Advances in Fracture and Damage Mechanics X

Edited by
Z. Tonković and M.H Aliabadi

TRANS TECH PUBLICATIONS

Advances in Fracture and Damage Mechanics X

Edited by
Z. Tonković
M.H. Aliabadi

Advances in Fracture and Damage Mechanics X

Selected, peer reviewed papers from the
10th International Conference on
Fracture and Damage Mechanics
(FDM 2011),
September 19-21, 2011, Dubrovnik, Croatia

Edited by

Z. Tonković and M.H. Aliabadi

TTP

Copyright © 2011 Trans Tech Publications Ltd, Switzerland

All rights reserved. No part of the contents of this publication may be reproduced or transmitted in any form or by any means without the written permission of the publisher.

Trans Tech Publications Ltd
Kreuzstrasse 10
CH-8635 Durnten-Zurich
Switzerland
http://www.ttp.net

Volumes 488-489 of
Key Engineering Materials
ISSN 1013-9826
Full text available online at *http://www.scientific.net*

***Distributed** worldwide by*

Trans Tech Publications Ltd.
Kreuzstrasse 10
CH-8635 Durnten-Zurich
Switzerland

Fax: +41 (44) 922 10 33
e-mail: sales@ttp.net

and in the Americas by

Trans Tech Publications Inc.
PO Box 699, May Street
Enfield, NH 03748
USA

Phone: +1 (603) 632-7377
Fax: +1 (603) 632-5611
e-mail: sales-usa@ttp.net

Preface

This volume is a collection of edited papers presented at the 10th International Conference on Fracture and Damage Mechanics (FDM2011), held in Dubrovnik, Croatia. Previous meetings were held in London, UK(1999), Milan, Italy (2001), Paderborn, Germany (2003), Mallarca, Spain (2005), Harbin, China (2006), Madeira, Portugal (2007), Seoul, Korea (2008) and St. Julian's Bay, Malta (2009) and Nagasaki, Japan (2010)

The conference which was attended by researchers from 22 countries served as a forum to promote and exchange latest theoretical, computation and experimental research works on fracture and damage mechanics as well as structural integrity and durability.

The FDM2011 covers a wide range of topics: Fracture Mechanics, Failure analysis, corrosion, Creep, Non-linear problems, Dynamic Fracture, Residual Stress, Environmental effects, Crack Propagation, Repair Techniques, Composite, Ceramics, Polymers, Metallic and concrete materials, Probabilistic Aspects, Risk Analysis, Damage Tolerance, Fracture Control, Computer Modelling Methods (Finite Elements, Boundary Elements and Meshless), Microstructural and Multiscale Aspects.

The Editors would like to thanks the members of the Steering Committee and International Scientific Committee for their help and support that were essential to the success of the conference. Furthermore, we express our gratitude to the Croatian Society of Mechanics for help in promoting the meeting. Special thanks go to the Faculty of Mechanical Engineering and Naval Architecture, University of Zagreb, for issuing the letters of guarantee for participants who have requested a Croatian visa. Thanks are also due to Harbin Engineering University for their sponsorship of the meeting. Finally, we would like to thank all those who helped to organize this scientific event.

Editors
M.H.Aliabadi and Z. Tonković

International Conference on Fracture and Damage Mechanics X

19-21 September 2011, Dubrovnik, Croatia

Steering Committee

M.H.Aliabadi Imperial College, London
B.Abersek University of Maribor, Slovenia
J.Alfaiate Instituto Superior Tecnico, Portugal
Jin-Keun Kim KAIST, Korea
S-I.Nishida Saga University, Japan
Sung-Woo Shin Hanyang University, Korea
Qingfen Li Harbin Engineering University, China

Conference Organising Committee

Prof. Dr. Zdenko Tonković
Institute of Applied Mechanics
Faculty of Mechanical Engineering and Naval Architecture
University of Zagreb
Zagreb, Croatia

Professor Ferri M.H. Aliabadi
Department of Aeronautics
Imperial College, London
Prince Consort Road, South Kensington
London, UK

International Scientific Committee

Abersek,B University of Maribor, Slovenia
Alfaiate,J Instituto Superior Tecnico, Portugal
Ashcroft,I.A Loughborough University, UK
Baragetti,S Universita degli Studi di Bergamo, Italy
Čanađija,M University of Rijeka, Croatia
Cerny,I SVUM , Czech Rep
Chen, D-H Science University of Tokyo, Japan
Constantin,N University Politehnica of Bucharest, Romania
De Corte, W Ghent University, Belgium
Dhondt,G MTU Aero Engines, Germany
Doblare,M University of Zaragoza, Spain
Ebara,R Hiroshima Institute of Technology, Japan
Espinosa,C (ISAE), TOULOUSE, France
Flewitt,P.E.J BNFL Magnox Generation, UK
Fujimoto,T Kyushu Sangyo University, Japan
Galvez,J.C Universidad Politécnica de Madrid, Spain
Guagliano,M Politecnico di Milano, Italy
Hadavinia,H Kingston University, UK
Hashida,T Tohoku University, Japan
Hornikova,J Brno University of Technology, Czech, Republic
Horst,P IFL, Braunschweig, Germany
Ivankovic,A University College Dublin, Ireland
Jankowski,R Gdansk University of Technology, Poland
Kawagoishi,N Kagoshima University, Japan
Kikuchi,M Science University of Tokyo, Japan
Kim, Jeong Guk (Korea Railroad Research Institute, Korea)
Kisu,H Nagasaki University, Japan
Kolednik,O Austrian Academy of Sciences, Austria
Korsunsky,A.M Oxford University, UK
Kotoul,M Brno University of Technology, Czech Republic
Kozak,D University of Slavonski Brod, Croatia
Krstulović-Opara,L University of Split,Croatia
Kuna,M Technische UniversitÃ¤t Bergakademie Freiberg, Germany
Lee, Jinyi (Chosun University, Korea)
Li Li Harbin Engineering University, China
Li,Q.F Harbin Engineering University, China
Makabe,C University of Ryukus, Japan
Marsavina,L Politechnica University of Timisoara, Romania
Nobile,L University of Bologna, Italy
Pappalettere,C Politecnico di Bari, Italy
Pastor,J ESIGEC, University of Savoie, France

Piat,R Univeristy of Karlsruhe, Germany
Providakis,C Technical University of Crete, Greece
Rezaeepazhand,J Ferdowsi University of Mashhad, Iran
Schlangen,E Delft University of Technology, The Netherlands
Sedmak,A University of Belgrade, Serbia
Sluys,L.J Delft University, The Netherlands
Soprano,A Second University of Naples, Italy
Sorić,J University of Zagreb, Croatia
Susmel,L University of Ferrara, Italy
Takuda,H Kyoto University, Japan
Teranishi,T Kyushu Sangyo University, Japan
Theilig,H Univ. Appl. Sci. Zittau/Gorliz, Germany
Tohgo,K Tokyo Institute of Technology, Japan
Torii,T Okayama University, Japan
Toribio,J University of Salamanca, Spain
Tsukrov, Igor University of New Hampshire, USA
Watanabe, K Yamagata University, Japan
Wang,Z.Q Harbin Engineering University, China
Yan,S.Y. Harbin Engineering University, China
Yoon,I.S. Induk Institute of Technology, South Korea
Yufeng Zheng Harbin Engineering University, China
ZHANG,J-Z Harbin University of science and Technology, China
Zhu,S.F. Harbin Engineering University, China

Table of Contents

Preface and Committees

Corrosion-Fatigue of High Strength Steel Bars: Evolution of Crack Aspect Ratio
J. Toribio, J.C. Matos, B. González and J. Escuadra 1

Lamb-Wave Based Technique for Impact Damage Detection in Composite Stiffened Panels
Z. Sharif Khodaei, R. Rojas-Diaz and M.H. Aliabadi 5

The Measurement of Residual Stresses in Thermal Barrier Coated Model Aerofoils
D. Liu, P.E.J. Flewitt and K.R. Hallam 9

Development of Predictive Models for Fatigue Crack Growth in Rails
A. De Iorio, M. Grasso, G. Kotsikos, F. Penta and G.P. Pucillo 13

Fracture Analysis of a First Stage Turbine Blade by FRANC3D
S. Asadikouhanjani and R. Ghorbani 17

Fully Reversed Uniaxial Tension-Compression High Cycle Fatigue Behaviour of Shot-Peened Steels
A. Plumtree and M.M. Mirzazadeh 21

Solutions for Impact over Aerospace Protection
L. Neckel, D. Hotza, D. Stainer, R. Janßen, A.G.R. Lezana, A. Dias and H.A. Al-Qureshi 25

The Effect of Mesh Density in Lattice Models for Concrete with Incorporated Mesostructure
J. Eliáš and M. Vořechovský 29

Calibration of Constitutive Law and Ductile Failure Criterion for Very Thin Rectangular Al2024-T3 Aluminum Alloy Specimen
M. Giglio, A. Gilioli and A. Manes 33

Flexural Wave Scattering by Double Elliptic Holes in an Infinite Thin Plate
H.L. Li, J. Guo and X.H. Shao 37

Advanced Finite Element Analysis to Predict Off-Axis Crushing Behaviour of Composite Aero-Structures
N. Ghafari-Namini, H. Ghasemnejad and M. Limbachiya 41

Fatigue Fracture Mechanism of Extruded Al Alloy 7075-T6 in High Humidity
K. Kariya, N. Kawagoishi, H. Maeda, Q. Chen, M. Goto and Y. Nu 45

Validation of Modified Lemaitre's Anisotropic Damage Model with the Cross Die Drawing Test
M.S. Niazi, H.H. Wisselink and T. Meinders 49

Probabilistic Fracture Resistance of a Forged Quality Medium Carbon Alloy Steel
K.K. Ray and R.N. Jha 53

Spatial Statistical Analyses for Time-Dependent Corroded Surfaces of Uncoated Weathering Steel Plates in Various Corrosive Environments
S. Kainuma and Y.S. Jeong 57

Corrosion Inhibition of Stress Corrosion Cracking and Localized Corrosion of Turbo-Expander and Steam/Gas Turbines Materials
B. Bavarian, J. Zhang and L. Reiner 61

The Effect of Lamb Wave Interaction with Fatigue Crack in Thin Al Sheet
V. Pavelko, I. Pavelko and E. Ozolinsh 65

Modeling Ductile Fracture Using the Discontinuous Velocity Domain Splitting Method
I.R. Ionescu and E. Oudet 69

Notched Specimens Fracture Prediction with an Advanced GTN Model
J. Fansi, M. Ben Bettaieb, T. Balan, X. Lemoine and A.M. Habraken 77

Dynamic Characteristics of Composite Materials Body for Bi-Modal Tram
Y.S. Kim, S.K. Chang, K.H. Moon and J.K. Mok 81

Comparison between 3D FEM and Standard ISO Tooth Root Stresses
G. Marunić, G. Gregov and V. Glažar 85

Crystallographic Analysis of Specimens Used for Calibrate a Failure Model for an Al 6061 – T6 Alloy
M. Giglio, A. Manes, C. Mapelli, D. Mombelli, C. Baldizzone and A. Gruttadauria 89

Cyclic Mixed-Mode Crack Propagation due to Time-Dependent Multiaxial Loading in Jet Engines
G. Dhondt 93

Crack Growth Rates and Corrosion Fatigue of Austenitic Stainless Steels in High Chloride Solutions
C. Vichytil, G. Mori, R. Pippan, M. Panzenböck and R. Fluch 97

Rolling Contact Fatigue Crack Growth Prediction by the Asperity Point Load Mechanism
D. Hannes and B. Alfredsson 101

Mechanical Characterization of Friction Stir Channels under Internal Pressure and In-Plane Bending
C. Vidal, V. Infante and P. Vilaça 105

Numeric Simulation of Fatigue Crack Growth in a Material Graded Structure
B. Schramm, H.A. Richard, M. Fulland and V. Kloster 109

Lifetime Determination of the Raceway of a Large Three-Row Roller Slewing Bearing
P. Göncz, R. Potočnik and S. Glodež 113

Analysis of Combined Adhesive and Cohesive Cracking at Roughened Surfaces
O. van der Sluis, S.P.M. Noijen, J.B. Bouquet and P.H.M. Timmermans 117

Performance of Different Metal-Foam Stuffed Whipple Shield against Hypervelocity Impact of Space Debris
B. Jia, F. Li, H.P. Gong and B.J. Pang 122

Development of a Low-Constraint SE(T) Toughness Test
W.R. Tyson, G. Shen, J.A. Gianetto and D.Y. Park 126

Modelling of Crack Bifurcation in Laminar Ceramics with Large Compressive Stress
M. Kotoul, O. Ševeček and T. Profant 130

Finite Element Analysis of Composite Flywheel with Two-Layer Pre-Stressed Rotor Structure
Z.Y. Ren, J.N. Liu, Q.F. Li and K.F. Li 134

Identification of Slant Cracks in a Cantilever Beam Using Design of Experiment and Neuro-Genetic Technique
M. Hajhosseini and H. Nahvi 138

Non-Linear Behaviour of Base-Isolated Building Supported on Flexible Soil under Damaging Earthquakes
S. Mahmoud, P.E. Austrell and R. Jankowski 142

Coupling Infrared Thermography and Acoustic Emission Measurement to Quantify the Shakedown State of Shape Memory Alloys
C. Dunand-Châtellet and Z. Moumni 146

Modeling Fracture of Fiber Reinforced Polymer
J. Ožbolt, V. Lacković and J. Krolo 150

Modeling Radiation Effects on the Fracture Process in Simplified Nuclear Glass
L.H. Kieu, J.M. Delaye and C. Stolz 154

Crack Growth Modeling in a Specimen with Polymer Weld
M. Ševčík, P. Hutař, L. Náhlík, R. Lach, Z. Knésl and W. Grellman 158

Basic Modes of Crack Propagation through the Interface in a Polymer Layered Structure
M. Zouhar, P. Hutař, L. Náhlík and Z. Knésl 162

Effect of Notched Parameters on Low Cycle Fatigue Life of Shaft under Bending-Torsional Loading
P. Ma and Y.T. Li 166

Investigation of Eigen-Values for Matrix Cracks of Two Materials
Y.T. Li and R.F. Wang 170

Dimensionless Stress Intensity Factors of an Annular Notched Shaft
B. Chen and Y.T. Li 174

Fatigue Crack Shape Prediction Based on the Stress Singularity Exponent
P. Hutař, M. Ševčík, L. Náhlík and Z. Knésl 178

Experimental and Numerical Investigation of Fatigue Behaviour of Nodular Cast Iron
P. Čanžar, Z. Tonković, A. Bakić and J. Kodvanj 182

Modelling of Nonlinear Creep and Recovery Behaviour of Cortical Bone
M. Lovrenić-Jugović, Z. Tonković and I. Skozrit 186

Finite Element Analysis by Using Hyper-Elastic Properties for Rubber Component
C.S. Woo, H.S. Park and W.G. Shin 190

Assessment of Thermal Damage for Railway Wheel of Long-Term Running
S.J. Kwon, J.W. Seo, D.H. Lee and S.T. Kwon 194

Influence of Curing Temperature on the Mechanical Properties of Alkali-Activated Bottom Ash Geopolymer Mortar
G.S. Ryu, S.H. Kim, K.T. Koh, S.T. Kang and J.H. Lee 198

Investigation into Damage of AL-Mesh Bumper under Hypervelocity AL-Spheres Impact
G.S. Guan, B.J. Bang and R.T. Niu 202

Dynamic Antiplane Behavior for a Quarter Infinite Piezoelectric Medium with a Subsurface Circular Inclusion
T.S. Song, D. Li and T. Merhej 206

A Study on the Fracture Test in Railroad Truck
S.C. Yoon, J.G. Kim, K.S. Baik, B.C. Goo and K.Y. Choe 210

Fracture Behavior and Mechanical Properties of Bamboo Fiber Reinforced Concrete
M. Terai and K. Minami 214

Study on Welding Deformations of Shipboard of Container Vessel
H. Li, D.L. Qiu, G.L. Li and H.L. Ren 218

Variational Principle and Buckling Analysis of Functionally Graded Plate with Temperature Changes
T. Fan 222

The Scattering of SH-Wave Caused by Subsurface Circular Cavities in a Layered Half-Space
D.N. Chen, H. Qi and Y. Shi 226

Fatigue Damage in On-Axis and Off-Axis Woven-Fiber/Resin Composite
J. Montesano, Z. Fawaz, K. Behdinan and C. Poon 230

Effect of Hydrogen on Mechanical Properties of Type 310S Stainless Steel
N. Takano and Y. Kaidu 234

Fatigue Strength of Radical Nitrided Spheroidal Graphite Cast Iron
K. Morino, F. Nishimura and N. Kawagoishi 238

Combined Influence of Expansive and Shrinkage Reducing Admixtures on the Shrinkage Behavior of Ultra-High Performance Concrete
J.J. Park, D.Y. Yoo, S.W. Kim and Y.S. Yoon 242

Study on Gradient-Dependent Nonlocal Damage Constitutive Models of Concrete under Freeze-Thaw Action
Z.M. Liu, J.Z. Mao, H.Y. Song and X.D. Chen 246

Effect of $YbCl_3$-Zn-Epoxy Coating on MIC Behavior of Low Alloy Steel
Y.D. Fu, Q.F. Li, J. Wang and C.H. Li 250

Improvement of MIC Behavior of Ship Plate Steel with $LaCl_3$-Zn Epoxy Coating
Q.F. Li, J. Wang, Y.D. Fu and C.H. Li 254

Computational Analysis of the AFM Specimen on Mixed-Mode I+II+III Fracture
Q.F. Li, L. Zhu, S.Y. Yan and X.N. Zhang 258

MIC Behavior of the Low Alloy Steel with Different Zn-Epoxy Coating in SRB Solution
J. Wang, Q.F. Li, Y.D. Fu and C.H. Li 262

Crack Initiation Predictions of the AFM-Specimen under Bend and Torsion Loading
S.F. Zhu, L. Zhu and Q.F. Li 266

Numerical Simulation of Series Experiments of Concrete Fracture
A.M. Deng, X.D. Wang and D.Y. Xu 270

Influence of the Type of Silica Fume on the Rheological and Mechanical Properties of Ultra-High Performance Concrete
K.T. Koh, J.J. Park, S.T. Kang and G.S. Ryu 274

Strength Enhancement of Bottom Ash-Based Polymer Concretes
J.M. Zhao, Z.X. Yang, K.H. Hwang, J.K. Lee, M.C. Kim and G.D. Seo 278

Potential of Shape Memory Complex Materials SMC as Welfare Equipment Actuator
T. Aoki, K. Fukunaga and A. Shimamoto 282

Performance of Nylon Based Polymer Foams at Elevated Temperature under Tensile Loading
V.G. Izzard, C.H. Bradsell, H. Hadavinia, V.J. Morris, P.J.S. Foot, L.M. Wilson and K. Hewson 286

Effect of REM Finishing on Fatigue Behavior of a Shot Peened Low Alloy Steel
S. Bagherifard, R. Ghelichi, M. Guagliano and M. Bandini 290

Optimal Elastic Design of CFCs
G. Stasiuk, R. Piat and Y. Sinchuk 295

High Cycle Fatigue Parameters of High Chromium Steel
M. Drobne, P. Göncz and S. Glodež 299

Slow Crack Growth and Creep Rupture of $Ba_{0.5}Sr_{0.5}Co_{0.8}Fe_{0.2}O3 - \delta$
J. Malzbender, G. Pećanac and S. Baumann 303

Influence of Al-Si Diffusion Coating on Low Cycle Fatigue Properties of Cast Superalloy Inconel 738LC at 800 °C
M. Juliš, K. Obrtlík, S. Hutařová, T. Podrábský and J. Polák 307

Effect of Friction Stir Welding Condition on Fatigue Limit of Welded Non-Combustible Mg Alloy
K. Hayashi, S. Hamada, I. Shigematsu, M. Sakamoto and H. Noguchi 311

A Role of Destructive and Non-Destructive Tests in Creep Damage Identification
Z.L. Kowalewski, T. Szymczak, K. Makowska and B. Augustyniak 315

Small Fatigue Crack Growth Behavior from Artificial Notch with Focused Ion Beam in Annealed 0.45% Carbon Steel
J. Sakamoto, Y. Takahashi and H. Noguchi 319

Loading Frequency Effects on the Fatigue Crack Growth Rate and Fracture Surface Morphology of Low Carbon Steel in Case of Long-Term Use in Hydrogen Gas
A. Nishimoto, Y. Oda and H. Noguchi 323

Micromechanical Modeling of Heterogeneous Materials with Irregularly Shaped Pores
I. Tsukrov and B. Drach 327

Edge-Strengthening of Structural Glass with Protective Coatings
M. Lindqvist, C. Louter and J.P. Lebet 331

Residual Stresses in As-Welded Joints: Finite Element Modeling and Neutron Difraction Stress Measurements
C. Acevedo, J. Drezet, J.P. Lefebvre, L. D'Alvise and A. Nussbaumer 335

Cellular Automata Multiscale Model of Creep Damage for Metals
K. Nowak 339

Experimental Investigation of Fatigue Crack Growth in the Welding Nugget of FSW Joints of a 6060 Aluminum Alloy
P. Marcassoli, M. Longo, G. D'Urso, C. Giardini and T. Pastore 343

Experimental Study on Polymer Mass Used to Repair Damaged Structures
T. Falborski, R. Jankowski and A. Kwiecień 347

Shaking Table Experimental Study on Damage Mechanism of the Disconnecting Switch under Seismic Excitation
P. Dembowski and R. Jankowski 351

Peridynamic Theory for Damage Initiation and Growth in Composite Laminate
E. Oterkus and E. Madenci 355

Inelastic Dynamic Analysis and Non-Linear Static Analysis (Push-Over) of 3-Story and 6-Story RC Buildings of Ductile Frames
J.A. Avila and J.C. Manzano 359

Application of the Θ-Method to 3D BEM Analysis of Cracks in Piezoelectric Components
K. Wippler and M. Kuna 363

The Influence of the Weld Width on Fracture Behaviour of the Heterogeneous Welded Joint
P. Konjatić, D. Kozak and N. Gubeljak 367

Simulation of a Strategy for the Assessment of Damage in Human Bones by Using FEM and Signal Processing
M. Miniaci, A. Marzani and E. Viola 371

Effect of an Internal Open Crack on Pipes Wave Propagation
A. Marzani, M. Miniaci and E. Viola 375

On the Stress Intensity Factors of Cracked Beams for Structural Analysis
E. Viola, Y. Li and N. Fantuzzi 379

Cracks Interaction Effect on the Dynamic Stability of Beams under Conservative and Nonconservative Forces
E. Viola, N. Fantuzzi and A. Marzani 383

Finite Temperature Nanovoids Evolution in FCC Metals Using Quasicontinuum Method
M. Ponga, I. Romero, M. Ortiz and M.P. Ariza 387

Bone-Cement Interface Micromechanical Model under Cyclic Loading
J.A. Sanz-Herrera, H. Esteban and M.P. Ariza 391

Comparison of Solutions of Stress Field Based on Hertzian and Combined Numerical-Crystallographic Approaches Beneath Nanoindenter
J. Horníková, P. Šandera and J. Pokluda 395

Influence of Boundary Conditions on Higher Order Terms of Near-Crack-Tip Stress Field in a WST Specimen
V. Veselý, L. Šestáková and S. Seitl 399

Valuation of TMF Lifetime Calculation Methods and their Limitations of Usability
H. Köberl, G. Winter and W. Eichlseder 403

Fatigue Crack Growth Simulation in Railway Axles
A. De Iorio, M. Grasso, F. Penta and G.P. Pucillo 407

Effect on the Alkali-Activator Mixing Ratio of Geopolymer Mortar Using Bottom Ash
S.H. Kim, G.S. Ryu, K.T. Koh, S.T. Kang and J.H. Lee 411

Crack Propagation from Bi-Material Notches – Matched Asymptotic Procedure
J. Klusák, T. Profant, O. Ševeček and M. Kotoul 416

Evaluation of the Fatigue Resistance of Chromium Slurry Coating Steel Substrate Compounds by Means of an Improved Impact Testing Procedure
K.G. Anthymidis, C. David, A. Trakali and D.N. Tsipas 420

Stress Responses to Large Simple Shear Deformation in Elasticity Based on the Logarithmic Strain
L.H. Yang, J. Qu and Y.Z. He 424

Slow Crack Growth by Grain Boundary Dissolution of Hydroxyapatite in Water
D.S. Seo, K.H. Hwang and J.K. Lee 428

Research on Acoustic Emission Test Method for Metal Fatigue Fracture Based on Wavelet Packets Feature Extraction
Q. Wang, Y.S. Chen and K. Song 432

The Study of AE and ESSPI Technique on the CBF Composite
Z.L. Chang, G.P. Zou, S. Chen and L. Chen 436

Interaction of SH-Wave on Multiple Linear Cracks near Shallow-Embedded Structure
Z.L. Yang, H.N. Xu, M.J. Xu and B.T. Sun 440

Numerical Simulation of Multiple Fatigue Crack Growth with Additional Crack Initiation
D. Holländer, M. Wünsche, S. Henkel and H. Theilig 444

Study on Damage Parameters and its Size Effect of Concrete by Tension Test
X.D. Wang, Y.F. Wang, Y. Wang, Y.J. Wu and X. Hua 448

Elastic-Viscoplastic Field at the Mixed-Mode Crack-Tip under Compression and Shear
W.Y. Liang, Z.Q. Wang and F. Liu 452

Effect of Rotational Speed on Thin-Rim Gear Bending Fatigue Crack Initiation Life
M. Opalić, K. Vučković and D. Žeželj 456

Investigation on Damage Tolerance of Carbon/Epoxy Laminate for Aircraft Structural Design
H.B. Park, C.D. Kong and K.S. Lee 460

Damage Analysis of Concrete Subjected to Freeze-Thaw Cycles and Chloride Ion Erosion
J.Z. Mao, Z.Y. Zhang, Z.M. Liu and C. Sun 464

Measurements of Mode I and Mode III Fracture Toughness of Spring's Steel
N. Gubeljak, V. Močilnik and J. Predan 468

Numerical Implementation of Constitutive Material Law for Simulating the Kinkband Formation in Fiber Composites
B. Veluri and H.M. Jensen 472

Fatigue Crack Propagation in New Generation Aluminium Alloys
S. Richard, C. Sarrazin-Baudoux and J. Petit 476

An Effect of Shot Peening on Retardation and Growth of Short Fatigue Cracks in an Aircraft Al-Alloy
I. Černý 480

The Effect of Nonlinear Matrix on Crack Propagation in the Particulate Composite
Z. Majer and P. Hutař 484

On Effective Properties of Layers in Damaged Composite Laminates
J. Varna 490

Defect Size Measurement of Wall Thinned Pipe Using Shearography and Digital Image Correlation
K.S. Kim, C.S. Park, D.P. Hong, M.Y. Choi, H.S. Chang and H.C. Jung 494

Fatigue Focused Optimization of Treatment Parameters – A Case Study about Deep Cryogenic Treatment
P. Baldissera and C. Delprete 498

Fatigue Behaviour of Notched Ti-6Al-4V in Inert Environment
S. Baragetti, S. Cavalleri and F. Tordini 502

A Comprehensive Study of the Performances of PVD WC/C-Coated Racing Gears
S. Baragetti, S. Cavalleri and F. Tordini 507

Effect of Shot Peening on the Fatigue Behavior of some Sintered Steels
S. Baragetti, R. Gerosa, G. Silva and B. Rivolta 511

Effect of Heat Treatment on Fracture during Bending in AA6016 Aluminium Alloy Sheets
A. Davidkov, R.H. Petrov, P. De Smet and L.A.I. Kestens 521

K_I, ΔJ-Integral and *ΔCTOD* Parameter
Ž. Božić, S. Schmauder and M. Mlikota 525

Developed Random Tessellation for Modeling of Microstructure
K. Farhangdoost and S. Rahnama 529

Fracture Analysis of Cube- and Cylinder-Shaped WST Specimens Made of Cementitious Composites with Various Characteristic Length
L. Řoutil, V. Veselý and S. Seitl 533

Finite Element Simulation on Failure Assessment of Toughened Epoxy Adhesives
P. Akbarzadeh and K. Farhangdoost 537

Dynamic Behavior of Granular Mixture Solids
M. Buonsanti, G. Leonardi, F. Scoppelliti and F. Cirianni 541

Load Sequence Effect on Fatigue Damage
Y.G. Xu, L. Wang, Y. Chen and W. Tiu 545

An Experimental and Numerical Investigation of the Mixed-Mode Fracture Toughness and Lap Shear Strength of Aerospace Grade Composite Joints
J. Mohan, A. Karač, N. Murphy and A. Ivanković 549

Numerical Investigation into Dynamic Fracture of PCBN
D. Carolan, A. Ivanković and N. Murphy 553

A Methodological Approach to the Tolerance Problems during the Assembly Process of Deformable Bodies
F. Caputo, G. Lamanna, F.M. Pannullo and G. De Angelis 557

Energy Absorption Capabilities of a Square Tube System
F. Caputo, G. Lamanna and A. Soprano 561

Effects of Tolerances on the Structural Behavior of a Bolted Hybrid Joint
F. Caputo, G. Lamanna and A. Soprano 565

The Influence of Short Glass and Polypropylene Fibers on First Crack Formation and Toughness of Cement Based Composites after their Exposure to Fire Conditions
Z.G. Pandermarakis, A.B. Sotiropoulou and N.D. Nikoloutsopoulos 569

Characterisation of the Fracture Energy and Toughening Mechanisms of a Nano-Toughened Epoxy Adhesive
D. Mc Auliffe, A. Karač, N. Murphy and A. Ivanković 573

API J55 Steel Casing Pipe with an Initial Surface Crack under Internal Pressure - Determination of Fracture Parameters
M. Rakin, B. Medjo, M. Arsić, Ž. Šarkoćević, I. Ivanović and A. Sedmak 577

Structural and Mechanical Properties of CN_X and CP_X Thin Solid Films
E. Broitman, A. Furlan, G.K. Gueorguiev, Z. Czigány, H. Högberg and L. Hultman 581

Simulation of Rubber-Coated Fabric Material Damage
A. Derewonko, P. Baranowski and D. Rudnik 585

Elastic-Plastic FEM Modelling of the Single Overload Effect on the Fatigue Crack Front Shape
A. Materna and V. Oliva 589

Energy Principle in Crack Propagation
H.Y. Song and T. Fan 593

Infrared Thermographic Analysis of Railway Brake Disc during Braking
J.G. Kim, S.T. Kwon, S.C. Yoon and B.C. Goo 597

Structure Buckling Reliability Analysis for the Underwater Super-Speed Supercavitating Vehicle
H. An, W.G. An and L. Zhou 601

Finite Element Analysis of Secondary Cracks at a Crack Front under Pure Mode III Loading
M. Ressel and H. Theilig 605

On the Evaluation of the R-Curve Including the Self-Weight Contribution: Mortar
N. Dourado and S. Morel 609

Influence of the Secondary Raw Materials on the Mechanical Properties of Multilayer Films
R. Didžiokas, J. Janutėnienė, M. Gintalas and A. Tadzijevas 613

Analysis of the Influence of Microstructure Heterogeneity and Mechanical Properties of Welded Joint Constituents on Fracture Toughness for Plane Strain, K_{Ic}
I. Čamagić, N. Vasić, Z. Burzić and A. Sedmak 617

R-Curve and Size Effect in Quasibrittle Fracture: A Rewriting of the Bazant's Size Effect Law
S. Morel and N. Dourado 621

Interaction of Heat Checks in Aluminum Pressure Casting Dies and their Effect on Fatigue Life
P. Raninger, W. Ecker, T. Antretter, M. Leindl and R. Ebner 626

Dynamic *J*-Integral Evaluation of Three-Point-Bend Beams with Various Geometrical Dimensions
M. Gintalas, A. Ziliukas and K. Kalnins 630

Fracture Behavior of Directional TiAl Lamellar Structures
J. Zhang 634

Failure Mechanisms and Energy Absorption in Composite Elements under Axial Crush
A.F. Johnson and M. David 638

Experimental Fracture Behavior of Polypropylene Fiber Reinforced Concrete Specimens with Variable Width
H. Cifuentes and F. Medina 642

Influence of the Wall Thickness on the Allowable and Failure Pressures of Two- and Tree-Way Globe Valve Bodies
M. Opalić, I. Galić and K. Vučković 646

Analysis of Shear Strength of Wood
T. Štefić, A. Jurić and P. Marović 650

Application of Two Methods for Notch Fatigue Life Prediction
R. Negru, L. Marsavina, H. Filipescu and C. Caplescu 654

A Microstructural Sensitivity Study of 316H Austenitic Stainless Steel to Inter-Granular Creep Fracture
B. Chen, P.E.J. Flewitt, D.J. Smith and C.M. Younes 658

FEA of Fretting Fatigue: A Comparison between ANSYS and ABAQUS
M. Abdel Wahab, R. Hojjati Talemi and P. De Baets 662

Fatigue Behavior in Filled Natural Rubber: Study of the Mechanical Damage Dynamics
L. Munoz, L. Vanel, O. Sanseau, P. Sotta, D. Long, L. Guy and L. Odoni 666

High Rate and High Temperature Fracture Behaviour of Polycrystalline Diamond
M. Petrović, A. Ivanković and N. Murphy 670

Structural Analysis of Historic Masonry Arch Bridges: Case Study of Clemente Bridge on Savio River
L. Nobile, V. Bartolomeo and M. Bonagura 674

Explosion and Temperature Resistance of Underground Structures by Free Hexagons
P.P. Prochazka and T.S. Lok 678

Application of Gradient Based IR Thermography to the GRP Structures Inspection
L. Krstulović-Opara, E. Garafulić, B. Klarin and Ž. Domazet 682

Tensile Properties of Random Distribution Short SMA Fiber Reinforced Composites
H.S. Lei, B. Zhou, Z.Q. Wang and X.Q. Wang 686

Study on Static and Dynamic Mechanical Property of Sandwich Plate with Aluminum Foam Core under Confining Pressure
G.P. Zou, Z.L. Chang and R.R. Wang 690

Study on Quasi-Static Growing Crack Field in Visco-Elastic Compressible Material
Y. Yang, G.H. Wu and L.Q. Tang 694

Fatigue Life Prediction Investigation on Steel Honeycomb Sandwich Beams at High-Temperature
J. Lu, G.P. Zou and Y. Cao 698

Solving the Equivalent Function of Failure Mode Based on Multiple Correlation
W.D. Chen, J.C. Li and Y.C. Yu 702

Sensitivity Analysis for the Stiffened Plate Structure System with Crack Defects
W.G. An, H. An and X.H. Song 706

Failure Conditions from Push Out Tests of a Steel-Concrete Joint: Fracture Mechanics Approach
J. Klusák, S. Seitl, W. De Corte, P. Helincks, V. Boel and G. De Schutter 710

Failure Conditions from Push-Out Tests of a Steel-Concrete Joint: Experimental Results
P. Helincks, W. De Corte, J. Klusák, S. Seitl, V. Boel and G. De Schutter 714

Numerical Stress Intensity Factors Determination for Fabrication Defects in Coronary Stents
C.S. Nes, A. Enkelhardt, N. Faur and A. Birlan 718

3-Dimensional Stress Intensity Factor Determination for a Notched Shaft under Mixed Mode Loading
C.S. Nes, N. Faur and L. Marsavina 722

Overview of the Methods for Service Life Prediction on Gears
B. Aberšek and J. Flašker 727

Load-Rate Sensitivity in 1D Non-Linear Viscoelastic Model
I. Kožar, J. Ožbolt and T. Pecak 731

Effect of Tensile Dwell on Low Cycle Fatigue of Cast Superalloy Inconel 792-5A at 800°C
M. Šmíd, K. Obrtlík, M. Petrenec and J. Polák 735

Assessment of Existing Concrete Buildings
L. Nobile, M. Bonagura and V. Bartolomeo 739

Residual Fracture Toughness of Concrete Subject to Elevated Temperatures
J.T. Yu, K.Q. Yu and Z.D. Lu 743

Taking Full Advantage of Nominal Stresses to Design Notched Components against Variable Amplitude Multiaxial Fatigue
L. Susmel and D. Taylor 747

Semi-Permeable Cracks in Magnetoelectroelastic Solids under Impact Loading
M. Wünsche, A. Sáez, C.Z. Zhang and F. García-Sánchez 751

A Three Dimensional Graphical Aid for Fatigue Data Analysis
B. Atzori, G. Meneghetti and M. Ricotta 755

Meshfree Continuum Damage Mechanics Modelling for 3D Orthogonal Woven Composites
L.Y. Li, M.H. Aliabadi and P.H. Wen 759

A Novel Methodology for Fatigue Delamination Growth Analysis of Composites
O. Bacarreza and M.H. Aliabadi 763

Impact Detection Using Artificial Neural Networks
M. Ghajari, Z. Sharif Khodaei and M.H. Aliabadi 767

Failure Analysis of Bolted Composite Joint Based on Extended Finite Element
Z.Q. Wang, S. Zhou, J.S. Zhou and X.D. Wu 771

Influence of Drawing Straining Path on Hydrogen Damage of Prestressing Steel Wires
J. Toribio, M. Lorenzo and D. Vergara 775

Structural Integrity of CO_2 Transport Pipelines – A Review
A. Chahardehi 779

Damage Mechanics in G/E Tubes under Tension-Torsion Cyclic Loading
P.A. Carraro and M. Quaresimin 783

Acoustic Damage Analysis of a Gear System
A. Belsak and J. Prezelj 787

Meshless Local Integral Equation Method with Analytical Formulation and its Application to Computational Fracture Mechanics
P.H. Wen and M.H. Aliabadi 791

Experimental Study to Verify the Fatigue Limit Found by Thermal Analysis of Specimen Surface in Mono Axial Traction Test
G. Risitano and C. Clienti 795

Measurement of Deformation on Welding Specimen Using ESPI
K.S. Kim, D.S. Kim, K.S. Kim, C.D. Kee, J.W. Kim and M.Y. Na 799

© (2012) Trans Tech Publications, Switzerland
doi:10.4028/www.scientific.net/KEM.488-489.1

Corrosion-Fatigue of High Strength Steel Bars: Evolution of Crack Aspect Ratio

J. Toribio[1,a], J.C. Matos[1,b], B. González[1,c] and J. Escuadra[1,d]

[1]E.P.S., Campus Viriato, Avda. Requejo 33, 49022 Zamora, SPAIN

[a]toribio@usal.es, [b]jcmatos@usal.es, [c]bgonzalez@usal.es, [d]jeb@usal.es

Keywords: Numerical modelling, Fatigue crack propagation, Prestressing steel bars, $Ca(OH)_2$+NaCl corrosion-fatigue.

Abstract. This paper shows the evolution of the surface crack front in prestressing steel wires subjected to fatigue in air and to corrosion-fatigue in $Ca(OH)_2$+NaCl. To this end, a numerical modelling was made on the basis of a discretization of the crack front (characterized with elliptical shape), considering that the crack advance at each point is perpendicular to such a front according to a Paris-Erdogan law, and using a three-parameter stress intensity factor (SIF). Each analyzed case (a particular initial crack geometry) was characterized by the evolution of the semielliptical crack aspect ratio (relation between the semiaxes of the ellipse) with the relative crack depth and by the variation of the maximum dimensionless SIF at the crack front.

Introduction

The fatigue behaviour of cold drawn eutectoid steel, frequently used as reinforcement in prestressed concrete, has received attention in the past, both in air [1] and in aggressive environments [2-5]. NaCl corrosion-fatigue affects the fatigue performance of high strength steel by increasing the crack growth rate in relation to its value in inert environment [3,4], this effect being even higher if the environment is constituted by $Ca(OH)_2$+NaCl [5].

When cylindrical rods (bars, wires, shafts…) are used, transverse cracking by fatigue usually takes place in the form of surface cracks with semielliptical shape [6]. Growth of surface cracks in round bars due to fatigue can be modelled using different criteria, e.g., prediction of the 90º intersecting angle of the crack with the surface or the iso-K criterion along the crack front [7]. Another criterion is based on the crack growth according to the Paris-Erdogan law [8] considering the crack advance perpendicular to the crack front, assuming elliptic geometry for the crack [9,10] or avoiding the shape hypothesis, i.e., allowing the crack to grow with any shape [11].

Material

This paper studies the corrosion-fatigue crack propagation in prestressing steel wires (chemical composition: 0.82%C, 0.60%Mn, 0.18%Si, 0.010%P and 0.024%S). Mechanical properties of the steel were obtained by Singh and Sánchez-Gálvez [5] as follows: Young's modulus E=204.4GPa, yield strength σ_Y=1430MPa, ultimate tensile strength (UTS) σ_R=1670MPa and fracture toughness K_{IC}=119 MPam$^{1/2}$. Fatigue tests were performed [5] under 1Hz sinusoidal wave and R-ratio equal to 0.5 in both air and aggressive environment consisting of 1g/l $Ca(OH)_2$ + 1g/l NaCl solution at free corrosion potential, and results were fitted to the Paris-Erdogan laws [8] in the form:

$$\frac{\mathrm{d}a}{\mathrm{d}N} = C\Delta K^{\mathrm{m}} \qquad (1)$$

thus obtaining the coefficients of the Paris law for prestressing steel in both environments. With regard to Paris exponent m (the only parameter required for the purposes of the present paper) experimental results were m=2.27 for fatigue crack propagation in air and m=0.70 in the case of $Ca(OH)_2$+NaCl corrosion-fatigue, where a clear decrease in the m-exponent was observed in corrosion-fatigue in spite of the elevation of the curve via an increase of the C coefficient.

Numerical modelling

To study how a crack propagates in the cross section of a round bar under tensile cyclic loading, a computer program in Java language was developed to determine the geometrical evolution of the crack front. The basic hypotheses of the modelling consisted of assuming that the crack front can been modelled as an ellipse with centre on the bar surface [6] and the fatigue propagation takes place in a direction perpendicular to this crack front, following a Paris-Erdogan law [8].

Every elliptical arc of the crack was divided in z segments with exactly the same length using the Simpson method to discretize the front. The point at the cylinder surface was not taken into account, since it presents difficulties regarding the computation of the stress intensity factor (SIF) K because there is a plane stress state at the crack edge. After that, every single point was shifted according to Paris-Erdogan law perpendicular to the front, so as to keep constant the maximum crack depth increment, $\Delta a(\max) \equiv \max \Delta a_i$. The advance of every front point, Δa_i, can be obtained from the maximum crack increment and the ratio of the dimensionless SIF ($Y = K/\sigma\sqrt{\pi a}$, where σ is the remote stress applied far from the crack and a the crack depth), as follows:

$$\Delta a_i = \Delta a(\max)\left[\frac{Y_i}{Y(\max)}\right]^m \tag{2}$$

The newly obtained points, fitted by the least squares method, generate a new ellipse with which the process of crack advance is repeated iteratively until the desired crack depth is reached (the maximum crack advance was up to 80% of the bar diameter). Due to the existing symmetry, only half of the problem was used for the computations.

The dimensionless SIF used in the computations is that proposed by Shin and Cai [12] obtained by the finite element method together with a virtual crack extension technique, which depends on the crack geometry a/b (aspect ratio, relation between the semiaxes of the ellipse), the relative crack depth a/D and the relative position of the point considered on its front x/h (Fig. 1).

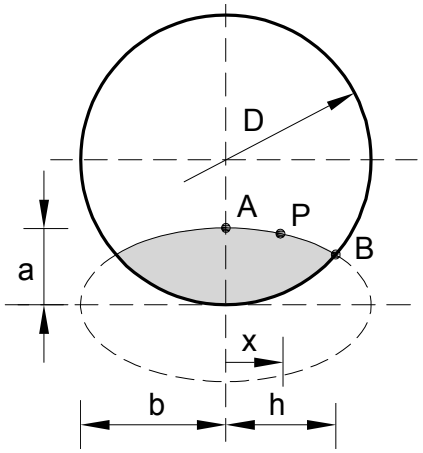


Fig. 1. Elliptical crack model used by Shin and Cai [12].

The analytical fitting on the basis of the finite element results provides three-parametrical expressions of the dimensionless SIF Y as follows,

$$Y = \sum_{i=0}^{2}\sum_{j=0}^{7}\sum_{k=0}^{2} M_{ijk}\left(\frac{a}{b}\right)^i\left(\frac{a}{D}\right)^j\left(\frac{x}{h}\right)^k \tag{3}$$

where the coefficients M_{ijk} used in the present paper are those calculated by Shin and Cai [12] for the particular case of tension loading with free ends.

Results and discussion

The geometrical evolution of the crack front, characterized as a part of an ellipse, was determined for each relative crack depth, a/D, through the crack aspect ratio, a/b. Fig. 2 shows how the crack grows in prestressing steel wires immersed in air and aggressive environment of $Ca(OH)_2$+NaCl for different initial crack geometries: relative crack depth $(a/D)_i$ from 0.03 to 0.5; crack aspect ratio $(a/b)_i$ from 0.08 (quasi-straight crack front) to 1 (circular crack front).

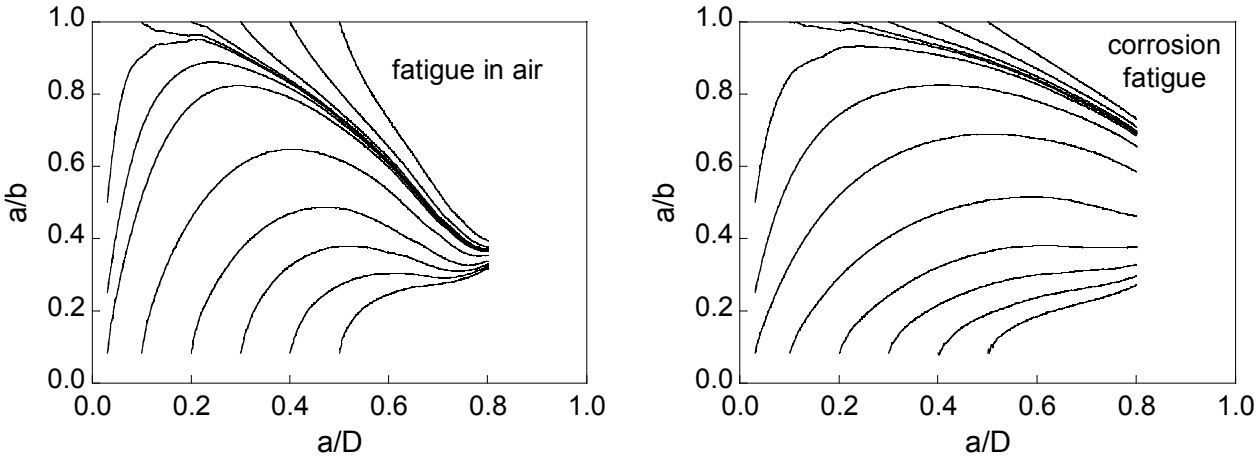


Fig. 2. Evolution of the crack aspect ratio: fatigue in air of prestressing steel (left) and $Ca(OH)_2$+NaCl corrosion-fatigue of prestressing steel (right).

Results show that fatigue crack propagation exhibits a preferential crack path towards which all a/b-a/D plots converge for the different initial crack geometries. This effect is quite quicker in air (higher exponent m of the Paris law) than in aggressive environment (with lower parameter m of the Paris law) [10]. If the initial crack front is quasi-straight, $(a/b)_i$=0.08, fatigue crack propagation takes place with more curved fronts initially in air and later in aggressive environment (with the exception of initially deep cracks where a/b is always higher in air). On the other hand, starting from initially circular cracks, $(a/b)_i$=1, fatigue crack propagation takes place with higher values of a/b (more curved fronts) in the case of aggressive environments.

Fig. 3 plots the evolution of maximum dimensionless SIF Y_{max} (the highest Y-value along the crack front) when the crack grows from different initial configurations in prestressing steel wires under conventional fatigue and corrosion-fatigue.

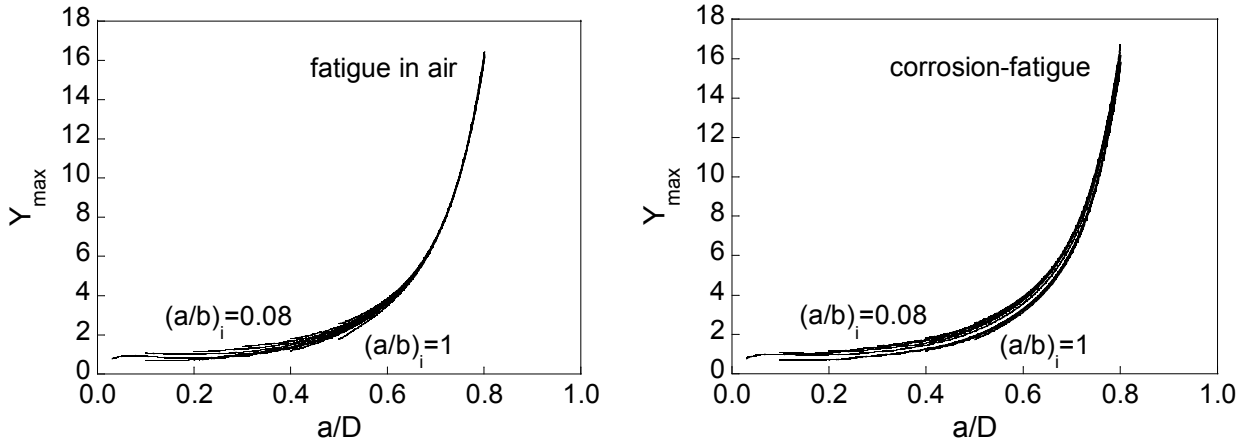


Fig. 3. Evolution of maximum dimensionless SIF: fatigue in air of prestressing steel (left) and $Ca(OH)_2$+NaCl corrosion-fatigue of prestressing steel (right).

Generally, the value of the Y_{max} increases when so does the relative crack depth (a/D) and diminishes with the crack aspect ratio (a/b). The influence of the relative crack depth is higher than that of the aspect ratio (with the exception of small crack depths) due to the existence of a preferential crack path in the fatigue crack growth (convergence in the plot a/b-a/D). Therefore, Y_{max} is higher in the case of quasi-straight initial crack front, $(a/b)_i$=0.08, than in the case of circular one, $(a/b)_i$=1, a situation more pronounced when the crack propagation is small and when the initial cracks are deeper. In addition, Y_{max} exhibits an elevated convergence with the fatigue crack growth in all initial geometries of cracks analyzed in this paper, quicker in air than in aggressive environment.

Conclusions

(i) In all initial crack geometries analyzed in this paper, fatigue crack propagation in prestressing steel exhibits a preferential crack path, where the convergence is quicker in air than in solution of $Ca(OH)_2$+NaCl, due the important decrease of the Paris exponent m in the case of aggressive environment.

(ii) If the initial crack front is quasi-straight, $(a/b)_i$=0.08, fatigue crack propagation takes place with more curved fronts initially in air and latter in aggressive environment (with the exception of initially deeper cracks, where a/b is always higher in air). For initially circular cracks, $(a/b)_i$=1, fatigue crack propagation takes place with higher values of a/b, i.e. more curved fronts, in the case of aggressive environment.

(iii) The dimensionless SIF (Y_{max}) exhibits, during fatigue crack propagation, a strong dependence on the relative crack depth and quite lower dependence on the crack aspect ratio (with the exception of shallow cracks of small depth), showing higher values for initially straight cracks than for circular ones. In addition, Y_{max} exhibits a quicker convergence during fatigue crack growth, higher in air than in aggressive environment.

Acknowledgements

The authors wish to acknowledge the financial support provided by the following Spanish Institutions: Ministry for Science and Technology (MCYT; Grant MAT2002-01831), Ministry for Education and Science (MEC; Grant BIA2005-08965), Ministry for Science and Innovation (MCINN; Grant BIA2008-06810), *Junta de Castilla y León* (JCyL; Grants SA067A05, SA111A07 and SA039A08).

References

[1] J. Toribio, J.C. Matos and B. González: Int. J. Fatigue Vol. 31 (2009), p. 2014.

[2] J. Toribio and V. Kharin: Int. J. Fract. Vol. 126 (2004), p. L57.

[3] G. Murtaza and R. Akid: Eng. Fract. Mech. Vol. 67 (2000), p. 461.

[4] A. Martín and V. Sánchez-Gálvez: Br. Corros. J. Vol. 23 (1988), p. 96.

[5] N. Singh and V. Sánchez-Gálvez: Br. Corros. J. Vol. 26 (1991), p.117.

[6] J. Toribio, J.C. Matos, B. González and J. Escuadra: Struct. Durab. Health. Monit. Vol. 123 (2009), p. 1.

[7] A. Levan and J. Royer: Int. J. Fract. Vol. 61 (1993), p. 71.

[8] P.C. Paris and F. Erdogan: J. Basic. Eng. Vol. 85D (1963), p. 528.

[9] A. Carpinteri: Int. J. Fatigue Vol. 15 (1972), p. 21.

[10] J. Toribio, J.C. Matos, B. González and J. Escuadra: Eng. Fail. Anal. Vol. 16 (2009), p. 618.

[11] X.B. Lin and R.A. Smith: Int. J. Fatigue Vol. 19 (1997), p. 461.

[12] C.S. Shin and C.Q. Cai: Int. J. Fract. Vol. 129 (2004), p. 239.

© (2012) Trans Tech Publications, Switzerland
doi:10.4028/www.scientific.net/KEM.488-489.5

Lamb-wave Based Technique for Impact Damage Detection in Composite Stiffened Panels

Z. Sharif Khodaei[1, a], Ramon Rojas-Diaz[1,b] and M.H. Aliabadi[1,c]

[1]Department of Aeronautics, Imperial College London, South Kensington Campus,

Roderic Hill Building, Exhibition Road, SW7 2AZ, London, UK.

[a]z.sharif-khodaei@imperial.ac.uk, [b]ramonrojasdiaz@gmail.com, [c]m.h.aliabadi@imperial.ac.uk

Keywords: Lamb wave, Impact damage, Probability-based imaging, damage identification, Piezoelectric sensor/actuator, Structural Health Monitoring

Abstract. The propagation characteristic of Lamb waves activated by Piezoelectric actuators and collected by sensors in a stiffened panel has been investigated. A network of actuators is used to scan the structure before and after the presence of damage. A diagnostic imaging algorithm has been developed based on the probability of damage at each point of the structure measured by the signal reading of sensors in the benchmark and damaged structure. A damage localization image is then reconstructed by superimposing the image obtained from each sensor-actuator path. Three-dimensional finite element model with a transducer network is modeled. Damage is introduced as a small softening area in the stiffened panel. Applying the imaging algorithm, the damage location was predicted with good accuracy. This method proves to be suitable for stiffened panels, where the complicated geometry and boundary reflections make the signal processing more complicated.

Introduction

Impact damage on critical structures such as aircraft structures can cause BVID (barely Visible Impact Damage) which can lead to material softening or delamination between plies and lead to catastrophic failures. Structural Health Monitoring (SHM) provides a system with the ability to detect and interpret adverse changes in a structure even though the structure is in service. SHM systems can reduce the risk of the catastrophic failures, prolong the lifespan of the structures and reduce the cost of inspections. A number of methods have been proposed for damage detection based on comparing signals to baseline recorded from the undamaged structure. Lamb wave based diagnosis method is one of the most effective techniques in plate-like structures due to its sensitivity to small defects.

Lamb waves are the most widely used guided waves for damage detection. Since the propagation properties of the ultrasonic waves depend on the mechanical properties of the laminates, the waveform of the ultrasonic waves propagating in the composite plates changes when damage occurs in the wave propagation path. The propagation of Lamb waves in the plate can be modeled using Finite Element Method (FEM) as explained in [1] or Boundary Element Method (BEM) in [2].

The simplest method for damage characterization is to subtract two signals from the damaged and undamaged case. This approach can be very effective if damage was the only factor causing the signals to change. In complex structures such as stiffened panels, the stiffeners and frames cause additional signal reflections and thus simple approaches such as ToF (Time of Flight) become unsuitable for damage localization. Gao*, et al* [3] used a signal difference coefficient 1-ρ, where ρ is the correlation coefficient between the two signals. Mal*, et al* [4] used a damage index which was computed based on the spectra of two signals being compared. Zhao*, et al* [5] determined the location of the defect by assuming that the probability of a defect occurrence at a certain point can be estimated from the severity of the signal changes of different sensor pairs as a result of this defect and its relative position to the sensor pair. In [6] Michaels and Michaels, digital bandpass filtering of the broadband signals was used to create a set of bandlimited signals with different centre

frequencies. Imaging methods are applied to these signals, creating different set of images corresponding to each centre frequency. These images are then fused to obtain more accurate localization with less noise. This methodology has been used in this paper and it is explained in the next section.

Damage identification and localization using Lamb waves

Received signals usually contain multiple Lamb wave modes. This broadband nature of signals has both advantages and disadvantages. However various modes are dispersive and travel at different velocities which result in difficulties analyzing the signals. The methodology used here is based on the approach presented by [7] which effectively utilizes broadband Lamb wave data using signal processing, image generation and image fusion.

Signal processing. The signal readings received by sensors which are surface-mounted or embedded in the panel are used so that a probability of damage at each point of the structure is obtained. The damage localization algorithm developed here searches for the location where the probability of the presence of damage is the highest. As the first phase of the algorithm, some signal preprocessing is necessary. This preprocessing includes two steps:

- Signal amplitudes are not necessarily consistent for all of the transducer pairs. Thus, they are scaled based upon the separation distances and the measured amplitudes of the direct arrivals for each filter frequency. If A_{ij} is the amplitude of the signal arriving to the sensor, each signal is scaled as

$$\widehat{\omega}_{ij}(t) = \frac{\omega_{ij}(t)}{A_{ij}} \sqrt{\frac{D_{ref}}{D_{ij}}} \tag{1}$$

  where ω_{ij} is the filtered but not scaled signal, D_{ij} is the distance between transducers i and j, and D_{ref} is a reference distance, usually set to 1m.

- subtract a baseline signal $u_{ij}(t)$ of the undamaged plate from the current signal of interest. The idea is to get the energy envelop at every point of the structure scattered by the damage wave.

$$u_{ij}(t) = \widehat{\omega}_{ij}(t) - \widehat{\omega}^{p}_{ij}(t) \tag{2}$$

  Image generation. The envelope-detected difference signal, $r_{ij}(t)$, is the magnitude of the complex analytic signal, formed from the signal and its Hilbert transform, $v_{ij}(t)$,

$$r_{ij}(t) = \sqrt{u_{ij}(t)^2 + v_{ij}(t)^2} \tag{3}$$

  The time of arrival at each point ($\mathbf{x}$) of the structure, of the signal transmitted by an actuator i located at ($\mathbf{x_i}$) and measured in sensor j located at ($\mathbf{x_j}$) is computed as

$$t_{ij}(\mathbf{x}) = \frac{d_i + d_j}{v_1}, \qquad d_i(\mathbf{x}) = \left\| \mathbf{x}_i - \mathbf{x} \right\| \tag{4}$$

All signals are averaged at each spatial location to obtain the image value, $E(\mathbf{x})$

$$E(\mathbf{x}) = \frac{1}{N_p} \sum_{i=1}^{N-1} \sum_{j=i+1}^{N} r_{ij}\left(t_{ij}\left(\mathbf{x}\right)\right) \tag{5}$$

Where N_p is the number of sensing paths considered. Let us remark that the higher the value of $E(\mathbf{x})$ is, the bigger is the probability of existence of damage.

Image fusion. For better localization of damage, images from each sensor-actuator path are combined or fused with each other. They are fused by considering one pixel at a time, with its value determined by the fused image from the corresponding individual images; that is the neighbouring pixels are not considered. Several different strategies for image fusion is possible. Averaging the individual pixels will reduce the noise. It may also be helpful in reducing the amplitude of artifacts, see [6]. This is the algorithm impemented here.

Application to stiffened panel

The damage localization algorithm here has been applied to a stiffened panel made from laminated composite skin layer with three stiffeners and three frames attached to it. The stiffeners and the Skin are made from laminated high tensile strength unidirectional carbon fibre prepreg HTA/977-2 $[45/-45/90/0]_s$. The numerical analysis was performed in ABAQUS FE program following [1]. The actuators are excited by a 5 cycle sineburst at 350 kHz in transducer 1 to 16 by applying a corresponding radial displacement in out of plane direction using SMART FEM model, see Figure 1.

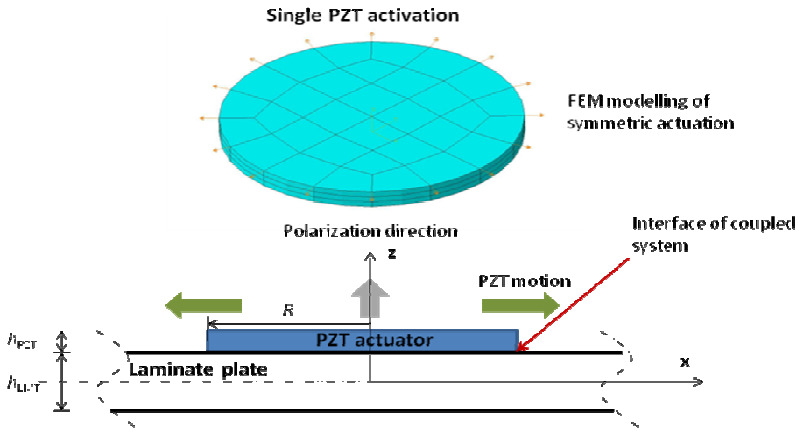


Figure 1. SMART FEM model for single acuator

An elliptic damage (semi-major axis: 30mm, semi-minor axis:15 mm, the angle: 135º) has been introduced as softening in the panel's skin as can be seen in Figure 2. The response is measured in each sensor. Magnitude $E(\mathbf{x})$ for each point of the panel is computed according to eq (5) and is shown in Figure 3, where a good agreement between the real location of the damage and the one obtained by applying the algorithm is seen.

Conclusion

In this paper an algorithm for damage detection based on probability of damage and image fusion has been proposed. The results show that the simulated damage was located with good agreement using Lamb wave signals from the numerical simulation of the damage and undamaged panel. Next step for this work is to validate the algorithm against experiments and to extend the algorithm to identification of different types of damage.

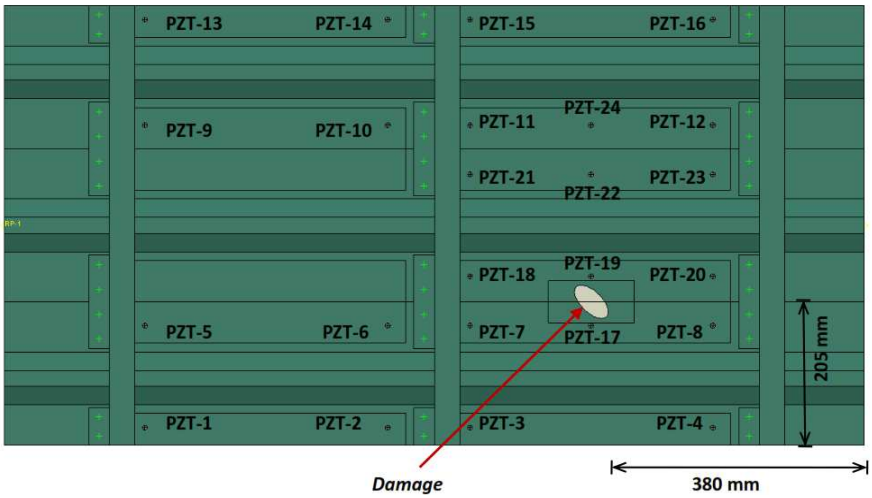


Figure 2. Sensorized Stiffened panel with damage location

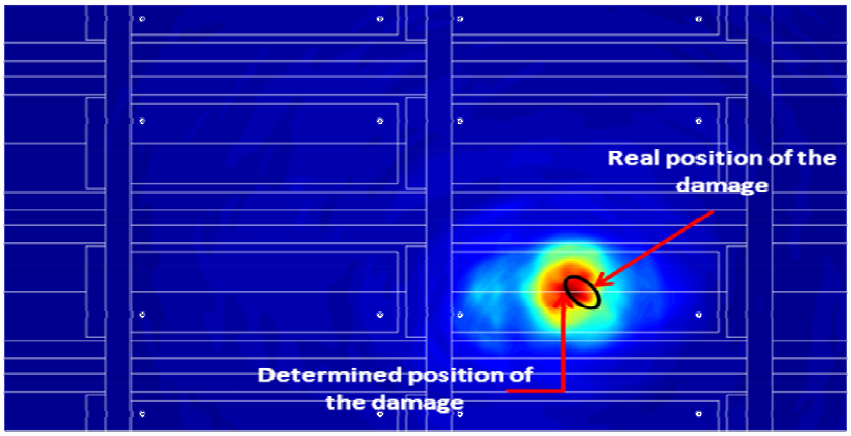


Figure 3. Damage localization using probability-based Imaging fusion

References

[1] S. Khodaei and M.H Aliabadi, "Damage Identification Using Lamb Waves," *Key Engineering Materials,* vol. 452, pp. 29-32, 2011.

[2] I. Benedetti, M H Aliabadi, A Milazzo "A Fast BEM for analysis of damaged structures with bonded piezoelectric sensors," Computer Methods in Applied Mechanics and Engineering Vol 199, p. 490-501, 2010.

[3] H. Gao, *et al.*, "Guided wave tomography on an aircraft wing with leave in place sensors," 2005, p. 1788.

[4] A. Mal, *et al.*, "A conceptual structural health monitoring system based on vibration and wave propagation," *Structural Health Monitoring,* vol. 4, p. 283, 2005.

[5] X. Zhao, *et al.*, "Active health monitoring of an aircraft wing with embedded piezoelectric sensor/actuator network: I. Defect detection, localization and growth monitoring," *Smart Materials and Structures,* vol. 16, p. 1208, 2007.

[6] J. E. Michaels and T. E. Michaels, "Guided wave signal processing and image fusion for in situ damage localization in plates," *Wave Motion,* vol. 44, pp. 482-492, 2007.

[7] J. Michaels, "Detection, localization and characterization of damage in plates with an in situ array of spatially distributed ultrasonic sensors," *Smart Materials and Structures,* vol. 17, p. 035035, 2008.

© (2012) Trans Tech Publications, Switzerland
doi:10.4028/www.scientific.net/KEM.488-489.9

The Measurement of Residual Stresses in Thermal Barrier Coated Model Aerofoils

Dong Liu[1,2,a] Peter EJ Flewitt[1,3,b] Keith R Hallam[1,c]

[1]Interface Analysis Centre, University of Bristol, Bristol, BS2 8BS, UK

[2]Department of Mechanical Engineering, University of Bristol, Bristol, BS8 1TR, UK

[3]School of Physics, HH Wills Laboratory, University of Bristol, Bristol, BS8 1TL, UK

[a]Dong.Liu@bristol.ac.uk [b]Peter.Flewitt@bristol.ac.uk [c]K.R.Hallam@bristol.ac.uk

Keywords: Superalloy CMSX4; Thermal barrier coating; Thermally grown oxide; Residual stress; Substrate curvature.

Abstract In this paper, we explored the relationship between thermal aging and the residual stresses developed within a thermal barrier coating (TBC) and the underlying thermally grown oxide (TGO). Superalloy model specimens (CMSX4) with a curved geometry designed to simulate key features of turbine blades coated with air plasma sprayed (APS) 7 wt.% Y_2O_3-stabilised ZrO_2 applied to an Amdry 995 bond coat were oxidised in the temperature range 900°C to 975°C for various lengths of time. Stress measurements on both the TBC and the underlying TGO were made at positions of known curvature using Raman and photo-stimulated piezo-luminescence spectroscopy (PLPS). The residual stress values reflect the interaction between TGO and TBC, which has the potential to be used as an indicator of service lifetime. The results are discussed with respect to the origin of the stress changes and the long term integrity of the coating.

Introduction

Thermal barrier coatings (TBC) when applied to gas turbine blades allow the engines to be operated at higher temperatures [1]. One application is for land-based power generation where the benefit of the coating is to increase thermal efficiency [2]. As a consequence, the continued use of these blades depends on ensuring the integrity of the thermal barrier coating. Within the range of TBC integrity evaluation methods, stress measurement can be carried out non-destructively. Therefore, if the stress values in the components are to be used as a lifetime indicator or integrity evaluation parameter, the non-destructive measurement would have to be applied at regular intervals to the in-service components to monitor the degradation. Here we consider residual stresses as measured in the TBC and TGO on five simulated aerofoil shaped model specimens using Raman spectroscopy (RS) and photo-stimulated pizeo-luminescence spectroscopy (PLPS). A relationship was found between the stresses produced in individual layers following exposure to temperatures in the range of 900ºC to 975ºC for various lengths of time. Compared with currently proposed life prediction methods [3, 4], a novel way is discussed based on these data for addressing the long term integrity.

Experiment Procedure

Model specimens with a curved geometry designed to simulate key features of coated blade were used. Each specimen comprised a superalloy substrate (CMSX4) with air plasma sprayed (APS) 7 wt.% Y_2O_3-stabilised ZrO_2 applied onto an Amdry 995 bond coat deposited using high velocity oxygen fuel (HVOF). The thickness of the TBC varied with position around the specimen from 130μm to 230μm. The as-coated specimens were thermally exposed at 900ºC for 100hr, 925ºC for 100hr, 975ºC for 1800hr and 975ºC until failure was observed. One as-coated specimen was used as a reference. Raman spectroscopic measurements were made using a Renishaw Ramascope model 2000 spectrometer, fitted with both argon and He-Ne laser sources operating at wavelengths of 514.53nm (30mW) and 632.80nm (25mW) respectively. The same spectrometer was used to determine the residual stresses in TGO by PLPS. As the TBC is transparent to the incident laser beam, it allows measurements to be made of stresses in the TGO [5].

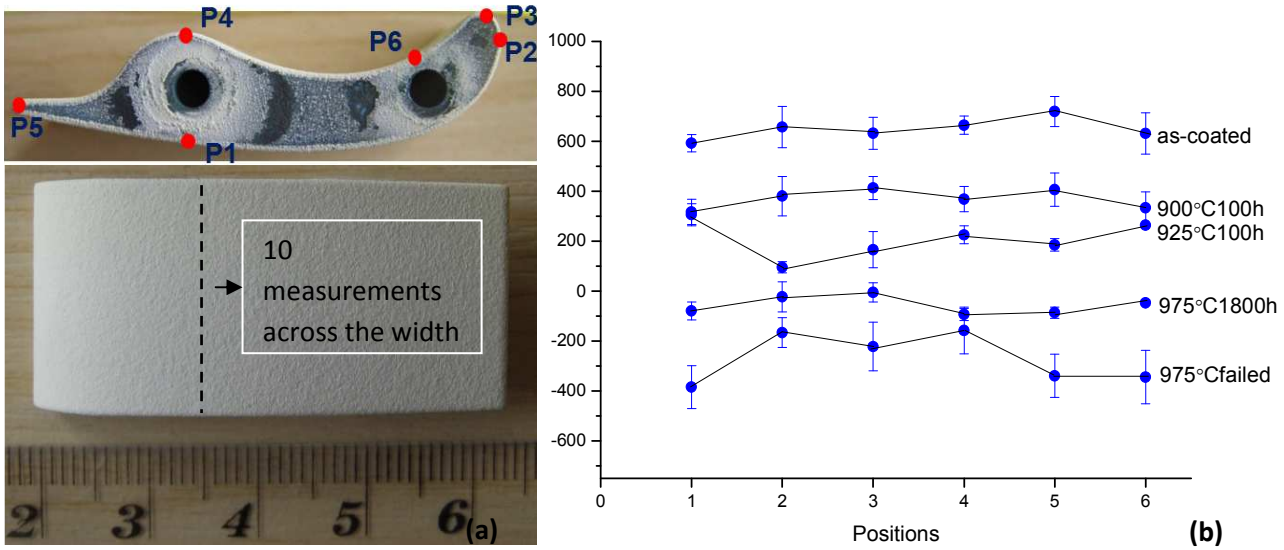


Figure 1 Residual stress in TBC coated specimens oxidised under various conditions: (a) positions measured; (b) stress variation as a function of aging

As shown in Figure 1(a), the curved specimens were about 43mm long and about 22mm in width. Six positions, P1 to P6, were measured and at each position 10 measurements were made along a line, evenly spaced, across the width of the specimen at the surface, Figure 1(a), for both the TBC and the TGO. For the former the red laser was used and for the latter the green laser. To relate Raman shifts with stress, a Raman conversion factor, Π, of 5.60±0.05cm^{-1}/MPa was obtained specifically for this TBC using a diamond anvil cell (DAC) [6]. The tetragonal ZrO_2 peak centred at a wavenumber of ~640cm^{-1} was considered because of the high signal-to-noise ratio achieved. The stress, σ, is calculated using a formula relating the shift of the peak centred at 640cm^{-1}, $\Delta\nu$, to stress:

$$\sigma = \Delta\nu \cdot \Pi^{-1} \tag{1}$$

Results and Discussion

The residual stresses measured for the five specimens are plotted in Figure 1(b). Regardless of the variation in the curvature and TBC thicknesses at six positions, the residual stresses tended to decrease uniformly from high tensile for the as-coated condition to compressive when failure of the coating occurred. A sharp decrease in level of stress to half of the original level for the as-coated specimen was observed after a short thermal exposure at 900ºC. At this point, it is not the creep of the bond coat that relaxes the stress, because the bond coat creep limit has been determined to be about 975ºC. Instead, we attribute this stress relaxation to limited pore shrinkage and nucleation and coalescence of cracks. To demonstrate microstructural evolution, two cross-sections are compared (Figure 2). After the initial decrease in the value of stress, further thermal exposure tended to continue to affect the stress progressively but with a lower rate.

To understand the interaction between TBC and TGO stresses, at the same measurement positions on the specimens, the residual stresses in TGO were determined (Figure 3). After a short period of oxidation at 900ºC, the stresses generated in TGO were small and compressive (0GPa to -0.85GPa), Figure 3, while, for the same thermal exposure at 925ºC, the TGO stresses became more compressive (-0.33GPa to -1.36GPa). The specimen oxidised at 975ºC for 1800hr showed, Figure 3, a significant variation of stress from position to position; correspondingly, the stress in TBC was about zero at this stage. Residual stresses in TGO reduced to near zero after a further 1200hr oxidation at 975ºC and showed the least variation from position to position for the specimens investigated.

A loop between the TBC and TGO stresses is found if the specimens are listed in the order of thermal aging and therefore oxidation severity, Figure 4. In Figure 4(a), each point represents 60 measurements around the specimen at positions with varying TBC/TGO/BC thicknesses and various curvatures. For comparison, the same positions with about the same TBC/TGO/BC thicknesses and substrate curvature are also investigated for all five specimens. Since all the positions show the same trend, the results for only one position are listed here. In Figure 4(b), the stress at P2 (see Figure 1(a)) was plotted for each of the five specimens. The similarity of the two plots in Figure 4 shows that it does not necessarily matter if the measurements are undertaken randomly around the specimens, or at one position that has about the same TBC/TGO/BC thickness and fixed curvature. The stresses in TBC and TGO follow the same rule with increasing thermal exposure oxidation. As shown for 5-5′ in Figure 4, the eventual failure of the TBC system occurred when a similar stress level was reached in the TBC and the TGO layers rather than when TBC stress was zero. The interactions between TBC and TGO stresses reflect the failure process of the system. If the area of the loop represents the stress difference that separates the TBC from the underlying layers, the closure of the loop at 5-5′ indicates that the difference has been accommodated by spallation of the TBC layer. Moreover, for points 4-4′, Figure 4(b), where the TGO and TBC stresses are equal after oxidation at 975ºC for 1800 hours, failure would be predicted.

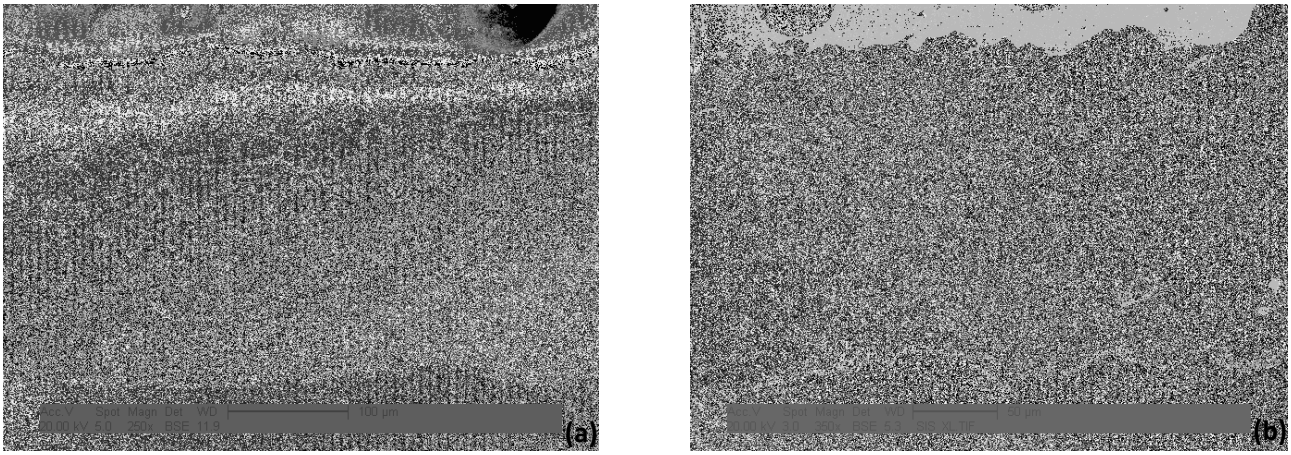


Figure 2 Cross-section of TBC with different aging: (a) as-coated TBC; (b) TBC oxidised at 900ºC for 2780 hr Courtesy of Cranfield University

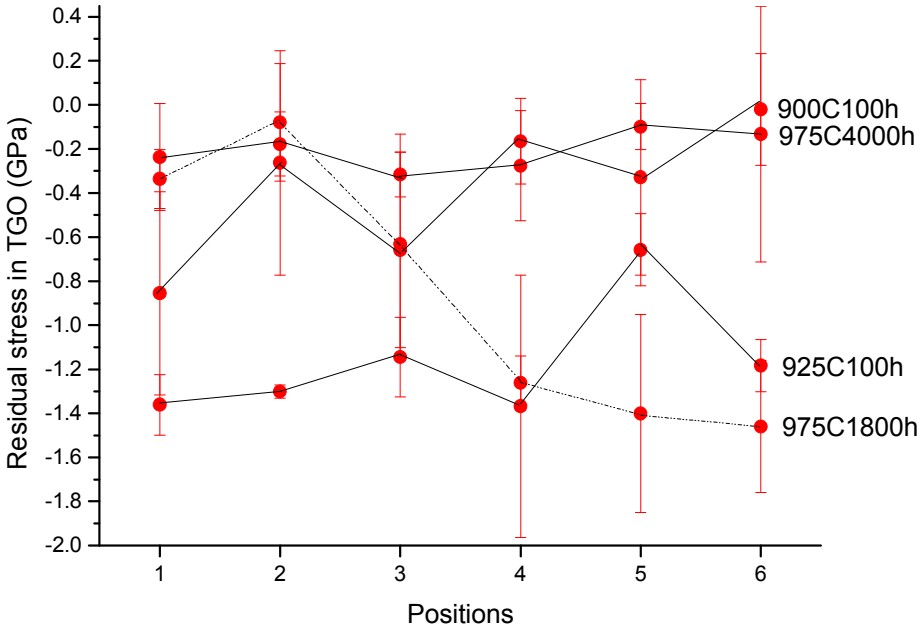


Figure 3 Residual stress in TGO on specimens with various oxidation conditions

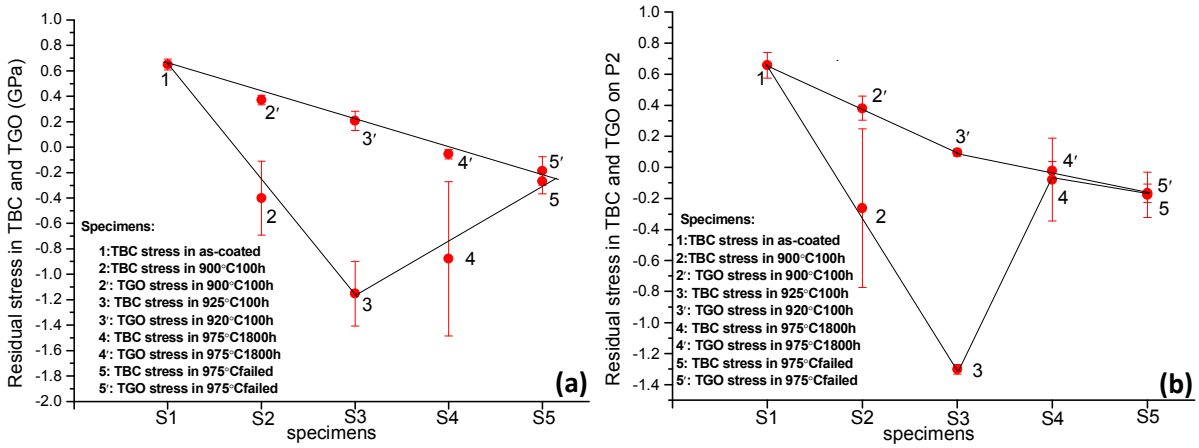


Figure 4 TBC and TGO stress loop: (a) TBC and TGO stress at positions P1 to P6; (b) TBC and TGO stresses at P2

Summary

A set of specimens prepared to simulate the geometry of aerofoils was investigated. The residual stresses in the TBC were found to change progressively with longer thermal exposure. Tensile stresses in TBC are initially accommodated by cracks and defect coalescence, but further alleviation relies on the detachment of ligaments. The stress difference between the TBC and TGO has the potential to predict the integrity of TBC system non-destructively for in-service components. This aspect will be explored and discussed in a future paper.

Acknowledgments

We would like to acknowledge the support of The Energy Programme, which is a Research Councils UK cross council initiative led by EPSRC and contributed to by ESRC, NERC, BBSRC and STFC, and specifically the Supergen initiative (Grants GR/S86334/01 and EP/F029748) and the following companies; Alstom Power Ltd., Corus, E.ON, Doosan Babcock, National Physical Laboratory, QinetiQ, Rolls-Royce plc, RWE npower, Sermatech Ltd. and Siemens Industrial Turbomachinery Ltd. for their valuable contributions to the project. Thanks go to Maud Seraffon (Cranfield University) for the SEM images, Figure 2.

References

[1] R.A. Miller: J. Am. Ceram. Soc. Vol. 67 (1984), p. 517

[2] S.M. Meier, D.K. Gupta, and K.D. Sheffler: J. of Metals Vol. 43 (1991), p. 50

[3] E.P. Busso, L. Wright, H.E. Evans, L.N. McCartney, S.R.J. Saunders, S. Osgerby, and J. Nunn: Acta Mater. Vol. 55 (2007), p.1491

[4] O. Trunova, T. Beck, R. Herzog, R.W. Steinbrech, and L. Singheiser: Surf. Coat. Technol. Vol. 202 (2008), p.5027

[5] Hilson G. PhD thesis, University of Bristol, 2008.

[6] D. Liu, P.E.J. Flewitt, and O. Lord: submitted to Engineering Structural Integrity Assessment Forum, 2011.

© (2012) Trans Tech Publications, Switzerland
doi:10.4028/www.scientific.net/KEM.488-489.13

Development of Predictive Models for Fatigue Crack Growth in Rails.

A. De Iorio[1,a], Grasso M. [2,b], Kotsikos G.[3,c], Penta, F. [4,d], Pucillo, G. P.[5,e]

[1), 2), 4),5)] University Federico II, P.le V. Tecchio. 80, 80125 Naples, Italy, fax n.: (+39) 081 9639948

[3)] Newcastle University, School of Mechanical & Systems Engineering, Newcastle upon Tyne, NE1 7RU,

[a)]antdeior@unina.it, [b)] marzio.grasso@unina.it, [c)] george.kotsikos@ncl.ac.uk,

[d)] penta@unina.it, [e)] gpucillo@unina.it,

Keywords: crack growth, rail defect, railway safety.

Abstract. Fatigue failures of rails often occur at the rail foot, since the geometry of this zone gives rise to stress concentrations under service loads or defects during rail manufacture and installation. In this paper, the fatigue behavior of cracks at the web/foot region of a rail is analyzed numerically. Analytical models in the literature for a semi-elliptical surface crack in a finite plate assume that the geometry of the front remains semi-elliptical during the whole propagation phase and the ellipse axes do not undergo translations or rotations. Fatigue tests show that this is not the case for such cracks in rails. A predictive model for crack growth has been developed by assuming an initial small crack at one probable initiation point between the web and foot of the rail in reference to a service condition loading. SIF values have been estimated by means of the finite element method and the plastic radius correction. The results attained were compared with crack growth experimental data.

Introduction

Catastrophic failures of rails due to cumulative fatigue damage are serious incidents for the rail industry as invariably they lead to vehicle derailment and high possibility of loss of life. Despite efforts by infrastructure managers to ensure that the integrity of rail track is preserved through up to date maintenance methods, cracks in rails are unavoidable requiring immediate remedial action.
Historically, cracks in rails had been appearing on the head of the rail as a result of wheel /rail contact stresses with the traction force acting as the crack opening force. Another source of cracking in rails is introduced by the presence of ail aluminothermic welds, where weld defects, such as porosity, shrinkage stresses or lack of fusion can lead to failure. As the rail material, weld procedures, rail head profile and bogie suspension systems have greatly improved in an effort to reduce the damage induced to the rail, fatigue cracks have been found to also initiate and propagate from small corrosion pits on the underside of the rail foot, requiring immediate repair or replacement of the rail.
Infrastructure managers have at their disposal some damage prediction tools based on empirical relations relating to the volume of traffic passing over a rail, which are not based on a scientific fracture mechanics approach to allow them to make an informed assessment of the severity of the flaw once this is detected by NDE inspections.
This work has undertaken the study of cracking in rails using FEA modelling to provide a tool for the assessment of the severity of surface breaking and embedded cracks in rails. The work does not investigate the well known crack initiation and propagation phenomena on the heads of rails, but concentrates mainly on cracks initiating and propagating from bending loads in the foot of the rail as a result of passing trains.

Background

The propagation of a crack is driven by the stress field that develops ahead of the crack tip. In fracture mechanics, the stress and strain fields can be characterized by parameters such as the stress intensity factors, K, under elastic conditions, or the J-integral or crack tip opening

displacement(CTOD) under conditions of extended plasticity. Such parameters describe the mechanics of the crack in terms that include the applied load and the length of the crack. The resistance of a material to fast fracture is given by the fracture toughness.
Under small scale yielding conditions, to predict crack propagation life and fracture strength, accurate stress-intensity factor solutions are needed both for initial, intermediate and final crack configurations. But, because of the complexities of such problems, exact solutions are not available. Instead, investigators have had to use approximate analytical methods, experimental methods, or engineering estimates to obtain the stress-intensity factors.
Closed form solutions for stress intensity factors of elliptical cracks in infinite bodies have been derived [1,2,3,4,5]. For finite bodies, all solutions have required approximate analytical methods with the use of the finite element analysis (FEA) method [6,7,8,9,10,11].
In this paper, a numerical approach that takes into account not only the finite geometry of the defected component but also the real elastoplastic behaviour of the component material. The implemented numerical model has been validated by means of full scale crack propagation test on a defected rail.

FEA

The finite element analysis has been carried out using the ANSYS package. Singular quarter-point elements for the small region around the crack front, where the stress field is K-dominated, have been used. The quarter-point elements allow to model singular displacement fields and thus to evaluate the stress intensity factor (SIF) with great accuracy and a relatively coarse mesh.
Several methods are actually available to obtain the SIF values during the post processing of the FE solution. Among them, the Displacement Correlation Method, applicable only when the material has linear elastic isotropic behaviour, makes use of the well-known relations between the SIF's values and the displacement field around the crack front. Otherwise, knowing the stress and strain field, the J values along the crack front have to be numerically evaluated and from them the SIF values can be derived.
The scientific code FRANC3D NG, developed by Cornwell University, has been used to generate the mesh around the crack front, which allows to manage both the preprocessing, i.e. it allows to create the crack in the uncracked model, and the postprocessing, i.e. the SIF evaluation in all the nodes of the front created in the previous phase. Starting from these SIF values, the crack growth has been evaluated using Paris' law whose parameters C and m has been obtained by means of crack propagation tests on DCB specimens, extracted from a rail. The obtained values for C and m are respectively, 3.3×10^{-13} and 4, if crack propagation rate is expressed in mm/cycle and the SIF in $MPa\cdot(mm)^{\mathbf{0.5}}$.
Since the aforementioned practice does not take into account the material ductility, a special code has been implemented in MATLAB, to correct the crack front shape with the plastic radius and evaluate the effective SIF values along the front. By the *theoretical* SIF values, K_I, and the following expression:

$$r_p = \frac{\pi}{8} * \left(\frac{K_I}{Y}\right)^2, \tag{1}$$

where, Y is the material yield stress, the plastic radius values, r_p, along the front have been evaluated, and a virtual crack front equivalent to the real one, but embedded in an elastic medium, has been generated.
The front so created has been imported in FRANC3D NG to evaluate the effective ΔK and with it the local increment Δa of the crack front, in order to obtain the new "theoretical" crack front corresponding to a given increment of number of cycles.

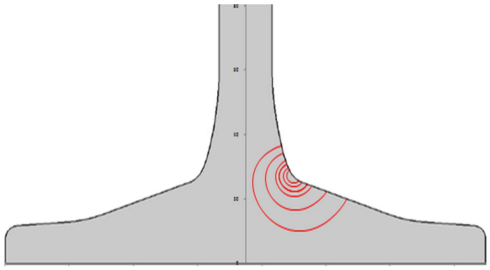


Figure 1 - Crack fronts obtained numerically starting from an initial semicircular flaw with radius equal to 2 mm.

In Fig. 1 some intermediate crack fronts obtained from an initial flaw having semicircular shape and radius equal to 2 mm are presented. The initial crack is located near the fillet between the foot and web rail and belongs to the cross section of the rail with the center on the external surface and at 27 mm far away from the underside of the rail foot.

Experimental

Four point fatigue tests have been carried out on a section of a rail to assess the accuracy of the numerical model. A UIC60 rail design section, the most common rail profile in European railways, was tested without a starter crack present.
Characterisation of the rail material was carried out to obtain all necessary mechanical properties for the analysis. Tensile tests were carried out according to BS EN 10002-1:2001. There was little variation in the tensile properties of the rail and the average Yield strength was determined as 540 MPa, the Ultimate strength 940 MPa and an elongation of approximately 12%.
The fracture mechanics tests were conducted according to BS7448 Part 2. The fracture toughness K_{IC} of the material could not be determined because the size of the specimens would not yield valid results. The K_Q value was determined and was equal to 27 MPa·$m^{1/2}$.

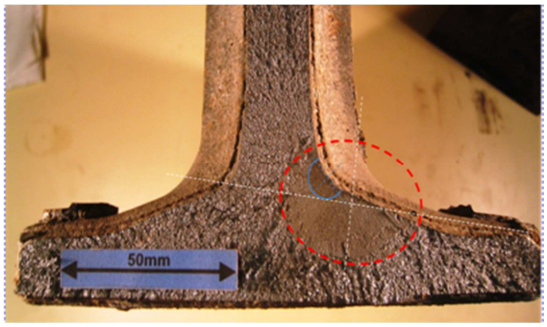


Figure 2 - Fatigue tested rail showing semicircular crack near initiation site (solid line) and semi-elliptical crack at failure (dotted line).

The rail fatigue tests were carried out with constant load amplitude and until final failure of the test sample. Once a crack has initiated, the test was stopped and the crack heat tinted. This was done to determine the shapes of the crack front during the initial propagation stage and how they change as the crack front propagates. It was observed that the crack initially has a semi-circular profile which changes to elliptical as the crack propagates. The crack front extends further towards the foot of the rail and less towards the web. This is reasonable as the stress increases the further away from the neutral axis towards the foot of the rail.

By overlapping the crack fronts of Fig. 1 and 2, it can be inferred that both the final experimental and numerical crack fronts are very close each other. This observation confirms the need of take account of the plastic region around the crack tip when the fatigue crack growth phenomenon in a ductile material has to be simulated.

Conclusions

A finite element analysis of the fatigue behaviour of a defected rail has been carried out by means of a commercial code integrated with an *ad hoc* macro written to iteratively evaluate the plastic radius, since the rail material is ductile, and the effective ΔK value that has to be used to evaluate the local growth of the crack front.
The good agreement between numerical result and experimental data obtained by fatigue testing of a rail segment with the same geometry, made of the same material, having the same defect and subjected to same load used in the numerical simulation, confirms the validity of the adopted modeling procedure and the need of directly introduce the effect of the plastic region at the crack tip when the problem of the crack growth in a ductile material has to be faced.

References

[1] Irwin, G. R.: The Crack Extension Force for a Part-Through Crack in a Plate, ASME,J. Appl. Mechs., Vol. 29, No. 4, 1962, pp. 651-654.

[2] Green, A. E. and Sneddon, I. N.: The Distribution of Stress in the Neighbourhood of a Flat Elliptical Crack in an Elastic Solid, Proc. Cambridge Phil. Soc., Vol. 47, 1950, pp. 159-164.

[3] Kassir, M. K. and Sih, G. C., Three-Dimensional Stress Distribution Around an Elliptical Crack Under Arbitrary Loadings, Journal of Applied Mechanics, Vol. 88, 1966, pp. 601-611.

[4] Shah, R. C.; and Kobayashi, A. S.: Stress-Intensity Factor for an Elliptical Crack Under Arbitrary Normal Loading, Engineering Fracture Mechanics, Vol. 3, 1971, pp. 71-96.

[5] Vijayakumar, Ko; and Atluri, S. N.: An Embedded Elliptical Flow in an Infinite Solid, Subject to Arbitrary Crack-Face Tractions, Journal of Applied Mechanics, Vol. 48, 1981, pp. 88-96.

[6] Smith, F. W.; Emery, A. F.; and Kobayashi, A. S.: Stress Intensity Factors for Semi-Circular Cracks, Part 2 - Semi-Infinite Solid, J. Appl. Mech., Vol. 34, No. 4, Trans. ASME, Vol. 89, Series E, Dec. 1967, pp. 953-959.

[7] Kobayashi, A. S.: Crack-Opening Displacement in a Surface Flawed Plate Subjected to Tension or Plate Bending, Proc. Second Intl_Conf. on Mechanical Behaviour of Materials, ASM, 1976, pp. 1073-1077.

[8] Raju, I. S.; and Newman, J. C., Jr.: Stress-Intensity Factors for a Wide Range of Semi-Elliptical Surface Cracks in Finite-Thickness Plates, Engineering Fracture Mechanics J., Vol. ii, No. 4, 1979, pp. 817-829.

[9] Newman, J. C., Jr._ and Raju, I. S.: Analyses of Surface Cracks in Finite Plates under Tension or Bending Loads, NASA TP-1578, Dec. 1979.

[10] Nishioka, T.; and Atiuri, S. N.: Analytical Solution for Embedded Elliptical Cracks, and Finite Element-Alternating Method for Elliptical Surface Cracks, Subjected to Arbitrary Loadings, Engineering Fracture Mechanics, Vol. 17, 1983, pp. 247-268.

[11] Tracey, D. M.,: 3D Elastic Singularity Element for Evaluation of K Along an Arbitrary Crack Front, Int. J. of Fracture, Vol. 9, 1973, pp. 340-343.

© (2012) Trans Tech Publications, Switzerland
doi:10.4028/www.scientific.net/KEM.488-489.17

Fracture Analysis of a First Stage Turbine Blade by FRANC3D

Saeed Asadikouhanjani[1,a], Reza Ghorbani[2,b]

[1,2] Mapna Turbine Blade Engineering & Manufacturing Co

Km 7 Malard Road, Mapna Boulevard, 31 67 64 35 97

Karaj, I.R.IRAN, P.O. Box: 31755-114

[a]asadi.saeed@Mapnablade.com, [b]ghorbani.reza@Mapnablade.com

Keywords: Fracture, Gas Turbine Blade, Fatigue, Tip Rubbing, Stress Intensity Factor

Abstract. The premature failure of a blade occurred after a service life of 8127 EOH operation houre. This paper presents the fracture analysis of the first stage blade through fractographic and mechanical analysis. Crack growth mechanisms were evaluated based on the microscopic observations of the fracture surfaces by SEM. The analysis of the different region of the fracture surface shows that crack propagation is mainly related with fatigue mechanism. The crack propagation occurred in the pressure-suction side direction. The dynamic characteristics of the blade were evaluated by FEM in order to identify the cause of blade failure. The result depicts that the second mode of vibration might be excited and the vibratory stresses cause to HCF damage of the blade. Eventully fracture analysis of the blade under the presence of a fatigue crack was analyzed by FRACNC3D software.

Introduction

Turbine blades in a typical gas turbine engine are identified as critical locations for stress fields and hence fatigue damage. Blade fatigue failures are often related to anomalies in mechanical behavior and manufacturing defects [1]. It this paper, a mechanical analysis has been performed with the metallurgical examinations to identify the possible causes of fatigue. Finite element method was utilized to determine the steady-state stresses and dynamic characteristics of the turbine blade under both laboratory and service conditions. Finally, the steady and dynamic stresses of blade have been checked by simulating the final crack through FRANC3D, state-of-the-art crack propagation software developed at Cornell University, which employs boundary elements and linear elastic fracture mechanics.

Background

A failure is addressed to a heavy duty land base gas turbine in hot section side. As a short history of failure can be mentioned that the unit was suffering from extraordinary turbine bearing vibration for period of the time which caused the unit forced outage. After casing removal; it was observed that among whole set of first stage rotary blades; four parts were fully broken in airfoil near meanline section. According to Fig. 1, out of four blades, one of them exhibited fatigue marks on the fracture surface (which is shown by two arrows), which has been proven by fractographic investigations [2]. The fracture surface of the failed blade was examined by a scanning electron microscope (SEM). Presence of fatigue striation lines reveals that HCF was the active mechanism of failure. However, the different analysis showed that the geometry and material characteristic complied with manufacturing requirements. In order to find out the root cause of fatigue cracking, the mechanical analysis has been carried out by using full featured model geometry including complex cooling passages of the blade which the results are presented hereinafter.

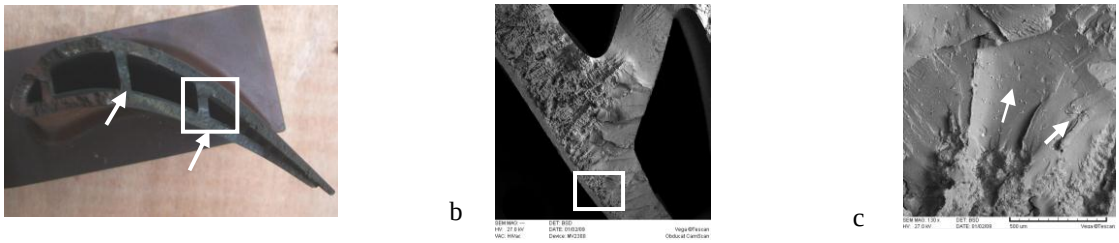


Fig. 1. a) General view b) SEM micrograph c) Higher magnification of Fig. 1b region

Finite Element Analysis

As above mentioned the metallurgical investigation showed that the blade failure was due to high cycle fatigue this means that the blade was exposed to cyclic loading. Fracture due to cyclic loading suggests that the blade can be subjected to resonance. So; modal analysis and dynamic FEM stress analysis have been conducted to extract blade natural frequencies, mode shapes and dynamic blade behavior. The FEM model is first validated by experimental results of the blade frequency test bench. The boundary condition which has been applied is clamped condition. Table 1 summarizes the results of experimental blade vibration measurements compared with the FE model predictions. The numerical analysis was performed by using commercial FEM software.

Table 1.Validation results for the FE model

Blade constraints	Mode no.	Tests [mean, Hz]	Model predication[Hz]	Mode type	Difference [%)]
clamped	1	562.2	569.4	Bending	1.2
	2	1303.3	1327.4	Torsion	1.8

A comparison of the natural frequencies is given in Table 1 depicting that there are good agreement between the test results and model prediction. In order to examine the dynamic behavior of the blade under service conditions, a pre-stressed modal analysis was performed. A FE analysis was conducted by exerting the centrifugal and gas pressure loads computed by CFD technique. The temperature dependency of relevant mechanical properties has been also considered in this analysis. The FE results were used as the initial conditions for a modal analysis. The stress distributions and mode shapes corresponding to the first and second vibration modal analysis are shown in Fig. 2. a & b.

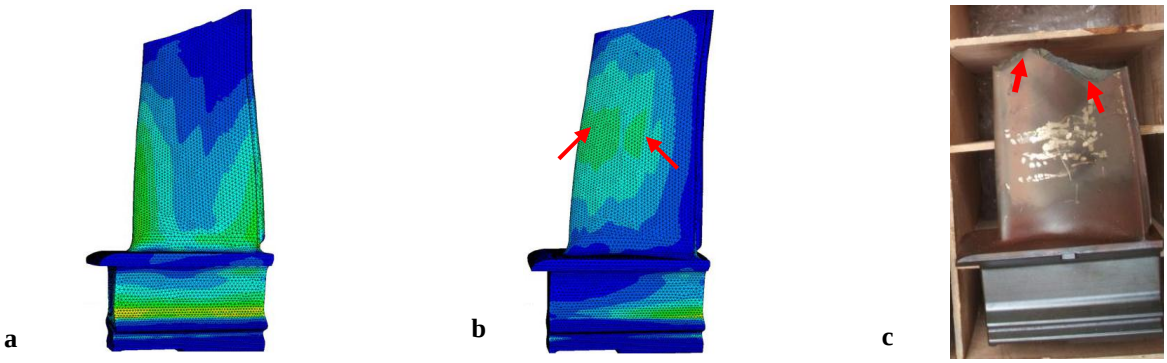


Fig. 2. Stress distribution for the blade in different vibration modes: (a) First mode-bending; (b) second mode- torsion; (c) arrows imply to initiation site of fatigue cracks in the damaged blade

In respect with the position of fatigue cracking in broken part (Fig. 2c) and comparing with stress plot of the second vibration modal shape; it can be easily recognized that the peak stress of the blade comply with where cracks initiated. Therefore; the second mode of blade vibration has probably been excited in this case of fracture. Generally; there are two possible vibration excitation

sources for the blade, (a) gas dynamic fluctuations and (b) blade tip rubbing. No significant evidence of gas dynamic pulsation abnormalities were found due to nozzle passing. As a consequence; normal gas dynamic fluctuations are most unlikely to be the excitation source. On the other hand; the rubbing between blades tip and vane upper shroud was evident from the vestige of wear at the tip of the blades which would occur in the form of an impulse load (Fig. 3a). It should be mentioned that in this turbine design; blades rotate under the vane upper-shroud roof functioning as shroud segment feature. This loading has been analyzed to determine whether it could contribute to the failure. Rubbing is essentially a "stick-slip" phenomenon [3]. In the case of a resonant or near resonant operation under these harmonic forces the blade can suffer a significant reduction in the design life. In a turbine stage, tip-rubbing can create a dynamic source of excitation that is most likely to vibrate blades at their second vibration mode. In among; the blade with fatigue marks was probably experienced most extensive rubbing and then has been fractured from the section with maximum vibratory stress near mean line section. The magnitude of stress was created by such a rubbing is impossible to predict preciously unless direct measurements of the tip displacement have been made. Therefore; in order to calculate the dynamic stress of second mode excitation, a harmonic analysis was performed in the condition of different harmonic force 100, 300, 500 and 700 N when applied as a tip rubbing force. Fig. 3c illustrates the stress distribution that resulted when rubbing was simulated.

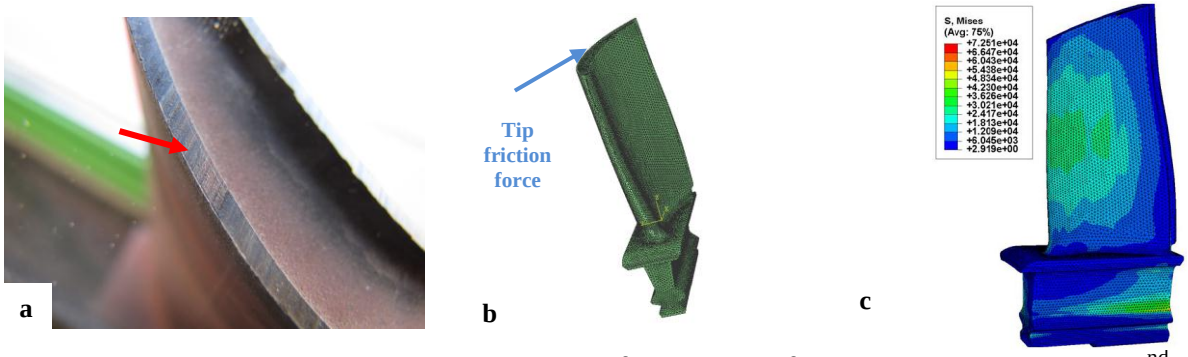


Fig 3.a) tip rubbing vestige b)Representation of tip rubbing force c) Resonant stress in 2nd mode-300 N rubbing force

Fracture Mechanics Analysis

In this step by using of FRANC3D software, the fracture mechanic behavior of a crack on the airfoil of the blade is simulated to predict whether crack initiate and propagate under already mentioned operation condition. According to the theory of facture mechanics, a certain level of vibratory energy is required to initiate a crack. The threshold stress intensity factor (ΔK_{th}) for IN738 material in gas turbine environment is approximately 8MPa$\sqrt{m}$ [4]. The values lower than threshold stress intensity factor is not providing sufficient energy to initiate and propagate a crack. For a complicated geometry and stress field produced by a complex three-dimensional structure like the airfoil of the gas turbine blade, the computer model is used to explicitly represent the damage and directly compute the ΔK along the crack front. So a boundary element model of the blade was constructed by OSM/FRANC3D [5]. In this approach; the complex geometry of the blade including sophisticated geometry of internal cooling system has been considered. Centrifugal and gas pressure loads were applied to the model as the boundary condition of the problem. The dynamic stress induced by alternative tip friction force has been calculated by FEM harmonic analysis and introduced into FRANC3D software as a cyclic stress. A semi-elliptical edge crack which is oriented approximately normal to the surface is introduced into the airfoil (Fig. 4a). The dimension is 0.5 mm length by 0.25 mm depth. The size and location of the initial flaw are taken from the

fractographic analysis. Fig.5 shows the normalized K_I along the crack front under steady state operation condition and cyclic stress when different tip rubbing forces of 100, 300, 500 and 700 N are applied in the blade.

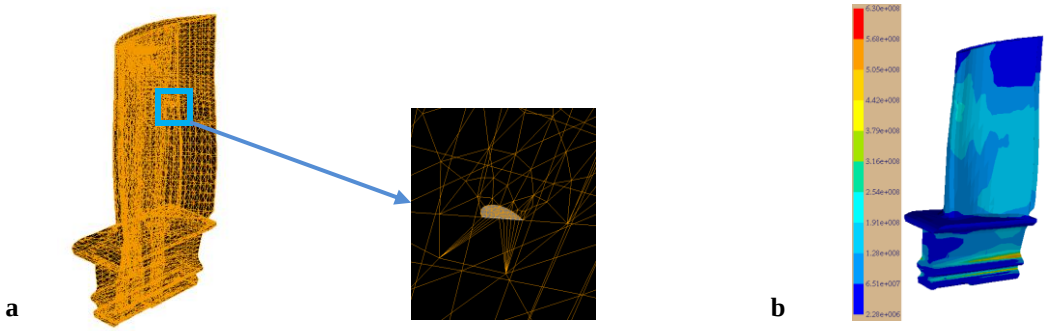


Fig 4. a) Typical model of blade in OSM. b) Superposition of centrifuge, Gas bending and 300 N harmonic forces in FRANC3D

According to Fig. 5b the calculated stress intensity factors indicate that only with the tip rubbing force more than 500 N, initiation and propagation of a fatigue crack is susceptible. This is in agreement with the result of Goodman diagram and FEM harmonic analysis (Fig. 5a). According to Goodman diagram an alternating stress of 110MPa is needed to occurrence of fatigue at the airfoil. Harmonic stress simulation by commercial FEM software shows this alternating stress is allocated in nearby the fracture region when 500 N tip rubbing friction forces is applied.

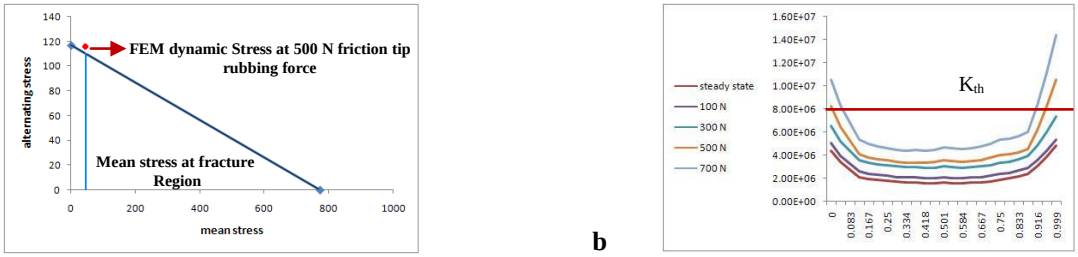


Fig 5. a) Goodman diagram. b)K_I stress intensity factor for different condition

Summary

In order to realize the root cause of happened failure; a fracture mechanics study has been carried out. The results indicate that sever rubbing between vane outer-shroud and blade squealer probably made blade excited which led to failure by HCF mechanism. The complementary FEM analysis also showing the 2nd vibration mode of the blade has been resonated. The calculated vibratory stress depicts that excitation of the 2nd vibration mode leading to fatigue crack initiation through the meanline section where the maximum and critical stress is experienced. In this case; the critical vibratory stress is introduced when blade tip friction forces would be higher than 500 N.

References

[1] Dj.M. Maric, P.F. Meier and S.K. Estreicher: ENG FAIL ANAL Vol. 9 (2002), p. 201.

[2] R. Ghorbani, S. Asadikouhanjani, K. Kusterer and A.H Ayed: Fracture Analysis of a First Stage Turbine Blade, Proceedings of ASME Turbo Expo 2010: Power for Land, Sea and Air.

[3] B. N. J. Persson, E. Tosatti: Physics of sliding friction, chapter I, Kluwer Academic Publishers (1996).

[4] W. Hoffelner: METALL TRANS A Vol. 13A (1982), p. 1245.

[5] Information on http://www.cfg.cornell.edu/software/software.htm.

© (2012) Trans Tech Publications, Switzerland
doi:10.4028/www.scientific.net/KEM.488-489.21

Fully Reversed Uniaxial Tension-Compression High Cycle Fatigue Behaviour of Shot-peened Steels

A. Plumtree[1,a] and M.M. Mirzazadeh[1,b]

Department of Mechanical and Mechatronics Engineering,

University of Waterloo, 200 University Ave. West,

Waterloo, N2L 3G1, Canada.

[a]plumtree@uwaterloo.ca, corresponding author
[b]m.m.mirzazadeh@gmail.com,

Keywords: Shot-peening, Fatigue life, Uniaxial cycling, Forged steels, Crackable steel.

Abstract. The effect of shot-peening on the uniaxial fatigue behaviour of four engineering steels, heat treated to a similar final hardness was investigated. Forged 0.39%C and 0.72%C steels, a quenched and tempered 0.51%C steel and a 0.50%C powder forged (PF) steel were fatigue tested under fully reversed (R=-1) push-pull loading conditions. Following long life (10^7) cycling, shot-peening had little effect on the fatigue limit of the 0.39%C and 0.72%C steels whereas the fatigue limit of the PF steel increased 10.4%. Conversely, the fatigue limit of the quenched and tempered steel decreased 12.0% after shot-peening. The results showed that the beneficial effects of shot-peening, such as compressive residual stresses and work hardening, balanced the effects of surface roughness since crack initiation tended to occur below the surface. Microhardness profiles showed that the greatest amount of cyclic softening in the shot-peened regions occurred in the hot rolled steels. Softening was accompanied by a decrease in the depth of surface hardness.

Introduction

Fatigue resistance is an important property when considering the service life of engineering components, such as connecting rods used in automobile internal combustion engines subjected to constant or variable cyclic loading. The durability of these components is of critical importance since they are usually designed for infinite life, with fatigue limit being the primary criterion [1].
Recently, the development of innovative one piece “crackable” forged steel connecting rods has reduced production costs. On breaking the rod at the big end and reassembly around the crankshaft, the broken surfaces match perfectly. Efficiency is increased and the tolerances are very close.
Shot-peening is generally applied to extend the fatigue life of these components by work hardening, simultaneously inducing compressive residual stresses at the surface. However, these beneficial effects can be offset by the accompanying surface roughness [2].
In this study the effect of shot-peening on the high cycle fatigue behaviour of four connecting rod steels, including the higher carbon crackable steel (C70S6), are investigated. Their respective lives are related to the surface treatment. The role of shot-peening, surface compressive stress and work hardening will be considered in influencing their long life fully reversed push-pull fatigue behaviour.

Materials and Experimental Procedure

Four different engineering steels of similar hardness have been investigated. AISI 1141, powder forged (PF) 0.50%C and crackable C70S6 (AISI 1070) steels were tested in their normalized conditions whereas AISI 1151 steel was tested after quenching and tempering. Their respective chemical compositions and mechanical properties are given in Tables1and 2.

Steel	Table 1. Chemical Composition %									
	C	Mn	S	P	Si	Cu	Cr	Mo	Ni	V
AISI 1141	0.39	1.41	0.12	0.01	0.24	0.05	0.1	0.01	0.03	0.06
AISI 1151	0.51	0.85	0.11	0.04	-	-	-	-	-	-
PF	0.50	0.31	0.12	-	-	3.06	-	-	-	-
C70S6	0.72	0.5	0.065	0.009	0.22	-	0.061	-	-	0.04

Table 2.Mechanical properties

Material	Yield Strength (MPa)	Tensile Strength (MPa)	Elongation (%)	Reduction of Area (%)
AISI 1141	575.7	855.0	17.0	39.0
AISI 1151	930.8	999.8	12.0	31.0
PF	565.4	889.5	15.0	30.0
C70S6	575.7	1006.7	13.0	27.0

The specimens were machined with a gauge section of 62 mm x17mm x 2mm and a generous 22mm shoulder radius. They were then divided into two groups. The first was polished to a surface finish of 0.26 ± 0.03µm. The second group was shot-peened using 1mm diameter steel shot, Almen scale 14-18A resulting in surface profile of 3.60 ± 0.44 µm. The specimens were then cycled under fully reversed (R=-1) tension-compression loading conditions.

Results

Through-thickness mircohardness tests were conducted on the gage and grip sections of selected samples before and after fatigue testing. An example is shown in Figure 1 for the crackable C70S6 steel. The mircohardness profile is typical for the other normalized steels (AISI 1141 and PM).

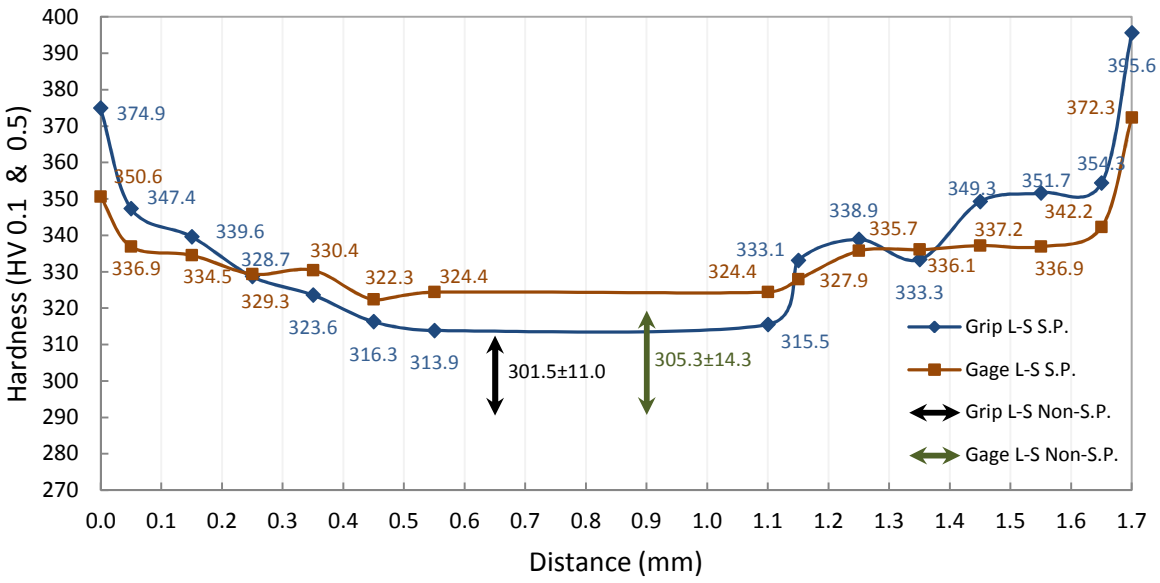


Figure 1. C70S6. Cross-section microhardness profiles.

Figure 1 shows the microhardness profile in the grip and gage sections of selected shot-peened and non shot-peened C70S6 specimens. After 10.1×10^7 cycles at σ_a=347.4MPa the shot-peened surface hardness decreased 6.0%. Also, the depth of surface hardness decreased from 0.55mm to about 0.25mm.The grip and gage hardness in the center were similar: 313.9±15.5 and 324.4±12.3 HV0.1, 0.5 respectively, as were the hardness values in the grip and gage of the non shot-peened sample after 10.6×10^7cycles at 341.8 MPa, indicating that neither cyclic softening nor hardening occurred.

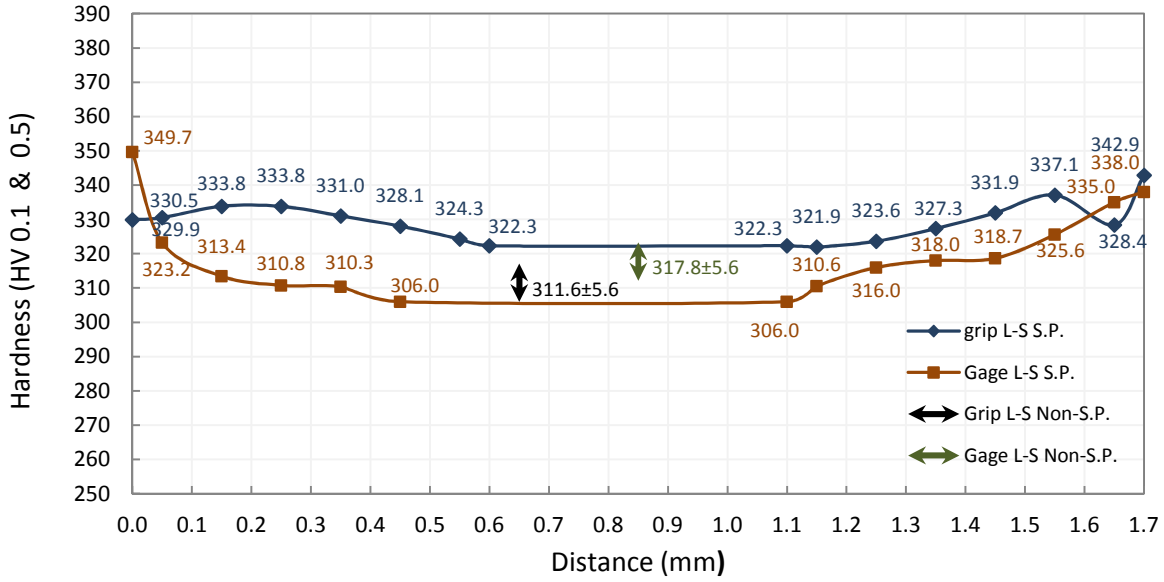


Figure 2. AISI 1151. Cross-section microhardness profiles.

Figure 2 shows that the initial shot-peened depth of the quenched and tempered AISI 1151steel specimens was about 0.5mm, and after 2.9×10^4 cycles at σ_a=461.1MPa, the shot-peened depth changed very little. The hardness decreased about 1% on one side and increased about 6% on the other. The grip and gage hardness values in the center were 322.3±11.2 and 306.0±11.6 HV0.1-0.5 respectively, indicating some cyclic softening had taken place at this stress. At lower cyclic stresses approaching the fatigue limit of 375.9±32.7MPa more cyclic softening is expected to occur due to relaxation of the internal stresses.

The hardness in the grip and gage sections of the non shot-peened sample after 6.5×10^5 cycles at σ_a=440.8MPa were 311.6±5.6 HV0.5 and 317.8±5.6 HV0.5 respectively, similar to the center of the shot-peened sample.

Table 3 lists the fatigue limits (N~10^7) of the four steels. In general, the effect of shot-peening ranged from a decrease in the fatigue limit stress of -12.0% to an increase of 10.4%.

Table 3. Fatigue Limits MPa 10^7Cycles

STEEL	SHOT-PEENED	NON SHOT-PEENED	INCREASE AVE. %
AISI 1141 Air Cooled	331.6 ± 2.6	324.3 ± 5.1	2.3
AISI 1151Heat Treated	375.9 ± 32.7	427.3 ± 7.6	- 12.0
Powder Forged	343.2 ± 22.4	311.0 ± 19.5	10.4
C70S6 Air Cooled	341.3 ± 7.4	348.8 ± 5.5	-2.2

Table 3 indicates that shot-peening the forged AISI 1141 and C70S6 steels had very little effect (2.3% and - 2.2% respectively) on their fatigue limit stresses.

For the powder forged steel, shot- peening was beneficial with a 10.4% increase in the fatigue limit, although the standard deviation was relatively high.

The decrease of 12.0% in the fatigue limit stress of the shot-peened heat treated AISI 1151 steel was the result of cyclic softening.

In general, for shot-peened steels cycled under reversed loading conditions close to the fatigue limit, the stress amplitudes exceed the local fatigue strength below the surface because of the shallow stress gradient and cracks tend to initiate below the surface. Although, in the present push-pull cycling tests the loading stress gradients were relatively shallow compared to cyclic bending, the fatigue cracks initiated just below the surface. This resulted in increases in the local fatigue strength which were further reduced by relaxation of compressive residual stresses.
Guechichi and Castex [3] presented a model based on the initiation of fatigue cracks in the subsurface layers which predicted the fatigue limit stress of shot-peened steel. Surface roughening caused by shot-peening was of lesser importance. Their model was substantiated by experimental data. This was in agreement with the earlier work of Wang et.al. [4] showing that the fatigue limit of shot-peened steels could be predicted based on the local fatigue limit at the crack source under the surface hardened layer. The effect of shot-peening was to shift the crack source into the residual tensile stress region beneath the surface hardened layer. Hence, fatigue crack initiation takes place in the sub-surface regions and the detrimental effects of the rough shot-peened surface fatigue life become less significant, as shown in the present work.

Summary

1. Surface roughness caused by shot-peening was not a large factor in controlling the balanced uniaxial push-pull fatigue lives of the steels investigated.

2. Following long periods of uniaxial push-pull cycling, the surface hardness of the normalized shot-peened medium AISI 1141steel and higher carbon crackable C70S6 steel decreased 3.0% to 7.0% and the hardness depth decreased about 70.0%.

3. Shot-peening had a very small beneficial effect of 2.3% on the uniaxial push-pull fatigue limit ($N\sim10^7$) of the air cooled AISI 1141 steel whereas shot-peening had an equally small negative effect of 2.2% on the push-pull fatigue limit of air cooled higher carbon crackable steel (C70S6).

4. Shot-peening negatively affected the fatigue properties of a quench and tempered AISI 1151 steel subjected to uniaxial push-pull cycling. The fatigue limit ($N\sim10^7$) decreased 12.0%.

5. The uniaxial push-pull fatigue limit ($N\sim10^7$) of the 0.50%C powder forged steel increased 10.3% on shot-peening, albeit with a large standard deviation.

Acknowledgments

Financial support was supplied by the Natural Sciences and Research Council of Canada. The authors are most grateful to Dr. Guangxu Cheng, Xi'an Jiatong University, Shaanxi, China for his diligent and careful work in carrying out the fatigue tests.

References

[1] A. Afzal and A. Fatemi, "A Comparative Study of Fatigue Behavior and Life Predictions of Forged Steel and PM Connecting Rods", SAE Int., 2004, SAE Paper No. 2004-01-1529.

[2] R. Fathallah, A. Laamouri, H. Sidhom, and C. Braham: Int. J. Fatigue, Vol. 26 (2004), p.1053.

[3] H. Guechichi and L. Castex: J. Mats. Processing Technology, Vol. 172 (2006), p. 381.

[4] S. Wang, Y. Li, M. Yao and R. Wang: J. Mats. Processing Technology, Vol. 73 (1998), p. 57.

© (2012) Trans Tech Publications, Switzerland
doi:10.4028/www.scientific.net/KEM.488-489.25

Solutions for Impact over Aerospace Protection

L. Neckel[1, a], D. Hotza[2,b], D. Stainer[3,c], R. Janßen[4,d] A.G.R. Lezana[5,e], A. Dias[5,f], H.A. Al-Qureshi[5,g]

[1]Universidade Federal de Santa Catarina (UFSC)

Departamento de Engenharia Mecânica - Centro Tecnológico

88040-970 Florianópolis–, SC, Brazil

[2]Universidade Federal de Santa Catarina (UFSC)

Departamento de Engenharia Química - 88040-970 Florianópolis–, SC, Brazil

[3]Construções Mecânicas Cocal Ltda. - 88845-000 Cocal do Sul, SC, Brazil

[5]Hamburg University of Technology - Institute of Advanced Ceramics - D-21073 Hamburg, Germany

[3]Universidade Federal de Santa Catarina (UFSC)

Centro de Engenharia da Mobilidade –89219-905 Joinville, SC, Brazil

[a]neckel.leandro@gmail.com; [b]dhotza@gmail.com; [c]daniel@cmc.ind.br;

[d]janssen@tu-harburg.de [e]lezana@deps.ufsc.br; [f]acires@emc.ufsc.br; [g]alhazim@emc.ufsc.br

Keywords: Composite structures, Modeling, Impact Absorption, Armor

Abstract. New ballistic protection systems based on alternative materials have been recently developed. One of the industry's objectives is to develop lighter and stronger defensive systems, which allow higher mobility and safety for both vehicles and humans. This work studies the behavior of an aerospace protection against a projectile impact, seeking an optimized construction. The Al-Qureshi et al. model suggests a ceramic-metal layer system and describes its behavior. The literature shows, due to the considered parameters, the erosion tax and the loss of velocity. The phenomenon is described in steps, presenting particular effects for each. The equations are not equal between the stages showing different properties. The present work searches for a solution that can show the expression for mass and velocity, for each stage of the phenomenon. The results from the numerical method used were plotted and analyzed. The treatment was performed using Maplesoft Maple software. As a result, graphs were generated, which allow a deeper analysis of the model. Finally, advance in the knowledge of fracture processes in materials by high velocity impact can be concluded. This fact permits developments in materials that can perform shock absorption.

Introduction

Al-Qureshi et al. [1] have developed a mathematical approach to the behavior of a two-layer system protection of ceramic-metal composite against high speed impact. The ceramic layer erodes the projectile and the back metal plate is responsible for absorbing the remaining energy by plastic deformation. The mathematical model separates the penetration in three different stages and proposes a deterministic equation that explains the deflection of the metal plate.

The equations were manipulated to find a single problem for velocity and mass separately for each stage. The data and initial parameters provided by the original work [1] were used for the differential equations found. To find the solution, the software Mapplesoft Maple V12 was used. Finally, the solution was plotted and compared to former results [1].

Materials and Methods

The software Maplesoft Maple V12 was used to solve the system. Al-Qureshi`s work [1] provided all materials constant values and initial parameters necessary. Moreover, the projectile specifications used were from rifle bullets.

The mathematical model of the penetration process is divided in three stages. The first represents the initial impact and erosion of the head of the projectile. In this situation there is no penetration in the protection. The force against the projectile is

$$m(t)\frac{d}{dt}v(t) = -YA_p \tag{1}$$

and the variation in the geometry is given by

$$\frac{d}{dt}m(t) = -A_p\rho_p v(t) \tag{2}$$

where Y is the dynamic yielding of the projectile and A_p is the effective contact area of the projectile. Also, ρ_p is the density of the projectile`s material.

The impact generates a shock wave that travels through the material and reflects back cracking the ceramic plate. In the second stage the penetration starts pushing an interface projectile-ceramic with velocity *u(t)*. The force against the projectile is the same but the difference of the velocities *v(t)* and *u(t)* gives the erosion ratio:

$$\frac{d}{dt}m(t) = -A_p\rho_p\big(v(t)-u(t)\big). \tag{3}$$

The modified hydrodynamic theory given by Tate [2] introduced the dynamic yielding (Y) and the resistance against penetration (R) adopted for the ceramic in this case. Tate`s law is given by

$$Y + \frac{1}{2}\rho_p\big(v(t)-u(t)\big)^2 = R + \frac{1}{2}\rho_c u(t)^2 \tag{4}$$

where ρ_c is the density of the ceramic material. This stage ends when *v(t)=u(t)*. After this the erosion stops and the final part of the movement is given by

$$m_{pr}\frac{d}{dt}v(t) = -RA_p \tag{5}$$

where m_{pr} is the remaining mass of the projectile. The metal plate absorbs the final kinetic energy by plastic deformation. The total plastic energy absorbed can be expressed in terms of the stress and strain as

$$E_p = \int_v\left(\int_0^{\bar{\varepsilon}}\bar{\sigma}\partial\bar{\varepsilon}\right)dV \quad . \tag{6}$$

It is considered a stress-strain curve given by the power law

$$\bar{\sigma} = A.(\bar{\varepsilon})^n \tag{7}$$

and the deflection profile of the plate given by

$$w(r) = w_0 e^{\left(-\frac{kr}{D}\right)}. \tag{8}$$

where w_0 is the maximum deflection of the dimple shape, D is the radius of the projectile and k is a deflection profile constant that can be determined experimentally. Considering a geometry of dimple given by $2\pi rh\delta r$, where h is the thickness of the plate [3-5], the manipulation of the equations gives

$$w_0 = \left(\frac{m_{pr} v_p^2 (n+1)^3}{\pi h A \left(\frac{k}{D} \right)^{2n}} \right)^{\frac{1}{2n+2}} \tag{9}$$

where v_p is the velocity of the projectile at the end of the second stage.

Results and Discussion

The solutions were obtained divided by the stages and by mass and velocity. First it was necessary to find a differential equation with a unique function. For the first stage it was

$$\frac{d^2}{dt^2} v(t) = -\frac{\rho_p v(t) \left(\frac{d}{dt} v(t) \right)^2}{Y} \tag{10}$$

for the velocity and

$$\frac{d^2}{dt^2} m(t) = \frac{Y A_p^2 \rho_p}{m(t)} \tag{11}$$

for the mass. The equations for the second stage were

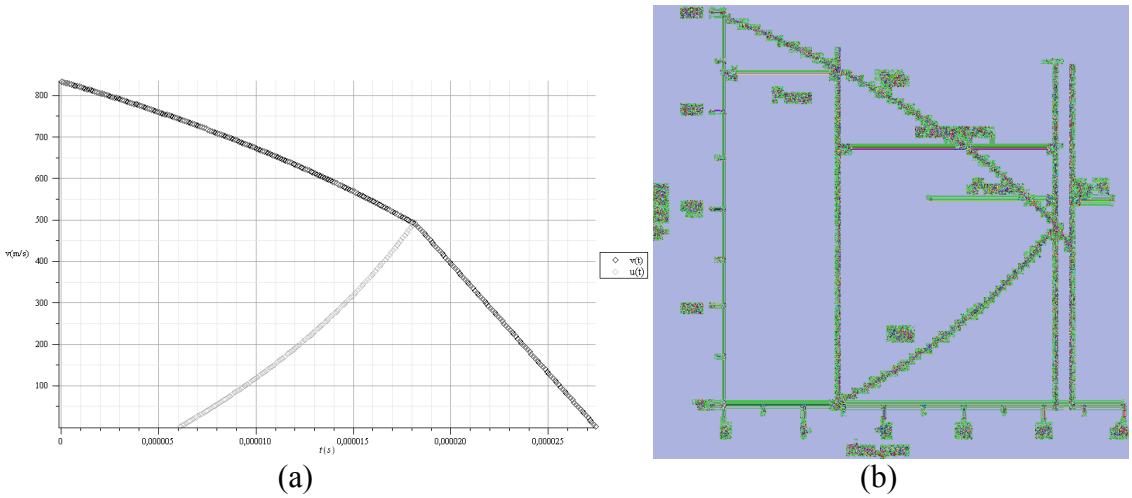
$$\frac{d^2}{dt^2} v(t) = \frac{\rho_p \left(\frac{d}{dt} v(t) \right)^2 \left(v(t)(2\rho_p - \rho_c) + \sqrt{2\rho_p R - 2\rho_p Y + 2\rho_c Y - 2\rho_c R + \rho_c \rho_p v(t)^2} \right)}{Y(\rho_c - \rho_p)} \tag{12}$$

for the velocity and

$$\frac{d^2}{dt^2} m(t) = -\frac{YA^2 \rho_c \rho_p}{m(t) \left(-\rho_c + \frac{\left(\frac{d}{dt} m(t) \right) \rho_c \rho_p}{\sqrt{\left(\frac{d}{dt} m(t) \right)^2 \rho_c \rho_p - 2\rho_c \rho_p^2 A_p^2 R + 2\rho_c \rho_p^2 A_p^2 Y}} \right)} \tag{13}$$

for the mass.

In Fig. 1 (a and b), *u(t)* corresponds to the lower curve. With the solutions it is possible to estimate the fraction of mass, velocity and energy lost in each stage. These values are presented in Table 1.



(a) (b)

Figure 1 : Velocity against time for (a) this work and (b) original work [1], respectively.

Table 1: Fraction of loss of velocity, mass and energy of the projectile in the three stages

Stage	Velocity Loss (%)	Erosion (%)	Absorbed Energy (%)
1°	10.62	19.18	35.73
2°	30.27	40.77	50.32
3°	59.10	-------	13.93

It was also possible to calculate how much the back metal plate will deflect using Eq. 9. The values of the constants were given by the former work [1] and the mass and velocity were given by the numerical solution. With these data the equation returned 17 mm as the value for the deflection. The experiment from Al-Qureshi`s work [1] provides values between 16.5 and 20.0 mm for the same conditions.

Conclusions

The values obtained from the model demonstrate how important the ceramic plate is in the protection, responsible for absorbing approximately 85% of the total energy. Moreover, the value for the deflection of the metal plate was close to the experimental data, which validates the model. The solved model allows future studies with simulation for different properties and projectile types.

Acknowledgments

The authors wish to thank CAPES and CNPq for supporting this work.

References

[1] D.P. Gonçalves; F.C.L. de Melo; A.N. Klein; H.A. Al-Qureshi: Analysis and Investigation of Ballistic Impact on Ceramic/Metal Composite Armour, International Journal of Machine Tools & Manufacture 44 (2004) 307–316

[2] A. Tate: A Theory for the Deceleration of Long Rods after Impact, J. Mech. Solids 15 (1967) 387–399.

[3] R. Hill: The Mathematical Theory of Plasticity, Oxford University, Press, (1950) 264.

[4] D. Ishikura; H.A. Al-Qureshi: An investigation of perforation of metallic and composite plates by projectiles, Proc Fifth Pan American Congress of Applied Mechanics—PACAM V, San Juan, Puerto Rico, 5, (1997) 194–197.

[5] M.L. Wilkins: Mechanics of penetration and perforation, Int. J. Eng. Sci. 16 (1978).

© (2012) Trans Tech Publications, Switzerland
doi:10.4028/www.scientific.net/KEM.488-489.29

The effect of mesh density in lattice models for concrete with incorporated mesostructure

Jan Eliáš[1,a], Miroslav Vořechovský[1,b]

[1]Institute of Structural Mechanics, Faculty of Civil Engineering, Brno University of Technology, Brno, Czech Republic

[a]elias.j@fce.vutbr.cz, [b]vorechovsky.m@fce.vutbr.cz

Keywords: lattice, brittle elements, mesh density dependency, concrete, grains, mesostructure

Abstract. This paper shows that mesh density dependency in brittle element lattice models cannot be completely removed by incorporating material mesostructure. This is concluded as a result of a series of simulations of fracturing in concrete using a 2D rigid-body-spring network. In the case of notched beams loaded in three-point-bending (TPB), adding finer grain structure led to a significant reduction in the dependency of the peak force on the mesh density. However, the energy dissipated during the fracture simulation was still affected significantly by the mesh density.

Introduction

Lattice models are a well established tool for fracture modeling and they appear to be very helpful, especially thanks to the increasing power of modern computers. In classical lattice models, the material is represented by a set of discrete elements inter-connected by springs. The use of a combination of simple constitutive models with a material structure incorporated from the meso-level [1,2], or alternatively of material parameters whose randomness somehow mimics this material structure [3,4], makes such models powerful tools able to model quasibrittle structural response. It is an alternative to the relatively complex constitutive laws applied in classical continuum mechanics-based models. The simplest models are those involving only elasto-brittle springs. Only this type of model is studied in this contribution.

The weak point of using purely brittle springs is the strong dependency of the results on network density. Since the network does not represent any real underlying structure, this dependency is understood as a bias which should be removed. If one insists on keeping the brittleness of elements, as we do (no softening of elements is incorporated), the mesh size dependency can be overcome e.g. by scaling the strengths of elements according to their lengths and a chosen internal length parameter [5] or, as is believed to be effective, by incorporating the material's inhomogeneities (voids, grains, microcracks), which introduces an internal length as well.

The paper presents a numerical study of the effect of grain microstructure projected on lattice elements in networks with varying densities (the grain layout properties to be used to classify elements is kept, but the network density is varied). Attention is particularly focused on how two of the most important characteristics are affected: the peak load and the dissipated energy. Conclusions are drawn from the presented series of simulations of fracturing in concrete using a 2D rigid-body-spring network.

Brief description of the model

Several lattice-type models can be found in the literature. In this research, the rigid-body-spring network developed by Kawai [6] is used. Fundamentally, the model is very similar to the one published by Bolander & Saito [7]. The fracture criteria are taken from the same article, i.e. a Mohr-Coulomb surface with tension cut-off is adopted. A more detailed description can be found in Eliáš [8]. Irregular geometry is used for the network in order to avoid directional bias. The meshing algorithm is based on Voronoi tessellation, which is performed on a set of pseudo-randomly placed triangulation nodes within the domain. The only restriction is that their minimal mutual distance equals a predefined parameter, $l_{\min}$.

When a notch is to be modeled, it is included by mirroring nodes along the notch line in the notch vicinity, see Figure 1b. Voronoi tessellation then creates a straight (notch) line and all springs lying on that line are subsequently removed to model the notch. In order to place the notch tip exactly at the desired coordinate, three points are placed with a prescribed distance from the tip. This procedure guarantees the exact location of the shared vertex of the three corresponding rigid bodies at the notch tip.

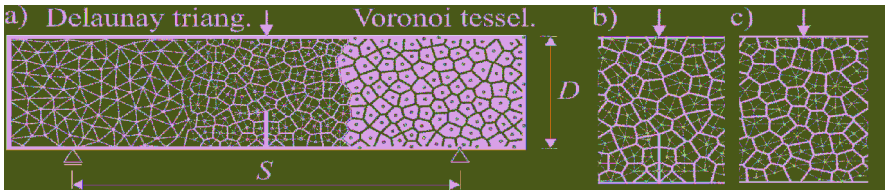


Figure 1: Specimens with and without a central notch (rel. notch depth $\alpha = 1/3$, depth $D = 0.1$ m, span $S = 0.4$ m). a) Illustration of the Delaunay triangulation corresponding to the dual graph of the Voronoi tessellation; b) and c) sketch of the central part of the specimen: with and without a notch.

Reduction of spurious mesh density effect via the incorporation of concrete mesostructure

In the homogeneous version of the model, the strength criterion defined by the breaking stress is identical for all springs. Also, the elastic normal and shear moduli are the same for all springs. The influence of network (mesh) density has to be understood as a spurious phenomenon because the mesh is arbitrary, artificial and does not arise from any real material structure. It is generally believed that the dependency of results on the network density might be removed by projecting material inhomogeneities onto the lattice. Incorporation of the grain structure introduces an internal length that decreases this dependency. In the following paragraphs this expectation is subjected to critical study which shows the limits of such a procedure.

The grain structure that is used here is generated by a computer algorithm using a Fuller curve. Typically, the maximal grain diameter d_{max} is chosen according to the real batch contents, and the minimal d_{min} according to the network density. The length of network elements should be at least three times smaller than d_{min} [9], otherwise the particles coalesce in the mesh. Grains smaller than d_{min} are ignored in the procedure. The larger the d_{min}, the smaller amount of grains included, yet changing d_{min} has no effect on coarse grains. Having small d_{min} enriches the model with small aggregates. Simulated grains are then projected onto the lattice to attribute springs with the three material phases – aggregate, matrix and the interfacial transitional zone (ITZ). These are distinguished according to the positions of nodes with respect to the mesostructure (see [9]). Each phase has a different strength and Young's modulus; values from [10] are used here.

The hypothesis tested the claim that the finer the mesostructure considered, the lower the mesh sensitivity of the model observed. To test the hypothesis, six different grain contents were generated. The first corresponds to a homogeneous case without any grains; the others differ by d_{min} (Figure 2); however, the maximum grain diameter d_{max} is kept equal to 32 mm. The mesh density varied from l_{min} equal to 2.5 mm up to a density of 0.625 mm. Note that not all the densities can be used for all the grain contents. The finer the grains, the finer the mesh required. For all possible combinations, 50 realizations of notched and unnotched TPB were simulated. In order to provide an idea of the model's behavior, Figure 3 shows average load-deflection diagrams for some of the considered densities and mesostructures. Notice the drastic strength decrease when one incorporates even only a few grains in the unnotched structure. The crack position can be sampled from many possible locations and thus the fracture always propagates along the weak ITZ. Such a steep drop in strength is not observed with notched structures: the crack propagates from the deep notch independently of the positions of the grains.

The results for the peak loads are shown in Figure 4. The homogeneous model of the notched TPB follows a straight line with a slope of 0.424. This slope differs from the expected 0.5 due to the probability of the occurrence of an inclined facet in the early stages of the crack [11, 12]. Models with grain content seem to reduce this dependency. The best results (almost a horizontal line) are achieved by the most detailed grain content. For this setting, the peak load hardly depends on the mesh density at all. In the unnotched case, the more detailed the structure, the less dependency is visible. However, for unnotched beams the trend is less apparent.

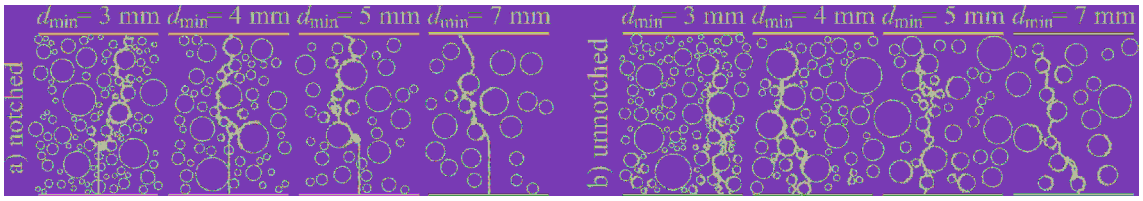


Figure 2: An example of crack patterns observed for (a) notched TPB and (b) unnotched TPB with the lattice model including concrete mesoscopic grain structure of varying fineness.

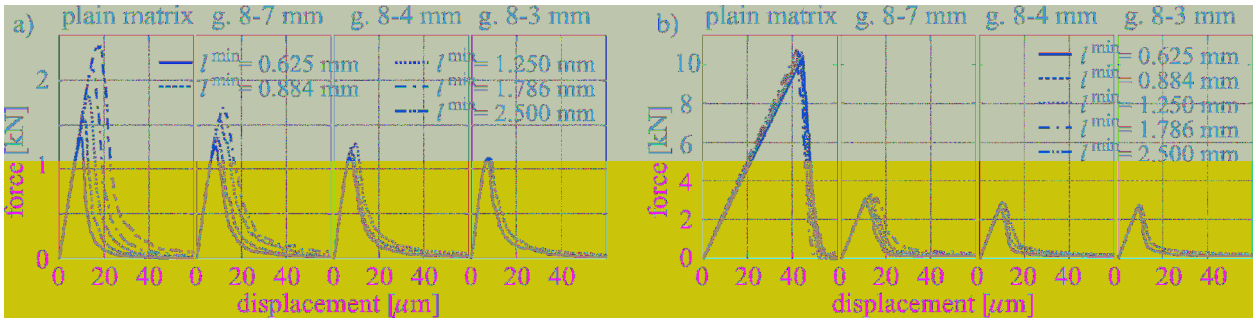


Figure 3: Average load-displacement diagrams of 50 realizations of (a) notched TPB and (b) unnotched TPB for some of the considered densities and mesostructures.

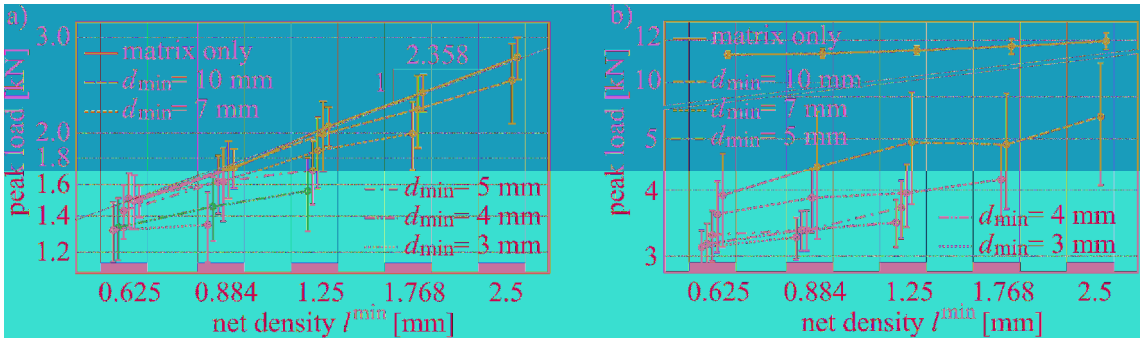


Figure 4: Dependence of maximum load for (a) notched TPB and (b) unnotched TPB on mesh density for varying incorporated grain structure.

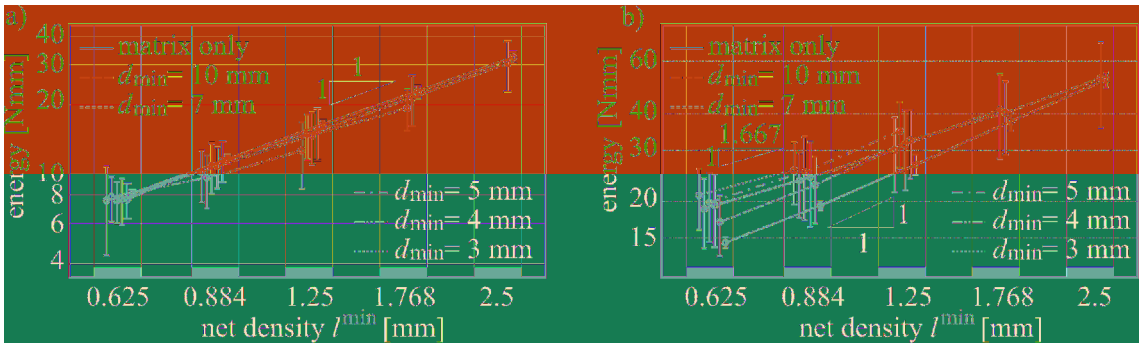


Figure 5: Dependence of the area under the load- displacement curve for (a) notched TPB and (b) unnotched TPB on mesh density for varying incorporated grain structure.

The second monitored parameter is the area under load-displacement curves, which represents energy. No substantial reduction in the dependence of this energy on the mesh density (by the incorporation of grain structure) was observed for the notched structure. Fig. 5a documents that all the lines share approximately the same rising slope. The energy dependency is only slightly reduced for the unnotched structure, see Fig. 5b. However, the line plotted for the finest resolution is far from being horizontal.

Summary

The effect of the discretization of brittle elements in lattice models for concrete was studied. Mechanical properties were assigned to the elements according to their correspondence to the three phases of concrete, namely matrix, aggregates and the interfacial transitional zone. Projecting of the concrete mesostructure onto the lattice has up to now been understood as a regularization technique that should overcome network mesh density dependency. The effect of such "regularization" was studied on both notched and unnotched beams loaded in three point bending. We report that even though the peak force dependence is reduced by the incorporation of mesostructure (and almost disappears in notched structures with the most detailed grain content), the strong dependence of the dissipated energy on mesh density is not removed.

Acknowledgement. This outcome has been achieved with financial support provided by the Czech Science Foundation under project no. P105/10/J028, and also by the Czech Ministry of Education, Youth and Sports under project no. 1M06005 (Civak). This support is gratefully acknowledged.

References

[1] E. Schlangen: *Experimental and numerical analysis of fracture processes in concrete* (Ph.D. thesis, Delft University of Technology, Netherlands 1993).

[2] J.E. Bolander, H. Hikosaka, W.-J. He: Eng. Computations Vol. 15 (1998), p. 1094–1116.

[3] P. Grassl, Z.P. Bažant: J. Eng. Mech. Vol. 135 (2009), p. 85–92.

[4] M.J. Alava, P.K.V.V. Nukala, S. Zapperi: Int. J. Fracture Vol. 154 (2008), p. 51–59.

[5] A. Jagota, S. J. Bennison: Modelling Simul. Mater. Sci. Eng. Vol. 3 (1995), p. 485–501.

[6] T. Kawai: Nucl. Eng. Des. Vol. 48 (1978), p. 207–229.

[7] J.E. Bolander, S. Saito: Eng. Fract. Mech. Vol. 61 (1998), p. 569–591.

[8] J. Eliáš: *Discrete simulation of fracture processes of disordered materials* (Ph.D. thesis, Brno University of Technology, Faculty of Civil Engineering, Brno, Czech Rep. 2009).

[9] J.G.M. van Mier: *Fracture Processes of Concrete: Assessment of Material Parameters for Fracture Models* (CRC Press, Boca Raton, Florida 1997).

[10] E.P. Prado, J.G.M. van Mier: Eng. Fract. Mech. Vol. 70 (2003), p. 1793–1807.

[11] M. Vořechovský, J. Eliáš, In: Proceedings of the Tenth International Conference on Computational Structures Technology, held in Valencia, Spain, Civil-Comp Press, Stirlingshire, Scotland, ISBN 978-1-905088-38-6, (2010) pp. 268, full papers on CD-ROM (20 pages).

[12] M. Vořechovský, J. Eliáš, In: EURO-C 2010, *Computational Modelling of Concrete Structures*, edited by Bicanic et al, CRC Press/Balkema, The Netherlands, ISBN 978-0-415-58479-1, (2010), p. 419–428.

© (2012) Trans Tech Publications, Switzerland
doi:10.4028/www.scientific.net/KEM.488-489.33

Calibration of constitutive law and ductile failure criterion for very thin rectangular Al2024-T3 aluminum alloy specimen

M.Giglio[1,a], A.Gilioli[1,b], A.Manes[1,c,*]

[1]Politecnico di Milano, Department of Mechanical Engineering,

Via la Masa 1, Milano, Italy

*Corresponding author, Politecnico di Milano, Department of Mechanical Engineering,

Via la Masa 1, 20156 Milano (ITALY),

phone ++39-02 2399 8630, Fax ++39-02 2399 8282

[a]marco.giglio@polimi.it, [b]andrea.gilioli@mail.polimi.it, [c]andrea.manes@polimi.it

Keywords: Virtual testing, FEA, Aluminum alloy, Ductile damage

Abstract. Thin plate structures are common in many industrial products and in particular they can be found as skins in sandwich panels. In order to develop complex FE analysis which involve the damage of these structures, it's crucial the knowledge of constitutive law and damage criterion of the material they are made. In this paper a complete characterization of both constitutive material law and damage criterion for very thin rectangular Al2024-T3 aluminum alloy specimen plate has been done. The specimens have been cut, using a water jet machine, directly from sandwich panel skins in order to take into account the modification of mechanical behavior due to the manufacturing process. A complete experimental campaign of tensile tests has been done and an accurate virtual testing methodology has been subsequently applied (by means on Finite Element Models) in order to numerically reproduce the tests. The calibration of a fitted constitutive law and of three ductile failure criteria allows the numerical model to reproduce the experimental tests with good agreement up to failure.

Introduction

In order to develop FE model that are able to reproduce complex phenomena it's crucial the knowledge of a detailed material constitutive law (CL). The use of general data [1] often could lead to erroneous results during simulations in extreme condition, especially in presence of technological process that can modify the mechanical behavior. In this paper a CL and three different ductile damage criteria (DC) for an Al2024-T3 aluminum alloy have been calibrated. The specimens are very thin plates (less than 1 mm) obtained by plastic deformation (rolling); therefore to take in account of the manufacturing history in the mechanical behavior, specimens have been cut directly from a sandwich panel skin. Once a robust CL has been obtained it has been possible to calibrate the DC. The approach followed in the research is virtual testing and the final results of the work are the CL and the DC which let to reproduce in the best way the real experimental curves up to failure.

Experimental test

Eight specimens have been cut from the skin of a real sandwich panel using a water jet machine. The nominal specimen dimensions have been chosen accordingly with [2]. Each specimen has been tested with an electro mechanical MTS testing machine. The load has been recorded with a load cell and displacement with an extensometer. All tests have been done in displacement control and they ended with the breakage of the specimen; the results are the load-displacement curves, Fig.1a. Experimental curves show some variability hence to find a reference curve for the FE comparison, a statistical approach has been chosen. It has been calculated the adsorbed energy for each test up to the same reference displacement of 1.1 mm. Then among the curves with the highest similarity in adsorbed energy, curve exp 331-2 has been selected as reference, Fig.1b.

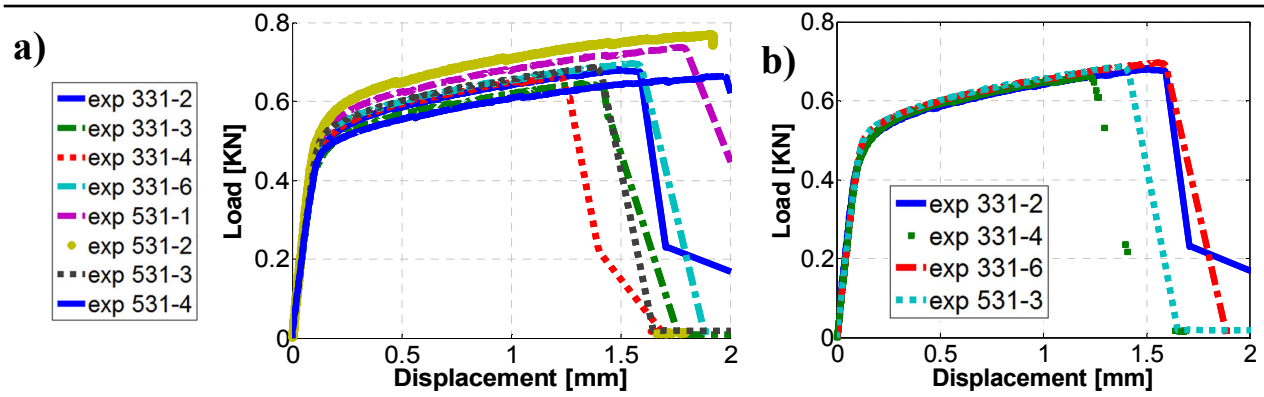


Fig.1. Experimental tensile test load-displacement curves: a) All the experimental results; b) Experimental curves with the highest similarity in adsorbed energy.

Virtual test

Numerical model

A numerical FE model has been built to numerically reproduce the tensile test. The analyses have been done with the commercial software Abaqus™ 6.9-1 with an explicit scheme. The simulations are quasi static accordingly with the approach proposed in Abaqus documentation [3]. The elements used are solid reduced brick elements C3D8R. In the model an encastre constrain has been set on one end of the specimen. On the other end the global displacement has been set, simulating the displacement of the test machine gripping. The numerical curves are obtained as matter what concerns the load as the reaction force measured at the constraint. The real displacements instead are obtained as the difference between nodal displacements of two points representing the real position of extensometer knives used during the experimental tests, Fig. 2.

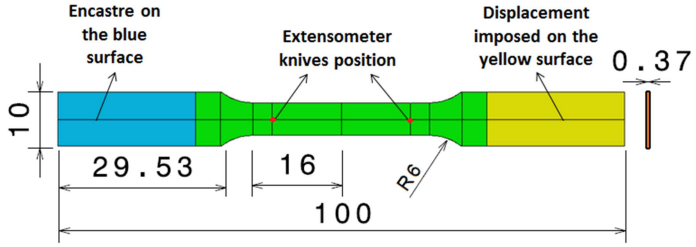


Fig.2. FE model of specimen with nominal dimensions.

Two different mesh dimensions have been tested to evaluate mesh sensibility. The first mesh has elements in the central zone of 0.5x0.375x0.6E-3 mm (6 elements through thickness). The refined mesh instead has element of 0.2x0.25x0.375x0.6E-3 mm (6 elements through thickness). In this range mesh doesn't affect results.

Calibration of constitutive law (CL) and ductile damage criterion (DC) for Al2024-T3

The calibration of the CL starts with the calculation of engineering stress and strain. Then true stress-strain curve is obtained using Eq.1, Eq. 2:

$$\varepsilon_{true} = ln(1 + \varepsilon_{eng}), \quad \sigma_{true} = \sigma_{eng} \cdot (1 + \varepsilon_{eng}) \tag{1, 2}$$

Eq. 1 and Eq. 2 are valid only before the necking phase. In the present work, due to the very low thickness of specimens, the necking practically doesn't appear thus application of Eq. 1 and Eq. 2 is correct up to specimen breakage. True stress-strain data are interpolated and the flow stress is described with a Johnson-Cook model (JC). JC plastic model can be written as:

$$\sigma = A + B \cdot \varepsilon^n \tag{3}$$

In order to find the most fitted CL, a trial and error approach has been used. In addition, according to the water-jet precision, the real geometry of the specimen can be slightly different from the nominal one; therefore all the specimens have been measured and a FE model with the average geometry has been built. The chosen material CL is described in Tab.1.

Tab.1. Material constitutive law parameters for Al2024-T3 aluminum alloy.

Material parameters for Al2024-T3			
E [MPa]	**A [MPa]**	**B [MPa]**	**n**
70000	162.5	462.2	0.2846

Once the CL has been found it is possible to calibrate DC. These criteria are based on the evaluation of the material mechanical quantities that are possible to identify during the FE analyses. The criteria used are based on the determination of the plastic strain and triaxiality (the ratio between mean stress and von Mises stress) in the most stressed area. Three different DC have been calibrated: Bao-Wierzbicki (BW) [4], void growth model (VGM) [5], stress modified critical strain (SMCS) [5]. These models are based on the determination of a damage variable which is calculated starting from a curve called fracture locus. The fracture locus is a curve that describes the plastic strain at failure depending from triaxiality. Therefore the calibration of a DC consists fundamentally in the determination of the fracture locus which let to obtain numerical fracture at the corresponding experimental displacement at failure. The DC calibrated in the present research are described by the following equations:

$$\text{VGM} \rightarrow VGI = \int_0^{\varepsilon_p^{failure}} \overline{\varepsilon_p^{failure}}(\eta)\, d\varepsilon_p = \int_0^{\varepsilon_p^{failure}} \exp(-1.5\eta)\, d\varepsilon_p > VGI_{critical}\,. \tag{4}$$

$$\text{SMCS} \rightarrow \varepsilon_p^{failure} = \alpha \exp(-1.5\eta^{critical}) > \varepsilon_p^{critical}\,. \tag{5}$$

$$\text{BW} \rightarrow D = \int_0^{\varepsilon_p^{failure}} \frac{d\varepsilon_{pl}}{\overline{\varepsilon_p^{failure}}(\eta)} = 1\,. \tag{6}$$

VGM and SMCS already have a defined shape for fracture locus, instead BW accordingly with [4] have a more complex form. BW fracture locus has to be partially arbitrary defined. Thus it has been chosen a hyperbola with equation:

$$\overline{\varepsilon_p^{failure}}(\eta) = \frac{C}{\frac{1}{3} + \eta}\,. \tag{7}$$

The results of calibration for all models are summarized in Tab.2.

Tab.2. Calibration parameters for each ductile damage criterion

VGM	**SMCS**			**BW**
$\mathbf{VGI_{critical}}$	**α**	$\boldsymbol{\varepsilon_p^{critical}}$	$\boldsymbol{\eta^{critical}}$	**C**
0.0343	0.0933	0.0566	0.333	0.0377

All the calibrated fracture locus can be seen in Fig. 3a. It's important to remark that each curve is related at a different criterion and this means that their interpretation is different. This explains why there is so much difference among them. In the same figure it can be seen the evolution of the equivalent plastic strain related with triaxiality in the most stressed area. The BW criterion is already implemented in the commercial FE software Abaqus^{TM} thus numerical simulation of tensile test has been done using this criterion. The results can be seen in Fig.3b.

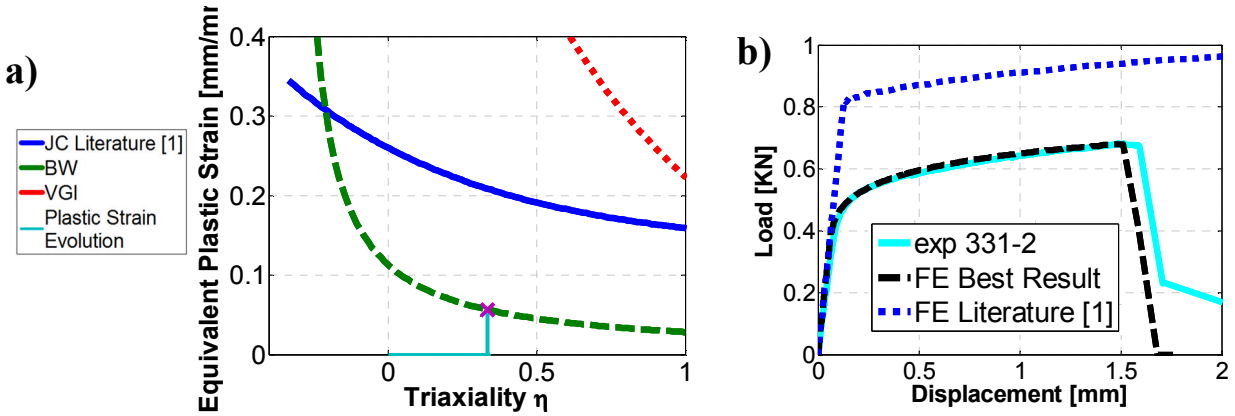


Fig.3. a) Fracture locus for Al2024-T3; b) Comparison between FE and experimental load-displacement curve with literature CL [1] and the calibrated CL with also BW DC implemented.

Conclusions

In this paper a complete characterization of very thin Al2024-T3 aluminum alloy plates have been carried on: three different DC have been calibrated. BW failure criterion has been also implemented in a FE model with very good results. As far as concerns the numerical reproduction of the real experimental tensile tests the error on the adsorbed energy between FE and experimental results is only 0.81%. The error between FE displacement at failure and the target displacement at failure (the experimental mean value between the displacements at failure of all the specimens) is equal to 5.95%. On the contrary the use of material data parameters from literature, in the implementation of material models in FE analyses, led to a not reliable result (Fig. 3b) that may effect in negative way further numerical simulations. Only BW criterion has been implemented mainly due to its wide diffusion and its high versatility. In fact adding further materials test (i.e. tensile test on notched specimens) could be very simple to assess and fit the validity of the criteria over a larger range of triaxialities. In this way is possible to get more realistic results of real components damage with various load conditions.

References

[1] Experimental Investigations of Material Models for Ti-6Al-4V Titanium and 2024-T3 Aluminum, U.S. Department of Transportation, September 2000.

[2] ASTM E8/E8M-09.

[3] Abaqus™ Analysis User's Manual v. 6.9-1.

[4] Y. Bao, T. Wierzbicki. A Comparative Study on Various Ductile Crack Formation Criteria. Journal of Engineering Materials and Technology, 126 (3) (2004), pp.314–324.

[5] A.M. Kanvinde, G.G. Deierlein, Void Growth Model and Stress Modified Critical Strain Model to Predict Ductile Fracture in Structural Steels, Journal of Structural Engineering 132 (12) (2006), pp.1907-1918.

© (2012) Trans Tech Publications, Switzerland
doi:10.4028/www.scientific.net/KEM.488-489.37

Flexural wave scattering by double elliptic holes in an infinite thin plate

HongLiang Li [1, a], Jing Guo[1,b], Xiaohua Shao[1,c]

[1]Department of Engineering Mechanics, College of Aerospace Engineering and Civil Engineering, Harbin Engineering University, Harbin, 150001, China

[a]leehl@sina.com, [b]guojing9232@hrbeu.edu.cn, [c]jiangping@hrbeu.edu.cn

Keywords: thin plate; flexural wave scattering; dynamic stress concentration factor; elliptic holes; multi local complex coordinates

Abstract. In mechanical engineering and aerospace engineering, thin plate structure is used widely. For the sake of fixing bolt, it often design open holes in the plate. Sometimes elliptic holes should be used inevitably. When the plate is overloaded or the load is changed regularly, flexural wave is propagating in the plate. Because there are holes, it can cause stress concentration. Stress concentration could decrease the bearing capacity of structure, and reduce the service life of structure. The problem of flexural wave scattering by holes in the plate is one of the important and interesting questions in aerospace engineering for the latest decades. There are lots of materials obtained by theoretical research and experimental investigation. The problem is complicated, because there are many factors influenced. It is hard to obtain analytic solutions except for several simple conditions. In this paper, based on the theory of elastic thin plate, by using wave function expansion method and multi local complex coordinates, scattering of flexural wave and dynamic stress concentration by double elliptic holes in the thin plate are investigated. In the complex plane, the displacement field aroused by incident wave and the scattering displacement field impacted by double elliptic holes comprised of Fourier-Bessel series with undetermined coefficients are constructed. Through applying the method of multi local complex coordinates, the equations with unknown coefficients can be obtained by using the stress-free condition of the double elliptic holes in the radial direction. According to orthogonality condition for trigonometric function, these equations can be reduced to a series of algebraic equations. Then the value of the unknown coefficients can be obtained by solving these algebraic equations. So the analytical solution of this problem is obtained. By using the displacement and stress expressions, an example is provided to show the effect of the change of relative location of the elliptic holes.

Introduction

In mechanical engineering and aerospace engineering, thin plate structure is used widely. For the sake of fixing bolt, it often design open holes in the plate. Sometimes elliptic holes should be used inevitably. The problem of flexural wave scattering by holes in the plate is one of the important and interesting questions in aerospace engineering for the latest decades. There are lots of materials obtained by theoretical research and experimental investigation[1-5]. The problem is complicated, because there are many factors influenced. It is hard to obtain analytic solutions except for several simple conditions.

In this paper, based on the theory of Kirchhoff thin plate, by using wave function expansion method and multi local complex coordinates, rotated coordinates system, complex function method and conformal mapping method, scattering of flexural wave and dynamic stress concentration by double elliptic holes in the thin plate are investigated. In the complex plane, the displacement field aroused by incident wave and the scattering displacement field impacted by double elliptic holes comprised of Fourier-Bessel series with undetermined coefficients are constructed. Through applying the method of multi local complex coordinates, the equations with unknown coefficients can be obtained by using the stress-free condition of the double elliptic holes in the radial direction. According to orthogonality condition for trigonometric function, these equations can be reduced to a series of algebraic equations. Then the value of the unknown coefficients can be obtained by solving these algebraic equations. So the analytical solution of this problem is obtained. By using the displacement and stress expressions, an example is provided to show the effect of the change of relative location of the elliptic holes.

Model and governing equation

The model is shown as Fig.1, an elastic infinite thin plate containing double elliptic holes. The incident angle of flexural wave is α. xoy is general coordinate system. $x_io_iy_i$ and $x_jo_jy_j$ are local coordinate system. θ_i and θ_j are angles between local coordinate system and general coordinate system.

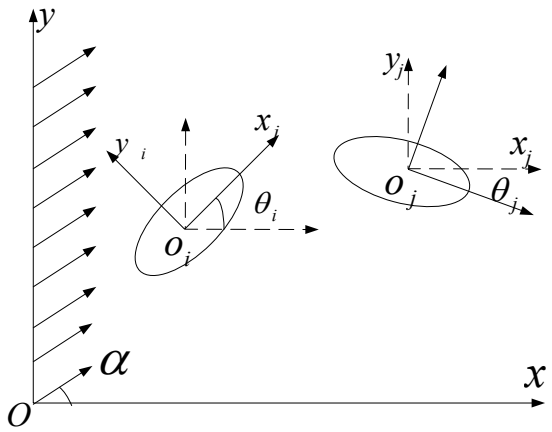


Fig.1 Model of the problem

The flexural wave equation in elastic plate can be shown as

$$D\nabla^2\nabla^2 W+\rho h\frac{\partial^2 W}{\partial t^2}=q \tag{1}$$

where $D=\dfrac{Eh^3}{12\left(1-\nu^2\right)}$ is the bending stiffness of plate, ρ is the density of plate, q is the transverse load.

Because frequency domain problem is studied in the paper, let $W(x,y,t)=W(x,y)e^{\pm i\omega t}$, and the flexural wave equation can be transformed to

$$\left(\nabla^2\nabla^2-k^4\right)W=0 \tag{2}$$

In general coordinate system generalized interior forces can be expressed as

$$M_{xx}=-D\left(\frac{\partial^2 W}{\partial x^2}+\nu\frac{\partial^2 W}{\partial y^2}\right),M_{yy}=-D\left(\frac{\partial^2 W}{\partial y^2}+\nu\frac{\partial^2 W}{\partial x^2}\right),M_{xy}=-D(1-\nu)\frac{\partial^2 W}{\partial x\partial y}=M_{yx},Q_x=-D\left(\frac{\partial^3 W}{\partial x^3}+\frac{\partial^3 W}{\partial x\partial y^2}\right),Q_y=-D\left(\frac{\partial^3 W}{\partial y^3}+\frac{\partial^3 W}{\partial x\partial y^2}\right)$$

By using complex function method, let $z=x+yi,\overline{z}=x-yi$ .For transforming elliptic holes to circular holes, conformal mapping method should be used. So let $z=\omega(\eta)$.

The scattering wave of elliptic holes can be expressed as

$$W_s^{(s)}=W_0\sum_{n=-\infty}^{+\infty}\left(A_{ns}H_{ns}^{(1)}\left(k\left|z-z_s\right|\right)\left[\frac{z-z_s}{\left|z-z_s\right|}\right]^n e^{in\theta_s}+B_{ns}H_n^{(1)}\left(ik\left|z-z_s\right|\right)\left[\frac{z-z_s}{\left|z-z_s\right|}\right]^n e^{in\theta_s}\right) \tag{3}$$

where W_0 is the transverse vibration amplitudes of incident flexural waves, $H_n^{(1)}(\cdot)$ the first kind of Hankel function and zero-order, A_{ns} and B_{ns} are unknown coefficients, z_s represents origin of local coordinates in general coordinate system.

Wave solution

The incident wave in general coordinate system should be expressed as

$$W^{(i)} = W_0 \sum_{-\infty}^{+\infty} (i)^n J_n(k|z|) \left\{ \frac{z}{|z|} \right\}^n e^{-in\alpha} \tag{4}$$

By using moving coordinate system method, it can be transformed to

$$W_s^{(i)} = W_0 \sum_{-\infty}^{+\infty} (i)^n J_n(k|z|) \left\{ \frac{z}{|z|} \right\}^n e^{-in(\alpha+\theta_s)} \tag{5}$$

The total wave is

$$W = W^{(i)} + \sum_{s=1}^{m} W_s^{(s)} \tag{6}$$

By using conformal mapping method, in local coordinate system ξ, generalized interior forces around the holes by incident wave can be given. Generalized interior forces around the holes by scattering wave can be given too.

Generalized interior forces around the holes for total wave should be express as

$$M_{rr}|_\xi = M_{rr}^{(s)}|_\xi + M_{rr}^{(i)}|_\xi, V_r|_\xi = V_r^{(s)}|_\xi + V_r^{(i)}|_\xi \tag{7}$$

The free boundary condition of elliptic holes should be express as

$$M_{rr}^{(s)}|_\xi + M_{rr}^{(i)}|_\xi = 0, V_r^{(s)}|_\xi + V_r^{(i)}|_\xi = 0 \tag{8}$$

Substituting expressions of generalized interior forces to this expression, the equations with unknown coefficients can be obtained. According to orthogonality condition for trigonometric function, these equations can be reduced to a series of algebraic equations. Then the value of the unknown coefficients can be obtained by solving these algebraic equations. So the analytical solution of this problem is obtained.

So it can be got that $M_{\theta\theta} = -D\left[\nabla^2 W - (1-\nu)\frac{\partial^2 W}{\partial r^2}\right]$. Let $M_{\theta\theta}^* = \left|\frac{M_{\theta\theta}}{M_0}\right|$, so Dynamic moment concentration factor(DMCF) around the holes could be given.

Example

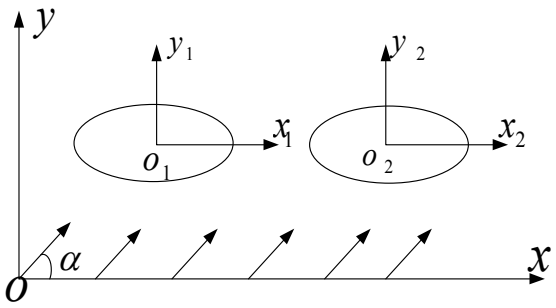


Fig.2 Calculating model

By using the expressions of total wave, an example is studied. It is shown as Fig.2. The sizes of two elliptic holes are same. The length of major axis is a, and the length of minor axis is b. The incident angle is α. The mapping function is

$$z = \omega(\eta) = r_0\left(\eta + \frac{m}{\eta}\right) \tag{9}$$

where $r_0 = \frac{1}{2}(a+b), m = \frac{a-b}{a+b}$.

The other parameters are shown in the figures.

From Fig. 3, it can be found that DMCF around the holes are symmetrical because the structure and the load are symmetrical. This result can prove that the method and the expressions got in this paper are correct.

In Fig. 4, it shows that with the increasing of ka, the value of DMCF at the tip of the left hole is changed violently. When one design such structure, this kind problem should be considered carefully.

Summary

In this paper, based on the theory of elastic thin plate, by using wave function expansion method and multi local complex coordinates, scattering of flexural wave and dynamic stress concentration by double elliptic holes in the thin plate are investigated. By using the displacement and stress expressions, an example is provided. It can be shown that the thought in this paper is useful.

Acknowledgments

Thanks for the support by the Fundamental Research Funds for the Central UniversitiesHEUCF100202.

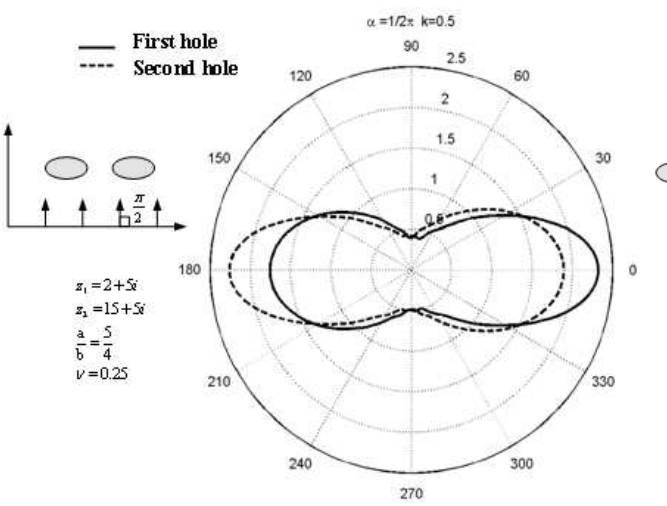


Fig.3 DMCF around the holes when $\alpha = 90^{\circ}$ and ka=0.5

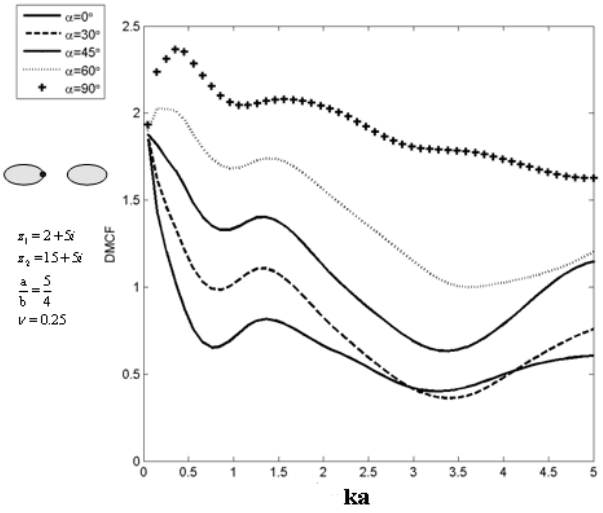


Fig.4 DMCF Vs. ka

References

[1] C. Hu, D. K. Liu: Scattering of flexural wave and dynamic stress concentrations in infinite plates. Acta Mechanica Sinica, Vol.27(1995), p.125～134(in Chinese)

[2] C. Hu, X. R. Ma, W. H. Huang: Dynamic stress concentrations in thin plates with two circular cutouts. Acta Mechanica Sinica , Vol.30 (1998),No.5, p.587-596

[3] C. Hu, X. Q. Fang, W. H. Huang: Multiple scattering of flexural waves in a semi-infinite thin plate with a cutout. International Journal of Solids and Structures,Vol.44(2007), p. 436-446

[4] K.L. Chan ,B. Smith, E. Wester: Flexural wave scattering in a quarter-infinite thin plate with circular scatterers. International Journal of Solids and Structures,Vol.46(2009), p.3669－3676

[5] W.M.Lee, J.T.Chen: Scattering of flexural wave in a thin plate with multiple circular holes by using the multipole Trefftz method. International Journal of Solids and Structures, Vol. 47 (2010), p.1118–1129

© (2012) Trans Tech Publications, Switzerland
doi:10.4028/www.scientific.net/KEM.488-489.41

Advanced finite element analysis to predict off-axis crushing behaviour of composite aero-structures

N. Ghafari-Namini[1,a], H. Ghasemenjad[1,b], M. Limbachiya[1,c]

[1,2,3] Faculty of Engineering, Kingston University, SW15 3DW, UK

[a]n.ghafari-namini@kingston.ac.uk , [b]h.ghasemnejad@kingston.ac.uk,

[c]M. Limbachiya@kingston.ac.uk

Keywords: Damage, Composites, Off-axis, FEA

Abstract: Advanced finite element analysis (FEA) is carried out to simulate the off-axis crushing process of glass/epoxy twill/weave composite box structures. The FE results were compared to relevant experimental result and it was shown that the applied model is capable to predict the damage behaviour and energy absorption of composite box aero-structures under off-axis loading condition.

Introduction

The energy absorbing capabilities of FRP composite structures have been investigated in literature by studying the effect of fibre type, matrix type, fibre architecture, specimen geometry, process conditions, fibre volume fraction and testing speed under axial loading. Most of these researches have studied crushing under axial loading. However, in a real crash event the more likely scenario is a non-axial collision. A few researches have investigated the energy absorbing capabilities of elements such as box under two types of non-axial loadings. In this paper, the off-axis crushing response of GFRP composite box is simulated by finite element software LS-DYNA and the results were verified by experimental results.

Finite element modelling (FEM)

In previous experimental study [1] the woven glass/epoxy composite box with fibre orientation of $[0]_{10}$ was crushed between two platen for 50mm stroke using a Universal Testing Machine with 500 kN load cell (see Figure 1). In the present work the GFRP composite box was modelled using finite element software LSDYNA. The size of outer cross section of the composite box was 80×80mm with a thickness of 3 mm. The composite box was modelled according to relevant angle to off-axis loading. Trigger mechanism was modelled by reducing the thickness of the first row of shell elements at the top of each box. The GFRP composite box model was based on Belytschko-Lin-Tsay quadrilateral shell elements. This shell element is based on a combined co-rotational and velocity strain. All surfaces of the model were meshed using quadratic shell element and the size of an element was 2.5×2.5mm. The striker was modelled as a rigid block using solid element.

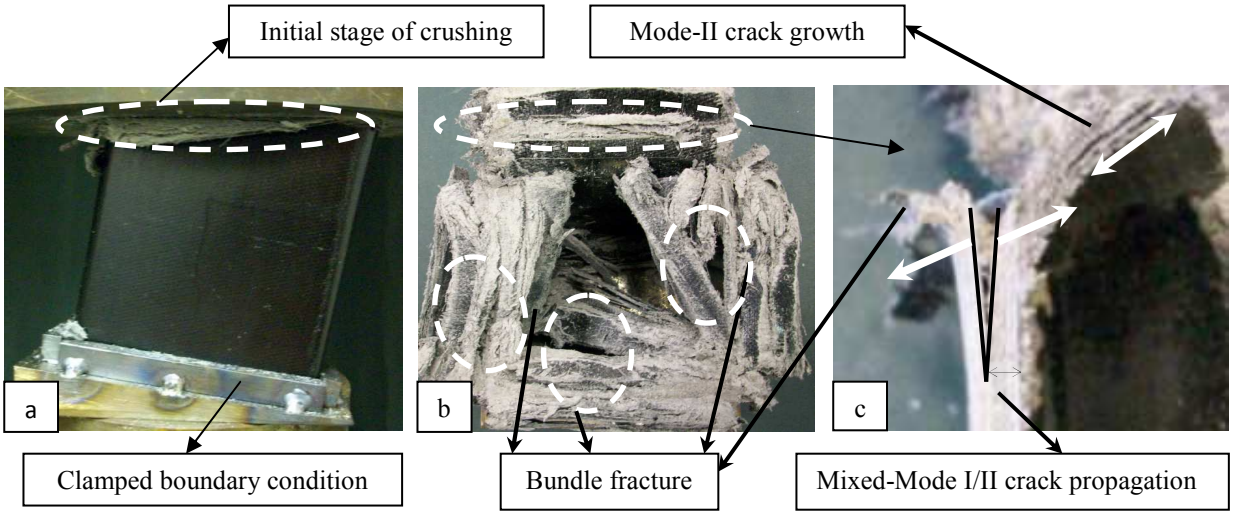


Fig. 1. Crushing process analysis of woven glass/epoxy composite box at off-axis loading of 10°, a) crushing process, b) plane view of crushed box and c) crack propagation in the wall of composite box.

Material model 54 of LS-DYNA was selected to model the damage of hybrid composite beams. The Chang-Chang failure criterion which is the modification of the Hashin's failure criterion was chosen for assessing lamina failure. The post-failure conditions in the Material 54 model are somewhat different from the original Chang-Chang equations. In this model four failure modes are categorised. These failure indicators are appointed on total failure for the laminas, where both the strength and the stiffness are set equal to zero after failure is encountered. In this model as described below all material properties of lamina are checked using the following laws to determine the failure characteristic [2, 3].

In this work the weight factor β which is defined as the ratio between shear stress and shear strength is set to 1. The material properties of GFRP were obtained from experimental work reported in [1].

The contact between the rigid plate and the specimens was modelled using a *nodes impacting surface* with a friction coefficient of 0.35 which was measured experimentally to avoid lateral movements. To prevent the penetration of the boundary by its own nodes, a *single surface* contact algorithm without friction was used. To simulate the quasi-static condition, the loading velocity of 1 m/s was applied to the rigid striker. However, the real crushing speed was too slow for the numerical simulation. The explicit time integration method is only conditionally stable, and therefore by using real crushing speed, very small time increment was required. In this study to decrease the time step increment the mass density of all materials was scaled-up by factors of 100 and 1000 with the same applied velocity. In both cases the response of internal energy was very similar with one another and the kinetic energy was negligible in comparison to internal energy. For satisfying quasi-static condition not only the total kinetic energy has to be very small compared to the total internal energy over the period of the crushing process but also the crushing force-displacement response must be independent from the applied velocity (see Figures 2 and 3).

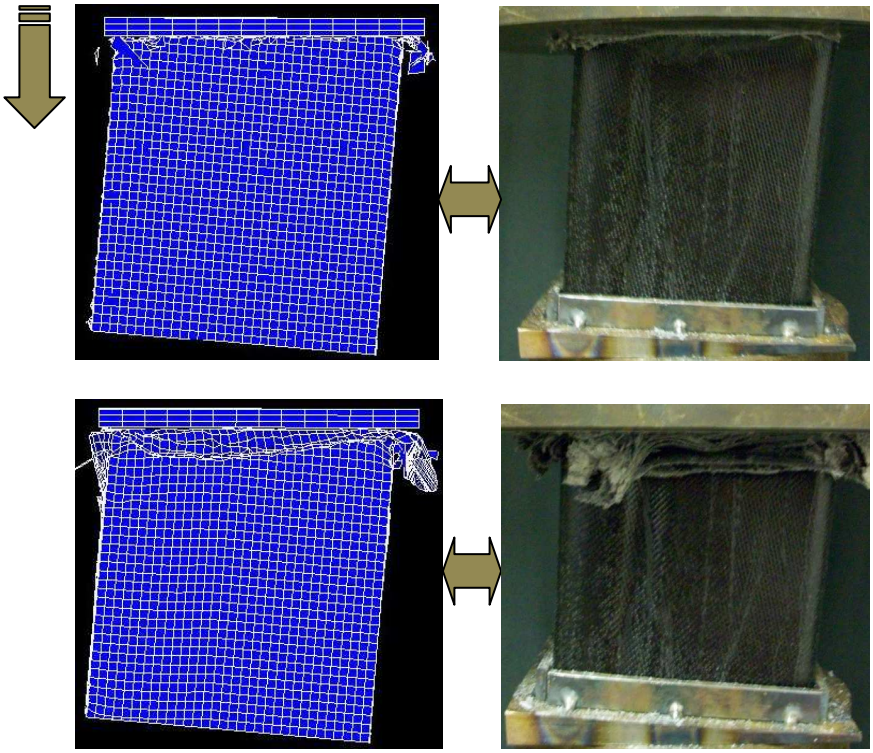


Fig. 2. Various stages of 5º off-axis angle at crushing process of GFRP composite box structures.

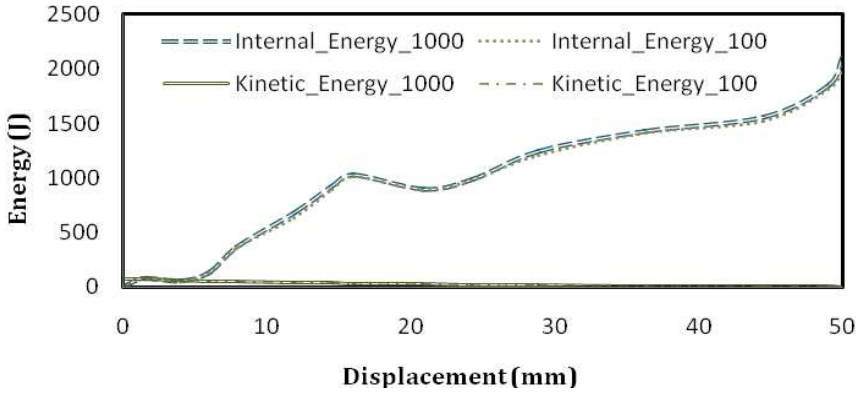


Fig. 3. Effect of mass scaling on the internal and kinetic energy in quasi-static simulation of off-axis loading of 5°.

Discussion and conclusion

In Figure 4 the force-crush distance of off-axis loading angle of 5º and 10º which were extracted from FEA model is compared with the experimental results. The difference in mean forces and energy absorption between the FEA models and experiments are less than 12% in these models.

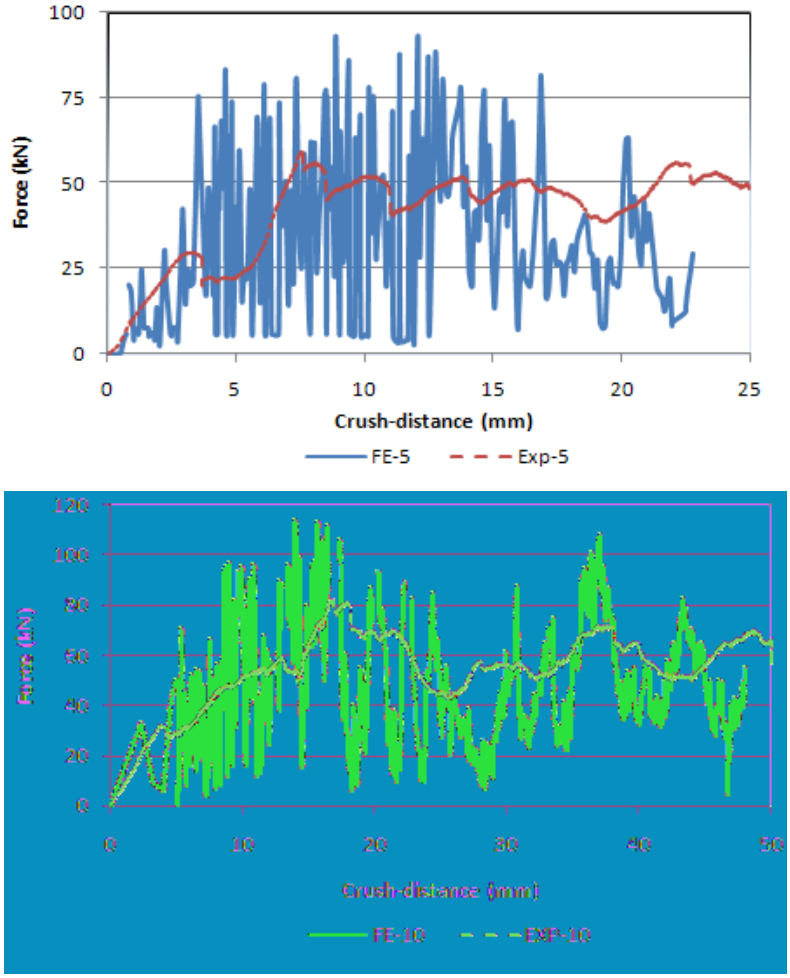


Fig.4. Comparison of experimental and FE force-crush distance results for woven GFRP composite box under off-axis loading of 5º and 10º.

References

[1] H. Ghasemnejad, H. Hadavinia, Off-axis crashworthiness characteristic of woven glass/epoxy composite box structures, in 'Journal of Reinforced Plastics and Composites', 29(15), August, pp. 2306-2330, (2010).

[2] LS-DYNA User's Manual (Non-linear Dynamic Analysis of Structures in Three Dimensions), Livermore Software Technology Corporation, 1997, Livermore, USA.

[3] H. Ghasemnejad, A.S.M. Furquan, PJ. Mason. Charpy impact damage behaviour of single and multi-delaminated hybrid composite beam structures. Materials and Design, 31(8):3653-3660, (2010).

© (2012) Trans Tech Publications, Switzerland
doi:10.4028/www.scientific.net/KEM.488-489.45

Fatigue Fracture Mechanism of Extruded Al Alloy 7075-T6 in High Humidity

K. Kariya[1,a], N. Kawagoishi[2,b], H. Maeda[2], Q. Chen [3,c], M. Goto[4,d] and Y. Nu [5,e]

[1] Dai-ichi College of Technology, 1-10-2 Kokubu-chuou, Kirishima, 899-4395, Japan
[2] Kagoshima University, 1-21-40 Korimoto, Kagoshima 890-0065, Japan
[3]Kochi National College of Technology, 200-1 Mononobe, Nankoku, 783-8508, Japan
[4]Oita University, 700 Dannoharu, Oita, 870-1109, Japan
[5] Chine Three Gorges University, Daxue road 8, Yichang, 4-43002, China
[a] k-kariya@daiichi-koudai.ac.jp, [b] hiro@mech.kagoshima-u.ac.jp,
[c] qchen@me.kochi-ct.ac.jp , [d] masagoto@cc.oita-u.ac.jp , [e] yan_nu@ctgu.edu.cn

Keywords: Fatigue, Extruded 7075-T6, Rotating bending, Humidity, Texture, Growth mechanism, Shear mode crack, Tensile mode crack

Abstract. Effect of high humidity on growth mechanism of a fatigue crack was investigated for an extruded bar of an age-hardened Al alloy 7075-T6 which had the marked texture of plane (111). Fracture in high humidity occurred by the growth of a shear mode crack under high stress levels, though a crack propagated in a tensile mode under low stress ones, macroscopically. Many voids and slip planes were observed on the fracture surface yielded by the shear mode crack. Especially most of the fracture surface was occupied by voids where the crack was small. The void percentage decreased with increasing in the crack depth. Fracture surface yielded by the shear mode crack was a plane (100). The growth direction of the shear mode crack to the cross section of specimen was about 55° corresponding to the angle composed by this plane and the texture of plane (111). These results suggest that the shear mode crack was related to microstructure, stress and environment. The growth mechanism of the shear mode crack assisted by hydrogen was proposed based on the results of the acceleration of crack growth and the formation of voids in high humidity.

Introduction

High strength Al alloys are sensitive to notch and humidity, causing the low endurance ratio. The effect of humidity on the fatigue strength is very large even in mild humidity which has no or little influence in low and medium strength alloys. It has been reported that the reason for the decrease in fatigue strength in high humidity was caused by hydrogen embrittlement [1-3]. On the other hand, the mechanism of fatigue fracture assisted by hydrogen, a ductile fracture, was proposed besides a brittle fracture. That is, some mechanisms for the degradation of strength by hydrogen have been proposed, e.g. hydrogen-induced decohesion [4], hydrogen-enhanced localized plasticity [5]. These different mechanisms may relate to stress condition and microstructure such as grain size, size and distribution of a precipitated particle, and so on. However the effect of humidity on fatigue properties was not fully understood.

In the present study, in order to investigate fatigue fracture mechanism of a high strength Al alloy in high humidity, fatigue tests were carried out for an extruded 7075-T6 which has a marked texture.

Material and experimental procedures

Material used was an extruded bar (20mm) of an age-hardened Al-Zn-Mg-Cu alloy, 7075-T6 which had the marked texture of plane (111). The chemical composition (wt. %) of the alloy was 0.09Si, 1.47Cu, 0.25Fe, 0.03Mn, 2.56Mg, 0.19Cr, 5.46Zn, 0.03Zr, 0.03Ti, and the remainder Al. The mean grain size was about 13 μm.

The mechanical properties were 527MPa of 0.2% proof stress, 673 MPa of tensile strength, 712 MPa of true fracture strength and 11.3% of reduction of area, respectively.

Fig.1 shows shape and dimensions of specimen. The specimen has a circumferential notch with a blunt and shallow shape to localize the crack initiation site and make easier the crack observation. However the stress concentration factor due to this notch is about 1.04, so this specimen can be regarded as a plain one. Prior to fatigue testing, all of the specimens were slightly electro-polished by 40 μm to secure the direct surface observation. The observations of the crack morphology and the fracture surface were conducted under a scanning electron microscope (SEM) or under an optical microscope by using the plastic-replica technique. The orientation of grain was measured by Electron Back Scatter Diffraction Pattern (EBSD) method. Fatigue tests were carried out using an Ono-type rotating bending fatigue testing machine operated at 50 Hz repetition in controlled humidity (RH) of 85% and distilled water. The deviation of humidity was RH±5% and temperature of water was 30℃±3℃.

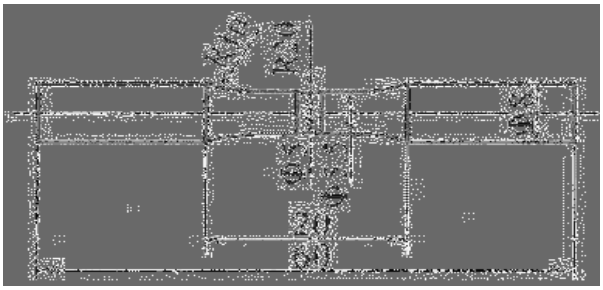
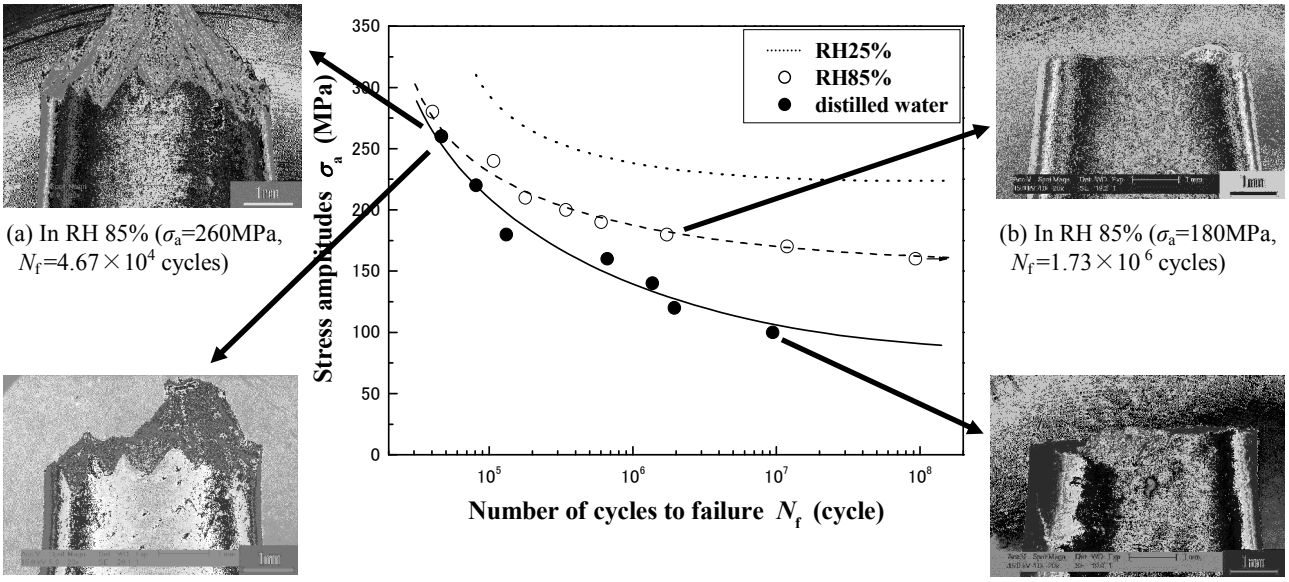


Fig. 1 Shape and dimensions of specimen.

Results and discussion

Fig.2 shows the *S-N* curves and typical morphology of a crack in RH85% and distilled water. In the figure, *S-N* relation in low humidity of RH25% [6] is also indicated by a line only. Fatigue strength was markedly decreased by high humidity and the fracture occurred by the growth of a shear mode crack in high stress levels, though most fractures yielded by the tensile one. The growth direction of a shear mode crack was about 55° to the cross section of specimen. The latter result was a well-known fracture reported in high strength metals including Al alloys by many studies [1-3]. In the following, the growth mechanism of a shear mode crack will be investigated through the detailed observation of fracture surface.



(a) In RH 85% (σ_a=260MPa, N_f=4.67×10^4 cycles)

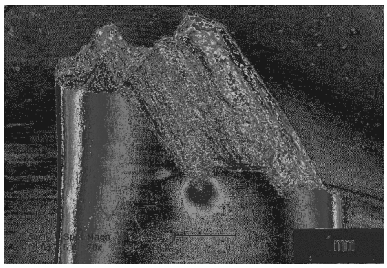
(b) In RH 85% (σ_a=180MPa, N_f=1.73×10^6 cycles)

(c) In distilled water (σ_a=260MPa, N_f=4.67×10^4cycles)

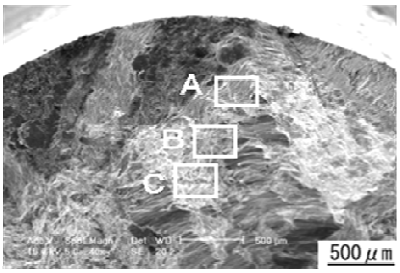
(d) In distilled water (σ_a=100MPa, N_f=9.46×10^6cycles)

Fig.2 S-N curves and morphology of a crack in RH85% and distilled water.

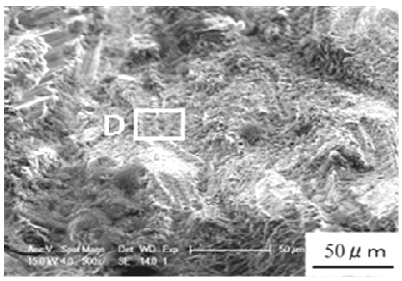
Fig.3 shows detailed fracture surfaces yielded by a shear mode crack in RH85%. There are many slip planes and voids on the fracture surface, meaning that the growth of a shear mode crack was yielded by a ductile fracture. Especially, most of fracture surface was occupied by voids when a crack length was small and the void percentage decreased with increasing in crack length. Moreover, precipitated particles are observed in voids. These features were similar to the ones in water, though the depth of void distribution was larger in water. On the other hand, as seen in Fig.4, many brittle facets were observed in addition to striations when a crack propagated in tensile mode under low stress levels in RH85% similar to the results in many studies [1-3].



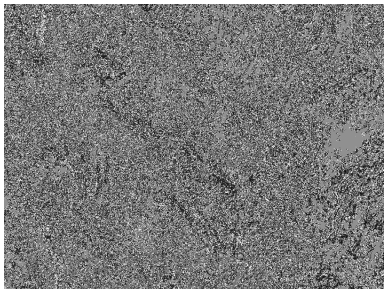
(a)Morphology of crack



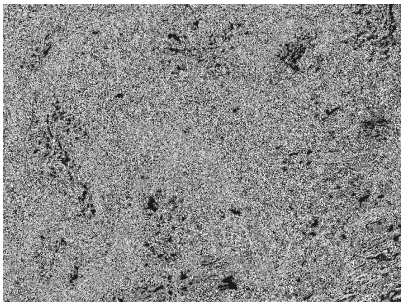
(b)Overview of fracture surface



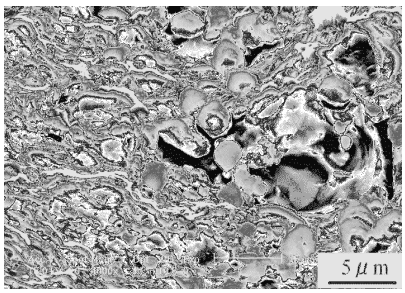
(c)Part A in Fig.(b)



(d)Part B in Fig.(b)



(e)Part C in Fig.(b)



(f)Part D in Fig.(c)

Fig.3 Fracture surface of shear mode growth (RH85%, σ_a=240MPa).

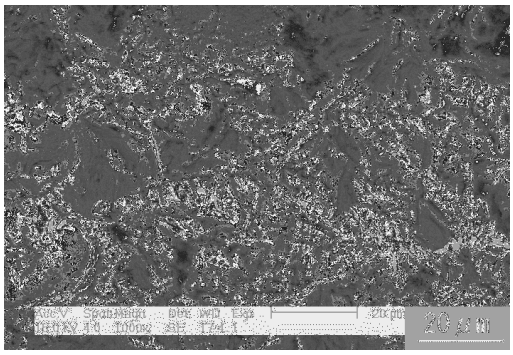


Fig.4 Fracture surface by tensile mode growth (RH85%, σ_a=180MPa).

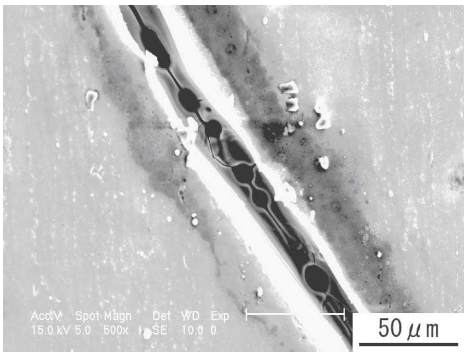


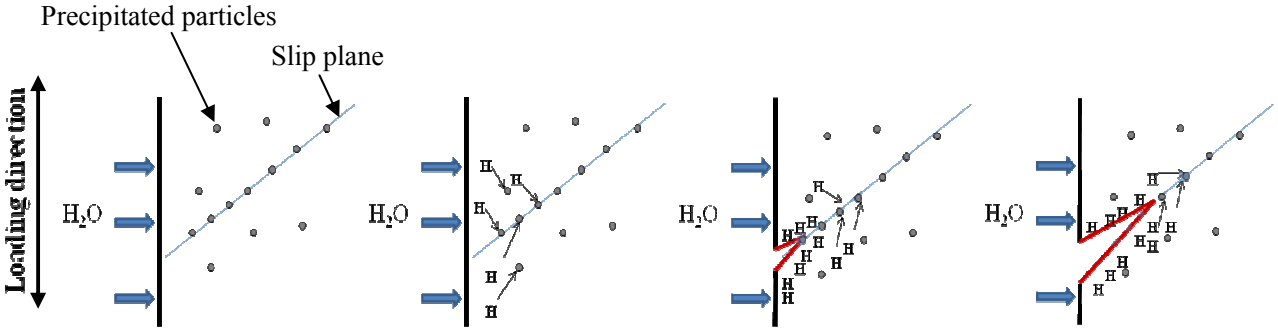
Fig.5 Opened state of a shear mode crack in water.

Fig.5 shows an example of the opened state of a shear mode crack in water. The configuration inside of a crack indicates that voids coalesced each other by shearing, corresponding to the fracture surface shown in Fig.3.

From the results mentioned above, the growth mechanism of a shear mode crack may be explained as follows: The growth of a shear mode crack yielded by formation and coalescence of voids and precipitated particles were observed inside of voids. Furthermore, the growth of a shear mode crack occurred in high humidity, meaning that hydrogen may diffuse into the alloy and accumulates at the plastic zone, i.e. dislocation, and a precipitated particle around a crack tip. Under stress loading, voids

may be formed and grow followed by hydrogen-enhanced localized plasticity mechanism and then voids coalesce each other by shearing. The coalescence and shearing of voids may be also assisted by hydrogen. This deformation and growth process yields on a slip plane, because many particles distribute on the slip planes [7]. On the other hand, it was confirmed that the alloy had a marked texture, plane (111) in cross section of the specimen [6] and fracture surfaces in both environments were a plane (100). Consequently, the growth of a shear mode crack was restricted to a specific direction, <100> of a plane (100), corresponding to the angle composed by both planes (111) and (100).

Fig.6 shows the above mentioned explanation schematically.



(a) Before fatigue test

(b)Transportation of hydrogen to precipitated particles

(c)Formation of void and its growth assisted by hydrogen

(d)Coalescense of voids and growth of a shear mode crack assisted by hydrogen

Fig.6 Schematic illustration of growth mechanism of a shear mode crack in high humidity.

Conclusions

Fatigue fracture mechanism of a high strength Al alloy in high humidity was investigated for an extruded 7075-T6. Fatigue fracture occurred by the growth of a shear mode crack and fracture surface was occupied by many voids and slip planes, meaning that the fracture was a ductile one, at high stress levels in RH85% and water. The void percentage decreased with increasing in crack length. As the growth mechanism of a shear mode crack, formation and coalescence of voids assisted by hydrogen was proposed.

Acknowledgement

The authors would like to acknowledge Mr. T. Fukudome, for his generous support on experiment.

References

[1] T. Broom and A. Nicholson, Journal of the Institute of Metals, Vol.89 (1961), p.183

[2] K. Endo and K. Komai, Jour. of the Society of Mater. Sci. in Japan, Vol.26 (1977), p.143

[3] R.E. Ricker and D.J. Duquette, Metallurgical Transactions, Vol.19A (1988), p.1775

[4] A.R. Troiano, Transaction of ASM, Vol.52(1960), p.54

[5] C.D. Beachem, Metallurgical Transactions, Vol.3 (1972), p.437

[6] N. Kawagoishi, K. Kariya, N. Yan, S. Furumoto and E. Kondo, Key Engineering Materials, Vols. 452-453(2010), p.745

[7] Microstructure and properties of aluminum, Ed. by Jour. of Japan Institute of Light Metals, (1991), p.302

© (2012) Trans Tech Publications, Switzerland
doi:10.4028/www.scientific.net/KEM.488-489.49

VALIDATION OF MODIFIED LEMAITRE'S ANISOTROPIC DAMAGE MODEL WITH THE CROSS DIE DRAWING TEST

M.S. Niazi[1, a], H.H. Wisselink[1, b] and T. Meinders[2, c]

[1] Materials Innovation Institute, P.O. Box. 5008, 2600 GA Delft, The Netherlands

Faculty of Engg. Tech., University of Twente, 7500 AE Enschede, The Netherlands

[a]M.Niazi@m2i.nl, [b]H.Wisselink@m2i.nl, [c]V.T.Meinders@utwente.nl

Keywords: Anisotropic damage, Cross die drawing, DP steels, Strain rate dependency.

Abstract. Dual Phase (DP) steels are widely replacing the traditional forming steels in automotive industry. Advanced damage models are required to accurately predict the formability of DP steels. In this work, Lemaitre's anisotropic damage model has been slightly modified for sheet metal forming applications and for strain rate dependent materials. The damage evolution law is adapted to take into account the strain rate dependency and negative triaxialities. The damage parameters for pre-production DP600 steel were determined. The modified damage models (isotropic and anisotropic) were validated using the cross die drawing test. The anisotropic damage model predicts the crack direction more accurately.

Introduction

Failure prediction of Dual Phase (DP) steels, during forming processes, is posing a challenge in the field of material modeling. The formability of these materials is limited mainly due to damage development [1]. In general, the process of damage development is anisotropic [2,3]. This article focuses on the development of a damage model which can accurately predict failure in advanced high strength steels. For this purpose the Lemaitre's damage models [4] have been modified and validated using a cross die drawing test. The cross die drawing is an appropriate test to check the formability of a material because of the variety of stress states and strain path changes that occur during the drawing process [5].

Modified Lemaitre's Anisotropic Damage Model

Lemaitre's anisotropic damage model is based on the hypothesis of strain equivalence. The damage variable is taken as a second order tensor denoted by $\mathbf{D}$. The damage evolution is defined as a function of the plastic strain rate.

$$\dot{\mathbf{D}} = \left(\frac{\overline{Y}}{S}\right)^{s} \left|\dot{\boldsymbol{\varepsilon}}_p\right| \quad \text{from } \varepsilon_I^p > \varepsilon_D^p \quad \text{up to } D_I > D_c \quad \text{where} \quad \overline{Y} = \frac{\tilde{\sigma}_{eq}^2 \tilde{R}_v}{2E} \,. \tag{1}$$

Where $|...|$ represents the absolute principal values of the plastic strain rate tensor, $\tilde{\sigma}_{eq}$ is the equivalent effective stress, S and s are damage parameters, ε_D^p is the threshold for damage development, D_c is the critical damage value, E is the Young's modulus and $\tilde{R}_v$ is a function of the triaxiality based on the effective stress. Further details of the model can be found in [4].

In this work some modifications are made to Lemaitre's model to improve its accuracy:

1. The damage evolution defined in Eq. 1 gives the same damage development under tension and compression states. This is not true for metals where damage development mainly constitutes of void growth. Therefore the parameter S in Eq. 1 is modified to S_c using a factor u_f for negative hydrostatic stresses.

$$S_c = S \times u_f \qquad \text{for} \qquad \tilde{\sigma}^H < 0 \,. \tag{2}$$

Selecting a high value of u_f will give negligible damage development under compression.

2. The post localization strain for DP steels increases with increase in the deformation rate [6]. This phenomenon is linked to the temperature rise in the material with increasing strain rates. The temperature rise enhances the ductility and thus reduces void nucleation and allows the voids to grow larger. Hence, the two damage parameters s and D_c are made a function of strain rate to account for the strain rate effect on damage evolution. These functions are selected such that to fit tensile experiments at different strain rates.

$$D_c = D_{c0}\left[\ln\left(1+\frac{\dot{\varepsilon}_{eq}^{p}}{\dot{\varepsilon}_0}\right)+0.3068\right] \text{ with } D_c = \min\left(D_c,1\right) \text{ and } D_c = \max\left(D_c, D_{c0}\right). \quad (3)$$

$$s = s_0\left[\ln\left(1+\frac{\dot{\varepsilon}_{eq}^{p}}{\dot{\varepsilon}_0 \cdot s_0}\right)+0.6517\right]^{-\frac{1}{s_0}} \text{ with } s = \min\left(s, s_0\right). \quad (4)$$

Where D_{c0} and s_0 are the reference parameters determined at the reference strain rate $\dot{\varepsilon}_0$. These modifications slow down the damage development and initiates fracture at higher damage values for a higher strain rate.

The above mentioned modifications were also made to the Lemaitre's isotropic damage model.

Damage Parameter Identification

There are four damage parameters which need to be determined i.e. ε_D^p, D_{c0}, S and s_0. The fast identification method [4] given by Lemaitre was used to determine these parameters. This methodology uses the data from a tensile test and a low cycle fatigue test. The tensile test was taken at a very low average strain rate i.e. 0.001/sec. This value is the reference strain rate which is used in Eq. 3 and 4. The values obtained from the fast identification methodology are given in Table 1. These parameters are validated by simulating the tensile test at the reference strain rate (Fig. 1). No inverse fitting was used to fit the parameters and the same parameters are used for the isotropic and anisotropic damage models. Von Mises yield criterion was used as the material was found to be almost isotropic. A physically based strain rate dependent isotropic hardening model 'Extended Bergstrom hardening' [7] was used. The parameters for this model were fitted to tensile tests at different strain rates.

Table 1: Damage parameters for DP Steel determined from the fast identification method.

Parameter	ε_D^p	D_{c0}	S	s_0
Value	0.18	0.1789	1.398	2.3

High strain rates tend to increase the post localization strain in DP steels [6]. This behavior is incorporated in the damage model using Eq. 3 and 4. A tensile test was carried out at a higher strain rate i.e. 0.038/sec which gave ~2% higher strain than that achieved from the test at the reference strain rate. This test was then simulated with the same damage parameters given in Table 1. The comparison of the simulations with experiments is shown in Fig. 2. The damage models predicted the failure approximately at the correct maximum strain for this test whereas the simulation without damage over predicts the failure considerably. If Eq. 3 and 4 are not used then the damage models under predict the failure strain.

Validation of the Modified Lemaitre's Damage Model

The damage models are validated using the cross die drawing test. These tests were carried out at an average strain rate of 1/sec. Fig. 3 compares the force displacement curves of the simulations with the experiments. Among the two experiments shown in Fig. 3, one localized (slightly cracked) at a punch displacement of 39.6mm whereas the other did not localize. The simulation without damage

clearly shows an over prediction of the critical punch depth whereas the simulation with the damage models predicts localization at ~39mm punch depth. The damage models under predict the critical punch depth when Eq. 3 and 4 is not used. Fig. 4 shows the comparison of the major strain distribution along the section where the maximum principal strains occurs in the experiments. The strain distribution was measured on the inner surface (facing the punch) of the blank. The strain distribution presented in Fig. 4 is taken from the experiment which did not localize at 39.6mm. The strain did not localize for the simulation without damage and thus gives good agreement with the experimental strain. The strains obtained from the simulations with damage are in good agreement throughout the section except for the part where localization took place. The slight crack in the other experiment occurred almost at the same location as predicted by the damage models. This region is found to be under the plane strain condition.

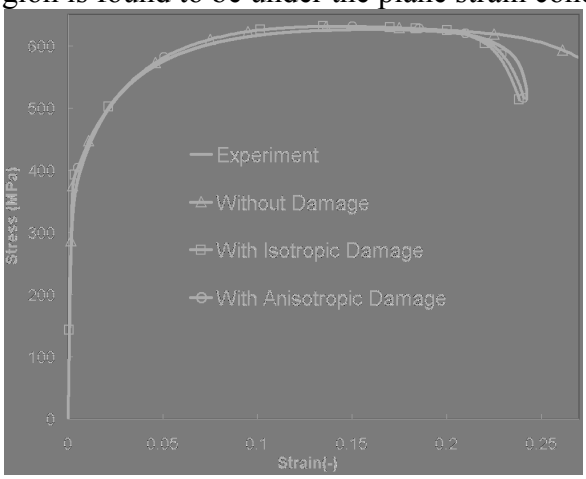


Figure 1: Validation of the damage parameters at reference strain rate tensile test.

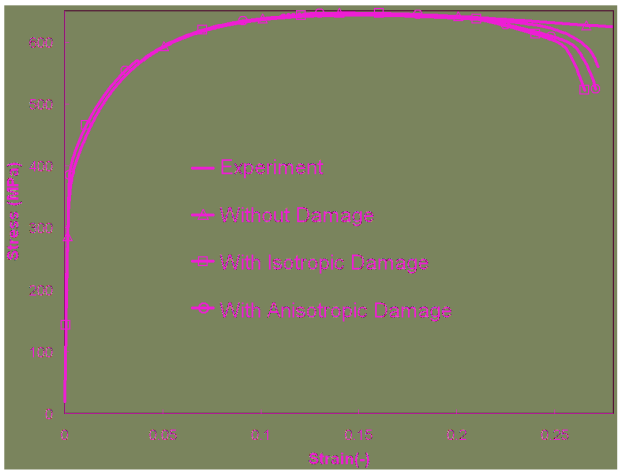


Figure 2: Validation of Eq. 3 and 4 using tensile test at strain rate 0.038/sec

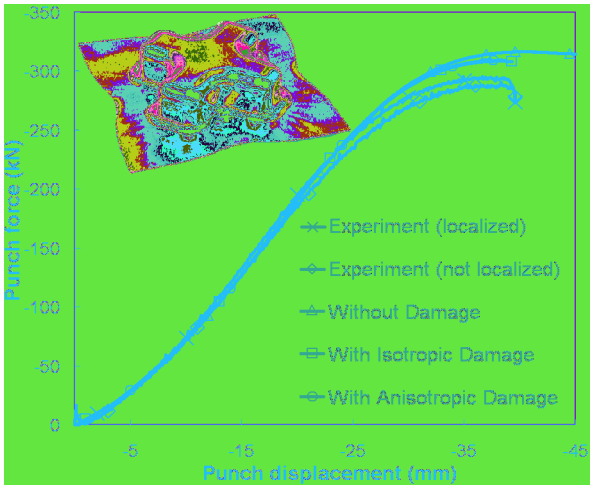


Figure 3: Force-Displacement curve for the cross die test.

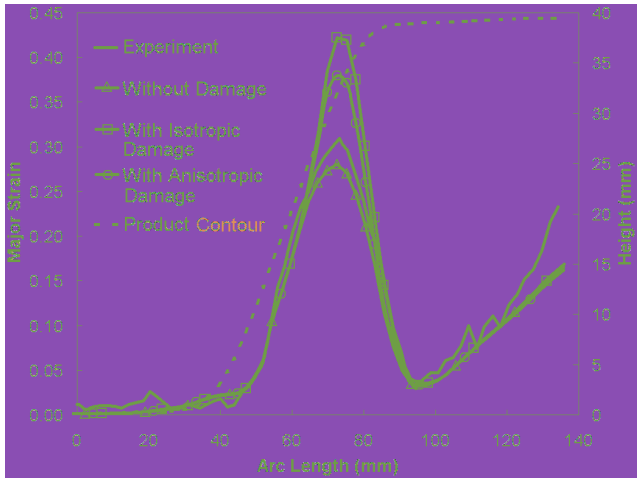
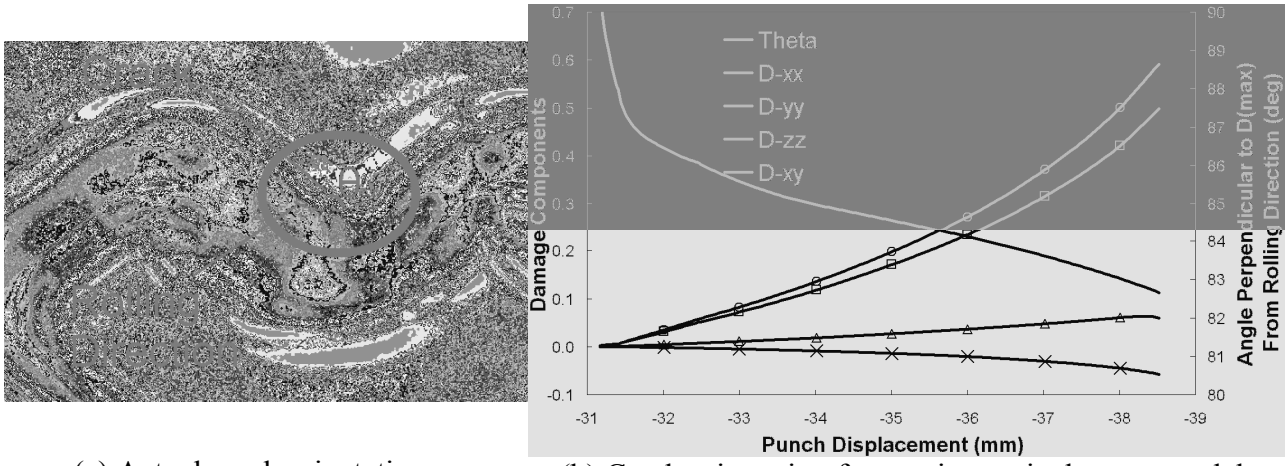


Figure 4: Major strain distribution along the section with maximum strain in the cross die test.

A scalar damage variable is used in isotropic damage model; therefore the information regarding the crack direction can not be obtained from the damage variable. A common approach is to take the crack propagation plane orthogonal to the maximum principal stress direction. This assumption gives inaccurate crack directions if the material undergoes non-proportional load path changes. The crack angle θ, as shown in Fig. 5(a) was determined for the isotropic damage model and the value of θ is found to be ~68^{o}, which is not very accurate. For anisotropic damage, the crack direction can be determined based on the principal damage direction. Fig. 5(b) shows the principal damage direction for anisotropic damage. The crack angle θ is found to be ~83^{o}, which is very close to what is found in the experiments. Using anisotropic damage is clearly advantageous for predicting the crack direction.

Conclusions

The Lemaitre's damage model was modified to take into account strain rate dependency and negative triaxialities. The modified model was validated with the cross die test. The simulation results are in good agreement with the experiments. The crack direction predicted from the isotropic damage model simulation deviates from the experiments whereas the anisotropic damage model simulation predicted the crack direction more accurately. This difference is mainly due to non-proportional strains. All the damage parameters were obtained from uniaxial conditions and were successfully used to predict failure in a forming process with a variety of triaxilities ranging from compression to biaxial conditions. The failure was predicted in a region with plane strain condition at almost the exact critical punch depth found from experiments.



(a) Actual crack orientation. (b) Crack orientation from anisotropic damage model.

Figure 5: Prediction of crack direction.

This research was carried out under the project number M61.1.08308 in the framework of the Program of the Materials innovation institute M2i (www.M2i.nl).

References

[1] C.C. Tasan, J.P.M. Hoefnagels, C.H.L.J. ten Horn and M.G.D. Geers, Mechanics of Materials Vol. 41(2009), p. 1264–1276.

[2] M.S. Niazi, H.H. Wisselink, V.T. Meinders and C.H.L.J. ten Horn, Steel Research International Vol. 81-9(2010), p. 1396-1399.

[3] C.L. Chow and J. Wang, International Journal of Fracture Vol. 33(1987), p. 3–16.

[4] J. Lemaitre and R. Desmorat: Engineering Damage Mechanics (Springer).

[5] E.H. Atzema, C.H.L.J. ten Horn and H. Vegter, In Proceeding of European congress on computational methods in applied sciences and engineering (2004).

[6] H. Huh, S.B. Kim, J.H. Song and J.H. Lim, International Journal of Mechanical Sciences Vol. 50(2008), p. 918–931.

[7] H. Vegter, C.H.L.J. ten Horn, Y. An, E. Atzema, H.H. Pijlman, T.H. van den Boogaard and H. Huétink, In Proceedings of COMPLAS VII (2003).

© (2012) Trans Tech Publications, Switzerland
doi:10.4028/www.scientific.net/KEM.488-489.53

Probabilistic fracture resistance of a forged quality medium carbon alloy steel

K. K. Ray[1, a] and R. N. Jha[2,b]

[1]Department of Metallurgical and Materials Engineering, Indian Institute of Technology, Kharagpur-721302, India

[2]Metal and Steel Factory, Ishapore-743144, India

[a]kkrmt@metal.iitkgp.ernet.in, [b]rnjha75in@yahoo.co.in

Keywords: Probabilistic fracture; Quality control; impact toughness; fracture toughness; alloy steel;

Abstract. Impact and fracture toughness of a large number of medium carbon alloy steel specimens have been ascertained using standard ASTM procedures, apart from examining their chemistry, microstructure, cleanliness, tensile behaviour and fracture surfaces. The results indicate that the scatter associated with ductility, impact and fracture toughness is considerable unlike that for strength or hardness. Analyses of the role of undesirable elements on toughness properties indicate that the scatter associated with fracture resistance of the steel primarily originates from the amount of tramp elements

Introduction

Low alloy steels with medium carbon-content having Ni, Cr, Mo and V as primary alloying elements e.g. AISI 4335 steels are widely used in several heavy-duty components like various armaments for their suitable combination of hardness, strength and toughness properties. The manufacturing process for these steels usually consists of primary melting in electric arc furnace, secondary refining in ladle furnace facilitated with vacuum degassing, casting in to ingots, electro slag refining followed by forging and heat treatment, which consists of homogenizing, quenching and tempering. The resultant tempered martensitic microstructure exhibits the desired combination of strength, ductility and toughness properties in these steels [1-5]. The processing of the material up to ESR is aimed to reduce the inclusion content and the undesirable elements whereas the heat treatment is done to achieve suitable degree of ductility and toughness at the cost of hardness and strength. In general these steels are often used in critical service conditions, and the current design concepts necessitate database on fracture toughness and crack growth characteristics. Unfortunately limited information [6] is available on fracture toughness and fatigue behaviour of AISI 4335 steel. The primary motivation in this report is to generate a suitable database for fracture toughness of AISI 4335 steel and to examine its reliability for design considerations by analyzing its variation in different production batches.

The possible threats to consistent fracture toughness of AISI 4335 steel could originate from the uncertainties associated with the extent of tramp elements, volume fraction of inclusions, homogeneity of the cast and forged ingots, and improper heat treatment. An attempt has been made, therefore, to examine the overall influence of these processing factors on the probabilistic fracture resistance of a selected commercial grade of vanadium bearing AISI 4335 steel, termed henceforth as 4335V steel.

Experimental Details

Material, Heat treatment and Microstructure. A large number (125 heats) of commercial AISI 4335V steel forgings were selected for this study. These steels were produced through electric arc furnace-ladle furnace-vacuum degassing-electroslag remelting route. The compositions of the steels

exhibit C = 0.33-0.40, Si = 0.09-0.38, Mn = 0.26-0.51, S = 0.001-0.006, P = 0.002-0.012, Ni = 2.96-3.35, Cr = 0.84-1.11, , Mo = 0.48-0.66, V = 0.13-0.19, Sn = 0.001-0.011, Sb = 0-0.009, As = 0-0.015 wt. % and balance Fe. The as-received forgings were subjected to heat treatment schedule as described earlier [3] and exhibit tempered martensitic microstructure.

Conventional Mechanical Properties. Hardness measurements of the samples were done using Brinell hardness tester at a load of 3000 kg. Tensile tests were performed using 40 Ton universal testing machine at a nominal strain rate $4.2x10^{-4}sec^{-1}$ using an extensometer of 50mm gauge length at room temperature following ASTM standard E8M-03 [7]. The tensile properties were obtained by analyzing the load elongation data. Charpy Impact Tests were carried out at ambient temperature and at sub-zero temperature (-50°C) as per ASTM Standard E23-03 [8].

Fracture Toughness Test. Fracture Toughness (FT) tests were carried out using 25 mm thick Compact tension specimens with C-R orientation having dimensions as per ASTM standard E399-05 [9], at room temperature in a 250 kN INSTRON Machine (Model: 8803). The specimens were first subjected to fatigue pre-cracking at a stress ratio of R = 0.1 using a frequency of 10Hz. The load-CMOD plot for each specimen was recorded using a clip gauge for subsequent analysis to estimate their fracture toughness values. The lengths of the machined and the fatigue pre-cracked regions were measured on the broken fracture surfaces. Fractured surfaces were next examined using a JEOL (model: JSM-5800) scanning electron microscope to record a series of fractographs for subsequent analysis.

Results and Discussion

Composition, Microstructure and Mechanical Properties. The compositions of the selected steels are closely at par with that of AISI 4335 grade [3,6] having small addition of vanadium. The variations in the alloying elements (Ni, Cr, Mo, V), in general, are less as compared to that of the undesired elements (S, P, Sn, Sb and As). The volume fraction of inclusions (VI) of the steels measured for 25 heats is found to be between 0.033-0.064%. The estimated conventional mechanical properties like Brinell hardness (BHN), yield strength (YS), ultimate tensile strength (UTS), %elongation (EL) and %reduction in area (RA), impact energies (IE) at room temperature (RT) and at sub-zero temperature (-50°C) were examined as bar charts; a typical variation of YS with heat number is shown in Fig. 1(a). The estimated values of mechanical properties averaged over all the heats of the selected steels are: hardness: 428.3±9.0 BHN. YS: 1330±29.4 MPa, UTS: 1434±24.4 MPa, %elongation: 12.51±0.83, %reduction of area: 47.18±3.39, Impact energy (RT): 45.89±5.56 J and Impact energy (-50°C): 36.05±4.16 J.

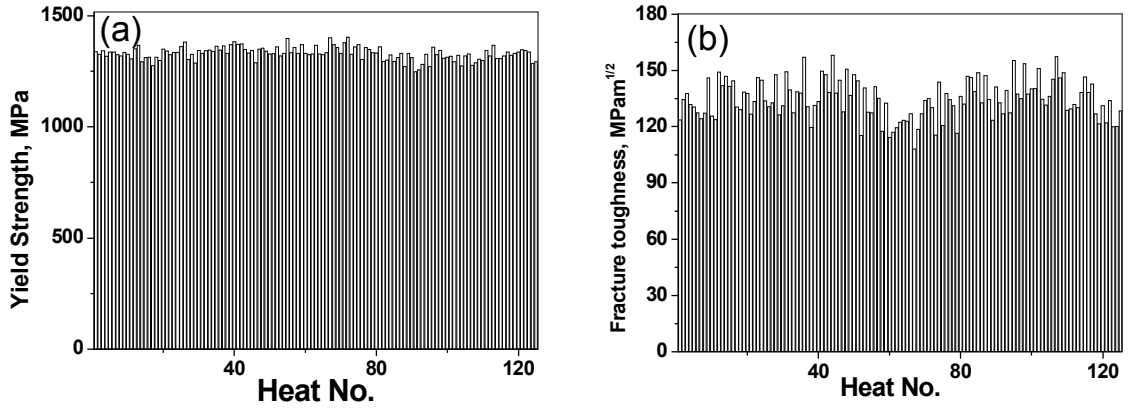


Fig. 1 Bar chart indicating variation of (a) yield strength (b) fracture toughness for various production batches

The tensile properties of the selected AISI 4335V steels are in good agreement with the reported values by Hertzberg [6] and Kerns and Stahle [10]. Quantitative comparisons of the nature of variations in the constituent elements and mechanical properties are made using their co-efficient of

variations (CEV=SD/Mean) in Fig. 2. The estimated results indicate that the relative scatter associated with strength and hardness values are insignificant compared to those associated with ductility and toughness values. Examinations of Fig. 2(a) and Fig. 2(b) infer that the significant scatter associated with ductility and toughness properties can be attributed to the variations in the undesired elements.

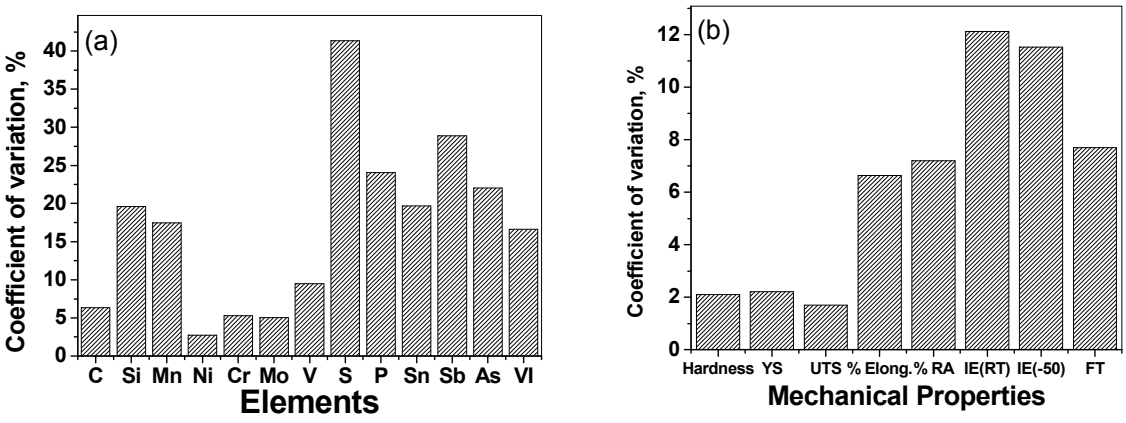


Fig. 2: Coefficient of variation plotted against (a) elements and (b) mechanical properties of the selected grade of steels

Fracture Toughness Test Results. The critical load for crack initiation (P_Q) for estimating equivalent fracture toughness values (K_Q) was determined by the standard 5% secant method while the K_Q values of the specimens were calculated using equation A4.1 and A4.2 given in ASTM standard E 399-05 [9] and are depicted in Fig. 1(b). Almost 80% of the estimated K_Q values could be considered as K_{IC}; valid thickness criterion for K_{IC} could not be achieved when K_Q is > 139 MPa√m. The average K_Q for the selected steels is calculated as 134.6 ±10.3MPa√m which is in good agreement with some reported results on similar steels [6,11]. In general, it can be inferred that like IE and ductility, fracture toughness values also reveal large variation from batch to batch (Fig. 2(b)). The fractured surfaces of the broken samples exhibited primarily quasi-cleavage feature with microvoids and intergranular facets, typically representative of fractured specimens having tempered martensitic structures.

Influence of Tramp Elements on Toughness Characteristics. An examination of the variations in the tramp elements (P, Sn, Sb and As) vis-à-vis that of the mechanical properties infers that the former have pronounced influence on the ductility and toughness of the selected steels; this gets particularly evident when one compares their corresponding CEV values of their inter-dependence as shown in Fig. 3, which lead to the obvious conclusion that the primary origin of scatter in ductility and toughness of the selected steels is due to the total amount of the tramp elements.

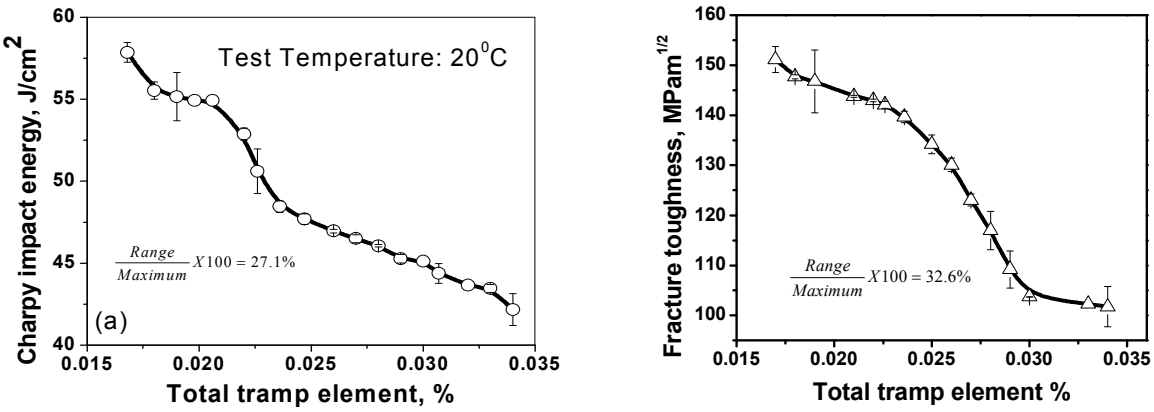


Fig. 3: Influence of tramp elements on (a) Charpy impact energy and (b) fracture toughness

Probabilistic Fracture Resistance. The estimated K_Q values were subjected to various types of probability distributions followed by assessment of the correlation coefficients (CC) of the probability plots. The generated data of K_Q could be excellently described (Fig. 4) by normal distribution (CC=0.997) rather than by Weibull distribution (CC=0.978) for 99% confidence level. The lower bound of the average value of FT from the distribution analysis was found to be 132.6 MPa√m which is well above the required specification for the commercial grade of these steels being investigated.

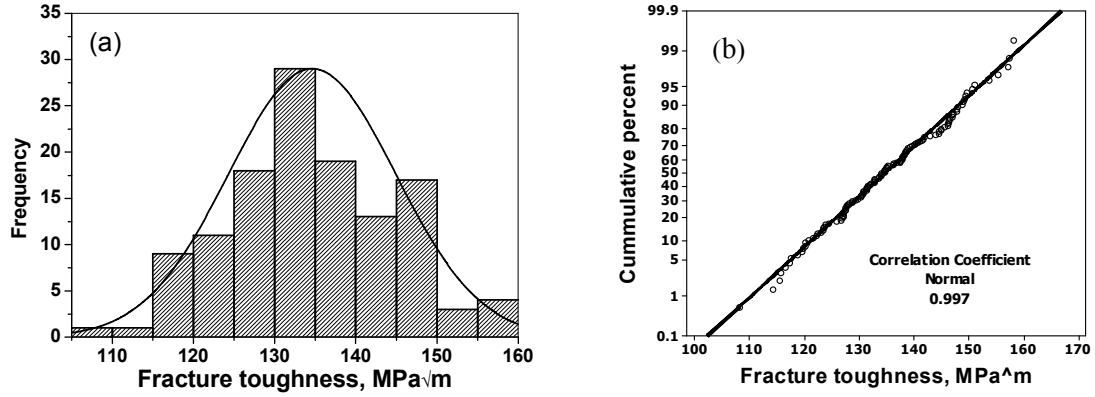


Fig. 4 (a) Normal distribution and (b) normal probability plots for the estimated fracture toughness values of the selected steels

Conclusions

1. The scatter associated with strength and hardness is marginal, but that associated with ductility, impact and fracture toughness of the selected AISI 4335V steels are considerable.
2. Fracture toughness values of AISI 4335V steels selected from various production batches vary in a wide range and the variation originates primarily from the amount of tramp elements.
3. Processing route influences the structural integrity of the selected steels even when their microstructure remains almost invariant.

Acknowledgement

The financial assistance received from Metal and Steel Factory, Ishapore, towards carrying out this investigation and the encouragement provided by its General Manager Mr. V. Gandhi, Additional General Manager Mr. S.K. Chopra and Director Mr. P. S. Bandopadhyay are gratefully acknowledged.

References

[1] W.S. Lee and T.T. Su: J. Mater. Proc. Technol. Vol. 87 (1999), p. 198.
[2] K. J. Irvine: J. Iron Steel Inst., Vol. 12 (1962), p. 620.
[3] R.N. Jha, K. Dutta and K.K. Ray: ISIJ Int, Vol. 50 (2010), p. 607.
[4] C. L. Briant and S. K. Banerji: Int. Met. Rev., Vol. 23 (1978), p. 164.
[5] D. H. Huang and G. Thomas: Metall. Trans. A, Vol. 2A (1971), p. 1587.
[6] R.W. Hertzberg: *Deformation and Fracture Mechanics of Engineering Materials*, 3rd Edition, (John Wiley and Sons, US 1989), p. 631.
[7] E8M-03. Annual Book of ASTM Standards, 2003.
[8] E23-03. Annual Book of ASTM Standards, 2003.
[9] E399-05. Annual Book of ASTM Standards, 2005.
[10] G.E. Kerns and R.W. Staehle: Scripta Met. Vol. 6 (1972), p. 631.
[11] S.K.Putatunda: Engg. Fract. Mech. Vol. 25 (1986), pp. 429-439.

© (2012) Trans Tech Publications, Switzerland
doi:10.4028/www.scientific.net/KEM.488-489.57

Spatial Statistical Analyses for Time-dependent Corroded Surfaces of Uncoated Weathering Steel Plates in Various Corrosive Environments

Shigenobu Kainuma[1,a], Young Soo Jeong[1,b]

[1]Department of Civil Engineering, Kyushu University,
744, Motooka, Nishi-ku, Fukuoka 819-0395, Japan

[a]kai@doc.kyushu-u.ac.jp, [b]jeong@doc.kyushu-u.ac.jp

Keywords: Corrosion, Weathering Steel, Atmospheric exposure test, Spatial Statistical Analysis

Abstract. To ensure the safety of steel structures, it is important to evaluate the time-dependent corrosion behavior. The purpose of this research is to develop a method of predicting time-dependence of the corrosion surfaces of uncoated weathering steel plates in various corrosive environments. Atmospheric exposure tests were carried out on the uncoated steel plates for 0.5, 1, 2 and 4-years in Okinawa Island, Japan. Spatial statistical analyses were carried out on the corrosion surfaces of the tested specimens. In addition to this, the time-dependence of the corrosion surfaces were simulated by the spatial statistical technique.

Introduction

In some of uncoated weathering steel bridges, severe corrosion damages have been reported at the structural members. It is important to devise a method of predicting the time-dependent corrosion behavior of the members to maintain safety the structures with corrosion failures. However, the method in various atmospheric environments has not yet been established.

Here, we describe a method for evaluating the time-dependence of corrosion at the surfaces of uncoated weathering steel plates in various corrosive environments. Atmospheric exposure tests were carried out on the steel plates for 0.5, 1, 2 and 4-years period in Okinawa Island, Japan. Specimens were mounted on racks at an angle of 0°, 45° and 90° to horizontal to obtain corrosion data in various corrosive environments. Spatial statistical analyses were also conducted using the corrosion depth data obtained from the exposed specimens. On the basis of the analytical results, numerical simulations also were carried out to predict the corrosion surfaces after a few decades.

Atmospheric exposure tests

Atmospheric exposure tests were carried out on uncoated specimens for periods of 0.5, 1, 2 and 4-years on Okinawa (Latitude 26°15′N, Longitude 127° 46′E). Annual mean values of temperature, relative humidity, airborne salt and total precipitation during four years were 23ºC, 75%, 0.3mdd (mg/100cm^2/day) and 172mm, respectively. The specimens were 400×60×9-mm JIS G 3114 SM490AW (Japanese Industrial Standard) structural weathering steel plate. Its chemical composition is shown in Table 1. The specimens were mounted on a rack at angles of 0°, 45° and 90° to the horizontal. These mounted angles were not used to investigate the influence of angle on the corrosion behavior as such, but rather to obtain data on different corrosive environments. The mean corrosion depth of the specimens was measured using a laser and also calculated from the weight loss of the specimens. Corrosion products of the skyward-facing surface of the specimen exposed for 1-year was analyzed by X-ray diffraction (XRD).

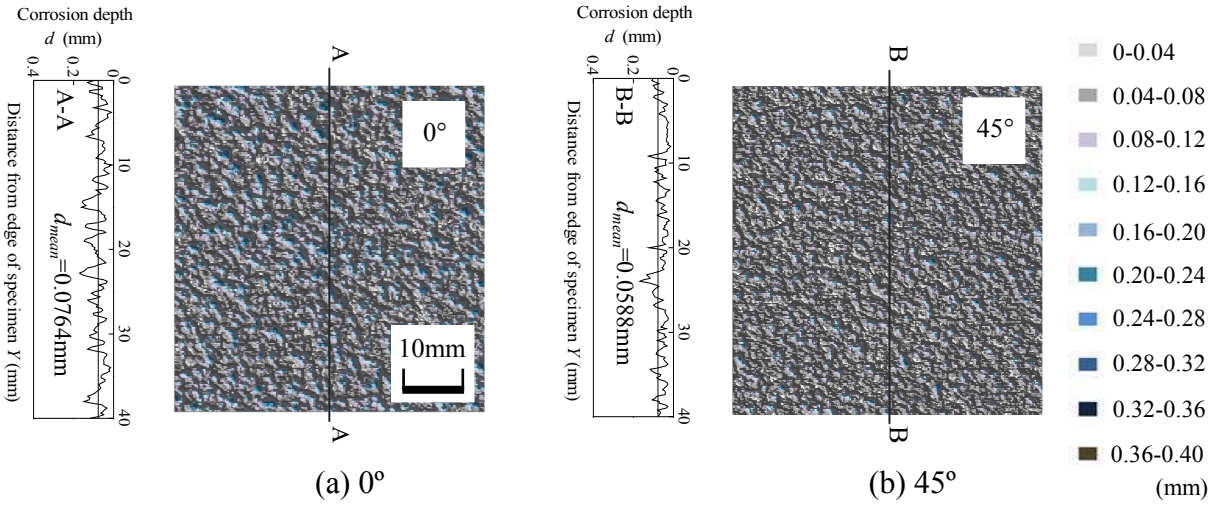
Composition of corrosion products is shown in Table 2. β-FeOOH which is formed in chloride environment is contained in corrosion products, of which content is 1.6%. Therefore, the corrosion behavior of the tested specimens is said to be affected by airborne salt from sea.

Table 1 Chemical composition of parent material (mass%).

C	*Si*	*Mn*	*P*	*S*	*Cu*	*Cr*	*Ni*
0.14	0.26	1.0	0.012	0.008	0.32	0.49	0.09

Table 2 Composition of corrosion products of specimen exposed for 1 year (wt%).

α-FeOOH	β-FeOOH	γ-FeOOH	Fe_3O_4	Amorphism
14.2	1.6	35.4	1.9	46.9



(a) 0º (b) 45º

Figure 1 Corrosion depth at skyward-facing surfaces of specimens exposed for 4-years.

Figure 1 shows the corrosion depth at two skyward-facing surfaces after exposure for 4-years following removal of the rust. These images correspond to the central area of tested specimens. The surface roughness was different for each mounted angle. In particular, more localized corrosion was observed on the specimen at the mounted angle of 0° than that of 45°.

The mean corrosion depth d_{mean} of the specimens is shown in Figure 2. Solid and dashed lines indicate regression curves for d_{mean} as function of exposed period t. The value of d_{mean} depends on the mounting angle and surface direction. Table 3(a) shows the coefficient of a, b and correlation coefficient R of the regression curves.

Spatial Autocorrelation Structure of the Corroded Surfaces

The spatial autocorrelation of each corroded surface was analyzed using a variogram [1,2]. The spherical model was used as a covariance function, given by the following equation [1] :

$$\gamma(h;\theta)=\begin{cases}\theta_1\left(1-\dfrac{3}{2}\dfrac{|h|}{\theta_2}+\dfrac{1}{2}\dfrac{|h|^3}{\theta_2^3}\right) & \left(0\le|h|\le\theta_2\right)\\ 0 & \left(|h|\ge\theta_2\right)\end{cases} \tag{1}$$

where $\gamma(h;\theta)$ is the covariance function of the spherical model, θ_1 and θ_2 are the sill and range, respectively, and h is the Euclidean distance.

Spatial regression analysis of the variograms was performed by applying a nonlinear least squares method to the covariance function. The spatial autocorrelation structures were estimated using the values of θ_1 and θ_2 obtained from the analytical results. Here, the equation for the weighted least squares standard, $WRSS(\theta)$, was applied as a nonlinear least squares approximation as follows [1] :

$$WRSS(\theta)=\sum_{k=1}^{K}\frac{|N(h_k)|}{\gamma(h_k;\theta)^2}\left(\gamma(h_k)-\gamma(h_k;\theta)\right)^2 \tag{2}$$

Table 3 Coefficient of a, b and correlation coefficient R.

(a) $d_{mean}=a\cdot t^{b}$

		Coefficient		Correlation coefficient R
		a	b	
0°	Skyward	0.0303	0.660	0.99
	Groundward	0.0386	0.509	0.91
45°	Skyward	0.0225	0.646	0.99
	Groundward	0.0260	0.606	0.95
90°	Skyward	0.0201	0.673	0.99
	Groundward	0.0209	0.668	0.99

(b) $h=a\cdot d_{mean}^{b}$

		Coefficient		Correlation coefficient R
		a	b	
0°	Skyward	3.293	0.393	0.87
	Groundward	7.942	0.677	0.94
45°	Skyward	2.394	0.324	0.90
	Groundward	5.214	0.527	0.96
90°	Skyward	1.859	0.185	0.54
	Groundward	5.363	0.523	0.90

where k is the Euclidean distance (or lag), $|N(h_k)|$ is the total number of pairs, K is the number of lags in the experimental variogram, $\gamma(h_k)$ is the value of the experimental variogram, and $\gamma(h_k; \theta)$ is the value of the theoretical spherical variogram model.

Figure 3(a) shows the range of h for each corrosion surface plotted against d_{mean}. Table 3(b) shows the coefficient of a, b and correlation coefficient R of the regression curves. When d_{mean} is less than 0.05 mm, the scatter of value of h is large. This is because corrosion surface of some specimens are significantly different even though the same exposure period. Therefore, their data plots were not used in calculation of regression analyses. The regression curves varied widely for the different corrosive environments. These curves are given by the equation in Figure 3(a).

The relationship between $\gamma^{1/2}$ and d_{mean} is shown in Figure 3(b). This relationship holds for all the corrosive environments. Thus, they can be expressed as the equation in Figure 3(b).

Numerical Simulation of the Time-Dependent Corrosion Surfaces

Procedure for the Spatial Statistical Simulation

The time-dependence of the corrosion at the different surfaces was simulated using spatial autocorrelation and is described by the following procedure [3].

(1) The range, h, and sill, γ, were calculated using equations in Figure 3(a) and (b).
(2) Random numbers with spatial autocorrelation structures using a mean of 0 mm and covariance of Σ were generated according to the covariance function of the spherical model.
(3) Normal distributions were calculated by adding the mean values of equation in Figure 2 to the values from Step (2).
(4) The surface data were calculated by superposing the probability distributions of Step (3).

The following assumptions were made in the numerical simulations, as described in Reference [3].

(1) The autocorrelation structure of the corrosion depth followed the covariance function of the spherical model.
(2) The probability distributions of the corrosion depths were described by normal distributions.

Simulated Results

The simulated corroded surfaces were compared to the corroded surfaces of the specimens under test to verify the numerical results. The simulated corrosion surfaces and their histogram of the corrosion depth were good agreement with that of experimental corroded surfaces. The maximum corrosion depth of the simulated results was also similar to that for the experimentally measured specimen. We can therefore conclude that the numerical simulations accurately describe the corroded surfaces.

Figure 4 shows simulated surfaces of skyward-facing at a mounted angle of 0°. The size and depth of the corrosion pits increase with time.

Summary of Findings

Atmospheric exposure tests were carried out on uncoated weathering steel plates for periods of 0.5, 1, 2 and 4-years on the island of Okinawa in Japan. Spatial statistical analyses were also carried out on the corroded surfaces. The experimental and analytical results led to a method for predicting the corrosion surfaces of uncoated weathering steel plates.

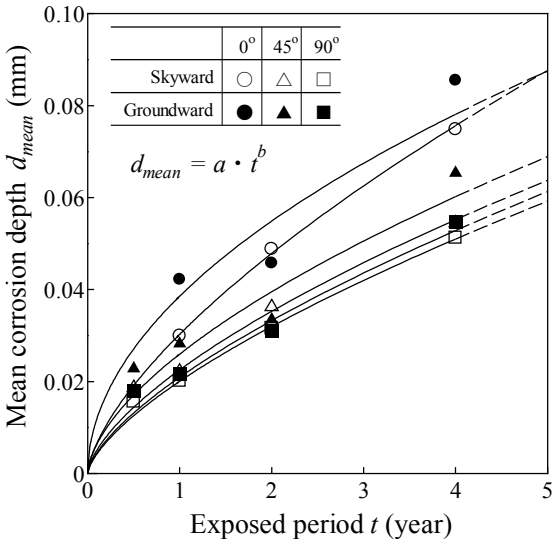
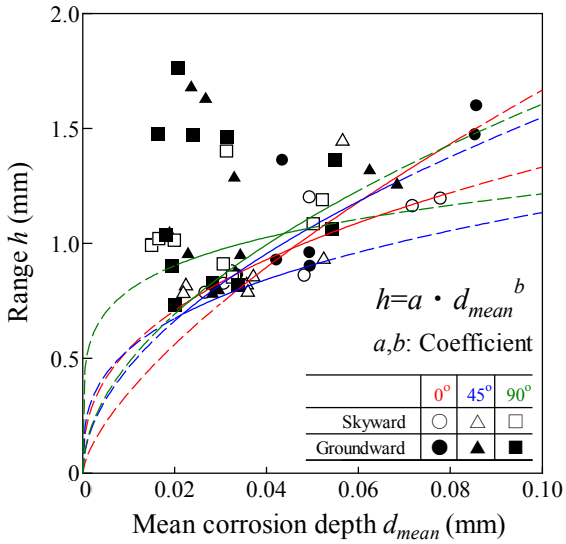


Figure 2 Mean corrosion depth d_{mean} as a function of exposed period t.



(a) Relationship between range h and d_{mean}.

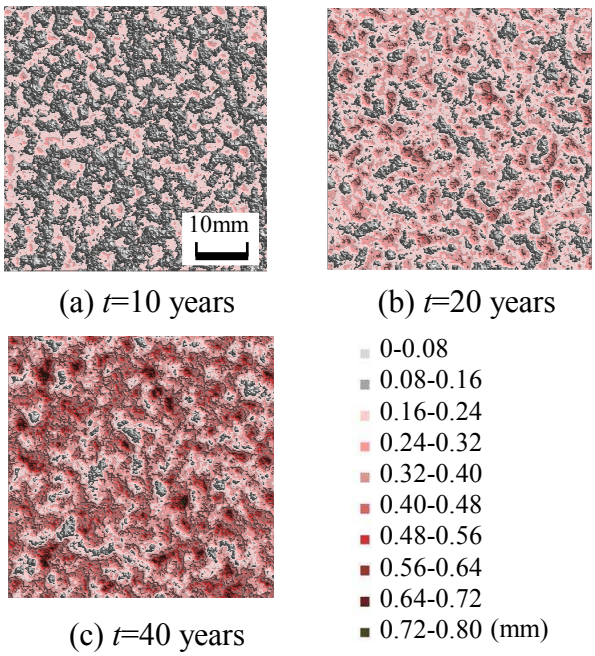
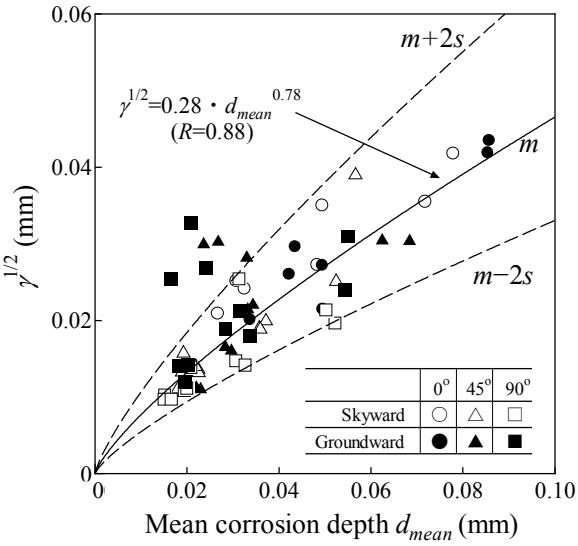


Figure 4 Simulated corrosion surfaces of skyward-facing at a mounted angle of 0°.



(b) Relationship between sill $\gamma^{1/2}$ and d_{mean}.

Figure 3 Relationship between the spatial statics and mean corrosion depth d_{mean}.

References

[1] N.Cressie : Fitting Variogram Models by Weighted Least Squares, J. Internat. Assoc. Math. Geol., 17, pp.563-586 (1985).

[2] H.Wackernagel : Multivariate Geostatistics, Springer (1998).

[3] S.Kainuma and N.Hosomi : Fatigue Life Evaluation of Corroded Structural Steel Members in Boundary with Concrete, Int. J. of Fracture, Vol.158, No.1, pp.149-158 (2009).

© (2012) Trans Tech Publications, Switzerland
doi:10.4028/www.scientific.net/KEM.488-489.61

Corrosion Inhibition of Stress Corrosion Cracking and Localized Corrosion of Turbo-Expander and Steam/Gas Turbines Materials

Behzad Bavarian, Jia Zhang and Lisa Reiner
Dept. of Manufacturing Systems Engineering & Management
College of Engineering and Computer Science
California State University, Northridge
Northridge, CA 91330
bavarian@csun.edu, j.zhang@csun.edu, l.reiner@csun.edu,

Keywords: stress corrosion, vapor phase inhibitors, turbo-expander, steam turbine, 7050 aluminum alloys, ASTM A470, corrosion inhibition

ABSTRACT. Stress corrosion cracking of 7050 aluminum alloys and ASTM A470 steel in the turbo expander and steam/gas turbine industry can cause expensive catastrophic failures, especially for turbo machinery systems performing in hostile, corrosive environments. Commercially available inhibitors were investigated for their effectiveness in reducing and controlling the corrosion susceptibility. Inhibitor effectiveness was confirmed with electrochemical corrosion techniques in different solutions. Polarization resistance increased with concentration of corrosion inhibitor due to film formation and displacement of water molecules. Cyclic polarization behavior for samples in the 1.0% and 5.0% inhibitors showed a shift in the passive film breakdown potential. The substantial increase in the passive range has positive consequences for neutralizing pitting and crevice corrosion cell chemistry. The strain to failure and tensile strength obtained from the slow strain rate studies for both alloys showed pronounced improvement due to corrosion inhibitor ability to mitigate SCC; the fractographic analysis showed a changed morphology with ductile overload as the primary failure mode instead of transgranular or intergranular cracking.

INTRODUCTION

The accumulation of damage due to localized corrosion (pitting, stress corrosion cracking [SCC] and corrosion fatigue [CF]) in low pressure steam turbine components, such as blades, discs and rotors, has consistently been identified as a main cause of turbine failure [1,2]. Accordingly, the development of effective localized corrosion inhibitors is essential for the successful avoidance of unscheduled downtime in steam turbines or other complex industrial and infrastructural systems and for the successful implementation of life extension strategies. Most damage occurs during the shutdown period due to chemistry changes and localized stagnant conditions. The environmental changes during the shutdown period significantly influence the probability of failure for the blades and discs in low pressure steam turbines. [O_2], [Cl^-], temperature, pH, and time spent in shutdown under aerated conditions increase the probability of localized corrosion attacks. Increase in [Cl^-] concentration and pH changes affect the stability of the protective oxides and eventually its breakdown pitting, stress corrosion cracking and corrosion fatigue [3-5].

Vapor phase corrosion inhibitors are often a complex mixture of amine salts and aromatic sulfonic acids that provide direct contact inhibition and incorporate volatile carboxilic acid salts as a vapor phase inhibitor for metal surfaces not sufficiently coated. A surface active inhibitor component will be strongly adsorbed at active sites having energy levels complimentary to the energy levels of the polar group, thereby forming a tighter, more uniform protective layer over the metal surface [6].

EXPERIMENTAL PROCEDURES

Electrochemical polarization tests were conducted (ASTM-G61) to evaluate the effects of these inhibitors on the ASTM A470 steel and 7050 aluminum alloy. The studies were conducted using a Gamry PC4/750™ Potentiostat/Galvanostat/ZRA and DC105 corrosion test software. These alloys

were tested in a solution of 1.0% and 5.0% inhibitor plus 200 ppm Cl- solution. Gamry electrochemical impedance spectroscopy EIS300™ systems were used to conduct cyclic polarization tests in temperatures ranging from 20 ^{o}C to 50 ^{o}C and to gather data for adsorption isotherms, tests were conducted in different inhibitor concentrations. The resistance polarization values were used to model adsorption isotherms. Crevice corrosion was conducted on both alloys in an eight-station alternate immersion system. Test were conducted per ASTM G44 and G47 for 200 cycles, the samples were examined and photographed to document their crevice corrosion resistances. The susceptibility to SCC was performed using slow strain rate tests (ASTM G128) under controlled electrochemical conditions using a strain rate of $5x10^{-7}$ sec^{-1}. To determine the degree of inhibitor effectiveness, anodic potentials close to breakdown potentials (-400mV for the 7050 alloy and -200 mV for ASTM A470) were applied.

RESULTS

Electrochemical Polarization Behavior. Electrochemical polarization behavior for two alloys in 200 ppm Cl- and 1.0% or 5.0% VCI inhibitor solutions showed a positive shift in the breakdown potentials by more than 500 mV. The inhibitor altered the electrochemistry, increased the passivation range significantly, and had beneficial consequences for pitting and localized corrosion. The extension of the passive zone contributes to the stability of the protective oxide film over a wider electrochemical range; therefore, corrosion attacks during shutdown period will be minimized.

Crevice Corrosion. Both alloy samples showed significant improvement in resistance to crevice corrosion after 200 hours of alternate immersion in various solutions. The samples immersed in 200 ppm Cl- and 5.0% VCI showed better corrosion resistance. The corrosion damage and discoloration were reduced with the addition of inhibitor for both alloys immersed in 1.0 and 5.0% VCI solutions. The passive film stability has improved the corrosion resistance for the inhibitor treated samples.

Stress Corrosion Cracking. Susceptibility to SCC was determined for both alloys close to their breakdown potentials. A noticeable increase in susceptibility with intergranular cracking modes is seen for the samples tested without inhibitor. The greatest reduction in degree of susceptibility is seen around -200 mV for ASTM A470 and around -400 mV for 7050 samples. Therefore, effectiveness of inhibitors was examined at these applied potentials. The morphology of the samples tested in non-protected solutions showed more intergranular attacks. Samples tested in the presence of VCI inhibitors showed mainly ductile overload failure with less localized corrosion damage. The slow strain rate tests showed that the protection afforded by the inhibitor is noticeable in the active anodic potential range. Both alloys showed a degree of SCC susceptibility of 95% in 5.0% VCI, 84% for 1.0% VCI compared with 45% for unprotected solutions (Figure 1). Corrosion fatigue tests on 7050 Al-alloy showed that the fatigue crack growth rate in the presence of inhibitor is more similar to inert environments. Tests conducted in 5.0% VCI solution showed no evidence of crack arrest effects that were observed in 200 ppm Cl- solution, mainly due to less corrosion product formation.

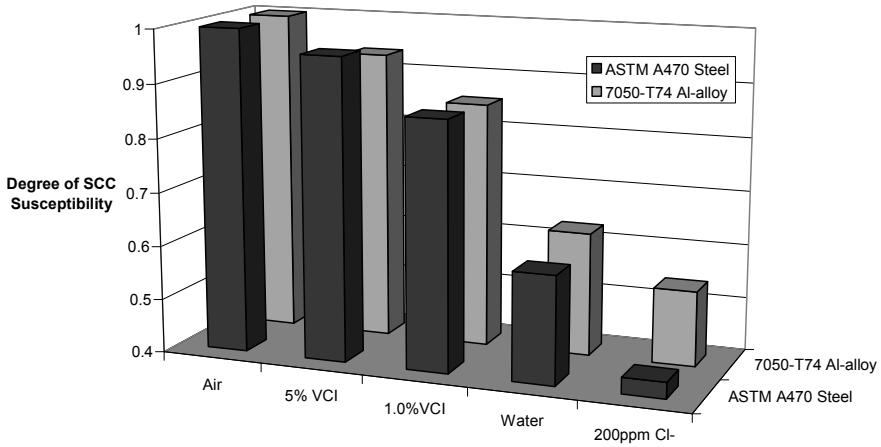
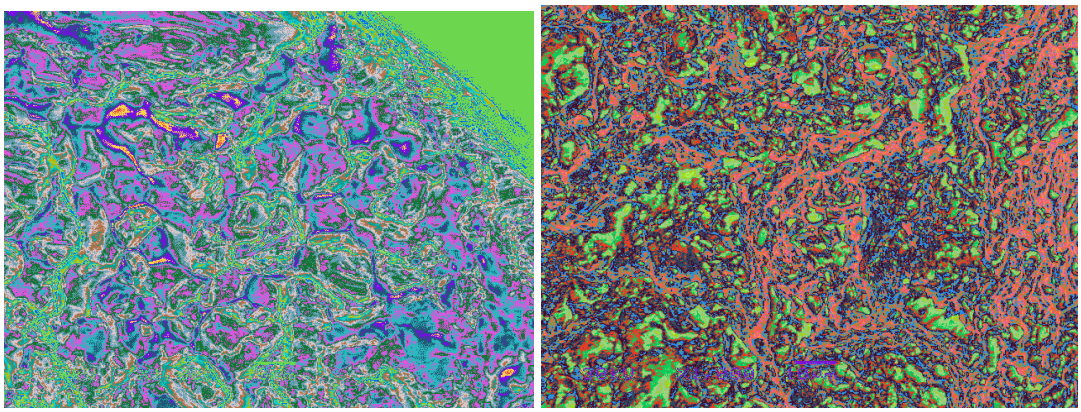


Figure 1: Slow strain rate tests on 7050-T74 Al-alloy (-400 mV_{SCE}) and ASTM A470 (-200 mV_{SCE}) per ASTM G128 in different solutions at $5x10^{-7}$ sec^{-1}.



200ppm Cl- at -200mVsce 200ppm Cl- +5%VCI at -200mVsce

Figure 2: SEM fractographs of ASTM A470 in unprotected and protected condition, showing failure mode changes in SCC tests.

Verification of the Inhibitor Mechanism: To explore the activation energy of the corrosion process and the adsorption thermodynamics, cyclic polarization and EIS were conducted in temperatures ranging from 20°C to 50°C in 1.0% and 5.0% VCI solutions. The results show that the corrosion behavior of both had less fluctuation during EIS tests. Therefore, EIS results and a modified Randles model were used to obtain the polarization resistance (Rp) values. The Bode plots show that VCI increases the polarization resistance of both alloys with higher inhibitor concentrations (Table 1). The addition of inhibitor has increased the Rp value and can be attributed to the film formation on the metal surfaces.

Table 1: Polarization resistance (KΩ) for ASTM A470 aluminum alloys generated by EIS in 200 ppm Cl-.

	VCI Concentration (%)		
Alloy	0.0%	1.0 % VCI	5.0 % VCI
ASTM A470	2.8	220	766
7050-T74	5.4	29	83

The thermodynamics of adsorption can provide valuable information about the mechanism of inhibition. The important thermodynamic values (changes in enthalpy of adsorption and changes in free standard energy of adsorption) can be obtained with adsorption isotherms and classical thermodynamics. The value of ΔG_{ad} is important for the identification of an adsorption mechanism. In chemisorption (chemical adsorption), ΔG_{ad} is usually much higher than physisorption (physical

adsorption). The criterion for chemisorption varies, for example, Bridka has suggested that chemisorption requires about -100 kJ/mol energy, whereas Metikos-Hukovic believes that chemisorption needs about -40 kJ/mol energy [7]. Still others assert that physisorption requires energy between -5 to -20 kJ/mol. Analysis of the VCI inhibitor showed that inhibitor adsorption to these alloys surfaces fits with the Langmuir adsorption isotherm; the enthalpy of adsorption is roughly between -14 to -18 kJ/mol, which suggests that this product is borderline between a strong physical adsorption or a weak chemical adsorption response with the metal surface.

CONCLUSIONS

A comprehensive investigation was undertaken to characterize the corrosion behavior of turbo machinery systems in vapor phase corrosion inhibitors. Effectiveness of the inhibitor was confirmed with electrochemical impedance spectroscopy at elevated temperature studies. As well, identification of the adsorption mechanism and corrosion activation energy was explored. The data acquired from EIS tests showed that inhibitor adsorption to these alloys surfaces fits with the Langmuir adsorption isotherm; the enthalpy of adsorption is about -14 to -18 kJ/mol, suggesting that this product is a relatively strong physical adsorption and weak chemisorption compound.
Cyclic polarization behavior for samples in the vapor phase inhibitor showed a shift in the passive film breakdown potential by roughly +500 mV. This increase in the passivation range will improve localized corrosion resistance. Crevice corrosion test results showed improved corrosion behavior compared with unprotected samples. The stress corrosion studies showed less SCC susceptibility for the samples in VCI inhibitors in the solution. Furthermore, ductile overload failure mode was observed for the alloys tested in the 5.0 % VCI inhibitor solution.

In summary, this investigation demonstrated that the addition of VCI inhibitor to the environment provides effective corrosion protection for both ASTM A470 and 7050 alloys during shutdown period for the blades and discs in low pressure steam turbines.

ACKNOWLEDGEMENT: The authors would like to express their appreciation to the W.M. Keck Foundation, AHPMC/DOD and CORTEC Corp. for their sponsorship of this project.

REFERENCES

1. H. McCloskey, R. B. Dooley and W. P. McNaughton, Turbine Steam Path Damage: Theory and Practice, Vols. 1 and 2, EPRI, Palo Alto, CA: 1999.
2. G. Engelhardt and D. Macdonald, Development of Code to Predict Stress Corrosion Cracking and Corrosion Fatigue of Low Pressure Turbine Components. EPRI, Palo Alto, CA: February 2004. 1004190.
3. G. Engelhardt and D. Macdonald, Corros. Sci., 46, 2755: 2004.
4. M. R. Saleh, A.M. Shams El Din, Corros. Sci. 12 (1981) 688.
5. M. L. Free, "A new corrosion inhibition model for surfactants that more closely accounts for actual adsorption than traditional models that assume physical coverage is proportional to inhibition," Corrosion Science, In Press, Corrected Proof, 10 May 2004.
6. M. Lagrenée, B. Mernari, M. Bouanis, M. Traisnel and F. Bentiss, "Study of the mechanism and inhibiting efficiency of 3,5-bis(4-methylthiophenyl)-4H-1,2,4-triazole on mild steel corrosion in acidic media," Corrosion Science, Vol 44, Issue 3 , March 2002.
7. R. Gasparac, C. R. Martin and E. Stupnisek-Lisac, "In situ Studies of Imidazole and its Derivatives as Copper Corrosion Inhibitors," Journal of The Electrochemical Society, 147 (2) 548-551 (2000).

© (2012) Trans Tech Publications, Switzerland
doi:10.4028/www.scientific.net/KEM.488-489.65

The Effect of Lamb Wave Interaction with Fatigue Crack in Thin Al Sheet

Vitalijs Pavelko[1, a], Igors Pavelko[2,b] and Eriks Ozolinsh [3,c]

[1] Lubanas iela 8-104, Riga LV-1019, Latvia

[2] Lomonosova iela 1B, Room B-211, Riga LV-1019, Latvia

[3]Lomonosova iela 1B, Room B-123, Riga LV-1019, Latvia

[a]vitaly_pavelko@hotmail.com, [b]Igors.Pavelko@rtu.lv, [c]eriks_ozolins@inbox.lv

Keywords: Lamb wave, fatigue crack, interaction

Abstract. The phenomenon of the Lamb wave interaction with fatigue crack in Al2024-T3 sheet was investigated at cyclic loading. Mentioned effect is associated with the crack open/close that change acoustic impedance of a crack. Analytical simulation of fatigue crack opening using the generalized Dugdale's model of a crack in thin plate shows good accordance between the intensity of ultrasonic signal and a crack opening.

Introduction

The guided Lamb wave technology (LWT) is one of the most effective means of structural damage detection in the thin-walled structural elements. Its application for structural health monitoring (SHM) of aircraft is very perspective [1,2]. This technology is applicable as for Al alloy as composite structure and has many important advantages in comparison with others methods. The main of them is the ability to detect large surface of structure at distance about some meters. Therefore the properties of LWT are intensively investigated in view of practical use in the systems of SHM.

Usually two approaches are used for structural damage detection: ‚pitch-catch' and 'pulse-echo'. Both suppose that there is initial data of a structural element, so called baseline. It is the ultrasound portrait of undamaged structure which comparison with current state allows to detect damage. But there is probability that the change of received ultrasound signal can be associated also with degradation of some elements of the SHM system. Therefore the research of any methods those are free from this disadvantage is very actual [2,3]. One of them is discussed in this article.

Set-up, Fatigue Test, and Measurement.

Some regularities of ultrasonic wave propagation in Al2024-T3 sheet with fatigue crack were investigated using a rectangular sample 80x300 mm of 1mm Al sheet (Fig.1). For fatigue crack initiation the 4 mm hole was drilled in center of a sample. Cyclic load 12/4 kN and 10 Hz was performed using 100kN hydraulic test machine 'Instron'. It means the maximal tensile stress was equal to 150 MPa, minimal 50MPa.

Two types of piezoceramics transducer were used. One is the PIC151 0.5x10x50mm (***T1*** and ***T2***) other transducer pz27 1x6.35x6.35mm (***t1*** and ***t2***). The ultrasound Lamb waves were excited by piezoceramics transducer(actuator) and received the same transducer(echo-signal) or other one(transmitted signal). Five sine burst with basic frequency in rage 250-300 kHz was exciting.

At first stage of testing the fatigue crack was initiated. The ultrasound signal generated by the transducer ***A*** (T_1) was received by the sensor ***S*** (T_2) (Fig.1). In other serie the generating-sensing was opposite: ***A*** (T_2) - ***S*** (T_1). After each 20000 cycles the serie of measurements was performed: the received signal at the static load 0, 6, and 12 kN was recorded and the impedance of all transducers was measured for estimation of they technical condition. Macro fatigue 5 mm crack (including a hole diameter 4 mm) was observed after 100000 cycles. At next stage of fatigue testing the same ultrasound and impedance measurements were performing after crack increment about 2 mm.

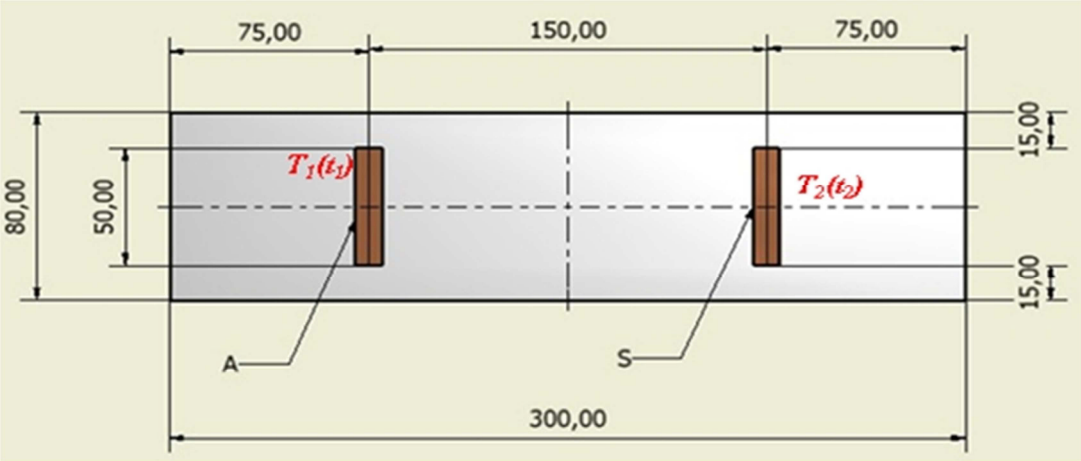


Fig.1. Test sample of Al2024-T3 1mm sheet

Test Results

Before the fatigue crack initiation intensity of a transmitted signal remains practically independent from the number of cycles (Fig.2). Since the fatigue crack occurrence the significant decreasing of the received signal as a function of cycle number is seen. Similar effect of the crack growth is observed for all variants: unloaded, loaded by 6 kN, and 12 kN. Easy see this effect is the same for both loaded states, and that is significantly more than for unloaded sample.

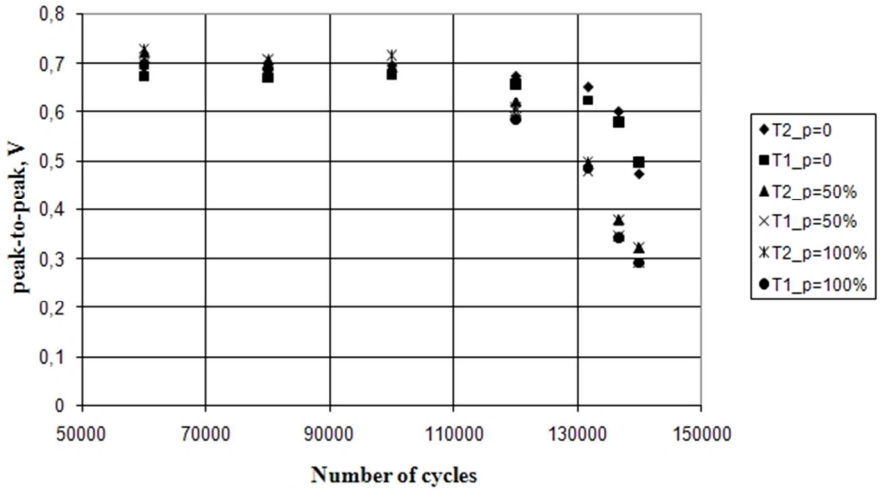


Fig.2. Peak-to-peak of received signal as function of number of cycles

Results of measurement of signal intensity as a function of crack length are presented in Fig.3. Note the direction of wave generating-sensing ($T_1 \rightarrow T_2$, $T_2 \rightarrow T_1$) does not affect the measurement result. Easy to suppose the effect of loading is connected with crack opening which decreases the acoustic transparency of a crack. But as it was mentioned above the loading effect is the same for both load 6 and 12kN. Therefore logically suppose that there is some threshold of load of the beginning of the crack closing at unloading. It can also suppose it can be defined by ultrasound detection.
Special test shows that these suppositions are substantiated. After 133990 cycles of loading the crack reached a 27mm length, and the static test with 0.5 kN load increment was performed. Joined result of all tests is presented in Fig.4. It can see the load increasing induces decreasing of ultrasound signal intensity to about 40 MPa stress, and at the larger load remains constant.

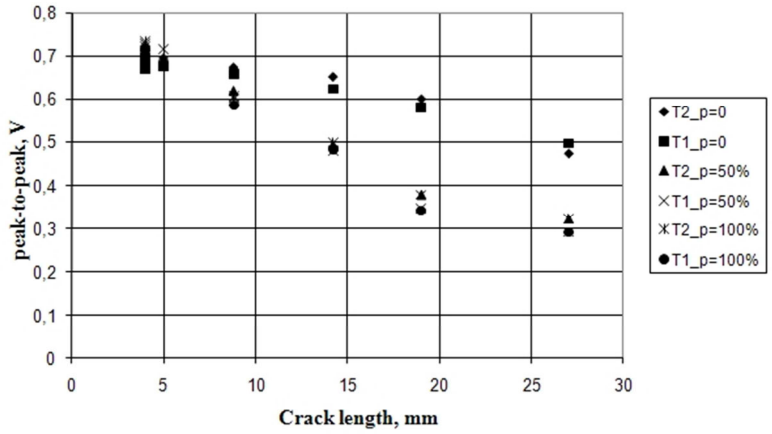


Fig.3. Peak-to-peak of received signal as function of crack length

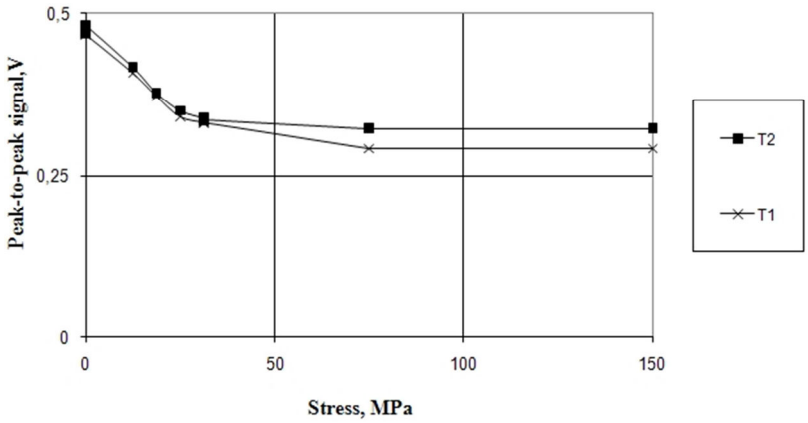


Fig.4. Peak-to-peak of received signal as function of stress (crack length 27mm)

Wave reflection- transmission phenomena.

The crack in the plate is a boundary at the way of crack propagation. It is known the properties of that one define the wave reflection-transmission features. At the crack-close configuration the contact of crack sides decreases the acoustic resistance of a crack and transmitted signal intensity increases. At the crack-open configuration the acoustic resistance of a crack increases and transmitted signal intensity decreases. The level of crack opening defines the degree of crack effect. Analytical simulation of fatigue crack opening using the generalized Dugdale's model of a crack in thin plate was performed. The isolated $2l_0$ length crack in infinite plane has a plastic layer that formed at cyclic loading. In basic configuration the crack side displacements is distributed in accordance to following expression:

$$\bar{v}(\bar{x}) = \frac{v(\bar{x})}{\frac{\sigma_Y}{E} l_0} = (\bar{x}-1) ln \frac{\bar{l}^2 - \bar{x} - \sqrt{(\bar{l}^2-1)(\bar{l}^2-\bar{x}^2)}}{\bar{l}^2 - \bar{x} + \sqrt{(\bar{l}^2-1)(\bar{l}^2-\bar{x}^2)}} - (\bar{x}+1) ln \frac{\bar{l}^2 + \bar{x} - \sqrt{(\bar{l}^2-1)(\bar{l}^2-\bar{x}^2)}}{\bar{l}^2 + \bar{x} + \sqrt{(\bar{l}^2-1)(\bar{l}^2-\bar{x}^2)}}$$

where $\bar{x} = \frac{x}{l_0}$, $\bar{l} = \frac{l}{l_0}$, σ_Y is yield stress, E is the elasticity modulus Using known theorem about plastic deformation at cyclic loading the shape of a crack during unloading was investigated. In Fig.5 the series of crack shapes at maximal load of cycle and after partial unloading to 33%, 24.75%, 16.5%, 8.25% of maximal load, and full unloading is showed. It was accepted the maximal stress is equal to half of the yield stress and the cycle ratio is 0.333.

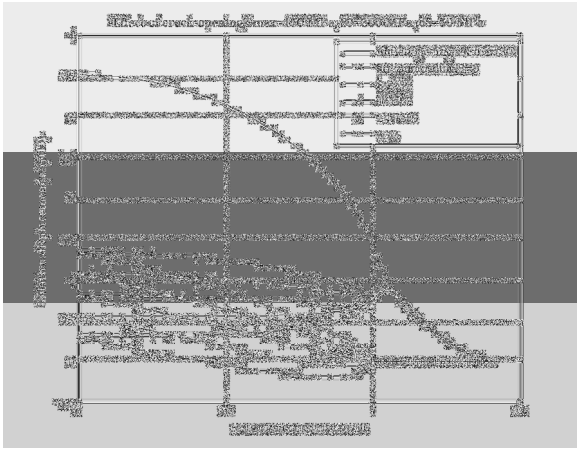


Fig.5. The crack shapes at maximal load and after partial unloading

Relative coordinate to equal 1 is corresponded to the crack tip, but the inside regione at $\bar{x} > 1$ is active plastic zone. Couple of the lines with the same marcers shows the passive plastic zone, that remins behind crack tip after partial unloading. Presented results is similar so called the strip-yield model of fatigue crack [4]. It can see the closing of a crack is started at about 16.5% of maximal load.

Summary

There is stable crack-opening effect (COE) to ultrasonic signal in Al alloy sheet. This effect can be explained by fracture mechanics. COE allows to develop the technology of a fatigue crack detection without using prior baseline data. On other side the Lamb wave technology can be useful for investigation of fatigue crack growth.

Acknowledgement

The research leading to these results has received funding from the European Community's Seventh Framework Program [FP7/2007-2013] under grant agreement n°212912. The authors are grateful to European Commission for financial support and all partners for scientific and technological collaboration.

References

[1] Adams D.E. (2007) Health Monitoring of Structural Materials and Components: Methods with Application, John Wiley & Sons, Ltd. (2007).
[2] Giurgiutiu, V. *Structural Health Monitoring with Piezoelectric Wafer Active Sensors*, Elsevier Academic Press, (2008).
[3] Hoon Sohn, Seung Bum Kim and Seung Die Kim. Guided Wave Based Nondestructive Testing: A Reference-Free Pattern Recognition Approach.//Ultrasonic and Advanced Methods of Nondestructive Testing and Material Characterization. World Scientific Publishing Co.Pte.Ltd. NJ (2007), 117-138.
[4] Newman Jr JC. A crack opening stress equation for fatigue crack growth. Int. J. Fract., 24(3), (1984), R131–135.

© (2012) Trans Tech Publications, Switzerland
doi:10.4028/www.scientific.net/KEM.488-489.69

Modeling ductile fracture using the discontinuous velocity domain splitting method

Ioan R. Ionescu[1, a] and Edouard Oudet[2,b]

[1]LSPM, University Paris13, 99 Av. J-B. Clement, 93430 Villetaneuse, France

[2]LAMA, University of Savoie, 73376 Le Bourget-du-Lac, France

[a]ioan.r.ionescu@gmail.com, [b]edouard.oudet@univ-savoie.fr

Keywords: Limit analysis, Collapse flow, Mesh free method, Localized déformations, Level sets, Genetic minimization algorithms.

Abstract. Discontinuous velocity domain splitting method (DVDS) is a mesh free method which focuses on the strain localization and completely neglect the bulk deformations. It considers the kinematic variational principle on a special class of virtual velocity fields to get an upper-bound of the limit load. To construct this class of virtual velocity fields, the rigid-plastic body is splinted into simple connected sub-domains and on each such sub-domain a rigid motion is associated. The discontinuous collapse flow velocity field results in localized deformations only, located at the boundary of the sub-domains.
In the numerical applications of the DVDS method we introduce a numerical technique based on a level set description of the partition of the rigid-plastic body and on genetic minimization algorithms. In the case of in-plane deformation of pressure insensitive materials, the internal boundaries of the sub-domains are parts of circles or straight lines, tangent to the collapse velocity jumps. In this case, DVDS reduces to the block decomposition method, which was intensively used to get analytical upper bounds of the limit loads. When applied to the two notched tensile problem of a von Mises material, DVDS gives excellent results with a low computational cost. Furthermore, DVDS was applied to model collapse in pressure sensitive plastic materials. Illustrative examples for homogenous and heterogeneous Coulomb and Cam-Clay materials shows that DVDS gives excellent prediction of limit loads and on the collapse flow.

Introduction

The numerical solutions methods in limit analysis are based on the discretization of the kinematic or static variational principles using the finite element method technics and on the convex and linear programming. The first results were obtained in [1],[2] while the literature on FE to limit analysis is very extensive. Despite great progress in the last decades (X-FEM, re-meshing techniques, ...), the finite element method remains associated to continuos fields and it is not so well adapted for modeling strain localization and velocities discontinuities on unknown surfaces.

The discontinuous velocity domain splitting (DVDS) method, introduced in [3], is a mesh free method which does not use a finite element discretization of the solid. DVDS focuses on the strain localization and completely neglect the bulk deformations.

Concerning the numerical approaches to be used in conjunction with DVDS, the main difficulty is to find a mesh free method to describe a domain partition and then to develop a numerical method to minimize the partition dependent plastic dissipation power. Even if some results have been obtained recently the "partition optimization" problem is a new challenge and the results obtained are not yet relevant.

In all the examples we have testes the numerical approach associated to DVDS appears to be robust. Concerning efficiency, the comparison of the DVDS with others (finite element) methods is not simple. DVDS, which is a mesh free method, has a very low memory cost but it uses genetic algorithms which need more computational time. If parallel computing techniques are used then the computational time is drastically reduced and DVDS becomes an efficient method.

The limit load problems are sometimes involved in the homogenization techniques used to deduce the macroscopic plastic properties of heterogeneous materials. Since the heterogeneity is captured in DVDS through the (analytical) expression of the plastic potential the computational effort of DVDS is almost the same for homogenous and heterogeneous materials. This is not the case when one uses a finite element approach. Indeed, the FE mesh has to be fine enough to capture the spatial distribution of the each heterogeneity, which will result in an important computational cost.

Description of DVDS

The main idea of DVDS, presented in details in [3], is to consider the kinematic variational principle on a special class of virtual velocity fields to get an upper-bound of the limit load. To construct this class of virtual velocity fields, the rigid-plastic body is splinted into simple connected sub-domains and on each such sub-domain is associated a rigid motion. The limit load problem is thus reduced to the minimization of a mesh free functional (plastic dissipation power) depending on the domain partition. The collapse flow velocity field, which is discontinuous, is associated to a domain partition and a set of rigid motions. It has localized deformations only, located at the boundary of the sub-domains.

The numerical minimization of the plastic dissipation functional depends on partitions of the rigid-pastic body. Since we would like to reduce the number of parameters in the optimization process, the main numerical difficulty of this problem is to find a mesh free method to describe a domain partition and then to develop a numerical method for the minimization of the partition dependent plastic dissipation functional, that avoids, as much as possible, local minima. Even if some results on optimal partition have already been obtained (see [4] for instance) for certain functionals efficient algorithms need to be formulated for general functionals. Since the topology of the optimal sets is unknown, a classical boundary variation optimization is not applicable here. To tackle this difficulty, we use an optimization procedure based on standard genetic algorithm techniques (see [5] for details on stochastic optimization methods). Thus, the main features of our approach are the parameterization of domains and the cost evaluation. Finally, the proposed algorithm consists in the following principal ingredients: description of the set with a small number of parameters, description of the vector field, reconstruction of the topology of the set and the computation of the cost function.

The parameterization of the level set function, which describe the partition, is based on Fourier's series. To parametrize the space of admissible vector fields, we add parameters to describe a rigid displacement on every connected component of the plastic domain (more precisely, a translation vector and a rotation angle for each connected component). With this information, we can proceed to the computation of our cost function. Notice that in our particular situation, we can avoid the time consuming step of generating a mesh of the interior of the plastic domain: all the integrals that have to be computed can be transformed into boundary integrals by Green's formula.

Slope stability

We analyse here a classical soil stability problems to demonstrate the accuracy and efficiency of the DVDS method for yield criteria which depends on the mean stress (or pressure). We consider the classical slope stability problem in the case when the material obeys Mohr-Coulomb yield potential, with C the cohesion and ϕ the internal frictional angle. The slope is of of height H and angle θ (see Figure 1). The soil in the slope is in contact with a rigid foundation while the other part of the boundary is stress free. The flow of the soil in the slope is gravity driven. Notice that the limit load depends only on the slope geometry, given by the angle θ, and the factor $C/(\gamma H)$, where γ is the gravity constant. In all the computations we have normalized the factor $C/(\gamma H)$ (set it to unity) and set the friction angle $\phi=20°$.

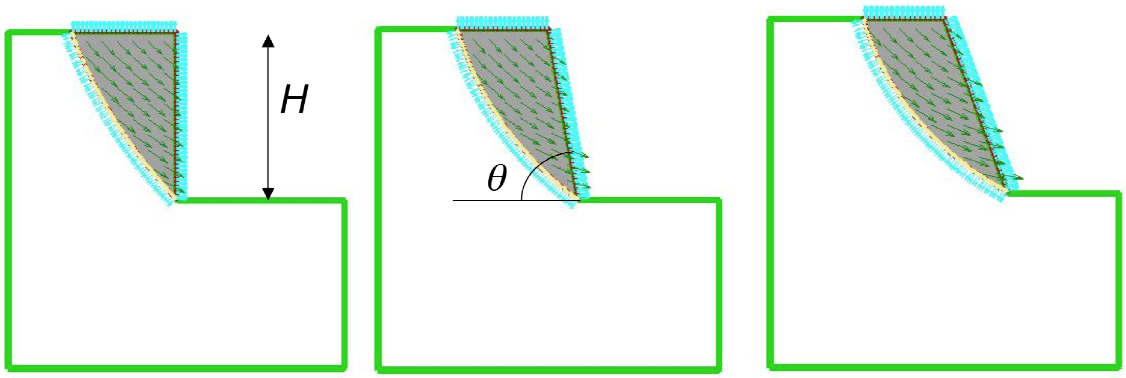


Figure 1. The fracture obtained with DVDS and the associated collapse flow for a Mohr-Coulomb material. Left: $\theta=90°$; Middle: $\theta=80°$; Right: $\theta=70°$.

The "reference" values of correspond to the analytical upper bound solution of Chen and Liu [6]. The computed limit load upper bound obtained with the DVDS method are given in Table 1 and the corresponding fracture configurations are plotted in Figure 1 for three slope configurations. Remark the good agreement with the analytical results, the accuracy of DVDS being less than 1%. For comparison, the DVDS accuracy is better, for the first two angles, than the method developed by Krabbenhoft et al [7] using a low-order discontinuous finite elements technique.

Table 1. The computed upper bound of the limit load of the slope problem.

Limit load	$\theta=90°$	$\theta=80°$	$\theta=70°$
Chen and Liu [6]	5.50	6.75	8.30
Krabbenhoft et al [7]	5.67	6.89	8.44
DVDS	5.50	6.78	8.48

Fracture in heterogeneous materials

We consider the same Mohr-Coulomb material, as in the previous section but in an uni-axial experiment. In Figure 2 left we have plotted the fracture obtained with DVDS for and the associated collapse flow in the case of a homogeneous material. We remark that in this case the DVDS gives exactly the theoretical fracture angle $\alpha= \pi/4 + \phi/2=55°$. We consider now two types of heterogeneity. First, we consider the presence of some voids (white spots in Figure 2 middle). To model that in the DVDS context, it is sufficient to put the cohesion $C=C(x,y)$ to vanish on the voids. The fracture, computed with DVDS and plotted in Figure 2 middle, is almost a straight line but with a different angle (approx 64°). This a consequence of the voids distribution on the specimen. The same number of voids (i.e. with the same porosity) but with a different distribution will give a different fracture surfaces and different limit loads. The second heterogeneity

concerns rigid grains (black spots in Figure 2 right), which is included in the DVDS modeling through by considering C(x,y) very large on the rigid grains. The fracture, computed with DVDS and plotted in Figure 2 right, is not anymore a straight line.

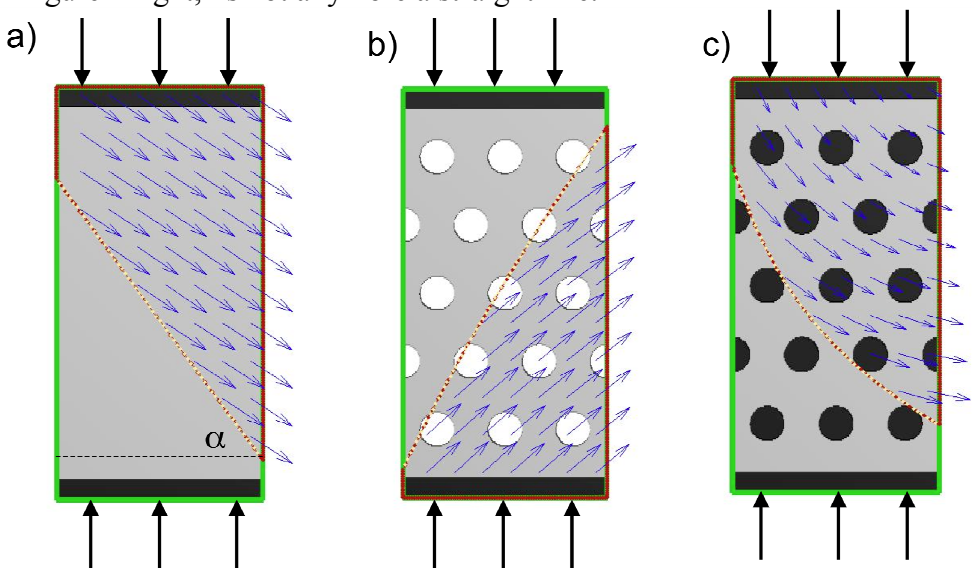


Figure 2. The fracture obtained with DVDS and the associated collapse flow for the uni-axial test of a Mohr-Coulomb material. Left: homogeneous (grey); Middle: voids (white) heterogeneity; Right: rigid grains (black) heterogeneity.

Let us notice that the heterogeneity is involved in DVDS through the analytical expression of the plastic potential (spatial distribution of the cohesion in the present case). That means that the computational effort of DVDS is almost the same in the homogenous and heterogeneous cases. This is not the case when one uses a finite element approach. Indeed, the FE mesh has to be fine enough to capture the spatial distribution of the each heterogeneity, which will result in an important computational cost.

References

[1] D.G. Hayes and P.V. Marcal, Determination of upper bounds for problems in plane stress using finite element techniques, *Internat. J. Mech. Scie.,* vol 9, 245--251, (1964), 349-364

[2] P.G. Hodge and T. Belytschko, Numerical methods for the limit analysis of plates, *J. Appl. Mech*., vol 35, 796--802 (1968), 349-364

[3] I.R. Ionescu and E. Oudet, Discontinuous velocity domain splitting in limit analysis, *Int. J. Solids and Structures*, vol. 47 (2010), 1459-1468

[4] B. Bourdin, D. Bucur and E. Oudet, Optimal Partitions for Eigenvalues, *SIAM J. Sci. Comput.* 31, 4100 (2009)

[5] Panos M., Pardalos and H. Edwin Romeijn (eds), *Handbook of global optimization*, Vol. 2. Nonconvex Optimization and its Applications, 62. Kluwer Academic Publishers, Dordrecht, (2002)

[6] Chen W.F., Liu X.L., *Limit Analysis in Soil Mechanics*, Elsevier Science Publishers B.V., Amsterdam, 1990.

[7] K. Krabbenhoft, A. V. Lyamin, M. Hjiaj and S. W. Sloan, A new discontinuous upper bound limit analysis formulation, *Int. J. Numer. Meth. Engng* (2005) 63, 1069--1088

© (2012) Trans Tech Publications, Switzerland
doi:10.4028/www.scientific.net/KEM.488-489.77

Notched Specimens Fracture Prediction with an Advanced GTN Model.

Joseph FANSI[1,2,3*], Mohamed BEN BETTAIEB[1], Tudor BALAN[3],

Xavier LEMOINE[2,3], Anne Marie HABRAKEN[1]

[1] Department ArGEnCo, Division MS²F, University of Liège, Chemin des Chevreuils 1, 4000 Liège, Belgium

[2] ArcelorMittal R&D Global Maizières S.A., voie Romaine, 57238 Maizières-lès-Metz, France

[3] LEM3, UMR CNRS 7239 Arts et Métiers ParisTech – Metz, 4 rue A. Fresnel, 57078 Metz cedex 03, France

* Corresponding author email: jfansi@doct.ulg.ac.be

Keywords: ductile fracture, dual phase steel, notched specimens, advanced Gurson model.

Abstract. This present contribution consists of implementing an advanced GTN damage model as a "User Material subroutine" in the Abaqus FE code. This damage model is based on specific nucleation and growth laws in order to predict the void coalescence properties of the material. When applied, this implementation predicts the damage evolution and the stress state of notched specimens made from dual phase steel. By comparing numerical predictions with experimental results, the numerical approach was improved and then validated.

1. Introduction.

One of the most powerful steel sheet damage modeling laws was introduced by Gurson [5]. Using mathematical models and experimental observations, he broke down this phenomenon into two areas: nucleation and growth of voids. Since the Gurson model [5] doesn't take into account plastic anisotropy, mixed hardening of matrix nor nucleation and coalescence of voids, numerous authors have extended this law. For instance Tvergaard and Needleman [6] introduced the nucleation and coalescence constant parameters (q_1, q_2, q_3), plastic anisotropy was developed by Benzerga [7], and advanced-isotropic hardening was studied by Pardoen [8] etc…
Motivated by industrial needs, an extended advanced GTN model [1] has been defined by Ben_Bettaeib [2] which includes a more accurate model plastic anisotropy, kinematic hardening and, chiefly, the nucleation function of the void volume fraction based on measurement using X-Ray tomography [4]. The first section of the present paper introduces the GTNB (Gurson, Tvergaard, Needleman, Ben Bettaieb) model. The second section describes its numerical integration. In the last section, the GTNB model is applied to a notched tensile specimen calculation.

2. GTNB model description.

The main goal of this damage law is to predict the void volume fraction evolution with the stress rate of in a dual-phase (DP) steel.
The total strain $\underline{\varepsilon}$ representing the matrix and voids is divided into $\underline{\varepsilon}^e$ and $\underline{\varepsilon}^p$ elastic and plastic contributions.

$$\underline{\varepsilon} = \underline{\varepsilon}^e + \underline{\varepsilon}^p \qquad \text{Eq.1}$$

The Elastic Law simply states $\underline{\sigma} = \underline{\underline{C}}^e : \underline{\varepsilon}^e$ Eq.2

$\underline{\sigma}$ is the macroscopic Cauchy stress tensor and $\underline{\underline{C}}^e$ is the elasticity matrix (isotropic and linear).

The plastic flow rule is defined by the normality relationship in the associated plasticity:

$$\underline{\dot{\varepsilon}}^{p} = \dot{\lambda}\frac{\partial F_P}{\partial \underline{\sigma}} \quad ; \quad \begin{cases} \dot{\lambda} = 0 & if \quad F_p < 0 \\ \dot{\lambda} \geq 0 & if \quad F_p = 0 \end{cases} \qquad \text{Eq.3}$$

The GTN yield function modified with Benzerga [7]coefficient κ

$$F_p = \frac{\tilde{\sigma}_{eqa}^2}{\sigma_Y^2} + 2q_1 f \cosh\left(-\frac{3\, q_2 \tilde{\sigma}_m}{\kappa \sigma_Y}\right) - 1 - q_3 f^2 = 0 \qquad \text{Eq.4}$$

DP steel is constituted of martensitic islands embedded in a ferritic ductile matrix. The mechanical choice to model this microstructure is to apply the Hill anisotropic yield function modified with a Benzerga coefficient [7] and coupled with the mixed hardening law (Ben Bettaeib). The hardening model is defined by the well known isotropic Swift law Eq.5, and by Amstrong-Frederick for the kinematic part Eq.6.

$$\sigma_Y = K(\varepsilon_0 + \varepsilon_m^p)^n \qquad \text{Eq.5}$$

Where K , n and ε_0 are material parameters and ε_m^p represents the equivalent plastic strain in the dense matrix only.

$$\underline{X} = (1 - q_1 f)\underline{X}^* \quad ; \quad \underline{\dot{X}}^* = C(s\underline{\dot{\varepsilon}}^p - \underline{X}^* \dot{\varepsilon}_{eqa}^p) \qquad \text{Eq.6}$$

$\underline{X}$: Backstress.

f :Porosity or void volume fraction.

C and $s$are material parameters, $\underline{\dot{\varepsilon}}^p$ is the plastic strain rate in the macroscopic and $\dot{\varepsilon}_{eqa}^p$ is its equivalent value defined as:

$$\dot{\varepsilon}_{eqa}^p = \sqrt{2\,(\underline{\dot{\varepsilon}}^p : \underline{\underline{H}}^{-1} : \underline{\dot{\varepsilon}}^p)} \qquad \text{Eq.7}$$

$\underline{\underline{H}}^{-1}$ is the pseudoinverse of $\underline{\underline{H}}$ Hill ($\underline{\underline{H}}$ is singular) for more details see [2].

The evolution of the first state variable σ_Y is defined by:

$$\tilde{\underline{\sigma}} : \underline{\dot{\varepsilon}}^p = (1 - f)\sigma_Y \dot{\varepsilon}_m^p \qquad \text{Eq.8}$$

Since it is difficult to predict each porosity evolution due to the material's heterogeneity , Bouaziz [4] proposed to take an evolution of a representative volume element (RVE) of the real and of the virtual materials at time t1 and t2.

The porosity is formally described by a single equivalent void evolution with the following Eq.4:

$$\frac{dR_{eq}}{R_{eq}} = \left(\frac{3 q_2{}^2 \sigma_Y \sinh\left(\frac{3\, q_2 \tilde{\sigma}_m}{\kappa \sigma_Y}\right)}{2\kappa \tilde{\sigma}_{eqa}}\right) d\varepsilon_{eqa}^p \qquad \text{Eq.9}$$

The damage evolution (porosity variable) is linked to the variable q_2 (q_1=1.5*q_2; q_3=$q_1$²). In the GTNB, the damage parameter q_2 (explicit method) is adjusted at each time increment to verify an evolution rule based on experimental observation.

3.Numerical integration.

The constitutive equations integrated is incrementally explicit for the porosity and implicit for the others .Parameter q_2 is recomputed at each step to verify Eq1. The complete set of equations of the constitutive model was rearranged in a condensed form of eight non-linear equations [2], to be solved by an iterative Newton-Raphson method for non linear system. These equations are scalar with exception of one tensorial equation: The GTN yield function Eq.4 has one unknown $\Delta\varepsilon_{matrix}^p$:

$$F_p(\underline{\sigma}, \underline{X}, f^t, q_2^t, \sigma_Y) = F_p(\Delta\varepsilon_{ij}^p, f^t, q_2^t, \sigma_Y) = 0 \quad (i, j = 1,2,3) \qquad \text{Eq.10}$$

The flow rule Eq.3 has 2 unknowns $\Delta\varepsilon^p$ and $\Delta\varepsilon^q$.

$$\Delta\varepsilon^p\left(\frac{\partial F_p}{\partial\sigma_{eqa}}\right)+\Delta\varepsilon^q\left(\frac{\partial F_p}{\partial\sigma_m}\right)=0 \qquad \text{Eq.11}$$

The Energy density Eq.6 has one unknown $\Delta\varepsilon^p_{matrix}$.

$$\Delta\varepsilon^p_{matrix}=\left(\frac{\tilde{\sigma}_m*\Delta\varepsilon_p+\tilde{\sigma}_{eqa}*\Delta\varepsilon_q}{(1-f)\sigma_y}\right)=0 \qquad \text{Eq.12}$$

Where $\Delta\varepsilon^p=\Delta\varepsilon_{plastic}(matrix+void)$,$\Delta\varepsilon^q=\Delta\varepsilon^{plastic}_{eqa}(matrix+void)$ and the unit-length deviated direction of plastic strain (5 unknowns) is:

$$n_{1\to5}=\left(\frac{\underline{\underline{H}}:\tilde{\sigma}_d}{(2\sigma_{eqa}}\right) \qquad \text{Eq.13}$$

The unknowns of this system are $(\Delta\varepsilon^p,\Delta\varepsilon^q,\Delta\varepsilon^p_{mat},\underline{n})$. The 8 equations are solved with the Newton-Raphson method for a non-linear system. The GTNB model has been developed and tested with Lagamine (implicit software). The law has been implemented and tested with one element in Abaqus-explicit through a VUMAT (user subroutine).

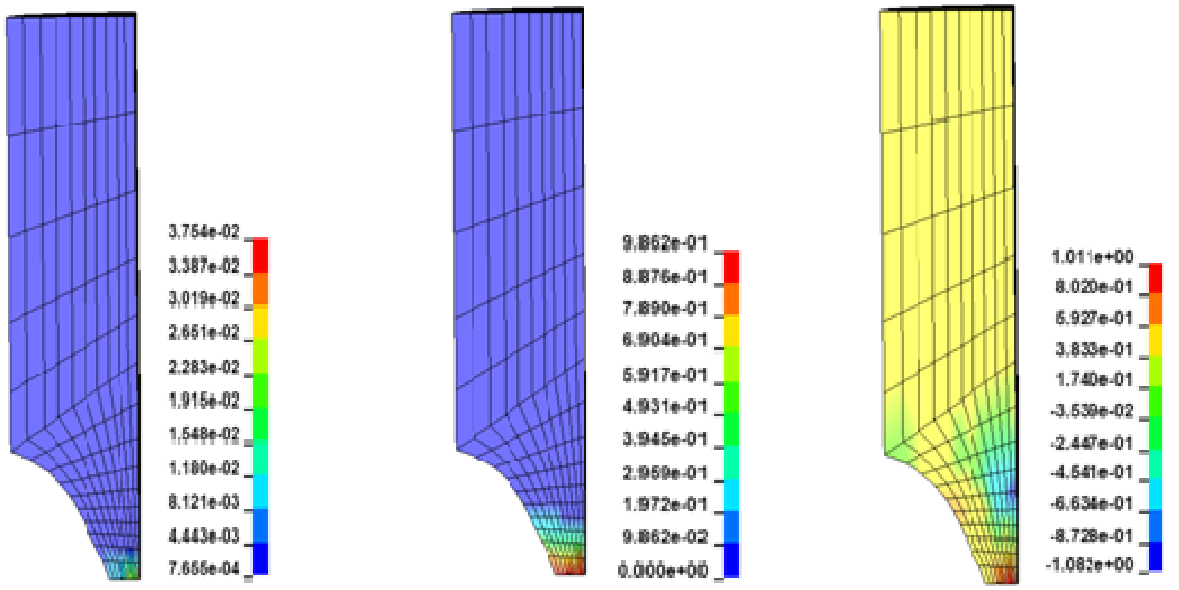
4.Application on Notched specimen.

The GTNB model described in this paper has been applied on a cylindrical notched specimen (1mm initial diameter at critical zone) to predict the damage evolution during a tensile test. Only one-eighth of the geometry has been meshed in 3D. Symmetry conditions have been applied in the 3 faces and the loading displacement was assigned at the top of the edge. The material data set for DP600 is listed in Table 1. The initial damage parameter f_0 equals 0.001 and q_2 equals 1.

Table1: Matrix *Material Parameters.*

Elasticity		Hill Plasticity			Isotropic hardening			Kinematic hardening	
E (GPa)		r_0	r_{45}	r_{90}	K (MPa)	ε_0	n	C	s (MPa)
210	0.35	0.85	1.04	0.94	891	0.02	0.245	92.04	58.02

The isovalues of the plastic strain in the matrix, the triaxiality factor and the porosity f are presented in fig.1 at the moment the maximum plastic strain was close to unity. The damage variable f is at a maximum at the core of the notch due to the high concentration of the plastic deformation and the triaxiality.



(a) porosity (b) matrix plastic strain (c) triaxiality

Fig.1 : Tensile test on notched specimen: isovalues

5.Conclusions.

The advanced GTN is developed to take into account the X-Ray porosity experimental results. A new explicit-implicit integration is also implemented. The results obtained with a notched specimen are promising in terms of equivalent plastic strain, porosity and triaxiality. Industrial application and comparison with experimental tests is in development.

Acknowledgements

The authors acknowledge Arcelor-Mittal Research S.A. (Olivier Bouaziz), and the Interuniversity Attraction Poles Program - Belgian State – Belgian Science Policy (P6/24) for its support. Eric Maire and Caroline Landron at the INSA de Lyon (France) are greatly recognized for providing the experimental database related to the tensile test.

References

[1] M. Ben Bettaieb, X. Lemoine, O. Bouaziz, L. Duchêne, A-M. Habraken, Damage initiation and growth in DP steel sheets, *Mechanics of Materials.*

[2] M. Ben Bettaieb, X. Lemoine, L. Duchêne, A-M. Habraken, On the numerical integration of an advanced Gurson model, *International Journal for Numerical Methods in Engineering,* DOI: 10.1002/nme.3010

[3] E. Maire, O. Bouaziz, M. Di Michiel, C. Verdu, Initiation and growth of damage in a dual-phase steel observed by X-ray microtomography, *Acta Materialia* 56 (18), 2008, 4954-4964

[4] C. Landron, O. Bouaziz, E. Maire, J. Adrien, Characterization and modeling of void nucleation by interface decohesion in dual phase steels, *Scripta Materialia* 63 (10), 2010, 973-976

[5] Gurson, A.L., 1977. Continuum theory of ductile rupture by void nucleation and growth: part I-yield criteria and flow rules for porous ductile media, J. Eng. Mater. Technol., 99, 2-15

[6]Tvergaard, V., Needleman, A., 1984. Analysis of the Cup-cone Fracture in a Round Tensile Bar. Acta Metall. 32, 157-169.

[7]Benzerga, A.A., Besson, J., 2001. Plastic potentials for anisotropic porous solids, Eur. J. Mech. A-Solids. 20, 397-434.

[8]Pardoen, T., 2006. Numerical simulation of low stress triaxiality ductile fracture, Comput. Struct., 84, 1641-1650.

© (2012) Trans Tech Publications, Switzerland
doi:10.4028/www.scientific.net/KEM.488-489.81

Dynamic Characteristics of Composite Materials Body for Bi-Modal Tram

Yeon Su Kim[1, a], Seky Chang[2,b], Kyeong-Ho Moon[3,c] and Jai-Kyun Mok[4,d]

[1,2,3,4] Korea Railroad Research Institute, Uiwang-si, Gyeonngi-do, South Korea
[a]yskim@krri.re.kr, [b]seky@krri.re.kr, [c]khmoon@krri.re.kr, [d]jkmok@krri.re.kr

Keywords: Bi-Modal Tram, Composite Material Body, Dynamic Characteristics.

Abstract. The car body of the bi-modal tram has been designed and built to have low floor to provide the old and the handicapped with easy access considering Korean physical standard, passenger capacity (standee, seated, handicapped), and bus and urban railway regulations in Korea. The car body has been composed of composite materials (light-weight sandwich constructions) with glass epoxy skins, aluminum honeycomb cores and aluminum inner-frames. This paper was aimed to evaluate dynamic characteristics of the car body while the bi-modal tram was running in the test track. Based on the results from vibration accelerations measured on the floor level of centers of car bodies and axle, dynamic characteristics of the composite materials car body were discussed in this paper.

Introduction

Generally, it is known that rubber-tired railway vehicles have better accelerating/decelerating performance and climbing capacity compared with conventional steel-wheeled railway vehicles. This has led lots of local governments in Korea to make plans to introduce rubber-tired light rail system such as bi-modal tram, monorail, AGT (automatic guide way transit). Among those, the bi-modal tram can travel on both dedicated track (lane) and public roadway, which can reduce construction cost and increase operational efficiency. It has passengers' capacity 1,000 to 5,000 persons/direction/hour (2-car or 3-car articulated vehicle). The bi-modal tram would be driven by CNG hybrid (series type) propulsion. All driving wheels were driven by electric traction motor-gearbox sets independently, which can eliminate differential gears to reduce turning radius and make low floor provide the old and the handicapped with easy access. The bi-modal tram has been developing in Korea since 2003 [1,2]. The car body of the bi-modal tram has been already designed and built to have low floor to provide the old and the handicapped with easy access considering Korean physical standard, passenger capacity (standee, seated, handicapped), and bus and urban railway regulations in Korea. The car body has been composed of light-weight composite materials with glass epoxy skins, aluminum honeycomb cores, and aluminum inner-frames [2,3].

This paper was aimed to evaluate dynamic characteristics of the car body while the bi-modal tram was running in the test track. Based on the results from vibration accelerations measured on the floor level of centers of car bodies and axle, dynamic characteristics of the composite materials car body were discussed in this paper.

Bi-Modal Tram

Vehicle Specifications. Trams can be classified into two groups, conventional steel-wheeled type and rubber-tired type (bi-modal tram). The bi-modal tram is developing to have articulated-two cars propelled by CNG hybrid (series type) propulsion in Korea since 2003, which can improve fuel efficiency and exhausting. The bi-modal tram can be also driven, steered, and guided by the AGS (automatic guidance system) which can calculate the vehicle position, wheel steering angles, vehicle speed and orientation to measure magnets coordinates and polarity installed on road per 4-5m. The AGS also makes the tram have a precision docking funcion in stations to provide passengers with easy access. Fig. 1 and Table 1 show vehicle configuration and general specifications for the bi-modal tram (2-car articulated vehicle) [1,2,4,5].

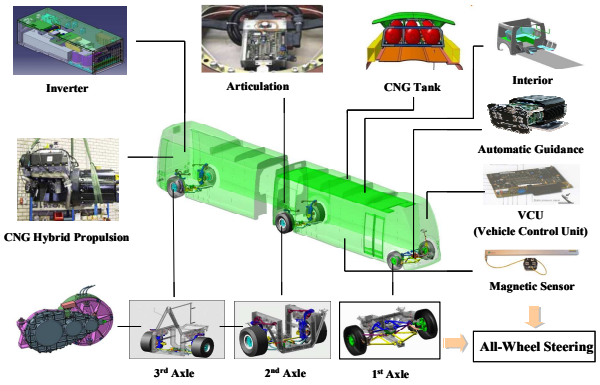


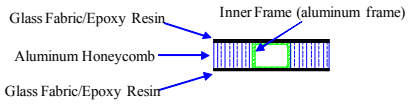
Figure 1 Configuration of the bi-modal tram.

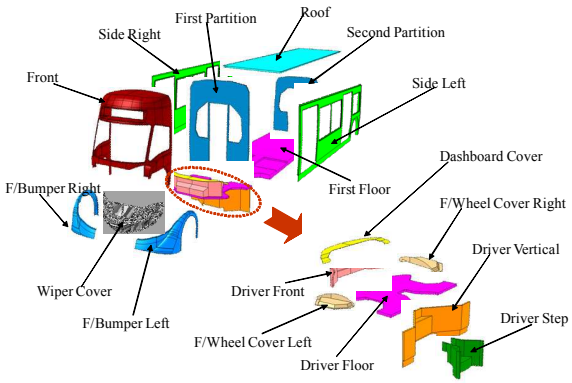
Table 1 Specifications of the bi-modal tram.

Length×Width×Height	18,000 × 2,480 × 3,393 [mm]
Weight	182kN (252kN including passengers)
Propulsion	Series Hybrid [CNG Engine + Generator + Li-Polymer Battery]
Floor Height	340 [mm] from the ground
Maximum Speed	80 [km/h]
Maximum Gradient	12 [%] under 50% of passenger load
Steering	All Wheels Steering
Minimum Turning Radius	12 [m]
Suspension	1st : rubber tires, 2nd : air spring

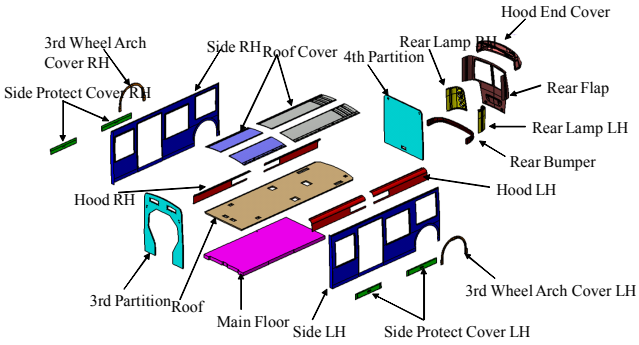
Composite Materials Car body. Figure 2 shows the composite materials composition (aluminum honeycomb sandwich panel) and car body configuration for the bi-modal tram. The car body was composed of 17 sections for carriage 1, and 18 sections for carriage 2. The roof, side, partition, and floor were built by the sandwich panels composed of glass fiber and epoxy resin (skin), aluminum frames (inner frame), and aluminum honeycomb panels. For the parts to support vehicle load, aluminum frames were installed to reinforce the strength and stiffness of the car body [2,3].

(a) composite materials





(b) carriage 1



(c) carriage 2

Figure 2 Composite materials car body of the bi-modal tram.

Vehicle Building and Test Track. The bi-modal tram composed of two articulated cars has been built completely as shown in Fig. 3. After checking the functions of the prototype tram, various tests and evaluations have been performed in both test track and public roadway since 2010. The test track has been constructed to evaluate the performance of the developed bi-modal tram system. It is a loop track to have 14m minimum radii of curvatures, 1~2% maximum gradient, and straight sections. Fig. 3 shows the bi-modal tram in operation at the test track.



Figure 3 Bi-modal tram in operation at the test track.

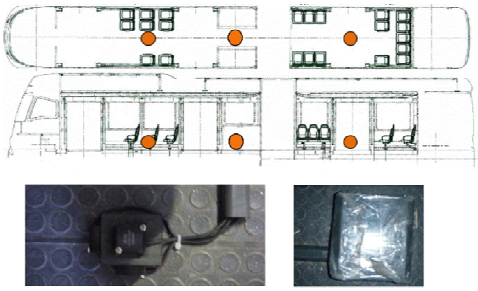


Figure 4 Vibration accelerometers on floor.

Dynamic Characteristics

Vibration Measurement. Vibration accelerometers were installed on the floor level of the center of carriage 1, axle 2, and carriage 2 as shown in Fig. 4. Two single axial accelerometers were fixed to vertical and lateral direction at the positions. Table 2 shows the specifications of the accelerometers for dynamic characteristics evaluations [1]. These were installed on the floor not to be affected by the resonance or local vibration during the vibration measurement.

Table 2 Specifications of vibration accelerometers

range (g)	sensitivity (mV/g)	frequency (kHz)	residual noise (μVRMS)	non-linearity (%FSO)	transverse sensitivity(%)	zero acceleration output (V)	thermal sensitivity (-20 to +85℃) %/ ℃
±200	10	0-1.5	±200	±0.5	±3	2.5±0.1	±0.028

Measuring Conditions. Vibration accelerations were measured at three positions simultaneously while the bi-modal tram was running at about 40~45 km/h maximum speed in the test track (maximum speed was limited to consider the length of the test track). Dynamic characteristics were evaluated on the condition of tare weight except measuring equipments, driver, and two researchers. Whenever the bi-modal tram turned around the test track, zero-to-peak values filtered by low-pass filter (20Hz) were calculated in vertical and lateral directions.

Results and Discussions. Fig. 5 shows a part of measured data (vehicle running speed, lateral and vertical vibrational accelerations) on the floor level of the center of carrage 1 while the bi-modal tram was running in the test track. Fig. 6 shows the lateral and vertical zero-to-peak accelerations (g) filtered by the low pass filter (20 Hz) on the basis of the measured data as shown in Fig. 5. Most of the zero-to-peak accelerations were less than 0.3g except vertical direction on the floor level of the center of axle 2. The lateral dynamic characteristics showed better results than the vertical directions. This results indicated the possibility that vertical vibrations occurred in the axle 2 (wheel, axle, electric motor, gearbox, and etc.) were transmitted directly into the composite materials car body. Fig. 6 also implied that the composite materials car body should be reinforced to have more stiffness for the improvement of the vertical dynamic characteristics.

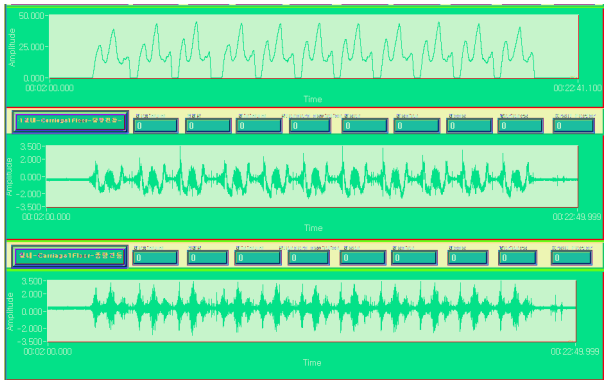


Figure 5 Vehicle speeds and vibration accelerations measured on the center of the carriage 1.

On the basis of the results, two design modifications were suggested in this paper in order to improve the dynamic characteristics of the composite materials car body. Mechanical vibrations transmitted into the car body from propulsion unit (electric motor, gearbox) and running wheels in the axle 2 should be isolated by removing physical contacts between the car body and rotating parts (like gearbox, electric motor, etc.), or changing bushing characteristics in connections between the carbody

and sub frames in axle 2. In addition, the floor parts of the car body should be reinforced by modifing structural composition or materials properties (aluminum frames in the composite materials can be installed more densely) to increase vertical stiffness which can improve vertical dynamic characteristics at the center of the car body. For the more generalized evaluations, however, it was expected that additional long-term tests and evaluations were necessary.

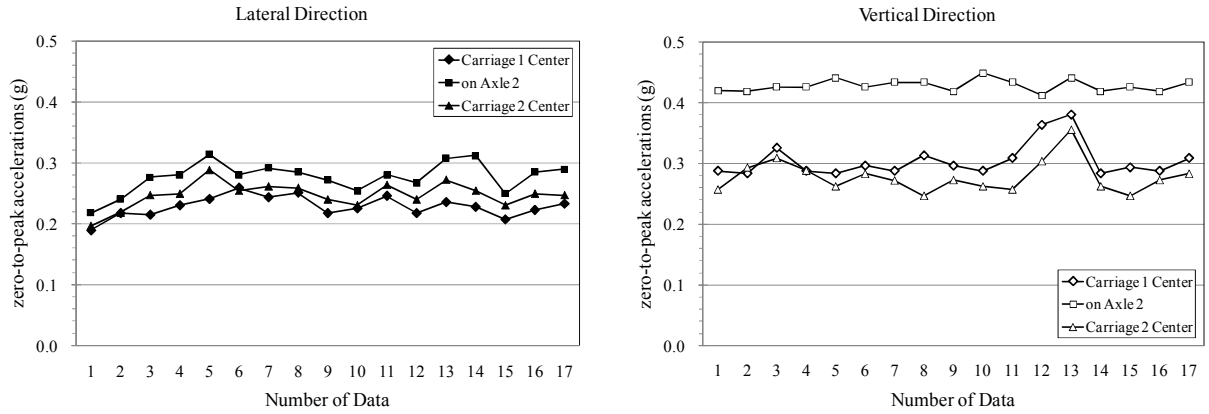


Figure 6 Lateral and vertical zero-to-peak accelerations evaluated in the test track.

Conclusions

Dynamic characteristics of the composite materials car body were evaluated while the bi-modal tram was running in the test track. On the basis of the results, in this paper, two design modifications were suggested to improve the dynamic characteristics of the composite materials car body: (1) mechanical vibrations transmitted into the car body from propulsion unit and running wheels in the axle 2 should be isolated, and (2) structural composition or materials properties in the floor parts should be modified to increase the vertical stiffness of the car body.

Ackonwledges

This work was a part of the R&D Project (bi-modal tram) supported by the Ministry of Land, Transport and Maritime Affairs (Korea). In addition, authors thank all people concerned in the Hankuk Fiber Glass Ltd., and the University of Sheffield for supporting this works.

References

[1] Korea Railroad Research Institute, in: Development for the bi-modal articulated low-floor vehicle, 1st-7th Annual Research Report (R&D/03 Transportation Essence B01), 2003-2010.

[2] Kim, Y.S., Lee, K.W., Mok, J.K., Leem, S.G. and Jeong, J.C., in: Structural analysis of body under 3-points supporting for bi-modal tram, Key Engineering Materials, Vols 417-418, pp. 401-404, 2010.

[3] Kim, Y.S., in: Strength and stiffness estimation for center fram of low floor vehicle, Materials Science Forum, Vols 654-656, pp. 2664-2667, 2010.

[4] Rudolf, B. Grool, in: The Frog Automated Transportation System Supervisor, Frog Navigation System B.V., The Netherlands, 2006.

[5] APTS, in: Phileas Driver's Manual, The Netherlands, 2005.

© (2012) Trans Tech Publications, Switzerland
doi:10.4028/www.scientific.net/KEM.488-489.85

Comparison between 3D FEM and Standard ISO Tooth Root Stresses

Gordana Marunić, Goran Gregov and Vladimir Glažar

University of Rijeka Faculty of Engineering, Vukovarska 58, 51000 Rijeka, Croatia

gmarunic@riteh.hr, gregovg@riteh.hr, vladimir.glazar@riteh.hr

Keywords: Thin-Rimmed Gear, Tooth Root Stress, 3D FEM, ISO Standard

Abstract. The paper deals with the discussion how nominal spur tooth root stress of thin-rimmed gear determined in accordance with the standard ISO 6336-3:2006, method B, agrees with the results of the 3D FEM stress analysis.

The procedure proposed by standard ISO for the tooth root stress calculation doesn't identify the stress behaviour related to mutual affects of characteristic thin-rimmed gear geometrical parameters. Therefore, the 3D FEM analysis of tooth root stress has been performed for gear structures with middle and offset web with various rim and web thickness. The rim thickness has covered and slightly overcome the backup ratio defined by ISO procedure, while the web thickness has covered the range of practical interest.

Introduction

Many researchers have been involved in the reappraisal and definition of new criteria based upon real gear stress conditions that can encourage the reduction of dimensions. A survey of available literature has underlined the following.

The approach to the tooth root stress determination has been firstly 2D and nowadays is always 3D one [1, 2]. Different numerical models of gear, gear pair or gear transmission have been utilised as well as the way the loading or the teeth contact phenomenon have been modelled [3, 4]. The investigations started with the gear tooth root stress and then entire gear structure stress have been embraced [5, 6, 7]. Various accompanying calculation methods and numerical environment to predict the gear state of strain and stress have been developed [8, 9].

The results of tooth root stress investigations for thin-rimmed gear have proved from the beginning that conventional calculation procedures proposed by standards are not applicable for the gear structure where teeth support suffers from considerable deformations [10, 11]. The rim thickness factor K_B for the correction of nominal tooth root stress for flexibly supported gear teeth, was firstly introduced by the standard AGMA [12]. The factor Y_B was adopted later by the standard ISO [13], too. These factors are both expressed as the function of backup ratio i.e. the ratio of rim thickness and the tooth height.

In this work, the results of the 3D FEM analysis [14] are the basis for the comparison of the obtained highest values of normal maximum principal spur tooth root stress, and nominal tooth root stress according to the standard ISO 6336-3, method B calculation procedure. The gear geometrical parameters under consideration are the rim and web thickness of middle and offset web gear structures. The affects of these parameters are investigated in relation to the magnitude of the mentioned maximum tooth root stress.

Nominal Tooth Root Stress Calculation According to Standard ISO

The standard ISO 6336-3, method B starts from the assumption that maximum tooth root stress occurs when the load is acting at the outer point of single pair tooth contact. The position of maximum nominal normal tooth root stress σ_{F0} is defined by the tangent to the tooth fillet, at the angle $\varphi = 30°$ to the tooth centre line.

Among the correction factors proposed for nominal tooth root stress calculation, the rim thickness factor is separated as it is used for the evaluation of rim thickness influence when detailed calculations of stresses in both tension and compression or experience are not available. The ratio s_R/h_t of the rim thickness s_R and the tooth height h_t, called backup ratio, is used for the determination of rim thickness factor Y_B. The case when $s_R/h_t \leq 0{,}5$ is to be avoided, and for $1{,}2 > s_R/h_t > 0{,}5$, the equation as well as the possibility of graphical determination, are given for factor Y_B.

Geometrical and Numerical Model of 3D Pinion-Wheel System

The stress calculation and analysis is performed for the gears having the same geometrical parameters of the tooth. Thin-rimmed wheel geometrical parameters of interest, the rim and web thickness are varying to cover thin rim range in accordance to the standard ISO and web thickness of practical interest. The backup ratio s_R/h_t is taken from 0,44; 0,64; 0,92 to 1,33. The web thickness b_s expressed by the tooth face width b, b_s/b is adopted b_s/b=0,1; 0,2; 0,3 and 0,4. In this work the gear under consideration i.e. the wheel of gear pair, was considered with middle and offset web arrangement.

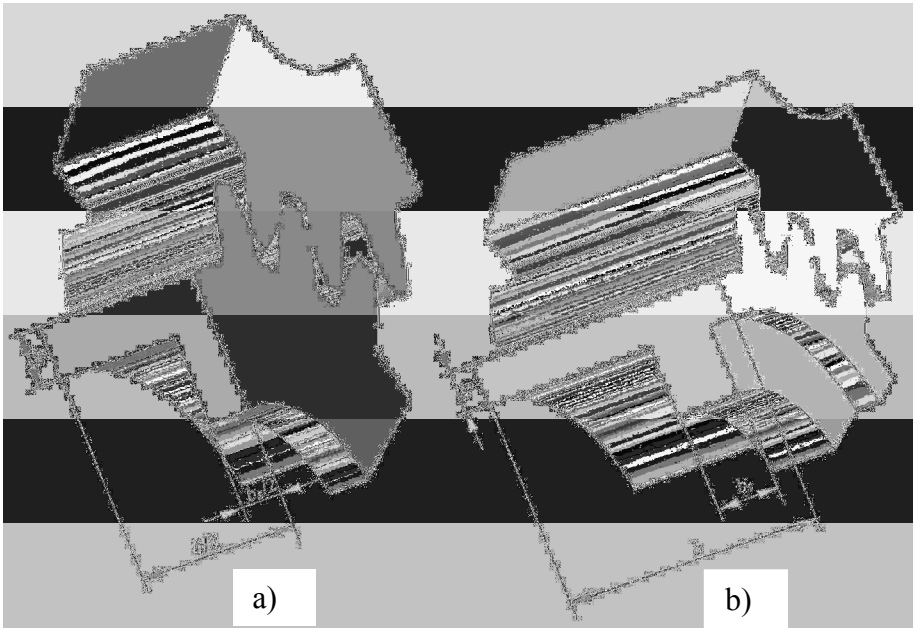


Figure 1. Geometrical model of gear pairs of a solid pinion mating with thin-rimmed wheel with middle web (half face width model) (a), and thin-rimmed wheel with offset web (b)

The face width of pinion and wheel was chosen $b_1=b_2$=100 mm (b/m=10). The angular extension of pinion and wheel models corresponds to four teeth, while three teeth are modelled above the rim (Fig. 1). The engagement and loading were accomplished through the middle teeth at the outer point of single pair tooth contact.

In order to minimize the time and effort for the modelling and calculation, numerical models were developed based upon the previously described partial geometrical models [8, 9]. By imposing the proper boundary conditions, the torque was simulated by tangential traction at the pinion internal rim surface.

The areas of interest i.e. the teeth surfaces in contact and the tooth root fillet were meshed with calculated and examined grid density and the compromise was found on the convergence of results for the wheel model with middle web (half of the face width) and wheel with offset web arrangement. The contact between the pinion and wheel surfaces was found for geometrical contact

line positioned approximately at the middle of contact surfaces. The contact width was adopted in accordance with [15] and the used software solver detects the frictionless contact between the teeth surfaces at the established engagement position.

Comparison of Tooth Root Stresses

The tooth root stress is normal maximum principal stress σ_1 at the tooth surface of tensile side of the loaded tooth calculated by means of 3D FEM (later on – tooth root stress). The highest values of maximum principal stress σ_{1max} are excluded regardless of their position along the tooth fillet as well as along the face width. These stress values are compared with the corresponding normal nominal tooth root stresses σ_{FO} determined in accordance with the standard ISO 6336-3, method B i.e. at the tooth fillet location determined by the 30° tangent.

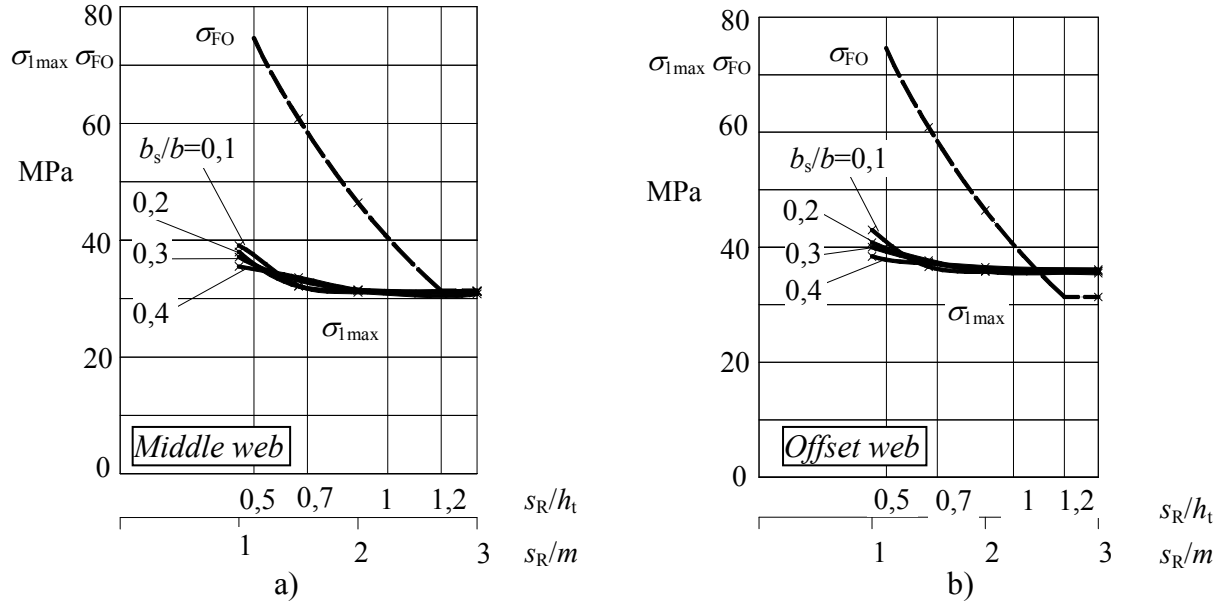


Figure 2. Maximum tooth root stress σ_{1max} related to the rim and web thickness, and normal nominal tooth root stress σ_{FO} according to the standard ISO related to the rim thickness, for middle web position (a) and offset web position (b)

In Fig. 2 a, b the tooth root stress σ_{1max} is related to the backup ratio s_R/h_t and web thickness ratio b_s/b, and the stress σ_{F0} is related to the s_R/h_t. The rim thickness is expressed additionally by very often used ratio s_R/m.

The difference of maximum tooth root stresses σ_{1max} considering various web arrangements is greater for thicker rims when maximum stress for gear with offset web is larger than maximum stress for gear with middle web about 15%, regardless of web thickness.

For middle web gear structure with the thinnest web, maximum stress for the thinnest rim is about 27% greater than the stress for the thickest considered rim, and for the gear structure with offset web, the stress is greater about 21%. It means that the rim thickness affects the tooth root stress maximum values more in the case of middle web.

As regards the influence of web thickness it can be noticed only for the thinnest rims. The stress for the gear with offset web is greater for the thinnest web about 12% than the stress for the thickest web, and for the gear with middle web it is greater about 10%.

The differences between two stresses σ_{1max} and σ_{F0} determined by different methods are more expressed for middle web arrangement (Fig. 4a) where lower maximum stresses determined by 3D FEM are detected, in comparison with offset web arrangement. When the backup ratio is larger than s_R/h_t =1,2 (s_R/m=2,7) and the influence of rim thickness doesn't exist anymore according to ISO calculation procedure, the stresses σ_{1max} and σ_{FO} coincide well, regardless of web thickness.

For offset web arrangement the difference of tooth root stresses σ_{1max} and σ_{FO} is more obvious for lower values of backup ratio, but exists too for the backup ratio values greater than s_R/h_t =1,2(s_R/m=2,7), Fig. 4b, when the stress values of σ_{FO} are lower than the values of σ_{1max}.

In the case of the adopted gear geometry, loading and material properties, the stress σ_{1max} is found approximately 2,2 times greater than σ_{FO} for the lowest backup ratio (s_R/h_t =0,5; s_R/m= 1,125) for middle, and about 2,1 times for offset web arrangement. For the gear with offset web and the thickest rim (s_R/h_t =1,33; s_R/m= 3) the tooth root stress σ_{FO} is approximately 1,14 times lower than the stress σ_{1max}.

Conclusions

The rim thickness of the chosen gear structures generally contributes more to the teeth support stiffness than the web thickness, and consequently maximum tooth root stress variation is more effected by the rim thickness, regardless of web arrangement.

For the backup ratio of about s_R/h_t = 0,8 (s_R/m = 1,8) and greater, the influence of rim thickness on tooth root stress is found neglect able regardless of web thickness and its arrangement. This limit value of rim thickness is less than the proposed one by the standard ISO 6336-3, method B, where the backup ratio is equal to s_R/h_t = 1,2 (s_R/m = 2,7).

The comparison of the 3D FEM and the standard ISO tooth root stresses indicates that nominal tooth root stress is highly overestimated for thinner rims in relation to the 3D FEM stress, regardless of web arrangement and web thickness. For thicker rims and backup ratio greater than s_R/h_t =1,2 (s_R/m=2,7), stresses coincide well for middle web arrangement, but in the case of offset web arrangement nominal tooth root stress becomes underestimated related to the stress values according to the 3D FEM.

References

[1] S. Oda, K. Nagamura and K. Aoki: Bulletin of the JSME, Vol. 24, (1981), p. 1273

[2] G. Curti, et al., in: *Proceedings of JSME International Conference on Motion and Power Transmissions*, JSME, Hiroshima (1991).

[3] L. E. Wilcox: Machine Design, No. 23, (1978), p. 88

[4] H. C. Kim, et al.,in: *Proceedings of International Congress – Gear Transmissions - `95*, edited by K. Arnaudov, TUME - Bulgaria, Sofia (1995).

[5] T. Sayama and S. Oda : Bulletin of JSME, Vol. 27, No. 230, (1984), p. 1773

[6] T. Sayama, S. Oda, and K. Umezawa : Bulletin of JSME, Vol. 29, No. 256, (1986), p. 3582

[7] S. Li: Journal of Mechanical Design, No.124, (2002), p. 129

[8] C. Baret, G. Coccolo and F.A. Raffa, in: *Proceedings of International Gearing Conference*, Newcastle Upon Tyne, (1994), p.149

[9] M. S. Prabhu, D . D. R. Houser, in : *Proceedings of International Conference of Gears,* Dresden, (1996), p. 201

[10] J. Hiremagalur, B. Ravani: Mechanics Based Design of Structures and Machines, Vol. 32, No. 4 (2004), p. 423

[11] E. Conrado, P. Davoli: GearTechnology (2007), p.52

[12] ANSI/AGMA C95 (2001)

[13] ISO 6336 -3 (2006)

[14] I-DEAS, SRDC, (2000)

[15] S. Li : Journal of Mechanical Design, Vol. 124, (2002), p. 511

© (2012) Trans Tech Publications, Switzerland
doi:10.4028/www.scientific.net/KEM.488-489.89

Crystallographic analysis of specimens used for calibrate a failure model for an Al 6061 – T6 alloy

M. Giglio[1,a], A. Manes[1,b*], C. Mapelli[1,c], D. Mombelli[1,d], C. Baldizzone[1,e], A. Gruttadauria[1,f]

[1]Politecnico di Milano, Department of Mechanical Engineering,

Via la Masa 1, Milano, Italy

*Corresponding author, Politecnico di Milano, Department of Mechanical Engineering,

Via la Masa 1, 20156 Milano (ITALY),

phone ++39-02 2399 8630, Fax ++39-02 2399 8282

[a]marco.giglio@polimi.it, [b]andrea.manes@polimi.it, [c]carlo.mapelli@polimi.it, [d]davide.mombelli@mail.polimi.it, [e]claudio.baldizzone@mecc.polimi.it, [f]andrea.gruttadauria@mecc.polimi.it

Keywords: Al 6061– T6, Bao-Wierzbicki method, EBSD analysis, failure, textures

Abstract. Calibration and exploitation of failure criterion is at present a challenging field in the structural integrity scenario. Calibrated failure criteria allow the simulation/reproduction of damages using virtual approach and eventually further assessment of the residual integrity of the components. Therefore the increase of awareness in failure issues makes the numerical simulation an actual, useful and reliable tool for the analysis of complex structures under extreme loads, especially in aerospace field where full scale tests are often very expensive and difficult to carry out. With this aim, the constitutive relations of an Aluminium Al 6061-T6 alloy have been calibrated with dedicated focus on failure criterion. The results obtained have been discussed considering the crystallographic measurements that permit to point out the dissipative behavior on the basis of texture formation as a function of the load type. The final aim is to confirm and explain the different failure behavior depending on the different stress triaxiality.

Introduction

Numerical assessment of the ductile fracture in metallic components represents an innovative and challenging field in the structural integrity scenario especially for aerospace, automotive and manufacturing industries. However, in order to obtain reliable and realistic results, a complete calibration both of true stress-strain curve and failure is required. With this aim a complete characterization of the mechanical properties of Al 6061-T6 aluminium alloy for how concern material hardening and fracture locus has been carried on in a previous work [1]. Al 6061-T6 belongs to the aluminium series 6000 with silicon and magnesium as principal alloying components. These alloys are developed for heat treatment (in present case T6) and they show good formability, workability, weldability and shaving. The chemical composition of Al 6061-T6 is described in *Tab. 1*.

Tab. 1 Chemical composition of Al 6061-T6

Chemical composition (wt.%) of Al 6061-T6 alloy								
Al	**Mg**	**Si**	**Fe**	**Cu**	**Mn**	**Cr**	**Zn**	**Ti**
98	0.8-1.2	0.4-0.8	0.7	0.15-0.4	0.15	0.04-0.35	0.25	0.15

Calibration has been carried on through a series of experimental tests on simple specimens, with similar geometry, but subjected to different stress triaxiality, thanks to the use of a multiaxial hydraulic test machine. The calibration of a versatile fracture criterion which covers a large range of

conditions requires different experimental tests. All the experimental tests have been numerically simulated (by means of Finite Element Models) and, based on the results of these analyses, a complete material constitutive model has been calibrated. In particular the methodology used have been focused on the calibration of a ductile failure criterion using the Bao-Wierzbicki [2] framework: this approach represents the state of the art about the criteria based on the stress triaxiality η and it is indirectly already implemented in most common finite element codes. All the details of this calibration are fully reported in [1]. In *Fig. 1* the fracture locus found in [1] is reported compared with a Johnson – Cook model from literature [3]. In *Fig. 2* the different specimens after the tests are presented.

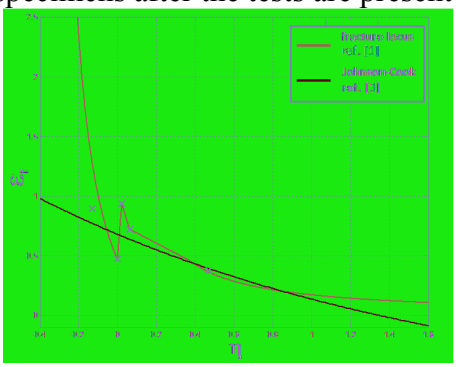


Fig. 1 Comparison between the new calibrated fracture locus for Al 6061-T6 and a literature Johnson-Cook criterion (ε_f strain at failure - η stress triaxiality)

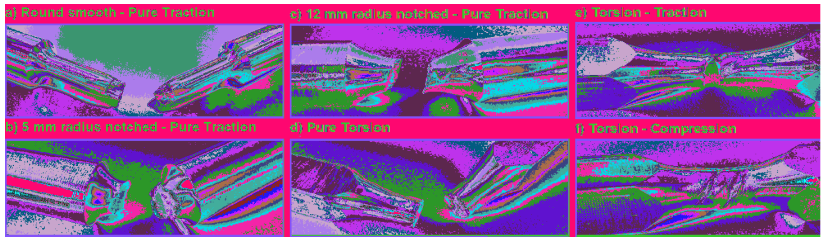


Fig. 2 Specimens after failure

The proposed model considers only the dependence of the failure strain from the stress triaxiality. The obtained indications point out a critical condition associated to the plane strain state caused by the torsion test, approximately with η equal to zero.

Experimental procedures

The experimental procedure for the metallographic and texture investigations involves mechanical grinding followed by chemical electro-polishing or chemical micro-etching, in case of, respectively Electron Backscattered Diffraction analysis or optical microscopy observation. Following the standard procedure for mechanical grinding, the samples are polished using an aqueous solution of colloidal SiO_2 (0.2 μm), while the electro-polishing is carried out using a Struers Movipol equipment using the following electrolyte composition. Such treatment is designed to remove the surface oxide layer in order to enhance the backscattered signal emitted by the surface, a crucial requirement for the EBSD analysis. Concerning the chemical micro-etching the authors employ the so called Berker solution, whose composition is reported in the table below (*Tab. 2*).

The SEM instrumentation employed for the experimental work is a Carl Zeiss AG - EVO® 50 Series and the rolling direction taken during the measurement corresponds to the axis of the specimens for the tensile test (RD in *Fig. 3*). Moreover, in order to correctly interpreter the EBSD images reported in the following section it is worth to mention the resolution and other crucial parameters employed during the analysis. Specifically, the pixel area of the digital image for the texture corresponds to 7.02 μm^2, the magnification used is 500x, meaning that the EBSD picture includes about 800x600 μm^2, the working distance of the EBSD probe is 16.5 mm and 20 kVx1 nA is applied.

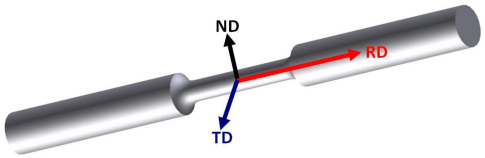


Fig. 3 Sketch of the test specimen featuring the reference system employed for the EBSD analysis

Tab. 2 Chemical composition of etchants used to prepare aluminium Al 6061-T6 alloy samples [4]

Chemical composition of etchant solution				
	H_2O	C_2H_5OH	HBF_4	$HClO_4$
Electro-polishing sol.	500 ml	-	4-5 ml	-
Berker sol.	140 ml	800 ml	-	60 ml

Analyses were performed on specimens (*Fig. 2*) representing four stress state studied to calibrate the ductile failure criterion using the Bao-Wierzbicki method: pure traction *(Fig 2.a,b,c)*, pure torsion *(Fig 2.d)*, torsion-traction *(Fig 2.e)* and torsion-compression *(Fig 2.f)*. Preliminary optical microscopy investigation was carried out to select the best magnification to use during the crystallographic analysis.

Results and discussion

The study involves a detailed crystallographic investigation concerning the texture modifications related to the different load modality applied to the specimens. Specifically, the load cases considered consists in: traction (referred to test sample *Fig 2.c*), torsion (*Fig 2.d*), torsion-traction (*Fig 2.e*) and torsion-compression (*Fig 2.f*). The texture analysis confirms the assumption that the load configuration affects directly the observed texture. Actually, the EBSD images performed in the fracture region indicate clearly the presence of cube texture around $\{100\}<001>$ (*Fig. 3, Fig. 4*), for the torsion-traction and torsion-compression cases, while in the case of pure traction the diffraction images point out a strong rotated cube $\{100\}<001>$ (*Fig. 5*).

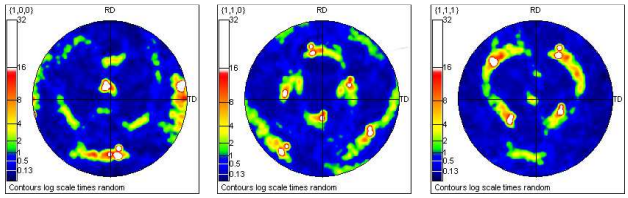


Fig. 3 Direct Polar Diagram near the fracture region of specimens that have undergone a loading modality of torsion-traction.

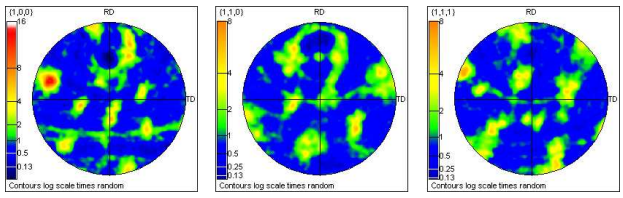


Fig. 4 Direct Polar Diagram near the fracture region of specimens that have undergone a loading modality of torsion-compression.

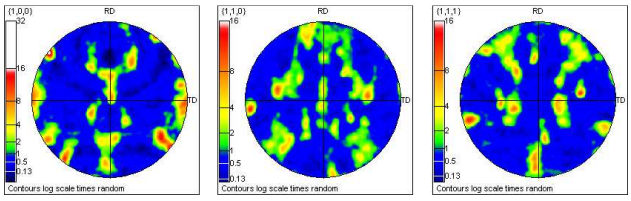


Fig. 5 Direct Polar Diagram near the fracture region of specimens that have undergone a loading modality of pure traction.

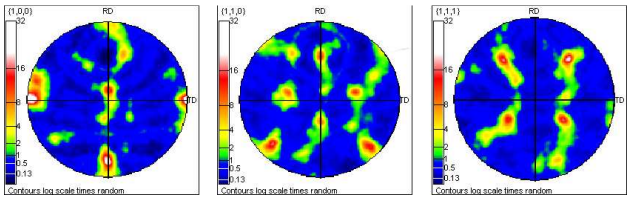


Fig. 6 Direct Polar Diagram near the fracture region of specimens that have undergone a loading modality of pure torsion.

The induction of cube and rotated cube components is typical of plastically deformed aluminium alloys and it intensifies strongly just before the fracture point is reached.

On the other hand, the inverse polar diagram points out a different behaviour that is very consistent with the revealed ductile fracture locus. The inverse polar diagram related to simply torsional loading condition shows a strong alignment of <100> direction of the elementary cells along the three reference directions (*Fig. 7*).

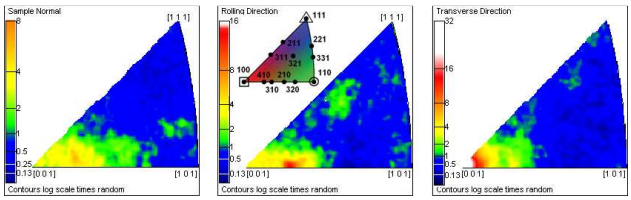


Fig. 7 Inverse Polar and the EBSD map for torque.

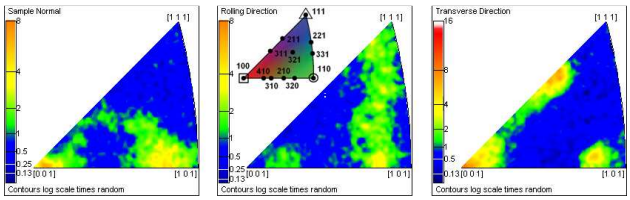


Fig. 8 Inverse Polar and the EBSD map for tensile stress.

A situation of strong concentration of elementary cells along two main direction has been shown also by the traction loading modality typical of notched stress, but in this case also the alignment of <112> along TD direction has been pointed out (*Fig. 8*).

In the case of combined loading (torsion-compression and torsion-traction) the texture development is wider and the texture distribution is much more distributed (*Fig.9, Fig. 10*).

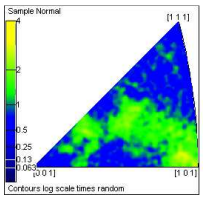


Fig. 9 Inverse Polar and the EBSD map for compression-torque loading.

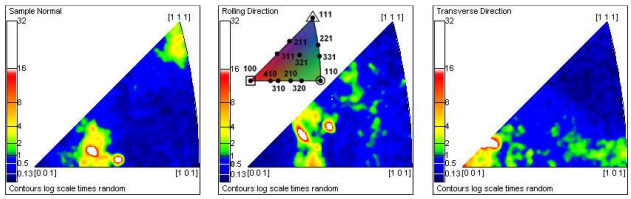


Fig. 10 Inverse Polar and the EBSD map for tensile-torque loading.

The higher diffusion of the texture components indicates the activation of different deformation patterns followed by the activated deformation system of the crystal lattices. The increase in the number of the deformation patterns followed by system taking part to plastic deformation is associated to the higher work to be performed to produce fracture. Actually, this is consistent with the statement of the first part of this work: a larger deformation extent has been associated to the load cases that include a tensile stress, as both in *e-case* and *f-case* the deformation process seems to have been more intense, leading to a narrower dispersion of lattice orientations.
Thus, the ductile fracture locus appears to be strictly related to the rotation and straining performed at the level of crystal lattice. The introduction of tensile loading condition and especially the combined loading modalities induce a less dangerous effect than the torque modality, because a higher number of deformation patterns followed by the activated system of the elementary cells implies an increase of the dissipated work, as proved by the comparison between measured polar diagram and EBSD maps and the results of ductile fracture locus.

Conclusions

Finally, from the EBSD survey involved in the result and discussion section the following are drawn:

- the defined ductile fracture locus is consistent with the revealed distribution of the texture components;
- the higher the number of the deformation modalities interesting the lattice systems taking part to the deformation process, the higher is the work to be spent for reaching the fracture point;
- the torque modality induces the activation of deformation system that tend to deform following a unique pattern and this deformation modality is characterized by a low value of work dissipation, while the combined conditions are features by a more diffused distribution of the final textures indicating different and concurrent modalities of deformation that are associated to a highest dissipation efficiency of the work that leads the material to fracture.

References

[1] A. Gilioli, A. Manes, M. Giglio, “Calibration of a constitutive material model for AL-6061-T6 aluminum alloy”, Proceeding of the ACE X, July 8-9, 2010, Paris, (France).

[2] Y. Bao, T. Wierzbicki. A comparative study on various ductile crack formation criteria. Journal of Engineering Materials and Technology, 126(3):314–324, (2004).

[3] D. R. Lesuer, G.J Kay, M. M. LeBlanc. Modeling large-strain, high rate deformation in metals, UCRL-JC-134118, Lawrence Livermore National Laboratory (2001).

[4] AA.VV. ASM Metal Handbook, Vol. 9, Metallography and Microstructure, pagg. 694,712, 1688 (2004)

© (2012) Trans Tech Publications, Switzerland
doi:10.4028/www.scientific.net/KEM.488-489.93

Cyclic Mixed-Mode Crack Propagation due to Time-dependent Multiaxial Loading in Jet Engines

Guido Dhondt[1, a]

[1]MTU Aero Engines, Postfach 50 06 40, 80976 Munich, Germany

[a]guido.dhondt@mtu.de

Keywords: Cyclic crack propagation, mixed-mode, mission analysis, cycle extraction.

Abstract. Components in jet engines are subject to time-dependent multiaxial loading. This creates a time-varying mixed-mode stress state at the crack tip. Mixed-mode loading leads to out-of-plane crack propagation and has been treated in previous articles [1,2]. This paper concentrates on coping with the time-dependent character. Key issues are the crack propagation rate and the crack propagation direction in three-dimensional space. In order to determine the prevalent crack propagation direction the dominant loading case is determined based on its crack propagation rate. Then, a mixed-mode equivalent K-factor is calculated for all other loading cases based on the closeness of their associated crack propagation direction with the dominant one. Subsequently, a cycle extraction is performed on the crack propagation rate for all loading cases. The extracted cycles are processed based on their mimimum and maximum equivalent K-factor and the maximum temperature. The mission crack propagation rate consists of the sum of the rate of all extracted cycles.

Introduction

Crack growth in real engine components usually exhibits mixed-mode, i.e. the crack does not necessarily stay in-plane. Since most crack propagation tests are performed under mode-I conditions, a procedure has to be defined to reduce the mode-I, mode-II and mode-III stress intensity (K) factors to just one equivalent K-factor which can be used in the well-known Paris crack propagation law (or any equivalent law). Furthermore, a bending and twist angle has to be calculated in order to determine the local crack propagation angle. Several criteria fulfilling the above conditions have been formulated in the past [1,2]. They often lead to similar results, however, due to the limited amount of mixed-mode testing further verification is needed. In the present paper it is assumed that the mixed-mode crack propagation procedure of [1] is used for the evaluation of the crack propagation rate and direction of any single cycle. The primary objective of the paper is to extend this procedure to the evaluation of complete missions. A mission is characterized by a sequence in time of loading points, each leading to a different mixed-mode state at any point along the crack front. An example of such a mission is a complete flight of an airplane, leading to time-dependent temperature and stress conditions at any location in its jet engines. Focusing on one location, the resulting mixed-mode state changes in time leading to several issues to be solved: what is the parameter to be used in the cycle extraction procedure and how does one cope with the different crack propagation angle of the lower and upper state of the extracted cycle. The next sections try to answer these questions.

Equivalent K-factor and crack propagation angles

The MTU mixed-mode crack propagation criterion[1] is based on a local analysis of the linear elastic asymptotic stress field along the crack front. Denoting the cylindrical coordinates in a local coordinate system at a location along the front by r, θ and z, the asymptotic stress field $\sigma_{ij}(r, \theta)$ depends on r only through a factor of $r^{-1/2}$. Therefore, multiplying this stress field by $r^{1/2}$ leads to the self-similar stress field $\sigma_{ij}^*(\theta)$. Notice that this stress field has the dimension of stress intensity factor. The eigenvalues corresponding to the self-similar stress tensor are denoted by $\sigma_1^*(\theta) \geq \sigma_2^*(\theta) \geq$

$\sigma_3^*(\theta)$, and the principal planes are described by $\varphi_1(\theta)$, $\varphi_2(\theta)$, $\varphi_3(\theta)$ (bending angles) and $\psi_1(\theta)$, $\psi_2(\theta)$, $\psi_3(\theta)$ (twist angles, Fig. 1). It is assumed that crack propagation will occur in a principal plane through the crack tip perpendicular to the largest principal self-similar stress. The condition that the principal plane must contain the crack tip is equivalent to postulating that the bending angle equals θ. So we are looking for $j \in \{1,2,3\}$ and $\theta^0 \in [-\pi/2, \pi/2]$ such that

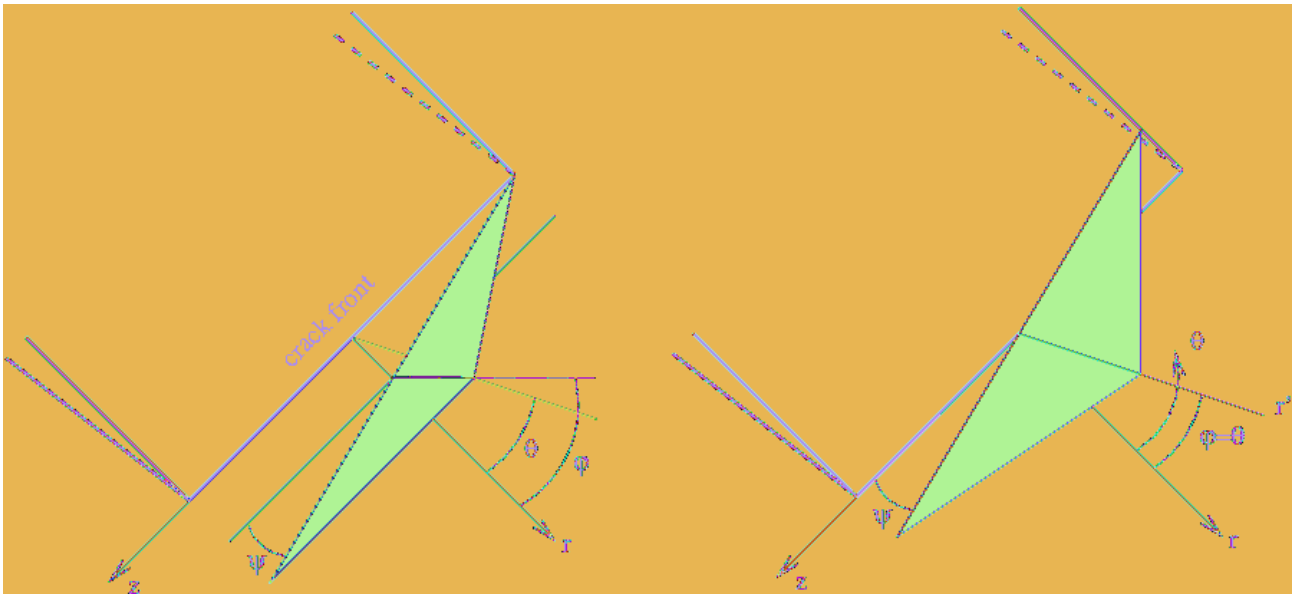


Figure 1: Principal plane not containing (left)/containing (right) the crack tip

$$\sigma_j^*(\theta^0) = \max\{\sigma_i^*(\theta) \mid \theta = \varphi_i(\theta)\},\ i \in \{1,2,3\}. \tag{1}$$

θ^0 is the bending angle of the crack propagation at the location considered. Generally speaking, the crack propagation is characterized by the largest principal stress, which is defined as the equivalent K-factor $K_{eq} \equiv \sigma_j^*(\theta^0)$, the normal vector on the crack propagation plane $\vec{n} \equiv \vec{n}_j(\theta^0)$, the bending angle $\varphi \equiv \varphi_j(\theta^0) = \theta^0$ and the twist angle $\psi \equiv \psi_j(\theta^0)$. By rotating the original crack plane φ radians about the local z-axis and subsequently ψ radians about the rotated r-axis r', one obtains the final position of the crack propagation plane. The complete set of principal stresses (not just the equivalent K-factor) and the complete set of principal directions is denoted by $\sigma_i^0 \equiv \sigma_i^*(\theta^0)$ and $\vec{n}_i^0 \equiv \vec{n}_i(\theta^0)$, respectively. These quantities depend on z (the location along the crack front) and time. So, up to now we have defined for each location along the crack front and for each time data point an equivalent K-factor and a direction the crack would like to take. However, in reality the time data points are not independent since cycle extraction links them as pairs, and the crack propagation direction for the upper and lower data point in a cycle should be the same. Therefore we are looking for a dominant crack propagation direction.

Identifying a dominant crack propagation direction

For the sake of the identification of a dominant crack propagation direction the standard Paris cyclic crack propagation law is taken in the form

$$\frac{da}{dN} = 10^{-7}\left(\frac{\Delta K_{eq}}{\Delta K_z}\right)^n \text{ (da/dN in m/cycle, K-factors in MPa.m}^{1/2}\text{)}, \tag{2}$$

where ΔK_z and n are temperature-dependent material constants. Since the equivalent K-factor and the temperature are known for all times, one can plot the crack propagation rate for a given crack front location assuming 0-max cycles, i.e. $\Delta K_{eq} = K_{eq}$ (Fig. 2, dropping the constant factor 10^{-7}).

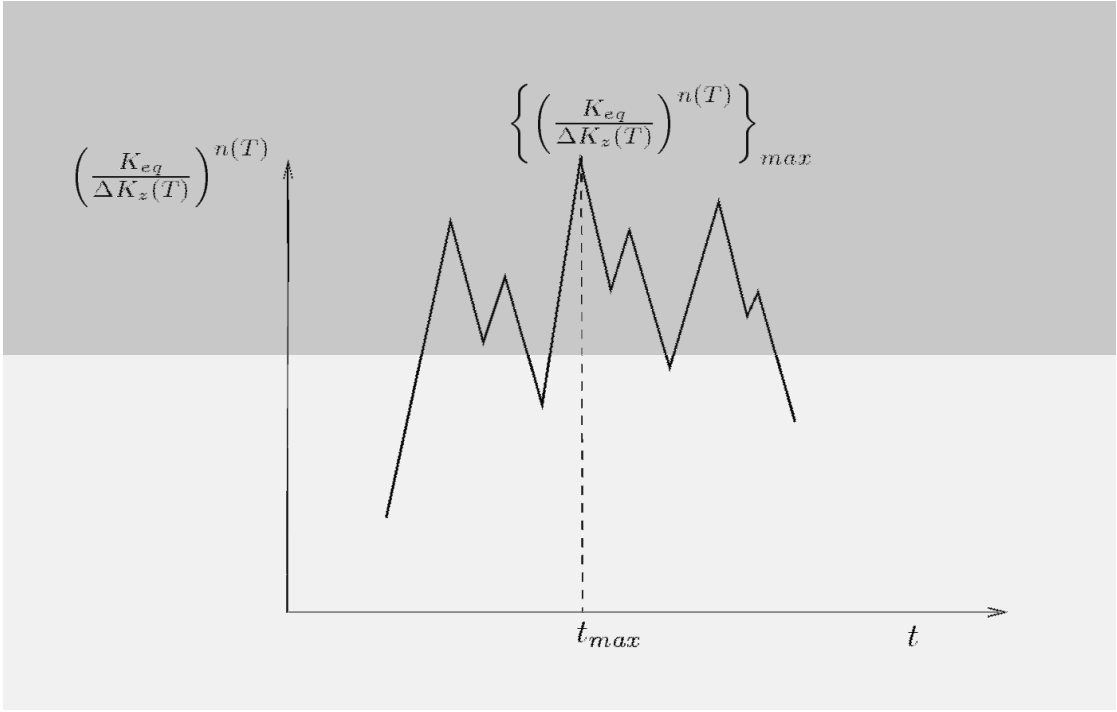


Figure 2: Definition of the dominant crack propagation time point

The time at which the crack propagation rate is maximum is called $t_{\max}$. The crack propagation direction $\theta^0(t_{\max})$ is considered as the dominant direction. The crack propagation at all other times is assumed to take place in a principal plane as close as possible to the dominant crack propagation direction, irrespective whether the corresponding principal self-similar stress is the maximum one at that time or not. This means that for all times t we are looking for $j \in \{1,2,3\}$ such that

$$\left|\vec{n}_j^{\,0}(t)\cdot\vec{n}(t_{\max})\right| \geq \left|\vec{n}_i^{\,0}(t)\cdot\vec{n}(t_{\max})\right|, i \in \{1,2,3\}, i \neq j. \tag{3}$$

The selected direction and the corresponding equivalent K-factor are called $\vec{n}^{\,s}(t) \equiv \vec{n}_j^{\,0}(t)$ and $K_{eq}^s(t) \equiv \sigma_j^0(t)$, respectively. Summarizing, after determining a dominant crack propagation direction based on the maximum crack propagation rate (looking at each time point separately, as if evaluating a 0-max cycle), the propagation direction (and equivalent K-factor) for all other time points is determined based on its proximity to the dominant direction.

Cycle extraction

Now, the crack propagation rate based on the selected equivalent K-factor is plotted as a function of time (Fig. 3). Notice that the material constants are temperature-dependent and that the correct time-dependence of the temperature has to be taken into account. A subsequent cycle extraction, e.g. performed with the algorithm explained in [3] yields a upper and a lower data point for each extracted cycle. Denoting the corresponding times by t_1 and t_2, these data points are characterized by a selected equivalent K-factor and a temperature: $\{K_{eq}^s(t_1), T(t_1)\}$ and $\{K_{eq}^s(t_2), T(t_2)\}$. To evaluate

the crack propagation due to this cycle, a K-factor range is defined by $\Delta K_{eq} = K_{eq}^{\max} - K_{eq}^{\min}$ based on the maximum value $K_{eq}^{\max}$ and minimum value $K_{eq}^{\min}$ of the selected K-factors $K_{eq}^{s}(t_1)$ and $K_{eq}^{s}(t_2)$. The temperature $T_{\max}$ is the maximum of the temperatures at the upper and lower cycle data point. Substituting ΔK_{eq} and $T_{\max}$ into Eq. 2 yields the crack propagation rate for the extracted cycle. The influence of the R-ratio ($K_{eq}^{\min} / K_{eq}^{\max}$), the threshold value and the critical value can be taken into account by extra multiplicative terms in Eq. 2. The crack propagation rate for the mission is the sum of the crack propagation rate of all extracted cycles. The corresponding bending and twist angle is $\varphi(t_{\max})$ and $\psi(t_{\max})$, respectively.

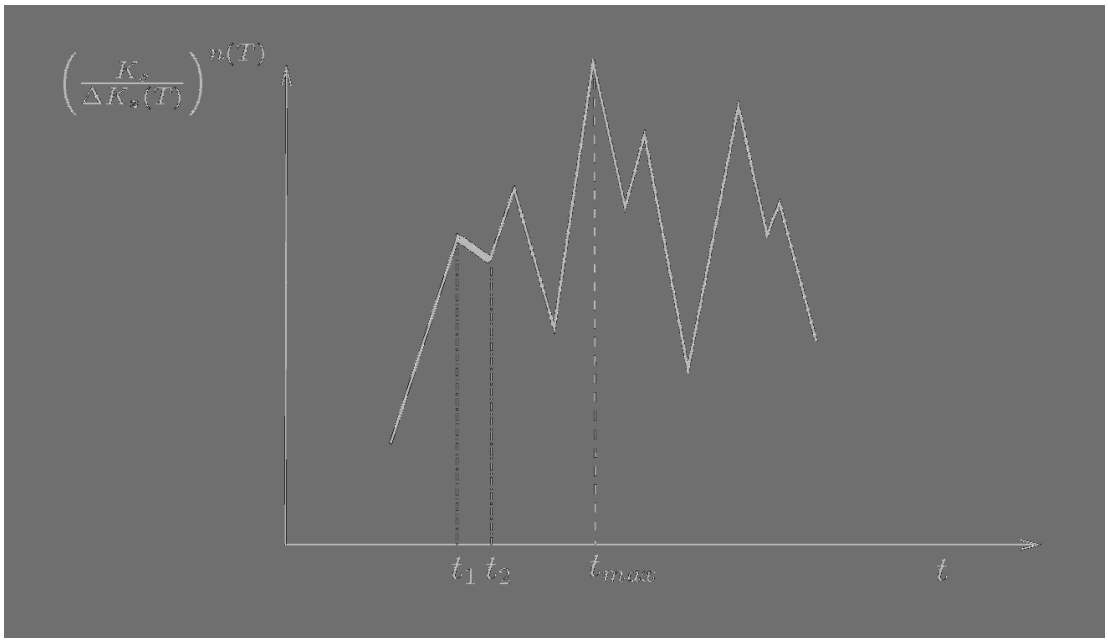


Figure3: Cycle extraction

Summary

Calculating crack propagation due to mixed-mode for complete missions introduces extra difficulties due to the change of the mixed-mode state during the mission. The present paper has presented a straightforward algorithm how to circumvent these problems. It is based on the identification of a dominant crack propagation direction and the calculation of the equivalent K-factors at all other times based on proximity of the principal self-similar stress planes. A subsequent cycle extraction and summation of the individual crack propagation rates leads to the crack propagation rate, bending angle and twist angle for the complete mission.

References

[1] G. Dhondt: Key Engineering (2003), p. 251-252, 209.

[2] M. Schöllmann, G. Kullmer, M. Fulland and H.A. Richard, in: Proc. of 6th Int. Conf. on Biaxial/Multiaxial Fatigue & Fracture, edited by M. de Freitas (2001), Lissabon, p 589-596.

[3] S.D. Downing and D.F. Socie Int. J. Fatigue (1982), p. 31-40.

© (2012) Trans Tech Publications, Switzerland
doi:10.4028/www.scientific.net/KEM.488-489.97

Crack growth rates and corrosion fatigue of austenitic stainless steels in high chloride solutions

C. Vichytil[1a], G. Mori[1b], R. Pippan[2c], M. Panzenböck[3d], R. Fluch[4e]

[1] Christian Doppler Laboratory of Localized Corrosion, Department of General, Analytical and Physical Chemistry, Montanuniversität Leoben, Franz-Josef-Straße 18, A-8700 Leoben, Austria

[2] Erich Schmid Institute of Materials Science, Austrian Academy of Science, Jahnstraße 12, A-8700 Leoben, Austria

[3] Department of Physical Metallurgy and Materials Testing, Montanuniversität Leoben, Franz-Josef-Straße 18, A-8700 Leoben, Austria

[4] Böhler Edelstahl GmbH & Co KG, Research and Development Special Materials, Mariazeller Straße 25, A-8605 Kapfenberg, Austria

[a]clemens.vichytil@unileoben.ac.at, [b]mori@unileoben.ac.at, [c]reinhard.pippan@oeaw.ac.at, [d]pan@unileoben.ac.at, [e]rainer.fluch@bohler-edelstahl.at

Keywords: corrosion fatigue, austenitic stainless steel, crack propagation,

Abstract, Purpose: Applications for highly corrosive environments and cyclic loading are often made out of austenitic stainless steels. Corrosion fatigue and crack propagation behaviour has been studied to determine failure processes and damage mechanisms.
Approach: CrNiMo stabilized austenitic stainless steel and CrMnN austenitic stainless steel in solution annealed and cold worked condition are compared. S/N curves and crack propagation rate curves are recorded in 43 wt% $CaCl_2$ solution at 120 °C, which resembles most severe potential service conditions. For comparison these experiments are also performed in inert glycerine. Additionally, the electrochemical behaviour of these materials has been studied.
Findings: The CrMnN steels have excellent mechanical properties but are very susceptible to stress corrosion cracking in the test solution. The fatigue limit as well as the threshold for long crack growth are significantly reduced in corrosive environment. Moreover these steels exhibit a remarkable increase in the propagation rate, which is extremely pronounced in the near threshold region. This effect is enhanced by cold working. CrNiMo steels also show a reduction in the fatigue limit, but it is less pronounced compared to CrMnN steels. The threshold is significantly reduced in corrosive environment, but propagation rate is lower in corrosive environment compared to inert glycerine. Possible explanations of this surprising behaviour are discussed.

Introduction

CrMnN austenitic stainless steels have good mechanical properties and a high potential in replacing CrNiMo steels, which stand out through their excellent corrosion resistance. In literature a lot of data on corrosion fatigue (CF) behaviour of CrNiMoN steels can be found [1,2], but hardly anything about CrMnN steels. Some contributions to a fundamental understanding have been published by Magnin [3]. Generally accepted failure mechanisms [3], which can be applied to both steels, strongly depend on the applied potential according to Magnin [4]. Especially crack initiation often occurs through a localized attack by the surrounding environment (e.g. pitting) [5]. Endo observed that increasing Cl^- concentration will enhance local dissolution and influences crack growth rates [6]. CF and stress corrosion cracking (SCC) are two phenomena which show similar mechanisms, especially during initiation and propagation. A clear distinction by analysing fracture surfaces is hardly possible, as both cracking modes result in similar characteristics on the fracture surface like facetted cleavage and factory roof structures [7].

Experimental

Experiments were performed with a CrNiMo and a CrMnN austenitic stainless steel. Chemical composition and pitting resistance equivalent number (PREN) are given in Table 1. PREN was calculated using Eq. 1.

$$PREN=\%Cr+3.3x\ \%Mo + 20x\ \%N\ (w/w). \quad (1)$$

Table 1: Chemical composition in [wt%] and PREN of the investigated materials

Alloy	C	Cr	Ni	Mo	Mn	N	PREN
CrNiMo	<0.05	26-29	28-31	2.0-4.5	2.0-3.5	0.2-0.35	~43
CrMnN	<0.05	18	1.7	0.5	21	0.66	~33

CF samples were machined according to ASTM E466, compact tension (CT) specimens for crack growth rate curves according to ASTM E647. All samples were electropolished using a H_3PO_4-H_2SO_4 based electrolyte. CT specimens were precracked under cyclic compression to create a fatigue precrack with a length of approximately 100 µm [8]. Corrosion fatigue experiments and crack growth rate curves were recorded in a calibrated servohydraulic universal testing machine with a 32 kN load cell or a 5 kN load cell respectively. All samples were mounted in a double walled glass cell, which could be heated. Experiments were performed in 43 wt% $CaCl_2$ aqueous solution and in inert glycerine as reference medium. Both media were heated to 120 °C, a frequency of 20 Hz was chosen for the S/N curves as well as the crack growth rate curves and a stress ratio of lower to upper stress (R-value) of 0.05 was applied. The fatigue strength was defined as the maximum stress where three samples endured $1.2*10^7$ cycles. Crack growth was monitored by using the direct current potential drop method. Fracture surfaces of selected samples were investigated with an SEM (Zeiss EVO 50). To characterize the corrosion properties of the investigated materials under testing conditions cyclic polarization curves were recorded in 43 wt% $CaCl_2$ at 120 °C with a scan rate of 200 mV/h. A platinum counter electrode and an Ag/AgCl reference electrode were used. Moreover exposure testing has been performed.

Results and Discussion

In glycerine fatigue cracks in both materials are initiated at evolved slip steps which consequently form extrusions and intrusions. All fracture surfaces show pure fatigue cracking with typical striations. In inert glycerine the CrMnN steel has better mechanical properties under static and cyclic loading compared to the CrNiMo material. The fatigue limits are listed in Table 2.

Table 2: Fatigue limits of investigated materials in [MPa] at 120°C

Alloy	Degree of cold working [%]	Fatigue limit in glycerin [MPa]	Fatigue limit in 43wt% $CaCl_2$ [MPa]
CrNiMo	0/SA	340±10	270±10
	14	380±10	240±10
CrMnN	0/SA	380±10	290±10
	14	400±10	240±10

In 43 wt% $CaCl_2$ solution cracks are initiated at slip steps which are chemically dissolved by the surrounding medium at the CrNiMo material. This leads to a shorter crack initiation period and a reduction of fatigue strength. The fracture surface around the initiation point shows thick oxide layers (Figure 1), but typical fatigue fracture is predominant on the fracture surface. Solution annealed and cold worked samples show the same fracture surface characteristics. At the CrMnN steel cracks are initiated at dissolved slip steps and also at pits. Fatigue limits are reduced to roughly the same values of the CrNiMo steel. The whole fracture surface, irrespective of the degree of cold working, is covered with oxide layers. The fracture surfaces reveal facetted cleavage (Figure 2) and factory roof structures which are usually known from SCC. Moreover a fine network of cracks in radial and axial direction was found on the residual fracture surfaces, which are also identified as SCC.

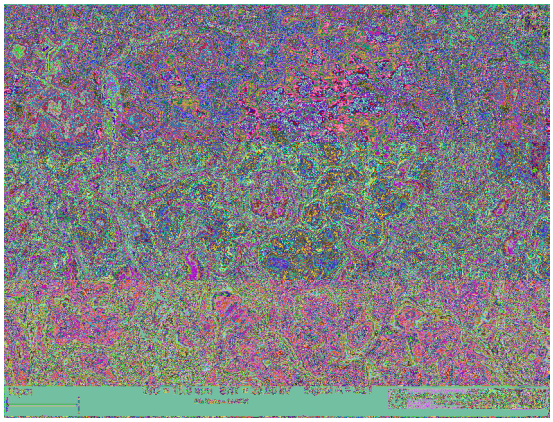


Figure 1: Fracture surface of CrNiMo-SA, 43 wt% $CaCl_2$ solution, 120 °C, oxides close to initiation point of fracture, fatigue specimen

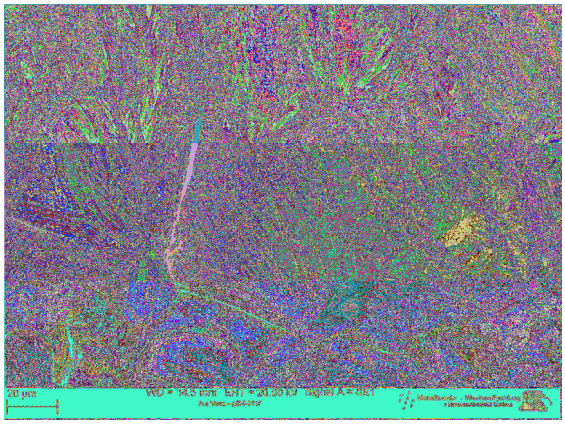


Figure 2: Fracture surface of CrMnN-SA, 43 wt% $CaCl_2$ solution, 120 °C, facetted cleavage, fatigue specimen

Crack growth rate curves (Figure 3) recorded in glycerine showed that precritical crack growth and crack stopping is present in both materials, as well as a slight reduction of ΔK_{th} with increasing degree of cold working. In 43 wt% $CaCl_2$ solution the threshold for long crack growth is significantly reduced in both materials in. Surprisingly the CrNiMo material shows very slow crack propagation in corrosive environment, and no influence of cold working could be noted. The cyclic polarization curves reveal that the CrNiMo material has a pronounced passive range compared to the CrMnN steel [9]. This particular CrNiMo material seems to repassivate very fast and besides roughness and plasticity induced crack closure, corrosion debris or oxide induced crack closure effects seem to be the main reason for the retarded crack growth at ΔK values between 5-11 MPa√m. Additional experiment at an R-value of 0.5 shows the same behaviour in the near threshold region and the Paris region. Very fine striations and some oxide layers on the fracture surface confirm this. The CrMnN steel exhibits a different behaviour. ΔK_{th} is also decreased, but cracks already propagate fast at ΔK values below 5 MPa√m. In 43 wt% $CaCl_2$ solution a sudden rise of the crack length occurs in the region around the threshold value, which might be due to SCC. ΔK_{th} is even further reduced with increasing degree of cold working and exhibits an even faster crack propagation.

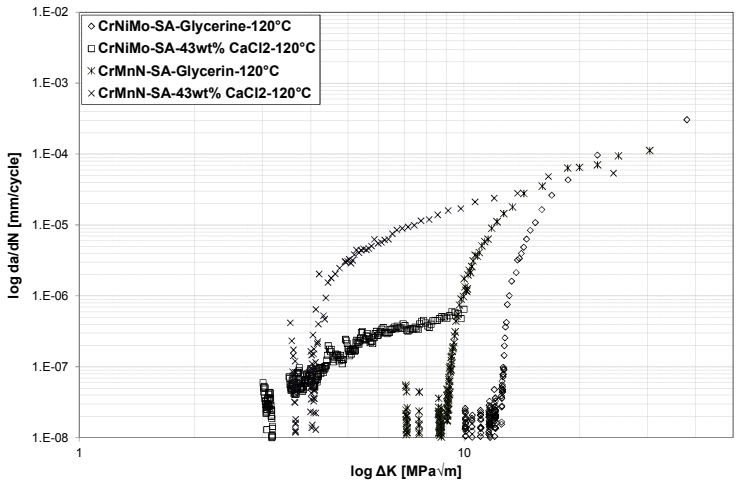


Figure 3: Crack growth rate curves of CrNiMo and CrMnN steel in glycerine and 43 wt% $CaCl_2$ solution at 120 °C

The fracture surfaces reveal typical signs for SCC like facetted cleavage (Figure 2) and factory roof structures, which also have been found on the fracture surfaces of the CF specimen. Moreover corrosion products and pitting could be found on the fracture surfaces of the CrMnN steel. Corrosion debris or oxide induced crack closure effects have an effect on crack propagation, but acceleration due to SCC seems to be predominant in this CrMnN steel. These effects are even more pronounced in the cold worked material. From the recorded data it can be derived that the CrMnN steel is susceptible to SCC under testing conditions and SCC susceptibility is increased with increasing degree of cold working [9].

Exposure test revealed, that even after one day the solution annealed CrMnN samples showed pitting and SCC could be observed at the 14 % cold worked material due to residual stresses of the cold working process. The CrNiMo material in solution annealed condition showed no corrosion at all after 7 days (which are equal to $1.2*10^7$ cycles at 20 Hz) of exposure and only some slight pitting in 14 % cold worked condition. After an exposure of 21 days (~500 hours) SCC was observed at the 14 % cold worked CrNiMo austenite.

SCC and CF show similar mechanisms and can interfere. A clear distinction under cyclic loading is very hard, especially if steels susceptible to SCC under given testing conditions are investigated. Crack initiation period is obviously decreased in CrMnN material due to its lower corrosion resistance and higher SCC susceptibility. Exposure tests showed [9] that the CrNiMo material with its excellent corrosion properties showed SCC, but an interference of SCC and CF can be ruled out as the crack initiation period is very long and propagation is very slow, which was proven by exposure testing and crack growth rate measurements. Both steels show a strong influence of crack propagation by the aggressive medium, but an enhancement with increasing degree of cold working could only be observed for the CrMnN steel.

Summary

In corrosive environment fatigue strength and ΔK_{th} for long crack growth is decreased in CrNiMo and CrMnN material irrespective of the degree of cold work. SCC affects and enhances crack propagation only the CrMnN steel. The CrNiMo material even shows slower crack propagation rates in 43 wt% $CaCl_2$ solution in the threshold and the Paris region compared to inert glycerine, nevertheless ΔK_{th} for long crack growth is lower in corrosive environment. This behaviour seems to be due to oxide or corrosion debris induced crack closure effects. The CrMnN steel has better mechanical properties over all, but only in inert environments. The investigated CrNiMo steel has better corrosion properties, which are not influenced by cold working.

References

[1] R.P. Wei, *Electrochemical and microstructural considerations of fatigue crack growth in austenitic stainless steels*, Proceedings of the 36th MWSP Conference, ISS-AIM, Vol. 32, p. 541-549, 1995

[2] Y.R. Qian, J.R. Cahoon, *Crack initiation mechanisms for corrosion fatigue of austenitic stainless steel*, Corrosion (USA), Vol. 53, no. 2, p. 135, 1997

[3] T. Magnin, *Advances in corrosion deformation interactions*, Trans Tech Publications Ltd, Switzerland, p.11-15, 69, 80, 87, 88, 1996

[4] T. Magnin, *Recent advances for corrosion fatigue mechanisms*, ISIJ Int. Vol. 35, no. 3, p. 224-225, 231-232. 1995

[5] C.-K. Lin, I.-L. Lan, *Fatigue behavior of AISI 347 stainless steel in various environments*, Journal of Materials Science 39, pp 6901-6908, 2004

[6] K. Endo, K. Komai, *Influence of Cl- Concentration on Corrosion Fatigue Crack Growth of an Austenitic Stainless Steel*, Bulletin of the JSME, Vol. 26, No 218, pp 1281-1287, 1983

[7] S.P. Lynch, *Progress towards understanding mechanisms of hydrogen embrittlement and stress corrosion cracking*, Corrosion 2007, Nashville, NACE, Houston, paper no. 07493, pp. 1-55, 2007

[8] R. Pippan, L. Plöchl, F. Klanner, H. P. Stüwe, *The Use of Fatigue Specimens Precracked in Compression for Measuring Threshold Values and Crack Growth*, ASTM Journal of Testing and Evaluation (USA), Vol. 22, no.2, pp. 98-103, 1994

[9] R. Sonnleitner, C. Vichytil, G. Mori, M. Panzenböck, R. Fluch, *Corrosion Fatigue Investigations on Austenitic Stainless Steels with Different Alloying Concepts*, Corrosion 2010, San Antonio, NACE, Houston paper no. 14458, pp. 1-15, 2010

© (2012) Trans Tech Publications, Switzerland
doi:10.4028/www.scientific.net/KEM.488-489.101

Rolling contact fatigue crack growth prediction by the asperity point load mechanism

D. Hannes[1,a], B. Alfredsson[1,b]

[1]Department of Solid Mechanics, KTH (Royal Institute of Technology), Stockholm, Sweden

[a]daveh@kth.se, [b]alfred@hallf.kth.se

Keywords: rolling contact fatigue; spalling; asperity; fatigue crack path; mode I; plane mixed-mode.

Abstract. The crack path and growth life of surface initiated rolling contact fatigue was investigated numerically based on the asperity point load mechanism. Data for the simulation was captured from a gear contact with surface initiated rolling contact fatigue. The evolvement of contact parameters was derived from an FE contact model where the gear contact had been transferred to an equivalent contact of a cylinder against a plane with an asperity. Crack propagation criteria were evaluated with practically identical crack path predictions. It was noted that the trajectory of largest principal stress in the uncracked material could be used for the path prediction. The mode I fracture mechanism was applicable to the investigated rolling contact fatigue cracks. The simulated path agreed with the spall profile both in the entry details as in the overall shape, which suggested that the point load mechanism was valid not only for initiation but also for rolling contact fatigue crack growth. Different equivalent stress intensity factor ranges were used to estimate the fatigue life, which agreed with the life of the investigated gear wheels.

Introduction

Gears are one example of applications with highly loaded rolling contacts that eventually will suffer from rolling contact fatigue (RCF) or spalling. The damage consists of cracks and craters or spalls in the contact surfaces [1]. Typical examples of surface initiated RCF craters are shown in Figs.1 and 2. After initiation below the pitch line, the cracks grew in the rolling direction.

Since the work by Way [2] in 1935, numerous researchers have investigated the damage process behind spalling. A two-dimensional description of the gear contact would suggest damage along the contact width, but not separate craters as shown in Fig.1. Olsson [3] proposed the asperity point load mechanism, where a three-dimensional asperity disturbs the two-dimensional load transfer and acts locally as a stress raiser at contact entry. Tensile surface stresses are then introduced in front of the asperity and allow for fatigue crack growth.

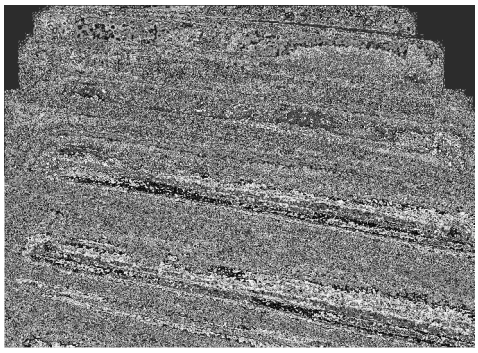


Figure 1. Pinion or driving gear wheel with separate spalls on the flacks.

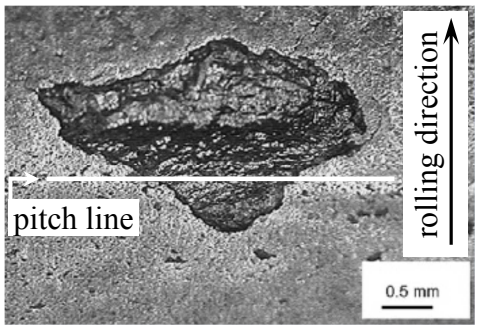


Figure 2. V- or sea-shell shaped surface initiated spall [4].

Problem description

The surface initiated RCF damage on the gear wheel in Fig.1 was modelled using the asperity point load mechanism. Both the cross-sectional shape of the spalls as a fatigue life estimation were computed.

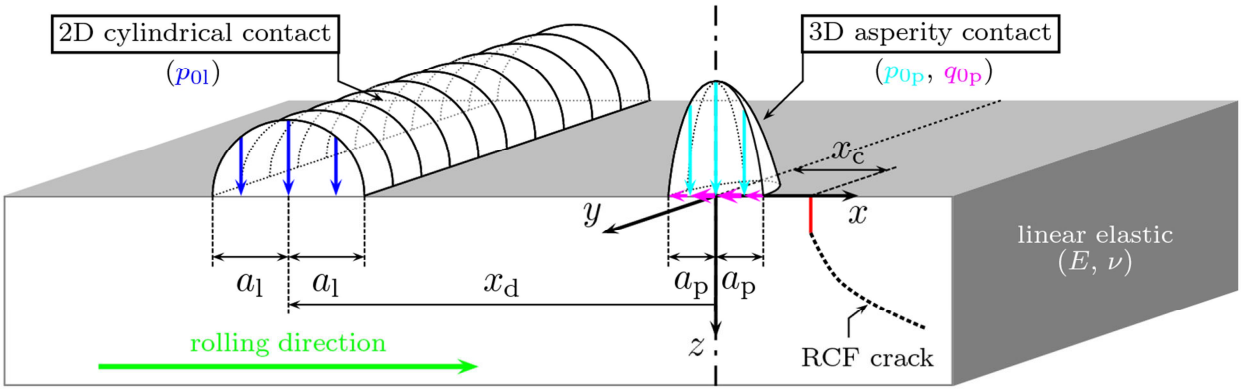


Figure 3. The asperity point load model for RCF crack growth in the xz-plane (symmetry plane).

The RCF crack propagated in the homogeneous [4] upper part of the hardened gear case. After running-in of the gear, the material behaved linear elastically with $E = 206$ GPa and $\nu = 0.3$, and the residual surface stress in the rolling direction was close to zero [5].

The complex rolling contact was simplified to a cylinder (follower) rolling against a flat surface (pinion) with a small cosine-shaped axisymmetric asperity. Talysurf measurements motivated an asperity height of 1.5 μm and a radius of 50 μm. The cylinder radius was given by the equivalent curvature at the pitch line for the gear in Fig.1. The lubricated follower-pinion contact was assumed frictionless, except at the asperity where the coefficient of friction was set to 0.3. The asperity was assumed to break through the lubrication film for both normal and tangential loads. It was situated slightly below the pitch line and thus subjected to negative slip.

The asperity point load model included a moving two-dimensional cylindrical load with constant maximum cylinder pressure $p_{0l} = 2.39$ GPa and a fixed asperity load with normal, p_{0p}, and tangential, q_{0p}, maximum loads depending on the position of the cylindrical load, x_d, see Fig.3. The contact half-width, a_l, and contact radius, a_p, were given by Hertzian contact theory [6].

An initial straight crack perpendicular to the contact surface was introduced in front of the asperity, at $x = x_c = 20$ μm, where a substantial tensile surface stress was expected to occur, as illustrated in Fig.4.

Computational models

An FE model was used to characterize the rolling contact load which was then used in a crack growth model to determine the load on the fatigue crack and simulate crack propagation.

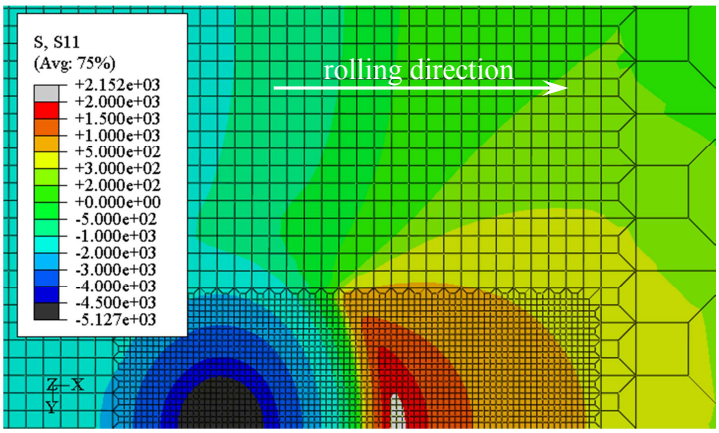


Figure 4. FE surface stress σ_x in MPa at the vicinity of the asperity when $x_d = -260.6$ μm. Large tensile stresses occurred in front of the asperity.

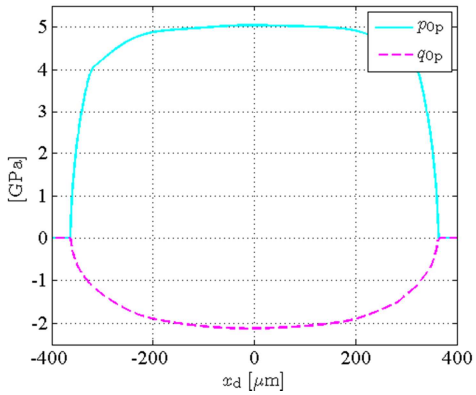


Figure 5. Evolvement of the maximum spherical loads. A moving average filter was applied.

FE model. An FE simulation of the equivalent geometry allowed to isolate the spherical and cylindrical pressures along the x-axis. The spherical loads p_{0p} and q_{0p} were identified by fitting Hertzian pressure distributions for consecutive positions of the cylinder, see Fig.5. The position of the initial crack was motivated by the large tensile surface stress $\sigma_x > 2$ GPa observed in the FE model, see Fig.4.

Crack growth model. Both the crack growth direction and the crack growth rate required prediction, in order to estimate fatigue life for a crack subjected to plane mixed-mode loading.

Crack growth direction. Knowing the cylindrical and spherical loads, the stresses normal and tangential to the crack in the uncracked symmetry plane were computed by using closed-form expressions for the stresses below Hertzian contacts [6,7]. The mode I and II stress intensity factors (SIF) were then derived from the stress field along the curved crack and weight functions for an equivalent through-thickness straight edge crack [8]. The load cycle subjected the crack tip to a non-proportional plane mixed-mode fatigue cycle. The non-proportionality requested a criterion for selection of a propagation instance. Two different criteria were evaluated during the period when the crack was opened: the instance when K_{I} was maximum and the instance when the hoop stress in the crack tip field was maximum. The criteria gave practically equal crack paths and the $K_{\mathrm{I,max}}$ criterion was selected for numerical stability. At the selected propagation instance, the direction for the next crack growth increment was evaluated with five different criteria from the literature [9] that were based on the mode I fracture mechanism, which resulted in quasi-identical crack path predictions. Therefore, the direction of the next crack increment was given by the maximum tangential principal stress criterion. In this criterion crack growth was assumed to occur in the direction perpendicular to the largest principal stress direction at the crack tip position in the uncracked material. The other four criteria were based on stress intensity factors, but were less stable numerically [9].

Crack growth rate. During the major part of the load cycle $K_{\mathrm{I}} < 0$ and crack closure became an issue. When closure occurred, it was assumed that K_{I} was equal to the constant crack closure limit $K_{\mathrm{I,cl}}$ and that K_{II} remained constant and equal to its value prior to crack closure. With the stress intensity factors corrected for closure, mode I and II effective SIF ranges were computed. The fatigue life computations for mixed-mode crack growth were based on an equivalent SIF range. Four different formulations were investigated [10] with the most conservative prediction by the crack tip displacement model [11].

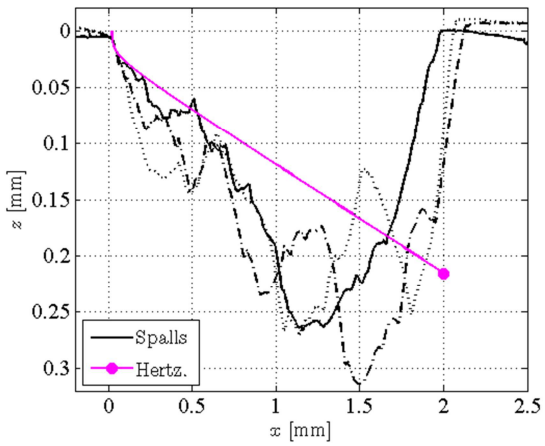


Figure 6. Crack path prediction (Hertz.) superimposed to three spall profiles (Spalls).

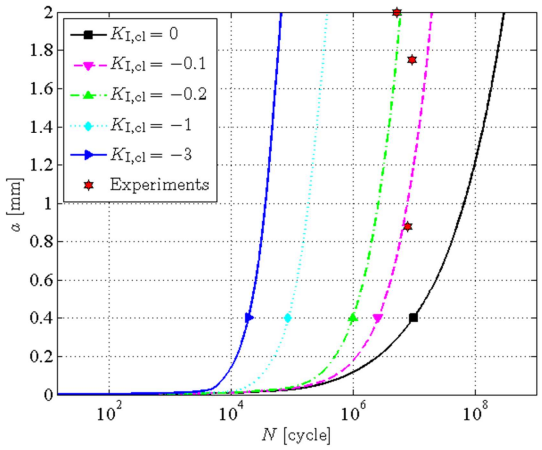


Figure 7. The influence of negative crack closure limits on RCF life predictions. $K_{\mathrm{I,cl}}$ in MPa$\sqrt{\mathrm{m}}$.

Results

The crack path prediction compared well to experimentally measured spall profiles on the gear wheel in Fig.1: both entry angle and propagation in the forward rolling direction were features recovered by the predicted crack path, see Fig.6. Fatigue life was computed along the crack path for different constant negative crack closure limits, see Fig.7. Indeed negative crack closure limits were observed during negative R-ratio fatigue experiments [10]. Small negative $K_{\mathrm{I,cl}}$ agreed best with experimental fatigue life lengths observed on gears [4]. The work by Yu *et al* [12] showed that for large negative peak stress the fatigue threshold could be extrapolated to zero, which was the result of a decreasing crack tip opening limit. It was also reported that crack growth rates increased with increasing magnitude of the negative peak stress.

Conclusions

Starting with data collected from a gear contact with surface initiated RCF, the simulated crack path agreed with experimental spall profiles. The mode I fracture mechanism was applicable to the investigated RCF cracks with propagation along the trajectory of largest principal stress in the uncracked material. The computed fatigue life based on a small negative crack closure limit and an equivalent stress intensity factor range also agreed with RCF life in the evaluated gears. All these results suggested that the asperity point load mechanism was valid not only for initiation but also for rolling contact fatigue crack growth.

References

[1] T.E. Tallian: Failure Atlas for Hertz Contact Machine Elements, ASME Press (1992).

[2] S. Way: Journal of Applied Mechanics 2 (1935), A49-A58.

[3] M. Olsson, in: Engineering Against Fatigue, edited by J. Beynon, M. Brown, T. Lindley, B. Tomkins, A.A. Balkema (1999).

[4] J. Dahlberg, B. Alfredsson: International Journal of Fatigue 30 (2008), 1606-1622.

[5] J. Dahlberg, B. Alfredsson: International Journal of Fatigue 29 (2007), 909-921.

[6] K.L. Johnson: Contact Mechanics, Cambridge University Press (1985).

[7] G.M. Hamilton, in: Proceedings of the Institution of Mechanical Engineers, volume 197C (1983).

[8] H. Tada, P.C. Paris, G.R. Irwin: The Stress Analysis of Cracks Handbook, Paris Production, Inc. (1985).

[9] D. Hannes, B. Alfredsson: submitted for international publication (2010).

[10] D. Hannes, B. Alfredsson: submitted for international publication (2011).

[11] K. Tanaka, Engineering Fracture Mechanics 6 (1974), 493-507.

[12] M.T. Yu, T.H. Topper, D.L. DuQuesnay, M.S. Levin: International Journal of Fatigue 8 (1986), 9-15.

© (2012) Trans Tech Publications, Switzerland
doi:10.4028/www.scientific.net/KEM.488-489.105

Mechanical Characterization of Friction Stir Channels under Internal Pressure and In-Plane Bending

Catarina Vidal[1, a], Virgínia Infante[2,b], Pedro Vilaça[3,c]

[1, 3]Instituto Superior Técnico, TULisbon, Av. Rovisco Pais, 1049-001 Lisboa, Portugal

[2]ICEMS - Instituto de Ciência e Engenharia de Materiais e Superfícies, Instituto Superior Técnico, TULisbon, Av. Rovisco Pais, 1049-001 Lisboa, Portugal

[a]catarina.vidal@ist.utl.pt, [b]virginia@dem.ist.utl.pt, [c]pedro.vilaca@ist.utl.pt

Keywords: Friction Stir Channelling, AA7178-T6, Bending tests, Internal pressure tests.

Abstract. Friction Stir Channelling (FSC) is a simple and innovative technique of manufacturing integral and continuous channels (also referred as conformal channels) in monolithic plates in a single step.
This paper is focused on the mechanical behaviour of integral and continuous FS channels produced in a monolithic plate of the aluminium alloy AA7178-T6 with 13mm of thickness, typically used in structural aircraft applications. Internal pressure tests were conducted on specimens with a longitudinal friction stir channel. In-plane bending tests were carried out in specimens with longitudinal and transversal channels; different conditions were analysed for each FSC parameters set. Results were analysed and compared concerning the FS channels microstructure and base material mechanical properties.
Bending tests results show that tool rotation speed has more influence in the FSC specimens bending strength than tool travel speed and internal pressure tests show that increase tool rotation speed increases the minimum pressure that leaking points arise.

Introduction

Friction Stir Channelling (FSC) is a non-traditional technique of creating continuous, integral channels in a monolithic plate in a single step [1] that derives from the Friction Stir Welding (FSW).
During FSW, a defect referred to as a "wormhole" is generated if the processing parameters and tool shoulder contact are not proper. FSC is based on converting this defect formation process into a manufacturing technique [2].

Nomenclature

d	channel depth
t	plate thickness
v	tool travel speed

Greek symbols

ω	tool rotation speed

The FSC uses the "wormhole" defect and produces integral channels inside a metal component. This can be accomplished by choosing the right processing parameters and reversing the material flow during processing.
FSC relies on the frictional heat generated between the tool material and the metal workpiece to soften and deform the material to facilitate the creation of a continuous channel [3].
The channel is formed due to the separation of the plasticized material around the pin from the base of the pin and which is then moved upwards towards the shoulder by the rotation of the pin and orientation of the threads. The material that is moved upwards is pushed out by the scrolls on the shoulder [2].
The channel shape, size, and integrity depend on the processing parameters. The shape and size of the channel can be controlled by varying the following process parameters [2]: tool rotation speed, tool travel speed, pin geometry and length, shoulder geometry and vertical downward forjing force. The continuous channel formed by FSC has a high potential in heat exchanger industry [1-3], in conformal cooling systems and in aerospace, automative and railway industries.

Figure 1 shows a schematic representation of the FSC process and Figure 2 shows a cross section of a FS channel. A combination of the orientation of the threads on the pin and the direction of tool rotation results in the displacement of material from the pin base to the surface. The flow arm is along the advancing side.

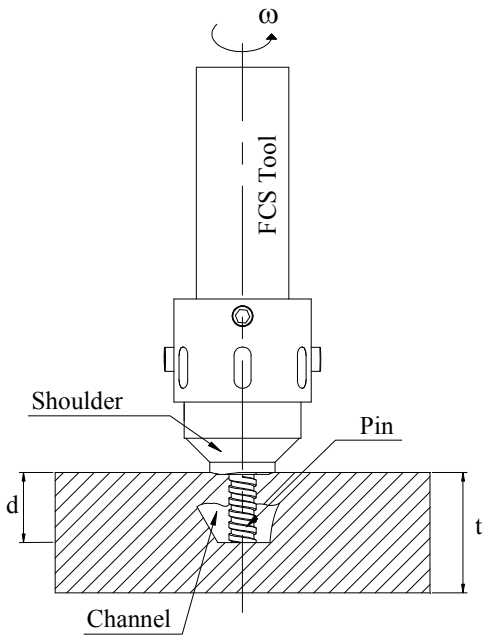


Figure 1. Schematic representation of a cross section view of the friction stir channelling (FSC) process.

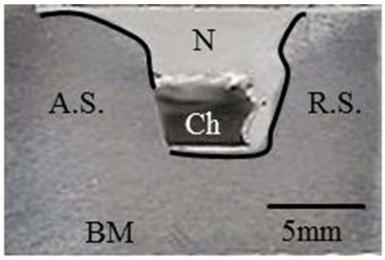


Figure 2. Example of a cross section macrograph of a FS channel showing the channel (Ch), the nugget (N), the base material (BM), the advancing side (A.S.) and the retreating side (R.S.) localization.

Experimental Procedure

The aeronautic aluminium alloy AA7178-T6 was used in this work. The nominal composition (by %weight) of AA7178-T6 is 85.76Al–8.73Zn–2.55Mg–2.46Cu–0.42Fe–0.08Cr. Friction stir channels were produced on 13mm thick plates of this alloy using an ESAB Legio FSW 3UL equipment. Plunge and dwell periods ($v = 0$) and processing period ($v > 0$) were performed under vertical position control.

A patented modular concept of a FSW tool that enables internal forced refrigeration was used to perform all channels. This tool is based on three main components: *body*; *shoulder* and *pin*. It was selected, for all the runs, a conical pin with a 5mm bottom diameter and left-handed threads along its length and a plane shoulder with two spirals striates scrolling an angle of 360º with outer and inner diameters of 20mm and 9mm, respectively.

The pin was penetrated to a depth of 5.5mm (without any gap between the shoulder and the workpiece). The tool tilt angle was 0° for all the runs. The tool was rotated in the counter clockwise direction.

To study the influence of processing conditions on channels' bending and internal pressure resistance the tool rotation speed and the tool travel speed were varied as listed in Table 1.

Table 1. FSC variable parameters.

Tool rotation speed (rpm)	Tool travel speed (mm/min)	FSC Condition symbol
600	80	A
600	150	B
800	80	C
800	150	D

Results and Discussion

Bending Tests

Bending tests were performed on an Instron 1342 servo-hydraulic machine, with a load cell of 250kN. The span distance (distance between the centres of support rolls) was 59mm. Support rolls diameter is 10mm and mandrel radius is 5mm. Mandrel velocity used throughout the trial was 1mm/min. From each condition two specimens were taken and bended. Base material and three different conditions of friction stir channelled specimens were tested: (a) specimens with a transversal channel with the processing zone (channel ceiling) under tensile stress, (b) specimens with a longitudinal channel with the processing zone (channel ceiling) under tensile stress and (c) specimens with a longitudinal channel with the non-processing zone (channel bottom) under tensile stress. All mechanical trials were performed at room temperature.

Table 2. Maximum load (kN) results.

Base Material	76.65		
	Bending test condition		
FSC Condition	(a)	(b)	(c)
A	28.06	53.31	72.44
B	26.40	51.39	72.19
C	34.39	40.49	56.72
D	Not tested	40.61	58.69

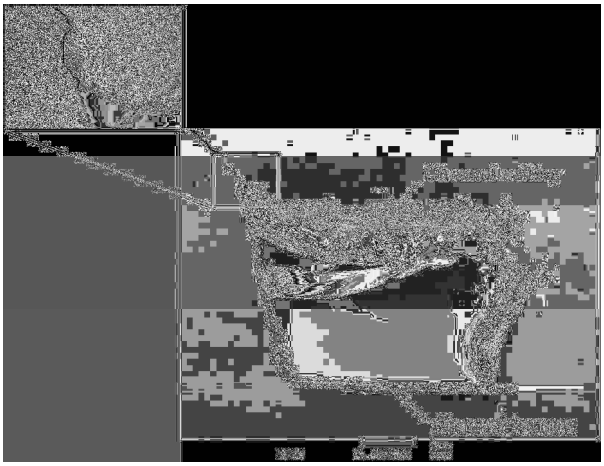


Table 3. Channel area (mm^2).

FSC Condition	Area
A	13.49
B	14.01
C	12.75
D	12.88

Figure 3. Fracture localization on specimens tested under bending test condition (a).

From the analysis of Table 2 it is possible to verify that tool rotation speed has more influence in the FSC specimens bending strength than tool travel speed. For bending test condition (a), increase tool rotation speed increases the maximum bending load. All specimens with a transversal channel fractured at the advancing side, namely in the boundary between the nugget and the thermo-mechanically affected zone (Figure 3).

For bending tests conditions (b) and (c) the highest loads were obtained for specimens produced with a tool rotation speed of 600rpm. According to the results of these two conditions, the channel bottom is more resistant than the channel ceiling. For specimens produced in FSC conditions A and B and tested under bending test condition (c) the maximum load is similar to the base material result.

Considering the friction stir channel area, the specimens tested were similar; however the channel area decreases with an increase in the tool rotation speed (Table 3).

Internal Pressure Tests

Specimens with a longitudinal channel were tested under internal pressure using an oil pressing machine. FSC conditions A (600rpm; 80mm/min) and C (800rpm; 80mm/min) were selected for the internal pressure tests. All specimens were subjected to a pressure of 100bar. In the A FSC condition specimen three leaking points were observed on the specimen surface, in the advancing side of the processed zone by 20bar. In FSC condition C only one leaking point was detected in the center of the beginning of the processed zone for a pressure of 40bar.
Comparing FSC conditions A and C it is possible to verify that increase tool rotation speed increases the minimum pressure that leaking points arise. In this specific case, increasing 200rpm, duplicated the minimum pressure stands by specimens without leakage.

Conclusions

This paper evaluates the friction stir channels bending and internal pressure strength. The work shows an innovative process, based on the friction stir welding principles, of manufacturing conformal channels in monolithic plates of AA7178-T6 in a single step.
From the bending tests, it is possible to verify that tool rotation speed has more influence in the FSC specimens bending strength than tool travel speed. For bending tests specimens with a transversal channel with the processing zone under tensile stress when the tool rotation speed increases the maximum bending load increases. All the specimens with a transversal channel fractured at the advancing side. According to the bending tests results of the specimens with a longitudinal channel with the processing zone (channel ceiling) and with the non-processing zone (channel bottom) under tensile stress, the channel bottom is more resistant than the channel ceiling.
The internal pressure tests show that for the FSC conditions tested it is possible to conclude that increase tool rotation speed increases the minimum pressure that leaking points arise.
Further studies are necessary to understand better the friction stir channel process.

Acknowledgements

The authors would like to acknowledge Portuguese Foundation for the Science and Technology (FCT) for its financial support through the PhD scholarship FCT SFRH/BD/62963/2009.

References

[1] Mishra, R.S., Integral Channels in Metal Components and Fabrication Thereof, US Patent 6,923,362 B2, Aug., 2, 2005.

[2] Balasubramanian, N, Mishra, R.S., Krishnamurthy, K, Friction stir channeling: Characterization of the channels, Journal of Materials Processing Technology 209, pp. 3696–3704, 2009.

[3] Balasubramanian, N, Mishra, R.S., Krishnamurthy, K, Process forces during friction stir channeling in an aluminum alloy, Journal of Materials Processing Technology 211, pp. 305-311, 2011.

© (2012) Trans Tech Publications, Switzerland
doi:10.4028/www.scientific.net/KEM.488-489.109

Numeric simulation of fatigue crack growth in a material graded structure

Britta Schramm[1, a], Hans A. Richard[1,b], Markus Fulland[2,c] and Viktor Kloster [1,d]

[1]Institute of Applied Mechanics, University of Paderborn, Germany

[2]Institute of Applied Mechanics, University of Zittau/Görlitz, Germany

[a]schramm@fam.upb.de, [b]richard@fam.upb.de, [c]mfulland@hs-zigr.de, [d]kloster@fam.upb.de

Keywords: crack growth, material gradation, numeric simulation, ADAPCRACK3D, collaborative research centre Transregio 30, Mixed Mode.

Abstract. This article deals with the development of functional graded materials which is pursued by the collaborative research centre Transregio 30. The functional gradation is produced by a thermo-mechanical production process and is characterized by different fracture mechanical specific values. Because cracks are by all means responsible for failure of structural elements crack growth has to be considered during the development of these materials. In this contribution simulations of crack growth which were carried out with the system ADAPCRACK3D are presented to illustrate the influence of a material gradation on crack growth.

Introduction

Innovative manufacturing and application-oriented products considering lightweight construction are more and more brought into the scientific and the economical focus. Thereby a significant position is taken by graded materials. These materials possess an application matched functional gradation and therefore they meet different local demands such as absorbability, abrasion and fatigue of structures. Besides the development and manufacturing of these innovative materials the task of the collaborative research centre Transregio 30 is to characterize their properties [1]. In consideration of gradation complex residual stresses and fracture mechanical properties have to be examined. The latter is very important because gradation has a remarkable influence on the fracture mechanical behavior. Taking into account the material gradation answers to the following questions are supposed to be found:

- Under which condition is crack growth possible?
- In which direction does the crack grow in case of stable crack growth?
- How fast does the crack grow?
- When does the unstable crack growth start?

Answers to these questions can be found by using fracture mechanics and simulation tools. A possible program to simulate crack growth in three-dimensional structures is ADAPCRACK3D, which was developed by the Institute of Applied Mechanics of the University of Paderborn in Germany.

Collaborative research centre Transregio 30

Within the collaborative research centre Transregio 30 different institutes of the Universities of Dortmund, Kassel and Paderborn concentrate on producing and characterizing functional graded components and structures based on thermo-mechanical phenomena. The intention is to meet different demands with only one material. For example a highly stressed region has available good mechanical strength properties, whereas another region of the structure has good absorbability and abrasion properties [1]. In cooperation the Institute of Analysis and Applied Mathematics of the University of Kassel and the Institute of Applied Mechanics of the University of Paderborn examine the crack growth in graded materials. The challenge is the functional gradation itself because it has a remarkable influence on the fracture mechanical properties [2].

Programsystem ADAPCRACK3D

For simulation of crack growth starting from user-defined cracks and under user-defined loadings in three-dimensional structures the program ADAPCRACK3D [3,4,5] has been established. This program, whose functionality can be seen in Fig. 1, consists of the three functional modules NETADPAT3D, ABAQUS™ und NETCRACK3D. The module NETADAPT3D is responsible for the automatic adaption of the FE-mesh in consideration of the modified geometry which is caused by the crack growth. A component including an initial crack and a submodel of the immediate area of the crack front are created. Afterwards the FE-calculation is carried out by the commercial FE-program ABAQUS™. The module NETCRACK3D is responsible for the fracture-mechanical evaluation on the basis of the submodel. In case of stable crack growth the program provides among other things stress intensity factors, load cycles and the coordinates of the new crack front. These coordinates are given to the first module NETADAPT3D which expands the crack area incrementally.

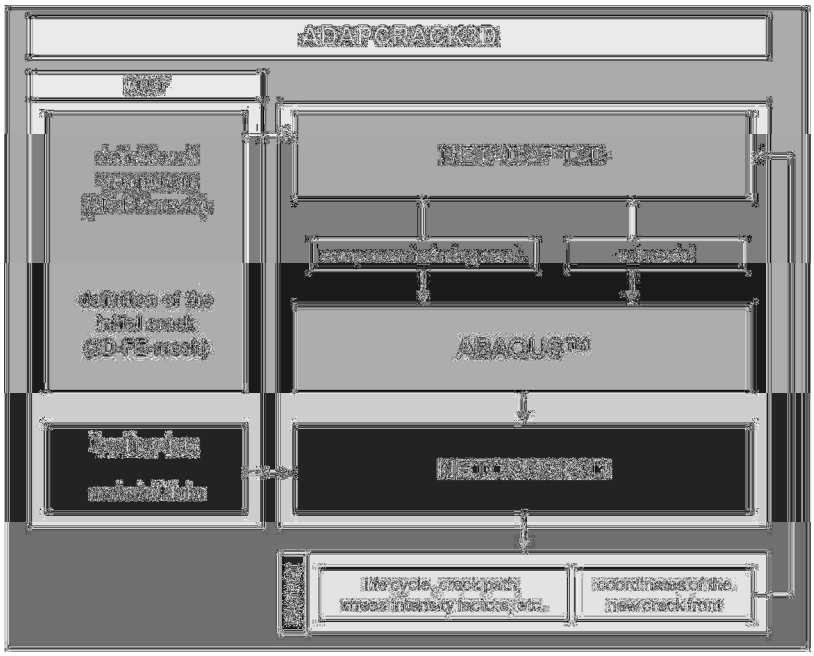


Fig. 1: Structure and functionality of ADAPCRACK3D

Simulation of crack growth

The collaborative research centre Transregio 30 uses standardized demonstrator objects to be able to compare and validate the different scientific findings and results with the help of the same objects. One of these objects is the thermo-mechanically produced flanged shaft. For this structure different simulations of crack growth were carried out with the program ADAPCRACK3D. The initial crack, a half-elliptical one with a width of c=4mm and a depth of a=2mm was positioned in the flange region (Fig. 2a). To eliminate the degrees of freedom the flanged shaft is mounted at the upper end with a bearing in x-y-z-direction and at the lower end with a bearing in x-z-direction. In addition there is another bearing in x-direction at the point of load incidence. The load is 15kN and causes a bending load.

The used material is the heat treatable steel 51CrV4. Due to the thermo-mechanical production process an almost pure martensite structure is generated in the formed flange, whereas the unformed outer regions of the shaft consist of base material (compare Fig. 2b). These structures show a remarkable difference in the fracture-mechanical properties. The basic structure has a Threshold value of ΔK_{th}=387MPamm$^{1/2}$ and a fracture toughness K_{IC}=3700MPamm$^{1/2}$. In contrast to this the Treshold value (ΔK_{th}=143MPamm$^{1/2}$) and the fracture toughness (K_{IC}=500 MPamm$^{1/2}$) of the martensitic phase are considerably smaller.

In the simulations the different phases have to be taken into account. Therefore the CAD-model (Fig. 2c) consists of two different material partitions. The transition zone, which can be seen in Fig. 2b, is not considered in the simulations.

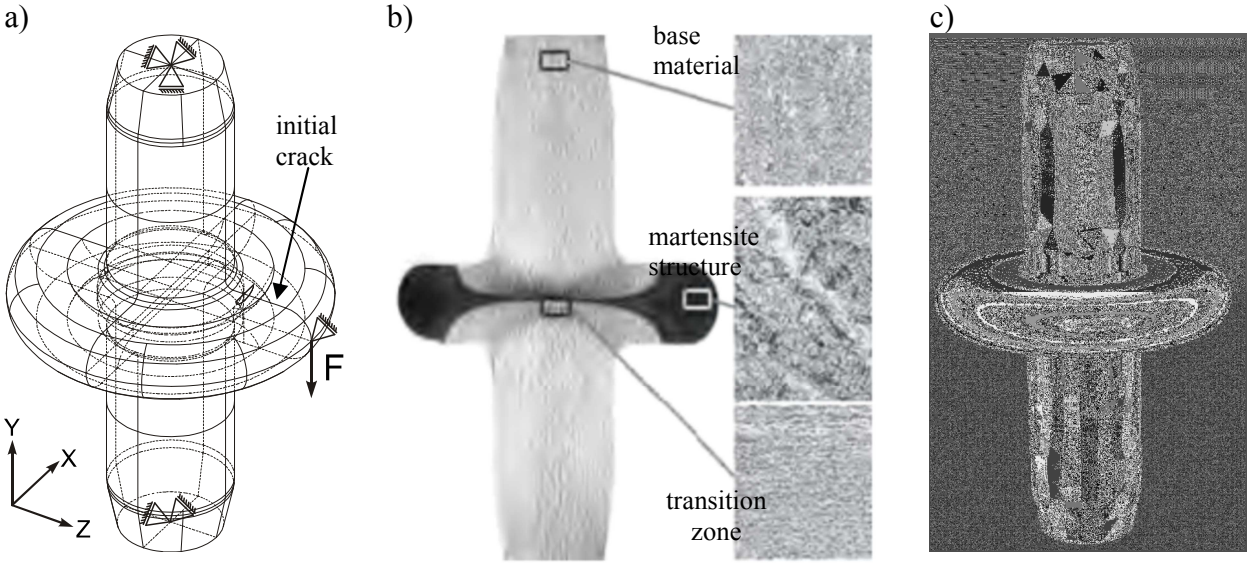


Fig. 2: a) Boundary conditions for the simulation (inclusive initial crack), b) Metallographic polished micrograph section of the graded flanged shaft, c) CAD-model of the graded flanged shaft

In the following simulations the width of the martensite region, marked with the letter *b*, is varied in 4 steps (compare Fig. 3a-d) to register the influence of the martensite region on crack growth.

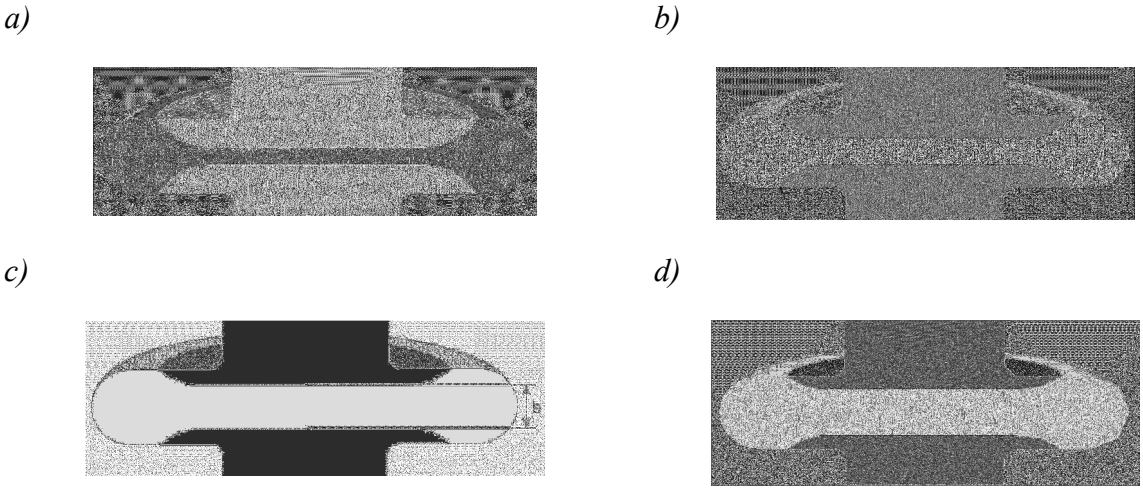


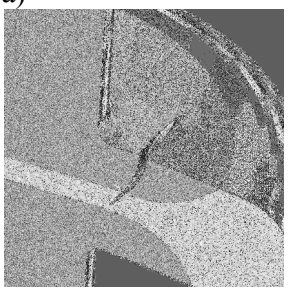
Fig. 3: Width of the martensitic phase b: a) b=3mm, b) b=5mm, c) b=7mm, d) b=9mm

In Fig. 4a-b the unstable crack growth in the demonstrator object flanged shaft with different width of the martensitic region (*b*=3mm and *b*=9mm) can be seen. The pictures show that the crack starts in the base material and becomes unstable after reaching the martensitic phase.

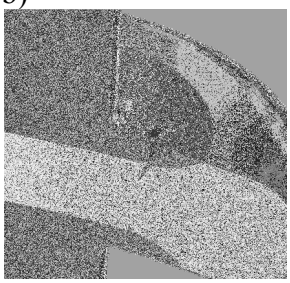
In Fig. 4c the crack depth *a* is plotted vs. the load cycles *N* in dependency of the width of the martensitic region *b*. Apparently the critical crack depth a_c is on the one hand smaller, on the other hand it is reached faster if the flanged shaft has a large martensite structure. For instance with a martensite width of *b*=9mm the critical crack depth a_c is only 3,4mm. In contrast the unstable crack growth is reached in the flanged shaft with *b*=7mm after a_c=4,4mm, with *b*=5mm after a_c=6,1mm and with *b*=3mm after a_c=6,5mm.

In addition a remarkable difference can be found by looking at the load cycles. The smaller the martensite region is, the more load cycles are tolerated until final fracture by the structure. For example with a martensite region of *b*=3mm 2.700.000 load cycles are possible, whereas those are clearly smaller with a larger martensitic region with 1.280.000 (b=5mm), 9.200 (b=7mm) and 2.400 (b=9mm) cycles.

a)



b)



c)

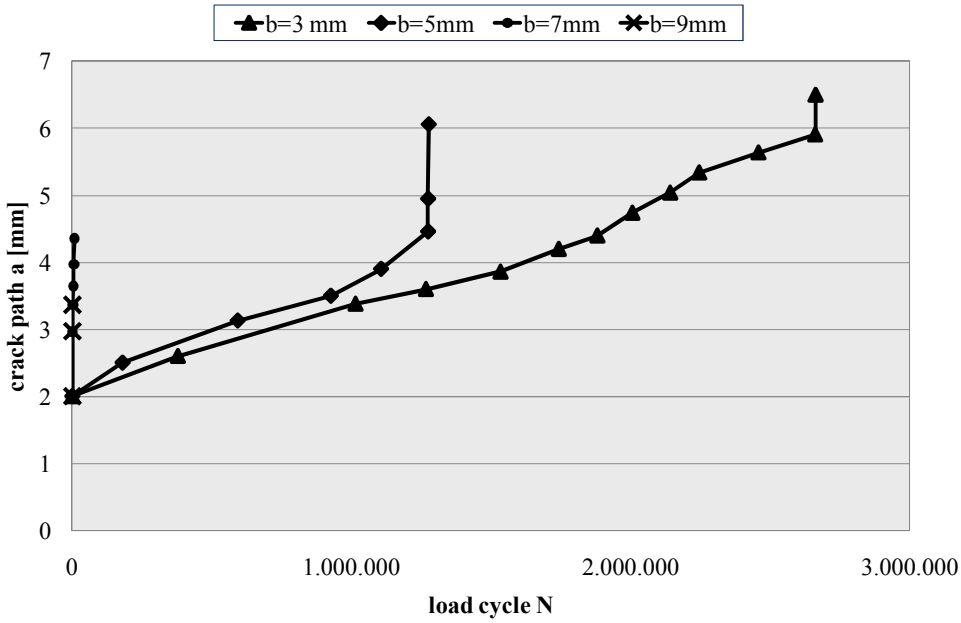


Fig. 4: a) Crack growth in a graded material with the martensite region b=3mm,
b) Crack growth in a graded material with the martensite region b=9mm,
c) Dependency of the size of the martensite region in a crack depth-load cycles-diagram

Summary

The presented simulations make clear that the martensitic region has an essential influence on the life cycles of a component. The inserted crack grows from the base material into the martensite phase and leads to failure of the structure immediately after reaching the graded region. Therefore it is suggested to produce only a small region of martensite structure to avoid an early unstable crack growth. Another possibility to minimize the critical influence of the martensite on crack growth is to produce a clearly defined transition zone with better fracture-mechanical properties.

Acknowledgment

This contribution is based on investigations of the collaborative research centre SFB/TR TRR30, which is kindly supported by the DFG.

References

[1] Maier, H.J.; Richard, H.A.: Funktional gradierte Materialien und Strukturen. In: ForschungsForum Paderborn, 2007.

[2] Steinhoff, K.; Maier, H.J.; Biermann, D.: Functionally Graded materials in Industrial Mass Production. Verlag Wissenschaftliche Scripten, Auerbach, 2009.

[3] Fulland, M.; Richard, H.A.: Finite-Element-based fatigue crack growth simulation in real structures. In: F.G. Buchholz, H.A. Richard, M.H. Aliabadi (Eds.): Advances in Fracture Mechanics, Trans Tech Publications, Zuerich, 2003, pp.79-84.

[4] Richard, H.A.; Fulland, M.; Schöllmann, M.; Sander, M.: Simulation of fatigue crack growth using ADAPCRACK3D. In: Blom, A.F. (ed.): Fatigue 2002. Proceedings of the 8th International Fatigue Congress, Stockholm, Sweden, 2002, S. 1405-1412.

[5] Schöllmann, M.; Fulland, M.; Richard, H.A.: Development of a new software for adaptive crack growth simulations in 3D structures. In: Engineering Fracture Mechanics 70, 2003, pp. 221-230.

© (2012) Trans Tech Publications, Switzerland
doi:10.4028/www.scientific.net/KEM.488-489.113

Lifetime determination of the raceway of a large three-row roller slewing bearing

Peter Göncz[1,a], Rok Potočnik[2,b] and Srečko Glodež[1,c]

[1]University of Maribor, Faculty of Natural Sciences and Mathematics, Koroška cesta 160, 2000 Maribor, Slovenia

[2]Rotis d. o. o., Brodišče 5, 1236 Trzin, Slovenia

[a]peter.goncz@uni-mb.si, [b]rok.potocnik@rotis-lj.si, [c]srecko.glodez@uni-mb.si

Keywords: large three-row roller slewing bearings, contact load distribution, numerical model, contact fatigue

Abstract. This paper deals with calculation procedure for lifetime determination of a large three-row roller slewing bearing. First, the contact force distribution between the rollers and the bearing raceway is determined both analytically and numerically. Then, the position and the magnitude of the maximum contact force are identified. In a separate numerical model finite element analyses are performed to determine the subsurface stress distribution as the result of contact between the raceway and different rollers. These stress fields serve as an input for the fatigue lifetime calculation, which is done in accordance with the stress-life approach (*S*-*N*). At the end the influence of roller geometry on the calculated fatigue life is presented.

Introduction

Slewing bearings are large bearings used in different engineering applications, such as turning tables, wind turbines, cranes, excavators, wind turbines, etc. [1]. Their main function is to establish a connection between structural parts, allow relative rotation between them and transmission of loads. Besides radial F_r and axial force F_a, which are usually acting on typical rolling bearings, slewing bearings are usually alsoloaded with an overturning (tilting) moment M_T. A typical three-row roller slewing bearing is schematically shown in Fig. 1. For general purpose there are some well-established industry standards for the calculation of static and dynamic load ratings of rolling bearings. However, as pointed out in [2] many assumptions used in these standards are not valid for large slewing bearings, such as: only parallel relative displacement of the bearing rings/raceways, no clearances, no ring deformations, no changing mechanical properties of the raceway, etc.

In this paper a calculation procedure for determination of the load capacity of a three-row roller slewing bearing's raceway in presented. First, two methods for the contact force distribution between the rollers and the raceway are described. Then, the numerical model for calculation of stress field distribution in the roller slewing bearing is presented. This is followed by the description of fatigue lifetime calculation. At the end the results of some computational examples are presented.

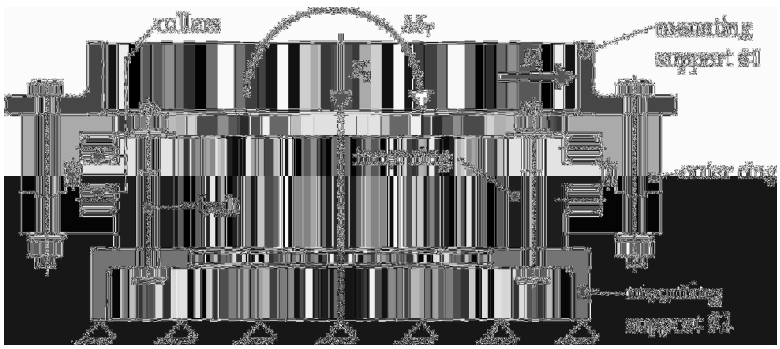


Fig. 1. Schematic structure of a typical three-row roller slewing bearing assembly

Computational model

Contact force distribution. In most cases, large slewing bearings are loaded with radial F_r and axial force F_a and an overturning moment M_T (Fig. 1). A simple analytical expression for the determination of the maximum contact force Q_{max} between the axial roller and the raceway can be found in [3]:

$$Q_{max} = \frac{4 \cdot M_T}{n \cdot D_L} \pm \frac{F_a}{n}. \tag{1}$$

This expression assumes that there is no axial deformation of the slewing bearing rings and that the axial contact load linearly varies across the diameter of the raceway (i.e. sinusoidal distribution). However, in real life situations the slewing bearing rings often undergo considerable deformations during operation. In such cases specialized calculation approaches [2] and numerical simulations [4, 5] should be used for the determination of contact load distribution.

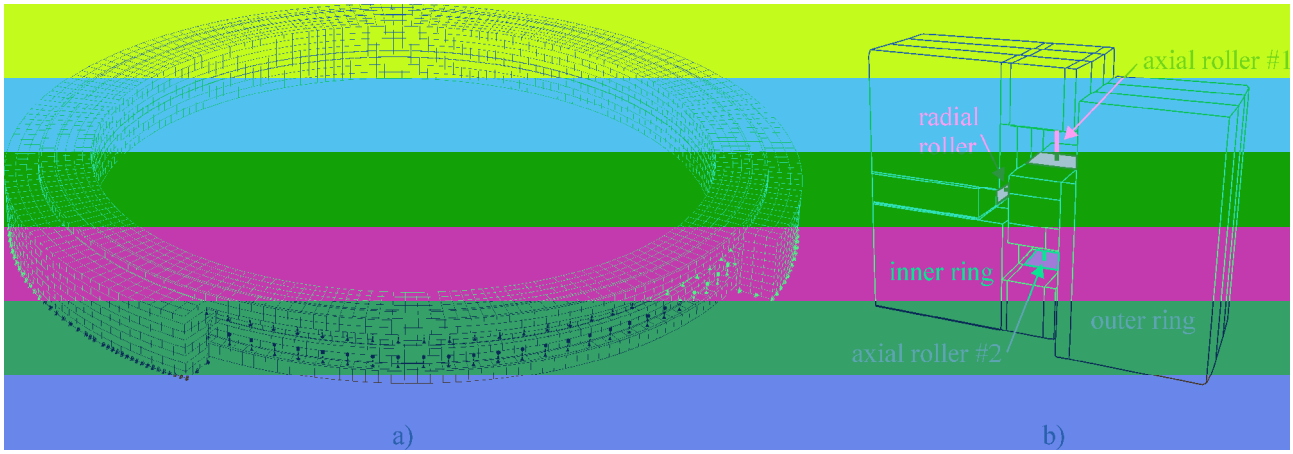


Fig. 2. (a) Numerical model of three-row roller slewing bearing, (b) detailed view of the coupled connectors

In the presented computational model both a simple analytical expression and a numerical simulation were employed to determine maximum contact force acting on the raceway. In the numerical simulation the whole three-row roller slewing bearing was modeled as a deformable 3D body, for which finite element software was used (Fig. 2a). The contacts between the particular rollers and the raceway were modeled as coupled nonlinear elastic connectors (Fig. 2b): no stiffness in tension, nonlinear stiffness in compression. This simplification was used to simulate the relation between the raceway/roller/raceway contact displacement and contact force.

Rolling element – raceway contact model. Stress distribution field in the slewing bearing raceway was determined by numerical calculation of the contact between the roller and the raceway. The numerical calculations were performed with the computer program Abaqus/Standard [6] as a static simulation with elastic material properties (E, ν) taken into account. Due to the symmetry of the problem, a 1/8 model was employed (Fig. 3a).

Three different types of rollers (all with the same nominal dimensions ϕ25x25 mm) were investigated. The first roller had a straight profile with an end chamfer (1/45°), the second had and end fillet (R1) and the third roller had a modified side profile [7]:

$$P(x) = 0.00035 D_{we} \ln\left[\frac{1}{1-(2x/L_{we})^2}\right], \tag{2}$$

where D_{we} is the roller diameter in mm, L_{we} effective roller length in mm and x is the position in the axial direction of the roller.

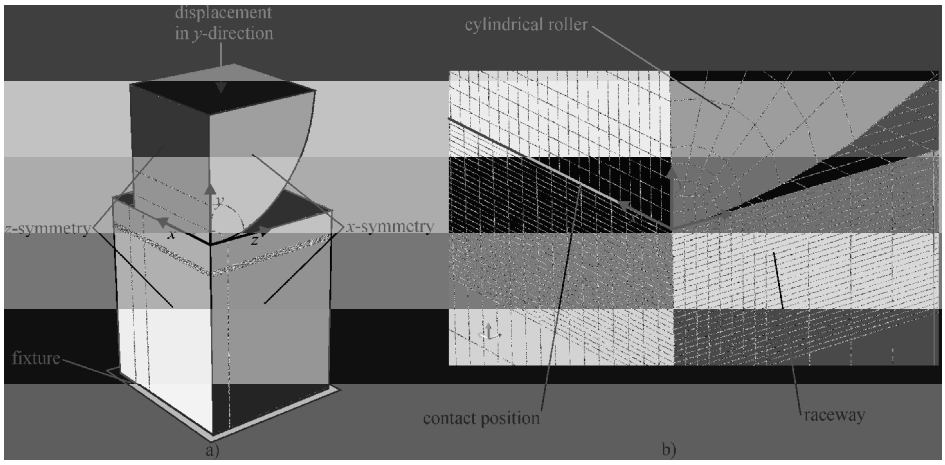


Fig. 3. (a) 1/8 symmetry model of the roller – raceway contact, (b) FE mesh of the numerical model

Numerical models of all three types of rollers consisted of approx. 100,000 8-node linear brick elements. The contact between the roller and the raceway was defined as "hard" contact (Fig. 3b). The contact loading was prescribed as a vertical displacement (in direction of y) of the roller segment. The resulting contact force Q was then determined for every vertical displacement Δy_i from the results of the numerical simulation.

As a result of these numerical calculations both the contact pressure distribution $p(x)$ along the x axis of the different rollers (Fig. 4) and the stress distributions in the raceway were determined.

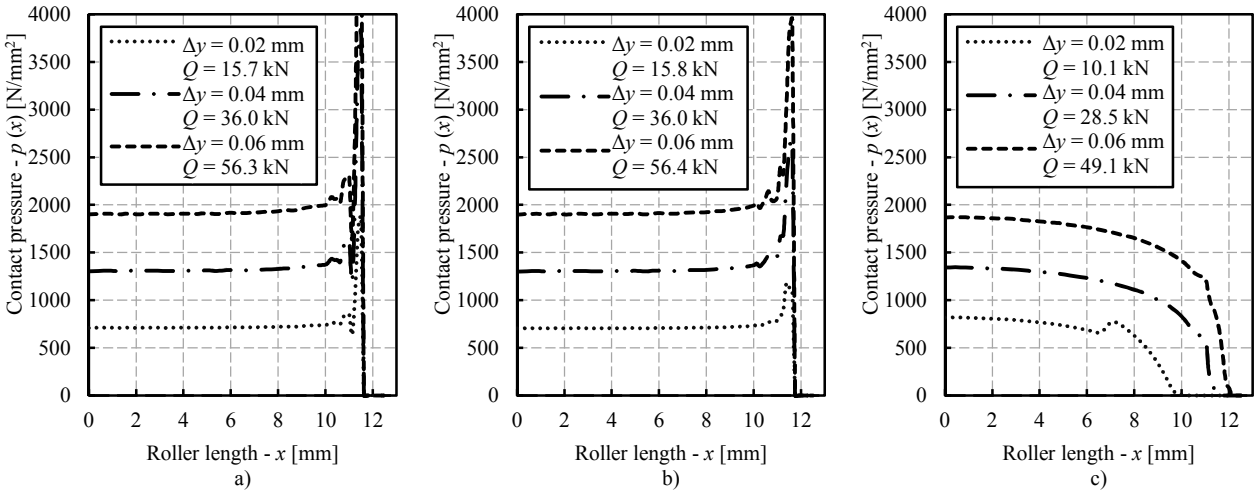


Fig. 4. Contact pressure distribution for: (a) unprofiled roller with edge chamfer, (b) unprofiled roller with edge fillet and (c) logarithmically profiled roller

Fatigue lifetime calculation. As mentioned in the introduction, stress-life approach (S-N) was used to calculate fatigue lifetime of the raceway. This approach is applicable to dynamically loaded machine elements, which undergo between 10^3 and 10^7 load cycles [8]. The number of loading cycles until failure can be determined with the Basquin [8] equation:

$$N_{\mathrm{f}} = \left(\frac{\sigma_{\mathrm{eq}}}{2^{\mathrm{b}} \cdot \sigma'_{\mathrm{f}}} \right)^{1/\mathrm{b}} . \tag{3}$$

Computational results

Fig. 5a shows the relation between the contact force Q and the max. equivalent stress σ_{eq} in the raceway while Fig. 5b shows the influence of the roller type and contact force magnitude on the calculated fatigue life N_f. For the purpose of comparison Fig. 5a also shows the relation between Q and σ_{eq} in the center of the roller.

It is evident from the results that the most critical region in the roller – raceway contact (in the case of unprofiled rollers) is at the end of the contact. However, at lower contact forces the unprofiled roller has an even more advantageous influence on the fatigue life.

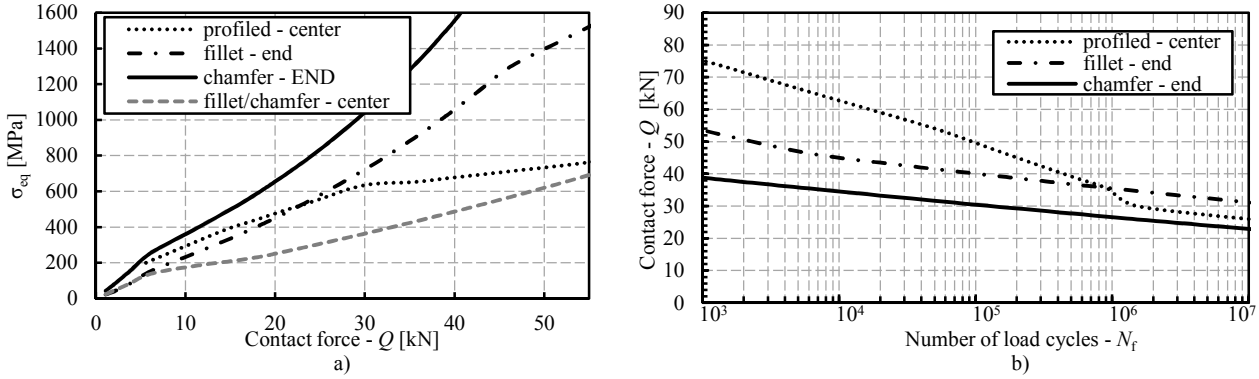


Fig. 5. (a) Relation between the max. contact force Q_{max} and the equivalent stress σ_{eq}, (b) relation between the calculated fatigue lifetime N_f and the max. contact force Q_{max}

Summary

The presented paper describes a computational model for the fatigue lifetime determination of a three-row roller slewing bearing's raceway. The contact force distribution between the rollers and the raceway is determined both analytically and numerically. Then, the most loaded roller is taken into account for the purpose of the determination of the subsurface stress distribution. The fatigue lifetime of the raceway is then determined from these results, according to the stress – life method. The results show that usage of profiled rollers result in significantly longer life times than usage of unprofiled rollers.

References

[1] *Slewing Bearings* [Product Catalog]. 2007, Rothe Erde.

[2] Potočnik, R., *Static capacity and lifetime of large double-row slewing ball bearings* [PhD Thesis], in Faculty of Mechanical Engineering. 2010, University of Maribor: Maribor.

[3] *DNV-2.22 - Lifting appliances*. 2008, DET NORSKE VERITAS.

[4] Kania, L., *Modelling of rollers in calculation of slewing bearing with the use of finite elements*. Mechanism and Machine Theory, 2006. **41**(11): p. 1359-1376.

[5] Smolnicki, T., D. Derlukiewicz, and M. Stanco, *Evaluation of load distribution in the superstructure rotation joint of single-bucket caterpillar excavators*. Automation in Construction, 2008. **17**(3): p. 218-223.

[6] *Abaqus Simulia 6.10-1 Documentation*. 2010, Dassault Systémes.

[7] *ISO/TS 16281: Rolling bearings — Methods for calculating the modified reference rating life for universally loaded bearings*. 2008, International Organization for Standardization: Switzerland.

[8] R. I. Stephens, A.Fatemi, R. R. Stephens, H. O. Fuchs, *Metal Fatigue in Engineering, 2nd Ed*. 2001: John Wiley & Sons, Inc.

© (2012) Trans Tech Publications, Switzerland
doi:10.4028/www.scientific.net/KEM.488-489.117

Analysis of combined adhesive and cohesive cracking at roughened surfaces

O. van der Sluis[1,2,a] S.P.M. Noijen[1,3,b] J.B. Bouquet[4,c] P.H.M. Timmermans[1,d]

[1]Philips Research, High Tech Campus 7, 5656AE Eindhoven, The Netherlands
[2]Department of Mechanical Engineering, Eindhoven University of Technology, 5600MB Eindhoven, The Netherlands
[3]Department of Precision and Microsystems Engineering, Delft University of Technology, 2628CD Delft, The Netherlands
[4]George W. Woodruff School of Mechanical Engineering, Georgia Institute of Technology, Atlanta, USA

[a]olaf.van.der.sluis@philips.com, [b]sander.noijen@philips.com, [c]jb.bouquet@imelavi.fr, [d]p.h.m.timmermans@philips.com

Keywords: Delamination, adhesion, roughness, fracture mechanics, cohesive zone modeling

Abstract. Macroscopic delamination of polymer-metal interfaces is one of the main failure modes observed in micro-electronic components. Due to the irregularly shaped metal roughness profile, this delamination not only consists of interface separation but also bulk cracking at the micro-scale of the roughness. In fact, one of the key mechanisms that results in increased adhesion toughness at roughened interfaces is the transition from adhesive to cohesive failure. A semi-analytical approach is discussed in which the competition between adhesive and cohesive cracking is analyzed by means of the theoretical relation between interface and kinking stress intensity factors. The parameters that define this relation, the solution coefficients, are quantified by finite element (FE) simulations. Accordingly, the crack kinking location and kinking angle into the softer polymer is readily calculated. Furthermore, the geometrical effect of roughness is evaluated by means of FE simulations in which the interface topology follows from measured roughness profiles while also including interface delamination using cohesive zone elements.

Introduction

Delamination of metal-polymer interfaces is one of the major failure modes occurring in micro- and nano-electronics. In the past, several numerical techniques at macro-scale have been applied successfully to predict the delaminating behavior of such electronic devices, see e.g. [1, 2, 3]. These phenomenological models rely on extensive experimental characterization of the interface strength and toughness. Alternatively, a sequential multi-scale approach, as illustrated in Fig. 1, could prevent the need for such extensive characterization work. At each scale information of the interface behavior is obtained and passed onto the next scale. At the atomic scale, the polymer-metal adhesive properties are due to chemical and physical interactions and can be obtained by molecular simulations or by experiments. This information is passed onto the micro-scale which accounts for roughness effects at the

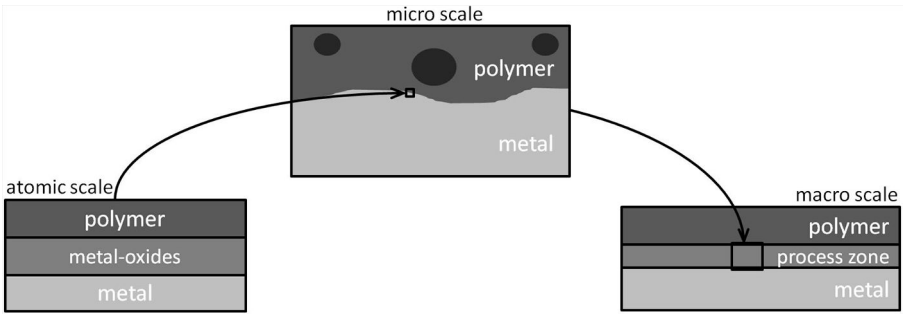


Figure 1: Sequential multi-scale framework for interface delamination (not to scale)

interface. These effects include surface increase, mechanical interlocking and the competition between cohesive and adhesive failure around the interface [4, 5, 6]. Subsequently, the macro-scale interface properties are then established as function of mode angle by means of an appropriate homogenization method, see e.g. [7].

This paper starts with a semi-analytical approach that enables the identification of crack kinking based on fracture mechanics theory combined with FE simulations. Next, a FE model is developed to determine the geometric effect of measured roughness profiles by calculating the resulting macroscopic traction-separation curve. It is remarked that currently, this model is limited to adhesive failure.

Semi-analytical approach to crack kinking at an interface

This approach is based on the work performed by He and Hutchinson [8, 9, 10] and more recently by Jakobsen et al [11]. In essence, the method uses the theoretical relation between kinking and interface stress intensity factors (SIFs) for an interface crack of length L between two semi-infinite dissimilar materials 1 and 2, loaded under remote uniform stress σ_{22}^{∞} and σ_{12}^{∞} and normal stress σ_{11} along the interface, and assuming that the kinking crack length a is small with respect to all relevant in-plane length quantities [10]:

$$K_I + iK_{II} = cKa^{i\varepsilon} + d\bar{K}a^{-i\varepsilon} + b\sigma_{11}\sqrt{a}, \tag{1}$$

in which (K_I, K_{II}) are the kinking SIFs, K is the complex interface SIF, $\bar{(\cdot)}$ denotes complex conjugation, and b, c, d are complex-valued solution coefficients. [9] provides tabulated solution coefficients c and d for certain material combinations, while [10] includes the parallel normal stress term $b\sigma_{11}$. Upon introducing the kinking crack energy release rate (ERR) into material 2, $G = (K_I^2 + K_{II}^2)(1-\nu_2^2)/E_2$, and the interface crack ERR $G_0 = (1-\beta^2)(K_1^2 + K_2^2)/E_*$, with $E_*^{-1} = (\bar{E}_1^{-1} + \bar{E}_2^{-1})/2$, the criterion for crack kinking from an initially delaminated area can be written as [12]

$$G_R \equiv \frac{G}{G_0} > \frac{\Gamma_k}{\Gamma_i(\psi)} \equiv \Gamma_R, \tag{2}$$

where Γ_k is the fracture toughness of material 2 and Γ_i corresponds to the interface toughness. In [13], the dependency of G_R-values for different mode angles, kinking angles, kinking crack lengths and Dundurs' parameter values is illustrated. The tabulated solution coefficients of He and Hutchinson [9] are based on numerical solutions of singular integral equations resulting from a basic solution for an edge dislocation in material 2 under the assumption that $L \gg a$. The tables restrict crack kinking predictions to the available tabulated material combinations and kinking angles. In order to generalize the tabulated solution coefficients, it is therefore proposed to derive an analytic expression that renders solution coefficients for any material combination (α, β) and kinking angle ω. An FE procedure is employed in this paper to determine the solution coefficients (b, c, d) for any (α, β, ω) combination. To this end, the method proposed by Jakobsen et al [11] is slightly adapted. Response Surface Modeling (RSM) is utilized to derive empirical equations describing the aforementioned dependency. To establish the solution coefficients, the SIFs are calculated for three mode angles which results in the following system of equations by rewriting Eq. 1

$$\begin{bmatrix} \Re c(\omega) \\ \Im c(\omega) \\ \Re d(\omega) \\ \Im d(\omega) \\ \Re b(\omega) \\ \Im b(\omega) \end{bmatrix} = \begin{bmatrix} f_1^{\psi_1} & -f_2^{\psi_1} & f_1^{\psi_1} & -f_2^{\psi_1} & f_3^{\psi_1} & 0 \\ f_2^{\psi_1} & f_1^{\psi_1} & -f_2^{\psi_1} & -f_1^{\psi_1} & 0 & f_3^{\psi_1} \\ f_1^{\psi_2} & -f_2^{\psi_2} & f_1^{\psi_2} & -f_2^{\psi_2} & f_3^{\psi_2} & 0 \\ f_2^{\psi_2} & f_1^{\psi_2} & -f_2^{\psi_2} & -f_1^{\psi_2} & 0 & f_3^{\psi_2} \\ f_1^{\psi_3} & -f_2^{\psi_3} & f_1^{\psi_3} & -f_2^{\psi_3} & f_3^{\psi_3} & 0 \\ f_2^{\psi_3} & f_1^{\psi_3} & -f_2^{\psi_3} & -f_1^{\psi_3} & 0 & f_3^{\psi_3} \end{bmatrix}^{-1} \begin{bmatrix} K_I^{\psi_1}(\omega) \\ K_{II}^{\psi_1}(\omega) \\ K_I^{\psi_2}(\omega) \\ K_{II}^{\psi_2}(\omega) \\ K_I^{\psi_3}(\omega) \\ K_{II}^{\psi_3}(\omega) \end{bmatrix}, \tag{3}$$

with $f_1^{\psi_i} = K_1^{\psi_i}\cos(\varepsilon \ln a) - K_2^{\psi_i}\sin(\varepsilon \ln a)$, $f_2^{\psi_i} = K_1^{\psi_i}\sin(\varepsilon \ln a) + K_2^{\psi_i}\cos(\varepsilon \ln a)$ and $f_3^{\psi_i} = \sqrt{a}\sigma_{11}^{\psi_i}$. The only requirement for this system to be regular is $\psi_1 \neq \psi_2 \neq \psi_3$. In a forthcoming publication [13], the accuracy of this method is proven by means of two benchmark cases: an isolated

and a finite interface crack. FE analysis is required to calculate the SIFs and ERR of an interfacial crack accurately for arbitrary geometries and loading conditions. Consequently, K_I and K_{II} of the kinking crack are calculated by means of Eq. 1. Performing these calculations for different kinking angles gives G_R as function of ω. By applying the kinking condition Eq. 2, it is determined if crack kinking occurs and at which angle ω_k. This semi-analytical approach to perform crack kinking analysis by a combination of FE calculations for the interface crack and analytic equations is generalized in this section by constructing an RSM that makes the solution coefficients immediately available as a function of α, β and ω.

As indicated in [12], physically admissible material combinations in plane strain are restricted to $\alpha \in [-1, 1]$ and $\alpha - 4\beta \in [-1, 1]$. A design of experiments (DOE) is set-up to derive solution coefficients for these material combinations with $\omega = \pm$ [20°, 40°, 60°, 80°, 100°]. For each material combination FE simulations consisting of stress simulations to determine σ_{11}, interface crack SIF calculations, and kinking crack SIF calculations are performed for three loading conditions. Solution coefficients for a total of 1250 α, β and ω combinations are determined. Cubic RSMs including interaction terms for each solution coefficient for all α, β and ω are established. Now that expressions are available that couple the solution coefficients to the material combinations and kinking angle, only the ERR and stress state of an interfacial crack need to be determined numerically to find G_R.

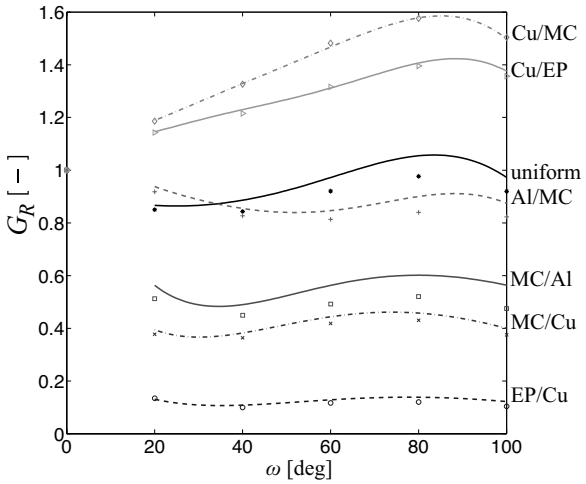
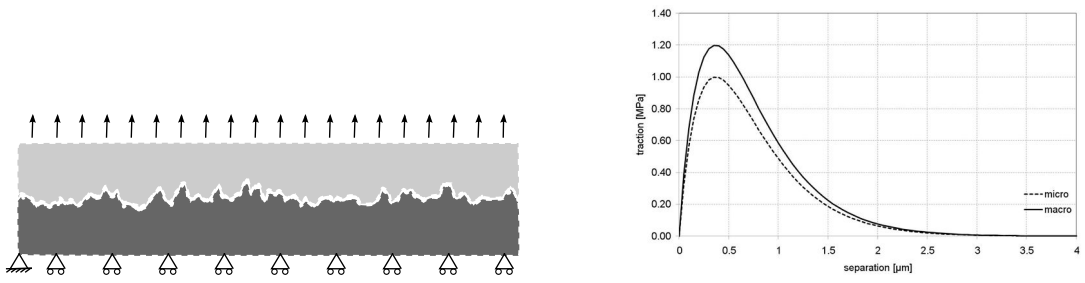


Figure 2: Semi-analytical (lines) and FE (symbols) results for different material combinations (MC: molding compound; EP: epoxy)

Fig. 2 shows the resulting G_R values as a function of ω for the case of an isolated interface crack. From these results, it can be concluded that the semi-analytical results reflect the FE values rather well with a maximum error of about 10%. For Cu/MC and Cu/EP, kinking is most likely to occur at 85°. It can thus be concluded that the semi-analytic approach is a very cost-effective method to perform crack kinking analyses at interface cracks. It must be noted, however, that the accuracy by utilizing the RSM is limited to approximately 90% of FE analysis. In cases that a higher accuracy is required it is recommended to recalculate the solution coefficients of the particular problem and apply Eq. 1. More detailed results can be found in [13].

Roughness modeling

Fig. 3a shows a FE model of a surface profile taken from a white light interferometer measurement of a copper leadframe with an accuracy of 0.5 μm, which is well below the typical size of the measured roughness of $R_a = 4.1\ \mu m$. One drawback of this measurement technique is that cavities cannot be detected. It appears that the length of the actual profile L is approximately 20% higher than the length



(a) (b)

Figure 3: (a) 2D micro-scale plane strain model for a measured surface roughness under mode I loading conditions; (b) micro-scale and macro-scale traction-separation curves for a rough interface

of the straight profile L_0. Now, if the surface is subjected to a vertical tensile force F_y, the macroscopic interface toughness increases by a factor L/L_0 (similar to the Wenzel factor $r = A/A_0$ [14]), assuming that the interface properties at this scale are indeed mode independent and no cavities causing interlocking are present. In the model, mode I loading is prescribed while interface delamination is modeled with cohesive zone (CZ) elements employing an exponential Smith-Ferrante law [15]. At this analysis scale, the interface properties are only due to chemical and physical interactions which can be found by molecular simulations (e.g., [16]) or by experiments (e.g., [17]). The bottom metal layer is constrained in vertical direction while at the top polymer layer a vertical displacement is prescribed. The macro-scale tractions are calculated by summation of the nodal reaction forces at the top edge of the micro-scale model divided by the width, see Fig. 3(b). The increase of interface toughness for the rough surface is apparent.

Discussion

The competition between cohesive and adhesive failure at a bimaterial interface was described by a semi-analytical model based on [8, 9, 10, 11]. The tabulated solution coefficients from [9] were generalized for any material combination and kinking angle by means of RSMs. In this approach SIFs of the interface crack and the normal stress field along the interface are calculated by FE simulations. These interface results are used in combination with solution coefficients to analytically determine the SIFs of kinking cracks based on relations presented in [10]. Furthermore, results for relevant polymer-metal interfaces from the presented semi-analytical approach were compared to FE results. The semi-analytical approach reflected the dependency of G_R on ω well: the maximum deviation of the results from FE results was within 10%. In addition, a 2D FE model was presented that accounted for the geometrical effect of surface roughness on macroscopic interface properties. The micro-scale interface properties are limited to chemical and physical interactions, while the resulting macroscopic interface properties reflect the effect of all micro-scale dissipation processes as well as the increase of interface surface area. An example on the effect of surface increase for mode I loading was given.

Future work will focus on the addition of transient bulk cracking of the surrounding materials by means of initially rigid cohesive zone elements, plasticity in the metal and friction to arrive at meaningful calculations for mode-dependent interface toughness values as function of roughness geometry. These numerically obtained results will be validated with results from experimental interface testing using mixed-mode bending [18].

Acknowledgements

We thank the European Commission for partial funding of this work under project NanoInterface (NMP-2008-214371).

References

[1] G.Q. Zhang, W.D. van Driel, and X.J. Fan. *Mechanics of Microelectronics*. Springer, Dordrecht, 2006.

[2] O. van der Sluis, C.A. Yuan, W.D. van Driel, and G.Q. Zhang. Advances in delamination modeling. In J.E. Morris, editor, *Nanopackaging: Nanotechnologies and Electronics Packaging*, pages 61--91. Springer, 2008.

[3] O. van der Sluis, Y.Y. Hsu, P.H.M. Timmermans, M. Gonzalez, and J.P.M. Hoefnagels. Stretching induced interconnect delamination in stretchable electronic circuits. *Journal of Physics D: Applied Physics*, 44:034008, 2011.

[4] K.L. Devries and D.O. Adams. Mechanical testing of adhesive joints. In D.A. Dillard and A.V. Pocius, editors, *The Mechanics of Adhesion*, pages 193--234. Elsevier, 2002.

[5] Q. Yao and J. Qu. Interfacial versus cohesive failure on polymer-metal interfaces in electronic packaging effects of interface roughness. *Journal of Electronic Packaging*, 124:127--134, 2002.

[6] P.D. Zavattieri, L.G. Hector Jr, and A.F. Bower. Cohesive zone simulations of crack growth along a rough interface between two elastic-plastic solids. *Engineering Fracture Mechanics*, 75: 4309--4332, 2008.

[7] C.V. Verhoosel, J.J.C. Remmers, M.A. Gutiérrez, and R. de Borst. Computational homogenisation for adhesive and cohesive failure in quasi-brittle solids. *International Journal for Numerical Methods in Engineering*, 83:1155--1179, 2010.

[8] M.Y. He and J.W. Hutchinson. Kinking of a crack out of an interface. *Journal of Applied Mechanics*, 111:270--278, 1989.

[9] M.Y. He and J.W. Hutchinson. Kinking of a crack out of an interface: Tabulated solution coefficients. Technical report, Harvard University, 1989.

[10] M.Y. He, A. Bartlett, A.G. Evans, and J.W. Hutchinson. Kinking of a crack out of an interface: Role of in-plane stress. *Journal of the American Ceramic Society*, 74:767--771, 1991.

[11] J. Jakobsen, J.H. Andreasen, and E. Bozhevolnaya. Crack kinking of a delamination at an inclined core junction interface of a sandwich beam. *Engineering Fracture Mechanics*, 75:4759--4773, 2008.

[12] J.W. Hutchinson and Z. Suo. Mixed mode cracking in layered materials. *Advances in Applied Mechanics*, 29:63--191, 1992.

[13] S.P.M. Noijen, O. van der Sluis, P.H.M. Timmermans, and G.Q. Zhang. A semi-analytic method for crack kinking analysis at interfaces. *submitted*, 2011.

[14] D.E. Packham. Surface energy, surface topography and adhesion. *International Journal of Adhesion & Adhesives*, 23:437--448, 2003.

[15] B.A.E. van Hal, R.H.J. Peerlings, M.G.D. Geers, and O. van der Sluis. Cohesive zone modeling for structural integrity analysis of IC interconnects. *Microelectronics Reliability*, 47:1251--1261, 2007.

[16] I. Yarovsky. Atomistic simulation of interfaces in materials: theory and applications. *Australian Journal of Physics*, 50:407--424, 1997.

[17] O. Hölck, J. Bauer, O. Wittler, K. Land, B. Michel, and B. Wunderle. Experimental contact angle determination and characterisation of interfacial energies by molecular modelling of chip to epoxy interfaces. In *Proceedings of ECTC 2011, Florida*, 2011.

[18] M. Kolluri, J.P.M. Hoefnagels, J.A.W. van Dommelen, and M.G.D. Geers. An improved miniature mixed-mode delamination setup for *in situ* microscopic interface failure analyses. *Journal of Physics D: Applied Physics*, 44:034005, 2011.

© (2012) Trans Tech Publications, Switzerland
doi:10.4028/www.scientific.net/KEM.488-489.122

Performance of Different Metal-Foam Stuffed Whipple Shield against Hypervelocity Impact of Space Debris

Bin Jia[1,a], Feng Li[2,b], Hai-peng Gong[1,c] and Bao-jun Pang[1,d]

[1]Department of Astronautic Engineering, Harbin Institute of Technology, Harbin 150001, China

[2]Chengdu Aircraft Design and Research Institute, Aviation Industry Corporation of China, Chengdu, 610041, China

[a]jiabin@hit.edu.cn, [b]billy6229878@126.com, [c]gonghaipeng@sina.com, [d]pangbj@hit.edu.cn

Keywords: space debris, hypervelocity impact, stuffed Whipple shield, metal foam

Abstract. Hypervelocity impacts on spacecraft in low earth orbit by meteoroids and space debris poses a threat to space missions, and the use of a shield can significantly decrease the probability of a catastrophic failure. Tests have identified that metallic foams have a good shielding performance against hypervelocity impact by micro-meteoroids and orbital debris. A metal-foam stuffed Whipple shield was presented under the concept of light-weight shield structure. A meso-structure model of geometry for metallic foams was set up simulating their manufacturing process and validated by comparison with experimental results using own SPH code. Three base materials of foam, including Al 7075-T651, Ti and Al ZL102, were researched for their performances as stuff of shield by means of numerical simulation. The results indicated that different base materials show the best shield performance at different impact speeds with other conditions the same. The foam of Al ZL102 stuffed can cause the strongest radial dispersion of the secondary debris cloud and is more likely to provide the best shield performance, which is proved at the higher part of the speed range investigated.

Introduction

All spacecraft in low earth orbit are subject to the risk of hypervelocity impact by meteoroids and space debris. These impacts can damage flight-critical systems, which can in turn lead to catastrophic failure of the spacecraft [1]. The use of a shield can significantly decrease the probability of a catastrophic failure. Fred Whipple proposed in the 1940s a meteoroid shield for spacecraft consisting of a thin "sacrificial" bumper followed at a distance by a rear wall [2]. The function of the first sheet or "bumper" is to break up the projectile into a cloud of material containing both projectile and bumper debris. This cloud expands while moving across the standoff, resulting in the impactor momentum being distributed over a wide area of the rear wall. For most conditions, a Whipple shield results in a significant weight reduction over a single plate, which must contend with deposition of the projectile kinetic energy in a very localized area. Considerable advances have been made in the development of constructive schemes based on the idea of a Whipple shield at present time [3]. In spite of these advances, attempts continue to find structures or materials that will provide better fragmentation of the projectile. A possible solution can be the use of bumpers of inhomogeneous materials. European Space Agency carried out experiments of hypervelocity impact on shields containing Al-foam bumpers, whose results indicate that the by-layered Al-foam or Al-foam sandwiched configurations have outstanding capabilities to induce multiple shocks to the projectile in the completely velocity range [4-6]. The tests showed the multiple shocking process capable to completely melt the impacting projectile both at about 6 and about 4 km/s, and quite a good deal of melting was observed also at velocities as low as 2.6 km/s [4]. As a result, metal-foam is a promising material in the shield design of spacecrafts in the future.

SPH method

Smoothed Particle Hydrodynamics (SPH) is a technique for problem solving in Computational Continuum Dynamics. Recently, SPH has become widely recognized for numerical simulation of hypervelocity impact. An own three-dimensional SPH code for simulations of foams was developed. The simulation was performed in the usual three typical steps using the own code, the first one being the building of the model by means of the internal pre-processor, the second step being the nonlinear dynamic analysis and the final one being the post-processing of the analysis results using the Tecplot for the interpretation and visualization of the computed data.

Foam model. In order to understand the behavior of metal foams subjected to hypervelocity impact processes, the impact experiments need to be complemented by material modeling of the foam behavior under numerical simulations. When a projectile traveling at hypervelocity reaches the foam, it fragments into smaller particles, which hit single cell walls and cause fragmentation and phase transitions on the mesoscopic scale. Therefore, for numerical simulations, it is not possible to use a continuum discretization of the foam; instead, a mesoscale model of the foam has to be generated.

The method of discretisation of foams presented here is similar to processing of foams. Light-weight foam metals can be produced by casting liquid metal around inorganic or even organic granules or hollow spheres of low density, or by introducing such materials into a metallic melt. The granules either remain in the metallic product after casting — yielding what is called a "syntactic foam" — or are removed by leaching in suitable solvents or acids or by thermal treatment (Fig. 1). The unique physical properties of solid foams can be attributed to random cellular morphology, which usually forms in the liquid state when gas bubbles become highly concentrated. The discretisation was created with an own particle code, that is based on the randomly disturbance of a regular structure. Then material parameters needed for metallic foams are just those of original metal material, which have been developed extensively and successfully.

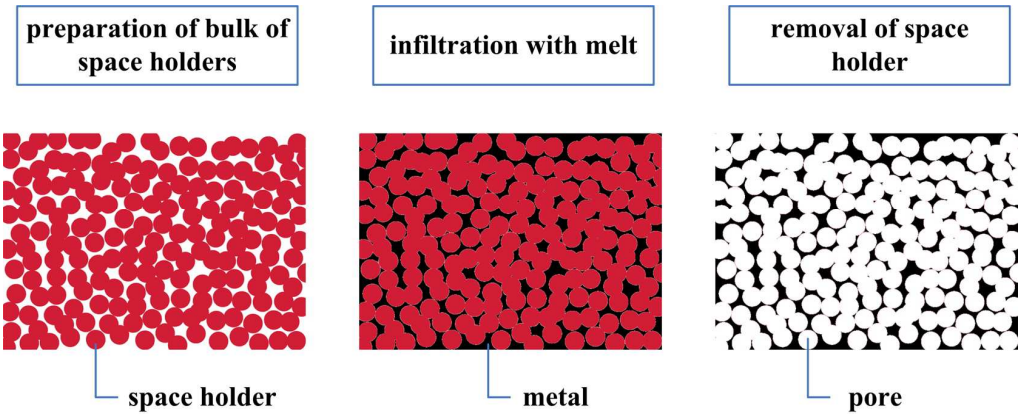


Fig. 1 Production of metallic foam using space-holding fillers

Validation of numerical approach. A metal-foam stuffed Whipple shield was presented under the concept of light-weight shield structure. Hypervelocity impact tests of Al-sphere projectile on Al-foam stuffed Whipple shield as shown in Fig. 2 were performed using two-stage light gas gun at a speed range from 2km/s to 4km/s. The first bumper of the shield is an Al 2A12 plate of 2mm in thickness. The second bumper is an Al Zl102 (AlSi12) open-cell foam plate with a thickness of 10mm placed in the middle of the first bumper and the rear wall. The foam has a relative density of 27% and a mean pore diameter of 1mm. The rear wall is an Al 5A06 plate of 2mm in thickness. The projectile is an Al 2017 sphere of 6.35mm in diameter and the incident angel is 0^{o}. Numerical simulations were conducted at the same impact speed with experiments through own SPH code combined with the foam model presented. Mie-Grüneisen equation of state and Johnson-Cook strength model was adopted for all the metals involved. Fig. 3 and Fig. 4 give the damage of Al-foam plate at the speed of 4.06km/s by experiment and simulation respectively. And Table 1 gives the result comparisons between experiments and simulations. The simulation is in good agreement with the experimental result.

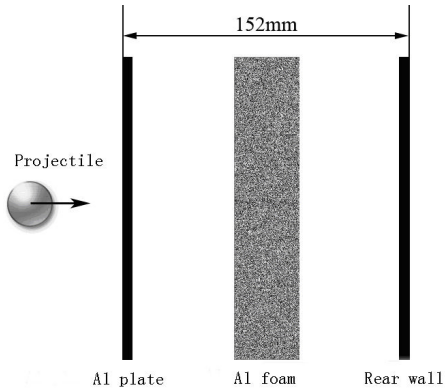


Fig. 2 Schematic configuration of Al-form stuffed Whipple shield

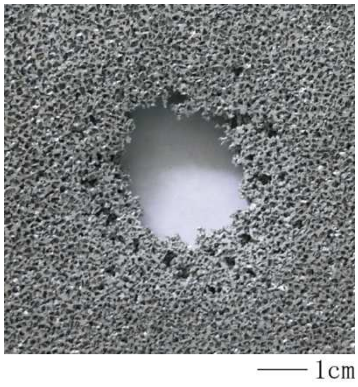


Fig. 3 Experimental result of Al-foam at 4.06km/s

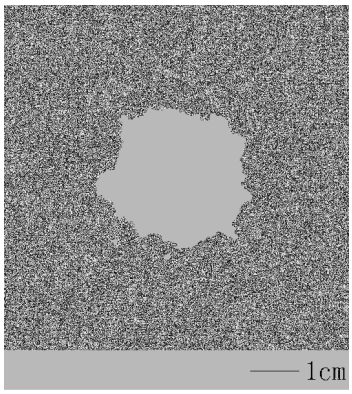


Fig. 4 Numerical result of Al-foam at 4.06km/s

Table 1 Results of experiments and simulations

Impact velocity [km/s]	Hole diameter of the first bumper [mm]		Hole diameter of the second bumper [mm]		Hole diameter of the rear wall [mm]	
	Experiment	Simulation	Experiment	Simulation	Experiment	Simulation
2.19	9.26	9.44	12.81	14.46	9.46	8.36
3.41	10.84	10.91	29.72	34.01	No bulge	No bulge
4.06	11.48	11.39	38.87	42.76	Bulge	Bulge

Simulation of different metal foams

Three base materials of metal foam were selected for their possible application in space and their performances as stuff of shield were investigated by means of numerical simulation. The materials include Al 7075-T651, Ti and Al ZL102 for their comprehensive property and low density.

The shield configuration is shown in Fig. 2 but the thickness of the first bumper was reduced by half to make the areal density of the whole shield lower. The foams of the three materials all have a relative density of 30% and a mean pore diameter of 1mm. The thicknesses of Al 7075-T651, Ti and Al ZL102 foam plate are 3.27, 2.05 and 3.3mm respectively to maintain the same areal density but significantly lower than that of the Al ZL102 foam stuffed in Fig. 1. The impact speed was chosen to be 2, 4, 6 and 8 km/s with the projectile being Al 2017 sphere and the incident angel being 0^{o}. The simulation results are listed in Table 2. From Table 2, performances of the three metal-foam stuffed Whipple shield can be compared with each other at different impact speeds.

At 2km/s of impact speed by a projectile of 3.97mm in diameter, the AL ZL102 foam stuffed shield was perforated in the rear wall but the other two were not. The AL 7075-T651 foam stuffed shield had smaller max bulge height to show the best performance at this speed. At higher speeds, the diameter of projectile was increased to be 6mm in order to magnify the damage on rear wall.

At 4km/s, all three shields were not perforated even the projectile had the larger diameter because the Al-projectile was fragmented beyond 3km/s and the shield can work effectively on the debris cloud formed. The damage of the three shields on rear wall was not distinct and the Ti foam stuffed shield had the smallest max bulge height to show the best performance at this speed.

At 6km/s, all three shields were perforated due to the higher kinetic energy of projectile and the higher momentum of debris cloud. The Ti and AL ZL102 form stuffed shield had the equally smaller hole size in rear wall and they have better shield performance than that of AL 7075-T651.

At 8km/s, the two Al-alloy foam stuffed shields had better performance than that of Ti. And the AL ZL102 foam stuffed shield had a slightly smaller hole size than that of AL 7075-T651 to show the best shield performance at this speed.

Table 2 Results of simulations

Impact velocity [km/s]	Projectile diameter [mm]	Base material of foam	Hole diameter of front wall [mm]	Hole diameter of foam plate [mm]	Damage of rear wall [mm]
2	3.97	AL 7075-T651	5	4	Max bulge height: 0.8
		Ti	5	5	Max bulge height: 1.0
		AL ZL102	5	5	Hole size: 4.0×4.2
4	6	AL 7075-T651	12	9	Max bulge height: 7.0
		Ti	12	12	Max bulge height: 6.3
		AL ZL102	12	14	Max bulge height: 6.4
6	6	AL 7075-T651	11	24	Hole size: 2.2×5.8
		Ti	11	37	Hole size: 2.5×2.5
		AL ZL102	11	40	Hole size: 2.5×2.5
8	6	AL 7075-T651	12	28	Hole size: 8×10
		Ti	12	38	Hole size: 15×9
		AL ZL102	12	40	Hole size: 8×9

It should be noticed that at all speeds, the AL ZL102 form stuffed shield had the largest hole diameter in the foam plate stuffed. This implies that the AL ZL102 form can cause the strongest radial dispersion of the secondary debris cloud and is more likely to provide the best shield performance, which is proved at the higher speed range simulated.

Summary

The SPH modeling of metal foam configurations under hypervelocity impact using an own three-dimensional SPH code was presented. A meso-structure model of geometry for metallic foams subjected to hypervelocity impact was set up simulating their manufacturing process. Experiments and numerical simulations of configurations with Al-foam stuffed Whipple shield were implemented and compared. Good agreement was obtained. Performances of three metal-foam stuffed Whipple shields were compared through numerical simulation. The three base materials of foam included Al 7075-T651, Ti and Al ZL102 for their comprehensive property and low density. The results indicated that different base materials show the best shield performance at different impact speeds with other conditions the same. And the foam of Al ZL102 stuffed can provide the best performance at the higher part of the speed range investigated.

References

[1] E.L. Christiansen: *Meteoroid/Debris Shielding* (NASA TP-2003-210788, 2003**)**.

[2] F.L. Whipple: Astron. J. Vol. 52 (1947), p. 132

[3] E.L. Christiansen, J.H. Kerr: Int. J. Impact Eng. Vol. 26 (2001), p. 93

[4] R. Destefanis, F. Schäfer, M. Lambert, et al: Int. J. Impact Eng. Vol. 29 (2003), p. 215

[5] K. Thoma, F. Schäfer and S.Hiermaier: Adv. in Space Research Vol. 34 (2004), p. 1063

[6] R. Destefanis, F. Schäfer, M. Lambert, et al: Int. J. Impact Eng. Vol. 33 (2006), p. 219

© (2012) Trans Tech Publications, Switzerland
doi:10.4028/www.scientific.net/KEM.488-489.126

Development of a Low-Constraint SE(T) Toughness Test

W.R. Tyson[1,a,*], G. Shen[1,b], J. A. Gianetto[1,c], D.-Y. Park[1,d]

[1] CANMET Materials Technology Laboratory, Natural Resources Canada

183 Longwood Road South, Hamilton, Ontario, L8P 0A5

[a]btyson@nrcan.gc.ca, [b]gshen@nrcan.gc.ca, [c]jgianett@nrcan.gc.ca, [d]dopark@nrcan.gc.ca

* Corresponding author

Keywords: low-constraint toughness, tension test, high strength steel pipe, girth welds

Abstract. CANMET-MTL has developed a low-constraint test designed to reduce unnecessary conservatism in the measurement of toughness for use in the assessment of flaws in pipeline girth welds. The design is based on tension loading using fixed (clamped) grips of a single-edge-notched BxB SE(T) specimen, side-grooved to promote plane-strain conditions. Equations have been developed to derive J-integral, CTOD and crack growth from measurement of load and crack-mouth opening displacement. Loading conditions (essentially distance between the grips) have been chosen to reproduce the crack-tip constraint of a circumferential surface flaw in a pipe in service under tensile or bending loads. In this paper, the development of the test and the principal findings from its use will be described.

Introduction

It is well known that constraint affects toughness. The term "constraint" reflects the extent to which plastic deformation is inhibited, which is essentially the degree of stress triaxiality. Constraint is intentionally high in conventional test specimen geometries in order to obtain conservative results, but is low in many structural geometries. An example that is the focus of the present paper is a circumferential flaw (e.g. a girth weld defect) in a pipe as shown in Fig. 1. Measurement of the relevant toughness for this geometry is of great practical interest, since it governs repair decisions that can cost millions of dollars. There is significant incentive to replace the current high-constraint test with a test that more closely simulates the actual constraint in service. For this purpose, work has been under way at CANMET to develop a low-constraint toughness test based on a single-edge tension SE(T) specimen. The procedure has been described in a CANMET report [1] and in proceedings of a conference [2], and is being applied to characterization of welds, including both weld metal (WM) and heat effected zone (HAZ) regions in high-strength steel pipe. Results are being used to predict crack growth in curved-wide plates to assess transferability to structural geometries, and it is expected that the method will be standardized for use in strain-based design of pipelines.

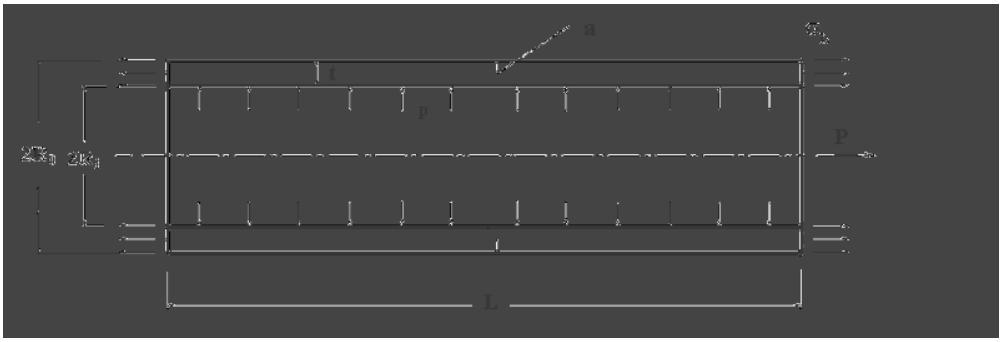


Fig. 1 Thin-walled pipe with a circumferential crack under axial tension and internal pressure [1]

Test Development

The first problem to be addressed was to ensure that the constraint developed in the test specimen represents the structural situation. This was ensured by comparing the stress field calculated by Finite Element Analysis (FEA) of a crack tip in a pipe with that of the proposed geometry (single-edge tension specimen, "daylight" between grips H/W=10, B=W (cross-section BxB)). The results are shown in Figs. 2 and 3 [3].

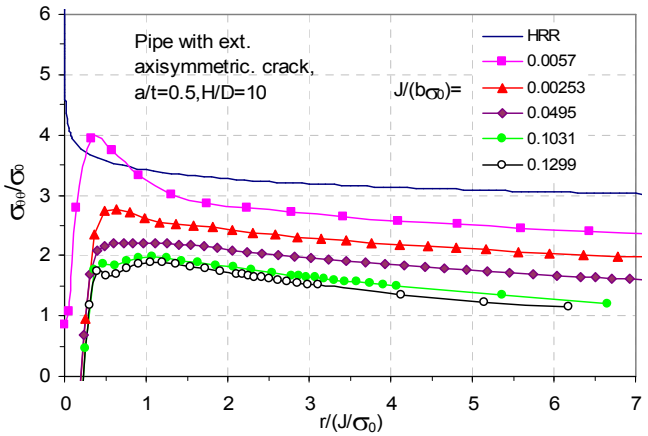


Fig. 2 Crack-tip opening stress for an external axisymmetric crack in a pipe (2-D), a/t=0.5, H/D=10 [3]

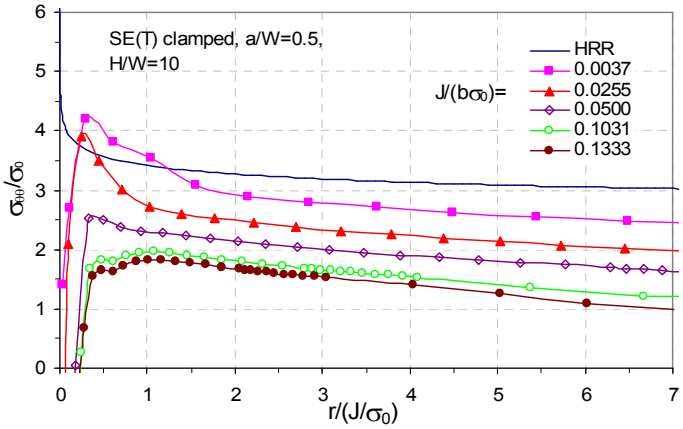


Fig. 3 Crack-tip opening stress for SE(T) clamped sample, a/W=0.5, H/D=10 [3]

Evidently, the stress profiles of the test specimen and the circumferential crack are similar. In particular, there is no marked decrease of stresses toward the centre of the ligament as would be found in bend specimens.

The degree of constraint can be measured by a variety of parameters, and we have chosen to use the conventionally-defined "Q" [3] which essentially compares the magnitude of the hydrostatic stress field at the crack tip to the yield stress. As J increases, the constraint varies as shown in Fig. 4 which shows J-Q relations for cracks in pipe and SE(T) specimens for two crack depths. The good constraint matching shown in Figs. 2 and 3 is supported by the good agreement of the J-Q relations.

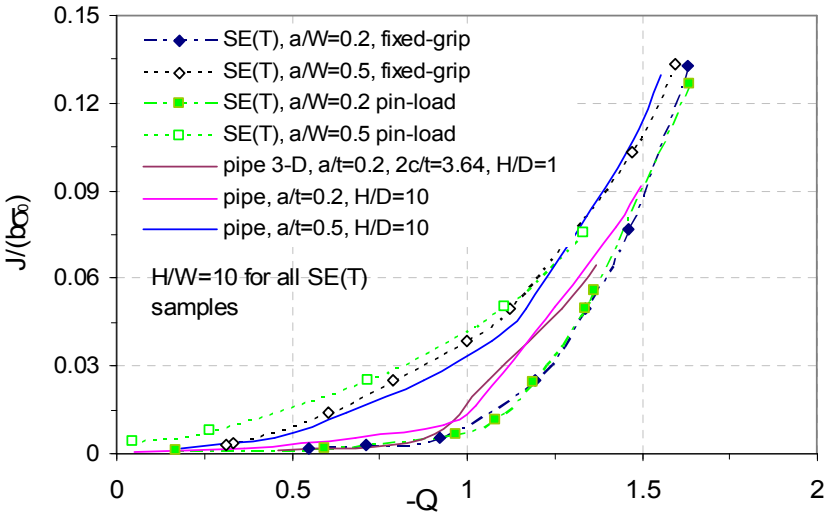


Fig. 4 J - Q relations for pipe and SE(T) samples [3]

The test procedure involves loading the specimen by "fixed grips" as shown in Fig. 5 [1] to restrain bending of the specimen, and the load and crack mouth opening are recorded. Equations for J and compliance have been developed by FEA and have been reported in [1] and [2]. Crack length is measured by unloading compliance [4], and CTOD is obtained using relations between CTOD and J developed by FEA [5]. Side grooves are employed to approximate plane strain conditions and to

promote straight-fronted crack growth; it has been found by trial and error that a total side-groove depth of 15% (7.5% each side) and root radius of 0.5 mm gives adequate crack-front straightness. All specimens in this work were pre-cracked in fatigue.

Results

The test procedure has been applied to homogeneous specimens of various sizes and at temperatures down to -40˚C. Welds have also been tested, although work remains to be done on detailed aspects such as verification that the crack tip samples the desired microstructure and allowable deviation of the crack path.

The unloading compliance method has proven convenient and reliable for measurement of crack size. As shown in Fig. 6, both initial and final crack sizes can be measured to good accuracy.

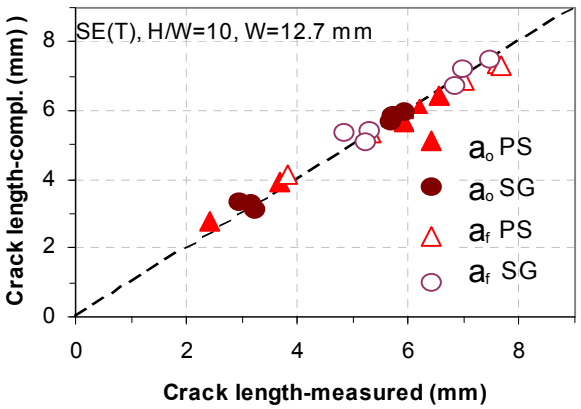


Fig. 6 Crack size for clamped SE(T) specimens. a_o, a_f : initial and final crack size (SG: side-grooved, PS: plain-sided) [2]

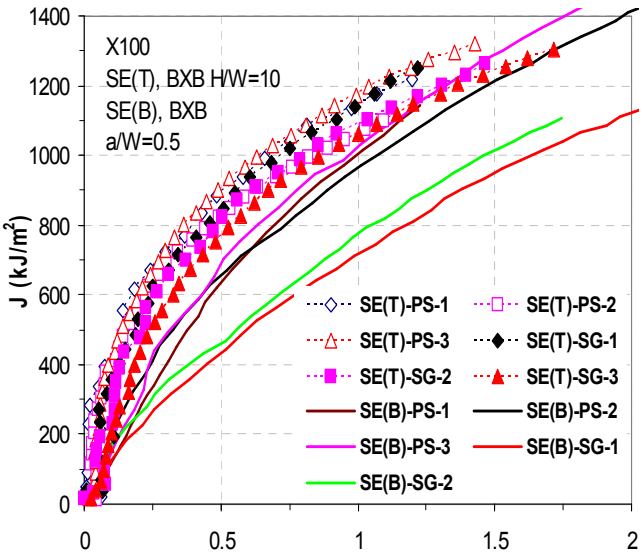


Fig. 7 J-R curves measured using SE(T) and SE(B) specimens, a/W=0.5 [2]

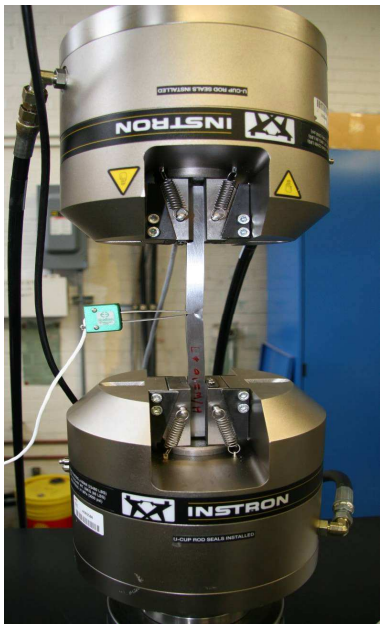


Fig. 5 SE(T) specimen under load [1]

Some typical J-R curves are shown in Fig. 7 [2]. This figure shows results for specimens with a/W=0.5, both SE(T) and SE(B), plain-sided (PS) and side-grooved (SG). Reproducibility is good. The effect of the side grooves is to lower the R curves (although the side grooves in this case were only 10% of thickness (total of both sides) for SE(T); the preferred side-groove depth of 15% would give a greater reduction in resistance. The side-groove depth was 20% for the SE(B) specimens, and it is clear in Fig. 7 that this lowered the R curves more than was the case for SE(T) specimens. The principal observation from Fig. 7 is that the effect of the lower constraint in the SE(T) specimens is to significantly raise the R curves. The increase in this case is as much as a factor of two, although typically somewhat smaller than this. Subsequent work has supported this conclusion.

Results of tests at lower temperatures have shown that the resistance curves were somewhat higher at lower temperatures (corresponding to higher yield stresses), although the increase was not large.

Summary

A procedure has been developed at CANMET to enable measurement of resistance (R) curves in a low-constraint SE(T) geometry. The objective of the work was to provide R curves for use in assessing flaws in pipe girth welds, and the specimen geometry was chosen to give good constraint matching for this application. The unloading compliance method has been shown to enable accurate monitoring of crack length, and equations have been developed to estimate J and CTOD from measurements of the load and crack-mouth opening displacement (CMOD). The method has been used to characterize WM and HAZ regions in high-strength steel pipe, and transferability is being assessed by comparison of the results with crack growth measurements in curved wide plates.

Acknowledgments

The work reported here is part of a consolidated program jointly funded by the Canadian federal government Program of Energy Research and Development (PERD), the Pipeline and Hazardous Materials Safety Administration of the U.S. Department of Transportation (DOT), and the Pipeline Research Council International, Inc. (PRCI). The views and conclusions in this paper are those of the authors and should not be interpreted as representing the official policies of any of these organizations. The contributions of research partners from Center for Reliable Energy Systems (CRES), National Institute of Standards and Technology, (NIST), and Lincoln Electric Company, LECO) is acknowledged.

References

[1] G. Shen, J.A. Gianetto and W.R. Tyson, "Development of Procedure for Low-constraint Toughness Testing using a Single-Specimen Technique", MTL 2008-18(TR), Natural Resources Canada, Nov. 2008

[2] G. Shen, J.A. Gianetto and W.R. Tyson, "Measurement of J-R curves using single-specimen technique on clamped SE(T) specimens", Proc. 18th Int. Offshore and Polar Engineering Conf., Osaka, Japan, 21-26 June 2009

[3] G. Shen, R. Bouchard, J.A. Gianetto and W.R. Tyson, "Fracture Toughness Evaluation of High-strength Steel Pipe", PVP2008-61100, Proc. ASME PVP 2008 Conf., Chicago, July 2008

[4] G. Shen and W.R. Tyson, "Crack size evaluation using unloading compliance in single-specimen single-edge-notched tension fracture toughness testing", Jour. of Testing and Evaluation Vol. 37 (4), paper ID JTE102368, ASTM (2009)

[5] G. Shen and W.R. Tyson, "Evaluation of CTOD from J-integral for SE(T) Specimens", Pipeline Technology Conference, Ostend, Belgium, 12-14 October 2009

© (2012) Trans Tech Publications, Switzerland
doi:10.4028/www.scientific.net/KEM.488-489.130

Modelling of Crack Bifurcation in Laminar Ceramics with Large Compressive Stress

Michal Kotoul[1, a], Oldrich Sevecek[1,b] and Tomas Profant[1,c]

[1]Full Institute of Solid Mechanics, Mechatronics and Biomechanics, Faculty of Mechanical Engineering, Brno University of Technology, Technická 2, 616 69, Brno, Czech Republic
[a]kotoul@fme.vutbr.cz, [b]sevecek@seznam.cz, [c]profant@fme.vutbr.cz

Keywords: Laminar Ceramics, Compressive Stress, Crack Bifurcation, Finite Fracture Mechanics

Abstract. Ceramic laminates designed with strong interfaces have shown crack growth resistance (R-curve) behaviour through microstructural design (e.g. grain size, layer composition) and/or due to the presence of compressive residual stresses, acting as a barrier to crack propagation. The goal of the contribution is to model the mechanism of crack bifurcation in laminar ceramics with large compressive stress which still have not been satisfactory explained. Experimental observations of the crack path in the multilayered ceramics tested under several kinds of loading showed crack penetration (i.e. crack propagating normal to the layers followed by crack bifurcation when the crack propagated from the tensile to the compressive layer. Numerical results [1] show that the initiation of crack bifurcation can be explained by the near-tip J-integral, provided that micro-cracks exist near the crack tip. We revisit the problem using the concept of Finite fracture mechanics and the matched asymptotic expansion method in order to evaluate the energy release rate criteria describing the competition of the crack bifurcation and straight crack propagation near behind the bimaterial interface.

Introduction

It is now well recognized that a design of layered ceramic composites provides a promising way for to enhance the strength reliability of ceramic component as well as to improve their fracture toughness by e.g. crack deflection or crack bifurcation. Moreover, expansion coefficients between different layers inevitably generate thermal residual stresses during subsequent cooling of layered ceramics with *strong interfaces*. Compressive residual stresses significantly contribute to toughening effect and resulting R-curve behaviour. The elastic mismatch of the layers induces an additional crack driving force term which also should be taken into account. The apparent R-curve behaviour is usually studied assuming straight crack propagation perpendicularly across layer interfaces. Nevertheless, the propagation of the crack through the layers may occur with an angle different from straight propagation. The compressive stress ensures that crack growth leading to failure in the laminar system is mediated by threshold strength, but, in some cases, it also leads to bifurcation of the propagating crack. Unfortunately, none of the theories regarding the directional growth of a crack in a brittle material such as deviation to maximize the crack tip energy release rate, deviation from the established path when there is a positive T-stress, and cracks that choose the path that gives a zero value of the Mode II stress intensity factor is in agreement with the observed behaviour in the layered composites. For that reasons we have decided to revisit the problem using the concept of Finite fracture mechanics (FFM) [2]. The criterion used in this method can be stated as follows: failure will occur if there is sufficient energy available to allow a finite amount of crack growth denoted as a_p. It tells that the fracture process is thermodynamically possible. This criterion is further combined with the stress criterion assuming that the stress at a distance a_p is equal to the strength σ_f. Such approach is particularly useful in case of general stress concentrators where the singularity exponent differs from ½. This is the case of a crack impinging an interface between elastically mismatched materials.

Model description

FE modelling of a cracked for points bending specimen was carried out assuming that the specimen was fabricated from ATZ/AMZ ceramic laminate. The commercial FE code ANSYS 11.0 has been used. The multilayer consists of nine alternating layers of different thickness, while the total thickness of the laminate body is kept constant (W = 3 mm). All the layers made of the same material, ATZ (alumina with 5% tetragonal zirconia), or AMZ (alumina with 30% monoclinic zirconia), respectively have the

same thickness, so the laminate is well defined by the thicknesses t_{ATZ} and t_{AMZ}, or the total thickness W and the ratio $\lambda = t_{ATZ}/t_{AMZ}$. Table 1 gives the values of the constituent material properties employed in the calculations. Two values of the layer thickness ratio λ =2 and 10 were used in the numerical study.

Table 1: Material properties of the alumina-zirconia layers according to [3]

Property	Units	ATZ	AMZ
Young´s modulus E	GPa	390±5	280±5
Poisson's ratio ν	-	0.22	0.22
Coefficient of thermal expansion α (20-1200°C)	$10^{-6}K^{-1}$	9.8±0.2	8.0±0.2*
Fracture toughness K_{IC}	$MPa.m^{1/2}$	3.2±0.1	2.6±0.1
Strength σ_f	MPa	422±30	90±20

* The low thermal expansion coefficient value is due to the volume increase associated with the $t \rightarrow m$ zirconia phase transformation in the AMZ layers during cooling.

A simplified 2D model of the ceramic laminate specimen with a crack propagating under plane strain conditions has been developed. Prior to any other calculations, thermal residual stresses are induced in the model by simulation of the cooling of the specimen from 1230 C° below the stress-free temperature. Note that this produces a slight discrepancy from the experimental case, since plane strain is used in this calculation and the equal biaxial thermal residua stress in the experimental specimen is not reproduced. Next the displacement U_y =0.05mm is prescribed at the upper surface supports, see Fig. 1. The crack tip impinges the third interface between ATZ layer and AMZ layer, cf. Fig.1. Because the Young modulus of the ATZ layer is greater than the Young modulus of the AMZ layer, see Tab.1, the exponent of the singularity δ is smaller than ½, (the case of a strong singularity).

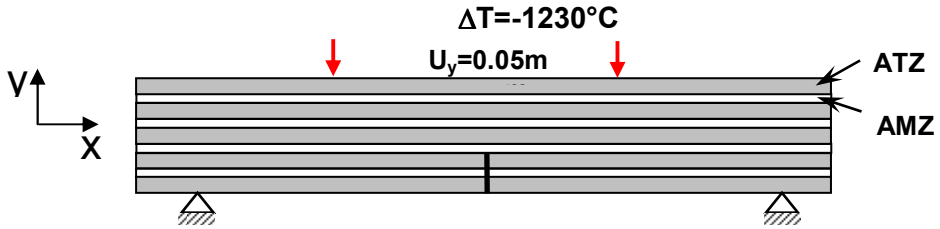


Fig. 1 Scheme of the numerical model of ceramic laminate specimen with 9 layers.

The singular stress field and displacement field are given by

$$\sigma_{ij} = H_1 \cdot r^{\delta_1 - 1} \cdot f_{ij1}(\theta) + H_2 \cdot r^{\delta_2 - 1} \cdot f_{ij2}(\theta), \quad \mathbf{U}^0 = H_1 \cdot r^{\delta_1} . \mathbf{u}_1(\theta) + H_2 \cdot r^{\delta_2} . \mathbf{u}_2(\theta), \tag{1}$$

where H_1 and H_2 are generalized stress intensity factors (GSIF) and δ_1, δ_2 are the corresponding singularity exponents. It can be shown that H_1 is negligible and makes no contribution. GSIF is calculated using the path independent Ψ-integral, see e.g. [4] and the references herein. For the case of residual stresses it requires a modification

$$H = \frac{\int_{\Gamma_2} \left(\sigma^h_{kl\,kl}(\mathbf{U}^0) n_l V^{aux}_k - \sigma^{aux}_{kl}(\mathbf{V}) n_l U^h_k \right) ds + \int_D \sigma^{aux}_{kl}(\mathbf{V}) \delta_{kl} \alpha \Delta T \, \mathrm{d}S}{\int_{\Gamma_1} \left(\sigma^s_{kl}(\mathbf{U}^0) n_l V^{aux}_k - \sigma_{kl}(\mathbf{V}^{aux}) n_l U^{0s}_k \right) ds} \tag{2}$$

where superscripts h, aux, and s denote a FEM solution, auxiliary solution, and the singular solution from Eq. (1) with H=1, respectively, Γ_2 is a remote path while Γ_1 is a path shrunk to the crack tip, D is a domain enclosed between the contours Γ_1 and Γ_2. The stress field and the displacement field, calculated by FEM at the distance R=0.0214 mm from the crack tip using a very fine mesh, was compared with the

analytical singular field (1) making use of the calculated value of GSIF from Eq. (2). A very good agreement can be observed except of the stress components σ_{xx} and σ_{yy}, where singular solution and total FEM solution are mutually shifted by a constant value. In the case of the stress component σ_{xx} this shift is attributed to the negative residual stresses in the AMZ layer, while in the case of the stress component σ_{yy} the shift is attributed to the combination of T-stress and residual stresses. A very important conclusion is that the constant stress term σ_{yy} in the asymptotic expansion is negative and thus cannot explain the crack bifurcation as it is often done.

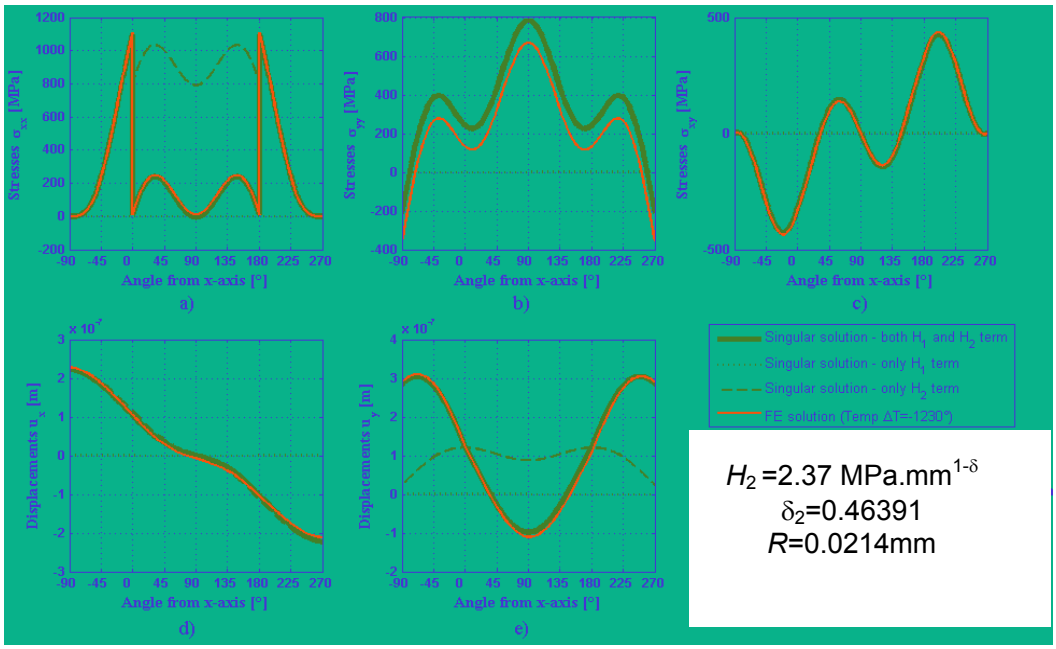


Fig. 2. Comparison of FE solution and the analytical singular field on the circular path of the radius R=0.0214 mm.

Matched asymptotic procedure see e.g. [4] is used to derive the change of potential energy due to the perturbation caused by a branched crack extension of the total length a_p or a straight penetrating crack extension of length a_p, The small perturbation parameter ε is defined as $\varepsilon=a_p/W<<1$. A second scale to the problem can be introduced, represented by the scaled-up coordinates $(y_1,y_2)=(x_1/\varepsilon,x_2/\varepsilon)$ which provides a zoomed-in view into the region surrounding the crack, see Fig.3. The change of the potential energy δW between the unperturbed state $\mathbf{U}^0$ (without the crack extension) and perturbed state $\mathbf{U}^\varepsilon$ (with the small finite crack extension) is given by the relation

$$\delta\Pi=\Pi^0-\Pi^\varepsilon=H_2^2K_{2p}(\varphi_p)\varepsilon^{2\delta_2}+\sigma_r\cos^2\varphi_pH_2\varepsilon^{1+\delta_2}\int_0^{1/2}\mathcal{V}_{2y_1'}(y')dy_2'-\frac{1}{2}\sigma_r\sin 2\varphi_pH_2\varepsilon^{1+\delta_2}\int_0^{1/2}\mathcal{V}_{2y_2'}(y')dy_2', \quad (3)$$

for a single deflected crack extension, similar results holds for branched crack. σ_r stands for resiudal stress ≅ 750 MPa (see also Fig. 1a). The factor $K_{2p}(\varphi_p)$ and the opening of the crack extension $\mathcal{V}_{2y_1'}(y')$ $\mathcal{V}_{2y_2'}(y')$ are calculated by FEM on the inner domain once for all, since they depend only on the local geometry and material properties.

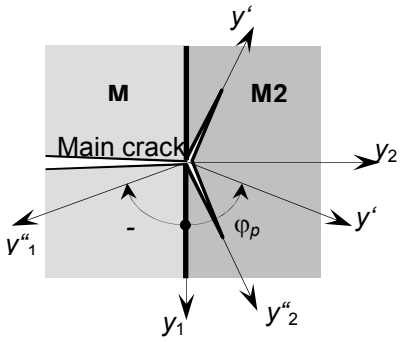


Fig. 3 Scheme of the crack bifurcation and local coordinate systems in the inner domain.

Critical length of the crack extension is found from energetic and stress conditions mentioned in the Introduction:

$$G_p = \frac{\delta\Pi\left(\varphi_p, H_2, \varepsilon\right)}{\varepsilon W} \geq G_c^{(2)},\ \sigma_c^{(2)} \leq H_2 \left(\varepsilon W\right)^{\delta_2 - 1} f_{11}^{(2)}\left(\varphi_p\right) + \sigma_r \cos^2\left(\varphi_p\right) \tag{4}$$

and the branching angle is found from the condition $\partial\Pi\left(\varphi_p\right)/\partial\varphi_p = 0$. The results of $G_p(\varphi_p)$ are shown in Figs. 4 and 5. The predicted angle of crack branching and/or single deflection is in good accord with experimental observation.

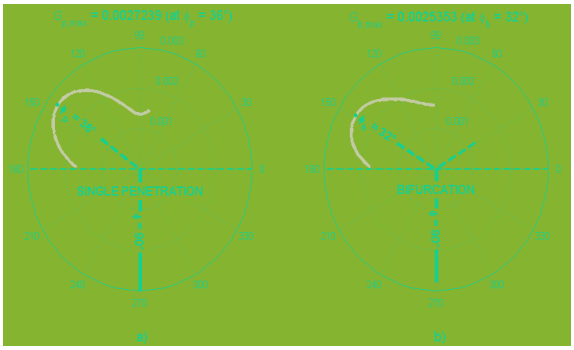


Fig. 4 Variation of the ERR G_p with the angle of crack extension for the ratio $\lambda = t_{ATZ}/t_{AMZ} = 2$. a) single crack deflection, b) crack bifurcation.

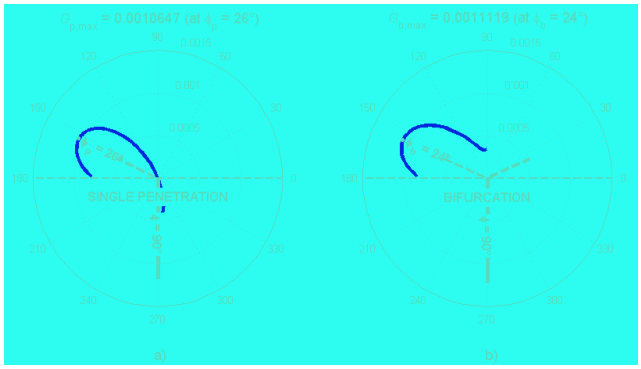


Fig. 5 Variation of the ERR G_p with the angle of crack extension for the ratio $\lambda = t_{ATZ}/t_{AMZ} = 10$. a) single crack deflection, b) crack bifurcation.

Summary

The application of FFM combined with the stress criterion explains the crack path in investigated ceramic composites without making any other assumptions concerning e.g. the presence of microcracks.

Acknowledgment

The authors gratefully acknowledge a financial support of the Czech Science Foundation under the Projects No. 101/09/1821

References

[1] Chen, C.R. et al.: Eng. Frac. Mech. 77 (2010), p.2567.

[2] Taylor, D.:*The Theory of Critical Distances* (Elsevier, UK 2007)

[3] Bermejo R, et al.: Compos. Sci. Technik, 67 (2007), p. 1930.

[4] Kotoul, M.; Ševeček, O.; Profant, T.: Eng. Fract. Mechanics, 77 (2009), p.229.

© (2012) Trans Tech Publications, Switzerland
doi:10.4028/www.scientific.net/KEM.488-489.134

Finite Element Analysis of Composite Flywheel with Two-layer Pre-stressed Rotor Structure

Ren Zheng-yi[1,a], Liu Jing-na[2,b], Li Qing-fen[2], Li Ke-fei[2]

[1]Engineering Training Center, Harbin Engineering University, Harbin 150001, China

[2]College of Mechanical and Electrical Engineering, Harbin Engineering University, Harbin 150001, China

[a]zyren8005@vip.sina.com, [b]liujingna2003@163.com

Keywords: composite flywheel; pre-stressed rotor; finite element method; stress distribution

Abstract. In this paper, considering the material properties of the composite flywheel and the characteristics of the pre-stressed structure, stresses and strains induced by rotor rotation and interference fit were calculated by finite element (FE) method based on the plane stress hypothesis, in the commercial software ANSYS. Based on the given material properties and the main dimension with a certain speed of rotation, three 2D FE-models of hybrid composite flywheel rotors with two-layer rotor structure were built with the unit property of plane stress, axisymmetric and plane strain respectively. Followed, the radial stress, circumferential stress and radial displacement of the rotor were obtained. The three simulation results are almost accordant with the present theoretical results. It shows that the numerical analyses are reliable. It can be shown that is advisable to design and optimize the flywheel rotor.

Introduction

Flywheel energy-storage is a novel energy storage device which can realize energy conversion between mechanical energy and electric energy .It has many advantages including high energy storage，high power, no pollution，high storage efficiency, wide application，noise free，long cycle life，and so on[1]. Energy-storage flywheel rotors are preferably made from high-strength and low-density fiber-reinforced polymer composites which can greatly enhance storage efficiency in the kinetic energy per unit mass.

The composite flywheels consist of the single ring structure and multi-ring structure. The multi-ring flywheel adopts the pre-stressed structure with multi-ring interference fit. And the strength analysis of the rotor is the base of the rotor structure design. Currently, the methods of strength analysis include analytical method based on plane stress /plane strain hypothesis and finite element method. The stress distribution analytical method of the composite rotor has been discussed in detail by a lot of literatures. Recently, the representative ones are that S.M Arnold [2] and Sung. Kyu. Ha [3] has worked on the theoretical analysis of the single and multi-ring composite rotors with interference.. The finite element method has been more widely used in the actual structure design of the rotor.

In this paper the introduction of the analytical method based on plane stress hypothesis is given firstly, and the finite element method is carried out in the commercial software ANSYS.

Flywheel Rotor Stress Analysis

The stresses and deformations of a rotating disk having constant thickness and an inner radius *a* and outer radius *b,* can be obtained from 3-dimensional equilibrium equations for a continuum that are formulated based on the principle of conservation of linear momentum (i.e. Newton's second law of motion). The equations are expressed in cylindrical coordinates as [4]:

$$\frac{\partial \sigma_r}{\partial r}+\frac{1}{r}\frac{\partial \tau_{r\theta}}{\partial \theta}+\frac{\partial \tau_{rz}}{\partial z}+\frac{\sigma_r-\sigma_\theta}{r}+F_r=0 \tag{1}$$

$$\frac{\partial \tau_{r\theta}}{\partial r}+\frac{1}{r}\frac{\partial \tau_{\theta}}{\partial \theta}+\frac{\partial \tau_{\theta z}}{\partial z}+\frac{2\tau_{r\theta}}{r}+F_\theta=0 \tag{2}$$

$$\frac{\partial \tau_{rz}}{\partial r}+\frac{1}{r}\frac{\partial \tau_{\theta z}}{\partial \theta}+\frac{\partial \tau_{z}}{\partial z}+\frac{\tau_{rz}}{r}+F_z=0 \tag{3}$$

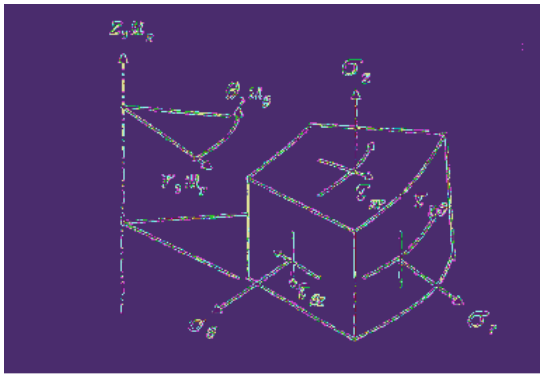


Figure 1.Stresses and displacements for a stress element in cylindrical coordinates.

Stress components on planes normal to the cylindrical coordinates were previously shown in Figure.1. They are designated, correspondingly, $\sigma_r,\sigma_\theta,\sigma_z,\tau_{r\theta},\tau_{rz}$, and $\tau_{\theta z}$ .In the above equations, F_r,F_θ,F_z are body forces for a unit volume in the cylindrical coordinate directions.

Assuming that the thickness of the rotating disk is small in comparison to its radius, then the variation of radial and circumferential stresses over the thickness can be neglected and $\sigma_z=0$. Due to loading/geometric symmetry Eqs.(1-3) reduce to:

$$\frac{d\sigma_r}{dr}+\frac{\sigma_r-\sigma_\theta}{r}+\rho r\omega^2=0 \tag{4}$$

The physical condition is:

$$\varepsilon_r=\frac{\sigma_r}{E_r}-\frac{v_{\theta r}}{E_\theta}\sigma_\theta \quad ,\varepsilon_\theta=\frac{\sigma_\theta}{E_\theta}-\frac{v_{r\theta}}{E_r}\sigma_r \tag{5}$$

The geometric condition is:

$$\varepsilon_\theta=\frac{u_r}{r} \quad ,\varepsilon_r=\frac{\partial u_r}{\partial r} \tag{6}$$

Based on the Eqs.(5-6) ,the Eqs (4) is replaced by Eqs (7)：

$$E_r r^2\frac{d^2u}{dr^2}+E_r r\frac{du}{dr}-E_\theta u=-\rho\omega^2 r^3\left(1-v_{r\theta}v_{\theta r}\right) \tag{7}$$

The radial and circumferential stresses are therefore:

$$\begin{aligned}\sigma_r&=\frac{3+v_{\theta r}}{9-K^2}\rho V_1^2\left[\frac{1-m^{3+K}}{1-m^{2K}}\left(\frac{r}{R_0}\right)^{K-1}-\frac{m^{2K}-m^{3+K}}{1-m^{2K}}\left(\frac{r}{R_0}\right)^{-K-1}-\left(\frac{r}{R_0}\right)^2\right]\\ \sigma_\theta&=\frac{3+v_{\theta r}}{9-K^2}\rho V_1^2\left[K\cdot\frac{1-m^{3+K}}{1-m^{2K}}\left(\frac{r}{R_0}\right)^{K-1}+K\cdot\frac{m^{2K}-m^{3+K}}{1-m^{2K}}\left(\frac{r}{R_0}\right)^{-K-1}-\frac{K^2+3v_{\theta r}}{3+3v_{\theta r}}\left(\frac{r}{R_0}\right)^2\right]\end{aligned} \tag{8}$$

But Eqs.(8) is only radial and circumferential stresses for the single layer. The radial and circumferential stresses of composite flywheel with the mult-layers are not be easily carried out.So in the next section of this paper, based on the given material properties and the main dimension with a certain speed of rotation, three 2D FE-models of hybrid composite flywheel rotors with two-layer rotor structure were built with the unit property of plane stress, axisymmetric and plane strain respectively.

Finite Element Analysis of Composite Flywheel

Because a 3-dimensional model requires decisively more computational resources, 2-dimensional model has been adopted in this paper. Based on the given dimension shown in Table1, three 2-dimensional finite element models with two-layer rotor structure were built with the unit property of plane stress, axisymmetric and plane strain respectively using PLANE 183 for the composite flywheel rotor.

Table 1 The physical dimension of the composite flywheel

Items		E-Glass/epoxy layer	Carbon/epoxy layer
ANSYS model of the plane stress /plane strain	Inner radius/mm	130	160
	Outer radius/mm	160	190
	Magnitude of interference/mm	0.2	
ANSYS axisymmetric	Axial dimension/mm	30	30

According to the composite material is anisotropic and the different coordinate system will be used, so material properties must be adjusted to be fit for the analysis of the plane stress model, plane strain model and axisymmetric model . Cartesian coordinate is used in the axisymmetric analysis: z is the fiber direction, x is radial direction and y is the axial direction. Cylindrical coordinate is used in the plane stress/ strain analysis: x is the radial direction, y is fiber direction and z is the axial direction. According to the definition of major and minor Poisson coefficient in ANSYS, composite material properties have the following transformation shown in the Table 2 :

Table 2 The material property transformation of the composite flywheel

	Items	ANSYS plane stress /plane strain	ANSYS axisymmetric
E-Glass /epoxy	Young'smodulus:	$E_{xy}=20\text{Gpa}, E_{yz}=70\text{Gpa}, E_{xz}=20Gpa$	$E_{xy}=20\text{Gpa}, E_{yz}=20\text{Gpa}, E_{xz}=70\text{Gpa}$
	Poisson's ratio	$\upsilon_{xy}=0.28, \upsilon_{yz}=0.08, \upsilon_{xz}=0.3$	$\upsilon_{xy}=0.3, \upsilon_{yz}=0.28, \upsilon_{xz}=0.28$
Carbon /epoxy	Young'smodulus:	$E_{xy}=10\text{Gpa}, E_{yz}=155\text{Gpa}, E_{xz}=10Gpa$	$E_{xy}=10\text{Gpa}, E_{yz}=10\text{Gpa}, E_{xz}=155Gpa$
	Poisson's ratio	$\upsilon_{xy}=0.25, \upsilon_{yz}=0.016129, \upsilon_{xz}=0.3$	$\upsilon_{xy}=0.3, \upsilon_{yz}=0.25, \upsilon_{xz}=0.25$

In view of the model with the unit property of plane stress and plane strain respectively have been only built a quarter of the model shown in Figure.2, the corresponding symmetry boundary conditions must be imposed on the corresponding side and the axial displacement restraint is imposed in the inner side of the E-Glass/epoxy layer. In view of the model with the unit property of axisymmetric, the displacement constraint of axial direction is imposed on bottom side of two layers shown in Figure.3 .

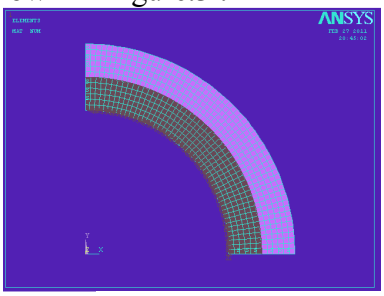
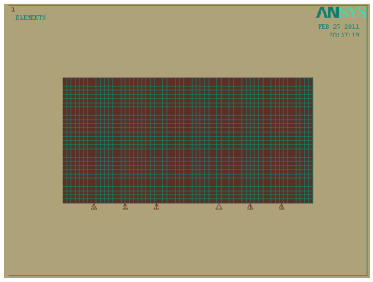


Figure 2. Plane stress/ strain model


Figure3. Axisymmetric model

There are two ways to set the magnitude of interference in ANSYS, one is to set the 0FFSET in the KEYOPT options of the unit; the other is to build the finite element model directly with the geometrical interference, and the stress distribution can be obtained by the contact analysis in the calculation (define as two surfaces which will be contact with the interference fit as the contacting surfaces). In this paper, the second way has been chosen to set the magnitude of interference. When set the contact surface pairs, set KEYOPT (9) = 4 of the contact element, that is to make ANSYS only consider CNOF set value (which is magnitude of interference referred value in the Table 1) in the contact calculations.

All the previously mentioned, numerical solutions obtained from the developed finite element model were validated using analytical stress solutions. For a rotational speed of 2000 RPM, radial stresses along the radial-direction obtained from numerical analysis were shown on in Figure.4-Figure.5.

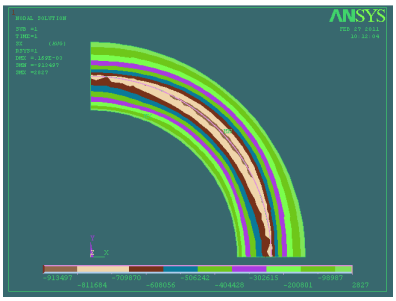


Figure 4. Radial stress calculated by the plane-stress model

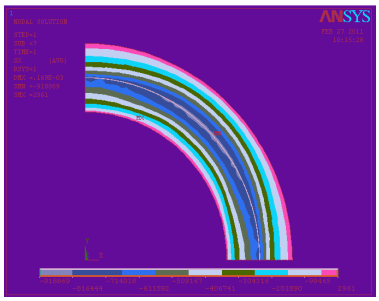


Figure5. Radial stress calculated by the plane-strain model

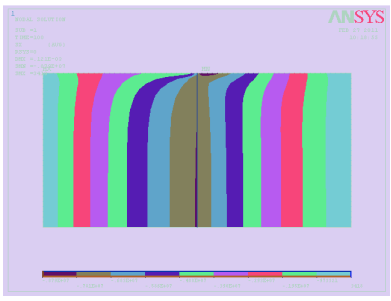


Figure 6. Radial stress calculated by the axisymmetric model.

Comparing the results in Figure.4- Figure.6, although there are same differences in values of the radial stress, the trend of the radial stress with radius is the same, which shows that the results of three models is desirable on certain aspects.The results of the three models are compared in Table 3 at the same time.

Table 3 The stress calculation results of the composite flywheel

Items	ANSYS plane stress	ANSYS plane strain	ANSYS axisymmetric
E-Glass/epoxy layer: radial displacement on the inner side/mm	0.388	0.387	0.316
Carbon/epoxy layer: radial displacement on the outer side/mm	0.169	0.168	0.121
E-Glass/epoxy layer: the maximum of the radial stresses /Mpa	0.918	0.917	8.790
Carbon/epoxy layer: the maximum of the radial stresses /Mpa	0.812	0.811	7.810
E-Glass/epoxy: radial stress on the inner side/Mpa	5.140	5.035	42.90
E-Glass/epoxy: radial stress on the outer side/Mpa	0.350	0.341	32.50
Carbon/epoxy layer: radial stress on the inner side/Mpa	9.271	9.193	51.80
Carbon/epoxy layer: radial stress on the outer side/Mpa	6.072	6.061	40.70
The joint of two layeres : radial stress/Mpa	-0.883	-0.882	-7.890

Compared the results of table 3, we can see all the results of the plane-stress model and plane-strain model are similar,and that are according with the theoretical analysis based on the plane stress.But only the radial displacement of the axisymmetric model is similar with the ones of the the plane-stress model and plane-strain model .And all the trends of the radial stresses with radius are the same shown in Figure.4- Figure.6, which shows the method of the axisymmetric model is not deviated from the theoretical analysis. Through the further analysis and calculation, it will be stated that the result of the 2D axisymmetric model is more accurate. In sum, all the analysis can provide theoretical basis for design and optimization of the flywheel rotor.

References

[1] S.Y. Jiang , H.G Wei, Z.P Sheng , ACTA ENERGIAE SOLAUIS SINICA. Vol. 21(2000) p. 427-433

[2] Arnold, S.M., Saleeb, A.F., and Al-Zoubi, N.R.,Deformation and Life Analysis of Composite Disk and Multi-Disk System, NASA Report NO.TM-2001-210578, Glenn Research Center, Cleveland, OH(2001).

[3] Sung K H, Kim D J, Sung T H.. International Journal of Mechanical Science, Vol. 43(2001), p. 993-1007

[4] Sung K. H., Hee_Moon Jeong ,Young-Soo Cho, , Journal of Composite Materials, Vol. 32(1998), p. 851-873

© (2012) Trans Tech Publications, Switzerland
doi:10.4028/www.scientific.net/KEM.488-489.138

Identification of slant cracks in a cantilever beam using design of experiment and neuro-genetic technique

M. Hajhosseini [a], H. Nahvi [b]

[1]Mechanical Engineering Department, Isfahan University of Technology, Isfahan 8415683111, Iran

[a] Mohammad.hajhosseini@yahoo.com, [b] hnahvi@cc.iut.ac.ir

Keywords: Slant crack, Natural frequency, Full factorial design, Neural network, Genetic algorithm

Abstract. Cracks present a serious threat to the performance of beam-like structures. In this paper, the flexural vibration of a cantilever beam having a slant crack is considered. The beam natural frequencies are obtained for various crack locations, depths and angles, using the finite element method. These natural frequencies and crack specifications are then used to train a neural network. The input of the neural network is the crack specifications and the output is five natural frequencies of the beam. With the trained neural network, genetic algorithm is then used to determine the beam crack specifications by minimizing the differences from the measured frequencies. Simulations are performed to evaluate performance of the neural network. Results show that the proposed scheme can detect slant cracks in cantilever beams with good accuracy.

Introduction

Most of the failures that cause serious damage to the structures can be attributed to cracks. Crack in a structure introduce local flexibility and changes in the stiffness and the dynamic behavior of the structure [1]. Many studies have been done on identification of the crack location and depth, using vibration parameters of the structures. The objective of any damage assessment technique is to inquire whether any structural damage, such as the initiation of a crack has occurred, and if so, to determine its specifications. Crack detection based on modal frequency has been a common and widely used approach [2-4]. Most of the studies on crack detection have used system identification, neural networks, fuzzy logic and genetic algorithm to solve the inverse problem of predicting crack specifications from the frequency data of structure [5-8]. Recently, Etemad and Ghaisari [9] used three neural networks separately to detect the location, depth and width of a crack in a shaft.

To identify the location, depth and angle of a slant crack in a cantilever beam, a method is presented where the beam natural frequencies, full factorial design method and a neuro- genetic technique are used. A two-layer neural network is designed and trained to estimate crack specifications. In the literature, very few researches have addressed the identification of slant cracks that plays an important role when a twisting moment is applied to a beam or a shaft. The detection of slant cracks in a cantilever beam is particularly studied in this paper.

Structural model

The cantilever beam shown in Fig. 1 has a length of 300 *mm*, and a rectangular cross-section of 20×20 mm^2. It contains a slant crack of depth D at a distance L from the clamped end, measured at the top side of the beam. Also in this figure α is the crack angle measured from the transverse plane. The material properties are E = 2.06×10^5 *Mpa* and ρ = 7850 $kg\,m^{-3}$.

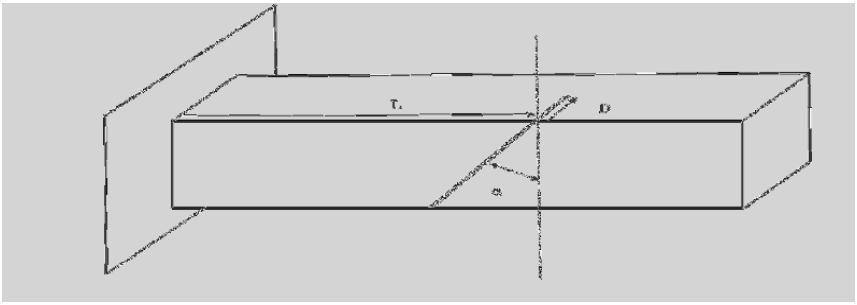


Fig. 1. A cantilever beam with a crack.

Design of experiment method (Full factorial design)

To train the neural network, many actual sets of input-output data are required. The actual data are obtained using the finite element method via Ansys software for a number of cracks with different specifications. To determine different specifications of the crack, full factorial design is employed. The full factorial design is a comprehensive method which considers the effects of original factors. By using the full factorial design, eight crack locations at L = 40, 68, 97, 124, 170, 200, 232, 260 *mm*, five crack depths at D = 0, 2, 6, 10, 14 *mm*, and six crack angles, α = 0, 11, 22, 34, 46, 60 degrees are considered for this study. Totally 240 sets of data are examined to obtain 5 natural frequencies of the cracked beam, including the first 3 natural frequencies (f_1 , f_2 , f_3), the 5th and 11th natural frequencies (f_5 , f_{11}). The 5th and 11th natural frequencies which relate to the beam twisting mode shapes are mostly influenced by the crack angle. The variations of f_5 and f_{11} with the crack angle are shown in Figs. 2 and 3, respectively, for a crack at L = 68 *mm* with different depths. It can be seen that at lower depth and angle values, f_5 and f_{11} are less sensitive to the crack angle.

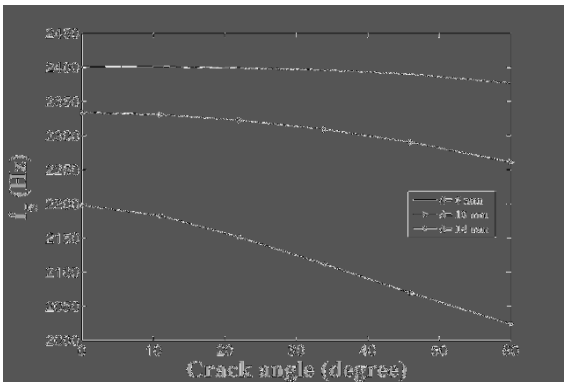


Fig. 2. Variations of f_5 with crack angle.

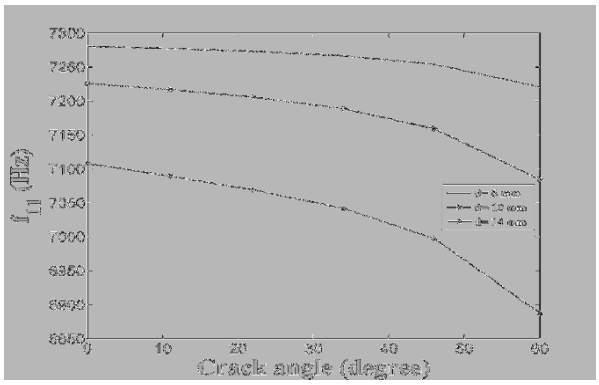


Fig. 3. Variations of f_{11} with crack angle.

Proposed neural network

In this study, the neural network is used to find a relation between the specifications of the crack and the beam natural frequencies. To train the neural network, the crack specifications and the five natural frequencies of the beam are selected as the network inputs and outputs, respectively. The proposed back-propagation network which is a multi-layer feed-forward neural network with one hidden layer is shown in Fig. 4. The feed-forward back propagation network consists of the input, the hidden, and the output layers. The hyperbolic tangent sigmoid activation function and the linear activation function are used for the hidden and output layers, respectively. The hyperbolic tangent sigmoid function can estimate a linear and a nonlinear relation between the inputs and outputs. The linear activation function can give the outputs in the range of −1 to 1.

Ansys software provides natural frequencies of the beam with given crack's specifications including the location, depth and angle. These actual data are used for training the proposed network. Table 1 presents some of the actual data obtained using Ansys. The trained network is then tested by new data to check its accuracy. Figs. 5-7 show the accuracy of the proposed neural networks in estimating the beam natural frequencies.

Table 1. Actual data obtained using Ansys software.

L (mm)	D (mm)	α (deg)	f_1 (Hz)	f_2 (Hz)	f_3 (Hz)	f_5 (Hz)	f_{11} (Hz)
40	10	46	153.41	172.40	1070.0	2295.0	7009.70
97	6	60	179.16	181.72	1125.40	2380.70	7288.70
124	10	46	172.26	179.95	1052.30	2322.70	7285.80
232	14	0	182.16	183.76	922.88	2077.80	6537.40

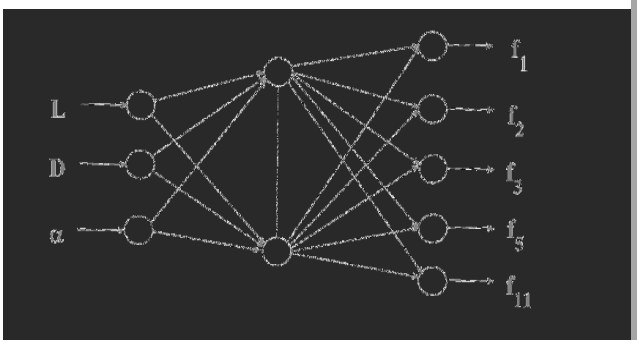


Fig. 4. Proposed two-layer neural networks.

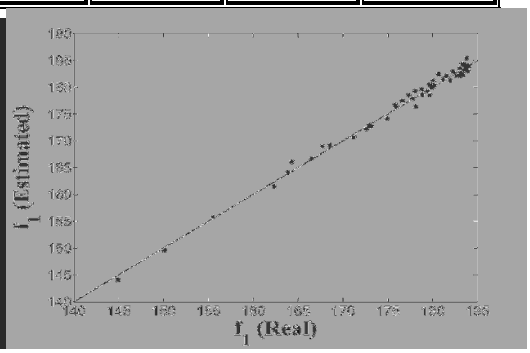


Fig. 5. Trained network for f_1 (Hz).

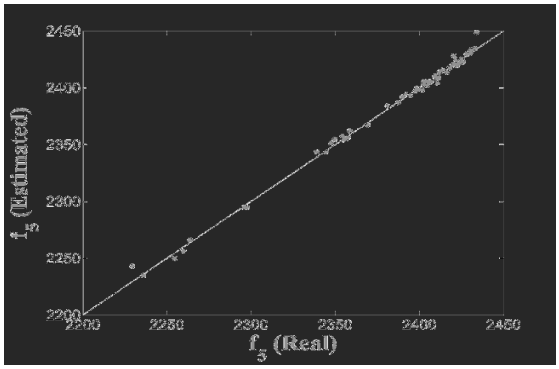


Fig. 6. Trained network for f_5 (Hz).

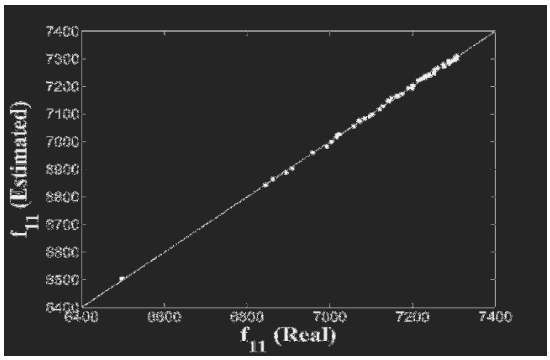


Fig. 7. Trained network for f_{11} (Hz).

Genetic algorithm

Genetic algorithm, a probabilistic optimization scheme based on the model of natural evolution, has demonstrated its capability to create good approximate solutions in complex optimization problems [7]. In this study, the fitness function which is minimized by the genetic algorithm is described as

$$F = \sqrt{(f_1 - f_1^*)^2 + (f_2 - f_2^*)^2 + (f_3 - f_3^*)^2 + (f_5 - f_5^*)^2 + (f_{11} - f_{11}^*)^2} \quad (1)$$

where f^*_1, f^*_2, f^*_3, f^*_5, f^*_{11} are five reference natural frequencies. Through several test problems, the genetic algorithm is set-up with: population size, N = 100; crossover rate, C = 0.25; mutation rate, M =0.01. Table 2 shows a sample of the results including the location, depth and crack angle that are estimated by the neuro-genetic algorithm. These results are compared with their actual ones and relative errors are computed. It can be seen that at lower depth and angle values, the relative errors are higher which is due to the less sensitivity of the frequencies f_5 and f_{11} to the crack angle.

Table 2. Crack identification results.

Actual calculated value			Neuro-Genetic technique value			Relative Error (%)		
Location (mm)	Depth (mm)	Angle (degree)	Location (mm)	Depth (mm)	Angle (degree)	Location	Depth	Angle
50	4	30	45.985	3.652	34.873	-8.029	-8.695	16.246
70	7	17	71.249	7.201	15.454	1.785	2.882	-9.091
83	9	20	82.338	9.123	19.573	-.796	1.373	-2.131
100	10	45	103.444	9.622	48.674	3.444	-3.771	8.165
164	14	60	165.944	13.911	59.860	1.185	-.635	-.232
230	7	45	234.114	7.441	45.982	1.788	6.301	2.183
245	9	20	240.981	8.747	18.768	-1.640	-2.806	-6.158

Conclusion

A neuro-genetic technique is introduced and implemented to identify the crack location, depth and angle in a cantilever beam from the natural frequencies. In addition to the first 3 frequencies, the 5^{th} and 11^{th} frequencies which are more sensitive to the crack angle are used to train the neural networks. The neural network is used to find natural frequencies as a function of the crack parameters and also the genetic algorithm is employed to find crack parameters that minimizes the difference between the obtained frequencies and the reference ones. Simulations are carried out to evaluate the performance of the neural networks. Results show that the crack specifications are estimated with good accuracy. However, at low depth and angle values the error is higher. This is due to the fact that in these cases f_5 and f_{11} are not so sensitive to the variations of the crack angle.

References

[1] A. Anifantis, P. Rizos and A.D. Dimarogonas: Identification of cracks on beams by vibration analysis, Proceedings of 11^{th} Biennial ASME Conf. on Mech. Vib. and Noise (1987), Boston.

[2] G.M. Owolabi, A.S.J. Swanidas and R. Seshadri: Crack detection in beams using changes in frequencies and amplitudes of frequency response function, J. S. Vib., Vol. 265 (2003), p. 1-22.

[3] F. Leonard, J. Lanteigne, S. Lalonde and Y. Thrcottey: Free vibration behavior of a cracked beam and crack detection, Mech. Syst. Signal Process., Vol. 15 (2001), p. 529-48.

[4] H. Nahvi and M. Jabbari: Crack detection in beams using experimental modal data and finite element model, International Journal of Mechanical Sciences, Vol. 47 (2005), p. 1477-1497.

[5] J.P. Sawyer and S.S. Rao: Structural damage detection and identification using fuzzy logic, AIAA J., Vol. 38 (2000), p. 2328-2335.

[6] K.M. Saridakis, A.C. Chasalevris, A.J. Dentsoras and C.A. Papadopoulos: Applying neural networks, genetic algorithms and fuzzy logic for the identification of cracks in shafts by using coupled response measurements, Computers and Structures, Vol. 86 (2008), p.1318-1338.

[7] M.W. Suh, M.B. Shim and M.Y. Kim: Crack Identification using hybrid neuro – genetic technique, Journal of Sound and vibration, Vol. 238 (2000), p.617-635.

[8] S. Suresh, S. Omkar, R. Ganguli and V. Mani: Identification of crack location and depth in a beam using modular neural network approach, Smart Mat. and Stru., Vol. 13 (2004), p. 907-15.

[9] S.A. Etemad and J. Ghaisari: Estimating shaft crack specifications using shaft vibration analysis and neural networks, IEEE Int. Conference on Testing and Diagnosis, China (2009), p. 1-5.

© (2012) Trans Tech Publications, Switzerland
doi:10.4028/www.scientific.net/KEM.488-489.142

Non-linear behaviour of base-isolated building supported on flexible soil under damaging earthquakes

Sayed Mahmoud[1,a], Per-Erik Austrell[1,b] and Robert Jankowski[2,c]

[1]Department of Construction Sciences, Division of Structural Mechanics, Lund University, Lund, Sweden

[2]Faculty of Civil and Environmental Engineering, Gdansk University of Technology, ul. Narutowicza 11/12, 80-233 Gdansk, Poland

[a]elseedy@hotmail.com, [b]Per_Erik.Austrell@construction.lth.se, [c]jankowr@pg.gda.pl

Keywords: Non-linear analysis, seismic isolation, structural damage, soil-structure interaction, earthquakes.

Abstract. Seismic isolation is a strategy to reduce damage of structures exposed to devastating earthquake excitations. Isolation systems, applied at the base of buildings, lower the fundamental frequency of the structure below the range of dominant frequencies of the ground motion as well as allow to dissipate more energy during structural vibrations. The effectiveness of the base-isolated buildings in damage reduction has been confirmed numerically for the models of structures with fixed supports. The aim of the present paper is to show the results of the non-linear analysis of the response of a base-isolated building supported on soft soil incorporating soil-structure interaction. The detailed study has been conducted for the building equipped with high damping rubber bearings used as isolation devices. The results of numerical simulations demonstrate that soil flexibility has a significant influence on the behaviour of isolated base of the structure. Considering the flexibility of soil significantly affects the rigid superstructure response lowering its potential to reduce structural damage.

Introduction

Seismic isolation is considered to be an effective strategy to reduce damage in structures during earthquakes [1]. Isolation systems are generally effective due to their flexibility and energy dissipation characteristics. Flexibility in the horizontal direction will lower the fundamental frequency of the building below the range of frequencies which dominate general earthquake input. Providing means of energy dissipation reduce the seismic energy transmitted to the system.

The seismic design of isolated structures is often based on the rigid base assumption and soil-structure interaction (SSI) is ignored [1]. Ignoring the SSI effects may lead to incorrect structural response assessment. Two general methods are available for rationally incorporating SSI effects into structural analysis [2]. The first one is a direct method, in which the structure and a portion of the base soil are both incorporated into a finite element mesh. In the second method, known as a substructure method, the structure and the soil are analyzed separately. A simplified model, which is typically composed of one or more springs or spring-damper combinations to approximate the behaviour of the soil, is coupled with the structural model at its base. The most common analytical model is the one in which the soil domain is considered to be a homogeneous elastic half-space.

Quite extensive research work has been conducted in order to investigate the impact of considering SSI effects on the response of isolated bridges (see [3] for example). However, very limited research works have been carried out for the response of seismically isolated buildings with SSI effects. The aim of this paper is to evaluate the influence of the base isolation together with SSI effects on the structural response of buildings during ground motions. A large number of

simulations, using single degree-of-freedom (SDOF) systems subjected to three damaging earthquakes with different peak ground accelerations (PGA), have been first performed. Then, the sensitivity of the response has been investigated for a variety of soil properties so as to investigate the effectiveness in reduction of structural damage in the case of different soil conditions.

Numerical model

Fig. 1 shows the idealized SDOF mathematical model of the isolated one-storey building of height h_1. A rigid floor of mass m_1 is connected to a rigid mat of mass m_b through massless columns of stiffness k_1 and damping c_1. The dynamic equation of motion for the superstructure and the base of the isolated system, incorporating the horizontal and rotation motions of the soil at the structure's base can be written as:

$$\mathbf{M}\ddot{\mathbf{U}} + \mathbf{C}\dot{\mathbf{U}} + \mathbf{K}\mathbf{U} + \mathbf{F_b} = -\mathbf{M}\ddot{\mathbf{U}}_\mathbf{g} \tag{1}$$

where $\mathbf{M}, \mathbf{C}$ and $\mathbf{K}$ is the mass, damping and stiffness matrix, respectively; $\ddot{\mathbf{U}}$, $\dot{\mathbf{U}}$, and $\mathbf{U}$ represent the acceleration, velocity and displacement vectors, respectively; $\ddot{\mathbf{U}}_\mathbf{g}$ is the ground acceleration vector and $\mathbf{F_b}$ denotes vector containing the forces mobilized in the isolation bearing.

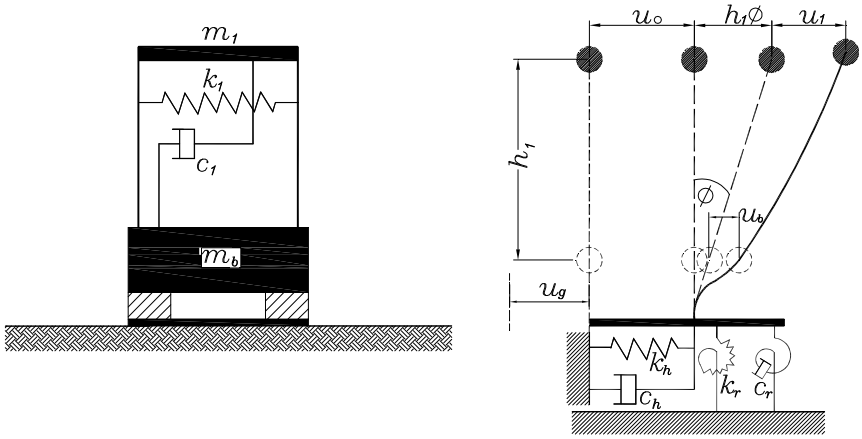


Fig. 1. Idealized SDOF mathematical model

High damping rubber bearings (HDRB) are used in the present study for the isolation devices. In order to simulate the behaviour of HDRB, a non-linear strain rate dependent model (see [4]) is applied. The model describes the behaviour of the bearing by a non-linear elastic spring-dashpot element with stiffness k_b and damping c_b defined as [4]:

$$k_b = a_1 + a_2(u_b)^2 + a_3(u_b)^4 + \frac{a_4}{\cosh^2(a_5\dot{u}_b)} + \frac{a_6}{\cosh(a_7\dot{u}_b)\cosh(a_8u_b)},\ c_b = \frac{a_9 + a_{10}(u_b)^2}{\sqrt{a_{11}^2 + (\dot{u}_b)^2}} \tag{2}$$

where u_b, $\dot{u}_b$ are actual displacement and velocity of the isolated base and $a_1 - a_{11}$ are parameters of the model obtained by fitting the experimental data using the method of the least squares.

The building model is assumed to rest on a half-space elastic flexible soil with no slippage between the base and the soil. The soil flexibility allows for horizontal translation and rocking at the structural base (see [5] for details). The building superstructure fundamental period, damping ratio and mass are: $T_n = 1\,\text{s}$, $\xi = 0.05$ and $m_1 = 30\times10^3$ kg. The storey height is $h = 3.5$ m. The base mass is $m_b = 90\times10^3$ kg. The soil mass density and Poisson's ratio are: $\gamma = 1.89\times10^3$ kg/m^3 and $\nu = 0.3$. The shear wave velocity is given by $V_s = 196$ m/sec. The radii of equivalent circular foundation for swaying and rocking have been estimated to be of equal values $r_h = r_r = 4$ m [6].

Response analysis

Extensive non-linear numerical simulations have been conducted in order to investigate the influence of soil flexibility on the response of base-isolated buildings having different natural periods. The analyses have been carried out under the El Centro earthquake (18.05.1940, PGA=0.34*g*), the N. Palm Springs earthquake (08.07.1986, PGA=0.59*g*) and the Chi-Chi (Taiwan) earthquake (20.09.1999, PGA=1.13*g*). The representative results for one sandy soil type with different shear wave velocities at depth of 15 m are presented in this paper. The Newmark method with $\gamma = 0.5$ and $\beta = 0.25$ has been used to solve the non-linear equation of motion (1).

Fig. 2 shows the peak displacement, velocity and acceleration responses for different natural structural periods with and without SSI effects under different earthquakes. It can be observed from the figure that as the structural period increases, the peak response of the isolated building without SSI effects increases as well. Similar trends can be observed for the system with incorporation of soil flexibility. Moreover, for the ground motion with high PGA (Chi-Chi earthquake) with the increase in the structural natural period a slight increase trend can be observed for the peak response curves with SSI effects and with further increase in the building period, the peak response of the system keeps constant values.

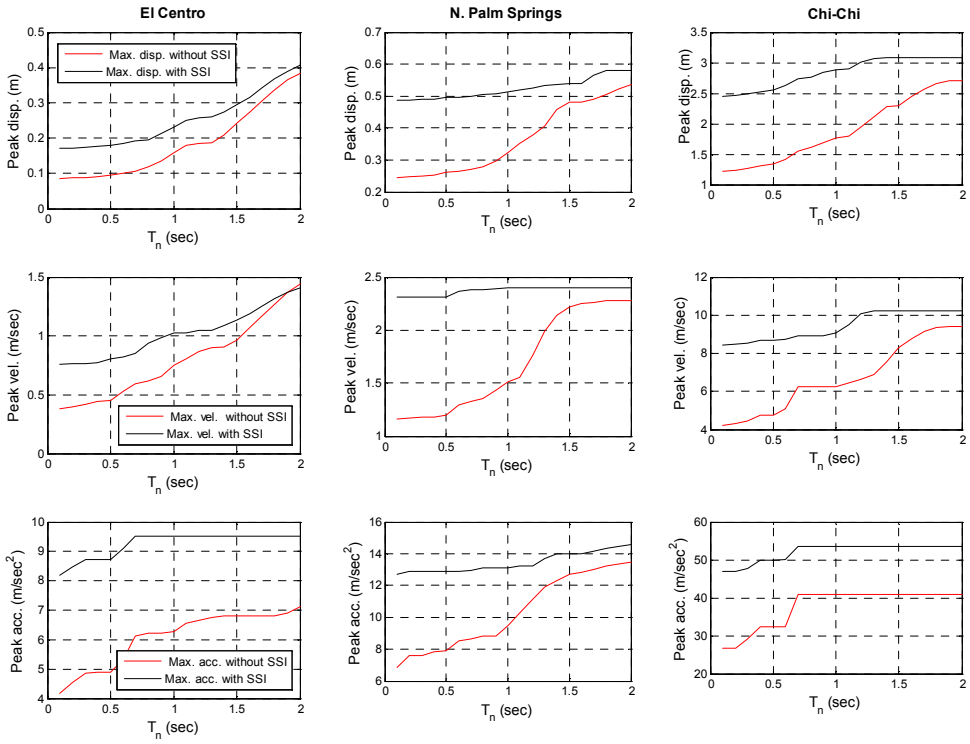


Fig. 2. Peak displacement, velocity and acceleration response for the system with different natural periods with and without SSI effects under different earthquakes

Fig. 3 shows the peak displacement and acceleration amplification factors (AF) for the non-isolated and isolated buildings with respect to the structural natural period under the El Centro earthquake with different shear wave velocities in the soil. It can be seen from the figure that, for the non-isolated building, variations in shear wave velocities significantly change the values obtained for the peak response AF, especially for low structural natural periods. Moreover, as the soil becomes soft, i.e. shear wave velocity decreases, the corresponding peak displacement AF increases, while the peak AF for the acceleration decreases. Fig. 3 also shows that the response of the base-isolated building is not altered by the shear wave velocity variations, although it is highly affected

by the soil flexibility. The simulation results indicate that as the natural period of the building increases the peak displacement and acceleration AF significantly decrease. For all the considered shear wave velocities in the soil, the peak response of the isolated building is uniformly amplified. Similar trends have been observed for other earthquakes considered in the study.

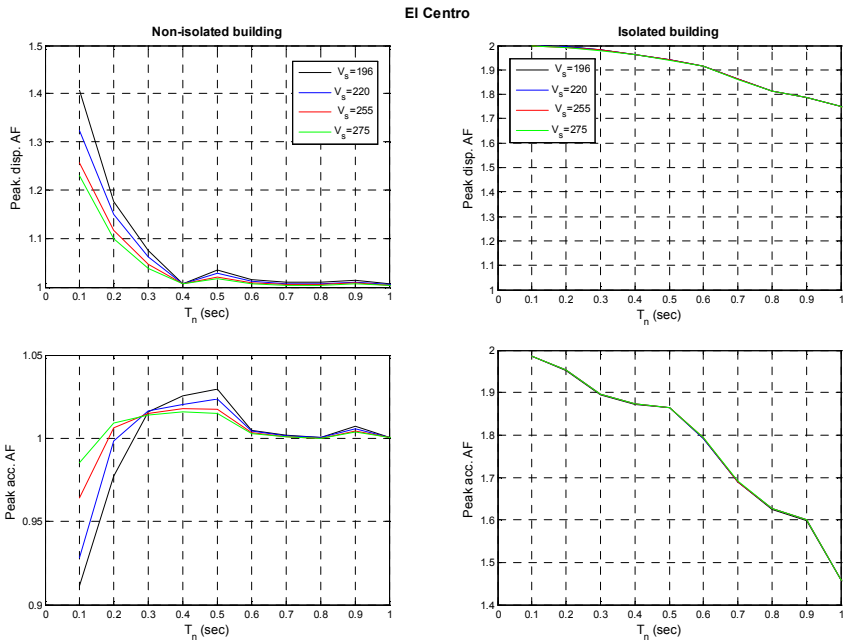


Fig. 3. Peak displacement and acceleration AF with respect to the structural natural period for different shear wave velocities in the soil (El Centro earthquake)

Conclusions

The results of the study indicate that soil flexibility has a significant influence on the earthquake-induced response of base-isolated buildings lowering its potential to reduce structural damage. Considering the flexibility of soil significantly affects the rigid superstructure response and is unable to influence the behaviour of the flexible base-isolation system. Moreover, the influence of the SSI effects on the response of base-isolated buildings is more significant for structures with longer natural period, particularly in the case of damaging earthquakes with high PGA. The results of further analyses demonstrate that the response of non-isolated buildings has been found to be much sensitive to the variations in shear wave velocity in the soil, especially for low structural natural periods. On the other hand, the response of the base-isolated buildings seems to be insensitive to the shear wave velocity variations.

References

[1] J.M. Kelly: *Earthquake-resistant design with rubber* (Springer, New York 1997).

[2] J.P. Wolf: *Foundation vibration analysis using simple physical models* (Prentice-Hall, Englewood Cliffs 1994).

[3] N.P. Tongaonkar and R.S. Jangid: Soil Dyn. Earthquake Engng. Vol. 23 (2003), p. 287.

[4] R. Jankowski: Bull. Earthquake Engng. Vol. 1 (2003), p. 397.

[5] R.V. Whitman and F.E. Richart: J. Soil Mech and Foundations. Vol. 93 (1967), SM6.

[6] I. Takewaki: Soil Dyn. Earthquake Engng. Vol. 25 (2005), p. 741.

© (2012) Trans Tech Publications, Switzerland
doi:10.4028/www.scientific.net/KEM.488-489.146

Coupling infrared thermography and acoustic emission measurement to quantify the shakedown state of shape memory alloys

C. Dunand-Châtellet[1, a], Z. Moumni[1,b]

[1]Mechanical Engineering Laboratory, chemin de la Hunière 91761 Palaiseau Cedex France

[a]clement.dunand-chatellet@ensta-paristech.fr, [b]ziad.moumni@ensta-paristech.fr

Keywords: shape memory alloys, shakedown, thermography, acoustic emission, pseudoelasticity

Abstract. This paper provides an original experimental characterization of the shakedown state of a shape memory alloy structure under cyclic pseudo-elastic loading. This analysis is performed through the observation of the dissipated energy at a macroscopic scale as well as the temperature on the surface of the sample through infrared thermography measurement. Morevover, a deeper study is led thanks to acoustic emission to quantify the shifts between microscopic evolutions at a lower scale. The main conclusion is that these 3 quantities are correlated and enable us to identify different stages the structure crosses until the shakedown state.

Introduction

Solid-solid phase transition between different crystal structure of shape memory alloys (S.M.A.) was widely studied over the past few years [1]. Recently, special interest was devoted to understand the thermo-mechanical coupling taking place during pseudo-elastic loading [2-5]. This stress induced martensitic transformation reveals an exothermic character, while the reverse transformation reveals an endothermic one [6,7] . Beyond this general fact, a strain rate dependance was observed and the higher the strain rate, the higher the temperature change. The pattern formation of strips is the core of several papers [6-8] to understand how these bands appear and how they are linked to the mechanical loading and the micro-structural properties of SMA.

Nevertheless, few studied are addressing the evolution of heat generated through cycling [9,10]. Here, The idea is to study these interlocked thermo-mechanical properties of SMA in fatigue through an experiment coupling infrared thermography measurements as well as acoustic emission measurement. Since, infrared thermography measurements permitted to notice complex behavior of the temperature field over one cycle, one can hope that change in temperature will occur regarding the change between dissipative regime established for the mechanical activity. Owing to the thermo-mechanical coupling, infrared thermography provides an other real time instrument, in addition to acoustic emission, to quantify the intrinsic dissipation. In this paper, the thermo-mechanical coupling which exists inside SMA until the shakedown state will be investigated.

Experimental setup

Quasi-equiatomic NiTi (50.3% at. Ni) SMA specimens were used for experiments and received the following heat treatment: an annealing at 673K during 30 minutes and a cooling by air were performed. The transformation temperatures are Ms=261K for the martensitic starting temperature and As=303K for the austenite start temperature. The geometry of the specimen is a simple wire of 3 mm diameter and 100 mm long. Since we are dealing with pseudo-elastic behavior, experiments were conducted at 324K using an uni-axial loading machine and a thermal chamber. The cyclic pseudo elastic loading was force controlled and fatigue failure occurs after 3158 cycles (Sine loading between 0.1MPa and 650 MPa with a frequency of 0.05 Hz).

Regarding acoustic emission measurement, a 20 dB recording threshold was determined during experiments associated to pre-amplifiers of 60dB and analogical filters with the following bandwidth [400kHz, 1MHz]. Acoustic sensors were glued on the wire to ensure acoustic coupling that was check thanks to pencil lead break procedure before and after the experiment. Regarding infrared thermography measurement, an infrared camera (FRLI S60 IR) was used with a 50 micron macro lens at a 50 Hz image frequency. To record the temperature field, one specimen surface was coated using black candle powder. The data acquisition and the post-processing was realized thanks to ThermaCam Researcher.

Results and discussion

Our aim is to demonstrate that the shakedown state of the material is reached after a given number of cycle. The shakedown state is the result of different periods inside the material characterized by 3 characterictic times relevant of the transient states through the final stable state. Let us define these times, T1, T2 and T3 which respectively correspond to cycles 12, 110 and 250. The interpretation of these periods will be lead thanks to the figures 1 to 8 which illustrate different features of our experiment.

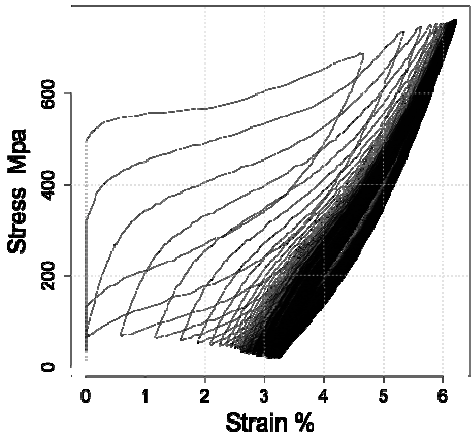


Figure 1: Cyclic strain stress Curve

One can see in Fig. 1 the cyclic pseudo-elastic curve. From this curve, macroscopic mechanical dissipation can be easily computed since it's revealed by the area of the hysteresis loop during pseudo elastic loading. This dissipated energy is shown in Fig. 2. One can clearly see the shakedown of the material through the stable state looking at the evolutive shape of the stress strain curve. One can notice 2 important features looking at the Fig. 1. From cycles 1 to 12, the shape of the loop exhibits some phase transition plateau which seems to disappear after T1. Moreover the accumulated residual strain is visible during this first period and becomes more difficult to distinguish after even if it continues to exist. These empirical facts are revealed looking at the dissipated energy in Fig. 2. During the first 12 cycles, the material dissipates a huge amount of energy which is visible regarding macroscopic quantities as the dissipated energy or the temperature on the surface of the sample in one point as shown in Fig. 3.

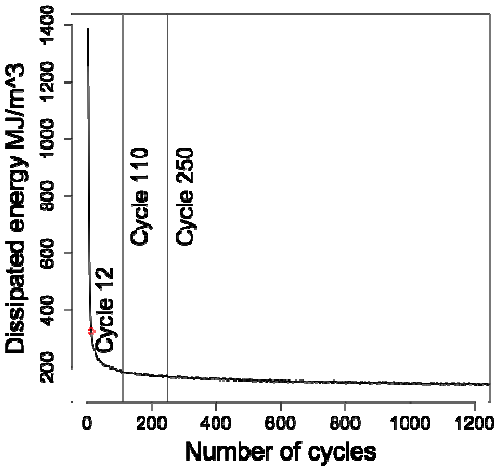


Figure 2: Dissipated energy VS Number of cycles

Indeed, one can quantify the large decrease of temperature which takes place from cycle 1 to cycle 12. In the same time, the formation of bands during the forward and backward transition is visible as shown in Fig. 4. These bands are relevant of the complex pattern of the phase transition and are no more visible after T1 as it is shown in Fig. 5. One explanation is that the formation of bands is linked to the volume fraction of martensite inside the material. From cycle 1 to 12, one can see a clear phase transition plateau in Fig. 1 and bands can emerge since a large ratio of the material shifts from one phase to another as explained in [2]. Meanwhile, when the volume fraction of residual martensite increases, the volume of material able to transform is lower and consequently,

complex patterns of bands are more difficult to create. Then, the volume fraction of residual martensite stabilizes and the temperature range also. This first period can also be analyzed looking at the cumulative energy of acoustic waves generated inside the material which are relevant of the microstructure evolution as shown in Fig. 6. One can underline that from cycle 1 to T1, there is an increase of the cumulative energy of acoustic waves generated inside the material before it reaches a quiet linear regime. This must be correlated to the two previous analysis regarding mechanical and thermal dissipation. The microscopic organization related to the disappearance of thermal bands and the huge decrease of mechanical and thermal quantities is also found here. The material relaxed a large amount of energy at the microscopic scale before reaching a first stationary state where it continues to dissipate energy but in a slower way, this is the second period from T1 to T2.

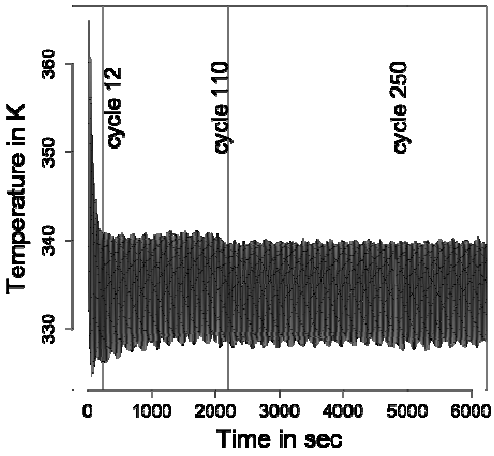


Figure 3: Temperature in 1 point of the sample

Looking at the Fig. 1 and 2, one can see that the plastic strain continues to increase but by indistinguishable steps. Nevertheless, one can appreciate the true bend formed by the dissipated energy curve which means that energy is dissipated. This must be linked with the range of temperature from T1 to T2 in Fig. 3 which is greater than the one from T2 to T3. A step between these regimes can be noticed and is linked to the intern dissipation which continue to evolve whereas after T2, the dissipated energy curve of Fig. 2 is almost flat as well as the temperature variation from one phase to an other which is constant. In the same time, the acoustic cumulative energy is linear which is relevant of a stable state of dissipation inside the material but the slope reveals that dissipation continues to exist but in a smoother way. This second phase from T1 to T2 is a transient phase to the macroscopic shakedown state which seems established after T2 since no variation of the dissipated energy is noticeable as well as no variation of the temperature amplitude is seen.

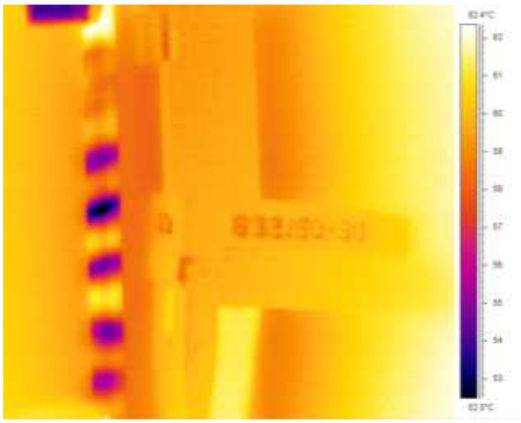


Figure 4: Thermal photography of the wire

Meanwhile, looking at the microscopic activity in Fig. 7, one can see that a huge change occurs in the dissipated energy between T2 and T3 since there is a really high increase of this quantity. This transition is crucial since one can see that after T3, the cumulative energy displays a linear behavior for a large number of cycle and then the material is also stabilized at the microscopic scale.

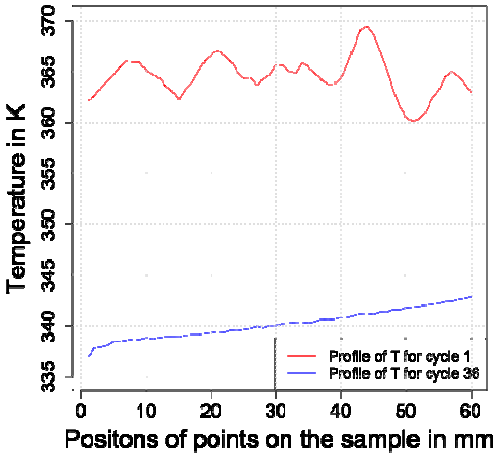


Figure 5: Temperature's profiles in the sample

But, to well understand what happened, one should pay attention to Fig. 8 which represents the coefficients of the cumulative distribution function followed by the energies of waves along cycling. This distribution is a power-law with exponential cut-off of the following form $p(E) \approx E^{-\varepsilon}\exp(-\lambda E)$ where E denotes the energy of the wave, ε the slope of the distribution in a log-log plot and λ is the variable quantifying if the distribution follows a pure

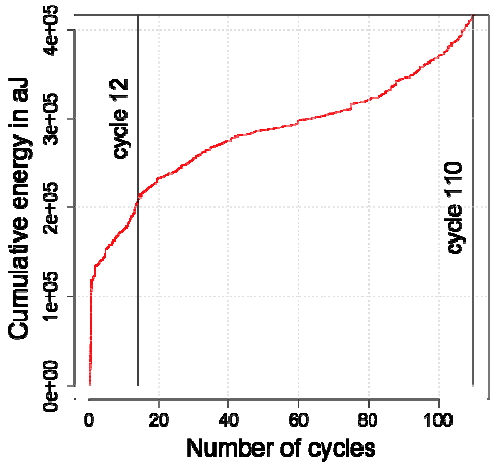


Figure 6: Cumulative energy of acoustic waves

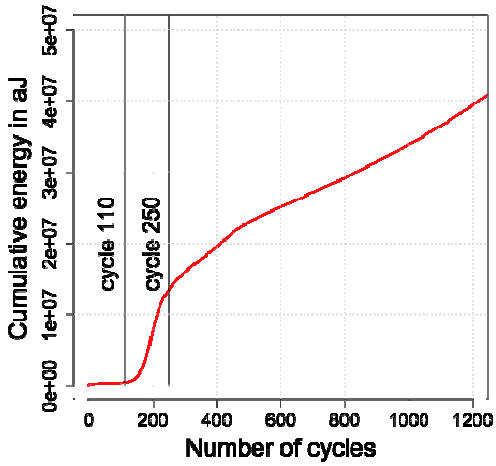


Figure 7: Cumulative energy of acoustic waves

power-law distribution or a power-law distribution with exponential cut-off. One can see that for cycle 1 to 12, the distribution of energies is not stabilized and is not a power-law distribution whereas from T1 to T2 we are in a transient regime where ε stabilizes and λ decreases continuously to 0. After T3, ε and λ are stabilized which means that the distribution follow a pure power-law distribution. This is physically very strong since it implies that a wave of given energy has the same probability to occur cycle after cycle which is relevant of stabilization at microscopic scale.

As a conclusion, one can appreciate the different periods which lead to the shakedown state and the correlation which exist whatever the variables investigated.

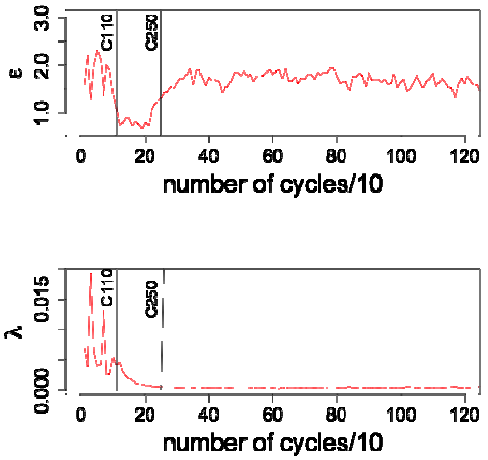


Figure 8: Evolution of power-law exponents

References

[1] Delaey, L. and Krishnan, R. V. and Tas, H. and Warlimont, H., Journal of Materials Science, 1974, Vol. 9, N.9, p.1521

[2] L.C.L. Catherine Brinson and Ina Schmidt and Rolf Lammering, Journal of the Mechanics and Physics of Solids, 2004, Vol.52, N.7, p. 1549

[3] Shaw, John A., International Journal of Plasticity, 200, Vol.16, N.5, p.541

[4] He, Y. J. and Sun, Q. P., International Journal of Solids and Structures, 2009, Vol.46, N.16, p.3045

[5] C. Morin, Z. Moumni and W. Zaki, International journal of plasticity, 2010 doi:10.1016/j.ijplas.2010.09.005

[6] Pieczyska, E. and Gadaj, S. and Nowacki, W. and Tobushi, H., Experimental Mechanics, 2006, Vol.46, N.4, p.531

[7] Daly, S. and Ravichandran, G. and Bhattacharya, K., Acta Materialia, 2007, Vol.55, N.10, p.3593

[8] Gadaj, S. P. and Nowacki, W. K. and Pieczyska, E. A., Infrared Physics & Technology, 2002, Vol.43, N.3-5, p.151

[9] Y J He and Q P Sun, Smart Materials and Structures, 2010, Vol.19, N.11

[10] Kim, K. and Daly, S., Experimental Mechanics, 2010, p.1

© (2012) Trans Tech Publications, Switzerland
doi:10.4028/www.scientific.net/KEM.488-489.150

Modeling Fracture of Fiber Reinforced Polymer

Joško Ožbolt[1,2a], Vesna Lacković[2,b] and Joško Krolo[3,c]

[1]Institute of Construction Materials, University of Stuttgart, 70560 Stuttgart, Germany

[2]IGH Institute, 10000 Zagreb, Croatia

[3]Faculty of Civil Engineering, University of Zagreb, 10000 Zagreb, Croatia

[a]ozbolt@iwb.uni-stuttgart.de, [b]vesna.lackovic@igh.hr, [c]josko.krolo@grad.hr

Keywords: Fiber-reinforced composite, polymer, glass fibers, numerical modeling, finite elements, fracture, microplane model.

Abstract. In the present paper 3D rate sensitive constitutive model for modeling of laminate composites is presented. The model is formulated within the framework of continuum mechanics based on the principles of irreversible thermodynamics. The matrix (polymer) is modeled using 3D rate sensitive microplane model. For modeling of fibers (glass) a uni-axial constitutive law is employed. The fibers are assumed to be uniformly smeared-out over the matrix. The formulation is based on the assumption of strain compatibility between matrix and fibers. To account for the de-lamination of fibers, the matrix is represented by the periodically distributed bands with non-uniform strength properties over the band width. The input parameters of the model are defined by the mechanical properties of matrix and fibers (elastic properties, strength and fracture energy), the volume content of fibers and by their orientation in 3D space. The model is implemented into a 3D finite element code. To assure mesh objective results, the localization limiter is based on the assumption of constant energy dissipation within each finite element, i.e. the crack band method is used. The performance of the model is shown on one numerical example for specimens loaded in uni-axial tension. It is demonstrated that the proposed model is able to realistically predict the resistance and failure mode of complex fiber-reinforced composite for different orientation of fibers.

Introduction

Due to the high efficiency of composites they are nowadays frequently used in design of modern structures in civil and mechanical engineering. To design efficient and economical structures and to support experiments, there is an obvious need for numerical models that can realistically predict behavior of composite structures for arbitrary geometry and loading. In the past different failure criteria and a number of macroscopic constitutive laws were proposed, which are, with more or less success, used in computational mechanics [1,2]. At the macroscopic level of modeling there are principally two approaches: (i) Modeling in the framework of continuum theory and (ii) Discrete modeling of composite (particle models). Due to the complexity of particle models, where the components of the composite and their interfaces are modeled in a discrete manner, in engineering practice usually continuous models are used. In continuous model there is an integral failure criterion, which is related to the so-called representative volume of the composite. The main difficulty with such continuum models is the modeling of de-lamination.

In the here presented model somewhat different approach is proposed. The matrix (polyester resin) is modeled using 3D rate sensitive microplane model, which is combined with the uni-axial constitutive law for glass fibers. The model input parameters are mechanical properties of matrix and fibers (separately), volume fraction of fibers in the composite, their orientation and number of layers. Damage and fracture are treated in a smeared way [3]. The model is implemented into a 3D finite element code and is first calibrated using a simple procedure that is based on a few basic test data. After calibration, the model is verified through simulations of experimentally tested specimens loaded in tension [4].

Numerical model for fiber reinforced polymer

Modeling framework and basic concept. The constitutive law for fiber-reinforced composite discussed in the present paper is formulated in the framework of continuum mechanics following basic principles of irreversible thermodynamics. The aim is to formulate a realistic model for composite where the required input parameters are only elastic and fracture properties of its components (matrix and fibers).

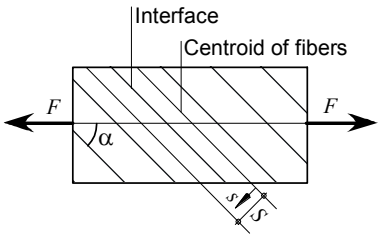


Figure 1. Idealisation of the weak matrix interface zone and the centroid of the group of fibers that is represented by the bandwidth S

The polymer (polyester resin) is treated as initially isotropic quasi-brittle material, similar to concrete like materials. The fibers are modelled as elastic-brittle material with different tensile and compressive properties. The main assumption is that the glass fibers, whose direction is defined in a 3D space, are uniformly smeared-out over the polymer. The total stress tensor consists of the contribution of the polymer and that of the fibers. Both stress tensors are calculated assuming compatibly of strains. Damage and fracture phenomena are modelled within the framework of smeared crack approach [3]. To assure mesh objective results the crack band method is employed. The decomposition of the total stress tensor is performed as (index notation):

$$\sigma_{ij} = (1-\phi)\xi(\phi,\eta)\sigma_{ij}^{m} + \phi\sigma_{ij}^{f} \qquad \text{for} \qquad i,j = 1,2,3 \tag{1}$$

in which σ^{m}_{ij} and σ^{f}_{ij} are contributions of the polymer and the fibers, respectively, ϕ is the volume fraction of fibers in the composite, $\xi(\phi,\eta)$ is a function, which varies in the range $0 \le \xi \le 1$ and η is the local space variable defined below. To formulate the model in the framework of continuum and to account for de-lamination of fibers, a periodic spatial imperfection of matrix is assumed. The imperfection is non-uniformly distributed over the bandwidth S that is parallel to fibers (see Fig. 1). Function $\xi(\phi,\eta)$ in (1) is defined in the local co-ordinate system of fibers as:

$$\xi(\phi,\eta) = 1 - \sin(\eta\pi)\phi^{\kappa} \qquad \text{with:} \qquad \eta = \frac{s}{S} \quad (0 \le s \le S) \tag{2}$$

where η is the relative distance of the matrix integration point from the centroid of the fiber group (see Fig. 1). It is assumed that the initial imperfection is proportional to the volume content of fibers. Parameter κ is a constant, which has to be obtained from the calibration of the model through inverse analysis of the basic set of tests. From Eq. (2) it follows that for $s = 0$ there is no imperfection (fiber centroid) and for $s = S/2$ (center of the interface zone) the imperfection is maximal.

Constitutive law of the polymer. The contribution of the polymer to the total stress tensor is calculated by employing microplane model. The version of the model that is originally developed for concrete is used [3]. The rate senistive model is based on the so-called relaxed kinematic constraint approach. Microplane strains are assumed to be the projections of the macroscopic strain tensor ε_{ij} (kinematic constraint). Note, however, that because of unrealistic microplane model response in the case of dominant tensile damage, the kinematic constraint must be relaxed. For more detail see [3,5].

Constitutive law for glass fibers. As mentioned before, it is assumed that the fibers are uniformly smeared-out over the matrix. Although the present formulation is restricted only to one layer of fibers, the model can principally deal with more layers of fibers that are uniformaly smeared-out in the matrix, each in different direction. The contribution of fibers to the total stress tensor is accounted for by adopting uni-axial linear elastic-brittle constitutive law in local direction of fibers, however, tensile and compressive properties of fibers are not the same. Tensile stress is calculated as:

$$t^f = E_t^f e^f \quad \text{with}: \quad e^f = l_i \varepsilon_{ij} l_j \tag{3}$$

where t^f is fiber traction (stress), E_t^f is tensile Young`s modulus and l_i is the orientation vector of fibers. The fiber strain e^f is calculated from the projection of the total strain tensor ε_{ij} into the fiber direction. Knowing stress in the direction of fiber, the contribution of fiber to the total stress tensor is calculated by transformation of the fiber traction into the global coordinate system in which the structure is discretized:

$$\sigma_{ij}^f = t^f l_i l_j \tag{4}$$

Young`s modulus for tension is obtained directly from uni-axial tensile test on fibers. The compressive Young`s modulus is lower than the tensile modulus. Moreover, the compressive limit strain is higher than the tensile limit, which is also obtained from direct tensile test on fibers. The reason for different behavior of fibers in compression and tension is due to the effect of geometrical instability of fibers under compressive load. Based on experimental results, the following relations are proposed:

$$E_c^f = c_3(\phi) E_t^f \qquad e_{cL}^f = c_4(\phi) e_{tL}^f \tag{5}$$

in which E_c^f, E_t^f, e_{cL}^f and e_{tL}^f are Young`s moduli of fibers for compression and tension and the corresponding limit strains, respectively. Functions c_3 and c_4 are obtained from the fit of the test data. Note, however, that Eq. (5) is valid only under the assumption that there is no global instability failure under compressive load. For more detail see [6].

Numerical Example – Uniaxial Tension

The presented model is implemented into a 3D finite element code and the calibration and verification of the model was carried out [6]. In the present paper the performance of the model illustrated on the specimen loaded in tension. The predicted and experimentally obtained relations between tensile strength as a function of orientation of fibers (angle α, measured from the loading direction), for volume fraction of fibers $\phi = 0.47$, is shown in Fig. 2. It can be seen that for $30^0 \le \alpha \le 90^0$ the tensile strength is not much influenced by the orientation of fibers. For $\alpha < 30^0$ tensile strength significantly increases and reaches the maximum at $\alpha = 0^0$. When the load direction is inclined to the direction of fibers, especially for $\alpha > 30^0$, the load needs to be transferred over the interface layers between fibers and matrix. Since the interface is a weak region of the composite, the failure takes place in this zone with the consequence that the tensile strength decreases with increase of α. This is illustrated in Fig. 5, which shows typical failure mode for the case $\alpha = 30^0$. Shown are maximal principal strains localized in the bands that represent idealized zones of weak interfaces between fibers and matrix. The failure is caused by mixed-mode failure (shear-tension) of the interface zone. From Fig. 2 it can be seen that there is a good agreement between predicted and experimentally obtained results.

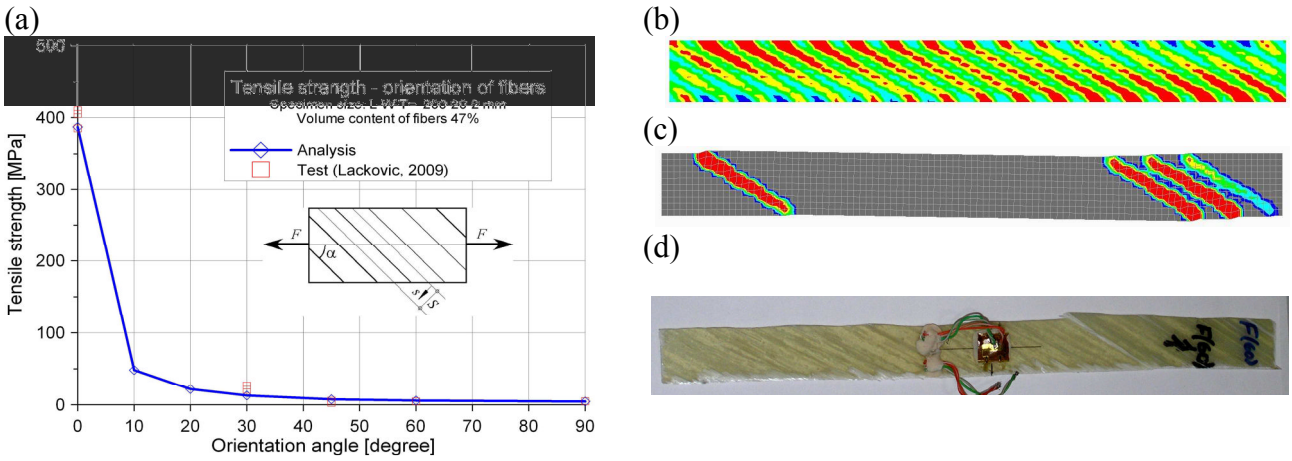


Figure 2. (a) Relation between tensile strength and orientation of fibers for volume fraction of fibers ϕ= 0.47; Maximal principal strains (damage) for load applied in horizontal direction with α= 30º: (b) at peak load, (c) at failure - deformed and (d) experimentally obtained failure mode

Summary

The paper discusses the 3D rate sensitive constitutive model for fiber-reinforced polymer. The matrix (polymer) is modeled by the 3D rate sensitive microplane model and for the glass fibers the uniaxial elasto-brittle constitutive law is used. Assuming continuity of the strain field, the stress tensor is additively decomposed into contribution of the matrix and the fibers. The advantage of the model is that the finite element discretization is not related to the orientation of the fibers. The basic mechanical properties of the composite are defined by the mechanical properties of matrix and fibers. The interaction between the matrix and the fibers is controlled by the volume fraction of the fibers and additional internal model parameters that controls the imperfection of the matrix-fiber interface. The model parameters are calibrated by fitting uniaxial tensile and compressive test data for specimens loaded parallel and perpendicular to the fiber direction. The model performance is demonstrated on the specimen loaded in uniaxial tension. The comparison between numerical and experimental results shows that the model is able to correctly predict the failure mode and the resistance of the specimens for different orientations of fibers with respect to the loading direction.

References

[1] I. I. Gol`denblatt and V. A. Kopnov, V. A., in: Journal of Polymer Mechanics, Vol. 1, No. 2, pp 54-59 (1966).

[2] R. Hill, in J. Mech. Phys. Solids, No. 3, pp. 405-417 (1990).

[3] J. Ožbolt, Y. Li and I. Kožar, in: International Journal of Solids and Structures, 38, 2683-2711 (2001).

[4] V. Lacković: Influence of the amount and structure of glass fibers on the mechanical properties of polymer composites. PhD. Thesis, Faculty of Civil Engineering Zagreb, Croatia, (2009).

[5] J. Ožbolt, K. K. Rah and D. Mestrović, in: Int. Journal of Fracture 139:239–252 (2006).

[6] J. Ožbolt, V. Lacković and J. Krolo, submitted for publ. in: Int. Journal of Fracture, (2011).

© (2012) Trans Tech Publications, Switzerland
doi:10.4028/www.scientific.net/KEM.488-489.154

Modeling Radiation Effects on the Fracture Process in Simplified Nuclear Glass

Le-Hai Kieu[1,a], Jean-Marc Delaye[1,b], Claude Stolz[2,c]

[1] Service d'Études et Comportement des Matériaux de Conditionnement, DEN/DTCD/SECM, CEA EA Marcoule, BP 17171, 30207 Bagnols sur Cèze cedex, France

[2] Laboratoire de Mécanique des Solides, CNRS UMR7649, École Polytechnique, 91128 Palaiseau cedex, France

[a] le-hai.kieu@cea.fr, [b] jean-marc.delaye@cea.fr, [c] stolz@lms.polytechnique.fr

Keywords: nuclear glass, radiation effect, fracture, molecular dynamics

Abstract. Experimentally, the evolution of several mechanic properties (hardness, density, Young's modulus, fracture toughness) is observed in nuclear glasses under irradiation. In this work, classical molecular dynamics calculations are performed to better understand fracture mechanisms in simplified nuclear glasses at atomistic scale and to explain the radiation effects. Fractures are simulated in more disordered glasses, representative of irradiated samples, to reveal radiation effects. We observe a lower elastic limit and a greater plasticity in the irradiated glass that can explain its larger fracture toughness.

Introduction

Nuclear waste glasses are aluminoborosilicate glasses containing more than thirty oxide constituents, and are used for immobilization of unrecycled minor actinides. Volume expansion together with a reduction in hardness and Young's modulus have been observed in glass doped with ^{238}Pu and ^{244}Cm [1-3]. In addition, microindentation measurements revealed an increase in the fracture toughness of doped glass compared with pristine glass [2,3], reflecting greater resistance to crack propagation.

The purpose of this study is to better understand the atomic-scale mechanism of cracking in simplified nuclear glasses using classical molecular dynamics simulations. Molecular dynamics is already routinely used to simulate cracking processes in silica glass [4,5].

Given that it is impossible to model the complexity of the actual nuclear glass, a model glass with its main constituents (SiO_2-B_2O_3-Na_2O) was used instead. This glass presents the same qualitative behavior as the real one [6].

Glass simulation

Fabrication of the pristine glass. To obtain the unirradiated glass structure, a liquid was equilibrated at 5000 K starting from a configuration in which the atoms were randomly distributed. The liquid was then quenched incrementally to room temperature at a rate of 5×10^{12} K/s. The final glass was first relaxed in the NPT ensemble to determine its equilibrium volume, then in the NVE ensemble to stabilize its structure. We fitted composition-dependent Buckingham potentials to simulate sodium borosilicate glass. The potentials were validated over a wide range of compositions [7]. The structural properties — especially modifications in the environment of boron atoms (tri- and tetracoordinate) with the composition, and the mechanical properties of the CJ1 glass used here (see *Table 1*) — are correctly reproduced.

Fabrication of the irradiated glass. We modeled the irradiated glass structure based on the analogy between the effects of irradiation and quenching [8]. The glass structure becomes increasingly disordered under irradiation: the network is depolymerized (increasing $B^{[3]}/B^{[4]}$ ratio and higher concentration of nonbridging oxygen), the angular and ring-size distributions expand, and mixing increases between species [6,8].

We modulated the quenching rate to reproduce these effects. A pristine glass sample previously equilibrated as described above was preheated to 3000 K for 50 ps, then quenched to room temperature at 10^{14} K/s. The resulting structural changes reproduce the effects of irradiation : swelling of 7%, 10% increase of $^{[3]}$B atoms, 3% increase of non-bridging oxygen, decrease of the Si-O-Si and Si-O-B angles.

Table 1. Comparison of simulated and experimental CJ1 glass elastic properties

CJ1 glass composition [mol%]			Density [g/cm^3]		Young's modulus [GPa]		Bulk modulus [GPa]	
SiO_2	B_2O_3	Na_2O	Sim	Exp	Sim	Exp	Sim	Exp
67.73	18.04	14.23	2.46	2.45	76.0	82	40.6	45

Simulation of cracking. The cracking mechanism was investigated by fracturing pristine and irradiated CJ1 glass samples by molecular dynamics. A tensile load was applied to a rectangular parallelepiped sample containing 100 000 atoms. The dimensions of the pristine and irradiated specimens along the XYZ axes were 250 Å × 50 Å × 100 Å and 256 Å × 51 Å × 102 Å, respectively. The specimen was initially notched by removing several atoms on one edge; the notch was 30 Å deep and 20 Å high. The tensile load was applied to the sample by imposing progressive movements on the Z-axis. The motion was fitted to obtain a tensile elongation rate of 40 m/s.

Results and discussion

Mechanical behavior. During cracking, we observed a mechanism involving the formation and coalescence of cavities (Fig. 1a and Fig. 1b). This mechanism has already been observed for cracking of silica glass by molecular dynamics [9] and was confirmed by atomic force microscope observation [10]. The cracking stress was calculated using the virial theorem [11,12].

For small deformations, the pristine and irradiated glass samples exhibit linear elastic behavior (*Fig. 1*c). Young's modulus for the pristine glass (75 GPa) satisfactorily reproduces the experiment value (82 GPa), as does the 25% reduction in Young's modulus in the irradiated glass. This decrease is consistent with the 15−30% experimental reduction measured in the actual nuclear glass [1-3].

The elastic limit for the irradiated glass is lower than for the pristine glass. The material becomes plastic when greater strain is applied. In the plastic region the nanocavities begin to grow. Above a certain strain threshold, coalescence begins to occur. The coalescence accelerates and the crack propagates to failure. In irradiated CJ1 glass, the plastic zone extends over a greater strain interval (*Fig. 1*c). The plasticity of the irradiated glass is therefore greater.

Cavity growth and coalescence mechanism. The volume fraction occupied by the cavities was determined using percolation theory [13]. This method consists in dividing the simulation cell into cubic unit volumes [14] with an edge length L long enough to avoid including interstitial sites in addition to the pore volumes. As the interstitial sites were less than 3 Å, we chose L = 4 Å. Adjacent empty unit volumes were then combined to identify growing pores.

In *Fig. 2*a the pore volume fraction curve is divided into 4 regions: (1) formation of cavities, (2) growth of cavities, (3) coalescence of cavities, and (4) decohesion between the two parts of the sample. In the first region the porous fraction increases linearly. Due to the lower elastic constants, the cavity nucleation rate is slightly higher in the irradiated glass than in the pristine glass. The more or less uniform nucleation of cavities in the irradiated glass prevents the occurrence of strongly deformed zones. Above the elastic limit, the growth rate increases significantly in the pristine glass and less sharply in the irradiated glass. This is attributable to the greater plasticity around the cavities in the irradiated structure.

The difference in the coalescence rate between the pristine and irradiated glass is clear in the third region. Coalescence begins for 13% strain in the pristine glass and 16% in the irradiated glass. The greater plasticity of the irradiated glass probably accounts for the delay in coalescence. These two differences — lower elastic limit and greater plasticity — between the irradiated and pristine glass could account for the increased fracture toughness. The rate of change of the porous fraction decreases in the last phase. A the moment of decohesion, relaxation is observed around certain cavities away from the failure zone. This phase is virtually identical in the pristine and irradiated glass.

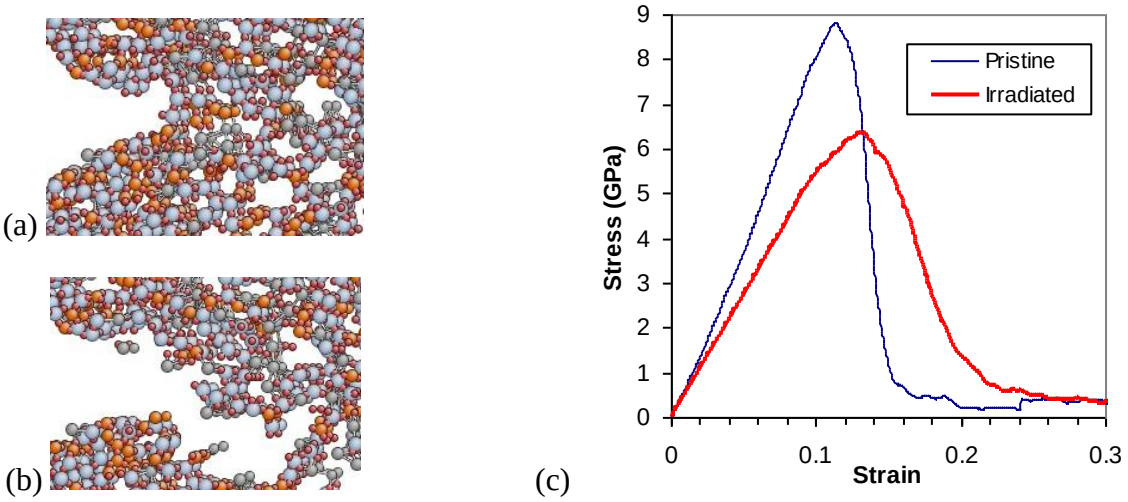


Fig. 1. (a) Initial crack (notch is on the left) and appearance of cavities; (b) Coalescence of cavities and propagation of the crack; (c) Stress-strain curves during cracking (thin : pristine glass; bold : irradiated glass)

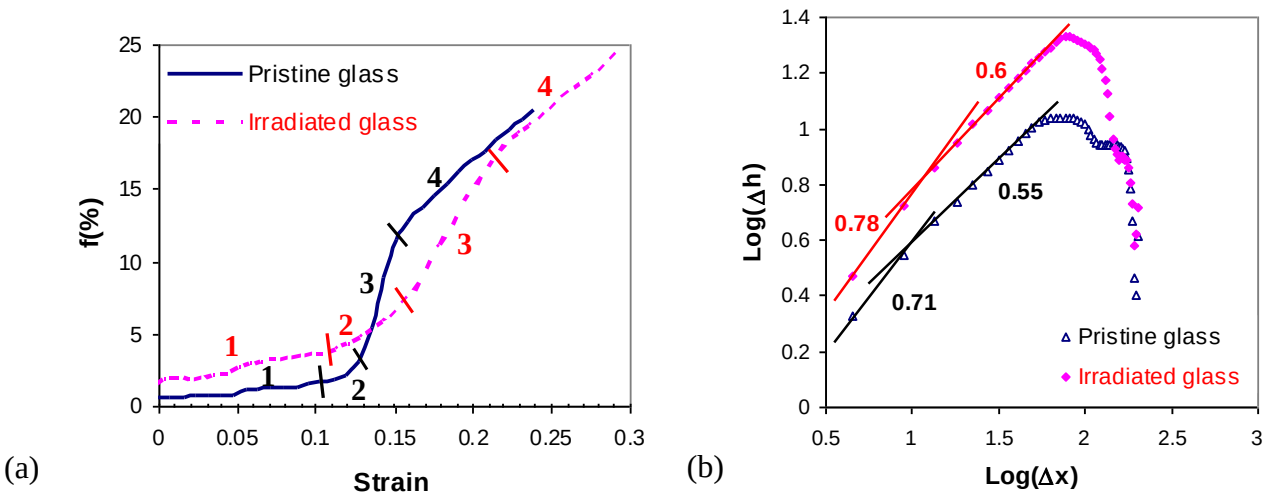


Fig. 2. (a) Pore volume fraction versus strain in pristine glass (solid line) and irradiated glass (broken line); (b) Roughness measurement by the 1D height-height correlation method

Roughness measurement and comparison with experimental result. The fracture surface was analyzed to measure the roughness by the 1D height-height correlation method [15] along the propagation direction. A roughness of 0.55 was measured on the pristine glass (*Fig. 2*b). Experimentally, common roughness values of 0.5 (short-range) and 0.8 (longer range) have been reported in many materials. Rountree found only exponent 0.5 in silica glass fractured by classical molecular dynamics for reasons related to the size of the simulation cell [16]. Atomic force microscope (AFM) observation yielded roughness values of 0.75 in CJ1 glass and 0.8 in silica at a scale exceeding 5 nm [17]. The short-range regime was not observed. The exponent measured here corresponds to a short-range roughness. The roughness coefficient increases under irradiation.

Moreover, we observed roughness exponents of 0.71−0.78 at very small scale (< 1 nm). The cutoff distance between the initial regime and the regime characterized by an exponent near 0.5 may be related to the size of the cavities: in fact, the cutoff distance corresponds to a visual estimate of the cavity size.

The size of the process zone in the pristine glass was measured by plotting the profile height versus the distance r from the crack front. The distance corresponding to the transition from plastic to elastic behavior ($1/r^{0.5}$ dependence) is about 7 nm. In pure silica, a difference between the size of the simulated process zone and the zone determined experimentally was reported by Rountree (150−300 nm

experimentally, 10 nm for the simulation) [14]. This difference is attributable to the crack propagation rate (10^{-11}−10^{-9} m/s experimentally compared with 10−1300 m/s for the simulation) [14]. A comparable difference can be expected for the calculations presented here.

Conclusion

By varying the thermal quenching rate, we modeled a SiO_2-B_2O_3-Na_2O glass structure similar to that of the irradiated glass in order to analyze the effect of irradiation on the cracking mechanism. The elastic limit diminishes in the irradiated glass while its plasticity increases; this results in slower coalescence of the cavities and delayed failure compared with the pristine glass.

References

[1] S. Peuget, J.N. Cachia, C. Jégou, X. Deschanels, D. Roudil, V. Broudic, J.M. Delaye, J.M. Bart, J. Nucl. Mater. 354 (2006), p. 1

[2] Y. Inagaki, H. Furuya, Y. Ono, K. Idemitsu, T. Banba, S. Matsumoto, S. Muraoka, *Mater. Res. Soc. Symp. Proc.* 294 (1993), p. 191

[3] H. Matzke, in: CEA/Varlhô Summer Session Proceedings on Glass: Scientific Research for High Performance Containment, Méjannes-Le-Clap (1997), p.149.

[4] C.L. Rountree, R.K. Kalia, E. Lidorokis, A. Nakano, L. Van Brutzel, P. Vashishta, Annu. Rev. Mater. Res. 32 (2002) p. 377.

[5] A. Pedone, J. Phys. Chem. C 113 (2009) p. 20773.

[6] J. de Bonfils, S. Peuget, G. Panczer, D. de Ligny, S. Henry, P.-Y. Noel, A. Chenet, B. Champagnon, J. Non-Cryst. Solids, 356 (2010) p. 388.

[7] L.H. Kieu, J.M. Delaye, L. Cormier, C. Stolz, submitted to J. Non-Cryst. Solids

[8] G. Bureau, J.-M. Delaye, S. Peuget, G. Calas, Nucl. Instr. Meth. Phys. Res. B 266 (2008) 2707.

[9] L. Van Brutzel, Ph.D. thesis, Université Paris VI (1999).

[10] F. Célarié, S. Prades, D. Bonamy, L. Ferrero, E. Bouchaud, C. Guillot, C. Malière, Phys. Rev. Lett. 90 (2003), p. 075504

[11] S.J.V. Frankland, V.M. Harik, G.M. Odegard, D.W. Brenner, T.S. Gates, Compos. Sci. Technol. 63 (2003) p.1655

[12] A. Adnan, C.T. Sun, H. Mahfuz, Compos. Sci. Technol. 67 (2007), p. 348

[13] D. Stauffer, *Introduction to Percolation Theory*, Taylor & Francis, Washington, DC (1992)

[14] C.L. Rountree, D. Bonamy, D. Dalmas, S. Prades, R.K. Kalia, C. Guillot, E. Bouchaud, Phys. Chem. Glasses: Eur. J. Glass Sci. Technol. B 51 (2010), p. 127

[15] E. Bouchaud, J. Phys. Condens. Matter 9 (1997), p. 4319

[16] C.L. Rountree, S. Prades, D. Bonamy, E. Bouchaud, R. Kalia, C. Guillot, J. Alloy. Compd. 434-435 (2007) p. 60

[17] S. Prades, PhD thesis, Université Paris VI (2004)

© (2012) Trans Tech Publications, Switzerland
doi:10.4028/www.scientific.net/KEM.488-489.158

Crack growth modeling in a specimen with polymer weld

Martin Ševčík[1,2,a], Pavel Hutař[1,b], Luboš Náhlík[1,2,c], Ralf Lach[3,d],

Zdeněk Knésl[1,e] and Wolfgang Grellman[3,f]

[1]Institute of Physics of Materials, Žižkova 22, 616 62 Brno, Czech Republic

[2]Brno University of Technology, Technická 2, 616 69 Brno, Czech Republic

[3]Martin-Luther University Halle-Wittenberg, Centre of Engineering, Halle/Saale, Germany

[a]sevcik@ipm.cz, [b]hutar@ipm.cz [c]nahlik@ipm.cz, [d]ralf_lach@web.de, [e]knesl@ipm.cz

[f]wolfgang.grellmann@psm.uni-halle.de

Keywords: polymer weld; crack propagation; graded structure; fracture mechanics

Abstract: Secure and cost effective joining methods are key points for practical applications of plastic pipelines. The morphology and material structure of welded joints are complicated in comparison with the base pipe material. The formation of the weld is highly dependent on both thermal history and stress state. Consequently, the material parameters characterizing the weld joint and corresponding heated zone influence the reliability and safety of the welded pipe system as a whole. In the contribution a welded polymer-polymer butt joint is considered and its possible damage caused by slow crack growing in the weld zone is numerically analyzed. The numerical model takes into account the geometry of the bead and changes in material properties inside the weld zone. The results obtained from welded specimens are compared with those for a smooth specimen from the base material. The conclusions described in the paper can be used for a better transfer of fracture mechanics characteristics between laboratory specimens and real pipes.

Introduction

Polymeric pipes are candidates for use in chemical processing plants, where they can transmit liquid chemicals [1]. One of the possible joining methods is a butt-fusion welding. This welding process consists of heating of the pipes' ends and pressing the heated ends together. The typical sign of butt welding is a bead that occurs due to the pressing of the pipes' ends, see Fig. 1. In reality, the morphology and material structure of welded joints are more complicated in their relationship with the base pipe material [2]. The geometry of the bead and its mechanical properties are highly dependent on both the thermal history and stress state of the weld process. Consequently, the material parameters characterizing the weld joint and corresponding heated zone are changed and influence the reliability and safety of the whole welded pipe system. In general, good quality butt welded joints should guarantee that the strength of the joint is about the same as that valid for basic pipe material [3,4]. Due to the butt-welding technology currently used, the changes of mechanical properties in the weld zone are continuous [5].

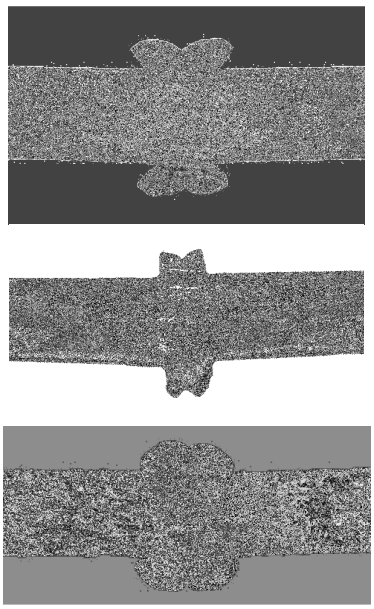


Fig. 1. Specimens used for testing of butt-weld quality; shape of the weld bead resulting from optimal welding conditions (up), lower welding pressure (middle) and higher welding pressure (down).

The typical testing specimen is cut out from the pipe in such a way that the weld bead is in the middle of the specimen, see Fig. 1. The specimens are usually subjected to tensile creep tests [6]. There are numerous works which focus specifically on polymeric pipe testing [6,7] however only a few of them engage in numerical simulation of the weld bead and estimation of the corresponding fracture parameters [8]. The main aim of this work is to model crack propagation in the specimen used for testing (similar as in Fig.1) and to compare these results with a single edge cracked tension specimen taken from the pipe. From this comparison the weld bead influence on the fracture behaviour of the welded joint is estimated and the possible transfer of the experimental data from laboratory specimens to pipeline structure is discussed.

Numerical model

A polymeric pipe with outer diameter D = 125 mm and wall thickness s = 7.4 mm was considered. The geometries of the beads were taken from real specimens, see Fig. 1. The variation of Young's modulus distribution E(z) across the butt weld was experimentally determined in work [5] and can be described aproximately using the following relation:

$$E(z) = h_1(z)E_{\max} + [1 - h_1(z)]E_{\min} \quad \text{for} \quad 0 \le z \le w/2$$

$$\text{where} \quad h_1(z) = \frac{1}{2}\left(\frac{z}{w/2}\right)^p$$

or (1)

$$E(z) = h_2(z)E_{\max} + [1 - h_2(z)]E_{\min} \quad \text{for} \quad w/2 \le z \le w$$

$$\text{where} \quad h_2(z) = 1 - \frac{1}{2}\left(\frac{w - z}{w/2}\right)^p$$

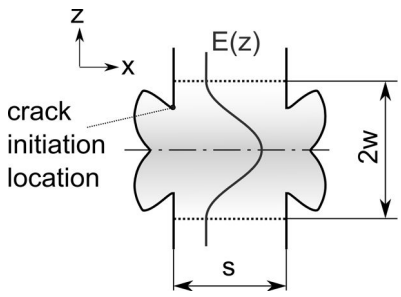


Fig. 2. Scheme of the bead with Young's modulus distribution across the weld.

where E_{max} is the highest Young's modulus measured in the centre of the butt weld, E_{min} is the base pipe, Young's modulus p is the degree of polynomial change (here used p = 2), and 2w is the thickness of the region influenced by the welding process, see Fig. 2. According to [5] the thickness of this region is between 4-7 mm for the given pipe geometry. In this study the ratio of E_{max}/E_{min} is a parameter characterizing the material property gradient across the weld. In the case of polypropylene/polypropylene weld the typically measured value of E_{max}/E_{min} is about 1.3, in the case of polyethylene/polyethylene E_{max}/E_{min} is about 1.1 [5]. A finite element model is shown in Fig. 3. Finite elements are strongly non-homogenously distributed due to high stress concentrations close to the weld bead and the crack front.

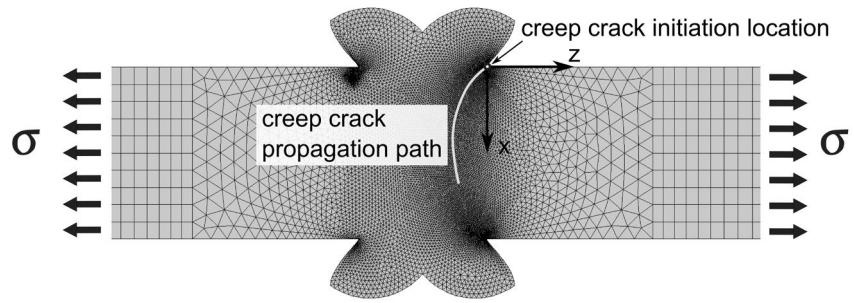


Fig. 3. Typical model of specimen with weld bead with highlighted crack path location.

Using numerical simulation the location of a possible crack initiation was found, see Fig. 3. Then, a specific algorithm for determination of the crack path was used in order to study the influence of the graded structure on the crack behavior. The algorithm calculates at each step the

stress intensity factors and the MTS criterion estimates the crack direction needed for prediction of further crack propagation. The core of the algorithm is similar to those published in [9,10]. The crack initiation location and numerically predicted crack path is in good agreement with experimental observations, see e.g. [6].

Influence of weld bead on the crack propagation path and fracture parameters

Specimens with various weld bead geometry and specimens without weld bead were numerically analyzed and crack propagation paths were estimated using the algorithm described above. The influence of material non-homogeneity can be seen in Fig. 4.

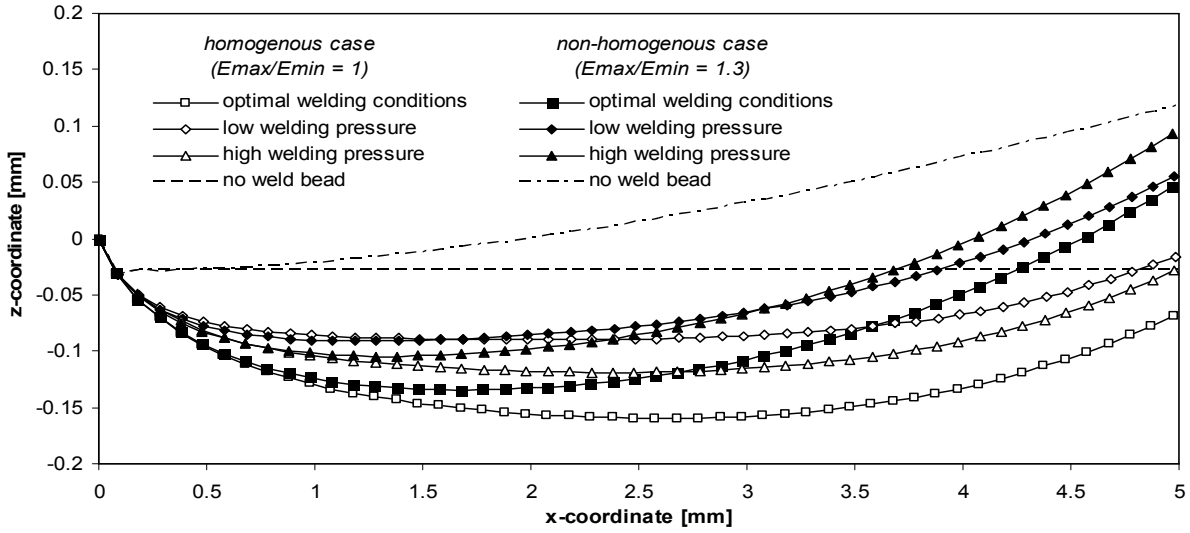


Fig. 4. Crack propagation paths for various configurations estimated numerically.

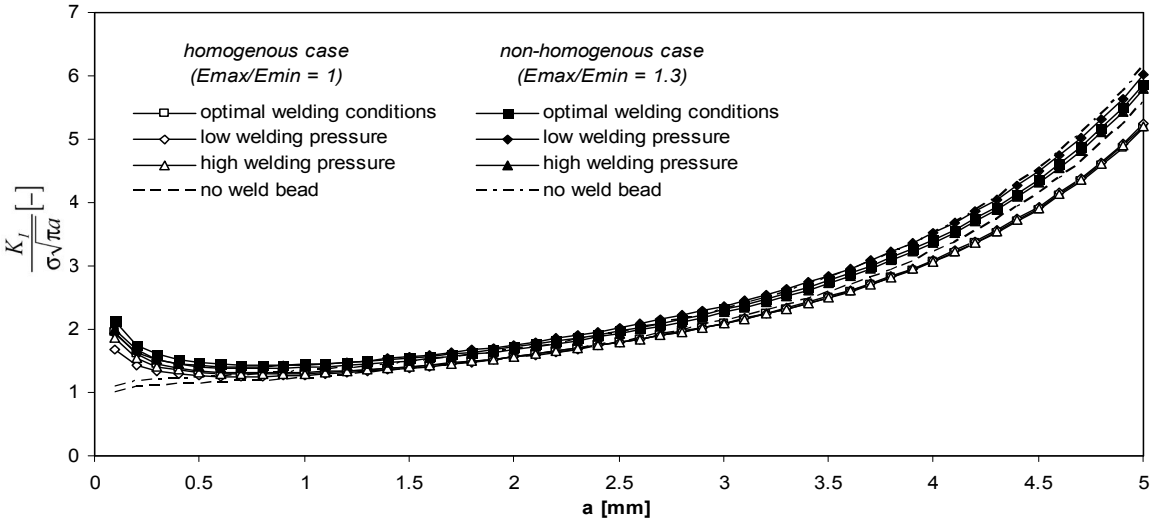


Fig. 5. Normalized stress intensity factor for different crack paths and weld bead configurations.

In cases where material non-homogeneity was taken into account the crack paths tend to deviate more from the weld center than in the case of a homogenous specimen. This tendency is also clearly visible for specimens without weld bead, so crack kinking is the consequence of the material non-homogeneity and does not come from stress concentration caused by notches in the weld bead. There is still no uniform view on the presence of the weld bead during testing. The notches in weld beads represent strong stress concentrators. However, the weld bead can in some cases increase the stiffness of the weld. To discover the influence of the weld bead on the fracture behavior the stress intensity factors were plotted in Fig. 6 for the calculated crack paths. The stress intensity factors

obtained for all types of weld bead geometries are almost identical, when material non-homogeneity is not taken into account. The difference in K_I between a specimen without weld bead and models with weld bead is significant only for short cracks, where the stress concentration of the notch influences the stress field. Taking the material non-homogeneity of the weld into account, the stress intensity factor slightly increases. Nevertheless, the values of K_I are roughly similar for all geometries of the weld. Therefore, it can be concluded that the shape of the weld bead has a minor influence on the stress intensity factor (smaller than 5%). The weld bead can decrease the time for crack initiation, but for crack propagation it has only a minor influence. We therefore conclude that the presence of the weld bead during testing of the specimens, according to our results, can be regarded as negligible in its effect.

Conclusions

The paper presented focuses on a numerical modeling of the fracture behavior of polymer weld testing specimens. The geometry of the weld bead depends on the welding conditions. Three typical geometries of the weld bead were analyzed, namely a weld bead produced during optimal welding conditions, lower welding pressure and higher welding pressure. The crack propagation paths and stress intensity factors were estimated numerically for all studied geometries of the weld bead and for both homogenously and non-homogenously distributed material properties across the weld and compared with crack paths obtained from smooth specimens.

It was found that the material non-homogeneity of the weld causes a slight increase of the stress intensity factor. In the case of a polyethylene/polyethylene weld (E_{max}/E_{min} is about 1.1) this can be effectively neglected, but in the case of polypropylene/polypropylene weld (E_{max}/E_{min} is about 1.3) the influence is stronger. Nevertheless, material non-homogeneity influences the crack path more than the values of the fracture parameters. Similarly, the presence of the weld bead has a significant influence only for the creep crack initiation due to the strong stress concentration in the notch between the weld bead and the smooth surface. Thus the presence of the weld bead during the testing of the specimens, according to our results, is not of great significance in the majority of cases.

Acknowledgement: This work was supported by grants 101/09/J027 and 106/09/H035 of the Czech Science Foundation and Deutsche Forschungsgemeinschaft (DFG) grants GR 1141/30-1 – 32-1.

References

[1] H. Chen et al.: Journal of Materials Engineering and Performance, Vol. 6(5) (1997), p. 473

[2] K. Leskovics, M. Kollár, P. Bárczy: Material Science and Engeneering A, Vol.419 (2006), p.138.

[3] A.S. Wood: Chemical Engineering Science, Vol. 48(17) (1993) p. 3071.

[4] L.E. Janson, *Plastics Pipes for Water Supply and Sewage Disposal*, Borealis, Stockholm, 1999.

[5] R. Lach et al.: Key Engineering Materials, Vol.465 (2011), p. 427.

[6] J. Hessel: *Erweitertes Anwendungsspektrum für PE-HD Rohrsysteme mit hoher Spannungsrißbeständigkeit*,Vortrag, Wiesbadener Kunststoffrohrtage 2001.

[7] G. Pinter, R.W. Lang, M. Haager: Monatshefte für Chemie, Vol.138 (2007) 347.

[8] M. Ševčík, Z. Knésl, P. Hutař, L. Náhlík: Key Engineering Materials, Vol.465 (2011), p.175.

[9] Kramberger, J., et al.: Engineering Fracture Mechanics*, Vol.*71 (2004), p.647.

[10] Španiel M, Jurenka J, Kuželka J: Meccanica Vol.44 (2008), p.189.

© (2012) Trans Tech Publications, Switzerland
doi:10.4028/www.scientific.net/KEM.488-489.162

Basic modes of crack propagation through the interface in a polymer layered structure

Michal Zouhar[1,2,a], Pavel Hutař[1,b], Luboš Náhlík [1,2,c] and Zdeněk Knésl[1,d]

[1]Institute of Physics of Materials, Žižkova 22, 616 62 Brno, Czech Republic

[2]Brno University of Technology, Technická 2, 616 69 Brno, Czech Republic

[a]zouhar@ipm.cz, [b]hutar@ipm.cz [c]nahlik@ipm.cz, [d]knesl@ipm.cz

Keywords: fracture mechanics, slow crack growth, multilayer polymer pipe

Abstract: The multi-layered structure components of dissimilar materials are used in many engineering applications to protect the base structure from outer damage. Typical examples of coated structures are pipes with the dimensional addition of protective layers (multi-layer pipes). The purpose of this development is to protect the main (functional) part of the pipes from damages (e.g. surface scratches, internal crack propagation). In the contribution the attention is paid to cracks existing and propagating in inner protective layer. In many cases the cracks are stopped at the interface between protective and functional layers. The important task is to decide if they penetrate further through the interface in the bulk material and thus cause the failure of the system. The critical stress for the crack propagation through the interface depends on the relation between bulk and coating materials as well as on the crack geometry. All these important topics are taken into account and their effect on crack propagation is broadly discussed.

Introduction

A crack perpendicular to a bi-material interface has attracted the attention of many investigators, e.g. Lin and Mar [1], Meguid et al. [2]. Bogy [3] has investigated the stress singularity of the semi-infinite crack terminating at the interface with an arbitrary angle. Gupta et.al [4] extended this work into the area of anisotropic materials. These papers mainly describe the stress field around the crack tip in the framework of linear elastic fracture mechanics. The basic problem is the influence of an interface on a crack penetrating that interface from one material into to the second one in a bi-material body. Many papers in this field are focused on crack behaviour in the case of layered ceramic structures e.g. [5-8]. In the field of polymer materials crack behaviour at the bi-material interface is described in paper [9]. If the crack is perpendicular to the interface for mode I, the stress distribution can be expressed as:

$$\sigma_{ij} = \frac{H_I}{\sqrt{2\pi} r^p} \cdot f_{ij}(p,\theta) \qquad (1)$$

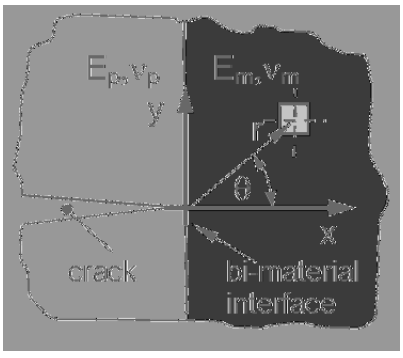


Fig. 1. Scheme of the crack terminating on the bi-material interface

where H_I is a generalized stress intensity factor, $p \neq 1/2$ is a stress singularity exponent and $f_{ij}(p,\theta)$ are known functions. The value of the stress singularity exponent $0 < p < 1$ depends on the elastic mismatch of the two materials, see [10]. The value of the stress singularity exponent p follows the boundary conditions, see e.g. [2,10] for details. The generalized stress intensity factor H_I has to be estimated for a given configuration numerically as a function of applied stress σ_{appl}, i.e. $H_I = H_I(\sigma_{appl})$. The fact that $p \neq 1/2$ complicates applications of linear elastic fracture mechanics procedures for studying crack behaviour, see e.g., [8,10]. On the basis of the idea of equality strain

energy density expressed by stress intensity factor K_I and strain energy density expressed by generalized stress intensity factor H_I ($\Sigma(K_I) = \Sigma(H_I)$), it is possible to a find relation between H_I and the effective value of a stress intensity factor at an interface K_{eff} [10]:

$$K_{eff} = \left(\frac{1-2\nu_m}{(1-p)^2\left(4(1-2\nu_m)+(g_r-p)^2\right)} \right)^{-\frac{1}{2}} d^{\frac{1}{2}-p} H_I \tag{2}$$

were d is the critical distance ahead of the crack tip and is usually correlated with the process zone [11]. g_r is a function of the stress singularity exponent and the composite parameters of the bi-material, see [10] for details. K_{eff} can be used as a standard value of the stress intensity factor and stability condition for creep crack penetration can be expressed as:

$$K_{eff} < K_{th}. \tag{3}$$

In the case of the validity of eq.(3), the crack is arrested on the interface. This is also an important factor for multi-layered polymer structures such as multilayer polymer pipes. In this contribution, attention is paid to cracks existing and propagating in protective layers. Because creep damage to this type of pipe is usually brittle and plastic deformations are localized just around the crack tip, small scale yielding conditions are valid and the concept proposed above for the crack terminating at the interface can be used. The conditions necessary for crack penetration through the interface between the protective layer and the main pipe is estimated for the 2D and 3D numerical model. The critical stress corresponds to the critical inner pressure p_{crit} and for the crack propagation through the interface depends on the relation between bulk and coating materials as well as on the crack shape. Taking into account the assumptions of linear elastic fracture mechanics, the critical stress (pressure in our case) can be expressed as:

$$p_{crit} = \frac{K_{th}}{K_{eff}\left(p_{appl}\right)} \cdot p_{appl} \tag{4}$$

were K_{th} is threshold for the creep crack propagation in the main material, p_{appl} is applied pressure.

Numerical model

The finite element model of a polymer multilayer pipe was created. Geometry of the pipe is shown in Fig. 2. The geometry of the pipe considered was: the outer diameter of the pipe $D_o = 110$ mm, the total thickness $t = 10$ mm, the thickness of both inner and outer layer $t_p = 2.5$ mm and the main pipe thickness $t_m = 5$ mm. Slow crack propagation from the inner surface through the protective layer is analyzed. The critical point for this application is the crack penetration to the main pipe. Therefore, a crack touching the interface between the inner protective layer and the main pipe is studied. The material properties of each layer were characterized by ratio E_p/E_m and Poisson's ratio $\nu_m = \nu_p = 0.35$. The ratio of E_p/E_m differs from 0.4 to 1.5. The threshold value for the creep crack propagation in the main pipe material was $K_{th} = 0.2$ MPa.m$^{1/2}$ [12] and the tensile strength of the main material $\sigma_c = 30$ MPa.

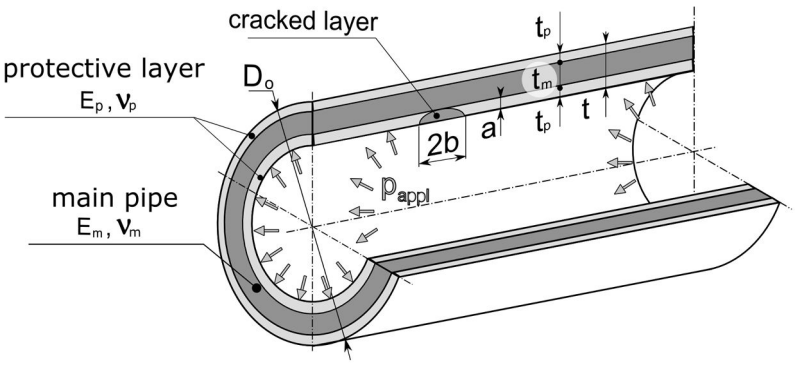


Fig. 2. Geometry of three-layer pipe with cracked inner layer

A three dimensional numerical model was created for two different crack shapes loaded by inner pressure p_{appl}. Two planes of symmetry were used. A model of the elliptical crack, characterized by ratio c/a (c/a = 1.2; 1.6) which is touching the interface, was used; see Fig. 3 left. It was then assumed that the crack is arrested on the interface and grows continuously sideways only in the

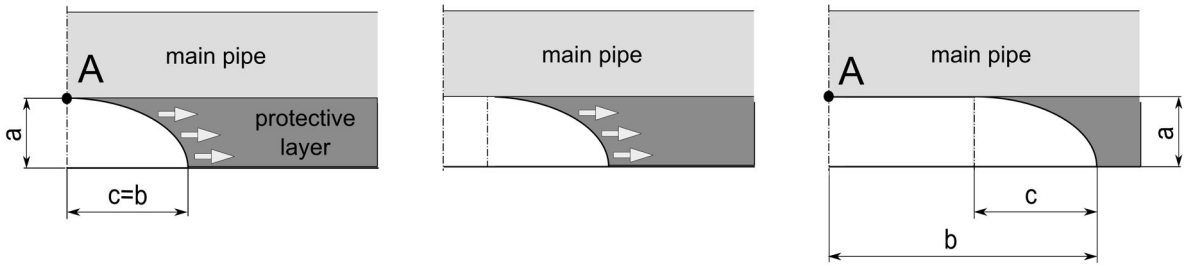


Fig. 3. Creep crack propagation along the interface

protective layer, see Fig. 3. This corresponds to a situation where the main pipe is tough or the threshold value of the main pipe is higher than in the case of protective layer [13]. The crack is characterized by the ratio c/a and its length b, see Fig. 3. The goal of this study is the evaluation of the critical pressure necessary for crack propagation through the interface as a function of b.

Results and discussion

The stability of a crack with its tip on the material interface was numerically investigated. The geometry of the three-layer pipe model with a cracked internal protective layer corresponds to Fig.2 and modeled crack shapes correspond to Fig.3. The different material properties of main pipe and protective layers, characterized by ratio E_p/E_m, depending on the value of K_{eff} for 2D and 3D model was calculated, see Fig.4. The resulting values of K_{eff} are approximately two times higher for the 2D model than for the 3D model with elliptical crack (Fig.3 left picture). Therefore, the 2D model of the creep crack propagation through the protective layer is not adequate and a 3D model is

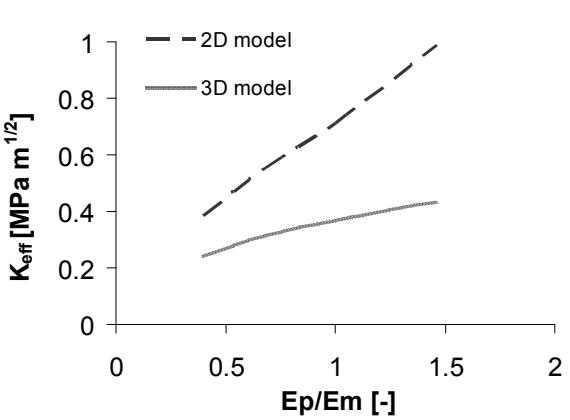


Fig. 4. K_{eff} dependence on E_p/E_m for three-layer pipe with cracked inner layer

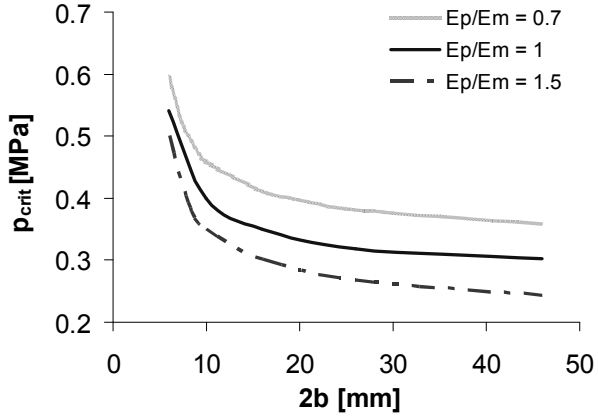


Fig. 5. Relation between p_{crit} for different crack length $2b$ (c/a = 1.2).

necessary. It is shown that the creep crack can be arrested at the interface, especially in a case where the main pipe material is tougher than the protective layer. In this case, the crack can propagate along the interface (see Fig.3) and the critical pressure for interface penetration decreases, see Fig.5. The value of the critical inner pressure causes crack propagation through the material interface given by the eq. (4). The influence of different material properties characterized by ratio E_p/E_m in relation to p_{crit} and crack length $2b$ is shown in Fig.5. In the case of a tough main pipe material ($E_p/E_m < 1$) the critical inner pressure is higher than for a homogenous case ($E_p/E_m = 1$).

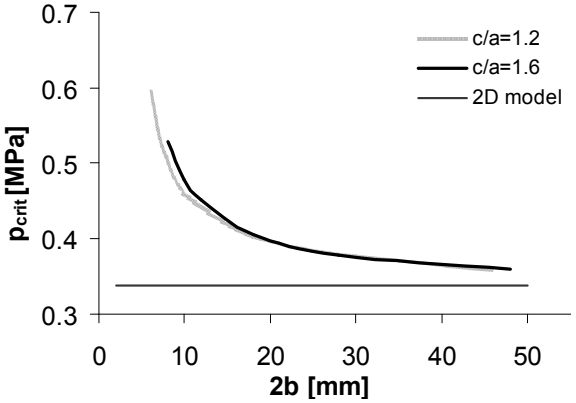


Fig. 6. Relation between p_{crit} for different crack length $2b$ ($E_p/E_m = 0.7$).

The dependency of p_{crit} on different crack lengths for an arrested crack at the material interface corresponding to $E_p/E_m = 0.7$ is shown in Fig. 6. The critical inner pressure p_{crit} which is necessary to apply for interface penetration by creep crack decreases with respect to the crack length. The limit value of p_{crit} is the value taken from a 2D solution under plain strain conditions. The different shapes of crack propagation along the interface expressed by c/a can be neglected, especially in the case of longer cracks.

The results obtained can be summarized by the following points:

- 2D description of the creep crack in the case of pipe structure is not sufficient.
- proper selection of the ratio E_p/E_m between Young's moduli of the main pipe and protective layer leads to better crack resistance of the interface.
- different crack shapes characterized by ratio c/a are important only for short cracks. For long cracks ($2b > 15$ mm) the value of p_{crit} is independent of the geometry of the elliptic part of the crack.
- the limit threshold value of p_{crit} leading to creep crack penetration of the main pipe corresponds to the 2D model.

Acknowledgement: This work was supported by grants 106/09/0279 and 106/09/H035 of the Czech Science Foundation and through the Specific academic research grant of the Ministry of Education, Youth and Sports of the Czech Republic provided to Brno University of Technology, Faculty of Mechanical Engineering.

References

[1] K.Y. Lin, J.W. Mar: International Journal of Fracture, Vol. 12 (1976), p. 451.

[2] S.A. Meguid, M. Tan, Z.H. Zhu: International Journal of Fracture, Vol. 73 (1995), p. 1.

[3] D.B. Bogy : International Journal of Fracture, Vol. 38 (1971), p. 911.

[4] V. Gupta, J. Yuan, D. Martinez: J. Am. Ceram. Soc., Vol. 76 (1993), p. 305.

[5] K. Kaddouri et al.: Computational Material Science, Vol. 35 (2006), p. 53.

[6] L. Marsavina, T. Sadowski : Computational Material Science, Vol. 44 (2009), p. 941.

[7] L. Náhlík et al.: Engineering Fracture Mechanics, Vol. 77 (2010), p. 2192.

[8] L. Náhlík, L. Šestáková, P. Hutař: Key Engineering Materials, Vol. 417-418 (2010), p. 301.

[9] P. Hutař et al.: Composite Structures, Vol. 92 (2010), p. 1120.

[10] L. Náhlík, L. Šestáková, P. Hutař: Computational Materials Science, Vol. 46 (2009), p. 614.

[11] Irwin, G.R., Journal of applied mechanics, Vol.24, pp. 361-364, 1957

[12] P. Hutař et al.: ANTEC 2009, ISBN: 1-61567-327- X, s. 2163-2168, 2009

[13] J. Menčík: Mechanics of components with Treated or coated surface, ISBN 0-7923-3700-X, 1996

© (2012) Trans Tech Publications, Switzerland
doi:10.4028/www.scientific.net/KEM.488-489.166

Effect of notched parameters on low cycle fatigue life of shaft under bending-torsional loading

Ping Ma[1], Youtang Li [2,a]

[1]College of Electrical and Information Engineering, Lanzhou University of Technology, Lanzhou 730050, China

[2]Key Laboratory of Digital Manufacturing Technology and Application, Ministry of Education, Lanzhou University of Technology, Lanzhou 730050, China

[a]liyt@lut.cn

Keywords: Low cycle fatigue, Medium carbon steel, Notched parameters, Bending-torsional loading

Abstract. A special clamp for fatigue of shaft under bending-torsion that used on the fatigue machine is designed and manufactured. For the medium carbon steel, the low-cycle fatigue experiments of shaft with annular notch under bending-torsion have been made on Shimadzu EHF-EM100kN high-frequency electro-hydraulic fatigue testing machine. Through experiments and analysis, the effects of tip radius, depth and open angle of notch on low cycle fatigue life of shaft with annular notch under bending-torsion are obtained. The method and results will play an important role on the fatigue life prediction and anti-fatigue design.

Introduction

The shafts are the typical parts in machine, which are mainly used to support transmission parts and transfer torque. There are many factors affect the fatigue life, which including the parameters of notch, size, heat treatment methods, loading frequency, stress wave, corrosion, high temperature and so on. In addition, the fatigue life is affected greatly by the installation conditions, boundary and lubricant conditions, environment and other factors. However, which are secondary factors in a number of affecting factors, have not been determined until now.

The shaft is used in engineering widely, such as machine tool, automobile, steamship and so on. The mathematical model of reliability design for fatigue life of shaft was set up by Y.Q.Sun by using combined stress method [1]. The mode of reliability optimal design of transmission shaft was set up by C.Su based on strength and torsional rigidity of transmission shaft [2]. The design of random fatigue of vehicular transmission shaft was studied by X.Chen [3]. There are many factors to affect the fatigue life of component. Therefore, it is very difficulty for determining a designed criterion exactly. A uniform model and fracture criteria of annularly notched shaft under bending [4] and an anti-fatigued criterion of annularly notched shaft on mechanical design [5] have been put forward, respectively. An assessment rule of fatigue life of shaft with a circumferential notch based on Corten-Dolan's theory and modified Miner's rule has been put forward [6], and the effect of supporting conditions [7] and wear [8] on fatigue life of shaft are studied, respectively. The effect of parameters of notch on high fatigue life of shaft has been calculated [9].

A special fatigue testing machine clamp for bending-torsion fatigue is designed at first. The low cycle fatigued experiments of shaft with notch under bending-torsion loading are made in Shimadzu EHF-EM100kN hydraulic-electric servo-pulser fatigue testing machine. The effect of tip radius, depth and open angle of notch on fatigue life of shaft with notch under bending-torsion are discussed by the experiments.

Test Specimen and Experimental Method

Test Specimen. The test specimen is shown in Fig.1, it is machined in lathe. The diameter of specimen is 2*b*, the tip radius of notch is ρ, depth of notch *t*, open angle of notch α.The material of test specimen is 45 medium carbon steel, it's σ_b=734Mpa, σ_s=468Mpa, and it is thermal refined. The chemical constitutions of 45 medium carbon steel are shown in Table 1.

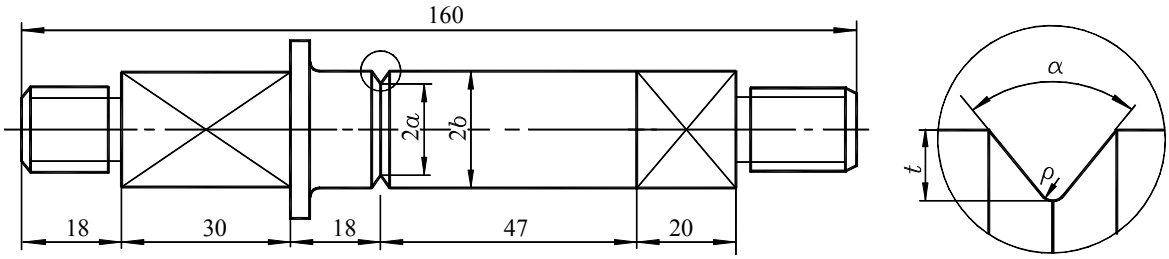


Fig.1 Geometrical figure and dimension of test specimen

Table 1 Chemical constitutions of 45 steel (%)

C	Si	Mn	P	S	Cr	Ni
0.45	0.20	0.59	0.04	0.04	0.25	0.25

Experimental method and Equipment. The special clamp and the Shimadzu EHF-EM100kN electric and hydraulic servo high frequency fatigue testing machine were used in the experiment. The experiments are made in room temperature. The maximum load is dynamically ± 100 kN, the maximum amplitude is ± 25 mm, and error of strain can be controlled within ± 0.001%. The testing equipment is controlled by computer and full-numerically measuring controlling mode with 32 bit processing device. The loading mode (level of stress, loading wave form, loading frequency) is automatically controlled by programs, the end data of intensity and deformation during loading process is automatically collected and stored in computer and can be taken out at any moment. The control software used for experiment is Gluon Testing, and the software for data processing of the experiment results is Gluon Data Processing.

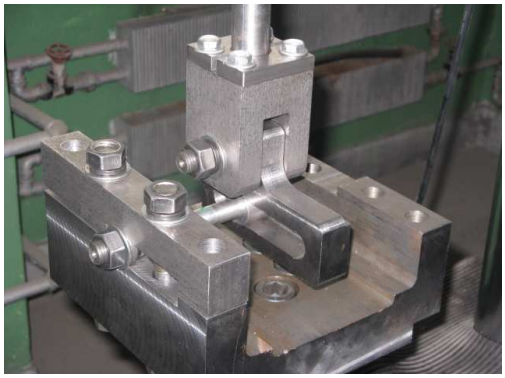


Fig.2 Special clamp

The special clamp for fatigue of shaft for bending-torsion fatigue that used on the fatigue machine is designed and manufactured that is shown in Fig.2. The sine wave of cyclic loading is chosen in the experiments. The transverse force can be expressed as $P=f(t)$, here, the cyclic stresses are affected by bending moment and torsional moment. The bending moment *M* and torsional moment *T* should be expressed as $M=f(t)l$ and $T=f(t)L$, where *l* and *L* are the distance of bending and torsion, respectively. The ratio of L/l is 11/9, the bending moment and torsional moment are 675N•m, 825N•m in the experiments.

Effect of Notched Parameters on Low Cycle Fatigue Life of Shaft

Effect of Tip Radius of Notch on Fatigue Life of Shaft. The relations between the fatigue life and ratio of diameter of shaft in different tip radius ρ of notch under bending-torsion are shown in Fig.3, in which the open angle of notch is 60^o. We can know from Fig.3 that the fatigue life will increase with the increase of the tip radius of notch under the same ratio of diameter, which shows that the stress concentration factor is changed and the fatigue life is shorten for the small tip radius of notch. The smaller the tip radius of notch is, the shorter the fatigue life of shaft is. The smaller the ratio of diameter a/b is, the larger the effect of tip radius of notch on fatigue life is.

We can know from Fig.3 also that the fatigue life will increase with the increase of the ratio of diameter (*a/b*) under the same tip radius of notch. The increase is linear nearly when *a*/*b* is larger then 0.85, and it is nonlinear when 0.85<*a*/*b*<0.95. The fatigue life is in the maximum when *a*/*b*=0.90 and ρ=2.0mm. Therefore, there is greater effect of tip radius of notch on fatigue life of shaft. For improving the fatigue life of shaft, the tip radius ratio of notch should be larger.

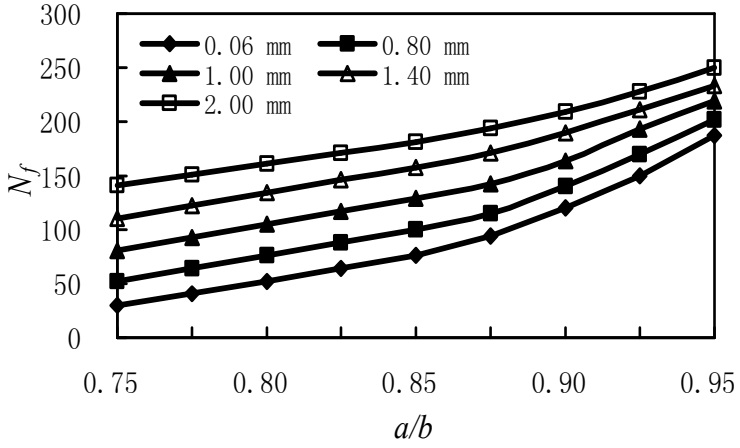


Fig.3 Relations of fatigue life vs tip radius of notch

Effect of Depth of Notch on Fatigue Life of Shaft. The relations between the fatigue life and the depth of notch under different tip radius ρ of notch under bending-torsion are shown in Fig.4, in which the open angle of notch is 60^o. We can know from Fig.4 that the fatigue life will decrease with the increase of the depth of notch (*t*/2*b*) under the same tip radius of notch. The decrease is linear nearly when *a*/*b* is larger then 0.0875, and it is nonlinear when 0.0875>*t*/2*b*>0.0125. The results show that the anti-fatigue strength of structure is changed with the depth of notch. The deeper the depth of notch is, the lower the anti-fatigue strength is for the same tip radius of notch, which shows that the deeper the depth of notch is, the larger the effect of tip radius of notch on fatigue life is.

Therefore, for improving the fatigue life of shaft, the depth of notch should be smaller under all tip radius of notch.

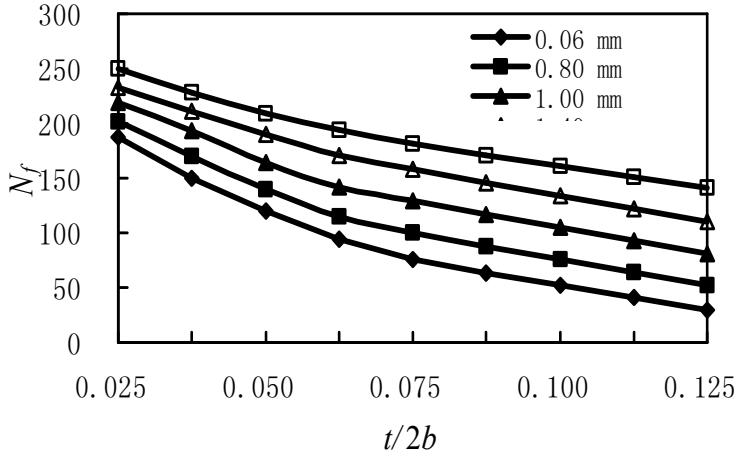


Fig.4 Relations of fatigue life vs depth of notch in different tip radius of notch

Effect of Open Angle of Notch on Fatigue Life of Shaft. The relations between the fatigue life and the open angle of notch in different tip radius of notch under bending-torsion are shown in Fig.5, in which the ratio of diameter of shaft, *a/b*, is 0.85. We can know from Fig.5 that the fatigue life will increase with the increase of the open angle of notch (α). The increase is linear nearly for all tip radius of notch, and the smaller the tip radius of notch is, the larger the slope of line is. Therefore, the effect of open angle of notch on fatigue life in smaller tip radius of notch is greater then that in greater tip radius of notch. The fatigue life of shaft is constant nearly when the tip radius of notch is 2.0 mm.

In engineering design, the open angle of notch is not important when the tip radius is larger than 2.0mm, and it should be considered when the tip radius of notch is very small.

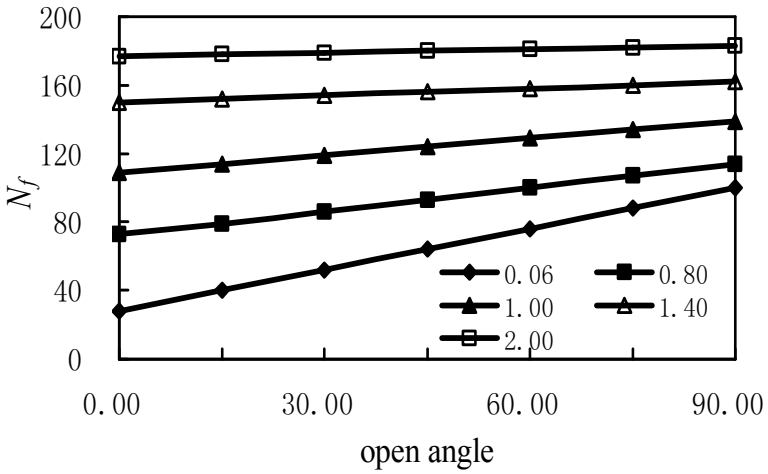


Fig.5 Relations of fatigue life vs open angle of notch in different tip radius of notch

Conclusion

1) The fatigue life of shaft under bending-torsion will increase with the increase of the tip radius of notch. The smaller the tip radius of notch is, the shorter the fatigue life of shaft is. The smaller the ratio of diameter *a/b* is, the larger the effect of tip radius of notch on fatigue life is.

2) The fatigue life of shaft under bending-torsion will decrease with the increase of the depth of notch diameter (*t*/2*b*). The deeper the depth of notch is, the larger the effect of tip radius of notch on fatigue life is. The depth of notch is the main factor to affect the fatigue life of shaft when the tip radius of notch is constant.

3) The effect of open angle of notch on fatigue life is not obvious. The effect of open angle of notch on fatigue life in smaller tip radius of notch is greater then that in greater tip radius of notch. The fatigue life of shaft is constant nearly when the tip radius of notch is 2.0 mm. is.

Acknowledgment: The work is supported by Funds of Ministry of Education, China (208152)

References

[1] Y.Q.Sun: Machinery Design & Manufacture Vol.15 No.8 (2006), p.39

[2] C.Su: Journal of Machine Design and Research Vol.14 No.1 (1997), p.35

[3] X. Chen, D.S.Chen: Journal of Machine Design Vol.19 No.6 (2002), p.50

[4] Y.T.Li, Z.Y.Rui and C.F.Yan: Key Engineering Materials Vol.321-323 (2006), p.751

[5] Y.T.Li, P.Ma and C. F. Yan: Key Engineering Materials Vol.321-323 (2006), p.755

[6] Y.T.Li, P.Ma and J.T.Zhao: Materials Science Forum Vol.561-565 (2007), p. 2253

[7] Y.T.Li, P.Ma, and M. Song: Key Engineering Materials Vol. 385-387 (2008), p.109

[8] Y.T.Li, Z.Y.Rui and C.F.Yan: Key Engineering Materials Vols. 417-418 (2009), p.469

[9] Y.T.Li, B.Chen and C.F.Yan: Materials Science Forum Vols. 638-642 (2009), p.3864

© (2012) Trans Tech Publications, Switzerland
doi:10.4028/www.scientific.net/KEM.488-489.170

Investigation of Eigen-values for Matrix Cracks of Two Materials

Youtang Li[a], Ruifeng Wang

Key Laboratory of Digital Manufacturing Technology and Application, Ministry of Education, Lanzhou University of Technology, Lanzhou 730050, China

[a]liyt@lut.cn

Keywords: Matrix crack, Eigen-values, Eigen-equation, Stress field, Fracture design

Abstract: The eigen-values problem of matrix cracks is studied in this paper. The stress field and displacement field of plane matrix crack is setup at first. The eigen-equation of matrix cracks is founded on the basis of the stress field and displacement field. The factors to affect the eigen-values are discussed. The effect of shearing modulus and Poisson ratio of matrix material and attaching material on eigen-values are analyzed. The results show that the bigger shearing modulus of material should be selected for attaching material and the shearing modulus of attaching material should bigger than that of matrix material in fracture design.

Introduction

Inverse problem in fracture subject has not only scientific value but also wide prospects of application in industry [1, 2]. Although there are some achievements of inverse problem in fracture mechanics [3, 4], the fracture design needs to study the appearance and action of a propagating crack and it is still in the early stage. In the applying research of crack theory, how to make crack quickly is a key problem that meets demand high efficient production in engineering. The ways to manufacture artificial crack in common using such as turning, milling etc. can not satisfy with the efficiency demands of modern production at present. Using matrix cracks that formed with different material should be a feasible way to achieve efficient production.

The study of interface crack is a main point of fracture theory and the research of matrix crack that can be used in active fracture has been commenced. But most of them are based on passive avoiding crack and limited to ceramic matrix composites [5, 6]. The stress field and displacement field of plane matrix crack is setup at first in this paper. The eigen-equation of matrix cracks is founded on the basis of the stress field and displacement field. The factors to affect the eigen-values are discussed. The effect of shearing modulus and Poisson ratio of matrix material and attaching material on eigen-values are analyzed. The result lays a theoretic and applied foundation for practical engineering application.

Singularity Stress Field of Matrix Crack

Two plates of elastic moduli E_1 and E_2, Poisson's radio v_1 and v_2 are perfectly joined along their common interface 1 and interface 2 (Fig.1). Material 1 is attaching material and material 2 is matrix material. There is a crack perpendicular to the interface in material 1. The crack tip is exactly at the interface of the two plates. Following the approach of Zak and Williams [7], the Ariy stress function $\Phi(r,\theta)$ which satisfied the biharmonic equation

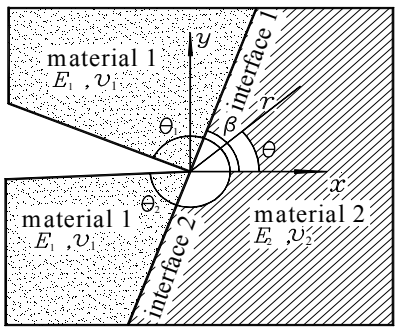


Fig.1 Geometry of bi-material

$$\nabla^2\nabla^2\Phi = \left(\frac{\partial^2}{\partial r^2} + \frac{1}{r}\frac{\partial}{\partial r} + \frac{1}{r^2}\frac{\partial^2}{\partial \theta^2}\right)\Phi = 0 \tag{1}$$

is assumed to take the form

$$\Phi(r,\theta) = r^{\lambda+1}F(\theta) = r^{\lambda+1}a\sin(\lambda+1)\theta + b\cos(\lambda+1)\theta + c\sin(\lambda-1)\theta + d\cos(\lambda-1)\theta \tag{2}$$

The stress and displacement components in polar coordinate are given by

$$\sigma_r = r^{\lambda-1}[F''(\theta)+(\lambda+1)F(\theta)] \qquad \sigma_\theta = r^{\lambda-1}[\lambda(\lambda+1)F(\theta)] \qquad \tau_{r\theta} = -\lambda r^{\lambda-1}F'(\theta) \tag{4}$$

$$u_r = r^{\lambda}\{-(\lambda+1)F(\theta)+(\lambda\omega)^{-1}\ [F''(\theta)+(\lambda+1)^2F(\theta)]\}/2\mu$$

$$u_\theta = -r^{\lambda}\{F'(\theta)+[\lambda\omega(\lambda-1)]^{-1}\ [F'''(\theta)+(\lambda+1)^2F'(\theta)]\}/2\mu \tag{5}$$

where μ is the shear modulus and ω=1+ν for plane stress and ω=1/(1-ν) for plane strain. The stress function Φ_1 and Φ_2 in material 1 and 2 have the form of eq.(2) with different values of coefficients a, b, c and d. However, the eigen-values for material 1 and material 2 must be equal in order to assure continuity of displacement along the interface. The boundary conditions of the bi-material plate comply that the normal stress σ_θ and the shear stress $\tau_{r\theta}$ vanish along both sides of the matrix crack (θ=θ_1 and θ=θ_2), the normal stress σ_θ and the shear stress $\tau_{r\theta}$ and the displacement u_r and u_θ are continuous along the interface. If we consider a linear symmetrical matrix crack (θ_1=θ_2=π and φ=$\pi/2$), a series equations for λ can be obtained from the boundary conditions in conjunction with equations (4) and (5) as following.

$$\begin{aligned}
&a_1\sin(\lambda_n+1)\theta_1 + b_1\cos(\lambda_n+1)\theta_1 + c_1\sin(\lambda_n-1)\theta_1 + d_1\cos(\lambda_n-1)\theta_1 = 0\\
&(\lambda_n+1)[a_1\cos(\lambda_n+1)\theta_1 - b_1\sin(\lambda_n+1)\theta_1] + (\lambda_n-1)[c_1\cos(\lambda_n-1)\theta_1 - d_1\sin(\lambda_n-1)\theta_1] = 0\\
&a_1\sin(\lambda_n+1)\theta_2 + b_1\cos(\lambda_n+1)\theta_2 + c_1\sin(\lambda_n-1)\theta_2 + d_1\cos(\lambda_n-1)\theta_2 = 0\\
&(\lambda_n+1)[a_1\cos(\lambda_n+1)\theta_2 - b_1\sin(\lambda_n+1)\theta_2] + (\lambda_n-1)[c_1\cos(\lambda_n-1)\theta_2 - d_1\sin(\lambda_n-1)\theta_2] = 0\\
&a_1\sin(\lambda_n+1)\varphi + b_1\cos(\lambda_n+1)\varphi + c_1\sin(\lambda_n-1)\varphi + d_1\cos(\lambda_n-1)\varphi -\\
&a_2\sin(\lambda_n+1)\varphi - b_2\cos(\lambda_n+1)\varphi - c_2\sin(\lambda_n-1)\varphi - d_2\cos(\lambda_n-1)\varphi = 0\\
&(\lambda_n+1)[a_1\cos(\lambda_n+1)\varphi - b_1\sin(\lambda_n+1)\varphi] + (\lambda_n-1)[c_1\cos(\lambda_n-1)\varphi - d_1\sin(\lambda_n-1)\varphi] -\\
&(\lambda_n+1)[a_2\cos(\lambda_n+1)\varphi - b_2\sin(\lambda_n+1)\varphi] - (\lambda_n-1)[c_2\cos(\lambda_n-1)\varphi - d_2\sin(\lambda_n-1)\varphi] = 0\\
&a_1\sin(\lambda_n+1)\varphi_1 + b_1\cos(\lambda_n+1)\varphi_1 + c_1\sin(\lambda_n-1)\varphi_1 + d_1\cos(\lambda_n-1)\varphi_1 -\\
&a_2\sin(\lambda_n+1)\varphi_1 - b_2\cos(\lambda_n+1)\varphi_1 - c_2\sin(\lambda_n-1)\varphi_1 - d_2\cos(\lambda_n-1)\varphi_1 = 0\\
&(\lambda_n+1)[a_1\cos(\lambda_n+1)\varphi_1 - b_1\sin(\lambda_n+1)\varphi_1] + (\lambda_n-1)[c_1\cos(\lambda_n-1)\varphi_1 - d_1\sin(\lambda_n-1)\varphi_1] -\\
&(\lambda_n+1)[a_2\cos(\lambda_n+1)\varphi_1 - b_2\sin(\lambda_n+1)\varphi_1] - (\lambda_n-1)[c_2\cos(\lambda_n-1)\varphi_1 - d_2\sin(\lambda_n-1)\varphi_1] = 0
\end{aligned} \tag{6}$$

In order for the system of the homogeneous equation to have a solution for the unknown a, b, c and d, the determinant of the coefficients of the unknowns should be zero. This condition leads to the following equation for the determination of λ by discarding the roots λ=0, λ=1

$$2\alpha\cos\pi\lambda - \beta\lambda^2 - \gamma = 0 \tag{7}$$

where

$$\alpha = (m+\kappa_2)(1+m\kappa_1), \quad \beta = 4(m+\kappa_2)(m-1),$$
$$\gamma = (1-m)(m+\kappa_2) + \alpha - m(1+\kappa_1)(1+m\kappa_2), \qquad m = \mu_2/\mu_1 \tag{8}$$

where $\kappa_{1,2} = (3-\nu_{1,2})/(1+\nu_{1,2})$ for plane stress and $\kappa_{1,2} = 3-4\nu_{1,2}$ for plane strain. Restricting attention to the singular part and the leading nonsingular, the near field solution reads

$$\begin{aligned}
\sigma_{ir} &= Q_1 r^{\lambda_1-1} f_{1r}(\lambda_1,\theta) + Q_2 r^{\lambda_2-1} f_{2r}(\lambda_2,\theta) + Q_3 f_{3r}(1,\theta)\\
\sigma_{i\theta} &= Q_1 r^{\lambda_1-1} f_{1\theta}(\lambda_1,\theta) + Q_2 r^{\lambda_2-1} f_{2\theta}(\lambda_2,\theta) + Q_3 f_{3\theta}(1,\theta)\\
\tau_{ir\theta} &= Q_1 r^{\lambda_1-1} f_{1r\theta}(\lambda_1,\theta) + Q_2 r^{\lambda_2-1} f_{2r\theta}(\lambda_2,\theta) + Q_3 f_{3r\theta}(1,\theta)
\end{aligned} \tag{9}$$

$$u_{ir} = Q_1 r^{\lambda_1} g_{1r}(\lambda_1,\theta)/2\mu_i + Q_2 r^{\lambda_2} g_{2r}(\lambda_2,\theta)/2\mu_i ; \quad u_{i\theta} = Q_1 r^{\lambda_1} g_{1\theta}(\lambda_1,\theta)/2\mu_i + Q_2 r^{\lambda_2} g_{2\theta}(\lambda_2,\theta)/2\mu \quad (10)$$

In the above expressions i=1, 2 correspond to the material 1 and material 2 shown in Fig.1, λ_1 and λ_2 are two orders of singularity.

Eigen-values of Matrix Cracks

For matrix cracks problem, we can know from eq. (7) that the eigen-values are affected by coefficients α, β, γ. The coefficients α, β, γ have relation to shearing modulus and Poisson's radios of two materials. Therefore, the eigen-values are affected by shearing modulus and Poisson's radios. Attaching material is alloy steel and it's shearing modulus is 79 GPa and Poisson's radios is 0.28. Matrix material is grey pig iron and it's shearing modulus is 44 Gp and Poisson's radios is 0.25. The eigen-values of matrix cracks are determined by the expansion of Taylor series and the QR method of real number algebraic equation.

Effect of Poisson's Radios of Matrix Material to Eigen-values. For certain material 1, Fig.2 and Fig.3 show the effect of v_2 on the eigen-values, λ_1 and λ_2, respectively. It is clear that the eigen-value λ_1 is increased and λ_2 is decreased when v_2 is increased. When v_2 increase from 0.14 to 0.44, λ_1 increase from 0.342 to 0.356, increasing 4.338% only and λ_2 decrease from 1.200 to1.192, decreasing 0.629% only.

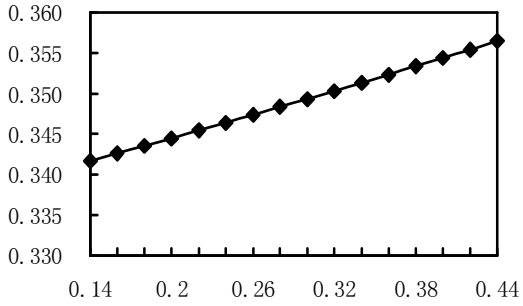


Fig.2 The effect of v_2 on λ_1

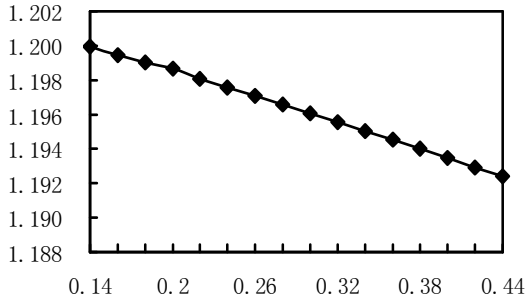


Fig.3 The effect of v_2 on λ_2

Effect of Shearing Modulus of Matrix Material to Eigen-values. For certain material 1, Fig.4 and Fig.5 show the effect μ_2 on the of eigen-values, λ_1 and λ_2, respectively. We can know from Fig.4 and Fig.5 that the eigen-value λ_1 and λ_2 are increased when μ_2 is increased. When μ_2 increase from 1 GPa to 100 GPa, λ_1 increase from 0 to 0.525 and λ_2 increase from 1 to 1.559. It is thus clear that the shearing modulus of attaching material should bigger in the application of fracture design.

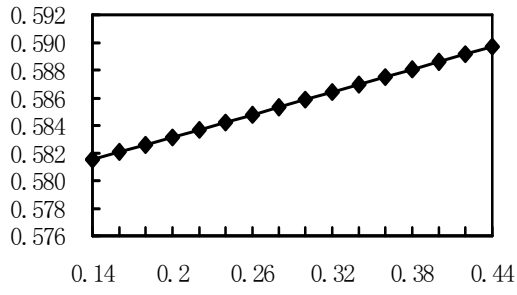


Fig.4 The effect of μ_2 on λ_1

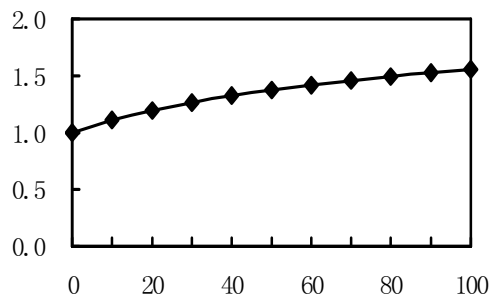


Fig.5 The effect of μ_2 on λ_2

Effect of Poisson's radios of attaching material to eigen-values. For certain material 2, Fig.6 and Fig.7 show the effect of v_1 on the eigen-values, λ_1 and λ_2, respectively. We can know from Fig.6 and Fig.7 that the eigen-value λ_1 and λ_2 are increased when v_1 is increased. When v_1 increase from 0.14 to 0.42, λ_1 increase from 0.582 to 0.560, and λ_2 increase from 1.687 to 1.793, increasing 6.3% only.

Effect of Shearing Modulus of Attaching Material to Eigen-values. For certain material 2, Fig.8 and Fig.9 show the effect of μ_1 on the eigen-values, λ_1 and λ_2, respectively. We can know from Fig.8 and Fig.9 that the eigen-value λ_1 and λ_2 are decreased when μ_1 is increased. When μ_1 increase from 10 GPa to 100 GPa, λ_1 decrease from 0.652 to 0.409, decreasing 59.6% and λ_2 decrease from 1.888

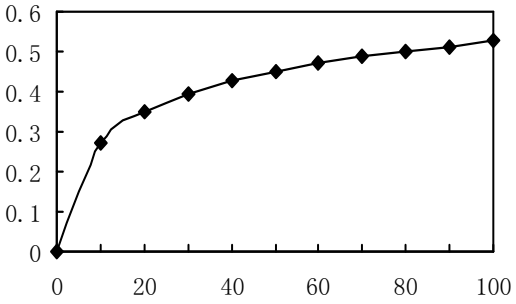


Fig.6 The effect of v_1 on λ_1

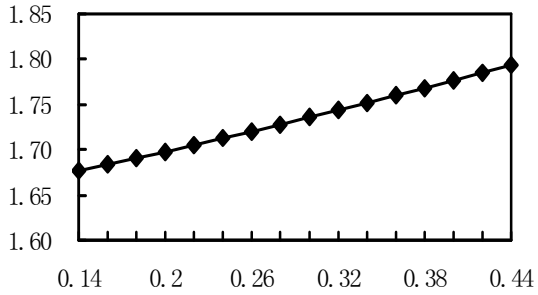


Fig.7 The effect of v_1 on λ_2

to 1.296, decreasing 45.6%. It is thus clear that the shearing modulus of matrix material should smaller than attaching material in the application of fracture design.

Conclusions

The stress field of matrix cracks is affected by eigen-values. For determining the stress field, the eigen-values of matrix cracks must be solved at first. The eigen-values of matrix cracks can be determined by the expansion of Taylor series and the QR method of real number algebraic equation. The eigen-values are affected by shearing modulus and Poisson's radios of attaching material and matrix material. The effect of Poisson's radios is not quite and the effect of shearing modulus is quite. The bigger shearing modulus of material should be selected for attaching material in fracture design, and the shearing modulus of attaching material should bigger than that of matrix material.

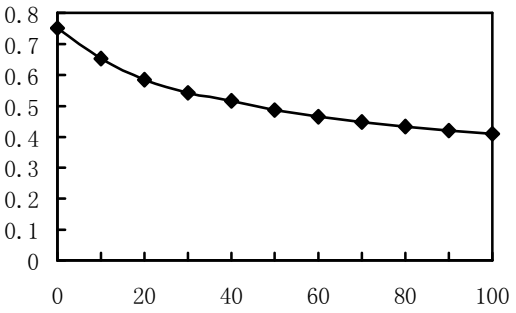


Fig.8 The effect of μ_1 on λ_1

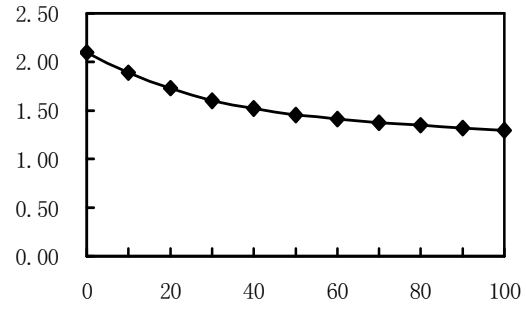


Fig.9 The effect of μ_1 on λ_2

References

[1] Y.Li, Y.Wei & Y.Hou. *Key Engineering Material Vols.*183 (2000) pp.319-324

[2] B.J.Zhao, Q.T.Wei, F.Y.Lang. *Int. J. Fracture.* 55, R43~R46(1990)

[3] N.Tada, T.Kitamura, R.Ohtani. *Engng Frac. Mech*.52, 1015~1026(1995)

[4] D.J.Herrmann & B.M.Hillberry. *Engng Frac. Mech*.56, 711~726 (1997)

[5] F.G.Yuan & S.Yang. *Int. J. Fracture*, 103, 71~84 (2000)

[6] F.O.Riemelmoser & R.Pippan. *Int. J. Fracture*, 103, 397~418 (2000)

[7] A.R.Zak & M.L.Williams. *J. Appl. Mech.* 30, 142-143 (1963)

© (2012) Trans Tech Publications, Switzerland
doi:10.4028/www.scientific.net/KEM.488-489.174

Dimensionless Stress Intensity Factors of An Annular Notched Shaft

Bo Chen, Li Youtang[a]

Key Laboratory of Digital Manufacturing Technology and Application, Ministry of Education, Lanzhou University of Technology, Lanzhou 730050, China

[a]liyt@lut.cn

Keywords: Annular notched shaft, Dimensionless stress intensity factors, Stress concentration factor, V-notch, U-notch, Stress field

Abstract: The tip radius ρ, depth t and field angle α of notch and the geometrical sizes a and b of shaft are looked as descriptive parameters in the annular notched shaft. Taken the crack, blunt crack and notch as breach, the stress field and displacement field near the tip of breach which serve dimensionless factor $f_\alpha(a/b)$ as descriptive parameter are obtained. The effects of parameters ρ, t and α to $f_\alpha(a/b)$ are analyzed. The connections between stress intensity factor of crack and stress concentrator factor of notch, between sharp V-notch and crack, between V-notch and U-notch have been founded.

Introduction

In traditional strength theory, the stress near the tip of notch is calculated usually by means of stress concentration factor for notched component, and the allowable stress is used for the basis design. The stress intensity factor is used to indicate the stress field near the tip of the crack in fracture mechanics. The fracture toughness of material is used for fracture criteria in safety design. The stress intensity factor of crack and the stress concentration factor of notch are independent at present. It is feasible that the strength is designed by means of stress concentration criterion in safety design because the tip radius of notch is usually not small. In fracture design, for increasing the intensity of stress field near notch tip, the tip radius of notch should as small as possible. The notch in fracture design is similar with blunt crack and blunt crack is situated between crack and notch. It is necessary that crack, blunt crack and notch be described in the same way.

The stress field and displacement field of blunt crack in two-dimension and three-dimension were obtained [1-3]. But there are no connected factor between the stress intensity factor of crack and the stress concentration factor of notch. The information in more detail about the connected factor among crack, blunt crack and notch have not been found at present. Therefore, there are many difficulties in fracture design of crack technique. For overcoming the difficulties in fracture design, crack, blunt crack and notch are called breach and the stress field of the shaft with annular breach will be given by means of dimensionless factor $f_\alpha(a/b)$ in this paper. The connection between the stress intensity factor of crack and the stress concentration factor of notch, between sharp V-notch and crack, between V-notch and U-notch have been set up. The dimensionless factors $f_\alpha(a/b)$ are studied, and the informations about brittle fracture design are discussed in detail.

The Described Parameters and the Forms of Breach

The stress concentration factor of notch that is described through tip radius ρ,depth t and field angle α of notch and parameters a and b of the shaft is very important in safety design of component. On the other hand, intensity of stress field at crack tip is usually measured by stress intensity factor.

The stress intensity factor is judged by geometric parameters a and b of the annular breach shaft. In fact, the stress field near the tip of breach is affected by the field angle α of breach. If the breach (crack, blunt crack and notch) is described through tip radius ρ,depth t and field angle α of breach and the geometrical sizes a and b of the shaft. The forms of breach listed in Table 1.

Table 1 The forms of breach

t=0			Smooth body
$t\leq\rho$			An arc notch
$t>\rho$	$\rho\rightarrow 0$	$\alpha=0^o$	Linear crack
		$\alpha\neq 0^o$	Sharp V-notch
	$\rho=\varepsilon$ (ε is small)	$\alpha=0^o$	Blunt crack
		$\alpha\neq 0^o$	V-blunt crack
	$\rho=c$(c is not small)	$\alpha=0^o$	U-notch

The Stress and Displacement Fields near the Tip of Breach

If the surface of breach are plane except the tip part and α=0, the stress and displacement fields near breach in three-dimension can be obtained [3]. If the facts that the stress intensity factor of annular crack and sharp V-notch are described through dimensionless factor $f(a/b)$ [4] and the stress and displacement fields near the breach tip are affected by field angle α have been taken into account, for the annular breach shaft showing in Fig.1, the stress and displacement fields can be expressed as following

$$\sigma_{zz}=\frac{\sigma}{4}\sqrt{\frac{b}{2r}}f_\alpha(a/b)\left(5\cos\frac{\theta}{2}-\cos\frac{5\theta}{2}+\frac{2\rho}{r}\cos\frac{3\theta}{2}\right)$$

$$\sigma_{nn}=\frac{\sigma}{4}\sqrt{\frac{b}{2r}}f_\alpha(a/b)\left(3\cos\frac{\theta}{2}+\cos\frac{5\theta}{2}-\frac{2\rho}{r}\cos\frac{3\theta}{2}\right)$$

$$\sigma_{uu}=2\mu\sigma\sqrt{\frac{b}{2r}}f_\alpha(a/b)\cos\frac{\theta}{2}\qquad \sigma_{zu}=\sigma_{nu}=0 \tag{1}$$

$$u_z=\frac{\sigma}{4G}\sqrt{\frac{rb}{2}}f_\alpha(a/b)\left[(7-8\mu)\sin\frac{\theta}{2}-\sin\frac{3\theta}{2}+\frac{2\rho}{r}\sin\frac{\theta}{2}\right]$$

$$u_n=\frac{\sigma}{4G}\sqrt{\frac{rb}{2}}f_\alpha(a/b)\left[(5-8\mu)\cos\frac{\theta}{2}-\cos\frac{3\theta}{2}+\frac{2\rho}{r}\cos\frac{\theta}{2}\right]\qquad u_u=0 \tag{2}$$

where $f_\alpha(a/b)$ is dimensionless stress intensity factor near breach tip. For mode I problem, the effect of σ_{zz} is maximum, so we discuss the first formula of eq.(1), when $\rho\rightarrow 0$, this formula will be

$$\sigma_{zz}=\sigma\sqrt{b/r}f_\alpha(a/b)\cos\frac{\theta}{2}\left(1+\sin\frac{\theta}{2}\sin\frac{3\theta}{2}\right) \tag{3}$$

When ρ is a limited value which is not small, the term of $2\rho/r\ f(\theta)$ not only affect the main queer term, but have the same level of amount with the main term. In the tip of breach, there is

$$\sigma_{zz\max}=2\sigma\sqrt{b/\rho}f_\alpha(a/b)=k_{t\alpha}\sigma \tag{4}$$

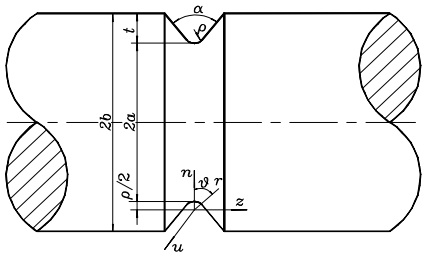


Fig. 1 Annular breach and it's descriptive parameters

where $k_{t\alpha}=2\sqrt{b/\rho}f_\alpha(a/b)=\sigma_{z\max}/\sigma$ is the stress concentration factor of V-notch. The dimensionless factor $f_\alpha(a/b)$ of an annular notched shaft can be shown as following

$$f_\alpha(a/b)=\sigma_{z\max}/\sigma\sqrt{\rho/b} \tag{5}$$

Dimensionless Factor of an Annular Notched Shaft

For determining the effect of ρ, t and α of breach on dimensionless factor, the numerical results of $f_\alpha(a/b)$ in different ρ/b,a/b and α have been calculated with Boundary Element Method, For the convenience of discussing, the dimensionless factor of notch is write as $f(a/b)$ when [ ] and the dimensionless factor of crack is written as $f_c(a/b)$.

The Effects of ρ and a/b on Dimensionless Factor. If the annular breach shaft is in tension, $\sigma = P/\pi a^2$, when [ ], the dimensionless factor can be written as following

$$f(a/b) = \frac{\pi a^2 \sigma_{\max}}{2P}\sqrt{\frac{\rho}{B}} \tag{6}$$

The numerical results of $f(a/b)$ in tension with ρ/b and a/b when field angles $\alpha = 0^o$ are shown in Fig.2. If the annular breach shaft is in bending, $\sigma = 4M/\pi a^2$, when $\alpha = 0^o$, the dimensionless factor can be written as following

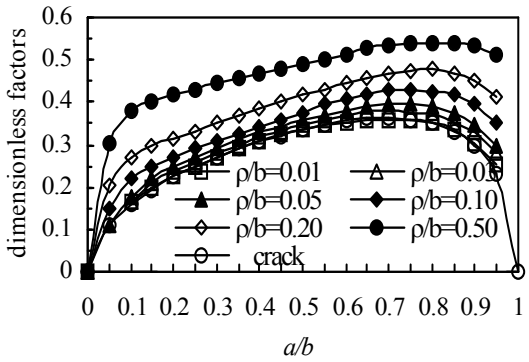


Fig. 2 $f(a/b)$ in tension with ρ/b and a/b

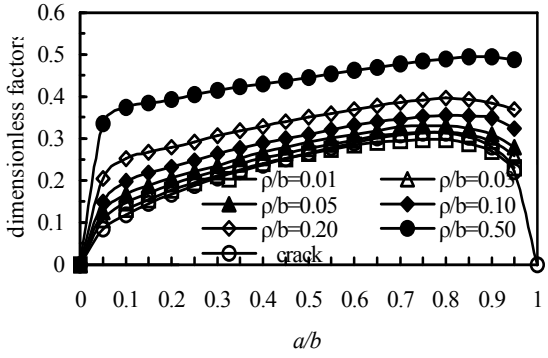


Fig. 3 $f(a/b)$ in bending with ρ/b and a/b

$$f(a/b) = \frac{\pi a^3 \sigma_{\max}}{8M}\sqrt{\frac{\rho}{b}} \tag{7}$$

The numerical results of $f(a/b)$ in bending with ρ/b and a/b when field angles $\alpha = 0^o$ are shown in Fig.3. We can know from Fig.2 and Fig.3 that the $f(a/b)$ of breach which are calculated through BEM and $f_c(a/b)$ of crack which are given by [4,5] are roughly the same even $f(a/b)$ are smaller than $f_c(a/b)$ when ρ/b is very small. It is inappropriate that the traditional theory of stress concentration be used in these conditions. The theory of stress intensity factor should be used when ρ is very small. Notch can be taken for blunt crack when ρ/b is small and crack can be regarded as the limit of notch. In these conditions, the fracture toughness of material should be the fracture criteria in safety design fracture design.

The Effect of Field Angle α on Dimensionless Factor. For the tension problem, Fig.4 and Fig.5 show the numerical results of $f_\alpha(a/b)$ in different α when ρ/b =0.01 and ρ/b =0.1, respectively. For the bending problem, Fig.6 and Fig.7 show the numerical results of $f_\alpha(a/b)$ in different α when ρ/b =0.01 and ρ/b =0.1, respectively.

Figs 4-7 indicate that either for tension or bending, the smaller ρ/b, the greater the effect of field angle α to dimensionless factor $f_\alpha(a/b)$. When α=60^o, the values of different field angle α be obtained by the following equation.

$$f_\alpha(a/b) = \tfrac{1}{2}\sqrt{\tfrac{\rho}{b}} + \left[f(a/b) - \tfrac{1}{2}\sqrt{\tfrac{\rho}{b}}\right] \times \left[1 - \left(\frac{\alpha}{180^o}\right)^{1+2.4\sqrt{\rho/t}}\right] \tag{8}$$

Conclusions

If the tip radius ρ, depth t and field angle α of breach and the geometrical sizes a and b are looked on as descriptive parameters in the annular breach shaft, every breach forms, e.g. crack, blunt crack, V-notch and U-notch etc. can be described. The dimensionless factor $f_\alpha(a/b)$ is taken as descriptive parameter, the stress and displacement fields of crack, blunt crack and notch have the same formulas. When $\rho \to 0$, it is the problem of mode I crack. When ρ is a limited value, it is the problem of stress concentration. There are connections between stress intensity factor of crack and stress concentration factor of notch, sharp V-notch and crack, V-notch and U-notch. Dimensionless factor $f_\alpha(a/b)$ is the function of tip radius ρdepth t and field angleα. Whenρ/ b is smaller than 0.01, the dimensionless factor $f_\alpha(a/b)$ of notch are similar with crack. Field angle α affect $f_\alpha(a/b)$. The smaller the tip radius ρ, the greater the effect of field angle α to dimensionless factor $f_\alpha(a/b)$.

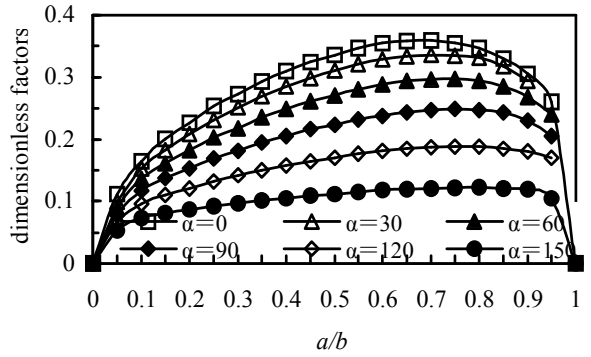


Fig. 4 $f_\alpha(a/b)$ in tension with□when ρ/b=0.01

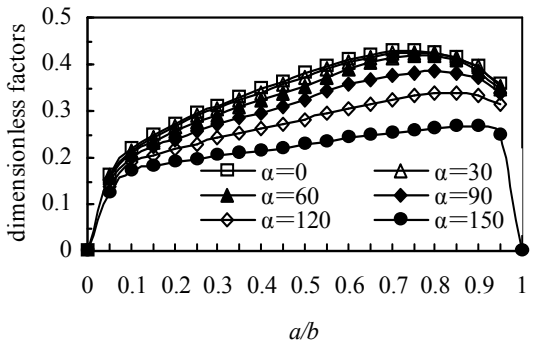


Fig. 5 $f_\alpha(a/b)$ in tension with α when ρ/b=0.1

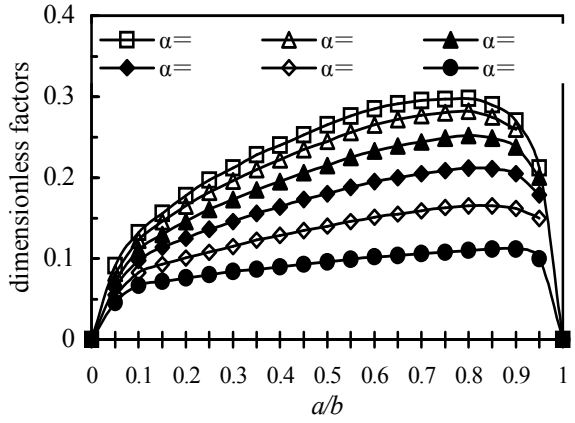


Fig. 6 $f_\alpha(a/b)$ in bending with α when ρ/b=0.01

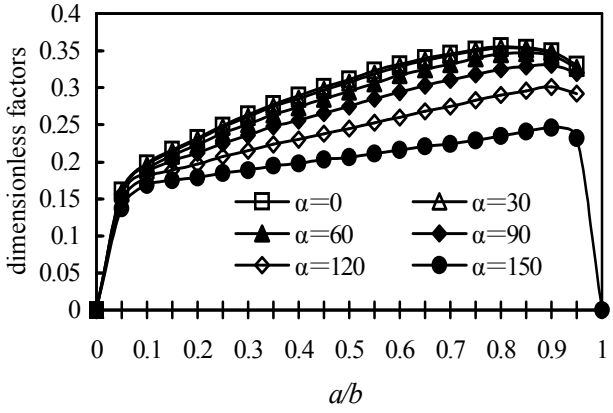


Fig. 7 $f_\alpha(a/b)$ in bending with α when ρ/b=0.1

References

[1] M Careger, P.C Paris. *Int. J. Fracture*, 3 (1967) p.247

[2] Z.B Kuang. *Engng. Fracture. Mech.* 1 (1982) p.19

[3] Y.Y Zhang. in: *The collection of 7th National Fracture Academi* (Huazhon University of Science and Technology Press. Wuhan, 1993, P.40 (in Chinese)

[4] China Research Institute of Aeronautics, *Stress intensity factor handbook* (Science press, Beijing 1981) (in Chinese)

[5] Y.Murakami. *Stress intensity factor handbook* (Pergumon Press, New York 1989)

[6] A.B.Verkhovsky. *The determination of stress for the dangerous section of complicated shape part* (Chinese Industry Press, Beijing 1962) (in Chinese)

[7] H.Z Neuber. *Stress concentration* (Science press, Beijing 1958) (in Chinese)

[8] H. Li. *Fracture Mechanics* (Shandong Science and Technology Press, China 1980)

[9] R.E.Peterson. *Stress concentration design factor* (John Wiley & Sons Inc. New York 1953)

© (2012) Trans Tech Publications, Switzerland
doi:10.4028/www.scientific.net/KEM.488-489.178

Fatigue crack shape prediction based on the stress singularity exponent

Pavel Hutař[1, a], Martin Ševčík[1,2,b] Luboš Náhlík[1,2,c] and Zdeněk Knésl[1,d]

[1]Institute of Physics of Materials, Žižkova 22, 616 62 Brno, Czech Republic

[2]Brno University of Technology, Technická 2, 616 69 Brno, Czech Republic

[a]hutar@ipm.cz, [b]sevcik@ipm.cz [c]nahlik@ipm.cz, [d]knesl@ipm.cz

Keywords: stress singularity exponent, crack front curvature, vertex singularity, free surface effect

Abstract: In many industrial applications it is necessary to predict fatigue lifetime of the structures where the stress field near the crack front have a three-dimensional nature. Due to the existence of vertex singularity in the point where the crack front touches free surface, crack propagation in 3D structures cannot be reduced to a series of plane strain or plane stress problems along the crack front. The paper describes the influence of the vertex singularity on crack shape for three-dimensional structure. The iterative process for estimation of a real crack front based on a stress singularity exponent is presented. In each node defining the crack front the stress singularity exponent has been estimated and complete crack front shape corresponding to the constant stress singularity exponent was found. The methodology presented can help to estimate crack front shape in a linear elastic fracture mechanics framework and estimate fracture parameters of fatigue cracks more accurately.

Introduction

Current three-dimensional fracture mechanics theories are based on the assumption that the local stresses around three-dimensional crack have similar stress distribution as those around two-dimensional crack and correspond to the square-root stress singularity. However, for the crack which is influenced by the free surface, this conclusion is invalid [1]. Stress singularity and distribution of the stresses at the intersection between crack and free surface have been topic of many investigators e.g. [2-7]. Despite of this, the effect of the 3D stress distribution on crack behaviour is still not fully understood.

The formation of the fatigue crack shape due to the influence of a free surface was studied in paper [8]. Crack front angle (the angle between crack front and free surface) obtained by numerical simulations corresponds well with literature data [4,6] for a particular Poisson's ratio. The stress distribution around the crack tip in each single plane perpendicular to the crack front was generally approximated in the form [9,10,11]:

$$\sigma_{ij} \approx \frac{H_I}{r^p} \cdot f_{ij}\left(p,\theta\right) \qquad (1)$$

where H_I is a generalized stress intensity factor, p is a stress singularity exponent and $f_{ij}(p,\theta)$ are corresponding shape functions. r,θ are local polar coordinates with origin at the crack tip O*, see Fig.1.

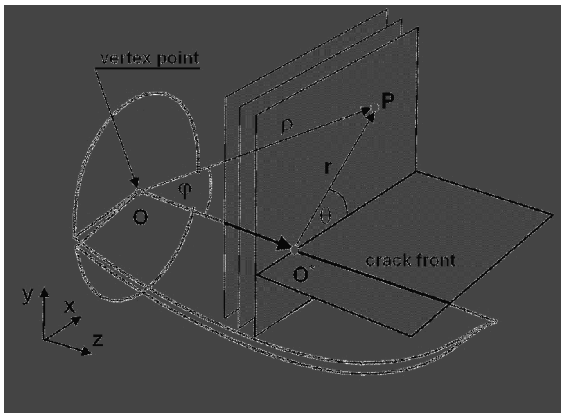


Fig. 1. Scheme of singular stress field close to free surface with origins of the coordinate systems used.

Than a new criterion based on Sih's strain energy density concept was developed [8]. Based on this criterion it is possible to find relation between generalized stress intensity factor and effective value of the stress intensity factor K_{eff}. The effective stress intensity factor can be used as a parameter controlling fatigue crack propagation rate according to the Paris-Erdogan law in the usual form:

$$\frac{da}{dN} = C\left(K_{eff}\right)^m, \tag{2}$$

where C and m are material parameters characterizing the fatigue crack propagation rate in given material. This methodology can describe 3D crack shape formation based on local increase or decrease of the fatigue crack propagation rate along crack front. The result is crack shape with constant fatigue crack growth rate along crack front [8]. For final shape of the crack the stress singularity exponent is uniform along whole crack front.

The main aim of the article is to compare shape of the fatigue crack for two different geometries (middle tension specimen and tension specimen with surface elliptical crack) based on stress singularity exponent. It is assumed that final crack shape corresponds to the state with constant stress singularity exponent along crack front. This algorithm can effectively describe real crack front shape based on linear elastic fracture mechanics and then estimate the relevant fracture mechanics parameters used for fatigue life prediction.

Numerical model

The standard Middle Tension (MT) and tension specimen with surface elliptical crack was studied and fatigue crack shape was predicted. The dimensions of considered MT specimen, see Fig. 2 was $2b = 20$ mm, $2h = 200$ mm, $2w = 50$ mm with crack length $a = 0.5w$. The crack front was assumed to be initially straight across the specimen thickness. In case of plate with surface crack the dimensions were $2h = 100$ mm, $t = 12$ mm with crack depth $a = 1$ mm. Length of the crack at surface $2b$ is a function of crack depth a. The homogenous linear elastic material model with Young's modulus $E = 210$ GPa and varying Poisson's ratio $\nu = (0 - 0.49)$ was taken into account for both specimens.

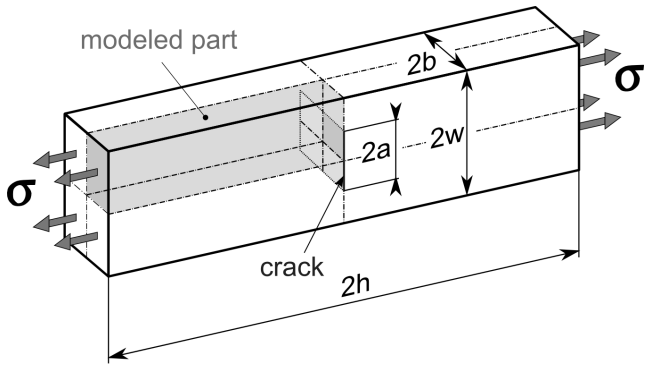


Fig. 2. MT specimen

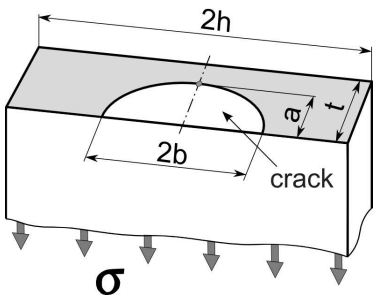


Fig. 3. Plate with surface semi-elliptical crack under tension

Results and discussion

The stress singularity exponent estimated along the straight crack front of MT specimen, taken from [12] is shown in Fig. 4. The influence of free surface ($z/b = 1$) on stress singularity exponent increases with increase of Poisson's ratio ν. According to [8,9] the fatigue crack propagation rate (FCPR) is related to stress singularity exponent p in such a way that the decrease of p leads to retardation of FCPR. It is assumed that the crack in real structures propagates keeping the stress singularity exponent constant along the whole crack front. Based on results plotted in Fig. 4 the curvature of the crack front near the free surface can be numerically estimated.

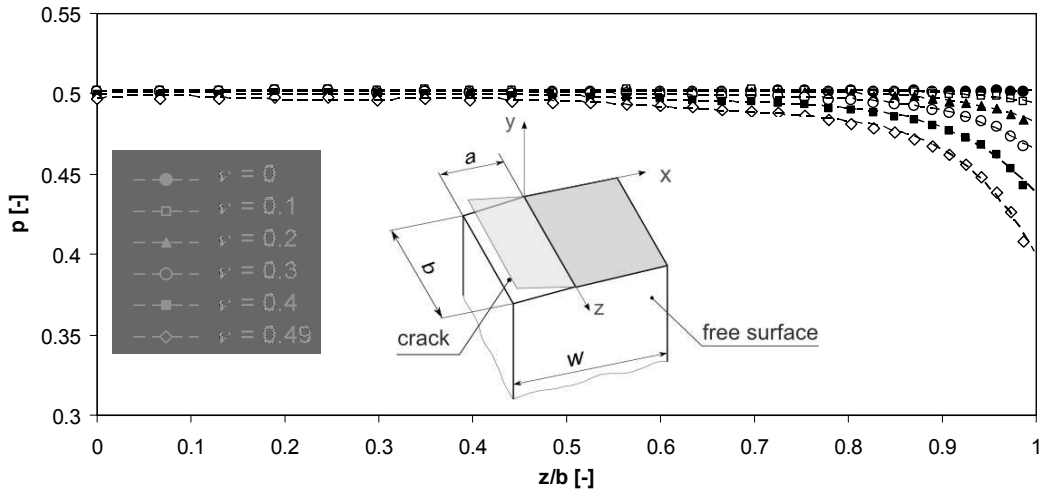


Fig. 4. Stress singularity exponent p estimated along the straight crack front of MT specimen as a function of Poisson's ratio ν [13].

Similarly to MT specimen the stress singularity exponent was estimated for semi-elliptical surface crack in tensioned plate. The effect of the free surface is insignificant between points A and B, so that the stress singularity exponent is plotted only between points B and C, see Fig. 5. The influence of Poisson's ratio on stress singularity exponent is considerable mainly for Poisson's ratio higher than 0.2. Effect of vertex singularity on influenced area close to the free surface is similar as for MT specimen with strong decrease of p for high Poisson's ratios.

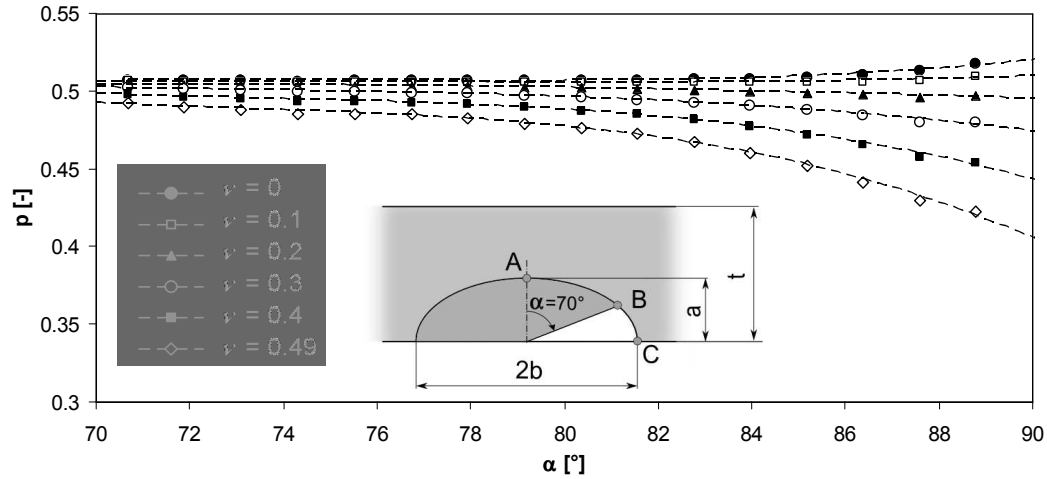


Fig. 5. Stress singularity exponent p estimated along the crack front in plate with elliptical crack under tension load as a function of Poisson's ratio ν.

An important parameter providing information about free surface influence is an intersecting angle γ_r between crack front and normal to the free surface at the vertex point C, see Fig. 5. According to [4,6] the angle γ_r depends only on Poisson's ratio ν. An iterative procedure was developed in order to numerically estimate the angle γ_r in considered cracked structures. The procedure modifies initial elliptical crack front in such a way that resulted crack front has constant stress singularity exponent. Finally, the intersecting angle γ_r is estimated in point C. Fig. 6 shows the influence of Poisson's ratio on intersecting angle γ_r for both plates with surface crack under tension and MT specimen together with results obtained by Pook. Very good agreement can be found between angles γ_r estimated on MT specimen and Pooks results. The angles γ_r obtained in case of plate with surface crack are slightly lower than for MT specimen. However, trends and values of estimated angles are similar.

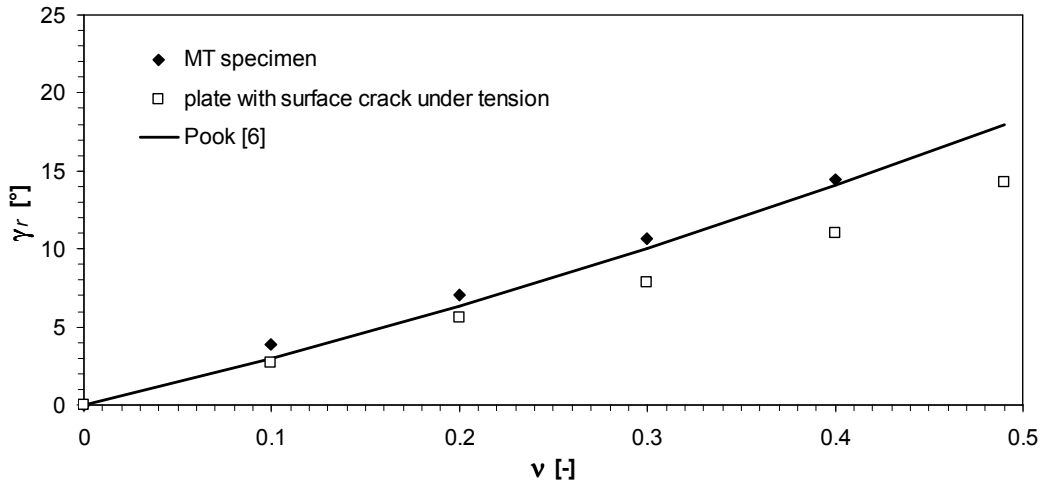


Fig. 6. Obtained intersecting angle γ_r as a function of Poisson's ratio ν.

Conclusions

This paper is focused on numerical estimation of the crack front shape in region influenced by free surface. The numerical analyses were performed on two different specimens – middle tension specimen and plate with surface semi-elliptical crack. It was found that the stress singularity exponent near the free surface decreases with increasing Poisson's ratio. Based on knowledge of stress singularity exponent variation along the crack front crack front shape can be numerically estimated based in iterative algorithm. Presented results can be helpful for better understanding of the crack behaviour close to the free surface and more accurate lifetime prediction of the structures considered.

Acknowledgement: This work was supported by grant 101/09/0867 of the Czech Science Foundation and project M10041090 of the Academy of Sciences of the Czech Republic. The research was also supported through the Specific academic research grant of the Ministry of Education, Youth and Sports of the Czech Republic provided to Brno University of Technology, Faculty of Mechanical Engineering.

References

[1] W.X. Zhu, Engineering Fracture Mechanics, Vol. 36 (1990), p. 239.

[2] Z.P. Bažant, L.F. Estenssoro : Int. J. Solids Structures, Vol. 15 (1979), p. 405.

[3] J.P. Benthem : Int. J. Solids Structures, Vol. 13 (1977), p. 479.

[4] M. Heyder, G. Kuhn : International Journal of Fatigue, Vol. 28 (2006), p. 627.

[5] C.R. Pictu, V. Gupta : J. Mech. Phys. Solids, Vol. 45 (1997), p. 1495.

[6] L.P. Pook : Engineering Fracture Mechanics, Vol. 48 (1994), p. 367.

[7] K.N. Shivakumar, I.S Raju : International Journal of Fracture, Vol. 45 (1990), p. 159.

[8] P. Hutař, L. Náhlík, Z. Knésl: International Journal of Fatigue, Vol. 32 (2010), p. 1265.

[9] P. Hutař, L. Náhlík, Z. Knésl: Computational Materials Science, Vol. 45 (2009), p. 653.

[10] P. Hutař, L. Náhlík, Z. Knésl: Key Engineering Materials, Vol. 385-387 (2008), p. 317.

[11] P. Hutař, L. Náhlík, Z. Knésl: Key Engineering Materials, Vol. 348-349 (2007), p. 377.

[12] P. Hutař et al.: Procedia Engineering, Vol. 2 (2010), p. 2095.

© (2012) Trans Tech Publications, Switzerland
doi:10.4028/www.scientific.net/KEM.488-489.182

Experimental and Numerical Investigation of Fatigue Behaviour of Nodular Cast Iron

P. Čanžar[a], Z. Tonković[b], A. Bakić[c] and J. Kodvanj[d]

Faculty of Mechanical Engineering and Naval Architecture, University of Zagreb,

I. Lučića 5, 10000 Zagreb, Croatia

[a]predrag.canzar@fsb.hr, [b]zdenko.tonkovic@fsb.hr, [c]ante.bakic@fsb.hr, [d]janos.kodvanj@fsb.hr

Keywords: nodular cast iron, fatigue, experiment, crack growth, finite element modelling.

Abstract. This paper presents an experimental and numerical study on two different types of the nodular cast iron EN-GJS-400-18-LT. The experimental procedure includes symmetrical and unsymmetrical strain controlled tests on the cylindrical specimens as well as crack initiation and propagation tests on the compact tension and single edged notched specimens. Different loading regimes are applied, and monitoring of the crack length during the tests is performed by an optical system. Within the framework of numerical investigations an efficient algorithm for modelling of cyclic plasticity is examined. Experimental results show that two material types have significantly different the crack behaviour.

Introduction

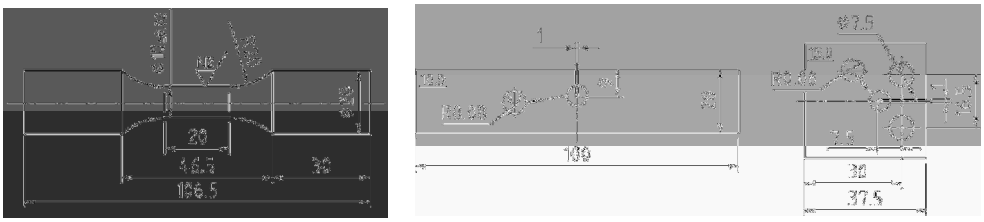
Specific shape of the graphite in the ferritic microstructure of nodular cast iron acts as the crack arrester and lowers the stress intensity in front of the crack. This feature, qualifies it as an appropriate material for structures under fatigue loading. The nodular cast iron grade EN-GJS-400-18-LT, in which graphite spheroids or nodules in a ferritic matrix provide large ductility and fatigue strength, is widely used [1]. It is well-known that fatigue strength is influenced by the size and the shape of graphite nodules [2, 3]. As reported in [4], when a fatigue crack is nucleated and propagates into the vicinity of the notch, the crack growth rate of short cracks is generally higher than that can be predicted by using the stress intensity factor concept based upon linear elastic fracture mechanics. Thus, it becomes essential to incorporate the effect of plasticity on initiation and growth behaviour of short fatigue cracks [5].

Two types of cast iron EN-GJS-400-18-LT referred to as Type 200 and Type 400, produced by different technologies are considered in this study. The Type 200 has a nearly ferritic matrix (approximately 95% ferrite–5% pearlite), while the Type 400 has purely ferritic matrix. For producing nodular cast iron two methods are applied: flotret (Type 200) and inmould (Type 400).

Uniaxial cycle tests

Uniaxial cycle tests are conducted at room temperature on a Walter Bai servohydraulic testing machine with a load capacity of ±50 kN. The strain is controlled with an extensometer of a gauge length of 10 mm. A series of the uniaxial strain-controlled cyclic loading experiments with several combinations of strain amplitudes are performed. In this section, a short description of test procedure is given, and some selected test results are presented. The present paper forms the continuation of work already reported in [6]. Mechanical properties of the nodular cast iron (Type 200) are 0.2% proof stress of 256.5 MPa, the tensile strength of 417.2 MPa, the modulus of 182.4 GPa and the elongation of 23.5%, respectively.

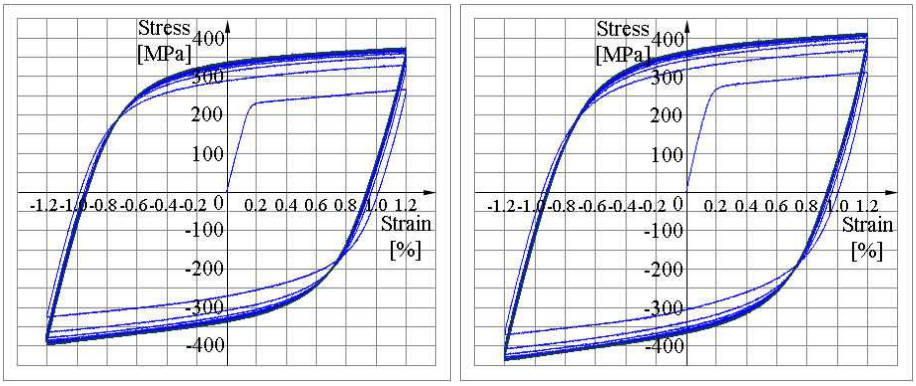
Fig. 1 illustrates the schematic shape and geometry of specimens required for the cycle fatigue tests. It consists of a polished cylindrical specimens used for cyclic testing (Fig. 1a), single edge bending (SEB) specimen (Fig. 1b) and compact tension (CT) specimen (Fig. 1c) according to the standards ASTM E606 and ASTM E1820.



a) b) c)

Fig. 1 Shape and dimensions of specimens: a) cylindrical specimen for cyclic testing, b) SEB specimen for three-point bending testing, c) CT specimen

The cyclic tests are carried out with the constant strain rate of 10^{-3} s^{-1} limited by applied strain amplitude ($\Delta\varepsilon/2$). Different strain amplitude is applied from the 0.2% up to the 1.2% with the increment of 0.2%. In each test 40 stress–strain hysteresis loops are obtained which is more than enough to achieve a stabilized curve. Fig. 2 show the representative symmetrical tests ($\Delta\varepsilon/2=\pm1.2\%$) for two types of nodular cast iron. In these tests mean strain is always equal to zero, and significant cyclic hardening can be observed.



a) b)

Fig. 2 Symmetrical stress–strain hysteresis loops for: a) type 200 and b) type 400 of the nodular cast iron

Crack initiation and propagation tests

This part of research is concerned with the investigation of the crack initiation and propagation under cyclic loading conditions. For this purpose SEB and CT specimens (Fig. 1b) and 1c)) are made according to the ASTM E1820 and ASTM E647 standards. Fig. 3 shows cracked specimen with exposed nodular cast iron microstructure.

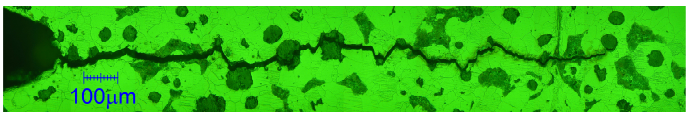
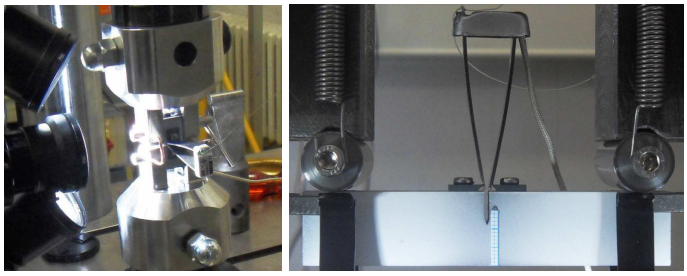


Fig. 3 Microstructural crack exposure

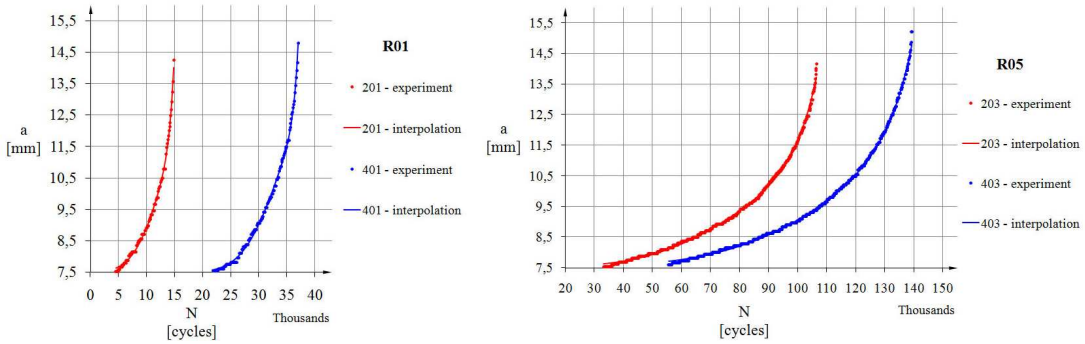
Derived microstructure with opened crack is shown, and is clearly how crack propagates through the grain boundaries. Specific shape of the graphite in the ferritic microstructure acts as the crack arrester and lowers the stress intensity in front of the crack. The test load is applied in sinusoidal form with the frequency of 10Hz, defined by a maximum load of 12kN and load ratio R. Two different loading regimes (R=0.1 and R=0.5) for both material types are performed. During the crack propagation tests length is measured by an optical measuring system. Specimen testing and crack measurement is shown in the picture below (Fig. 4). Besides of measuring crack propagation i.e. the crack size, crack mouth opening displacement (CMOD) is also measured using special extensometers.



a) b)

Fig. 4 Specimen and testing configuration for: a) CT and b) SENB specimen

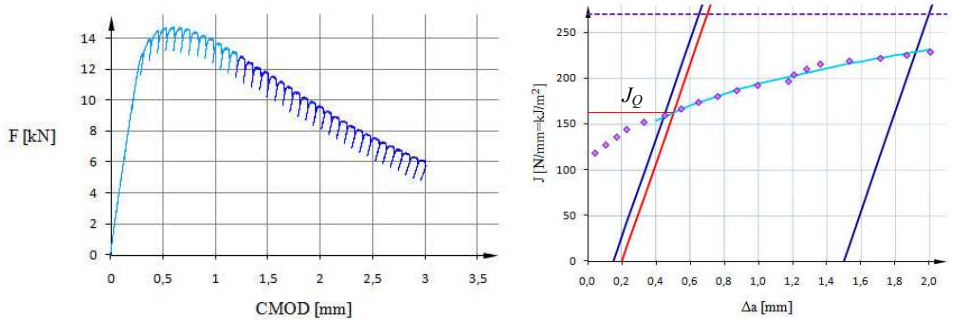
Fig. 5 shows dependence between crack length, a, and the number of cycles, N, for different load ratios (R=0.1 and R=0.5). For the most rigorous load ratio R=0.1, there is the most pronounced difference in material types considering crack propagation. Material type 200, produced by the flotret process, shows the least crack resistance. On contrary, material type 400, produced by the inmould technique, lasts approximately 2.5 times longer, till the final specimen fracture.



a) b)

Fig. 5 Number of cycles vs. crack length for: a) R=0.1 and b) R=0.5 load ratio

Compliance test, as well as crack resistance curve is shown on the picture bellow (Fig 6). Critical J value for the type 200 of nodular cast iron is J_Q=162kJ/m^2



a) b)

Fig. 6 a) Load vs. crack mouth opening displacement curve, b) J-R curve for material type 200

Modelling of cyclic plasticity

The accurate and realistic modelling of inelastic deformations as well as damage and failure behaviour of ductile materials under general loading conditions is still a complicated problem. In this study the algorithm which enables numerical modelling of cyclic elastoplastic deformation of shell structures presented in [5] is modified to simulate elastoplastic behaviour of a nodular cast iron. The derived computational algorithm is implemented in the software ABAQUS/Standard by using the user-defined material subroutine UMAT [7]. The cyclic plasticity model is afterwards applied to study the fatigue damage in the CT type specimen near the notch and the crack tip by employing a damage initiation and evolution criteria.

Modelling of damage initiation and growth

The direct cyclic analysis procedure from Abaqus/Standard is used in this work to compute the stabilized response of the structure directly [7], without need to compute a number of sequential cycles that would lead to such stabilized cycle. Additionally, Abaqus/Standard damage initiation and evolution criteria are adopted to determine the low-cycle fatigue damage. These two criteria are based on the stabilized accumulated inelastic hysteresis strain energy per cycle, Δw.

The cycle number in which damage is initiated is written in the form:

$$N_0 = c_1 \Delta w^{c_2}, \tag{1}$$

where c_1 and c_2 are material constants. Once the damage criterion is satisfied at the material integration point, rate of damage per cycle is given by:

$$\frac{\mathrm{d}D}{\mathrm{d}N} = \frac{c_3 \Delta w^{c_4}}{L}, \tag{2}$$

where c_3 and c_4 are material constants, L is the characteristic length associated with an integration point, while D stands for fatigue scalar damage variable which assumes the degradation of the elastic stiffness. For the cast iron type 200 specimen, the cyclic plasticity and fatigue material constants are: A_1=15.8 GPa, A_2=107.4 GPa, B_1=263.2, B_2=2090.1, C_1=16.8, C_2=0, D_1=102.3 MPa, D_2=0, c_1=13.84, c_2=-0.20. The material parameters are calibrated using test data from a constant amplitude tests (Fig. 2) and multiple step tests conducted on the smooth specimens.

Conclusion

The cyclic deformation and low-cycle fatigue behaviour of the nodular cast iron EN-GJS-400-18-LT has been studied experimentally and numerically. Two types of the cast iron produced by different technologies are considered.

In the first part of the experimental investigation, the cyclic, symmetrical and unsymmetrical strain controlled tests are performed on the smooth cylindrical specimens. In the second part, the crack initiation and propagation tests for different loading ratios are carried out on the SENB and CT specimens. The results show that the size, shape and distribution of the graphite nodules as well as the microstructure phase (ferritic and pearlitic) have significant influence on the material fatigue behaviour. The specimen produced with the flotret technology shows the worst resistance to crack growth, while the inmould shows the best results.

Within the framework of numerical investigations the new cyclic plasticity model together with the Abaqus/Standard damage initiation and evolution criteria are applied to study the fatigue damage in the specimen near the notch and the crack tip. The correlation of the numerical predictions and the experimental data is subject of the current research.

References

[1] F. Fan, S. Kalnaus and Y. Jiang: Mechanics of Materials, Vol. 40 (11) (2008), p. 961-973.
[2] P. Hübner, H. Schlosser, G. Pusch and H. Biermann: Int. Journal of Fatigue Vol. 29 (2007), p. 1788–1796.
[3] N. Costa, N. Machado and F.S. Silva: Int. Journal of Fatigue, Vol. 32 (2010), p. 988–995.
[4] F. Ding, M. Feng and Y. Jiang: Int. Journal of Plasticity, Vol. 23 (2007), p. 1167–1188.
[5] Z. Tonković, J. Sorić and I. Skozrit, CMES Vol. 26 (2) (2008), p. 75-90.
[6] P. Čanžar, Z. Tonković, J. Kodvanj, A. Bakić and Z. Tomičević, Key Engineering Materials, Vols. 452-453 (2010), p. 825-828.
[7] ABAQUS/Standard: Version 6.9, Hibbitt, Karlsson & Serensen, Inc. (2009).

© (2012) Trans Tech Publications, Switzerland
doi:10.4028/www.scientific.net/KEM.488-489.186

Modelling of Nonlinear Creep and Recovery Behaviour of Cortical Bone

Martina Lovrenić-Jugović[1,a], Zdenko Tonković[1,b] and Ivica Skozrit[1,c]

[1] Faculty of Mechanical Engineering and Naval Architecture, University of Zagreb, I. Lučića 5, 10000 Zagreb, Croatia

[a]martina.lovrenic@fsb.hr, [b]zdenko.tonkovic@fsb.hr, [c]ivica.skozrit@fsb.hr

Keywords: cortical bone, viscoelasticity, viscoplastcity, creep, recovery, finite element modelling.

Abstract. A new one-dimensional constitutive model for human cortical bone is proposed to simulate the viscoelastic–viscoplastic behaviour occurring during creep-recovery tests. The material parameters are determined by fitting experimental results of creep-recovery tests reported in the published literature. An efficient computational algorithm for the integration of the proposed constitutive model at the material point level is derived. The derived algorithm in conjunction with the Jacobian matrix is implemented in the finite element code ABAQUS. The model predictions are found to be in good agreement with the experimental data presented in literature.

Introduction

Experimental results show that the cortical bone behaves as a linear viscoelastic material during tensile creep for stress levels below some threshold value of stress. Beyond this value, it behaves as a viscoelastic-viscoplastic damaging material [1, 2]. In order to better represent the actual behaviour of the cortical bone tissue during creep, the irreversible viscoplastic strains should be included in the constitutive model in addition to the time-dependent, reversible viscoelastic strains [3].

In recent years, the ideas and approaches developed for engineering materials are used for the modelling of bone behaviour [3, 4]. The presented research is motivated by the experimental data reported by Melnis [2] and Parsamian [3] for nonlinear time-dependent response of human cortical bone, and viscoelastic and viscoplastic models presented by Schapery [5], Dassapa et al. [6] and Marklund et al. [7, 8]. These models, originally proposed by Zapas and Crissman, are commonly used for viscoplastic strains in polymeric and composite materials.

An algorithm which enables numerical modelling of viscoelastic-damage behaviour of cortical bone is proposed in [9]. The present paper is a continuation of that work where the viscoplastic deformation associated with creep and creep-damage is analyzed in detail for more accurate predictions. The objective of this study is to develop a new constitutive model for cortical bone tissue that predicts the experimental viscoelastic-viscoplastic behaviour in creep-recovery tests. The derived algorithm for the integration of the proposed constitutive model at the material point level is implemented in the finite element code ABAQUS [10]. The accuracy of the computational procedure is tested by comparing the computed results with the real experimental [2] and numerical [11] data. Thereby, creep-recovery deformation processes in the cortical bone under different loading levels are considered.

Constitutive model

The constitutive modelling of viscoelastic−viscoplastic cortical bone behaviour is based on the assumption of small strains. The total creep strain $\varepsilon(t)$ of this concept is additively decomposed into the reversible viscoelastic part ε_{VE}, and the irreversible viscoplastic part ε_{VP}, as follows

$$\varepsilon(t) = \varepsilon_{VE} + \varepsilon_{VP}\,. \tag{1}$$

Schematic representation of the stress history and strain response of cortical bone during the creep and recovery period is presented in Fig. 1. As can be seen, upon removal of the applied load, the viscoelastic strain is recovered, while the viscoplastic strain is permanent.

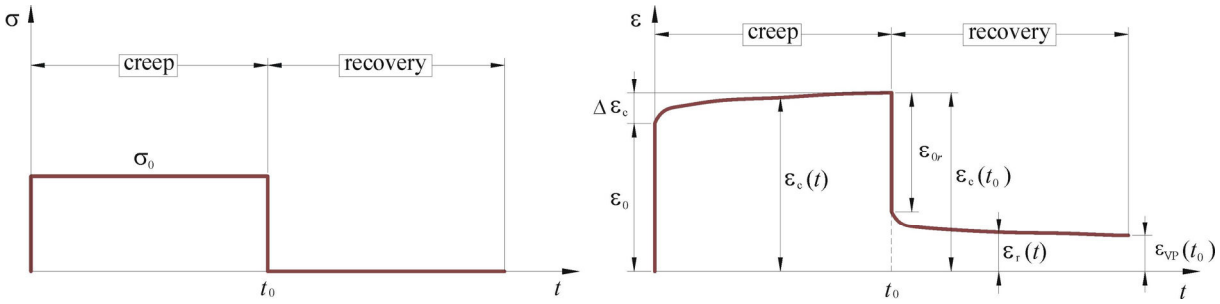


Fig. 1 Schematic representation of stress history and strain response during creep - recovery period

The model developed by Schapery [5] is applied for describing the viscoelastic components. In the case of uniaxial tensile loading, the total viscoelastic strain may be written in the form

$$\varepsilon_{\mathrm{VE}} = \int_0^t J(t-\tau)\frac{\mathrm{d}\sigma}{\mathrm{d}\tau}\,\mathrm{d}\tau\,, \tag{2}$$

where J denotes the viscoelastic compliance of the virgin material, while t and τ stand for time and retardation time, respectively. In Eq. (2) σ represents the Cauchy stress. According to Parsamian [3] and Abdel-Tawab and Weitsman [4], the following expression for the compliance is adopted

$$J = J_0 + J_1 t^{\gamma}\,, \tag{3}$$

where J_0, J_1 and γ are material parameters**.** After inserting Eq. (3) in Eq. (2), the viscoelastic strain during creep and recovery is expressed by the following equations

$$\varepsilon_{\mathrm{VE}} = J_0\,\sigma + J_1\,\sigma\,t^{\gamma}\,,\ \text{for}\quad 0<t<t_0\,, \qquad \varepsilon_{\mathrm{VE}} = J_1\,\sigma\left[t^{\gamma}-\left(t-t_0\right)^{\gamma}\right],\ \text{for}\quad t>t_0\,, \tag{4}$$

where t_0 stands for recovery time (Fig.1).

According to Dasappa et al. [5], the following viscoplastic model, initially proposed by Zapas and Chrissman, is adopted

$$\varepsilon_{\mathrm{VP}} = \alpha\left\{\int_0^t h\left[\sigma(\eta)\right]\mathrm{d}\eta\right\} = \left\{\int_0^t h\left[\sigma(\eta)\right]\mathrm{d}\eta\right\}^n, \quad \text{where } \varepsilon_{\mathrm{VP}}=0, \text{ when } \sigma=0 \text{ or } t=0\,. \tag{5}$$

In Eq. (5) α is a function which depends on the stress history ($h\left[\sigma(\eta)\right]$ with $h[0]=0$) and $h\left[\sigma(\eta)\right]=C\sigma^m$. Now, the expression (5) for the viscoplastic strain can finally be transformed into the following relation: $\varepsilon_{\mathrm{VP}} = \left[C\left(\sigma^m\right)t\right]^n$. Thus, viscoplastic model considers the viscoplastic strain as a nonlinear function of stress and time. The threshold value of stress, σ_{th}, beyond which viscoplastic strain starts to accumulate, is obtained by analyzing experimental data for the recovery period reported in [2]. In this publication recovery time is five times longer than creep period. The obtained threshold stress value is about 45 MPa. Finally, the viscoplastic strain may be expressed in the form

$$\varepsilon_{\mathrm{VP}} = A\cdot\left\langle\sigma-\sigma_{th}\right\rangle^{m\cdot n}\cdot t^{n},\ \text{for}\quad 0<t<t_0\,, \qquad \varepsilon_{\mathrm{VP}} = A\cdot\left\langle\sigma-\sigma_{th}\right\rangle^{m\cdot n}\cdot {t_0}^{n},\qquad \text{for}\quad t>t_0\,. \tag{6}$$

Material parameters

For the constitutive model presented, the material parameters are determined by fitting experimental results of creep-recovery tests carried out by Melnis et al [2]. As described in this paper, the experimental samples are taken from the middle segment of the tibia diaphysis of five males ranging in age from 30 to 35 years. The samples were cut along the longitudinal axis of the bone in six cross-sectional zones. Thereafter creep testing is carried out at six different stress levels between 30 and 105 MPa. The separation of the viscoelastic and viscoplastic strains from the total creep strain, based on the multiple creep-recovery tests is done using a method described in [6]. The determined viscoelastic and viscoplastic parameters are given in Table 1. Graphical representation of the creep strain as a function of time and stress for human cortical bone is shown in Fig. 2.

Table 1. The material parameters determined by fitting experimental results of creep-recovery tests

viscoelastic parameters			viscoplastic parameters		
J_0	$5.2217\cdot10^{-5}$	MPa^{-1}	A	$6.54007\cdot10^{-9}$	$\mathrm{MPa}^{-mn}\cdot\mathrm{sec}^{-n}$
J_1	$8.61449\cdot10^{-7}$	$\mathrm{MPa}^{-1}\cdot\mathrm{sec}^{-\gamma}$	m	1.05615	-
γ	0.27124	-	n	0.74835	-

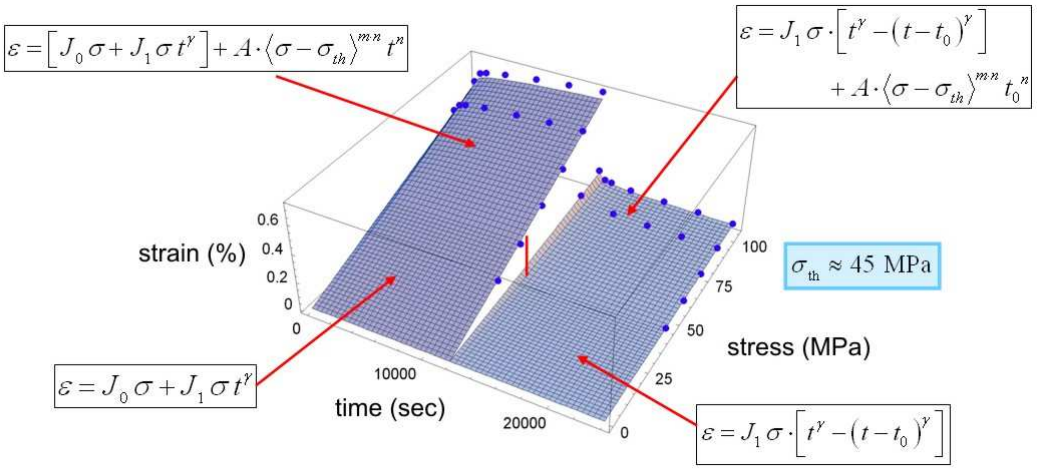


Fig. 2 The creep strain as a function of time and stress

Numerical formulation and results

The implicit integration scheme is used to integrate the rate form of the presented constitutive model. The updated values of the state variables, $\sigma(t_n+\Delta t)$ and $\varepsilon(t_n+\Delta t)$, at the end of the time step $(t_n, t_n+\Delta t)$ have to be found for a given value of the incremental strain $\Delta\varepsilon(t_n)$ at time t_n. The constitutive equations are transformed into an incremental form by using finite differences. The obtained non-linear equations:

$$\varepsilon = \left[J_0 + J_1(t+\Delta t)^{\gamma}\right](\sigma+\Delta\sigma) + A\cdot\langle\sigma-\sigma_{th}+\Delta\sigma\rangle^{m\cdot n}\cdot(t+\Delta t)^{n} - \Delta\varepsilon, \qquad \text{for} \quad 0<t<t_0, \quad (7)$$

$$\varepsilon = J_1\left[(t+\Delta t)^{\gamma} - (t+\Delta t-t_0)\right](\sigma+\Delta\sigma) + A\cdot\langle\sigma-\sigma_{th}+\Delta\sigma\rangle^{m\cdot n}\cdot(t_0)^{n} - \Delta\varepsilon, \quad \text{for} \quad t>t_0, \quad (8)$$

are solved by the Newton-Raphson algorithm to find unknown variables. The derived updating algorithm is implemented at the material point level of the available finite elements in the software ABAQUS/Standard [10] by using the user subroutine UMAT. The creep simulation is performed and uniaxial tension load is first applied to the FE model using an elastic calculation at time t = 0.

The load is then kept constant and subsequent time-dependent creep analyses are performed. In addition, Fig. 3 shows a comparison of strain versus time between the solutions obtained in the present paper and the published experimental [2] and numerical [11] solutions for creep and recovery. It is the first step after which the viscoplastic strain can be seen in recovery period.

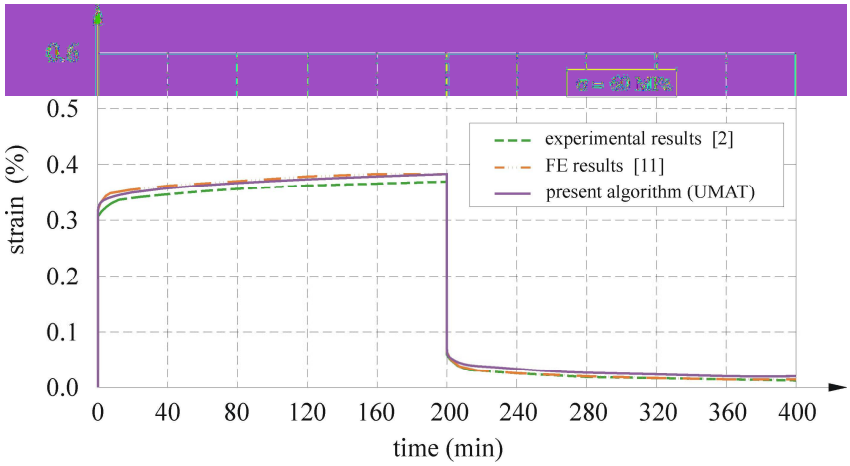


Fig. 3 A comparison of strain versus time between the present work and the published experimental [2] and numerical [11] solutions

Conclusion

The one-dimensional constitutive model is developed for human cortical bone tissue to predict the experimental viscoelastic-viscoplastic behaviour in creep-recovery tests. For the proposed constitutive model, the material parameters are determined by fitting experimental results of creep-recovery tests carried out by Melnis et al [2]. The computational algorithm for the integration of the proposed constitutive model is derived and implemented in the Abaqus UMAT subroutine. The accuracy of the computational procedure is tested by comparing the computed results with the published real experimental data [2] and numerical [11] solutions. Thereby, creep deformation processes in the cortical bone are considered. Formulation and implementation of three-dimensional time integration algorithm for modelling of nonlinear orthotropic viscoelastic-viscoplastic-damage behaviour of cortical bone is the subject of the current research.

References

[1] M. Fondrk, E. Bahniuk, D.T. Davy and C. Michaels,: J. Biomech., Vol. 21 (1988), p. 623-630.
[2] A.E. Melnis, I.V. Knets and P.A. Moorlat: Mech. Compos. Mater. Vol. 15 (1980), p. 574-579.
[3] G.P. Parsamian: Ph.D.Thesis, West Virginia University, (2001).
[4] K. Abdel-Tawab and Y.J.Weitsman: Contract technical report, The Univer. of Tennessee, 1997.
[5] R.A. Schapery: Int J Fract Vol. 97 (1999), p. 33–66.
[6] P. Dasappa, P. Lee-Sullivan and X. Xiao: Compos. Part B: Eng. Vol. 41 (2010), p. 48-57.
[7] E. Marklund, J. Eitzenberger and J. Varna: Compos. Sci. Technol. Vol. 68 (2008), p. 2156-2162.
[8] E. Marklund, J. Varna and L. Wallstrom: J. Eng. Mater. Technol. Vol. 128 (2006), p. 527-536.
[9] M. Lovrenić-Jugović, Z. Tonković and I. Skozrit: Key. Eng. Mater. Vol. 417-418 (2010), p. 273-276.
[10] ABAQUS/Standard: Version 6.9, Hibbitt, Karlsson & Serensen, Inc., (2009).
[11] A.N. Natali, E.L. Carniel and P.G. Pavan: Medical Eng. & Physics, Vol. 30 (2008), p. 905-91.

© (2012) Trans Tech Publications, Switzerland
doi:10.4028/www.scientific.net/KEM.488-489.190

Finite Element Analysis by using Hyper-elastic Properties for Rubber Component

Chang-Su Woo[1, a], Hyun-Sung Park[1,b], Wae-Gi Shin[2,c]

[1]Korea Institute of Machinery & Materials, 171, Jang-Dong, Yuseong-Gu, Daejeon, 305-343, Korea.

[2]PAVCO Ltd., 291-7, Bonro-Ri Nongong-Eup, Dalseong-Gun, Daegu, 711-855, Korea

[a]cswoo@kimm.re.kr, [b]hspark@kimm.re.kr, [c]wgshin@ph.co.kr

Keywords: Rubber component, Hyper-elastic properties, Finite element analysis, Mooney-Rivlin, Ogden model, Material constant, Fatigue failure.

Abstract. The material modeling of hyper-elastic properties in rubber is generally characterized by the strain energy function. The strain energy functions have been represented either in term of the strain in variants that are functions of the stretch ratios, or directly in terms of the principal stretch. Successful modeling and design of rubber components relies on both the selection of an appropriate strain energy function and an accurate determination of material constants in the function. Material constants in the strain energy functions can be determined from the curve fitting of experimental stress-strain data. The uniaxial tension, equi-biaxial tension and pure shear test were performed to acquire the constants of the strain energy functions which were Mooney-Rivlin and Ogden model. Nonlinear finite element analysis was executed to evaluate the behavior of deformation and strain distribute by using the commercial finite element code. Also, the fatigue tests were carried out to obtain the fatigue failure. Fatigue failure was initiated at the critical location was observed during the fatigue test of rubber component, which was the same result predicted by the finite element analysis.

Introduction

Characteristics and lifetime prediction on the rubber component was increasing according to the extension of warranty period of the automotive components. A design of rubber components against failure is one of the critical issues to prevent the failures during the operation. Therefore, characteristic analysis and lifetime prediction are the key technologies to assure the safety and reliability of mechanical rubber components. Recent advance in finite element analysis technology has resulted in industrial application of simulation tools in the design of rubber components. With the availability of simple to use numerical procedures for handling the contact problem, many manufacturers of rubber components such as mount, insulator, seal has recognized the potential of numerical analysis [1,2]. Finite element analysis is used extensively in the design of structures and sub-components. Finite element analyses can provide information needed to determine the performance and behavior. This information includes a load–deflection curve and stress and strain distribution. Accurate predictions of component properties require both suitable material models and accurate material properties data. Non-linear material laws for rubber materials are nowadays well established and form a natural part of the material library of commercial nonlinear finite element codes [3]. But these well established material models may cause serious problems in practical applications, if insufficient testing is done when calibrating the material constants. A large variety of fine constitutive models for rubber materials are available already since quite some time. Material laws like the Mooney-Rivlin and Ogden model are well acknowledged and substantially tested. In order to determine the material constants, uniaxial tension, equi-biaxial tension and pure shear test were performed. Nonlinear finite element analysis was executed to evaluate the behavior of deformation and strain distribute by using the commercial finite element code.

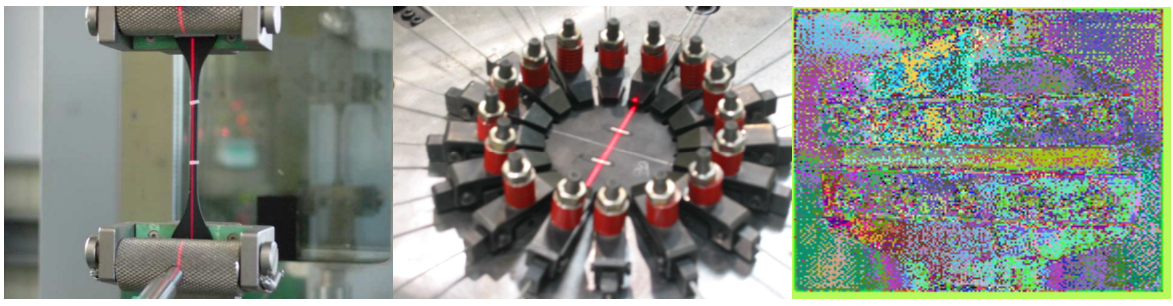
Mechanical Test

The rubber material property, which is essential in finite element analysis, is expressed with the coefficient values of strain energy function and these values are determined by fitting stress-strain data obtained from the material tests under various load conditions into the stress-strain curve induced from strain energy function [4,5]. And it is determined to minimize the differences between the test values and calculated values. Therefore, we analyzed the property of the material and determined the nonlinear material constant, which is necessary in finite element analysis, by conducting uniaxial tension, equi-biaxial tension and pure shear test [6].

Figure 1 shows the mechanical test of rubber material by using non contacting strain measurement with laser extensometer. Rubber materials are deformed, their network structure lose their stiffness due to modification and reformation, and damping properties change. Mullins suggested this is due to the stress-strain response, called the Mullins effect [7]. This is more prevalent in carbon black-filled rubbers. In other words, the stiffness of rubber depends on its history and strain range. In addition, the stress-strain curve in initial stage is not repeated anywhere and the curve stabilize after receiving approximately five repetitive loads within the same strain range. The stress-strain curve exhibits yet another change when the rubber material is subjected to a larger strain than the previous one. Lastly, the rubber material possesses properties in which fixed permanent deformation occurs when the material returns to the initial strain value; the strain is not equal to 0 even if the stress is equal 0. Figure 2 shows the stress-strain curves obtained from the uniaxial tension, equi-biaxial tension and pure shear tests in which we applied five repetitive loads in each of the vertical and horizontal direction with 25%, 50% and 100% of the strain range for rubber material. According to Figure 2, the stress-strain curves during the second repetition showed a greater decline than in the first repetition. The stress-strain curve gradually decreased as the number of repetitions increased, and ultimately stabilized to a fixed stress-strain value. In order to predict the behavior of the rubber components using the finite element analysis, the rubber material constants must be determined from the stabilized cyclic stress-strain curve. The stress-strain curve varies significantly depending on the cyclic strain levels. A 5^{th} loading cycle was selected as the stabilized stress-strain relationship in this study. But this stabilized relation should be shifted to pass through the origin of the curve, to satisfy the hyper-elastic nature of rubber. Figure 3 shows the stress-strain relation of rubber material for various physical tests. The shift of curve meant that the gage length and initial cross sectional area were changed as shown in Eq. (6).

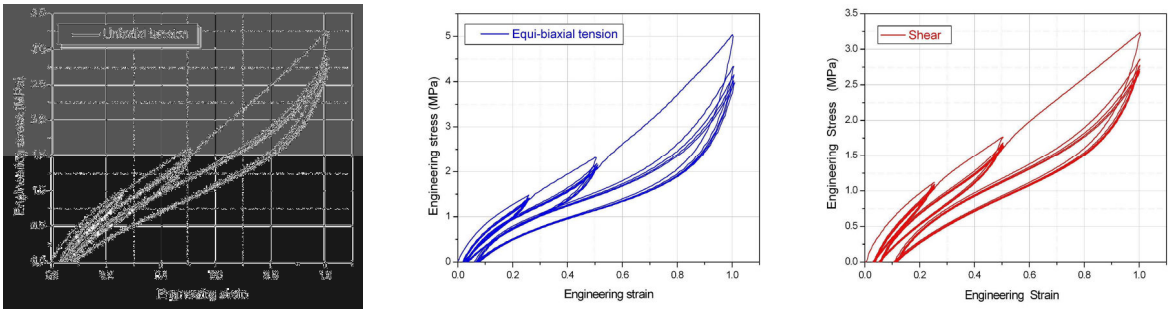
$$\varepsilon = \frac{\varepsilon' - \varepsilon_p}{1+\varepsilon_p} \qquad \sigma = \sigma'(1+\varepsilon_p) \tag{6}$$

We performed the curve fitting with uniaxial tension, equi-biaxial tension and pure shear test data. Mooney-Rivlin 2-terms and Ogden 3-terms fits that uses progressively more information as the basis for the curve fitting [8]. Table 1 contains the values of rubber material coefficient calculated in each case.



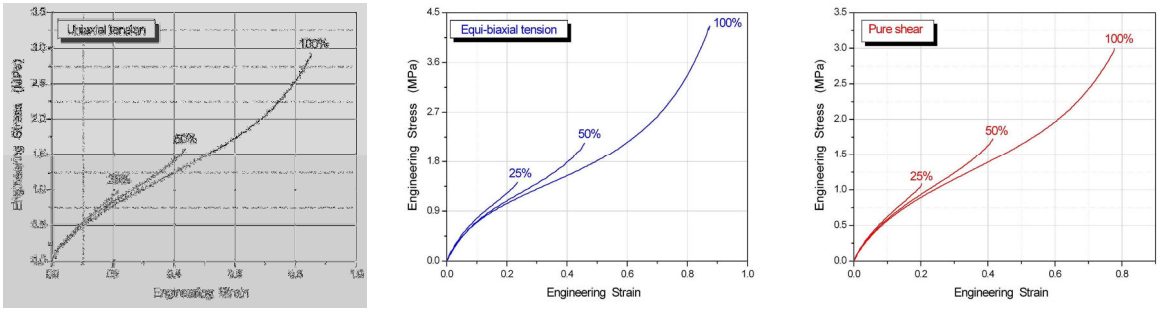
(a) uniaxial tension (b) equi-biaxial tension (c) pure shear

Figure 1 Mechanical test of rubber material



(a) uniaxial tension (b) equi-biaxial tension (c) pure shear

Figure 2 Stress-strain curves at various loading and strain range



(a) uniaxial tension (b) equi-biaxial tension (c) pure shear

Figure 3 Stabilized stress-strain curve and shift curve to zero

Table 1 Mooney-Rivlin and Ogden function of rubber material

Strain	Mooney-Rivlin			Ogden						
	C_{10}	C_{01}	G	μ_1	α_1	μ_2	α_2	μ_3	α_3	G
25%	0.889	0	1.779	1.1e-4	2.291	0.968	3.710	4.5e-4	3.080	1.796
50%	0.772	0	1.543	2.0e-5	1.030	2.140	1.3e-6	1.182	2.602	1.532
100%	0.723	0.0091	1.463	0.028	4.391	5.813	0.031	0.953	2.593	1.390

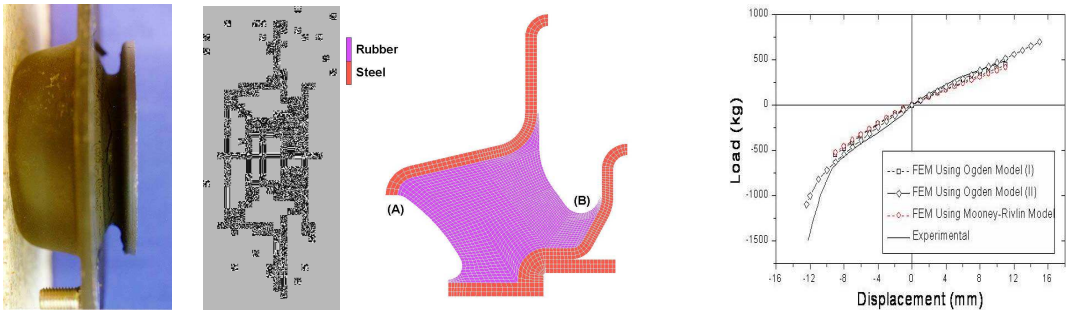
Finite Element Analysis

Strut rubber insulator is used in a suspension component of automotive vehicle. Finite element analysis was performed to investigate the deformation and strain distribution behavior of strut rubber insulator. Material constants representing the Mooney-Rivlin and Ogden strain energy potential of order 3 were used for defining a constitutive relation of the natural rubber in this study. Strut rubber insulator was modeled with Full-Herrmann formulation quad 4 element as shown in Figure 4(a). Contact is specified between the rigid steel and the regions on the inner surface of the strut rubber insulator. Figure 4(b) shows the load-displacement curve comparison between simulations using the hyper-elastic models and static test data. Results of the finite element analysis are a good agreement with experimental test. Figure 5 shows the deformed shape and strain distribution under tension and compression load. The maximum stress and strain occurred at the "A" and "B" position as indicated in Figure 4(a). Fatigue failure was initiated at the critical location was observed during the fatigue test of rubber component, which was the same result predicted by the finite element analysis.

Summary

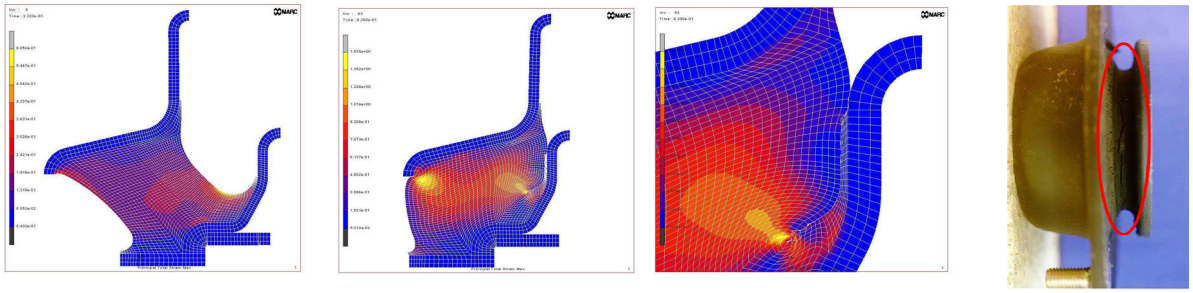
The material modeling of hyper-elastic properties of rubber was characterized by the strain energy functions and determined by the curve fitting of experimental stress-strain data from uniaxial tension, equi-biaxial tension and pure shear test. The behaviors of the deformations and strain

distributions of strut rubber insulator were evaluated by using commercial finite element analysis code. And, it was shown that the results by finite element analysis simulations were in close agreement with the experimental test. The technologies developed in this study are expected to be widely used applied in design, analysis and development of several rubber components which are used in automotive, railroad and mechanical elements etc.



(a) strut rubber insulator (b) load-displacement curve

Figure 4 Finite element model of strut rubber insulator



(a) tension (b) compression (c) position of failure

Figure 5 Strain distribution and failure of strut rubber insulator

References

[1] W. V. Mars, A. Fatemi, A Literature Survey on Fatigue Analysis Approaches for Rubber, Int. J. Fatigue, Vol. 24, **No.** 9, pp. 913–1012. (2002)

[2] K. Legorju-jago, C. Bathias, Fatigue Initiation and Propagation in Natural and Synthetic Rubbers, Int. J. Fatigue, Vol. 24, **No.** 2, pp. 85–97. (2002)

[3] D. M. Tuner, Problems with equations for rubber elastic behavior, Rubber Engineering Using FEA, IMechE London, Vol. 4. (1995)

[4] F. J. H. Peeters, M. Kussner, Material law selection in the finite element formulation of rubber-like materials and its practical application in the industrial design process, Constitutive models for rubber I, pp. 29-36. (1999)

[5] R. K. Luo, W. J. Mortel, Finite element analysis on bolster springs for metro railway vehicles, Constitutive models for rubber I, pp. 275-280. (1999)

[6] R. P. Brown, *Physical Testing of Rubber*. Chapman & Hall, London. (1996)

[7] L. Mullins, Chemistry and Technology, Vol. 42, pp. 339. (1969)

[8] R. W. Ogden, *Non-linear elastic deformations*, Chichester Ellis Horwood Limited. (1984)

© (2012) Trans Tech Publications, Switzerland
doi:10.4028/www.scientific.net/KEM.488-489.194

Assessment of Thermal Damage for Railway Wheel of Long-term Running

Seok Jin KWON[1, a], Jung Won SEO[2,b], Dong Hyung LEE[3,c], and Sung Tae Kwon[4,c]

[1]Korea Railroad Research Institute, 360-1, Woram-dong, Uiwang-city, Gyeongi-do, Korea

[a]sjkwon@krri.re.kr, [b]jwseo@krri.re.kr, [c]dhlee@krri.re.kr, [d]stkwon@krri.re.kr

Keywords: Railway wheel, Replication test, Wheel tread, Defect, Residual stress, Thermal damage

Abstract. The railway wheel in long-term running had experienced the wheel damage due to fatigue crack and shelling. The damaged wheel in railway vehicle would cause a poor ride comfort, a rise in the maintenance cost and even fracture of the wheel, which then leads to a tremendous social and economical cost. It is necessary to evaluate long-term damage of railway wheel in order to ensure the safety of wheel. To evaluate the damage for railway wheels, the measurements for the replication of wheel surface and residual stress of railway wheel using x-ray diffraction system were carried out. The result shows that the residual stress of wheel is depend on the running distance and thermal gradient during brake application also that the replication test can be applied in new evaluation method of wheel damage.

Introduction

The railway wheels which are running on rails under a complicated load conditions require safety assessment since their defect or partial fracture can cause derailments resulting in enormous economic and social loss. While the mechanical performance of railway wheels are managed by local and international standards and the quality policies of manufacturers, the quality performance has been strengthened in addition to the standard of maintenance and new, better materials are being developed in Europe, Japan and the USA to keep pace with the continuous improvement of the performance of rolling stock which in turn leads to severer operating and loading conditions.

The cracks on the tread braking wheels for railway usually initiate from the boss of wheel, center of wheel flange or rim of wheel, and propagate in radial direction, and may result in fracture under severe load condition, followed by derailment accompanied with personal and property loss. Since the derailments caused by wheel fracture influence large impact on the economy and society, it is required to strengthen the quality standard and safety assessment of railway wheels.

In the present paper, the thermal damage of the wheels of power car for high speed train by replication test and residual stress measurement has been evaluated.

2. Replication test of railway wheel

2.1 Test points

The wheel tread occur various microstructural changes due to the contact stress with rail and the thermal stress caused by tread braking. To inspect such microstructural changes, the specimen taken from the wheel tread should be examined with an electron microscope. However, obtaining specimen from the railway wheels in operation is possible only in very limited cases. The replication method which replicates the concerned metal microstructure to another material was used to examine and analyze the changes in the replica in laboratory environment.

To investigate the damage of the high speed railway wheels, the surface microstructure of the wheels with and without thermal damage were compared and analyzed, as shown in Fig. 1. In addition, the replication tests were conducted to compare the left and right side wheels with reference to the direction of running. Fig. 1 shows the inspection points of the friction surface of a thermally damaged wheel.

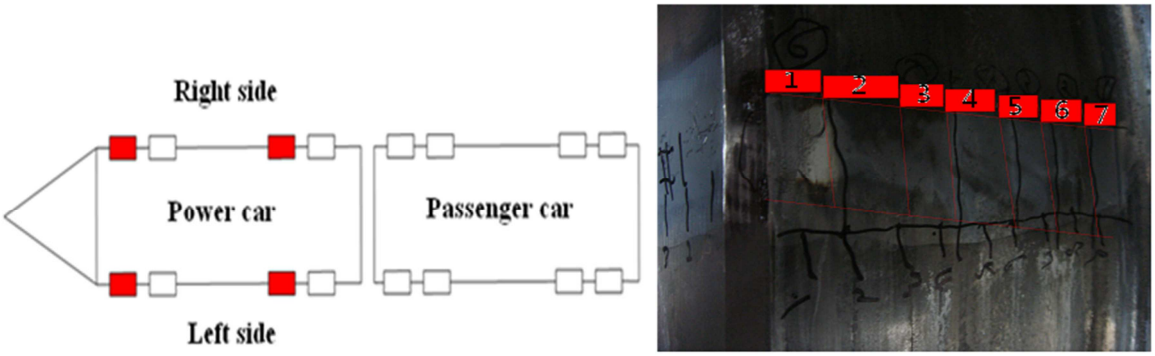
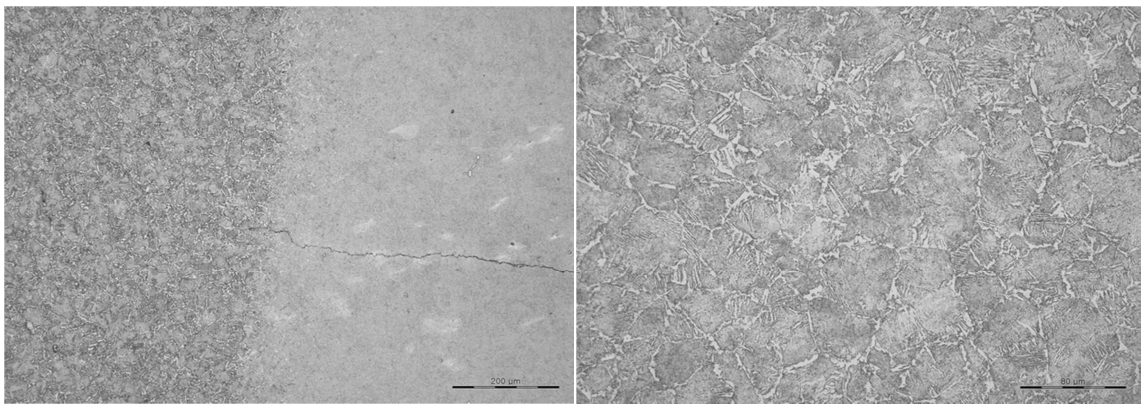


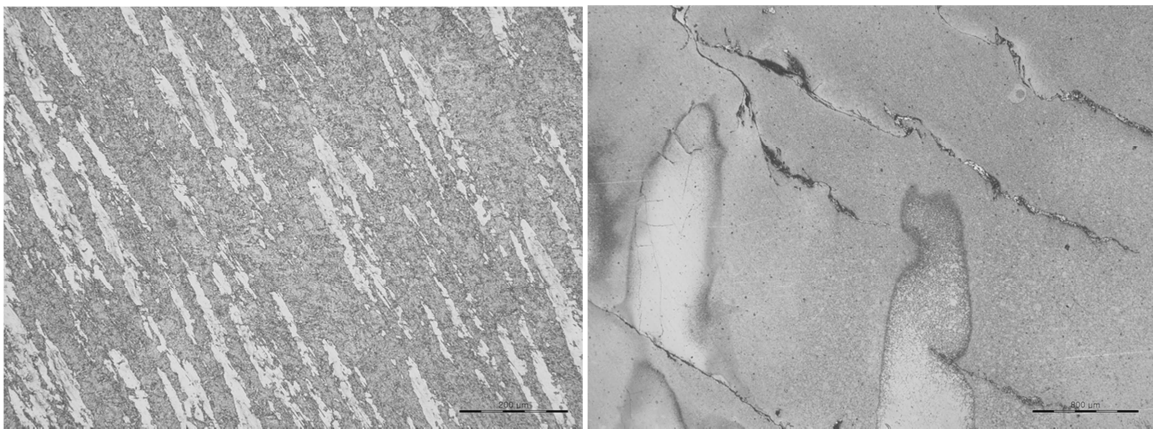
Fig. 1 Measurement points of replication test

2.2 Results of the replication test

Fig. 2 ~ Fig. 3 show the results of the replication inspections on the friction surfaces of the power car wheels. In Fig. 2(a), Friction Surface-Section 1 on the outer side of the wheel is the part where the deformation by the friction with brake block is the severest.



(a) between section 1 and section 2 (b) section 2



(c) section 4 (d) section 6

Fig. 2 Microstructure of power car wheel

This section 1 showed development of reticular cracks in the white layer formed on the wheel surface caused by rapid heating close to the melting point and cooling. The Friction Surface-Section 1 seems to have been affected by heat generated from friction with brake block most severely, which was the major cause of the severe thermal discoloration on the side.

The Section 4 also was formed with recrystallized layer by the friction heat, and in the Section 6, it was though that the structure had been deformed and cracks were generated by friction with rail.
It was assumed that the main causes of the wear and damage of the wheels were the friction between the wheel and brake block and the wheel and rail for the inner and outer sides of the wheel, respectively. It was also assumed that the partial difference of the deformation layer was due to the uneven friction forces between the wheel and brake block and rail. The boundaries between the deformation layers showed micro-cracks vertical and horizontal to the axis of friction.

3. Measurement of the residual stress of wheels

3.1 Test procedures

The residual stresses of the damaged and undamaged wheels of high speed train were measured on the tread within 20 mm from the rim, as shown in Fig. 3. Residual stress can be measured by punching method, cutting and strain gauge method, or ultrasonic method. In this study, an X-ray measurement system was used to measure the residual stress of wheels of power car, as shown in Fig. 3(a). The measurement points were arranged at the intervals of 90° in the circumferential direction, and the X-ray irradiation angle was -45°~45 at 25° intervals. Table 1 illustrates the measurement conditions of the residual stress of the wheels.
The measurement apparatuses of the residual stress of the wheels were XSTRESS 3000 (Stresstech, Finland). The direction of measurement was in circumferential direction. Regarding the diffraction condition of the X-ray, the shifts of diffraction peak were measured at the diffraction angle of 2θ, according to the stress measurement method, and tilted in both ± directions for 5 times (ψ = 0°, 20.7°, 30.0°, 67.8°, and 45°) each to measure the lattice spacing d and measure the residual stress by $d-\sin^2\psi$ method.

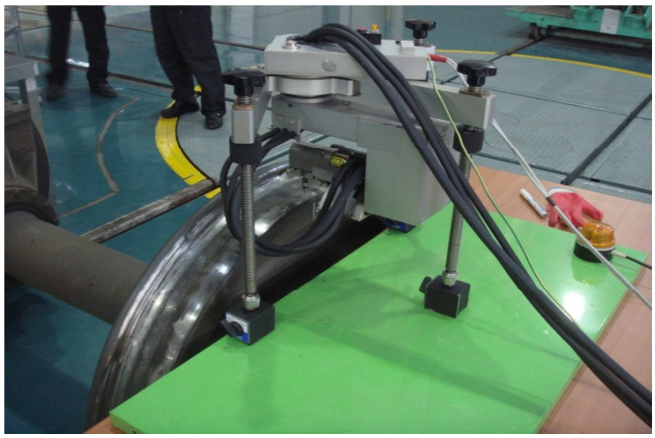


Table 1 Test conditions

Test condition	α-Ferrite
Characteristic X-ray	Cr-Kα
Diffraction plane	{211}
Diffraction angle	156.4°
No. of Oscillation,	-
Irradiated area	ϕ3
Time constant	5 ~ 25sec

Fig. 3 Residual stress measurement of railway wheel

3.2 Result of the residual stress measurement

Fig. 4 shows the residual stress measured on the wheel tread in radial direction. For damaged wheel, the tensile residual stress had distributed in location 0 and 90 degree. In Fig. 4 shows the maximum tensile residual stress of 117.6 MPa was measured on the wheel rim. The residual stress in wheel rime is higher than that of wheel flange. While the wheel had thermally damaged, the wheel rim has the weak points with respect to crack initiation.
With reference to the rim (back face), tensile residual stress (+86.9 MPa) distributed at the certain part of the wheel surface, and the compressive residual stress which existed in the new wheel decreases as approaching the flange.
The result of the residual stress measurement showed no tensile residual stress exceeding the wheel replacement standard of UIC (+300 MPa). However, the compressive residual stress of railway wheel in manufacturing reverse to tensile residual stress due to thermal damage between wheel and brake block during long term running of railway wheel.

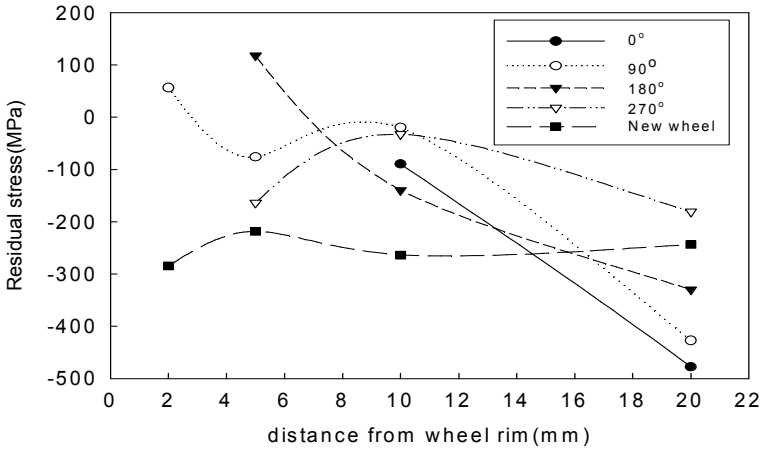


Fig. 4 Residual stress for damaged and new wheel

Summary

The replication test and residual stress measurement were performed with thermally damaged high speed railway wheels to obtain following conclusions.

1) The outer side close to the friction surface of the wheels showed thermal discoloration caused by friction heat, softening of metal structure, and decrease of hardness.
3) In the microstructural inspection of the wheels, a structural deformation by friction heat could be identified on the rim of the power car wheels
4) On the tread of the power car wheels having thermal damage, thermal cracks caused by the friction heat with the brake block were identified, and the tread on the opposite side of the flange showed more thermal cracks than other areas.
5) On the thermally-damaged wheels, tensile residual stress distributed on the certain part of the wheel from the rim (back face).
6) On the thermally-damaged wheels, thermal cracks occurred where there was no tensile residual stress. These cracks were thought to be caused by the braking friction heat from brake block and the rolling contact fatigue with rail.

References

[1] Gordon, J., and Perlman, A. B., Estimation of Residual Stresses in Railroad Commuter Car Wheels Following Manufacture, Proceedings, International Mechanical Engineering Congress and Exhibition, ASME RTD Vol. 15, pp.13 - 18, (1998)
[2] Gordon, J., Jones, J. A., and Perlman, A. B., Evaluation of Service-Induced Residual Stresses in Railroad Car Commuter Wheels, Proceedings, International Mechanical Engineering Congress and Exhibition, ASME RTD Vol. 15, pp. 25 – 32, (1998)
[3] S.J.Kwon, D.H.Lee, J.W.Seo, Damage evaluation of wheel tread based on contact position between wheel and rail, Key Engineering Materials Vols. 417-418, pp 645-648,(2010)
[4] A. Ghidini, S. Cantini : Mechanical Comparison between American and European Materials for Railway Wrought Solid Wheels in Terms of RCF Resistance,14th Wheelset Congress, (2004)

© (2012) Trans Tech Publications, Switzerland
doi:10.4028/www.scientific.net/KEM.488-489.198

Influence of Curing Temperature on the Mechanical Properties of Alkali-activated Bottom Ash Geopolymer Mortar

Gum-Sung Ryu[1,a], Si-Hwan Kim[1,b], Kyung-Taek Koh[1,c], Su-Tae Kang[1,d] and Jang-Hwa Lee[1,e]

[1]Structural Engineering & Bridges Research Division, Korea Institute of Construction Technology, Goyang, 411-712, Korea

[a]ryu0505@kict.re.kr, [b]shkim@kict.re.kr, [c]ktgo@kict.re.kr, [d]alphard@kict.re.kr, [d]jhlee@kict.re.kr

Keywords: Bottom Ash, Alkali-activated, Geopolymer, Compressive strength, Curing temperature

Abstract. The fabrication of Portland cement causes numerous problems accompanying the large exhaustion of gas. Even if fly ash, an industrial by-product produced in thermoelectric power plants, is recycled in concrete by partial replacing of cement, more than 50% remains still discharged in marine and ashore landfills and, continue to provoke environmental problems. Recently, active research has been dedicated to alkali-activated concrete that does not use cement as binder. This alkali-activated concrete as a *cement zero concrete* activated by alkali solution using bottom ash rich in Si and Al instead of cement is effective in reducing gas exhaustion. This study is a basic research for the fabrication of concrete without cement and using 100% of bottom ash among the industrial by-products. Therefore, the purposes are to develop cement zero concrete by evaluating the mechanical properties by age according to the change of the molar concentration and ratio (SH/SS) of the alkali-activator and the curing temperature, and to investigate the reaction mechanism. From the test results, the compressive strength increased with larger molar concentration and the optimal curing temperature was 60°C. In addition, the measurement of the leaching according to the molar concentration of fly ash having similar chemical composition showed that the leaching of Si^{4+} and Al^{3+} increased. Compared to 6M, the leached quantities of Si^{4+} and Al^{3+} were twice larger for 9M and 12M. The formation of gel at the surface of fly ash indicated that fly ash was more activated in higher alkaline environment.

Introduction

Chindaprasirt et al. [2] conducted a comparative analysis of a geopolymer fabricated using fly ash as binder and a geopolymer using bottom ash. The results showed that the compressive strength of the geopolymer using bottom ash ranged between 9 MPa and 18 MPa when measured after 48 hours of curing at 65°C. On the other hand, the geopolymer using fly ash as binder developed less than half of this compressive strength. The authors found out that this difference was caused by the difference in the reactivity through a series of chemical analyses. Sathonsaowaphak et al. [3] evaluated the changes of the strength and fluidity according to the effects of the fineness of bottom ash (2100, 3400, 5000 cm^2/g), ratio of alkali-activator to bottom ash, ratio of water glass to NaOH, and concentration of NaOH. The compressive strength measured after 48 hours of high temperature curing at 75°C reached 59 MPa. Slavik et al. [4] carried out a study on the possibility to fabricate geopolymers with bottom ash obtained from fluidized bed combustion. The resulting compressive strength was 52 MPa at 90 days after curing at ambient temperature. Satisfactory resistance to free-thaw was also reported.

Accordingly, this study as a basic research for the fabrication of concrete without cement and using 100% of bottom ash among the industrial by-products intends to develop cement zero concrete and verify its reaction mechanism by evaluating the mechanical properties per age with respect to the curing temperature and the change of the molar concentration of the alkali-activator.

Reaction Mechanism

Inorganic material like F-class bottom ash rich in Si and Al is applied as binder by being activated by an alkaline aqueous solution. In this case, the chemical reaction that occurs is the polymerization. Such polymerization means the formation process of the polymer Si-O-Al-O through the chemical reaction of Al-Si minerals in highly alkaline state. This can be expressed as follows.

$$M_n[-(Si-O_2)_2-Al-O \cdot wH_2O \quad (1)$$

where M is the alkali element; (–) indicates the existence of binding; *z* takes value of 1, 2 or 3; and, *n* is the degree of polymerization.

In addition, Si and Al in bottom ash act as binder through the activation by a compound of sodium hydroxide and sodium silicate solution. In general, a compound of sodium hydroxide (or potassium hydroxide) and sodium silicate (or potassium silicate) is used as alkali-activator. High temperature curing is commonly performed since the chemical reaction accelerates under heating.

Test Planning and Method

Test Planning. The binder used in this study is the bottom ash dry-produced at the power plant of Hadong. The results of a preliminary test using raw bottom ash (fineness of about 1600 cm^2/g) revealed that the strength was not developed. Therefore, a fineness of 4000 cm^2/g similar to that of fly ash was secured using a vibration mill. The test variables of the geopolymer using bottom ash are the molarity (NaOH 6M, 9M, 12M, 15M), the curing temperature (30, 60, 90°C) and the weight ratio of NaOH to sodium silicate (SH/SS ratio: 80/20, 65/35, 50/50, 35/65, 20/80). Table 1 lists the chemical composition and physical properties of fly ash and bottom ash prior and after crushing by vibration mill. The quantity of unburned carbon in the bottom ash obtained through dry-process appeared to be extremely small. In the case of Hadong power plant, the bottom ash showed smaller quantity of unburned carbon than fly ash. The vibration mill did not affect the chemical composition of bottom ash but had effect only on the change of the density and fineness.

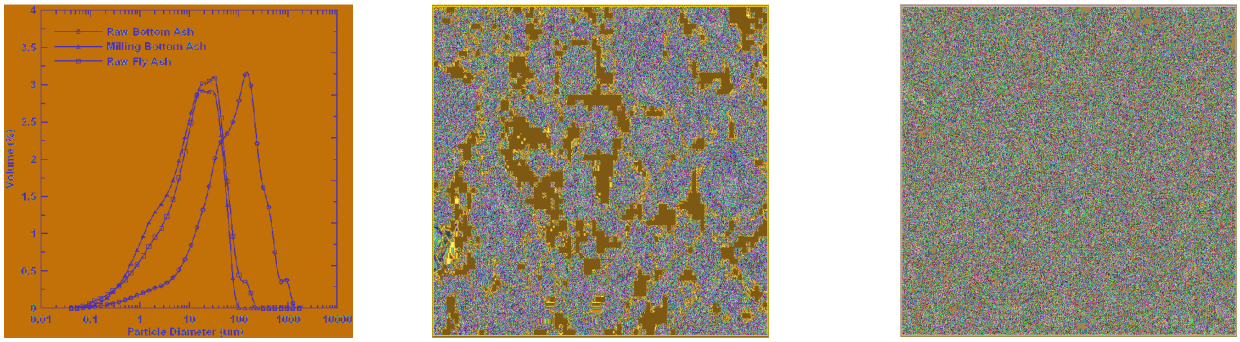
Table 1. Physical and chemical properties of fly ash and bottom ash

	SiO_2 (%)	Al_2O_3 (%)	Fe_2O_3 (%)	CaO (%)	MgO (%)	SO_3 (%)	K_2O (%)	Na_2O (%)	L.O.I	Density (g/cm^2)	Fineness (cm^2/g)
Bottom ash (raw)	57.7	23.6	9.36	4.57	0.16	0.71	2.56	0.82	0.01	2.39	1642
Bottom ash (crushed)	58.3	22.4	8.8	4.53	1.37	0.42	2.38	0.7	0.04	2.51	4061
Fly ash	57.5	24.6	5.26	4.72	1.34	0.73	1.8	0.38	2.5	2.08	3669

Mixing and Curing Method. The mixing of mortar using 100% of bottom ash was conducted by introducing bottom ash and sand in the mixer with capacity of 10 liter, executing dry mixing during 3 minutes, followed by 5 minutes if mixing after introduction of the water and the activator composed of sodium hydroxide and sodium silicate. In order to measure the developed strength according to the change of the molar concentration of the alkali-activator, the specimens were fabricated using a 50×50×50 mm cubic mold. After placing the specimens, sealing was disposed using a vinyl to prevent the evaporation of moisture produced by the elevation of temperature according to the change of curing temperature. Curing at 60°C was conducted during 24 hours in an oven followed by dry-air curing at 23±2°C. Thereafter, the compressive strength was measured at 1, 3, 7 and 28 days.

Test Results and Discussion

Fig. 2 shows the particle size distribution after crushing of the dry-produced bottom ash using the vibration mill. The fineness of the uncrushed bottom ash runs around 1600 cm^2/g and the mean grain size is 82.57 μm. Besides, the crushed bottom ash exhibits a particle size distribution similar to fly ash with a fineness of 4061 cm^2/g and mean grain size of 11.75 μm.



(a) Particlesize distribution curve (b) Uncrushed bottom ash (1600 cm^2/g) (c) Crushed bottom ash (4061 cm^2/g)

Fig. 2 Granulometry according to vibration mill treatment

Fig. 3 analyzes the effect of the molar concentration of the alkali-activator on the compressive strength. The compressive strength increases with higher molarity of NaOH but the values at 28 days being 56 MPa for 15M and 56.4 MPa for 12M remain small. This is caused by the activation of the Si and Al components contained in bottom ash induced by the high alkalinity according to the increase of the molar concentration of NaOH. Moreover, the strength of the geopolymer not based on bottom ash seems to be highly influenced by the ratios SiO_2/Na_2O and Al_2O_3/Na_2O.

Fig. 4 presents the results of the compressive strength test according to the SS/SH. The compressive strength at 28 days for SH/SS of 50:50 and 35:65 runs about 40 MPa. Solidification that is the crystallization of the alkali-activator is observed for SH/SS of 80:20 and 65:35 following the increase of SH. Accordingly, the most optimal SH/SS appears to be 50:50 and 35:65. Together with the Al/Si ratio, the ratios SiO_2/Na_2O, Na_2O/Al_2O_3 and H_2O/SiO_2 are also important for the alkali-activated bottom ash cement because H_2O plays a critical role in the dissolution process between the Al and Si ions. However, there is still no clear understanding of the geopolymerization, which is an important hardening reaction of the alkali-activated bottom ash cement.

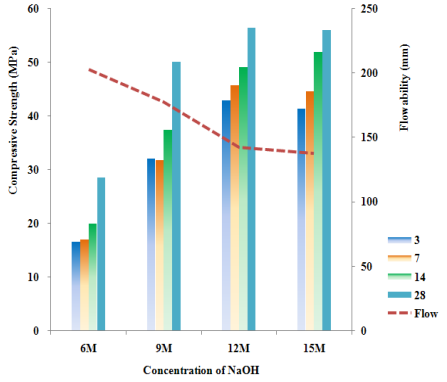


Fig. 3 Compressive strength wrt molar concentration

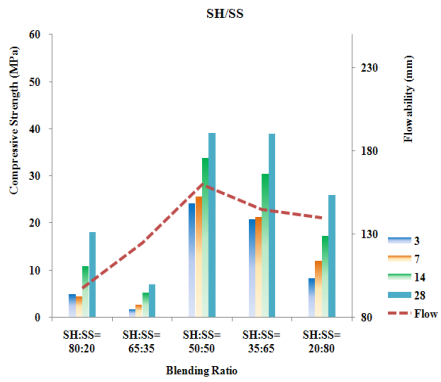


Fig. 4 Compressive strength wrt SH/SS

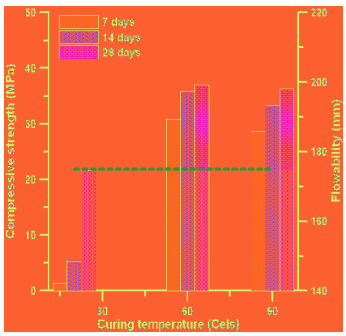


Fig. 5 Strength development wrt curing temperature

Fig. 5 illustrates the change of strength according to the curing temperature. Strength does not develop at 7 and 14 days at 20°C while reaches about 21 MPa at 28 days. Considering that the minimum design strength ranges between 37 and 35 MPa regarding the durability of concrete, the requirement relative to the strength is not satisfied. Especially, such result will provoke the problem of delaying construction due to the slow development of strength at early age. Therefore, need is for solutions accelerating the development of early strength together with the improvement of the strength to enable curing at ambient temperature. Besides, strength developed mostly (more than 75%) at the first 7 days for curing temperature of 60°C and 90°C to reach a value larger than 30 MPa. In addition, a comparison of the results at 60°C and 90°C shows that curing at high temperature of

90°C was without effect on the promotion of the strength according to the activation of the reaction compared to 60°C. On the contrary, a slight loss of strength was observed. Accordingly, in view of the present results, the most satisfactory development of strength can be expected when curing at temperature near 60°C.

Conclusions

The following conclusions can be drawn from the SEM analysis and compressive test of zero cement mortar with 100% bottom ash as binder using the molar concentration, curing temperature and ratio of alkali-activator as test variables.

(1) The vibration mill did not affect the chemical composition of bottom ash but had effect only on its physical properties through change of its density and fineness.

(2) The strength increased with higher molar concentration of NaOH but the values at 28 days being 56 MPa for 15M and 56.4 MPa for 12M remained small. This could be explained by the activation of the Si and Al components contained in bottom ash induced by the high alkalinity according to the increase of the molar concentration of NaOH.

(3) The ratios of 50:50 and 35:65 for the alkali-activator (SH/SS) led to compressive strength of about 40 MPa and appeared to be the most appropriate in terms of workability and strength.

(4) Need is for solutions accelerating the development of early strength together with the improvement of the strength to enable curing at ambient temperature. A comparison of the results at 60°C and 90°C showed that curing at high temperature of 90°C was without effect on the promotion of the strength according to the activation of the reaction compared to 60°C. On the contrary, a slight loss of strength was observed. Accordingly, in view of the present results, the most satisfactory development of strength can be expected when curing at temperature near 60°C.

Acknowledgements

The study was supported through the R&D Project “Development of Technology for High Volume Bottom Ash Concrete the Reduce CO_2 Emission (Project No.20101020100180)” of the Korea Institute of Energy Technology Evaluation and Planning. The authors acknowledge the support.

References

[1] Ryu G.S., Koh K.T., Kang S.T., Ahn K.H., Kim S.W., Lee J.H.,(2008), ″An Experimental Study on the Development of Strength of Mortar Using 100% of Fly Ash as Binder” Proceedings of Spring Conference of the Korea Concrete Institute, 2008

[2] Prinya Chindaprasirt et al.(2009), "Comparative study on the characteristics of fly ash and bottom ash geopolymers", Waste Management

[3] Apha Sathonsaowaphak et al.(2009), “Workability and strength of lignite bottom ash geopolymer mortar”, Journal of Hazardous Materials

[4] R. Slavik et al.(2008), “Preparation of geopolymer from fluidized bed combustion bottom ash”, J. Materials Process Technology.

© (2012) Trans Tech Publications, Switzerland
doi:10.4028/www.scientific.net/KEM.488-489.202

Investigation into Damage of AL-Mesh Bumper under Hypervelocity AL-Spheres Impact

Guan Gongshun[1, a], Bang Baojun[1, a] and Niu Ruitao[1, a]

[1]P. O. Box 3020, Science Park, Harbin Institute of Technology, Harbin, 150080, P. R. China

[a]ggsh@hit.edu.cn

Keywords: Hypervelocity impact; Mesh bumper; Damage; Crack; Experiment

Abstract. The aluminum mesh/plate bumper was designed by improving on AL-Whipple shield, and a series of hypervelocity impact tests were practiced with a two-stage light gas gun facility at Harbin Institute of Technology. Impact velocities of Al-spheres were varied between 3.5km/s and 5km/s. The diameters of projectiles were 3.97mm and 6.35mm respectively. The hypervelocity impact characteristics of 5052 aluminum alloy mesh bumper were studied through hypervelocity impact on aluminum mesh/plate bumpers. The fragmentation and dispersal of hypervelocity particle against mesh bumpers varying with material and specification were analyzed. It was found that the mesh wall position, diameter of wire and separation distance arrangement and mesh opening had high influence on the hypervelocity impact characteristic of aluminum mesh/plate shields. At similar impact velocity, hypervelocity impact characteristics comparison with aluminum sheet bumpers of equal areal mass was thrust. The optimized design idea of aluminum mesh/plate bumpers was suggested.

Introduction

Space debris is a recognized threat for any space mission. Hypervelocity impacts on spacecraft in low earth orbit by meteoroids and space debris can damage flight-critical systems, which can in turn lead to catastrophic failure of the spacecraft [1]. Therefore, the design of spacecraft for an earth-orbiting mission must take into account the possibility of such impacts and their effects on the spacecraft structure. The Whipple shield is the conventional shield type used to protect space structures from hypervelocity meteoroids and orbital debris impacts [2,3]. This shield decreases the momentum flux density of after-impact residual fragments acting on the rear wall. Comparing Whipple shield structure, The aluminum mesh/plate bumper shield structure is better resistance shielding systems because of its low mass and high flexibility [4]. A number of experiments elucidating the integral dispersing and fragmentation properties of meshes due to their interaction with a projectile were also carried out as well [5]. The crater distribution and crater depth on the rear wall can be used to evaluate the protection ability of shield configuration. In this paper, by hypervelocity impact experiment, performance of aluminum mesh/plate bumper shield was investigated. For different shield configurations with the same mesh, the results indicated that the first aluminum mesh wall did not help enhancing the performance of shields, and the last aluminum mesh wall did not help reducing the damage area on the rear wall. For the same shield configurations with different aluminum mesh, the results indicated that mesh opening and diameter of wire were the important parameters for enhancing the performance of shields.

Experimental Set-Up

Test bumpers. The impact tests were performed onto aluminum mesh/plate shields, each of them consisting of 5052 aluminum alloy mesh and 2A12 aluminum alloy bumpers with a 3mm thickness 5A06 aluminum alloy rear wall. The overall space between bumper and rear wall was 100mm. The spherical projectile was made of 2017 Aluminum alloy. The meshes of 5052 aluminum alloy mesh were 14, 17, 20 and 28 respectively. The details of the mesh targets are shown in Table 1. The geometry parameters D and S in Table 1 are diameter of the wires and spacing between the wires respectively.

Table 1 Details of mesh target s

No.	*Mesh*	*D (mm)*	*S (mm)*	*Areal density (g/cm2)*
1	14	0.42	1.39	0.039
2	14	0.20	1.61	0.009
3	17	0.25	1.24	0.017
4	17	0.20	1.29	0.011
5	18	0.26	1.15	0.018
6	20	0.20	1.07	0.013
7	28	0.30	0.61	0.036

Aluminum mesh/plate shield was designed by improving on AL Whipple shield, and a series of hypervelocity impact tests were practiced. The aluminum alloy mesh would disperse fragments generated by an impact of space debris. The aluminum alloy mesh/plate shield configurations in the test are shown in Fig.1.

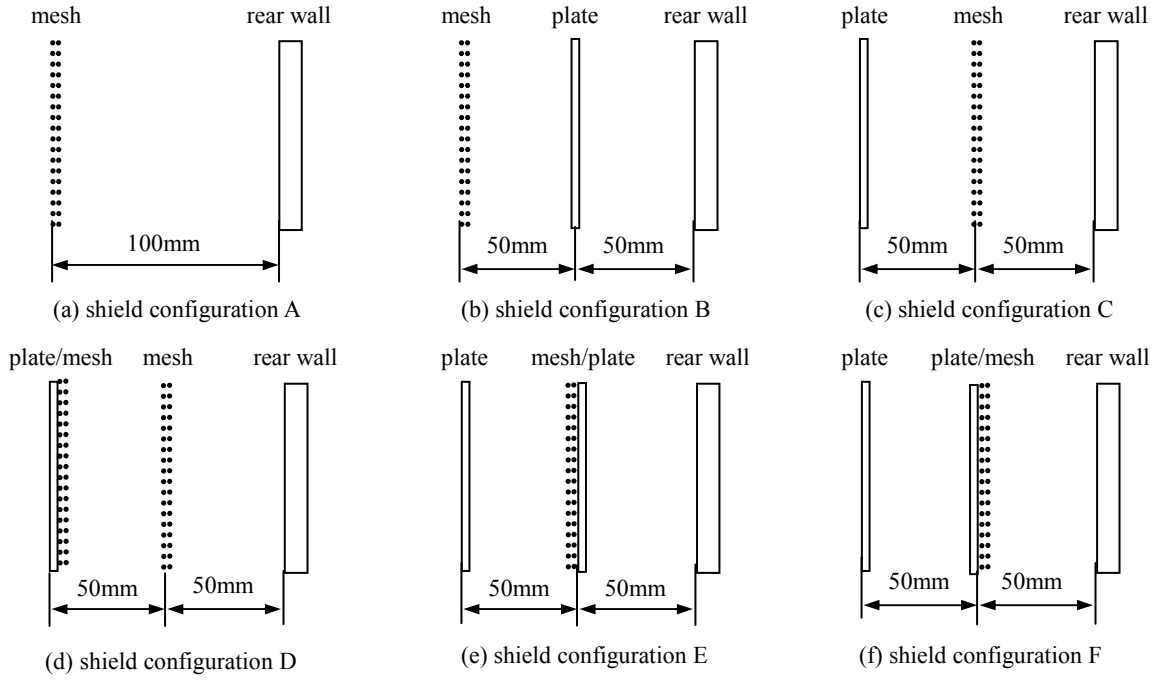


Fig.1 Shield configurations in the test

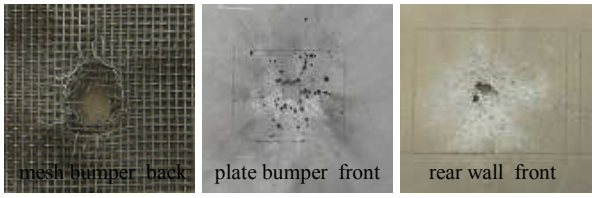
Test facility. The hypervelocity impact tests were performed with a gas driver two-stage light gas gun at Harbin Institute of Technology. For this study, 2017-T4 aluminum alloy spheres were launched, with the protection of sabots, at velocities between 3.5km/s and 5km/s. The diameters of projectiles were 3.97mm and 6.35mm respectively. The impact angle was 0° for all the tests. The projectile velocities were measured by magnetic induction. The uncertainty in these measurements is approximately ± 2%. The pressure of nitrogen gas in the first stage reservoir ranged from 7MPa to 12MPa. The pressure of hydrogen gas in pump tube ranged from 0.1MPa to 0.12MPa. The pressure in test chamber was approximately 200Pa.

After each test, a digital microscope was used to measure the perforation diameter of bumper and the diameter of crater distribution areas on the rear wall of aluminum. The images of the rear wall were processed to identify the damage zones and the distribution and size of craters on the rear walls.

Results and Discussion

Table 2 presents the data from the impact tests. The geometry parameters d_p in Table 2 is projectile diameter; the parameters V, D_{99}, P_s and H_b are the projectile velocity, the diameter of covering 99% of spray area, sink depth of the rear wall front surface, and bulge height of the rear wall back surface respectively.

After Al-sphere projectile penetrated through bumper, debris clouds comprising particles of projectile and bumper was brought behind the bumper. Particles size and material state in debris clouds depends on projectile impact velocity and material characteristics of projectile and bumper. Accordingly, debris clouds impact can generate craters, spallations and perforation on the rear wall. The rear wall damage is characterized by front surface sink and back surface bulge of the rear wall surrounding the impact center and a large splash of finely fragmented and liquid material. Test results are presented in Fig.2.



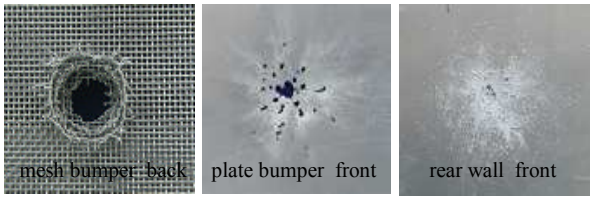
(a) d=3.97mm, v=4.01km/s, No.1 meshes configuration B



(b) d=3.97mm v=3.98km/s No.4 meshes configuration B



(c) d=3.97mm v=4.03km/s No.6 meshes configuration B



(d) d=3.97mm v=4.02km/s No.7 meshes configuration B

Fig.2 Representative test results

Table2 Damage results of aluminum mesh/plate shields

No.	*V (km/s)*	*d_p (mm)*	*D (mm)*	*D_{99} (mm)*	*p_s (mm)*	*H_b (mm)*	*Rear wall damage*
A01-1	3.92	3.97	8.30	152	-	-	Perforation
B01-1	4.01	3.97	7.30	128	-	-	Perforation
B02-4	3.98	3.97	8.02	127	-	-	Perforation
B03-6	4.03	3.97	-	133	4.33	2.90	No perforation
B04-7	4.02	3.97	-	131	3.89	2.20	No perforation
C01-1	4.00	3.97	3.17	138			Perforation
C02-1	4.51	3.97	-	148	2.13	1.18	No perforation
C03-3	3.50	3.97	2.25	121			Perforation
C04-3	4.80	3.97	-	150	-	-	No perforation
C05-4	3.85	3.97	-	130	2.01	0.71	No perforation
C06-4	4.70	3.97	-	143	2.01	3.21	No perforation
C07-2	3.58	3.97	2.85	129	-	-	Perforation
C08-2	4.00	3.97	-	137	2.89	0.76	No perforation
C09-2	5.00	3.97	-	151	-	-	No perforation
D01-3	4.01	3.97	3.01	138	-	-	Perforation
E01-5	3.73	6.35	1.55	144			Perforation
E02-5	4.00	6.35	-	153	1.00	0.51	No perforation
F01-5	3.57	6.35	2.95	141	-	-	Perforation
F02-5	4.03	6.35	-	153	2.11	1.05	No perforation

For shield configuration B with different aluminum meshes is shown in Fig.1, when projectile impact conditions including impact velocity, projectile diameter and impact angle are same, the damage on the rear wall are different. It was found that the rear wall was perforation failure when aluminum mesh bumpers were 14 and 17 meshes respectively. When aluminum mesh bumpers were 20 and 28 meshes respectively, the rear walls of shields were no failure, and only sink and bugle of the rear wall were occurred (see Fig. 2). These results suggest the finer meshes provide more interactions with the debris, thus comminuting, decelerating and dispersing the debris more readily. The finer meshes are to be preferred, as long as they possess sufficient mass to induce substantial projectile fragmentation. So, the ratio of mesh opening size to projectile diameter was an important parameters affecting projectile fragmentation. There is an optimal ratio of mesh opening size to projectile diameter for the same meshes material.

Comparing with shield configuration B, the aluminum mesh wall of shield configuration C was located the site of the second bumper (see Fig. 1). For the same aluminum mesh and impact conditions, the results showed that the rear walls of shield configuration B were perforation failure, and the rear walls of shield configuration C were all no perforation , and only sink and bugle of the rear wall were occurred. Therefore, comparing with the same areal density aluminum alloy plate, the first projectile comminuting capability of aluminum mesh wall was less than that of 0.5mm thickness 2A12 aluminum alloy plate, and AL-plate lead to qualitatively similar projectile comminution and rear wall damage.

At the same time, when the impact velocity was constant, the damage area on the rear wall of configuration B was less than that of configuration C. Thereby, if there is not any other prevention wall between mesh wall and rear wall, the diameter of damage area on the rear wall increased as spacing between mesh wall and rear wall increased. Because of time after time comminution, deceleration and dispersion of the projectile from anterior aluminum plates, the size of debris was very small. The mesh wall makes for small debris passing.

Summary

This paper discussed the results obtained from all impact tests performed by launching aluminum spheres onto aluminum mesh shield configuration. This was done to search for the effects of aluminum mesh on the prevention performance. In this study, effects of aluminum mesh wall position and mesh opening on damage of the rear wall were analyzed. The results showed that mesh wall position, mesh opening and wire diameter had high influence on the hypervelocity impact characteristic of shields. For different shield configurations with the same aluminum mesh, the results indicated that the first mesh wall did not help enhancing the performance of shields, and the last stainless steel mesh wall did not help reducing the damage area on the rear wall. The optimized mesh/plate shield for preventing debris impact should be that: the first bumper possesses the ability to dissipate sufficient kinetic energy of projectile, thus comminuting, decelerating and dispersing the debris more readily; the mesh wall is not fit for the first bumper of shield.

References

[1] M. Lambert: Adv. Space Res. Vol.19 (1997), p. 369.

[2] E. L. Christiansen and J. H. Kerr: Int. J. Impact Eng. Vol. 26(2001), p. 93.

[3] G. Gongshun, P. Baojun, Z. Wei and H. Yue: Int. J. Impact Eng. Vol. 35(2008), p. 1541.

[4] N. N. Myagkov, V. A. Goloveshkin, and A. V. Sulimov: Int. J. Impact Eng. Vol. 36(2009), p. 468.

[5] F. Horz, M. J. Cintala, R. P. Bernhard and T. H. See: Int. J. Impact Eng. Vol. 17(1995), p. 431.

© (2012) Trans Tech Publications, Switzerland
doi:10.4028/www.scientific.net/KEM.488-489.206

Dynamic Antiplane Behavior for a Quarter Infinite Piezoelectric Medium with a Subsurface Circular Inclusion

Tianshu Song[1,a], Dong Li[1,b] and Tamman Merhej[1,c]

[1] School of Aerospace and Civil Engineering, Harbin Engineering University, Harbin, 150001, China

[a]songts@126.com, [b]lidong242@163.com, [c]merhej78@126.com

Keywords: quarter infinite piezoelectric medium; subsurface circular inclusion; dynamic antiplane behavior; dynamic stress concentration factor; electric field intensity concentration factor

Abstract. Dynamic antiplane behaviors are investigated theoretically in this paper for a quarter infinite piezoelectric medium with a subsurface circular inclusion. Based on complex variable and mirror image method, the expressions are obtained on dynamic stress concentration factor (DSCF) and electric field intensity concentration factor (EFICF) at the inclusion's edge caused by the interaction between the inclusion and the right angle edge under time-harmonic anti-plane shearing. While some calculating cases are plotted, so as to show how the frequencies of incident wave, the piezoelectric material's parameters and the structure's geometry influence on DSCF and EFICF. The calculating results indicate that dynamic analyses are important to a quarter-infinite piezoelectric medium with defects at the surface vicinity.

Introduction

There has been an explosion of interest in the field of piezoelectric materials in recent years. The electro-mechanical response of piezoelectric materials is complex as it involves a mechanical response, an electrical response, and a mutual coupling between the mechanical and electrical domains. Due to the coupling behavior, piezoelectric materials have been widely used in various fields. In order to predict the performance and integrity of these devices, it is important to analyze and study the behavior of various defects such as cracks, dislocations and inclusions under the electrical and mechanical fields.

Numerous attempts have been made to analyze the inclusion problems in piezoelectric materials. In the work by Shindo[1], the dynamic theory of anti-plane piezoelectricity was applied to solve the problem of a circular piezoelectric inclusion embedded in an infinite piezoelectric matrix subjected to horizontally polarized shear waves and a steady-state in-plane electrical load. Feng[2] analyzed the scattering of SH-wave by a cylindrical piezoelectric inclusion partially debonded from its surrounding piezoelectric material using the wave function expansion method and singular integral equation technique. Chen[3] carried out the piezoelastic investigation for a circular inclusion embedded in a sandwich. Shodja[4] examined the effect of couple stresses on anti-plane electro-mechanical behavior of piezoelectric media. A piezoelectric-inhomogeneity system consisting of a circular piezoelectric inclusion or void inside an infinite body made of piezoelectric or solely elastic material. Based on the complex variable method, Yang[5] studied the interactions between N randomly-distributed cylindrical inclusions which were subjected to an anti-plane shear stress and an in-plane electric field at infinity. In the work of Pak[6], a closed-form solution of the model of an elliptical piezoelectric inclusion embedded in an infinite piezoelectric matrix for the case of a far-field anti-plane mechanical load and an in-plane electric load.

In the present paper, the dynamic theory of linear piezoelectricity is applied to investigate the scattering of antiplane shear waves by a piezoelectric circular inclusion in a quarter infinite piezoelectric medium. This study is useful in designing piezoelectric composites. Numerical results for the dynamic stress and electric field concentrations are computed, and they are plotted in terms of the wave frequency and the piezoelectric materials' constants.

Basic Governing Equations

The medium is assumed to have been poled along the *z*-axis perpendicular to the *xy*-plane. In the absence of body forces and free charges, the basic governing equations of linear piezoelectricity for dynamic antiplane shearing with exponential time-harmonic factor $exp(-i\omega t)$ are given by

$$c_{44}\nabla^2 w + e_{15}\nabla^2\phi + \rho\omega^2 w = 0\,,\quad e_{15}\nabla^2 w - \kappa_{11}\nabla^2\phi = 0 \tag{1}$$

where c_{44}, e_{15} and κ_{11} are shear elastic modulus, piezoelectric constant and dielectric constant of the medium, respectively; while w, ϕ, ρ and ω are out-of-plane displacement, electric potential, mass density and frequency of the incident wave, respectively. The factor $exp(-i\omega t)$ will be omitted here and after. Introduced a complex variable $\eta = x + iy$, $\overline{\eta} = x - iy$, Eq.1 can be simplified further

$$\frac{\partial^2 w}{\partial\eta\partial\overline{\eta}} + \frac{1}{4}k^2 w = 0,\quad \phi = \frac{e_{15}}{\kappa_{11}}w + f\,,\quad \frac{\partial^2 f}{\partial\eta\partial\overline{\eta}} = 0 \tag{2}$$

where $k^2 = \rho\omega^2 / c_{44}(1 + e_{15}{}^2 / c_{44}\kappa_{11}) = \rho\omega^2 / c_{44}(1+\lambda)$.

The constitutive relation can be written in complex plane $\eta = re^{i\theta}$

$$\begin{aligned}
&\tau_{rz} = c_{44}\left(\frac{\partial w}{\partial\eta}\mathrm{e}^{\mathrm{i}\theta} + \frac{\partial w}{\partial\overline{\eta}}\mathrm{e}^{-\mathrm{i}\theta}\right) + e_{15}\left(\frac{\partial\phi}{\partial\eta}\mathrm{e}^{\mathrm{i}\theta} + \frac{\partial\phi}{\partial\overline{\eta}}\mathrm{e}^{-\mathrm{i}\theta}\right),\quad \tau_{\theta z} = \mathrm{i}c_{44}\left(\frac{\partial w}{\partial\eta}\mathrm{e}^{\mathrm{i}\theta} - \frac{\partial w}{\partial\overline{\eta}}\mathrm{e}^{-\mathrm{i}\theta}\right) + \mathrm{i}e_{15}\left(\frac{\partial\phi}{\partial\eta}\mathrm{e}^{\mathrm{i}\theta} - \frac{\partial\phi}{\partial\overline{\eta}}\mathrm{e}^{-\mathrm{i}\theta}\right),\\
&D_r = e_{15}\left(\frac{\partial w}{\partial\eta}\mathrm{e}^{\mathrm{i}\theta} + \frac{\partial w}{\partial\overline{\eta}}\mathrm{e}^{-\mathrm{i}\theta}\right) - \kappa_{11}\left(\frac{\partial\phi}{\partial\eta}\mathrm{e}^{\mathrm{i}\theta} + \frac{\partial\phi}{\partial\overline{\eta}}\mathrm{e}^{-\mathrm{i}\theta}\right),\quad D_\theta = \mathrm{i}e_{15}\left(\frac{\partial w}{\partial\eta}\mathrm{e}^{\mathrm{i}\theta} - \frac{\partial w}{\partial\overline{\eta}}\mathrm{e}^{-\mathrm{i}\theta}\right) - \mathrm{i}\kappa_{11}\left(\frac{\partial\phi}{\partial\eta}\mathrm{e}^{\mathrm{i}\theta} - \frac{\partial\phi}{\partial\overline{\eta}}\mathrm{e}^{-\mathrm{i}\theta}\right)
\end{aligned} \tag{3}$$

in which τ_{rz}, $\tau_{\theta z}$, D_r and D_θ are shear stresses and electric displacements, respectively.

Boundary Value Problem on DSCF and EFICF

Consider a quarter infinite piezoelectric medium with a circular inclusion at the surface vicinity subjected to an antiplane steady-state shearing wave directed at an incident angle α_0 with the opposite *x*-axis, as show in Fig.1. The boundary conditions at the right angle surface are considered to be traction free and electrically impermeable, while the inclusion is considered to be an electrically permeable continuum to the medium. The boundary conditions can be expressed as

$$\begin{aligned}
&\tau_{yz} = 0, D_y = 0\,,\quad y = h \quad \textbf{or} \quad x = d\\
&w = w^{\mathrm{I}}\,,\quad \tau_{rz} = \tau_{rz}^{\mathrm{I}}\,,\quad D_r = D_r^{\mathrm{I}}\,,\quad \phi = \phi^{\mathrm{I}}\,,\quad r = R
\end{aligned} \tag{4}$$

in which, superscript "I" denotes the physical parameter or variable in the inclusion.

Based on geometric symmetry and of the structure, the solutions for elastic displacement and electric potential of the inclusion and the medium can be given respectively by

$$w^{\mathrm{I}} = \sum_{n=-\infty}^{+\infty} F_n J_n(k^{\mathrm{I}}|\eta|)\cdot\left(\frac{\eta}{|\eta|}\right)^n\,,\quad \phi^{\mathrm{I}} = \frac{e_{15}^{\mathrm{I}}}{\kappa_{11}^{\mathrm{I}}}\cdot w^{\mathrm{I}} + \sum_{n=0}^{+\infty} L_n\eta^n + \sum_{n=1}^{+\infty} M_n\overline{\eta}^n \tag{5}$$

and

$$w = w^i + w^r + w^s, \quad \phi = \phi^i + \phi^r + \phi^s \tag{6}$$

in which, superscripts "*i*", "*r*" and "*s*" denote incident, reflecting and scattering wave fields in the medium, respectively; $J_n(\cdot)$ expresses Bessel function; F_n, L_n and M_n are unknown constants, respectively. The expressions of physical variables in Eq.6 are given as follows.

$$\begin{aligned}
w^i &= w_0 \exp\left\{ik[(\eta - \mathrm{i}h)\mathrm{e}^{-\mathrm{i}(\pi-\alpha_0)} + (\overline{\eta} + \mathrm{i}h)\mathrm{e}^{\mathrm{i}(\pi-\alpha_0)}]/2\right\} \\
w^r &= w_0 \exp\left\{ik[(\eta + 2d - \mathrm{i}h)\mathrm{e}^{-\mathrm{i}\alpha_0} + (\overline{\eta} + 2d + \mathrm{i}h)\mathrm{e}^{\mathrm{i}\alpha_0}]/2\right\} + w_0 \exp\left\{ik[(\eta - \mathrm{i}h)\mathrm{e}^{\mathrm{i}(\pi-\alpha_0)} + (\overline{\eta} + \mathrm{i}h)\mathrm{e}^{-\mathrm{i}(\pi-\alpha_0)}]/2\right\} \\
&\quad + w_0 \exp\left\{ik[(\eta + 2d - \mathrm{i}h)\mathrm{e}^{\mathrm{i}\alpha_0} + (\overline{\eta} + 2d + \mathrm{i}h)\mathrm{e}^{-\mathrm{i}\alpha_0}]/2\right\} \\
w^s &= \sum_{n=-\infty}^{\infty} A_n \{H_n^{(1)}(k|\eta|)[\eta/|\eta|]^n + (-1)^n H_n^{(1)}(k|\eta + 2d - 2\mathrm{i}h|)[(\eta + 2d - 2\mathrm{i}h)/|\eta_1 - 2\mathrm{i}h|]^n \\
&\quad + (-1)^n H_n^{(1)}(k|\eta + 2d|)[(\eta + 2d)/|\eta + 2d|]^{-n} + H_n^{(1)}(k|\eta - 2\mathrm{i}h|)[(\eta - 2\mathrm{i}h)/|\eta - 2\mathrm{i}h|]^{-n}\} \\
\phi^i &= e_{15}/\kappa_{11} \cdot w^i, \quad \phi^r = e_{15}/\kappa_{11} \cdot w^r \\
\phi^s &= \frac{e_{15}}{\kappa_{11}} w^s + \sum_{n=1}^{\infty} B_n[\eta^{-n} + (\overline{\eta} + 2\mathrm{i}h)^{-n} + (-1)^n(\eta + 2d - 2\mathrm{i}h)^{-n} + (-1)^n(\overline{\eta} + 2d)^{-n}] \\
&\quad + \sum_{n=1}^{\infty} C_n[\overline{\eta}^{-n} + (\eta - 2\mathrm{i}h)^{-n} + (-1)^n(\eta + 2d)^{-n} + (-1)^n(\overline{\eta} + 2d + 2\mathrm{i}h)^{-n}]
\end{aligned} \tag{7}$$

where A_n, B_n and C_n are unknown constants, respectively; $H_n^{(1)}(\cdot)$ denotes Hankel function of first kind. Obviously, Eq.7 can meet electromechanical boundary conditions at the right-angle's surface.

All the unknown constants in Eqs.5 and 7 can be obtained solving the boundary value problem. And dimensionless DSCF τ^* and EFICF E^* around the inclusion can be expressed as follows

$$\tau^* = |\tau_{\theta z}|_{r=R}/\tau_0|, \quad E^* = |E_\theta|_{r=R}/E_0|, \quad E_\theta = -\mathrm{i}(\partial\phi/\partial\eta \cdot \mathrm{e}^{\mathrm{i}\theta} - \partial\phi/\partial\overline{\eta} \cdot \mathrm{e}^{-\mathrm{i}\theta}) \tag{8}$$

where $\tau_0 = c_{44}(1 + \lambda\ )kw_0$ and $E_0 = \frac{e_{15}}{\kappa_{11}}(1 + \lambda)kw_0$ refer to the magnitudes of shear stress and electric field intensity of the incident field, respectively.

Calculating Cases

As cases, some of the calculating results based on Eq.8 are plotted for DSCFs and EFICFs. Fig.2 indicates that DSCFs of this paper coincide well to document[7] when the problem is reduced to a quarter infinite elastic medium with a subsurface circular cavity. Figs.3, 4, 5 and 6 show variations of DSCFs and EFICFs with dimensionless wave number *kR* and with different piezoelectric parameter's ratio $e_{15}/e_{15}^{\mathrm{I}}$ or different dielectric parameter's ratio $\kappa_{11}/\kappa_{11}^{\mathrm{I}}$, respectively. It can be seen that both of DSCF and EFICF decrease with increment of *kR* in oscillating form. The influence of $e_{15}/e_{15}^{\mathrm{I}}$ and $\kappa_{11}/\kappa_{11}^{\mathrm{I}}$ on EFICF is more significant than that on DSCF. While EFICFs increase with the increment of $\kappa_{11}/\kappa_{11}^{\mathrm{I}}$.

Summary

Dynamic analyses are more important for a quarter infinite piezoelectric medium with a subsurface inclusion at lower frequencies. At the situation of particular parameters' selection, DSCF and EFICF may be very large due to the influence of right-angle surface. The theoretical method employed in this paper can serve as a reference for modeling of piezoelectric media with complex defects and for the design of piezoelectric components.

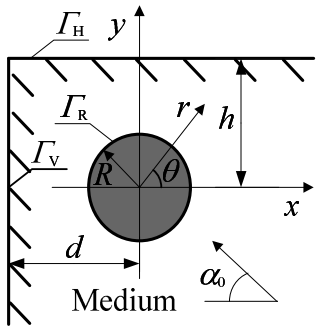


Fig.1 Geometric model

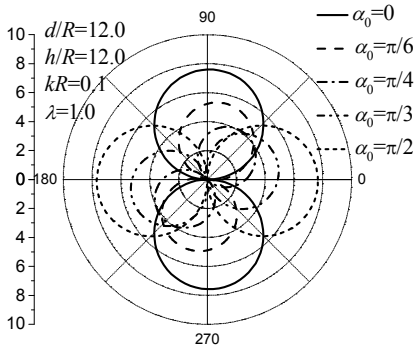


Fig.2 Reduction situation

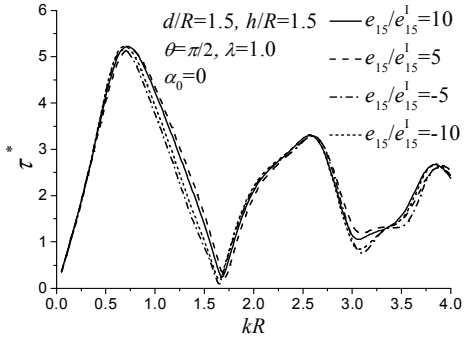


Fig.3 DSIFs varied with $e_{15}/e_{15}^{\mathrm{I}}$

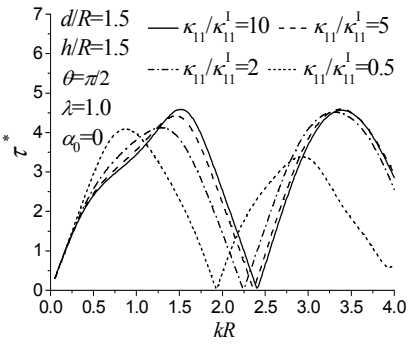


Fig.4 DSIFs varied with $\kappa_{11}/\kappa_{11}^{\mathrm{I}}$

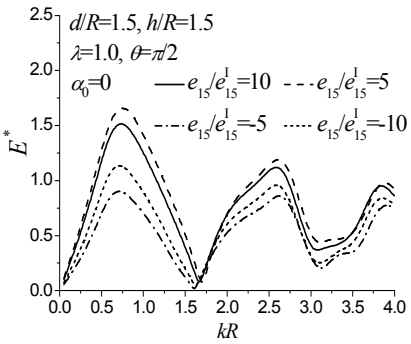


Fig.5 EFICFs varied with $e_{15}/e_{15}^{\mathrm{I}}$

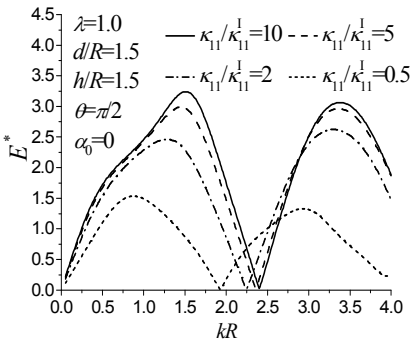


Fig.6 EFICFs varied with $\kappa_{11}/\kappa_{11}^{\mathrm{I}}$

Acknowledgment

The present work is supported by the Fundamental Research Funds for the Central Universities (HEUCF100202).

References

[1] Y. Shindo, H. Moribayashi and F. Narita: Scattering of antiplane shear waves by a circular piezoelectric inclusion embedded in a piezoelectric medium subjected to a steady-state electrical load, ZAMM .Z. Angew. Math. Mech., 82(1): 43-49(2002).

[2] W. Feng, L. Wang, Z. Jiang and Y, Zhao: Shear wave scattering from a partially debonded piezoelectric cylindrical inclusion, Acta Mechanica Solida Sinica, 17(3): 258-269(2004).

[3] F.M. Chen, M.H. Shen and S.N. Chen: Piezoelastic study on singularities interacting with circular and straight interfaces, Int. J. of Solids and Structures, 43: 5541-5554(2006).

[4] H.M. Shodja, M. Ghazisaeidi: Effects of couple stresses on anti-plane problems of piezoelectric media with inhomogeneities, European J. of Mechanics A/Solids, 26: 647-658(2007).

[5] B.H. Yang, C.F. Gao and N. Noda: Interactions between N circular cylindrical inclusions in a piezoelectric matrix, Acta Mechanica, 197(1-2): 31-42(2008).

[6] Y.E. Pak: Elliptical inclusion problem in antiplane piezoelectricity: Implications for fracture mechanics, Int. J. of Engineering Science, 48: 209-222(2010).

[7] Y. Shi, H. Qi and Z.L. Yang: Scattering of SH-wave by circular cavity in right-angle plane and seismic ground motion, J. of Applied Mechanics, 25(3): 392-397(2008).

© (2012) Trans Tech Publications, Switzerland
doi:10.4028/www.scientific.net/KEM.488-489.210

A Study on the Fracture Test in Railroad Truck

Sung-Cheol Yoon [1,a], Jeongguk Kim [1,b], Kwang-Sun Baik [1,c],
Byeong-Choon Goo[1,d] and Kang-Youn Choe[1,e]

[1] Korea Railroad Research Institute, 360-1, Woulam, Uiwang, Kyunggi, South Korea 437-718

[a]scyoon1@krri.re.kr, [b]jkim@krri.re.kr, [c]ksbaik@krri.re.kr kr, [d]bcgoo@krri.re.kr, [e]kchoe@krri.re.kr

Keywords: Truck, Yield stress, Fatigue limit, Goodman diagram.

Abstract. The truck that is used as running equipment for freight car support is a core structural part that supports the load of the car body and that greatly influences the safety of freights and vehicles, as well as their running performance. The running equipment is composed of truck frames, wheels and wheel axles, independent suspensions, and brakes. Among these components, the truck frame supporting the load of the vehicles and freights may be the most important one. This study was carried out to analyze the structure of truck frames and to determine whether they are safe when the maximum vertical load, breaking load, and front and rear loads are applied to them. This was done by subjecting the truck frames to stress tests and then measuring the stress on each of their parts. Before the load test, a structural-analysis program was used for the stress distribution analysis of the truck frame. To measure the stresses based on the results of the structural analysis, strain gages were attached to the surfaces of truck frames. The results of the stress tests showed that truck frames have a safe vehicle load design.

Introduction

The freight trains in Korea that use the railroads are punctual, compared with other transportation means. It is convenient because it is possible to transport the freight in large volumes. Truck frames for Freight trains are among the most critical parts of freight train actuators designed for freight transport [1, 2]. To verify the condition of the structural design of truck frames for freight trains, the study seeks to conduct a test on their load. The objective of the test is to determine the strength of such truck frames and to verify the security of the design. The configuration of truck frames for freight trains are shown in the figure below. The truck frames for freight trains have a welding structure that uses a coil spring for a suspension system. The methods for the load test were in accordance with JIS E 4208 (Test Methods of Static Load for Truck Frames of Railway Rolling Stock) with employment of maximum rigorous conditions for load conditions [3].

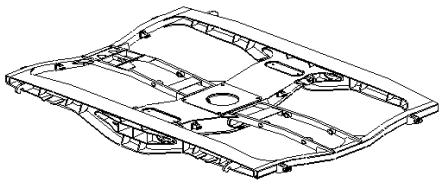


Fig. 1. Configuration of truck frames

Table 1. Weight conditions

Type	Weight (kg)
Tare Weight	20,000
Freight weight	50,000
Spring bottom weight	5,400
Weight per bogie	32,300

Verification Test [4]

Installation of Strain Gauge

As the left and right and front and back of the truck frames for freight trains are symmetrical, a total of 45 channels, consisting of 24 uni-axial strain gauges alongside 7 Rosette strain gauges, were attached to the 1/4 area where stress concentration is expected to occur.

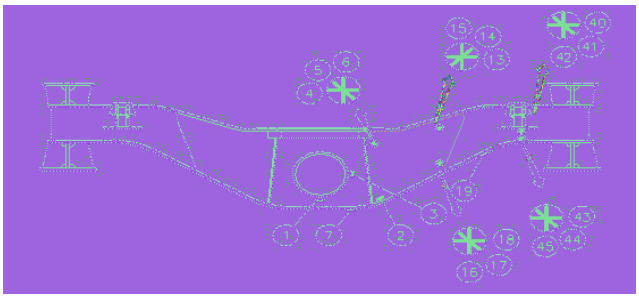


Fig. 2. Side-view of bolster

Vertical Load Test

Vertical load is a load supported by truck frames for freight trains against the weight of a freight car and loaded loads. Vertical static load is a load without consideration to dynamic effects in maximum loading, whereas vertical dynamic load is assumed under the deteriorated conditions with consideration to 0.5g of vertical acceleration of a car body, representing 1.5 times of vertical static load consideration.

Supporting truck frames for freight trains at the axle center of the axle box in which a coil spring is installed, the addition of vertical static load and vertical dynamic load at the dummy center pivot was made.

The Load Test for Brakes

For the load test on the brakes, load incurred by the weight of brake equipment parts was introduced onto each brake hanger bracket by dividing the upper and the bottom direction. Under the identical condition to the vertical load test, load was introduced onto a hanger bracket while exerting vertical dynamic load onto a dummy center pivot with the following order of hanger bracket 1&8, 2&7, 3&6 and 4&5 for the test to be conducted. As for load, the acceleration of 10g onto the load of brake parts was considered.

The Front and Rear Load Test

In consideration of the dynamic effects of front and rear direction of a car body, 40% of the vertical static load was exerted to the front and rear direction of truck frames for freight trains.

The said truck frames were supported at the position of the axle box with the installation of the dummy center pivot and the front and rear load jig. Following restraining the displacement in the front and rear direction of axle box, the front and rear load was exerted while exerting the vertical dynamic load.

The Left and Right Load Test

In consideration of the dynamic effects of the right and left direction of a car body, 30% of vertical static load was exerted to the right and left of truck frames for freight trains.

The said truck frames were supported at the position of the axle box, with the installation of the dummy center pivot and the front and rear load jig. Following restraining the displacement in the front and rear direction of axle box, the front and rear load was exerted while exerting the vertical dynamic load.

The Torsional Load Test

The torsion in the truck frames for freight trains occur due to the unevenness between wheels and rails, as well as the difference in a round running angle.

In the first torsional load test, a liner was inserted onto a coil spring supporting part at the diagonal direction of the truck frames for freight trains with the addition of 15-mm prescribed displacement along with 63 tons of vertical load.

In the second test conducted under further deteriorated conditions, a liner was inserted onto the top of the axle box with the addition of 15-mm prescribed displacement along with 68.9 tons of vertical load.

Table 2. Load condition for test

Load condition	Load (ton)	Remarks
Vertical static load	34.8	W_t
vertical dynamic load	52.2	$W_t+(0.5\times W_t)$
the load of brake parts	5.3	$10\times W_f$
Left and right load	10.4	$0.3\times W_t$
Front and rear load	13.9	$0.4\times W_t$
Torsional load 1	63	
Torsional load 2	68.9	



Fig. 3. Loading test equipment

Table 3. Mechanical properties of used material

Material	Yield stress	Tensile stress	Fatigue Limit			Remarks
			Base metal	Welding and grinding	Welding	
SWS490A	324	490	157	110	70	MPa

Test Result

The test results show that the combined mean stress and combined dynamic stress were obtained using stress obtained from the load test in accordance with KRS 9210 (truck frames for railway rolling stock-general rules for design) with an illustration of them in the stress limit evaluation diagram.

Stress incurred by the torsional load in calculating the combined stress, combined stress was calculated under further deteriorated conditions.

The three-phase strain gauge was compared and is shown in the stress limit diagram after calculating the principal stress and combined mean stress and combined dynamic stress.

Stress Limit Diagrams

Material used in truck frames for freight trains is SWS490A and its mechanical properties are shown in Table 3. At each measured position, the combined mean stress and combined dynamic stress were obtained and presented in the Goodman diagram as shown in figure 4.

According to the test results, high stress occurred in the following positions: the spot where the lower bolster is bent (gauge No. 19, base metal), the lower sideframe is bent (gauge No. 23, base metal) and the end beam surface (gauge No. 32, Welding and grinding).

The test results found that all combined stresses were positioned within the secure area in the Goodman diagram.

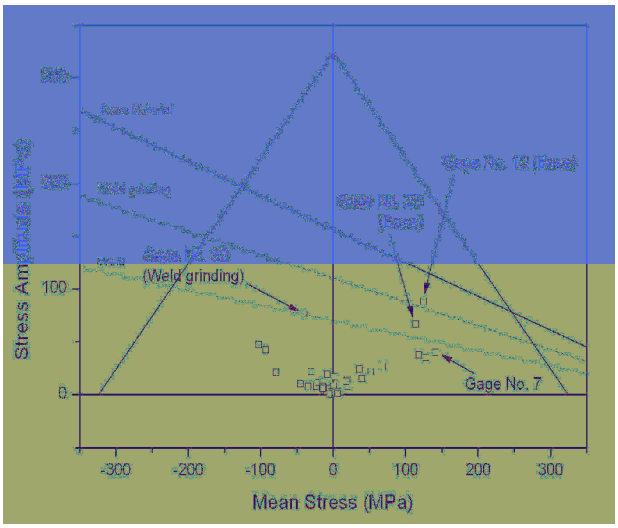


Fig. 4. Goodman diagram

Conclusions

The load test on weld-truck frames for freight trains has the following results:

High stress occurred in the following areas: Gauge No. 19 was the base metal and the spot where the lower bolster was bent; Gauge No. 23 was the base metal and the spot where the lower side frame was bent; and Gauge No. 32 was the grinding area following the end beam welding, satisfying allowable stress. The test results show that all combined stresses were positioned within the secure area in the Goodman diagram.

The load test results show that the truck frames for freight trains, the most critical part of freight train actuators designed for freight transport, fully satisfied the design requirements.

References

[1] J.G. Kim, S.C. Yoon, et al, : Key Engineering Materials, Vols. 385-387 (2008), p. 653.

[2] Japanese Industrial Standards, Truck Frames for Railway Rolling Stock-General Rules for Design, E 4207(1992).

[3] Japanese Industrial Standards, Test Methods of Static Load for Truck Frames and Truck Bolsters of Railway Rolling Stock, E 4208(1988).

[4] Y.S. Ham, H.C. Chung, et al, A Study on Improvement method of Running Safety for Welded Bogie Structure of Railway Freight Car, KRRI Research Report(2004).

[5] Korea Standard Association, General code of design for bogie stock for railway rolling stock, 9210(1996).

© (2012) Trans Tech Publications, Switzerland
doi:10.4028/www.scientific.net/KEM.488-489.214

Fracture Behavior and Mechanical Properties of Bamboo Fiber Reinforced Concrete

Masakazu TERAI[1, a] and Koichi MINAMI[1, b]

[1] Fukuyama University, 985 Aza-sanzo Higashimura-cho, Fukuyama 729-0292, Japan

[a]terai@fuarc.fukuyama-u.ac.jp, [b]minami@fucc.fukuyama-u.ac.jp

Keywords: Fiber Reinforcement, Bamboo, Fracture behavior, Compression Strength, Splitting-tensile Strength, Flexural Strength.

Abstract. Fiber reinforced concrete is superior to plain concrete in toughness, which is the energy absorption at fracture. This study is intended to use fibers extracted from bamboo for tensile reinforcement of concrete. Some experiments were carried out to explore the possibility of bamboo fiber reinforced concrete. As a result, the compressive strength of concrete with 1-2% bamboo fiber is little different from the case without reinforcement. On the other, the splitting tensile and the flexural strength significantly increased with an increased volume fraction of fibers. The strength of bamboo fiber reinforced concrete increased with increasing fiber content as a result of fiber bridging.

Introduction

In recent years, steel prices have soared. For developing countries, steel is difficult to obtain because of expensive prices, and for the construction industry, usage of steel is currently limited heavily. The production of steel has high consumption of fossil fuels, so, the steel discharge in the construction of structures has been presented, showing the possibility of drastic reduction by research institutes. Meanwhile, for developing countries, it is important to make the development of buildings construction; low cost, no requirement of sophisticated technologies and reliable construction methods.

Recently, in the attention in response to global warming issues and sustainable society, the manufacturing using natural materials has become actively. Bamboo, low cost, fast growing, and broad distribution of growth, is expected to contribute significantly to earthquake-resistant construction and seismic retrofit technology in developing countries. The authors also have been studied for the possibility of effective using of 'Bamboo'. The experimental study is carried out in our laboratory on understanding the mechanical behavior of bamboo reinforced concrete member and clarifying the differences of structural properties between steel reinforced concrete and bamboo reinforced concrete.

This paper investigates the application to explore the possibility of bamboo fiber reinforced concrete. Some experiment on bamboo fiber reinforced concrete with the parameters of W/C ratio, the mixing amount of bamboo fiber, aggregate and so on, has been carried out. The mechanical properties and the fresh workability on the Bamboo Fiber Reinforced Concrete (BFRC) are studied.

Experimental procedures

Materials and Mixtures. Three kinds of bamboo, fiber, chip and stick, were used in this study. The Shape of bamboo fibers is shown in Photo 1 and their dimentions are shown in Table 1. The fiber contents were 0, 1 and 2% by volume. Table 2 shows the mix proportions of BFRC. The water to cement ratios (W/C) of BFRC was 50% on all specimens. Cement, aggregates and bamboo were premixed for 60 seconds by means of a two-axis concrete mixer. After that, water were added and mixed for 2 minutes. Mixed concrete was cast in molds of 150×150×530mm for bending tests and

φ100×200mm (cylinder) for compressive and tensile tests. After curing in a laboratory (in the air) for 1 week, A total of specimens were remolded and cured in the air of 10°C until the testing age of 28 days.



(a)Bamboo Fiber (b)Bamboo Stick (c)Bamboo Chip

Photo 1 Bamboo Reinforcement

Table 1 Detail of Bamboo fibers

Bamboo	Size (mm)			Aspect ratio	Photo
	Thickness	Width	Length		
Bamboo Fiber	0.40	0.70	30.0	50.0	
Bamboo Stick	ϕ 1.8		30.0	16.7	
Bamboo Chip	0.27	2.54	30.0	32.3	

Table 2 Mix proportion of concrete

Type of Concrete	W/C (%)	G_{max} (mm)	Unit content(kg/m^3)					Fiber content (%)
			Cement	Water	Fine Aggregate	Caorse Aggregate	Bamboo	
Plane	50.0	15.0	450	225	44.55	30.25	-	0.0
Fiber 1					43.75	29.75	7.86	1.0
Fiber 2					45.25	30.8	15.72	2.0
Stick					43.75	29.75	7.86	1.0
Chip					43.75	29.75	7.86	1.0



Photo 2 Third point loading Test

Test. 5MN Universal Testing Machine was used onto the all test. The 4-point gending tests as shown in Photo2 were carried out on the beam specimens and the fracture loads were recorded. The load was applied in the direction normal to the casting direction. The axial strains are obtained by measuring strain gauges of 30mm length applied on the surface. In addition, the compressometer designed to conduct a strength test was adopted to measure the post peak behaviors. The splitting tests, that is widely used to evaluated the tensile strength of concrete, were carried out with φ100×200mm cylindrical concrete specimen.

Experimental results and Study

Figure 1 shows the compressive strength changes of concrete with and without bamboo reinforcement. However, the temperature in laboratory is kept low at 10°C, the compressive strengt of plane concrete at 28 days was 31.5MPa. Compressive strength – strain curve of BFRC was shown in Figure 2.



Fig. 1 Compressive Strength

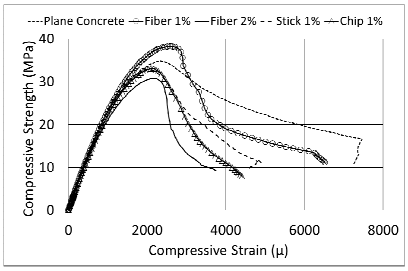


Fig. 2 Compressive Strength – Strain Curves for BFRC

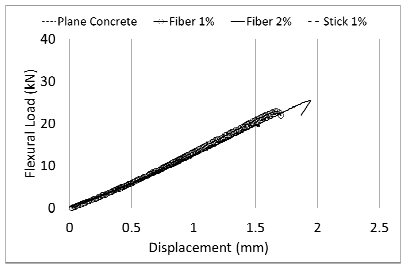


Fig. 3 Flexural Load – Deformation Curves for BFRC

Examples of measured flexural load – displacement curves of BFRC were shown in Figure 3. The influence of the fiber content on the strength was not recognized. After the initial crack occured, the crack was growing. As the load was decreased, the bending crack progressed rapidly, then the data of strain softening behavior could not be recorded.

Photo 3 and 4 shows the concrete debris formed crack surfaces and the fracture surfaces of BFRC specimen with 2% bamboo fiber, respectively. These photos show that the bamboo fibers are evenly distributed over the fracture surface of specimen and have contributed to the failure behavior by the pullout mechanism at the interface between the fiber and interface.



Photo 3 Debris of Fracture Surface



Photo 4 Fracture Surface of Specimen with 2% Bamboo Fiber

The flexural strength, the tensile strength and the compressive strength of three specimens reinforced with different fiber contents are shown in Figure 4. These strength of the SFRC significantly increased with an increased volume fraction of fibers.

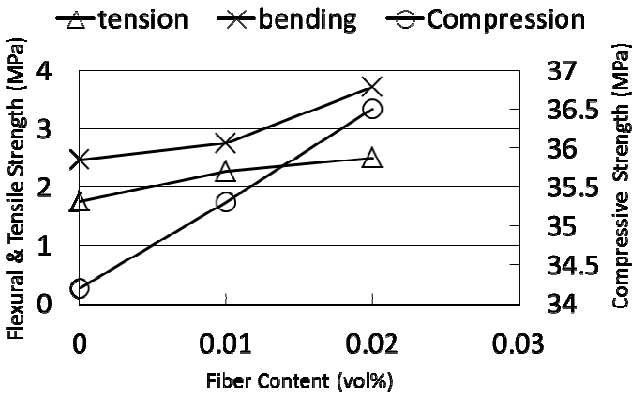


Fig. 4 Strength of BFRC vs. Fiber Content

Figure 5 shows the gravity and the modulus of elasticity of the BFRC specimens measured at the compressive strength test. No effect in both gravity and modulus of elasticity by bamboo reinforcement content can be appeared.

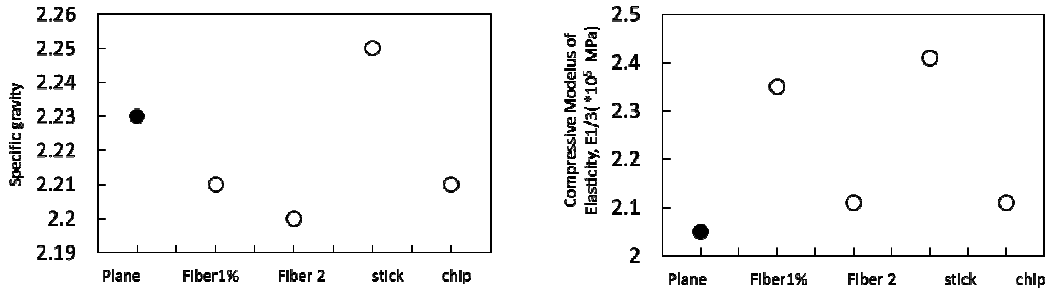


Fig. 5 Gravity & Compressive Modulus of Elasticity of BFRC

The flexural strength, the tensile strength and the compressive strength of three specimens reinforced with different kind of bamboo are shown in Figure 6. This results show that in case of 1% volume fraction of the fibers, the strength of SFRC is not significantly affected by the shape of bamboo reinforcement.

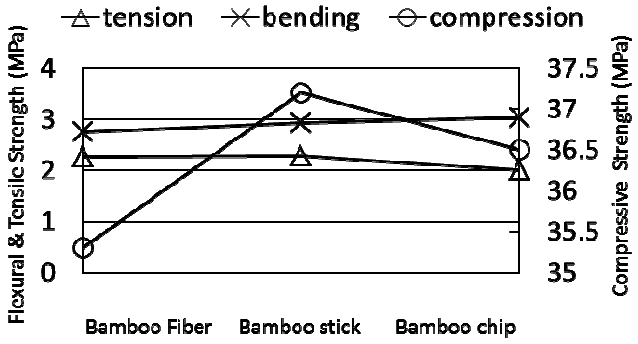


Fig. 6 Strength of BFRC with Fiber Content 1%

Summary

To evaluate the compressive, tensil and flexural strength of bamboo fiber reinforced concrete, influence of the fiber content and the shape of bamboo was experimentally studied.

1）The flexural strength, the tensile strength and the compressive strength of three specimens reinforced with different fiber contents significantly increased with an increased volume fraction of fibers.

2）In case of 1% volume fraction of the fibers, the flexural strength, the tensile strength and the compressive strength of BFRC reinforced with different shape of bamboo is not significantly affected by the kind of bamboo fiber.

Acknowledge

The preparation of some specimens was performed by a research grant of the 2010 Satoru Hiroshi Satake and Technology Foundation of Japan.

Preferences

[1] Ishihara Seiichiro et al. (2006) Influence of Water-Binder Ratio on Bending Fracture Behavior of Hybrid Fiber Reinforced Cementitious Composites, *Proceedings of the Japan Concrete Institute*, 28(1), pp.377-382 (in Japanese)

[2] Ohama Yoshihiko, Demura katsunori and Kondo satoshi (1994) Fundamental Properties of Bamboo Fiber Reinforced Polymer-Modified Pastes, *Proceedings of AIJ Tohoku Chapter Architectural Research Meeting*, 57, pp.265-268 (in Japanese)

© (2012) Trans Tech Publications, Switzerland
doi:10.4028/www.scientific.net/KEM.488-489.218

Study on welding deformations of shipboard of container vessel

Hong Li [1, a], Dalu Qiu[1, b], Guanglei Li[1, c] and Huilong Ren[2, d]

[1]College of Aerospace and Civil Engineering, Harbin Engineering University, Harbin 150001, China

[2]College of Shipbuilding Engineering, Harbin Engineering University, Harbin 150001, China

[a]leeh2005@sohu.com, [b]402138365@qq.com, [c]okliguanglei@126.com, [d]renhuilong@263.net

Keywords: Container vessel; Residual deformation; Equivalent load; Inherent strain; Gaussian heat source

Abstract. Residual plastic strains of the shipboard are the product of nonlinear behaviors during welding. Deformations of a welded shipboard injure the beauty of appearance of the ship, cause errors during the assembly of the shipboard and reduce the strength of the ship. Residual welding deformations of shipboard of a container vessel are studied in this paper. Nonlinear three dimensional transient temperature fields are analyzed by FEM first. The heat source is modeled as a moving heat flux following a Gaussian distribution. Then, applying the equivalent loads induced by the inherent strain on the shipboard, the final in-plane shrinkage and out-of-plane deformations are calculated. Being compared with the experimental results of deformations, the simulated results show mostly conformity.

Introduction

A welding process involves multifarious physical phenomena, such as heat transferring, metal melting and freezing, phase-change, welding stress and deformation and so on. The welding process has always played a major role in industrial production, especially in the automotive, maritime and aerospace industries. Due to high centralized instantaneous heat input in the process of the welding, a great deal of residual stresses and deformations should be brought in the welded structure, which can heavily influence the capability and reliability of the structure. If welding process can be simulated with computer, the best design, procedure method and optimum welding parameter can be obtained before building. The long term goal is to specify an optimal welding procedure, and hence, to minimize deformation and residual stresses due to welding [1]. Therefore it is essential to calculate and analyze the residual deformations of the welded structure.

Based on experimental method and finite element method, the residual deformations of shipboard of container vessel are studied in this paper. In the simulation, the distribution of the temperature field in the welded region must be calculated first. According to the results of temperature and degree of restraint, welding residual plastic strains of shipboard are analyzed in order to get the equivalent loads. Applying the equivalent loads on the shipboard, the final deformations are calculated [2].

Shipboard Model and Welding Conditions

The shipboard of a container vessel is studied in this paper (shown as Fig.1). It consists of outer plate, eleven longitudinal pieces, two stiffened plates, one deck and inner plate. The welding voltage is U=36V. The current is I=300A. The velocity is v=20mm/s. The shrinkage displacements

and out-of-plane displacements of the inner plate are measured after the shipboard is welded in the shipyard. At the same time, according to the equivalent loads method based on inherent strains, the deformations of the shipboard are calculated. The model of finite element analysis is shown as Fig.2. Then the calculation results are compared with the results of the experiments.

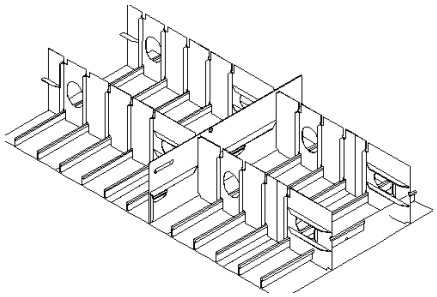


Fig.1 Shipboard of a container vessel

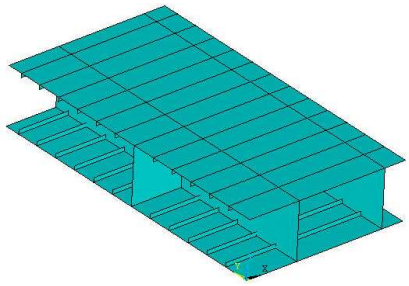
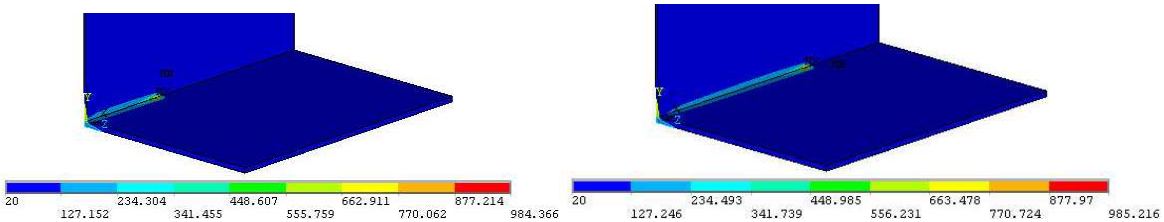


Fig.2 Finite element analysis model

Simulation of Temperature Field

To determine the welding deformations, heat conduction analysis is required first. The most significant factors affecting the analysis are the heat input rate, the moving speed of the heat source, the thickness of the plate, the geometry of the heating line and the properties of the material. The three-dimensional transient temperature field is analyzed by FEM. The heat source is modeled as a moving heat flux following a Gaussian distribution. In the process of analysis, the temperature dependent properties of materials and enthalpy are considered [3].

According to the field equation of heat conduction, the highest temperatures that points experience during the whole welding process everywhere in the welded structure are different. The calculation results are shown as Fig.3. When the center of the heat source moves at a constant velocity along the straight welding line, the temperature profile seen from the heat source will become quasi-stationary. The highest temperature is almost the same. The grads of the temperature in front of the heat source center are much larger than that behind the heat source center. The magnitudes of the temperature far away from the welding line go down to the environment temperature rapidly.



(a) $t = 10s$ (b) $t = 20s$

Fig.3 Calculated results of temperature field

Welding Deformations of Shipboard

The equivalent load method based on the inherent strain is an efficient method for predicting the welding deformation of complicated structures. When using this method, the distribution of the inherent strain in the welded region and equivalent loads induced by the inherent strain must be calculated. Then the final deformations are calculated by elastic finite element analysis. The inherent strains can be expressed as a function of the highest temperature in the welded region and

degree of restraint, which shows the rigidity of the welded region and the adjacent region [4]. The welding deformations discussed and measured in this experiment are transverse shrinkage, longitudinal shrinkage and angular distortion. The welded shipboard is shown as Fig.4.



Fig.4 Welded shipboard of a container vessel

The longitudinal shrinkage and transverse shrinkage results of simulation are shown as Fig.5 and Fig.6. Analyzing the contour of shrinkage, the maximum of shrinkage happen at the edge of the base plates. They are symmetrical about the structure. The transverse stiffened plate can restrain the longitudinal shrinkage. The longitudinal deck can restrain the transverse shrinkage.

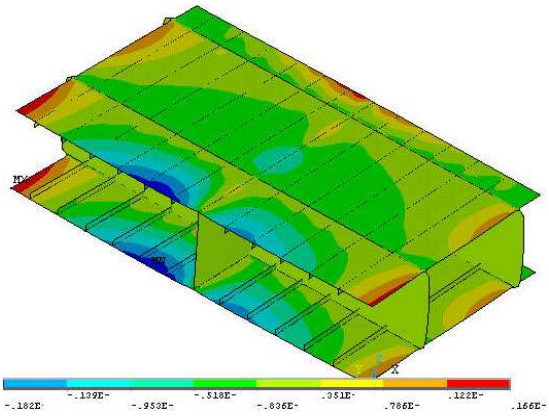


Fig.5 Longitudinal shrinkage contour

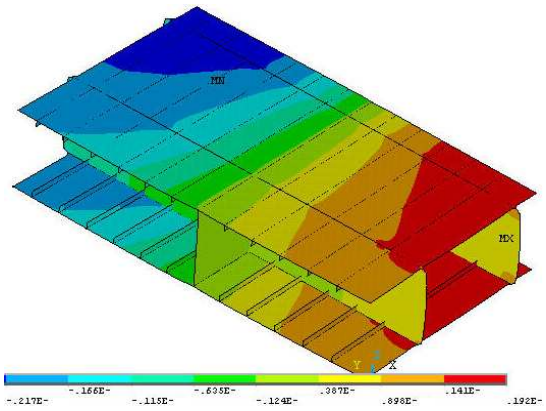


Fig.6 Transverse shrinkage contour

In order to compare the simulated results with the experimental results, some points on the inner plate are selected to inspect the deformation (shown as Fig.7). The out-of-plane deformations are collected from the points numbered 1 to 39. They are near to the stiffened plate 1, stiffened plate 2 and deck respectively. The curves of deformation are shown as Fig.8, Fig.9 and Fig.10. The shrinkage deformations are collected from the points numbered 40 to 46. They locate at the edge of the inner plate. The curve of shrinkage deformation is shown as Fig.11.

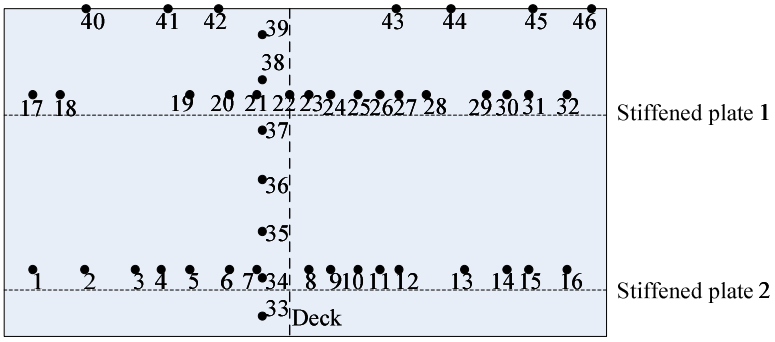


Fig.7 Positions of the measured points

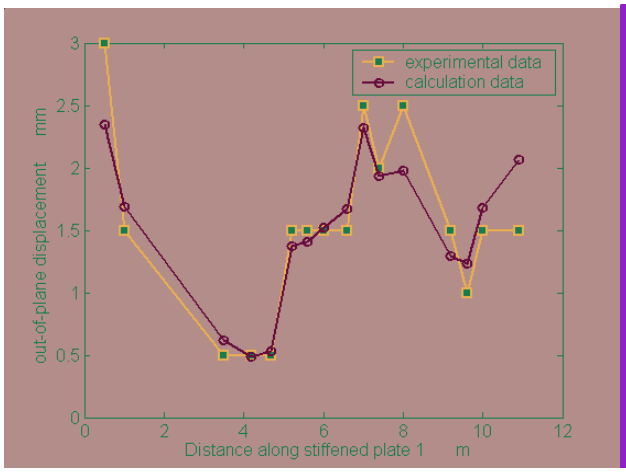


Fig.8 Vertical displacement near stiffened plate 1

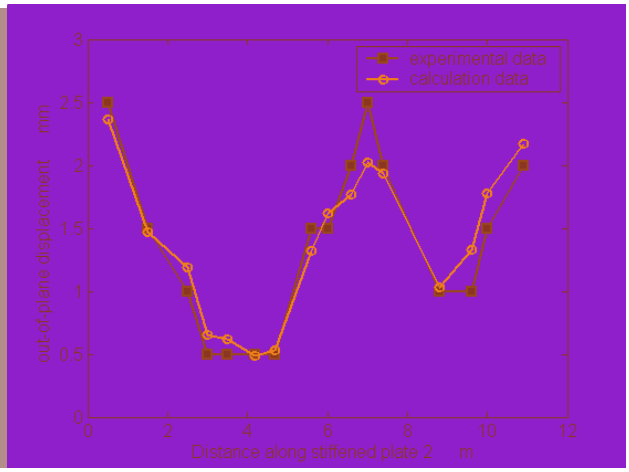


Fig.9 Vertical displacement near stiffened plate 2

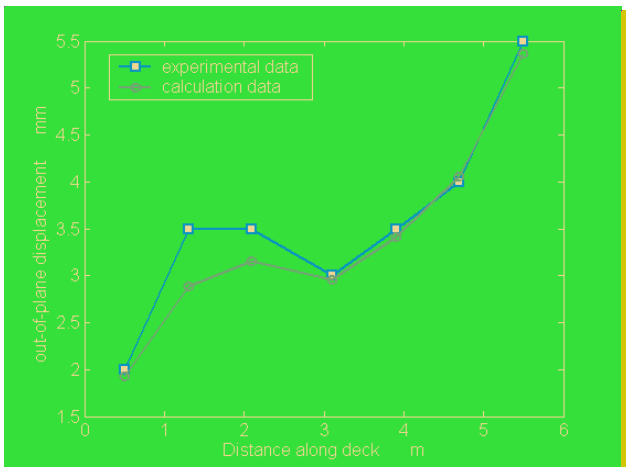


Fig.10 Vertical displacement near deck

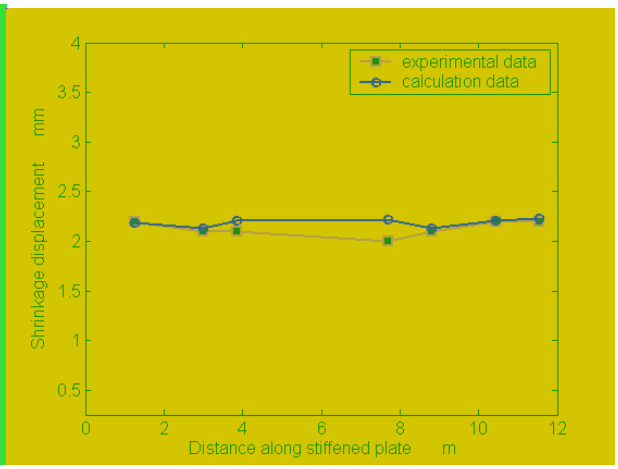


Fig.11 Longitudinal shrinkage of plate

Summary

There are larger out-of-plane deformations and shrinkage deformations left after welding on the shipboard of a container vessel. The equivalent loads method based on inherent strains is accurate and available to predict the deformations in a ship structure, which provides theory foundation and instruction on welding mechanics analysis and engineering.

The way of predicting the residual deformations can prepare an error-minimizing guide at design stage and can be used in accuracy management.

References

[1] D.Radaj. Heat Effects of Welding. Springer-Verlag Berlin Heidelberg ,1992

[2] Chang Doo Jang, Seung II Seo and Dae Eun Ko. A Study on Prediction of Deformations of Plates Due to Line Heating Using a Simplified Thermal Elasto-Plastic Analysis. Journal of Ship Production. 1997, 13(1):22-27

[3] Hong Li, Huilong Ren. Prediction of Welding Distortions of Stainless Steel Ship. Key Engineering Materials, Vols. 348-349 (2007): 373-376

[4] LI Hong, REN Huilong. Simulation of Welding Deformations of Ship Sections. Ship Engineering. Vol.28 No.5 2006: 19-22 (in Chinese)

© (2012) Trans Tech Publications, Switzerland
doi:10.4028/www.scientific.net/KEM.488-489.222

Variational Principle and Buckling Analysis of Functionally Graded Plate with Temperature Changes

Tao Fan

College of Aerospace and Civil Engineering, Harbin Engineering University,

Harbin, China, 150001

fantao19812005@yahoo.com.cn

Keywords: variational principle; FGM; temperature changes; buckling

Abstract. In this paper, the variational principle for the simply supported FGM plate is presented by the variational integral method. Then, the stationary value conditions are obtained with the derivation of the varitional principle. At last, the vibration governing equation is illustrated, which will be benefit for the numerical simulation with finite element method in further investigations. From the stationary value conditions deduced by the variational principle, it can be observed that the buckling characteristics of the simply supported FGM plate can be influenced by the temperature changes.

Introduction

With the remarkable excellent properties, the works of functionally graded materials (FGM) have drawn a lot of attention[1-4]. Due to the characteristics, the FGM are expected in the application of aerospace, nuclear, biological engineering and many other fields. With the development of material science and technology, it is found that the static and dynamic characteristics of FGM can be turned by the temperature changes. As a result, some relevant works are reported on the properties of FGM with thermal effects[5-7]. In this paper, the simply supported FGM plate is studied, which is widely used in high-temperature working environment. Taken the thermal-mechanical coupling into account, the variational principle for the simply supported FGM plate is presented by the variational integral method. With the derivation of the varitional principle, the stationary value conditions are obtained. At last, the vibration governing equation is illustrated, which will be benefit for the numerical simulation with finite element method in further investigations. From the stationary value conditions deduced by the variational principle, it can be observed that the buckling characteristics of the simply supported FGM plate can be influenced by the temperature changes. It is expected to be useful for the design and application of the FGM under high temperature environment.

Vibration Equation

The thermal stress caused by temperature change can be expressed as the following form

$$\sigma^T = -\frac{\overline{E}\alpha T}{1-\upsilon}. \tag{1}$$

where $\overline{E}$ is Young's modulus of FGM plate, $\overline{E}(z) = E(cz^2+1)$, which is supposed to have the gradient along the z direction, α the coefficient of thermal expansion, T the amount of of temperature change and υ the Poisson's ratio, respectively.

The thermal stress caused by the longitudinal loads can be expressed as

$$\overline{N}_x^T = \overline{N}_y^T = \overline{N}^T = \int_{-\frac{h}{2}}^{\frac{h}{2}} \sigma^T dz = N^T(1+\frac{ch^2}{12}), \quad N_{xy}^T = \tau_{xy}^T h = 0. \tag{2}$$

where h is the thick of FGM plate, c the graded coefficient , $N^T = -\frac{E\alpha T}{1-\upsilon}h$.

The bending moment and torsional moment can be expressed as the following form:

$$M_x = -\bar{D}(\frac{\partial^2 w}{\partial x^2} + \upsilon \frac{\partial^2 w}{\partial y^2}), M_y = -\bar{D}(\frac{\partial^2 w}{\partial y^2} + \upsilon \frac{\partial^2 w}{\partial x^2}), M_{xy} = M_{yx} = -\bar{D}(1-\upsilon)\frac{\partial^2 w}{\partial x \partial y}. \quad (3)$$

where w is the deflection of the FGM plate, $\bar{D} = D(1+3ch^2/20)$ the bending stiffness of the FGM plate, and $D = Eh^3/12(1-\upsilon^2)$.

Considering the thermal effect，Hamilton principle of FGM plate can be expressed as

$$\pi_H = \int_{t_0}^{t_1} \iint_S \frac{1}{2}\rho(\frac{\partial w}{\partial t})^2 dxdydt - \frac{1}{2}\int_{t_0}^{t_1} \iint_S \bar{D}\{(\frac{\partial^2 w}{\partial x^2} + \frac{\partial^2 w}{\partial y^2})^2 - 2(1-\upsilon)[\frac{\partial^2 w}{\partial x^2}\frac{\partial^2 w}{\partial y^2} - (\frac{\partial^2 w}{\partial x \partial y})^2]\}dxdydt - \int_{t_0}^{t_1} \iint_S [\bar{N}_x^T \cdot \frac{1}{2}(\frac{\partial w}{\partial x})^2 + \bar{N}_y^T \cdot \frac{1}{2}(\frac{\partial w}{\partial y})^2]dxdydt - \int_{-\frac{t}{2}}^{\frac{t}{2}} (\int_{-\frac{a}{2}}^{\frac{a}{2}} \bar{V}_y w dx + \int_{-\frac{b}{2}}^{\frac{b}{2}} \bar{V}_x w dy + \int_{-\frac{a}{2}}^{\frac{a}{2}} \bar{M}_y \frac{\partial w}{\partial y} dx + \int_{-\frac{b}{2}}^{\frac{b}{2}} \bar{M}_x \frac{\partial w}{\partial x} dy)dt . \quad (4)$$

where ρ is the density， a, b the length and width of FGM plate.

The variation operation is done on π_H in Eq. (4) and letting $\delta\pi_H = 0$, the following equation is obtained

$$\delta\pi_H = \int_{t_0}^{t_1} \iint_S \{\rho \frac{\partial w}{\partial t}\delta(\frac{\partial w}{\partial t}) - \frac{1}{2}\bar{D}[2\frac{\partial^2 w}{\partial x^2}\delta(\frac{\partial^2 w}{\partial x^2}) + 2\frac{\partial^2 w}{\partial y^2}\delta(\frac{\partial^2 w}{\partial y^2}) + 2\upsilon\frac{\partial^2 w}{\partial x^2}\delta(\frac{\partial^2 w}{\partial y^2}) + 2\upsilon\frac{\partial^2 w}{\partial y^2}\delta(\frac{\partial^2 w}{\partial x^2}) + 4(1-\upsilon)\frac{\partial^2 w}{\partial x \partial y}\delta(\frac{\partial^2 w}{\partial x \partial y})] - [\bar{N}_x^T \frac{\partial w}{\partial x}\delta(\frac{\partial w}{\partial x}) + \bar{N}_y^T \frac{\partial w}{\partial y}\delta(\frac{\partial w}{\partial y})]\}dxdydt - \int_{-\frac{t}{2}}^{\frac{t}{2}} [\int_{-\frac{a}{2}}^{\frac{a}{2}} \bar{V}_y \delta w dx + \int_{-\frac{b}{2}}^{\frac{b}{2}} \bar{V}_x \delta w dy + \int_{-\frac{a}{2}}^{\frac{a}{2}} \bar{M}_y \delta(\frac{\partial w}{\partial y})dx + \int_{-\frac{b}{2}}^{\frac{b}{2}} \bar{M}_x \delta(\frac{\partial w}{\partial x})dy]dt = 0 . \quad (5)$$

Using the integration by parts in Eq. (5)

$$\int_{t_0}^{t_1} \rho \frac{\partial w}{\partial t}\delta(\frac{\partial w}{\partial t})dt = \int_{t_0}^{t_1} \rho \frac{\partial w}{\partial t}\frac{\partial}{\partial t}\delta w dt = \rho \frac{\partial w}{\partial t}\delta w\Big|_{t_0}^{t_1} - \int_{t_0}^{t_1} \rho \frac{\partial^2 w}{\partial t^2}\delta w dt . \quad (6)$$

$$\iint_S \frac{\partial^2 w}{\partial x^2}\delta(\frac{\partial^2 w}{\partial x^2})dxdy = \int_{-\frac{b}{2}}^{\frac{b}{2}} \frac{\partial^2 w}{\partial x^2}\delta(\frac{\partial w}{\partial x})dy - \int_{-\frac{b}{2}}^{\frac{b}{2}} \frac{\partial^3 w}{\partial x^3}\delta w dy + \iint_S \frac{\partial^4 w}{\partial x^4}\delta w dxdy . \quad (7)$$

$$\iint_S \frac{\partial^2 w}{\partial y^2}\delta(\frac{\partial^2 w}{\partial y^2})dxdy = \int_{-\frac{a}{2}}^{\frac{a}{2}} \frac{\partial^2 w}{\partial y^2}\delta(\frac{\partial w}{\partial y})dx - \int_{-\frac{a}{2}}^{\frac{a}{2}} \frac{\partial^3 w}{\partial y^3}\delta w dx + \iint_S \frac{\partial^4 w}{\partial y^4}\delta w dxdy . \quad (8)$$

$$\iint_S \frac{\partial^2 w}{\partial x^2}\delta(\frac{\partial^2 w}{\partial y^2})dxdy = \int_{-\frac{a}{2}}^{\frac{a}{2}} \frac{\partial^2 w}{\partial x^2}\delta(\frac{\partial w}{\partial y})dx - \int_{-\frac{a}{2}}^{\frac{a}{2}} \frac{\partial^3 w}{\partial x^2 \partial y}\delta w dx + \iint_S \frac{\partial^4 w}{\partial x^2 \partial y^2}\delta w dxdy . \quad (9)$$

$$\iint_S \frac{\partial^2 w}{\partial y^2}\delta(\frac{\partial^2 w}{\partial x^2})dxdy = \int_{-\frac{b}{2}}^{\frac{b}{2}} \frac{\partial^2 w}{\partial y^2}\delta(\frac{\partial w}{\partial x})dy - \int_{-\frac{b}{2}}^{\frac{b}{2}} \frac{\partial^3 w}{\partial y^2 \partial x}\delta w dy + \iint_S \frac{\partial^4 w}{\partial y^2 \partial x^2}\delta w dxdy . \quad (10)$$

$$2\iint_S \frac{\partial^2 w}{\partial x \partial y}\delta(\frac{\partial^2 w}{\partial x \partial y})dxdy = 2\iint_S \frac{\partial^2 w}{\partial x \partial y}\frac{\partial}{\partial x}\delta(\frac{\partial w}{\partial y})dxdy$$

$$= 2\int_{-\frac{b}{2}}^{\frac{b}{2}} \frac{\partial^2 w}{\partial x \partial y}\delta(\frac{\partial w}{\partial y})dy - 2\iint_S \frac{\partial^3 w}{\partial x^2 \partial y}\delta(\frac{\partial w}{\partial y})dxdy$$

$$= 2\int_{-\frac{b}{2}}^{\frac{b}{2}} \frac{\partial^2 w}{\partial x \partial y}\frac{\partial}{\partial y}\delta w dy - 2\iint_S \frac{\partial^3 w}{\partial x^2 \partial y}\frac{\partial}{\partial y}\delta w dxdy$$

$$= 2\frac{\partial^2 w}{\partial x \partial y}\delta w\Big|_{corner} - 2\int_{-\frac{b}{2}}^{\frac{b}{2}} \frac{\partial^3 w}{\partial x \partial y^2}\delta w dy - 2\int_{-\frac{a}{2}}^{\frac{a}{2}} \frac{\partial^3 w}{\partial x^2 \partial y}\delta w dx + 2\iint_S \frac{\partial^4 w}{\partial x^2 \partial y^2}\delta w dxdy . \quad (11)$$

$$\iint_S \bar{N}_x^T \frac{\partial w}{\partial x}\delta(\frac{\partial w}{\partial x})dxdy = \int_{-\frac{b}{2}}^{\frac{b}{2}} \bar{N}_x^T \frac{\partial w}{\partial x}\delta w dy - \iint_S \bar{N}_x^T \frac{\partial^2 w}{\partial x^2}\delta w dxdy \ . \tag{12}$$

$$\iint_S \bar{N}_y^T \frac{\partial w}{\partial y}\delta(\frac{\partial w}{\partial y})dxdy = \int_{-\frac{a}{2}}^{\frac{a}{2}} \bar{N}_y^T \frac{\partial w}{\partial y}\delta w dx - \iint_S \bar{N}_y^T \frac{\partial^2 w}{\partial y^2}\delta w dxdy \ . \tag{13}$$

Substituting Eqs. (6) - (13) into Eq. (5), it is obtained that

$$-\int_{t_0}^{t_1}\iint_S \{\bar{D}[\frac{\partial^4 w}{\partial x^4}+\frac{\partial^4 w}{\partial y^4}+2\frac{\partial^4 w}{\partial x^2\partial y^2}]-\bar{N}_x^T\frac{\partial^2 w}{\partial x^2}-\bar{N}_y^T\frac{\partial^2 w}{\partial y^2}+\rho\frac{\partial^2 w}{\partial t^2}\}\delta w dxdydt$$

$$+\int_{t_0}^{t_1}\int_{-\frac{a}{2}}^{\frac{a}{2}} \{\bar{D}[\frac{\partial^3 w}{\partial y^3}-(2-\upsilon)\frac{\partial^3 w}{\partial x^2\partial y}]-\bar{N}_y^T\frac{\partial w}{\partial y}-\bar{V}_y\}\delta w dxdt$$

$$+\int_{t_0}^{t_1}\int_{-\frac{b}{2}}^{\frac{b}{2}} \{\bar{D}[\frac{\partial^3 w}{\partial x^3}-(2-\upsilon)\frac{\partial^3 w}{\partial x\partial y^2}]-\bar{N}_x^T\frac{\partial w}{\partial x}-\bar{V}_x\}\delta w dydt$$

$$-\int_{-\frac{a}{2}}^{\frac{a}{2}} \bar{D}[(\frac{\partial^2 w}{\partial y^2}+\upsilon\frac{\partial^2 w}{\partial x^2})+\bar{M}_y]\delta(\frac{\partial w}{\partial y})dx-\int_{-\frac{b}{2}}^{\frac{b}{2}} \bar{D}[(\frac{\partial^2 w}{\partial x^2}+\upsilon\frac{\partial^2 w}{\partial y^2})+\bar{M}_x]\delta(\frac{\partial w}{\partial x})dy\}dt$$

$$+2\bar{D}(1-\upsilon)\frac{\partial^2 w}{\partial x\partial y}\delta w\Big|_{corner}+\iint_S \rho\frac{\partial w}{\partial t}\delta w\Big|_{t_0}^{t_1} dxdy = 0\,. \tag{14}$$

Considering the arbitrary of δw , the vibration equation is obtained,

$$\bar{D}[\frac{\partial^4 w}{\partial x^4}+\frac{\partial^4 w}{\partial y^4}+2\frac{\partial^4 w}{\partial x^2\partial y^2}]-\bar{N}^T(\frac{\partial^2 w}{\partial x^2}+\frac{\partial^2 w}{\partial y^2})+\rho\frac{\partial^2 w}{\partial t^2}=0\,. \tag{15}$$

Natural Frequency

Considering the case of simply supported FGM plate, let the deflection function be

$$w(x,y,t)=\sum_{m=1}^{\infty}\sum_{n=1}^{\infty}(A_m\cos\omega_m t+B_m\sin\omega_m t)\sin\frac{m\pi x}{a}\sin\frac{n\pi y}{b} \ . \tag{16}$$

where ω is natural frequency of FGM plate, $m, n = 1, 2, 3\cdots$.

Substituting Eq. (16) into Eq. (15), the natural frequency of different vibration mode is obtained,

$$\omega_{mn}=\pi\sqrt{\pi^2(\frac{m^2}{a^2}+\frac{n^2}{b^2})^2\frac{\bar{D}}{\rho h}+(\frac{m^2}{a^2}+\frac{n^2}{b^2})\frac{\bar{N}^T}{\rho h}}\,. \tag{17}$$

Numerical Results and Discussions

In this part, the effects of the temperature changes on the vibration characteristics are presented. The relation between the coefficient of functionally graded and natural frequency is illustrated for different cases of temperature changes in Fig. 1 and Fig. 2, where a = 10m, b = 15m, h =0.5m, T = 40,50,60K. It can be observed that the effect of the temperature change on the deflection is obvious. Furthermore, both of the natural frequency ω_{11} and ω_{21} decrease as the amount of of temperature change increases in the chosen domain.

Conclusions

In the present work, based on the variational principle, the vibration equation and the natural frequency are derived, respectively. The influences of the temperature changes on the buckling characteristics of the simply supported FGM plate are presented. The results are expected to be useful to the FGM under high temperature environment.

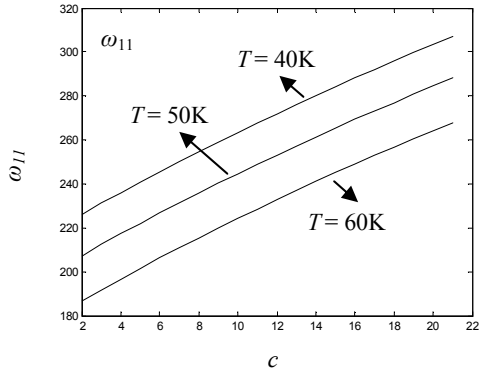


Fig. 1 The relation between ω_{11} and c.

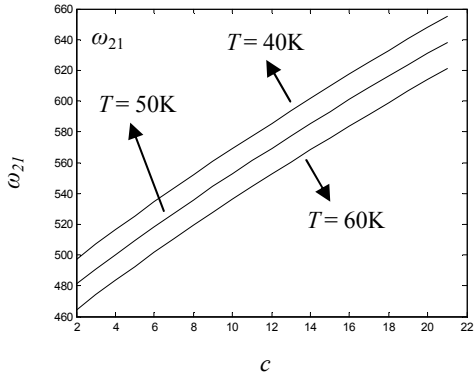


Fig. 2 The relation between ω_{21} and c.

Acknowledgment: This work is supported by the fundamental research foundation of Harbin Engineering University under Grant No.002020260728.

References

[1] L. Ma, L.Z. Wu, L.C. Guo, Z.G. Zhou. On the moving Griffith crack in a non- homogeneous orthotropic medium. European Journal of Mechanics A. Vol. 24,(2005), p.393-405

[2] X.F.Li, B.L.Wang, J.C. Han. A higher-order theory for static and dynamic analyses of functionally graded beams. Archive of Applied Mechanics. Vol. 80, (2010), p.1197-1212

[3] W.Q.Chen, H.J. Ding, J. Liang. The exact elasto-electric field of a rotating piezoceramic spherical shell with a functionally graded property. International Journal of Solids and Structures. Vol. 38, (2001), p.7015-7027

[4]W.J.Feng, R.K.Su. Dynamic internal crack problem of a functionally graded magneto- electro-elastic strip. International Journal of Solids and Structures. Vol. 43, (2006), p.5196-5216

[5]L.C. Guo, N. Noda. An analytical method for thermal stresses of a functionally graded material cylindrical shell under a thermal shock. Acta Mechanica. Vol. 214, (2010), p.71-78

[6]Y.Y.Lee, X. Zhao, J.N. Reddy. Postbuckling analysis of functionally graded plates subject to compressive and thermal loads. Computer Methods in Applied Mechanics and Engineering. Vol. 199, (2010), p.1645-1653

[7]F.Ebrahimi, A. Rastgoo, M.N.Bahrami. Investigating the thermal environment effects on geometrically nonlinear vibration of smart functionally graded plates. Journal of Mechanical Science and Technology. Vol. 24, (2010), p.775-791

© (2012) Trans Tech Publications, Switzerland
doi:10.4028/www.scientific.net/KEM.488-489.226

The Scattering of SH-wave Caused by Subsurface Circular Cavities in a Layered Half-space

CHEN Dong-ni [1,a], QI Hui [1,b], SHI Yong [1,c]

[1]College of Aerospace and Civil Engineering, Harbin Engineering University, Harbin 150001, P.R. China

[a]cdn1230@126.com, [b]qihui205@sina.com, [c]shiyong@hrbeu.edu.cn

Keywords: Scattering of SH-wave, Subsurface circular cavities, Surface elastic layer, Big circular arc postulation method, Dynamic stress concentration

Abstract. The scattering of SH-wave caused by the subsurface circular cavities in an elastic half-space covered with an elastic layer was discussed, which was based on the complex function method ,wave functions expansion method and big circular arc postulation method in which the circular boundary of large radius was used to approximate straight boundary of surface elastic layer. By the theory of *Helmholtz*, the general solution of the *Biot's* wave function was achieved. Utilizing the complex series expansion technology and the boundary conditions, we could transform the present problem into the problem in which we needed to solve the infinite linear algebraic equations with unknown coefficients in wave functions. Finally, the dynamic stress concentration factors around the circular cavities were discussed in numerical examples.

Introduction

Scattering of elastic wave and dynamic stress concentration under the theoretical background was studied from sixties and seventies last century and a great deal of research results [1,2] has been achieved. The solving methods to scattering of SH-wave are mainly two kinds, one is numerical method and the other is analytical method.

In 1982, the complex function method was successfully extended to two-dimensional scattering analysis by LIU Dian-kui [3] et al. The scattering of SH-wave which was discussed in this paper was based just on the complex function method [4-6] and big circular arc postulation method [7] .

Model of problem

The model of an elastic half-space covered with an elastic layer was shown in Figure 1. There were cavities underground. The upper and lower boundaries of elastic layer covered on surface were labeled as T_U and T_D , thickness was marked as h ; shallow cavities were marked as $T_S\left(S=1,...m\right)$, while its radius was expressed by a_s; c_j was the origin of local coordinate system $X_jO_jY_j$; big circular arc center of upper and lower boundaries of elastic layer was marked as O' , radius of big circular arc were marked as R_U and R_D .

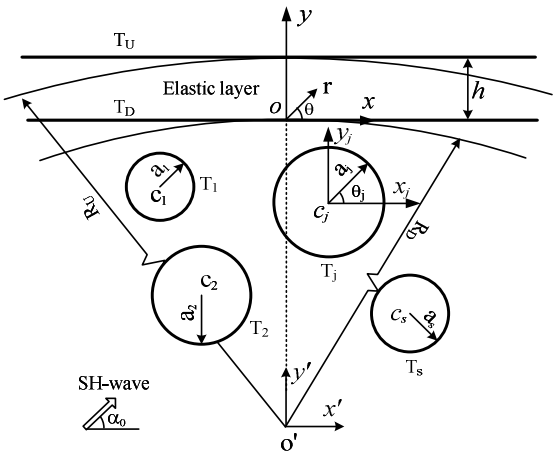


Fig.1 The model of scattering of SH-wave by subsurface
circular cavities in elastic half-space covered with an elastic layer

The general coordinate system XOY and the local coordinate system $X_jO_jY_j$ were established.

As the problem was mixed boundary value problem, so a "partition" idea was used to divide the solution region into two parts I and II. II was the surface elastic layer, and the remaining half-space which contained a number of cavities was I. T_D was the public boundary of two areas.

Basic equations

By using complex variable, $z = x + iy$, $\bar{z} = x - iy$, in complex plane $\left(z, \bar{z}\right)$ the governing equation of W_i was written as

$$\frac{\partial^2 W_i}{\partial z \partial \bar{z}} + \frac{1}{4}k^2 W_i = 0 . \tag{1}$$

The stress was

$$\tau_{xz} = \mu_i\left(\frac{\partial W_i}{\partial z} + \frac{\partial W_i}{\partial \bar{z}}\right), \quad \tau_{yz} = \mu_i\left(\frac{\partial W_i}{\partial z} - \frac{\partial W_i}{\partial \bar{z}}\right) . \tag{2}$$

While in polar coordinate, stress was expressed as

$$\tau_{rz} = \mu_i\left(\frac{\partial W_i}{\partial z}e^{i\theta} + \frac{\partial W_i}{\partial \bar{z}}e^{-i\theta}\right), \ \tau_{\theta z} = i\mu_i\left(\frac{\partial W_i}{\partial z}e^{i\theta} - \frac{\partial W_i}{\partial \bar{z}}e^{-i\theta}\right). \tag{3}$$

Theoretical analysis

In area I, scattering wave $W^{(SI)}$ should be made of $W_{T_S}^{(SI)}$ and $W_{T_D}^{(SI)}$. $W_{T_S}^{(SI)}$ was caused by subsurface cavities T_S, $W_{T_D}^{(SI)}$ was caused by T_D. So

$$W^{(SI)} = W_{T_S}^{(SI)} + W_{T_D}^{(SI)} . \tag{4}$$

Similarly, in area II, scattering wave $W^{(SII)}$ should be made of $W_{T_U}^{(SII)}$ and $W_{T_D}^{(SII)}$. $W_{T_U}^{(SII)}$ and $W_{T_D}^{(SII)}$ were caused by T_U and T_D. So

$$W^{(SII)} = W_{T_U}^{(SII)} + W_{T_D}^{(SII)}. \tag{5}$$

As shown in figure 1, there was an incident steady SH-wave with the incident angel α_0 to positive direction of x axis in half-space, in complex plane $\left(z', \overline{z'}\right)$, the incident wave could be expressed as W_i.

Finally, the equations for solving the problem could be derived from boundary conditions:

$$\begin{cases} (a)\ T_S\left(\left|z_j\right| = a_j\right): \tau_{rz}^{(i)} + \tau_{rz,T_S}^{(SI)} + \tau_{rz,T_D}^{(SI)} = 0 \quad \left(j = 1,...m\right) \\ (b)\ T_D\left(\left|z'\right| = R_D\right): \tau_{rz}^{(i)} + \tau_{rz,T_S}^{(SI)} + \tau_{rz,T_D}^{(SI)} = \tau_{rz,T_U}^{(SII)} + \tau_{rz,T_D}^{(SII)} \\ (c)\ T_D\left(\left|z'\right| = R_D\right): W^{(i)} + W_{T_S}^{(SI)} + W_{T_D}^{(SI)} = W_{T_U}^{(SII)} + W_{T_D}^{(SII)} \\ (d)\ T_U\left(\left|z'\right| = R_U\right): \tau_{rz,T_U}^{(SII)} + \tau_{rz,T_D}^{(SII)} = 0 \end{cases}. \tag{6}$$

Numeric solution

The example discussed in this paper was only the distribution of dynamic stress concentration factor $\tau_{\theta z}^{*}$ around the circular cavity. The model of calculation was shown in figure 2.

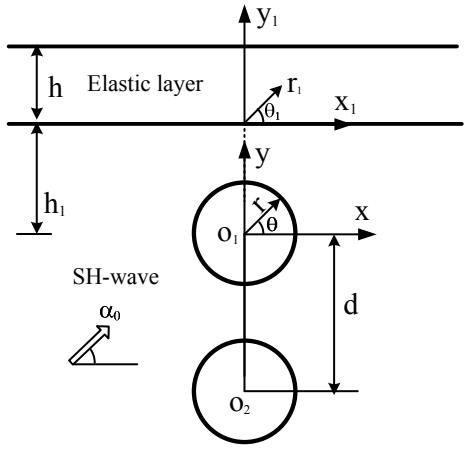


Fig.2 The model of incident of SH-wave to double circular cavities being located in same vertical plane

The numeric solution was shown in figure 3. When α_0=90° or α_0=45°, the distribution of dynamic stress concentration factor $\tau_{\theta z}^{*}$ around upper circular cavity under different medium parameter combination was given in figure 3-1, 3-2, 3-3. It was shown that scattering of SH-wave was shielded and the dynamic stress concentration was weakened while arrangement direction of double cavities was the same with incident wave compared with single circular cavity.

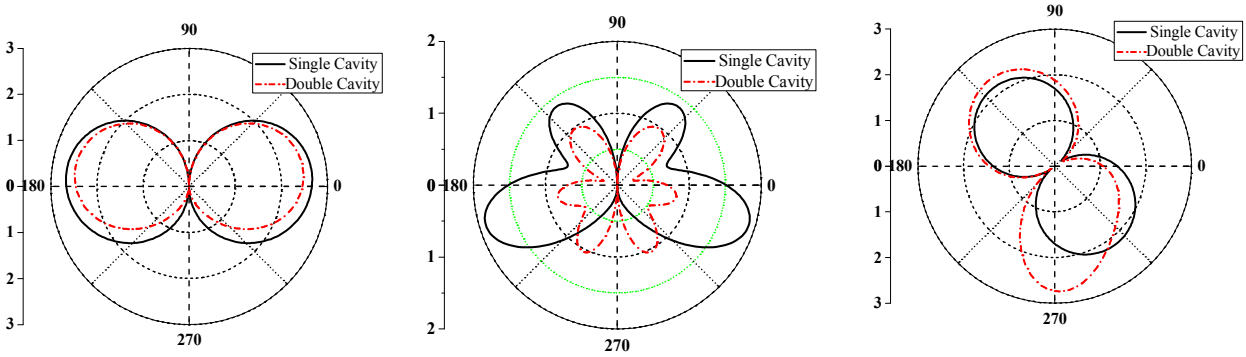


Fig 3-1: $k_1 = 0.1, k_2 = 0.5$, $h_1 = 10.0, h = 5.0$, $d = 2.5$, $\alpha_0 = 90°$

Fig 3-2: $k_1 = 2.0, k_2 = 0.1$, $h_1 = 10.0, h = 5.0$, $d = 2.5$, $\alpha_0 = 90°$

Fig 3-3: $k_1 = 0.1, k_2 = 0.5$, $h_1 = 3.0, h = 5.0$, $l = 20.0$, $\alpha_0 = 45°$

Fig.3 Distribution of DSCF around left circular cavity while double circular cavities were located in same vertical plane ($\mu_1 = \mu_2 = 1.0$)

Conclusion

By using complex function method, multi-polar coordinate movement technology and big arc postulation method, the approximate analytic solution of SH-wave scattering by circular cavities was given. The numeric solution showed that the existence of surface elastic layer could change the distribution of dynamic stress concentration around circular cavities obviously. When the arrangement direction of double cavities was the same with incident wave, the dynamic stress concentration caused by scattering of SH-wave was weakened, conversely, the dynamic stress concentration factor was enlarged remarkably. Therefore, the existence of surface elastic layer in half-space and subsurface cavities must be minded seriously in engineering practice.

References

[1] Lin Gao: submitted to World Earthquake Engineering (1990)

[2] Pao. Yih-hsing: submitted to Applied Mechanics Review (1998)

[3] Liu D.K. Gai. B.Z. and Tao G..Y: submitted to Acta Mechanica Sinica (1981)

[4] Liu D.K. Gai. B.Z. and Tao G..Y: submitted to Wave Motion (1982)

[5] Shi S.X. Liu D.K: submitted to Acta Mechanica Sinica (2001)

[6] Lin H. Liu D.K: submitted to Earthquake Engineering and Engineering Vibration (2002)

[7] Liang J.W. Wei X.L. Vincent W.Lee: submitted to Chinese Journal of Geotechnical Engineering (2009)

© (2012) Trans Tech Publications, Switzerland
doi:10.4028/www.scientific.net/KEM.488-489.230

Fatigue Damage in On-Axis and Off-Axis Woven-Fiber/Resin Composite

John Montesano[1, a], Zouheir Fawaz[1, b], Kamran Behdinan[1, c], Cheung Poon[1, d]

[1]Dept. of Aerospace Eng., Ryerson University, 350 Victoria St., Toronto, ON, Canada M5B 2K3
[a]gmontesa@ryerson.ca, [b]zfawaz@ryerson.ca, [c]kbehdina@ryerson.ca, [d]c1poon@ryerson.ca

Keywords: Fatigue; Damage Progression; Polymer Matrix Composites; Mechanical Properties

Abstract. In this study the tensile static and fatigue behaviour of a woven-fabric laminate is investigated in both the on-axis and off-axis material directions. Emphasis is placed on the development of damage and its influence on the stress-strain behaviour of the laminate. The test results illustrate that there is a high degree of anisotropic behaviour due to anisotropic damage development, which is evident by the variation of the material behaviour between the on-axis and off-axis test specimens. The fatigue tests also suggest that the on-axis specimens exhibit noticeable stiffness degradation, while the off-axis specimens do not. The qualitative results provide significant insight into the type of damage mechanism responsible for the observed behaviour.

Introduction

Recently advanced polymer matrix composite (PMC) materials have been more frequently employed for aerospace applications. Specifically, textile composites such as woven-fabric PMCs have been shown to have numerous advantages when compared to more conventional unidirectional-ply PMC laminates [1, 2]. Extending the usable range of woven fabric-reinforced PMCs for primary load-bearing aerospace structures is consequently of great importance. In service, composite components may be subjected to local on-axis and off-axis static and cyclic loading due to the variation of the fiber orientation throughout the component. As a result, an improved understanding of the on-axis and off-axis behaviour of these advanced materials is warranted.

In general, few experimental fatigue studies on woven fabric-reinforced composites have been reported in the open literature [1, 3-5], fewer of which consider off-axis loading (i.e., applied loading is not parallel to the warp or weft yarns) [2, 6]. In the present study, the on-axis and off-axis tensile static and fatigue behaviour of a woven-fabric laminate at room temperature is examined. The focus of the study is on monitoring the development of damage and determining its corresponding effect on the material stress-strain behaviour.

Material and Experimental Details

Material and Test Specimens. The material used for the experiments was a two-dimensional 8-harness-satin (8HS) woven carbon fiber-reinforced thermosetting resin. Each laminate panel consisted of 6 plies of the woven carbon/resin. The weave direction of all plies for the on-axis panels was oriented along the loading axis, while for the off-axis panels the weave direction of all plies was oriented at 45° bias from the loading axis. On-axis test specimens were cut to nominal dimensions of 300 mm × 25 mm, while off-axis test specimens were 470 mm × 25 mm. Tapered aluminum end tabs 50 mm in length were then bonded to each specimen in compliance with testing standard ASTM D 3479 [7].

Experimental Protocol. All static and fatigue tests were performed on an MTS 322 loading frame equipped with hydraulic wedge grips. Both surface bonded resistance strain gages and a clip-on extensometer were employed to monitor strain. Ultimate static tension tests were performed in displacement control with a constant crosshead speed of 0.8 mm/min at room temperature to determine the on-axis and off-axis tensile strengths. Tension-tension fatigue tests were performed at room temperature under load control with a constant stress ratio of 0.1, loading frequency of 5 Hz, and maximum stress of 65% of the respective ultimate stress. Fatigue tests were interrupted at predefined intervals to perform displacement controlled static tests up to the maximum cyclic stress in order to monitor the change in the specimen stiffness. In addition, all test specimens were inspected *post-mortem* using an optical microscope and a scanning electron microscope (SEM).

Experimental Results and Discussion

Static Tensile Tests. The axial stress-strain results of the on-axis and off-axis ultimate static tension tests are shown collectively in Fig. 1. Note that the calculated stress and strain data values in all the presented plots have been scaled respectively by different scalar values. It is not surprising that the on-axis specimens have a significantly higher failure stress and stiffness compared to that of the off-axis specimens. It is also noteworthy that the failure strain for the off-axis specimen was more than 2x greater than that of the on-axis specimen. In addition the on-axis specimens exhibited linear behaviour up until failure, while the off-axis specimens initially exhibited linear behaviour followed by nonlinear behaviour as shown in Fig. 1. These characteristics can be mainly attributed to the fact that the on-axis specimens have a fiber-dominated nature, while the off-axis specimens are matrix-dominated. Since the thermosetting matrix is weak relative to the fibers, the off-axis specimens are typically more susceptible to damage development at lower applied stresses.

The fracture surface for each test specimen consisted of a dominant crack across the specimen width. For the on-axis specimens, the failure surface was perpendicular to the loading direction without any appreciable delamination or fiber pullout. This would indicate that the failure morphology was brittle-natured. For the off-axis specimens, the failure surface was oriented at 45° from the loading axis (i.e., along the fiber direction) with some delamination and more of a brushy appearance in the vicinity of the fracture. The overall area affected by these failure modes was however minimal, which again is an indication of a brittle-natured failure. This localized failure behaviour does nevertheless explain the elongation observed in the off-axis specimens approaching failure. This highly localized damage pattern may also explain the fact that the off-axis specimen initially exhibits linear stress-strain behaviour followed by nonlinear behaviour closer to fracture.

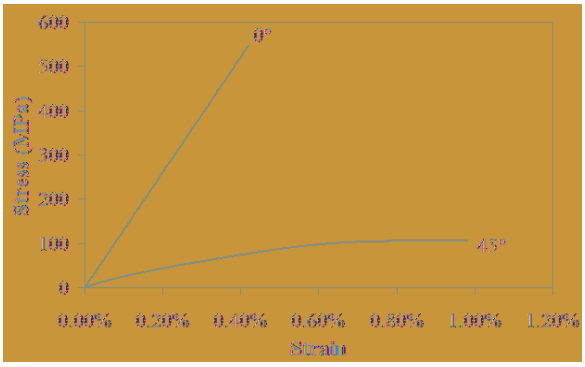


Figure 1. Ultimate static tensile axial stress-strain behaviour.

(a) (b)

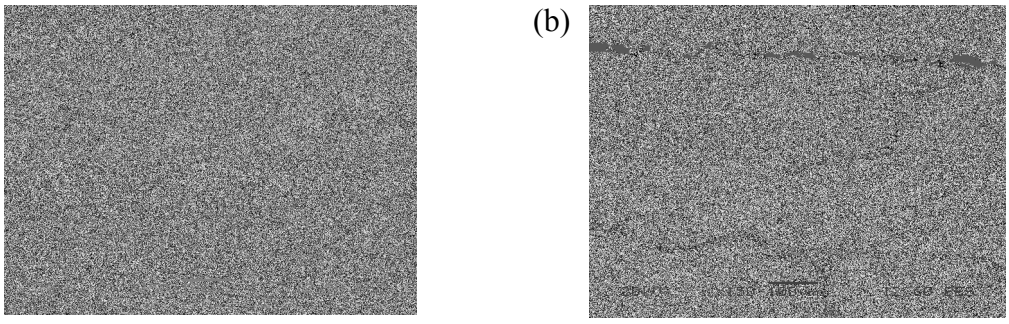


Figure 2. SEM photomicrographs (150x magnification): (a) on-axis static and (b) off-axis static.

Cross-sectional photomicrographs of an on-axis and off-axis specimen are shown in Fig. 2. In both specimens, the extent of damage in the vicinity of the fracture surface is far greater than that away from the fracture surface. Typical damage modes were through-thickness cracking in the fiber yarns (at the fiber/matrix interface, propagating along the axis of the yarns), intra-ply cracking between adjacent yarns at the crossover locations, and local matrix cracking in the matrix-rich zones. Intra-ply cracking at yarn crossover locations is a common damage mode for textile composites due to the shearing effect between the crossing fiber yarns [8]. This was more severe for the off-axis specimen due to the tendency of the off-axis fiber yarns to rotate towards the loading

axis (see Fig. 2). This may further explain the significant elongation exhibited by the off-axis specimen before failure, where weakening of the crossover locations due to this shearing effect allowed reorientation of the fiber yarns. In both cases, the orientation of the fibers dictated the direction of damage propagation and the locations of the observed anisotropic damage patterns.

Fatigue Tests. The axial stress-strain results of the intermittent static tests for the on-axis and off-axis fatigued specimens are shown in Fig. 3 as successive stress-strain curves. Note that the fatigue life of the on-axis specimens was about 10x greater than that of the off-axis specimens. The permanent deformation (observed by the degree of shifting or ratcheting of the stress-strain curve) and the energy dissipation exhibited by the off-axis specimens were significantly greater than that of the on-axis specimens. For the off-axis specimens the majority of the dissipated energy and permanent deformation occurs in the early stages of cycling. For the on-axis specimens the degree of dissipated energy is consistent throughout cycling, while the permanent deformation is relatively minimal. In addition, the on-axis specimen exhibited notable stiffness loss during cyclic loading, approximately 25% reduction in the modulus after 3,000,000 cycles, while the off-axis specimen did not exhibit any stiffness loss. In fact, the off-axis specimen exhibited a minor increase in stiffness during cyclic loading. The off-axis specimens also exhibited nonlinear stress-strain behaviour in the early stages of cycling, which became more linear as the fatigue cycles increased.

The fracture surface for the on-axis fatigued specimens was similar to that observed for the on-axis static specimens; a dominant crack normal to the loading axis with little delamination or fiber pullout. Edge effects were also observed for the on-axis fatigue specimen, including edge cracking and surface fiber yarn protrusion near the edges. The fracture surface for the off-axis fatigued specimen was however quite different from that observed in the off-axis static specimen. Significant necking was observed as the off-axis fiber yarns reoriented towards the loading axis, with fracture occurring in both the ±45° directions. Significant delamination, fiber pullout and matrix fallout occurred in a large area surrounding the fracture surface. This is indicative of more matrix-dominated damage modes and fiber-matrix interface failure modes.

Cross-sectional photomicrographs of on-axis and off-axis fatigue specimens are shown in Fig. 4. Similar to the static specimens, an increased amount of damage was found in the vicinity of the fracture surface for each specimen. Commonly observed damage modes in both on-axis and off-axis test specimens include through-thickness cracking in the fiber yarns propagating along their axes, intra-ply cracking between adjacent yarns at the crossover locations, and local matrix cracking in the matrix-rich zones. The damage was however more widespread throughout the length of each specimen in contrast to that observed with the static test specimens, with the on-axis specimen generally containing more damage throughout. Again, the observed anisotropic damage patterns and the directions of damage propagation were a direct result of the fiber yarn orientations.

Some test specimens were fatigue tested and sectioned prior to failure in order to observe the pre-failure damage states. SEM analysis of the off-axis specimens indicated that there was little damage present in the material until just before failure, suggesting that fracture was triggered when a critical amount of damage developed locally. This may explain why the stiffness of the specimen remained fairly constant until close to failure. This also suggests that the energy dissipation and permanent deformation exhibited by the off-axis specimens is a result of fiber reorientation and/or characteristic material dissipative behaviour in the early stages of cycling. Regarding the specimen stiffness, it may be that accumulated fatigue damage during the initial portion of cycling was offset by the reorientation of the off-axis fiber yarns. In addition, as the fiber yarns continue to straighten during cycling, the behaviour of the material would tend to be more fibre-dominated. This was shown as the stress-strain curves became more linear during cycling. Recall that significant intra-ply cracking was observed between adjacent fiber yarns at the off-axis crossover locations.

SEM analysis of the on-axis specimen indicated that significant damage was present in the specimen before failure occurred, which suggests that damage accumulation was more gradual and more widespread. The degree of energy dissipation and permanent deformation is relatively minor when compared to the off-axis specimen, suggesting that cumulative damage is the main source of this characteristic behaviour. This indicates that the gradual stiffness loss exhibited by the specimen

is mainly due to fatigue damage accumulation. The main observed microscopic damage modes affecting the specimen compliance include through-thickness cracking in the transverse fiber yarns propagating like mode 1 cracks, and intra-ply/matrix cracking at the yarn crossover locations causing weakening of these zones and more compliance of the specimen.

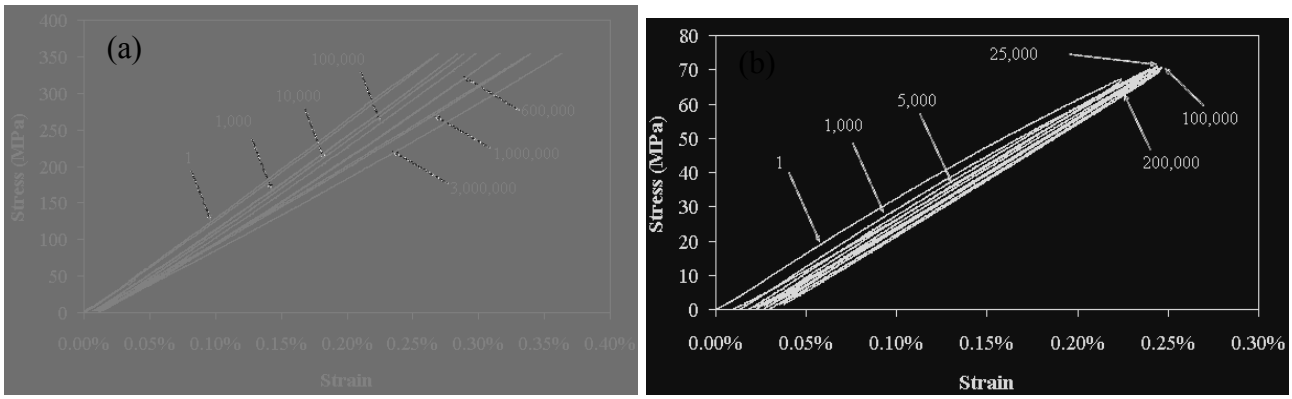


Figure 3. Fatigue stress-strain behaviour at indicated loading cycle: (a) on-axis, and (b) off-axis.

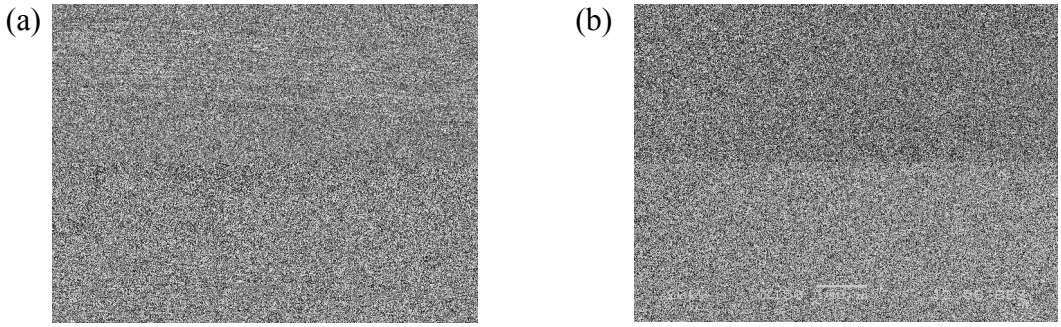


Figure 4. SEM photomicrographs (150x magnification): (a) on-axis fatigue and (b) off-axis fatigue.

Conclusion

The development of microscopic damage and its resultant effect on the tensile stress-strain behaviour of a woven-fabric PMC laminate loaded in on-axis and off-axis directions was presented. Ultimate static tensile tests indicate that off-axis specimens exhibited matrix-dominated behaviour with significant elongation to failure due to damage at fiber yarn crossover locations. On-axis static specimens exhibited fiber-dominated behaviour with minor elongation. Fatigue tests indicate that in the off-axis specimens gradual damage accumulation at the fiber yarn crossover locations causes significant fiber yarn reorientation which offsets the effects of damage accumulation causing the effective specimen stiffness to remain constant. Gradual damage accumulation in the on-axis fatigue specimens does however cause measurable stiffness degradation. An analytical fatigue model is currently being developed to consider these on-axis and off-axis characteristics.

References

[1] U. Hansen: J. Compos. Mater. Vol. 33 (1999), p. 614.
[2] M. Kawai and T. Taniguchi: Compos. Part A Vol. 37 (2006), p. 243.
[3] L. Toubal, M. Karama and B. Lorrain: Int. J. Fatigue Vol. 28 (2006), p. 1867.
[4] Y. Miyano, M.K. McMurray, J. Enyama and M. Nakada: J. Compos. Mater. Vol. 28 (1994), p. 1250.
[5] T. Shimokawa, Y. Kakuta, D. Saeki and Y. Kogo: J. Compos. Mater. Vol. 41 (2007), p. 2245.
[6] V. Tamuzs, K. Dzelzitis and K. Reifsnider: Applied Compos. Mater. Vol. 11 (2004), p. 259.
[7] ASTM D 3479/D 3479M-96: Standard test method for tension-tension fatigue of polymer matrix composite materials. ASTM International 2007.
[8] S.V. Lomov, D.S. Ivanov, T.C. Truong, I. Verpoest, F. Baudry, K. Vanden Bosche and H. Xie: Compos. Sci. Technol. Vol. 68 (2008), p. 2340.

© (2012) Trans Tech Publications, Switzerland
doi:10.4028/www.scientific.net/KEM.488-489.234

Effect of hydrogen on mechanical properties of type 310S stainless steel

Noriyuki Takano[a], Yutaka Kaidu

Advanced Materials Processing Research Laboratory, Kanazawa Institute of Technology,
3-1 Yatsukaho, Hakusan, Ishikawa 924-0838, JAPAN
[a]ntakano@neptune.kanazawa-it.ac.jp

Keywords: Hydrogen embrittelment, SSRT, Austenitic stainless steel, Martensite

Abstract. It is known that type 310S stainless steel is insensitive to hydrogen embrittlement. Then, the effect of hydrogen on the mechanical properties has not been studied in detail. In the present work, SSRT was carried out under hydrogen cathodic charging condition. Elongation increased by hydrogen charging, while reduction of area decreased. A lot of micro-cracks were observed on the side surface of fractured specimens into which hydrogen was charged, while no cracks were observed on the side surface of fractured specimens without hydrogen charging. Micro-cracks were also observed on the surface of unloaded specimens that were annealed after hydrogen charging. Therefore, it is considered that cracks occur from the defects induced by hydrogen charging.

Introduction

It is known that austenitic stainless steels are less susceptible to hydrogen embrittlement because of low hydrogen diffusivity and high hydrogen solubility. Austenite stability, however, influences susceptible of hydrogen embrittlement [1,2]. Hydrogen embrittlement occurs in type 304, which austenite stability is low, because of stress induced α' martensitic transformation, but it does not occur in type 310S, which is most stable austenitic steel [3]. On the other hand, Eliezer at al. have reported that stressing of type 310 with cathodic charging produce shallow, nonpropagating cracks [1]. It implies that micro-cracks are also induced by hydrogen in austenitic stainless steels without α' martensite. It is interested in the mechanism of micro-crack initiation in austenitic stainless steels without α' martensite. The purpose of the present paper is to investigate the origin of the micro-cracks and the effect of them on the mechanical properties. Then, tensile tests were carried out in air on both the hydrogen charged specimen and discharged specimen to make a role of hydrogen clear.

Experimental procedure

Specimens were machined from ϕ8mm drawing rods of type 310S stainless steel, whose chemical composition is shown in Table 1. The dimensions of the tensile specimen are shown in Fig. 1. Its surface was polished chemically by the aqueous solution that contains 2.9mass% of hydrofluoric acid and 29mass% of hydrogen peroxide after polishing mechanically by alumina powder (0.1μm) .

Table 1 Chemical compositions [mass%].

C	Si	Mn	P	Ni	Cr	S
0.02	0.3	1.07	0.028	19.26	24.1	0.001

Hydrogen was charged electrochemically into specimens during 48 hours at the cathode current density of 445 $A \cdot m^{-2}$ in 0.5 $kmol \cdot m^{-3}$-H_2SO_4 electrolytic solution with 1.4$kg \cdot m^{-3}$ thiourea as a recombination poison. Some specimens were annealed at 673K during 2 hours after hydrogen charged to discharge dissolved hydrogen. Tensile tests were carried out at room temperature in air for no-charged, charged and discharged specimens. Strain rate was 10^{-5} s^{-1}. Fracture surface and side surface were observed with SEM.

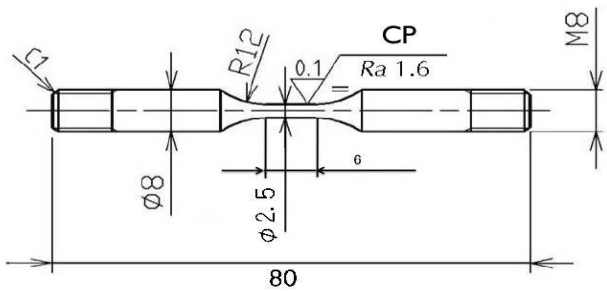
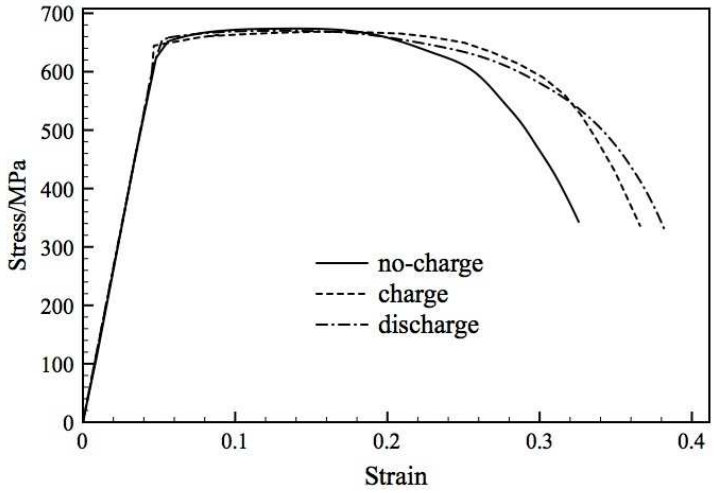


Fig.1 Dimensions of the tensile specimen.

Results and discussion

Stress-strain curves are shown in Fig.2. Though these curves are the same to maximum stress, more elongation is shown in both hydrogen-charged and discharged conditions than no-charged one. It is known that hydrogen enhances the localized plasticity [4]. However, the elongation also increased in the discharged condition in comparison with no-charged condition. Hydrogen is hardly contained in the discharged specimen. Then, the reason of the increase of elongation is not due to the hydrogen enhanced localized plasticity.



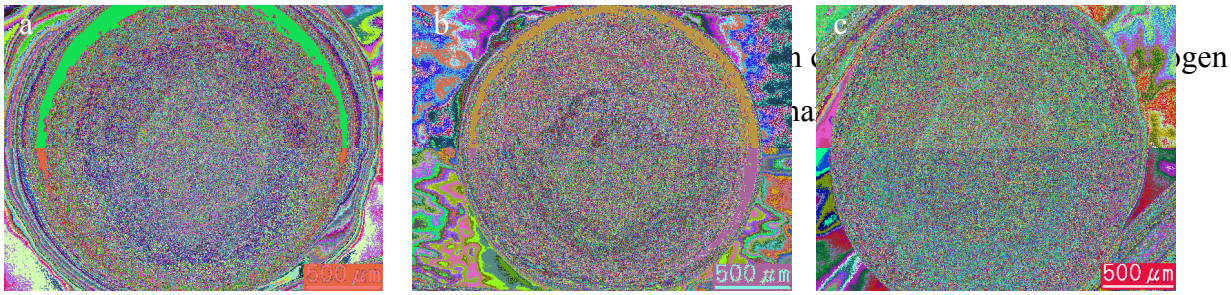


Fig. 3 SEM photographs of fracture surfaces as a) no-charged, b) charged and c) discharged.

Any fracture surfaces, as shown in Fig.3, show cup and cone, which is typical ductile fracture

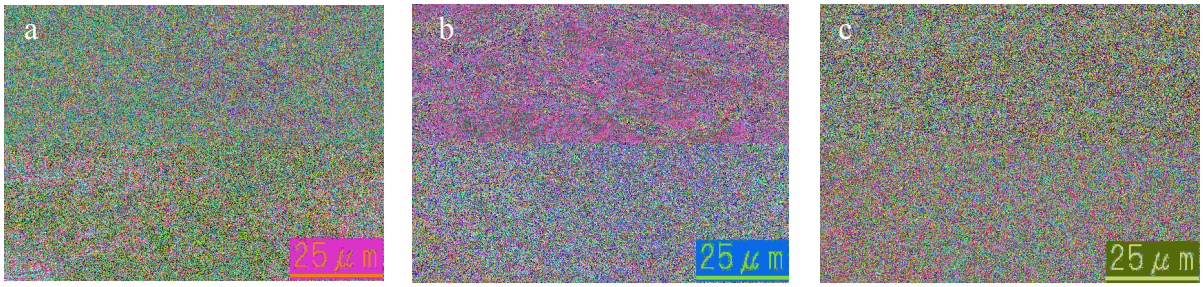


Fig. 4 SEM photographs of side surfaces of fractured specimens as a) no-charged, b) charged and c) discharged.

surface. Reduction of area in no-charged condition is higher than in the others in contrast to elongation. It is considered that the vicinity area of specimen's surface contributes to the increase of elongation. Side surfaces of fractured specimens are shown in Fig.4. Slip bands but no cracks are observed in no-charged condition (Fig.4 a). In the other conditions, a number of cracks are observed (Fig.4 b,c). Then, it is considered that these cracks were initiated during hydrogen charging and opened by tensile stress, because cracks are also observed in discharged condition. The opening of the cracks leads to enhance the elongation. Fracture surface is hardly affected by these cracks, since they are limited to very neighborhood of the surface. Hydrogen diffusivity D is $4.13\text{x}10^{-14}\text{m}^2\bullet\text{s}^{-1}$ in type 310S [5]. Diffusion distance of hydrogen during 48 hours (=t) is estimated at 85μm by eq. $\sqrt{Dt}$.

Fig.5 shows the surfaces of unloaded specimens. A lot of micro-cracks are observed on the surface of the discharged specimen (Fig.5 a), though obvious cracks are hardly observed on the charged specimen (Fig.5 b). Fig.5b shows that the micro-cracks is not due to corrosion during hydrogen charging. It has been reported that hydrogen induces the ε martensite into austenitic stainless steels [6]. Annealing in discharged process decomposes the ε martensite induced by hydrogen charging. Micro-cracks are considered to initiate during its decomposition process. In the charged specimen without annealing, the decomposition was probably occurred during a tensile test. As a result, micro-cracks were observed on the fractured specimen, not but on the unloaded specimen without annealing.

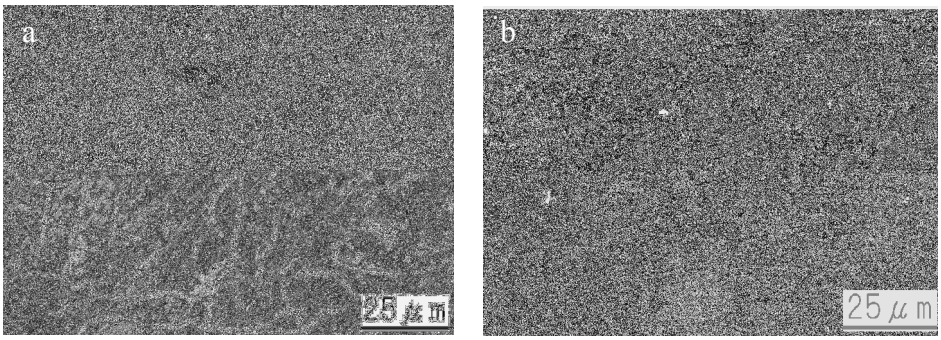


Fig. 5 SEM photographs of surfaces of unloaded specimens as a) discharged and b) charged.

Summary

Elongation increases in type 310S stainless steel by hydrogen charging. This enhancement also occurs on the annealed specimen after hydrogen charging. It is caused by micro-cracks induced during hydrogen charging and/or discharging. They are considered to concern the hydrogen induced ε martensite.

References

[1] D.Eliezer, D.G.Chakrapani, C.J.Altstetter and E.N.Pugh: Metall. Trans. Vol.10A (1979) p.935.

[2] M.Imade, S.Fukuyama and M.Yokokawa: CAMP-ISIJ vol.20 (2007) p.1058.

[3] R.B.Jr. Benson, R.K.Dann and L.W.Jr. Roberts: Trans. Metall. Soc. AIME Vol.242 (1968) p.2199.

[4] C.D.Beachem: Metall. Trans. Vol.3 (1972) p.437.

[5] Y.Mine, C.Narazaki, S.Matsuoka and Y.Murakami: Tetsu-to-Hagane Vol.93 (2007) p.247.

[6] A.Inoue A, Y.Hosoya and T.Masumoto: Trans. ISIJ Vol.19 (1979) p.170.

© (2012) Trans Tech Publications, Switzerland
doi:10.4028/www.scientific.net/KEM.488-489.238

Fatigue Strength of Radical Nitrided Spheroidal Graphite Cast Iron

K. Morino[1,a], F. Nishimura[1,b] and N. Kawagoishi[2,c]

[1]Tokuyama College of Technology, Gakuendai, Shunan 745-8585, Japan

[2]Kagoshima University, 1-21-40 Korimoto, Kagoshima 890-0065, Japan

[a]morino@tokuyama.ac.jp, [b]nisimura@tokuyama.ac.jp, [c]hiro@mech.kagoshima-u.ac.jp

Keywords: Fatigue, Spheroidal Graphite Cast Iron, Nitriding, Fracture Mode, Fracture Origin.

Abstract. In order to investigate the effect of radical nitriding on fatigue strength of spheroidal graphite cast iron FCD400, rotating bending fatigue tests were carried out at room temperature. Fatigue strength was increased by nitriding. Fracture started from microshrinkages or abnormal graphites in the same manner as that of as cast iron. However, fracture mode was different according to the stress level. That is, fracture occurred from specimen surface at high stress levels and it occurred from defects in subsurface at low stress levels. The cause of these results was the hardened layer and the compressive residual stress, which suppressed the initiation of the surface crack.

Introduction

Spheroidal graphite cast iron(SGI) has high strength and high toughness in the static property. However, it is well known that the fatigue strength is not so great. In fatigue, fracture always starts from microshrinkages or abnormal graphites that exist on the neighboring surface[1]. The sizes of these defects are comparatively large. Existence of these casting defects is the main reason of low fatigue strength. On the other hand, surface treatment that hardens surface and generates the compressive residual stress is an effective method to relay the crack initiation[2,3]. So many studies on fatigue strength of surface treated SGI have been done. However, sufficient results have been not obtained yet[4].

In this study, radical nitriding[5], one of superior surface treatment methods, was applied to ferritic spheriodal graphite cast iron and the effect of nitriding on the fatigue strength was investigated in comparison with as cast one by rotating bending fatigue tests.

Materials and experimental procedures

The material used was ferritic spheriodal graphite cast iron (JIS FCD400). The chemical composition is shown in Table 1. Table 2 shows some characteristics of spheroidal graphite which are measured by the image processing analysis technique. The threshold value of graphite is 12 μ m.

Figure 1 shows the shape and dimensions of specimen. All of the specimens were finished with alumina paste after machining and emery paper grinding. Nitrided specimens were prepared by heat treating at 530℃ for 10h in H_2 and NH_3 gases. Figure 2 shows microstructure of nitrided specimen. Compound layer of 2～3 μ m in thickness was formed on the specimen surface and diffusion layer of about 150 μ m in thickness was formed. Figure 3 and Fig.4 show the distribution of hardness and residual stress in the depth of nitrided specimen, respectively. Hardness of ferrite and graphite were measured separately by Micro Vickers hardness tester. Used weight is 0.245N. Graphite was not hardened, though ferrite was hardened by nitriding. Marked hardening (*HV*740) was observed on the surface, which was caused by the formation of compound. The hardness decreases gradually approaching to the value of as cast ones. Compressive residual stress was generated near the surface layer and the distribution of it was nearly the same as one of hardened ferrite.

Fatigue tests were carried out using a rotating bending fatigue testing machine operating at 50 Hz.

Table 1 Chemical composition [wt. %]

	Si	Mn	P	S	Mg
3.72	2.5	0.56	0.016	0.008	0.041

Table 2 Characteristics of spheroidal graphite

D_m (mm)	N_g (1/mm^2)	f_g (%)	h_g (%)
30.1	115	9.83	75.4

D_m : Average graphite diameter N_g : Nodule count
f_g : Area fraction of graphite h_g : Nodularity

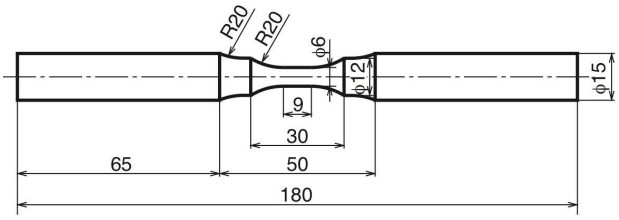


Fig.1 Shape and dimensions of specimen

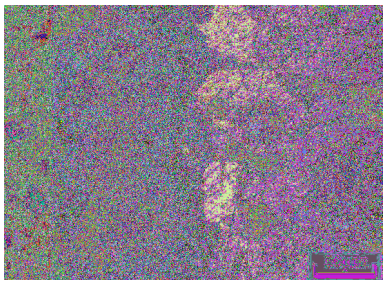


Fig.2 Microstructure of nitrided FCD400

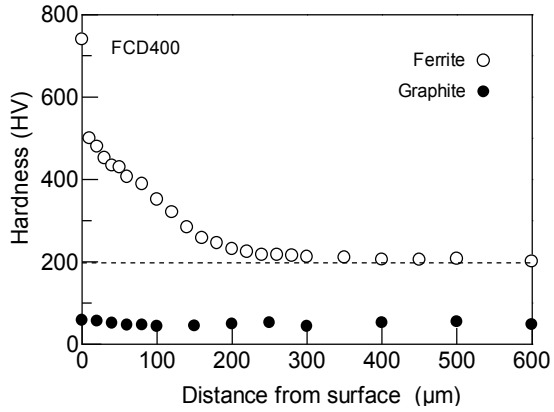


Fig.3 Hardness distribution

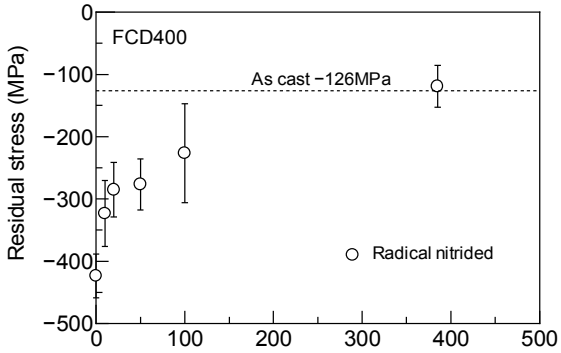


Fig.4 Residual stress distribution

Results and discussion

Figure 5 shows S-N curves of as cast specimens and nitrided ones. Open marks in the figure mean that fracture occurred from specimen surface and solid marks mean the internal fracture, which is described in detail hereinafter. Fatigue strength of FCD400 is increased by nitriding in wide life region. S-N curves in most of surface hardened steels show a two-step shape caused by the change in fracture mechanism [2-4] . However, the shape of two-step is not recognized clearly in S-N curves of nitrided FCD400.

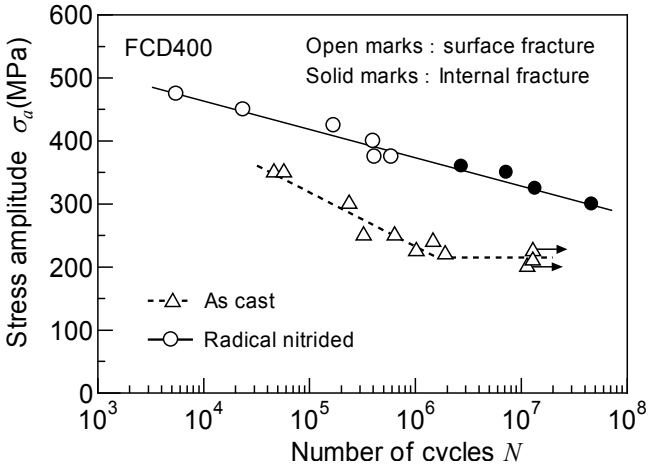
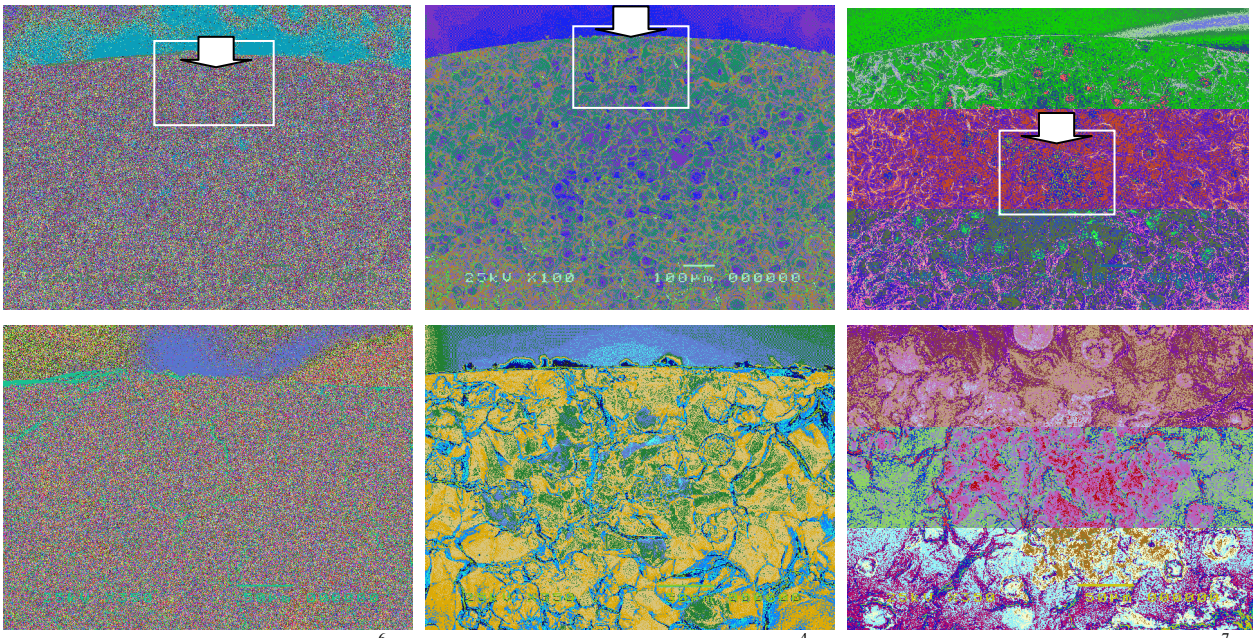


Fig.5 S-N curves



σ_α= 225MPa, N_f= 1.01×10^6 σ_α= 450MPa, N_f= 2.36×10^4 σ_α= 300MPa, N_f= 4.63×10^7

(a) As cast (b-1) Nitrided (b-2) Nitrided

Fig.6 Observation of fracture origin (: Fracture origin)

Figure 6 shows SEM photographs of fracture origin of as cast specimen (Fig.6(a)) and nitrided ones (Fig.6(b-1)(b-2)). Lower photographs expand the part □ in upper ones and arrow marks show the fracture origin, respectively. Fracture of as cast iron always occurred from specimen surface and casting defects (for example: microshrinkages or abnormal graphites) existed on the neighboring surface. Fracture of nitrided specimens starts from casting defects in the same as that of as cast iron, though ring-shaped failure zones corresponding to diffusion layer are observed and cracks propagate in brittle manner in these zones. However, fracture mode differed according to the stress levels. That is, fracture occurred from specimen surface at high stress levels as shown in Fig.6(b-1) and inner fracture occurred from casting defects in subsurface at low stress levels as shown in Fig.6(b-2).

Figure 7 shows the relationship between the depth from specimen surface of casting defects of fracture origin and the stress amplitude. Data of as cast iron was plotted together. At high stress levels, casting defects observed on nitrided specimens exist on the neighboring surface. Also, the size of defects was projected on the surface ranges from 100 μ m to 250 μ m. These results were the same as that of as cast iron. On the other hand, the depth of fracture origin at low stress levels was deeper than that at high stress levels, though the size of casting defects was almost the same as that at high stress levels. The depth from specimen surface was almost the same at low stress levels, too. However, these

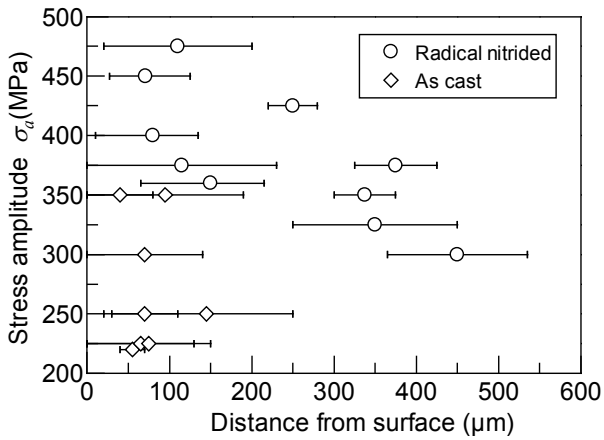


Fig.7 Relationship between the depth from surface of casting defects of fracture origin and stress amplitude

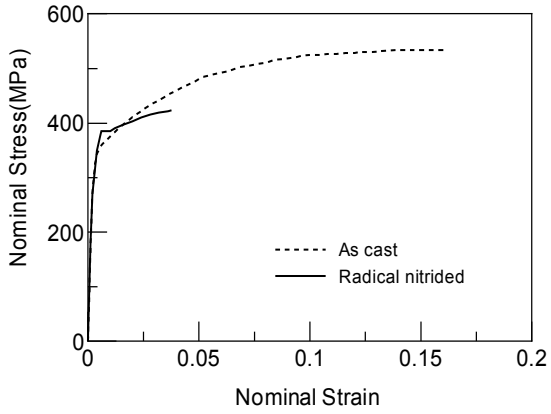


Fig.8 Stress-strain curves

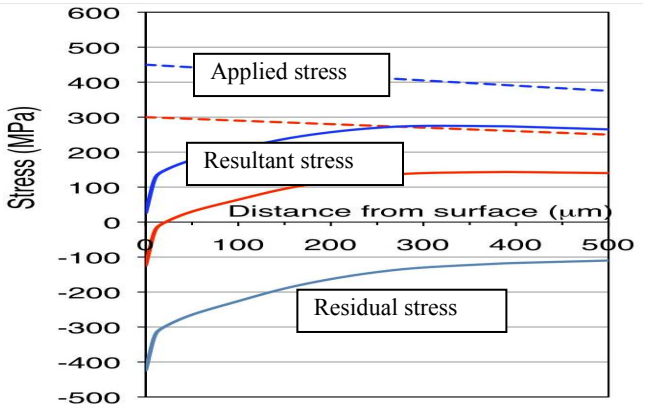


Fig.9 Resultant stress due to applied stress and residual stress

defects that caused fatigue fracture located in 250～550 μ m depth. This means that crack initiates from casting defects in the non-hardened layer. That is, fracture mode changes from the specimen surface to subsurface with decrease in stress levels. The stress changed mode was about 370MPa.

Figure 8 shows the stress-strain curves. Elongation of nitrided one becomes large at stress above 380MPa and some cracks occur on the specimen surface. This is the cause why the surface fracture occurred at stress amplitude above 370MPa on nitrided FCD400.

Figure 9 shows the resultant stress due to applied stress and residual stress. Depth where the resultant stress is maximized is about 250～550 μ m. This value agrees well with the experimental results. These results mean that the increase in fatigue strength at stress amplitude below 370MPa on FCD400 by nitriding is mainly caused by the suppression of crack initiation due to the presence of the hardened thick layer and the compressive residual stress. Above 370MPa, existence of hardened layer , which was not very brittle one, and compressive residual stress caused the suppression of crack initiation increases in fatigue strength.

Conclusions

Rotating bending fatigue tests were carried out for radical nitrided spheroidal graphite cast iron FCD400 in order to investigate the effect of nitriding on fatigue strength. Fatigue strength was increased by nitriding. Fracture occurred from casting defects in the same manner as that of as cast iron. However, fracture mode changed from the specimen surface to subsurface with decrease in stress level. The increase in fatigue strength was mainly caused by suppression of crack initiation due to the presence of the hardened layer and the compressive residual stress. However, the cause is different in each fracture mode.

Acknowledgement

The authors would like to acknowledge Mr. S. Fukaji(Kohan Kogyo Ltd.) for his support on nitriding.

References

[1] K.Morino et al.: Japan Soc. Mech. Eng. Int. J., Ser. A, Vol.41, No.2 (1998), p.243

[2] N.Kawagoishi et al.: Japan Soc. Mech. Eng., Ser. A, Vol.67, No.654 (2001), p.314

[3] K.Morino et al.: Japan Soc. Mech. Eng., Ser. A, Vol.69, No.686 (2003), p.1490

[4] Y.Ochi et al.: Int. J. Fatigue, Vol.23, No.5 (2001), p.441

[5] K.Fukada: J. Japan Soc. Tech. Plasticity, Vol.40, No.464 (1999), p.847

© (2012) Trans Tech Publications, Switzerland
doi:10.4028/www.scientific.net/KEM.488-489.242

Combined Influence of Expansive and Shrinkage Reducing Admixtures on the Shrinkage Behavior of Ultra-High Performance Concrete

Jung-Jun Park[1,a], Doo-Yeol Yoo[2,b], Sung-Woo Kim[1,c] and Young-Soo Yoon[2,d]

[1]Structural Engineering & Bridges Research Division, Korea Institute of Construction Technology, Goyang, 411-712, Korea

[2]School of Civil, Environmental and Architectural Engineering, Korea University, Seoul, 136-713, Korea

[a]jjpark@kict.re.kr, [b]dooyeol@korea.ac.kr, [c]swkim@kict.re.kr, [d]ysyoon@korea.ac.kr

Keywords: Ultra high performance concrete, Restrained shrinkage, Shrinkage reducing agent, Expansive admixture.

Abstract. Since ultra-high performance cementitious composite (UHPCC) exhibits remarkable compressive strength and ductility, its application for structural member provides significant reduction of the section. The use of low water-to-binder ratio and admixtures with high fineness induce large shrinkage strain, leading to the possibility of large occurrence of shrinkage cracks due to the restraints of the form and reinforcing bars. Therefore, this study admixes a combination of expansive and shrinkage reducing agents as a solution to reduce the shrinkage of UHPCC. The eventual appropriateness is computed to evaluate the free shrinkage and restrained shrinkage behaviors. From the test results, the admixing of a combination of expansive and shrinkage reducing agents is seen to achieve a reduction of the free shrinkage by 30% to 50% at 28 days and a reduction of the strain of the external steel by about 19%.

Introduction

Among the construction materials, concrete offers the best economic efficiency together with remarkable mechanical properties and durability. However, concrete presents also several problems like the poor strength characteristics developed compared to its weight and its brittle failure characteristics. Recently, research has been extensively conducted on the development and practicability of ultra-high performance concrete (UHPC) in order to overcome these limitations [1]. UHPC adopts a low water-to-binder ratio (W/B) and does not use coarse aggregate. Since the grain sizes of cement, filler and admixtures are optimized based on the packing theory before mixing, UHPC presents a very dense structure. Such features result in the large occurrence of early autogenous shrinkage. This shrinkage taking place at a time where sufficient strength is not developed induces cracking that degrades the service life and structural performance of the structure. Accordingly, research should be imperatively conducted to understand and evaluate exactly the shrinkage behavior and to provide preventing solutions for the application of UHPC in real structures [2]. Therefore, this study performs free shrinkage and restrained shrinkage tests of UHPC by adopting the eventual presence of expansive agent (EA) and shrinkage reducing agent (SRA) as test variables for the comparative evaluation of the shrinkage reduction effect and drying shrinkage.

Materials

The cement used in this study is ordinary Portland cement. Silica fume presenting specific surface of about 200,000 cm^2/g is used as admixture. Sand with grain size below 0.5 mm is used as fine aggregates and coarse aggregates are discarded. The adopted sand presents density of 2.62 g/cm^3 with characteristics corresponding to approximately 98% of SiO_2. The filler exhibits mean particle size of about 2 μm and is composed of material with density of 2.65 g/cm^3 and content of SiO_2 larger than 99%. Polycarbonate-based superplasticizer in dark brown liquid form with density of 1.01 g/cm^3 is used. Highly elastic steel fibers with tensile strength of 2,500 MPa, diameter of 0.2 mm, length of

13 mm and shape coefficient of 65 are introduced. Glycol-based agent is introduced as material for the reduction of the autogenous shrinkage of UHPC and, CSA-based material is adopted as expansive agent. Both agents are in powder form.

Mix Design and Test Method

Table 1 arranges the mix design of UHPC in terms of the relative ratios.

Table 1. Mix design of concrete (in relative ratios*)

Mix type	W/B (%)	Cement	Silica fume	Sand	Filler	Steel fiber	Super-plasticizer	SRA	EA
Mix A	0.2	1	0.25	1.1	0.3	V_f = 2%	0.02	–	–
Mix B								0.01	0.075

(*) Relative ratios: weight ratio to cement, except steel fiber expressed as volumetric ratio to the whole volume

Flow test was conducted in compliance with the regulations of ASTM C 1437. The compressive strength was measured with respect to KS F 2405 on ϕ100×200 mm cylinders. In order to secure sections identical to those of the drying shrinkage crack test, the free shrinkage was measured using molds with dimensions of 100×100×400 mm. Teflon sheets were disposed to minimize the shrinkage restraining force due to friction between concrete and the mold and tests were performed in a constant temperature and humidity chamber at 23±1°C and humidity of 60±5%. The molds were removed 24 hours after placing. For the autogenous shrinkage, the exposed surface was completely sealed using aluminum tape to prevent loss of volume due to the evaporation of humidity after the removal of the mold. Drying shrinkage crack test was conducted in compliance with KS F 2959 to evaluate the restrained shrinkage behavior of UHPC. Fig. 1 illustrates the test. Drying started since the removal of the restraining mold one day after placing of concrete. Concrete was restrained by means of the protrusions at the top and bottom ends of the mold. The section of the restrained concrete at the center was 100×100 mm and test was carried out by exposing all the faces of the specimen. The drying shrinkage crack test was performed in a constant temperature and humidity chamber identically to the free shrinkage test. The time of initiation of crack due to the shrinkage of concrete was defined as the time at which the steel gage bonded in the restraining mold measured sudden change of the strain. Embedded gages were installed in the restrained concrete to compare the restrained strain and unrestrained shrinkage. Quantitative evaluation was performed for the shrinkage restrained by external steel.

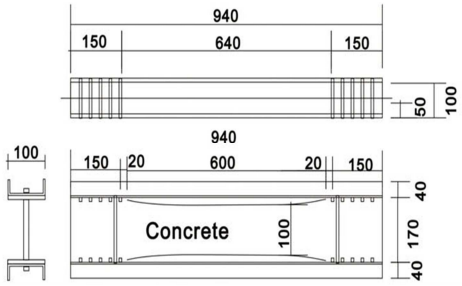


Fig. 1 Drying shrinkage crack test

Table 2. Properties of fresh and hardened concrete

Designation	Flow (mm)	fc (MPa)			
		1 day	3 days	7 days	28 days
Mix A	235	78.8	105.6	126.2	152.4
Mix B	240	70.7	98.7	127.3	152.2

Experimental Results and Discussion

Table 2 arranges the results of the flow and compressive strength tests. Mix B including SRA and EA exhibits a flow similar to Mix A. The early compressive strength of Mix B is seen to be slightly smaller than Mix A but turns out to a nearly identical value after 7 days. Accordingly, the admixing of a combination of 7.5% EA and 1% SRA appears to have nearly insignificant effect on the compressive strength and flow of UHPCC.

Fig. 2 plots the autogenous shrinkage measured with respect to the age of UHPC. The temperature was calibrated based on the change of the internal temperature measured using a thermocouple.

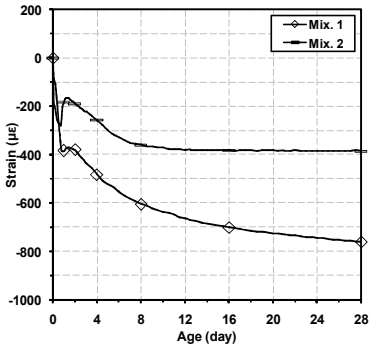


Fig. 2 Measured autogenous shrinkage of UHPC

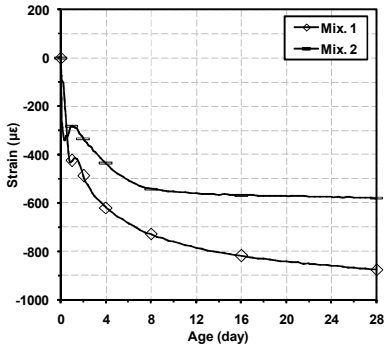


Fig. 3 Measured total shrinkage of UHPC

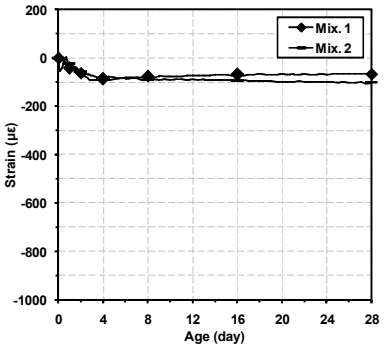
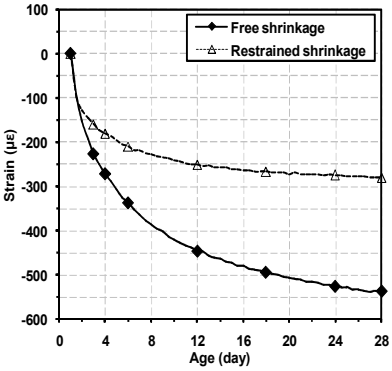


Fig. 4 Measured drying shrinkage of UHPC

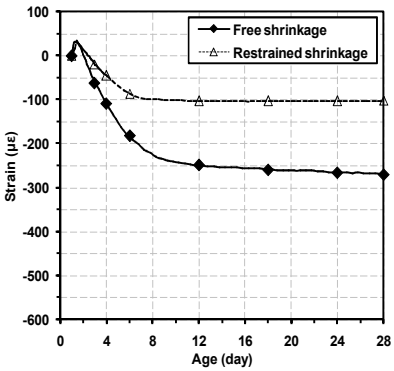
Mix B exhibits large shrinkage compared to Mix A. It appears that expansion occurred between 0.7 to 1.2 days after placing of concrete. In addition, the shrinkage of Mix A tends to increase continuously whereas Mix B shows practically no change of the shrinkage from 7 to 8 days after placing of concrete and indicates effective reduction of the shrinkage of UHPC. The strains of Mixes A and B at 28 days are -775 με and -387 με, respectively.

As shown in Fig. 3, the total shrinkage of Mixes A and B tends to exhibit similar graph to that of the autogenous shrinkage. The strains of Mixes A and B at 28 days are -876 με and -581 με, respectively.

The drying shrinkage of Mixes A and B at 28 days ran about -67 με and -103 με (Fig. 4). In the case of UHPC, the low W/B and the use of high fineness admixture lead to a very dense structure and the drying shrinkage caused by the evaporation of humidity appears to be rather insignificant. The reason for the drying shrinkage of Mix B to be larger than Mix A can be explained by the easier migration of the water content owing to the numerous internal voids formed through early expansion induced by the introduction of EA.



(a) Mix A



(b) Mix B

Fig. 5 Restrained and free shrinkages of UHPC

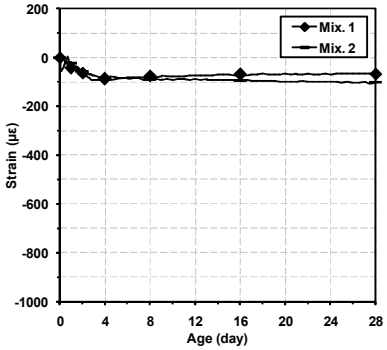


Fig. 6 Restrained strain of external steel

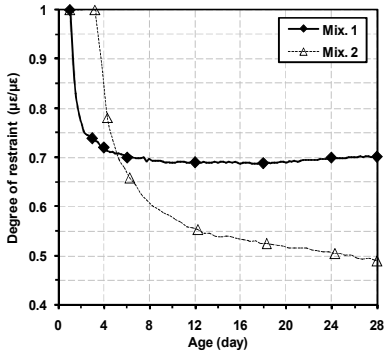


Fig. 7 Degree of restraint of external steel

Fig. 5(a) plots the results of the free shrinkage and restrained shrinkage of Mix A. The restraint effect occurred about 14 hours after the removal of the mold and the shrinkage showed a difference in shrinkage of about 257 με at 28 days. Poor difference was observed between the free and restrained shrinkages at early age. This can be explained to the large occurrence of tensile creep before concrete has hardened sufficiently. Besides, Mix B exhibited a difference of about 168 με between the free and restrained shrinkages at 28 days. Similarly to the result of the ring test, the restrained shrinkage showed poor change since 8 days after the placing of concrete as shown in Fig. 5(b).

Fig. 6 illustrates the restrained strain pattern of the external steel. Strains of approximately -160 με and -129 με were measured at 28 days for Mix A and Mix B, respectively. The shrinkage of Mix B remained poor since 8 days after placing of concrete leading to the decrease of the steel strain due to tensile creep. Assuming that the thickness of the concrete ring is relatively small and that shrinkage occurs uniformly, the shrinkage of concrete, $\varepsilon_{sh}(t)$, is the sum of the restraint strain of inner steel ring, $\varepsilon_{st}(t)$, the elastic strain of concrete, $\varepsilon_e(t)$, and the creep of concrete due to restraint stress, $\varepsilon_{cp}(t)$.

$$\varepsilon_{sh}(t) = \varepsilon_{st}(t) + \varepsilon_e(t) + \varepsilon_{cp}(t) \quad (1)$$

If we assume that concrete is perfectly restrained by the internal steel ring, the corresponding restraint strain $\varepsilon_r(t)$ can be expressed as follows:

$$\varepsilon_r(t) = \varepsilon_e(t) + \varepsilon_{cp}(t) \quad (2)$$

Accordingly, the degree of restraint (ψ) can be defined as the value obtained the restraint strain by the total drying shrinkage.

$$\psi = \frac{\varepsilon_r(t)}{\varepsilon_{sh}(t)} = \frac{\varepsilon_{sh}(t) - \varepsilon_{st}(t)}{\varepsilon_{sh(t)}} = 1 - \frac{\varepsilon_{st}(t)}{\varepsilon_{sh}(t)} \quad (3)$$

As shown in Fig. 7, the evaluation of the degree of restraint conducted by applying Eq. (3) revealed that Mix A experienced a degree of restraint of about 0.7 at 28 days while Mix B showed a value of 0.5. The cause of such decrease of the degree of restraint can be attributed to the reduction of the shrinkage through the introduction of EA and SRA, which in turn decreased the strain of the external steel.

Conclusions

The following conclusions could be derived from the results of the free and restrained shrinkage tests of UHPC selecting the presence of EA and SRA as test variables.

(1) For Mix B, poor change of the compressive strength and flow was observed according to the introduction of EA and SRA.

(2) The introduction of the combination of EA and SRA enabled to achieve reduction of the free shrinkage by about 34% to 50% at 28 days. The strain of the external steel was seen to decrease by approximately 19%.

(3) The tensile strength of UHPCC appeared to be larger than the residual tensile stress from the drying shrinkage crack test. Shrinkage cracking did not occur. The values of the degree of restraint were 0.7 and 0.5 for Mix A AND Mix B, respectively. The degree of restraint tended to decrease in Mix B following the combined introduction of EA and SRA.

Acknowledgements

This study was carried out as a partial research of the "Development of Ultra High Performance Concrete for Hybrid Cable Stayed Bridges (Manual of Manufacturing UHPC)" in the Korea Institute of Construction Technology. The authors express their gratitude for the support.

References

[1] Pierre Richard; Marcel Cheyrezy: *Composition of Reactive Powder Concretes*, Cement and Concrete Research, Vol.25, No.7(1995), p.1501-1511.

[2] Korea Institute of Construction Technology: *Ultra High Performance Concrete for Hybrid Cable Stayed Bridges (Manual of Manufacturing UHPC)* (2010).

© (2012) Trans Tech Publications, Switzerland
doi:10.4028/www.scientific.net/KEM.488-489.246

Study on gradient-dependent nonlocal damage constitutive models of concrete under freeze-thaw action

LIU Zongmin[1, a], MAO Jize[1, b], SONG Haiyan[1, c], CHEN Xuedong[2, d]

[1] Smart Structures and Advanced Composites Laboratory, College of Aerospace and Civil Engineering, Harbin Engineering University, Harbin 150001, China

[2] Heilongjiang Research Institute of Electric Power Exploration and Design, Harbin 150010, China

[a] lzm1976@yahoo.com.cn, [b]maojize@hrbeu.edu.cn, [c]shyivg@yahoo.com.cn, [d]cxd0451@163.com

Keywords: gradient-dependent, nonlocal, damage, freeze-thaw

Abstract. Concrete materials with a large number of micro-cracks were defined as inhomogeneous materials. And the mechanical properties of inhomogeneous materials were regarded as high-order deformation gradient dependent. Starting from the nonlocal thermodynamics theory and the hypothesis of total energy equivalence, the gradient-dependent nonlocal damage constitutive models of concrete under freeze-thaw action would be established in this paper.

Introduction

Concrete is a composite material which consists of coarse aggregate, fine aggregate and cement paste. The composition of concrete materials is often ignored. And concrete materials are regarded as homogeneous continuum. What's more, concrete materials are customarily assumed to be initially isotropic. But concrete materials contain a large number of microcracks, especially at the interface between aggregate and mortar, even before the application of external load. When microcracks produced, the mechanical properties of concrete materials are no longer isotropic. So Noll defined the materials as inhomogeneous materials[1].

Due to the inhomogeneities in the calculation, many scholars presented non-local models based on the concept of space average[2,3]. Under freeze-thaw action, area weighted average nonlocal constitutive models of concrete was presented in ref.[4]. But the nonlocal constitutive models could not model strain-softening in the calculation. For inhomogeneous materials, the mechanical properties were regarded as high-order deformation gradient dependent[1]. The gradient-dependent nonlocal damage constitutive models of concrete for elasto-plasticity were presented in refs.[5,6]. Starting from the nonlocal thermodynamics theory and the hypothesis of total energy equivalence[7], the gradient-dependent nonlocal damage constitutive models of concrete under freeze-thaw action would be established in this paper.

Nonlocal thermodynamics theory

The nonlocal first law of thermodynamics can be described as the time change rate of kinetic energy $\dot{T}$ and the internal energy $\dot{U}$ is equal to the sum of the rate-work $\dot{W}$ done upon the body by the external forces and heat energy rate $\dot{Q}$. Thus mathematically

$$\dot{T}+\dot{U}=\dot{W}+\dot{Q} \tag{1}$$

The variables $\dot{T}$, $\dot{U}$, $\dot{W}$ and $\dot{Q}$ can be written as follows respectively

$$\dot{T} = \int_V \rho \boldsymbol{v} \cdot \dot{\boldsymbol{v}} dV \tag{2}$$

$$\dot{U} = \int_V \rho \dot{e} dV \tag{3}$$

$$\dot{W} = \int_V \rho \boldsymbol{f} \cdot \boldsymbol{v} dV + \int_A \boldsymbol{\sigma} \cdot \boldsymbol{n} \cdot \boldsymbol{v} dA \tag{4}$$

$$\dot{Q} = \int_V \rho \dot{r} dV - \int_A \boldsymbol{q} \cdot \boldsymbol{n} dA \tag{5}$$

where, ρ is mass density, $\boldsymbol{v}$ is velocity vector, e is internal energy density per unit mass, $\boldsymbol{f}$ is external body forces vector per unit mass, $\boldsymbol{\sigma}$ is stress tensor, $\boldsymbol{n}$ is surface direction cosine vector, $\boldsymbol{q}$ is the heat flow vector, $\dot{r}$ is distributed internal heat sources.

Substituting Eqs.(2)~(5) into Eq.(1) , we get

$$\int_V (\rho \boldsymbol{v} \cdot \dot{\boldsymbol{v}} + \rho \dot{e}) \, dV = \int_V (\rho \boldsymbol{f} \cdot \boldsymbol{v} + \rho \dot{r}) dV + \int_A \boldsymbol{\sigma} \cdot \boldsymbol{n} \cdot \boldsymbol{v} dA - \int_A \boldsymbol{q} \cdot \boldsymbol{n} dA \tag{6}$$

Using Green theorem

$$\int_A \boldsymbol{\sigma} \cdot \boldsymbol{n} \cdot \boldsymbol{v} dA = \int_V (\nabla \cdot \boldsymbol{\sigma}) \cdot \boldsymbol{v} dV + \int_V \boldsymbol{\sigma} \cdot (\nabla \cdot \boldsymbol{v}) dV \tag{7}$$

$$-\int_A \boldsymbol{q} \cdot \boldsymbol{n} dA = -\int_V \nabla \cdot \boldsymbol{q} dV \tag{8}$$

And equilibrium equation can be expressed as follow

$$\rho \dot{\boldsymbol{v}} = \nabla \cdot \boldsymbol{\sigma} + \rho \boldsymbol{f} \tag{9}$$

Substituting Eqs.(7)~(9) into Eq.(6) , we get

$$\int_V \rho \dot{e} dV = \int_V [\boldsymbol{\sigma} \cdot (\nabla \cdot \boldsymbol{v}) + \rho \dot{r} - \nabla \cdot \boldsymbol{q}] dV \tag{10}$$

Eq.(10) is another expression of the nonlocal first law of thermodynamics.

Gradient-dependent nonlocal damage constitutive models under freeze-thaw action

Kachanov[8] considered the damage in a cross section to be measured by the relative area of voids. Most of the early damage theories followed this idea using a scalar as damage variable. And damage variables may be a scalar or a tensor. When selecting a scalar as damage variable, it implies that the damage is isotropic. However the mechanical properties of concrete with microcracks are no longer isotropic. A tensor should be selected as internal variable which can be described nonlocal damage properties of concrete. In ref.[5,6], strain gradient $\nabla \varepsilon$ and damage gradient ∇D were adopted respectively. It was verified that nonlocal effect of material could be described by a nonlocal internal variable[9]. So only damage gradient ∇D is adopted as internal variable of gradient-dependent nonlocal damage constitutive models of concrete in this paper.

Under freeze-thaw action, concrete is subjected to cyclic temperature field. Except for the outflow heat $\nabla \cdot \boldsymbol{q}$ and the inflow heat $\rho \dot{r}$, the dissipated energy with internal and external state change can all be transformed into heat. And the heat which is absorbed in the body raise entropy s. For volume V, one can obtain as follow

$$\int_V \rho \dot{s} dV = \int_V \frac{1}{T}[\boldsymbol{\sigma}_p : \dot{\boldsymbol{\varepsilon}}_p + Y\dot{D} + \boldsymbol{Y}^{(\nabla D)} \cdot (\nabla \dot{D}) + \rho \dot{r} - \nabla \cdot \boldsymbol{q}] dV \tag{11}$$

Where, $\boldsymbol{\sigma}_p$ is plastic stress tensor, $\boldsymbol{\varepsilon}_p$ is plastic strain tensor, T is temperature, D is damage variable, ∇D is damage gradient, Y, $\boldsymbol{Y}^{(\nabla D)}$ are the conjugate forces of thermodynamics corresponding to damage variable D and damage gradient ∇D respectively[6].

Substituting Eq.(11) into Eq.(10) , we get

$$\int_V \rho \dot{e} dV = \int_V [\boldsymbol{\sigma} : \dot{\boldsymbol{\varepsilon}} - \boldsymbol{\sigma}_p : \dot{\boldsymbol{\varepsilon}}_p - Y\dot{D} - \boldsymbol{Y}^{(\nabla D)} \cdot (\nabla \dot{D}) + \rho T \dot{s}] dV \tag{12}$$

Where, $\boldsymbol{\varepsilon}$ is strain tensor. The potential function of thermodynamics is generally adopted in the expression of constitutive models, namely Helmholtz free energy function.

$$\psi = e - Ts \tag{13}$$

The time derivative of Eq.(13) is as follow

$$\dot{\psi} = \dot{e} - \dot{T}s - T\dot{s} \tag{14}$$

Substituting Eq.(14) into Eq.(12) , we get

$$\int_V \rho \dot{\psi} dV = \int_V [\boldsymbol{\sigma} : \dot{\boldsymbol{\varepsilon}} - \rho s \dot{T} - \boldsymbol{\sigma}_p : \dot{\boldsymbol{\varepsilon}}_p - Y\dot{D} - \boldsymbol{Y}^{(\nabla D)} \cdot (\nabla \dot{D})] dV \tag{15}$$

The free energy is a function of all the state variables. The rate of the free energy ψ is expressed as follow

$$\dot{\psi}(\boldsymbol{\varepsilon}, T, \boldsymbol{\varepsilon}_p, D, \nabla D) = \frac{\partial \psi}{\partial \boldsymbol{\varepsilon}} : \dot{\boldsymbol{\varepsilon}} + \frac{\partial \psi}{\partial T}\dot{T} + \frac{\partial \psi}{\partial \boldsymbol{\varepsilon}_p} : \dot{\boldsymbol{\varepsilon}}_p + \frac{\partial \psi}{\partial D}\dot{D} + \frac{\partial \psi}{\partial (\nabla D)} \cdot (\nabla \dot{D}) \tag{16}$$

Substituting Eq.(16) into Eq.(15) , we get

$$\begin{aligned} &\int_V [(\boldsymbol{\sigma} - \rho \frac{\partial \psi}{\partial \boldsymbol{\varepsilon}}) : \dot{\boldsymbol{\varepsilon}} - \rho(s + \frac{\partial \psi}{\partial T})\dot{T} - (\boldsymbol{\sigma}_p + \rho \frac{\partial \psi}{\partial \boldsymbol{\varepsilon}_p}) : \dot{\boldsymbol{\varepsilon}}_p - \\ &(Y + \rho \frac{\partial \psi}{\partial D})\dot{D} - (\boldsymbol{Y}^{(\nabla D)} + \rho \frac{\partial \psi}{\partial (\nabla D)}) \cdot (\nabla \dot{D})] dV = 0 \end{aligned} \tag{17}$$

Because of the arbitrariness of $\dot{\boldsymbol{\varepsilon}}$, $\dot{T}$, $\dot{\boldsymbol{\varepsilon}}_p$, $\dot{D}$ and $\nabla \dot{D}$, we get

$$\boldsymbol{\sigma} = \frac{\partial \psi}{\partial \boldsymbol{\varepsilon}} \tag{18}$$

$$s = -\frac{\partial \psi}{\partial T} \tag{19}$$

$$\boldsymbol{\sigma}_p = -\frac{\partial \psi}{\partial \boldsymbol{\varepsilon}_p} \tag{20}$$

$$Y = -\frac{\partial \psi}{\partial D} \tag{21}$$

$$\boldsymbol{Y}^{(\nabla D)} = -\frac{\partial \psi}{\partial (\nabla D)} \tag{22}$$

The strain energy density expression of coupled thermo-elasto-plastic anisotropic damage is expressed as follow

$$\psi = \frac{1}{2}\boldsymbol{\varepsilon}:\tilde{\boldsymbol{E}}^{(e)}(D):\boldsymbol{\varepsilon} + \frac{1}{2}\boldsymbol{p}:\tilde{\boldsymbol{E}}^{(p)}(D):\boldsymbol{p} + \frac{1}{2}(\nabla D)\cdot\tilde{\boldsymbol{E}}^{(\nabla D)}(D)\cdot(\nabla D) + \theta\tilde{\boldsymbol{H}}^{(e)}(D):\boldsymbol{\varepsilon} + \theta\tilde{\boldsymbol{H}}^{(p)}(D):\boldsymbol{p} + \theta\tilde{\boldsymbol{H}}^{(\nabla D)}(D)\cdot\nabla D + \frac{1}{2}\tilde{\xi}(D)\theta^2 \quad (23)$$

Where, $\tilde{\boldsymbol{E}}^{(e)}(D)$ is the effective elastic modulus tensor with damage, $\tilde{\boldsymbol{E}}^{(p)}$ is the plastic hardening modulus tensor with damage, $\boldsymbol{p}$ is the accumulated plastic strain tensor, $\tilde{\boldsymbol{E}}^{(\nabla D)}(D)$ is the effective damage gradient modulus tensor with damage, θ is the temperature difference, $\tilde{\boldsymbol{H}}^{(e)}(D)$ is the effective thermal modulus tensor coupled with thermo-elasto-damage, $\tilde{\boldsymbol{H}}^{(p)}(D)$ is the effective thermal modulus tensor coupled with thermo-plasto-damage, $\tilde{\boldsymbol{H}}^{(\nabla D)}(D)$ is the effective thermal modulus vector coupled with thermo-damage and damage gradient, $\tilde{\xi}(D)$ is the effective specific heat coefficient with damage. The specific forms of parameters above are related to material properties and microscopic properties of damage. Due to the limit of space, they are not described in more details.

Summary

The mechanical properties of concrete materials with a large number of micro-cracks were regarded as high-order deformation gradient dependent. In the paper, damage gradient ∇D is adopted to describe nonlocal damage properties of concrete. Subjected to elasto-plastic field and cyclic temperature field, the gradient-dependent nonlocal damage constitutive models of concrete under freeze-thaw action are established.

Acknowledgement

This research is supported by the National Natural Science Foundation of P. R. China through Grant number 50908059.

References

[1] W. Noll: submitted to Arch. Rational Mech. Anal., 1987, vol.27, pp. 1-32.

[2] E. Kroner: submitted to Int. J. Solids Struct., 1967, vol.3, pp. 731-742.

[3] A. C. Eringen: submitted to Int. J. Solids Struct., 1972, vol.10, pp. 233-248.

[4] Zongmin Liu, Jize Mao and Haiyan Song: Study on Non-local Damage Constitutive Model of Concrete under Freeze-thaw Action, Key Engineering Materials, 2011, vols.452-453, pp.133-136.

[5] Lu Yang, Fusheng Zhu and Xinpu Shen: submitted to Chinese Journal of Materials Research, 2007, vol. 21(5), pp. 477-481.

[6] X.P. Shen, L. Yang: *Damage theory and experiment of concrete* (Science Press, Beijing 2009).

[7] K. Saanouni, C. Forster and F. B. Hatira: submitted to Int. J. Dama. Mech., 1994, vol.3, pp. 140-169.

[8] L. M. Kachanov: submitted to IZV. AN. SSR. Otd. Tekhn. Nauk., 1958, vol.8, pp. 26-31.

[9] S.Murakami, K. Kamiya: submitted to Int. J. Mech. Sci., 1997, vol.39(4), pp. 473-486.

© (2012) Trans Tech Publications, Switzerland
doi:10.4028/www.scientific.net/KEM.488-489.250

Effect of $YbCl_3$-Zn-Epoxy Coating on MIC Behavior of Low Alloy Steel

Fu Yu-dong [1,a], Li Qing-fen[2,b], Wang Jun[1], Li Chun-hui[2]

[1] College of Material Science and Chemical Engineering, Harbin Engineering University,

[2] College of Mechanical and Electrical Engineering, Harbin Engineering University,

Harbin 150001, China

[a]fuyudong@hrbeu.edu.cn, [b]qingfli@yahoo.com.cn

Keywords: $YbCl_3$-Zn-epoxy coating; microbiological influenced corrosion (MIC); low alloy steel; marine environment

Abstract. In the present study, the rare earths element $YbCl_3$ was added into the Zn-epoxy coating, and the MIC behavior of the low alloy steel specimen with $YbCl_3$-Zn-epoxy coating in the sulfate-reducing bacteria (SRB) solution was investigated and compared with the specimen of Zn-epoxy coating. Experimental results show that both the $YbCl_3$-Zn-epoxy and Zn-epoxy coating may offer effective protection for the basic low alloy steel. However, the corrosion potential of the specimen with $YbCl_3$-Zn epoxy coating was obviously higher than the Zn-epoxy coating, suggesting that the $YbCl_3$-Zn-epoxy coating may offer more favorable protection. Results of X-rays diffraction (XRD) and surface micrographs of specimens show that more sulfides and corrosion products of $YbCl_3$-Zn-epoxy coating were produced which increased the shielding property of the coating. The mechanism about the effect of $YbCl_3$-Zn-epoxy coating on MIC behavior was further discussed.

Introduction

There are lots of microorganisms in seawater. When immersed in seawater, many metals would suffer serious microbiological influenced corrosion (MIC) damage, and the cost of such damage may reach billions of dollars annually. Among them, the sulfate-reducing bacteria (SRB) influenced corrosion is one of the most severe one in marine environment [1, 2]. Some techniques to control such corrosion are used, such as coatings, biocides, UV irradiation, etc. Among these, application of suitable coatings appears to be a promising method of corrosion control in terms of cost effectiveness and service life.

Previous work pointed out that it is effective to coat the steel with Zn-rich epoxy which may apply cathodic polarization for protection and increase of service life of the material [3, 4], and that the rare earths have special bacteriostasis / sterilization effect which may reduce the microbiological influenced corrosion [5, 6]. It is therefore possible to reduce corrosion effectively by adding the rare earths into Zn-epoxy coating.

In the present study, the rare earths element $YbCl_3$ was added into the Zn-epoxy coating, and the effect of $YbCl_3$-Zn-epoxy coating on the MIC behavior of the low alloy steel was investigated.

Experimental

The chemical composition of the low alloy steel used in the present investigation is shown in Table 1. The size of specimen coated with Zn-epoxy or $YbCl_3$-Zn epoxy is 30 x 25 x 6 mm (with working area of 6 cm^2). A copper wire was soldered to the lower surface. Samples were

successively polished up to 1000 grit, cleaned with deionized water, dried with air and finally coating with Zn-epoxy or $YbCl_3$-Zn epoxy. The dry film thickness of the coating is about 30 μm. All specimens were sterilized under UV for 3 hours before test.

Tests were carried out in the SRB solution. The SRB strains were isolated from the sea-mud in Qingdao seashore. The composition of the SRB solution is given in table 2.

MIC behaviors in SRB were investigated with EIS, EDS, ESEM of XL30, and a XRD-D8 Advance. Corrosion potential and impedance measurements were performed using the IM6 electrochemical workstation of ZAHNER. Tests were carried out at ambient temperature using a three-electrode system.

Table 1 Chemical Composition of the Low Alloy Steel [wt %]

C	Si	Mn	S	P	Cr	Ni	Mo	V
0.09~0.14	0.17~0.37	0.30~0.60	≤0.03	≤0.035	0.09~1.20	2.60~3.00	0.20~0.27	0.04~0.10

Table 2 Composition of the SRB Solutions [g/L]

Seawater	PH	$K_2HPO_4.3H_2O$	$MgSO_4.7H_2O$	$CaCI_2$	Na_2SO_4	NH_4Cl	Sodium lactate	Vc
1	7.00	0.50	2.00	0.10	0.50	1.00	3.50	0.10

Results and discussion

The variation of corrosion potential over time of the specimen with $YbCl_3$-Zn-epoxy and Zn-epoxy coating in SRB solution is given in Fig.1. Where, we can see that the corrosion potential of the $YbCl_3$-Zn-epoxy sample was obviously higher than that of the Zn-epoxy coating sample. Commonly, the higher the potential, the better the corrosion resistance property of the electrode, and the better the protection effect of the coating will be. It is obvious that the protection effect of the $YbCl_3$-Zn-epoxy coating specimen is better than the Zn-rich coating one.

The EIS vs time of different specimens in SRB solution is given in Fig. 2. We may see that when the specimens immersed in the SRB solution at about 0.5 hour, the low-frequency impedance value is about $1x10^{8.8}$ (ohm) for Zn-epoxy coating specimen and $1x10^{8.5}$ (ohm) for $YbCl_3$-Zn-epoxy specimen, both are pretty high. It suggests that the shielding property of both coating specimen are fine.

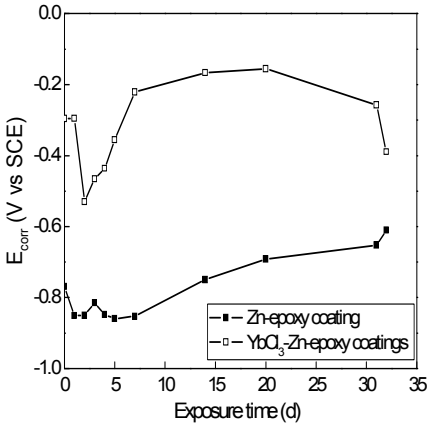
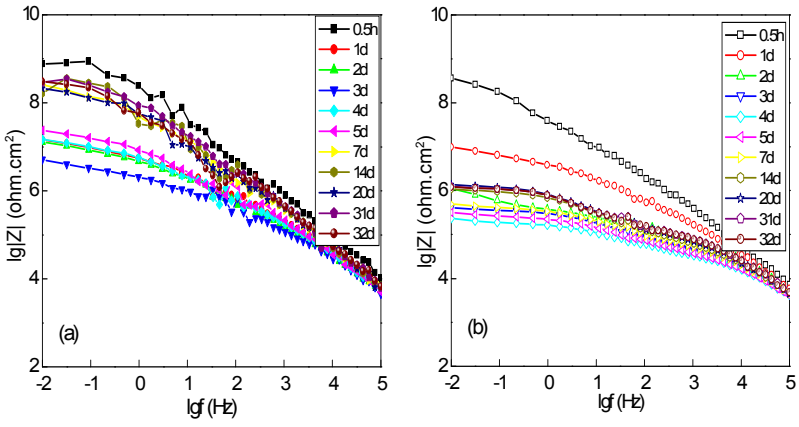


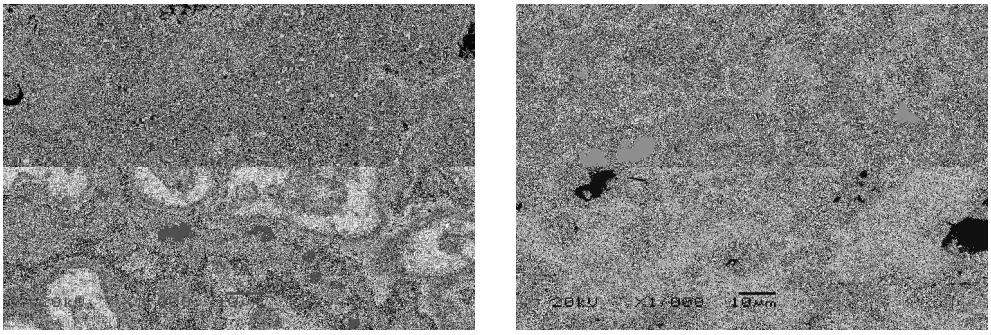
Fig.1 E_{corr} vs time of different specimens in SRB solution



(a) Zn-epoxy coating (b) $YbCl_3$-Zn-epoxy coating

Fig.2 EIS vs time of different specimens in SRB solution

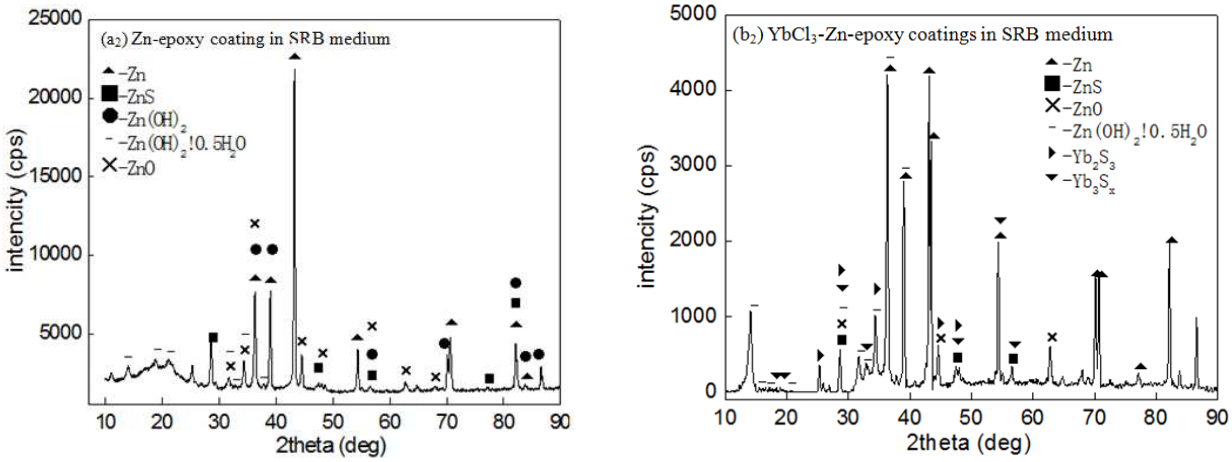
The SEM of Zn-epoxy and $YbCl_3$-Zn-epoxy coating specimens after 30 days exposure in SRB solution are shown in Fig. 3 (a) and (b) respectively. Where, there is no local corrosion can be seen for both the two coatings. It is obvious that the basic low alloy steel was effectively protected by the two coatings.



(a) Zn-epoxy coating (b) $YbCl_3$-Zn-epoxy coating

Fig.3 SEM of specimen after 30 days exposure in SRB solution

Results of X-rays diffraction (XRD) of specimens after 30 days exposure in SRB solution are given in Fig. 4. We may see from Fig.4 (a) that the Zn, ZnS, ZnO, and $Zn(OH)_2$ are the main surface corrosion products of Zn coating specimens. Where, the ZnO and $Zn(OH)_2$ were produced by H_2O and O_2, and the H_2S was produced by the sulfate-reducing bacteria (SRB). In Fig.4 (b), manifold sulfides such as Yb_2S_3 / Yb_3S_x were observed except for the above mentioned corrosion products of Zn. It is obvious that more sulfides and corrosion products of $YbCl_3$-Zn-epoxy coating were produced which increased the shielding property of the coating. There was no corrosion product of Fe existed, indicating that the basic low alloy steel was not eroded at all. We may see that both Zn-epoxy and $YbCl_3$-Zn-epoxy coatings are effective against the attack of SRB.



(a) Zn-epoxy coating (b) $YbCl_3$-Zn-epoxy coating

Fig.4 XRD of specimen after 30 days exposure in SRB solution

The corrosion mechanism of $YbCl_3$-Zn-epoxy coating in the SRB solutions is analyzed as follow:

SRB is anaerobic bacteria and it gets energy from the reduction process of $SO_4^{2-} \rightarrow S^{2-}$. SRB bio-film restrained the corrosion process in the early stage of the test, but the corrosion process was promoted with the increasing amount of SRB then.

The reaction of cathodic depolarization in SRB is as follow:

$$4Zn \rightarrow 4Zn^{2+} + 8e \qquad \text{(anodic reaction)}$$

$$8H_2O \rightarrow 8H^+ + 8OH^- \qquad \text{(hydrolyzation reaction)}$$

$$8H^+ + 8e \rightarrow 8H \qquad \text{(cathodic depolarization reaction)}$$

$$SO_4^{2-} + 8H \rightarrow S^{2-} + 4H_2O \qquad \text{(cathodic reaction caused by bacteria)}$$

The corrosion products came from the follow reaction:

$Zn^{2+} + S^{2-} \rightarrow ZnS$ (corrosion product)

$2Yb^{3+} + 3S^{2-} \rightarrow Yb_2S_3$ (corrosion product)

$3Zn^{2+} + 6OH^- \rightarrow 3Zn(OH)_2$ (deposition reaction)

The whole reaction is:

$$17Zn^{2+}+2Yb^{3+}+4SO_4^{2-}+16H_2O \rightarrow 16Zn(OH)_2+ZnS+Yb_2S_3$$

The Yb^{3+} ions may dissolve out when the specimen coated with $YbCl_3$-Zn-epoxy immerge in the SRB solution, due to the water-solubility effect of the $YbCl_3$. The Kulun adsorption effect of the positive charge Yb^{3+} ions with the sulfate-reducing bacteria (SRB) may destroy the protein configuration of the bacteria, and restrain the upgrowth of the bacteria or perish the bacteria. The corrosion rate will therefore be reduced with the attenuation of SRB. Besides, the sulfides produced by the Yb^{3+} ions from the $YbCl_3$-Zn-epoxy coating in the SRB solutions may decrease the denseness of corrosive ions and decrease the attackable ability of the SRB. At the same time, the sulfides accumulated on the specimen surface may increase the shielding property of the coating. It is obvious that more sulfides and corrosion products of $YbCl_3$-Zn-epoxy coating were produced which increased the shielding property of the coating. The basic low alloy steel is therefore more effectively protected by the $YbCl_3$-Zn-epoxy coating.

Summary

Effect of $YbCl_3$-Zn-epoxy coating on MIC behavior of the low alloy steel in SRB solution was investigated. Experimental results show that the $YbCl_3$-Zn-epoxy coating may offer more effective protection for the basic steel than the Zn-epoxy coating. The Yb^{3+} ions may destroy the protein configuration of the bacteria, and restrain the upgrowth of the bacteria or perish the bacteria and therefore reduce the corrosion rate of specimen in the sulfate-reducing bacteria (SRB) solution. At the same time, the $YbCl_3$-Zn-epoxy coating may produce more sulfides and corrosion products which may increase the shielding property of the coating.

Acknowledgement

The paper is financially supported by the Nature Science Foundation of Heilongjiang Province (E200910).

References

[1] L. P. Chen: J. Corrosion Science & Protection Technology Vol. 17 (1996), p. 248

[2] R. P. George, D. Marshall, R. C. Newman: Corrosion Sci. Vol. 45 (2003), P. 1999

[3] G. Z. Liu: Marine Science Vol. 29 (2005), p. 87

[4] D. Liu, Q. F. Li, C. H. Li and L. L. Xue: Key Engineering Materials Vols. 348-349 (2007), P. 509.

[5] N. Yang, X. M. Zhang, L. Tian: Applied Chemistry Vol. 11 (2008), p.1362.

[6] J. Yang, H. Zhang, J. C. Wang: Rare Earth Vol. 1 (2009), p.35.

© (2012) Trans Tech Publications, Switzerland
doi:10.4028/www.scientific.net/KEM.488-489.254

Improvement of MIC Behavior of Ship Plate Steel With $LaCl_3$-Zn Epoxy Coating

Li Qing-fen [1,a], Wang Jun[1], Fu Yu-dong[2], Li Chun-hui[2]

[1] College of Mechanical and Electrical Engineering, Harbin Engineering University,

[2] College of Material Science and Chemical Engineering, Harbin Engineering University,

Harbin 150001, China

[a]qingfli@yahoo.com.cn

Keywords: Microbiological influenced corrosion (MIC); ship plate steel; $LaCl_3$-Zn epoxy coating; marine environment

Abstract. The MIC behavior of the ship plate steel specimen with $LaCl_3$-Zn epoxy coating in the sulfate-reducing bacteria (SRB) solution was investigated in this paper. The variation of corrosion potential over time of different specimens in SRB solution show that the corrosion potential of the specimen with $LaCl_3$-Zn epoxy coating was obviously higher than the Zn-epoxy coating, suggesting that the $LaCl_3$-Zn epoxy coating may offer better protection. The variations of $lgf_{lg\,|Z|=4.5}$ and f_h with time show that the property of anti-infiltration and corrosion resistance of $LaCl_3$-Zn coating is much better than the ones of Zn-epoxy coating. Results also show that more sulfides and corrosion products of $LaCl_3$-Zn epoxy coating were produced which increased the shielding property of the coating. The experimental results of XRD and SEM are in good agreement with the ones of $E_{corr,}$ and EIS, etc. They all show that the $LaCl_3$-Zn epoxy coating exhibits more favorable corrosion resistance property than the Zn-epoxy coating. It is obvious that coating the ship plate steel with $LaCl_3$-Zn epoxy is an effective and promising method against the attack of SRB in marine environment.

Introduction

Marine is a rigorous corrosive environment. There exit many kinds of salts and halobios in seawater and many metals working in it would suffer serious corrosion damage. A variety of microorganisms in the marine environment may cause microbiological influenced corrosion (MIC), one of the most serious forms of degradation. The cost of MIC failures may reach billions of dollars annually and it has received increasing consideration in the last years [1].

Some techniques to control such corrosion are used, such as biocides, UV irradiation, and coating. Previous work pointed out that it is effective to coat the steel with Zn-rich epoxy which may increase the service life of the material [2,3], and that the rare earths have special bacteriostasis / sterilization effect which may reduce the microbiological influenced corrosion [4, 5].

In the present work, the rare earths element $LaCl_3$ was added into the Zn-epoxy coating, and the effect of $LaCl_3$-Zn-epoxy coating on the MIC behavior of the ship plate steel was investigated and compared with the Zn-epoxy coating.

Experimental

The chemical composition of the ship plate steel used in the present investigation is shown in Table 1. The size of specimen is 30 x 25 x 6 mm (with working area of 6 cm^2). A copper wire was soldered to the lower surface. Specimens were successively polished up to 1000 grit, cleaned with deionized water, dried with air and finally coating with Zn-epoxy or $LaCl_3$-Zn epoxy. The dry film thickness of the coating is about 30 μm. All specimens were sterilized under UV for 3 hours before test.

Tests were carried out in the SRB solution. The SRB strains were isolated from the sea-mud in Qingdao seashore. The composition of the SRB solution is given in table 2.

MIC behaviors in SRB were investigated with EIS, EDS, ESEM of XL30, and a XRD-D8 Advance. Corrosion potential and impedance measurements were performed using the IM6 electrochemical workstation of ZAHNER. Tests were carried out at ambient temperature using a three-electrode system.

Table 1 Chemical Composition of the Ship Plate Steel [wt %]

C	Si	Mn	S	P	Cr	Ni	Mo	V
0.09~0.14	0.17~0.37	0.30~0.60	≤0.03	≤0.035	0.09~1.20	2.60~3.00	0.20~0.27	0.04~0.10

Table 2 Composition of the SRB Solutions [g/L]

Seawater	PH	$K_2HPO_4.3H_2O$	$MgSO_4.7H_2O$	$CaCl_2$	Na_2SO_4	NH_4Cl	Sodium lactate	Vc
1	7.00	0.50	2.00	0.10	0.50	1.00	3.50	0.10

Results and discussion

The variation of corrosion potential over time of the specimen with $LaCl_3$-Zn-epoxy and Zn-epoxy coating in SRB solution is given in Fig.1. Where, the corrosion potential of the $LaCl_3$-Zn-epoxy specimen is obviously higher than that of the Zn-epoxy coating specimen, suggesting that the protection effect of the $LaCl_3$-Zn-epoxy coating specimen is much better than the Zn-rich coating one， because higher potential will give better corrosion resistance property of the electrode and endue better protection effect of the coating usually.

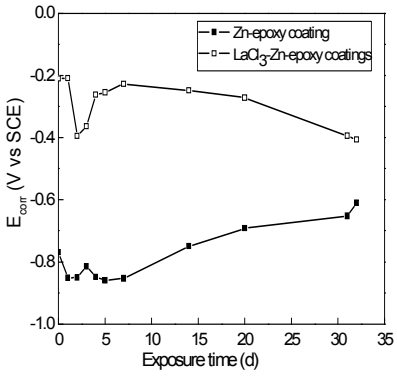
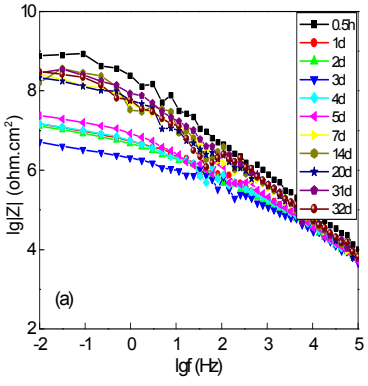
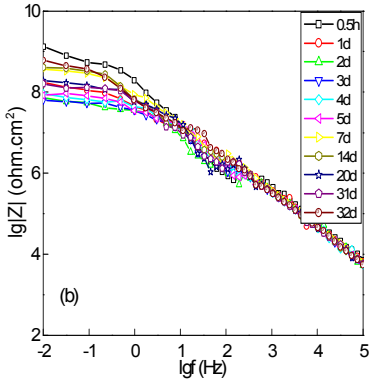


Fig.1 E_{corr} vs time of different specimens in SRB solution



(a) Zn-epoxy coating



(b) $LaCl_3$-Zn-epoxy coating

Fig.2 EIS vs time of different specimens in SRB solution

The EIS vs time of different specimen in SRB solution is given in Fig. 2. From which, we may see that the low-frequency impedance values of $LaCl_3$-Zn-epoxy coating specimen are much higher than those of the Zn-epoxy coating one, suggesting that the shielding property of $LaCl_3$-Zn-epoxy coating is much higher than the one of Zn-epoxy coating. Especially when specimen immersed in the SRB solution at the first 0.5 hour, it reached to $1\times10^{9.1}$ for $LaCl_3$-Zn-epoxy coating specimen, obviously higher than the one of Zn-epoxy coating specimen ($1x10^{8.8}$). Besides, the variation

range of $LaCl_3$-Zn-epoxy coating is smaller, suggesting that the electrochemistry reaction resistance of $LaCl_3$-Zn-epoxy coating is higher, and therefore the corrosion resistance property is better than the Zn-epoxy coating.

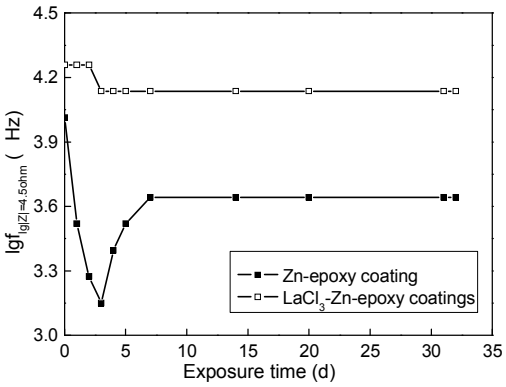


Fig.3 Variations of $lgf_{lg|Z|=4.5}$ with time

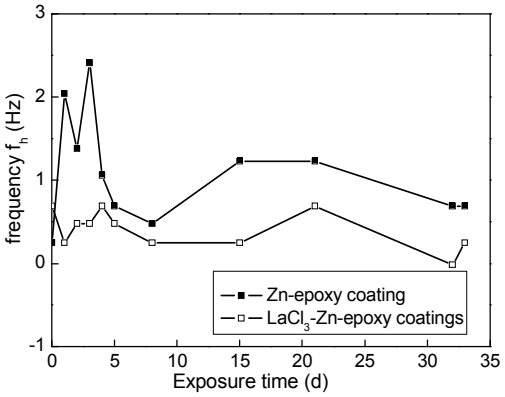


Fig.4 Variations of f_h with time

The variations of $lgf_{lg\ |Z|=4.5}$ and f_h with time are given in Fig.3 and 4 respectively. From Fig.3, we see that the $lgf_{lg\ |Z|=4.5}$ value of $LaCl_3$-Zn-epoxy coating specimen was very high and kept constant at the first 2 days, indicating that the $LaCl_3$-Zn-epoxy coating was very compact and it was very difficult for the solution infiltrating into the coating. The $lgf_{lg\ |Z|=4.5}$ value decreased a little in the next day and kept constant in the following days, showing that the infiltration reached saturation quickly and the infiltrating amount was very little. It indicates that the $LaCl_3$-Zn-epoxy is much more compact than the Zn-epoxy coating, and therefore the property of anti-infiltration is much better.

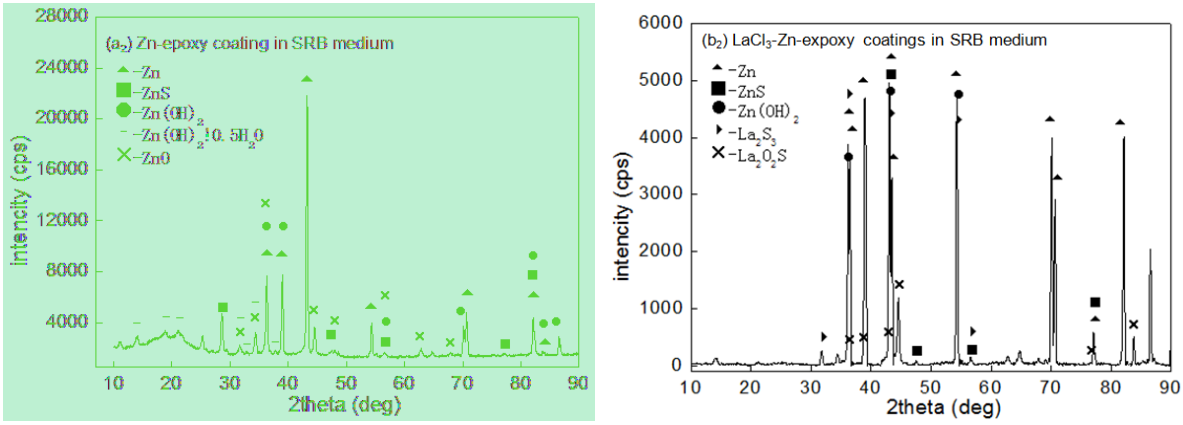
From Fig. 4, we see that the characteristic frequency value (f_h) of $LaCl_3$-Zn-epoxy is obviously lower than the one of Zn-epoxy coating. It is known that the characteristic frequency value increases with the increasing peel-off-area of coating. Therefore, the lower the f_h value is, the better the corrosion resistance property of the coating will be. Fig. 4 shows that the anticorrosion property of $LaCl_3$-Zn-epoxy coating is much better than the Zn-epoxy coating.

Results of X-rays diffraction (XRD) of specimens after 30 days exposure in SRB solution are given in Fig. 5. We may see from Fig.5 (a) that the Zn, ZnS, ZnO, and $Zn(OH)_2$ are the main surface corrosion products of Zn coating specimens. Where, the ZnO and $Zn(OH)_2$ were produced by H_2O and O_2, and the H_2S was produced by the sulfate-reducing bacteria (SRB). In Fig.5 (b), manifold sulfides such as La_2S_3，La_2O_2S were observed except for the above mentioned corrosion products of Zn. It is obvious that more sulfides and corrosion products of $LaCl_3$-Zn-epoxy coating were produced which increased the shielding property of the coating. There was no corrosion product of Fe existed, indicating that the basic low alloy steel was effectively protected by the coatings.

The SEM of Zn-epoxy and $LaCl_3$-Zn-epoxy coating specimens after 30 days exposure in SRB solution are shown in Fig. 6 (a) and (b) respectively. From Fig. 6 (b), we see that the flaky-Zn was enwrapped by the organic rosin and the corrosion products filled in the organic rosin. It is obvious that the continuity of organic rosin of $LaCl_3$-Zn-epoxy coating is much better than the one of Zn-epoxy coating, and therefore the basic low alloy steel was more effectively protected by the $LaCl_3$-Zn-epoxy coating.

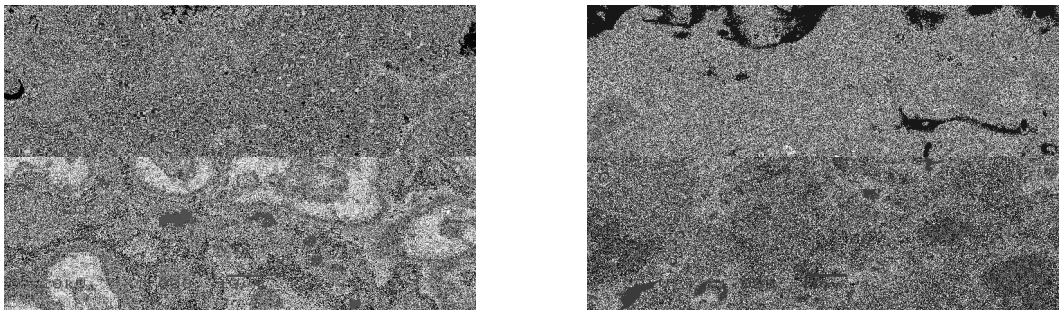
It can be explained that due to the water-solubility effect of the $LaCl_3$, the La^{3+} ions may dissolve out when specimen coated with $LaCl_3$-Zn-epoxy immerged in the SRB solution. The Kulun-adsorption-effect of the positive charge La^{3+} ions with the sulfate-reducing bacteria (SRB) may destroy the protein configuration of the bacteria, and restrain the upgrowth of the bacteria or perish the bacteria. The corrosion rate will therefore be reduced with the attenuation of SRB. Besides, the sulfides produced by the La^{3+} ions from the $LaCl_3$-Zn-epoxy coating in the SRB

solutions may decrease the denseness of corrosive ions and decrease the attackable ability of the SRB. Synchronously, the sulfides accumulated on the specimen surface may increase the shielding property of the coating. It is obvious that more sulfides and corrosion products of $LaCl_3$-Zn-epoxy coating were produced which increased the shielding property of the coating. The basic low alloy is therefore more effectively protected by the $LaCl_3$-Zn-epoxy coating.



(a) Zn-epoxy coating (b) $LaCl_3$-Zn-epoxy coating

Fig.5 XRD of specimen after 30 days exposure in SRB solution



(a) Zn-epoxy coating (b) $LaCl_3$-Zn-epoxy coating

Fig.6 SEM of specimen after 30 days exposure in SRB solution

All the experimental results ($E_{corr,}$ EIS, XRD, SEM etc.) are in good agreement with each other. They all show that the $LaCl_3$-Zn epoxy coating exhibits more favorable corrosion resistance property than the Zn-epoxy coating. It is obvious that coating the ship plate steel with $LaCl_3$-Zn epoxy is an effective and promising method against the attack of SRB in marine environment.

Acknowledgement

The paper is financially supported by the Nature Science Foundation of Heilongjiang Province (E200910).

References

[1] R. P. George, D. Marshall, R. C. Newman: Corrosion Sci. Vol. 45 (2003), P. 1999

[2] G. Z. Liu: Marine Science Vol. 29 (2005), p. 87

[3] D. Liu, Q. F. Li, C. H. Li and L. L. Xue: Key Engineering Materials Vols. 348-349 (2007), P. 509.

[4] N. Yang, X. M. Zhang, L. Tian: Applied Chemistry Vol. 11 (2008), p.1362.

[5] J. Yang, H. Zhang, J. C. Wang: Rare Earth Vol. 1 (2009), p.35.

© (2012) Trans Tech Publications, Switzerland
doi:10.4028/www.scientific.net/KEM.488-489.258

Computational Analysis of the AFM Specimen on Mixed-mode I+II+III Fracture

Li Qing-fen[a], Zhu Li[b], Yan Sheng-yuan[c], and Zhang Xiao-nan

College of Mechanical and Electrical Engineering, Harbin Engineering University, Harbin 150001, China

[a]qingfli@yahoo.com.cn, [b]zhuli0712@hrbeu.edu.cn, [c]yanshengyuan@hrbeu.edu.cn

Keywords: computational analysis; all fracture modes (AFM) specimen; mixed-mode I+II+III fracture; strain energy release rates (SERRs)

Abstract. The computational analysis of an all fracture modes (AFM) specimen on mixed-mode I+II+III fracture is presented in this paper. The separated energy release rates (SERRs) along the crack front of the AFM-model are calculated by the modified virtual crack closure integral (MVCCI)-method and the commercially available software ANSYS. A transition model is built by adopting several 3D elements of SOLID45 and one point element of MASS21 in the ANSYS program. Under the related constraint conditions, the separate force and moments are respectively applied on the point element of the transition model, so the corresponding desired reaction forces can be obtained. When the desired loads are superimposed and applied on the AFM-model, the mixed-mode I+II+III fracture can then be achieved. Thereby, the SERR results are calculated. The calculation results show that the facture behavior of G_{II} and G_{III} appears complex due to the global deformation and Poisson's ratio, although the distribution of SEERs G_I is symmetrical with respect to the middle point along the crack front. The total SERRs, G_{Tn}-values increase along the crack front with the minim value at one corner and the maxim value at the other corner. It can therefore be predicted that the fracture will occur initially at one corner on the crack front of the AFM-specimen in this case.

Introduction

The understanding and analysis of mixed mode fracture is an important subject in fracture mechanics, since fracture processes are in many cases of the three dimensional (3D) character in the real engineering structures, where cracks may experience superimposed tensile, shear and torsion stress for the complex geometries and loading conditions. Although the investigation of 3D crack configurations has been a major task of fracture-mechanical research for a long time, only a few 3D fracture criteria have been proposed so far [1, 2]. The AFM-specimen has been used to investigate 3D fracture problems but only for pure mode I, pure mode II, and pure mode III [3]. The mixed-mode I+III and II+III were investigated recently in the previous work [4, 5]. However, the simulation of mixed-mode I+II+III fracture is still a challenging problem, in particular that it is difficult to apply loads on the test model.

In this paper, the computational analysis of an all fracture modes (AFM) specimen on mixed-mode I+II+III fracture is presented by using a transition model. The separated energy release rates (SERRs) along the crack front of the AFM-model are calculated by the modified virtual crack closure integral (MVCCI)-method and the commercially available software ANSYS.

AFM-specimen and FE-mesh

The AFM loading device and specimen designed by Richard [3] are shown in Fig. 1 a) and b). Through the AFM loading device all single types of loading can be generated and furthermore arbitrary combinations of external tension, in-plane shear and out-of-plane shear loadings can be achieved. The AFM-specimen is a special type of single edge notched (SEN) specimen (Fig. 1 b))and the AFM loading device consists of two specially designed parts of spheres as illustrated in Fig. 1 a)

through which the load F of a standard uniaxial tensile/compression testing machine is introduced. The design is such that the load line intersects the centre of the SEN-specimen and the front of the notch that is machined there.

When the load F is acting under the angles α and β with respect to the local crack or notch tip coordinate system the components of F can be expressed as follow:

$$F_y = N = F\cos\alpha\cos\beta \quad (1a)$$

$$F_x = Q = F\sin\alpha\cos\beta \quad (1b)$$

$$F_z = T = F\sin\beta \quad (1c)$$

$$M_Q = FH_2\sin\alpha\cos\beta \quad (1d)$$

$$M_T = FH_1\sin\beta \quad (1e)$$

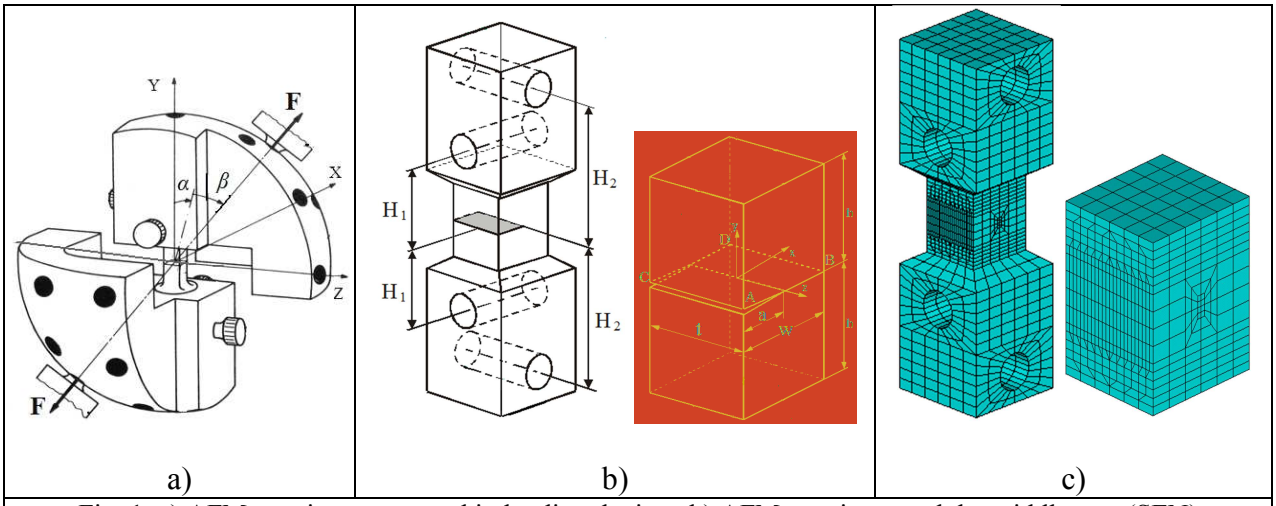
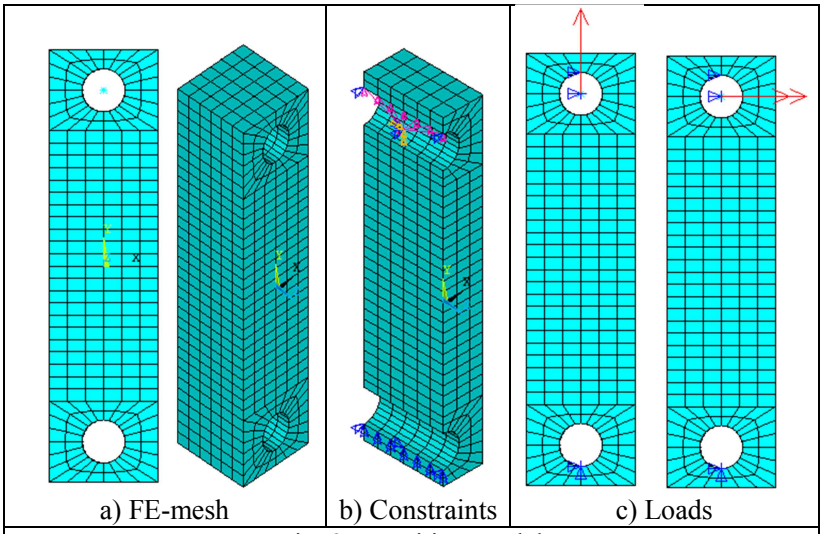


Fig. 1 a) AFM-specimen mounted in loading device; b) AFM-specimen and the middle part (SEN) c) FE-model of AFM-specimen and the middle part (SEN)

The geometrical parameters of AFM-specimen, in Fig. 1 b), are as follows: width w =27mm, height h =20mm, thickness t =24.3mm, crack length a =0.5 w (straight crack front), H_1 =32.5mm, and H_2 =57.5mm. The material parameters are chosen as follows: Young's modulus $E = 2.1\times10^5$ N/mm^2 and Poisson's ratio ν=0.3. The specimen is subject to a static loading of F =6561N.

The 3D FE-model of the AFM-specimen, shown in Fig. 1 c), is assembled of some standard 6- but predominantly of non-singular, standard 8-node volume elements. The total mesh consists of 3,528 six- or eight-node SOLID45 elements with a total of 4,858 nodes, and about 30,000 degrees of freedoms. A spider-web-like mesh around the crack front is employed near the crack front to capture detailed stress/strain variations and their singularity behavior. Considering the singular stress behavior at the crack front some mesh refinement is incorporated in the model adjacent to the crack front and with respect to the MVCCI-method the crack front is formed by a homogeneous mesh with elements of constant size ($0.1\times0.1\times0.1$mm^3 with $\Delta a = 0.1$mm and $\Delta a/a = 0.0074$).

It is a challenging problem to apply loads on the test model for simulation of mixed-mode I+II+III fracture. In order to simulate mixed-mode I+II+III fracture and in particular apply loads on the AFM-model, an uncracked transition model is used to overcome this problem. The transition model has a similar physical configuration with the AFM-model, and consists of several 3D elements of SOLID45 and a point element of MASS21 (see Fig. 2 a)). The point element MASS21 is added in the centre of the upper hole (x=0, y=H_2, z=0). Besides, the y-DOF of the MASS21 is coupled with the nodes along the top line in the upper hole (see Fig. 2 b)). Meanwhile all displacements of the nodes along the bottom line in the lower hole are suppressed in the y-direction (also see Fig. 2 b)). When the corresponding forces (N, Q, T) and moments (M_Q, M_T) are respectively applied on the point element of the transition model, the reaction forces of the nodes can be obtained from these supports (see Fig. 2 c)). The negative values of the reaction are the desired loads, which represent tensile, shear, and torsion loads. When the loads are applied on the AFM-model at corresponding nodes, the mixed-mode I+II+III fracture can then be achieved (see Fig. 3).



a) FE-mesh b) Constraints c) Loads

Fig. 2 Transition model

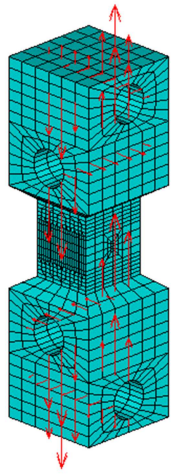


Fig. 3 Loads on the AFM-model

3D Computational Fracture Analysis and Discussion of Results

The normalized SERRs along the crack front of the AFM-specimen under superimposed mode I+II+III loading (α =45°, β =45°) are given in Fig. 4. Where, it is found that the mode I loading condition $G_{In}(a, z/t)$- values along the straight crack front through the thickness of the specimen (-0.5 $\leq z/t \leq$ +0.5) are symmetric with respect to the center point of the crack front, and nearly constant in the inner part of the specimen (-0.25< z/t <0.25). Besides, adjacent to the free surfaces of the specimen, the well known 3D-effect is apparently observed that the G_{In}(a, z/t)-values decrease with increasing $|z/t|$ values, and with a stronger gradient when $z/t \rightarrow \pm 0.5$.

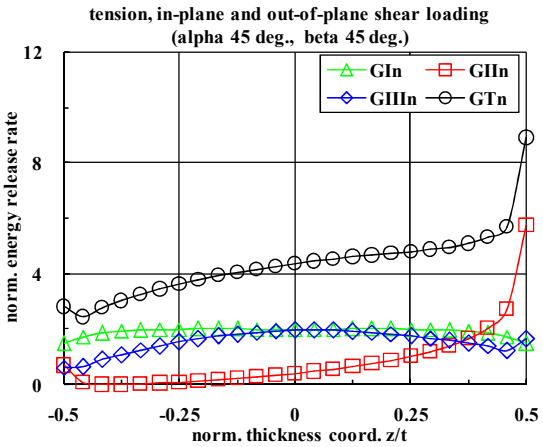
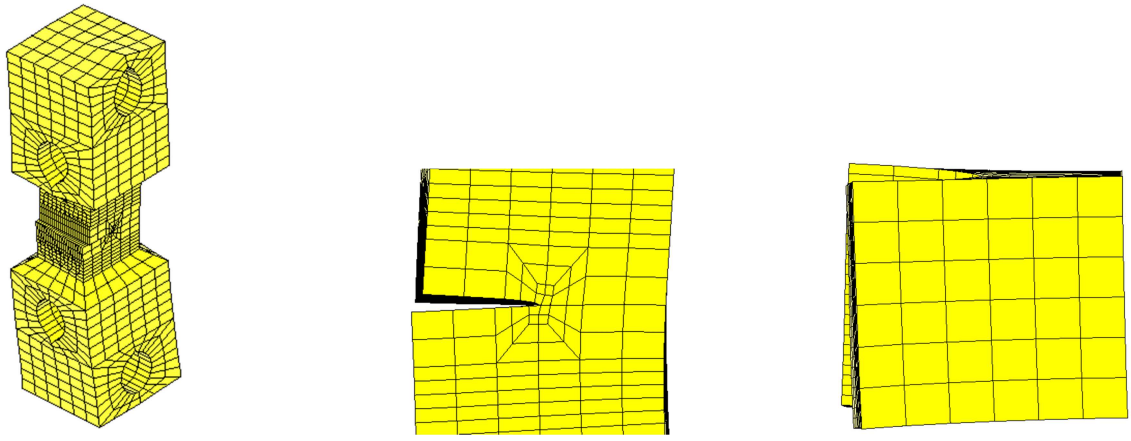


Fig. 4 Normalized SIFs along the crack front under mixed-mode I+II+III loading condition

For mode II and III loading conditions, the SERRs achieved along the crack front are more complex that the applied and induced modes are generated simultaneously due to the global deformation and Poisson's ratio. The G_{IIn} and G_{IIIn} values for z/t <0 are obviously smaller than the ones for $z/t \geq 0$. This behavior is owing to that for $z/t \geq 0$, the induced mode loads and the applied ones along the crack front are both in the positive direction, whereas for z/t <0, the two mode loads are in opposite direction. Consequently, the $G_{IIn}(a, z/t \geq 0)$-values and $G_{IIIn}(a, z/t \geq 0)$-values are the results of the applied modes plus the induced ones, whereas the $G_{IIn}(a, z/t$ <0)-values and $G_{IIIn}(a, z/t$ <0)-values are the results of the applied modes offset the induced ones. Thus, the presence of mode II or mode III always induces the other, especially in the vicinity of the crack corner points.

The total SERRs, G_{Tn}-values, are finally evaluated. From Fig. 4, we see that the G_{Tn}-values increase along the crack front with the minim value of $G_{Tn}(a, z/t = -0.5)$ at one corner and the maxim value of $G_{Tn}(a, z/t = +0.5)$ at the other corner. It can therefore be predicted that the fracture will occur initially at one corner on the crack front of the AFM-specimen in this case.

Qualitatively, the deformed crack details of the FE-model of the AFM-specimen under mixed-mode I+II+III loading condition are given in Fig. 5 a) – c) respectively. Where, we can see that besides the globally torsion behavior (Fig. 5 a)), the expected crack opening, in-plane and out-of-plane sliding displacements around the crack front (Fig. 5 b, c)) are apparently observable.



a) Whole model b) Side view of crack tip c) Top view on the center part

Fig. 5 Deformed crack details of the AFM-specimen under mixed-mode I+II+III loading condition

Thus, the computational analysis of the AFM specimen on mixed-mode I+II+III loading condition is successfully investigated by using a transition model in conjunction with the MVCCI-method and commercial software ANSYS.

Acknowledgement

This paper is financially supported by the High-level Creative Talents and International Exchange Project Foundation of Harbin Engineering University.

References

[1] R. Citarella, G. Cricrì: Engng. Fract. Mech., vol. 77, no. 11 (2010), p. 1730-1749

[2] G. Dhondt: Key Engineering Materials, vol. 251-252 (2003), p. 209-214

[3] H. A. Richard, M. Kuna: Engineering fracture Mechanics, vol. 35, no. 6 (1990), p. 949-960

[4] Q. F. Li, L. Zhu, F. G. Buchholz, S. Y. Yan: Key Engineering Materials, Vols. 452-453 (2010), p. 173-176

[5] Q. F. Li, L. Zhu, S. F. Zhu: SDHM, Vol. 158, no.1 (2010), p. 1-16

© (2012) Trans Tech Publications, Switzerland
doi:10.4028/www.scientific.net/KEM.488-489.262

MIC Behavior of the Low Alloy Steel with Different Zn-Epoxy Coating in SRB Solution

Wang Jun[1,a], Li Qing-fen [1,b], Fu Yu-dong[2]，Li Chun-hui[2]

[1] College of Mechanical and Electrical Engineering, Harbin Engineering University,

[2] College of Material Science and Chemical Engineering, Harbin Engineering University,

Harbin 150001, China

[a]wangjun@hrbeu.edu.cn, [b]qingfli@yahoo.com.cn

Keywords: Microbiological influenced corrosion (MIC); granular-Zn-epoxy coating; flaky-Zn-epoxy coating; sulfate-reducing bacteria (SRB) solution.

Abstract. The microbiological influenced corrosion (MIC) behavior of the low alloy steel with granular-Zn-epoxy and flaky-Zn-epoxy coating in the sulfate-reducing bacteria (SRB) solution was investigated with electrochemical impedance spectroscopy (EIS), X-rays diffraction (XRD), scanning electron microscope (SEM) etc. Results show that the protection effect of the flaky-Zn coating specimen is much better than the granular-Zn coating one. The dissolution of zinc is more severe in granular-Zn coating than in flaky-Zn coating when the specimen immersed in the SRB solution. The shielding property of flaky zinc is much higher than granular zinc in the coating. The flaky-Zn coating is much more compact than the granular-Zn coating and therefore the property of anti-infiltration is much better. We may conclude that the flaky-Zn coating exhibited more favorable corrosion resistance property than the granular one.

Introduction

The microbiological influenced corrosion (MIC) failures exit in many industries and the cost of such damage may reach billions of dollars annually [1]. The corrosion caused by the sulfate-reducing bacteria (SRB) is the most severe one among MIC. Although many research studies of MIC caused by SRB have been carried out [2-4]，corrosion behavior of steel in the marine microbiological environment has not been investigated in detail and the corrosion mechanism is not totally clear yet.

Previous work pointed out that the MIC behavior of low alloy steel with Zn-rich epoxy coating was improved obviously. The protection mechanism is that the Zn-rich epoxy coating cemented with epoxy binder and zinc powder can be considered as porous coating due to the metallic content. The potential of zinc is lower comparing with steel, and when exposed to the corrosive environment the zinc particles are devoted to corrode and will therefore provide cathodic protection to the base steel in a first period. Later, when zinc corrosion products form and fill the coating holes, the cathodic protection terminates and an improved barrier type protection is offered by the coating. In the SRB solution, the protection of the coating was affected by the culture medium and life activity of the bacteria mainly. With the rapid increase of SRB, the activation of zinc was enhanced, and zinc coating protect the test steel by cathodic protection. With the increasing of zinc consumption and corrosion product depositions, the steel is protected with physical barrier [5].

Different structure of Zn-epoxy coating may have different effect on the MIC behavior. However, few data for such coating used in the marine microbiological environment is available.

In the present study, the effect of granular-Zn epoxy coating and flaky-Zn epoxy coating on the MIC behavior of the low alloy steel in SRB solution was investigated.

Experimental

The chemical composition of the low alloy steel used in the present investigation is shown in Table 1. The size of specimen coated with Zn-epoxy is 30 x 25 x 6 mm (with working area of 6 cm^2). A copper wire was soldered to the lower surface. Specimens were successively polished up to 1000 grit, cleaned with deionized water, dried with air and finally coating with Zn-epoxy. The dry film thickness of Zn-epoxy coating is about 30μm. All specimens were sterilized under UV for 3 hours before test.

Tests were carried out in the SRB solution. The SRB strains were isolated from the sea-mud in Qingdao seashore. The composition of the SRB solution is given in table 2.

MIC behaviors in SRB solution were investigated with EIS, EDS, ESEM of XL30, and a XRD-D8 Advance. Corrosion potential and impedance measurements were performed using the IM6 electrochemical workstation of ZAHNER. Tests were carried out at ambient temperature using a three-electrode system.

Table 1 Chemical Composition of the Low Alloy Steel [wt %]

C	Si	Mn	S	P	Cr	Ni	Mo	V
0.09~0.14	0.17~0.37	0.30~0.60	≤0.03	≤0.035	0.09~1.20	2.60~3.00	0.20~0.27	0.04~0.10

Table 2 Composition of the SRB Solutions [g/L]

Seawater	PH	$K_2HPO_4.3H_2O$	$MgSO_4.7H_2O$	$CaCl_2$	Na_2SO_4	NH_4Cl	Sodium lactate	Vc
1	7.00	0.50	2.00	0.10	0.50	1.00	3.50	0.10

Results and discussion

The variation of corrosion potential over time of the granular-Zn epoxy coating and flaky-Zn epoxy coating in SRB solution is given in Fig.1. Where, we can see that the corrosion potential of the flaky-Zn coating sample was obviously higher than that of the granular-Zn coating sample. It is obvious that the protection effect of the flaky-Zn coating specimen is better than the granular-Zn coating one.

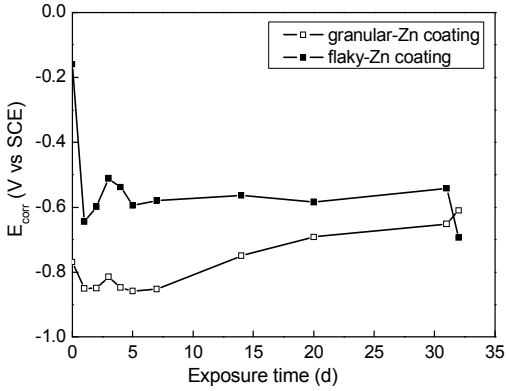


Fig.1 E_{corr} vs time of different specimens in SRB solution

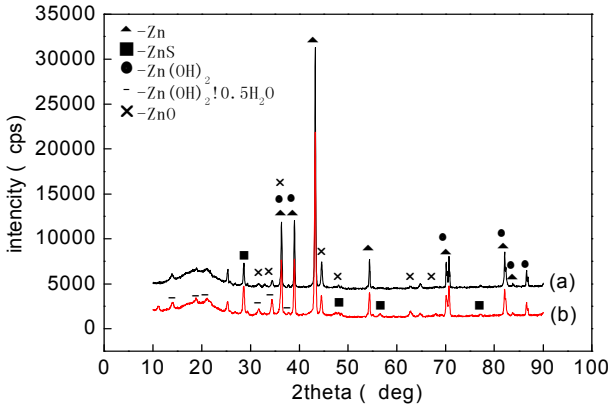
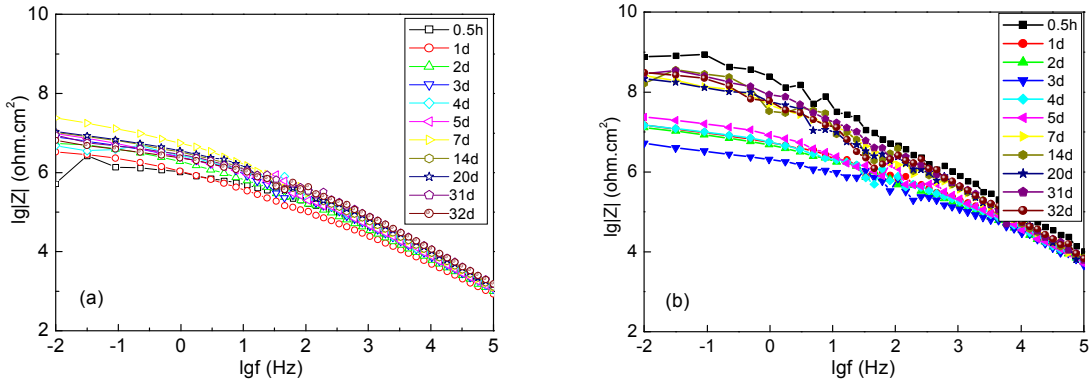


Fig.2 XRD of specimen after 30 days exposure in SRB solution
(a) Granular-Zn coating (b) Flaky-Zn coating

Results of X-rays diffraction (XRD) of specimens after 30 days exposure in SRB solution (see Fig.2) show that surface corrosion products of both granular-Zn coating and flaky-Zn coating specimens are similar. Where, the ZnO and $Zn(OH)_2$ were produced by H_2O and O_2, and the H_2S was produced by the sulfate-reducing bacteria (SRB). However, the content of zinc is much higher

in granular-Zn coating than in flaky-Zn coating. It is obvious that the dissolution of zinc is more severe in granular-Zn coating than in flaky-Zn coating when the specimen immersed in the SRB solution.

The EIS vs time of different specimens in SRB solution is given in Fig. 3. The variations of $lgf_{lg\ |Z|=4.5}$ with time and variations of θ_{fmax} with time are given in Fig. 4 and 5 respectively. The SEM of both granular-Zn coating and flaky-Zn coating specimens after 30 days exposure in SRB solution are shown in Fig. 6.



(a) Granular-Zn coating (b) Flaky-Zn coating

Fig.3 EIS vs time of different specimens in SRB solution

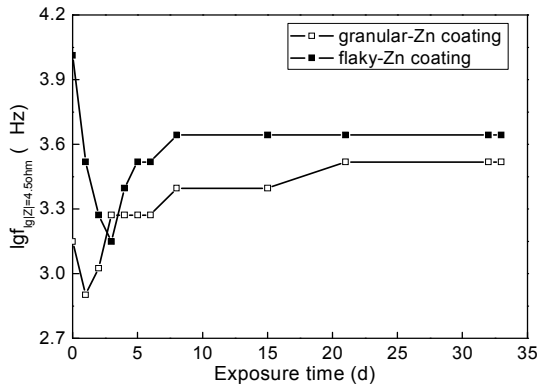


Fig.4 Variations of $lgf_{lg|Z|=4.5}$ with time

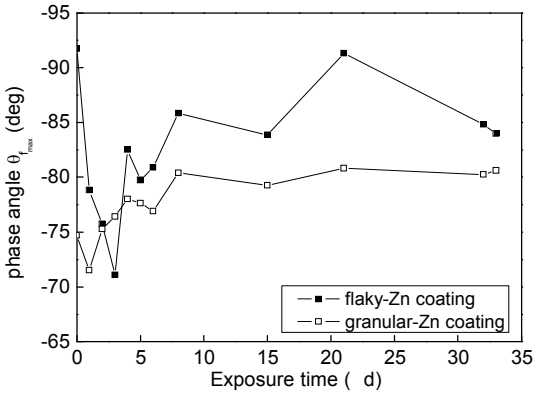
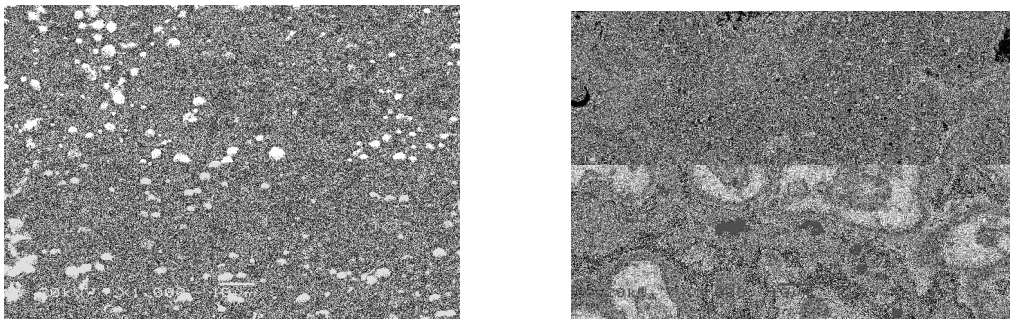


Fig.5 Variations of θ_{fmax} with time



(a) Granular-Zn coating (b) Flaky-Zn coating

Fig.6 SEM of specimen after 30 days exposure in SRB solution

From Fig. 3, we may see that the low-frequency impedance value of flaky-Zn coating specimens is obviously higher than that of the granular-Zn coating specimens, especially when the specimen immersed in the SRB solution at about 0.5 hour, it is about $1x10^{8.8}$, much higher than the one of granular-Zn coating specimens. It suggests that the shielding property of flaky zinc is much higher than the one of granular zinc in the coating.

Fig. 4 shows that the $lgf_{lg\ |Z|=4.5}$ value of granular-Zn coating decreased quickly at the first day, increased in the next 20 days, and kept constant in the following days. It suggests that the SRB solution infiltrated through the coating quickly at the first day, and then in the next 20 days, the more and more velum and corrosion products accumulated over the specimen surface and filled in the coating pores, which decreased the solution infiltration through coating. Finally, it was saturated and the $lgf_{lg\ |Z|=4.5}$ value kept constant. As for the flaky-Zn coating specimen, the $lgf_{lg\ |Z|=4.5}$ value was very high at first and decreased quickly in the first 3 days, then increased in the next 8 days and kept constant in the following days. It indicates that the flaky-Zn coating is much more compact than the granular-Zn coating, and therefore the property of anti-infiltration is much better.

Fig. 5 shows that the high-frequency phasic angle of flaky-Zn coating is also higher than the one of granular-Zn coating, indicating that the anticorrosion property of flaky-Zn coating is better.

Surface micrographs of specimens after 30 days immersion are shown in Fig 6, where no local corrosion can be seen for both the two coatings. It is obvious that the basic low alloy steel was effectively protected by the two Zn-rich epoxy coatings. However, it can be seen from Fig 6(a) that the spherical zinc powder and corrosion products were serried distributed on the granular-Zn coating surface, whereas, few zinc flake or corrosion products can be seen on the flaky-Zn coating surface from Fig 6 (b). It is obvious that the dissolution of zinc is much less in flaky-Zn coating than in granular-Zn coating when the specimen immersed in the SRB solution, and therefore the shielding property of flaky zinc is much higher than granular zinc in the coating. These results of SEM are in good agreement with the results of $E_{corr,}$ XRD and EIS, etc.

All the experimental results show that the flaky-Zn coating exhibited more favorable corrosion resistance property in SRB solution than the granular one. We therefore pitch on the flaky-Zn coating and eliminate the granular-Zn coating for further investigation and engineering application.

Summary

The effect of granular-Zn epoxy coating and flaky-Zn epoxy coating on the MIC behavior of the low alloy steel in SRB solution was investigated. Experimental results show that the flaky-Zn coating exhibited more favorable corrosion resistance property than the granular one in SRB solution. It is obvious that the flaky-Zn coating should be pitched on and the granular-Zn coating be eliminated for further investigation and engineering application.

Acknowledgement

The paper is financially supported by the Nature Science Foundation of Heilongjiang Province (E200910).

References

[1] L. P. Chen: J. Corrosion Science & Protection Technology Vol. 17 (1996), p. 248

[2] G. Z. Liu: Marine Science Vol. 29 (2005), p. 87

[3] S. Z. Song, L. H. Yin, and J. Wu: Journal of Chemical Industry and Engineering Vol. 56 (2005): p.121-125.

[4] G. F. Cui, N. Li, D. Y. Li, J. Zheng, and Q. L. Wu: Surface & Coatings Technology Vol. 200 (2006), P. 6808–6814.

[5] D. Liu, Q. F. Li, C. H. Li and L. L. Xue: Key Engineering Materials Vols. 348-349 (2007), P. 509.

© (2012) Trans Tech Publications, Switzerland
doi:10.4028/www.scientific.net/KEM.488-489.266

Crack Initiation Predictions of the AFM-specimen under Bend and Torsion Loading

Zhu Shi-fan[a], Zhu Li[b], Li Qing-fen[c]

College of Mechanical and Electrical Engineering, Harbin Engineering University, Harbin 150001, China

[a]zhushifan@hrbeu.edu.cn, [b]zhuli0712@hrbeu.edu.cn, [c]qingfli@yahoo.com.cn

Keywords: crack initiation predictions; all fracture modes specimen; maximum principal stress σ_1'-criterion; modified virtual crack closure integral method

Abstract. In this paper, the computational predictions of crack initial breakpoint and deflection angles under bend and torsion loading conditions are investigated in conjunction with the modified virtual crack closure integral (MVCCI)-method by using the all fracture modes (AFM) specimen and commercial software ANSYS. The separated strain energy release rates (SERRs) along the crack front are calculated and subsequently converted to the stress intensity factors (SIFs) by using Irwin´s equations. Based on the SIFs results, the crack initiation predictions are presented by the maximum principal stress σ_1'-criterion. Results show that when the AFM-model under a series of combined proportional bend and torsion loading conditions, asymmetrical stress fields are produced along the crack front. The presented investigation also shows that the maximum principal stress σ_1'-criterion in conjunction with the MVCCI-method provides a powerful numerical tool for general computational approach to the fracture analysis of complex loading conditions.

Introduction

Mixed mode fractures, which are most likely to be found in various structures in service, such as pressure vessels, pipeline systems, off-shore structures and aircraft components, have been recognized as real cases for such components [1]. Crack growth may lead to abrupt failure of structures in many practical cases, and it is of great importance to predict the crack initial breakpoint and deflection angles in different cases.

In this paper, investigations are focused on the influence of the loading angles to the stress intensity factors (SIFs) distributions and the crack initiation angles. The calculation of the strain energy release rates (SERRs) along the crack front is performed by the numerically very accurate and reliable modified virtual crack closure integral (MVCCI) method. By this method, the forces at the crack front are combined with the displacements just to the open side of the crack front to calculate the strain energy release rate in post processing. In particular, not only the total strain energy release rate (G_T) is calculated, but also the mode I, II and III components of strain energy release rates (G_I, G_{II}, G_{III}) are calculated respectively, which are subsequently converted to the stress intensity factors (SIFs) by using Irwin´s equations [2].

The computational approach is carried through the maximum principal stress σ_1'-criterion in conjunction with the MVCCI-method. It is well known that under mode II loading the crack kinks with a kink angle φ_0 and that under mode III loading the crack front grows into a new plane that is twisted about the angle ψ_0 referred to the pre-crack plane [3]. In order to investigate the initiation of crack front, a recently developed and proposed 3D fracture criterion is utilized, which can take into account all three basic fracture modes I, II and III. This so called the maximum principal stress σ_1'-criterion (where the σ_1' is the maximum principal stress on a virtual cylindrical surface around the crack front) reduces to the well established MTS-criterion, in case of plane mixed mode I and II loading conditions along the crack front, and thus can be taken as its 3D generalization. The details of the σ_1'-criterion are given in reference 3.

FE-model of the AFM-specimen under Bend and Torsion Loading

The all fracture modes (AFM)-specimen and the loading device in this study are similar to that employed by Richard [4]. The diagram of the modified AFM-specimen and test fixture under investigation are shown in Fig. 1. The AFM-specimen is supported at its two ends and loaded by four pins, which are connected with the fixture, in Fig. 1 a. For the specimen with different loading conditions, the node position of the pins may need to be changed. The pinhole locations on the spatial surface of the fixture provide a range of loading angles, α and β, where α=90° and β=0° correspond to bend loading (Fig. 1 b), α=90° and β=90° correspond to torsion loading (Fig. 1 c), and α=90° plus $0° < \beta < 90°$ correspond to mixed-mode bend and torsion loading.

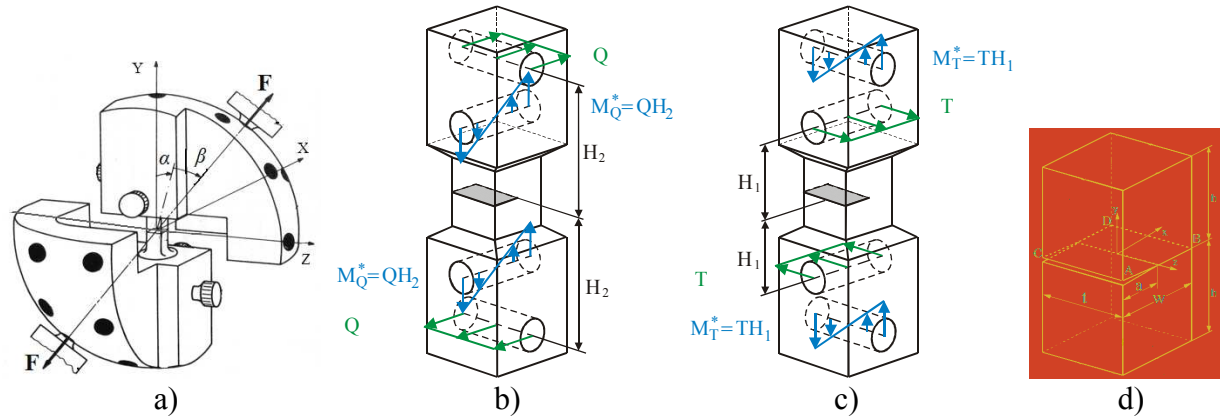
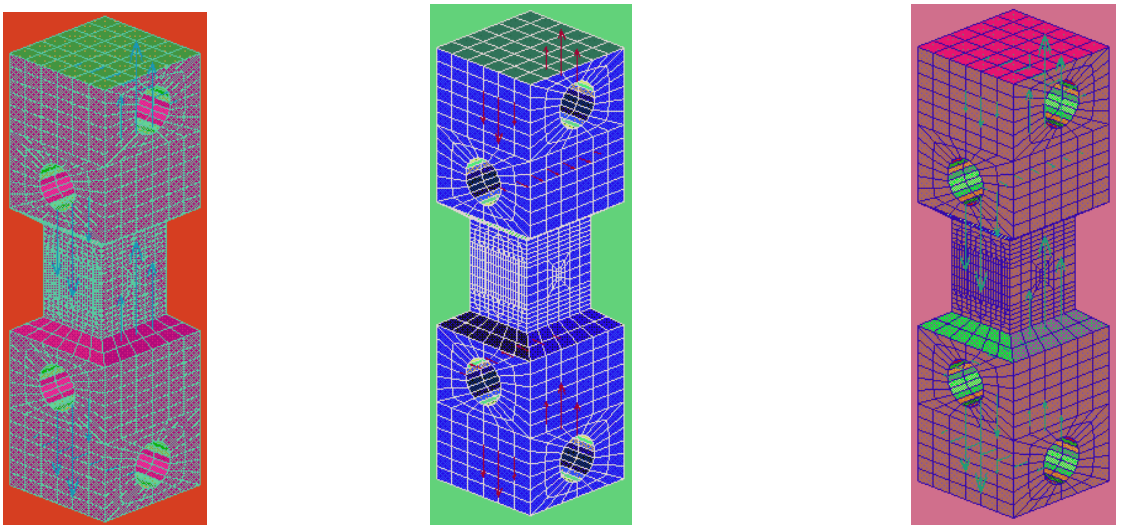


Fig. 1 Schematic 3D view and loading conditions of the AFM-specimen
a) The AFM-specimen mounted on the fixture b) Bend loads
c) Torsion loads d) The center part of the AFM-specimen

The geometrical parameters of the AFM-specimen, in Fig. 1 are as follows: width w =27mm, height h =20mm, thickness t =24.3mm, crack length a =0.5 w (straight crack front), H_1 =32.5mm, and H_2 =57.5mm. The material parameters are chosen as follows: Young's modulus $E = 2.1 \times 10^5$ N/mm^2 and Poisson's ratio ν=0.3. The specimen is subject to a static loading of F =6561N. The straight crack front is located along the z-axis at the center of the AFM-specimen. In this work, the coordinate origin is positioned at the middle point of the crack front (Fig. 1 d).



a) Bend loads b) Torsion loads c) Mixed bend and torsion loads

Fig. 2 Loads on the AFM-model

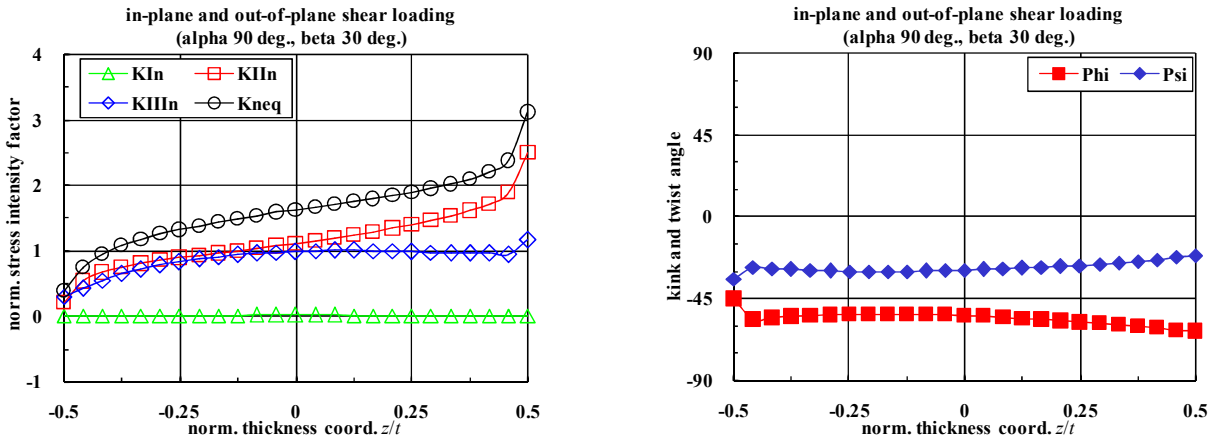
The mesh and the loading conditions of the specimen are shown in Fig. 2. Due to geometrical symmetry of the AFM-specimen with respect to the *x*-*z* plane, only a half of the specimen ($y \geqslant 0$) is modeled with a regular 8-node solid element mesh initially, by using commercial software HyperMesh as a pre-processor. Then, by reflection command, the whole mesh is established. Fig. 2 also shows the mesh in and behind the crack that a spider-web-like mesh is around the crack front. It might be expected that a prerequisite for good MVCCI values is a mesh with equal size crack tip elements with element boundaries perpendicular to the crack front. Thus, smaller elements, with constant edge sizes of 0.1 mm, are distributed along the crack front, while elements with larger edge sizes are used further away from the crack front.

The output of HyperMesh program is an input mesh used for further analysis with ANSYS program as a generic FE-solver. The bend loading consists of in-plane shear forces Q on the outside two holes and compensation moments M_Q on the inside holes (see Fig. 1 b and Fig. 2 a). The torsion loading includes out-of-plane shear forces T on the inside holes and compensation moments M_T on the outside holes (see Fig. 1 c and Fig. 2 b). When bend and torsion loads are combined, the mixed mode is generated (see Fig. 2 c). Changing the fixed angles of the specimens, namely the loading combination ratios of bend and torsion, the fractures under various modes can be obtained.

Computational Fracture Analysis Results and Discussion

For space limitation, the specimens with loading angles of α=90° plus β= 30°, and α=90° plus β= 60° are taken as examples.

For α=90° plus β=30°, by the MVCCI method, the normalized SIF K_{In}, K_{IIn}, and K_{IIIn} results are plotted in Fig. 3 a. Besides, according to the σ_1'-criterion, the normalized equivalent SIF K_{neq} values are depicted in Fig. 3 a, and the crack angles φ_0 and ψ_0 are given in Fig. 3 b.

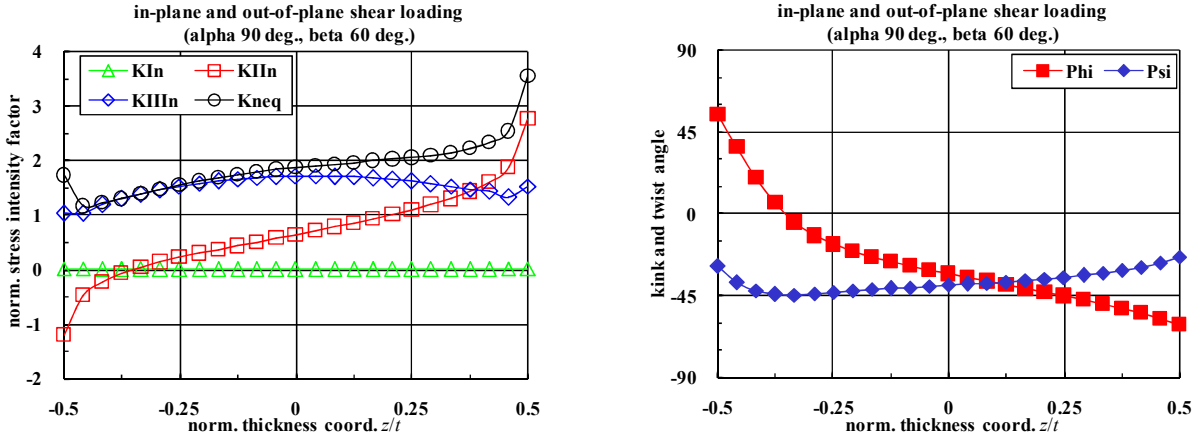


a) Normalized SIFs b) Crack angles

Fig. 3 Normalized SIFs and crack angles of the AFM-specimen for α=90° plus β=30°

From Fig. 3 a, it is obvious that the K_{IIn} and K_{IIIn} curves are varied and irregular through the thickness direction of the AFM-specimen. Due to the combination of the bend and torsion loads, the mode II and the mode III loading conditions influence each other locally along the crack front, especially in the vicinity of two corners. In detail, with respect to the effect of Poisson's ratio, the applied bend loads induce the mode III loading condition along the crack front and more pronouncedly when approach to the free surfaces. In the meantime, owing to the global deformation behavior by the applied torsion loads, the mode II loading condition is induced along the crack front and more intensively toward the two corners. As the induced mode II has a negative effect with the applied bend loads for z/t <0, and the induced one is positive to the applied one for $z/t \geq 0$, the K_{IIn}-values are weaken for z/t <0 while intensified for $z/t \geq 0$. So are the K_{IIIn}-values.

In terms of the σ_1'-criterion, the position corresponding to the maximum equivalent SIF is regarded as the fracture initiation point. In this case, from Fig. 3 a, we can conclude that the crack will initially break at one side of the AFM-specimen. From Fig. 3 b, the crack deflection angles are negative and approximately constant along the crack front. Thus, it can be predicted that the crack front will fracture to a series of narrow facets with approximate deflection angles.



a) Normalized SIFs b) Crack angles

Fig. 4 Normalized SIFs and crack angles of the AFM-specimen for α=90° plus β=60°

The similar analysis is carried out for α=90° plus β=60°, and the results of normalized SIFs and crack angles are given in Fig. 4 a and b respectively. The differences between Fig. 4 a and Fig. 3 a are remarkable that the values of K_{IIn} at -0.5<z/t<-0.3 are negative for α=90° plus β=60° while positive for α=90° plus β=30°, since the proportion of the mode II and mode III for α=90° plus β=60° is distinct with that for α=90° plus β=30°. Correspondingly, the distributions of the crack kink angle φ_0 and twist angle ψ_0 are pronouncedly different with that for α=90° plus β=60° (Fig. 3 b). In Fig. 4 b, the kink angle φ_0 are higher at one side ($z/t \to -0.5$) and then decreases towards to the other side ($z/t \to +0.5$) with a further drop as the surface is approached. The twist angle ψ_0 varies along the crack front with negative values. Thus, it can be predicted that the crack will initially fracture at one corner ($z/t \to +0.5$), and grow in a non-coplanar manner and kink in opposite orientation at the two sides. Besides, the crack will curve more intensively on surfaces than the middle along the crack front.

The presented investigation also shows that the maximum principal stress σ_1'-criterion in conjunction with the MVCCI-method is feasible and effective for further computational analysis under complex loading conditions.

Acknowledgement

This paper is financially supported by the High-level Creative Talents and International Exchange Project Foundation of Harbin Engineering University.

References

[1] Q. Liu, J. Qiu, S. Ge, W. Guo: ICIC 2009, vol. 4, art. no. 5169202 (2009), p. 362-365

[2] G. Dhondt, A. Chergui, F.-G, Buchholz: Engineering Fracture Mechanics, vol. 68, no. 4 (2001), p. 383-401

[3] M. Schöllmann, H.A. Richard, G. Kullmer, M. Fulland: International Journal of Fracture, vol. 117, no. 2 (2002), p. 129-141

[4] H. A. Richard, M. Kuna: Engineering fracture Mechanics, vol. 35, no. 6 (1990), p. 949-960

© (2012) Trans Tech Publications, Switzerland
doi:10.4028/www.scientific.net/KEM.488-489.270

Numerical Simulation of Series Experiments of Concrete Fracture

Deng Aimin [1,a], Wang Xiangdong [1,b], Xu Daoyuan [1,c]

[1] Department of Engineering Mechanics, Hohai University, Nanjing 210098, China
[a]d-a-m@sohu.com,[b]wwang90@sohu.com, [c]wwwkkty2002@yahoo.com.cn

Key words: numerical simulation; concrete fracture; ANSYS; experiment; non-linear

Abstract: With progress of the computer technology and numerical simulation method, the numerical simulation of the fracture process of concrete materials has become possible. In this paper, the numerical simulation models of the two types of samples were carried out with the SOLID65 concrete element based on the ANSYS software platform. According to the results, the non-linear characteristic of the concrete material exhibited in the loading process is reflected by the phenomenon that the slope of the later stage shows some reduction in the simulated load - loading point displacement curve. That is to say, the behavior of the appearance and development of cracks can be simulated with SOLID65 concrete element in ANSYS.

Introduction

Numerical simulation has many merits under the physical conditions that the structure to be numerically simulated and the real structure are sufficiently similar, for example, time-saving, labor-saving, no equipment restrictions, repeatability, feasibility for simulation of complex loading paths that the load equipment is difficult to achieve, and stability of the results, i.e. the results are affected by the various factors in the tests [1,2]. The emergence and development of micro-cracks can be reflected in numerical simulation, and the influence of the fracture process zone can also be reflected in the load-displacement curve obtained by numerical simulation. So, the critical effective crack length corresponding to the peak load can be determined by the load-displacement curve, and the effective fracture toughness considering the impact of fracture process zone can be calculated by inserting the peak load and the critical effective crack length into the formula derived from the LEFM, and the *K* criterion considering the impact of fracture process zone can be established [3,4].

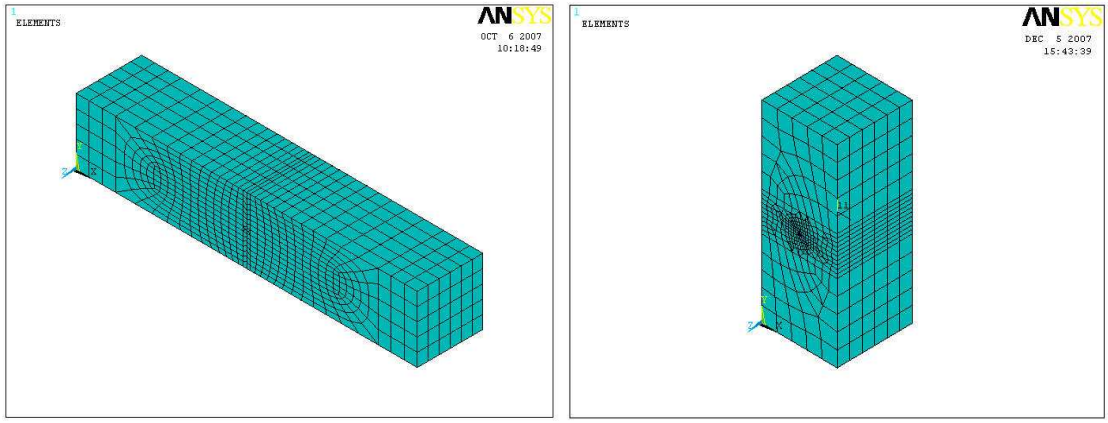
Taking into account the nonlinear characters of concrete materials, the SOLID65 element is introduced in ANSYS. The element is applicable to the simulation of the process of fracture damage to the concrete structure. The material of the element is linear when the stress at these integral points has not reached the concrete compressive strength or tensile strength. The cracks or crushing zone will appear when the main stress exceeds the tensile strength or compressive strength of concrete material at one of these integral points. The cracks zone or crushing zone is formed in the position perpendicular to the direction of principal stress at the corresponding point with the re-distribution of stress in a local part of the element. At this time, the material of the element is non-linear, and the iterative solver is required [5].

Macro-reflection of the emergence and development of micro-cracks in numerical simulation is introduced into the above-mentioned methods, and the impact of fracture process zone can be reflected in the load-displacement curve obtained in the numerical simulation. So, the critical effective crack length considering the impact of fracture process zone can be calculated based on the curve, and by inserting the peak load and the critical effective crack length into a formula developed from LEFM, the effective fracture toughness considering the impact of fracture process zone is calculated. In the end, the *K* criterion considering the impact of fracture process zone is established.

Numerical simulation results of the fracture process of different types of cracks

The numerical simulation is carried out with the SOLID65 concrete element based on the ANSYS software platform. The sizes of the numerical model from the literature [6] are adopted, and the initial crack length a_0 of all samples is 50mm. The solid model feature is generated from the bottom up. That is, key-points are created, then lines are defined by these key-points, after that areas are defined by the lines, and volumes are defined by the areas. The PLANE42 is defined first when the areas are meshed, and then the SOLID65 concrete element is defined when the solid model is stretched along the z direction.

The two types of samples models of the numerical simulation are presented in Fig.1. Those are the beam specimen model and the column specimen model. The load-displacement curves before the peak loads are obtained in the numerical simulation by simulating the load stage. The peak loads for simulation from the literature [6] are adopted, and further divided into 5-6 load steps, each load step being divided into several sub-steps automatically in the process. According to simulation results, the typical load versus loading point displacement curve is drawn, as shown in Fig.2.



(a) The beam specimen model **(b) The column specimen model**

Fig.1 The numerical simulation models

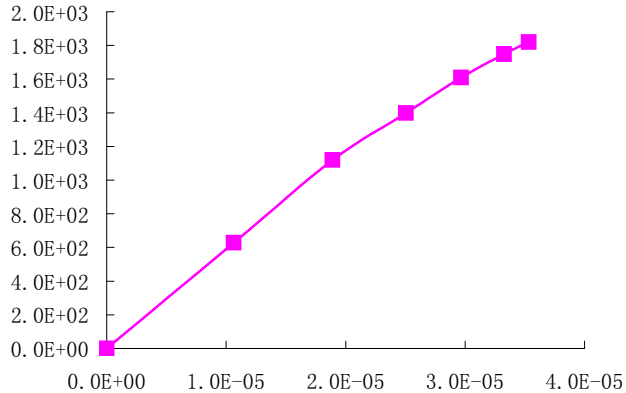


Fig.2 Typical load vs. loading point displacement

The non-linear characteristic of the concrete material exhibited in the loading process is reflected by the phenomenon that the slope of the later stage shows some reduction in the simulated load - loading point displacement curve. That is to say, the flexibility of the sample decreases gradually before unstable fracturing of the concrete specimen, and the initial crack in

the sample has a certain degree of propagation. So, the stress intensity factor calculated by the peak load and initial crack length is clearly inappropriate, and therefore, the critical effective crack length corresponding to the peak load needs to be determined.

Based on the linear asymptotic superposition assumption, the approaches of linear elastic fracture mechanics can be adapted to the description of the complete fracture process so that the nonlinear characteristic of crack propagation is reflected. And the non-linear fracture process of concrete material can be simplified to a series of linear fracture process superposition. For this purpose, a series of concrete specimens are made with the same geometry and are pre-cracked for the same dimensions for the growing of elastic cracks equivalent to their different lengths, then loads are applied to the specimens of the variety of fracture models until deformation becomes nonlinear. Hence, a series of load - loading point displacement curves will be straight lines. In this way, the relationship between loading point displacement and load is obtained for the process of crack propagation, and the relationship can be unified approximately as follows

$$b \cdot E \cdot \frac{\delta}{F} = \alpha + \beta \tan^2\left(\frac{\pi}{2}\frac{a}{h}\right) \tag{1}$$

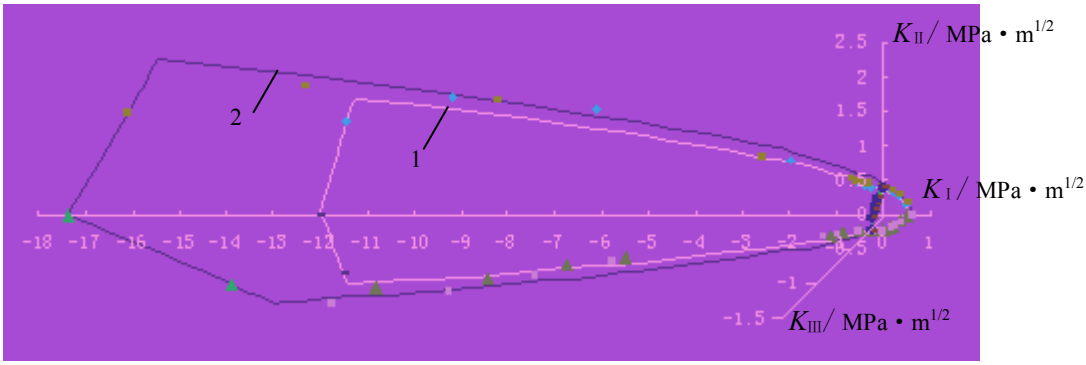
Where, b is the thickness of specimen, E is the elastic modulus of the material, δ is the loading point displacement, F is the load corresponding to δ, a is the crack length, h is the height of specimen, and α and β are the parameters of fracture modes and can be obtained by approximating the results of numerical calculation of the specimen for the variety of fracture models.

Based on the curves obtained from the results of numerical simulation, the critical effective crack lengths corresponding to the peak loads of the specimen in each group can be determined. The formula of stress intensity factor for the crack tip is approximated by the finite element method, and transformed into a dimensionless form. Then, the stress intensity factor K_{I}, K_{II}, and K_{III} for each group of samples are calculated by inserting the critical effective crack length and the corresponding peak load into the corresponding dimensionless form of the stress intensity factor formula.

Critical curve and fracture criterion of concrete fracture derived from numerical simulation

Through the analysis of results of numerical simulation, it is in appropriate to fit the Ⅰ-Ⅱ mixed mode, Ⅰ-Ⅲ mixed mode or Ⅰ-Ⅱ-Ⅲ mixed mode data with a curve or surface. According to the expression form literature [6], the critical curves for the Ⅰ-Ⅱ mixed mode, and Ⅰ-Ⅲ mixed mode fracture are divided into curve and line segments, and the curve segments are approximated with a parabola, the critical curve for the Ⅱ-Ⅲ mixed mode fracture is approximated with an elliptical type curve, and the critical surface for the Ⅰ-Ⅱ-Ⅲ mixed mode is divided into curve and plane segments, with the elliptical parabolic surface used to fit the curve segment.

Based on numerical simulation results, the critical curve of the complete series of concrete compound fracture criterion is shown in Fig.3. For comparison, the original critical curve without considering the influence of fracture process zone is also given in Fig.3 [6]. As can be seen from Fig.3, the critical curve based on the present results of numerical simulation is outside the original critical curves. It shows that, because of taking into account the nonlinear properties of concrete, the results of numerical simulation reflect the impact fracture process zone, and the results are safe compare to the results in literature [6].



1. Original critical curve 2. Critical curve from numerical simulation

Figure.3 Critical curve and critical surface of concrete fracture

Conclusions

The critical effective crack lengths of specimens of each single model and the mixed model fracture of concrete corresponding to the peak load are calculated based on the curves obtained from the numerical simulation, and the stress intensity factor of unstable fracture is calculated with the peak load and the corresponding critical effective crack lengths. Finally, according to the results, the complete series K criterion of concrete fracture considering the influence of fracture process zone is established. In the numerical simulation, the material of concrete is regarded as homogeneous, and William-Warnke five-parameter failure criterion is used in ANSYS program, so, there is some difference between the results of numerical simulation and the measured results of fracture test, but the regularities of the critical curves are the same. In the absence of actual test data or lack of laboratory equipment, numerical simulation is still an effective estimation method, and the results can be adopted for engineering projects.

Acknowledgements

This work is supported by the National Nature Science Foundation of China(Nos.10972072 and 50878077)

References

[1] Peng Yijiang, Li Baokun:Numerical Simulation of Meso-level Mechanical Properties of Roller Compacted Concrete[J]. Journal of Hydraulic Engineering, Vol.11 (6) ,2001,pp.19-22.

[2] Zhu Wanchun, Zhao Qinlin:Mechanical Model and Numerical Simulation of Fracture Process of Concrete [J]. Advances in Mechanics, Vol.32 (4) ,2002, pp.579-598.

[3] Xu Shilang: Determination of Double-K Criterion for Crack Propagation in Quasi-Brittle Fracture,Part Ⅱ:Analytical Evaluating and Practical Measuring Methods for Three-Point Bending Notched Beams[J].International Journal of fracture, Vol.98, 1999,pp.151-177.

[4] Wang Guoqiang: Practical Numerical Simulation of Engineering Technology and its Application in ANSYS[M]. Xi'an: Northwest Industry University Press., China,2000,pp.35.

[5] Zhang Yaoting, Qiu Jisheng: Application of ANSYS in Nonlinear Analysis of Prestressed Reinforced Concrete Structure[J]. Journal of Huazhong University of Science and Technology(Urban Science Edition), Vol.20 (4) ,2003, pp.20-23.

[6] Xu Daoyuan, Zhu Weixuan: Research on Concrete Damage-Compound Fracture Failure Mechanism and Evaluation Standards[M], Nanjing: Hohai University, 1995,pp.15.

© (2012) Trans Tech Publications, Switzerland
doi:10.4028/www.scientific.net/KEM.488-489.274

Influence of the Type of Silica Fume on the Rheological and Mechanical Properties of Ultra-High Performance Concrete

Kyung-Taek Koh[1, a], Jung-Jun Park[1,b], Su-Tae Kang[1,c] and Gum-Sung Ryu[1,d]

[1]Structural Engineering & Bridges Research Division, Korea Institute of Construction Technology, Goyang, 411-712, Korea

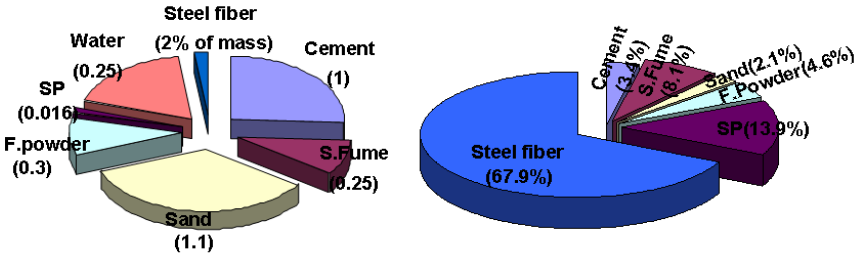
[a]ktgo@kict.re.kr, [b]jjpark@kict.re.kr, [c]alphard@kict.re.kr, [d]ryu0505@kict.re.kr

Keywords: Silica fume, UHPC, Viscosity, Flowability, Compressive strength.

Abstract. Ultra-high performance concrete (UHPC) is a new generation of concrete developed through microstructure enhancement techniques for cementitious materials. UHPC exhibits extremely high compressive and flexural strengths exceeding 180 and 30 MPa, respectively, and remarkable durability compared to normal concretes. The fabrication of UHPC requires very low W/B ratio reaching merely 0.2, the use of large quantities of fine binder and superplasticizer without coarse aggregates, and the incorporation of steel micro-fibers. This study investigates the effect of the type of silica fume on the rheological and mechanical properties of UHPC. The adopted silica fume presents various contents of SiO_2 and surface areas. From the experimental results, UHPC using silica fume with 94% of SiO_2 3% of ZrO_2, and surface area of 80,000 g/cm^3 shows better flowability than UHPC using silica fume with 98% of SiO_2 and surface area of 200,000 g/cm^3 by lowering the viscosity of the cementitious composites without decreasing the compressive strength. Therefore, the fabrication cost of UHPC can be reduced by smaller dosage of superplasticizer when using silica fume with Zr content .

Introduction

Ultra-high performance concrete (UHPC) is featured by a compressive strength larger than 180 MPa and an elastic modulus ranging between 45 and 55 GPa. Its flexural strength exceeds 30 MPa through the addition of steel fiber making large improvement of its tensile behavior and toughness [1,2]. Moreover, the densification of the structure of the cementitious composite leads to remarkable improvement of its material durability compared to conventional concretes [3]. The performances of UHPC are achieved through large amounts of steel fibers, silica fume and superplasticizer, as well as a very small water-to-binder ratio (W/B) below 0.2. Since the fabrication of UHPC requires large quantities of expensive materials, its fabrication cost is known to be significantly higher than that of ordinary concrete. Fig. 1 presents the mix proportions of UHPC developed by the authors[4] and the economic efficiency analysis results per material. It can be seen that the materials which have the largest contribution to the fabrication cost are successively steel fiber, superplasticizer, and silica fume. The superplasticizer shows the largest demand for the fabrication of the cementitious composite.



(a) Mix proportions (b) Economic efficiency

Fig. 1 Mix proportions and economic efficiency of UHPC

Silica fume is indispensable in UHPC[5]. The fineness of silica fume being approximately 200,000 g/cm^3 is extremely smaller than that of the cement particles, which enables it to play the role of filler filling the voids between the cement particles and to increase the strength through the generation of hydrates according to the hydration and pozzolanic reaction[6,7]. The use of microscopic powders like silica fume also increases significantly the viscosity during the mixing of UHPC. In order to secure a high flowability with flow beyond 200 mm, UHPC requires the introduction of large quantities of superplasticizer, which in turn induces the problem of increasing the fabrication cost. Accordingly, this study investigates the effects of the type of silica fume on the viscosity, the rheological characteristics of the flowability and the mechanical properties of the compressive strength to reduce the quantity of superplasticizer involved in the fabrication of UHPC.

Mix Proportion and Test Methods

Table 1 lists the properties of the binder used in this study. SiO_2 is set as the main component of silica fume including Zr content. Apart from these components, ZrO_2 is present in a proportion of about 2% and, MgO and SO_3 are practically absent. In addition, the specific surface area is 80,000 g/cm^3, which is smaller than silica fume. Table 2 arranges the mix proportion of UHPC analyzed in this study. Classification is done into Series I, replacing silica fume, and Series II, substituting the filler.

Table 1. Properties of cementitious materials

Items / Types	Surface area (cm^2/g)	Density (g/cm^3)	L.O.I	Chemical composition (%)						
				SiO_2	Al_2O_3	Fe_2O_3	CaO	MgO	SO_3	ZrO_2
Cement	3,413	3.15	1.40	21.0	6.4	3.1	61.3	3.0	2.3	-
Silica fume	200,000	2.10	1.50	98.0	0.25	0.12	0.38	0.2	0.3	-
Zr Silica fume	80,000	2.50	0.1	94.0	-	-	-	0	0	3.0

Table 2. Mix proportion

Type	Reference mix
W/B	0.2
Cement	1
Silica Fume*	0.25
Sand	1.1
Filling Powder**	0.3
Superplasticizer	0.016
Steel fiber(Vf)	2%

*Series I: : Zr 0.00, 0.05, 0.10, 0.15, 0.20, 0.25
**Series II : Zr 0.0, 0.1, 0.2, 0.3



Fig. 2 Brookfield viscometer

The flowability is evaluated by means of flow test. The viscosity is assessed by obtaining the plastic viscosity using the Brookfield viscometer shown in Fig. 2. The compressive strength of UHPC is measured on ϕ100×200 mm cylinders that were subjected to 2 days of wet curing in molds after the fabrication, followed by 48 hours of high temperature steam curing at 90°C and atmospheric curing at 20°C until 7 days.

Experimental Results and Discussion

Fig. 3 shows the flowability of UHPC with respect to the adopted quantity of Zr silica fume. In the case where Zr silica fume is used as replacement material of silica fume, the fluidity increases with large quantities of Zr silica fume with a maximum flow of about 260 mm for a Zr content of 20%. When Zr silica fume is used as substitute the filler, a maximum flow of about 220 mm is observed for

a Zr content of 10% but the fluidity tends on the contrary to diminish for larger quantities. Accordingly, it appears that using Zr silica fume as an admixture together with silica fume improves the fluidity rather than using it as filler.

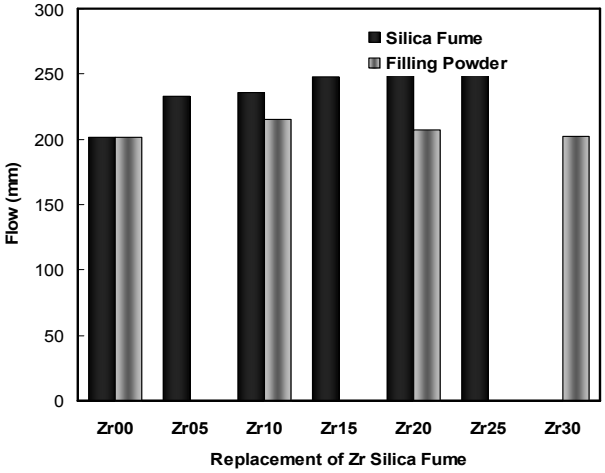


Fig. 3 Fluidity wrt replacement ratio of Zr silica fume

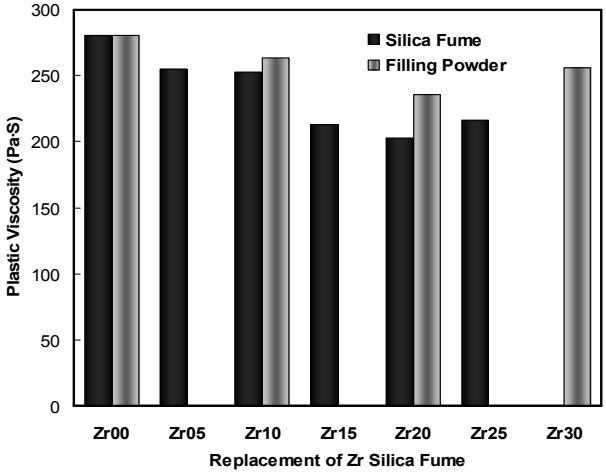


Fig. 4 Viscosity wrt replacement ratio of Zr silica fume

Fig. 4 presents the measured plastic viscosity of UHPC with respect to the quantity of Zr silica fume. When Zr silica fume is used to replace silica fume, the viscosity of UHPC decreases with large quantities of Zr. The viscosity decreases until a proportion of 15% of Zr but this decrease slows down for larger proportions, which indicates the existence of an optimal replacement rate of silica fume. The experimental results reveal that this optimal replacement ratio is 15%. When Zr is adopted to replace the filler, the plastic viscosity reduces until a proportion of 20% whereas increases for larger rates. However, the decrease if the plastic viscosity brought by the substitution of filler appears to be smaller than that caused by the replacement of silica fume. Therefore, it seems that there is some limitation in reducing the viscosity of UHPC by replacing the filler.

Fig. 5 plots the relationship between the fluidity and plastic viscosity of UHPC. It can be observed that a close relation exists between these two properties. Concretely, the plastic viscosity decreases as much as the increase of the fluidity. Especially, when silica fume is used as replacement material, this effect appears to be larger. Following, when Zr silica fume is adopted to replace silica fume, the reduction of the viscosity and the improvement of the fluidity of UHPC can be explained by the difference in the fineness of those materials.

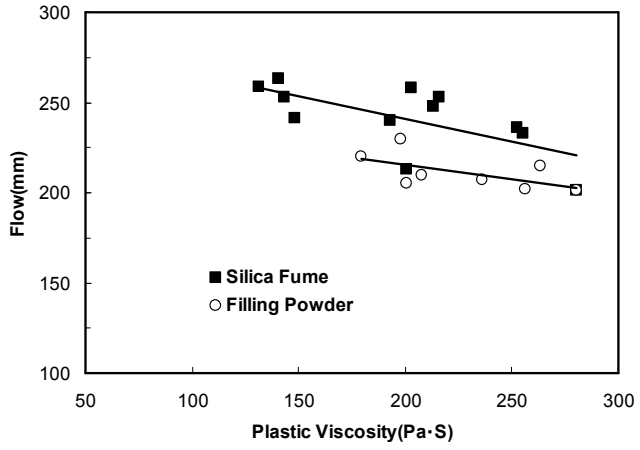


Fig. 5 Relation between the fluidity and viscosity of UHPC

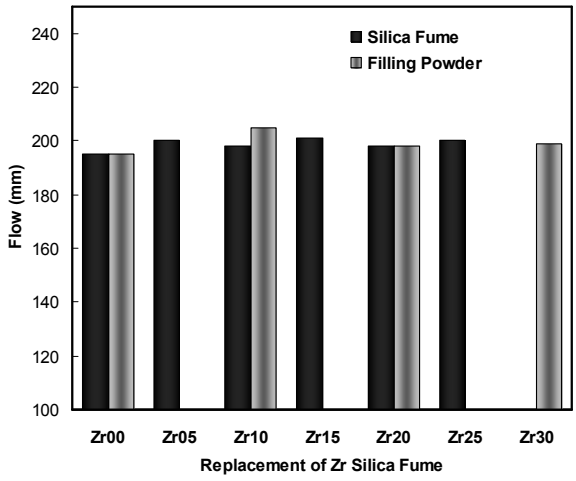


Fig. 6 Compressive strength of UHPC

Fig. 6 shows the resulting compressive strength of UHPC according to the adopted quantities of Zr silica fume. Regardless of the replacement method and replacement ratio of Zr silica fume, the compressive strength appears to be equivalent or superior to that of the previous UHPC using silica fume and filler. Since Zr silica fume also exhibits smaller particle size than that of cement similarly to silica fume, Zr silica fume plays the role of filler and the resulting compressive strength can be attributed to the occurrence of the pozzolanic reaction with $Ca(OH)_2$ produced by the hydration of cement with more than 90% content of SiO_2. Moreover, the quartzite filler is known not only to play the role of filler filling the voids between the cement particles and aggregates but also to improve the strength by strengthening the bond at the interface between the aggregates and cement. Similarly to the quartzite filler, Zr silica fume appears to play the role of filler as well as improving the bond performance at the interface without loss of the strength compared to the quartzite filler.

Conclusions

As a result of the replacement of silica fume and quartzite filler in previous UHPC by Zr silica fume, the viscosity of the cementitious composite appeared to reduce with improvement of the fluidity by about 26% without loss of the strength when replacing silica fume. In such case, the economic efficiency can be secured since the fabrication cost of UHPC is decreased by a comparable reduction of the required quantity of superplasticizer. In addition, significant effect on the mixing time being also realized, the adoption of Zr silica fume is promising to contribute to the practicability of UHPC in the future.

Acknowledgements

The work presented in this paper was founded Korea Institute of Construction Technology (KICT) via the Project ‘Hybrid Cable-Stayed Bridge 2020.

References

[1] P. Richard and M. Cheyrezy, in: *Composition of Reactive Powder Concrete*, Cement and Concrete Research, Vol.25, No.7, 1995, pp.1501-1511.

[2] K.T. Koh et al., in: *A study on selection of the mix proportions of ultra-high strength steel fiber reinforced cementitious composites*, Proceedings of JSCE, 2004.

[3] O. Bonneau et al., in*: Mechanical and Durability of Two Industrial Reactive Powder Concretes*, ACI Materials Journal, Vol.94, No.4, 1997, pp.286-290.

[4] K.T. Koh, et al., in: *Development of the Advanced Technology of Toughness in Ultra High Performance Concrete for hybrid Cable Stayed Bridge*, KICT 2009-077, 2009.

[5] A.H. Toutanji and Z. Bayasi, in: *Effect of curing procedures on properties of silica fume concrete*, Cement and Concrete Researches, Vol.33, 1999, pp.497-501.

[6] C. Artelt and E. Garica, in: *Impact of superplasticizer concentration and of ultra-fiber particles on the rheological behaviour of dense mortar suspensions*, Cement and Concrete Research, Vol.38, 2008. 633-642.

[7] A. Zenati et al., in: *Influence of cementitious additions on rheological and mechanical properties of reactive powder concretes*, Physics Procedia, Vol.2, 2009, pp.1255-1261.

© (2012) Trans Tech Publications, Switzerland
doi:10.4028/www.scientific.net/KEM.488-489.278

Strength Enhancement of Bottom Ash-based Polymer Concretes

J.M.Zhao[1], Z.X.Yang[1], K.H.Hwang[1], J.K.Lee[2], M.C.Kim[3], and G.D.Seo[4]

[1]Eng. Res. Inst., *i*-Cube Center, Gyeongsang Nat'l Univ., 660-701, Jinju, S.Korea

[2]Chosun Univ., [3]RDK Co., Ltd., [4]Jungwon Co., Ltd., S.Korea

Email: khhwang@gnu.ac.kr

Key words: Bottom ash, compressive strength, CO_2 emission, green concrete

Abstract:

To replace bottom ash for natural sand completely, the mix proportions of bottom ash in concrete was adjusted according to tab density and replacement ratio of polymeric resin/Potland cement(PC) were established. And then testing for slump, setting time, and compressive strength was conducted. According to test results, the compressive strength of concrete using the bottom ash was lower than that of concrete using natural sand (BA0 concrete). But by adjusting the amount of bottom ash in concrete according tab density so that the fine aggregate proportions change 44% to 38%, the compressive strength of concrete using the bottom ash could even be higher than BA0 concrete. And as the polymeric resin content of bottom ash concrete increased, strength would be increased drastically, but proper dispersant should be cooperated with polymeric resin cement with fine bottom ash powders.

1. Introduction

Nowadays, more researches are focused on environment-friendly construction materials. To reduce CO_2 emission, bottom ash concrete is expected to replace the natural aggregate based cement concrete.[1] Recently the coal-ash production has been increased by increase of consumption of electric power. So it is important to secure a reclaimed land and treatment utility for coal-ash.[2]

Coal-ash is classified into fly ash, cinder ash, and bottom ash according to produced positions. Among these ashes, bottom ash are produced 10~15% and mostly land filled so that recycling would be important year by year. Moreover, recent natural aggregate limit of supply of sand and sea (maritime) depending on regulation of collection to replace the concrete aggregate is used as a substitute for sand, sea, sand and crushed the three can complement the loss of the use is significant. [3] The physical and chemical properties of bottom ash itself as a replacement for fine aggregate in concrete in order to get enough of this review should consist of is considered.

So in this experiment to compare and analyze the properties of concrete according to replacement of bottom ash to natural sand, the mix proportions of concrete according to W/C(40,50,60%) and r eplacement ratio of polymeric resin to Portland cement(0,10,20,35,50%) were established, and then tested for slump and compressive strength.

2. Experimental procedures

The ordinary Portland cement, water soluble poly-acrylic resin(PAMM), styrene butadiene rubber(SBR) latex, coarse crushed gravel near the mountain, river sand, and metakaolin were used as raw materials. Mixing of concrete was done in mixer with capacity of 100L. Aggregate, cement, and bottom ash were first dry mixed for 3min then wet mixed for another 5min with water addition. Polymeric resin was mixed with water at different concentration before wet mixing. After mixing, the concrete mortar was poured into moulds for compressive strength test. The specimens were cured in air for 24hr and in water for 7-days and 28-days. Then the compressive strength was measured respectively. The amount of polymeric resin concentration, bottom ash, aggregate type and sand type were varied for application investigation. 5 types of resin are taken into test marked as I, II (PAMM), III, IV (SBR), V (PAMM & SBR copolymer).

Fly ash was also added to enhance the strength of resin bonded bottom ash concrete at amount of 0 to 10wt.%. And the bottom ash/aggregate ratio, polymeric resin/Portland cement were also varied to get a optimal compressive strength value for practical applications. The particle size distribution of bottom ash and natural sand were measure by sieving test. The microstructure of each specimen was investigated by a scanning electron microscope.

3. Results and discussion

Particle size distribution curve of the bottom ash was shown in Fig. 1 with the upper and lower limit of particle size distribution of natural sand. The amount of fine particles in bottom ash that are less than 0.3mm is so large that the strength of bottom ash concrete reduced drastically mainly due to large amount of fine particles than sand as shown in Fig.2a).

Firstly, the bottom ash containing coarse and fine particles are used as raw material, and 5 types of resin are added as bonder. Highest strength was reached when adding 30% resin IV as shown in Fig.2b). Resin I and II showed little effect for strength enhancement when the amount is below 10%. No more strength increase is observed when keeping increasing the resin amount. The addition of resin III causes strength loss when the amount is 10% above. The result from resin V is preferable because it brings a higher strength at lower concentration of polymer solution.

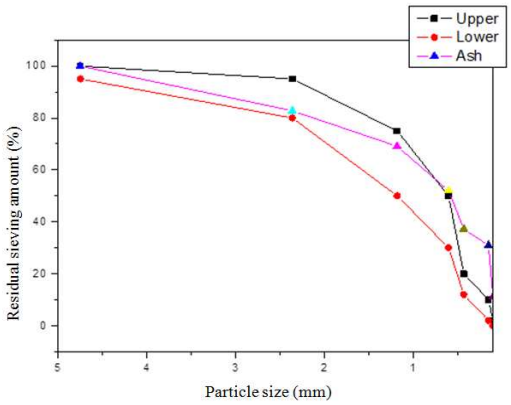
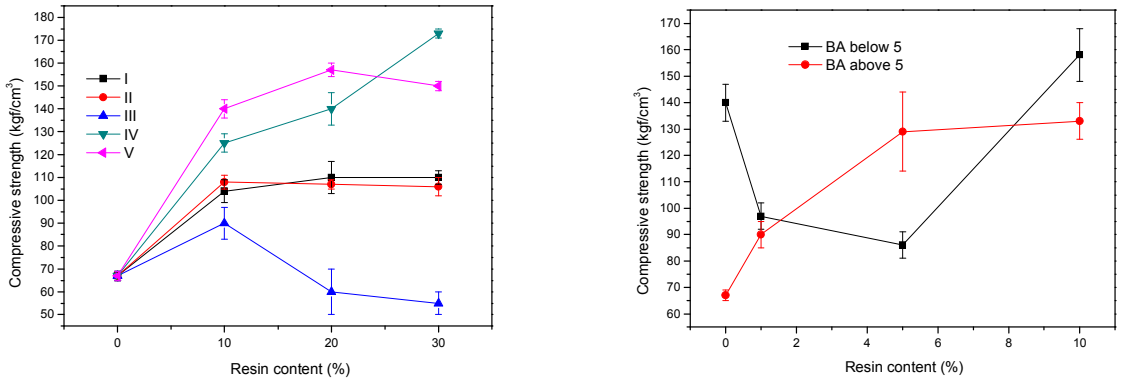


Fig.1. The particle size distribution curves of used bottom ash.



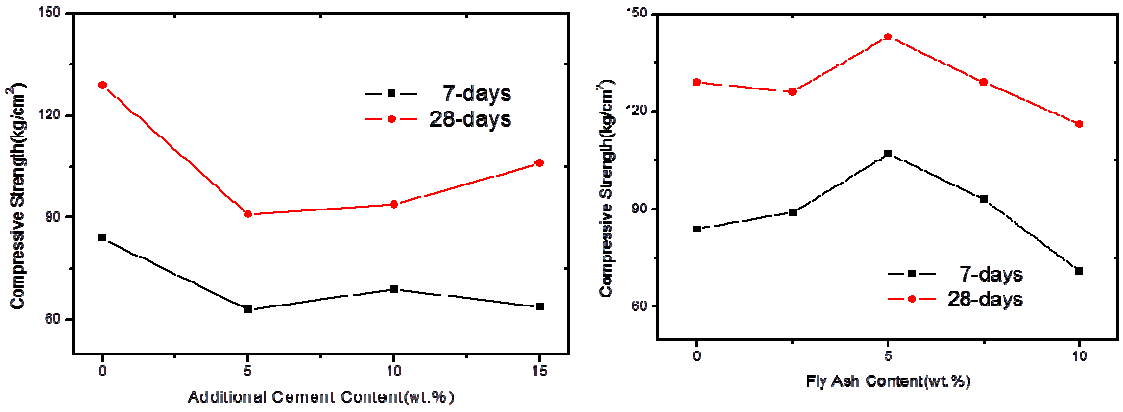
a) b)

Fig.2. The compressive strength of bottom ash used concrete and the effect of fine particles in Bottom ash.

According to the first test, resin V is proved to be the proper admixture for bottom ash based concrete. So resin V is chosen as the main additive for other experiment afterwards. Fig.2 b) indicates the effect of resin bonder on varied grain size of bottom ash. Larger grain is found to be much more appropriate for getting a higher strength for the lower consumption of water and smaller specific area for bonding.

As an ordinary strength increasing method of the concrete, the amount of Portland cement would be increased. But as shown in Fig.3a), the strength also decreased as the amount of cement increases due to the high Water/Cement ratio. So the ratio of cement to bottom ash is varied with certain amount of bottom ash of 30% (total amount) and 30% (matrix part) of cement/bottom ash ratio was found to be the optimal value for the highest strength. In this case the strength increased for the cement amount increase and decreased for the high W/C ratio, which could be seen as Fig.3b).

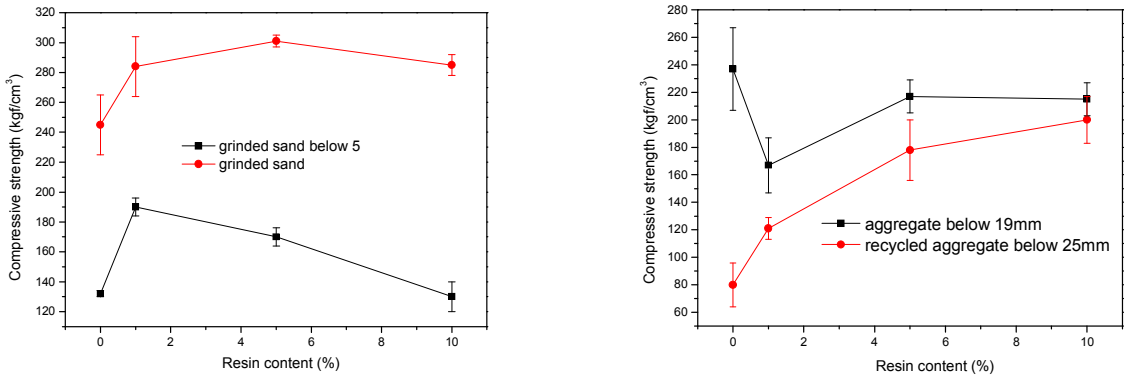
Highest strength was reached when adding 5% fly ash as shown in Fig.2b). The pozzolana and hydraulic activity of fly ash have mainly been pointed out as well as the possibility to use this addition as a concrete component.[4] The fly ash addition, in considered range of FA/C values, has no significant effect on specific gravity and water absorbability of concrete but the addition reduces the capillary suction of water. However, too much amount could cause the water consumption increase that reduce the strength.



a) b)

Fig.3. The compressive strength of bottom ash used concrete with the amount of Portland cement and fly ash.

Recycled aggregate and grinded sand are also taken into experiment for replace traditional natural aggregate and river sand. Larger grains lead to a higher strength and the effects of polymer solution modification are more obvious on both test, which are shown as Fig.4. Smaller grains both in matrix and aggregate parts would consume more water then cause a porous structure. Concrete fabricated by recycled aggregate with grain size below 25mm could reach a similar strength than that of natural aggregate below 19mm with 10% resin V modification.



a) b)

Fig.4. The compressive strength of resin modified concrete with different type of a) sand and b) aggregate

The microstructure comparison of bottom ash based concrete with polymer modification is shown in Fig.5. The introduction of fly ash smoothes the matrix structure for its self-cementing feature(Fig.5b). When finer fly ash particles partially replace Portland cement, the heterogeneities in microstructures of hydrated Portland cement paste are reduced greatly. Further, when the

pozzolanic reaction proceeds, there is a gradual decrease in both the size of capillary pores and crystalline hydration products, thus eliminating the weak link in the concrete microstructure. Thus the product is highly crack resistant and durable. The structure becomes stronger when polymer resin is introduced. The cured polymer bonded matrix and aggregate well by the enhancement of frameworks. (Fig.5c)).

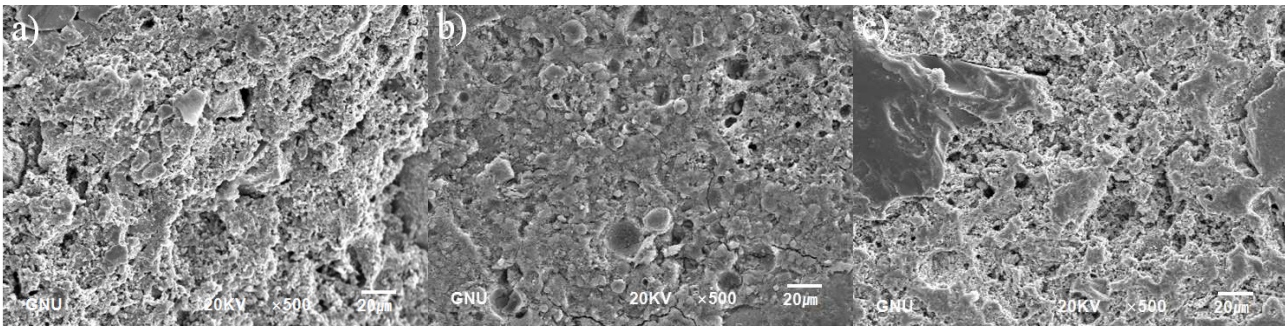


Fig.5 SEM microstructures of a) bottom ash only contained, b) with 5% fly ahs addition, and c) with 5% resin V modification

4. Conclusions

The replacement of bottom ash for natural sand and aggregate is researched to improve the engineering properties of concrete. The following results were reviewed.

1) The copolymer of PAMM and SBR latex performs a better modification effect on strength enhancement than that of 2 types simplex polymer on bottom ash based concrete.

2) The rate of addition of extra cement doesn't give contribution for strength enhancement for the higher W/C ratio. And 30% is found to be the optimal ratio for cement/bottom ash ratio.

3) Proper amount of fly ash addition is helpful for strength increasing, for its pozzolanic and hydraulic activity. Too much amount (>5%) would cause a reduction of strength because the fine particle of fly ash consumes water a lot.

4) For both recycled aggregate and sand, the distribution of grains is important and the effect of polymer resin modification is obvious with larger particles.

Acknowledgement

This work was supported by Korea Sanhak Foundation(2010).

References

[1] L. B. Andrade, J. C. Rocha and M. Cheriaf, "Aspects of Moisture Kinetics of Coal Bottom Ash in Concrete", Cement and Concrete Research, Volume 37, Issue 2, February 2007, Pages 231-241

[2] L. B. Andrade, J. C. Rocha and M. Cheriaf, "Evaluation of Concrete Incorporating Bottom Ash as a Natural Aggregates Replacement", Waste Management, Volume 27, Issue 9, 2007, Pages 1190-1199

[3] Apha Sathonsaowaphak, Prinya Chindaprasirt and Kedsarin Pimraksa, "Workability and Strength of Lignite Bottom Ash Geopolymer Mortar", Journal of Hazardous Materials, Volume 168, Issue 1, 30 August 2009, Pages 44-50

[4] Haldun Lurama and Mine Kaya, "Usage of Coal Combustion Bottom Ash in Concrete Mixture", Construction and Building Materials, Volume 22, Issue 9, September 2008, Pages 1922-1928

© (2012) Trans Tech Publications, Switzerland
doi:10.4028/www.scientific.net/KEM.488-489.282

Potential of Shape Memory Complex Materials SMC as Welfare Equipment Actuator

Teruko Aoki[1,a], Keigo Fukunaga[1,b], Akira Shimamoto[2,c]

[1]1666 maki, oita, Oita,870-0152, Japan

[32]1690 fusaiji, fukaya, Saitama,369-0293, Japan

[a]aokit04@oita-ct.ac.jp, [b]fukunaga@oita-ct.ac.jp, [c]shimamot@sit.ac.jp

Keywords: SMC, SMA, SMP, Shape Recovery, Actuator, Deflection coefficient

Abstract. Intelligent materials have been studied in various fields. In this study, Shape Memory Composite (SMC) is produced as one of those intelligent materials. SMC consists of Shape Memory Polymer (SMP) and Shape Memory Alloy (SMA). These two materials possess different characteristics in temperature changes. Therefore, we investigated the possibility of the SMC's actuator function as an intelligent material. The actuator function is achieved by applying a current to SMA fiber of SMC to grab and release objects. As a result of this investigation, meaningful data for actuator to design SMC is obtained.

Introduction

Shape memory materials such as Shape Memory Alloy (SMA), Shape Memory Polymer (SMP) and so on are attracting attention as an intelligent material. [1][2][3]

In this study, Shape Memory Composite (SMC) material consists of SMA and SMP is produced. The mechanical property of SMC is clarified experimentally by applying current to heat control to SMA, and the potential of welfare equipment actuator is examined.[4][5][6][7]

Experiment

Specimen. SMC is consists of SMP sheet and SMA fiber. SMP's glass transition temperature (T_g) is between 313K and 333K. SMA's phase transformation temperatures are as follows; A_s=309K, A_f=328K, M_s=269K, M_f=225K. SMC is manufactured using a mold shown in figure 1. The shaped SMC specimen measurement is shown in figure 2.

The number of SMA fibers to be sandwiched in SMC is found using low of mixture of composite materials shown in equations (1) and (2).

$$D_C = V_A D_A + V_P D_P \quad (1)$$

$$V_A + V_P = 1.0 \quad (2)$$

D_C and D_P in this case are the deflection coefficient of SMC and SMP found from three bent test, and they are equal to Young's modulus E of linear elastic body. V_A and V_P are volume fraction of SMA fiber and SMP consisting SMC. D_A, D_P differ substantially at high temperature side (over A_f) and low temperature side (under T_g) as shown in Table 1. The shape recovery force is expected to be determined by the product of the volume fraction (V) and deflection coefficient (D) of SMA fiber and SMP sheet in SMC. Thus each $(V \times D)$ ratio of SMA/SMP at high temperature side and SMP/SMA at low temperature side is calculated.

The result is shown in table 2.

In this study, the target is to develop the actuator which can utilize shape recovery force at both high and low temperature side. In Table 1, therefore, a smaller difference between high and low temperature side is desirable. Consequently, the pair of ten ϕ0.2mm fibers and four ϕ0.4mm fibers in Table 2 shows the smallest differences in $(V*D)$ ratio of high and low temperature. It is also

considered that to have more SMA fiber is better in order to transmit SMA fiber emitted heat to SMP effectively while applying current to heat. SMC used in this experiment, therefore, consists of ten ϕ0.2mm SMA fibers sandwiched in SMP.

Shape recovery of SMC. SMC specimen is assumed to grab and release an object as a welfare equipment actuator, thus shape memorized to the C-shape prior to the experiment. In order to shape memorize C-shape, SMC is put in boiled (373K) water to make it softer and set it into round fixture (inner diameter ϕ70mm) to fix the specimen. After that, kept the SMC again in the boiled water for ten minutes and cool it down immediately. The shape memory temperature of SMA fiber is about 473K therefore SMA fiber kept its linear shape and base material SMP is shape memorized to C-shape.

Current was applied using low electrical current power unit to the C-shaped SMA fiber sandwiched in between SMC and heat entire SMC. At the time, SMA fiber tries to shape recover in linear, C-shape SMC starts to open. Subsequently, power source is switched off, SMP tries to shape recover to C-shape. This mechanism is shown in figure 3 and the displacement and surface temperature is measured every ten seconds.

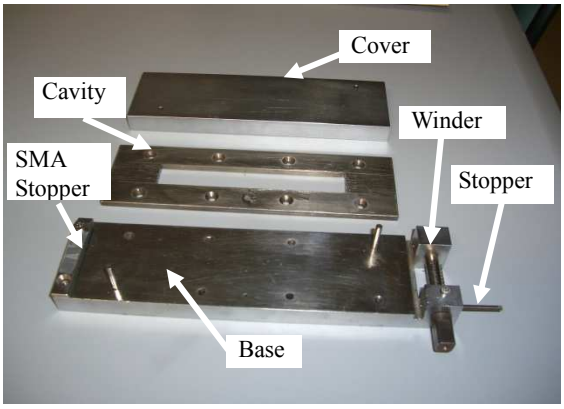


Figure 1 Molding tool

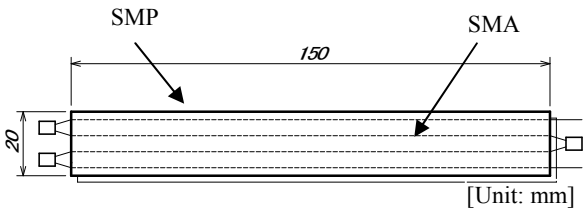


Figure 2 SMC specimen

Table 1 Deflection Factor D_A and D_P of SMA & SMP [MPa]

	Over A_f of SMA	Under T_g of SMP
SMA	50000	10000
SMP	30	1150

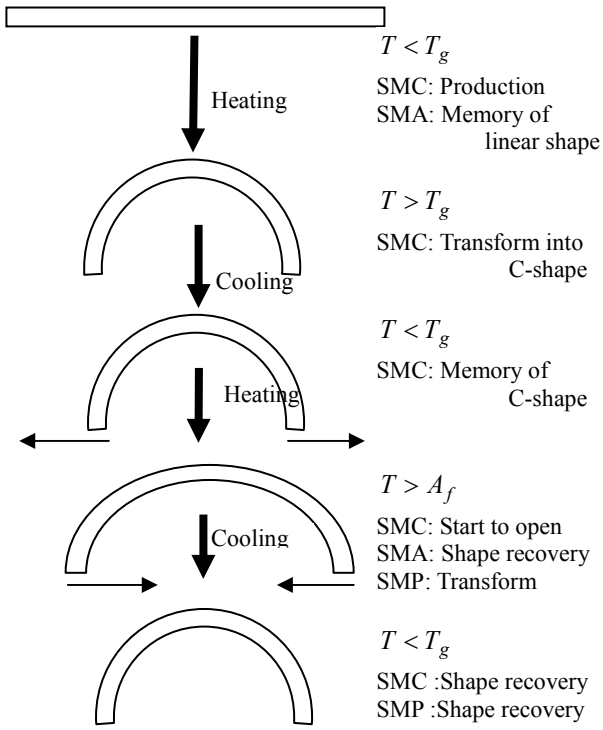


Figure 3 Process of SMC's shape memory recovery

Table 2 Ratio between SMA and SMP

	ϕ 0.4mm SMA			ϕ 0.2mm SMA	
Number of fibers	2	4	8	8	10
$(V_A D_A) / (V_P D_P)$ over A_f	9.1	18.2	36.4	9.1	11.0
$(V_P D_P) / (V_A D_A)$ under T_g	21.0	10.5	5.3	21.0	16.8

Results and considerations

Surface temperature. The changes of surface temperature of the specimen are shown in figure 4. As it is shown in figure 4, the surface temperature reached around T_g by electrical current value of 0.5A with current time of one minute. Additionally, the maximum surface temperature after thirty seconds of stopping electrical current is 333K in case of electrical current of 0.5A to heat for two minutes.

Consequently, it takes time to transmit the heat from SMA fiber to SMP surface (that is SMC surface) therefore the surface temperature keeps growing after stopping the electrical current. The surface temperature of the specimen becomes 303K about ten minutes after the test starts. It is seen that the fall of surface temperature after stopping the current draws a gentle curve compared to when applying the current to heat.

When applying current to heat for ten minutes by 0.25A, the surface temperature of the specimen grows gradually and saturated at 323K.

Shape recovery value. The calculation method of SMC shape recovery value is the same as the method of SMP shown in figure 5.

Figure 5 shows the relationship of current time and recovery value $(X_1\text{-}X_0)$. As an example, when current of 0.5A is applied for two minutes, the specimen starts opening after thirty seconds. Then stopping the current, the shape recovery value is maximized in thirty seconds. After that, the shape recovery value decreases gradually and the specimen becomes close to the initial shape of C-shape after 8 minutes. The same results are obtained by applying current for three minutes.

When a current of 0.25A is applied for ten minutes, the specimen starts opening in about two minutes. The shape recovery value increases gradually and becomes close to the saturated condition after seven minutes. It however did not return to the initial condition after stopping the current. It can be concluded that the memory of initial C-shape has disappeared due to overheat SMP by applying current SMA fiber.

The relationship between time and recovery value shown in figure 6 is nearly equal to the relationship between time and surface temperature shown in figure 4. Subsequently, it is clear that optional displacement can be obtained by electrically controlling the current applied to the SMC.

In order for the SMC to operate as an actuator, it is important to be able to control the surface temperature of SMC by applying current to SMA fiber. It starts to recover to the linear shape by the shape recovery effect of SMA fiber when applying current to hear SMA fiber higher than A_f. At the time, D_A gets bigger but D_P gets smaller and SMC starts opening. When the surface temperature reaches around T_g and stopping current to SMA fiber, SMC stops opening. Additionally, the shape memory effect of matrix that is SMP makes SMC returns to C-shape.

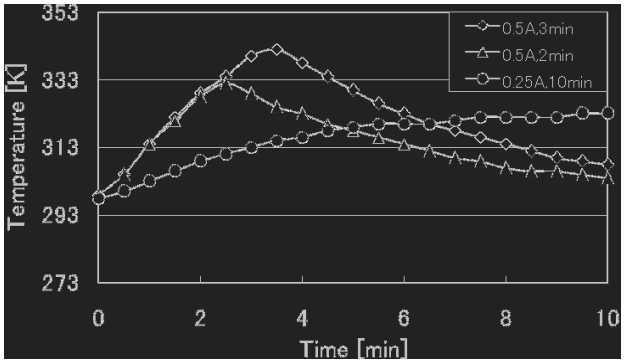


Figure 4 Relationship between time and temperature

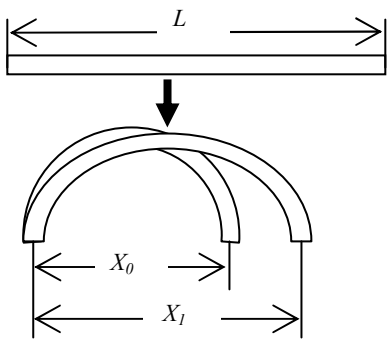


Figure 5 Shape recovery ratio dimension

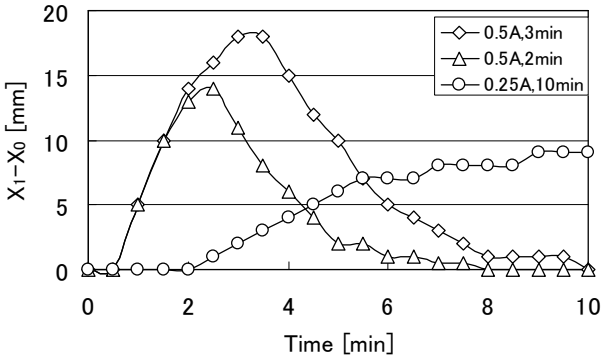


Figure 6 Relationship between time and $X_1 - X_0$

Conclusion

SMA fiber is sandwiched in between two sheets of SMP to produce SMC. In this study, the possibility of SMC as an assistive equipment actuator is investigated. As a result, the ability to be able to open and shut SMC by applying current to control SMA fiber was confirmed.

The results of this study are shown below.

(1) The surface temperature of SMC reaches around T_g in one minute of applying current with the current value of 0.5A.

(2) SMC specimen starts to open in thirty seconds of applying current with current value of 0.5A for two minutes. Then after stopping current, the recovery value is maximized in thirty seconds and eight minutes after that it becomes close to the initial shape of C-shape.

Consequently, it is clear that there are possibilities of welfare equipment actuator for grab an object by electrically controlling SMC.

Reference

[1] Iguchi, N., Shape Memory Materials and their Applications, *Agune Pub* (in Japanese). (1984), pp.16-35

[2] Ohkata, I., Part 1 Applications of Shape Memory Alloy in Medical Devices, *The Japan Society of Mechanical Engineers* (in Japanese),Vol.107, No.1028 (2004), pp26-29

[3] Ohkata, I., The Shape Memory Alloy Can Be Used in Many Ways, *The Chemical Society of Japan* (in Japanese), Vol.36, No.2 (1988), pp.30-31

[4] Endou, Y., Ogawa, A., Katou, A., Nakazato, Y., Sakada, T. and Takeda, Y., Development of Medical Rehabilitation Equipment for Fingers Using SMA Actuator ~First report: Trial Manufacture of The Mechanism of Equipment~ , *The Japan Society of Mechanical Engineers* (in Japanese), No.05-44 (2005), pp.31-32

[5] Miyazaki, A., Minemura, A., Yuasa, K. and Nakazato, Y., Development of Micro-SMA Actuator for Small Medical Rehabilitation Equipment, *The Japan Society of Mechanical Engineers* (in Japanese)

[6] Tobushi, H., Hayashi, S., Hoshio, K., and Makino, Y., Characteristics of Shape Memory Composites with SMA and SMP, *Proceedings of the 2005 Annua Meeting of the Japan Society of Mechanical Engineers* (in Japanese), No.05-1 (2005), pp.475-476

[7] Tobushi, H., Hoshio, K., Makino, Y. and Hayashi, S., Mechanical characteristic of Shape Memory Composite Material, *Proceedings of the 54 Regular Meeting of the Japan Society of Mechanical Engineers,* (in Japanese)

© (2012) Trans Tech Publications, Switzerland
doi:10.4028/www.scientific.net/KEM.488-489.286

Performance of Nylon Based Polymer Foams at Elevated Temperature under Tensile Loading

V.G. Izzard[1], C.H. Bradsell[1], H. Hadavinia[1*], V.J. Morris[1], P.J.S. Foot[1], L. M. Wilson[2], K. Hewson[2]

[1]Kingston University, London, UK, [2]Zotefoams plc, Croydon, UK

[*] Address all correspondence to h.hadavinia@kingston.ac.uk

Keywords: Cellular Solid, Polyamide Foam, Nylon, Elastic Modulus, Glass Transition Temperature

Abstract: One of the primary applications of polymer based cellular solids is to act as an energy absorbing material during impact where compressive strain rates may reach 500-800/s. In reality, impacts occur over a wide range of temperatures and velocities at different angles of incidence. Understanding and modelling the behaviour of the polymer foams requires characterisation of the material response in detail. The stress-strain response that covers both compressive and tensile behaviour for a wide range of strain rates and temperatures are needed to characterize the mechanical performance of polymer foams as polymeric foams are highly nonlinear materials that undergo large deformation in crashworthiness related cases. It is reported in literature that any increase or decrease in temperature over the glass transition region can cause changes by order of magnitude in elastic modulus of polymeric foams. However, creation of cross linking at high temperature can affect the elastic modulus.

In this work, the behaviour of two, polyamide-6 (PA-6) based closed cell foams at elevated temperatures were investigated covering the glass transition temperature. This work presents the variation of elastic and tangent modulus of two low densities PA-6 and PA-6/polyolefin (Nylon alloy) based foams. Empirical equations have been proposed to allow the prediction of modulus over a temperature range of 23^{o}C to 120^{o}C for these materials.

Introduction

Zotefoams plc is a world leader in the manufacture and distribution of speciality foam materials, manufactured using a unique, proprietary technology [1]. An advantage of this technology is the wide range of materials to which it can be applied. For PA-6 based materials the foaming process has traditionally been an insurmountable technical challenge or otherwise limitations have existed to the reduction in density possible.

The ZOTEK N B50 and N A30 grade foams have nominal densities of 50kg/m^3 and 30kg/m^3, respectively. N B50 is produced from a PA-6 base material and N A30 is produced from a PA-6 and Polyolefin alloy base material. Generally, the properties of both foam materials reflect those of this class of polymer, with high temperature performance, resistance to hydrocarbon fuels and oils combined with impact performance, buoyancy and low thermal conductivity from the cellular structure. It is these characteristics which make the ZOTEK N B50 and N A30 grade foams ideal for energy absorption and cushioning applications in extreme environmental conditions.

In isotropic polymer foams Young's modulus, shear modulus and Yield stress are important to be characterised [2]. Any temperature dependency of these properties must also be understood. It is reported that over the glass transition region, the elastic modulus of a polymer can fluctuate by orders of magnitude [2], however, it is also reported that this large change can be harnessed by the

presence of cross linking within the base polymer of the foam [3]. As a result, characterising the variation of the elastic and tangent modulus of our foams and establishment of any linear stabilisation in behaviour as temperature increases is the goal of this research.

Method

All samples were taken from a single foam sheet to minimise the effects of density variation on results. Cylindrical, 50mm dia × 25mm thick, samples were conditioned for a minimum of 6 days at 23^{o}C, 50% RH [4]. All dimensions were carried out in accordance with ISO 1923 [5]. Tensile tests were carried out in accordance with methods outlined as per type B specimen given in ASTM D1623-03[6] where Scotch-Weld Acrylic Structural Adhesive DP810 is used as a sample gripping method. This is supported by those investigating fatigue properties of similar materials [7]. One sample is glued between two 52 mm dia × 25 mm thick Aluminium discs and cured at room temperature and conditioned for a further 48 hrs.

The sample is encased in a thick walled brass tube and installed in to a Mayes Universal Tensile Tester with, rotating self centring hydraulic grips. The assembly is wrapped in a heating jacket whose temperature is monitored using thermocouples used to control the temperature of the sample. The sample is then conditioned for a minimum of 2 hrs after the experiment temperature is achieved.

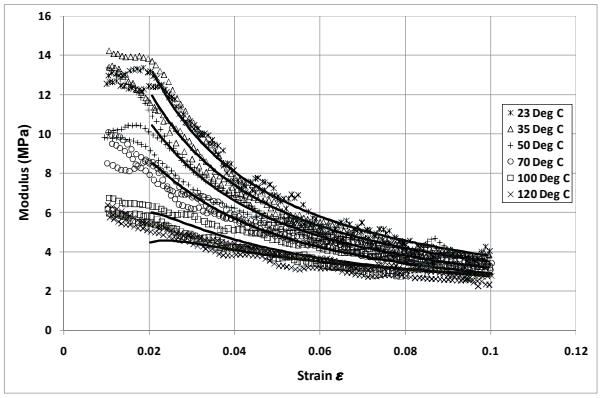
The tensile test was conducted at a strain rate of 0.01s^{-1} where displacement is data logged via an externally installed LDVT, connected directly to the sample holder. Expansion of metallic components due to the loading is accounted for in the data analysis. Further works are underway at higher strain rates.

Results and Discussions

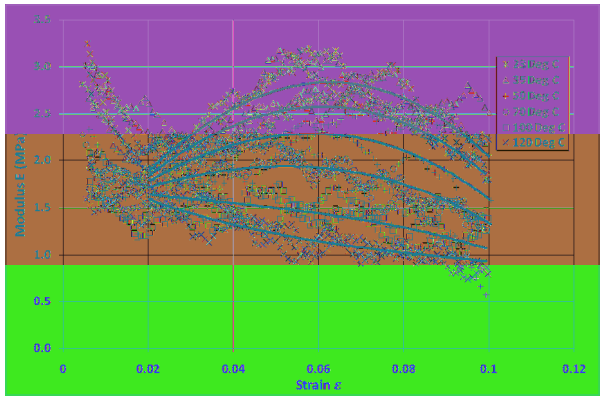
All data has been analysed based on a moving point average, covering a range of approximately 20 data points over 0.01 stain range from 0.01 to 0.10 strain.

As shown in Fig.1a, the variation of tangent modulus of N B50, show a general decrease in value, with the steepest decline shown at the lower end of the temperature scale. As the temperature increases, the severity of the drop becomes less marked until the highest temperature shows a near linear relationship between tangent modulus and strain. This is a characteristic behaviour of polymer based materials. When considering the behaviour of N A30 Fig.1b, the tangent modulus increases until a peak at approximately 0.06 strain. The value then decreases, giving a non linear relationship. However, this is only evident at the lower temperatures. As the temperature increases, the fluctuation in modulus decreases until a near linear relationship is achieved at 100^{o}C.

It is also interesting to note that at the lower end of the temperature scale, N B50 shows an approximate drop of two thirds in modulus. This is only applicable until the glass transition temperature of 50°C is reached. Once this temperature is crossed, the variation is approximately halved over a range of 0.02-0.10 strain.



a. N B50 at Strain Rate of $0.01s^{-1}$



b. N A30 at Strain Rate of $0.01s^{-1}$

Fig.1: Variation of tangent modulus vs strain at various temperature from tensile tests- Experiments and empirical curve fitting

N A30 shows that over the same range, although there is significant deviation of the modulus between 0.02 and 0.10 strain, the modulus returns to the same value. This is the case until 50-70°C (Tg) is achieved, after this the start and end value appears to differ, which becomes greater with temperature but the fluctuation is virtually eliminated. When investigating further, this behaviour is not a result of glue, machine or rate dependency.

It is reported that the elastic modulus changes by orders of magnitude over the glass transition temperature (Tg). This is not evident in this investigation. It is also reported that cross linking can and does harness this effect [3]. In order to produce this foam, cross linking is occurring, and therefore, there are not large differences in modulus. It is over the glass transition range (50-70°C) that the fluctuation in elastic modulus begins to be harnessed. For both materials, conducting tests at higher temperatures, lowers and stabilises the fluctuation in elastic modulus.

As described, the two materials show different behaviours. N A30, is manufactured from a PA-6 polyolefin alloy. By definition, this base material is a mix of two polymers and since such fluctuations are not seen in N B50, this may also contribute to the initial variation of modulus described in this paper. For N B50 and N A30, polynomials equations 1 and 2, respectively, can be used to predict the tangent modulus at a given temperature and strain. Table 1 gives the required coefficients and the accuracy of the fit. However, these functions are only valid within the limits of this paper.

$$E = a + bT + \frac{c}{\varepsilon} + dT^2 + \frac{e}{\varepsilon^2} + f\frac{T}{\varepsilon} \quad (1)$$

$$E = a + bT + c\varepsilon + dT^2 + e\varepsilon^2 + fT\varepsilon + gT^3 + h\varepsilon^3 + iT\varepsilon^2 + jT^2\varepsilon \quad (2)$$

Where: E = Modulus in MPa
T = Temperature in °C
ε = Strain
a-j = Material dependent coefficients

Table 1: Coefficients of empirical curve fitting function

N B50 (R^2 = 0.958)									
a (10^{-1})	b (10^{-2})	c (10^{-1})	d (10^{-4})	e (10^{-3})	f (10^{-3})	g	h	i	j
7.86236	-1.58849	3.92949	1.89810	-1.69475	-2.09482	N/A	N/A	N/A	N/A
N A30 (R^2 = 0.843)									
a (10^{-1})	b (10^{-2})	c (10^{1})	d (10^{-5})	e (10^{2})	f (10^{-1})	g (10^{-7})	h (10^{2})	i (10^{0})	j (10^{-4})
5.80049	1.01808	8.32384	3.24620	-5.7209	-9.71344	-1.70370	-6.69754	6.37092	7.18107

Conclusions

The elastic and tangent modulus of both foam materials is affected by temperature. The nature of the effect can be described relative to the glass transition region of the material.

1. Below the glass transition, the elastic modulus is higher, however large fluctuations are observed in tangent modulus as strain is increased
2. Above the glass transition, the elastic modulus is lower, however there is little fluctuation as strain is increased, therefore a more constant behaviour can be assumed

The tangent modulus of both above and below the glass transition region for both foam materials can be predicted using Eqs. (1) and (2).

Acknowledgements

The authors would like to acknowledge the financial support from EPSRC Award CASE/CNA/06/29. Many thanks go to the technical staff at Zotefoams plc for the supply of the samples. In addition our thanks also go to Bryan Ruby and Chris Pickles for the manufacture of the test fixtures.

References

[1] Izzard VG, Bradsell CH, Hadavinia H, Morris VJ, Foot PJS and Witten N, *Investigation of the Compression Recovery Properties of Polyamide-6 Cellular Solid over Temperature Range of -5°C to 90°C,* (June 2010) Key Engineering Materials Vols. 417-418 p.933-936

[2] Gibson LJ, and Ashby MF, *Cellular Solids- Structures and Properties, Second Edition*, Cambridge University Press 1997

[3] Ashby MF and Jones DRH, *Engineering Materials 2, An Introduction to Microstructures Processing and Design, Second Edition*, Butterworth Heinemann 2001

[4] BS EN ISO 291:2008: *Plastics-Standard Atmospheres for Conditioning and Testing*

[5] BS EN ISO 1923:1995: *Cellular Plastics and Rubbers-Determination of Linear Dimensions*

[6] ASTM D1623-03: *Tensile and Tensile Adhesion Properties of Rigid Cellular Plastics*

[7] Zenkert D, Shipsha A and Burnam M, *Fatigue of Closed Cell Foams,* (2006) Journal of Sandwich Structures and Materials Vol. 8 p.517.

© (2012) Trans Tech Publications, Switzerland
doi:10.4028/www.scientific.net/KEM.488-489.290

Effect of REM Finishing on Fatigue Behavior of a Shot Peened Low Alloy Steel

S. Bagherifard[1, a], R. Ghelichi[1, b], M. Guagliano[1, c] and M. Bandini[2, d]

[1]Politecnico di Milano, Department of Mechanical Engineering, Via La Masa, 1, 20156, Milan-Italy

[2] Peen service s.r.l., Via Augusto Pollastri, 7, 40138, Bologna-Italy

[a]sara.bagherifard@mail.polimi.it, [b]ramin.ghelichi@mail.polimi.it, [c]mario.guagliano@polimi.it, [d]m.bandini@peenservice.it

Keywords: Shot peening, fatigue, surface roughness, finishing.

Abstract. The effect of slight surface REM finishing, that is a chemically accelerated polishing process, in order to reduce surface roughness after shot peening has been studied on different series of specimens shot peened by varied peening parameters. Room temperature rotating bending fatigue tests have been performed on the shot peened series and the series subjected to shot peening and successive REM finishing process. The results represent how REM finishing affects the final fatigue behavior of differently treated specimens in two ways: decreasing surface roughness and removing a thin layer of material with compressive residual stresses.

Introduction

Shot peening is a well-known mechanical surface treatment generally used to improve fatigue behavior of metallic components. Final aim of the process is creation of compressive residual stresses close to the surface and work-hardening of the same layer of material. These effects are very useful in order to totally prevent or greatly delay the failure of the part [1-2].

On the other hand increasing the roughness is well-recognized as a side effect of shot peening process. Since fatigue cracks initiate predominantly at the free surface of a material, the surface condition of the treated part becomes decisive. Irregularities along the surface act as stress concentrations and may aid crack initiation at the surface. Accordingly surface roughness has generally a deteriorating effect on fatigue life improvement obtained via shot peening process.

REM Chemicals finishing, is a chemically accelerated vibratory polishing technique generally applied to surface hardened steels [3]. The REM process involves two steps: the first, referred to as the refinement process involves a chemical interaction on the surface of the part. An active chemistry is used in a vibratory machine in conjunction with high-density, non-abrasive ceramic media. The rubbing motion across the metal surface developed by the machine and media effectively wipes the conversion coating off the peaks of the surfaces, but leaves the valleys untouched. The conversion coating is continually re-formed and rubbed off producing a surface smoothing mechanism till the surfaces are free of asperities. In the final step, commonly referred to as burnishing, the active chemistry is rinsed from the machine with a neutral soap. The conversion coating is completely rubbed off to produce the isotropic superfinished surface [3-5].

In this research, shot peening effects on fatigue resistance of quenched and tempered steel have been experimentally investigated with special focus on the role of surface roughness. Rotating bending fatigue tests have been performed on different series of quenched and tempered steel smooth specimens, shot peened with unlike combinations of peening parameters. Some series have been REM polished in order to study the effect of roughness on the fatigue strength. The specimens of each series have been characterized using roughness measurements and X-ray diffraction measurements.

Experimental Procedure

Quenched and tempered steel 40NiCrMo7 (SAE4340) specimens with the chemical composition represented in Table 1 were shot peened by peening parameters inducing different Almen intensities presented in Table 2.

Table 1. Nominal chemical composition of 40NiCrMo7 quenched and tempered steel [%]

C	Si	Mn	S	P	Ni	Cr	Mo	Cu
0.389	0.29	0.68	<0.003	<0.009	1.81	0.84	0.23	0.09

Table 2. Aspects of the performed shot peening treatments

Shot type and diameter (mm)	Almen Intensity (0.0001 inch)	Coverage%
CE70 (ceramic, ϕ=0.1)	10N	100
S110 (steel, ϕ=0.3)	6A	100
S170 (steel, ϕ=0.43)	12A	100

Roughness measurement. Roughness measurements have been performed on some specimens of as received not peened (NP) and shot peened series. The results presented in Table 3 are the mean value of three measurements performed on each series. As expected by intensifying the Almen intensity of the process that is its kinetic energy, the surface roughness increases.

The average of the measurements performed on REM finished specimens of each series are also presented in Table 3. The results indicate of clear decrease in surface roughness after finishing process. The average thickness of removed material for each series after the same finishing treatment duration is measured to be 0.03 mm, 0.03 mm and 0.01 mm respectively for 10N, 6A and 12A series.

Table 3. Surface roughness parameters of RSSP and SSP specimens

Treatment	l_r [mm]	l_n [mm]	R_a [μm]	R_z [μm]	R_t [μm]
NP	0.80	4.0	1.37	5.84	6.21
10N	0.80	4.0	1.49	8.50	9.80
10N-REM	0.80	4.0	0.22	2.00	2.96
6A	0.80	4.0	1.73	9.28	12.36
6A-REM	0.80	4.0	0.28	2.07	3.04
12A	0.80	4.0	2.35	12.07	14.32
12A-REM	0.80	4.0	1.26	7.26	9.93

X-ray diffraction (XRD) measurements. The state of the induced residual stresses has been investigated by using an AST X-Stress 3000 X-ray diffractometer (radiation Cr Kα, irradiated area 1mm^2, $\sin^2\psi$ method, diffraction angles (2θ) scanned between -45 and 45). To obtain the in-depth profile of residual stresses, measurements have been carried out in depth step by step removing a very thin layer of material using an electro-polishing device.

XRD measurement results as presented in Fig. 1, demonstrate that increasing the applied Almen intensity leads to continuous increase in the on-surface and maximum values of residual stresses.

XRD measurements are not conducted on specimens after REM finishing. However in the literature the REM process is reported to have no measurable effect on residual stresses [3].

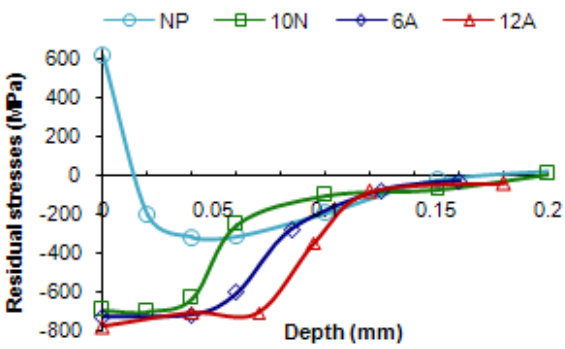


Fig 1. Distribution of residual stresses obtained by XRD for different shot peened series

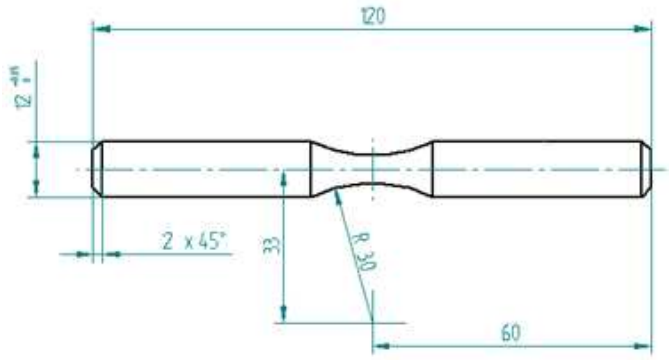


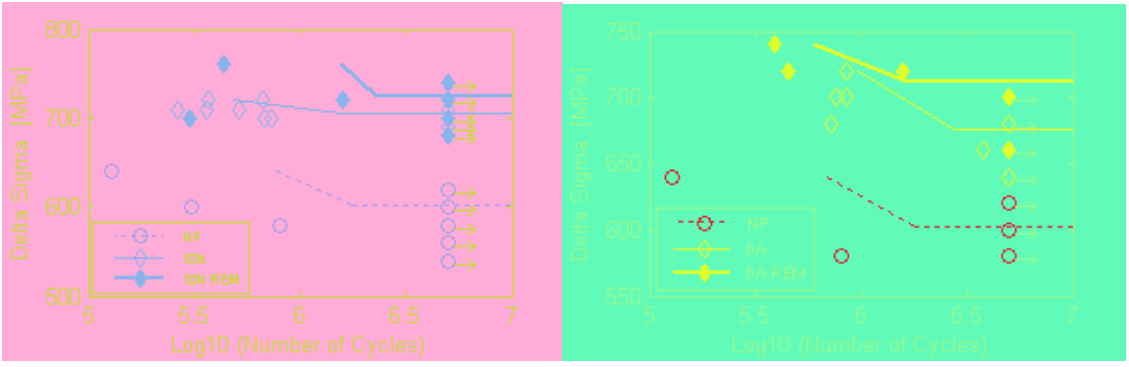
Fig 2. Fatigue smooth specimens' geometry (All dimensions are given in mm)

Fatigue tests. Rotating bending fatigue tests (stress ratio R=-1) have been carried out at room temperature at a nominal frequency of 20 Hz on the NP and shot peened smooth specimens the geometry of which according to ISO 1143 [6] is presented in Fig. 2. Fatigue strength corresponding to a fatigue life of 5 million cycles has been obtained by a staircase procedure, planned by employing 15 specimens.

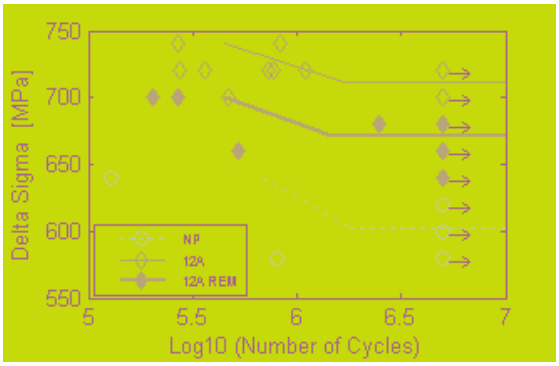
The results of the reverse bending fatigue tests are compared in Fig. 3 for the different treated series of specimens. The fatigue endurance at $5x10^6$ cycles are listed in Table 4. The data are elaborated according to ASTM standard E739-91 [7].

As indicated in Fig.3 and Table 4, all the applied peening treatments have been effective in prolonging the fatigue strength of the material. This improvement depends on the applied Almen intensity and specially the surface characteristics of the treated specimens. Notwithstanding the fact that surface roughness is well-known to have detrimental effects on fatigue strength, the 12A series which have the highest surface roughness, result in the highest fatigue limit, due to the more effective residual stress field and of the induced surface work-hardening.

For the just shot peened series the percentage of this increment increases by intensifying the Almen intensity. In case of shot peened and REM finished series, It is observed that the more intense peening treatments (12A) did not result in a further improvement of the fatigue behavior as compared to the mildest one (10N). In fact the results of 10N series and 6A series show fatigue strength enhancement while in case of 12A, the fatigue strength decreases with respect to the not finished series. This worsening can be attributed to the fact that even though by REM finishing, the roughness is somehow decreased, at the same time a layer of material with high compressive residual stresses is removed too. In other words, the partial decrease in roughness is not enough to result in the fatigue strength improvement with respect to only shot peened series.



3.a 3.b



3.c

Fig. 3. Bending fatigue test of the as received and shot peened series of specimens

Table 4. Fatigue strenghth of shot peened & shot peened-REM finished series

Treatment	Fatigue strength (MPa) peened series	Fatigue strength (MPa) peened & REM finished series
NP	602	-
10 N	705	724
6 A	676	712
12 A	712	672

Conclusions

REM finishing applied after shot peening process obviously results in surface roughness decrease; however the amount of fatigue strength improvement depends on the original surface roughness and the material removal extent; that is the deteriorating effect of removal of a thin layer of material with high compressive residual stresses shall be taken into consideration. As demonstrated by the presented results, REM finishing is beneficial to enhance fatigue strength mainly in case of light shot peening treatments, while for the more intense treatment, since it results in removing a layer with high compressive residual stresses and leaves still a comparatively high surface roughness, the fatigue strength does not improve compared to the not REM finished series. It is to be mentioned that further experiments to investigate the fatigue behavior of REM finished specimens are on course.

References

[1] K.J. Marsh, *Shot Peening: Techniques and Applications.* (London: EMAS; 1993).
[2] V. Schulze, *Modern Mechanical Surface Treatment, states, stability, effects*. (WILEY-VCH; 2006).
[3] S. Rao, D. McPherson and G. Sroka, Repair of Helicopter Gears, Technical Paper of American Gear Manufacturers Association, 2005.
[4] B. Hansen, M. Salerno and L. Winkelmann, Isotropic Superfinishing of S--76C+ Main Transmission Gears, Technical Paper of American Gear Manufacturers Association, 2006.
[5] Information on http://www.taylor-race.com/isotropic.cfm
[6] ISO 1143: 1975. Metals- Rotating bar bending fatigue testing.
[7] ASTM standard E739-91: Standard Practice for Statistical Analysis of Linear or Linearized Stress-Life and Strain-Life Fatigue Data, 2004.

© (2012) Trans Tech Publications, Switzerland
doi:10.4028/www.scientific.net/KEM.488-489.295

Optimal elastic design of CFCs

Galyna Stasiuk [1, a], Romana Piat[,b] and Yuriy Sinchuk[3,c]

[1]Institute of Engineering Mechanics, Karlsruhe Institute of Technology, Kaiserstraße 12
D-76131 Karlsruhe, Germany

[a]galyna.stasiuk@kit.edu, [b]romana.piat@kit.edu, [c]yuriy.sinchuk@kit.edul

Keywords:carbon/carbon composites, optimal elastic design, optimization, fibers distribution, porosity

Abstract. The aim of the proposed studies is the development of the carbon/carbon composite with prescribed elastic properties. To achieve this, a microstructure optimisation problem for estimation of the microstructure with prescribed stiffness is formulated. The design variables of the posed problem are the local fibers distribution and porosity. The volume fractions of the fibers and pores in the whole microstructure are fixed. Material properties of the local microstructure of the composite are calculated using virtual models. Semi-analytical homogenization procedures were used for the development of these models. Modeling results are compared with elastic properties obtained experimentally by tension and compression test and ultrasonic studies of the bulk material. Approach to design microstructure for three point bending test is proposed.

Introduction

The estimation of the optimal topology of advanced materials is very important for industrial applications, especially for carbon/carbon (C/C) composites. These materials consist of two kinds of microconstituents: carbon fibers and pyrolytic carbon (PyC) [1-3]. Both materials are transversely isotropic. The production of C/Cs allows varying of orientation and volume fractions of fibers in the composite [4]. The topology optimization on the microlevel can dramatically influence the material response for this kind of composites with high anisotropy of constituents.

Microstructure of the studied materials

In our previous studies [5-7] we have proposed methodology for microstructure characterization of the C/C composites. This procedure consists of two steps, firstly the characterization of the fiber distribution and secondly, the characterization of the pores distribution.

Fibers distribution The three dimensional distribution of fibers can be determined by X-ray computed microtomography (μCT) of the non-infiltrated preform. An example of such a microstructure characterization is presented for a special case of preform consisting of layers with mostly fibers in one preferred orientation (Fig.1a) [5].

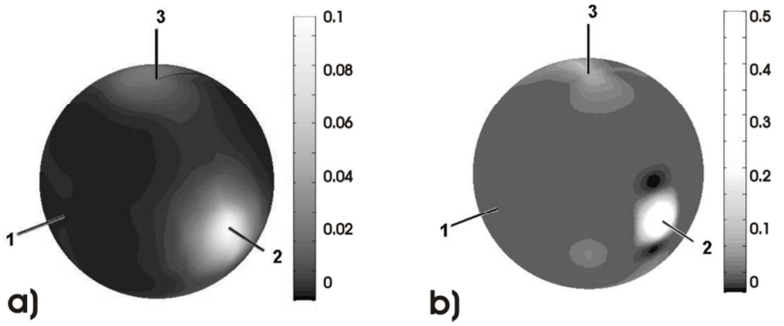


Fig.1: Typical distribution functions of the a) fibers in preform and b) pores in the whole composite.

Porosity characterization Porosity is one of the important characteristics of C/C composites. Even though the architecture of the fiber preform is the same, different duration of the infiltration results in a different volume of the pores. μCT analysis was utilized for 3D description of the porosity [6, 7] and the following procedure was used:

- The μCT data was segmented into pores and solid material with a region growing algorithm;
- The pores were labeled and analyzed using the following procedure:

1. The pore surface was extracted as a point cloud;
2. An ellipsoid with the same volume as the pore under consideration was fit using principal component analysis;
3. The Euler angles, principal half axes and the volumes of the pores were tabulated.

Using the described procedure, the 3D information about porosity of the material was gathered. All pores were approximated as oblate and prolate spheroids. The example of the distribution function of the pores is presented in Fig.1b.

Microstructure modeling

For the prediction of the effective elastic properties of C/C composites we propose the homogenization procedure by the Mori-Tanaka model [8]:

$$\mathbf{C}^{MT} = \mathbf{C}^{M} + \left(+ \sum_{i=1}^{n} f_i \left(\mathbf{C}^{F} - \mathbf{C}^{M} \right) : \mathbf{B}_i - \sum_{i=1}^{m} \rho_i^p \mathbf{C}^{M} : \mathbf{A}_i^p \right) : \left(\mathbf{I} + + \sum_{i=1}^{n} f_i \left(\mathbf{B}_i - \mathbf{I} \right) + \sum_{i=1}^{m} \rho_i^p \left(\mathbf{A}_i^p - \mathbf{I} \right) \right)^{-1} \quad (1)$$

where $\mathbf{C}^i$ are the stiffness tensors of the micro constituents, f and ρ are experimentally obtained distribution functions of the virtual fibers and pores (see Fig. 1 and 2), $\mathbf{A}$ and $\mathbf{B}$ are the influence tensors. Obtained stiffness tensor $\mathbf{C}^{MT}$ presents the effective properties of the material with pores and fibers.

For verification of the proposed modeling the comparison of the calculated and experimental [5] material properties was provided.

Microstructure optimization

The objective function of the optimization problem is the compliance of the specimen and the design variables are the local volume fractions and the local orientations of the fibers.

The specimen for which the optimal microstructural distribution is required occupies domain $\Omega \subset \mathrm{R}^3$. For this formulation we introduce the energy bilinear form $a(\mathbf{u}, \mathbf{v})$ and the load linear form $l(\mathbf{v})$:

$$a(\mathbf{u}, \mathbf{v}) = \int_{\Omega} C_{ijkl}(\mathbf{x}) \varepsilon_{ij}(\mathbf{u}) \varepsilon_{kl}(\mathbf{v}) \, d\Omega, \quad (2)$$

$$l(\boldsymbol{v}) = \int_{\Omega} \boldsymbol{f} \boldsymbol{v} \, d\Omega + \int_{\Gamma_T} \boldsymbol{t} \boldsymbol{v} \, ds,$$

with the linearized strain ε_{ij}, the components of the stiffness tensor C_{ijkl} of the element, the body forces $\mathbf{f}$ and the boundary tractions $\mathbf{t}$ on the traction part $\Gamma_T \subset \Gamma \equiv \partial\Omega$ of the boundary. The minimum compliance (maximum global stiffness) problem has the form [9]:

$$\min_{\mathbf{u}\in U, f_c, \alpha, \beta} \quad l(\mathbf{u}) \tag{3}$$

$$s.t.: a_{\mathbf{C}}(\mathbf{u},\mathbf{v}) = l(\mathbf{v}), \qquad \forall \mathbf{v} \in U,$$

$$C_{ijkl}(\mathbf{x}) = \widetilde{C}_{ijkl}(f_c(\mathbf{x}), \alpha(\mathbf{x}), \beta(\mathbf{x})),$$

$$\int_{\Omega} f_c(\mathbf{x}) d\Omega \le F_c; \; f_{c\,\min} \le f_c(\mathbf{x}) \le f_{c\,\max}, \; \mathbf{x} \in \Omega.$$

Here U is the space of kinematically admissible displacement fields; F_c is the given amount of fibers in Ω; and $f_{c\min}, f_{c\max} \in (0,1)$ are the limits on the fibers volume in the elements.

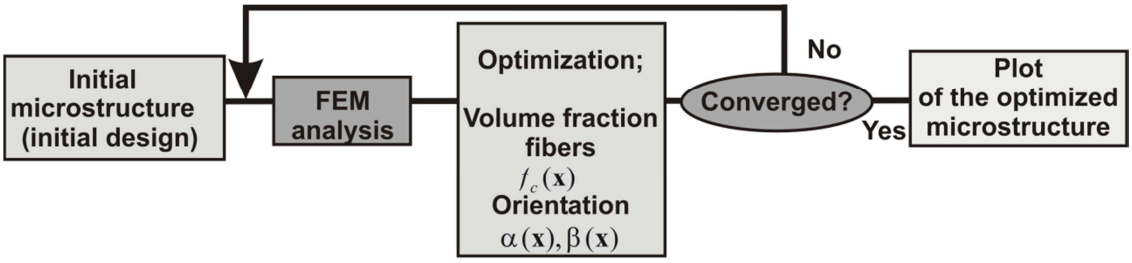


Fig.2: Calculation flow for the optimization problem with three design variables.

The optimal orientation and local volume fractions of the fibers were achieved iteratively on each step of this procedure using the finite element method. The design problem consists in finding the optimal choice of the stiffness tensor in each element $C_{ijkl}(\boldsymbol{x}_i) = \widetilde{C}_{ijkl}(f_c(\boldsymbol{x}_i), \alpha(\boldsymbol{x}_i), \beta(\boldsymbol{x}_i)), \; \boldsymbol{x}_i \in \Omega$ which depends on three design variables – the volume fraction of the fibers and two angles of fiber orientation in R^3 space.

The components of the effective stiffness tensor $\widetilde{C}_{ijkl}(\boldsymbol{x}_i)$ of the element are calculated using the homogenization procedure. For our studies we have utilized the simplified form of Eq.1:

$$\widetilde{\mathbf{C}}^{MT} = \mathbf{C}^M + \left(f\left(\mathbf{C}^F - \mathbf{C}^M\right) : \mathbf{B} - \rho \mathbf{C}^M : \mathbf{A}^p\right) : \left(\mathbf{I} + f\left(\mathbf{B} - \mathbf{I}\right) + \rho\left(\mathbf{A}^p - \mathbf{I}\right)\right)^{-1} \tag{4}$$

We suppose that in each element all fibers have the same orientation and volume fraction f; the volume fraction of the pores is ρ and all pores are spherical.

The optimization procedure was provided as presented in Fig. 2.

Numerical results

The optimal orientation of the fibers and their volume fractions in the C/C composite specimen (dimensions 25:8:5) subjected to the three-point bending test are presented in the Fig. 3 and 4.

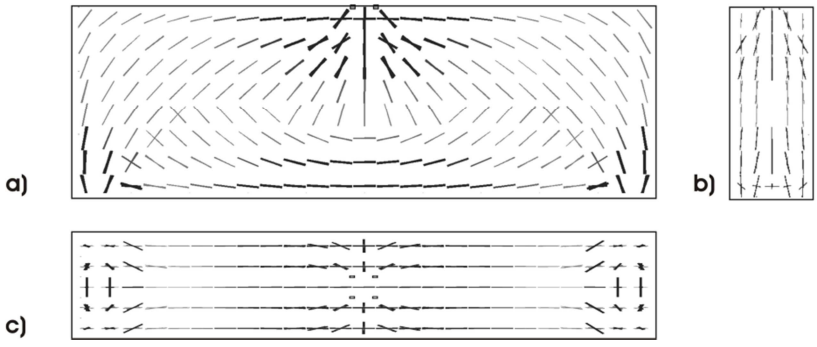


Fig. 3: Projections of the optimal fibers distributions on: a) xy, b) yz and c) xz.

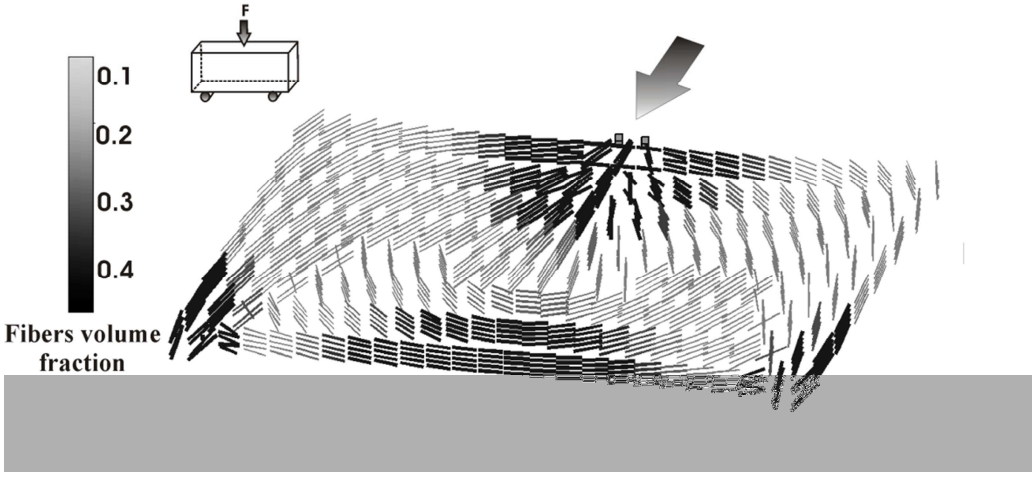


Fig. 4: Fibers orientations and volume fraction distributions inside 3D specimens.

Summary

A short overview of the microstructure characterization, estimation of the fibres and pores distributions is presented. The obtained distributions are used for calculation of effective elastic properties of C/C composites. The homogenization methods are utilised for the microstructure modeling. Developed and experimental verified models are applied for the 3D microstructure optimization. The minimum compliance problem was solved for the three-point bending test. The optimal distribution of the fibers volume and orientation for each element was determined.

In the present studies the volume of the pores was constant und the volume of the fibers/PyC were the design variables. In the future studies different shapes of the pores and their volume fraction will be the also design variables.

Acknowledgements
The financial support of the DFG (PI 785) is gratefully acknowledged.

References

[1] W.G. Zhang, K.J. Hüttinger: Carbon*,* Vol. 41(2003), p. 2337.

[2] T. Gross et al.: *Carbon,* Vol.49 (2011), p. 2147.

[3] J.-M. Gebert et al. : *Carbon*, Vol. 48 (2010), p.3650.

[4] R. Piat : *Key Engineering Materials* Vol. 348-349 (2007), p. 668.

[5] R. Piat et al., in: *High Temperature Ceramic Materials and Composites*, edited by W. Krenkel, J. Lamon AVISO, Berlin, Germany (2010), p. 597.

[6] B. Drach et al.: *Int. J. Solids Struct.*, submitted, 2010.

[7] J.-M. Gebert et al. : *Mechanics of Advanced Materials and Structures*, Vol. 15 (2008), p. 473.

[8] A. Giraud et al.: *Mechanics of Materials*, Vol. 3(2007), p.1024.

[9] M.P. Bendsoe, O. Sigmund: *Topology optimisation. Theory, methods and applications* (Springer, 2003).

© (2012) Trans Tech Publications, Switzerland
doi:10.4028/www.scientific.net/KEM.488-489.299

High cycle fatigue parameters of high chromium steel

Matej Drobne[1, a], Peter Göncz[2, b], Srečko Glodež[2, c]

[1]Valji, production of rolls and castings, d.o.o., Železarska cesta 3, Si – 3220 Štore

[2]University of Maribor, Faculty of Natural Sciences and Mathematics, Koroška cesta 160, Si – 2000 Maribor

[a]matej.drobne@valji.si, [b]peter.goncz@uni-mb.si, [c]srecko.glodez@uni-mb.si

Keywords: rolling contact fatigue; hot strip mills; high chromium steel; stress method

Abstract. The determination of monotonic mechanical properties and high cycle fatigue parameters of high chromium steel (HCS) is presented. The monotonic mechanical properties (ultimate compressive and ultimate tensile strength) are determined using standardized testing procedures according to DIN 50125 standard. The high cycle fatigue parameters are determined using uniaxial fatigue test where the tests specimens are loaded with pure pulsating compression load (load ratio R=0 in compression) at different load levels. Therefore, a typical S-N curve and appropriate fatigue parameters (fatigue strength coefficient σ_f' and fatigue strength exponent b) are determined. The experimental results determined in this study can serve as a basis for the determination of service life of rolls using stress-life approach. However, a few guidelines for the further research work considering increased temperatures and multiaxial fatigue are given in the conclusions of this study.

Introduction

The main aim of the rolling process is to reduce the thickness of the work piece, from the initial thickness to a pre–determined final thickness. This is accomplished on a rolling mill, in which rotating rolls draw the strip or plate to be rolled into the roll gap and force it through to the exit, causing the required reduction of the thickness [1, 2]. To achieve this goal, the appropriate material of rolls should be chosen considering the appropriate manufacturing process and thermal treatment in such a way that the rolls will operate certain service life under given loading conditions.

Different type of rolls according to dimensions and material of rolling plates may be used for different stands in mill. Rolls which operate at roughing stands in hot strip mills are normally double layered. Shells of rolls are usually spin casted and made of high chromium steel, where for cores a combination of pherlitic–ferritic nodular graphite iron is used. The result of high spinning speed is a centrifugal force which pushes the molten metal to fill the mold.

The stress–strain state when contact between roll and metal is established can be for simple cases analytically determined by using the contact theories as described in [4]. For more comprehensive studies the influence of the multi–axial state of stress and also the influence of thermal loading due to hot forming metal should be taken into account in the subsequent computational analyses. The numerical procedure using FEM-method is usually used for that purpose. When the stress field and the contact area and the material parameters (fatigue strength coefficient σ_f'and the fatigue strength exponent b) are known, the fatigue behaviour of rolls can be analysed using the following equations:

$$\sigma_a = \sigma_f' \, (2N)^b. \tag{1}$$

$$N = (\sigma_a / (\sigma_f' \, 2^b))^{1/b}. \tag{2}$$

From Eq. (1) the allowable alternating stress σ_a can be determined if the service life (number of cycles N) is known or given in advance. For known alternating stress the appropriate number of loading cycles in the expected service life can be determined from Eq. (2).

Experimental testing

The determination of fatigue strength coefficient σ_f' and the fatigue strength exponent b has been performed by using the test specimens as shown in Fig. 1. Specimens were cut out of the roll shell by using an abrasive water blast, where the influence on specimen material because of tooling is reduced to minimum.

Before the fatigue tests the monotonic compressive test has been made using the same specimen as shown on Fig. 1. To compare the differences between compressive and tensile strength of HCS the monotonic tensile test has also been done using a specimen B 10 x 50 according to DIN 50125 standard [6].

The fatigue tests have been performed on the servo – hydraulic fatigue test machine Instron 1255 with a computer aided control unit and an Instron 8500 data recording system. Ten specimens have been tested by using the different load levels. On the basis of the monotonic compression test the first load level which belongs to the first specimen was set up a little bit lower in comparison to the compressive yield stress taken from the monotonic compression test. The compressive loading of the subsequent test specimens has then been reduced in order to increase the loading cycles to failure. The experimental results have then been plot in $S - N$ diagram as presented in section Results.

According to the operating conditions of rolls which are subjected to the compressive contact loading, the test specimens have been loaded with dynamic pulsating compression load (load ratio $R = 0$ in compression).This is not in agreement with the standard rotating bending test according to DIN 50113 standard [5], where the specimen is exposed to fully reversed loading (load ratio $R = -1$). The proposed testing procedure ($R = 0$ in compression) enables the direct determination the service life of real contacting components (rolls) using Eq. (2) without consideration of mean stress effect. However, it is not the case when determining the service using material parameters σ_f' and b previously determined for fully reversed loading.

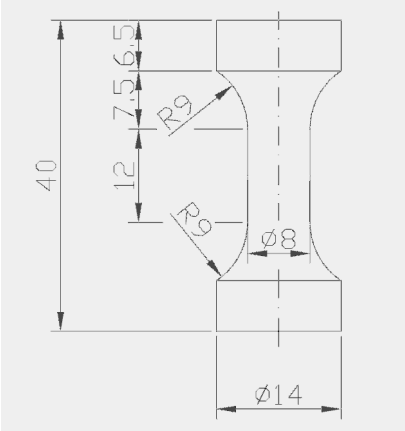


Fig. 1. Test specimen

Results

Fig. 2 represents the tensile vs. compression stress–strain curve, from which the ultimate compression and ultimate tensile strengths can be recorded. It is obvious that the ultimate compression strength (≈ 2345 N/mm^2) is for treated material HCS almost 2.5 – times larger than the ultimate tensile strength (≈ 932 N/mm^2).

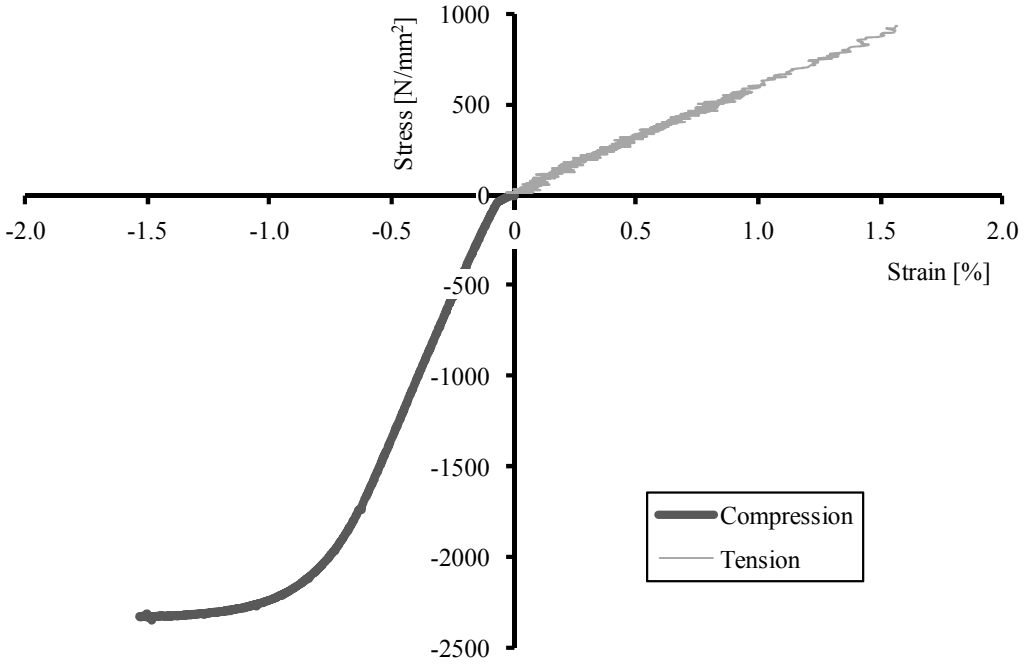


Fig. 2. Tension vs. compression stress - strain curve

Fig. 3 shows the stress – life fatigue curve plotted on log – log scales for compression pulsating stress. Six specimens have been tested to determine the material parameters σ_f' and b in the median fatigue area. Additional four tested specimens were not taken into account when determining the parameters σ_f' and b because the number of loading cycles until the failure exceeded 10^7 cycles (area of the fatigue limit). It is evident from Fig. 3 that with the increasing of the loading cycles N, the alternating stresses σ_a decreases very slowly (the fall of the alternating stress is in the range of loading cycles 0 to 10^6 a little more than a 100 N/mm^2).

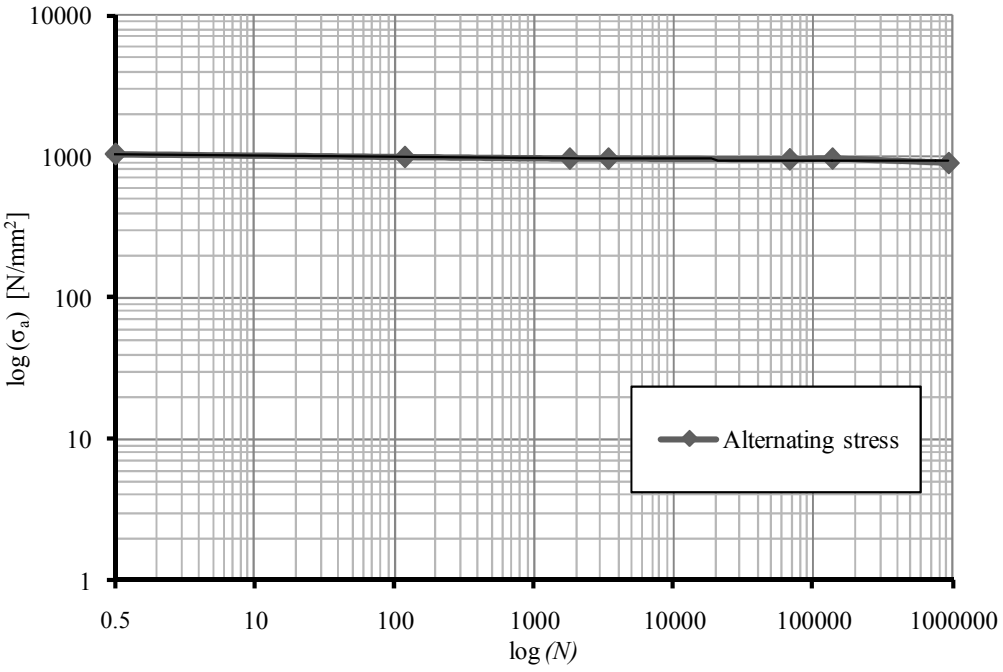


Fig. 3. Stress – life fatigue curve plotted on log – log scales for compression pulsating stress

The results ($S - N$ data) recorded from experiments have then been mathematically analyzed where the least squares method [7] has been used to determine the correlation line between experimental points. Therefore, the high cycle fatigue parameters for High Chromium Steel (HCS) for pulsating compression load ($R = 0$ in compression) result in:

- fatigue strength coefficient : $\sigma_f' \approx 1032$ N/mm^2
- fatigue strength exponent: $b \approx -0.008$

Conclusion

An experimental determination of the mechanical properties and the high–cycle fatigue parameters of High Chromium Steel (HCS) are presented. From the experimental results of the monotonic tensile and compressive test it is evident that the ultimate compression strength (≈ 2345 N/mm^2) is almost 2.5-times higher than the ultimate tensile strength (≈ 932 N/mm^2). The fatigue tests results (see $S - N$ diagram in Fig. 3) show a good resistance of treated material again compression pulsating loading (alternating stress σ_a decreases slowly by significant increasing of loading cycles to failure N).

The experimental results represented in this paper can be used for the further investigations regarding to fatigue behavior of high chromium steel for rolls. Because this type of rolls are usually intended to operate at roughing stands in hot strip mills, the similar fatigue test should be done by increased temperatures. To determine the service life of rolls regarding contact fatigue phenomenon the exact stress – strain field in the contact area between rolls and metal should be known. Therefore, a comprehensive numerical analysis considering the material properties of roll and metal under increased temperature should be done for that purpose. Considering the multi-axial state of stress in the contact area an appropriate fatigue criterion should also be used for real determination of service life of rolls.

Acknowledgements

Operation is part financed by the European Union, European Social Fund.

References

[1] Lenard, G.F., *Primer on Flat Rolling* – A monograph for those who need to understand the basics of the flat rolling process. Elsevier.

[2] ASM HANDBOOK, Volume 14, *Forming and Forging,* (1996).

[3] Stephens R.I., Fatemi A., Stephens R.R, Fuchs H.O., *Metal fatigue in Engineering*, John Wiley & Sons Inc., New York, 2001.

[4] Johnson K.L., *Contact Mechanics*, Cambridge University Press, 1985

[5] DIN 50113; Testing of metals; Rotating bar bending fatigue test; 1982.

[6] DIN 50125; Testing of metallic materials - Tensile test pieces; 2004.

[7] Lawson, C. L.; Hanson, R. J. (1974). *Solving Least Squares Problems*. Englewood Cliffs, NJ: Prentice-Hall.

© (2012) Trans Tech Publications, Switzerland
doi:10.4028/www.scientific.net/KEM.488-489.303

Slow Crack Growth and Creep Rupture of $Ba_{0.5}Sr_{0.5}Co_{0.8}Fe_{0.2}O_{3-\delta}$

J. Malzbender[1], G. Pećanac[2], S. Baumann[3]

Forschungszentrum Jülich GmbH, IEK, 52425 Jülich, Germany

[1]j.malzbender@fz-juelich.de, [2]g.pecanac@fz-juelich.de, [3]s.baumann@fz-juelich.de

Keywords: Fracture, Ceramics, Slow Crack Growth, Creep

Abstract. $Ba_{0.5}Sr_{0.5}Co_{0.8}Fe_{0.2}O_{3-\delta}$ is a mixed ion-electron conductor with high application potential as high-temperature gas separation membrane. However, in practical use the integrity of this brittle perovskite is challenged by the mechanical boundary conditions of transient temperature exposure. Moreover, long term failure mechanisms such as static fatigue at room temperature and creep rupture at operation temperature might occur. The relevance of both effects for BSCF has been investigated. The slow crack growth at room temperature has been determined using bi-axial bending under different loading rates. The creep rupture at elevated temperature has been analyzed from three-point bending tests. The results indicate favourable behaviour of BSCF in both cases. A low risk of failure due to slow crack growth exists and the strain to failure in combined tensile - compressive mode reaches up to 40 %.

Introduction

Based on the growing awareness to the long term climatic development the reduction of carbon dioxide emission has received increasing attention [1]. One of the most promising options to separate carbon dioxide in fossil power plants is the oxy-fuel combustion, where ceramic gas separation membranes provide the necessary oxygen [1]. Various mixed ion electron conducting (MIEC) perovskites have been suggested as possible oxygen transport membranes (OTMs). In particular $Ba_{0.5}Sr_{0.5}Co_{0.8}Fe_{0.2}O_{3-\delta}$ (BSCF) with its high oxygen permeation rate appears to be one of the most promising OTM materials [2].

Under the severe conditions of real application the materials stability is challenged by the high operation temperature, pressure gradients across the membrane and chemically induced strains. In addition to microstructural stability the mechanical integrity is a main requirement to warrant the long term functionality [3]. Actually the long-term performance of a ceramic component does not only rely upon the initial strength and fracture toughness of the material, but also depends on the long-term failure behaviour. Slow crack growth (SCG) of the component might be important at ambient temperature. SCG is generally not well addressed for perovskite type ceramic membrane materials. For the perovskite $La_{0.2}Sr_{0.8}Fe_{0.8}Co_{0.2}O_{3-\delta}$ (LSFC) SCG has been investigated [4]. The SCG is investigated in the present work measuring the stress rate dependence of the fracture strength [5]. Stress rate effects are important to evaluate the effect of thermally induced stresses, which can be generated by differences in components thermal expansion or temperature gradients and hence the rate of temperature changes during start-up and shut-down.

Long-term failure might also occur at the elevated operation temperature due to creep. Previous investigations on BSCF creep concentrated mainly on the deformation under compressive loads [6,7]. Between 600 °C and 800 °C the compressive creep rates of BSCF in air were almost constant but increased continuously up to 900 °C [7]. Since during operation tensile as well as compressive stresses act on OTM components an important thermo-mechanical aspect at elevated temperatures is also the creep rupture under tensile or combined tensile-compressive loads. Recently reported C-ring creep tests revealed the formation of pores along grain boundaries normal to the tensile stresses that ultimately lead to creep rupture [7]. In fact the authors estimated a critical strain of ~ 0.2 % for damage initiation under tensile loading of a C-ring specimen. Note that acceptable creep rates in a compressive mode for engineering ceramics are suggested to be about 10^{-10} s^{-1} yielding a tolerable strain of about 1% per year. The creep is analysed in 3-point bending.

Experimental

Disk-shaped (for SCG test, 22 mm × 2 mm) specimens were provided by Fraunhofer IKTS, Institutsteil Hermsdorf and bar geometry specimens (for creep test, 30 mm × 4 mm × 3 mm) were provided by IEK-1, Forschungszentrum Jülich GmbH. The initial powders were supplied by Treibacher Industrie AG, Austria. The powders were uniaxially pressed with a pressure of 105 MPa and sintered at 1000 °C for 12 h at a heating rate of 5 K/min and a cooling rate of 0.5 K/min. Some bar-shaped specimens received additional polishing to permit an optical measurement of the strain.

The slow crack growth was tested using biaxial bending under different loading rates at room temperature. The ring-on-ring bending test followed the procedures recommended in the ASTM C 1499-05. The experiments for the SCG analysis were performed with applied stress rates from 10 tests each at $3.2 \cdot 10^{-3}$, $3.2 \cdot 10^{-2}$, 3.2 MPa/s and 25 tests at $3.2 \cdot 10^{-1}$ MPa, thus permitting a rather accurate determination of the Weibull modulus following ASTM C1239-07.

The flexure tests were performed at RT. The fracture stress data σ were used to determine the characteristic strength σ_f and the Weibull modulus m using a maximum likelihood statistical analysis after ASTM C1239-07 based on the relationship for the failure probability.

The bending tests were carried out with a universal testing machine (Instron 1362). The central displacement of the specimen was recorded with a sensor that contacted the lower surface of the sample. The loading rate was 100 N/min in all tests. The displacement was measured with a ceramic extension rod attached to a Linear Variable Differential Transformer (Sangamo, LVDT, range ± 1 mm, precision 1.25 µm). The load was determined with a 1.5 kN load cell (Interface 1210 BLR). The temperature was monitored close to the outer specimen surface with a thermocouple.

The creep failure was investigated in a three-point bending arrangement. The tests were carried out up to failure between 850 and 900 °C in air (at 800 °C the creep rate was too low to reach failure relevant specimen deformations in a finite time). Note that these temperatures are also in the proposed operation range of gas separation membranes [1]. The three-point bending test followed the procedures recommended in ASTM C1-161. For the tests at elevated temperatures, a heating rate of 2 K/min was used. At higher temperatures a dwell time of 1 h was chosen to reach thermal equilibrium before testing. For some of the specimens the creep strain was measured directly using the change of distance between hardness impressions [8, 9] as illustrated in Fig. 1. The indentation marks were imprinted with a Fischer HC100 indentation system applying a load of 1N.

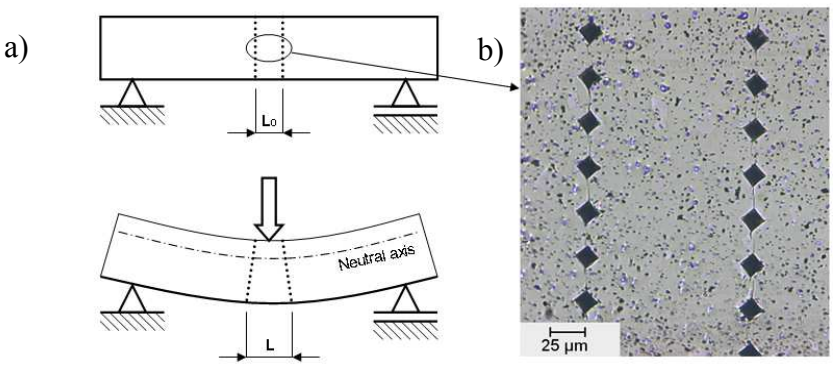


Fig. 1: a) Schematic drawing of the direct strain measurement using the change in position of hardness impressions, b) rows of imprints (load 1 N).

Results and discussion

Slow crack growth (SCG). The fracture stress values were analysed statistically to determine characteristic strength and Weibull modulus. The loading rate sensitivity of bending test data can be used to assess the slow crack growth sensitivity of a material. It has been shown that the strength is linked to a particular stress rate $\dot{\sigma}$ via [4,5]:

$$\sigma_f = \frac{1}{n+1} \log\dot{\sigma} + \log D\,, \tag{1}$$

where n and D are the SCG parameters. Fig. 2 gives a graphical representation of the data for BSCF. The resulting SCG parameters are $n \sim 30$ and $D \sim 94$ MPa, which compares well to the literature data of LSFC (n = 24, D = 95 MPa), another perovskite material considered for OTM application [4]. For both perovskites the crack kinetics parameter n is too high to expect pronounced SCG. For comparison much lower values of $n \sim 11$ - 18 have been reported for soda lime glass, a material prone to static fatigue [5].

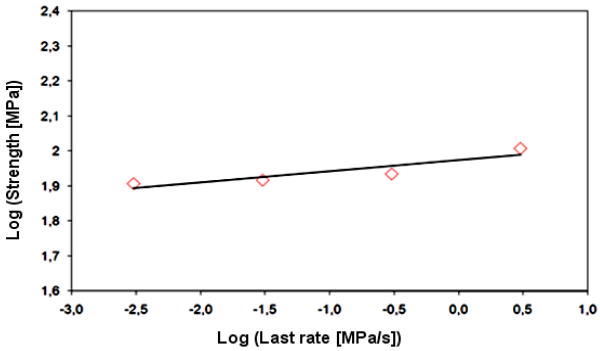


Fig. 2: Fracture strength as a function of stress rate. The line is a linear regression result.

Creep rupture. 3-point bending creep tests have been carried out at 850 and 900 °C. No significant creep occurred at 800 °C and below in agreement with the reported low compressive creep rate for this material [6,7]. The resulting creep rupture time as a function of the nominal applied stress is given in Fig. 3. The time to creep failure decreases with temperature and applied nominal stress. It can be seen that increasing the temperature by 50 °C decreases the time to failure by a factor of ~ 5 - 10.

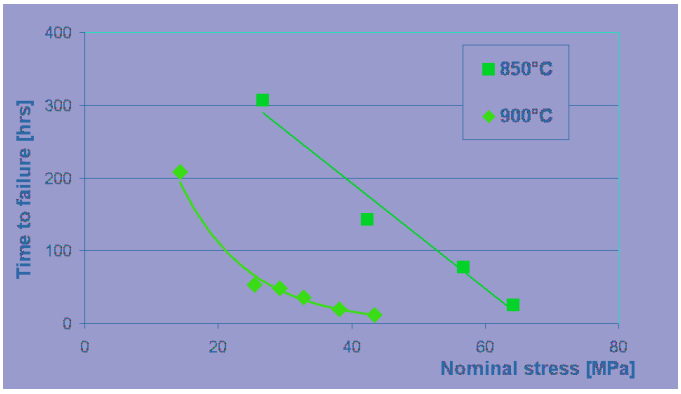


Fig. 3: Rupture time as a function of nominal applied stress.

Differences in creep rate under tensile and compressive load have been reported for ceramic materials in the past [8, 9]. Furthermore, although the simple three-point bending test permits to determine the rupture time as a function of the applied stress, it does not give information on the failure strain. In order to determine this important parameter additional bending tests were

performed where the strain distribution was measured microscopically by the change in distance between rows of hardness impressions in the cross-section (Fig. 1).

The tests were carried out at 900 °C with a nominal applied stress of 15 MPa. The distance between the rows of hardness impressions (initially ~120 μm) was re-measured after 25 h creep tests and then again after another additional 25 h under creep exposure. After the first 25 h of creep the direct strain measurement yielded a compressive strain of ~ -2 % and a tensile strain of 4.5 %. After the subsequent creep exposure the compressive strain remained almost unchanged at -2 %, whereas the tensile strain increased to almost 9 %. From the bending creep tests a compressive strain rate of $2 \cdot 10^{-7}$ s^{-1} is determined for the first 25 hrs step, which is in agreement with literature data $3 \cdot 10^{-7}$ s^{-1} for these conditions [6]. The tensile strain rate increases from $4.5 \cdot 10^{-7}$ s^{-1} for the first annealing step to $9 \cdot 10^{-7}$ s^{-1} after the additional 25 hrs exposure. Based on these results it can be estimated that the specimen that failed under identical conditions after ~ 210 h obtained a fracture strain of ~ 40 %.

Conclusions

The slow crack growth at room temperature was tested using biaxial bending under different loading rates. The results indicate a low risk of failure due to slow crack growth.

The creep rupture time at 850 and 900 °C was investigated using three-point bending tests. The creep rupture time decreases considerably with temperature and applied stress. A temperature increase by 50 K reduces the time to rupture by a factor of ~ 5 - 10. Under the combined tensile-compressive creep mode a failure strain of ~ 40 % was estimated, yielding ~ 40 years lifetime for a creep deformation of 1 % per year.

Acknowledgement

The work was financially supported by the EU through the FP7 NASA-OTM Project (NMP3-SL-2009-228701) and the Helmholtz Association of German Research Centers (Initiative and Networking Fund) through the MEM-BRAIN Alliance. The authors would like to express their gratitude to R. Küppers and J. Mönch for the excellent experimental support of the creep tests.

References

[1] M. Czyperek, P. Zapp, H. J. M. Bouwmeester, M. Modigell, K.-V. Peinemann, I.Voigt, W. A. Meulenberg, L. Singheiser and D. Stöver: Energy Procedia 1 (2009) p.303-310.
[2] J. Sunarso, S. Baumann, J. M. Serra, W. A. Meulenberg, S. Liu, Y. S. Lin and J. C. D. da Costa: J. Membrane Sci. 320 (2008) p.13-41.
[3] A. Atkinson and T.M.G.M. Ramos: Solid State Ionics 129 (2000) 259 - 269.
[4] N. Nagabhushana, T. Nithyanantham, S. Bandopadhyay and J. Zhang: Int. J. Appl. Ceram. Technol. (2009) DOI: 10.1111/j.1744-7402.2009.02440.x
[5] S. R. Choi, J. A. Salem and F. A. Holland: NASA Technical Memorandum 107369, 1997.
[6] J.X. Yi, H.L. Lein, T. Grande, S. Yakovlev and H.J.M. Bouwmeester: Solid State Ionics 180 (2009) p.1564-8.
[7] B. Rutkowski, J. Malzbender, T. Beck, R.W. Steinbrech and L. Singheiser: J. Europ. Ceram. Soc. 31 (2011) p.493.
[8] J.H. Kim, D.B. Han and K.T. Kim: Mater. Sci. Eng. A212 (1996) p.87-93
[9] C.F. Chen and T.J. Chuang: J. Am. Ceram. Soc. 73 (1990) p.2366.

© (2012) Trans Tech Publications, Switzerland
doi:10.4028/www.scientific.net/KEM.488-489.307

Influence of Al-Si diffusion coating on low cycle fatigue properties of cast superalloy Inconel 738LC at 800 °C

Martin Juliš[1,a], Karel Obrtlík[2,b], Simona Pospíšilová[1,c], Tomáš Podrábský[1,d] and Jaroslav Polák[2,e]

[1]Brno University of Technology, Faculty of Mechanical Engineering
Technická 2896/2, 616 69 Brno, Czech Republic

[2]Institute of Physics of Materials, Academy of Sciences of the Czech Republic
Žižkova 22, 616 62 Brno, Czech Republic

[a]julis@fme.vutbr.cz, [b]obrtlik@ipm.cz, [c]pospisilova@fme.vutbr.cz,
[d]podrabsky@fme.vutbr.cz, [e]polak@ipm.cz

Keywords: Low cycle fatigue, diffusion coating, Inconel 738LC, high temperature, fatigue life, cyclic stress-strain curve, cyclic hardening/softening curve.

Abstract. High temperature low cycle fatigue behaviour of cast nickel-based superalloy Inconel 738LC in as-received condition and coated with an Al-Si diffusion layer was studied. The Al-Si protective layer was deposited on the gauge section of cylindrical specimens using the slurry technique. Fatigue tests were performed on cylindrical specimens under total strain control in symmetrical cycle at 800 °C in air. The coating has a beneficial effect on fatigue life in the low amplitude domain. The stress response of the coated material is higher for high amplitudes in comparison with the uncoated one. Fracture surfaces and sections parallel to the specimen axis have been examined to study fatigue damage mechanisms.

Introduction

Precipitation strengthened nickel base superalloy Inconel 738LC is widely used for the production of blades and discs of gas turbine engines. Fatigue behavior of Inconel 738LC is reported rarely [1]. The critical parts of the engines are subjected to repeated elastic-plastic loading and erosion in aggressive environments at high temperatures. The component service life can be improved by suitable surface treatment [2].

The effect of diffusion coatings on the fatigue life of superalloys is ambiguous [3-5]. A Pt modified Al diffusion coating on Inconel 738LC led to fatigue life diminution at 850 °C in comparison with the uncoated material [3]. In René with Al diffusion coating, detrimental effect is reported at high strain amplitudes while fatigue lives become longer at low strain amplitudes [4]. The Al-Si diffusion coating applied on Inconel 713LC resulted in the beneficial effect on the Manson-Coffin life curve [5].

The objective of the present work was to study the low cycle fatigue behavior of cast nickel-based superalloy Inconel 738LC in as-cast condition and with an Al-Si diffusion coating at 800 °C in air.

Experimental

Polycrystalline Inconel 738LC was supplied by PSB Velká Bíteš, a.s. as conventionally cast rods in fully heat treated condition, i.e. after 1120 °C / 4 h / air cooling (AC) + 845 °C / 24 h / AC. Chemical composition of the superalloy is 15.9 Cr, 8.3 Co, 3.3 Ti, 3.3 Al, 2.5 W, 1.7 Mo, 0.15 Fe, 2.53 Nb+Ta, 0.11 C, <0.05 Si, <0.05 Mn, 0.03 Zr, 0.008 B, the rest Ni (all in wt. %). The average grain size, found using the linear intercept method, was 3.6 mm.

Fatigue tests were performed on button-end specimens having gauge length and diameter of 15 mm and 6 mm, respectively. Specimens were machined parallel to the rod axis and their gauge length was mechanically ground. Four specimens were surface-treated using a slurry technique. A suspension of Al and Si was deposited over the gauge length and the specimens were annealed in protective atmosphere at 950 °C for 5 hours followed by slow cooling. The thickness of the resulting surface layer was in the interval 50 to 60 μm.

Coated and uncoated specimens were fatigued in a closed-loop electro-hydraulic testing system at total strain rate of $2x10^{-3}$ s^{-1} with fully reversed total strain cycle (R_ε = -1) at 800 °C in air. Heating was provided by a three-zone resistance furnace and the temperature was monitored by three thermocouples. Strain was measured and controlled using sensitive extensometer with 12 mm base. Hysteresis loops for selected numbers of cycles were recorded in disk memory. Plastic strain amplitude derived from the half of the loop width and stress amplitude at half-life were evaluated.

Light microscopy (LM) and scanning electron microscopy (SEM) Philips XL30 were used to study fracture surfaces and polished sections of the gauge segment in both treated and untreated specimens.

Results and discussion

The stress amplitude σ_a as a function of the number of cycles N obtained for both treated and untreated specimens cycled at 800 °C is shown in Fig. 1. In the uncoated superalloy (see Fig. 1a), the stable stress response is typical for low amplitudes while the initial hardening followed by saturation and softening is observed in the high amplitude domain. In the coated material the saturated stress response can be seen for low and medium amplitudes while moderate softening is obvious at the highest strain amplitude (see Fig. 1b).

Fatigue life curves of the surface treated and untreated superalloy are plotted in Fig. 2. Fig. 2a shows the stress amplitude σ_a at half life vs. the number of cycles to fracture N_f in the bilogarithmic representation. Experimental data are fitted by the Basquin law

$$\log 2N_f = (1/b) \log \sigma_a - (1/b) \log \sigma_f' . \quad (1)$$

The fatigue strength coefficient, σ_f' = 1860 MPa, and the fatigue strength exponent, b = 0.164 , were

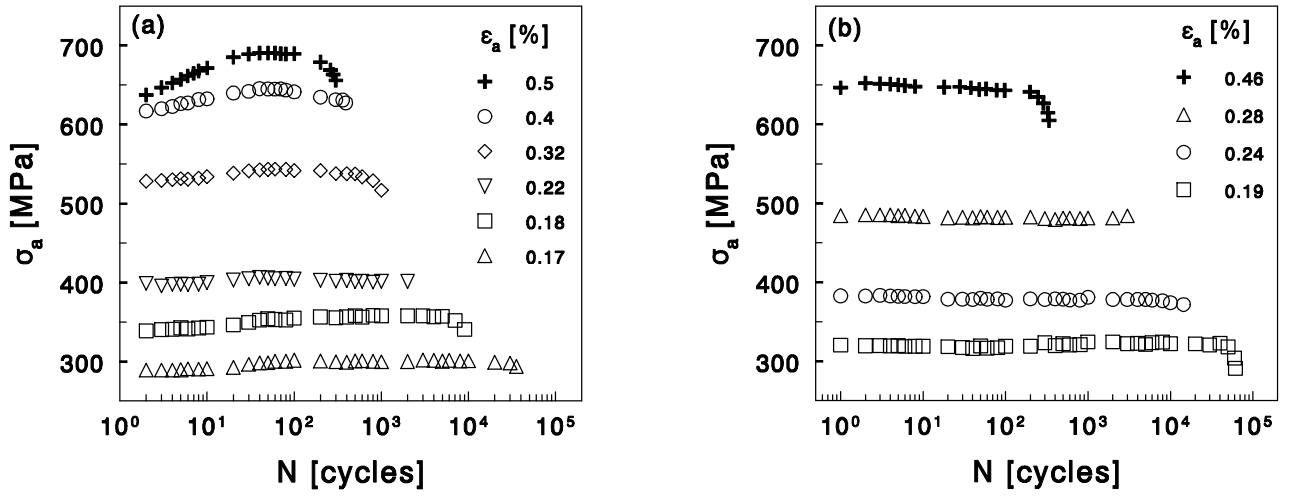


Fig. 1. Fatigue hardening/softening curves of the uncoated (a) and coated (b) superalloy Inconel 738LC.

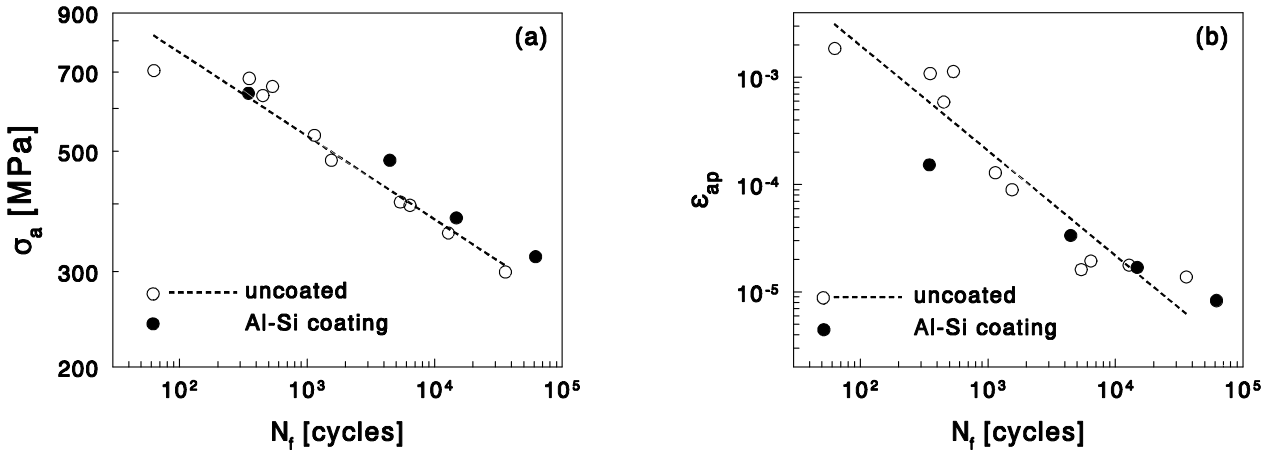


Fig. 2. Fatigue life curves of the surface treated and untreated Inconel 738LC in Basquin (a) and Manson-Coffin (b) representation.

evaluated using regression analysis for the uncoated material. Fatigue life curves in the representation of the plastic strain amplitude ε_{ap} at half life vs. the number of cycles to fracture N_f are shown in Fig. 2b. Experimental data were fitted by the Manson-Coffin law

$$\log 2N_f = (1/c) \log \varepsilon_{ap} - (1/c) \log \varepsilon_f' \quad . \tag{2}$$

The fatigue ductility coefficient, $\varepsilon_f' = 0.96$, and the fatigue ductility exponent, $c = 1.10$, were evaluated using regression analysis for the uncoated material. It can be seen from Fig. 2 that the effect of the Al-Si diffusion coating depends on amplitude. In the low amplitude domain, the surface treatment results in fatigue life improvement – see Fig. 1a. The detrimental influence of the coating is apparent for high amplitudes in the Manson-Coffin representation – see Fig. 2b.

Fig. 3 shows the cyclic stress-strain curve both for the uncoated and coated material. The stress amplitude σ_a is plotted vs. the plastic strain amplitude ε_{ap} at half-life. Experimental data were approximated by the power law

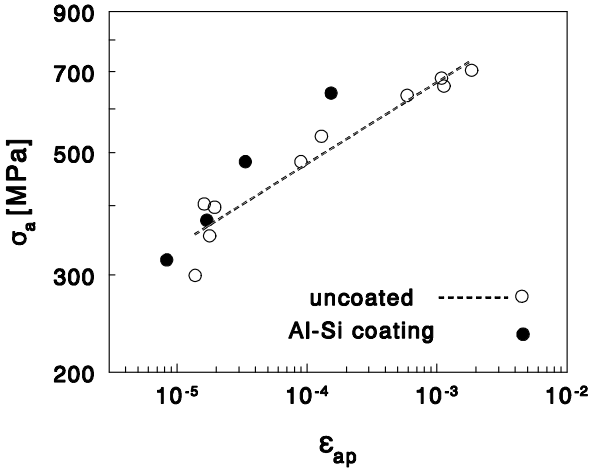


Fig. 3. Cyclic stress-strain curves of uncoated and coated Inconel 738LC.

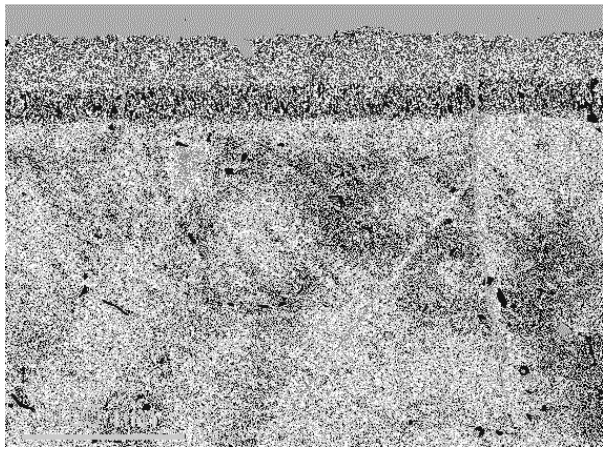


Fig. 4. Fatigue cracks growing from the surface to the substrate of a coated specimen (LM).

$$\log \sigma_a = \log K' + n' \log \varepsilon_{ap}. \quad (3)$$

Fatigue hardening coefficient K'= 1860 MPa and fatigue hardening exponent n'= 0.148 were evaluated using linear regression analysis in the uncoated material. The diffusion coating results in the increase of the stress response for high amplitudes. For the given plastic strain amplitude, the stress amplitude of the coated superalloy is increased in comparison with the uncoated material – see Fig. 3.

An optical micrograph of the etched section parallel to the loading axis of a coated specimen cycled to fracture (ε_a = 0.24 %, N_f = 14844 cycles) is shown in Fig. 4. Two fatigue cracks growing from the surface through the diffusion layer to the substrate can be seen in Fig. 4. The density of cracks initiated at the surface and propagated to the substrate is higher in coated specimens than in uncoated ones for similar strain amplitudes. Therefore, the surface crack initiation is more homogeneous in the coated material.

Present results show that Al-Si diffusion coating has beneficial effect on the fatigue life of Inconel 738LC in the high amplitude domain. Particularly the Basquin life curve of the coated material is shifted to higher fatigue lives in comparison with that of the uncoated superalloy – see Fig 2. The main crack initiates preferably at casting defects. Since surface defects are covered by the coating the crack initiation becomes more difficult because it is subsurface and in oxygen-free environment. This results in the life extension in comparison with the uncoated material.

Conclusions

The results of the total strain controlled tests both on the coated and uncoated Inconel 738LC led to the following conclusions.

1) Surface treatment of Inconel 738LC by the Al-Si diffusion coating results in changes of the fatigue behavior of Inconel 738LC.
2) The stress response at half-life of the coated material is higher than that of the uncoated superalloy at the same strain amplitude in the high amplitude domain.
3) The Al-Si diffusion coating has beneficial effect on the fatigue life of Inconel 738LC for low amplitudes. Basquin curve of the coated material is shifted to the higher fatigue life in comparison with the uncoated one.
4) Surface crack initiation is more homogeneous in the coated material.

Acknowledgements

The financial support of the research project AV0Z 20410507of the Academy of Sciences of the Czech Republic and the grants Nos. 106/09/P522 and P107/11/2065 of the Grant Agency of the Czech Republic and the grant No. 2E13800119 of the FME BUT is gratefully acknowledged.

References

[1] K. Obrtlík, A. Chlupová, M. Petrenec and J. Polák: Key Eng. Mater. Vols. 385-387 (2008), p. 581.

[2] M.J. Donachie and S.J. Donachie: *Superalloys: A Technical Guide.* (ASM International, Materials Park 2002).

[3] V. Bicego, P. Bontempi and N. Taylor, in: *Low cycle fatigue and elasto-plastic behaviour of materials*, edited by K.-T. Rie and P.D. Portella, Elsevier Science Ltd Amsterdam (1998), p. 137.

[4] K. Rahmani and S. Nategh,: Mater. Sci. Eng. Vol. A486 (2008), p. 686.

[5] M. Juliš, K. Obrtlík, S. Pospíšilová, T. Podrábský and J. Polák: Procedia Eng. Vol. 2 (2010) 1983.

© (2012) Trans Tech Publications, Switzerland
doi:10.4028/www.scientific.net/KEM.488-489.311

Effect of Friction Stir Welding Condition on Fatigue Limit of Welded Non-combustible Mg Alloy

Komei HAYASHI[1,a], Shigeru HAMADA[1,b], Ichinori SHIGEMATSU[2,c], Michiru SAKAMOTO[2,d] and Hiroshi NOGUCHI[1,e]

[1]Department of Mechanical Engineering, Faculty of Engineering, Kyushu University, 744 Motooka, Nishi-ku, Fukuoka-shi, Fukuoka 819-0395 Japan

[2]National Institute of Advanced Industrial Science and Technology (AIST),2266-98 Anagahora, Shimo-Shidami, Moriyama-ku, Nagoya, Aichi 463-8560 Japan

[a]hayashi@mech.kyushu-u.ac.jp, [b]hamada@mech.kyushu-u.ac.jp, [c]i-shigematsu@aist.go.jp, [d]michiru-sakamoto@aist.go.jp, [c]nogu@mech.kyushu-u.ac.jp

Keywords: Fatigue, Threshold Stress Intensity Factor Range, FSW, Non-combustible Mg Alloy

Abstract. The atigue strength of Friction Stir Welding is affected by the structure and the welding defect size. The welding defect sizes have a scatter. Therfore, the effect of Friction Stir Welding condition on fatigue limit of welded noncombustible Mg alloy was investigated with the specimen which has a controlled defect size. As a result, the good correlation between the fatigue limit and the hardness of the welding area was clarified.

Introduction

The optimum welding condition of FSW is judged by the value of welding efficiency, and the existence of the defect judged from external appearance in many cases. However, the optimal welding condition obtained by such methods is not possible to be the optimum welding condition from a viewpoint of fatigue strength. It is because the metallographic structure of a welding changes according to the welding condition.

Fatigue strength consist of the basic fatigue strength characteristic and the disturbances (welding defects, groove gaps, etc.). In this study, by introducing an artificial defect into a FSW specimen, we fix the defect size and clarify mutual relation between the threshold stress intensity factor range and the hardness of the metallographic structure.

Tested materials and test methods

The tested material is non-combustible magnesium alloy; AMX602. Table 1 shows the chemical composition of AMX602. Table 2 shows the welding condition of the test sample. In this study, in order to avoid the defect produced by groove gap etc., the friction stir processing is performed to the surface of one plate instead of butt welding of two plates. The size of the plate is 150 mm ×200 mm, and thickness is 2 mm. From one plate which performed friction stirring processing, three sheets were cut at a time for fatigue test specimens (after-mentioned). Figure 1 shows a welding outline view. The condition 2600-200 which is the large conditions of the input-heat per unit time is smoother as for a surface state. Figure 2 shows the size of the test specimen used for the fatigue tests, and the size of the artificial defect for pre-crack introduction. Figure 3 shows the photograph of the test specimen before and after polishing. After removing stress concentration zones, such as a step which exists in a welding surface, the surface was polished to the mirror finished surface and the artificial defect was introduced into the center of the welding surface. Then, some loads were applied in order to initiate a crack from the artificial defect. The load condition was σ_a=45MPa and the stress ratio R= 0.05 (since introduction of the fatigue crack was difficult about the welding condition 1000-400, the pre-crack has not introduced). After the pre-crack has initiated and propagated to predetermined length, and vacuum annealing for 200 °C 60 minutes was performed in order to remove the plastic-deformation history at the tip of a crack.

First of all, hardness tests were performed in order to investigate correlation of a welding condition and hardness. The conditions of the hardness test are load 2.94 N, and holding time 30 seconds. The indentations were given to the same position as the artificial defect of the fatigue test specimen, i.e., the welding central part of the welding surface, and hardness was tested. Next, the threshold stress intensity factor was measured using the fatigue test specimen. The tension-compression fatigue testing machine was used for the test. The stress ratio R = 0.05 and frequency are 20 Hz. After the fatigue test, a fractographic study was performed using scanning electron microscope (SEM) and optical microscope.

Results and discussions

As a result of the hardness test, the Vickers hardness of the conditions 1000-400 was HV73.9, and the Vickers hardness of the conditions 2600-200 was HV82.5. Both are the averages of six points.

Figure 4 shows the test result of the threshold stress intensity factor range. On the conditions 2600-200, the introduced pre-crack became a fracture origin. Figure 5 shows the crack tip before and after the fatigue test. Vacuum annealing was carried out to the specimen which has the non-propagating crack, and the fatigue test was done again. The fatigue test was carried out until the specimen is broken. The sizes of the pre-crack measured from the fracture surface are a = 390μm, b = 250μm and $\sqrt{area}$ = 390μm. On the conditions 1000-400, the large artificial defect was introduced as compared with the artificial defect introduced into the conditions 2600-200. However, before the crack initiated from the artificial defect, it fractured at 108,000 cycles (σ_a=45MPa). Figure 6 shows the SEM photograph of the fracture origin which appeared on the fracture surface. The elementary analysis result of the defect of a = 140μm, b = 55μm, and $\sqrt{area}$ = 110μm fracture origin of the size of a crack is the same as the result of base metallographic structure, and it turned out that a fracture origin is not an inclusion. Figure 7 shows the optical microscope photograph of the specimen side face. The crack which caused the fracture is just initiated on the boundary between a friction stir area and a base-metal area. It turns out that cracks were found besides the final fracture, and these cracks including the fracture origin crack are initiated in accordance with the history of tool rotation. Since there were few input-heats, sufficient plastic flow is not happened, but it is presumed that it became a defect like the flow line in a casting. In Fig.4, the broken line shows the relation between the threshold stress intensity factor range of a non-combustible magnesium alloy and a crack size in the small crack region obtained by our previous study. The equation is shown below.

$$\Delta K_{th} = 3.3\times10^{-3}(HV+25)(\sqrt{area})^{1/3}\sqrt{(1-R)/2}\text{ , R=0.05} \quad (1)$$

ΔK_{th} : Threshold stress intensity factor range [MPa$\sqrt{m}$] $\sqrt{area}$: Crack size [μm]

An alternate long and two short dashes line shows the predicted value of the threshold stress intensity factor range at $\sqrt{area}$ = 110μm. And an alternate long and short dash line shows the predicted value of the threshold stress intensity factor range at $\sqrt{area}$ = 390μm. On the conditions 1000-400, since the crack initiated on the boundary of base metal and a friction stir area, the hardness is considered same as the hardness of the base-metal. The Vickers hardness of the base-metal is HV60. In addition, the non-fracturing test result was not obtained on the conditions 1000-400. Then, fatigue limit of the specimen on the condition 1000-400 is predicted using modified S-N diagram. Modified S-N diagram is the S-N diagram normalized with the predicted value of the fatigue limit. The modified S-N diagram of a non-combustible magnesium alloy is shown in Figure 8. Using the fatigue test result and the modified S-N diagram, predicted fatigue limit of the condition 1000-400 is σ_w = 33MPa. In this study, defects existed in a friction stir area or the boundary of a stir area and base-metal. And from Fig. 4, it became clear that there are good mutual relation between hardness and fatigue limit in both cases.

Conclusions

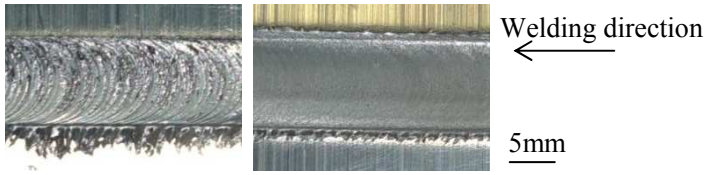
The fatigue tests were performed using friction stir welding material with the defect by which the size was controlled for the purpose of clarifying mutual relation of the fatigue limit of non-combustible magnesium alloy friction stir welding material, and the metallographic structure of the welding. The obtained results are shown as follows. 1) The discontinuous area of the structure which cannot delete by specimen surface lapping may exist in the boundary between a friction stir area and a base-metal area. This discontinuous area tends to produce the input-heat per unit time in few welding conditions. 2) When a defect exists in the friction stir area and the boundary between friction stir area and base-metal area, the fatigue limit of these parts has good correlation to the hardness of a fracture origin.

Table 1 Chemical composition

Al	Mn	Ca	Zn	Si	Cu	Ni	Fe	Mg
0.58	0.34	1.89	0.0024	0.029	0.001	<0.001	<0.001	Bal.

Table 2 Welding condition

Condition No.	Rotation speed [rpm]	Welding speed [mm/min]
1000-400	1000	400
2600-200	2600	200



(a) 1000-400 (b) 2600-200

Figure 1 Appearances of FSW

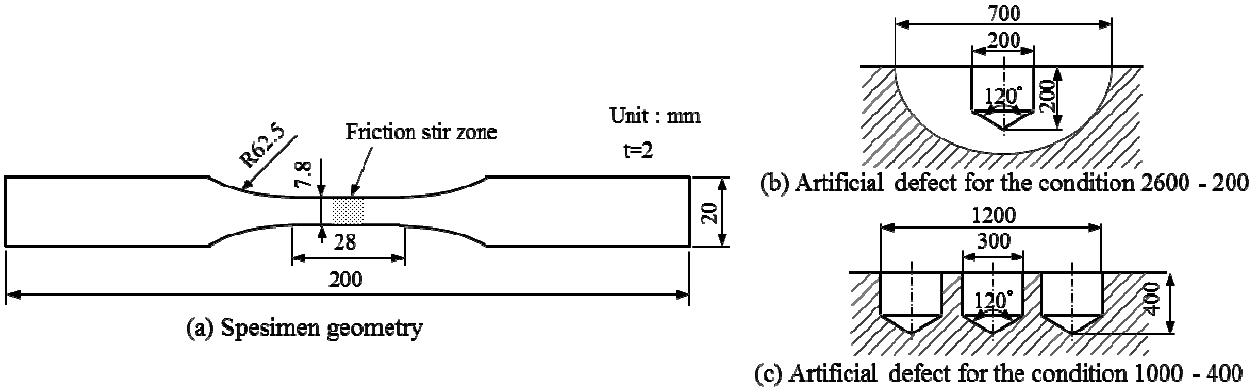


Figure 2 Shapes and dimensions of the specimen

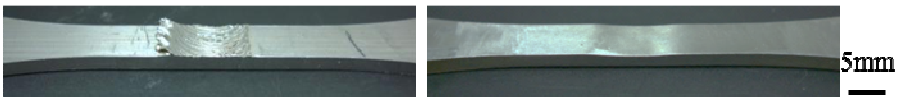


Figure 3 Appearances of FSW before and after polishing

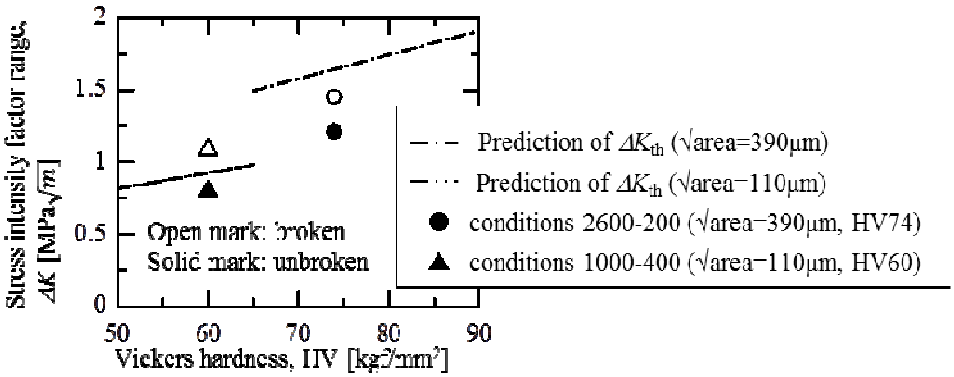


Figure 4 Relationship between ΔK_{th} and Vickers hardness

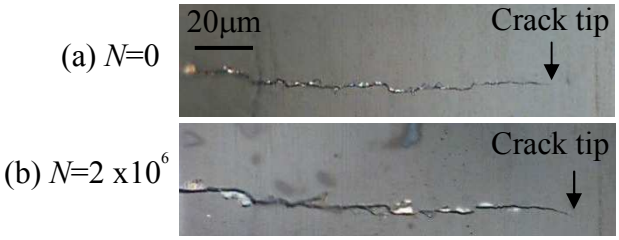


Figure 5 Non-propagation cracks

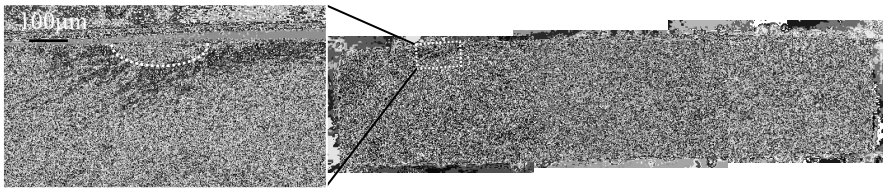


Figure 6 Scanning electron microscope photograph of the crack origin

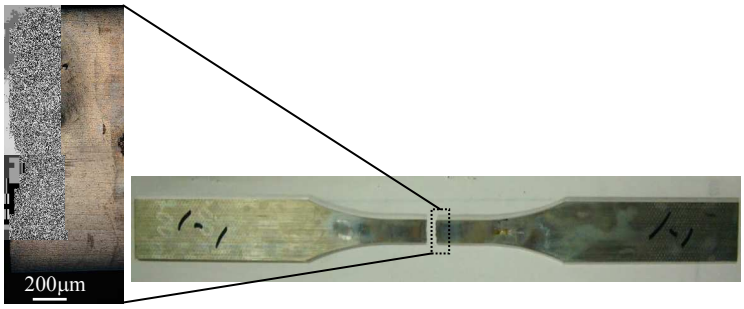


Figure 7 Optical microscope photograph of the specimen side face

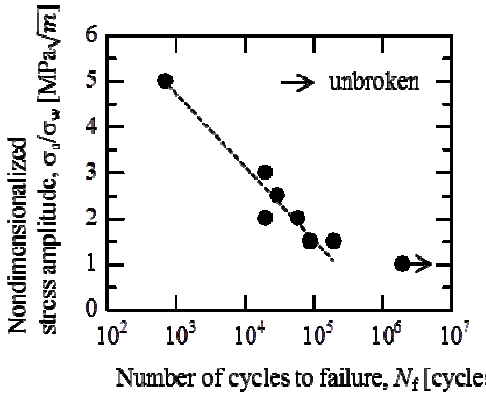


Figure 8 Modified *S-N* curve of non-combustible Mg alloy (R=0.05)

© (2012) Trans Tech Publications, Switzerland
doi:10.4028/www.scientific.net/KEM.488-489.315

A role of destructive and non-destructive tests in creep damage identification

Z. L. Kowalewski[1,a], T. Szymczak[2,b], K. Makowska[3,c] and B. Augustyniak[4,d]

[1]Institute of Fundamental and Technological Research Polish Academy of Sciences, 5B Pawinskiego Street, 02-106 Warsaw, Poland

[2,3]Motor Transport Institute, 80 Jagiellonska Street, 03-301 Warsaw, Poland

[4]Gdansk University of Technology, 11/12 Narutowicza Street, 80-233 Gdansk, Poland

[a]zkowalew@ippt.gov.pl, [b]tadeusz.szymczak@its.waw.pl, [c]katarzyna.makowska@its.waw.pl, [d]bolek@mifgate.mif.pg.gda.pl

Keywords: creep, damage, yield point, ultimate tensile stress, Young's modulus, acoustic birefringence, magnetoacoustic emission.

Abstract. The paper presents relationships between strain level generated by creep process and two parameters determined form non-destructive tests, i.e. acoustic birefringence and amplitude of magnetoacoustic emission for three kinds of steel: 40HNMA, P91 and 13HMF. Moreover, the relationships between prior deformation level and selected mechanical parameters resulting from the standard tensile tests subsequently carried out at room temperature were established. As a consequence, this enabled to formulate mutual relationships between these mechanical parameters and parameters obtained from the ultrasonic/magnetic investigations.

Introduction

The aim of this work was to find certain possible relationships between parameters achieved by means of non-destructive and destructive experimental techniques in order to provide a new effective tool for damage assessments in some very responsible structural elements. Nowadays, this task is extremely important for such industrial branches in which the fracture may have a serious consequences related to environment and human being security, i.e.: chemical enterprises, coal or nuclear power stations, etc.

The destructive investigations comprised creep tests interrupted for different time periods; followed by the first series of specimens was subjected to monotonic tension up to fracture, while the second one with the same levels of predeformation was tested using non-destructive techniques. This enabled to obtain variations of non-destructive test parameters versus prior deformation and also allowed to check an influence of creep prestrain on the stress-strain characteristics, and as a consequence, on variations of such conventional mechanical parameters as: Young's modulus, yield point and ultimate tensile stress. The second part of the experimental program was devoted to investigations of non-destructive parameters (acoustic birefringence, amplitude of magnetoacoustic emission) and their correlations with mechanical parameters determined on the basis of tensile tests. The special notice was devoted to the early stage of degradation of the materials.

Experimental procedure

Three steels commonly used in the petrochemical industry in Poland (40HNMA, P91 and 13HMF) were selected for investigations. The plane specimens having rectangular cross section of 5mm×7mm dimensions and gauge length of 40 mm were subjected to creep prestraining at 773K. The process was interrupted for different time periods. In the case of 40HNMA steel the creep stress level was equal to 250MPa and the process was interrupted at selected points of the creep curve to achieve the following strain levels: 0.36%, 0.81%, 1.13%, 1.20%, 2.30%, 4.00% and 6.51%. For the P91 steel the creep process was conducted under tensile stress equal to 290MPa, and interrupted to

obtain prior deformation levels of: 0.85%, 1.80%, 3.15%, 4.60%, 5.40%, 7.90% and 10.00%. In the case of 13HMF steel creep tests were carried out under 180MPa and the following prestrain levels were selected: 5.92%, 10.06%, 17.90%, 30.46%, 34.10% and 40.19%. The ultrasonic technique was applied to determine variation of the acoustic birefringence as a function of prior creep deformation. Similar relation was established for the magnetoacoustic emission on the basis of tests performed using magnetic method. A magnitude of the acoustic birefringence was estimated from velocity difference of two shear waves polarized in the perpendicular directions [1]. The magnetoacoustic emission, defined as an acoustic signal generated during the movement of 90° domain walls due to local volume changes in the material having a non-zero magnetostriction [2], was measured by means of the piezoelectric transducer. The measuring set used to investigate the magnetoacoustic emission was described in detail in the previous paper [3]. Relationships between prestrain levels and acoustic birefringence, and moreover, between prestrain levels and amplitude of the magnetoacoustic emission were determined. In the next step of the experimental program the standard tensile tests were carried out. The yield point, ultimate tensile strength and Young's modulus were calculated on the basis of these tests. The relations between prestrain levels and just mentioned mechanical parameters were analyzed. Having these results and those previously elaborated for the non-destructive parameters allowed finally to find mutual relationships between acoustic birefringence/magnetoacoustic emission and yield point/ultimate tensile strength.

Results

Chemical composition of the tested steels is presented in Table 1. The materials differ from each other in carbon content and microstructure. The microstructures of 40HNMA and P91 steels consist of the sorbite with remaining needle martensite configuration, whereas the microstructure of 13HMF steel consists of ferrite and carbide precipitations mixture.

Table 1. Chemical composition of tested steels. Numbers denote percentage by weight.

material	C	Si	Mn	P	S	Cr	Mo	Ni	V	Cu	Fe
40HNMA	0.36	0.58	0.45	0.015	0.010	0.80	0.43	1.82	0.01	0.16	rest
P91	0.08	0.40	0.45	0.013	0.010	8.80	0.90	0.31	0.21	0.12	rest
13HMF	0.13	0.15	0.55	0.030	0.012	0.40	0.62	0.05	-	0.04	rest

Figure 1 presents variation of the acoustic birefringence for each steel versus creep prestrain level. A decrease of the acoustic birefringence is caused by a diversification of the shear waves velocities polarized along theirs axes and in the perpendicular direction (a velocity of the longitudinal waves in the loading direction applied decreases more rapidly than that of the longitudinal waves in perpendicular direction). This is due to preferential orientation of microstructure [4].

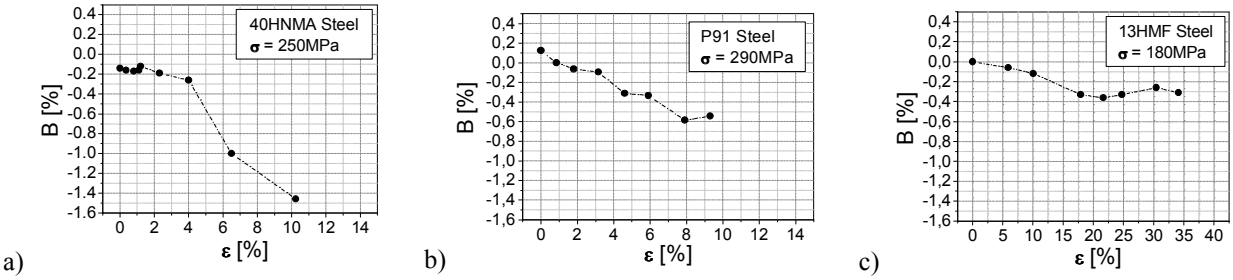


Fig. 1. The acoustic birefringence versus prestrain for: a) 40HNMA, b) P91, c) 13HMF

In the case of 40HNMA steel, the amplitude of magnetoacoustic emission increases at the first stage of creep and decreases at the second and tertiary periods of the process, whereas amplitude of the magnetoacoustic emission of the P91 and 13HMF steels decreases at all stages of creep (Fig. 2). The maximum visible for the 40HNMA steel (Fig. 2a) might be connected with the presence in this material a significantly greater amount of non-metallic inclusions in comparison to that for the P91 and 13HMF steels observed.

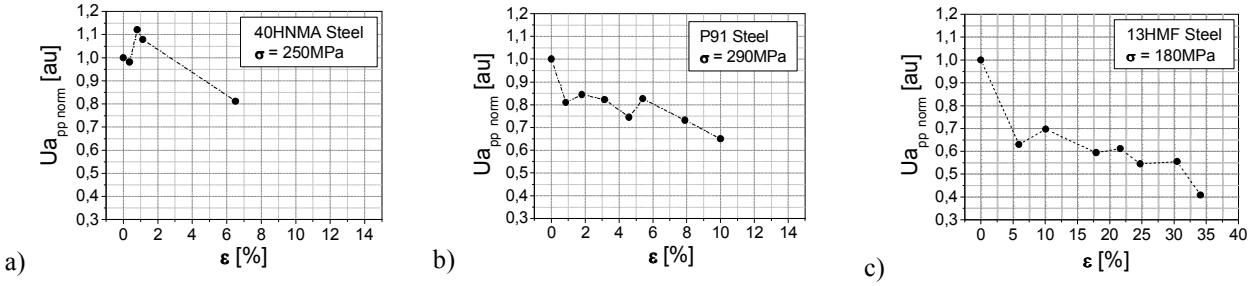


Fig. 2. Amplitude variation of the magnetoacoustic emission versus prestrain for: a) 40HNMA, b) P91, c) 13HMF

The yield point and ultimate tensile stress variation as a function of prestrain level and relationships between Young's modulus and prestrain are shown in Fig. 3a-f. The yield point and ultimate tensile stress of the 40HNMA steel decrease with prior deformation level increase (Fig. 3a). The slight drop of the yield point was observed for the P91 steel, whereas its ultimate tensile stress was almost insensitive to creep prestrains (Fig. 3b). In the case of 13HMF steel a prior deformation leads to the hardening effect. Additionally, it can be noticed that Young's modulus almost does not change with the creep prestrains (Fig. 3d-f).

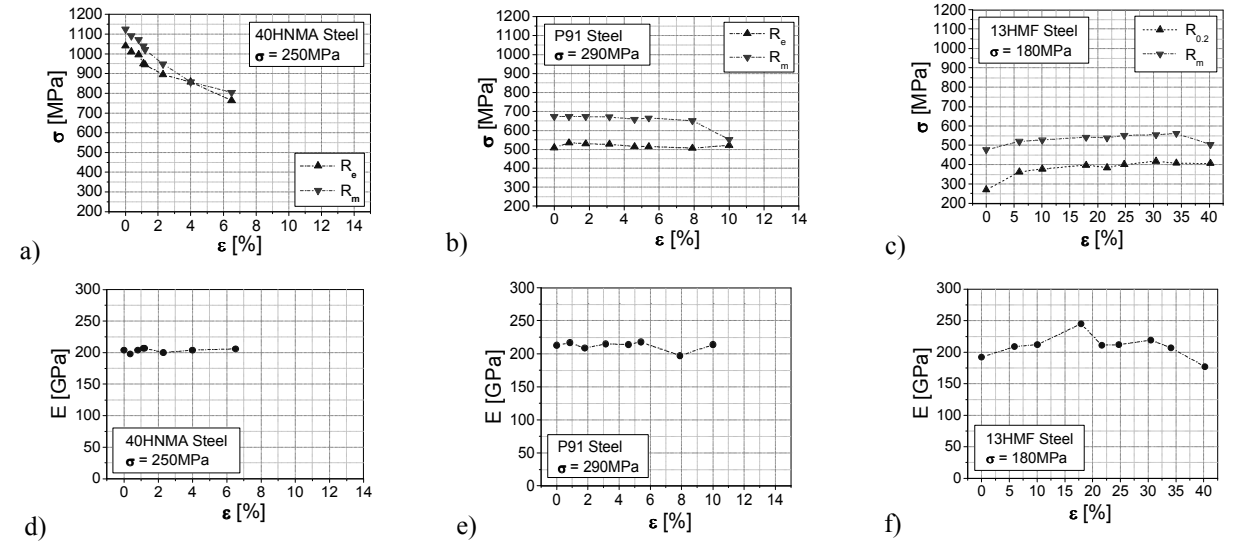


Fig. 3. Relationships between mechanical properties and creep pre-strains for: 40HNMA (a,d), P91 (b,e), 13HMF (c,f)

The relationships between mechanical properties and acoustic birefringence are presented in Fig. 4a-c, whereas in Fig. 4d-f the same mechanical properties are expressed as functions of the magnetoacoustic emission. The yield point and ultimate tensile stress of the 40HNMA steel as a function of the acoustic birefringence can be described with reasonably good accuracy by the linear relations in the range of the first and second periods of creep (Fig. 4a). The mechanical properties are almost insensitive to acoustic birefringence variations in the case of P91 steel (Fig. 4b). For the 13HMF steel a relation between the same parameters can be well expressed using non-linear functions (Fig. 4c). As it is seen in Fig. 4d-f, the yield point and ultimate tensile stress variations versus the amplitude of magnetoacoustic emission have almost the same character for all materials in question. In the case of P91 and 13HMF steels, they are mainly linear what is in contradiction to the results obtained for the 40HNMA steel. The yield point of the P91 steel in opposite to the 40HNMA and 13HMF steels versus the amplitude of magnetoacoustic emission does not change essentially (Fig 4e). The highest increase of the ultimate tensile stress with an increase of the magnetoacoustic emission amplitude was observed for the 40HNMA steel (Fig. 4d).

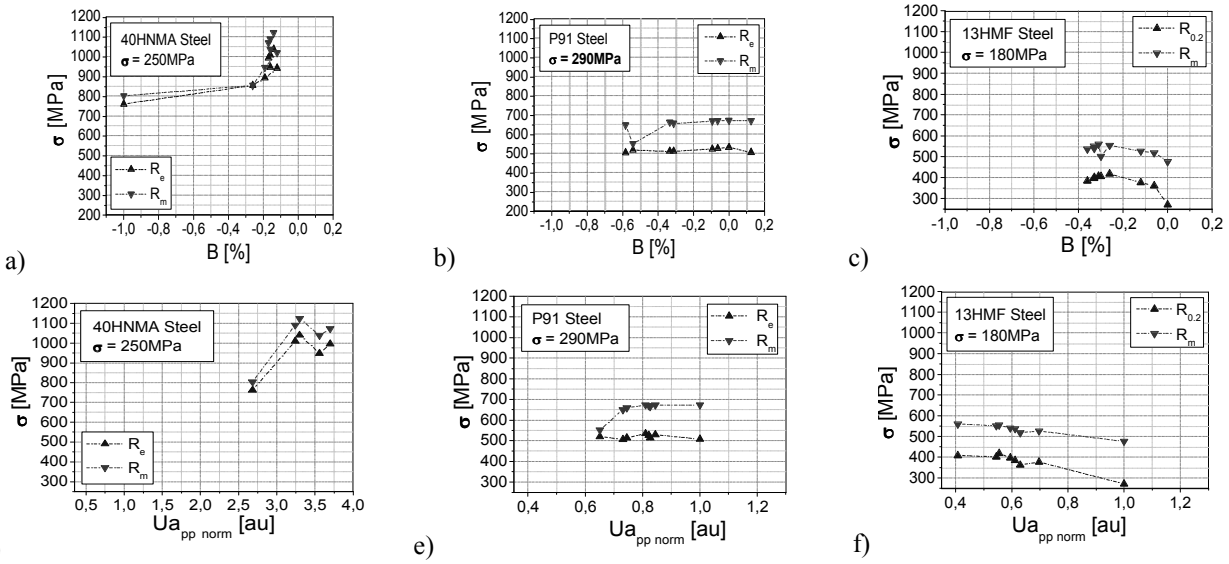


Fig. 4. Yield point and ultimate tensile stress versus acoustic birefringence (a-c) and magnetoacoustic emission (d-f) for: a,d) 40HNMA, b,e) P91, c,f) 13HMF

Summary

The results for the 40HNMA steel (in comparison to the P91 and 13HMF) exhibit the strongest variations of non-destructive and destructive parameters versus prior creep deformation. This is related to a quantity and distribution of non-metallic inclusions in the steel matrix. In the case of 40HNMA steel the quantity of non-metallic inclusions was significantly greater than for the other steels investigated in this research (P91 and 13HMF). Young's modulus variations for all tested steels were practically insignificant independently on the creep prestrain level.

The mutual relationships established between parameters of destructive and nondestructive testing techniques provide a new promising tool for better damage development evaluation. Such relationships give a great opportunities for the effective remaining lifetime predictions of many structural elements, what may decrease costs connected with pipelines maintenance in power stations for example.

Acknowledgments

The research was performed within the project R15004904 with financial support from the Ministry of Sciences and Higher Education of Poland.

References

[1] Z.L. Kowalewski, J. Szelążek, S. Mackiewicz, B. Augustyniak: *A role of interdisciplinarity in a damage degree investigations of power plant steels*, XVI Seminar on Nondestructive Material Testing, Zakopane, Poland (2009)

[2] D. Jiles: *Introduction to magnetism and magnetic materials* (Taylor and Francis Group, New York 1998)

[3] Z.L. Kowalewski, B. Augustyniak, J. Szelążek, S. Mackiewicz: *Destructive and non-destructive methods for damage assessment in steels used at power plants,* Proc. of Plasticity2008, ed. by A.S. Khan/NEAT Press, Full Ton, Maryland (2008)

[4] G. Sposito, C. Ward, P. Cawley, P.B. Nagy, C. Scruby*: A review of non-destructive techniques for the detection of creep damage in power plant steels*, NDT&E International Vol. 43 (2010)

© (2012) Trans Tech Publications, Switzerland
doi:10.4028/www.scientific.net/KEM.488-489.319

Small fatigue crack growth behavior from artificial notch with focused ion beam in annealed 0.45% carbon steel

Junji SAKAMOTO[1,a], Yoshimasa TAKAHASHI[2,b] and Hiroshi NOGUCHI[3,c]

[1,3]Department of Mechanical Engineering, Kyushu University, 744 Motooka, Nishi-ku, Fukuoka-shi, Fukuoka 819-0395 Japan

[2]National Institute of Advanced Industrial Science and Technology (AIST), 744 Motooka, Nishi-ku, Fukuoka 819-0395 Japan

[a]sakamoto@mech.kyushu-u.ac.jp, [b]yoshim.takahashi@aist.go.jp, [c]nogu@mech.kyushu-u.ac.jp

Keywords: artificial pre-crack, fatigue limit, focused ion beam, small fatigue crack growth analysis

Abstract The aim of this study is firstly to investigate the applicability of a sharp notch with Focused Ion Beam (FIB) as a crack for fatigue limit evaluation. Secondly we investigate a condition in which artificial defects (drilled hole, FIB notch) can be used as a crack for fatigue limit evaluation. To achieve the aim, the growth behaviors and the non-propagating crack sizes of small fatigue cracks initiated from a FIB notch and a drilled hole are carefully compared with those of an annealed fatigue crack which imitates an ideally sharp crack. The results show that a FIB notch can be used as a crack for fatigue limit evaluation under some conditions. The results also show that the condition which controls the applicability of an artificial defect as an ideal crack for fatigue limit evaluation is strongly dependent on the relation between (i) the length of a non-propagating fatigue crack and (ii) the crack length when the small fatigue crack growth behaviors from an artificial defect and an ideal pre-crack become almost the same. It is found that the length of (ii) can be obtained by the analyses using the number of cycles from a certain crack length to failure.

Introduction

The fatigue limits of metal components are usually controlled by the threshold stress against the propagation of small fatigue crack initiated from flaws or naturally initiated cracks. The threshold stress intensity factor range (ΔK_{th}) value of a long fatigue crack is constant irrespective of the initial crack size. On the other hand, the ΔK_{th} value of a small fatigue crack depends on the initial crack size [1]. Therefore, an artificial crack, whose size is precisely controlled, needs to be introduced for fatigue limit evaluation.

Various types of artificial defects have been used for fatigue limit evaluation in the previous studies. Some studies have used annealed fatigue pre-cracks which imitated an ideally sharp crack. The method, however, can only be applied to materials that exhibit no micron structure change during annealing [2]. Some other studies have simply introduced drilled holes on the specimen surface, but the shape of a drilled hole is completely different from a sharp crack [3].

Recently, a sharp notch introduced by FIB technique has been used as an artificial defect [4]. The growth behaviors of a small fatigue crack initiated from a FIB notch and a naturally initiated crack were found to be similar during the finite life regime. However, it is not clear whether or not a FIB notch can be used as a crack for fatigue limit evaluation.

The aim of this study is firstly to investigate the applicability of a FIB notch as a crack for a fatigue limit evaluation. Secondly we investigate a condition in which artificial defects (drilled hole, FIB notch) can be used as a crack for a fatigue limit evaluation. To achieve the aim, the growth behaviors and the non-propagating crack sizes of small fatigue cracks initiated from a FIB notch and a drilled hole are carefully compared with those of an annealed fatigue crack.

Materials and method

In order to achieve the aforementioned aim, an annealed S45C steel was used as the testing material as its microstructure is not changed by annealing. Tables 1 and 2 show the chemical composition and mechanical properties of a JIS S45C steel, respectively. Figure 1 shows the shape and dimension of the specimen. Three different kinds of artificial defects were introduced on each specimen surface; a drilled hole (specimen A), a FIB notch (specimen B) and an annealed fatigue crack (specimen C), whose surface lengths perpendicular to the axial direction were about 100 μm.

The fatigue test was conducted by using an Ono-type rotating bending machine (3000 rpm) in laboratory air at room temperature. Crack length (a) including the defect length was measured perpendicular to the axial direction by a replica method.

Table 1. Chemical composition (wt.%)

C	Si	Mn	P	S	Al
0.46	0.20	0.73	0.029	0.017	0.018

Table 2. Mechanical properties

σ_{sl}	σ_B	Hv
360	633	185

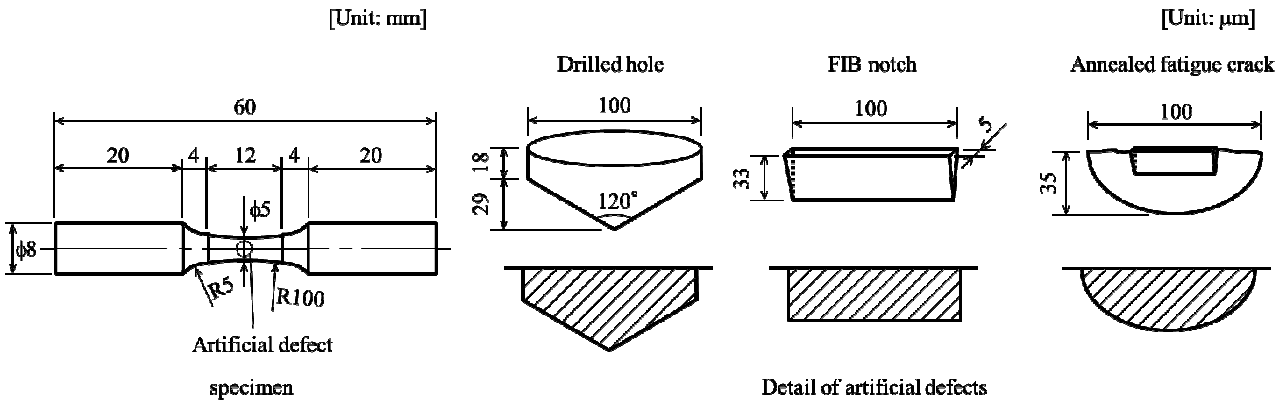


Figure 1. Shape and dimension of specimen

Results and discussion

Firstly, the applicability of a FIB notch as a crack for fatigue limit evaluation is investigated. Figure 2 shows the relation between the stress amplitude (σ_a) and the number of cycles to failure (N_f) of specimen A, B and C. In Fig. 2, the fatigue limits (σ_w) of specimen A, B and C are 258 MPa,

250 MPa and 255 MPa, respectively. This result shows that the fatigue limit changes according to the defect type even if the surface defect lengths are almost the same. The difference of fatigue limits may result from the difference of $\sqrt{area}$ parameter (the shaded area shown in Fig. 1 is *area*; the area projected on the principal stress plane). Therefore, the evaluation which is not affected by the *area* is tried. The fatigue limit values are then normalized by the fatigue limit predicted by using Eq. (1).

$$\sigma_{w,predicted} = 1.43(Hv + 120)/(\sqrt{area})^{1/6}. \quad (1)$$

Here, the $\sqrt{area}$ of each specimen was obtained by the fracture surface observation. The normalized fatigue limits ($\sigma_w/\sigma_{w,predicted}$) of specimen A, B and C are derived as 1.18, 1.10, 1.20, respectively. $\sigma_w/\sigma_{w,predicted}$ values of specimen B and C are almost the same while $\sigma_w/\sigma_{w,predicted}$ value of specimen A is different from that of specimen C. The result shows that a FIB notch can be used as a crack for fatigue limit evaluation in the present testing condition, on the other hand, a drilled hole cannot be used as a crack for fatigue limit evaluation.

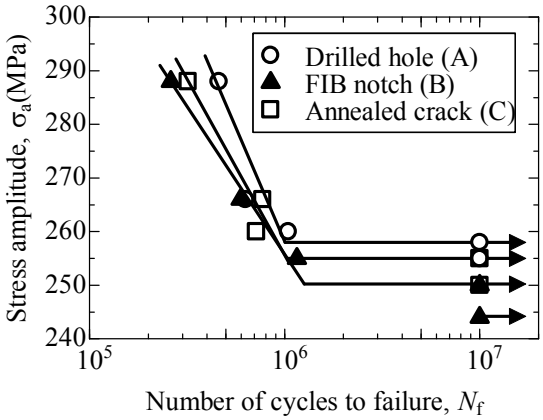
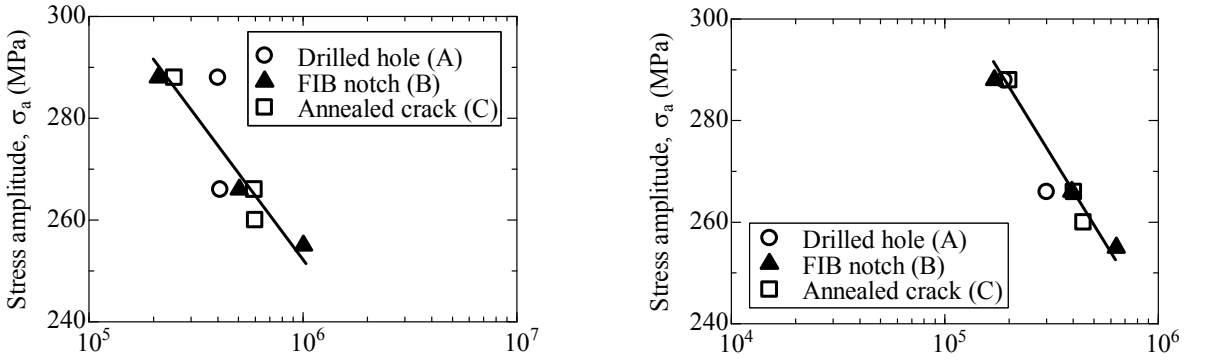


Figure 2. Relation between stress amplitude, σ_a, and number of cycles to failure, N_f, of specimen A, B and C.

Secondly, we focus on the condition which controls the applicability of an artificial defect as an ideal crack for fatigue limit evaluation. Figure 3 shows the relation between σ_a and the number of cycles from a certain crack length to failure for specimen A, B and C; (a) N_f-$N_{a=130}$, (b) N_f-$N_{a=200}$. In Fig. 2, the *S-N* curves for various types do not coincide in the finite life regime. In Fig. 3(a), the curves for specimens B and C coincide. In Fig. 3(b), the curves for all specimen types coincide. This means that the growth behaviors of small fatigue cracks in specimens B and C are essentially the same after the surface crack lengths reach 130 μm and, further more, the growth behaviors of small fatigue cracks are almost specimen independent after the surface crack lengths reach 200 μm. This indicates that the effect of defect shape on fatigue crack growth is almost negligible when the crack propagates to some extent. On the other hand, at the fatigue limit stress levels, non-propagating fatigue crack was not observed in specimen A, while the non-propagating fatigue crack lengths of specimen B and C were 150 μm and 182 μm, respectively. It is then postulated that the fatigue crack initiated from a FIB notch became non-propagating after the effect of defect shape

was almost negligible. Considering the difference of fatigue limits of specimen A, B and C, it seems that the fatigue limit of a specimen with artificial defect is different from that of a specimen with an ideal pre-crack when the fatigue crack initiated from the defect becomes non-propagating before the effect of defect shape is almost negligible. It is inferred from these results that whether or not an artificial defect, whose shape is not identical to a sharp crack, can be used as a crack for fatigue limit evaluation is defined by the relation between (i) the length of a non-propagating crack and (ii) the crack length when the small fatigue crack growth behaviors from an artificial defect and an ideal pre-crack become almost the same.



(a) Number of cycles from crack length 130 μm to failure, N_f-$N_{a=130}$

(b) Number of cycles from crack length 200 μm to failure, N_f-$N_{a=200}$

Figure 3. Relation between σ_a and number of cycles from a certain crack length to failure for specimen A, B and C

Conclusion

(1) A FIB notch can be used as a crack for fatigue limit evaluation under some conditions.

(2) The condition which controls the applicability of an artificial defect as an ideal crack for fatigue limit evaluation is strongly related to the relation between (i) the length of a non-propagating fatigue crack and (ii) the crack length when the small fatigue crack growth behaviors from an artificial defect and an ideal pre-crack become almost the same.

(3) The length of (ii) can be obtained by the analyses using the number of cycles from a certain crack length to failure.

References

[1] N. E. Frost, L. P. Pook and K. Denton: Engineering Fracture Mechanics, Vol. 3 (1971), p. 109

[2] N. E. Frost: Proc. Instn. Mech. Engrs, Vol. 173-35 (1959), p.811

[3] Y. Murakami, Metal Fatigue: Effects of small Defects and Nonmetallic Inclusion, (1993)

[4] M. Marx, W. Schaf, H. Vehoff, C. Holzapfel: Materials Science and Engineering A, Vol. 435-436 (2006), p. 595-601

© (2012) Trans Tech Publications, Switzerland
doi:10.4028/www.scientific.net/KEM.488-489.323

Loading frequency effects on the fatigue crack growth rate and fracture surface morphology of low carbon steel in case of long-term use in hydrogen gas

A. Nishimoto[1,a], Y. Oda[2,b], H. Noguchi[2,c]

[1]Graduate School of Kyushu University, 744 Moto-oka, Nishi-ku, Fukuoka 819-0395, Japan

[2]Kyushu University, Faculty of Engineering, Collaborative Research Scientist of AIST, 744 Moto-oka, Nishi-ku, Fukuoka 819-0395, Japan

[a]2TE09318G@s.kyushu-u.ac.jp, [b]oda@mech.kyushu-u.ac.jp, [c]nogu@mech.kyushu-u.ac.jp

Keywords: Fatigue, Hydrogen embrittlement, Crack propagation, Fractography

Abstract

Loading frequency effects on FCGR and fracture surface morphology were investigated on pre-strained low carbon steel in high FCGR range. Loading frequency effects showed the different trend between internal hydrogen and environmental hydrogen. The effects of combined condition hydrogen revealed similar tendency of environmental hydrogen.

Introduction

It is one of the important issues for the metallic components exposed to hydrogen gas environment for a long term to evaluate the loading frequency effects on the fatigue crack growth rate (FCGR). As to hydrogen condition, not only environmental hydrogen[1] but also hydrogen which entered materials over a long time (internal hydrogen[2]) and the combination of these hydrogen should be considered. In this study, first, the effects of internal hydrogen and environmental hydrogen on the FCGR and fracture surface morphology were examined individually, then, the effects of combined[3] condition.

Experimental procedure

Specimen. The material used in this study is a low carbon steel (JIS S10C). This steel was annealed completely at 1173 K. In order to introduce hydrogen into the material, specimen was strained up to 10 % total strain after annealing. Figure 1 shows the specimen geometry. Internal hydrogen was charged by immersing specimens in an aqueous solution of 4 % ammonium thiocyanate (HN_4SCN) at 313 K for 48 hours. The hydrogen content of a charged specimen was 0.1-0.2 ppm.

Testing. In order to investigate the loading frequency effects on FCGR and fracture surface morphology, loading frequency change tests were conducted. Figure 2 shows the test wave profiles. The loading frequency was changed from 6 Hz to 6-0.001 Hz. In the case of internal hydrogen, H-charged specimens were tested in nitrogen gas. In the case of environmental hydrogen, uncharged specimen was tested in hydrogen gas. In the case of combined hydrogen condition, H-charged specimen was tested in hydrogen gas. All the tests were conducted at a total strain range of $\Delta\varepsilon_t$ = 0.7 % under fully-reversed loading in gas environment at an absolute pressure of 0.18 MPa and at a temperature of 313 K. In this study, the condition on FCG tests is suitable for observing brittle-like fracture surface in order to examine the effects of hydrogen easily.

Results and Discussion

Figure 3 shows the crack growth behavior in nitrogen. The loading frequency change points of all specimens were converged for comparison. The FCGR at low frequency accelerated after the frequency change point. Figure 4 shows the FCGR at a crack length of 900 μm corresponding to Fig. 3. The FCGR had a peak around 0.005 Hz and no influence of internal hydrogen around 6 Hz. Figure 5 shows a map of fracture surface. SEM images were captured right before and after the frequency change point. Figure 6 shows SEM images of fracture surface in nitrogen. Images of (v) and (vi) shows ductile fracture surface occupies around over the whole surface at high frequency whether internal hydrogen exist or not. In contrast, images of (i) - (iv) show brittle-like (quasi-cleavage) fracture surface appears at low frequency when internal hydrogen exists.

Figure 7 shows the crack growth behavior in hydrogen. The loading frequency change points of both specimens are converged for comparison. Both of the FCGR at low frequency decelerate after frequency change point. The degree of deceleration on uncharged specimen is larger than that on H-charged specimen. Figure 8 shows SEM images of fracture surface on uncharged specimen in hydrogen gas. The image of (b) was captured just before the frequency change point, and the image of (a) was captured just after that. The brittle-like fracture surface occupies around over the whole surface at high frequency area (b). In contrast, the ductile fracture surface with striation-like pattern increased drastically at low frequency area of (a).

Figure 9 shows SEM images of fracture surface on H-charged specimen in hydrogen gas. The image of (b) was captured just before frequency change point, and the image of (a) was captured just after that. The brittle-like fracture surface occupies around over the whole surface at high frequency area (b). Ductile fracture surface appears in the brittle like fracture surface at low frequency area (a).

Conclusions

(1) As the effect of internal hydrogen, decreasing loading frequency led to increasing FCGR with the transition from ductile to brittle-like fracture surface.

(2) As the effect of environmental hydrogen, decreasing loading frequency led to decreasing FCGR with the transition from brittle-like to ductile fracture surface.

(3) The loading frequency effects of combined hydrogen revealed the similar FCG characteristics of environmental hydrogen.

(4) Within these experimental conditions, even if internal hydrogen shows the most powerful effect on FCG, the effect of environmental hydrogen is considered to overcome that of internal hydrogen.

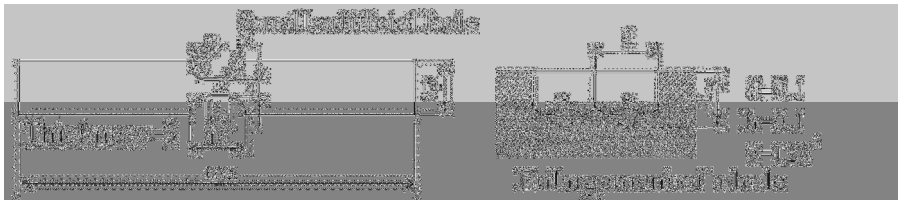


Fig. 1 Shapes and dimensions of specimen (in mm).

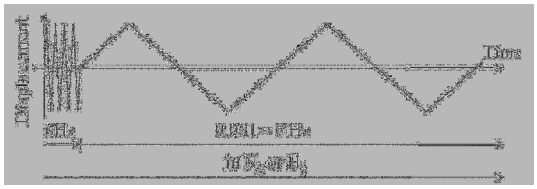


Fig. 2 Test wave profile.

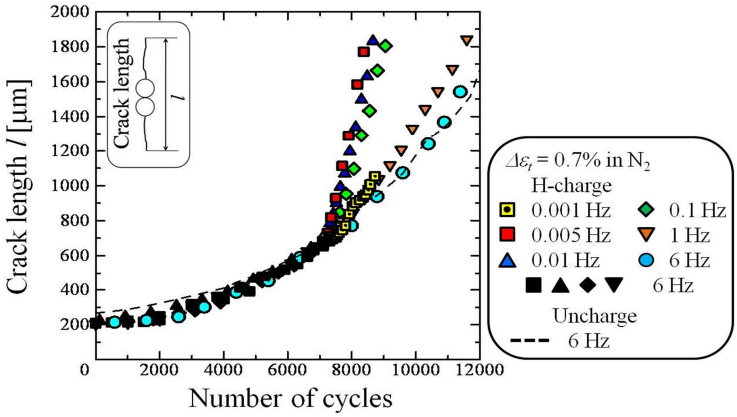


Fig. 3 Load frequency effect on crack growth behavior.

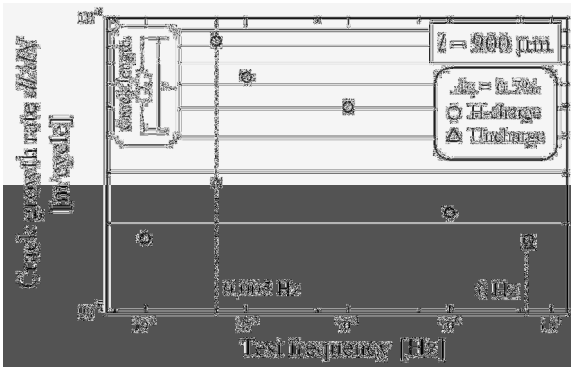


Fig. 4 Load frequency effect on FCGR.

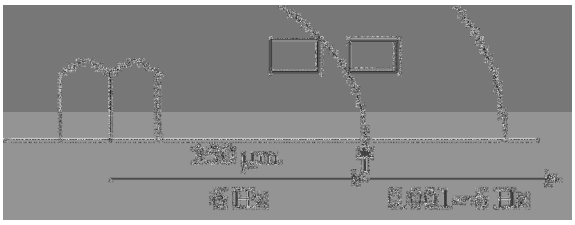
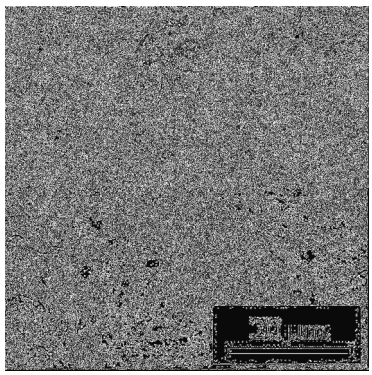
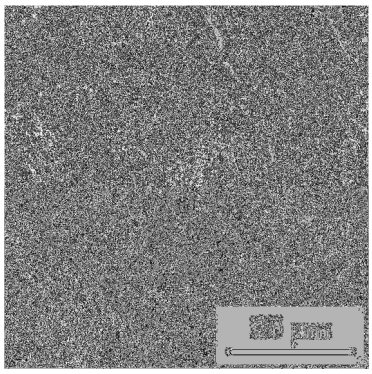


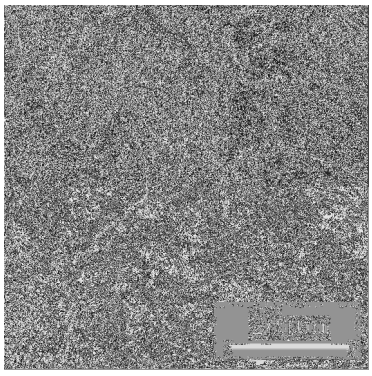
Fig. 5 Map on fracture surface.



(i) 0.005 Hz, H-charge



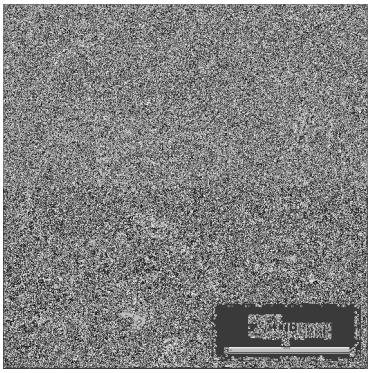
(ii) 0.01 Hz, H-charge



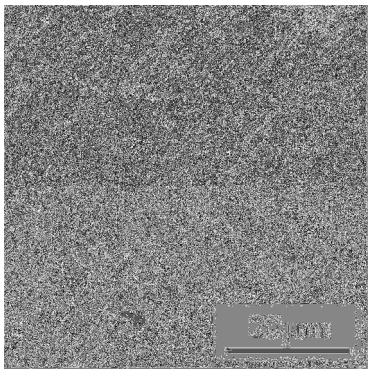
(iii) 0.1 Hz, H-charge



(iv) 1 Hz, H-charge



(v) 6 Hz, H-charge



(vi) 6 Hz, Uncharge

Fig. 6 SEM images of fracture surface in nitrogen gas.

The major part of this study has been conducted as a part of "Fundamental Research Project on Advance Hydrogen Science" funded by New Energy and Industrial Technology Development Organization (NEDO).

References

[1] H. Nishikawa, Y. Oda, H. Noguchi: Transactions of the Japan Society of Mechanical Engineers, A 75, No 759, (2009), pp. 1615-1623.
[2] S. Matsuoka, N. Tsutsumi, Y. Murakami: Transactions of the Japan Society of Mechanical Engineers, A 74, No 748, (2008), pp. 1528-1537.
[3] D.M. Symons: Engineering Fracture Mechanics, 68, (2001), pp. 751-771.

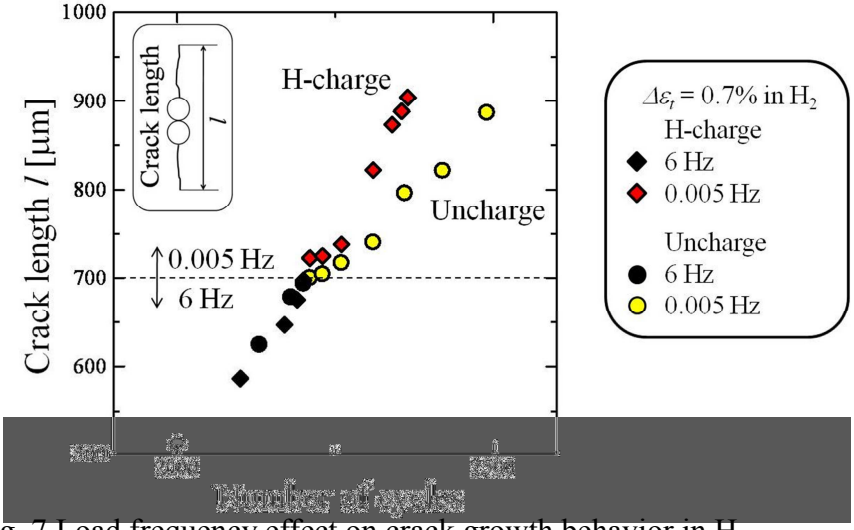
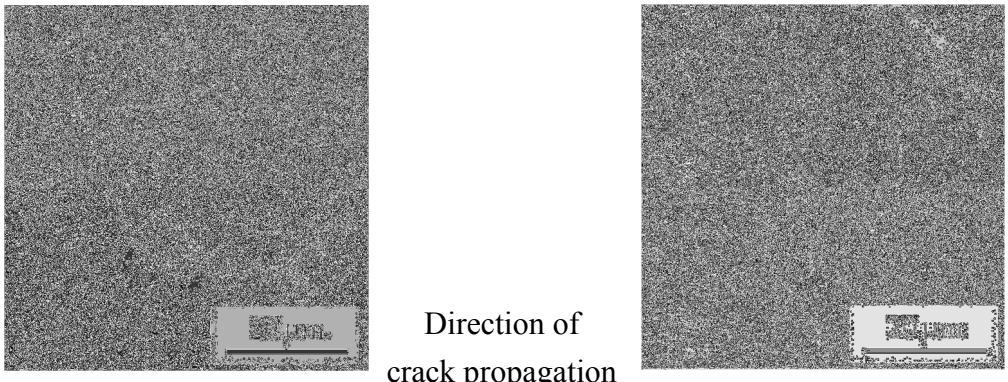
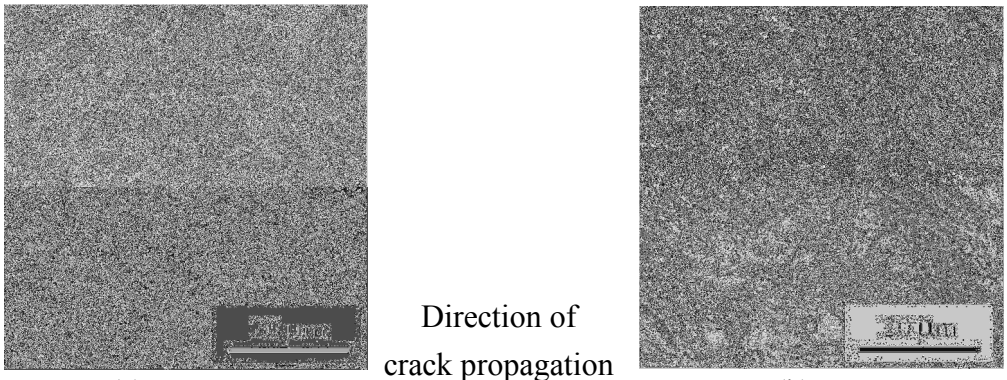


Fig. 7 Load frequency effect on crack growth behavior in H_2.



(a) 0.005 Hz (b) 6 Hz

Fig. 8 Fracture surfaces of uncharged specimen in hydrogen gas.



(a) 0.005 Hz (b) 6 Hz

Fig. 9 Fracture surfaces of H-charged specimen in hydrogen gas.

© (2012) Trans Tech Publications, Switzerland
doi:10.4028/www.scientific.net/KEM.488-489.327

Micromechanical modeling of heterogeneous materials with irregularly shaped pores

I. Tsukrov[1,a], B. Drach[1,b]

[1] Mechanical Engineering Department, University of New Hampshire, Durham, NH, USA

[a] igor.tsukrov@unh.edu, [b] borys.drach@unh.edu

Keywords: micromechanics, pores of irregular shapes, effective properties, stress concentrations

Abstract. An approach to predict the overall mechanical properties of materials containing pores of irregular shapes is described. Micromechanical modeling is performed by evaluating cavity compliance contribution tensors of individual pores [1] which are then used as an input for well-developed homogenization models. The cavity compliance contribution tensor can be found either analytically or numerically depending on the pore geometry and the level of anisotropy of the surrounding material. The results of numerical analysis can be used to compare the ability of differently shaped pores to initiate fracture.

1. Introduction

Overall mechanical properties of porous materials depend on elastic symmetry of matrix material, shapes of the pores, and their spatial and orientational distributions. In this paper, we restrict our attention to linearly elastic response in the case of pores randomly distributed in space. Two types of porous material properties are considered: effective elastic parameters (homogenization) and stress concentrations around cavities. Section 2 describes our approach to homogenization which is based on the evaluation of compliance contribution tensor of each pore type [1]. For some pore types this can be done analytically utilizing existing elasticity solution [2, 3]. The examples of such geometries are 3D ellipsoids and 2D ellipses and equilateral polygons. However, there are no convenient analytical solutions for irregular pore shapes, so that numerical techniques, e.g. finite element analysis (FEA), have to be used. The FEA procedure to determine the cavity compliance contribution tensor of an arbitrarily shaped cavity in some isotropic or anisotropic matrix is presented in section 3. The contributions of several pore shapes to the effective elastic properties are given as an example. Section 4 outlines our approach to evaluating the potential of pores to initiate fracture by analyzing stress concentrations obtained by FEA.

All pore shapes considered in this paper were obtained by X-ray computed microtomography (μCT) of a carbon/carbon composite sample [4]. Fig. 1 schematically shows the process of pore shape extraction from μCT data.

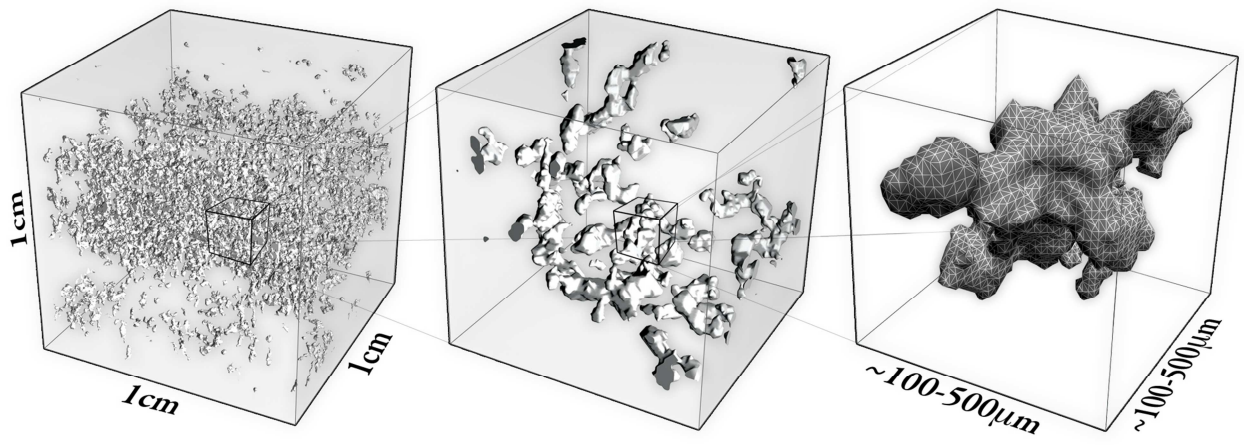


Fig. 1. Extraction of a pore shape from μCT data

2. Homogenization of materials with pores

According to [1], the overall compliance tensor of porous material can be represented as

$$\mathbf{S} = \mathbf{S}^{(0)} + \mathbf{H}_{RVE}, \tag{1}$$

where $\mathbf{S}^{(0)}$ is the compliance of the matrix and $\mathbf{H}_{RVE}$ is the fourth rank compliance contribution tensor of the representative volume element (RVE) of the material [5]. $\mathbf{H}_{RVE}$ is expressed in terms of contributions of individual cavities. These contributions are characterized by tensor $\mathbf{H}$ defined as a set of proportionality coefficients between remotely applied homogeneous stress field $\boldsymbol{\sigma}^{(0)}$ and the additional strain $\Delta\boldsymbol{\varepsilon}$ generated in the material due to the presence the cavity:

$$\Delta\boldsymbol{\varepsilon} = \mathbf{H} : \boldsymbol{\sigma}^{(0)}. \tag{2}$$

Depending on the concentration of pores, one of the well-developed micromechanical models can be used to construct $\mathbf{H}_{RVE}$. If pores are sufficiently away from each other (dilute limit), the non-interaction approximation is appropriate, the overall compliance contribution tensor for the RVE is then calculated by direct summation:

$$\mathbf{H}_{RVE}^{NI} = \sum \mathbf{H}^{(i)}, \tag{3}$$

where $\mathbf{H}^{(i)}$ is the compliance contribution tensor of an individual pore, and the summation is performed over all defects present in the RVE. For non-dilute distribution of pores, some more advanced micromechanical schemes can be used. For example, predictions for the overall elastic compliance by the Mori-Tanaka method [6] in terms of $\mathbf{H}_{RVE}^{NI}$ is given by a simple formula

$$\mathbf{H}_{RVE}^{MT} = \mathbf{H}_{RVE}^{NI} / (1 - p), \tag{4}$$

where p is the volume fraction of pores [1].

3. Evaluation of contribution of pores by finite element analysis

The pore compliance contribution tensor of a non-ellipsoidal pore can be calculated numerically using FEA. The following procedure utilizing MSC.MARC (www.mscsoftware.com) software package was implemented by the authors (for details, see [4]):

(a) The pore surface is placed into the reference volume in the shape of a cube with sides five times larger than the largest dimension of the pore. This setup is auto meshed with tetrahedral 3D elements;
(b) To obtain all 21 independent components of **H**-tensor, six loadcases (3 uniaxial tensions and 3 shear deformations in perpendicular directions) are considered;
(c) The FEA simulations are performed and the stress and strain fields are calculated;
(d) The components of the pore **H**-tensor are calculated based on the average values of strain. For example, from the uniaxial tension in x_1 direction $\sigma_{11}^{(0)}$ we obtain the H_{ij11} components ($i, j = 1, 2, 3$):

$$H_{ij11} = \frac{1}{\sigma_{11}^{(0)}} \left(S_{ij11}^{(0)} \sigma_{11}^{(0)} - \left\langle \varepsilon_{ij}^{(1)} \right\rangle_{RVE} \right). \tag{5}$$

The above procedure was utilized to evaluate contribution of irregularly shaped 3D pores to the overall properties of carbon/carbon composites. As an example, Table 1 provides contributions of several pore shapes to the effective material parameters. If non-interacting pores of the same shape are assumed to be parallel to each other, the parameters $\tilde{E}_i$ characterize contribution to the corresponding Young's moduli in the directions of coordinate axes:

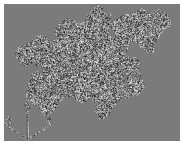
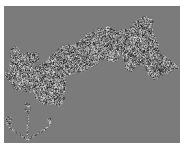
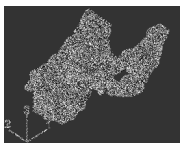
$$E_i = E^{(0)} / \left(1 + p\,\tilde{E}_i\right), \tag{6}$$

where p is the volume fraction of parallel pores of the corresponding shape. If the pores are randomly oriented, the overall response will be isotropic. The effective bulk and shear moduli can be represented as

$$K = K^{(0)} / \left(1 + p\,\tilde{K}\right) \quad \text{and} \quad G = G^{(0)} / \left(1 + p\,\tilde{G}\right) \tag{7}$$

with pore shape contribution parameters $\tilde{K}$ and $\tilde{G}$ given in Table 1.

Table 1. Contributions of selected pores to the effective Young's moduli

Cavity Shape	$\tilde{E}_1$	$\tilde{E}_2$	$\tilde{E}_3$	$\tilde{K}$	$\tilde{G}$	S_c
	2.070	2.661	2.154	5.605	2.056	0.091
	1.753	2.359	2.591	5.507	2.012	0.123
	1.711	2.674	2.176	5.327	1.964	0.129

4. Evaluation of stress concentration around pores

The FEA results can be utilized to evaluate the potential of pores to initiate fracture under various loading conditions. Let us consider, for example, a pore of the shape shown in Fig. 1 under remotely applied hydrostatic tension (Fig. 2a). This shape was extracted from μCT and contains sharp corners due to finite size of voxels of the μCT data. Linear elastic analysis (brittle material) of the pore response under applied loading produces high stress concentrations at sharp corners. A non-local approach is needed to compare different pore shapes in terms of their ability to initiate fracture. We introduce a normalized parameter

$$S_c = \frac{V_c}{V_p}, \tag{8}$$

where V_p is the volume of a pore and V_c is the volume of all finite elements with maximum principal stress higher than a certain threshold. For the considered example of the hydrostatic tension we chose the threshold to be $3\sigma_0$. The corresponding values (0.091, 0.123 and 0.129) of S_c

for three representative pore shapes are given in Table 1. We conclude that pore 3 is more prone to initiate fracture under hydrostatic tension. Fig. 2b shows distribution of principal stresses around one of the pore shapes.

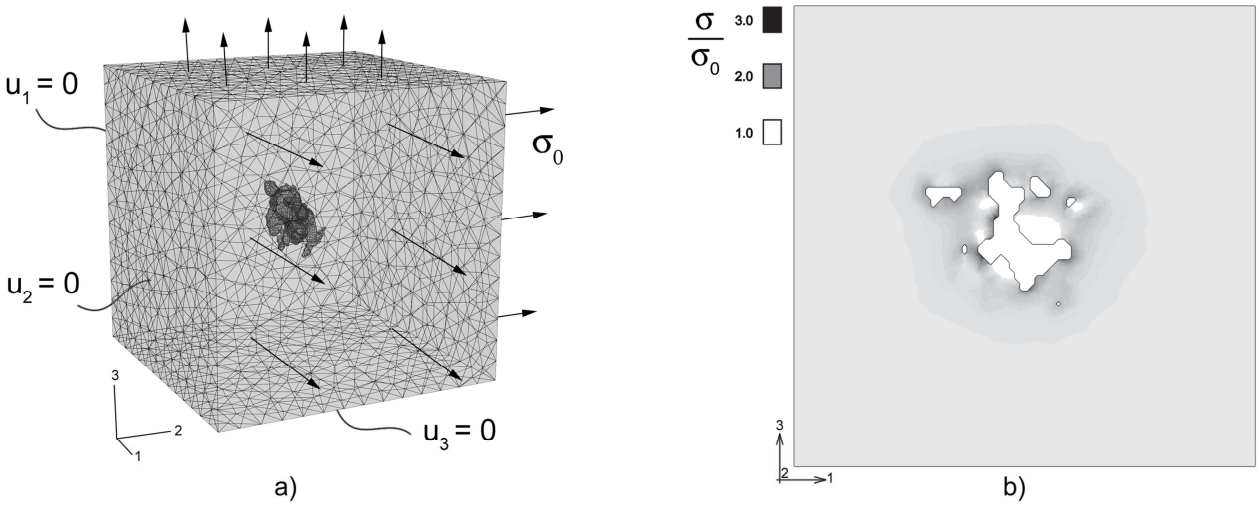


Fig. 2. FEA of one of the pore shapes: a) distribution of max principal stresses around the pore b) boundary conditions prescribed to the RVE

Acknowledgements

The authors gratefully acknowledge the financial support of the National Science Foundation (NSF) grant to the University of New Hampshire. We also thank Dr. Piat (Karlsruhe Institute of Technology, Germany) and Dr. Bayraktar (Albany Engineered Composites, USA) for valuable suggestions.

References

[1] M. Kachanov, I. Tsukrov, B. Shafiro "Effective moduli of solids with cavities of various shapes". *Applied Mechanics Reviews*, 47 (1994), S151–S174

[2] J.D. Eshelby "The determination of the elastic field of an ellipsoidal inclusion and related problems". *Proc. Roy. Soc. Lond. Ser. A*, 241 (1957), 376–396

[3] M. Kachanov, B. Shafiro, I. Tsukrov "*Handbook of Elasticity Solutions*". Kluwer Academic Publishers, Dordrecht (2003)

[4] B. Drach *et al.* "Numerical modeling of carbon/carbon composites with nanotextured matrix and 3D pores of irregular shapes". *Int. J. Solids Struct.*, *in press* (2011)

[5] R. Hill "Elastic properties of reinforced solids: some theoretical principles". *J. Mech. Phys. Solids,* 11 (1963), 357–372

[6] T. Mori, K. Tanaka "Average stress in matrix and average energy of materials with misfitting inclusions". *Acta Metall*., 21 (1973), 571–574

© (2012) Trans Tech Publications, Switzerland
doi:10.4028/www.scientific.net/KEM.488-489.331

Edge-Strengthening of Structural Glass with Protective Coatings

M. Lindqvist[1, a], C. Louter[1, b], J.-P. Lebet[1, c]

[1]Steel Structures Laboratory ICOM, ÉCOLE POLYTECHNIQUE FÉDÉRALE DE LAUSANNE (EPFL) School of Architecture, Civil and Environmental Engineering (ENAC), Lausanne, Switzerland
[a] maria.lindqvist@epfl.ch, [b] christian.louter@epfl.ch,
[c] jean-paul.lebet@epfl.ch

Keywords: Glass, coatings, edge strength, mechanical properties

Abstract. In modern buildings, glass is increasingly used as a load-carrying material in structural components, such as glass beams. For glass beams especially the edge strength of glass is important. However, the strength of glass is not a material constant but depends on various parameters, which makes glass, amongst other things, a challenging building material. One of the parameters influencing glass strength is the combination of humidity and stress, which may cause stress corrosion.

The aim of the current study is to limit the effect of humidity at the glass edge. This is done by the application of a protective coating. In this exploratory study several coating solutions are tested applying the coating at the edge of glass specimens. These specimens are then subjected to in-plane four-point bending tests to determine their failure strength. The effects of the coatings on the edge strength are analyzed using the failure strength data from the bending tests. The results indicate that only one of the tested coatings has an effect on the glass edge strength.

Introduction

In this study, the use of coatings in structural glass applications is investigated. Similar to Wen [1], the current study focuses on strengthening the glass edge. Earlier publications on the strengthening effects of glass coatings have been reported by several sources, using acrylate coatings [1], epoxy coatings [2] and silicon grease [3]. These authors attribute the strengthening effect of these coatings to their ability to protect the glass against stress corrosion.

Materials

Small-scale soda-lime silicate glass specimens were used, and the edge strength was investigated with and without a coating. All glass specimens were cut from polished glass panes and the polished edge was loaded in four-point bending tests. The nominal dimensions of the specimens were 110 x 10 x 4 mm with a support-span of 100 mm, and load-span of 50 mm.

Several coating solutions were tested:

1. Bioresin Biovest 578
2. Bluestar Silicones BP 9710
3. Rhodorsil Silicon grease Paste 4
4. Epoxy resin, Dow (DER 330, DER 732, DEH 26)
5. Tape, Gyso V712, Adhesive tape based on butyl rubber (0.8 mm) aluminum sheet coated with polyester.

Preparation and testing

Before testing, glass specimens were cleaned and heated up to 100 degrees in an oven for 48 hours. During heating, the specimens were covered with humidity absorbing molecular sieves (Zeochem, Z4-04) to absorb moisture. After cooling, the edges of the specimens were coated within a few seconds with one of the coatings listed above. Furthermore, the coatings dried following the instructions of each product specifications.

Thereafter, the glass specimens were loaded in-plane using an Instron 5948 MicroTester machine. Two stress rates used were 19 ± 2.5 MPa/s (high) and 0.14 ± 0.02 MPa/s (low). Each series contained 20 specimens per one stress rate. Thus, the series of specimens without a coating had 40 specimens including 20 specimens for both stress rates.

Test results

The effect of the coatings on the edge strength was analyzed using the failure strength data from the bending tests. The analysis was made using the two-parameter Weibull distribution function [4]. The experimental failure strength values are presented in Table 1. In addition, the Weibull fit to the failure strength values is shown in Fig. 1.

Table 1: Failure strength data analyzed using the two-parameter Weibull distribution.

Series	0 Uncoated	0 Uncoated	1 Bioresin Biovest 578	2 Bluestar Silicones BP 9710	3 Rhodorsil Silicon grease	4 Epoxy resin	5 Tape Gyso V712
Stress rate	high	low	low	low	low	low	low
Mean strength $\hat{\mu}$ [MPa]	81.18	63.16	62.41	63.96	79.40	63.20	68.96
Variation coefficient $\hat{V}$ [%]	12.03	13.27	11.53	16.73	8.99	11.78	17.47
Weibull scale parameter $\hat{\theta}$ [MPa]	85.33	66.69	65.48	68.36	82.49	66.37	73.89
Weibull shape parameter $\hat{\beta}$	10.00	9.02	10.46	7.03	13.59	10.22	6.71

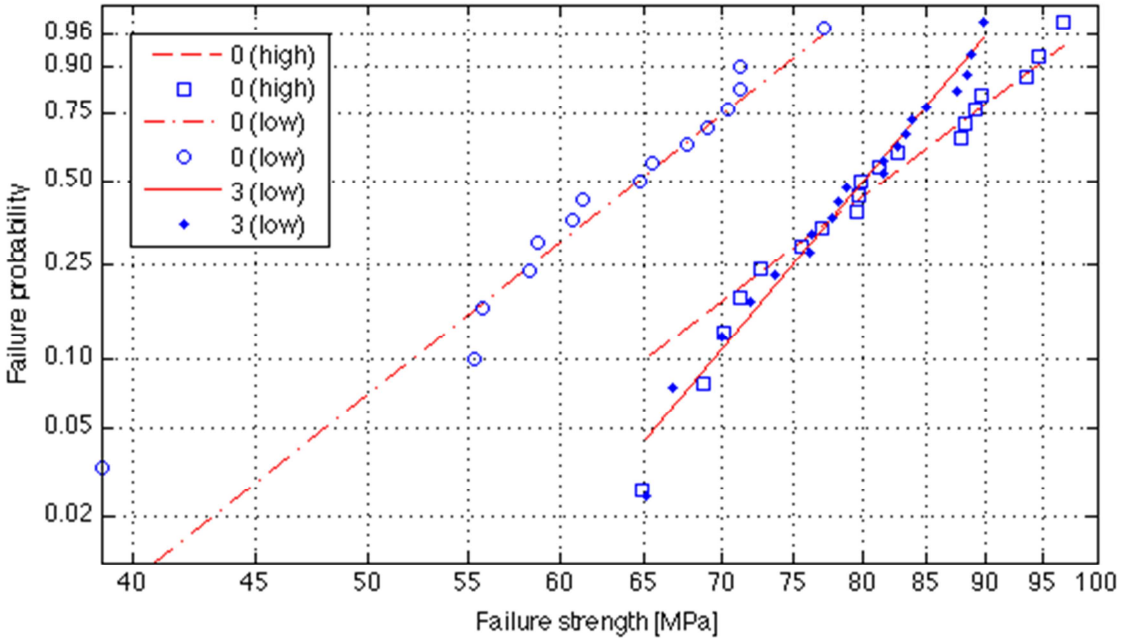


Fig. 1: The failure strength values (dots) with the Weibull distribution fitting (lines) for uncoated series (0) at the high and low stress rates and the coating 3 values at the low stress rate.

The thickness of the coatings was studied using a confocal microscope (LSM710). Fig. 2 a) and b) show an illustration of the glass cross-section after failure. The coating layer is situated on the glass edge. The study with the microscope showed that the thickness of the coatings varied between 20 μm and 200 μm depending on the viscosity of the coating product.

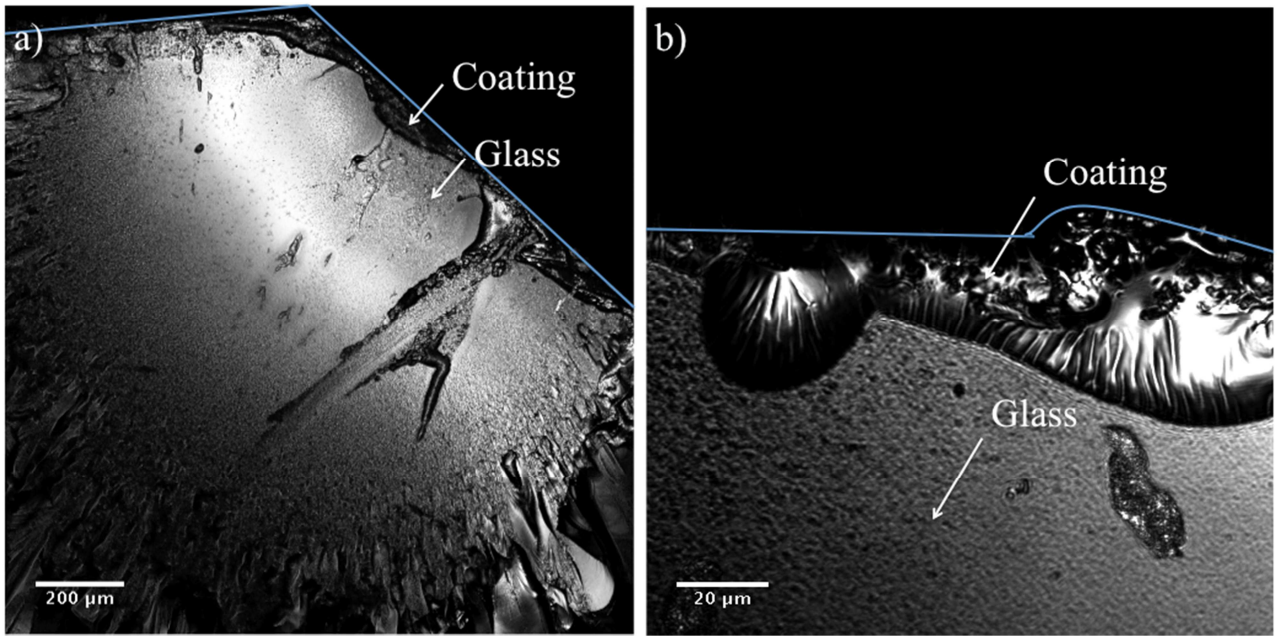


Fig. 2: a) An illustration of the glass edge at the failure location showing the layer of coating 3, Rhodorsil Silicon grease Paste 4, on top of the glass. The figure presents a part of the cross-section of the glass specimen as well as the location where a flaw initiates the failure. b) A layer of epoxy resin (coating 4) covering the glass edge-surface.

Discussion

Seven series of 20 specimens were tested in-plane in four-point bending. From the failure strength values the following is observed.

Firstly, the uncoated specimens loaded at a high stress rate reached higher average strength level than the uncoated specimens that were loaded at a low stress rate. The difference amounted to 22%. The difference is assumed to be related to the effect of humidity on the glass strength and was expected according to [3].

Secondly, it is observed that the specimens with coatings 1, 2 and 4 loaded at a low stress rate, reached similar strength levels as the uncoated specimens that were also loaded at low stress rate. From this it is observed that the coating 1, 2 and 4 had no significant effect on the edge strength of the glass specimens.

Thirdly, the specimens coated with coating 3 loaded at a *low* stress rate, reached similar strength levels as the uncoated specimens that were loaded at a *high* stress rate. Here, the coating had a 'strengthening' effect on the glass.

Finally, it is observed that coating 5 had an inconsistent effect on the edge strength of the glass specimens. The specimens with coating 5 showed a tendency for increased strength. However, as can be seen from Table 1 the scatter in the results of the specimens with coating 5 is rather large.

Conclusions

In this study, the use of coatings at the glass edge for structural glass applications is investigated. The use of a protective coating is proposed to limit the effects of humidity at the glass edge. The results showed that only one coating, Rhodorsil Silicon grease Paste 4, managed to protect the edge during testing. Coating 5, Tape Gyso V-712, had a small influence.

The microscope detection of the glass surface with coatings allowed to estimate the thickness of the coatings. However, further study is required to estimate why only the coating 3 had an effect on the glass edge strength.

The advantage of a protective coating is to decrease the scatter of strength levels, thus avoiding the dependency in stress rate. If this scatter in strength can be avoided by using a coating, such an improvement in strength would be significant in the design of structural glass.

In order to obtain more proof on the use of protective coatings, a future study is suggested on the details of the chemical and mechanical properties of coatings, their long-term effects, and the capability of coatings to protect the glass under changing environmental conditions. This includes a non-destructive evaluation on the micro level effects of coatings especially at the crack-tip area.

Acknowledgements
The study is made with the assistance of testing equipment provided by the Laboratory of Applied Mechanics and Reliability Analysis (LMAF) and the confocal microscope in BioImaging and Optics platform (PTBIOP) at EPFL. Also the financial support of Swiss National Science Foundation (SNSF) is acknowledged.

References

[1] M. Wen, J.-M. Chapagno, G. Silverman, M. Bourrel: submitted to Journal of Non-Crystalline Solids 354 (2008), p. 5060-5067.
[2] R.J. Hand, B. Ellis, B.R. Whittle, F.H Want: submitted to Journal of Non-Crystalline Solids 315 (2003), p. 276-287.
[3] M. Haldimann, Fracture strength of structural glass elements – Analytical and numerical modeling, testing and design. Thesis EPFL (2006).
[4] EN-12603:2002 Glass in building- Procedures for goodness of fit and confidence intervals for Weibull distributed glass strength data, European Committee for Standardization.

© (2012) Trans Tech Publications, Switzerland
doi:10.4028/www.scientific.net/KEM.488-489.335

Residual stresses in as-welded joints: finite element modeling and neutron diffraction stress measurements

C. Acevedo[1,a] , J.M. Drezet[2,b] , J.-P. Lefebvre[3] , L. D'Alvise[3,c] and A. Nussbaumer[1]

[1]ICOM Steel Structures Laboratory, ECOLE POLYTECHNIQUE FEDERALE DE LAUSANNE (EPFL), Lausanne, Switzerland

[2]LSMX Computational Materials Laboratory, ECOLE POLYTECHNIQUE FEDERALE DE LAUSANNE (EPFL), Lausanne, Switzerland

[3]CENAERO Excellence in Simulation Technologies for Aeronautics, Gosselies, Belgium

[a]claire.acevedo@a3.epfl.ch, [b]jean-marie.drezet@epfl.ch, [c]laurent.dalvise@cenaero.be

Keywords: Welded joints, Residual strain and stress, Finite element analysis, Neutron diffraction

Abstract. This paper describes the numerical analysis method used to estimate welding induced residual stresses in K-shape tubular bridge joints. The knowledge of residual stress distribution is required to design the geometry of K-joints loaded under fatigue stresses. Numerical simulations are focused on the arc welding MAG process, generally used to weld joints in bridge construction. Thermo-mechanical analyses are performed in 3D using two finite element codes: ABAQUS® and MORFEO®. ABAQUS has the advantage to offer large analysis capabilities (nonlinear, transient, dynamic, etc.) whereas MORFEO is more dedicated to welding processes and offers the possibility to analyze crack propagation under fatigue loads. Computed residual stresses in the region surrounding the weld are compared with measured residual stresses in order to estimate the ability of the codes to reproduce these stresses. Position, orientation and magnitude of the highest residual stress components are discussed.

Introduction

Residual stresses created by thermal induced deformations during welding are particularly high in the surface surrounding the weld. Combined with applied cyclic loadings, they influence the fatigue crack propagation (onset, rate and shape) [1, 2]. This study evaluates residual stresses in order to control and optimize the design of K-joints geometry.

Finite element simulations made in this paper are focused on the welding process of S355 steel. An uncoupled formulation is used; the transient thermal analysis is followed by an elasto-plastic mechanical analysis. These simulations provide the 3D residual stress distribution along the weld. The calculated residual stresses are compared with previously measured residual stresses in order to evaluate the accuracy of numerical models.

Presentation of the finite element analysis

A three dimensional thermo-mechanical finite element analysis is performed in order to simulate the stress generation during welding. In the case of a mild steel such as the S355 steel, it has been shown by [3] that phase transformations have a small effect on residual stresses generation, therefore phase transformations are not considered in this analysis.

An uncoupled approach is used to solve, first, the 3D transient temperature field and, then, the displacement field using the temperature field as input data.

Thermal analysis. The thermal analysis is based on transient non-linear heat conduction formulation (Eq. 1).

$$\rho\, C_{eq}\, \frac{\partial T}{\partial t} \;=\; \boldsymbol{\nabla}^T\, \mathbf{D} \boldsymbol{\nabla} T + s \tag{1}$$

where ρ is the material density [kg/mm^3], C_{eq} is the specific heat C combined with the latent heat L induced by melting [J/(kg.°C)], T is the temperature [°C], t is the time [s], D is the thermal conductivity tensor reduced to one coefficient k for isotropic case [W/(mm.°C))] and s is the volumetric heat source [W/mm^3].

The temperature-dependent thermal properties k, C and ρ are taken from the EN 1993-1-2:2005(E) for mild steel. The conductivity value is increased to three times its value at the solidus temperature [4, 5] to take into account the convection flow in the weld pool and kept constant at $T \geq T_{solidus}$. The latent heat L induced by fusion/solidification between solidus and liquidus temperatures (1465-1544 °C for S355 steel) is considered using a value of 247000 J/(kg.°C) [6]. Heat losses by radiation and convection (boundary conditions) are considered on all surfaces.

The 7-passes welding, generating the K-joint weld, is simulated as a single pass with an equivalent heat source. Each pass is made in four steps (half weld at the right brace toe, half weld at the left brace toe and the two symmetrical half welds). This heat source is composed of a volumetric flux moving along the weld path at a speed of 5.5 mm/s. The characteristics of the heat source are determined so that the computed size of the weld pool matches the one measured on a macrograph. In ABAQUS, the heat source is a sphere with a radius r = 15mm, in MORFEO, this is a truncated circular cone model with a radius r_1= 15 mm for its first base, r_2= 9.3 mm for its second base and a height h= 15 mm. To merge the seven weld passes into one equivalent pass, it is recommended by [7] to keep the total heat input of the seven weld passes, Q = 41500 W. Metal deposition of the MAG arc welding is not considered, the finite elements representing the weld are present in the model from the beginning.

Figure 1 depicts the 53966 nodes and 48549 elements used to model the K-joint composed of two braces (diameter 88.9 mm, thickness 8 mm) welded onto a chord member (diameter 168.3 mm, thickness 20 mm). The heat source traveling around the weld is also shown. 8-node brick linear elements for heat transfer are chosen for the thermal analysis.

Mechanical analysis. The mechanical analysis is based on an elastic-plastic material behaviour with a linear isotropic work hardening ignoring rate-dependent (creep) effects at high temperatures.

A variation of temperature, obtained as the thermal analysis output, implies thermal strain. In a thermo-elastic-plastic analysis, the generalised Hooke's law is expressed as follows (Eq. 2):

$$\boldsymbol{\sigma} = \mathbf{C}\boldsymbol{\epsilon}^{el} = \mathbf{C}(\boldsymbol{\epsilon} - \boldsymbol{\epsilon}^{pl} - \boldsymbol{\epsilon}^{th}) \tag{2}$$

where C is the elasticity tensor. The temperature-dependent mechanical properties required to solve the previous equation are the Young's modulus E [MPa] and the Poisson's ratio ν for the elastic part, the yield stress f_y [MPa] and the stress evolution as a function of the accumulated plastic strain $f_y + Hp$ (linear isotropic hardening assumption) for the plastic part and the thermal expansion coefficient α [/°C] for the thermal part.

The Young's modulus E is defined according to the EN 1993-1-2:2005(E) and the Poisson's ratio ν, the thermal expansion coefficient α and the yield stress f_y according to [8].

The mesh is identical to the one used for thermal analysis, but reduced integration is used for the mechanical part in the ABAQUS model. Concerning boundary conditions, displacements are set to zero at the chord right extremity, no traction or compression is applied.

Results and discussion

Residual strain measurements were conducted at the Institute Laue-Langevin (ILL) on a K-joint sample with a chord wall of 20 mm thick. This method enables to measure triaxial residual stresses non-destructively deep inside the sample. The residual stresses calculated from these measurements are

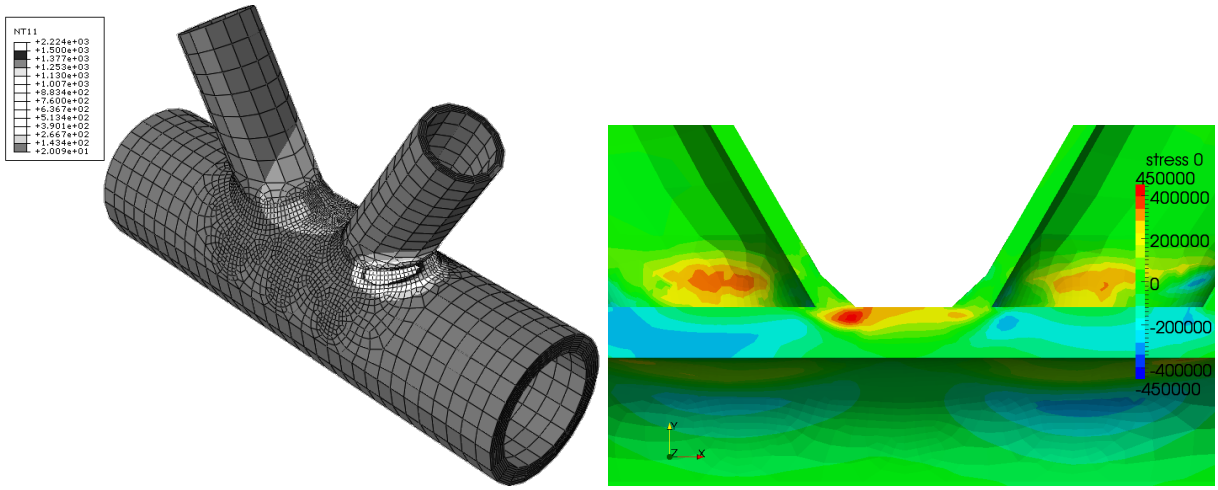


Fig. 1: On the left, temperature field from ABAQUS model during the movement of the torch. On the right, cut view of transversal residual stresses from MORFEO showing a restraining effect in the gap area between the braces (stress values in kPa).

compared in Fig. 2 with residual stresses resulting from numerical models. Stress distributions, along a vertical line passing through the 20 mm chord wall thickness underneath the weld toe, are given in the transverse direction (perpendicular to the weld), the longitudinal direction (parallel to the weld) and the radial direction (in the radial direction of the tube). The same simulation was performed with ABAQUS® [9] and MORFEO® [10] from Cenaero research center.

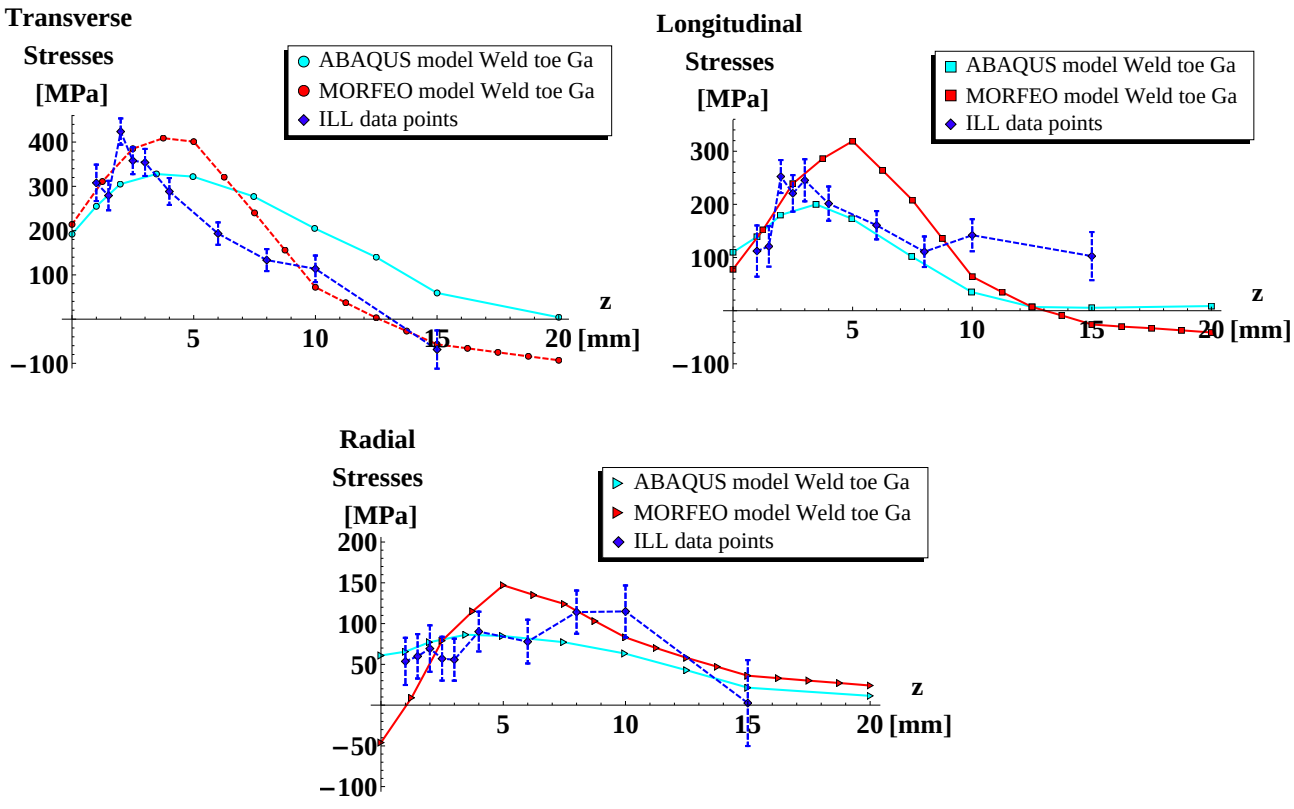


Fig. 2: Comparison of transverse, longitudinal and radial residual stress distributions (ABAQUS, MORFEO and experimental data) at the weld toe though the 20 mm chord wall thickness.

In Fig. 2, the results obtained numerically confirmed that transverse residual stresses are greater than longitudinal ones, which are greater than radial ones. Figure 1b also gives the proof that a strong restraining effect occurs between the braces keeping transversal residual stresses at a high value.

Figure 2 shows that the numerical distributions give the global magnitude of experimental residual stresses and that the maximum values they reach are quite close to the experimental ones. However, the transverse residual stress distribution obtained with ABAQUS is shifted to the right compared with the experimental distribution. It means that transverse residual stresses should be compressive at 13 mm depth but the models present tensile residual stresses through all the depth. MORFEO results predict more accurately the transverse residual stress distributions whereas ABAQUS results fit better the longitudinal stress distribution. The difference between both codes might be attributed to the different heat source models.

Globally, numerical results are in an acceptable agreement with experimental results.

Conclusion

The numerical results, obtained using the ABAQUS and MORFEO codes, have shown to be globally in good agreement with the experimental results obtained from neutron diffraction measurements. Our simplified model proved its ability to reproduce the residual stress distribution in the region surrounding the welds even though the peak values are not always well captured and the distribution is sometimes shifted.

Numerical simulations have clearly confirmed the importance of transverse residual stresses and the restraining effect occurring in the gap area. Transverse residual stresses are detrimental because they will superimpose with applied fatigue stresses which are also predominantly transversally oriented.

References

[1] T.R. Gurney: *Fatigue of Welded Structures*. Cambridge University Press (1979).

[2] K. Masubuchi: *Analysis of welded structures*. Pergamon Press (1980).

[3] P. Dong and J.K. Hong: *Recommendations for determining residual stresses in fitness-for-service assessment*. Welding Research Council Bulletin Vol. 476 (2002).

[4] V.J. Papazoglou and K. Masubuchi: J. Press. Vess.-T. ASME Vol. 83-87 (1982), p. 119.

[5] J. Goldak, A. Chakravarti and M. Bibby: Metall. Trans. B Vol. 15B Numb. 2 (1984), p. 299.

[6] L.O. Raymond and J. Chipman: Trans. Met. Soc. AIME Vol. 239 (1967), p. 630.

[7] L.-E. Lindgren: J. Therm. Stresses 24 (2001), p. 141.

[8] P. Michaleris. Courses at the Pennsylvania State University (2011).

[9] ABAQUS: *Analysis user's manual version 6.9* (Dassault Systèmes, 2009).

[10] MORFEO: *v1.3 user manual* (Cenaero, 2009).

© (2012) Trans Tech Publications, Switzerland
doi:10.4028/www.scientific.net/KEM.488-489.339

Cellular automata multiscale model of creep damage for metals

Krzysztof Nowak[1, a]

[1]Faculty of Civil Engineering, Politechnika Krakowska,
ul. Warszawska 24, 31-155 Krakow, Poland

[a]kn@limba.wil.pk.edu.pl

Keywords: creep damage, cellular automata, multiscale modeling

Abstract. Polycrystalline materials like metals fail in creep conditions due to development of inter- or intra-granular voids. The model of creep damage is proposed which simulates voids growth on microscale using Cellular Automata (CA) technique at RVE level, coupled with creep deformation on macroscale. It is assumed that experimentally observed creep deformation is a result of interaction between hardening and softening of a material. The softening process is mainly due to voids development and it is built in deformation model by weakening of effective stress by damage parameter calculated by CA part of the model. Parameters of model are based on primary and secondary stages of creep experiments. The results of simulations show that multiscale model predicts quite well times to failure and strains at failure.

Introduction

Polycrystalline materials like metals creep at elevated temperatures under constant loading. The uniaxial creep deformation exhibits so called normal creep curve that can be divided in three periods. In the first period deformation velocity is decreasing due to hardening of material (primary creep). The rate of deformation in the second period is approximately constant as softening of material compensates effects of hardening (secondary or steady-state creep). In the third period the softening prevails and deformation velocity starts to increase causing the specimen to fail (tertiary creep).

One of the main processes connected with softening of material is damage development. The damage in creep conditions is caused by development of voids, which are growing i.a. by deformation of surrounding material (cf. [1]). In such a way a positive feedback occurs accelerating both deformation and damage development. Macroscopic description of this phenomenon was proposed by Kachanov [2]:

$$\dot{\varepsilon}_c = B\left(\frac{\sigma}{1-\omega}\right)^n, \quad \dot{\omega} = A\left(\frac{\sigma}{1-\omega}\right)^m, \tag{1a,b}$$

where $\dot{\varepsilon}_c$ is rate of creep strain, ω is damage parameter, σ is applied stress, A, B, n, m are material parameters. This coupling between damage and strain complicates the determination of these parameters. To use B and n obtained from Norton law of creep (without coupling), one has to assume that damage parameter is negligible during secondary creep. But the voids occurs in creeping material already during primary period (cf. e.g. [3,4]) and neglecting damage in secondary period is questionable. In model proposed in this paper, not secondary but primary creep is assumed as a 'virgin' deformation according to [5]:

$$\dot{\varepsilon}_c = B_1 \varepsilon_c^{-\alpha}\left(\frac{\sigma}{1-\omega}\right)^{n_1}, \tag{2}$$

where B1, n1, α are material parameters describing primary creep. In paper [5] Kachanov equation (Eq. 1b) for damage development is applied. The damage parameter defined in such a way ignores any physical interpretation of damage; it is calibrated only by time to failure. The consequence of this approach is that strains obtained by this model do not coincide with experimental results. It regards both shape of creep curve and value of strain to failure.

Another way of describing damage is to find some physical interpretation of damage parameter. There are many proposals for damage measures and assigning them to values of damage parameters (see [6]). These measures can be of micro- or macroscopic nature. The microscopic measures are connected with measurement of some direct symptoms of damage like number of voids (or their cross-section or volume) using microscopic techniques. Using microscopic measures of damage one has to decide how large Representative Volume Element (RVE) is. It is obvious that damage is not distributed uniformly over all the specimen volume, especially at the end of its life. Additionally, it is rather impossible to set the minimum size of RVE to obtain value of damage parameter independent on RVE size. Therefore the law of damage evolution depends not only on assumed measure of damage but also on the size of RVE.

Model presented in this paper proposes to solve some of above mentioned problems by replacing the continuous damage evolution equation by simulation of damage development by means of Cellular Automata (CA) technique.

Multiscale model

Structure of material. As it is mentioned above, the process of damage development is not homogeneous over the specimen volume. Even small heterogeneity in material structure causes that damage development is non-homogeneous and induces positive feedback between deformation and damage enlarging initially small differences. But it manifests itself only in third period of creep. During secondary creep another mechanism prevails: the softened part of material takes less of the loading and the damage develops slower. It acts on damage as negative feedback and allows preserving nearly constant strain rate.

The main source of heterogeneity in pure metals is their polycrystalline structure. It is important for damage development process as grain boundaries are locus of initiation of intergranular voids. They grow due to grain boundary diffusion of vacancies and the final surface of failure is intergranular in most cases. Therefore the granular structure of material is the most important feature in simulation the damage development process.

Discrete Voronoi tessellation is used to adopt grain structure for CA simulation. The full procedure is described in paper [7]. It allows to obtain structure of different grain sizes and geometries with randomly distributed grain seed points. Number of grain seed point n_{seed} is the one parameter defining the grain structure in case of homogeneous seed point distribution. The other structure parameters are: N_0 is the linear size of initial RVE in cells, d_0 is a ratio of initially damaged cells to number of all cells in RVE. Parameter N_0 is connected with resolution of automaton, i.e. larger N_0 - smaller void can be modeled by automaton. The parameter d_0 can be related to microstructure parameter - initial void volume fraction.

Damage development model. The mechanism assuming here as dominating in softening process is development of microvoids and microcracks. There are four main stages of this process: microvoids nucleation, growth of microvoids along grain boundaries, voids coalescence, macrocrack formation and final rupture (see review in [8]). The two first stages are simulated by CA jointly. Two mechanisms are taken into account: voids growth by deformation and by diffusion. In real material these mechanisms can act separately, enhancing or inhibiting one another. In simulation similar effect is reached in dependence of conditions like current strain or damage level.

Deformation is treated as an input variable for CA simulation. The current size of RVE is calculated at beginning of every CA iteration. If deformation is noticeable by automaton then the size of RVE (in cells) is changing and deformation is spread over CA network (cf. [7]). During this process new damaged cells can be initiated especially on grains borders or at triple points. Number of damaged cells is controlled by empirical equation for relative variation of density (cf. [9]):

$$\rho = \rho_0\left(1 - H\varepsilon^{\gamma}\right), \tag{3}$$

where ρ_0 is the initial density of undamaged cells, ε is strain, H and γ are material parameters. According to Eq. 3 when strain is increasing, number of damaged cells is increasing as well, what allows for growth of voids enhanced by deformation.

The second implemented mechanism of void growth is diffusion. Damaged cells are moving freely inside grains simulating diffusion of vacancies. This movement is restricted by energy criterion allowing for aggregations of cells along grain boundaries (cf. [7]). The rate of diffusion is related to time step between subsequent CA iteration T_{step}, which is model parameter.

In model considered here there is no implementation of coalescence mechanism. Due to high localization of damage and strain the RVE in that stage should be very small. But it is assumed that time of this stage is very short, and error in time to failure is negligible. However, this mechanism is important in calculation of strain to failure, especially for large applied stress.

Damage evaluation. The value of damage parameter is calculated for RVE in every CA iteration. The linear sizes of all microcracks (cluster of connected damaged cells) are compared and their maximum found. Value of damage parameter is obtained by ratio of this maximum to current linear size of RVE. It is set to one if the longest microcrack joins the opposite sides of RVE. In such situation the element loses his bearing capacity and macrocrack starts to propagate resulting in final rupture.

Coupled deformation model. The CA damage microscale model is driven by deformation obtained from macroscale Finite Element (FE) model. Creep deformation is calculated by solving differential equation in form of Eq. 2. CA damage model is run in every Gaussian point of FE mesh and value of damage parameter is transferred to FE state variables. The total strains are obtained as sum of instantaneous strains and creep strains. CA damage model and FE model consist together multiscale model in frame of CAFE technology (cf. [10]).

Example

Model parameters. The model parameters were fitted to experimental data for OFHC high purity copper of mean grain size 30 μm in 823 K [11]. For FE model parameters the instantaneous and primary creep data were used. As the damage model produces also non-zero instantaneous damage to properly model primary creep Eq. 2 was transformed to:

$$\dot{\varepsilon}_c = B_1 \varepsilon_c^{-\alpha}\left(\frac{\sigma\left(1-\omega_0\right)}{1-\omega}\right)^{n_1}, \tag{4}$$

where ω_0 is average initial damage. In simulation of Cu in 823 K it was used: B_1=7.57E-24 $(MPa)^{-n_1}s^{-1}$, n_1=9.76, α=2, ω_0=0.15. The initial structure was built using N_0=641, n_{seed}=10, g_{dam0}=0.006. Variation of density parameters were obtained from data for copper in [3]: H=1.17 and γ=2.3. Damage model parameters were estimated by suiting the results to steady-state creep rate. Diffusion rate was controlled by time step T_{step} equals to 0.25 s.

Results. Simulations were run for simple tension test in plane strain state. Specimen was covered by 4 elements and 16 CA simulations were run. The model was examined in stress range 28-52 MPa. The results are presented in Fig. 1 as mean values of six simulations for every stress level. In most cases simulations produced normal creep curve, but sometimes without tertiary creep. Times to failure and strains to failure obtained in simulations show a very good agreement with experimental results.

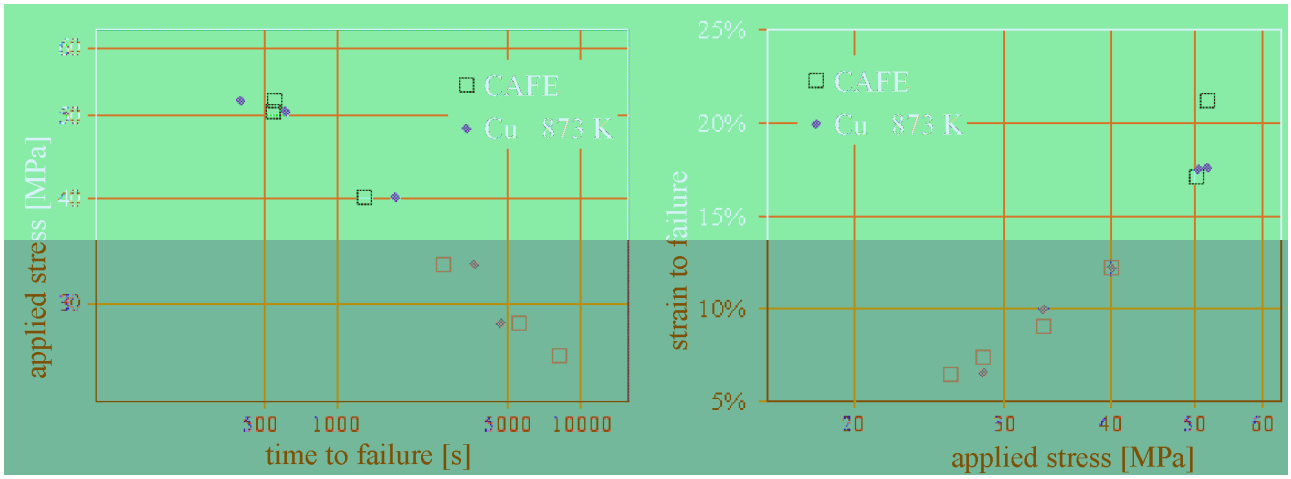


Fig. 1. Results of CAFE simulations in comparison with experimental results for copper [11].

Summary

Results obtained by simulations show that creep deformation can be modeled by superposition of two processes: hardening and softening of materials. Both of these processes are active all the creep life but with different intensity. Additionally, simulations demonstrate that coupling of deformation and damage product reasonable strain and time to failure. But the strains to be coupled are primary strains, as strains during secondary creep are already influenced by damage. The improvement of time and strain to failure evaluation was obtained due to replacing classical continuous Kachanov model by micromechanical simulations.

References

[1] A.C.F. Cocks, M. F. Ashby: Prog. Mater. Sci. Vol. 27(1982), p. 189

[2] L.M. Kachanov: Izv. Akad. Nauk. SSR Vol. 8 (1958), p. 26

[3] R.C. Boettner, W.D. Robertson: Trans. Metall. Soc. AIME Vol. 221 (1961), p. 613

[4] A. Gittins: Metal Sci. J. Vol. 1 (1967), p. 214

[5] M. Chrzanowski, Bull. Ac. Pol. Sc. Ser. Sc. Techn. Vol. XX (1972), p. 75

[6] J. Lemaitre, J. Dufailly: Eng. Fract. Mech. Vol. 28 (1987), p. 643

[7] M. Chrzanowski, K. Nowak: Journal of Multiscale Modelling Vol. 1 (2009), p. 389

[8] M.E. Kassner, T.A. Hayes: Int. J. of Plast. Vol. 19 (2003), p. 1715

[9] G. Belloni, G. Bernasconi, G. Piatti: Meccanica Vol. 12 (1977), p. 84

[10] A. Shterenlikht, I.C. Howard: Fatigue Fract. Engng. Mater. Struct. Vol. 29 (2006), p. 770

[11] P. Feltham, J.D. Meakin: Acta Metall. Vol. 7 (1959), p. 614

© (2012) Trans Tech Publications, Switzerland
doi:10.4028/www.scientific.net/KEM.488-489.343

Experimental investigation of fatigue crack growth in the welding nugget of FSW joints of a 6060 Aluminum Alloy

Marcassoli P.[a], Longo M.[b], D'Urso G.[c], Giardini C.[d], Pastore T.[e]

Department of Design and Technologies, University of Bergamo, Dalmine (BG), Italy

[a]paolo.marcassoli@unibg.it, [b]michela.longo@unibg.it, [c]durso@unibg.it, [d]claudio.giardini@unibg.it, [e]pastore@unibg.it

Keywords: friction stir welding, AA6060 alloy, fracture mechanics, fatigue, crack growth rate

Abstract. The work investigates the fatigue behavior of friction stir welded butt joints by means of fracture mechanics techniques. FSW joints of artificially aged AA6060 T6 aluminum alloy were studied. The welding was performed on 8 mm thick butt joined sheets by means of a CNC machine tool. Welding speed in the range between 117 and 683 mm/min and tool rotational speed between 838 and 1262 rpm were considered. Fatigue crack growth tests were performed according to ASTM E647 standard on CT specimens, under constant load amplitude conditions, at 0.1 minimum to maximum load ratio, with the notch placed in the dynamic recrystallization zone of weld nugget, oriented along the welding direction. The comparison of results demonstrates the crack growth rate is always equal or lower than the base material at low values of stress intensity range. At ΔK values above 12 MPa$\sqrt{m}$, crack growth rate was found to be higher than base material for high feed, low speed and high feed/speed ratio.

Introduction

Aluminum alloys are often considered as difficult to be welded by traditional techniques. A promising alternative process is offered by Friction Stir Welding (FSW), a solid-state welding technique patented by TWI in Cambridge (UK) and improved over the last twenty years [1]. Plates are welded by the action of a rotating tool, moving along the joining interface. The material is heated by friction, extruded around the tool pin and forged by the tool shoulder pressure. No specific preparation of plates is needed. Furthermore residual stresses are lower compared with conventional processes, because of lower temperatures, always below the melting point. FSW has increasing success in automotive, aerospace and naval applications, due to many advantages, such as quality, repeatability, precision, low material waste and low energy consumption.

A number of works in literature deal with fatigue behavior of FSW joints and several works focused on AA6060 alloy [2,3]. Anyway, crack propagation in the various zones with different microstructures produced by welding needs to be further investigated. Aim of the research project is to evaluate fatigue behavior of welding as a function of FSW parameters such as tool rotational rate (speed) and translation rate (feed). This paper resumes mechanical characterization and fatigue tests on welding nugget.

Experimental

The welding was carried out by means of a CNC machine tool. Butt joints were obtained on sheets having a thickness equal to 8 mm. An AA6060 aluminum alloy in the T6 artificially aged condition was used for this purpose. Sheets were welded by using a standard tool with smooth plane shoulder and cylindrical pin, varying process parameters, namely tool rotational speed and feed rate. The tool was fabricated using AISI 1040 steel, shoulder and pin diameters are respectively equal to 20 and 8 mm. For a first stage of study, 4 conditions were chosen among the 9 conditions defined according to the Design Of Experiment (DOE) adopted method. Specimens were identified by letter "S" followed by speed in rpm and letter "F" followed by feed in mm/min. Test were also performed on

the base material for comparison purpose. Macrostructure in the welding zone was revealed by alkaline etching in 200 g/L NaOH solution at 60°C on transversal section of the joints, after surface preparation up to 4000 grit with SiC emery papers. Vickers microhardness tests were carried out at 100 g and dwell time of 15 sec. For the base material specimen, microhardness profile was performed across thickness. For welded specimens, three series of indentations were performed respectively in the upper side, in the middle thickness and in the lower side, from the center of welding nugget to the base material. The distances of indentation from the edges and between indentations were according to UNI EN ISO 14577-1:2004. Tensile tests were performed orthogonally to the welding direction according to UNI EN 10002-1:2004 on standard specimens with 18 x 8 mm cross section, having welding nugget placed in the middle of gage length. Tests were carried out on 3 specimens for each welding condition, under strain control during elastic deformation by strain gage with length 25 mm and under speed control after yield point. Fatigue tests were performed on CT specimens with chevron notch placed in the middle of weld nugget, and crack orientation along the welding direction. Specimen geometry, preparation and testing were performed according to ASTM E647 standard. Before testing, specimens were pre-cracked for at least 3.2 mm at frequency of 20 Hz. Fatigue tests were carried out under constant load amplitude control, at 0.1 minimum to maximum load ratio and 7 Hz frequency. Crack length was monitored by the compliance method. Test was stopped after crack reached 45 mm length or at specimen breakage. Two tests for each condition were performed. Crack length vs cycles data were elaborated according to the "incremental polynomial method" for estimating da/dN vs ΔK propagation curves. After testing fracture surfaces were observed by means of an optical stereomicroscope and a scanning electron microscope (SEM), in order to evaluate morphology and presence of welding defects.

Results and discussion

According to literature, 4 zones were identified (Fig. 1): the base material, unaffected by welding, the heat affected zone (HAZ), produced by thermal cycle of heating and cooling near welding, the thermo-mechanically affected zone (TMAZ), partially recrystallized and modified by severe deformation and heating induced by friction, and the dynamic recrystallization zone (DRZ), with very fine and homogeneous microstructure. The nugget appearance is quite similar for all conditions. A large HAZ was observed for S1050F117 condition, related with high heating produced by low feed rate. Some voids were always found in TMAZ, more pronounced at low feed rate, already visible on transversal section after grinding and clearly evident after alkaline etching.

Microhardness of base material ranges from 74 to 84 $HV_{100,15}$ (Tab. 1). For the welded specimens, hardness values were lower in the DRZ and in the TMAZ with respect to the base material. The lowest microhardness was always measured in the HAZ, showing values of about 40 $HV_{100,15}$. In the HAZ hardness progressively increases up to reach base material values at 14-20 mm distance from center depending on welding parameters (Tab. 1). Figure 1 shows results obtained for the S1050F117 condition on the upper and the lower profile. Trends and results were analogue for all the welded specimens.

Table 1: Welding parameters and main results of tensile and microhardness tests (average values ± std. dev.)

Welding parameters		TYS [MPa]	UTS [MPa]	Elong. [%]	$HV_{100,15}$			BM-center distance [mm]
Speed [rpm]	Feed [mm/min]				DRZ	TMAZ	Min. in HAZ	
1050	117	75	137	14.1	58 ± 3	56 ± 2	40	20
838	400	85	149	11.0	53 ± 2	52 ± 3	42	18
1262	400	85	144	11.1	54 ± 3	54 ± 1	41	16
1050	683	88	148	11.5	54 ± 3	52 ± 2	42	14
Base Material (BM)		174	200	14.8	78 ± 2			-

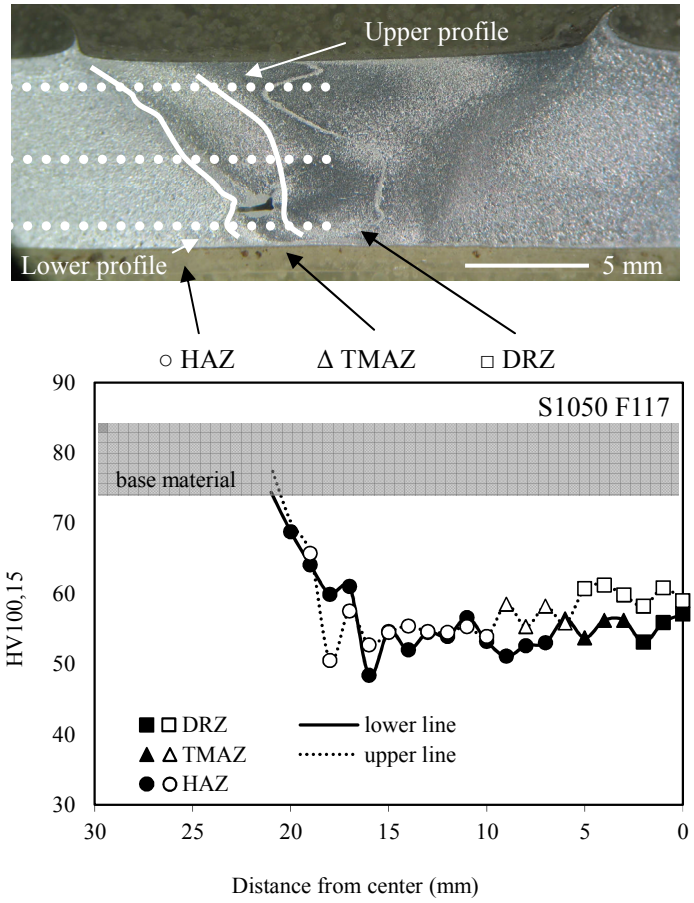


Fig. 1: Welding macrostructure and microhardness profiles on S1050F117 specimen

According to microhardness results, rupture during tensile tests was normally localized in the HAZ, as a matter of fact the specimens showed uneven plastic straining along the gage length, occurring mainly in this weak area, just after yielding. As reported in literature [2], the ultimate tensile strength decreases of about 25-30% as a function of process parameters affecting the geometry of welding zones and their properties (Tab. 1). Elongation decreases of about 5-25%. A significant decrease of tensile yield strength was also observed. Thus the mechanical properties are much lower than base material and the worst value was found for the lowest feed and lowest feed to speed ratio.

The microstructural analysis in all specimens always evidenced the presence of tunnels and kissing bonds caused by excessive or insufficient plastic straining and remnants of oxide layers dragged inside welding by the mixing action of the tool, respectively [4,5]. Despite of presence of these defects in all specimens, only on two specimens of S838F400 the rupture happened in the TMAZ, starting from marked tunnels. However, the rupture occurred after necking also in these cases.

Fatigue tests were performed mainly from 6 to 25 MPa√m producing fatigue rates in the range $2 \cdot 10^{-5}$ and $5 \cdot 10^{-2}$ mm/cycle. At low stress intensity range, below 12 MPa√m, fatigue crack growth rate is lower than base material for all welding conditions (Fig. 2). Above this value, the propagation on S1050F683 and S838F400 specimens becomes faster, approaching about two times the rates of base material at 18 MPa√m. For the other two welding conditions the fatigue behavior remains very similar to that of base material. The crack propagation was straight only for base material, whereas the propagation usually was more irregular on welded specimens. Although the requirements of the ASTM standards were always satisfied, in the welded specimens crack tends to deviate from the symmetry axis. Such propagation could be related by the different mechanical properties of the nugget and the near TMAZ and HAZ. Owing to its mechanical properties, the nugget could have a tendency to distribute stresses in the near weakest area. On the other hand the presence of areas with different microstructures and intrinsic fatigue resistance can also affect crack growth. In some specimens, the propagation was different on the two

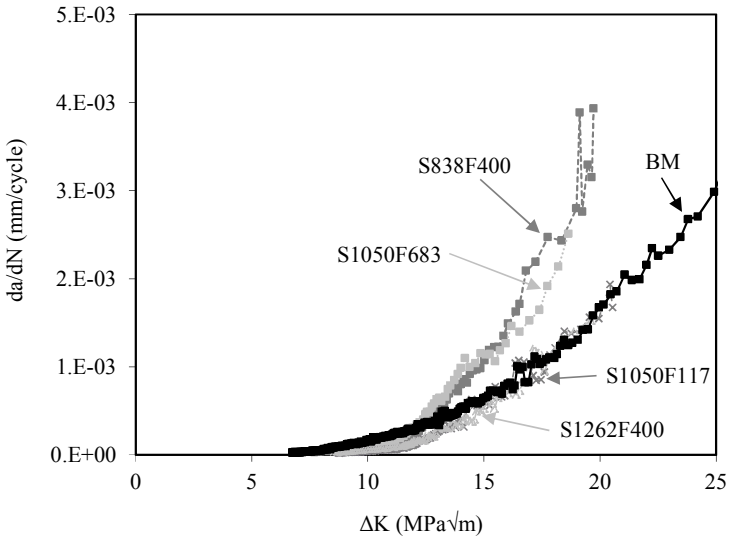


Fig. 2: Fatigue propagation curves

sides, showing high plasticization and deviation from symmetry axis on the upper side (tool side), whereas a straight and longer crack, in a very thin layer, was observed on the opposite side (Fig. 3). During fatigue testing the presence of a very thin brittle "skin" on the surface of base material was also observed. Defects and holes were often found below this layer.



Fig. 3: Uneven propagation on S1050F683 specimen

Several authors emphasized the contribution of compressive residual stresses produced by friction stir welding on the fatigue resistance of aluminum alloys [6,7]. Compressive stress in the transverse direction with respect to welding path reduces the effective stress intensity range acting at crack tip and thus reduces crack growth rate. Residual compressive stresses were already documented by techniques such as diffractometer [7] but their role has surely to be further investigated. FEM modeling of temperature, stress and strain distribution for evaluating this effect is in progress. However the results outlined that the retardation in propagation seems to occur only at low ΔK values, that is at low loading levels. By increasing stress intensity range, internal stress is expected to be negligible with respect to the fatigue loading. As a consequence crack growth approaches to the base material at 12 MPa$\sqrt{m}$. Above this value, the deleterious effect of inadequate welding parameters can be evident. In the test conditions adopted in this work, a clear worsening was observed at high feed, low speed and high feed to speed ratio.

Summary

The fatigue behavior of FSW joints of an AA6060 T6 aluminum alloy was studied. Crack growth rate in the weld nugget was evaluated by fatigue crack growth tests. The results confirm literature data, emphasizing a good fatigue behavior of the FSW butt-joints. Crack propagation rates comparable to the base material condition were observed on specimens welded at low feed, high speed and low feed to speed ratio. In the range of welding parameters adopted for testing, at low stress intensity range, fatigue crack growth in welding nugget was always slower than in base material. The effect of non-optimal welding parameters was evident at high ΔK. An increase of two times of rate was observed at 18 MPa$\sqrt{m}$. Further investigation is needed in order to evaluate the behavior in the near zones that were found to be weaker during mechanical and microstructural characterization.

References

[1] Mishra M.S., Mahoney, M.W., Friction Stir Welding and Processing, ASM International, 2007

[2] Moreira P.M.G.P. et al., Theoretical and Applied Fracture Mechanics, 50 2, 2008, 81-91

[3] Uematsu Y. et al., Fracture of Nano and Engineering Materials and Structures, 2T5, 2006, 287

[4] Li B., Materials & Design, 32, 4, 2011, 2073-2084

[5] James, M.N., International Journal of Fatigue, 25, 12, 2003, 1389-1398

[6] John R., Jata K.V., Sadananda K., Inter J Fatigue 25, 2003, 939

[7] Hong S. et al., Journal of Materials Science, 42, 23, 2007, 9888-9893

© (2012) Trans Tech Publications, Switzerland
doi:10.4028/www.scientific.net/KEM.488-489.347

Experimental study on polymer mass used to repair damaged structures

Tomasz Falborski[1,a], Robert Jankowski[1,b] and Arkadiusz Kwiecień[2,c]

[1]Faculty of Civil and Environmental Engineering, Gdansk University of Technology, ul. Narutowicza 11/12, 80-233 Gdansk, Poland

[2]Institute of Structural Mechanics, Cracow University of Technology, ul. Warszawska 24, 31-155 Kraków, Poland

[a]tomfalbo@pg.gda.pl, [b]jankowr@pg.gda.pl, [c]akwiecie@pk.edu.pl

Keywords: Repair of damage, experimental study, polymer mass, damaged structure, non-linear behaviour.

Abstract. A new method of repairing damaged structures by injecting the cracks with specially designed polymer mass (flexible two-component grout based on polyurethane resin) has been recently proposed. The technique is mainly dedicated to damaged masonries, especially historical structures where minimum intervention is permitted. The cracks are filled with the special injection, forming the flexible joints bonding the disrupted structural elements. The aim of the present paper is to show the results of the experimental study focused on properties of the polymer mass used for the injections. First, the material has been subjected to static compression tests. Then, the polymer mass has been examined dynamically under harmonic excitations with different frequencies and strain levels. The results of the study indicate that the tested polymer mass shows highly non-linear behaviour with relatively low resistance under small displacements and stiffening effect for higher strain levels. Moreover, it is substantially dependent on the strain rate having higher initial deformation modulus for higher strain rate values. Finally, the observed hysteretic behaviour of the material confirms its potential to dissipate the energy during vibrations preventing from further structural damage in the case of dynamic loading.

Introduction

Earthquake excitations are undoubtedly ones of the most dangerous and unpredictable threats to the structures all around the world. Dynamic loadings due to ground motions often lead to considerable damage to a number of structures and hence became an issue of major interests in many seismically active regions. This concerns especially masonry buildings, which are generally not strong enough to resist the cyclic horizontal loads induced by seismic excitations. Damage in such structures usually occurs due to their low tensile strength, contrary to their considerable compressive resistance. There are a lot of different methods which can be used to repair and reinforce cracked masonry structures (see [1]), but when it comes to damaged historical buildings and other heritage objects, it is not only safe exploitation but also aesthetical aspects which may play an important role. A new method of repairing damaged structures by injecting the cracks with specially designed polymer mass has been recently proposed [1-3]. The cracks are filled with the special injection, forming the flexible joints bonding the disrupted structural elements.

The aim of the present paper is to show the results of the experimental study focused on determination the properties of the polymer mass used for the injections. First, the material has been subjected to static compression tests. Then, the polymer mass has been examined dynamically under harmonic excitations with different frequencies and strain levels.

Polymer mass and flexible joint method

Polymer mass considered in the experimental study is a specially designed flexible two-component grout, which is based on polyurethane resin. Injecting of this polymer has been proposed as a method of repairing damaged structures (see [1,3]). The technique, which is known as Flexible Joint Method (FJM), is dedicated to cracked masonries, especially to historical structures where minimum intervention is allowed [2]. The cracks are filled with the special polyurethane mass injection, forming the flexible joints bonding the disrupted structural elements. This method is registered in the Polish Patent Department with No. P-368173. The FJM permits safe work of the retrofitted structure in the new stabilized state of balance. The method is particularly conductive to objects, in which a redistribution of stress occurred in consequence of damage (cracks). It permits further safe exploitation of the structure under additional static and dynamic loads. Filling the cracks in the previously damaged structure with specially designed polymer strengthens the disrupted structural elements. It assures that the damaged structure regains tensile, compression and shear resistance in place where bearing capacity was lost. The deformation of the flexible joint under load assures uniform distribution of stress along the joint over the total contact surface. The polymer mass bonds structural faults in places of cracks and limits development of the new stress concentrations [1].

Static compression tests

In order to determine the basic properties of the polymer mass used in the FJM, static compression tests were first conducted. For the purposes of the experiment, a number of cylinder specimens with a polymer part of 28 mm diameter and 28 mm height was prepared (Fig. 1). The tests were carried out under four different strain rates: $5 \cdot 10^{-1}$ 1/s, 10^{-1} 1/s, 10^{-2} 1/s and 10^{-3} 1/s in the testing machine (Fig. 2). The results of the experiment are shown in Fig. 3. It can be seen from the figure that for the higher strain rate the higher deformation modulus has been observed. Moreover, the behaviour of the polymer under static compression shows the stiffening effect of the material for higher strain levels.



Fig. 1 Cylindrical specimens made of polymer mass.

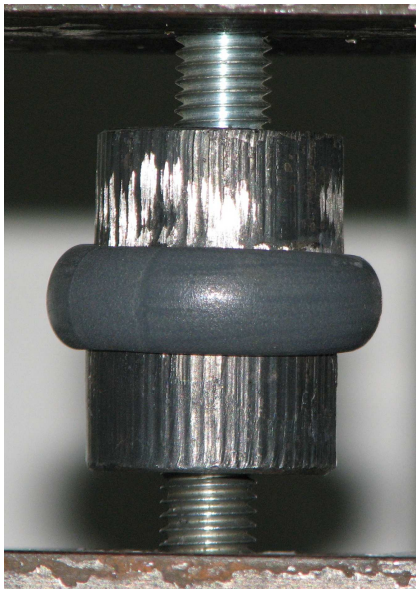


Fig. 2 Static compression test.

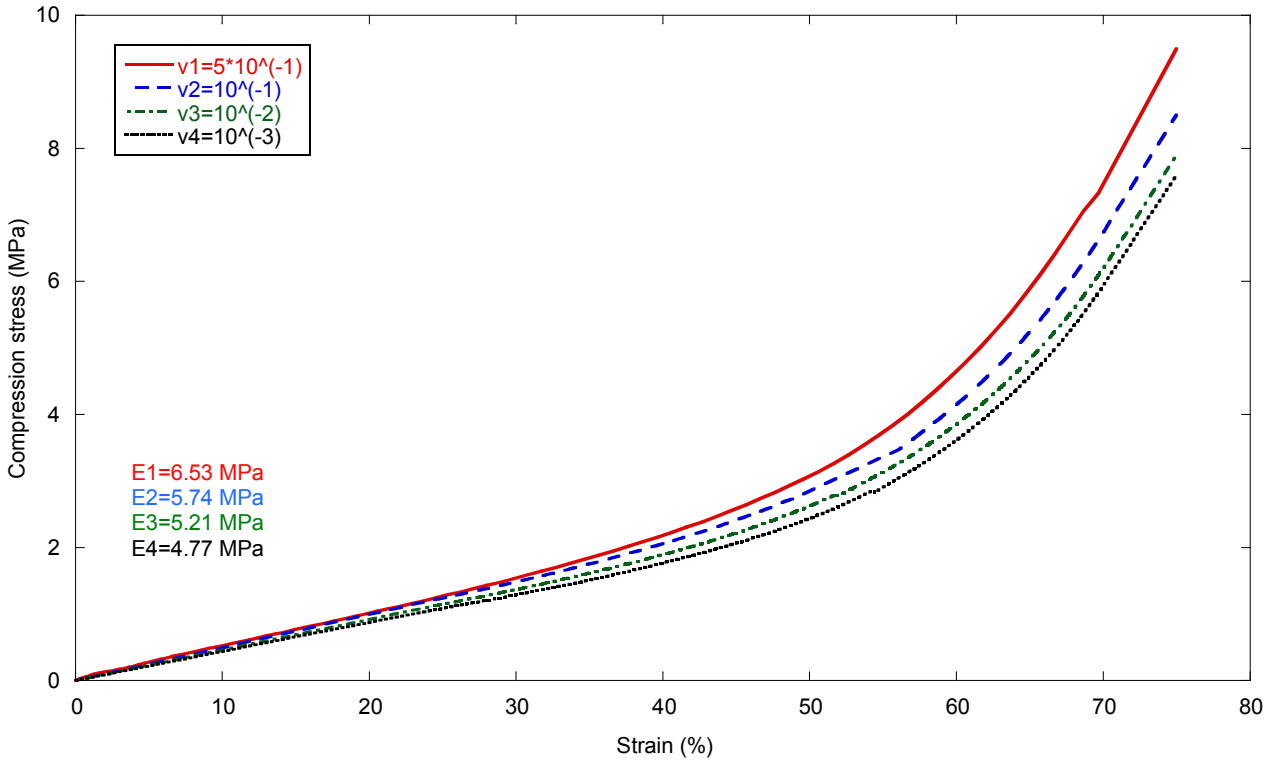


Fig. 3 Compression stress-strain diagrams for different strain rates.

Push-and-pull dynamic tests

Then, the push-and-pull tests were carried out in order to determine the dynamic properties of specimens made of polymer mass. During the tests, the devices were subjected to harmonic excitations with different frequencies. The strain levels of +/- 10%, 20%, 30% and 40% were attained. The examples of the results of the experiment in the form of the force-deformation hysteresis loops for the frequencies of 0.1 Hz, 0.5 Hz, 2 Hz and 5 Hz are presented in Fig. 4. It can be seen from the figure that the behaviour of the tested specimens is quite similar in the considered range of the frequency of excitation. The results indicate that the device shows relatively low resistance under small displacements, whereas it shows the stiffening effect for higher displacements.

Conclusions

The experimental investigation focused on properties of the polymer mass used in the FJM has been described in this paper. The results of two experiments (static compression and dynamic push-and-pull) have been presented.

The results of the study indicate that the tested polymer mass shows highly non-linear behaviour with relatively low resistance under small displacements and stiffening effect for higher strain levels. Moreover, it is substantially dependent on the strain rate having higher initial deformation modulus for higher strain rate values. Finally, the observed hysteretic behaviour of the material confirms its potential to dissipate the energy during vibrations (see [4]) preventing from further structural damage in the case of dynamic loading. This property is especially important in the case of damaged masonry structures, which have been strengthen by bonding the disrupted elements with the polymer mass.

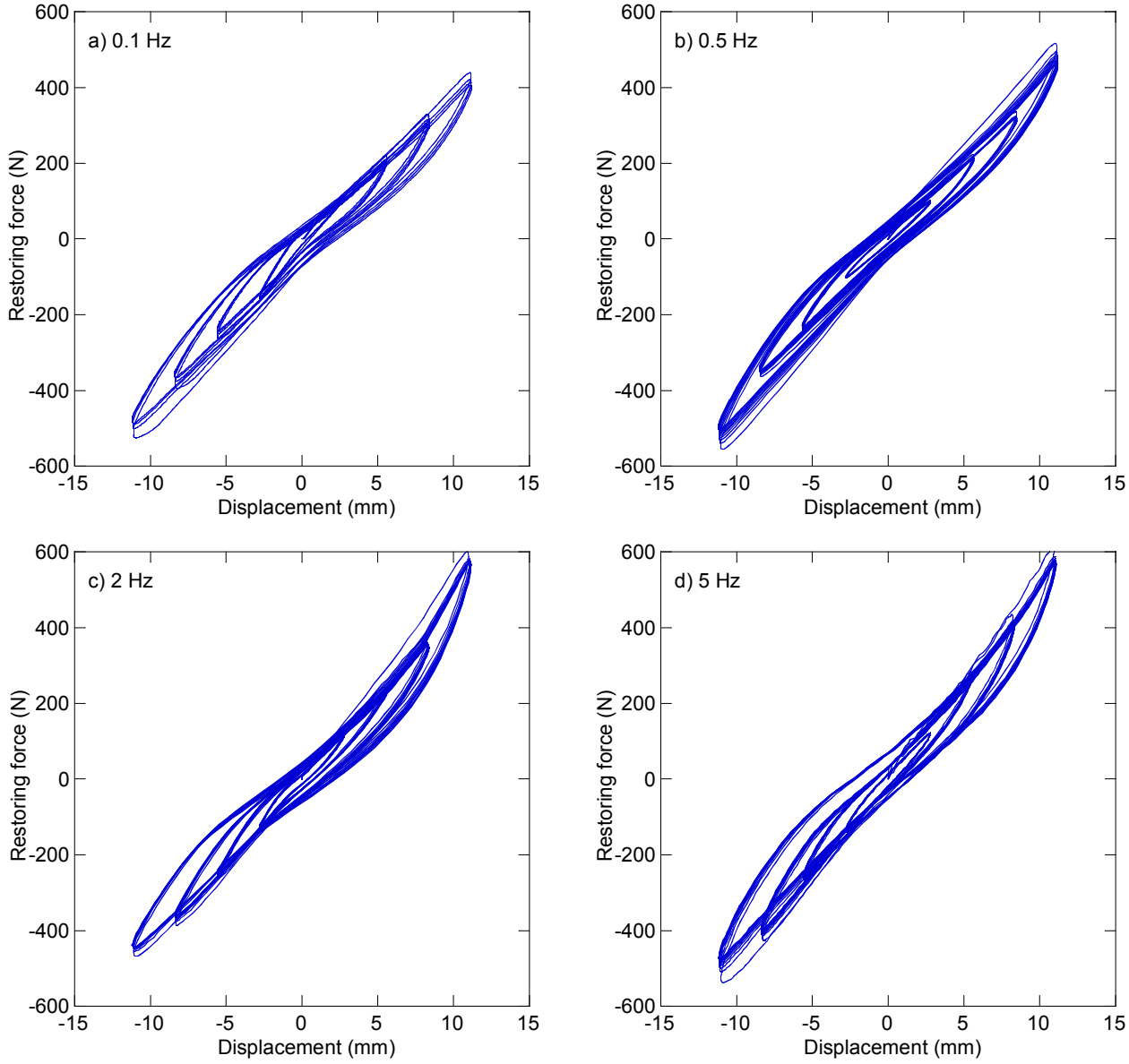


Fig. 4. Hysteresis loops for different excitation frequencies.

Acknowledgements

The authors would like to thank very much Mr. Bogusław Zając for his help in preparing the specimens made of polymer mass.

References

[1] A. Kwiecień, J. Kubica, P. Stecz and B. Zając, in: *First European Conf. on Earthquake Engineering and Seismology*, paper no. 282, Geneva, Switzerland (2006).

[2] A. Kwiecień, B. Zając and R. Jankowski, in: *Proc. of 6th Int. Conf. on Structural Analysis of Historic Construction*, volume 2, p. 931, Taylor & Francis/CRCPress/Balkema, London, UK (2008).

[3] A. Kwiecień and B. Zając, in: *Proc. of 7th European Conference on Structural Dynamics*, paper E 1, Southampton, UK (2008).

[4] R. Jankowski: Bulletin of Earthquake Engineering Vol. 1 (2003), p. 397.

© (2012) Trans Tech Publications, Switzerland
doi:10.4028/www.scientific.net/KEM.488-489.351

Shaking table experimental study on damage mechanism of the disconnecting switch under seismic excitation

Paweł Dembowski[1,a] and Robert Jankowski[1,b]

[1]Faculty of Civil and Environmental Engineering, Gdansk University of Technology, ul. Narutowicza 11/12, 80-233 Gdansk, Poland

[a]paweldembowski@wp.pl, [b]jankowr@pg.gda.pl

Keywords: Experimental study, damage mechanism, energetic network, earthquakes.

Abstract. The efficiency of the energetic network is a very import safety issue in the region experienced by the earthquake. High voltage disconnecting switches are important elements of the energetic infrastructure used to separate electric circuits (i.e. during repairs), which should not be damaged remaining fully operational. The aim of the paper is to show the results of the shaking table experimental investigation focused on damage mechanism of a high voltage disconnecting switch under seismic excitation. The real example of the two-column pantograph-type disconnecting switch was considered in the study. First, the tests were carried out by exciting the unit with the sweep-sine function. Based on the results, the structural dynamic properties of undamaged structure (natural frequencies, damping ratios) could be determined. Then, the so called rumbling seismic tests were conducted in order to determine the seismic strength of disconnecting switch according to the standards PN-EN 60068-3-3. After each experiment, the sweep-sine test was carried out so as to check the decrease in the natural frequencies of the unit. The results of the study show that the lower parts of the columns, which serve as isolators, are the most critical locations of the disconnecting switch considered. The unit was damaged due to failure of one of the rotational mechanisms installed at the bottom of columns.

Introduction

The efficiency of the energetic network is a very import safety issue in the region experienced by the earthquake. The power lines belong to critical lifelines, particularly soon after an earthquake. Lack of electricity makes difficulties in rescue operation, intensifies chaos and panic among the citizens. Meanwhile, many energetic infrastructure devices were seen damaged during past earthquakes. For example, after the Northridge earthquake in 1994, the damages were so extensive, that 2.5 million people of Los Angeles and surroundings were deprived of electricity [1].

High voltage disconnecting switches are important elements of the energetic infrastructure system used to separate electric circuits (i.e. during repairs), which should remain fully operational after the ground motion [2,3]. For their good and safe work conditions, usage of resistant and reliable materials is really essential. High voltage disconnecting switches have to pass rigorous and expensive seismic tests (see [4]) which are conducted on shaking tables (see [5]).

The aim of the present paper is to show the results of the experimental investigation focused on damage mechanism of the high voltage disconnecting switch under seismic excitation. The real example of the two-column-type disconnecting switch SGF 123, manufactured by HAPAM Poland Company, was considered in the study. In the first part of the investigation, the sweep-sine shaking table tests were conducted. Based on the results of the tests, the dynamic properties of the disconnecting switch were determined. In the next step, a set of dynamic experiments, so called rumbling seismic tests, were conducted in order to determine the seismic strength of analysed structure according to the standards [6]. After each experiment, the sweep-sine test was carried out so as to check the decrease in the natural frequencies of the structure.

Experimental tests

The experimental tests were conducted at the seismic laboratory of the Ship Design and Research Centre, Poland. First, the sweep-sine tests of undamaged structure were conducted in all three directions (two horizontal and one vertical) for two operating conditions (opened arms and closed arms). During the tests, the frequency of the harmonic excitation began at 2.0 Hz and it was increasing up to 35 Hz. The shaking table with the tested structure in the closed arms condition is shown in Fig. 1. The example of the results of one of the sweep sine tests is shown in Fig. 2. Based on the results, the structural dynamic properties of undamaged structure (natural frequencies, damping ratios) were determined.

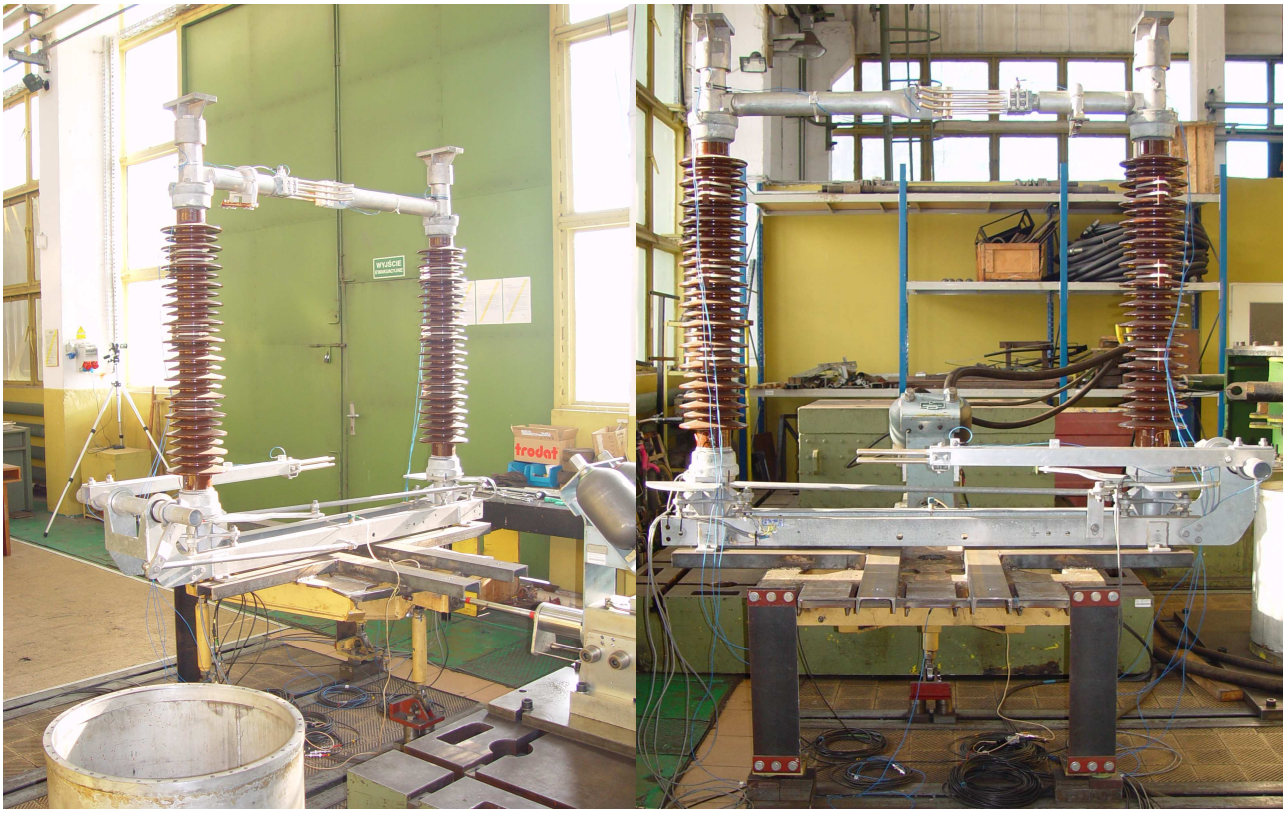


Fig. 1. Shaking table with tested disconnecting switch.

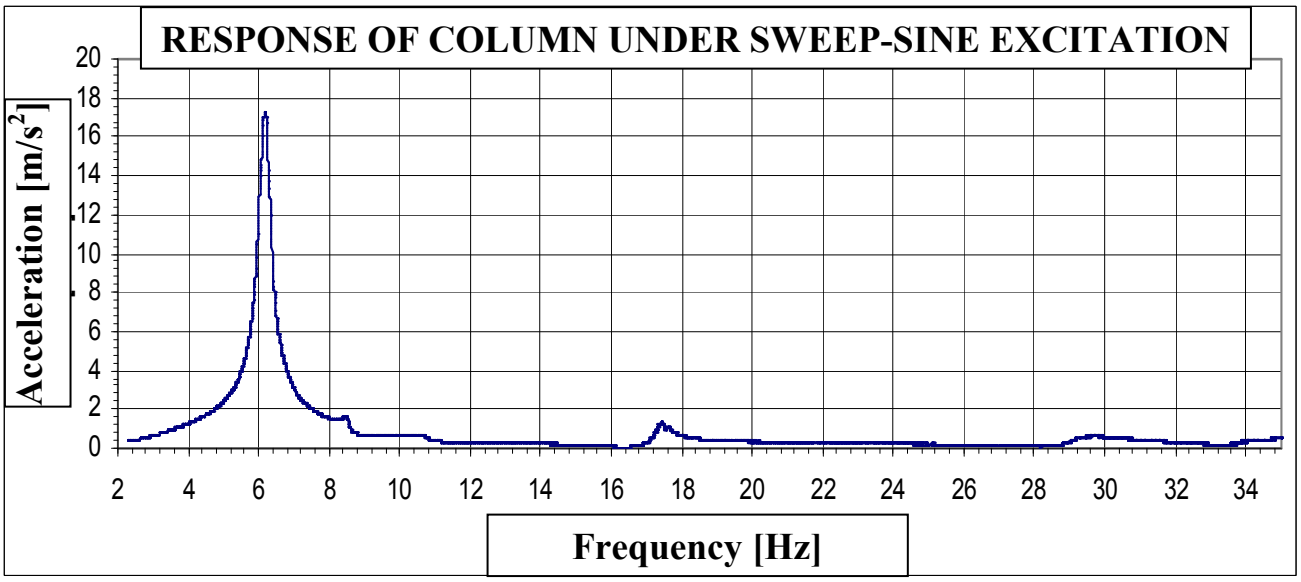


Fig. 2. Example of results from sweep-sine test of undamaged structure.

Then, the experiments were carried out in order to determine the seismic strength of the structure according to standards PN-EN 60068-3-3 [6]. The disconnecting switch was excited using the sinusoidal rumbling function with increasing level of acceleration until damage of the unit. After each experiment, the sweep-sine test was carried out so as to check the decrease in the natural frequencies of the structure. The results of the test, which caused damage of the disconnecting switch are shown in Fig. 3. The green line in the figure (first diagram) represents the acceleration time history of the shaking table excitation, whereas the blue line (second diagram) denotes the acceleration response time history of the upper part of the column. The example of the results of the sweep-sine test conducted after damaging experiment are presented in Fig. 4. Comparison between Fig. 2 and Fig. 4 shows that the drop in the first natural frequency of the unit was as large as 39%.

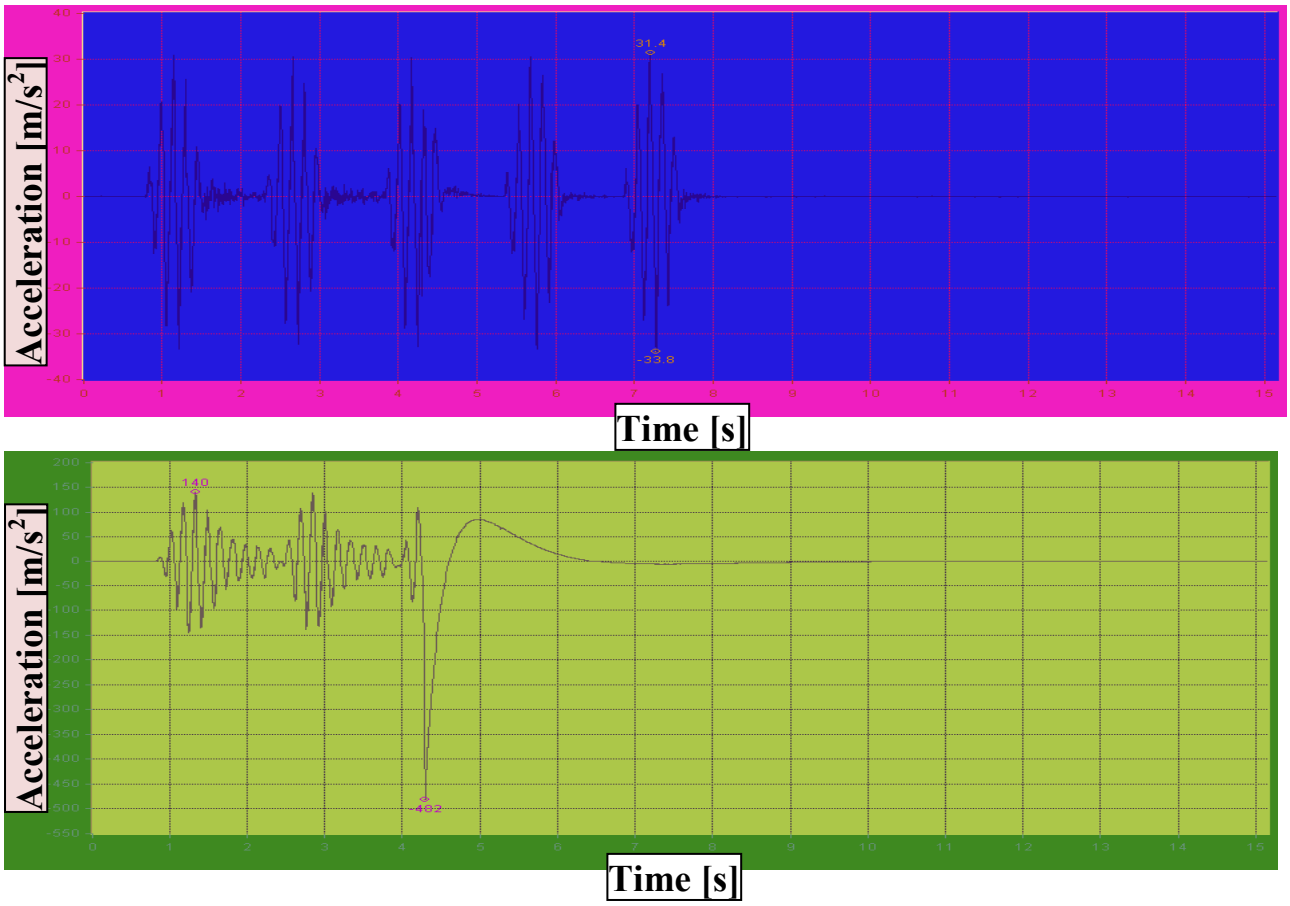


Fig. 3. Results of the test which caused damage.

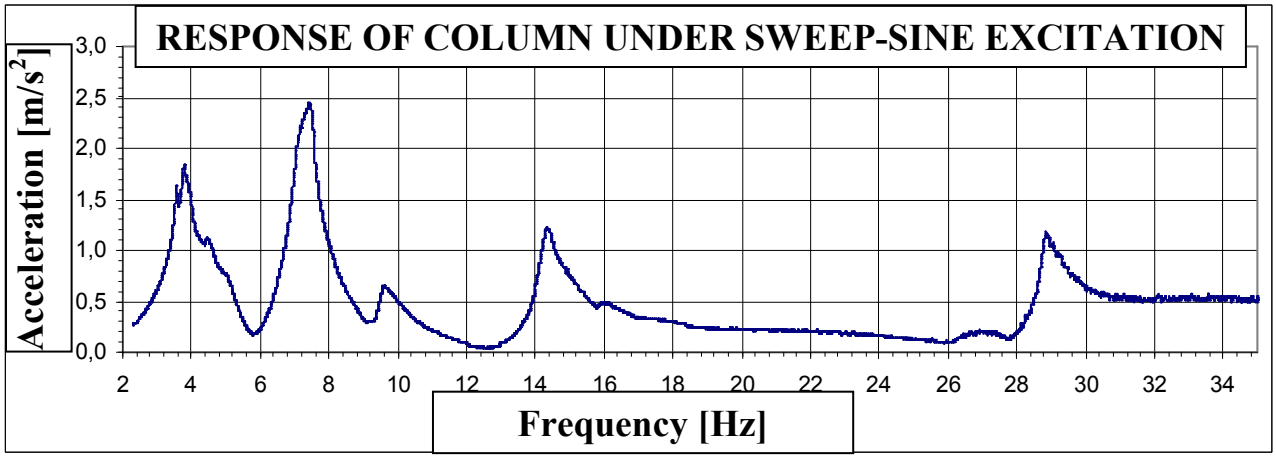


Fig. 4. Example of results from sweep-sine test of damaged structure.

Fig. 5 shows the damaged part of the disconnecting switch after rumbling seismic tests. The unit was damaged due to failure of one of the rotational mechanisms installed at the bottom of columns.

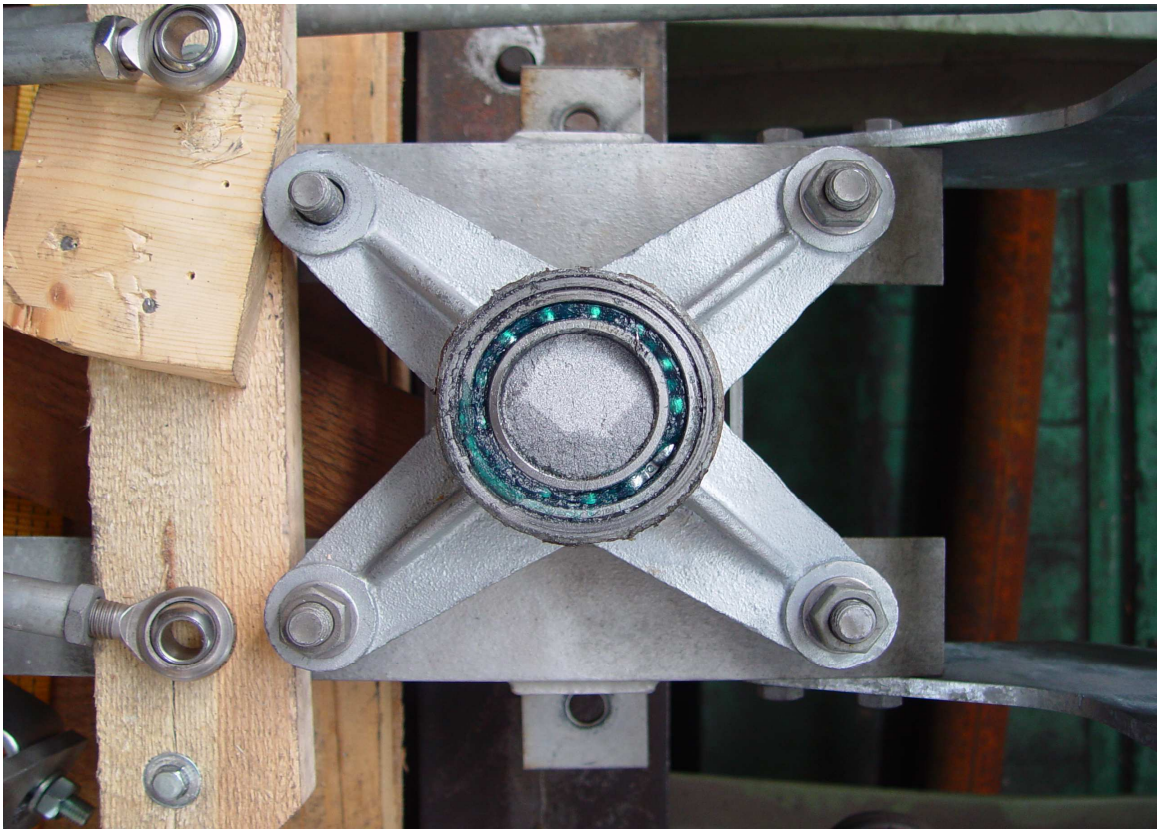


Fig. 5. Damaged rotational mechanism of the disconnecting switch.

Conclusions

The results of the study show that the lower parts of the columns, which serve as isolators, are the most critical locations of the disconnecting switch considered. The unit was damaged due to failure of one of the rotational mechanisms installed at the bottom of columns. The results of the experiments indicate, however, that the analysed structure is capable to endure very strong vibrations, highly exceeding third level of seismic exploitation according to the standards. A substantial drop in the natural frequencies of the unit was noticed as the result of seismic rumbling tests with increasing level of acceleration.

References

[1] F.Z. Hall: Earthquake Spectra Vol. 11 (1995), suppl. C.

[2] P. Dembowski and R. Jankowski, in: *Proc. of 10th International Conference on Recent Advances in Structural Dynamics – RASD 2010*, paper ID 58, Southampton, UK (2010).

[3] P. Dembowski, R. Jankowski and Z. Zembaty, in: *Proc. of 14th European Conference on Earthquake Engineering*, paper ID 844, Ohrid, Macedonia (2010).

[4] C.W. De Silva*:* Earthquake Engineering and Structural Dynamics Vol. 8 (1980), p. 337.

[5] R. Jankowski*:* Earthquake Engineering and Structural Dynamics Vol. 39 (2010), p. 343.

[6] Standard PN-EN 60068-3-3:1993 Environmental testing. Guidance. Environmental testing. Miscellaneous. Guide to seismic test methods for equipment (1993).

© (2012) Trans Tech Publications, Switzerland
doi:10.4028/www.scientific.net/KEM.488-489.355

Peridynamic Theory for Damage Initiation and Growth in Composite Laminate

Erkan Oterkus[1, a], Erdogan Madenci[2,b]

[1]National Institute of Aerospace, Hampton, VA 23666, USA

[2]Aerospace and Mechanical Engineering, The University of Arizona, Tucson, AZ 85721, USA

[a]erkan.oterkus@ninet.org, [b]madenci@email.arizona.edu

Keywords: Progressive; Failure; Composites, Nonlocal; Peridynamic theory

Abstract. A recently introduced nonlocal peridynamic theory removes the obstacles present in classical continuum mechanics that limit the prediction of crack initiation and growth in materials. Furthermore, damage growth in composites involves complex and progressive failure modes. Current computational tools are incapable of predicting failure in composite materials mainly due to their mathematical structure. However, the peridynamic theory removes these obstacles by taking into account non-local interactions between material points. This study presents an application of the peridynamic theory for predicting damage progression from a central crack in fiber reinforced composite plates subjected to uniaxial tension loading.

Introduction

Despite the development of many important concepts to predict material behavior and failure, the prediction of failure modes and residual strength of materials is a challenge within the framework of the finite element method (FEM). Furthermore, the previous methods cannot address the nucleation of damage in a continuous material. The field of fracture mechanics is primarily concerned with the evolution of pre-existing defects within a body, rather than the nucleation of new defects. Even when addressing crack growth, the FEM suffers from the inherent limitation that it requires remeshing after each incremental crack growth. In addition to the need to remesh, existing methods for fracture modeling also suffer from the requirement of an external crack growth criterion. This criterion prescribes how damage evolves a priori based on local conditions, and guides the analysis as to when and how damage initiates and propagates. Considering the difficulty in obtaining and generalizing experimental fracture data, providing such a criterion for damage growth, especially in composite structures, clearly presents a major obstacle to fracture modeling using conventional methods. This prevents such methods from being applicable to problems in which multiple damage growth occurs and interacts in complex patterns.

In order to overcome these problems, Silling [1] introduced a nonlocal theory that does not require spatial derivatives—the peridynamic (PD) theory. The main difference between the PD theory and classical continuum mechanics is that the former is formulated using integral equations as opposed to derivatives of the displacement components. This feature allows damage initiation and propagation at multiple sites, with arbitrary paths inside the material, without resorting to special crack growth criteria. In the PD theory, internal forces are expressed through nonlocal interactions between the material points within a continuous body, and damage is a part of the constitutive model. Interfaces between dissimilar materials have their own properties and damage can propagate when and where it is energetically favorable for it to do so.

Peridynamic theory

Silling [1] replaced the equations of classical continuum mechanics with the following equation of motion applicable whether or not a discontinuity exists in the structure:

$$\rho(\mathbf{x})\ddot{\mathbf{u}}(\mathbf{x},t)=\int_H \mathbf{f}(\mathbf{x}'-\mathbf{x},\mathbf{u}'-\mathbf{u})\,dH+\mathbf{b}(\mathbf{x},t)\ . \tag{1}$$

In Eq. (1), the horizon, H, includes all the material points that the material point $\mathbf{x}$ can interact with inside the body. The interaction force or peridynamic force between material points $\mathbf{x}$ and $\mathbf{x}'$ can be expressed as $\mathbf{f}(\mathbf{x}'-\mathbf{x},\mathbf{u}'-\mathbf{u})$, and it is a function of the relative position vector, $\mathbf{x}'-\mathbf{x}$, and relative displacement vector, $\mathbf{u}'-\mathbf{u}$. The peridynamic force is along the same direction of the relative position of these material points in the deformed configuration, i.e., $\mathbf{y}'-\mathbf{y}=(\mathbf{x}'+\mathbf{u}')-(\mathbf{x}+\mathbf{u})$. For an elastic isotropic material, the peridynamic force takes the form

$$\mathbf{f}=c\,s\frac{\mathbf{y}'-\mathbf{y}}{|\mathbf{y}'-\mathbf{y}|}, \tag{2}$$

where c, and s represent the peridynamic material parameter and stretch between material points $\mathbf{x}$ and $\mathbf{x}'$, respectively. The material parameter, c, can be related to the engineering material constants by equating the strain energy densities of the PD and classical continuum theories at a material point inside a body due to simple loading, such as uniform expansion.

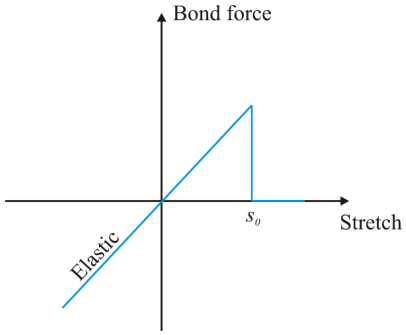


Figure 1. Constitutive relation between material points in an elastic material

It can also be assumed that two material points, $\mathbf{x}$ and $\mathbf{x}'$, cease to interact with each other if the mechanical stretch between these material points exceeds a critical stretch value, s_0, as shown in Fig. 1. This material model represents an elastic material behavior without allowing any permanent deformation. Termination of the interaction between material points can be associated with the failure of the material by modifying the peridynamic force relation given in Eq. (2) by introducing the failure parameter

$$\mu(\mathbf{x}'-\mathbf{x},t)=\begin{cases}1 & \text{if } s(\mathbf{x}'-\mathbf{x},t')<s_0 \text{ for all } 0<t'<t\\ 0 & \text{otherwise}\end{cases} \tag{3}$$

The local damage is the weighted ratio of the number of the broken interactions to the total number of interactions within the horizon, H. The extent of damage is defined by a value between 0 and 1, where 0 indicates that a material point has no damage and 1 indicates complete damage at the material point. Also, a damage value of 0.5 and above indicates possible cracking. In order to solve Eq. (1), a collocation method is adopted and the numerical treatment involves the discretization of the domain of interest into subdomains. The peridynamic formulation described above concerns an isotropic material where there is no directional dependence of the interactions between the material points. However, if anisotropic materials such as a fiber-reinforced composite structure are considered, the directional dependency must be included in the peridynamic analysis. Therefore, four different peridynamic material parameters are introduced, as shown in Fig. 2, to model a fiber-reinforced composite laminate. Note that a material point of interest can only interact with a material point located either in the same ply or in the adjacent plies.

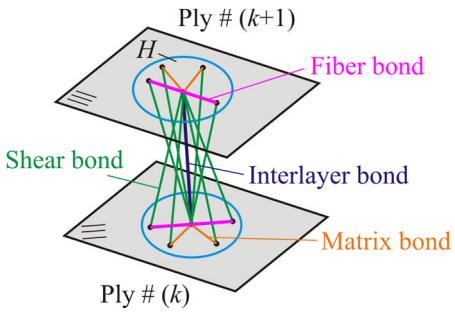


Figure 2. Peridynamic bonds for a fiber-reinforced composite laminate

Associated with a ply, the material parameter concerning the interaction of material points in the fiber direction only is denoted with c_f. The interaction of material points in all other directions within a ply is governed by the material parameter, c_m. The interaction between material points in adjacent plies is described by the material parameter c_{in} and c_{is} accounting for transverse normal and shear deformations between the neighboring plies.

As in the case of isotropic materials, the peridynamic material parameters, c_f, c_m, c_{in} and c_{is} can be expressed analytically in terms of the engineering material constants, E_1, E_2, E_3, G_{12}, and ν_{12}. The detailed derivations of these expressions are given by Oterkus [3].

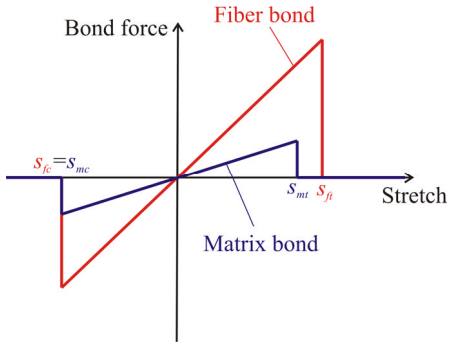


Figure 3. Force-stretch relation for fiber and matrix bonds.

The constitutive or the force-stretch relations for the in-plane interactions of two material points, referred to as fiber and matrix bonds, are shown in Fig. 3. The critical parameters that define the failure of these bonds under tension and compression are (s_{ft}, s_{mt}) and (s_{fc}, s_{mc}), respectively, and can be determined based on the experimental measurements. Interlayer damage represents the breakage of (interlayer) bonds between a layer and its adjacent layers above and below. Hence, it provides the extent of delamination between the adjacent layers. Therefore, the interlayer bonds are assumed to fail only in tension.

Numerical results

The failure prediction capability of the PD theory is demonstrated by introducing a central crack in the two laminate layups of $[0°/90°/0°]$ and $[0°/45°/0°]$. Its elastic moduli in the fiber and transverse directions are $E_1 = 159.96\,\text{GPa}$ and $E_2 = 8.96\,\text{GPa}$, respectively. The length and width of the lamina are specified as $L = 15.24\,\text{mm}$ and $W = 7.62\,\text{mm}$, respectively. Ply thickness is specified as $t = 0.1651\,\text{mm}$. As shown in Fig. 4, the crack is aligned with the y-axis and has a length of $2a = 0.01778\,\text{m}$. The laminates are subjected to a velocity boundary condition of $v_0 = 2.02\times10^{-7}\,\text{m/s}$ along the edges of the lamina through a volumetric region with a depth of $b = 2.54\times10^{-3}\,\text{m}$. The PD model is generated by using a single layer of material points with a grid size of $\Delta x = 6.35\times10^{-4}\,\text{m}$. The horizon radius is specified as $\delta = 3.015\Delta x$. The fiber and matrix bond constants are computed as $c_f = 5.72\times10^{23}\,\text{N/m}^6$ and $c_m = 1.86\times10^{22}\,\text{N/m}^6$. The critical stretch parameters specified for the fiber and matrix bonds are $s_{ft} = 0.027$ and $s_{mt} = 0.0135$, respectively. The critical stretch and angle values for interlayer and shear bonds can be specified as equal to the critical stretch of the matrix bond, i.e., $s_{in} = \varphi_c = 0.0135$. The quasi-static solution is obtained by using the adaptive dynamic relaxation technique by using a time increment of 1 and stable mass density value of $7.005\times10^{18}\,\text{kg/m}^3$.

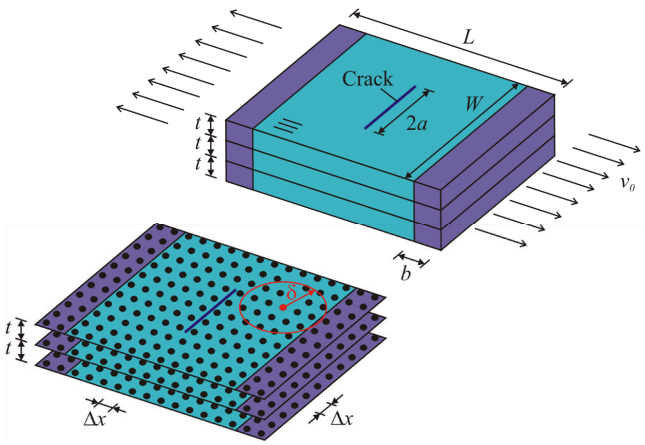
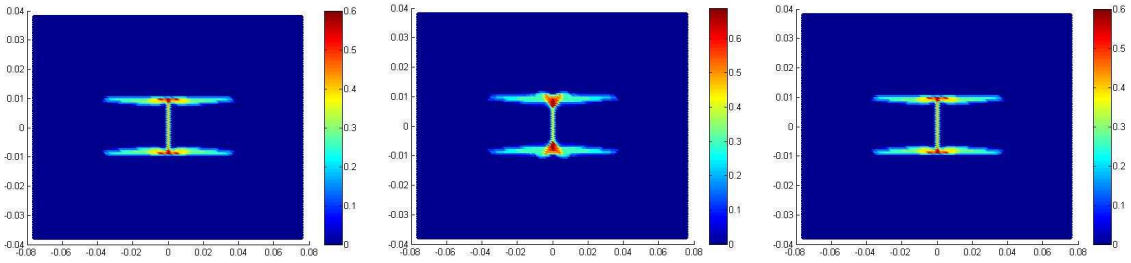


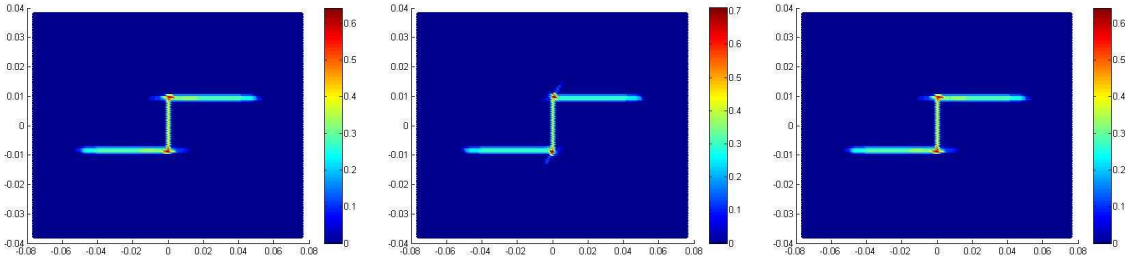
Figure 4. Loading and geometry of a laminate with a crack under tension loading.

For the $[0°/90°/0°]$ laminate, an "H"-type splitting failure mode is observed for all plies, as shown in Fig. 5. In this case, 0° plies are dominant in the loading direction; therefore, 0° plies determine the failure behavior of the laminate. However, in the $[0°/45°/0°]$ laminate, a "Z"-type failure mode is obtained in all plies due to the presence of a 45° ply, as shown in Fig. 6. These damage patterns are consistent with those observed in a study by Bogert et al. [4].



(a) **(b)** **(c)**

Figure 5. Matrix bond damage plots for a laminate of $[0° / 90° / 0°]$ with a pre-existing crack for $s_{mt} = s_{in} = \varphi_c$: (a) bottom ply, $0°$; (b) center ply, $90°$, and (c) top ply, $0°$.



(a) **(b)** **(c)**

Figure 6. Matrix bond damage plots for a laminate of $[0° / 45° / 0°]$ with a pre-existing crack for $s_{mt} = s_{in} = \varphi_c$: (a) bottom ply, $0°$; (b) center ply, $90°$, and (c) top ply, $0°$.

Summary

Based on the numerical results, the PD approach successfully predicts the damage growth patterns in fiber-reinforced laminates with a pre-existing crack while considering the distinct properties of the fiber and matrix, as well as of the interlayer material between the plies. The predictions capture the correct failure mechanisms of matrix cracking, fiber breakage, and delamination without resorting to any special treatments, and agree with the experimental observations published in the literature. The simulations also capture failure modes among each ply, which are usually distinct; they heavily depend on fiber direction, which is realistically exhibited in the current results. It can be concluded that the peridynamic theory is a powerful method that can be employed for failure analysis of composite materials.

References

[1] Silling, S.A., 2000, "Reformulation of elasticity theory for discontinuities and long-range forces," *J Mech Phys Solids*, Vol 48, pp. 175-209.

[2] Silling, S. A. and Askari, E., 2005, "A meshfree method based on the peridynamic model of solid mechanics," *Comput Struct,* Vol. 83, pp. 1526-1535.

[3] Oterkus, E., 2010, "Peridynamic theory for modeling three-dimensional damage growth in metallic and composite structures," *PhD Thesis*, University of Arizona.

[4] Bogert, P. B., Satyanarayana, A. and Chuncu, P. B., 2006, "Comparison of damage path predictions for composite laminates by explicit and standard finite element analysis tools," 47^{th} *AIAA/ASME/ASCE/AHS/ASC Structures, Structural Dynamics, and Materials Conference*, Newport, Rhode Island, AIAA 2006-1750.

© (2012) Trans Tech Publications, Switzerland
doi:10.4028/www.scientific.net/KEM.488-489.359

Inelastic dynamic analysis and non-linear static analysis (Push-over) of 3-story and 6-story RC buildings of ductile frames

Jorge A. Avila [1, 2, a] and Julio C. Manzano [2]

[1] Institute of Engineering, National University of Mexico (UNAM)

[2] Faculty of Engineering, National University of Mexico (UNAM)

Ciudad Universitaria, Coyoacan 04510, México, D.F.

[a] javr@pumas.iingen.unam.mx

Keywords: ductile frames, non-linear static analysis, inelastic dynamic step by step analysis.

Abstract. With 3-story and 6-story RC buildings of ductile frames, previously designed, non-linear static analysis with increased monotonically lateral loads (Push-over) are made in order to determine its collapse and their responses against the inelastic seismic analysis results with the SCT-EW-85 record are compared. It is designed with the Principal Body and with the Appendix A conditions of the Seismic Technical Norms of the Mexico City Code (RDF-04), satisfying the maximum story distortion limits of the service and collapse conditions; the buildings (offices) are in the III_b compressible seismic zone. The non-lineal responses were determined with nominal resistance and over-resistance effects. For the non-linear static analysis with increased monotonically lateral loads, was important to select the type of lateral forces distribution. The comparison were made with base shear force–roof lateral displacement relations.

Introduction

It is determined and compared the non-linear seismic (Push-Over) and the inelastic dynamic step by step performance in 3 and 6-story buildings with reinforced concrete (RC) frames located in the compressible zone of México City. The design was made with the RDF-04 Construction Code [1], according to the service and failure limit states established in its corresponding Complementary Techniques Norms (CTN-Seismic and CTN-Concrete). The structures were designed as follows: A) with the design spectrum of the Principal Body (PB), seismic zone III_b; B) with the design spectrum according to the soil dominant period, defined in the Appendix A (T_s= 2 seconds). The inelastic seismic responses in time history were analyzed with the SCT-EW record representative of maximum compressible soil damage in Mexico City during the earthquake of September 1985. For the Push-Over analyses, the responses under different lateral load distributions were calculated. It is included the influence of the possible over-resistance sources. With the results of this work it is to show that there are no important variations between cases B1 and D1 (Principal Body) and B2 and D2 (Appendix A). The criterion of Appendix A allows to determinate displacement of the conditions of service and collapse to the structure may be subject.

Structure description

They are office buildings of 3 and 6-story of reinforced concrete, symmetric and regular in plan and elevation. They have a foundation rigid box. The structural system is formed with reinforced concrete frames by girders and columns rigidly connected by a solid slab of 10 cm thick. Fig. 1 shows the principal details in plan and elevation of the buildings under study. The column and girder resistances were designed for the last mechanic elements of the spectral modal dynamic analysis, considering the three-dimensional structural performance more the vertical load effects (dead loads and live loads) and second order effects, and for the ductile frame special requirements established by Concrete Norms, due to the use of seismic performance factor Q= 4.

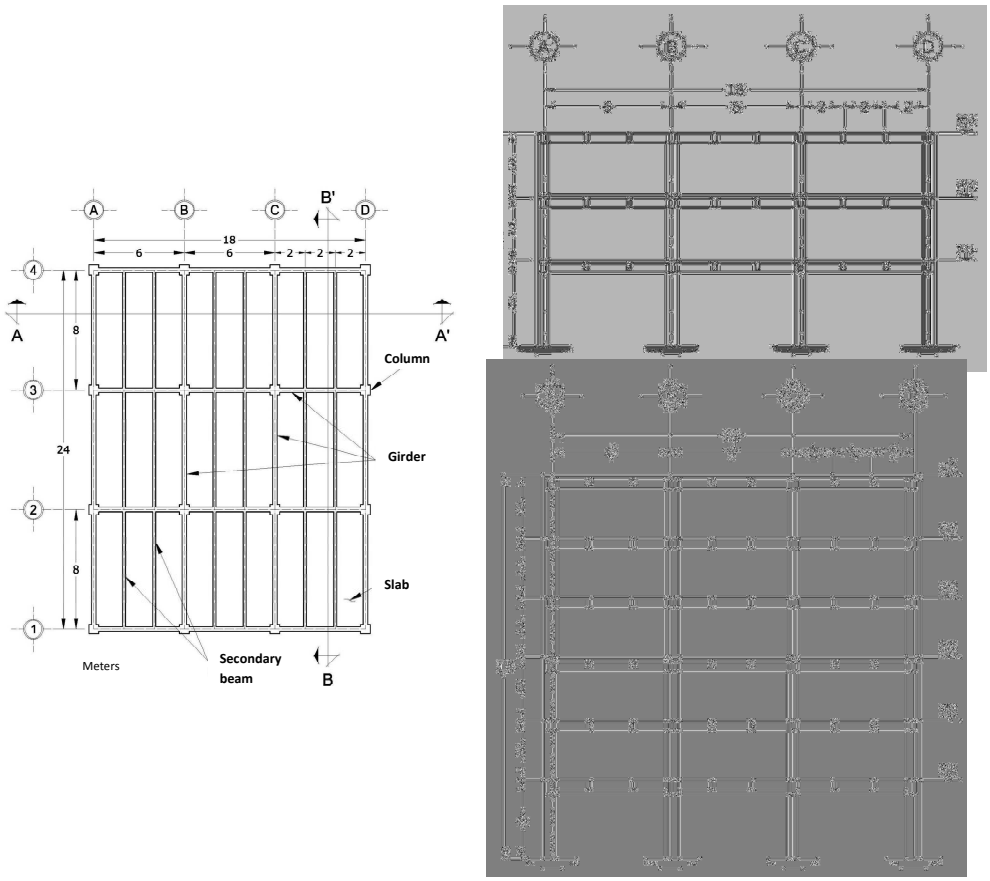


Figure 1: Structural plant-type (dimensions in meters) and transversal cuts (A-A´)

Elastic response

Periods of vibration. Periods in the direction X and Y are the same due to the symmetry of the structure. Fig. 2 shows the design spectra of the RDF-04 of the Appendix A (T_s= 2 seconds), the elastic and inelastic response spectra of SCT-EW-85 record (critical viscous damping of 5%) as well as the location of the fundamental periods of vibration of the 3-story building (T_{1X}= 0.663 seconds and T_{1Y}= 0.674 seconds) and 6-story building (T_{1X}= 0.832 seconds and T_{1Y}= 0.837 seconds).

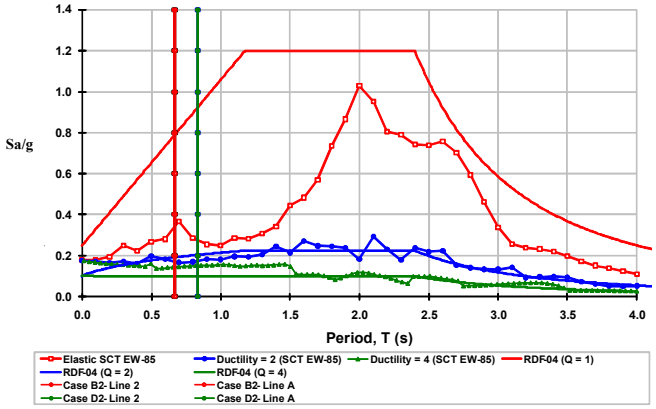


Figure 2: Location of fundamental periods of vibration, lines 2 and A of 3-story and 6-story structures, regarding the design spectra (Q= 1 y 4) of Appendix A (cases B2 and D2) and the response spectra (μ = 1 y 4) of SCT-EW-85 record

Maximum story drifts. The 3-story building under earthquake in both directions, accomplishes with the permissible limit of 0.006 specified in the Principal Body (case B1), and with the permissible limit of 0.002 for Appendix A (case B2); the collapse limit of 0.03 was not a condition to govern the performance of the design. The 6-story building accomplishes with both permissible limits (service condition); the story drifts in this structure are closer to the collapse limit that the 3-story model.

Inelastic response step-by-step

Inelastic dynamic responses step-by-step are determined by using the SCT accelerogram, E-W component, registered on September 19th 1985. The responses were calculated for the lines 2 (direction X) and A (direction Y) of the 3-story and 6-story buildings; such frames were "calibrated" to ensure static and dynamic performance similar to the three-dimensional model.

Maximum horizontal displacements and demands of global ductility. All cases of 3 and 6-story buildings, with nominal resistances, experiment inelastic performance; generally the models with over-resistance effects have lower global demands, μ_G ; the inelastic responses with over-resistance effects are practically the same in cases B and D. In the 6-story models, case D2 with nominal resistances, the μ_G values are higher; the cases D1 and D2, with over-resistances tend to behave elastically. In no case μ_G was over 4, equal to the value of the seismic performance factor (Q) with which the elastic design spectrum of cases B and D were reduced.

Non-linear static analysis (Push-over)

The non-linear static analysis with four different distributions of lateral load, without and with the over-resistance effects, were made: 1) SMD distribution with forces at the floor level (F_i), determined from spectral modal dynamic analysis, involving all modes of lateral vibration. 2) Elastic step-by-step distribution with forces at floor level (F_i), when the structure is working in the elastic range. 3) Inelastic step-by-step distribution with forces at floor level (F_i), for the maximum inelastic roof displacement. 4) Linear triangular distribution from F_i forces of static seismic analysis (linear); the results shown are for the distributions 1) and 3). The Push-over analyses were made to the following conditions: a) maximum demands of the local ductility in girders are equal to 35, b) maximum demands of the local ductility in columns are equal to 20, c) maximum story drift of the collapse condition is 0.03, according to Appendix A of the Seismic Norms of RDF-04 Code for structures for ductile concrete frames with Q= 4, d) the mechanism of collapse of the structure is reached.

Base shear force–roof lateral displacement relationship. Fig. 3 compares the results of the base shear force-roof lateral displacement relationships of the Push-over analyses against relationship of the corresponding inelastic step-by-step analyses without and with over-resistance effects, of the 3 and 6-story models for the line A, designed with Appendix A (cases B2 and D2). In the case B2 of the 3-story building, maximum displacement did not exceed 30 cm, due to the regulation of the limit condition previously established of maximum demands of ductility in columns of 20. For 6-story models, the resulting performance from Push-over analysis was governed generally by the condition of permissible drift of collapse of 0.03. The influence of over-resistance effects is very important.

Conclusions

Buildings designed with RDF-04 Code show satisfactory performance, with enough reserve of resistance, to avoid brittle failure. Significant variations between the designs of the cases B1 and D1 (Principal Body) and B2 and D2 (Appendix A) are not presented. With the help of the over-resistance effects, the maximum responses tended to be lower. The tendency of plastic hinges from step-by-step and non-linear static (Push-over) analyses show, in general, a strong column-weak girder performance according to the current design philosophy, which ensures a ductile behavior.

References

[1] Gaceta Oficial del Gobierno del Distrito Federal, "Reglamento de Construcciones de la ciudad de México y Normas Técnicas Complementarias para Diseño por Sismo, y para Diseño y Construcción de Estructuras de Concreto" (2004).

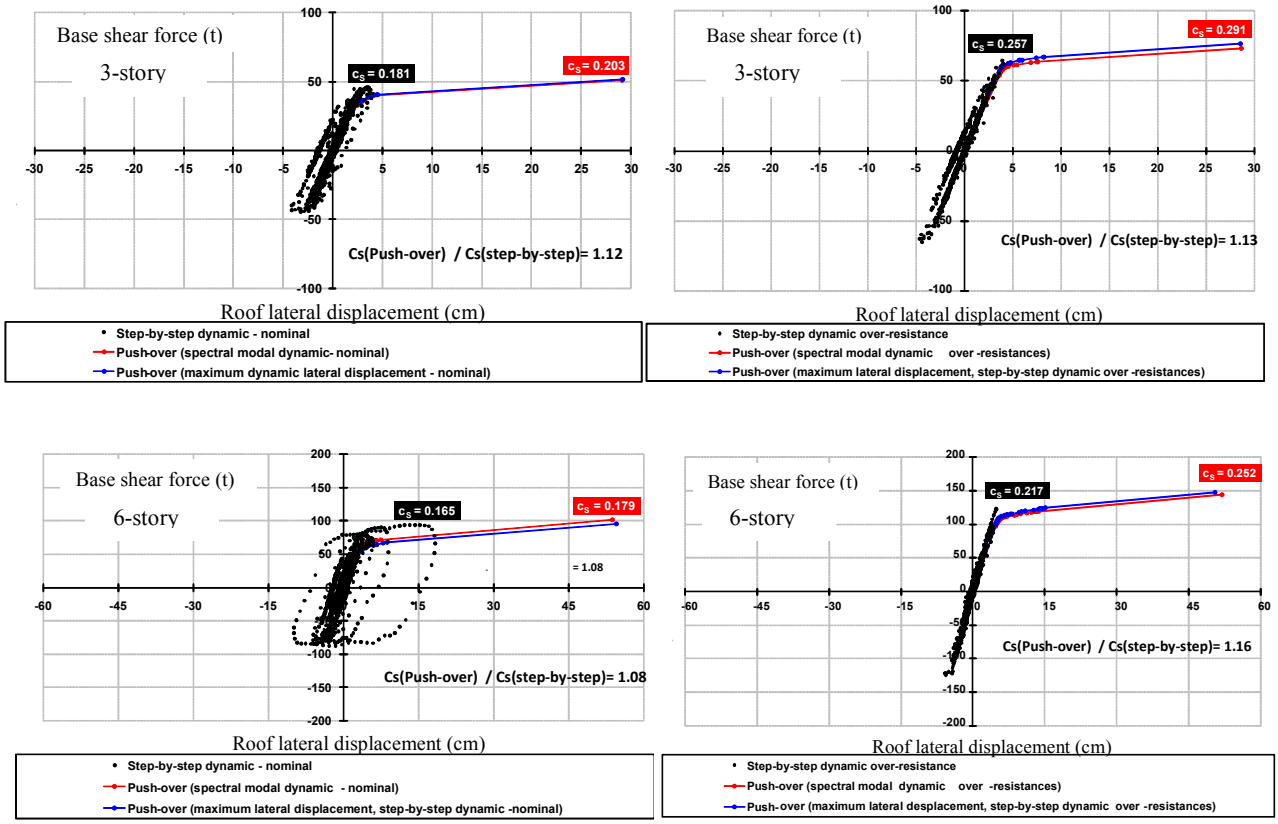


Figure 3: Base shear force–roof lateral displacement relationships comparison, non-linear static analysis (Push-over) and inelastic step-by-step dynamic analysis with nominal resistance and over-resistances effects, 3-story and 6-story structures, case D2 (Appendix A)

© (2012) Trans Tech Publications, Switzerland
doi:10.4028/www.scientific.net/KEM.488-489.363

Application of the Θ-method to 3D BEM analysis of cracks in piezoelectric components

Karsten Wippler[1,a] , Meinhard Kuna[2,b]

[1]Ingenieurbüro Enderlein, Wippler und Partner, Gostritzer Str. 63, 01217 Dresden, Germany
[2]Institute of Mechanics and Fluid Dynamics, TU Bergakademie Freiberg, 09596 Freiberg, Germany

[a]k.wippler@ewp-engineering.de, [b]Meinhard.Kuna@imfd.tu-freiberg.de

Keywords: piezoelectric materials, boundary element method, 3D crack analysis, θ-method.

Abstract. A general purpose direct BEM code has been developed for three-dimensional crack problems in piezoelectric structures. Special 3D non-continuous crack tip elements and several techniques for determining crack tip parameters were implemented. To calculate the electromechanical energy release rate for a virtual crack extension, the Θ-method is employed, which was originally suggested by Bonnet for linear elastic materials. The paper presents the generalization and numerical realization of the Θ-method to 3D piezoelectric cracks. The great advantage of the Θ-method is the direct computation of energy release rate, whereas the way via K-factors and the Irwin matrix is more complicated. The efficiency and accuracy of the technique are shown for various example problems by comparing with analytical solutions.

Introduction

In order to assess the strength and reliability of piezoelectric devices and smart composites, a crack analysis under mechanical and electrical loading has to be performed [1]. The Boundary Element Method (BEM) offers much comfort in handling discretization and high accuracy when dealing with singular crack tip fields. Recently, direct [2], mixed [3] and Galerkin-type [4] BEM approaches have been developed for 3D piezoelectric fracture problems.
The coupled electro-mechanical field problem is described by an extended formulation. The mechanical displacement vector u_k and the electric potential φ are merged as generalized displacements U_K. Indices in capital letters are running over $\{1,2,3,4\}$, whereas small ones comprise $\{1,2,3\}$. The generalized strains S_{Kl} are formed as gradients of U_K.

$$U_K = \begin{cases} u_k & \text{for } K=1,2,3 \\ \varphi & \text{for } K=4 \end{cases}, \quad S_{Kl} = \begin{cases} \frac{1}{2}(u_{k,l}+u_{l,k}) & \text{for } K=1,2,3 \\ \varphi_{,l} & \text{for } K=4 \end{cases} \tag{1}$$

Similar, the generalized stress tensor Σ_{Kl} consists of the mechanical stress tensor σ_{kl} and the dielectric displacement vector D_l. In absence of volume forces and charges, it has to satisfy the homogeneous balance equations of momentum and charge. By means of the Cauchy formula the generalized tractions are derived using the normal vector n_l.

$$\Sigma_{Kl} = \begin{cases} \sigma_{kl} & \text{for } K=1,2,3 \\ D_l & \text{for } K=4 \end{cases}, \quad \Sigma_{Kl,l}=0, \quad T_K = \Sigma_{Kl}\, n_l. \tag{2}$$

The constitutive relation for a piezoelectric material is described by the generalized matrix C_{iJKl}, assembling the anisotropic elastic, piezoelectric and dielectric constants.

$$\Sigma_{iJ} = C_{iJKl} S_{Kl}. \tag{3}$$

Boundary element code for 3D piezoelectric crack analyses

A universal direct BEM code has been developed in [5] to solve the above three-dimensional boundary value problems for a piezoelectric domain Ω with boundary Γ. Generalized displacements U^0 or tractions T^0 are prescribed at the boundary regions Γ^U and Γ^T, respectively. Starting point is the Somigliana-identity for 3D piezoelectricity. In order to avoid strongly singular integrals, the regularized form of the boundary integral equation (BIE) is used.

$$0 = \int_{\Gamma} T_K(x) U^*_{MK}(x,\xi) \mathrm{d}\Gamma - \int_{\Gamma} \left(U_K(x) - U_K(\xi)\right) T^*_{MK}(x,\xi) \mathrm{d}\Gamma. \tag{4}$$

The fundamental solutions for the generalized displacements U^*_{MK} and tractions T^*_{MK} in a 3D piezoelectric domain are computed best by means of the Radon-tansform and tabulated numerical results. For the numerical discretization preferably 8-noded isoparametric boundary elements have been used. At edges, corners and for crack front discretization non-continuous elements have been employed. A new recursive, auto-adaptive scheme has been developed for the numerical integration adopting Gauss-Kronrod quadrature rules [5]. Around the crack front special boundary elements have been constructed embedding the specific $\sqrt{r}$-behavior of U_K and $1/\sqrt{r}$-singularity of the tractions T_K.

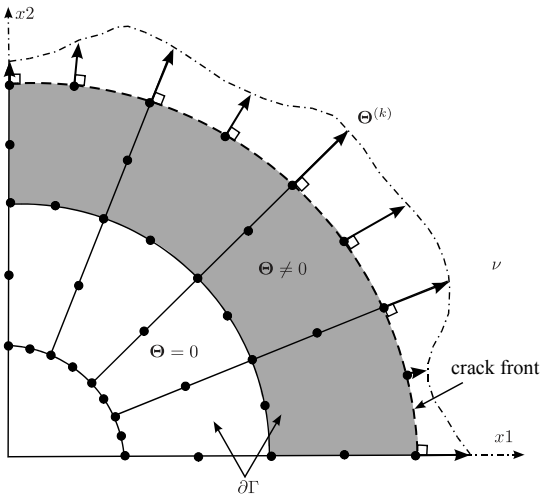


Fig. 1: Schematic sketch of Θ-method along the crack front

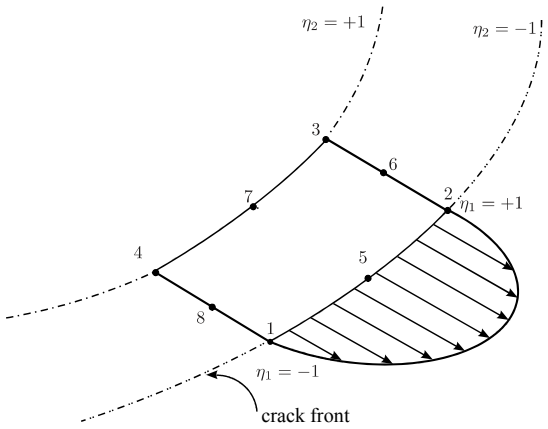


Fig. 2: Virtual crack front extension in the Θ-method

Computation of energy release rate by the Θ method

The Θ-method was originally created in design optimization [6] to determine the dependency of physical quantities, if the geometry of the structure is changed. A parameter p is introduced to describe the geometrical change of the current configuration $\mathbf{x} = \mathbf{\Phi}(\mathbf{X}, p)$ expressed by the reference configuration $\mathbf{X}$. The derivation with respect to the parameter p is called *Theta-function* $\mathbf{\Theta}(\mathbf{x}, p) = \partial \mathbf{\Phi}(\mathbf{X}, p)/\partial p$. Analogeous to the material time derivative, the differentiation of any field f with respect to the parameter p (denoted by $\lozenge$) can be obtained by

$$f^{\lozenge}(x_i, p) = f_{,p}(\mathbf{x}, p) + \boldsymbol{\nabla} f(\mathbf{x}, p) \cdot \mathbf{\Theta}(\mathbf{x}, p). \tag{5}$$

When applied to a virtual crack extension (see Fig. 2), $\mathbf{\Theta}(\mathbf{x}, p)$ simulates the variation of the crack front, i.e. the function is only non-zero for the crack tip elements as shown in Fig 1. The change of the total potential electromechanical energy δW due to the virtual crack front variation δa amounts to

$$-\delta W = \int_S G(s)\delta a(s) ds, \;\; W = \frac{1}{2}\int_{\Gamma^U} T_I U^0_I d\Gamma - \frac{1}{2}\int_{\Gamma^T} T^0_I U_I \, d\Gamma. \tag{6}$$

G means the local energy release rate at a position s along the crack front S. The energy W can be expressed by the generalizd boundary displacements and tractions, which are available as results of the BEM analysis. To determine the wanted dependency $G(s)$, the variation of the BEM-solution with respect to this geometric changes will be computed by parameter differentiation (5) of the BIE (4). This approach was suggested by [7] for 3D linear elastic crack problems. The lengthy analytic derivation for piezoelasticity can be found in [5]. Finally, an equation is obtained to determine the shape sensitivities $U_K^{\Diamond}$ and $T_K^{\Diamond}$ of the BEM-solution

$$\begin{aligned} 0 = &\int_\Gamma T_K^{\Diamond} U_{MK} \mathrm{d}\Gamma - \int_\Gamma \left(U_K^{\Diamond} - U_K^{\Diamond}(\xi)\right) T_{MK} \mathrm{d}\Gamma \\ &+ \int_\Gamma T_K \left(\Theta_r - \Theta_r(\xi)\right) U_{MK,r} \mathrm{d}\Gamma + \int_\Gamma T_K U_{MK} D_r \Theta_r \mathrm{d}\Gamma - \int_\Gamma D_{rj} U_K \left(\Theta_r - \Theta_r(\xi)\right) \Sigma_{MK}^j \mathrm{d}\Gamma. \end{aligned} \tag{7}$$

where $\Theta_r(\xi)$ and Θ_r mean the virtual velocities of source and field points, respectively. Two geometric differential operators D_r and D_{rj} (surface divergence) have been introduced.

$$D_r f = f_{,r} - n_r f_{,i} n_i, \quad D_{rj} f = n_r f_{,j} - n_j f_{,r}. \tag{8}$$

The first two terms of the integral equation (7) have exactly the same form as the original BIE (4), i. e. the coefficient matrices of the linear BEM equation system are identical with the already solved boundary value problem. The additional expressions in (7) contribute only to a modified right hand side of the system. They can be calculated from the BEM solution $T_K\,, U_K$ and the virtual crack extension prescribed as Θ-function.

In the numerical realization, the crack front is virtually displaced node by node, which results in a set of Θ-functions affecting only the crack front elements. The displacement vector δa lies always perpendicular to the local crack front and within the crack plane. The Θ-function along the crack front coordinate s is expressed by interpolating the nodal values $\boldsymbol{\Theta}^{(k)}$ of all N_C crack front nodes.

$$\boldsymbol{\Theta}(s) = \sum_{k=1}^{N_C} N_i^t(\eta_1) N^b(\eta_2) \boldsymbol{\Theta}^{(k)}, \quad G(s) = \sum_{l=1}^{N_C} N_l^t(\eta_1) G^{(l)} \tag{9}$$

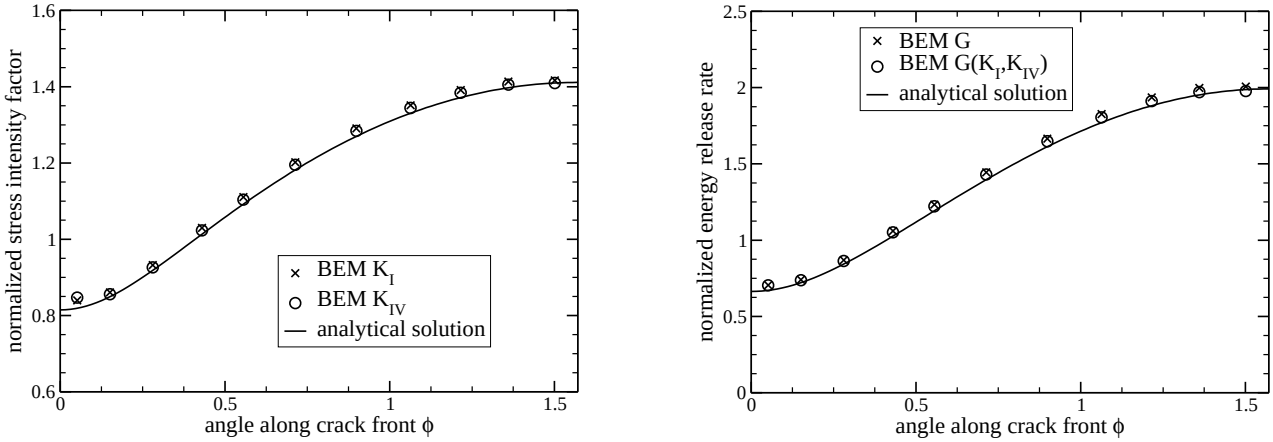
The interpolation function is constructed to achieve [7, 5] a quadratic dependency in the direction η_1 tangential to the crack front and a linear behavior with respect to the binormal orientation η_2, ensuring $\boldsymbol{\Theta}(\mathbf{x}, p)$ is non-zero at the crack front only This is illustrated in Fig. 2 for the three crack front nodes (1, 2, 5) of an element, whereby the crack front coincides with $\eta_2 = -1$. In a similar way the energy release rate $G(s)$ is interpolated by quadratic shape functions N_k^t along the crack front. For every $k \in \{1, N_C\}$ crack front variation $\Theta^{(k)}$ the corresponding sensitivities $T_K^{(k)\Diamond}$ and $U_K^{(k)\Diamond}$ are computed from (7). In combination with (9) a linear system of equations is obtained to calculate the $G^{(l)}$-values for every crack front node irrespective of the actual choice of $\Theta^{(k)}$ and thus $\boldsymbol{\Theta}(\mathbf{x}, p)$

$$\Theta^{(k)} \left[G^{(l)} \int_S N_k^t(s) N_l^t(s) \mathrm{d}s + \frac{1}{2} \int_{\mathrm{d}\Gamma^U} T_K^{(k)\Diamond} U_K \mathrm{d}\Gamma - \frac{1}{2} \int_{\mathrm{d}\Gamma^T} T_K U_K^{(k)\Diamond} \mathrm{d}\Gamma \right] = 0. \tag{10}$$

Numerical results

Analytical and numerical reference solutions [8] are available for elliptical cracks in an infinite domain loaded by generalized tractions T_N^∞ perpendicular to the crack faces. The mechanical (K_I) and electrical (K_{IV}) intensity factors have the same distribution along the crack as function of the elliptical angle ϕ. The energy release rate is related to the K_N-factors by means of the Irwin-matrix, which simplifies in the present case to the expression (c_T, e and κ are material constants for Ba TiO_3 [1, 8])

$$G = \frac{1}{2}\frac{K_I^2}{c_T} + \frac{K_I K_{IV}}{e} - \frac{1}{2}\frac{K_{IV}^2}{\kappa}. \tag{11}$$



(a) Normalized stress and field intensity factors

(b) Normalized total energy release rate

Fig. 3: Results for internal elliptical crack under mechanical and electrical loading

The results obtained with the present BEM for an elliptical crack ($a/c = 1/3$) are given in Fig. 3. Figure (a) represents the normalized angular behavior of mechanical K_I and electrical K_{IV} intensity factors, calculated by crack tip elements. In Figure (b) the energy release rates are compared between the direct result of the proposed Θ-method and the indirect way using the K_N-factors via equation (11). The agreement among the numerical results and with the analytic solutions is excellent. Further examples are given in [5].

References

[1] Kuna, M.: Engineering Fracture Mechanics 77 (2010), p. 309-326

[2] Hill, L., Farris, T.: Journal of intelligent materials systems and structures 9 (1998), p. 251-259

[3] Solis, M., Sanz,J., Ariza, M., Dominguez, J.: Engineering Analysis with Boundary Elements 33 (2009), p. 271-282

[4] Rungamornrat, J., Mear, M.: International Journal of Fracture 151 (2008), p. 1-27

[5] Wippler, K.: Entwicklung einer dreidimensionalen Randelementemethode zur Analyse von Rissen in piezoelektrischen Strukturen, Technische Universitet Bergakademie Freiberg, PhD Thesis 2010

[6] Bonnet, M.: Computers and Structures 56 (1995), p. 799-811

[7] Bonnet, M., Xiao,H.: Engineering Analysis with Boundary Elements 15 (1995), p. 137-149

[8] Shang, F., Kuna, M., Abendroth, M.: Engineering Fracture Mechanics 70 (2003), p. 143-160

© (2012) Trans Tech Publications, Switzerland
doi:10.4028/www.scientific.net/KEM.488-489.367

The Influence of The Weld Width on Fracture Behaviour of The Heterogeneous Welded Joint

Pejo Konjatić[1, a], Dražan Kozak[1, b], Nenad Gubeljak[2, c]

[1] Josip Juraj Strossmayer University of Osijek, Mechanical Engineering Faculty in Slavonski Brod, Trg Ivane Brlić-Mažuranić 2, HR-35000 Slavonski Brod, Croatia

[2] University of Maribor, Faculty of Mechanical Engineering, Smetanova ulica 17, SI-2000 Maribor, Slovenia

[a] pejo.konjatic@sfsb.hr, [b] drazan.kozak@sfsb.hr, [c] nenad.gubeljak@uni-mb.si

Keywords: heterogeneous welded joint, finite element method, yield load, weld width, fracture resistance, material mismatch

Abstract. Since welded constructions are widely used in engineering, a certain flaws in welded joints may occur either in process of welding or in exploitation period. Easiest way to prolong working life of such welded construction is to repair welded joint to eliminate possibility of construction failure. Process of repair welding usually gives heterogeneous welded joints because during process of repair additional material is introduced into welded joint, resulting in heterogeneity from the presence of materials in welded joint point of view. Such difference in materials usually results in yield strength difference between materials, represented with mismatch ratio, and it is commonly present in welds where high strength low-alloyed (HSLA) steels were welded. Since *I* butt welded joints are very common in welding, a systematic investigation of such welds is performed and presented in this paper. Therefore in this investigation the influence of present material in heterogeneous weld and geometry of weld is investigated in context of fracture resistance of welded joint represented as yield load solutions in the first place. A flaw in form of crack was implemented in such heterogeneous weld and using finite element method yield load solutions for different combinations of weld geometry and material strength are obtained and presented in form of diagrams.

Introduction

Repair welding is commonly used in welding industry when need to repair emerges due to occurrence of flaws or cracks during welding process or in period of exploitation. In this repair process an additional material is introduced into already heterogeneous structure. Such difference in materials usually results in yield strength difference between materials, represented with mismatch factor, and it is commonly present in welds where high strength low-alloyed steels were welded. This two level of heterogeneity was not often been investigated, just recently including investigations in [1,2,3]. Since *I* butt welded joints are very common in welding, a systematic investigation of such welds using finite element method is performed and presented in this paper. Different types of weld shapes have different weld geometry parameters, but weld width, as one of key parameters, is common for all weld shapes. Therefore, this paper concentrates to investigation of influence of weld width to fracture behaviour of welded joint. Fracture resistance is investigated in context of yield load solutions for a standard single notched three point bend specimen (SENB).

Material heterogeneity and key assumptions

As it is earlier mentioned, repair welding usually produces heterogeneous welds where some parts of welds have different strength of material compared to welded base material. This difference in strength is called strength mismatch and is represented with strength mismatch factor M:

$$M = \frac{\sigma_{YW}}{\sigma_{YB}} \tag{1}$$

where σ_{YW} represents yield strength of weld material and σ_{YB} yield strength of base material. Two mismatch factors can exist in repaired weld, for overmatched part of weld mismatch factor M_{om} and for undermatched part of weld mismatch factor M_{um}. This means that repaired weld is performed with material with higher or lower yield strength compared to original weld.

Certain idealization were usually considered in previous similar investigations including idealization of weld shape as weld strip, crack positioned in center of the weld and material behaviour as elastic ideally plastic [4,5,6] and they are implemented in this investigation as well.

Fracture toughness can be expressed in different ways, but here it is investigated in context of yield load solutions in the first place. A yield load represents load that causes yielding across whole cross section of welded joint indicating forming of plastic hinge and failure of the structure at the end. Yield load solutions are often used as key parameters in failure assessment procedures including widely used European Structural Integrity Procedure SINTAP [7] and R6 procedure [8].

Finite element analysis

Finite element analysis is performed on 2D plane strain model for number of simulations where two levels of mismatch were investigated. In one part of simulations, crack was positioned in overmatched part of weld, with strength mismatch factor of M_{om}=1,5, and in other in undermatched part of weld with strength mismatch factor of M_{um}=0,75. Crack length ratio (a/W - ratio of crack length and weld height) and weld width ($2H$) are varied in order to determine their influence on fracture resistance. Simulations are performed in ANSYS software [9] for finite element analysis and only one half of specimen is modeled due to existing symmetry (Fig. 1). Weld materials are considered as elastic almost ideally plastic with very small strain hardening not influencing results but only convergence rate.

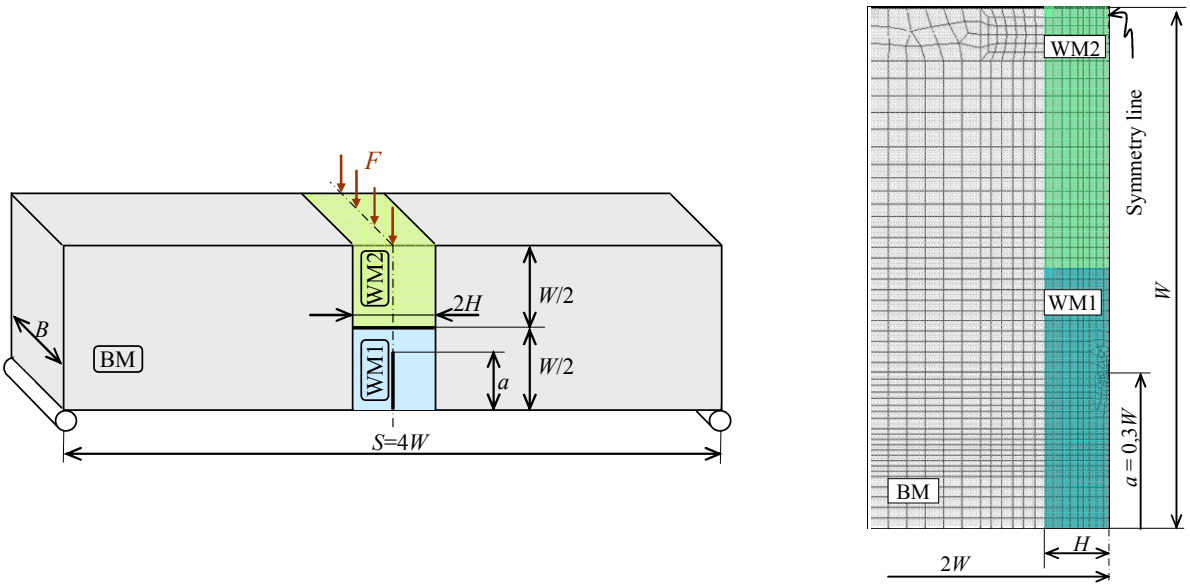


Fig. 1 Finite element model of SENB specimen with heterogeneous *I* butt welded joint

Results

Obtained yield load solutions are represented as ratio of yield load of heterogeneous weld and yield load of welded joint made of all base material. This ratio clearly shows is there a fracture resistance increase (value higher than 1) of decrease (value lower than 1) compared to all base material solutions.

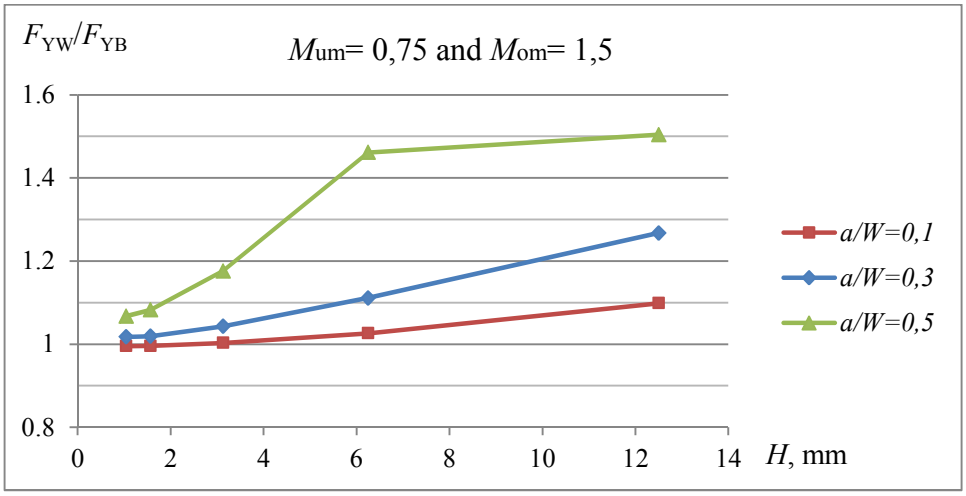


Fig. 2 Yield loads of heterogeneous *I* butt welded joint with crack in undermatched part of weld

On Fig. 2, where yield load solutions of heterogeneous *I* butt welded joint with crack in udermatched part of weld are presented, can be seen that deeper cracks generally lead to grow of fracture resistance for whole range of weld widths. This can be explained with higher influence of overmatched material in front of crack tip. For deeper cracks yielding zone is mainly contained in overmatched part of weld giving increase in fracture resistance. It is also evident that wider welds also give significant increase in fracture resistance.

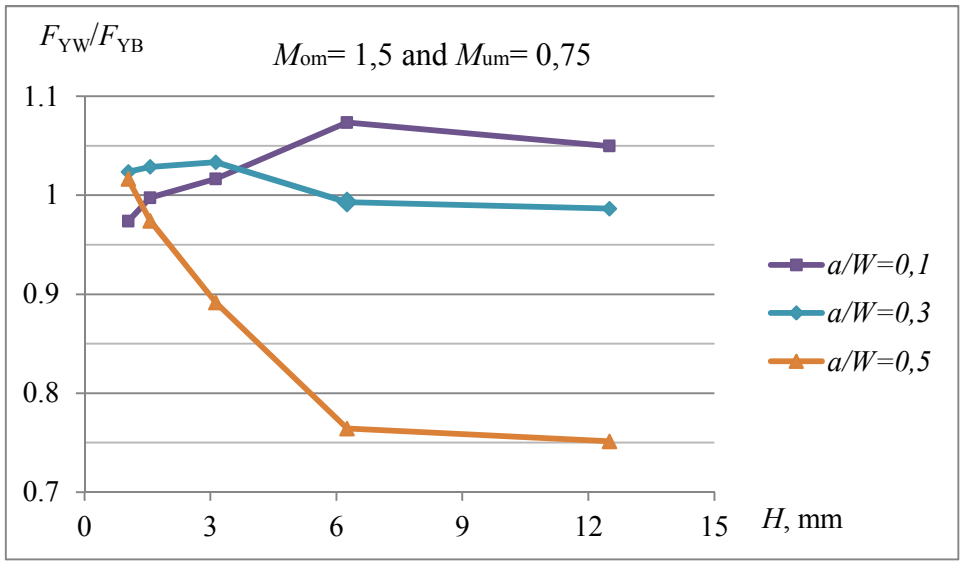


Fig. 3 Yield loads of heterogeneous *I* butt welded joint with crack in overmatched part of weld

This interaction of crack length and weld width on fracture resistance results in such a manner that for narrow welds solutions are contained is small band of value, whilst larger weld widths allow more scattering in yield loads regarding crack lengths. Generally, all solutions for this material mismatch combination, where crack is located in undermatched part of weld, give overmatch character of weld.

Fig. 3 shows yield load solutions of heterogeneous *I* butt welded joint with crack in overmatched part of weld and it can be seen that solutions do not, like on Fig 2, give overmatched nor just undermatched character of welded joint but mixed combination. Narrow welds show similar resistance regarding crack length, what clearly changes for larger weld widths. For widest welds it is obvious that material in front of crack, for deep cracks, dictates fracture behaviour of welded joint. That can be explained with yielding zone spreading mostly through material in front of crack tip. Also it can be noticed that weld width has less influence on welds with shallow crack.

Conclusions

Repair welded joint with two level of heterogeneity show complex fracture behaviour influenced not only with strength mismatch factors of materials present in weld but also with crack length and width of weld. Generally narrow welds show similar fracture resistance, in context of yield load, weather crack is located in overmatched or udermatched part of weld, while welds with larger width allow to material in front of crack, especially for deep cracks, to take a dominant role in fracture behaviour of heterogeneous welded joint. Narrow welds force yielding zone to spread through base material as well as through weld levelling yield load for welded joints with crack either in overmatched or in udermatched part of weld. Wide welds exhibit yielding just through weld itself, giving more influence to materials where crack is located i.e. material in front of crack. This investigation clearly shows that weld width is definitely one of key parameters for explaining fracture behaviour and quantifying fracture resistance of heterogeneous welded joint.

References

[1] N. Gubeljak, J. Predan, I. Rak, D. Kozak: Integrity assessment of HSLA steel welded joint with mis-matched strength, Structural Integrity and Life, (2009), 9, 3, p. 157-164

[2] D. Kozak, N. Gubeljak, P. Konjatić, J. Sertić: Yield Load Solutions of Heterogeneous Welded Joints, International Journal of Pressure Vessels and Piping, (2009), 86, 12, p. 807-812.

[3] D. Kozak, N. Gubeljak, J. Vojvodič Tuma: The effect of a material's heterogeneity on the stress and strain distribution in the vicinity of a crack front, Materials and technology, (2007), 41, 1, p. 41-46

[4] Y.J. Kim, K.H. Schwalbe: Mismatch effect on plastic yield loads in idealised weldments. I. Weld centre cracks, Engineering Fracture Mechanics (2001), 68, p. 163–182.

[5] Y.J. Kim, K.H. Schwalbe: Compendium of yield load solutions for strength mis-matched DE (T), SE (B) and C (T) specimens, Engineering Fracture Mechanics, (2001), 68, p. 1137–1151.

[6] Y.J. Kim: Experimental J estimation equations for single-edge-cracked bars in four-point bend: homogeneous and bi-material specimens, Engineering Fracture Mechanics, (2002), 69, p. 793–811.

[7] SINTAP, Structural Integrity Assessment Procedure, Final Revision, EU Project BE 95-1462, Brite Euram Programme, Brussels, 1999.

[8] R6, Revision 4, Assessment of the Integrity of Structures Containing Defects, Chapter IV.3, Stress Intensity Factor Solutions, British Energy Generation Ltd, Gloucester, 2003.

[9] ANSYS, software for finite element analysis, 2009, www.ansys.com

© (2012) Trans Tech Publications, Switzerland
doi:10.4028/www.scientific.net/KEM.488-489.371

Simulation of a strategy for the assessment of damage in human bones by using FEM and signal processing

Marco Miniaci[1,a], Alessandro Marzani[1,b] and Erasmo Viola[1,c]

Department of Civil, Environmental and Materials Engineering - DICAM, University of Bologna, Viale del Risorgimento 2, 40136, Bologna, Italy

[a] marco.miniaci2@unibo.it, [b]alessandro.marzani@unibo.it, [c]erasmo.viola@unibo.it

Keywords: Damage, Finite Element, Guided waves, Bone characterization, Health monitoring.

Abstract. The aim of this work is to propose a non-invasive technique aimed at assessing the evolution of damage in elongated bones that could be caused, for instance, by metabolic diseases. The technique exploits signals related to mechanical guided waves traveling along the bone to characterize its mechanical properties in a total non-destructive manner. Such properties can be used as an indicator of the damage level present in the bone. The preliminary results motivate future studies.

Introduction

Monitoring of damage is fundamental to increase the design lifetime of any structure. This becomes even more relevant if the structure in consideration is a human bone. Various techniques have been proposed over years to assess the status of human bones. Among the several, recently, researchers are exploiting guided ultrasounds because of their unique non invasive inspection capabilities [1,2].

In this context, the present study is aimed at simulating a non-invasive technique based on axial transmission of mechanical guided waves for structural parameters identification of human bones. The cortical bone only is considered in this study. Even though the cortical bone is anisotropic and porous at the microstructural level, it is possible to treat it as a linear, elastic, isotropic and homogeneous material if the waves wavelength, as in this case, are much greater than the heterogeneity of the microstructure. In fact, for typical shear (c_S) and compressional (c_L) velocities of about 1000 - 4000 m/s, ultrasonic wavelengths in the kHz frequency range are of the millimeter order, much greater than any structural heterogeneity [3]. If so, the cortical bone Young's modulus E, Poisson's coefficient ν as well as material density ρ remain the only structural parameters to identify. Nonetheless, such parameters can be used as indicators of the bone state of health.

The proposed technique identifies the structural properties of the bone as the outcomes of an optimization problem in which the discrepancy between measured and numerically simulated guided waves dispersion curves is minimized. In particular, here the wavenumber-frequency ($k-f$) curves are used. Such optimum is sought by varying the set of material properties to be identified, i.e. E, ν, ρ, into the numerical model used for the forward computation of $k-f$ curves.

Experimentally, such curves are obtained by exciting the bone via a opportune medical device capable to send mechanical energy into the bone in the ultrasonic regime. Next, the time transient responses detected along a series of points on the outer surface of the bone are post processed via a signal processing strategy called bi-dimensional Fast Fourier Transform (2D-FFT). The signal processing yields a wavenumber-frequency map that reveal the energy content of the propagating guided waves.

Numerically, the $k-f$ curves are obtained via a Semi-Analytical Finite Element formulation (SAFE) for a given set of material properties in input. Then, an algorithm based on an improved version of the Simplex search method [4] is used to update the material properties into the SAFE tool till the numerical $k-f$ curves resemble those obtained experimentally.

The partial results presented in this paper track the path for the development of a procedure aimed at characterizing the mechanical properties of the bone ina total non-destructive manner.

Strategy overview

A schematic flowchart of the proposed strategy is presented in Fig. 1. The experimentally determined wavenumber-frequency curves, **EXP**$(k-f)$, are on the left-hand side of the scheme. Such curves depend on the material properties of the cortical bone, denoted as E^T, ν^T and ρ^T, where the superscript T stands for target value. The numerically computed wavenumber-frequency curves, **NUM**$(k-f)$, are on the right-hand side of the figure. Such curves are obtained via a SAFE formulation for a given set of material properties E_i, ν_i and ρ_i [4]. By means of the experimental $k-f$ map and the numerical one it is possible to evaluate an objective function that senses the discrepancy (Δ) between the two maps. If $\Delta > tol$, where tol is an opportunely defined tolerance value, a sensitivity based scheme updates the input properties, i.e. E_{i+1}, ν_{i+1} and ρ_{i+1}, into the SAFE scheme for a new computation of the $k-f$ curves. The optimization process goes on till the tolerance is reached. In such case the E_i, ν_i and ρ_i mechanical properties are assumed as the identified ones E^{ID}, ν^{ID} and ρ^{ID}.

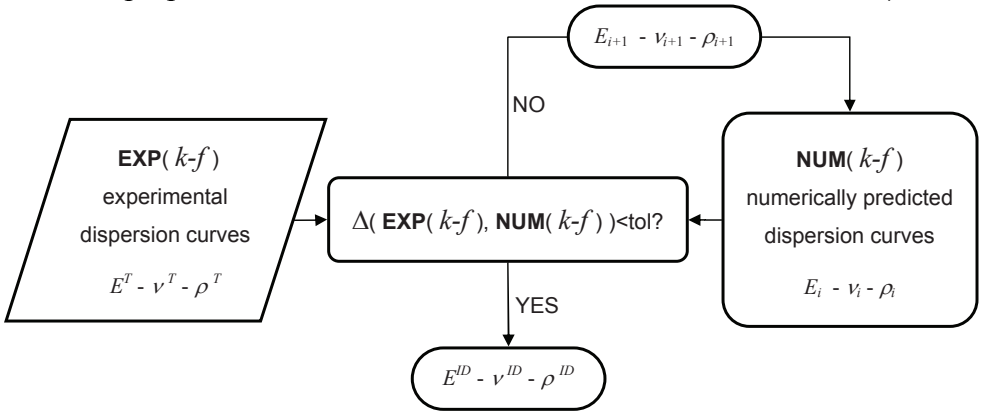


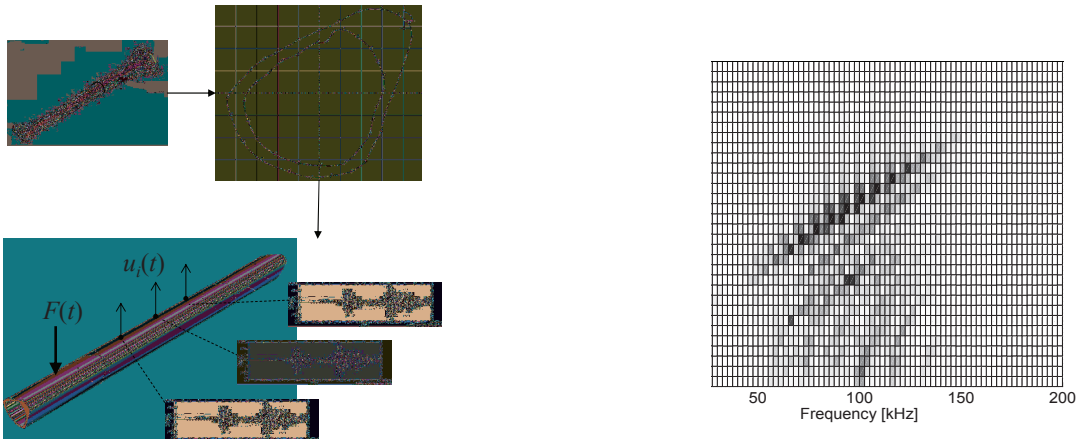
Fig. 1: Schematic representation of the optimization process.

Pseudo-experimental data

In this preliminary work, pseudo-experimental data are used. First, a significant cross-section of a human tibia is extracted and used to build a 3D Finite Element model of the bone (see Fig. 2a). The cross-section thickness varies from 10.7 mm (maximum value) to 1.8 mm (minimum value). The 3D model is created extruding the cross section for a total length of 400 mm. Such length has been chosen as good compromise between a measure of a real human tibia and the necessity of generating a computationally light model. The bone is supposed to be in vacuum and its mechanical properties have been assumed equal to $E^T = 14000$ MPa, $\nu^T = 0.37$ and $\rho^T = 1500$ kg/m^3 [3], with corresponding longitudinal and shear bulk waves speed $c_L = 4063$ m/s and $c_S = 1845$ m/s, respectively. A 3 cycle sinusoidal point force centered at 100 kHz and modulated by a Hanning window has been applied 100 mm from the left-end side of the bone in order to excite guided waves. Transient simulations have been carried out via ABAQUS EXPLICIT by using a mesh with 196200 *C3D8R* 8-node linear brick elements and an integration time of 1e^{-7} [s]. Such values guarantee solution accuracy [5].

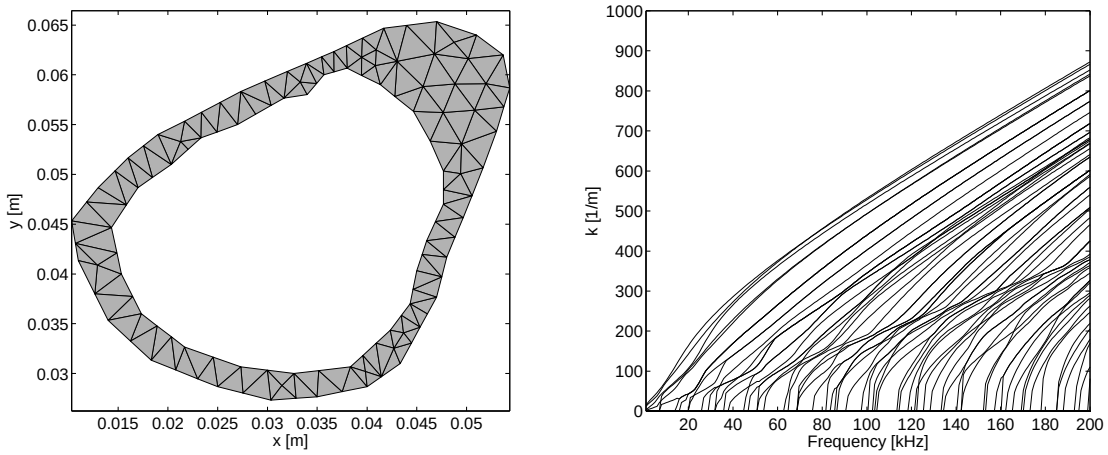
Displacement signals $u_i(t)$, sampled at 10 MHz, are acquired from the outer surface of the bone at 200 different positions equally spaced by 1 mm along the axis direction (see Fig. 2a). The positions were taken in the central 200 mm of the bone in order to avoid interference from the waves reflected and refracted back at the end sides of the model.

Next, the bi-dimensional Fast Fourier Transform (2D-FFT) is applied to all the collected signals in order to extract the two-dimensional wavenumber-frequency map. For the case under consideration such map is represented in Fig. 2b. From this figure it can be noted that several guided waves propagate along the bone. As expected, the energy carried by the waves is concentrated around the central frequency of the forcing function, i.e. 100 kHz.



(a) (b)

Fig. 2: a) Pseudo-experimental simulated signals; (b) pseudo-experimental $k - f$ map.



(a) (b)

Fig. 3: a) Mesh over the waveguide cross-section ; (b) SAFE computed $k - f$ curves.

Numerical data

In parallel a Semi-Analytical Finite Element formulation (SAFE) is used for the forward computation of the dispersion $k - f$ curves. This method requires the bi-dimensional finite element mesh of the waveguide cross-section only. Here a mesh of 143 constant strain triangular (CST) elements, with 3 dofs (degrees of freedom) per node, is used (see Fig. 3a). After the mechanical properties have been assigned and the guided wave equation built, the dispersion curves for the waveguide can be calculated. Mathematical steps are discussed in details in the reference [6].
The $(k - f)$ map for the bone cross-section under consideration are given in Fig. 3b. It must be pointed out that for the purpose of comparing the pseudo-experimental and the numerical $k - f$ maps, the SAFE curves in Fig. 3b have been computed directly starting from the target mechanical properties (E^T, ν^T, and ρ^T).

Discussion and future outlook

This study constitutes a staring point for the implementation of a strategy for bones assessment. The idea is to feed an optimization scheme with experimental and numerical wavenumber-frequency $(k - f)$ curves in oder to characterize the bone mechanical properties. Here, the experimental curves for a human tibia have been simulated by a two-stage approach: first, 3D finite element simulations

of guided waves propagating along the tibia are performed and next the bone responses are post-processed by means of the 2D-FFT transform. It has been shown that with such technique the $k-f$ map of the excited guided waves can be obtained. Numerically, the $k-f$ curves have been computed by an ad-hoc Semi-Analytical Finite Element (SAFE) formulation considering the same mechanical properties used for the pseudo-experimental phase.

By comparing Fig. 3b with Fig. 2b it can be clearly seen that the $k-f$ curves obtained by using the SAFE formulation closely resemble the pseudo-experimental curves. It is worth nothing that while the SAFE gives the curves of all the existing waves in the 0-200 kHz range, the FEM and 2D-FFT procedure only reveals the guided waves that propagate along the bone, i.e. those that have been excited by the applied forcing function.

Next steps will involve i) the extraction of only the excited branches from the SAFE curves (to this purpose the frequency response function of the waveguide must be computed [7]); ii) the design of the optimization function and finally iii) the development and testing of the optimization scheme.

Acknowledgement

This research involves one of the subjects of the Centre of Study and Research for the Identification of Materials and Structures (CIMEST) – "M. Capurso", University of Bologna, Italy.

References

[1] V.C. Protopappas, D.I. Fotiadis, K.N. Malizos. Guided ultrasound wave propagation in intact and healing long bones. *Ultrasound in Medicine and Biology*. Vol. 32 (2006), p. 693-708.

[2] M.G. Vavva, V.C. Protopappas et al.. Velocity dispersion of guided waves propagating in a free gradient elastic plate: Application to cortical bone. *The Journal of the Acoustical Society of America*. Vol. 125 (2009), p. 3414-3427.

[3] A. Marzani, E. Viola, I. Bartoli, F. Lanza di Scalea, P. Rizzo. A semi-analytical finite element formulation for modeling stress wave propagation in axisymmetric damped waveguides. *Journal of Sound and Vibration*. Vol. 318 (2008) p. 488-505.

[4] M. Sale, P. Rizzo, A. Marzani. Semi-analytical formulation for the guided waves-based reconstruction of elastic moduli. *Mechanical Systems and Signal Processing*. Vol. 25 (2011), p. 2241-2256. 2011;(available on line).

[5] I. Bartoli, F. Lanza di Scalea, M. Fateh, E. Viola. Modeling guided wave propagation with application to the long-range defect detection in railroad tracks. *NDT and E International*. Vol. 38 (2005) p. 325-334.

[6] I. Bartoli, A. Marzani, F. Lanza di Scalea, E. Viola. Modeling wave propagation in damped waveguides of arbitrary cross-section. *Journal of Sound and Vibration*. Vol. 295 (2006) p. 685-707.

[7] A. Marzani, I. Bartoli. High frequency waves propagating in octagonal bars: a low cost computation algorithm. *Algorithm*. Vol. 2 (2009) p. 227-246.

© (2012) Trans Tech Publications, Switzerland
doi:10.4028/www.scientific.net/KEM.488-489.375

Effect of an internal open crack on pipes wave propagation

Alessandro Marzani[1,a], Marco Miniaci[1,b] and Erasmo Viola[1,c]

Department of Civil, Environmental and Materials Engineering - DICAM, University of Bologna, Viale del Risorgimento 2, 40136, Bologna, Italy

[a] alessandro.marzani@unibo.it, [b]marco.miniaci2@unibo.it, [c]erasmo.viola@unibo.it

Keywords: Damage, FEM, Guided waves, Non-invasive technique, Health monitoring.

Abstract. Stress guided waves in the sonic and ultrasonic regime are acknowledged as a powerful tool to inspect pipes in a non-invasive manner.
A key point of the inspection procedure is related to the dispersive behavior of guided waves, that for a given pipe is defined by the so-called dispersion curves. Such behavior, is generally predicted by means of analytical formulations. However, when the geometry of the pipe cross-section is not axially symmetric, such as in the presence of an open internal crack running along the pipe length, analytical formulations fail. Here, the computation of the guided waves properties for such a scenario is addressed via a Semi Analytical Finite Element (SAFE) formulation in which the open crack is modeled at the mesh level. Different crack depths are considered and their effect on the waves dispersion curves are highlighted. The results could be of interest in pipeline inspection and monitoring.

Introduction

The nondestructive evaluation of structural integrity is a very important task in present-day industry. Recently, the interest to ultrasonic guided waves has increased. Compared to classical bulk waves based inspections, the use of ultrasonic guided waves has many advantages such as longer inspection range, higher sensitivity to small flaws and larger versatility. In general, guided waves develop in waveguides like plates, rods, pipes or elongated structures, after several reflections and refractions of the original incident wave. Generally, multiple guided waves can propagate. The majority of the propagating modes are dispersive, i.e. their principal features, known as phase and group velocity, attenuation, wavestructure and wavelength, are frequency dependant [1,2].
This work investigates how the presence of an open internal crack running along the cross section of a straight pipe affects dispersion curves. Guided waves phase velocity sensitivity to various depths of the open crack are highlighted. It can be seen from such curves that some modes, being particularly sensitive to the defect, can be good candidates for the non destructive detection of the crack depth.

Mathematical Formulation

A semi-analytical finite element formulation is used to set the guided wave equation. Such formulation requires a bi-dimensional finite element mesh over the waveguide cross-section only, here generated by using the *"pdetool"* of Mtalab.
Figure 1 shows a schematic representation of an infinitely long waveguide. The waveguide cross-section belongs to the $x-y$ plane and the z axis coincides with the longitudinal axis of the waveguide. The structure is considered to be in vacuum. The wave propagates along z direction. The problem variables at the general point $\mathbf{x} \equiv (x, y, z)$ of the waveguide are the displacement $\mathbf{u}$, the stress $\boldsymbol{\sigma}$ and the strain $\boldsymbol{\epsilon}$ vectors with components $\mathbf{u} = [u_x \quad u_y \quad u_z]^T$, $\boldsymbol{\sigma} = [\sigma_{xx} \quad \sigma_{yy} \quad \sigma_{zz} \quad \sigma_{yz} \quad \sigma_{xz} \quad \sigma_{xy}]^T$, $\boldsymbol{\epsilon} = [\epsilon_{xx} \quad \epsilon_{yy} \quad \epsilon_{zz} \quad \gamma_{yz} \quad \gamma_{xz} \quad \gamma_{xy}]^T$, where the T superscript means transposition.

The structure cross-section is discretized by constant strain triangular (CST) elements, with 3 dofs per node associated to the dispacement u_x, u_y and u_z. The generic displacement vector at a point within the generic $e-th$ element can be approximated as

$$\mathbf{u}_h(\mathbf{x}, t) = \mathbf{N}(x, y)\mathbf{q}(z, t) \tag{1}$$

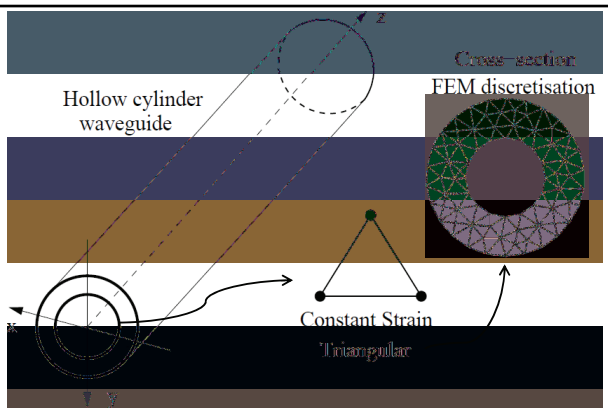


Fig. 1: Schematic representation of the waveguide and the cross-section bi-dimensional finite element mesh.

where $\mathbf{N}(x,y)$ is a matrix containing the element shape functions and $\mathbf{q}(z,t)$ is a vector with the $e-th$ element nodal displacements. Similarly, it is possible to write the approximated strain vector as

$$\boldsymbol{\epsilon}(\mathbf{x},t) = \mathbf{B}_{xy}\mathbf{q} + \mathbf{B}_z \frac{\partial \mathbf{q}}{\partial z} \tag{2}$$

where $\mathbf{B}_{xy} = \mathbf{L}_x \frac{\partial \mathbf{N}_x}{\partial x} + \mathbf{L}_y \frac{\partial \mathbf{N}_y}{\partial y}$, $\mathbf{B}_z = \mathbf{L}_z \mathbf{N}$, and the $\mathbf{L}_i$ operators are defined as

$$\mathbf{L}_x = \begin{bmatrix} 1 & 0 & 0 \\ 0 & 0 & 0 \\ 0 & 0 & 0 \\ 0 & 0 & 0 \\ 0 & 0 & 1 \\ 0 & 1 & 0 \end{bmatrix}, \qquad \mathbf{L}_y = \begin{bmatrix} 0 & 0 & 0 \\ 0 & 1 & 0 \\ 0 & 0 & 0 \\ 0 & 0 & 1 \\ 0 & 0 & 0 \\ 1 & 0 & 0 \end{bmatrix}, \quad \mathbf{L}_z = \begin{bmatrix} 0 & 0 & 0 \\ 0 & 0 & 0 \\ 0 & 0 & 1 \\ 0 & 1 & 0 \\ 1 & 0 & 0 \\ 0 & 0 & 0 \end{bmatrix} \tag{3}$$

By using Hamilton's principle, the waveguide Lagrangian reads

$$\mathcal{L} = \frac{1}{2} \bigcup_{e=1}^{n_{el}} \int_{-\infty}^{+\infty} \int_{\Omega_e} \left[\rho^e \dot{\mathbf{u}}_h^T \dot{\mathbf{u}}_h - \boldsymbol{\epsilon}_h^T \mathbf{C}^e \boldsymbol{\epsilon}_h \right] dxdydz \tag{4}$$

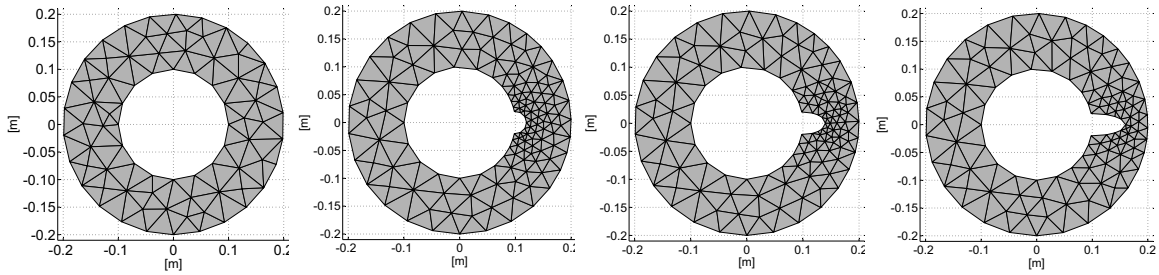
where ρ^e is the element mass density, $\mathbf{C}^e$ is the viscoelastic operator [3]. Those quantities are considered to be constant over Ω_e. After some algebraic manipulations the guided wave equation is obtained from equation (4)

$$\left[\mathbf{A} - \xi \mathbf{B}\right]_{2H} \mathbf{Q} = \mathbf{0} \tag{5}$$

where H is the total number of degrees of freedom of the cross-section mesh.
The solution of the wave equation is found using the *"eig"* command of Matlab [4], for a given frequency in input ($\omega = 2\pi f$). Then all the complex wavenumbers ξ^m and waveshapes $\mathbf{Q}^m$ exsisting at that frequency, where $m = 1, 2, 3, ..., 2H$, are obtained. Finally, phase velocity is calculated from these modal properties by means of simple formulae. Dispersion curves are traced repeating this procedure for all the frequencies of interest.
Mathematical steps are discussed in details in the reference [5].

Case	D0	D1	D2	D3
Defect semi diameters lengths	$a = 0$ cm $b = 0$ cm	$a = 2$ cm $b = 2$ cm	$a = 4$ cm $b = 2$ cm	$a = 6$ cm $b = 2$ cm

Table 1: Analysed cross-section denomination and defect description.



(a) D0 (b) D1 (c) D2 (d) D3

Fig. 2: Analysed cases: from a pristine cross-section (a) to damaged cross-sections (b,c,d).

Numerical Applications and Discussions

A hollow cylinder is considered. Inner and outer radius are $R_i = 10$ cm and $R_e = 20$ cm, respectively. The material is steel, with the following nominal properties: longitudinal bulk wave speed $c_L = 5875.1$ m/s, shear bulk wave speed $c_S = 3140.4$ m/s, density $\rho = 7800$ kg/m^3. Steel is modeled as an isotropic elastic material. Four cases are considered: the pristine hollow cylinder and three damaged cases with an elliptical notch of increasing depth. The notch is characterized by its semi-diameters lengths *a* and *b* (see Table 1). The location of the notch is identical for all the cases considered (see fig. 2). The mesh around the crack location is refined in order to obtain a more accurate solution.
The phase velocity dispersion curves for the pristine cylinder are represented in fig. 3. It can be noted that in the 0-8000 Hz range several dispersive waves exist. Larger slope of the curves denotes higher dispersion: in those zones, called *high dispersive zones*, waves are more distorted with propagating distance.

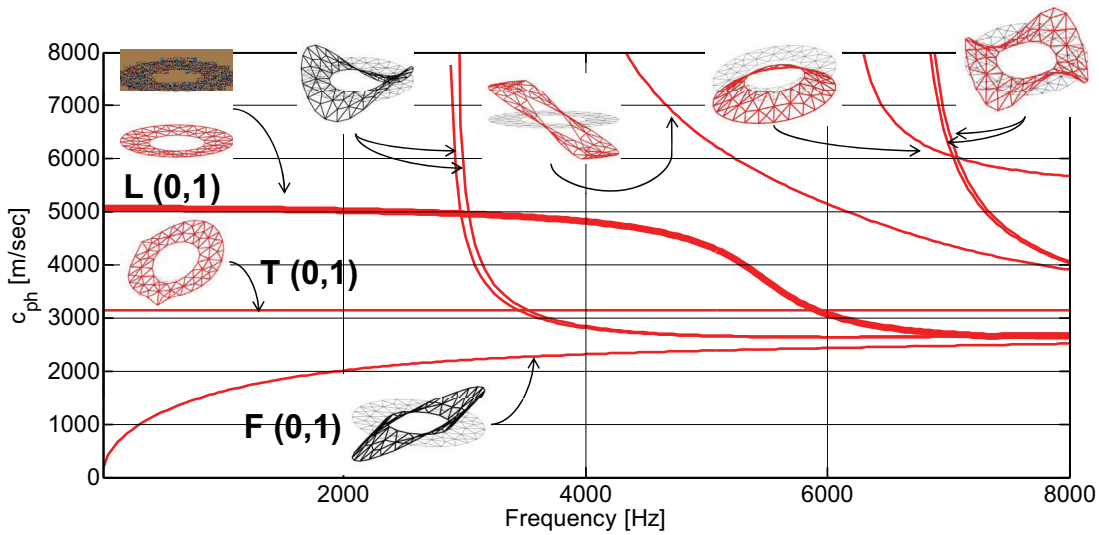


Fig. 3: Phase velocities curves and waveshapes for the pristine case.

Normalised waveshapes for each mode are also reported in fig. 3. It appears that below 3000 Hz three guided modes exist: a flexural one (F), a torsional one (T) and a longitudinal one (L). The F-mode and the L-mode are dispersive; the T-mode is non-dispersive. For upper frequency values, new dispersion curves exist.

A fundamental aspect in the inspection procedure is related to the sensitivity that each propagating wave shows with respect to the target defect. In this study, sensitivity is defined as the difference between the phase velocity for the intact case (chosen as a reference curve) and the phase velocity for the damaged cases (see fig. 4). As it can be seen, the longitudinal mode shows potential for detection of this kind of defect.
The above results indicate that the phase velocity of the L(0,1) mode in the 4000 - 8000 kHz frequency range decreases for increasing crack depths. In conclusion, this wave-phase velocity shift could be potentially used for detecting the presence of an internal open elliptical crack on pipes.

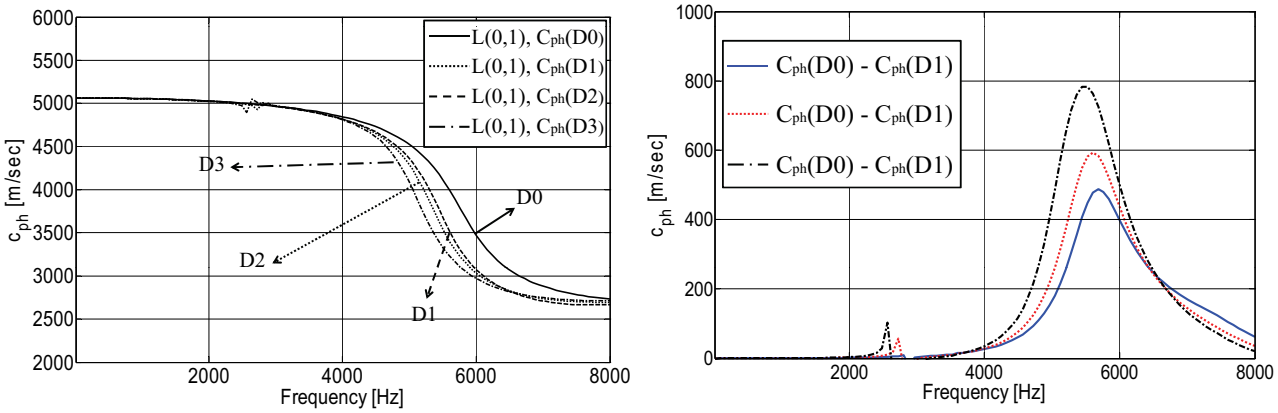


Fig. 4: (a) L(0,1) phase velocity dispersion curves for the four considered cases. (b) L(0,1) sensitivity curves for the elliptical notch.

Acknowledgement

This research involves one of the subjects of the Centre of Study and Research for the Identification of Materials and Structures (CIMEST) – "M. Capurso", University of Bologna, Italy.

References

[1] A. Marzani, E. Viola, I. Bartoli, F. Lanza di Scalea, P. Rizzo. A semi-analytical finite element formulation for modeling stress wave propagation in axisymmetric damped waveguides. *Journal of Sound and Vibration*. Vol. 318 (2008)p. 488-505.

[2] I. Bartoli, F. Lanza di Scalea, M. Fateh, E. Viola. Modeling guided wave propagation with application to the long-range defect detection in railroad tracks. *NDT and E International*. Vol. 38 (2005) p. 325-334.

[3] S. Coccia, I. Bartoli, A. Marzani, et al.. Numerical and experimental study of guided waves for detection of defects in the rail head. *NDT and E International*. Vol 44 (2011) p. 93–100.

[4] Mathworks. Matlab user's manual version V7.10 (R2010a) 2010.

[5] I. Bartoli, A. Marzani, E. Viola, et al.. Modeling wave propagation in damped waveguides of arbitrary cross-section. *J. of Sound and Vibration*, Vol. 295 (2006) p. 685-707.

© (2012) Trans Tech Publications, Switzerland
doi:10.4028/www.scientific.net/KEM.488-489.379

On the Stress Intensity Factors of Cracked Beams for Structural Analysis

Erasmo Viola[a], Yong Li[b], Nicholas Fantuzzi[c]

DICAM-Department, University of Bologna, Viale Risorgimento 2, Bologna 40136, Italy

[a]erasmo.viola@unibo.it , [b]yong.li@unibo.it, [c]nicholas.fantuzzi@unibo.it

Keywords: Fracture mechanics; Stress intensity factors; Circular section beam.

Abstract. In this paper simple engineering methods for a fast and close approximation of stress intensity factors of cracked beams and bars, subjected to bending moment, normal and shear forces, as well as torque, are examined. As far as the circular cross section is concerned, comparisons are made on the base of numerical calculations. The agreement between the present results and those previously published is discussed. New formulae for calculating the stress intensity factors are proposed.

Introduction

For cracked structures, the knowledge of the stress intensity factors (SIFs) plays a fundamental role in linear elastic fracture mechanics. There is an important class of crack problems, involving surface damage in the form of part-through cracks in round bars or beams, where a three-dimensional analysis becomes necessary. Because of the complexity of such problems, exact solutions for edge cracks in round bars are not available. For engineering estimations of the strength of cracked bodies, the use of procedures involving a smaller amount of computational work can be suitable, even if a lower accuracy is involved. The numerical methods for calculating the SIFs involve singular integral equations, weight functions, boundary collocation, finite element methods and boundary element methods.

Valiente [1] numerically obtained two solutions by the finite element method. Daoud and Cartwright [2, 3] computed SIFs in a circular bar with a straight-fronted crack under tension and bending using finite element numerical procedure. Ng and Fenner [4] built a three-dimensional finite element model with both straight and circular-arc crack fronts in an edge cracked circular bar to compute SIFs in tension and bending. Naik and Maiti [5] presented the formulation for analyzing the triply coupled free vibration of beams based on the compliance approach for an open edge crack in an arbitrary angular orientation. Some reviews [6] of the stress intensity factor solutions for surface cracks in round bars subjected to tension loading are presented. This paper deals with two simple engineering methods for a fast and close approximation of stress intensity factors in cracked or notched beams (Fig.1).

Kienzler and Herrmann's Method

Kienzler and Herrmann's method [7] is based on an elementary beam theory and assumes that the strain energy release rate G for crack extension is equal to that for crack widening so that the well known Irwin's G-K relation can be used to determine the stress intensity factors. Bazant [8] suggested that this hypothesis is approximately valid within a correction factor β (slope of the stress diffusion lines).

The incremental strain energy of beams with widening of the crack can be obtained by elementary beam theory [9]. The energy release rate due to crack extension based on Irwin's G-K relation is given in Ref. [10]. The SIFs can be calculated once the factor β is determined.

A tension N applied to a single-edge-crack circular section beam leads to a combined tension and bending moment, since the neutral axial of the ligament is shifted by $e = 2R^3(2\eta - \eta^2)^{3/2}/(3A^c)$, which gives rise to a bending moment $M^N = eN$, where A^c is the area of the cracked cross section of the beam,

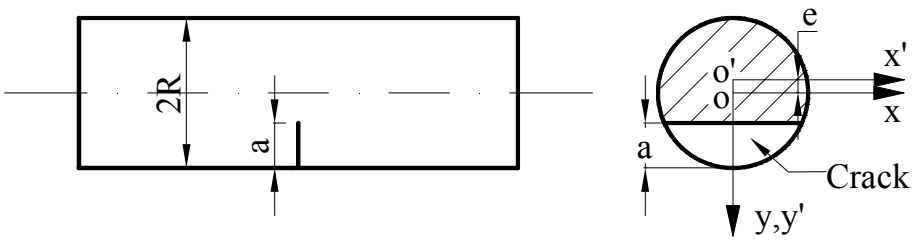


Fig.1. Cracked beam and cracked cross-section

R is the radius of the circular section, $\eta = a/(2R)$ is the dimensionless crack depth and a is the maximum crack depth. The SIF for Mode I K_{I_N} can be expressed as follows

$$K_{I_N} = \frac{N}{R^{3/2}} F_N(\eta) \tag{1}$$

where the geometric function $F_N(\eta)$ is reported in Ref. [10] and shown in Fig.3.

For the edge cracked circular section beam subjected to the bending moment M, the formula for the SIF K_{I_M} can be obtained as

$$K_{I_M} = \frac{M}{R^{5/2}} F_M(\eta) \tag{2}$$

where the geometric function $F_M(\eta)$ is reported in Ref. [10] and shown in Fig.2.

When a torque T is applied at the cracked circular section beam, one obtains the expression of the SIF as

$$K_{\mathrm{III}_T} = \frac{T}{\mathrm{R}^{5/2}} F_T(\eta) \tag{3}$$

where the geometric function $F_T(\eta)$ is reported in Ref. [10] and shown in Fig.5.

For the circular section beam under shear force S, putting shearing factor $\chi = 6/5$, Poisson's coefficient $\upsilon = 0.3$, the SIF's expression for K_{II_S} can be written as

$$K_{II_S} = \frac{S}{R^{3/2}} F_S(\eta) \tag{4}$$

where the geometric function $F_S(\eta)$ is reported in Ref. [10] and shown in Fig.4.

Section Method

The section method was proposed in Ref. [11] and modified by Ref. [12]. Considering a straight beam of constant circular-cross-section, subjected to a couple M, a tensile force N or a shearing force S, the singular stress distribution at the crack tip takes the form $\sigma_{ij}^s = K_i/\sqrt{2\pi r}$. The stress resultants arising at the crack tip are reported in Ref. [10].

The nominal stress is evaluated by the known stress distribution of the reduced solid cross-section passing through the crack tip (ligament). Then, the equivalent condition between singular stress and nominal stress resultant at the crack tip determines K_i approximately.

For pure bending, the normal stress is given by $\sigma_z = (M/I^c)y$, where I^c is the area moment of inertia of the cracked section. The force not transmitted through the crack section is given in Ref. [10]. The distance b determined from the condition that σ_z^s is equal to the normal stress at $r = b$, can be expressed as

$$K_{I_M}^* / \sqrt{2\pi b} = (M/I^c)(R + e - a - b) \tag{5}$$

The distance b can be solved numerically. Substituting such distance b into Eq. (5), the approximate stress intensity factor $K_{I_M}^*$ can be obtained and expressed as $K_{I_M}^* = (M/R^{5/2})F_M^*(\eta)$, where the geometric function $F_M^*(\eta)$ is reported in Ref. [10].

Considering pure tension, as described in the foregoing section, the normal stress on the cross-section of beams under pure tension is $\sigma_z = N/A^c + (Ne/I^c)y$. The force not transmitted through the crack section is given in Ref. [10]. The stress resultant arising at the crack tip is the same as for bending moment. The distance b can be determined from Eq. (6)

$$K^*_{I_N}/\sqrt{2\pi b} = N/A^c + (Ne/I^c)(R+e-a-b) \tag{6}$$

The procedure for determining the approximate stress intensity factor is similar to that used for pure bending. We get $K^*_{I_N} = (N/R^{3/2})F^*_N(\eta)$, where the geometric function as shown in Ref. [10].

When a shear loading S is applied to cracked beam, the average shearing stress acting on the ligament cross section passing through the crack tip takes the form $\tau_{zy} = SQ^*_x/(I^c t)$, where Q^*_x is the first moment of area of the part of the reduced cross section bounded by t which is the width of the ligament cross section at the current calculation stress point.

The force not transmitted through the crack section is given in Ref. [10]. The distance b is determined as

$$K^*{}_{II_S}/\sqrt{2\pi b} = SQ^*_x\big|_{y=R-a-b}/(2I^c\sqrt{R^2-(R-a-b)^2}) \tag{7}$$

By the above mentioned equations, the distance b can be solved. Substituting b into Eq. (7), the approximate stress intensity factor can be obtained as $K^*_{II_S} = (S/R^{3/2})F^*_S(\eta)$, where the geometric function $F^*_S(\eta)$ is shown in Ref.[10].

The torsion problem of circular bars with an edge crack is rather complicated. It will be investigated in a future paper.

Numerical results

The formulae derived for geometric functions are illustrated in Figs. 2-5 for a straight fronted edge cracked circular section bars subjected to bending moment, normal stress, shear force and torque, respectively. Comparisons for tension and bending moment are also considered.

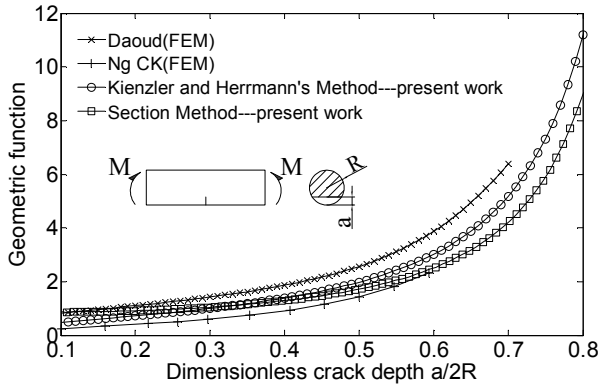


Fig.2. Geometric functions for circular section of beam under bending moment

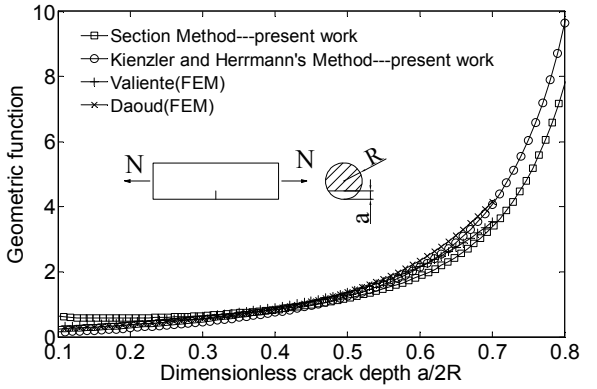


Fig.3. Geometric functions for circular section of beam under tension

As depicted in of Fig.2, 3, the geometric functions for axial force and bending moment show that the agreement between the reported results appear to be satisfactory for value of $a/2R$ from 0.1 to 0.7. Moreover, the geometric functions proposed in this paper are adequate for $0 < a/2R < 1$.

It should be noted that, for edge cracked circular section beams subjected shear force and torsion, authors did not find any relative results about stress intensity factors. The present results are shown in Fig. 4 and Fig. 5.

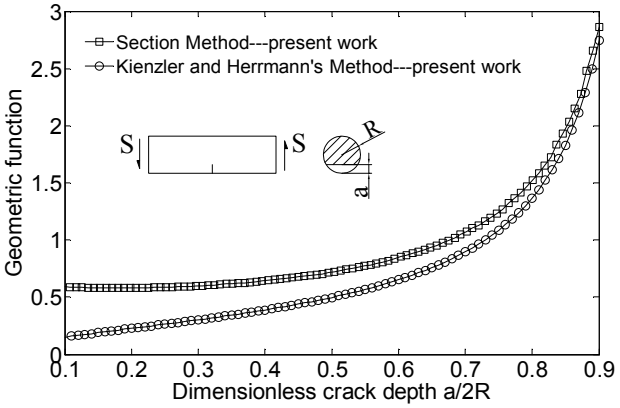


Fig.4. Geometric functions for circular section of beam under shear force

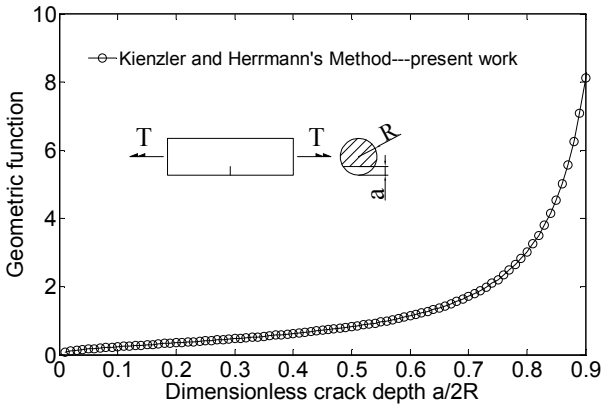


Fig.5. Geometric function for circular section of beam under torque

Conclusions

Two simple engineering methods for a fast and close approximation of stress intensity factors of cracked beams subjected to bending moment, normal and shear forces, as well as torque, are revisited. Moreover, the present work considers the shift of neutral axis of the ligament due to the axial load applied to a single-edge-notch circular section leads to a combined axial load and bending moment. The eccentricity effects on the stress intensity factors under axial load and bending moment is pointed out. Toque and shear force are also investigated. Especially for a deep crack, the eccentricity must be taken into account. As far as sections not considered up to now are concerned, comparisons are made on the base of numerical calculations. The agreement between the present results and those previous appear to be satisfactory.

References

[1] Valiente A. Criterios de fractura para alambres. PhD thesis, Polytechnic University of Madrid, Spain; 1980.

[2] Daoud OEK, Cartwright DJ, Carney M. Strain-energy release rate for a single-edge-cracked circular bar in tension. J Strain Anal Eng Des1978;13(2):83–9.

[3] Daoud OEK, Cartwright DJ. Strain energy release rate for a straight-fronted edge crack in a circular bar subject to bending. Eng Fract Mech 1984;19:701-707.

[4] Ng CK, Fenner DN. Stress intensity factors for an edge cracked bar in tension and bending. Int J Fract 1988;36:291–303

[5] Naik SS, Maiti SK. Triply coupled bending-torsion vibration of Timoshenko end Euler-Bernoulli shaft beams with arbitrarily oriented open crack. J Sound Vib. 2009; 324:1067-1085

[6] Toribio J, Alvarez N, Conzàlez B, ect. A critical review of stress intensity factor solution for surface cracks in round bars subjected to tension bending. Eng Fail Anal 2009;16:794-809

[7] Kienzler R, Herrmann G. An elementary theory of defective beams. Acta Mech 1986;62:37-46.

[8] Bazant ZP. Justification and improvement of Kienzler and Herrmann's estimate of stress intensity factors of cracked beam. Eng Fract Mech 1990;36:523-5.

[9] Ricci P, Viola E. Stress intensity factors for cracked T-sections and dynamic behaviour of T-beams. Eng Fract Mech. 2006;73(1):91-111

[10] Viola E, Li Y, Fantuzzi N. The stiffness matrix of cracked beams for structural analysis. Technical report –DICAM Department (2011), University of Bologna, Italy.

[11] Parton VZ, Morozov EM. Elastic–plastic fracture mechanics. Moscow: Mir Publishers; 1978.

[12] Nobile L. Mixed mode crack initiation and direction in beams with edge crack. Theor Appl Fract Mech 2000;33:107-116

© (2012) Trans Tech Publications, Switzerland
doi:10.4028/www.scientific.net/KEM.488-489.383

Cracks interaction effect on the dynamic stability of beams under conservative and nonconservative forces

E. Viola[1,a], N. Fantuzzi[1,b], A. Marzani[1,c]

Department of Civil, Environmental and Materials Engineering - DICAM, University of Bologna, Viale del Risorgimento 2, 40136, Bologna, Italy

[a] erasmo.viola@unibo.it, [b] nicholas.fantuzzi2@unibo.it, [c] alessandro.marzani@unibo.it

Keywords: non conservative forces, stability, interaction effect, crack, finite element.

Abstract. This study is an extension of the paper by E. Viola and A. Marzani [1] where the eigenfrequencies and critical loads of a single cracked beam subjected to conservative and nonconservative forces have been investigated. Here the aim is to analyze the dynamic stability of T cross section beams with multiple cracks. A doubly cracked Euler-Bernoulli beam subjected to triangularly distributed subtangential forces, which are the combination of axial and tangential forces, is considered. The governing equation of the system is derived via the extended Hamilton's principle in which the kinetic energy, the elastic potential energy, the conservative work and the nonconservative work are taken into account. The local flexibility matrix for a beam with T cross-section is used to model the cracked section. The results show that for given boundary conditions cracked beams become unstable in the form of either flutter or divergence depending on the crack parameters, the nonconservativeness of the applied load as well as the interaction of the two cracks.

Introduction

The dynamic stability of an elastic column subjected to subtangential forces has been investigated by several studies [1,2,3]. Subtangential forces are the combination of axial forces and tangential follower forces. The stability analysis of structures subjected to nonconservative forces requires special consideration with respect to the alternative modes of instability (e.g. divergence or flutter). In the divergence case, the structure passes through a nontrivial equilibrium position in becoming unstable, i.e. the transition of the structure from stability to instability occurs at a zero-eigenvalue. When the instability is in the form of flutter (oscillations with increasing amplitudes), the system loses stability at eigenvalues that are different from zero. In recent years, some authors have studied the dynamic stability of columns with a single crack under a distribution subtangential follower forces. However, there are no papers on the stability of multiple cracked columns. So, a study concerning the interaction between cracks, boundary conditions and instability behaviour of beams is required. The aim of this paper is to construct an algorithm for the analysis of the frequencies and the critical loads level of cracked beams under both static conservative and nonconservative forces. The finite element method is used to perform numerical analyses on the dynamic stability of restrained cracked beams subjected to triangularly distributed subtangential forces. This paper investigates not only how the crack depth and the crack location can effect the transition from divergence to flutter, or from flutter to divergence, but also the crack interaction effect on the dynamic behaviour of cracked beams. For a cracked element, the stiffness matrix has been calculated by a line-spring model in order to simulate the cracked section [4,5]. Such model is based on the knowledge of the stress intensity factors, which play an important role in fracture control.

Beam theory and calculation of the energetic terms

Fig. 1 shows an Euler-Bernoulli elastic beam in an undeformed configuration subjected to a distribution of axial and tangential forces as well as boundary forces. Let the axial force per unit length be denoted by p_h and the tangential force per unit length by p_t. Denoting by φ the angle between the *z*-axis and the beam slope, by $\alpha\varphi$ the angle between the z-axis and the subtangential force p_α, the resultant of p_h and p_t, one easily obtains the relations

$$p_\alpha = p_h + p_t, \qquad \alpha = \frac{p_t}{p_\alpha} \tag{1}$$

with the assumption of a small deflection. In (1) α is known as the *nonconservativeness parameter*. The use of this parameter allows one to replace the system of two forces p_h, p_t by a follower force p_α. By varying the parameter α one can investigate the stability for different loadings. The governing equation of the system is derived from the extended Hamilton's principle, and the crack is modeled via the theory of fracture mechanics. The finite element method is used to perform numerical investigation and to derive the line-spring stiffness matrix expressing the stiffness of the beam cracked sections. The fundamental equation is obtained through the above extended Hamilton's principle, which assumes the following aspect

$$\int_{t_1}^{t_2} \delta\left(\mathcal{T} - \Phi + W_c\right) dt + \int_{t_1}^{t_2} \delta W_{nc} dt = 0 \tag{2}$$

where $\mathcal{T}$ is the kinetic energy, Φ is the elastic potential energy, W_c and W_{nc} represent the conservative work and the nonconservative virtual work, respectively. From equation (2) the equation of motion can be obtained

$$\rho A \frac{\partial^2 v}{\partial t^2} - \frac{\partial}{\partial z}\left(N\frac{\partial v}{\partial z}\right) + \frac{\partial^2}{\partial z^2}\left(EI\frac{\partial^2 v}{\partial z^2}\right) - \alpha p_\alpha \frac{\partial v}{\partial z} = 0 \tag{3}$$

where v is the *y*-displacement, ρ is the mass density, A is the area of the uncracked section, E is the Young's modulus, I is the area moment of inertia of the uncracked section, and t the time variable.

Finite element formulation

For solving the problem at issue with the finite element method, the system equation (strong formulation) has to be written in the weak form. The beam of total length L can be subdivided into *n* finite elements, whose length is l. The governing equation in weak form reads

$$\sum_{i=1}^{N} \int_0^l \left(\rho A \frac{\partial^2 v}{\partial t^2}\delta v + N(z)\frac{\partial v}{\partial z}\frac{\partial \delta v}{\partial z} + EI\frac{\partial^2 v}{\partial z^2}\frac{\partial^2 \delta v}{\partial z^2} - \alpha p_\alpha \frac{\partial v}{\partial z}\delta v\right) dz = 0 \quad \forall \delta v \tag{4}$$

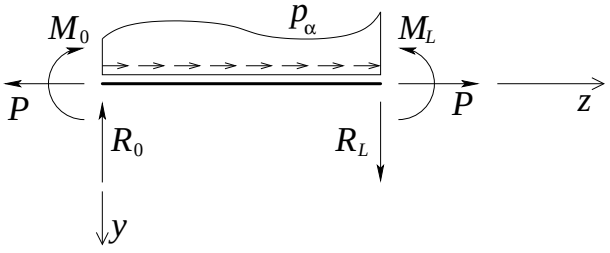


Figure 1: Uncracked beam model

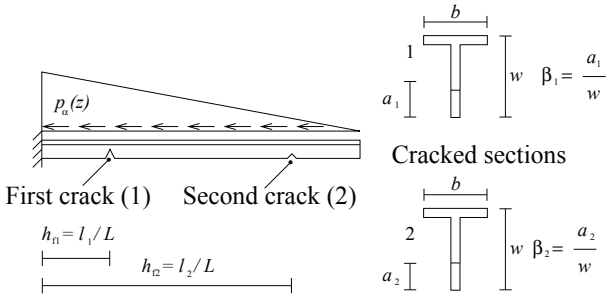


Figure 2: Cracked beam scheme

The displacement field can be approximated by means of the classical linear combination of the Hermitian shape functions with generalized nodal displacements v_1, φ_1, v_2, φ_2. Considering a T cross section beam, the theory developed by Ricci and Viola [2] can be used. The stiffness matrix of a line-spring is given as follows

$$\mathbf{k}_f = \begin{bmatrix} 1/\lambda_{ss} & 0 & -1/\lambda_{ss} & 0 \\ 0 & 1/\lambda_{mm} & 0 & -1/\lambda_{mm} \\ -1/\lambda_{ss} & 0 & 1/\lambda_{ss} & 0 \\ 0 & -1/\lambda_{mm} & 0 & 1/\lambda_{mm} \end{bmatrix} \tag{5}$$

where λ_{ss} and λ_{mm} are the compliances for the shear force and bending moment. By adopting a finite element assembling procedure where the cracks are taken into account, yields a global equation in the following form

$$\mathbf{M}\ddot{\mathbf{u}} + \mathbf{K}_T\mathbf{u} = \mathbf{0} \tag{6}$$

where $\mathbf{K}_T = \mathbf{K}_g + \mathbf{K}_e + \mathbf{K}_d - \mathbf{K}_f$ is the global stiffness matrix. Assuming the solution (6) as $\mathbf{u} = \mathbf{V}\exp(i\omega t)$, the study of the stability of the cracked system is reduced to the following eigenvalue problem

$$\left(\mathbf{K}_T - \omega^2\mathbf{M}\right)\mathbf{V} = 0 \tag{7}$$

Numerical analysis and results

In order to compute the natural frequencies, natural modes and critical distributed tangential forces, the eigenvalue problem associated with the undamped free vibration must be solved. Parametrical studies considering dimensionaless crack depths β_1, β_2, dimensionless crack locations h_{f1}, h_{f2}, as well as different values of nonconservativeness parameter α, have been carried out. The interaction effect of two cracks in the dynamic behaviour of Euler-Bernoulli beam has been investigated. It should be noted that while for the uncracked cantilever beam this problem is dimensionless, when a cracked system is considered the solution depends on crack position, cross section dimensions and beam length. In figs $3-6$ the variation of the two lowest eigenfrequencies $\Omega = (\rho AL^4\omega^2/EI)^{1/2}$ versus the dimensionless distributed force parameter $Q = p_0L^4/EI$ is represented for various values of the nonconservative parameter α. In the numerical results we have considered a beam 5 m long with a T cross section of $w = 80$ cm width, $b = 60$ cm height and 10 cm of thickness. Figs 3-4 show the eigenfrequency curves as a function of subtangential force when the two crack depths are considered variable and in figs 5-6 when the two crack locations are variable. It appears that flutter and divergence phenomena take place.

Conclusions

In this paper, a finite element procedure for cracked prismatic beams, under conservative and nonconservative forces is developed. The paper details the derivation of the global stiffness matrix for the cracked system. The crack effect on the dynamic stability is investigated and graphically presented. The influence of the degree of nonconservativeness of the load on the eigenfrequency curves is also shown for various boundary conditions, when different crack depths and a fixed crack position are considered. The main innovation introduced by the present work regards the formulation and the use of the line-spring model for calculating the interaction effect on frequencies and critical loads of cracked beams under triangularly distributed subtangential forces. The present approach can be extended to scenarious in which interaction between more than 2 cracks is considered, and also in which coupling between the various forms of motion such as bending, shear and torsion take place.

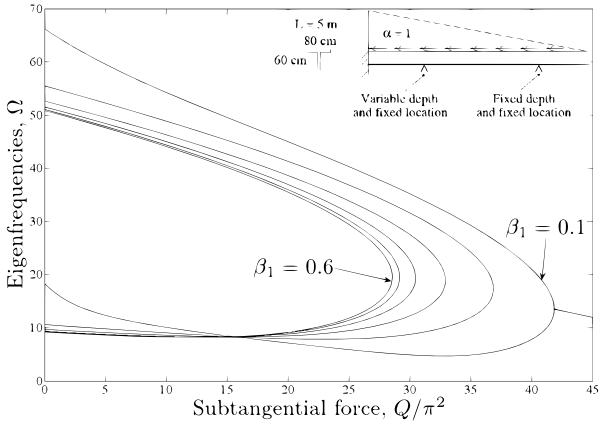


Figure 3: First crack depth variable

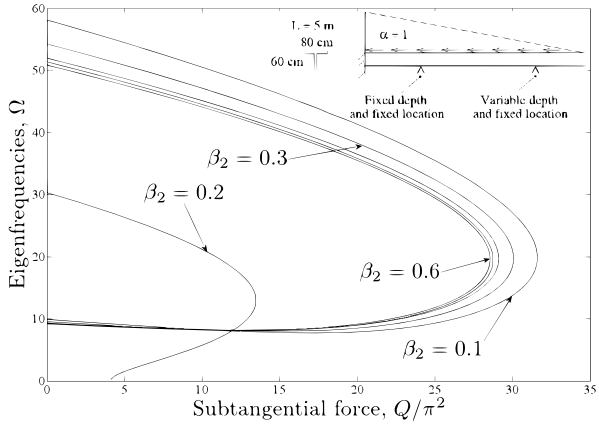


Figure 4: Second crack depth variable

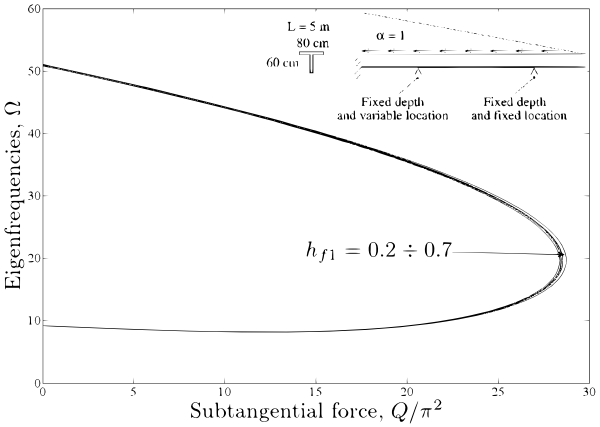


Figure 5: First crack location h_{f1} variable

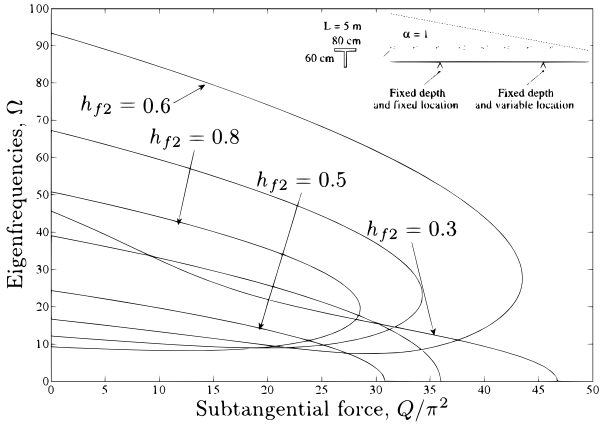


Figure 6: Second crack location h_{f2} variable

Acknowledgement

This research involves one of the subjects of the Centre of Study and Research for the Identification of Materials and Structures (CIMEST) – "M. Capurso", University of Bologna, Italy.

References

[1] Viola E, Marzani A. Crack effect on dynamic stability of beams under conservative and non-conservative forces. Eng. Frac. Mech. Vol. 71 (2004), p. 699 - 718.

[2] Ryu BJ, Sugiyama Y, Yim KB, Lee GS. Dynamic stability of an elastically restrained column subjected to triangularly distributed subtangential forces. Comp. & Struct. Vol. 76 (1975), p. 611 - 619.

[3] Sugiyama Y, Mladenov K. Vibration and stability of elastic columns subjected to triangularly distributed sub-tangential forces. J. Sound and Vib. Vol. 88 (1983), p. 447 - 457.

[4] Ricci P, Viola E. Stress intensity Factors for cracked T-sections and dynamic behavior of T-beams. Eng. Frac. Mech. Vol. 73 (2006), p. 91 - 111.

[5] Viola E, Ricci P and Aliabadi MH. Free vibration analysis of axially loaded cracked Timoshenko beam structures using the dynamic stiffness method. J. Sound and Vib. Vol. 304 (2007), p. 124-153.

© (2012) Trans Tech Publications, Switzerland
doi:10.4028/www.scientific.net/KEM.488-489.387

Finite Temperature Nanovoids Evolution in FCC Metals Using Quasicontinuum Method

Ponga M.[1,a] , Romero I.[2,b] Ortiz M.[3,c] and Ariza M.P.[1,d]

[1]ESTI, Universidad de Sevilla, Camino de los descubrimientos, s.n., 41092 Sevilla, Spain
[2]ETSII, Universidad Politécnica de Madrid, José Gutiérrez Abascal, 2, 28006 Madrid, Spain
[3]California Institute of Technology, 1200 E. California Blvd., Pasadena, CA-91125, USA

[a]mponga@us.es, [b]ignacio.romero@upm.es, [c]ortiz@aero.caltech.edu, [d]mpariza@us.es

Keywords: Quasicontinuum Method, Nanovoids, Multiscale Modelling, FCC Crystals.

Abstract. Tensile failure of metals often occurs through void nucleation, growth and coalescence. This work is concerned with the study of plastic nanovoid cavitation in face-centered cubic (FCC) crystals at finite temperature. In particular, the Quasicontinuum (QC) method, suitably extended to finite temperatures, is taken as the basis for the analysis. We specifically focus on nanovoids in copper single crystals deforming in uniaxial and triaxial tension. The complex structure of dislocations around the nanovoid and the evolution of stress, deformation and temperature of the sample is described in the present work.

Introduction

Atomistic simulations of materials have gained recent interest due to their applications in nano and micro mechanics. To understand the mechanical response of materials subject to dynamical loads the knowledge of the physical and thermodynamical properties of materials is required. Molecular dynamics (MD) techniques have been used by many authors to study the mechanical response of materials with nanovoids. However, a correct simulation of plastic phenomena requires the use of very large systems and appropriate boundary conditions, which may result in complex MD models. In this sense, multiscale (MS) modelling provides an alternative to MD simulation, especially for this type of problem. Particular MS technique, the Quasicontinuum method (QC) [1] has been succefully employed in the past. In the current work, QC method with extension to systems in thermodynamic equilibrium and non-equilibrium (HotQC) is used.

Results are shown for numerical tests according to a non-equilibrium finite temperature problem using QC method. This problem has been studied by many authors, but none of them have included systems outside equilibrium. Also, the purpose of these tests is to understand the nucleation of particular arrangement of atoms around a nanovoid and the evolution of the temperature field in this process.

QC Method for Non-Equilibrium Problems

QC is a multiscale modelling scheme that seamlessly spans continuum and atomistic descriptions. The method starts with a small and complete atomistic system around a core defect. Then the rest of the crystal is modelled in the geometry and reducing the configuration space of the crystal trough a judicious application of a finite element-based kinematic constraints. To avoid full lattice sums, only atoms in small clusters, surrounding the representative atoms must be visited for computing the effective out-of-balance forces. Additionally, the selection of representative atoms is performed adaptively based on the local strain of the elements. The tolerance governing the adaptation process is set so that the full atomistic resolution is attained only in the presence of dislocations.

The force among atoms is directly computed by empirical potentials. As in conventional continuum mechanics, QC permits the direct simulation of systems controlled through the application of remote

boundary conditions. Details of the implementation of QC used in the present study and an analysis of convergence of the method may be found in [1].

Extension of the QC method to systems in thermodynamic equilibrium and non-equilibrium was developed in [2]. This extension is possible by the application of a variational mean-field theory and the maximum-entropy (*max-ent*) formalism. Using this formalism, we can directly approximate the probability density function to find the system in a certain state, not necessarily in equilibrium. In this model, every atom within the system have its own local statistical parameters, temperature and entropy, in addition to position. Then, the *max-ent* variational principle provides the most likely probability density function within the assumed mean-field class and consistent with all constraints on the systems.

Attention to macroscopic processes that are quasi-static is performed. Under these conditions, the net result of the *max-ent* procedure is to define a non-equilibrium free energy depending on the positions and temperatures of all the atoms. The non-equilibrium free energy is computed explicitly by numerical quadratures and the result may be regarded as a temperature-dependent interatomic potential. The stable configuration of the system is found by minimization of the free energy for a given temperature field.

The next step in the development of the method therefore concerns the calculation of the evolving temperature field. We accomplish this by coupling the free-energy minimization problem to a diffusion form of the energy-balance equation. The proper form of the coupling is suggested by the variational formulation of coupled thermo-mechanical problems proposed in [3].

Numerical Test

A nanovoid triaxial expansion problem is studied using the HotQC method outlined previously. This problem has been studied by many authors but none of them have considered the system in thermodynamic non-equilibrium. The purpose of these tests is to understand the nucleation and evolution of dislocations emanating from the surface of the nanovoid, and also the evolution of the size and shape of the nanovoid with the applied deformation. Results are compared with similar ones obtained using MD techniques.

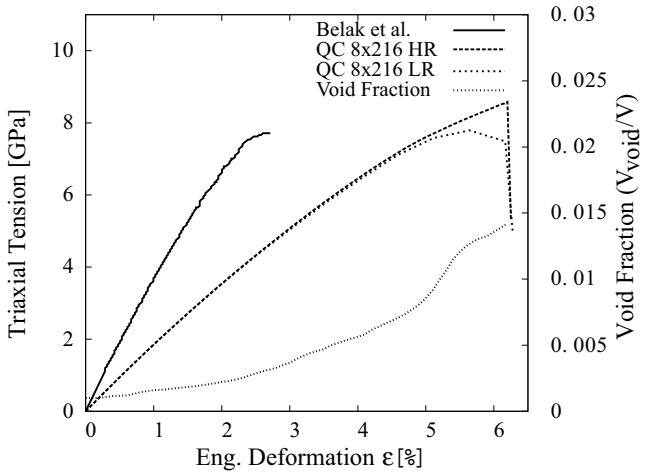
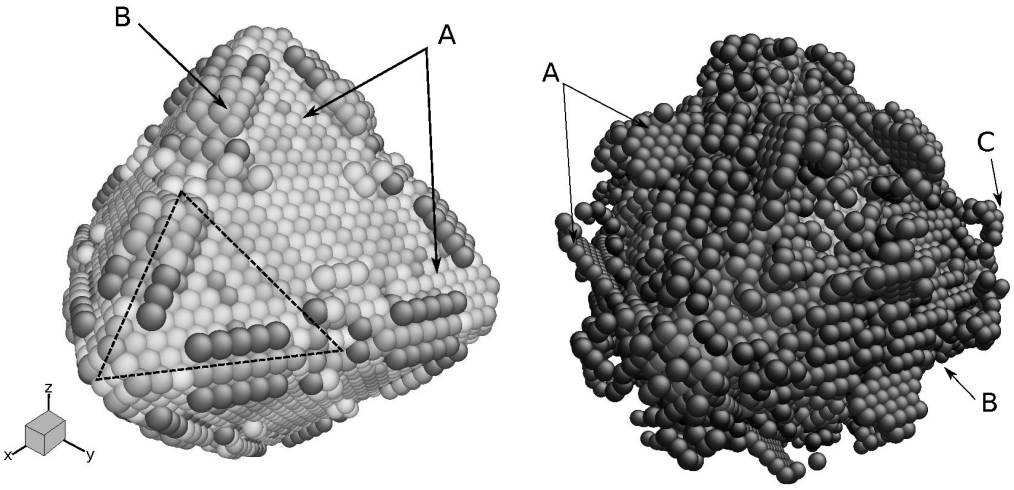


Fig. 1: Computed triaxial tension and normalized void volume expansion V_{void}/V vs deformation ε of the sample.

Problem definition. It is well establish that the nature of nanosized void growth in single crystals is sensitive to the crystal structure. In particular, an initially spherical void in FCC metals grows into an octahedral shape as observed in single crystal spall experiments [4]. We consider a computational cell of size $216a_0 \times 216a_0 \times 216a_0$ ($a_o = 0.3615$nm) of copper, containing a total of 51×10^6 atoms. A spherical void of radius $3.5a_0$ is created in the center of the cell with initial full atomistic resolution



(a) (b)

Fig. 2: (a) Octaedral shape of the void observed at $\epsilon = 3\%$. (b) Dislocation structures at $\epsilon = 6\%$.

within a $8a_0 \times 8a_0 \times 8a_0$ region surrounding the void. The applied load consists of a triaxial expansion of the void by prescribing pure dilatational displacements over the cell boundary, deformation is steadily increased by 0.1 % increments. At every step new stable equilibrium configuration is obtained by using the Polak-Ribiere variant of the non-linear conjugate gradient algorithm. Previously, the sample is allowed to expand isothermally at $T_0 = 300K$. In order to check the effect of the triangulation on the macroscopic behavior of the material, two distortion energies (HR and LR) have been implemented. Additionally, a second cell of $864a_0 \times 864a_0 \times 864a_0$ or 312.3 nm of length have been analyzed in order to better observed dislocation structures around the surface of the void. In this case the cell contains a $15a_0$ nanovoid. The total number of atoms in this cell is 323×10^6 and the initial nodes are 33×10^3.

Results and Discussion. Fig. 1 shows the evolution of tension and void volume expansion vs deformation. The behavior of the material is linear up to 5% of deformation followed by a hardening regime up to the failure of the material. A comparison with MD study is also shown, with higher slope value due to the characteristic high strain rate of MD simulations. The V_{void}/V curve shows that void growth is not linear with the deformation and following an exponential behavior as indicated by continuum theories. The dislocation structures that form after the first yield point are shown in Fig. 2a, fourfold assemblies of stacking-fault tetrahedra are observed in planes 111 around the nanovoid. Up to 6% of deformation the void growth rate increases again, atomic configurations are shown in Fig. 2b. At this point, the dislocation grows over the primary octahedron as shown in Fig. 2a. Atoms with label A are stacking faults dislocations in 111 planes and atoms with label B are perfect dislocations 1/2[110]100). Finally, an interval with strong non-linearity indicates the fragile failure of the material.

The evolution of the macroscopic temperature with respect to deformation is shown in Fig. 3. Up to 5% of deformation, the temperature decreases constantly according to the thermo-elastic behavior of the material. After 6.2% of deformation, the rate changes due to the formation of dislocations around the nanovoid, decreasing up to 238 K. Finally, when after failure the temperature value jumps up to 262 K due to the break of atomic bonds in the nanovoid surroundings.

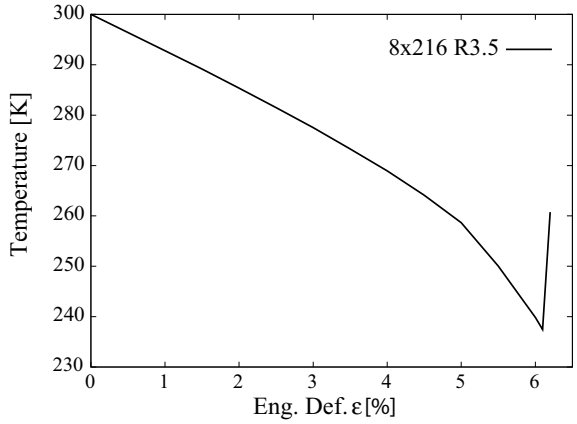


Fig. 3:

Conclusions

In this work we have applied an extension of the QC method to study the thermo-mechanical behavior of a nanovoid under tension in copper. The extension of the Quasicontinuum method to non-equilibrium systems has provided a detailed solution of the forces, deformation, and temperature at every point of the sample, with atomistic resolution close to the defect. In this region, both adiabatic as well as isothermal simulations indicate that a fragile fracture occurs in the material shortly after dislocation structures appear. The multiscale resolution of the Quasicontinuum approach then serves to compute a macroscopic response of the whole crystal, where fracture is clearly identified.

Acknowledgment

We gratefully acknowledge the support of the Ministerio de Educación y Ciencia of Spain (DPI2009-14305-C02-01/02), the support of the Consejería de Innovación of Junta de Andalucía (P09-TEP-4493) and the support of the Department of Energy National Nuclear Security Administration under Award Number DE-FC52-08NA28613 through Caltech`s ASC/PSAAP Center for the Predictive Modeling and Simulation of High Energy Density Dynamic Response of Materials.

References

[1] E.B. Tadmor, M. Ortiz and R. Phillips: Philos. Mag. Vol. 73 (1996), p. 1529

[2] Y. Kulkarni, J. Knap and M. Ortiz: J. Mech. Phys. Solids Vol. 56 (2008), p. 1417

[3] Q. Yang, L. Stainier and M. Ortiz: J. Mech. Phys. Solids Vol. 54 (2006), p.401

[4] A.L. Stevens, L. Davison, and W.E. Warren: Journal of Applied Physics Vol. 43(12) (1972), p. 4922

[5] C.L. Kelchner, S.J. Plimpton and J.C. Hamilton: Phys. Rev. B Vol. 58 (1998), p.11085

© (2012) Trans Tech Publications, Switzerland
doi:10.4028/www.scientific.net/KEM.488-489.391

Bone-cement interface micromechanical model under cyclic loading

J.A. Sanz-Herrera[1, a], H. Esteban[b] and M.P. Ariza[c]

[1]Escuela Técnica Superior de Ingeniería, Universidad de Sevilla. Camino de los descubrimientos s/n 41092 Seville (Spain)

[a]jsanz@us.es, [b]helgaem@gmail.com, [c]mpariza@us.es

Keywords: Bone-cement interface, Micromechanics, Fatigue damage, Viscoelasticity.

Abstract. Total hip replacement is one of the most common techniques in orthopaedic surgery, and one of the most important surgical advances of the last XX century. Normally, implant is fixed to bone by means of a polymer material known as bone cement, building an interface between implant and bone regions. Microscopically, two interfaces can be distinguished, namely, bone-cement and implant-cement interfaces. One of the main causes of failure is implant loosening due to fatigue of one of the two microscopic interfaces. In this work, a micromechanical analysis of bone-cement interface under cyclic forces is introduced. Both bone and cement are considered using different models based on fatigue damage over a statistically representative volume element (RVE) of the microstructure. This technique allows to homogenize mechanical stresses of the RVE yielding the effective macroscopic behavior of the bone-cement interface, avoiding experimental fitting case to case, once the interface geometry and mechanical characterization of the involved phases are known.

Introduction

Total hip replacement (THR) is one of the most common techniques in orthopaedic surgery, and one of the most important surgical advances of the last XX century [1]. The use of biomaterials for these applications has been widely extended. Implant design must be based on the individual kinematics as well as dynamic load transfer to the body region. THR has been available since the introduction by Dr. Charnley of the so-call bone cement to fix the implant to bone [2]. Bone cement acts like a filling material, and therefore, its clamping capability strongly depend on its capacity to go through trabecular bone during implant fixation. Since it is a viscoelastic polymer, it shows properties like damping or uniform load distribution which reduces contact stress concentration. One of the main causes of failure is due to interface loosening at the microscopic level, which takes place at one of the two well distinguished ones, namely, bone-cement and cement implant interfaces [3]. Loosening may induce fatigue failure at one of the above referenced interfaces. This work is focused on the micromechanical analysis of the bone-cement interface.

In this paper, two micromechanical models under cyclic loading both for bone and cement are considered in order to analyze their combined behavior of the interface from a microscopic point of view. Each model assumes the characteristic properties of bone and cement. The study is established over a representative volume element (RVE) of the bone-cement interface microstructure. This technique allows to homogenize macroscopic behavior of the interface through the homogenized damage as an internal variable. Numerical implementation is carried out using the finite element method.

Mathematical modeling

From a mechanical point of view, bone tissue may be assumed as a viscoelastic material which contains microcracks, which is treated from continuum damage mechanics approach,

$$\boldsymbol{\sigma} = (1 - d_b)\boldsymbol{C} \cdot \boldsymbol{\varepsilon} \tag{1}$$

where $d_b \in [0,1)$ is a dimensionless scalar parameter (considered as isotropic damage) which measures the damage and $\boldsymbol{C}$ being a fourth order tensor which contains the mechanical properties of the undamaged material. Bone tissue damage is decomposed by the fatigue and creep damage d_f and d_c, respectively. Fatigue damage is obtained by means of the Miner-Palgrem formula,

$$d_f = \sum_{i=1}^{m} \frac{n_i}{N_{fail_i}} \tag{2}$$

being n_i the current number of cycles applied at a given step *i*. On the other hand N_{fail_i} is the number of cycles of failure for a given stress level at step *i*. The latter parameter is obtained by experimental setup of fatigue tests, which results are fitted to [4],

$$N_{fail} = F\sigma^{-G} \tag{3}$$

F and *G* were experimentally fitted to $2.51 \cdot 10^{30}$ and 30.4 for stresses given in MPa [4]. σ is the maximum principal tension stress. On the other hand, creep damage depends of time as well as the applied load level, which increases until bone fracture is reached for a value of one of the damage variable. Under a constant stress, the failure time is defined as,

$$T_b = A\sigma^{-B} \tag{4}$$

A and *B* being experimentally obtained constants [4], with values of $3.02 \cdot 10^{35}$ and 17.95, respectively, for stress is given in MPa and time in seconds. Analogously, σ is the maximum principal tension stress. Therefore, using the Miner-Palmgren rule in (4) yields,

$$\frac{d}{dt}[\![(d]\!]_c) = \frac{1}{A\sigma^{-B}} \tag{5}$$

If we consider a time-harmonic loading, the number of cycles can be expressed as $n = \omega t / 2\pi$. Then, Eq. (5) yields to,

$$\frac{\frac{d}{dn}[\![(d]\!]_c)}{dn} = \frac{\frac{d}{dt}[\![(d]\!]_c)(dt)}{dn} = \frac{2\pi}{\omega A\sigma^{-B}} \tag{6}$$

The above introduced modeling is applied to the bone material. On the other hand, cement is used to attach the implant to bone, assumed as a viscoelastic passive material considering damage, such that the Hooke's law is written as,

$$\boldsymbol{\sigma} = (1 - d_{1m})\boldsymbol{C} \cdot (\boldsymbol{\varepsilon} - \boldsymbol{\varepsilon}_{\perp c}) \tag{7}$$

To obtain the accumulated damage we use the Miner-Palmgren law according to the following expression,

$$\frac{d}{dn(d_m)} = \frac{\alpha}{N^{\alpha}_{F_{cement}}(\sigma)} n^{\alpha-1} \tag{8}$$

$N^{\alpha}_{F_{cement}}$ being the number of cycles of failure for a given stress level, σ is the maximum principal tension stress, *n* is the number of load cycles, whereas α is an experimentally obtained fitting coefficient. Cement fatigue life, $N^{\alpha}_{F_{cement}}$, is experimentally obtained by means of S-N assays, which can be modeled to,

$$\sigma = I \cdot N^{J}_{F_{cement}} \tag{9}$$

where I and J are experimentally obtained parameters fitted to 74.805 and -4.68, respectively, and σ is the maximum principal tension stress given in MPa.
On the other hand, the following expression is used in order to compute the creep strain in the cement material,

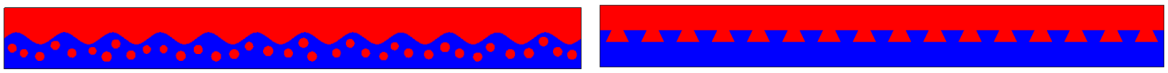
$$\varepsilon_c = R \cdot n^S \cdot \sigma_{VM}^T \tag{10}$$

being R=1.798·10^{-6}, S=0.283, and T=1.858, experimentally obtained data for Von Mises σ_{VM} stress. Eq. (10) is now differentiated with respect to the number of cycles as,

$$\frac{d}{dn}(\varepsilon_c) = R \cdot S \cdot n^{S-1} \cdot \sigma_{VM}^T + R \cdot n^S \cdot T \cdot \sigma_{VM}^{T-1} \cdot \frac{d}{dn(\sigma_{VM})} \tag{11}$$

Bone-cement micromechanics

The above introduced models both for bone and cement under cyclic loading are here applied over two representative volume elements (VRE's) of the bone-cement interface microstructure. Fig. 1 shows two idealized RVE's finite element models of the bone cement-interface, distinguishing from a smooth interface (Fig. 1a) and a sharp interface (Fig. 1b). The upper part of such interfaces corresponds to the cement, whereas the lower part to bone region (interdigitated cement).



(a) *(b)*

Figure 1. Geometry of the RVE of the interface microstructure. (a) Smooth bone-cement interface with cement inclusions into the bone region, and (b) sharp bone-cement interface.

Boundary conditions applied over the RVE microstructure are the following: periodicity of the displacement field between left and right edges, and clamped displacements at the upper and down edges. On the other hand, RVE's shown in Fig. 1 are subjected to a volumetric strain both at normal and tangential directions. Once the microscopic problem is solved, field and internal variables are homogenized at the macroscopic (or apparent) level according to the following operator,

$$\langle \blacksquare \rangle = \frac{1}{V} \int_V \blacksquare \, dV \tag{12}$$

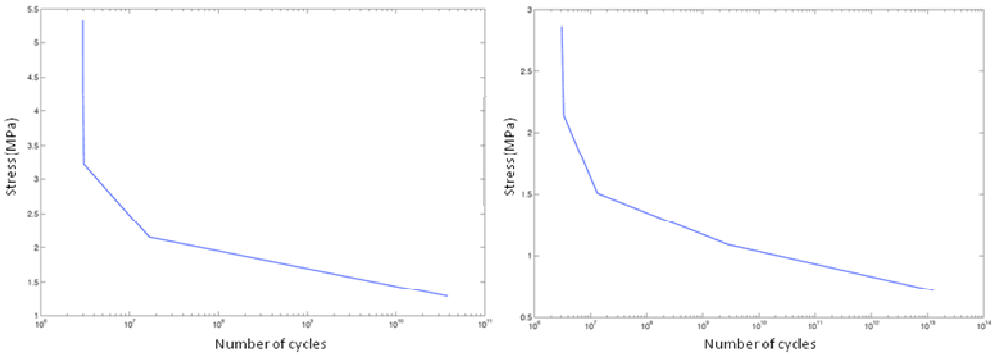
V being the RVE volume.
We can estimate at the macroscopic level the following adapted Miner's rule,

$$\langle d \rangle = \frac{n}{\langle N_f \rangle} \tag{13}$$

where $\langle d \rangle$ is the homogenized (averaged) damage for an imposed loading amplitude and for a given number of cycles n, and $\langle N_f \rangle$ the estimated number of cycles to failure of the interface at the macroscopic level.

Results

Macroscopic S-N curves for the interfaces with RVE's shown in Fig. 1 are obtained in this section. Fig. 2a plots the stress magnitude and the number of cycles to failure for the smooth interface introduced in Fig. 1a. On the other hand, tangential loading behavior for this interface is depicted in Fig. 2b.



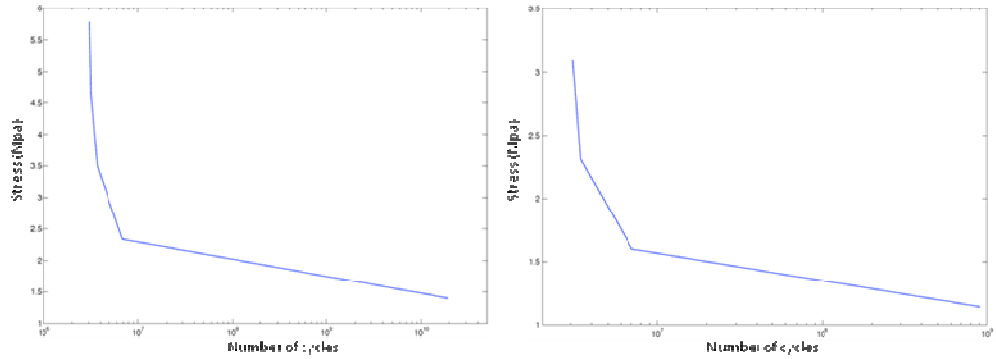
(a) *(b)*

Figure 2. Macroscopic S-N curves for the smooth interface. (a) Normal direction of loading, (b) tangential direction of loading.

S-N curves for the sharp interface are presented in Fig. 3, for normal loading (Fig. 3a) and tangential loading (Fig. 3b), providing an estimation of the overall interface macroscopic failure behavior.

Summary

A micromechanical modeling of bone-cement interfaces has been presented in this work. Results provide microscopic as well as macroscopic information of the interface mechanics. Future works includes a multiscale formulation for the analysis of implants and prosthesis from a micro and macromechanical point of view.



(a) *(b)*

Figure 3. Macroscopic S-N curves for the sharp interface. (a) Normal direction of loading, (b) tangential direction of loading.

References

[1] A.-K. Nilsdotter, A.-K. and F. Isaksson: BMC Musculoskeletal Disorders Vol. 11 (2010), p. 47

[2] J. Charnley, in: *Acrylic cement in orthopaedic surgery*, Churchill/Livingstone, Edinburgh, UK (1970).

[3] M. Jasty, W.J. Maloney, C.R. Bragdon, D.O. Connor, T. Haire and W.H. Harris: J. Bone Joint Surg. Am. Vol. 73-B (1991), p. 551

[4] D.R. Carter and W.E. Caler: J. Orthop. Res. Vol. 3 (1985), p. 84

© (2012) Trans Tech Publications, Switzerland
doi:10.4028/www.scientific.net/KEM.488-489.395

Comparison of Solutions of Stress Field based on Hertzian and Combined Numerical-Crystallographic Approaches beneath Nanoindenter

Jana Horníková[a], Pavel Šandera[b] and Jaroslav Pokluda[c]

Brno University of Technology, Technická 2, 616 69 Brno, Czech Republic
[a]hornikova@fme.vutbr.cz, [b]sandera@fme.vutbr.cz, [c]pokluda@fme.vutbr.cz

Keywords: Nanoindentation; Hertzian approach; Numerical solution; Pop-in effect; Crystallography.

Abstract. Nanoindentation is considered to be a very promising experimental approach to measuring the ideal shear strength since the stressed volume beneath the sharp indenter may be defect-free. The local shear component of the stress reaches its maximum value at some close distance from the indenter in the bulk. The value of the stress can reach the ideal shear strength and, consequently become high enough to nucleate dislocations. This process might be detected as a pop-in on the nanoindentation load-displacement curve. To model the nanoindentation test for that purpose, three different approaches have been used in this works. The first approach is based on the analytical Hertzian solution of the stress field beneath the nanoindenter where only a continuum mechanics is taken into account. The second concept is based on the numerical solution without crystallographic considerations and the third one respects the fact that the dislocation generation in the substrate is subjected to crystallographic rules. The aim of this article is to compare all these concepts by their application to the nanoindentation process performed on selected bcc and fcc metallic substrates.

Introduction

When the local shear component of the stress in the critical site under the nanoindenter reaches the value of the ideal shear strength τ_{id} (ISS), the dislocations can be spontaneously generate to produce a pop-in on the nanoindentation load displacement curve. Some authors already reported such behaviour and tried to compare the related stress to the theoretically determined ideal shear stress [1-4]. A relevant model of the nanoindentation test must be based on joining approaches on three different levels: (i) Atomistic (calculation of ISS); (ii) mesoscopic (crystallography); (iii) macroscopic (finite element analysis of stress strain response). In our previous works [5-8], such models were applied to predict the pop-in effect in Cu and Ni single crystals with a reasonable agreement with experimental data in the case of critical loads related to the pop-in effect. As a rule, however, the experimental values of the pop-in deformation lie slightly above the values obtained by a majority of published models. In this connection, one should take some possible imperfections of the numerical codes into account. Indeed, the results of the numerical FEM codes can be extremely susceptible to associated techniques as selection of the shape and type of elements, density of the mesh, distribution of contact elements, numerical procedures, number of iterations, convergence criteria, etc. On the other hand, the analytical Hertzian model (e.g. [9]) does not suffer from such, rather subjectively influenced, factors. Therefore, some adjustment of the numerical models with respect to the Hertzian model would be desirable. To our knowledge, such a comparison was not performed hitherto.

The aim of this article is to compare different concepts by their application to the nanoindentation process performed on single crystals of copper, nickel and tungsten.

Description of utilized procedure

A three-dimensional isotropic FEM analysis was performed by using the finite element ANSYS code. A frictionless sphere conical indenter with the radius $R = 0.5$ μm is pressed into a 50 μm thick substrate disc with the radius of 100 μm. In the vicinity of the interface, the sphere is meshed with

elements approximately 0.5 nm and the mesh of the substrate is refined from 1 μm at the outer edge of the disc to 0.5 nm directly beneath the indenter. The size of the elements near the contact is an order of magnitude smaller in comparison to the depth of penetration. Owing to the axial symmetry of the indentation model only 2D section could be analysed, as depicted in Fig. 1. The Young modulus E of the diamond indenter was taken to be of 1141 GPa and the Poisson ratio $\mu = 0.07$.

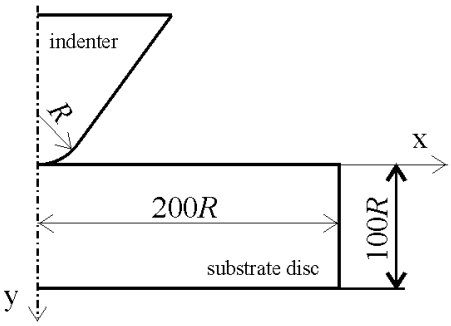


Fig. 1: The radial cross-section of the nanoindenter and the substrate disc.

To model a contact area between the indenter tip and the specimen one has to identify where the contact might occur during the deformation. The kinematics of the deformation process can be tracked after defining the potential contact surfaces via a target and contact elements. Further details concerning the contact surfaces can be found in [10]. As a contact algorithm the augmented Lagrangian method [11] was chosen. This penalty method with additional penetration control usually leads to better conditioning and is less sensitive to the magnitude of the contact stiffness coefficient comparing to other methods, e.g. pure penalty method or pure Lagrange multiplier method.

In 1882 Hertz solved the problem by involving contact between two elastic bodies with curved surfaces. In general, the Hertzian contact stress usually refers to the stress close to the area of contact between two spheres of different radii. Hertz made his analysis general by attributing a quadratic function to represent the profile of the two opposing surfaces and gave particular attention to the case of contacting spheres. He deduced that an ellipsoidal distribution of pressure would satisfy the boundary conditions of the problem and found the following relations relevant to the case of a sphere:

$$\sigma_x = \left[-(1+\mu)\left(1 - \frac{y}{a}\arctan\frac{a}{y}\right) + \frac{1}{2}\left(1+\frac{y^2}{a^2}\right)^{-1} \right] p_0 \tag{1}$$

$$\sigma_y = -\left(1+\frac{y^2}{a^2}\right)^{-1} p_0 \tag{2}$$

where σ_x and σ_y are stress components, p_0 is the contact pressure and a is the radius of the contact circle. Hertz did not calculate the magnitude of the stresses at points throughout the interior but offered a suggestion as to their character by interpolating between those he calculated on the surface and along the axis of symmetry y.

Results and discussion

Both above described methods were used for a calculation of stresses σ_x, σ_y and the maximum shear stress τ_m along the y axis under the indenter for fcc single crystals Cu and Ni (loaded in the [100] direction) and the bcc tungsten single crystal (loaded in the [111] direction). The resulting stresses are depicted in Fig. 2 for the tungsten crystal in dependence of the normalized depth y/R.

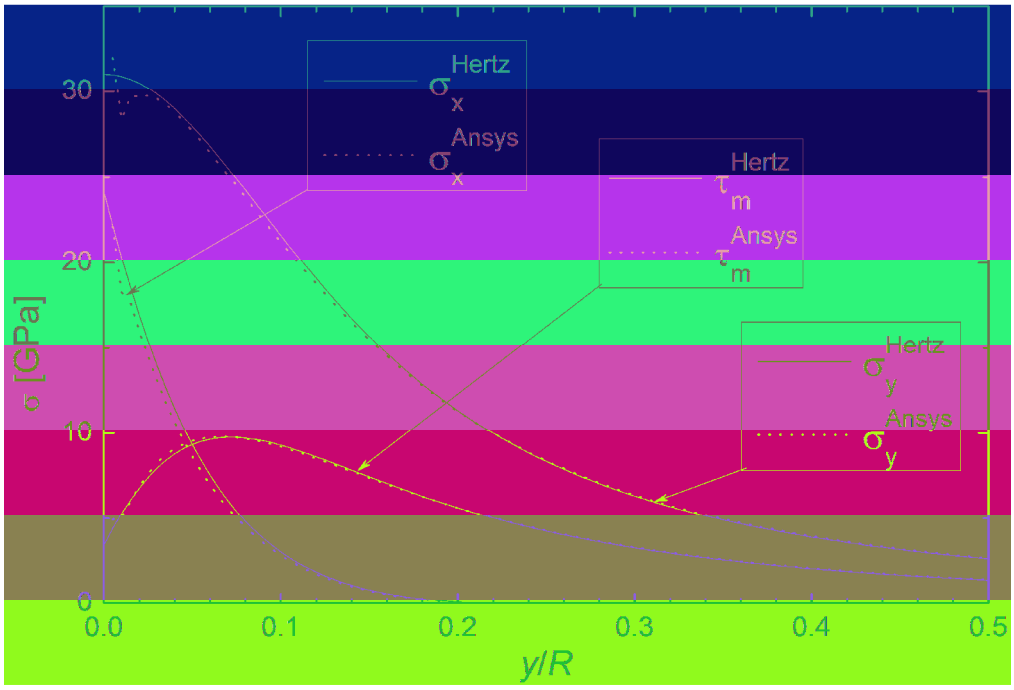


Fig. 2: Stresses σ_x, σ_y and τ_m computed by means of the Hertzian and the numerical model as functions of the normalized depth y/R for the tungsten crystal.

One can see that both models give a practically identical prediction of the stresses along the symmetry axis. This confirms the good properties of the numerical model.

The main difference between the continuum model and the multiscale model lies in the crystallography considered in the latter model. In order to identify the appropriate crystallographic plane in which the condition for the dislocation emission is firstly reached, the dislocation activity in the shear system $\{1\,\bar{1}\,1\}\langle 110\rangle$ for fcc crystals and the shear systems $\{1\,\bar{1}\,0\}\langle 111\rangle$, $\{11\bar{2}\}\langle 111\rangle$ for bcc crystals was considered in the calculations. With regard to the cylindrical symmetry of the solution, the stress tensor transformation was performed to obtain all possible positions of the crystallographic systems rotating according to the main coordinate system. This rotation enabled us to compute the maximum values of the shear stress τ in the respective slip system. The positions of the critical nodes and the corresponding values of the maximum shear stress for the crystals W and Cu are displayed in Tabs. 1 and 2. Note that the critical nodes 1418, 2001 (W) and 195 (Cu) are slightly shifted from the symmetry axis. This crystallographic effect was also found by Krenn et al. [4]. The maximum shear stress values in all crystallographic systems are less than those for the node 149 lying on the symmetry axis computed by the continuum model. This difference represents also a significant effect of the multiscale model.

Tab. 1: Location of critical nodes and the related maximum shear stresses for the continuum and multiscale model applied to the tungsten crystal.

node	x/R	y/R	$\tau_{\{110\}<111>}$	$\tau_{\{112\}<111>}$	τ_{max}
149	0	0.07000	5326.4	7532.7	9785.2
1418	0.05791	0.06946	7148.4	8564.0	9275.1
2001	0.09224	0.06817	7443.9	8249.9	8634.1

Tab. 2: Location of critical nodes and the related maximum shear stresses for the continuum and multiscale model applied to the copper crystal.

node	x/R	y/R	$\tau_{\{111\}<110>}$	τ_{max}
149	0	0.07000	3564.8	3781.1
195	0.02918	0.06828	3693.9	3732.2

Conclusion

The approach based on the analytical Hertzian solution of the stress field beneath the nanoindenter and the numerical method using the ANSYS code were applied to the single crystals of copper, nickel and tungsten. Both methods resulted in the same stress-strain fields along the symmetry axis. Moreover, the application of the numerical method combined with crystallographic considerations revealed that the position of the maximum shear stress related to the pop-in effect is slightly shifted away from the symmetry axis for all investigated crystals. The associated values of the maximum shear stress are lower than those located at the symmetry axis as predicted by continuum models without taking the crystallographic effects into account. The analysis revealed that the slight disagreement between theory and experiment should be identified in other possible imperfections of the multiscale model.

Acknowledgement

The support of the Ministry of Education, Youth and Sports of the Czech Republic in the frame of the project MSM0021630518 is gratefully acknowledged.

References

[1] Y. L. Chiu and A. H. W. Ngan: Acta Mater. Vol. 50 (2002), p. 2677–2691.

[2] M. Göken, M. Kempf and W. D. Nix: Acta Mater. Vol. 49 (2001), p. 903–911.

[3] M. Göken and M. Kempf: Z. Metallkd. Vol. 92 (2001), p. 1061–1067.

[4] C. R. Krenn, D. Roundy, M. L. Cohen, D. C. Chrzan and J. W. Morris Jr.: Phys. Rev. Vol. B65 (2002), 134111.

[5] J. Horníková, M. Černý, P. Šandera and J. Pokluda: Key Engng. Mater. Vol. 348–349 (2007), p. 8001–8004.

[6] J. Horníková, V. Buršíková, P. Šandera, M. Černý and J. Pokluda: Acta Metall. Slovaca, Vol. 13 (2007), p. 65–69.

[7] J. Horníková, P. Šandera, M. Černý and J. Pokluda: Engng Fract. Mech. Vol. 75 (2008), p. 3755–3762.

[8] J. Horníková, J. Pokluda, P. Šandera and M. Černý, in: *9th International Conference on Nanostructured Materials - Nano08*, Centro Brasileiro de Pesquisas Fisicas, Rio de Janeiro 2008, p. 271.

[9] K. L. Johnson. *Contact Mechanics* (Cambridge University Press, UK 1985).

[10] ANSYS Users Manual. Revision 12.0, I-IV (Swanson Analysis System, Houston, USA 2009).

[11] T. A. Laursen and J. C. Simo: Comp. Methods Appl. Mech. Engng. Vol. 108 (1993), p. 133–146.

© (2012) Trans Tech Publications, Switzerland
doi:10.4028/www.scientific.net/KEM.488-489.399

INFLUENCE OF BOUNDARY CONDITIONS ON HIGHER ORDER TERMS OF NEAR-CRACK-TIP STRESS FIELD IN A WST SPECIMEN

Václav Veselý[1,a], Lucie Šestáková[1,b] and Stanislav Seitl[2,c]

[1]Institute of Structural Mechanics, Faculty of Civil Engineering, Brno University of Technology, Brno, Czech Republic

[2]Institute of Physics of Materials, Academy of Sciences of the Czech Republic, v. v. i., Brno, Czech Republic

[a]vesely.v1@fce.vutbr.cz, [b]sestakova.l@fce.vutbr.cz, [c]seitl@ipm.cz

Keywords: wedge-splitting test, crack tip fields, higher order terms, boundary conditions, over-deterministic method.

Abstract. A precise description of the stress and deformation fields in a cracked body is provided using multi-parameter fracture mechanics based on the approximation of the fields by means of the Williams' power series. This paper presents a detailed analysis of the stress field in a wedge-splitting test geometry specimen aimed at the calculation of coefficients of the higher order terms (up to 14) of the Williams' expansion. The numerical study is conducted with the use of a conventional finite element package; however, for processing of the results an over-deterministic method is employed. Special attention is paid to the influence of boundary conditions of the test geometry on the values of the coefficients of the higher order terms of the Williams' series. The results are compared to data from the literature; a strong effect of the boundary conditions is observed.

Introduction and motivation

The characterization of materials which fail in a quasi-brittle manner is rather problematic. Fracture description must necessarily be carried out based on nonlinear fracture models involving the cohesive nature of quasi-brittle crack propagation. Fracture energy and softening parameters are among the most relevant characteristics in this field. However, methods and subsequent evaluation procedures for the determination of fracture parameters suffer from the considerable dependencies of the calculated values of the parameters on the specimen's size and shape and on the boundary conditions of the test, although several improvements have been proposed in recent decades [1], [2]. A possible way to diminish the size/geometry/boundary effect on the fracture characteristics may involve taking the features of the fracture process zone (FPZ – the zone where the material fails, *e.g.* its shape and volume) into account within the method of fracture parameters determination [3].

It has recently been proposed [3] that an estimation of the extent of the FPZ ahead of the tip of a propagating macro-crack in a quasi-brittle material can be performed based on a combination of several approaches to material failure modelling. To obtain a precise description of the stress field in a cracked body what is known as multi-parameter fracture mechanics is employed [4], [5]. This theory is based on the analytical description of the stress and deformation fields in the cracked body by means of their approximation using the Williams' power series [6]. Utilization of the first term or the first two terms of the series is common within the crack stability assessment of structures made of brittle or ductile (mainly metal) materials, see *e.g.* [5], [7]. However, in the case of quasi-brittle materials, a higher number of terms of the power series must be taken into account [3], as the extent of the zone around a crack tip with nonlinear material behaviour is very large in comparison to the typical structural dimensions.

In the paper, a detailed analysis of the stress field in a wedge-splitting test (WST [8], see Fig. 1) specimen is conducted by means of FEM [9]. Particular attention is paid to the influence of the typical variants of the boundary condition of the WST on the values of the higher order terms of the power series as functions of the relative crack length. An over-deterministic method [4] is used for the calculation of the values of the coefficients of the crack-tip stress and displacement fields.

Theoretical background

Description of the stress and displacement fields in a cracked body. Williams' solution for an elastic homogeneous 2D body with a crack [5], [6], [10] provides an approximation of stress and deformation fields by means of their expansion into a power series. For the stress tensor and displacement vector it holds that:

$$\begin{Bmatrix}\sigma_x\\ \sigma_y\\ \tau_{xy}\end{Bmatrix}=\sum_{n=1}^{\infty}\frac{n}{2}r^{\frac{n}{2}-1}A_n\cdot\begin{Bmatrix}\left[2+(-1)^n+\frac{n}{2}\right]\cos\left(\frac{n}{2}-1\right)\theta-\left(\frac{n}{2}-1\right)\cos\left(\frac{n}{2}-3\right)\theta\\ \left[2-(-1)^n-\frac{n}{2}\right]\cos\left(\frac{n}{2}-1\right)\theta+\left(\frac{n}{2}-1\right)\cos\left(\frac{n}{2}-3\right)\theta\\ -\left[(-1)^n-\frac{n}{2}\right]\sin\left(\frac{n}{2}-1\right)\theta+\left(\frac{n}{2}-1\right)\sin\left(\frac{n}{2}-3\right)\theta\end{Bmatrix}, \tag{1}$$

$$\begin{Bmatrix}u\\ v\end{Bmatrix}=\sum_{n=1}^{\infty}\frac{r^{n/2}}{2\mu}A_n\cdot\begin{Bmatrix}\left(\kappa+\frac{n}{2}+(-1)^n\right)\cos\frac{n}{2}\theta-\frac{n}{2}\cos\left(\frac{n}{2}-2\right)\theta\\ \left(\kappa-\frac{n}{2}-(-1)^n\right)\sin\frac{n}{2}\theta+\frac{n}{2}\sin\left(\frac{n}{2}-2\right)\theta\end{Bmatrix}, \tag{2}$$

respectively, where r and θ are polar coordinates centred at the crack tip (considering a crack with traction-free faces lying on the negative x-axis), $\mu = E/(2(1+\nu))$ is the shear modulus and κ equals $(3-\nu)/(1+\nu)$ for plane stress and $(3-4\nu)$ for plane strain; E and ν are Young's modulus and Poisson's ratio. Coefficients A_n are constants for fixed crack length a. Their values change with varying relative crack length $\alpha = a/W$, where W is the specimen's width, and can be expressed as dimensionless functions as follows (for the first five terms of Eq. 1):

$$k(\alpha)=\frac{A_1(\alpha)}{\sigma\sqrt{W}},\quad t(\alpha)=\frac{4A_2(\alpha)}{\sigma},\quad g_3(\alpha)=\frac{A_3(\alpha)}{\sigma}\sqrt{W},\quad g_4(\alpha)=\frac{A_4(\alpha)}{\sigma}W,\quad g_5(\alpha)=\frac{A_5(\alpha)}{\sigma}W^{3/2} \tag{3}$$

where $\sigma = P_{sp}/BW$, BW is the cross-sectional area of the specimen and P_{sp} is the splitting component of the loading force.

The over-deterministic method (ODM). The approach known as the over-deterministic method, which is based on the formulation of linear least-squares [4], has been chosen for the study. This is especially because of its minimal requirements on the FE software (it is not necessary to use any special crack finite elements). The ODM is based on the knowledge of the displacements field near the crack tip (Eq. 2); nodes displacements u and v were obtained from numerical calculations. The coefficients of higher-order terms A_i are then calculated from a system of $2k$ equations, where k is the number of nodes selected around the crack tip. The number of higher-order terms, n, can be chosen arbitrarily, but there are some restrictions and recommendations introduced in [4]. In our case, $n = 14$ was used as it is suitable to ensure sufficiently precise results.

Numerical Study

The study is aimed at investigation of the effects of boundary conditions on both sides of the cube-shaped WST specimen: in the load imposing area, *i.e.* in the groove for the insertion of the steel platens transferring the load from the wedge connected to the testing machine jaw (typically the top part), and in the supported (usually bottom) area. Typical variants of both sorts of boundary conditions published in the literature, *e.g.* [10], [11], were taken into account. In the top part, the loading was considered to be either concentrated (marked in the graphs as CL – concentrated loading) or distributed (DL) on vertical planes of the groove (according to and due to the possibility of comparison with [10]). When modelling the loading as distributed (*i.e.* transferred through the steel platens) an additional variant was considered – not only the splitting component of the loading force (Psp)

but also its vertical component (Psp+Pv) was taken into account. The WST specimen was modelled as being supported by one central support or two supports placed under the centres of gravity of each of its halves. The considered variants, including their dimensions, are sketched in Fig. 1.

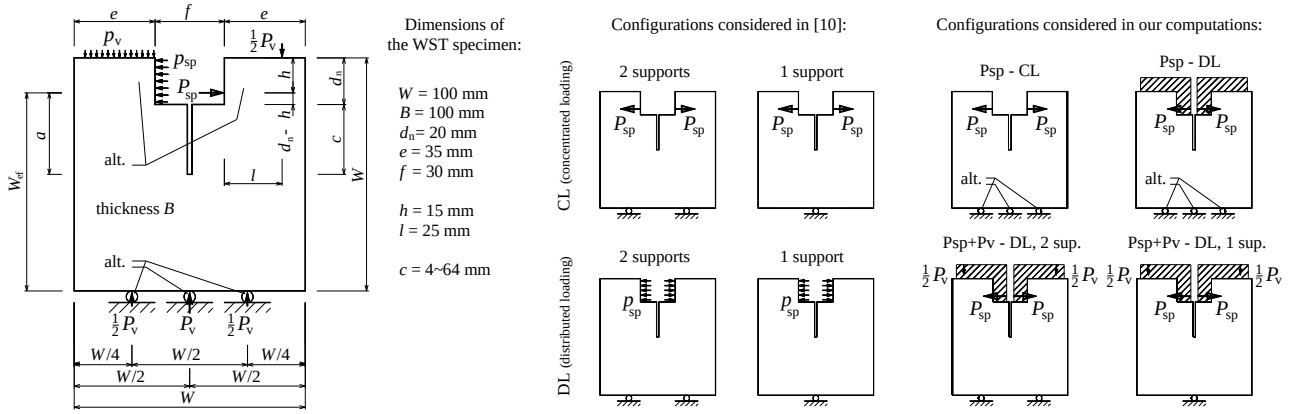


Fig. 1: Cube-shaped WST specimen with the considered variants of boundary conditions

Description of the models. Numerical models were created corresponding to the geometries introduced in Fig. 1. An example of the FE mesh near the crack tip can be seen in Fig. 2. The first row of elements is composed of what is known as crack elements with shifted mid-side nodes. The displacements of the 21 nodes highlighted in Fig. 2b) have been used for determination of the coefficients of the higher-order terms by means of the ODM.

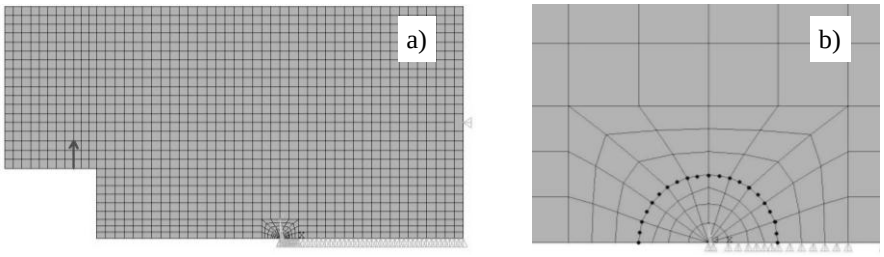


Fig. 2: FE mesh – a) symmetrical half of the specimen with corresponding loading and boundary conditions; b) detail around the crack tip with highlighted nodes used for determination of the A_n coefficients by means of the ODM

Results. As an example of results, the calculated values of the dimensionless coefficients of the first five terms of the Williams' power series for the approximation of stress and deformation fields (defined in Eq 3) are plotted as functions of the relative crack length α in Fig. 3. They can be compared to the corresponding functions published in [10]. The wide range of capabilities of the computational technique employed for the presented analyses is demonstrated here by an additional graph showing the course of function $g_9(\alpha)$, which corresponds to the ninth term of the series.

Discussion and conclusions

From the graphs in Fig. 3 following points are worth noticing: *i)* The utilization of the ODM on the results of common FEM calculations provides as precise an approximation of the stress and displacement fields as special FE formulations, e.g. hybrid crack elements (compare our calculated Psp - CL and Psp - DL curves with the corresponding ones from [10]). *ii)* The boundary conditions in the groove only influence the curves in the area of short cracks, and this up to approximately $\alpha = 0.3$. *iii)* Support variants slightly influence the functions for long cracks; the effect is more pronounced if the compressive component of the loading force is considered. *iv)* Differences between curves with different boundary conditions increase with increasing n.

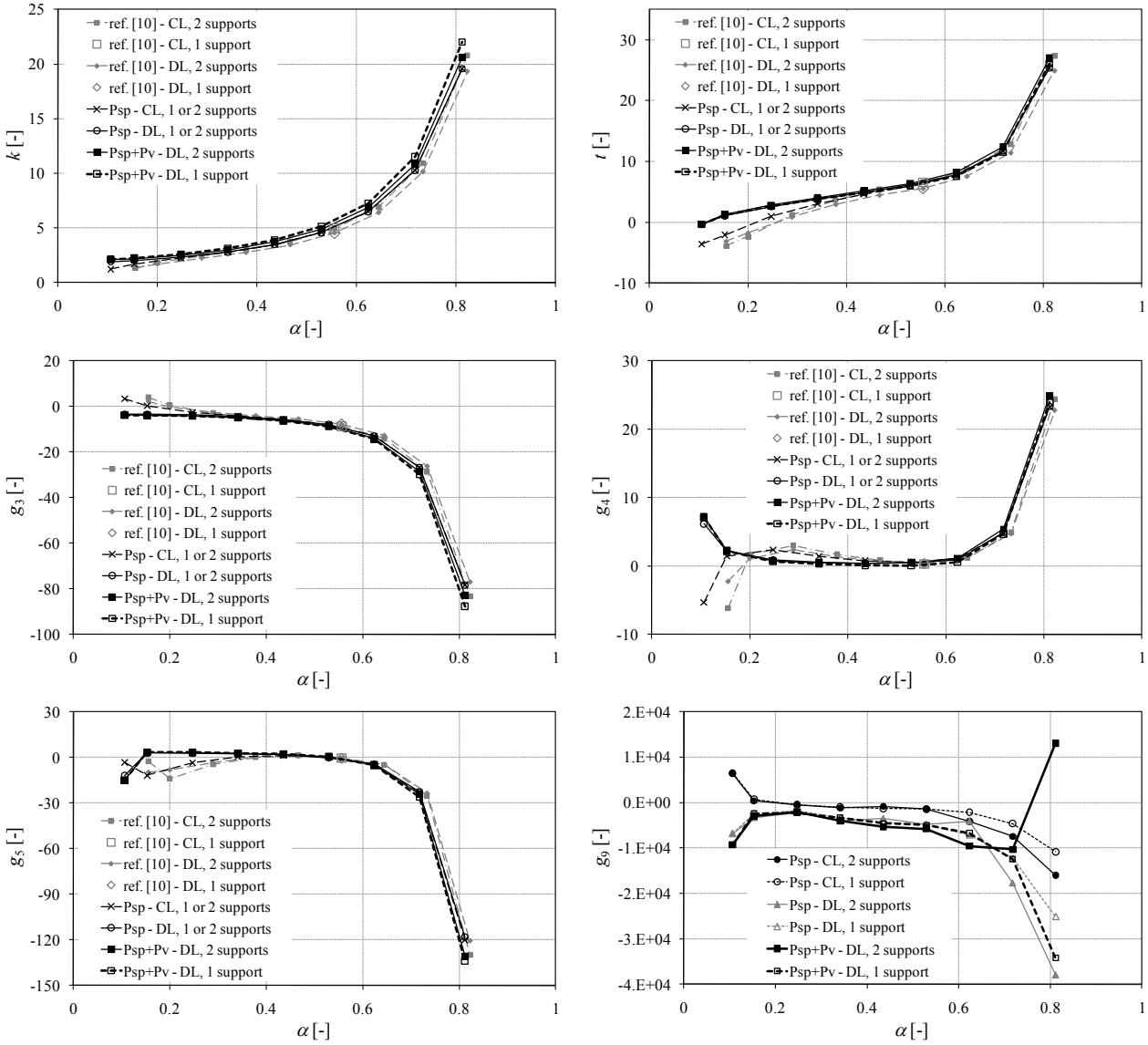


Fig. 3: Comparison of $k(\alpha)$, $t(\alpha)$, $g_3(\alpha)$, $g_4(\alpha)$, $g_5(\alpha)$, and $g_9(\alpha)$ functions for different boundary conditions

Acknowledgement: Financial support from the Ministry of Education, Youth and Sports of the CR (1M0579) and the Czech Science Foundation (P105/11/1551) is gratefully acknowledged.

References

[1] Z.P. Bažant: J Engng Mech (ASCE), 122(2) (1996), p. 138.

[2] K. Duan, X.-Z. Hu, F.H. Wittmann: Engng Fract Mech, 70(16) (2003), p. 2257.

[3] V. Veselý, P. Frantík: Appl Comp Mech, 4 (2010), p. 237.

[4] M.R. Ayatollahi, M. Nejati: Fatigue Fract Engng Mater. Struct, 34 (2011), p. 159.

[5] Z. Knésl, K. Bednář: *Two parameter fracture mechanics: calculation of parameters and their values* (Brno, IPM of the Academy of Sciences of the Czech Republic, 1997).

[6] M.L. Williams: J Appl Mech (ASME), 24 (1957), p. 109.

[7] T.L. Anderson: *Fracture mechanics: Fundamentals and applications* (CRC, Boca Raton 2005).

[8] H.N. Linsbauer, E.K. Tscheg: Zement und Beton, 31 (1986), p. 38.

[9] ANSYS Users manual version 10.0, Swanson Analysis System, Inc., Houston, 2005.

[10] B.L. Karihaloo, H. Abdalla, Q.Z. Xiao: Engng Fract Mech, 70 (2003), p. 2407.

[11] S. Seitl, Z. Knésl, V. Veselý, L. Řoutil: Appl Comp Mech, 3(2) (2009), p. 375.

© (2012) Trans Tech Publications, Switzerland
doi:10.4028/www.scientific.net/KEM.488-489.403

Valuation of TMF Lifetime Calculation Methods and their Limitations of Usability

H. Köberl[1, a], G. Winter[1, b], W.Eichlseder[1, c]

[1]Chair of Mechanical Engineering, Montanuniversität Leoben, Austria

[a]hubert.koeberl@unileoben.ac.at, [b]gerhard.winter@unileoben.ac.at, [c]wilfried.eichlseder@unileoben.ac.at

Keywords: Thermo-mechanical fatigue, Nickel alloys, Lifetime calculation

Abstract. Cyclic loading of metallic engineering components at constant elevated or fluctuating temperature causes a complex evolution of damage which can hardly be described. At the same time the thermal expansion is restricted in some regions, due to the complex geometry of the components. Therefore, mechanical stresses occur and cyclic plastic deformation leads to thermo-mechanical fatigue (TMF) of the material. A careful analysis and comparison of the experimental results, based on a systematical variation of the relevant influence factors, allow to develop empirical models for computing the fatigue life of thermo-mechanical loaded components made of Ni alloys (IN718, Ni200/201). Different lifetime calculation methods were executed and analyzed to fulfil the requirements for the fatigue analysis of components made of these alloys. In addition, the model parameters can be optimized using these results. Based on the parameters, which define the usability of the investigated lifetime models, e.g. temperature, stress, plastic strain, the limiting combination of the parameters can be described. This graphical representation of the "border line" or limiting combination can also be used for any other materials. The results show that the main lifetime calculation models can only applied in a limited range. This limited range is mainly defined by temperature, strain constraining and their combination.

Introduction

Thermo-mechanical fatigue, which induced through cyclic loading by temperature variation along with simultaneous constrained elongation, results in accompanied cyclic loads. This constraint leads to local plastic deformation which affects the fatigue behaviour of the material. Due to the low number of bearable thermo-mechanical cycles and the macroscopic plastic deformation, the thermo-mechanical fatigue takes place in the low cycle fatigue (LCF) region of the S-N curve [1].

In practice, time- and cost-intensive TMF-tests are often characterized by simple isothermal LCF-tests to estimate the lifetime of components under thermo-mechanical loads. Hence this characterization with LCF results in non-conservative lifetime calculation. This happens when, under TMF loading, the cyclic stress-strain behaviour or the effective damage mechanism deviates explicitly from the material behaviour observed under isothermal conditions. Therefore, special focus should be taken on the local and temporally unsteady temperature field acquiring the thermo-mechanical deformation behaviour (stress and strain), to avoid incorrect interpretations. Fundamental investigations of the stress-strain behaviour, as well as, the dominant damage mechanisms under TMF conditions are necessary for a correct lifetime assessment during a thermo-mechanical loading [2].

The cyclic thermo-mechanical deformation behaviour depends on thermally activated dislocation aspects at lower temperatures, cyclic aging processes at mid temperature ranges and diffusion conveyed creep at higher temperatures. Therefore, under both loading modes, IP-TMF (in-phase, i.e. temperature and stress are in-phase) as well as OP-TMF (out-of-phase, i.e. temperature and stress are opposite), the deformation and oxidation effects were predominantly formed in a range at the maximum temperature [3]. For example, under OP-testing conditions, the mechanical strain

works against the thermal strain, which causes a compression at maximum temperature. In comparison, during in-phase tests, the mechanical and thermal strains are cumulative, and thus results a tension at maximum temperature.
To find a correlation between the number of cycles of failure and loading parameters, different damage parameters are available as a function of lifetime [1]. Due to the interplay of strain and stress values under TMF loading, they are able to account for more specific influences as well as their interactions. It is shown in former works of Riedler [2, 4], that energy based criteria are very practical for lifetime approaches. To estimate the lifetime, a damage parameter which is based on the energy (elastic and plastic) of a hysteresis loop, has been developed [5].

Testing conditions

The investigated materials for this research are pure Nickel (Ni200/201) and IN718. Ni200/201 is an annealed cold worked rod and IN718 is forged.
The TMF tests were conducted for all investigated materials on a test rig developed on the Chair of Mechanical Engineering. With this test rig it was possible to allow defined phase shifts between thermal and mechanical strains. The temperature ranges were between 375°C and 525°C for Ni200/201 and 700°C for IN718; whereby the strain constraint values were between 0.75 and 2 for both. Temperatures of LCF and TMF tests were controlled with an induction coil, operated by a RF-generator.

Results

LCF and TMF tests were analyzed according to the Manson-Coffin-Basquin Model (Eq. 1).

$$\varepsilon_{a,t} = \varepsilon_{a,e} + \varepsilon_{a,p} = \frac{\sigma'_f}{E} \cdot (2N_f)^b + \varepsilon'_f \cdot (2N_f)^c \qquad \text{Eq. 1}$$

where $\varepsilon_{a,t}$, $\varepsilon_{a,p}$ and $\varepsilon_{a,e}$ are the total, plastic and elastic strain amplitude respectively; σ'_f is the fatigue strength coefficient; ε'_f is the cyclic ductility coefficient; b is the fatigue strength exponent; c is the cyclic ductility exponent; E is the Young's modulus; and N_f is the number of cycles to failure.

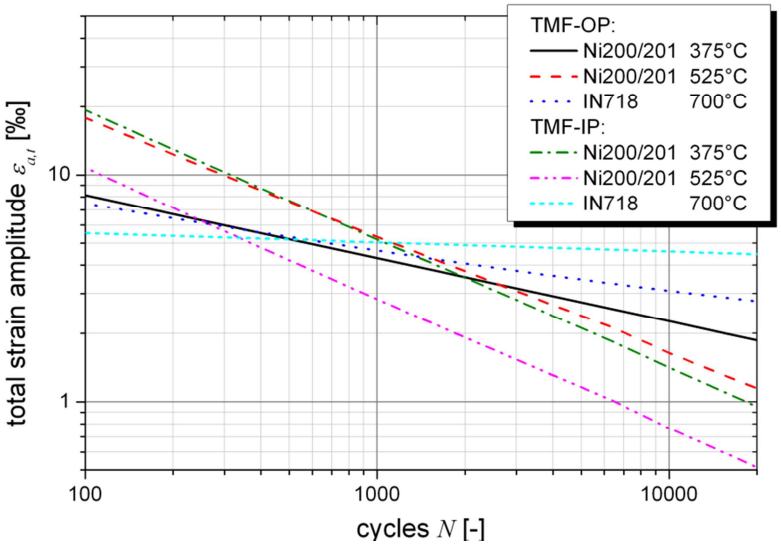


Fig. 1: Comparison of all TMF tests of Ni200/201 and IN718

The TMF behavior of Ni200/201 and IN718 is shown in Fig. 1. The lifetime decreases with an increase in the maximum temperature. Due to the high mechanical strain, resulting from the high thermal strain, the lifetime decreases due to a higher plastic deformation during one cycle. The main

difference can be observed by IP and OP test conditions. For Ni200/201 at 375 °C, the OP test demonstrated creep damage, but at 575 °C from OP to IP conditions, there was a balance between creep, pure fatigue and oxidation damage [5]. IN718 shows in contrast only a small difference at 700°C.

Simulation of the lifetime

The most common empirical model for lifetime estimation is the Manson-Coffin [6, 7] (P_{MC}) criterion, which exists with numerous modifications. Thereby, a lifetime can be calculated by the plastic strain.

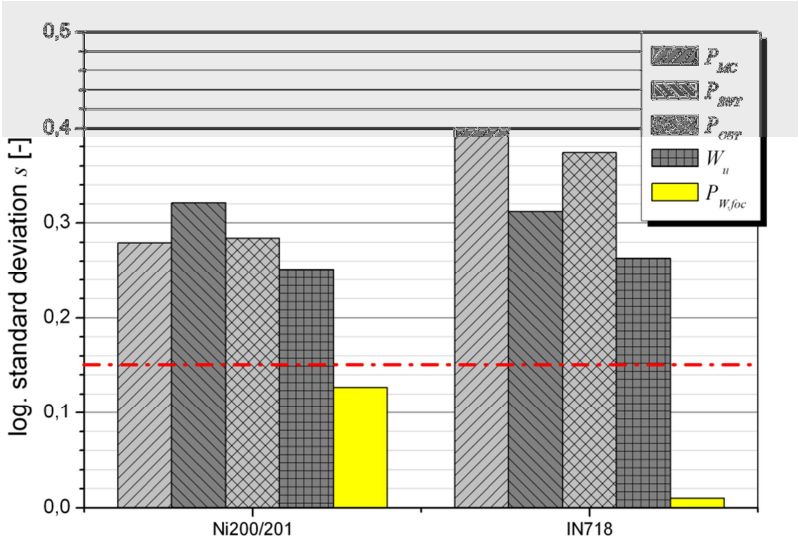


Fig. 2: Comparison of the logarithmic standard deviation

A classical description can be achieved by using the Smith-Watson-Topper [8] damage parameter (P_{SWT}). Ostergren [9] (P_{OST}) assumes a correlation between the lifetime of the material, and the hysteresis energy which is the area of the stress-strain-hysteresis in the tensile domain.

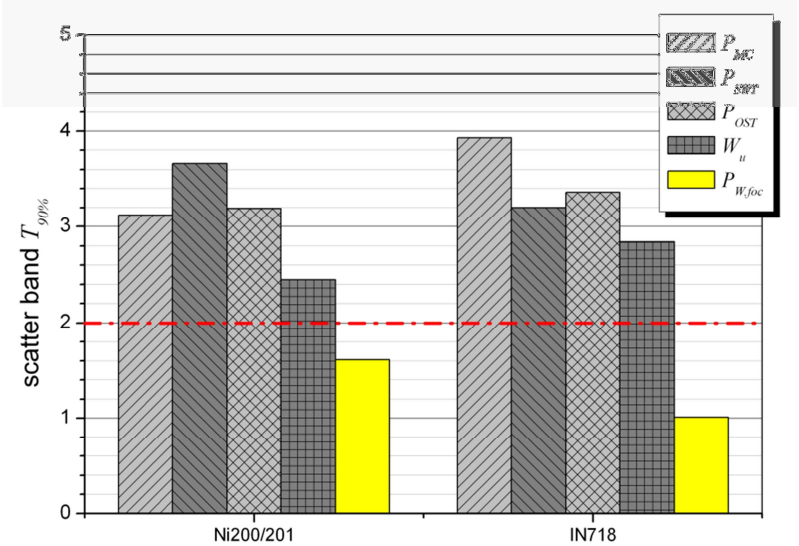


Fig. 3: Comparison of the 90% scatter band

Subsequent investigations of Riedler [4] (W_u) show the possibility of using a common energy criterion, which is the unified energy approach. Based on the consideration that the elastic loading part is affected by the maximum stress; while the plastic part is affected by the stress amplitude, a combined approach is developed in order to simulate the lifetime of out-of-phase TMF loaded materials. Continuative investigations of Köberl [3, 5] ($P_{W,foc}$) (Eq. 2) in different materials (AlSi-

cast-alloys, Cu-alloys, cast irons and nickel alloys) show that a combination of damage parts (pure fatigue, oxidation, creep) like Neu-Sehitoglu [10] and energy based criterion like Riedler gives a lifetime estimation with a very low logarithmic standard deviation and a small 90% scatter band, see Fig. 2 and Fig. 3.
The above pointed overviews are based on both the logarithmic standard deviation s, which is a typical statistic index for Gaussian distribution. The 90% scatter band, which means that the lifetime of 90% of the calculated tests has to be in the range of ±2.5 relative to the test results.

$$P_{W,foc} = \left(\Delta W_e + c_p \cdot \Delta W_p\right)\cdot\left(\xi_f + \xi_{ox}\right) + \left(c_p \cdot \Delta W_p\right)\cdot \xi_c =$$
$$= \left(\varepsilon_{a,e}\cdot\sigma_o + c_p \cdot \varepsilon_{a,p}\cdot\sigma_a\right)\cdot\left(\xi_f + \xi_{ox}\right) + \left(c_p \cdot \varepsilon_{a,p}\cdot\sigma_a\right)\cdot\xi_c \qquad \text{Eq. 2}$$

$\varepsilon_{a,e}$ describes the elastic, $\varepsilon_{a,p}$ is the plastic strain amplitude, c_p is the specific plastic energy parameter, σ_o is maximum stress, σ_a is the stress amplitude and ξ_f, ξ_{ox} and ξ_c are the weighted influence factors of fatigue, oxidation and creep, respectively at NB/2.

Conclusion

An extensive test program was conducted to investigate the influences (creep, oxidation and fatigue) of the selected alloys under TMF loading conditions. Based on the stress-strain loops obtained from the LCF tests at different temperatures, a variety of material models were adopted to describe the cyclic deformation behavior in order to gain the stress and strain values for different loading conditions. This was the basis for a subsequent lifetime calculation. To describe the TMF lifetime different lifetime calculation models were tested. The most models show limitations of their usability when both, OP and IP TMF-tests were used for lifetime calculation. Only $P_{W,foc}$ delivers a good estimation for lifetime under OP and IP-TMF loading for Nickel alloys.

References

[1] H. Köberl, G. Winter, M. Riedler and W. Eichlseder: *Failure mechanism of pure nickel (Ni 200/201) under thermo-mechanical loading.* Key Engineering Materials Vol. 348-349, Trans Tech Publications, Suiss, 2007, pp. 793-796, www.scientific.net.
[2] M. Riedler: *Methodology for the simulation of thermo-mechanically loaded components of engines made from aluminium alloys*. PhD Thesis, University of Leoben 2005.
[3] H. Köberl, G. Winter and W. Eichlseder: *Energy based lifetime calculation for Ni-alloys.* Materials Testing, Vol.51, No. 5, 2009, pp.276-285, www.materialstesting.de.
[4] M. Riedler, R. Minichmayr and W. Eichlseder: *Methods for the thermo-mechanical fatigue simulation based on energy criteria.* Proceedings of the 6th International Conference of Assessment of reliability of materials and structures: problems and solutions, RELMAS 2005, St. Petersburg, 2005 pp. 496-503.
[5] H. Köberl, G. Winter and W. Eichlseder: *Lifetime Calculation of Thermo-Mechanically Loaded Materials (Al, Cu, Ni and Fe Alloys) Based on Empirical Methods.* Journal of ASTM International, Selected Technical Papers STP 1526, Vol. 37, Baltimore 2011,pp. 589-604
[6] S.S. Manson: *Behaviour of materials under conditions of thermal stress.* NACA Report, 1170, 1954.
[7] L.F. Coffin: *A study of the effects of cyclic thermal stresses on a ductile metal.* Trans. ASME, 76, 1954, pp. 931-950.
[8] K.N. Smith, P. Watson and T.H. Topper: *A stress-strain function for the fatigue of metals.* Journal of Materials, Vol. 5(4), 1970, pp. 767-778.
[9] W.J. Ostergren: *A Damage Function and Associated Failure Equations for Predicting Hold Time and Frequency Effects in Elevated Temperature Low Cycle Fatigue.* Journal of Testing and Evaluation, Vol. 4, 327, 1976, pp. 327-339.
[10] R.W. Neu and H. Sehitoglu: Thermo-mechanical fatigue, oxidation and creep, part II: life prediction. Met Trans, 20A, 1989, pp. 1769-1783.

© (2012) Trans Tech Publications, Switzerland
doi:10.4028/www.scientific.net/KEM.488-489.407

Fatigue Crack Growth Simulation in Railway Axles

A. De Iorio[1,a], M. Grasso[1,b], F. Penta[1,c] and G.P. Pucillo[1,d]

[1]University of Naples Federico II, P.le V. Tecchio 80, 80125 Naples, Italy

[a] antonio.deiorio@unina.it, [b] marzio.grasso@unina.it, [c] penta@unina.it, [d] gpucillo@unina.it

Keywords: Railway Components, Fracture Mechanics, Finite Element Method, Damage Tolerance.

Abstract. In order to carry out the railway axle design according to the "Damage Tolerance" philosophy, reliable crack-growth models for these kind of components are necessary. Indeed, damage tolerance principles have received more and more attention from railway technical community, thanks to its ambitious task concerning the inspection intervals prevision of railway components subjected to non-stationary loading conditions. In this paper, a simple routine is exposed that is able to calculate the characteristic parameters of the Linear Elastic Fracture Mechanics (LEFM) for a generic cracked mechanical component. Such parameters are then used in a two parameters propagation law to estimate the necessary time for a crack to become critical.

Introduction

Railway components are usually designed to have an "infinite life. Although this approach could seem safe, mainly when every uncertainty has been conservatively removed by adopting very high safety factors, a number of failures still occurs in service. This is mainly due to both (inevitable) approximations about the hypothetical stress time history that the structural component will experience in service and because component surfaces are not free of flaws.

In the case of railway axles, an alternative approach that would allow of solving the problem, is the one based on the damage tolerance principles. Working in this way, the component is designed to have the residual strength needed to *tolerate* a defect under service loading and in addition it is possible to plan the inspection intervals to retire the unsafe components from the service. However, in order to implement this designing strategy, it is essential that reliable models for the structural behaviour of defected components are available.

In this paper, a numerical procedure for the simulation of the fatigue crack-growth in railway axle is presented. The work deals with the behaviour under rotary bending loads of an initial crack surfacing in the notched region of the axle, where the wheel is shrink-fitted, and having semi-elliptical shape. The numerical routine has been implemented in the ANSYS program and is essentially composed of two parts. The former generates a parametric finite element model of the axle and calculates the mode I stress intensity factor (K_I) distribution on the crack front. The latter corrects the K_I values to take into account the ductile behaviour of the common axle steel, calculates the crack length increments at specific locations along the crack front by means of a fatigue crack growth relationship and, finally, generates the new crack front. The previous two calculation steps are iteratively repeated in the FE environment until the greatest of the calculated K_I values along the crack front reaches the material fracture strength given by the material R-curve as a function of the actual crack length. Numerical results are presented in terms of changes of the crack aspect ratio, α, that is the semi-axes ratio of the elliptical flaw (see Fig. 1), for different values of the initial configuration of the defect. Plasticity-related K_I correction effects on crack shape evolution and on crack growth rates are also investigated.

Geometry and numerical model

The examined geometry is that of a stepped round bar (Fig. 1) whose maximum and minimum diameters are respectively D and d, with a shoulder fillet of radius r. The initial shape of the flaw has been assumed semi-elliptical. Furthermore, the flaw is surfacing in the initial point of the

circular fillet, where the curvature radius abruptly changes, and lies in the cross section of the bar. We choose to analyse this kind of flaw geometry because both numerical and experimental studies [1-6] showed that, in most cases, even if the initial crack front shape is not perfectly semi-elliptical, during the propagation phase its geometry approach to the semi-elliptical one.

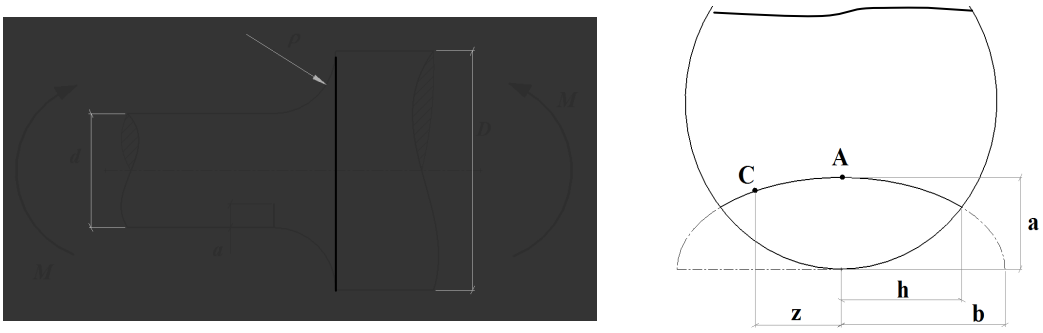


Figure 1 – Stepped round bar under rotary bending.

The geometry of the crack front is shown in Fig. 2: it is defined by its normal semi-axes, a, the aspect ratio, $\alpha = a/b$, and the location of its centre, y_E, with respect to the centre of the bar cross-section. In the present study, we constrain the centre of the ellipse to lie always on the cylindrical surface, namely $y_E = 0$. Each point of the crack front is characterized by its dimensionless distance from the symmetry plane of the bar, $\zeta = z/h$ (see Fig. 1).

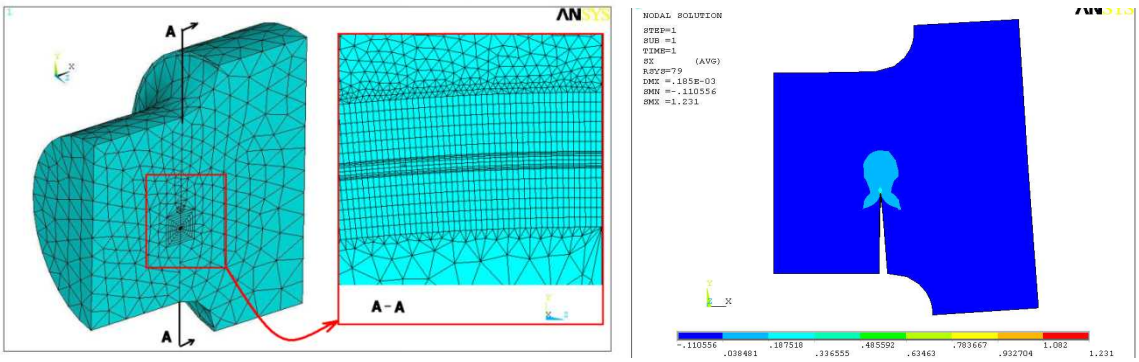


Figure 2 - Crack shape evolution (left) and FE model (right).

For each bar geometry and crack shape, the implemented subroutine gives instructions to the FEM code for building the mesh and solving the elastic problem (see Fig. 2).

The stress intensity factor values were evaluated by means of the force method [7, 8] implemented in an *ad hoc* written routine.

Crack tip plasticity

To investigate about plasticity effects on crack growth rate, a modified value of K_I has been considered during iterations. For a nominal stress range, $\Delta\sigma$, acting on the part of the axle with minimum diameter, and for a generic crack length, the *effective* crack length is obtained by adding the plastic radius to the *local* crack length (Eq. 1):

$$\Delta K_A = \Delta\sigma \cdot \overline{K}_I(A) \cdot \sqrt{a_A + r_p(A)}\,/\sigma_M, \qquad \Delta K_C = \Delta\sigma \cdot \overline{K}_I(C) \cdot \sqrt{a_C + r_p(C)}\,/\sigma_M, \tag{1}$$

were A and C are the points on the crack front at $\zeta = 0$ and $\zeta = 1$, respectively.

Many formulas have been proposed to take into account crack tip plasticity [10, 11] by means of a plastic radius, r_p, and each of them can be put in the subroutine. Due to its simplicity, however, we have chosen the Irwin's plastic zone correction.

Crack growth simulation results

Crack growth rate can be calculated by means of any phenomenological propagation law, using the ΔK_I values calculated in the first step. Due to its simplicity, we utilize a two parameters equation, namely the Paris law. The Paris law is written for points A and C, in terms of the corrected K_I, and the new position of points A and C are calculated with a vector perpendicular to the crack front, in these points, having modulus (see also Fig. 3):

$$\Delta a = C \cdot \Delta N \cdot (\Delta K_A)^m ; \qquad \Delta c = C \cdot \Delta N \cdot (\Delta K_C)^m \ .$$

Because SIF distribution is a function of θ, the angular position of the bending moment with respect to the horizontal semi-axes of the ellipse, b, it has been necessary to evaluate, for points A and B, the maximum ΔK in a full revolution of the bar around its axes (Fig. 3). Their values were calculated by a linear combination of $K_{I,\,0}$ and $K_{I,\,\pi/2}$, that are the SIF values calculated for $\theta = 0$ and $\theta = \pi/2$, respectively:

$$K\,(A) = \Delta\sigma/\sigma_M \cdot [\, K_{I,\,0}\,(\mathrm{A}) \cdot \cos\theta + K_{I,\,\pi/2}\,(\mathrm{A}) \cdot \sin\theta\,];$$

$$K\,(B) = \Delta\sigma/\sigma_M \cdot [\, K_{I,\,0}\,(\mathrm{B}) \cdot \cos\theta + K_{I,\,\pi/2}\,(\mathrm{B}) \cdot \sin\theta\,].$$

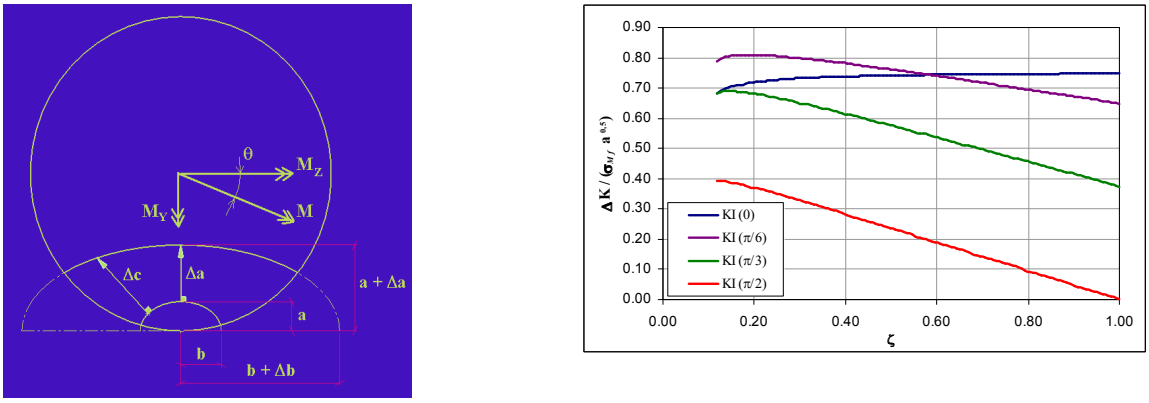


Figure 3 - Dimensionless K_I distribution along the crack front for different angular positions, θ, of the bending moment ($\xi = 0.2$; $\alpha = 0.3$).

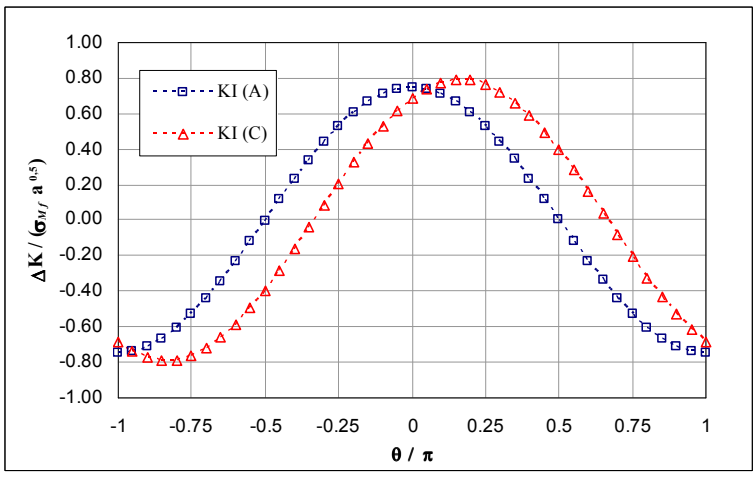


Figure 4 - Dimensionless K_I distribution vs. θ for points A and C ($\xi = 0.2$; $\alpha = 0.3$).

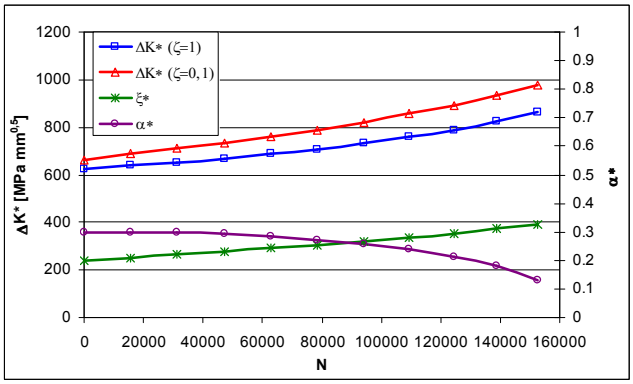


Figure 5 - ΔK_I evolution for points A and C and crack shape evolution vs. cycle number ($\xi = 0.2$; $\alpha = 0.3$).

Fig. 3 shows the results in terms of dimensionless $\frac{K_I}{\sigma_M \cdot \sqrt{\pi a}}$ distribution along the crack front for different values of θ, were σ_M is the nominal maximum bending stress in the minimum cross section.

In Fig. 4, dimensionless SIF vs. θ is shown for points A and B. Crack growth results are summarized in Fig. 5, where for a specified initial flow ($\xi_0 = 0.2$; $\alpha_0 = 0.3$) crack shape evolution is shown as a function of the applied number of load cycles.

Conclusions

A numerical practice for the structural analysis of railway axles has been defined; it is based on assumptions extensively verified by experimentation carried out until now on notched components having a geometry similar to that of the axle and subjected to the same loading conditions as the axle. Besides that, the practice is able to take into account both different propagation conditions arising as consequence of the material crack propagation properties, the ductility of this latter and, finally, the particular loading conditions to which the crack front is subjected due to the rotating bending acting on the axle.

References

[1] A. Carpinteri: Int. J. Fatigue Vol. 15 N. 1 (1993), pp. 21-26.

[2] A. Carpinteri and R. Brighenti: Int. J. Fatigue Vol. 18 N. 1 (1996), pp. 33-39.

[3] A. Carpinteri, R. Brighenti and S. Vantadori: Int. J. Fatigue Vol. 28 N. 3 (2006), pp. 251-260.

[4] A. Carpinteri, R. Brighenti and A. Spagnoli: Int. J. Fatigue Vol. 22 N. 1 (2000), pp. 1-9.

[5] X.B. Lin and R.A. Smith: Eng. Fract. Mech. Vol. 63 (1999), pp. 503-522.

[6] X.B. Lin and R.A. Smith: Eng. Fract. Mech. Vol. 63 (1999), pp. 523-540.

[7] I.S. Raju and J.C Newman, Jr.: NASA TM X-72825 (1977).

[8] I.S. Raju and J.C Newman, Jr.: NASA TN D-8414 (1977).

[9] A.B. de Morais: Eng. Fract. Mech. Vol. 74 (2007), pp. 739-750.

[10] Irwin, G.R., in: Handbuch der Physik VI, Flugge Ed., Springer (1958), pp. 551-590.

[11] Dugdale, D.S.: J. Mech. Phys. Sol., Vol 8 (1960), pp. 100-108.

© (2012) Trans Tech Publications, Switzerland
doi:10.4028/www.scientific.net/KEM.488-489.411

Effect on the Alkali-Activator Mixing Ratio of Geopolymer Mortar using Bottom Ash

Si-Hwan Kim [a] , Gum-Sung Ryu [b], Kyung-Taek Koh [c],

Su-Tae Kang [d], Jang-Hwa Lee [e]

[a-e]Structural Material Research Division, Korea Institute of Construction Technology , 2311 Daehwa-Dong, Ilsanseo-Gu, Goyang-Si Gyeonggi-Do, 411-712 Republic of Korea

[a]shkim@kict.re.kr, [b]ryu0505@kict.re.kr, [c]ktgo@kict.re.kr, [d]alphard@kict.re.kr, [e]jhlee@kict.re.kr

Keywords: bottom ash, alkali-activator, geopolymer mortar.

Abstract : This Study purposed to review on the strength of geopolymer mortar and the change in liquidity depending on the mixing ratio of alkali-activator in developing the geopolymer mortar using bottom ash as binder. Alkali-activator was used through mixing 9M-Sodium hydroxide (SH) and 3 kinds of Sodium sillicate(SS) and its strength was measured by material age after curing for 48 hours at 60°C. As a result, the pressure strength was shown as 40MP when the mass ratios of 9M-Sodium hydroxide and 3 kinds of Sodium sillicate were35 vs. 65 and 50 vs. 50, but the solution of the mass ratio of 50 vs. 50 showed the rapid solid phenomenon in the process of mortar manufacturing, thereby disadvantage in construction. In addition, in case of storing the mixed solution in room temperature, as the mix ratio of 9M-Sodium hydroxide increases, the solution solidified. Accordingly, when considering on strength, liquidity and storage, it's most preferable to fix the mass ratio of 9M-Sodium hydroxide and 3 kinds of Sodium sillicate at 35 vs. 65.

Introduction

Cement are comprehensively been using as the structural materials for construction including road, bridge and building. Especially, as the industrial structure has been advanced since 20th, the construction technique has been developed, so the cement has increased hugely in use amount and has developed in use technique by many researchers. Even though it has played the most roles of construction materials, it's recognized to deconstruct nature due to the huge amount of CO2 produced in time of manufacturing cement [1, 3]. On the other hand, the issue in terms of global warming has been recognized as a worldwide common challenge and the developed nations in the world are seeking a method to reduce emissions by 50% by 2050 compared to the present.

Table 1. Generation Amount of Coal Ash in Korea

	Generation Amount of Coal Ash	Fly ash	Bottm ash
2006	6037	4830	1207
2007	6247	4998	1249
2008	7870	6296	1574
2009	7300	5840	1460
2010	8348	6678	1670

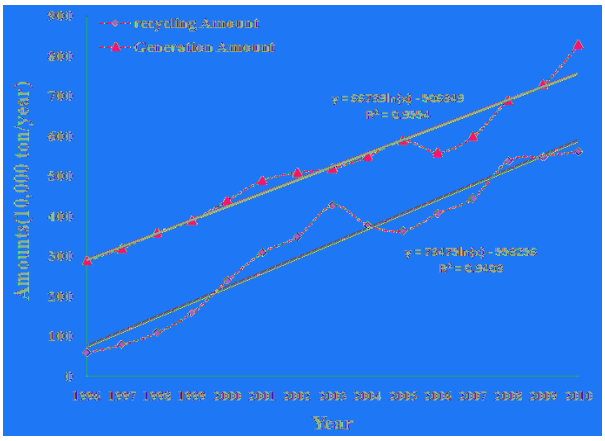


Figure 1. Generation and Recycling Amount of Coal Ash in Korea

Accordingly, each industry sector is taking effort to reduce the greenhouse gas emissions and furthermore the cement sector is seeking a way to reduce the use of cement to show a vast amount of CO2 emissions through developing alkali-activator geopolymer mortar using industrial by-products. Ash is largely used as binder in manufacturing alkali-activator geopolymer mortar and can be divided into two kinds: fly ash and bottom ash. In Korea, the ash production continued to increase up to 7.3 million tons in 2010: around 50-60% of that is recycled as concrete materials and the remaining 40% or more is buried in the neighboring landfill. Fly ash is mostly consumed as cememt raw materials and concrete admixture, but bottom ash, around 15-25% of ash production, is mostly buried, resulting in the economic loss caused by huge treatment cost and impeding the efficient use of land because of increased landfills [4]. From the background, this Study examined the strength, liquidity and storage of geopolymer mortar depending on the mixing ratio of alkali-activator in developing geopolymer mortar using fully the bottom ash produced in thermal power plant as cement substitutes.

Mix proportion and test methods

Table 2 shows the characteristics of binders used in this Study and each used ash was picked at a thermal power plant in Hadong-gun Korea simultaneously at the same day. In terms of main component and physical characteristics of bottom ash, SiO_2 and Al_2O_3 were shown almost similar compared to fly ash, which has widely been used as giopolymer binder, while the loss on ignition (LOI) lower compared to fly ash. The source sample of bottom ash showed alkali-activator reflection because its fineness was smaller than fly ash's, but was shown disadvantageous, so the fineness needs to be improved through mechanical grinding process. This Study used the sample after improving the fineness at 4061㎠/g through ball mill treatment for one hour and half, minimizing the factor decreasing the strength according to material characteristics.

Table 3, a mixing table for specimen production, sets the SH vs. SS variables as 5 kinds. SiO_2 (99%) from Australia was used as fine aggregate used at the mixing and Sodium hydroxide and Sodium sillicate were used after being stabilized through producing at least one day ahead. The mixing was conducted through dry mixing for 3 minutes at the speed of 30~40rpm after putting bottom ash and fine aggregate into a 10-liter mixer and then bottom ash mortar was produced through mixing for 4 minutes at the speed of 70~80rpm after pouring alkali-activator manufactured in advance. In order to measure the liquidity of the manufactured bottom ash mortar, flow was measured according to KS L 5105 and the compressive strength was measured at the 3, 7, 14 and 28-day age of material after manufacturing the specimen with 50x50x50 cubic mold, curing at oven at 60℃ for 48 hours and making it removed.

Table 2. Component analysis according to kinds of ash

Types \ Items	Chemical component ratio (%)					Density (g/㎤)	Fineness (㎠/g)
	SiO_2	Al_2O_3	Fe_2O_3	Na_2O	L.O.I		
Bottom Ash (source sample)	57.7	23.6	9.36	0.82	0.01	2.39	1642
Bottom Ash (ball mill treatment)	58.3	22.4	8.8	0.7	0.04	2.51	4061
Fly Ash	57.5	24.6	5.26	0.38	2.5	2.08	3669

Table 3. Test variables and mixing table (unit : g)

Sand	Bottom Ash	Activator	SH:SS	Liquid/binder	Curing condition
2,400	1,600	880	Variables*	0.55	Oven, 60°C, 48hr

* 80:20, 35:65, 50:50, 65:35, 20:80

Additionally, in order to identify the characteristics with regard to both the mixing of Sodium hydroxide and Sodium sillicate in advance and the mixing of them at the test day, this Study compared and analyzed them through manufacturing the mortar according to a standard of SH : SS = 50 : 50.

Experimental results and Discussions

Figure 2 shows the results of liquidity measurement prior to cure after manufacturing mortar with the alkali-activator manufactured in advance at the mixing ratio of 80:20 (Na_2O/SiO_2=0.30), 65:35 (Na_2O/SiO_2=0.58), 50:50 (Na_2O/SiO_2=0.93), 35:65 (Na_2O/SiO_2=1.36) and 20:80 (Na_2O/SiO_2=1.92) in terms of NaOH (sodium hydroxide, SH) and $Na_2O{\cdot}3SiO_2$ (sodium silicate, SS) in order to analyze the effect which the mixing ratio of alkali-activator had on liquidity. The most advantageous mixing ratio in liquidity was shown at 50: 50 and 35: 65 and in terms of sodium silicate, because it's high in cohesion, the increased mixing ratio resulted in the decreased liquidity. The more the mixing ratio of sodium hydroxide increase, the lower the proportion of Na_2O/SiO_2 , and the liquid of the mixing showed the condensation even at higher temperature, so it's judged that the change of properties had an effect on the liquidity. In addition, according to the observation of hardening after one hour at high temperature over each mortar enclosed with plastic bag, the mortar of the mixing ratio of 35: 65 and 20: 80 was showing the liquidity without hardening. The mortar using the other ratios hardened between 20 minutes and one hour, not securing the liquidity and workability.

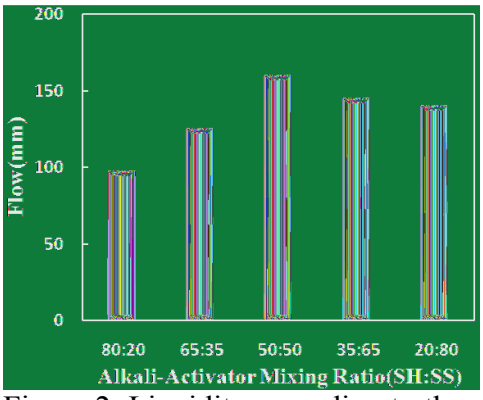


Figure 2. Liquidity according to the mixing ratio of alkali-activator

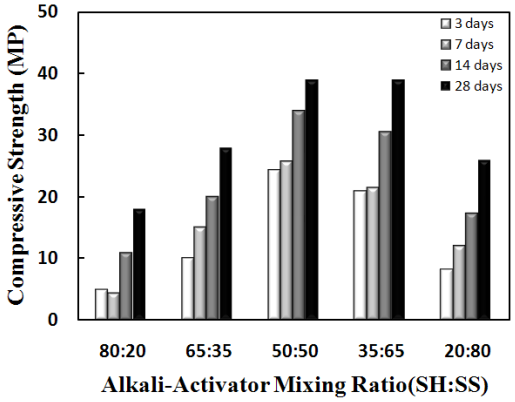


Figure 3. Compressive strength according to the mixing ratio of alkali-activator

Bottom ash mortar showed strength development through a hardening process by polymerization in the high alkali condition. This polymerization is a chemical reaction composing Si-O-Al-O combination through chemical reaction by Si-Al mineral in the high alkali condition, and sodium slicate forms a high alkali condition after producing NaOH through recating with water, promoting the polymerization. Figure 3 shows the age-specific compressive strength according to the mixing ratio of alkali-activator. The specimen for measuring the compressive strength was measured after conducting high cure for 48 hours in dry condition at 60℃ after mold formation. The better strength develpment was produced at the alkali-activator mixing ratio of 50: 50 and 35: 65, expressing the compressive strength of 40MP. It's judged to increase Si and Na component besides Si and Al components within bottom ash and induce the polymerization, so the strength was improved.

However, the more the sodium hydroxide, the less the Si component, and the more the sodium sillicate, the less the Na ion, which is disadvantageous in activating the polymerization and results in the strength degradation.

In addition, NaOH changes to Na_2O and H_2O through the mixing of Sodium hydroxide and Sodium sillicate and the stabilization process, and change the Na_2O/SiO_2 ratio of sodium sillicate. As a result of test, when the ratio of Na_2O/SiO_2 was 1.36, condensation occured in time of liquid storage and the properties changed, which resulted in the strength degradation.

Figure 4 shows the examination resules on effects according to the manufacturing time of alkali-activator and as seen at (a) and (b), unless alkali-activator was not stabilized through being manufactured in advance, it showed the hardening phenomenon before mold formation through reacting quickly with bottom ach [2].



(a)Individual input (b) Input after manufacturing in advance

Figure 4. Effects according to the manufacturing time of alkali-activator

Conclusions

Considering the analysis results on effects according to the mixing ratio of alkali-activator in manufacturing geopolymer mortar using bottom ash, the industrial by-product, the mixing ratio of 50: 50 and 35: 65 was shown to be most advantageous in terms of liquidity and strength. In case of 50: 50, however, liquid showed a condensation phenomenon in storing the alkali-activator and the properties changed. Accordingly, it's judged that the alkali-activator mixing ratio of 35: 65 would be most desirable in the comprehensive aspect.

Acknowledgements

This work presented in this paper was founded Korea Inst. Const. Tech. (KICT) via the Project 'Development of Technology for High Volume Bottom Ash Concrete to Reduce CO_2 Emission.

References

[1] Y.H. Oh et al., in: Synthesis of zeolite A from coal fly ash and adsorption characteristics of synthetic zeolite for ammonium ion, J. Korea Solid Wastes Eng. Soc. Vol.17, No.1, 2000.

[2] D. Hardjito and B.V. Rangan, in: Development and Properties of Low-Calcium Fly Ash-based Geopolymer Concrete, Research Rep. CC-1, Faculty of Eng., Curtin Univ. of Technology, 2005.

[3] B.W. Jo et al, in: Strength Development and Hardening Mechanism of Alkali Activated Fly Ash Mortar, J. of the Korea Concrete Institute, Vol. 18, No. 4, pp. 449~458, 2006.

[4] H.J. kim et al., in: Effect alkaline activator and curing condition on the compressive strength of cementless fly ash based alksli-activated mortar, J. of Korea inst. Res. Rec. Vol.18, No.2, 2009.

[5] H.Xu et al, in: Synthesis of thermostable geopolymer from circulating fluidized bed combustion (CFBC) bottom ashes, Journal of Hazardous Materials, vol.175, pp.198~204, 2010.

© (2012) Trans Tech Publications, Switzerland
doi:10.4028/www.scientific.net/KEM.488-489.416

Crack propagation from bi-material notches – matched asymptotic procedure

J. Klusák[1,a], T. Profant[2,b], O. Ševeček[2,c] and M. Kotoul[2,d]

[1]Institute of Physics of Materials, Žižkova 22, Brno, Czech Republic

[2]Faculty of Mechanical Engineering, BUT, Technická 2, Brno, Czech Republic

[a]klusak@ipm.cz, [b]profant@fme.vutbr.cz, [c]sevecek@fme.vutbr.cz, [d]kotoul@fme.vutbr.cz

Keywords: Orthotropic bi-material notch, two-state integral, Ψ-integral, matched asymptotic expansion, Betti's reciprocity theorem.

Abstract. The methods based on the properties of the two-state integrals allow one to calculate the amplitude of singular and the other terms of the Williams' asymptotic expansion. The paper is focused on the use of the Ψ-integral, whose application is conditioned by the knowledge of the so-called auxiliary solution of the solved problem. On the other hand, the Ψ-integral can be applied to the analysis of the problems with various geometries, e.g. the analysis of the bi-material notches. The application of the Ψ-integral can be also extended to the matched asymptotic procedure, which allows one to predict the behavior of the cracked notches or following crack growth near the bi-material interfaces.

Introduction

The method of Ψ-integral enables to determine the local stress field parameters in the vicinity of the crack or notch tip using the deformation and the stress field in the remote points, where the numerical results obtained e.g. using the finite element analysis are more accurate. This method is an implication of the Betti's reciprocity theorem, which states in the absence of the body forces and residual stresses the following integral is path independent

$$\Psi(\underline{u},\hat{\underline{u}}) = \int_{\Gamma} \left[\sigma_{ij}(\underline{u}) n_i \hat{u}_j - \sigma_{ij}(\hat{\underline{u}}) n_i u_j\right] ds, \tag{1}$$

where Γ is any contour surrounding the crack tip and $\underline{u}$, $\hat{\underline{u}}$ are two admissible displacement fields. The asymptotic expansion of the displacements $\underline{u}(r,\theta)$ for the bi-material notch at its tip is possible to write in the following form

$$\underline{u}^0(r,\theta) = H_1 r^{\delta_1} \underline{u}_1(\theta) + H_2 r^{\delta_2} \underline{u}_2(\theta) + \ldots, \tag{2}$$

where H_1 and H_2 are the generalized stress intensity factors (GSIFs), $\underline{u}_1$ and $\underline{u}_2$ are the angular distribution of the displacements corresponding to the singular terms in the stress asymptotic expansion. The application of the two-state integrals requires the knowledge of the so-called auxiliary solution $\hat{\underline{u}}$ in the form of eigenfunctions of the appropriate singular problem. The Stroh or Lekhnitskii formalisms provide the effective tools evaluating these eigenfunction for the case of the anisotropic, especially orthotropic bi-material notches [1], [2]. Considering the auxiliary solution $\hat{\underline{u}}$ in the form $\hat{\underline{u}}(r,\theta) = r^{-\delta_i} \underline{u}_{-i}(\theta)$ for $i = 1, 2$, one gets the relation allowing the H_1 and H_2 evaluation

$$\Psi\left(\underline{u}^h, r^{-\delta_i} \underline{u}_{-i}(\theta)\right) = H_i \Psi\left(r^{\delta_i} \underline{u}_i(\theta), r^{-\delta_i} \underline{u}_{-i}(\theta)\right), \tag{3}$$

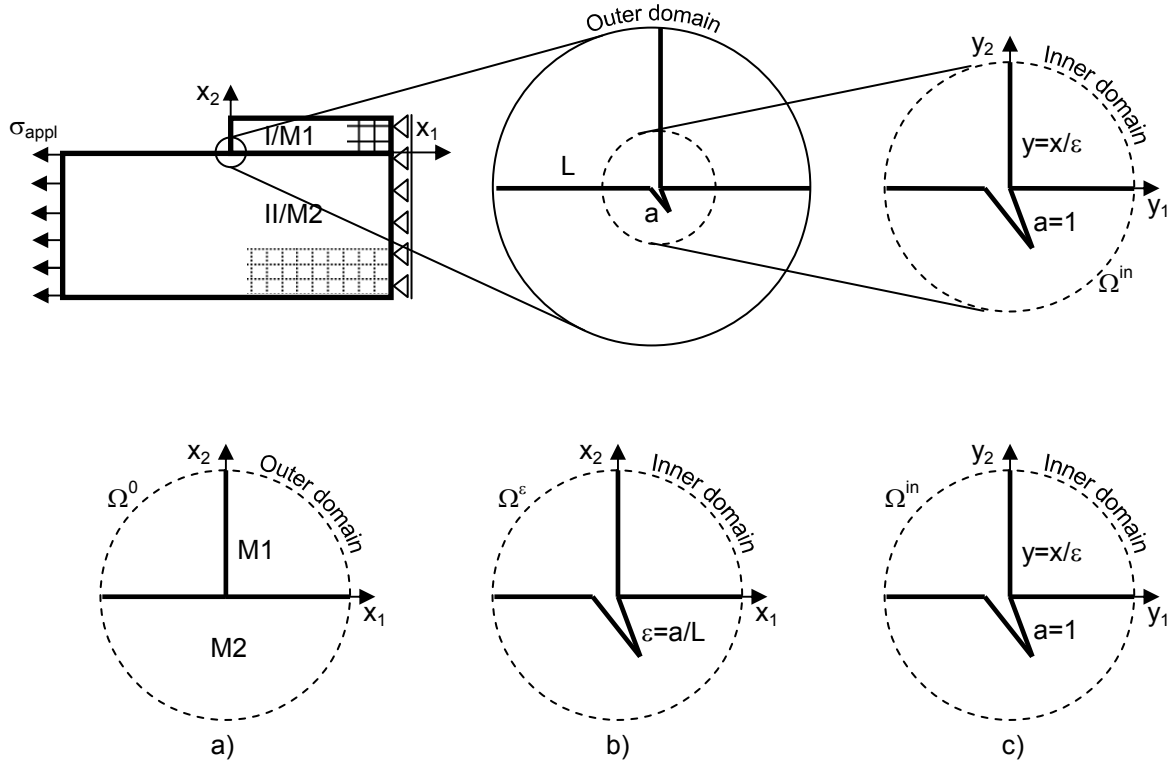


Figure 1: Outer and inner domain used in matched asymptotic analysis, zoomed-in view of notch neighbourhood perturbed by an initial crack increment. a) – c) coordinate system of the outer and inner domain

where the integrals on the right hand side are calculated along the path Γ_1 surrounding the crack tip with diameter r_1 approaching zero. Because of the path independence of the integrals, the left hand side integral can be computed along the path Γ_2, which is any remote integration path with diameter r_2. The $\underline{u}^h$ is a finite element approximation for the exact solution $\underline{u}$ along the path Γ_2.

Matched asymptotic procedure

Matched asymptotic procedure can be used to derive the change of potential energy and energy release rate (ERR) for the cracked bi-material notch, [2],

$$G = -\frac{1}{2\varepsilon L}\Psi\left(\underline{u}^{\varepsilon}, \underline{u}^{0}\right) = -\frac{1}{2\varepsilon L}\left[H_1^2\varepsilon^{2\delta_1}K_1 + H_1H_2\varepsilon^{\delta_1+\delta_2}\left(K_2 + K_1'\right) + H_2^2\varepsilon^{2\delta_2}K_2'\right], \tag{4}$$

where the exponents δ_i are real and $\underline{u}^{\varepsilon}$ corresponds to the perturbed state of the notch with the additional coefficients of the Williams asymptotic expansion

$$K_i = \Psi\left(\underline{u}_1^h, \rho^{\delta_i}\underline{u}_i\right), \quad K_i' = \Psi\left(\underline{u}_2^h, \rho^{\delta_i}\underline{u}_i\right). \tag{5}$$

The integrals K_i and K_i', respectively, are calculated on the perturbed scaled-up domain Ω^{in}, see Fig. 1, with the prescribed boundary conditions $u\big|_{\partial\Omega^{in}} = \rho^{\delta_1}\underline{u}_1(\theta)$ and $u\big|_{\partial\Omega^{in}} = \rho^{\delta_2}\underline{u}_2(\theta)$, respectively. The scale-up factor of the domain is given by the ratio $\varepsilon = a/L$, where a is the length of the crack perturbing the notch tip and L the characteristic dimension of the notch. The $\underline{u}_1^h$ and $\underline{u}_2^h$,

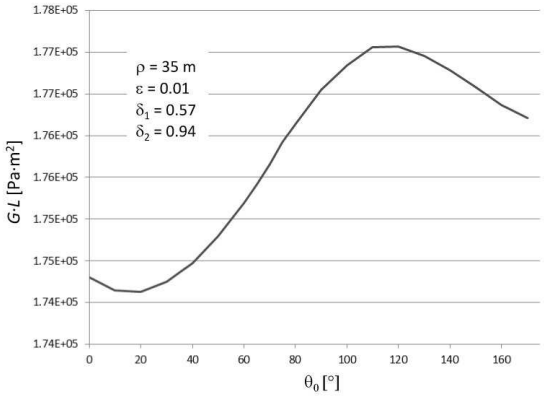


Figure 2: The product of the ERR and characteristic length of the outer domain L as a function of the perturbed crack inclination with respect to x_1-axis in material M2.

respectively, are the finite approximations to the first and second basis functions of Eq. 2 calculated along the remote integration path in the scaled-up coordinate system $(\rho,\theta) \equiv (r/\varepsilon,\theta)$.

Crack initiation direction

The stress field around a bi-material notch inherently covers combined normal and shear modes of loading. For mixed mode fields a crack may grow along the interface or at a certain angle θ_0 with the interface into one material of the notch. Following the procedure given in [3] it can be proposed that the crack is initiated in the direction θ_0 where the ERR in Eq. 4 has its maximum and reaches a critical value. To find the maximum of G and consequently the crack initiation direction in materials of the notch, following conditions have to be determined

$$\left.\frac{\partial G}{\partial \theta}\right|_{\theta=\theta_0} = 0, \quad \left.\frac{\partial^2 G}{\partial \theta^2}\right|_{\theta=\theta_0} < 0 \,. \tag{6}$$

The direction of potential crack initiation determined from Eq. 6 can exist in both materials of the notch. If there are more than one direction of possible crack initiation, it is necessary to consider all of them. The direction θ_0 enters to a stability criterion, and thus it is the necessary step in the reliable assessment of general singular stress concentrations.

Threshold values of generalized stress intensity factors

The threshold values of GSIFs used in stability criterion of the bi-material notches define the loading conditions above that a fatigue crack is initiated in the tip of the singular stress concentrator. In further it is assumed the cyclic loading with the minimum stress $\sigma_{min} = 0$. Thus the range of the (generalized) stress intensity factor corresponds to the values under maximum loading ($\Delta K = K_{max}$, $\Delta H = H_{max}$). Note that the subscript (max) is then omitted. To find the relation between the GSIFs and their critical values, consider the fact that the ratio of the values H_1 and H_2 is constant for a given bi-material configuration and boundary conditions and does not depend on the absolute value of the applied stress

$$\Gamma_{21} = \frac{H_2}{H_1} = \frac{H_{2th}}{H_{1th}} \,. \tag{7}$$

This assumption is justified because when changing the value of the applied stress, only the absolute values of GSIFs change, but their ratio is constant even for the threshold values H_{ith}. From the suggestion of the same mechanism of rupture and consequently the same value of ERR corresponding to threshold conditions in the case of a bi-material notch and a crack, one can determine the threshold value H_{1th}. Assuming crack growth to proceed straightforwards, the threshold value of the ERR of the crack in homogeneous orthotropic media can be defined as, [5,6]

$$G_{Ith} = \frac{K_{Ith}^2}{2L_{22}} \,, \tag{8}$$

where L_{22} is component of the Barnett-Lothe tensor, [6]. Considering the ERRs for the cases of the perturbed bi-material notch and the crack under the threshold condition $G = G_{Ith}$, the threshold value of GSIF is given from comparing relations Eq. 8 and Eq. 4

$$H_{1th} = K_{Ith}\left[\frac{-2\varepsilon L}{2L_{22}\left(\varepsilon^{2\delta_1}K_1 + \Gamma_{21}\varepsilon^{\delta_1+\delta_2}\left(K_2 + K_1'\right) + \Gamma_{21}^2\varepsilon^{2\delta_2}K'\right)}\right]^{\frac{1}{2}}, \tag{9}$$

where K_{Ith} is the threshold value of the studied material. Threshold value K_{Ith} is a material characteristic and is gained for the directions θ_0 of assumed crack initiation, [7]. The direction θ_0 in the case of a bi-material notch can be ascertained from criterion of maximum tangential stress, see [2, 3, 4]. Because of that fact the normal loading mode is predominant. Thus the comparison with crack propagation characterized by the threshold value K_{Ith} is justified.

Numerical example

As an example, the values of the input parameters for the matched asymptotic procedure and ERR as a function of the perturbed crack inclination are presented. For the rectangular bi-material orthotropic notch characterized by angles $\omega_1 = 90°$ and $\omega_2 = 180°$, thicknesses of the domain *I* and *II* as 4 and 25 [mm], respectively, under the remote loading $\sigma_{11} = 100$ [MPa], see Fig. 1, it is considered the bi-material with the Young's modulus $(E_1)_I = 100$, $(E_2)_I = 50$, $(E_1)_{II} = 400$, $(E_2)_{II} = 50$ [MPa]. The corresponding eigenvalues of the singularity are $\delta_1 = 0.57$ and $\delta_2 = 0.94$ and GSIFs $H_1 = 0.73$ [MPa.m$^{1-\delta_1}$] and $H_2 = 31.47$ [MPa.m$^{1-\delta_2}$]. There are given the values of the additional coefficients of the Williams's asymptotic expansion $\underline{u}^{\varepsilon}$ corresponding to the perturbed state of the notch in Table 1. Its numerical evaluation requires delicate handling because of the appearance of its integration path independence even some distance from the notch tip $\rho = r/\varepsilon$. The ERR as a function of the of the perturbed crack inclination with respect to x_1-axis in material M2 is given in Fig. 2.

Table 1: Additional coefficients of the Williams asymptotic expansion for several values of integration path radius

ρ	51.484	36.004	20.431
$K1$	-3.29E-10	-4.51E-10	-6.86E-10
$K2$	8.79E-10	9.95E-10	1.21E-09
$K'1$	-4.87E-08	-3.77E-08	-1.97E-08
$K'2$	6.79E-08	5.83E-08	3.29E-08

Acknowledgements

The authors are grateful for financial support through the Research projects of the Czech Science Foundation (P108/10/2049).

References

[1] T. Profant, J. Klusák and M. Kotoul: Key Engineering Materials. Vol. 452-453 (2010) p. 441

[2] T. Profant, J. Klusák and M. Kotoul: Key Engineering Materials. Vol. 465 (2011) p. 157

[3] J. Klusák, T. Profant, M. Kotoul: Procedia Engineering Vol. 2 (2010) p. 1635

[4] J. Klusák, Z. Knésl: Theor. Comp. Mater. Sci. Vol. 39(1) (2007) p 214

[5] K. B. Broberg: *Cracks and Frature* (Academic Press, 1999)

[6] Ch. Hwu: *Anisotropic Elastic Plates* (Springer, 2010)

[7] C. Carloni, L. Nobile, Theor. Appl. Fract. Mech. Vol. 38(2) (2002) p. 109

© (2012) Trans Tech Publications, Switzerland
doi:10.4028/www.scientific.net/KEM.488-489.420

Evaluation of the fatigue resistance of chromium slurry coating steel substrate compounds by means of an improved impact testing procedure

K.G. Anthymidis[1,a], C. David[2,b], A. Trakali[3,c] and D.N. Tsipas[4,d]

[1,2]Technical University of Serres, Mechanical Engineering Department,

Magnesias Campus, 62124 – Serres, Greece

[3]Technical University of Larisa, Agricultural Machinery Department,

TEI Campus, 41110 – Larisa, Greece

[4]Aristotele University of Thessaloniki, Mechanical Engineering Department,

Panepistimioupoli Campus, 54006 – Thessaloniki, Greece

[a]kanth@teiser.gr, [b]david@teiser.gr, [c]afrotrak@yahoo.gr, [d]tsipas@meng.auth.gr

Keywords: slurry coatings, impact testing, fatigue

Abstract. Chromium coatings have been used for the protection of gas turbine blades in power plants during the last years due to their very good resistance against steam corrosion. Microhardness, scratch, adhesion and pin-on-disk sliding tests are commonly used for rapid evaluation of the mechanical properties of these coatings [1,2]. However, very limited information exists on their fatigue resistance. In this paper we present the experimental results of the impact testing examination of the above coatings. This experimental method is capable to assess the fatigue and the impact wear resistance of coatings working under cyclic impact loading conditions. From the experimental results it was concluded that the slurry Cr, Zr coatings deposited on P91 steel showed adequate fatigue strength for the above-mentioned kind of use.

Introduction

The modern power generation steam turbines are being designed to have higher efficiencies and to meet the stringent environmental regulations, ensuring plant reliability, availability and maintainability, without increased costs. High efficiencies can be achieved by increasing the operating temperature of the whole process. At temperatures above 550°C coatings are implemented to protect turbine materials against corrosion, oxidation and degradation due to fatigue wear.

Chromium coatings, especially those with Al, or Zr, do meet the above requirements of the power plant industry. These coatings are being explored already for use in the power plants steam turbines that operate at superficial temperatures, but they have not been applied in production still.

In this paper we assess the wear fatigue resistance of chromium coatings working under cyclic loading conditions by means of the impact testing method. The impact testing method already has been introduced as a convenient experimental technique to evaluate the fatigue strength of coatings being exposed in successive impact loads during the last years [3-8]. According to this method the coated specimen is cyclically loading by a cemented carbide ball that repetitively impacts on the specimen surface at a frequency of 50 Hz. The superficially developed Hertzian pressure induces a complex stress field within the coating, as well as, in the interfacial zone between the coating layer and the substrate. Both these stress states are responsible for distinct failure modes, such as cohesive and/or adhesive one. The exposure of the layered compound against impulsive stresses creates the real conditions for the appearance of coating fatigue phenomena based upon structural transformation, cracking generation and cracking growth, which are responsible for the gradual microchipping and the coating degradation.

Experimental procedure

The examined slurry coatings were characterized regarding their fatigue resistance using the impact testing method illustrated in figure 1.

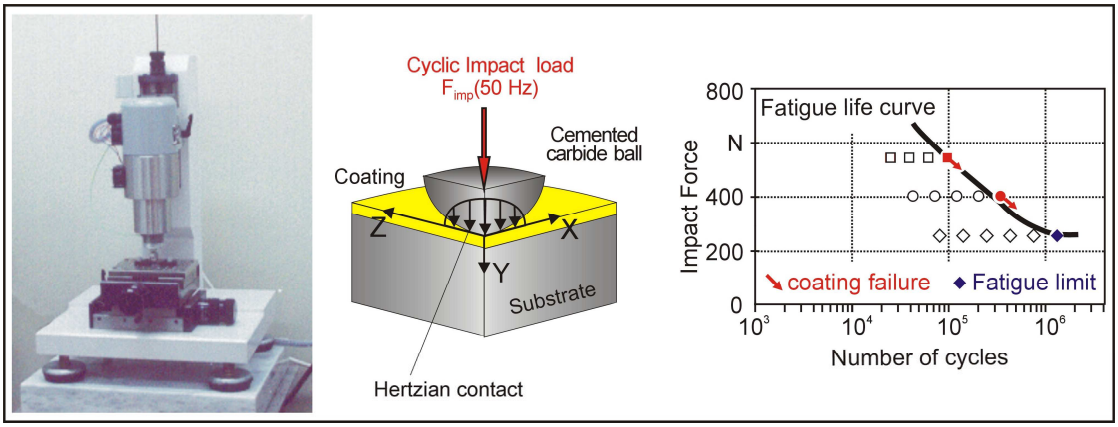


Figure 1: Impact testing method

The working principle of the impact testing is based on the alternate Laplace magnetic forces that are produced by an electromagnetic field, which is induced by a coil located in the mechanical unit. In order to enhance the impact testing efficiency the mechanical unit with the coil were analyzed by finite elements method to achieve the optimum magnetic flux density resulting in higher electromagnetic force and correspondingly in an increased impact load. The stress strain state related to the impact test is attributed to the Hertzian contact, which is developed between the spherical indentor (cemented carbide ball) and the examined layered space resulting in an impact crater. Gradual intrinsic coherence release and coating microchipping or abrupt coating adhesive fracture and consequent exposure of the substrate material designate the coating failure.

The coating failure mode and its extent in all conducted experiments were assessed by means of SEM observations and EDX analysis. The impact load leading to coating fatigue failure was recorded in fatigue diagrams versus the number of impacts applied. The impact load for which the coating after 10^6 impacts does not fail designates its fatigue limit.

Results and discussion

In Figure 2 the typical morphology of the Cr, Zr coatings deposited on P91 steel substrate is shown. The above coatings that are used for the purposes of the current investigation have been produced by slurry deposition method. This kind of coatings is characterized for their good dense structure in comparison to coatings produced by HVOF method [9]. In Figure 3 the high cycle fatigue diagram of the Cr, Zr slurry coating deposited on P91 steel substrate is shown. This coating had an average thickness of 40 μm and Vickers microhardness values of 330 Hv. From the conducted impact tests it was concluded that the fatigue limit of the current coating amounts approximately 200 N.

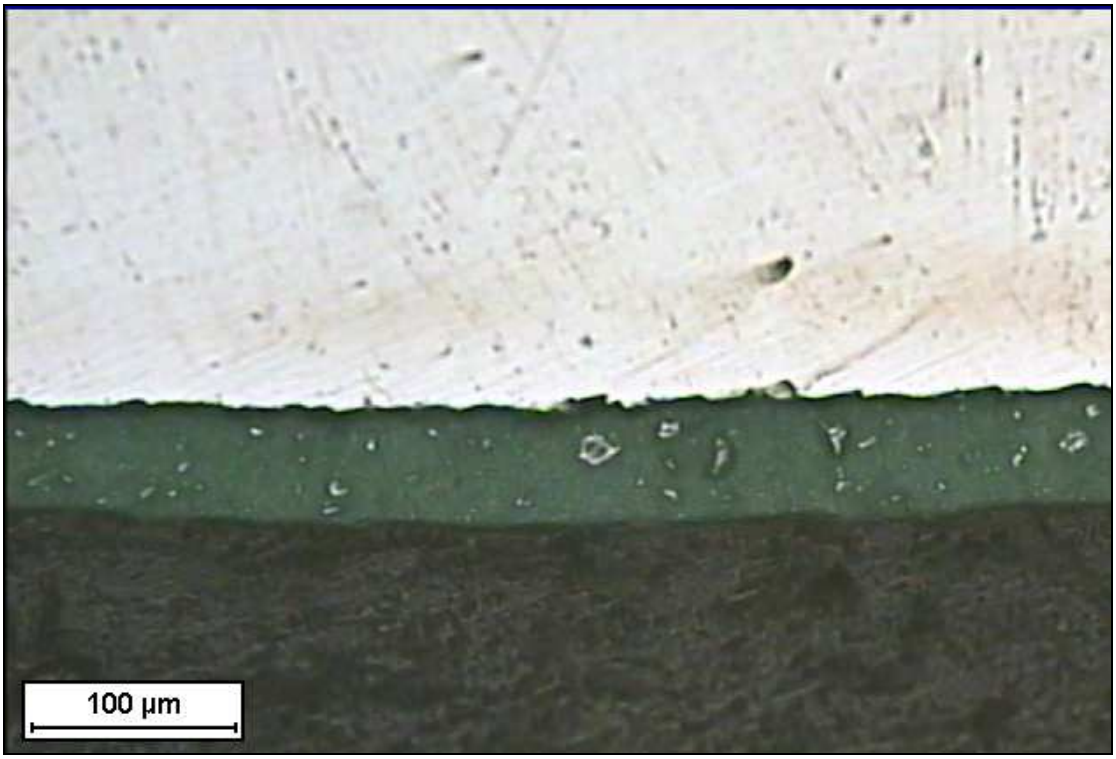


Figure 2: Typical morphology of the Cr, Zr coatings deposited on P91 steel substrate

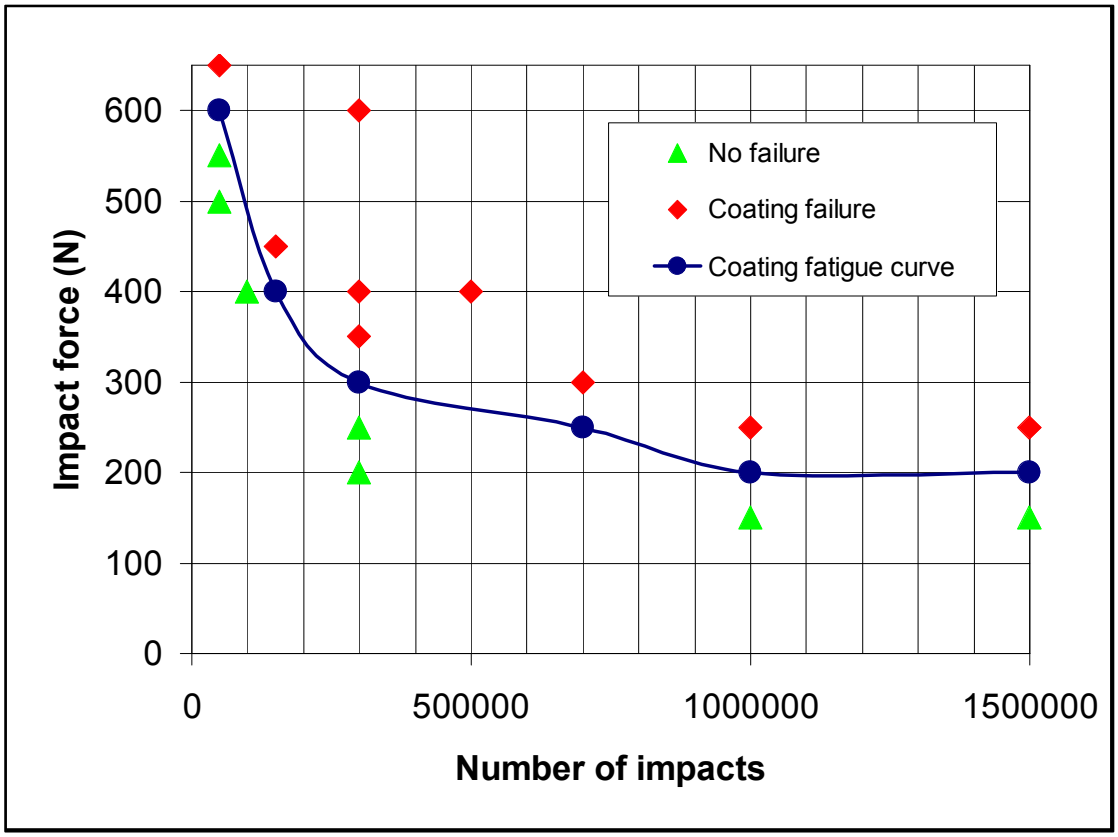


Figure 3: Fatigue curve of the Cr, Zr slurry coating deposited on P91 steel substrate

Conclusions

The work presented here reports the results of an experimental approach capable to investigate the endurance performance of coating systems with refer to their mechanical properties and to deliver a semi-empirical design approach. In this sense provides a feedback approach for optimizing the

design of surface engineering components that serve under impact wear operating conditions. Current impact testing investigations revealed the good fatigue strength of Cr, Zr slurry coatings due to their good dense.

Acknowledgment

Financial support by the Research Committee of the Technological Education Institute (TEI) of Serres, under grant 24/5/23-3-2011, is gratefully acknowledged. The authors would also like to express their gratitude to the Aristotles University of Thessaloniki for the use of its research facilities and the provision of the specimens used in the experiments.

References

[1] F. Loeffler: Thin Solid Films, Vol. 339 (1999), p. 181
[2] G. A. Saltzmann: Selection and Use of Wear Tests for Coatings, ASTM Spec. Tech. Publ., 769, R.G. Bayer, Ed., 1982
[3] A.A. Voevodin, R. Bantle and A. Matthews: Wear Vol. 185 (1995), p. 151
[4] R. Bantle and A. Matthews: Surface and Coatings Technology Vol. 74-75 (1995), p. 857
[5] W. Heinke, A. Leyland, A. Matthews, G. Berg, C. Friedrich, E. Broszeit: Thin Solid Films, Vol. 270, (1995), p. 431
[6] H. Ziegele, C. Rebholz, A.A. Voevodin, A. Leyland, S. L. Rohde, A. Matthews: Tribology International, Vol. 30 no. 12, (1997), p.845
[7] O. Knotek, B. Bosserhoff, A. Schrey, T. Leyendecker, O. Lemmer and S. Esser: Surface & Coatings Technology, Vol. 54-55, (1992), p. 102
[8] Xiaodong Zhu, Hailin Dou, Zhigang Ban, Yixiong Liu and Jiawen He: Surface and Coatings Technology, Vol. 201, No. 9-11, (2007), p. 5493
[9] L. Zhao, M. Mauer, F. Fischer, E. Lugscheider: Surface & Coatings Technology, Vol. 185, Issue 2-3, pp. 160-165, (2004)

© (2012) Trans Tech Publications, Switzerland
doi:10.4028/www.scientific.net/KEM.488-489.424

Stress responses to large simple shear deformation in elasticity based on the logarithmic strain

Yang Lihong [1, a], Qu Jia [1, b] and He Yunzeng [1, c]

[1]College of Aerospace and Civil Engineering, Harbin Engineering University, Harbin 150001, China

[a]yanglihong@hrbeu.edu.cn, [b]qujia@hrbeu.edu.cn, [c]hyz_1@sina.com

Keywords: Logarithmic strain; Large simple shear deformation; Elastic large strain constitutive model

Abstract: The logarithmic strain is more suitable for analyzing large strain problems because the volume invariability condition in small deformation is equivalent to volume invariability condition in large deformation when using the logarithmic strain. Large simple shear deformation has always been used in the analysis of large strain problems. In this paper, elastic large strain constitutive model was introduced based on the logarithmic strain and large simple shear deformation was analyzed by using the constitutive model given in the paper. The stress responses to large simple shear deformation were derived corresponding to four objective rates of tensors. The results show that normal stresses may maintain good monotonicity, but there exists different levels of oscillation of shear stress corresponding to various objective rates, and there was the most severe oscillation of stress when adopting Jaumann rate. The objective rate should not be the only factor bringing about oscillation of shear stress.

Introduction

Large strain constitutive models have been generally formulated in terms of the formation rate and an objective rate of stress by popularizing small deformation constitutive models. Dienes[1] found that the stress responses to large simple shear deformation were oscillating in elasticity when using this kind of constitutive model with Jaumann rate of stress and the monotonic increasing stress responses may be given if Green-Naughdi rate of stress was used. Nagtegaa and de Jong[2] had obtained the same conclusion for anisotropic kinematic hardening material. Thus, it had attracted wide attention to find appropriate objective stress rates which were suitable for describing large deformation problems[3, 4]. Volume invariability can not be satisfied when using the deformation rate in this popularized large strain constitutive model[5]. Small deformation volume invariability condition is the first invariant of strain I=0, but large deformation volume invariability condition is Jaccobi determinant J=1. For the deformation rate, I=0 is not equivalent to J=1 in large deformation condition and only logarithmic strain can make I=0 equivalent to J=1[5]. So, it is more reasonable to replace the deformation rate in large strain constitutive models by the objective rates of the logarithmic strain.

In this paper, large strain elastic constitutive models are discussed based on the logarithmic strain and elastic large simple shear deformation is analyzed based on several objective rates. The influence of objective rates on the stress responses to large simple shear deformation is discussed.

Elastic Large Strain Constitutive Model

Elastic constitutive model in small deformation condition is represented as

$$\dot{\boldsymbol{\sigma}} = 2\mu\dot{\boldsymbol{\varepsilon}} + \lambda J_1(\dot{\boldsymbol{\varepsilon}})\boldsymbol{I} . \tag{1}$$

Here, $\dot{\boldsymbol{\sigma}}$ is rate of Cauchy stress, $\dot{\boldsymbol{\varepsilon}}$ is rate of engineering strain, λ, μ are Lame parameters of material, $J_1(\dot{\boldsymbol{\varepsilon}})$ is the first invariant of $\dot{\boldsymbol{\varepsilon}}$ and $\boldsymbol{I}$ is second-order unit tensor.

If $\dot{\boldsymbol{\varepsilon}}$ is replaced by the objective rate of the logarithmic strain $\boldsymbol{H}^*$ and $\dot{\boldsymbol{\sigma}}$ is replaced by the objective rate of Kirchhoff stress $\boldsymbol{\tau}^*$ in Eq. 1, we may obtain the large deformation elastic constitutive model as follows

$$\boldsymbol{\tau}^* = 2\mu \boldsymbol{H}^* + \lambda J_1\left(\boldsymbol{H}^*\right)\boldsymbol{I}. \tag{2}$$

Deformation and motion analysis of simple shear

Motion model of simple shear is shown in Fig. 1. *Oabc* becomes *Oa'b'c* during simple shear deformation. Let Lagrange cartesian coordinates $X_i\left(i=1,2\right)$ coincide with Euler cartesian coordinates $x_i\left(i=1,2\right)$. So simple shear deformation may be described by the following expressions

$$x_1 = X_1 + v(X_2)t, \quad x_2 = X_2. \tag{3}$$

where, $v(X_2)$ is the velocity along direction x_1. The base vectors of coordinates are denoted by $\boldsymbol{e}_i\left(i=1,2\right)$. Then the deformation gradient of large simple shear deformation is given by

$$\boldsymbol{F} = \frac{\partial \boldsymbol{x}}{\partial \boldsymbol{X}} = \boldsymbol{e}_1\boldsymbol{e}_1 + \boldsymbol{e}_2\boldsymbol{e}_2 + \gamma \boldsymbol{e}_1\boldsymbol{e}_2. \tag{4}$$

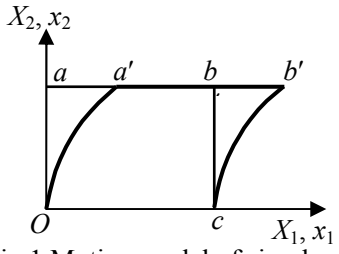


Fig.1 Motion model of simple shear

where, $\gamma = \dfrac{dv\left(X_2\right)}{dx_2}t$ is the shear strain of simple shear deformation. Using Eq. 4, the left Cauchy-Green deformation tensor is calculated as follows

$$\boldsymbol{B} = \boldsymbol{F}\cdot\boldsymbol{F}^T = \left(1+\gamma^2\right)\boldsymbol{e}_1\boldsymbol{e}_1 + \boldsymbol{e}_2\boldsymbol{e}_2 + \gamma\left(\boldsymbol{e}_1\boldsymbol{e}_2 + \boldsymbol{e}_2\boldsymbol{e}_1\right). \tag{5}$$

Then the left tension tensor is given by

$$\boldsymbol{V} = \boldsymbol{B}^{1/2} = \frac{1}{b}\left[\left(2+\gamma^2\right)\boldsymbol{e}_1\boldsymbol{e}_1 + 2\boldsymbol{e}_2\boldsymbol{e}_2 + \gamma\left(\boldsymbol{e}_1\boldsymbol{e}_2 + \boldsymbol{e}_2\boldsymbol{e}_1\right)\right]. \tag{6}$$

Here, $b = \sqrt{4+\gamma^2}$. Thus the logarithmic strain of simple shear deformation is derived from Eq.6, as

$$\boldsymbol{H} = \ln \boldsymbol{V} = \frac{a}{b}\left[\gamma\left(\boldsymbol{e}_1\boldsymbol{e}_1 - \boldsymbol{e}_2\boldsymbol{e}_2\right) + 2\left(\boldsymbol{e}_1\boldsymbol{e}_2 + \boldsymbol{e}_2\boldsymbol{e}_1\right)\right]. \tag{7}$$

Here, $a = \ln\left(b/2+\gamma\right)$.

Using Eq.3, the velocity vector of simple shear deformation is derived as follows

$$\boldsymbol{v} = \frac{\partial \boldsymbol{x}}{\partial t} = v\left(X_2\right)\boldsymbol{e}_1. \tag{8}$$

Then the velocity gradient is obtained as

$$\boldsymbol{l} = \frac{\partial \boldsymbol{v}}{\partial \boldsymbol{x}} = \dot{\gamma}\boldsymbol{e}_1\boldsymbol{e}_2. \tag{9}$$

The material spin is calculated as follows

$$\boldsymbol{w} = \frac{1}{2}\left(\boldsymbol{l} - \boldsymbol{l}^{\mathrm{T}}\right) = \frac{\dot{\gamma}}{2}\left(\boldsymbol{e}_1\boldsymbol{e}_2 - \boldsymbol{e}_2\boldsymbol{e}_1\right). \tag{10}$$

$\boldsymbol{V}$ can be rewritten as

$$\boldsymbol{V} = \boldsymbol{R}_{\mathrm{E}}\cdot\boldsymbol{\lambda}\cdot\boldsymbol{R}_{\mathrm{E}}^{\mathrm{T}}.$$

Here, $\boldsymbol{\lambda}$=diag[λ_1, λ_2, λ_3], and λ_1, λ_2, λ_3 are the eigenvalues of $\boldsymbol{V}$. The Eulerian spin is defined as $\boldsymbol{\Omega}^{\mathrm{E}} = \dot{\boldsymbol{R}}_E\cdot\boldsymbol{R}_E^{\mathrm{T}}$. Using Eq.6, we have

$$\boldsymbol{\Omega}^{\mathrm{E}} = \dot{\boldsymbol{R}}_{\mathrm{E}}\cdot\boldsymbol{R}_{\mathrm{E}}^{\mathrm{T}} = \frac{\dot{\gamma}}{b^2}\left(\boldsymbol{e}_1\boldsymbol{e}_2 - \boldsymbol{e}_2\boldsymbol{e}_1\right). \tag{11}$$

Rotation tensor of simple shear deformation is obtained from Eqs. 4 and 6 as

$$\boldsymbol{R} = \boldsymbol{V}^{-1}\cdot\boldsymbol{F} = \cos\theta\left(\boldsymbol{e}_1\boldsymbol{e}_1 + \boldsymbol{e}_2\boldsymbol{e}_2\right) + \sin\theta\left(\boldsymbol{e}_1\boldsymbol{e}_2 - \boldsymbol{e}_2\boldsymbol{e}_1\right). \tag{12}$$

where, $\theta = \arctan\left(\gamma/2\right)$. Then the spin of Euler configuration to Lagrange configuration is obtained as

$$\boldsymbol{\Omega} = \dot{\boldsymbol{R}} \cdot \boldsymbol{R}^{\mathrm{T}} = \frac{2\dot{\gamma}}{b^2}\left(\boldsymbol{e}_1\boldsymbol{e}_2 - \boldsymbol{e}_2\boldsymbol{e}_1\right) = 2\boldsymbol{\Omega}^{\mathrm{E}}. \tag{13}$$

The expression of logarithmic spin is given by[5]

$$\boldsymbol{\Omega}^{\log} = \boldsymbol{w} + \sum_{i\neq j}^{m}\left[\frac{1+b_i/b_j}{1-b_i/b_j} + \frac{2}{\ln\left(b_i/b_j\right)}\right]\boldsymbol{B}_i\boldsymbol{D}\boldsymbol{B}_j = \frac{\dot{\gamma}}{4}\left(\frac{4}{b^2} + \frac{\gamma}{ab}\right)\left(\boldsymbol{e}_1\boldsymbol{e}_2 - \boldsymbol{e}_2\boldsymbol{e}_1\right). \tag{14}$$

where, b_1, …, b_{m} are the distinct eigenvalues of $\boldsymbol{B}$ and $\boldsymbol{B}_1$, …, $\boldsymbol{B}_{\mathrm{m}}$ are the corresponding subordinate eigenprojections of $\boldsymbol{B}$.

Jaumman rate of logarithmic strain is derived from Eqs. 7 and 10 as

$$\boldsymbol{H}^{\mathrm{J}} = \dot{\boldsymbol{H}} - \boldsymbol{w}\cdot\boldsymbol{H} + \boldsymbol{H}\cdot\boldsymbol{w} = \frac{\dot{\gamma}}{b^3}\left\{\left[\gamma b - 2a\left(b^2-2\right)\right]\left(\boldsymbol{e}_1\boldsymbol{e}_1 - \boldsymbol{e}_2\boldsymbol{e}_2\right) + \left[2b + \gamma a\left(b^2-2\right)\right]\left(\boldsymbol{e}_1\boldsymbol{e}_2 + \boldsymbol{e}_2\boldsymbol{e}_1\right)\right\}. \tag{15}$$

Eulerian rate of logarithmic strain is derived from Eqs. 7 and 11 as

$$\boldsymbol{H}^{\mathrm{E}} = \dot{\boldsymbol{H}} - \boldsymbol{\Omega}^{\mathrm{E}}\cdot\boldsymbol{H} + \boldsymbol{H}\cdot\boldsymbol{\Omega}^{\mathrm{E}} = \frac{\dot{\gamma}}{b^3}\left[\gamma\left(\boldsymbol{e}_1\boldsymbol{e}_1 - \boldsymbol{e}_2\boldsymbol{e}_2\right) + 2\left(\boldsymbol{e}_1\boldsymbol{e}_2 + \boldsymbol{e}_2\boldsymbol{e}_1\right)\right]. \tag{16}$$

Green-Naghdi rate of logarithmic strain is derived from Eqs. 7 and 13 as

$$\boldsymbol{H}^{\mathrm{GN}} = \dot{\boldsymbol{H}} - \boldsymbol{\Omega}\cdot\boldsymbol{H} + \boldsymbol{H}\cdot\boldsymbol{\Omega} = \frac{\dot{\gamma}}{b^3}\left[\left(\gamma b - 4a\right)\left(\boldsymbol{e}_1\boldsymbol{e}_1 - \boldsymbol{e}_2\boldsymbol{e}_2\right) + \left(2b + 2\gamma a\right)\left(\boldsymbol{e}_1\boldsymbol{e}_2 + \boldsymbol{e}_2\boldsymbol{e}_1\right)\right]. \tag{17}$$

The logarithmic rate of logarithmic strain is derived from Eqs. 7 and 14 as

$$\boldsymbol{H}^{\log} = \dot{\boldsymbol{H}} - \boldsymbol{\Omega}^{\log}\cdot\boldsymbol{H} + \boldsymbol{H}\cdot\boldsymbol{\Omega}^{\log} = \frac{\dot{\gamma}}{2}\left(\boldsymbol{e}_1\boldsymbol{e}_2 + \boldsymbol{e}_2\boldsymbol{e}_1\right). \tag{18}$$

Stress analysis of Simple Shear Deformation

We know from Eq.4 that volume ratio of large simple shear deformation is $J = J_3(\boldsymbol{F}) = 1$. Then, Kirchhoff stress $\boldsymbol{\tau}$ is the same as Cauchy stress $\boldsymbol{\sigma}$ in simple shear deformation. So we have

$$\boldsymbol{\tau} = J\boldsymbol{\sigma} = \boldsymbol{\sigma} = \tau_{11}\boldsymbol{e}_1\boldsymbol{e}_1 + \tau_{22}\boldsymbol{e}_2\boldsymbol{e}_2 + \tau_{12}\left(\boldsymbol{e}_1\boldsymbol{e}_2 + \boldsymbol{e}_2\boldsymbol{e}_1\right). \tag{19}$$

Then, Jaumann rate of Kirchhoff stress may be obtained from Eqs.10 and 19 as

$$\boldsymbol{\tau}^{\mathrm{J}} = \dot{\boldsymbol{\tau}} - \boldsymbol{w}\cdot\boldsymbol{\tau} + \boldsymbol{\tau}\cdot\boldsymbol{w} = \left(\dot{\tau}_{11} - \tau_{12}\dot{\gamma}\right)\boldsymbol{e}_1\boldsymbol{e}_1 + \left(\dot{\tau}_{22} + \tau_{12}\dot{\gamma}\right)\boldsymbol{e}_2\boldsymbol{e}_2 + \left[\dot{\tau}_{12} - \frac{1}{2}\left(\tau_{22} - \tau_{11}\right)\dot{\gamma}\right]\left(\boldsymbol{e}_1\boldsymbol{e}_2 + \boldsymbol{e}_2\boldsymbol{e}_1\right). \tag{20}$$

Eulerian rate of Kirchhoff stress may be obtained from Eqs.11 and 19 as

$$\begin{aligned}\boldsymbol{\tau}^{\mathrm{E}} &= \dot{\boldsymbol{\tau}} - \boldsymbol{\Omega}_{\mathrm{E}}\cdot\boldsymbol{\tau} + \boldsymbol{\tau}\cdot\boldsymbol{\Omega}_{\mathrm{E}} \\ &= \left(\dot{\tau}_{11} - \frac{2}{b^2}\tau_{12}\dot{\gamma}\right)\boldsymbol{e}_1\boldsymbol{e}_1 + \left(\dot{\tau}_{22} + \frac{2}{b^2}\tau_{12}\dot{\gamma}\right)\boldsymbol{e}_2\boldsymbol{e}_2 + \left[\dot{\tau}_{12} - \frac{1}{b^2}\left(\tau_{22} - \tau_{11}\right)\dot{\gamma}\right]\left(\boldsymbol{e}_1\boldsymbol{e}_2 + \boldsymbol{e}_2\boldsymbol{e}_1\right)\end{aligned}. \tag{21}$$

Green-Naghdi rate of Kirchhoff stress may be obtained from Eqs.13 and 19 as

$$\boldsymbol{\tau}^{\mathrm{GN}} = \dot{\boldsymbol{\tau}} - \boldsymbol{\Omega}\cdot\boldsymbol{\tau} + \boldsymbol{\tau}\cdot\boldsymbol{\Omega} = \left(\dot{\tau}_{11} - \frac{4}{b^2}\tau_{12}\dot{\gamma}\right)\boldsymbol{e}_1\boldsymbol{e}_1 + \left(\dot{\tau}_{22} + \frac{4}{b^2}\tau_{12}\dot{\gamma}\right)\boldsymbol{e}_2\boldsymbol{e}_2 + \left[\dot{\tau}_{12} - \frac{2}{b^2}\left(\tau_{22} - \tau_{11}\right)\dot{\gamma}\right]\left(\boldsymbol{e}_1\boldsymbol{e}_2 + \boldsymbol{e}_2\boldsymbol{e}_1\right). \tag{22}$$

Logarithmic rate of Kirchhoff stress may be obtained from Eqs.14 and 19 as

$$\boldsymbol{\tau}^{\log} = \dot{\boldsymbol{\tau}} - \boldsymbol{\Omega}^{\log}\cdot\boldsymbol{\tau} + \boldsymbol{\tau}\cdot\boldsymbol{\Omega}^{\log} = \left[\dot{\tau}_{11} - c\tau_{12}\dot{\gamma}\right]\boldsymbol{e}_1\boldsymbol{e}_1 + \left[\dot{\tau}_{22} + c\tau_{12}\dot{\gamma}\right]\boldsymbol{e}_2\boldsymbol{e}_2 + \left[\dot{\tau}_{12} - c\left(\tau_{22} - \tau_{11}\right)\dot{\gamma}\right]\left(\boldsymbol{e}_1\boldsymbol{e}_2 + \boldsymbol{e}_2\boldsymbol{e}_1\right). \tag{23}$$

Here, $c = 2/b^2 + \gamma/(2ab)$.

Elastic stress response to simple shear deformation

Substituting Eqs. 15 and 20 into Eq. 2, the elastic constitutive model in simple shear deformation for Jaumann rate is given in the following component form

$$\dot{\tau}_{11} = -\dot{\tau}_{22} = \left\{\tau_{12} + d\left[\gamma b - 2a\left(b^2-2\right)\right]\right\}\dot{\gamma}, \quad \dot{\tau}_{12} = \left\{\frac{1}{2}\left(\tau_{22} - \tau_{11}\right) + d\left[2b + \gamma a\left(b^2-2\right)\right]\right\}\dot{\gamma}. \tag{24}$$

where, $d = 2\mu/b^3$. Similarly, substituting Eqs. 16 and 21 into Eq. 2, the elastic constitutive model for Eulerian rate is given in the following form

$$\dot{\tau}_{11} = -\dot{\tau}_{22} = \left(\frac{2}{b^2} \tau_{12} + \gamma db \right) \dot{\gamma}, \quad \dot{\tau}_{12} = \left[\frac{1}{b^2} \left(\tau_{22} - \tau_{11} \right) + 2db \right] \dot{\gamma} . \tag{25}$$

Substituting Eqs. 17 and 22 into Eq. 2, the elastic constitutive model for Green-Naghdi rate is given by

$$\dot{\tau}_{11} = -\dot{\tau}_{22} = \left[\frac{4}{b^2} \tau_{12} + d\left(\gamma b - 4a \right) \right] \dot{\gamma}, \quad \dot{\tau}_{12} = \left[\frac{2}{b^2} \left(\tau_{22} - \tau_{11} \right) + d\left(2b + 2\gamma a \right) \right] \dot{\gamma} . \tag{26}$$

Substituting Eqs. 18 and 23 into Eq. 2, the elastic constitutive model for logarithmic rate is given by

$$\dot{\tau}_{11} = -\dot{\tau}_{22} = c\tau_{12}\dot{\gamma}, \quad \tau_{12} = c\left(\tau_{22} - \tau_{11} \right) \dot{\gamma} + \mu \dot{\gamma} . \tag{27}$$

The shear stress responses to simple shear deformation corresponding to Jaumann rates are shown in Fig. 2. We can conclude from Fig.2 that the oscillation of shear stress still exist for the logarithmic strain when using Jaumann rate, but the oscillation amplitude is smaller than that obtained for the deformation rate. The elastic stress responses to large simple shear deformation corresponding to four objective rates of logarithmic strain are derived from Eqs. (24)~(27), as shown in Fig. 3. We can see from Fig, 3 that τ_{11} (or τ_{22}) are monotonic corresponding to this four stress rates in simple shear deformation, but τ_{12} is not monotonic corresponding to these stress rates.

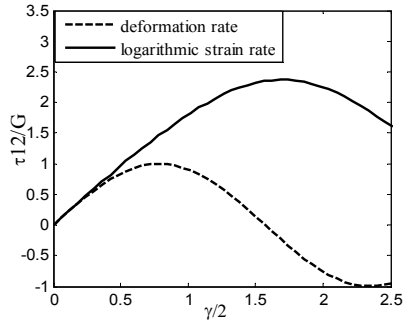
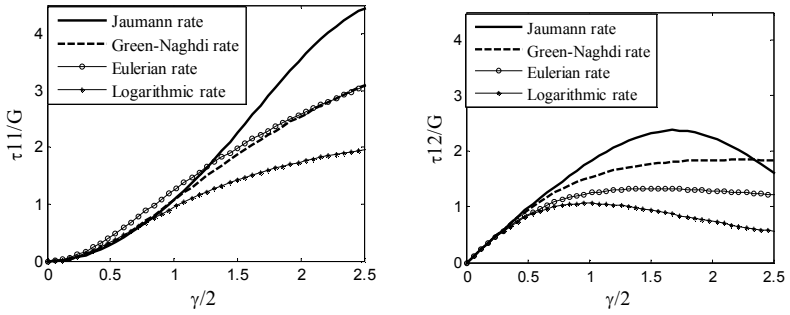


Fig. 2 Elastic shear stress responses to simple shear based on Jaumann rate



(a) (b)

Fig. 3 Elastic stress responses to simple shear based on objective rates of the logarithmic strain

Conclusions

In this paper, the small deformation elastic constitutive model is popularized to large deformation based on the logarithmic strain. Elastic large simple shear deformation is analyzed by using the constitutive model given in this paper. Elastic stress responses are given corresponding to four objective rates. The conclusions obtained are as follows: (1) Jaumann rate is not suitable for studying large deformation problems; (2) the normal stresses have better monotonicity in simple shear deformation, but shear stress has different levels of oscillation; (3) the objective rate of tensor is not the only factor resulting into the unreasonable stress response, and the methods of establishing large deformation constitutive model should be further discussed.

References:

[1] Dienes J K. On the Analysis of Rotation and Stress Rate in Deforming Bodies. Acta Mechanica. Vol. 32(1979), p. 217-232.

[2] Nagtegaal J C, de Jong J E. Some Aspects of Non-isotropic Work-hardening in Finite Strain Plasticity. Proceeding of the Workshop on Plasticity of Metals at Finite Strain: Theory, Experimental and Computation. Stanford University. 1981, p. 65-102.

[3] Yang Wei, Cheng Li, Huang Kezhi. Objective Corotational Rates and Shear Oscillation. International Journal Plasticity. Vol. 8(1992), p. 643-656.

[4] Yang Lihong, He Yunzeng, Wu Guohui. Analysis of Large Strain Constitutive Relationship based on Torsion Test. Journal of Harbin Engineering University. Vol. 27(2006), p. 816-820.

[5] Zhou Zhe, Li Mingriu, Huang Wenbin. Volume Invariability in Calculation of Finite Deformation. Chinese Journal of Applied Mechanics. Vol. 19(2002), p. 81-84.

© (2012) Trans Tech Publications, Switzerland
doi:10.4028/www.scientific.net/KEM.488-489.428

Slow Crack Growth by Grain Boundary Dissolution of Hydroxyapatite in Water

Dong Seok Seo[1,a], Kyu Hong Hwang[2,b] and Jong Kook Lee[1,c]

[1]Department of Advanced Materials Engineering, Chosun Univ., Gwangju, 501-759 Korea

[2]School of Materials Engineering, Gyeongsang National Univ., Jinju, 660-701, Korea

[a] dsseo30@naver.com, [b]khhwang@gnu.ac.kr, [c]corresponding to jklee@chosun.ac.kr

Keywords: Hydroxyapatite, Grain boundary dissolution, Crack crowth

Abstract. Mechanical degradation of hydroxyapatite ceramics due to the slow crack growth was observed in water. Microstructural crack on the surface of hydroxyapatite initiated by grain boundary dissolution in liquid environment resulting in particle loosening and microstructural-level degradation, followed by a drastic decrease of mechanical properties. In this study, slow crack growth by the dissolution behavior of hydroxyapatite ceramics was investigated based on microstructural observation by field emission microscopy. The crack growth and morphological change of hydroxyapatite surface, especially at the initial stage of dissolution and related surface roughness were observed with immersion time. The surface dissolution occurred from the initial stage of immersion showing increase in surface roughness. Following certain period of immersion time, the surface dissolution initiated at grain boundaries and generated many separated grains.

Introduction

Hydroxyapatite-based ceramics have an attention to significant applications as a bone graft materials to medical and dental fields [1]. But they were dissolved during exposure to the in vitro and in vivo environment due to its intrinsically poor mechanical properties especially in wet environments [2]. It is important to predict the possible harmful effects of materials on the surrounding bone tissues [3]. As a result of dissolution or particle loosening from implant materials, it will provoke inflammation or third body friction [4]. Therefore, it requires the fabrication of hydroxyapatite with dissolution and degradation resistance for a long time. Of the calcium phosphate ceramics, HA is expected to be stable in body fluid because it shows the lowest solubility of calcium phosphate materials in a very narrow pH range of >7.3 [5].

However, HA ceramics undergoes numerous dissolution and failure processes induced by biological fluids after implantation. This process begins to degrade the ceramic and influence later cellular degradation. Therefore, in this study, HA powder was prepared by a precipitation method and pure sintered HA body was obtained and its dissolution was demonstrated in distilled water of neutral pH.

Experimental procedure

HA powder with a Ca/P ratio of 1.67 was synthesized by an aqueous precipitation method from calcium nitrate tetrahydrate, $Ca(NO_3)_2 \cdot 4H_2O$ and orthophosphoric acid. The powders were uniaxially compacted and subsequently cold isostatic pressed (CIP) at 220 MPa. The obtained compacts were sintered at 1200℃ for 2 h in air with under moisture protection. The density of the sintered bodies was measured using the Archimedes technique. After sintering, the disks were polished to smoothness using 1㎛ diamond paste. The four disks were soaked in 40 ml of pH 7.4 in distilled water at 37℃ for 3, 7 and 14 days. The phase composition of all samples was analyzed by X-ray diffractometer. After the samples were taken out of the immersion solution, the overall microstructural characterization of HA disks was performed using scanning electron microscopy (SEM) in secondary electron mode. Surface roughness and fracture toughness were measured with immersion time.

Results and discussion

The relative density of the sintered body was calculated as 98% above of the theoretical density exhibiting a nearly fully densified microstructure, in which few intergranular and intragranular pores are present (Fig. 1(a)). The HA sintered body was consisted of fine grains of 300-400 nm with narrow size distribution. Figure 1(b) shows the XRD pattern of the HA sintered body. All detectable peaks are identical only to HA lattice planes without expressing any impurities.

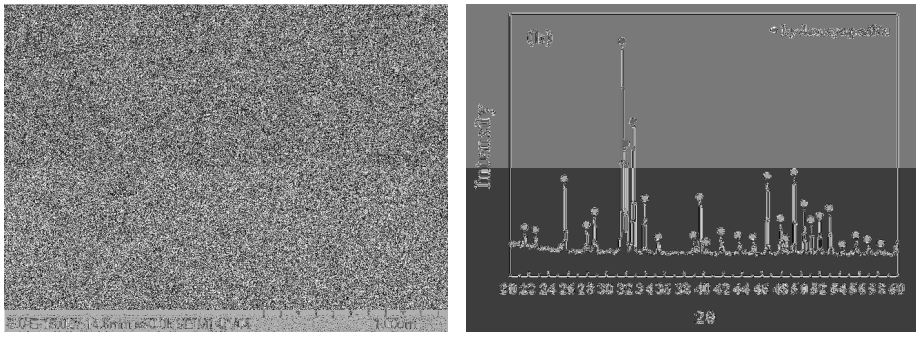


Fig. 1 (a) Microstructure and (b) XRD patterns of HA disk sintered at 1200℃.

Figure 2 presents surface morphology of HA with immersion period. The polished surface was smooth with a relatively low density of surface defects. The surface was slightly dissolved by water after 3 days of immersion. Grain boundaries, denoted as arrows, initiate to be appeared, the surface became rough and the defect like pores due to the dissolution was also observed. After 7 days of immersion, grain boundaries dissolution was pronounced showing similar morphology to the thermally etched surface of Fig. 1. Following the further immersion to 14 days, the dissolution at grain boundary continued and considerable dissolution of the surface occurred resulting in the formation of micron-scale cracks. In this region, the dissolution is assumed to progress gradually interior to the material along the grain boundary resulting in that the grains were separated into individual ones.

The dissolution should continue interior to the material along the grain boundaries is evidenced by fracture surfaces with increasing immersion period (Fig. 3(a)). After 7 days of immersion, intergranular fracture, due to the grain boundary dissolution, limited to near the surface. As the immersion time increased to 14days, the region of intergranular fracture was expanded resulting from proceeding of grain boundary dissolution into bulk (Fig. 3(b). Once dissolution of HA occurred along the grain boundaries, it extends into bulk following these paths. This dissolution is accompanied by separation of grains leading to the growth of microcracks on the surface. Also, the presence of a different fracture mode in the same specimen may be that the bonding strength of grains in dissolved area became weak by the grain boundary dissolution, therefore a crack during the fracture progresses along the grain boundaries resulting in intergranular fracture. However, transgranular fracture occurred where any significant dissolution was not happened because the bonding strength between grains obtained by sintering remains unchanged before and after the immersion in water.

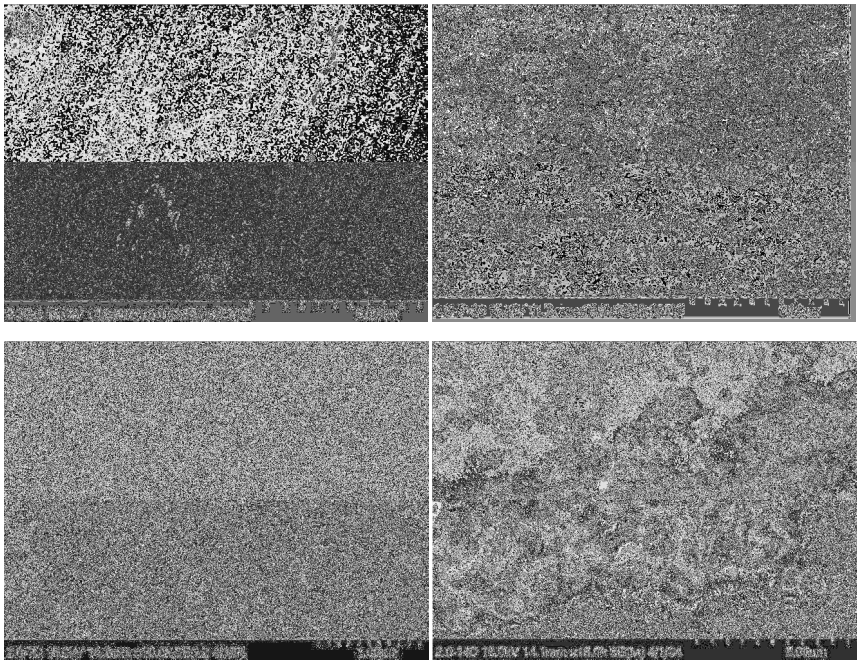


Fig. 2 SEM micrographs of HA; (a) polished, and immersed for (b) 3 days, (c) 7 days, and (d) 14 days. The shallow appearance of grain boundaries (arrows) is indication of dissolution. (c) represents a clear sign of grain boundary dissolution throughout the material. Grains are pulled out of the HA surface (curved arrow) with longer exposure to water.

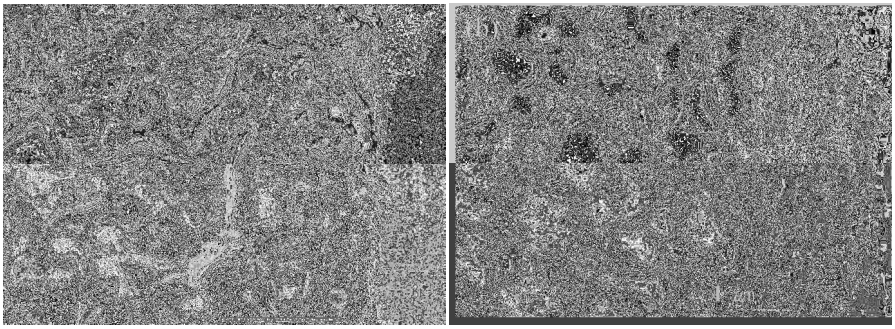


Fig. 3 Fracture surfaces of HA after immersion for (a) 7 days and (b) 14 days. In (a), the righthand portion (near the surface) shows intergranular fracture, whereas transgranular fracture in the lefthand portion marked with an asterisk (*).

From the crack growth to interior of HA, mechanical properties should be affected by surface dissolution. Figure 4 shows the fracture toughness (K_{Ic}) of HA with immersion period from 0 to 14 days. The K_{Ic} value of HA sintered body was approximately 1.0 $MPa \cdot m^{1/2}$, which is analogous to the value reported for monophase HA material [6]. The K_{Ic} value of the specimen immersed for 3 days was similar to that of the polished one because the surface of 3 day's specimen was not much damaged as shown in Fig. 2(b). Further immersion decreased the fracture toughness of HA to almost half of the initial value due to the severe surface dissolution and at least the formation of micron-scale defect. The variation of fracture toughness is in good agreement with microstructural change of HA with immersion period.

To improve mechanical performance of calcium phosphate-based bioceramics, Ca/P molar ratio should be precisely regulated because a very small deviation in the Ca/P ratio leads to

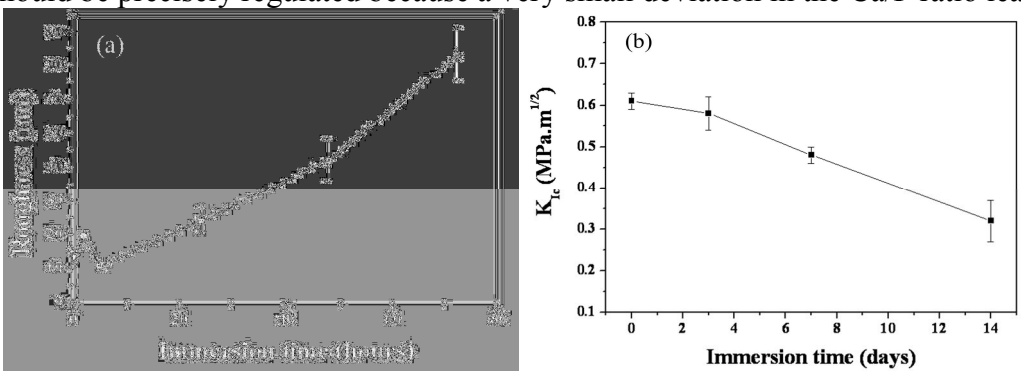


Fig. 4 Change of (a) surface roughness and (b) fracture toughness in HA with immersion time.

formation of soluble phase of TCP or CaO. Also, the microstructural defect like residual pores after sintering was detrimental to the reliability of HA ceramics. HA is subjected to be used in biological condition, so, the result in Fig. 4 can be a good example of how important is the dissolution and related to the slow crack growth dominate mechanical stability of HA ceramics. It suggests that the grain boundary dissolution and formation of micron-sized cavities can evoke a drastic decrease of the long term mechanical stability of bioceramics.

Summary

In this study, using the nano-sized HA powder, dense HA ceramics was prepared and its dissolution and slow crack growth were investigated. The surface dissolution is also evidenced by the increase of the value of roughness with immersion period. In the synthesized HA specimens, the surface was predominantly dissolved at grain boundaries and extended into bulk following this paths resulting in slow crack growth of the material. By the crack growth from the surface to the interior, fracture toughness decreased up to almost half of the initial value. From a mechanical point of view, grain boundary dissolution and formation of the related cavities can lead to a distinct decrease in the long term mechanical stability of bioceramics.

Acknowledgment

This research was supported by a grant from the National Research Foundation of Korea funded by the Ministry of Education, Science and Technology in Korea (20090085676).

References

[1] L. Hong, H. C. Xu and K. De Groot: J. Biomed. Mater. Res. Vol. 26 (1992), p. 7

[2] M. Jarcho: Clin. Orthop. Vol. 157 (1981), p. 259

[3] T. Futagami and T. Okamoto: Yogyo-Kyokai-Shi Vol. 95 (1987), p. 775

[4] M. Jarcho, C. H. Bollen, M. B. Thomas, J. Bobick, J. F. Kay and R. H. Doremus: J. Mater. Sci. Vol.11 (1976), p. 2027

[5] C. P. A. T. Klein, J. M. A. de Blieck-Hogervorst, J. G. C. Wolke, and K. de Groot: Biomaterials Vol.11 (1990), p. 509

[6] W. Suchanek and M. Yoshimura: J. Mater. Res. Vol. 13 (1998), p. 94

© (2012) Trans Tech Publications, Switzerland
doi:10.4028/www.scientific.net/KEM.488-489.432

Research on Acoustic Emission Test Method for Metal Fatigue Fracture Based on Wavelet Packets Feature Extraction

Wang Qi, Chen Yin-sheng, Song Kai

School of Electrical Engineering and Automation, Harbin Institute of Technology,

Harbin 150001, China

wangqi@hit.edu.cn

Keywords: acoustic emission test; metal fatigue fracture; wavelet packets; feature extraction

Abstract. The appearance and growth of the microcracks in the structure is an important factor that influences the structure safety and its service life. Thus it is very important to detect the crack and monitor its growth at the beginning of the crack. Aiming at the main style of failures in metal structure - fatigue fracture, this paper research acoustic emission waveforms analysis that base on wavelet packets feature extraction, through processing acoustic emission signal to test metal fatigue fracture. First, this paper analyses the reason of metal fatigue fracture and introduces the theory of acoustic emission. Based on that, we establish the time domain module of acoustic emission signal and extract the feature of acoustic emission signal using wavelet packets. According to the experimental results bending specimen, acoustic emission techniques monitoring fatigue crack propagation is certificated not only to resemble variable rule of fatigue crack propagation but also to catch generation of fatigue crack in real time. Compared with the method of parameter extraction, this method can not only realize real-time and dynamic monitoring, but also get the result that is similar with fatigue crack expanding rate curve.

Introduction

Fatigue fracture is the main style of failure in metal structure and it approximately accounts for 90% of the failure of the structure. Because of metal structure under cyclic loading and various reasons (such as stress concentration, etc), fatigue fracture causes the decrease of fatigue strength and cracks, by the expansion of cracks causing the invalidation of mental structure in final. Acoustic Emission (AE) is a phenomenon accompanied with quick energy release of snapshot flexible wave, when the material and structure emerge plastic deformation or the cracks form and extend, under the influence of internal force, external force or temperature. Acoustic Emission signal is a kind of stress wave which derives from internal defect, not in limit of specimen or geometry structure. Compared with traditional un-destructive detection, acoustic emission test gives the changes of defect instead of the value with dynamic, real-time characteristics. The acoustic emission technology not only can monitor the process of cracks extension, but also reflect the dynamic process of cracks extension. Therefore, it is an efficient way to study material fatigue fracture. Combining fatigue fracture theory and acoustic emission technology together, it has important significance of the theory and application prospect in monitoring fatigue fracture and cracks extension[1-3].

Acoustic emission signal can be divided into two types in time domain: continuous type and gusty type. The substance of acoustic emission signal in the process of metal fatigue fracture is gusty type acoustic emission signal.

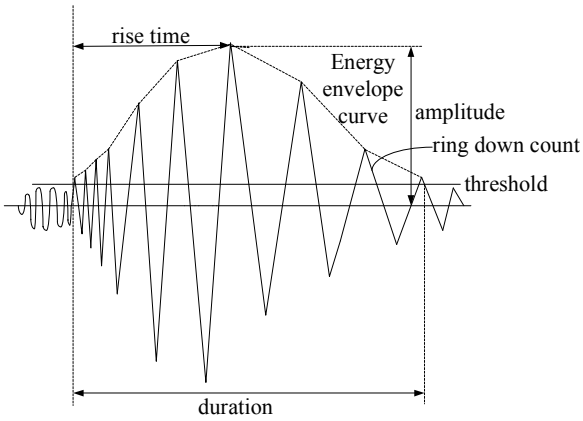


Fig.1 The characteristics of gusty type acoustic emission

Waveforms analysis and parameter extraction are two ways to extract acoustic emission signal, applying the second method in this paper. Gusty signal parameters are ring-down count, amplitude, energy count, rise time, duration, time difference, etc. The parameters closely related to fatigue fracture:

ring-down count—counting the quantity of ring-down pulse over the threshold, expressed by H.

energy count—the area under signal detection envelope curve, reflecting signal strength, not sensitive to threshold, working frequency, propagation characteristic, expressed by E[4,5].

Feature extraction based on wavelet packet decomposition

A. Basic Theory of Wavelet Packet

Wavelet transform has been used to obtain information of signals in many reports. The main advantages are that the results obtained by wavelet transform contain both the time and frequency domain information. Wavelet transform decomposes only the approximations of the signal, but the important information is mainly located in higher frequency so that feature can not be extracted exactly. Wavelet packet transform is an expansion of the classical wavelet decomposition, which contains more information for signal feature extraction. Fig. 2 shows the WPD process by taking a three-layer WPD as an example. Where A denotes low frequency, D is high frequency and serial number at the end denotes the layer numbers of WPD. Hence the signal can be described as X=AAA3+DAA3+ADA3+DDA3+AAD3+DAD3+ADD3+DDD3 . It is observed that WPT not only split low frequency components but also high frequency components [6].

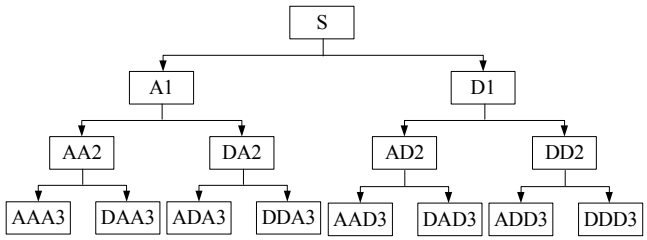


Fig. 2 Sketch map of three-layer WPD

B. Feature Extraction Steps of WPD

The steps of feature extraction using three-layer WPD are as follows:

1) Normalize the signal by

$$\widetilde{\mathbf{X}} = D_{\sigma}^{-1}[\mathbf{X} - E(\mathbf{X})] \tag{1}$$

Where $\mathbf{X}$ denotes the output sequence signal, $E(\mathbf{X})$ is the mean of $\mathbf{X}$ and D_σ is the standard deviation.

2) Decompose $\tilde{\mathbf{X}}$ with three-layer wavelet packet transform and get the coefficients vectors of the eight nodes in the third level described as $\tilde{\mathbf{x}}_{30},\tilde{\mathbf{x}}_{31},\tilde{\mathbf{x}}_{32},\tilde{\mathbf{x}}_{33},\tilde{\mathbf{x}}_{34},\tilde{\mathbf{x}}_{35},\tilde{\mathbf{x}}_{36},\tilde{\mathbf{x}}_{37}$ (rank from low to high).

3) Reconstruct the decomposition coefficients of each node in step 3 to obtain their corresponding data $\mathbf{S}_{30},\mathbf{S}_{31},\mathbf{S}_{32},\mathbf{S}_{33},\mathbf{S}_{34},\mathbf{S}_{35},\mathbf{S}_{36},\mathbf{S}_{37}$.

4) Calculate the energy sums of each frequency and normalize them by

$$ES_{3i}=\int|\mathbf{S}_{3i}|^2dt=\sum_{j=1}^{n}|S_{3i,j}|^2 \qquad \overline{ES_{3i}}=\frac{ES_{3i}}{\sqrt{\sum_{i=0}^{7}|ES_{3i}|^2}} \tag{2}$$

where n denotes the number of each frequency after reconstructing and $\overline{ES_{3i}}$ is the normalized energy.

5) Therefore, after three-scale wavelet packet decomposition, eight values will be obtained: $T=[\overline{ES_{30}},\overline{ES_{31}},\overline{ES_{32}},\overline{ES_{33}},\overline{ES_{34}},\overline{ES_{35}},\overline{ES_{36}},\overline{ES_{37}}]$

We think this is consistent with the idea of wavelet packet analysis. Due to the large value of E_{30} and for the purpose of simple and convenient computation, a relative energy value was adopted as a computing feature. The relative energy was computed by:

$$RE_{30}=\frac{E_{30}}{E} \tag{3}$$

Where RE_{30} is the relative energy, E the total energy of T, and E is given by:

$$E=\sum_{j=0}^{7}E_{3j} \tag{4}$$

Experimental results and discussion

In this paper, a computer simulates a mental fatigue crack curve, with time 40s and sampling rate of 0.1K. After filtering background noise with a higher threshold, we reconstruct the signal using wavelet packet, shown in Fig 3. Ring-down count can reflect the characteristics parameters of the changes in material properties, as it relates to the dislocation movement in materials, fracture of foreign inclusion and the released energy of cracks extension proportionally. For the detection of fatigue crack extension, the traditional method counts the number of ring-down count (the number of ring pulse count across threshold). Setting the threshold value of 2 here, and computing the slope of each sample point, if the pulse goes across the threshold and the slope changes from the positive to negative, this point is considered as the maximum point (considered as a ring-down count). Then the number of maximum points is ring-down count. In this paper, we put forward an acoustic emission waveform analysis method based on wavelet packet energy feature extraction. The energy feature contains a wealth of information of cracks. Using the wavelet packet feature extraction step of III part and extracting acoustic emission signals, we set the normalized energy threshold value of 0.3. If the value is more than the threshold, it indicates that fracture extension happens in material. Shown in Fig.4, compared with traditional ring-down count parameter extraction, the use of wave energy feature extraction method can effectively detect mental fatigue fracture. This method can not only realize real-time and dynamic monitoring, but also have faster calculation speed.

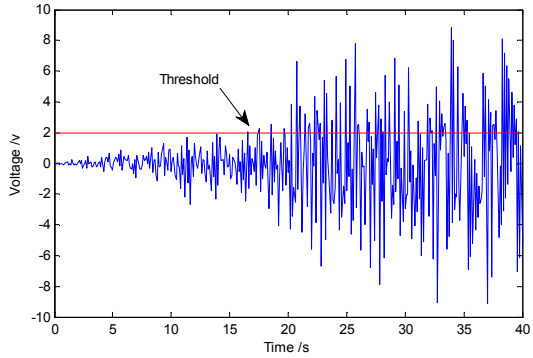


Fig.3 Acoustic emission waveform

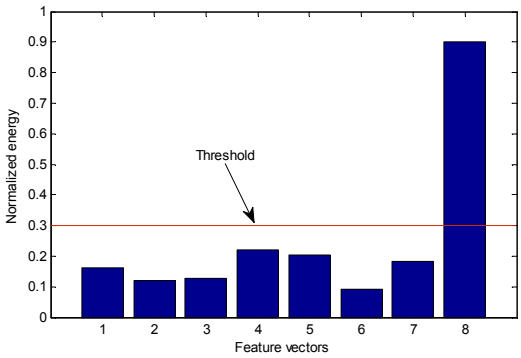


Fig.4 Acoustic emission signal feature

Metal fatigue fracture process is a very complex dynamic process of plastic accumulation of damage, using acoustic emission technology to monitor the process of the generation, development ad fracture of mental fatigue cracks. Compared with the traditional crack detection, acoustic emission not only achieve the real-time and dynamic monitoring of crack, but also get the similar results of fatigue crack extension rate curve in theory. Therefore, acoustic emission technique have a good prospect in mental fatigue fracture dynamic monitor, but the fatigue cracks estimates and fatigue life prediction remains to be further experimental research.

References

[1] Li Guang-hai, Liu Zheng-yi. “Based on the mental high-frequency fatigue acoustic emission monitoring” China Mechanical Engineering, vol.15, no.13, pp.1205-1209, 2004.

[2] Gong Z, DuQuesnay D L, McBride S L. “Measurement and Interpretation of Fatigue Crick Growth in 7075 Aluminum Alloy Using Acoustic Emission Monitoring” Journal of Testing and Evaluation, vol.26, no.6, pp.567-574, 1998.

[3] Zhou Jie, Mao Hanling，Huang Zhen-feng，Zeng De-liang “Acoustic emission technique for the detecting of metal fatigue fracture,” China Measurement Techology, vol.33, no. 3, pp. 7-9, 2007.

[4] Roberts T M, Talebzadeh M. “Acoustic Emission Monitoring of Fatigue Crack Propagation,” Journal of Construction Steel Research, vol.59, no. 6, pp.695-712, 2003.

[5] Geng Rong-sheng, Shen gong-tian, Liu shi-feng “Acoustic emission signal processing and analysis technology” *nondestructive test*, vol.24, no. 1, pp. 23-28, 2002.

[6] Yin Yong, Yu Hui-chun, Zhang Hong-chun. “A feature extraction method based on wavelet packet analysis for discrimination of Chinese vinegars using a gas sensors array,” *Sensors and Actuators B*, vol.134, no. 2, pp.1005-1009, 2008.

© (2012) Trans Tech Publications, Switzerland
doi:10.4028/www.scientific.net/KEM.488-489.436

The Study of AE and ESSPI Technique on the CBF Composite

Chang Zhongliang[1, a], Zou Guangping[1], Chen Si[1] and Chen Liang[1]

[1]College of Aerospace and Civil Engineering, Harbin Engineering University, Harbin 150001, China

[a]czl19820228@163.com

Keywords: CBF composite plate; non-destructive testing; ESSPI; AE technique.

Abstract. The CBF (continuous basalt fiber) composite as new and high mechanical property material have been widely applied in actual engineering. The composite material may inevitably occur all kinds of defects during fabrication and using, so in this paper, the AE (acoustic emission) and ESSPI (electronic shearography speckle pattern interferometry) technique are adopt to study the defects or damage of the CBF composite plate. The AE technique is adopted to detect the damage phenomenon of the CBF composit plate specimen tension experiment, and the ESSPI technique is adopt to study the defects of the CBF composite plate which its defects are made by artificial. From the experiment results it can be see that these techniques can detect the position and damage of the CBF composite plate, and these study can provide useful reference for the application of the CBF composite.

Introduction

The CBF (continuous basalt fiber)composite as new high mechanical property material have been widely applied in the actual engineering, and the component of the composite-CBF has many advantages, such as wide material sources, low cost, high-temperature resistance, acid-alkali resistance and electromagnetic wave transparent property, so the CBF composite have a broad application prospect in the fields of metallurgy, chemical engineering, construction and aerospace[1-3]. The CBF composite materials inevitably occur all kinds of defects during fabrication and using, such as fiber breakage, crack, bubble and delamination. These defects may generate stress concentration, it will decrease the strength of structure and lead to the failure of materials, what's more, it maybe lead to engineering accidents. So in this paper, the non-destructive testing method AE(acoustic emission) and ESSPI (electronic shearography speckle pattern interferometry) technique are adopt to study the defects or damage of the CBF composite plate. From the experiment results it can be see that these technique is very useful to detect the damage of the CBF composite plate.

AE Inspection of the CBF Composite Plate Tension Test

The AE is the physical phenomenon when the objects suffer the deformation and external forces, and his internal strain energy is quickly released by means of elastic waves. As a dynamic non-destructive testing technique, the AE can inspect on the accumulated damage about the materials deformation and invalidation, the AE technique has many advantage, such as real-time, high sensitivity, easy operation and so on[4-5]. In this paper, the INSTRON5505 electronic universal testing machine is used for testing the static tensile mechanical property of the CBF composite plate, and using the AE technique detect the acoustic emission phenomenon when the material is tension. The CBF composite plate which is made by laminate technology are used in the testing, the material's density is 1.886g/cm^3.

Testing and Analysis

Testing Specimen. According to GB/T 1447-2005, this standard provide the Ⅱ specimen which the length is 250 mm,the width is 25 mm, the thickness is 4 mm and bonding a 25 mm strengthening plate to its ends. The specimen parameters are shown as Fig.1.

Experiment instrument. The INSTRON5505 electronic universal testing machine is used for testing the tensile test. The AE detector which is made by PAC company is used for detecting the AE signal, and the strain gauge is used for detecting the strain of composite material tension..

Experimental Methods and Process. The electronic universal testing machine is used for testing the load-displacement curve and maximum load during the CBF composite plate tension process. Bonding 0/90 strain gage to the specimen surface to test the strain data. Installing the AE sensor to specimen, using the adhesive tape to fasten the AE probe and making the AEwin software of AE detector to output the AE signal and image. The experimental loading speed is 0.01mm/s, testing pattren is shown as Fig.2 and experiment schematic diagram is shown as Fig.3.

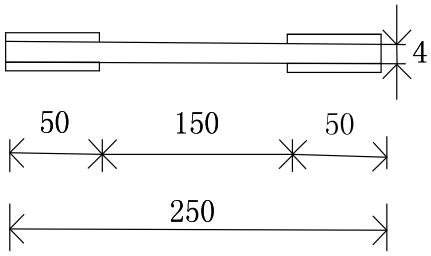


Fig.1 Specimen parameter



Fig.2 Testing pattern

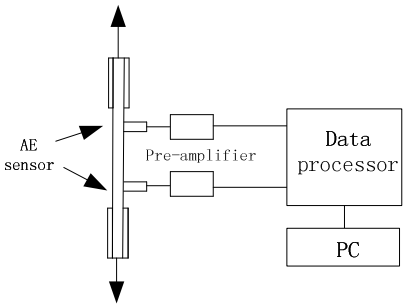


Fig.3 Testing schematic diagram

Experimental Result. By the tensile tesing, the typical load-displacement curve is shown as Fig.4. The maximum load is 28930N, the tensile strength is 289.30MPa. And bonding the strain gage to specimens, getting the elastic modulus is 38.34GPa, the Poisson's ratio is 0.11. The data graphs from AEwin software are shown in Fig5 and Fig6.

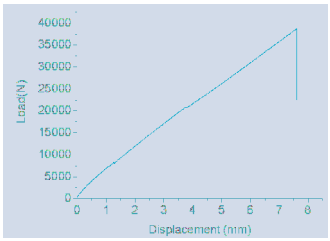


Fig.4 Load-displacement curve

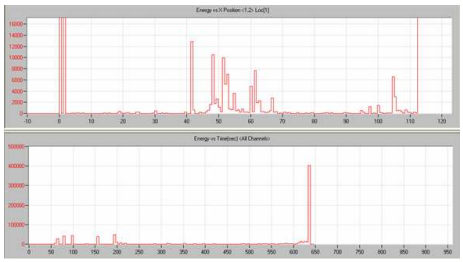


Fig.5 Energy-position curve(up) and energy-time curve(down)

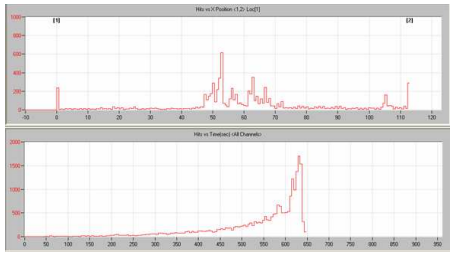


Fig.6 Hits-position curve(up) and hits-time curve(down)

Failure Analysis. From the load-strain curve of the CBF composite specimen during the tension test, the load-displacement curve is about proportion relationship, but it can be seen the fiber occur fracture during the test, the load-displacement curve is not severe proportion relationship. And form the AE data, the fracture can be divided into three stages.

The first stage is from 0 seconds to 300 seconds in Fig.5 and Fig.6, this stage has little the AE signal number and energy, and has barely increasing. The internal fibers of materials are fully on elastic stage. The second stage is from 300 seconds to 600 seconds in Fig.5 and Fig.6, in this stage the AE signal number is increasing with time and the AE energy is also increasing with signal number. At this time the internal fibers have been fractured, the fractured fibers also need other fibers to undertake the original load, so the fractured velocity of fibers is faster and faster. The third stage is from 600 seconds to end in Fig.5 and Fig.6, in this stage the growth rate of the AE signal numbers has obviously improved, the AE energy has radically increasing, at last the destructive materials produce enormous AE energy.

ESSPI Technique in the Non-Destructive Test of CBF Composite Plate

ESSPI is a new technique which measures the displacement derivative, it has many advantages, such as simple light path, low require of vibratory isolation, and it is very sensitive to the loading stress concentration of defects, ESSPI is a very good way to the non-destructive testing and strain measurement[6]. In this paper, the defected plate are simulated by making a hole ahead of time and detected the defected hole by ESSPI.

Testing Specimen. The first CBF composite plate thickness is 3 mm, and drilled three holes， their diameter is 8 mm, 6 mm and 4 mm respectively, and depth is 2 mm. The second plate thickness is 4 mm, and drilled three holes, their diameter is 8 mm, 6 mm and 4 mm respectively, and depth is 2 mm. The right side of the plate was sprayed coating to reduce the glaring shine marks. The spraying coating should be payed attention in order to get the best effect, the best process is that it should be sprayed white coating firstly, and sprayed the black coatings in the distance so that to make black coating flog fall on the plate slowly when the white coating has dried, the black coating can be equally covered half of the plates.

Experimental Equipment. The testing schematic diagram as shown in Fig.7, it consist of shearing prisma lens, lens, CCD, expander, laser, hair dryer, lamp, ruler. And the experiment equipment as shown in Fig.8.

Experiment Process and Results. According to the light path structure to adjust every equipment location, then put into the shearing prisma lens. Firstly there is a wood specimen which thickness is 10 mm and has a back hole which diameter is 10 mm and depth is 7-8 mm to check the light path. And then fix the wood specimen to workbench and confirm the hole within measured area. After close all light source without the laser, use the hair dryer to equally heat the holes, the screen may appear arc-shaped stripes which are shown as Fig.9 by capturing the pictures, the arc-shaped stripes are also called bull's eye stripe. The stripes can show the defect in the back of material.

The 8 mm hole of the first CBF plate is detected through this light path structure of ESSPI. The screen shows the defective bull's eye stripe which is shown as Fig.10 when the specimen is stopped heating, it is different to identify the stripe in the static picture but in the screen. The bull's eye stripe in a wood specimen is clearer than CBF composite plate specimen, the stripe picture is few number and quickly changeable, there are a lot of horizontal mobile stripes in the no defective location. The experimental data are shown as Table 4.1.

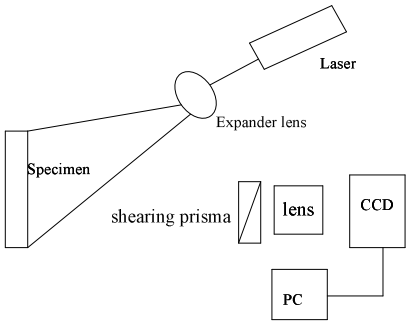


Fig.7 ESSPI experiment schematic diagram

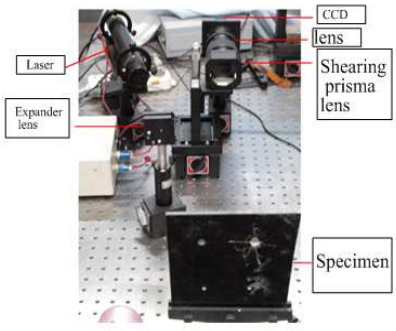


Fig.8 The ESSPI experiment equipment picture

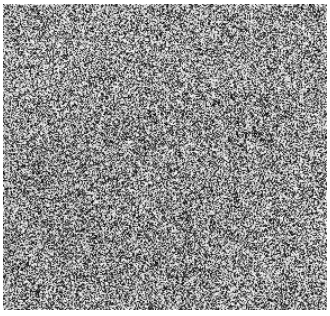


Fig.9 The bull's eye stripe of wood specimen

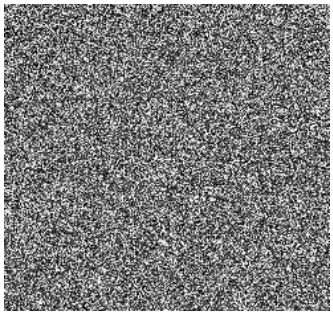


Fig.10 The bull's eye stripe of CBF composite plate

Table1 The holes' testing result of the first plate and the second plate

Materials' thickness	Defects' diameter	Defects' depth	Bull's eye stripe, clearness Yes or no
3mm	8mm	2mm	Yes, yes
3mm	6mm	2mm	Yes, general
3mm	4mm	2mm	No, no
4mm	8mm	2mm	Yes, general
4mm	6mm	2mm	Yes, no
4mm	4mm	2mm	No, no

Summary

In this paper, The electronic universal testing machine is used for testing the CBF composites plate tensile mechanical property, gained the tensile curve and used the AE detector to detect the AE signal during the tensile testing, according to the AE signal, analysed the fracture process of the CBF composite material. The experimental results show that the AE technique is very sensitive to the fracture signal of the CBF fibers and can monitor the internal damage condition of the CBF composite material. This is very suitable for engineering application. The ESSPI is used for detect the back defect of the CBF composite plate, this method is suitable for the CBF composite plate from the experimental stripes but the sensitivity is low,if the accuracy of ESSPI is ensured ,and the detected accuracy will be araise.

Acknowledgment

This work was supported by a grant from the Ph.D. Programs Foundation of Ministry of Education of China (No. 20092304110003).

References

[1] X.Q.Hu, Y.F.Luo, T.N.Shen: Hi-tech Fiber & Application,Vol. 27(2002),p.1-5.

[2] W. Li, X. Zhu, X.Q.Wang. Ordnance Material Science and Engineering,Vol.32 (2009),p.51-53.

[3] X.Q. Hu, T.N.Shen. Hi-tech Fiber & Application, Vol. 30(2005),p.7-13.

[4] S.L.Yang, J.Liu, D.M. Yang, X.F. Yin: Nonde structive testing. Vol. 22(2000),p.303-306.

[5] Z.K Wang. Journal of Textile Research, Vol.28(2007),p. 52-55.

[6] G.P. Zou, J. Lu, W.W.Wang. Journal of Harbin Engineering University Vol. 30 (2009),p.357-361.

© (2012) Trans Tech Publications, Switzerland
doi:10.4028/www.scientific.net/KEM.488-489.440

Interaction of SH-wave on Multiple Linear Cracks near Shallow-embedded Structure

Zailin Yang[1,2a], Huanan Xu[1,b], Meijuan Xu[1,c] and Baitao Sun[2,d]

[1]College of Aerospace and Civil Engineering, Harbin Engineering University, Harbin, 150001, China

[2]Institute of Engineering Mechanics, China Earthquake Administration, Harbin, 150080, China

[a]yangzailin00@163.com, [b]hntiger_86@126.com, [c]meijuan242@163.com, [d]sunbt@iem.net.cn

Keywords: scattering of SH-wave, multiple cracks, circular lining structure, Green's function, surface displacement

Abstract. The surface displacement of a circular lining structure and multiple cracks in an elastic half space by incident SH-wave is studied in this paper based on the methods of Green's function, complex function and multi-polar coordinates. Firstly, we construct a suitable Green's function which indicates a fundamental solution to the displacement field for an elastic half space possessing a circular lining structure and cracks while bearing out-plane harmonic line loads at arbitrary point. Then using the method of crack-division, a crack is created. Thus expressions of displacement and stress field are established at the existence of the structure and the cracks. Finally, the interaction of inclusion and two cracks is chosen as numerical examples and the influences of different parameters on the surface displacement are discussed.

Introduction

Since nature is in eternal motion and change, the media, artificial materials or structures inevitably produce various defects and uneven distribution of the formation also give rise to large amounts of heterogeneity, such as small faults, joints, multiple lens, etc., which distribute arbitrarily. These structures with diverse distribution can be simplified to be cracks in engineering practice. Therefore, it is of great significance to study interaction of subsurface structures and cracks. In this paper, the blast-resistance problems of underground structure can be regarded as the problem of SH-wave scattering caused by a circular lining structure and multiple cracks in elastic half-space.

Statement of the Problem

The infinite half space model with a circular lining structure and multiple cracks impacted by SH-wave is shown in Fig.1. There are different material constants $(\rho_1, \mu_1;\ \rho_2, \mu_2)$ of two different media. Some coordinates are established and the connection of them is given by

$$x' = x \qquad y' = y - h$$

$$x_1 = x\cos\beta_1 + y\sin\beta_1,\ y_1 = y\cos\beta_1 - x\sin\beta_1,\ h_{11} = \frac{\left(h_1 + b_1\sin\beta_1\right)}{\cos\beta_1} \tag{1}$$

$$x_n = x\cos\beta_n + y\sin\beta_n,\ y_n = y\cos\beta_n - x\sin\beta_n,\ h_{nn} = \frac{\left(h_n + b_n\sin\beta_n\right)}{\cos\beta_n}$$

The Scattering Waves around the Circular Lining Structure

Governing equation. This problem can be seen as the problem of blast resistance. In an isotropic medium, the scattering of SH-wave is the easiest problem of the study on scattering of elastic wave. The displacement $W(x, y, t)$ impacted by the incident wave is vertical to xy plane and irrespective with z axis, which should satisfy the governing equation [1, 2]

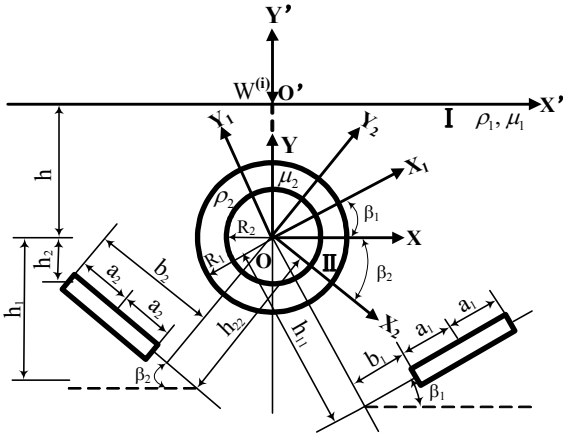


Fig.1.The infinite half space model with a circular lining structure and a crack under impact load

$$\frac{\partial^2 W}{\partial x^2}+\frac{\partial^2 W}{\partial y^2}+k^2 W=0 \tag{2}$$

in which, $k=\omega/c_s$, ω is the circular frequency of the displacement function, $c_s=\sqrt{\mu/\rho}$ stands for the velocity of the shear wave. ρ and μ are the mass density and shear modulus of the medium respectively.

In the polar coordinate, the corresponding stresses are given by

$$\tau_{rz}=\mu\left(\frac{\partial W}{\partial z}e^{j\theta}+\frac{\partial W}{\partial \bar{z}}e^{-i\theta}\right),\tau_{\theta z}=i\mu\left(\frac{\partial W}{\partial z}e^{j\theta}-\frac{\partial W}{\partial \bar{z}}e^{-i\theta}\right) \tag{3}$$

The scattering wave in the district Ⅰ. According to the symmetry of the scattering wave and multi-polar coordinates, the scattering wave in the medium induced by the circular lining structure can be constructed, which should satisfy the governing equation (2) and the radiation condition for infinite distance beside the stress free condition on the horizontal interface[3,4].

In the complex plane $(z,\bar{z})$, $G_{\mathrm{I}}^{(s)}$ can be expressed as

$$G_{\mathrm{I}}^{(s)}=\sum_{n=-\infty}^{\infty}A_n\left\{H_n^{(1)}\left(k_1|z|\right)\left[\frac{z}{|z|}\right]^n+H_n^{(1)}\left(k_1|z-2hi|\right)\left[\frac{z-2hi}{|z-2hi|}\right]^{-n}\right\} \tag{4}$$

where A_n are the unknown coefficients, which are determined by the boundary condition of the circular lining structure.

The scattering wave in the district Ⅱ. In the complex plane $(z,\bar{z})$, the scattering wave inside of circular lining structure can be expressed as

$$G_{\mathrm{II}}^{(s)}=\sum_{n=-\infty}^{\infty}B_n\left\{H_n^{(2)}(k_2|z|)\left(\frac{z}{|z|}\right)^n\right\}+\sum_{n=-\infty}^{\infty}C_n\left\{H_n^{(1)}(k_2|z|)\left(\frac{z}{|z|}\right)^n\right\} \tag{5}$$

where B_n and C_n are the unknown coefficients, which are determined by the boundary condition of the circular lining structure.

Green's Function

The Green's function G denotes an essential solution to the displacement field for an elastic half-space possessing a circular lining structure and multiple cracks with arbitrary length and arbitrary position while bearing out-plane harmonic linie loads at arbitrary point, which is expressed as $e^{-i\omega t}$ and satisfies the governing equation (2).

In a half elastic space, the incident wave $G^{(i)}$ excitated by the out-plane line loads takes the form of

$$G^{(i)}=\frac{i}{4\mu_1}H_0^{(1)}\left(k_1|z'-z_0'|\right)+\frac{i}{4\mu_1}H_0^{(1)}\left(k_1|z'-\bar{z}_0'|\right) \tag{6}$$

In the complex plane $(z,\bar{z})$, the boundary condition can be expressed as

$$G^{(i)}+G_{\mathrm{I}}^{(s)}=G_{\mathrm{II}}^{(s)},r=R_1\qquad \tau_{rz}^{(i)}+\tau_{rz,\mathrm{I}}^{(s)}=\tau_{rz,\mathrm{II}}^{(s)},r=R_1\qquad \tau_{rz,\mathrm{II}}^{(s)}=0,r=R_2 \tag{7}$$

Substitution of Eqs.(4)to(6) into Eq.(3), the stresses from $G^{(i)}$, $G_{\mathrm{I}}^{(s)}$ and $G_{\mathrm{II}}^{(s)}$ can be derived, then substituting these expressions into boundary conditions (7), the coefficients A_n,B_n,C_n will be solved.

The total wave field is

$$G_0 = G^{(i)} + G_{\mathrm{I}}^{(s)} \tag{8}$$

Then the total stresses can be performed. If the additional stresses with the same magnitude and opposite direction as the total stresses are applied at the same point, the ultimate stresses will be zero. Therefore, when a pair of forces with the same magnitude and opposite direction is loaded at the region where the crack will appear, the resultant forces at the region are zero, which can be thought as a crack.

$$G_1 = G_0 - \int_{(b_1,-h_{11})}^{(2a_1+b_1,-h_{11})} \tau_{\theta z,0} G_0 dz_1 \tag{9}$$

in which, $\tau_{\theta z,0}$ is the force with the same magnitude and opposite direction as the force caused by G_0 loaded at the region where the crack will appear.

In the same way, the Green's function of multiple cracks G_n can be solved.

$$G_2 = G_1 - \int_{(b_2,-h_{22})}^{(2a_2+b_2,-h_{22})} \tau_{\theta z,1} G_1 dz_2 \tag{10}$$

$$G_n = G_{n-1} - \int_{(b_n,-h_{nn})}^{(2a_n+b_n,-h_{nn})} \tau_{\theta z,n-1} G_{n-1} dz_n \tag{11}$$

Scattering of SH-wave by Circular Lining Structure and Cracks near the Interface

As shown in Fig.1, the incident steady SH-wave defined as $W^{(i)}$ can be given by

$$W^{(i)} = W_0 e^{-i(k_1 y' + \omega t)} \tag{12}$$

where W_0 is amplitude of incident wave.

The scattering waves $W_{\mathrm{I}}^{(s)}$ and $W_{\mathrm{II}}^{(s)}$ excited by the elastic circular lining structure can be described as Eqs.(4) and (5), respectively. And the process of solving A_n, B_n and C_n is the same as that of the Green's function discussed in preceding paper.

Then, the total wave field in domain I is

$$W_0^{(t)} = W^{(i)} + W_{\mathrm{I}}^{(s)} \tag{13}$$

Based on the above theoretical derivation, the total wave field in domain I can be obtained when two cracks coexist:

$$W_2^{(t)} = W^{(i)} + W_{\mathrm{I}}^{(s)} - \int_{(b_1,-h_{11})}^{(2a_1+b_1,-h_{11})} \tau_{\theta z,0} G_0 dz_1 - \int_{(b_2,-h_{22})}^{(2a_2+b_2,-h_{22})} \tau_{\theta z,1} G_1 dz_2 \tag{14}$$

Results and Discussion

The interaction of inclusion and two cracks is chosen as numerical examples here to discuss the effects of various parameters on the horizontal surface displacement. The expressions of horizontal surface displacement is given by Eq. (14).

Figs.2 to 5 give the graphical results of horizontal surface displacement. Fig.2 shows that the horizontal surface displacement amplitudes decrease rapidly and tend to be stable as h/R_2 increases. Fig.3 illustrates the trend of the surface displacement amplitudes can be seen intuitively from the figure, the vicinity of $X/R_2 = 0$ has the stronger response, it can be seen that as the wave number increases, the horizontal surface displacement amplitudes first increase and then decrease.

In Fig.4, it can be seen that the horizontal surface displacement amplitudes have the strongest response near $X/R_2 = 0$, and decrease rapidly and then tend to be stable as h_2/R_2 increases.

From Fig.5, we can see that the displacement amplitudes increase and then get smaller and smaller increase with the increasing of μ_1/μ_2.

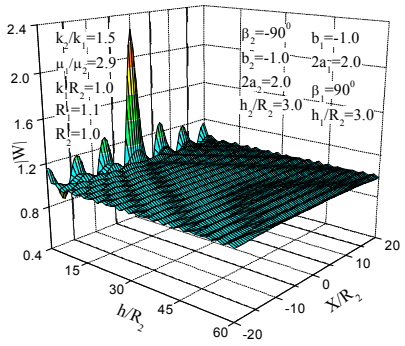


Fig. 2. The displacement changes with h / R_2 when SH-wave incident from upside

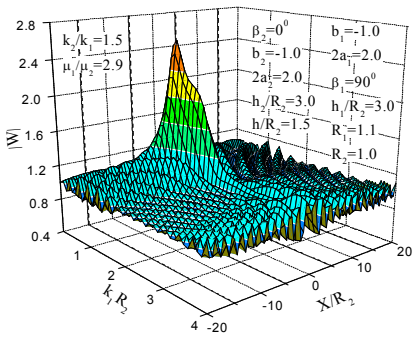
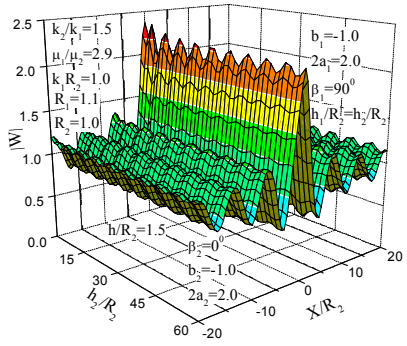
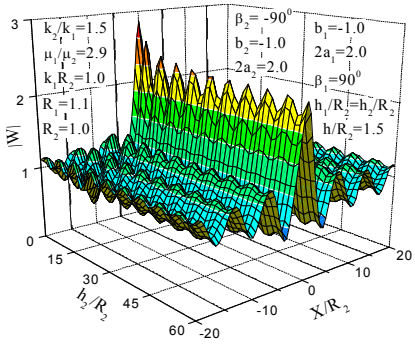


Fig.3. The displacement changes with $k_1 R_2$ when SH-wave incident from upside

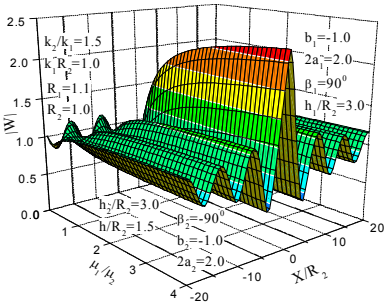


a

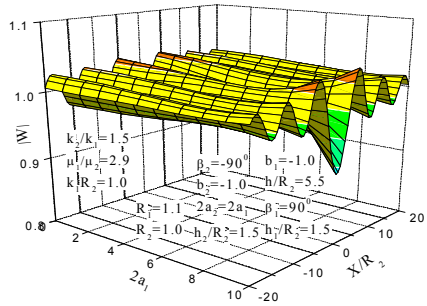


b

Fig. 4. The horizontal surface displacement changes with h_2 / R_2 when SH-wave incident from upside



a



b

Fig. 5. The horizontal surface displacement changes with μ_1 / μ_2 and $2a_1$ when SH-wave incident from upside

Acknowledgement

This Work was Supported by National Natural Science Foundation of China (No. 10972064), Key Laboratory of Earthquake Engineering and Engineering Vibration, China Earthquake Administration (No. 2009A06) and Key Laboratory of Damping Control and Structure Security, Guangzhou University (No. gzuf200905).

References

[1] Pao Yih-hsing: submitted to Applied Mechanics Review. (1998)

[2] Pao Y H, Mow C C: *Diffraction of Elastic Wave and Dynamic Stress Concentration* (Crane and Russak, New York, 1973).

[3] Zailin Yang, Peilei Yan: submitted to Journal of Key Engineering Materials (2008).

[4] Zailin Yang, Peilei Yan, and Diankui Liu: submitted to Acta Mechanica Sinica (2009).

© (2012) Trans Tech Publications, Switzerland
doi:10.4028/www.scientific.net/KEM.488-489.444

Numerical Simulation of Multiple Fatigue Crack Growth with Additional Crack Initiation

D. Holländer[1,a], M. Wünsche[2,b], S. Henkel[3,c] and H. Theilig[4,d]

[1]Faculty of Mechanical Engineering, Technische Universität Dresden, Germany

[2]Faculty of Science and Technology, University of Siegen, Germany

[3]Institute of Materials Engineering, Technische Universität Bergakademie Freiberg, Germany

[4]Department of Mechanical Engineering, University of Applied Sciences Zittau/Görlitz, Germany

[a]dirk.hollaender@tu-dresden.de, [b]wuensche@bauwesen.uni-siegen.de[c]henkel@ww.tu-freiberg.de, [d]h.theilig@hs-zigr.de

Keywords: multiple crack systems, crack path simulation, plastic limit load, failure assessment diagram, Smith-Watson-Topper parameter

Abstract. In this paper, advanced numerical simulations of curved crack growth in the case of multiple crack systems in combination with the analysis of the plastic limit load by the lower bound theorem of plasticity are presented. In order to take additionally initiated cracks during the crack growth process into account, the numerical simulation algorithm has been extended by using the Smith-Watson-Topper (SWT) parameter in combination with a linear fatigue damage accumulation.

Introduction

The numerical simulation of crack propagation is one of the important tasks in engineering applications. The obtained results have a direct relevance on the safety as well as the optimization of real components and structures. Especially the defect assessment methods are getting increasing attention in industrial regulations and standards. The program PCCS-2D has been successfully developed to analyse the crack growth and the plastic limit load at each crack simulation step automatically. It has been shown, that the proposed solution algorithm provides a powerful tool for flaw assessment with the FAD-procedure in combination with a numerical crack path simulation [1]. It is well known that additionally cracks can be initiated during the crack growth process and therefore an advanced numerical simulation algorithm is required to consider such problems in a fully automatic analysis. Numerical results of multiple crack growth under biaxial proportional loading are presented and compared with experimental findings in order to show the accuracy and the efficiency of the proposed algorithm.

Failure assessment diagram

An assessment point with the parameters $K_r = K/K_{mat}$ and $L_r = \sigma/\sigma_e$ is compared in the failure assessment diagram (FAD) with the failure line calculated from the material tensile properties. K is the stress intensity factor. In the case of an initial mixed mode loading the equivalent stress intensity factor K_{eq} should be taken while the K_I stress intensity factor is applied for a pure mode-I situation. On the other side the tensile stress σ is the loading of the component and σ_e defines the corresponding plastic limit load [2].

Crack path simulation

The numerical simulation of the crack propagation is done with a well-founded fracture mechanical predictor-corrector method based on the criterion of the local symmetry. This simulation concept fulfils the geometric conditions on crack growth by the use of a quadratic form function for the increments. Further it allows a fully automatically computation of the crack paths for a system of multiple growing cracks with compatible crack increments of the simulated crack trajectories [1].

Computation of the plastic limit load

For the practical use of the FAD it is necessary to compute the L_r parameter as a measure of plasticity effects. As a consequence the global plastic limit load σ_e has to be computed for an elastic-perfectly plastic material model with the lower bound theorem of plasticity and only primary loads are taken into account. In the numerical simulation a simple iterative solution strategy for proportional loading systems has been implemented in a special module of the PCCS-2D within the FE-code ANSYS. In the investigated 2D problems plane stress and the von Mises plasticity are taken into account. The plastic limit load is evaluated from the characteristic non-linear load-deformation curve. The CTOD of the crack tip with the maximum stress intensity factor is chosen as the deformation parameter. Based on the calculated elastic slope a plastic slope criterion is used.

SWT parameter and linear fatigue damage accumulation

In order to take additionally initiated cracks in the numerical solution into account, a damage model in combination with a linear fatigue accumulation is implemented in the PCCS-2D. In the present work the Smith-Watson-Topper (SWT) parameter based on the mechanism of the Coffin-Manson relationship is used for lifetime predictions [4]. The model includes the influence of cyclic mean stress and is described by

$$P_{SWT} = \sqrt{\sigma_{max}\varepsilon_{a,t}E} = \sqrt{(\sigma_a + \sigma_m)\varepsilon_{a,t}E} \tag{1}$$

with $\varepsilon_{a,t}$ as the total mechanical strain amplitude. E is the Young's modulus, σ_{max} is the maximum stress, calculated from the stress amplitude σ_a, and σ_m is the mean stress. In combination with the Wöhler line for variable middle stress and strain P_{SWT} is defined by

$$P_{SWT} = \sqrt{\sigma_f'^2(2N)^{2b} + \varepsilon_f'\sigma_f'E(2N)^{(b+c)}} \tag{2}$$

with σ_f', ε_f', b, c and N being the fatigue strength coefficient, the fatigue ductility coefficient, the fatigue strength exponent, the fatigue ductility exponent and the number of the cycles.The damage degree D according to the Palmgren-Miner hypothesis is defined as the sum of the cumulative damage fractions D_i with

$$D = \sum_i \Delta D_i = \sum_i \frac{n_i}{N_i}, \tag{3}$$

where n_i is the number of the applied cycles and N_i is the number of the cycles to failure. Crack initiation is assumed at D = 1.

Numerical and experimental results

In the following, numerical results are presented and compared with experimental findings to show the influence of the additionally initiated cracks on the crack paths and the FAD.

In the experimental investigations the crack observation was done optically by a high-resolution scanner camera system which is suitable to observe the specimen area of 120 x 120 mm with a resolution of 10,000*10,000 pixels. The high-resolution photographs are also suitable for the determination of crack lengths of curved cracks [2]. The considered planar biaxial sample (aluminum alloy 6061 T 651) and the crack propagation after 23,085 cycles are shown in Fig. 1. The sample failed after 23,098 cycles. The two initial cracks were inserted by EDM as slits with a thickness of 0.4 mm and length of 10 mm.

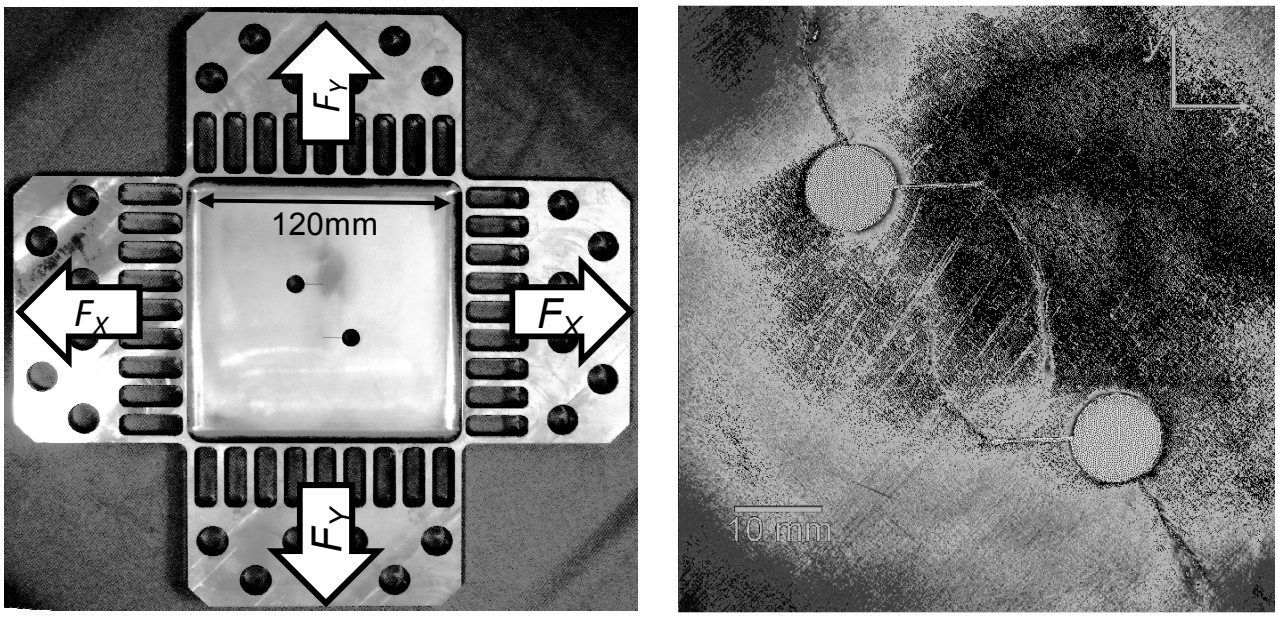
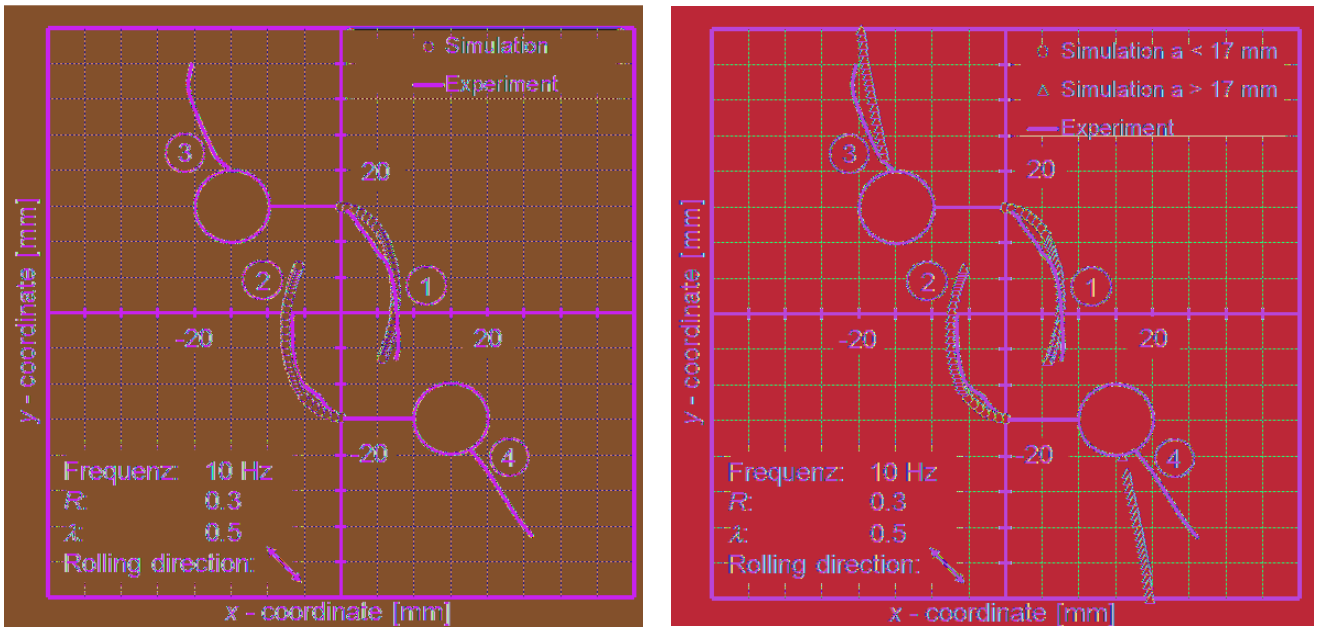


Fig. 1: Planar biaxial sample with starting notches and crack propagation after 23,085 cycles



a) b)

Fig. 2: Experimental and simulated crack paths without (a) and with consideration (b) of the two additionally initiated cracks

In the numerical simulation of the crack paths with PCCS-2D the quadratic element PLANE183 was chosen together with a crack extension increment $\Delta a_{max} = 0.5$ mm. The additionally initiated cracks were modeled with $a_0 = 1.5$ mm full automatically at $a_{1,2} = 17$ mm where D = 1 is obtained. Fig. 2 shows the comparison of the experimental and simulated crack paths without and with consideration of the two additionally initiated cracks. The results indicate a good accordance.

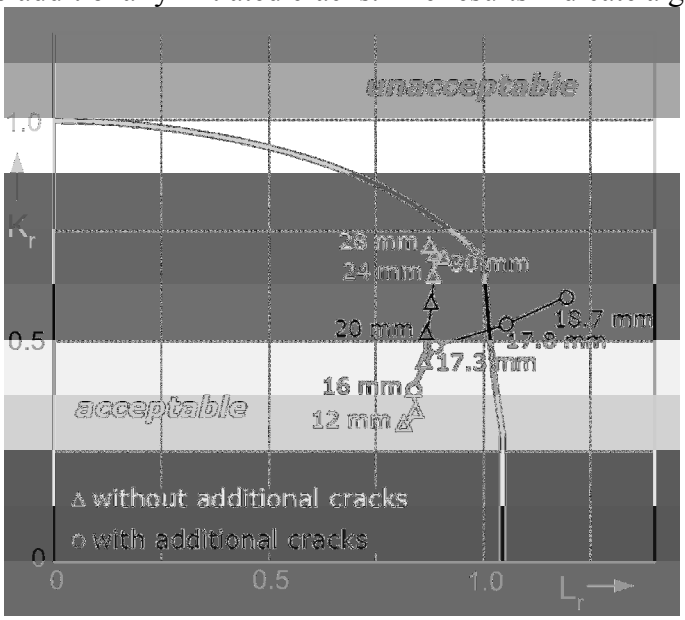


Fig. 3: Failure assessment diagram (crack 1 and 2) without and with consideration of the two additionally cracks

The numerical simulation of the crack paths without consideration of the additionally cracks leads always to save points (K_r, L_r) in the FAD. In contrast the consideration of the additionally cracks shows unacceptable points for crack lengths $a_{1,2} > 17.6$ mm, as clearly seen in Fig. 3.

Summary

The paper presents the numerical crack path simulation by taking into account additionally initiated cracks during the crack growth process in a fully automatic procedure. In the present simulation, the Smith-Watson-Topper (SWT) parameter in combination with a linear damage accumulation has been applied for this purpose. First numerical and experimental examples are presented and discussed.

References

[1] Theilig, H., Holländer, D., Wünsche, M.: Key Engineering Materials Vols. 417 - 418 (2009), pp. 45 - 48.

[2] Henkel, S., Holländer, D., Wünsche, M., Theilig, H., Hübner P., Biermann H., Mehringer S: Engineering Fracture Mechanics Vol. 77 (2010), pp. 2077 - 2090.

[3] Forschungskuratorium Maschinenbau: *FKM Richtlinie Bruchmechanischer Festigkeitsnachweis für Maschinenbauteile,* VDMA - Verlag GmbH (2006).

[4] Radaj, D., Vormwald, M.: *Ermüdungsfestigkeit, Grundlagen für Ingenieure,* Springer-Verlag Berlin Heidelberg (2007).

© (2012) Trans Tech Publications, Switzerland
doi:10.4028/www.scientific.net/KEM.488-489.448

Study on Damage Parameters and Its Size Effect of Concrete by Tension Test

Wang Xiangdong[1a]; Wang Yuefeng[1b]; Wang Yan[1]; Wu Yongjin[1]; Hua xi[1]

[1]Department of Engineering Mechanics, Hohai Univ., Nanjing 210098, China
[a]wwang90@sohu.com, [b]wyf20054005@qq.com

Key words: concrete; tension; damage; size effect; damage parameters

Abstract. The carrying capacity decreases continuously as the material property deteriorates under the action of some external factors. It is important to evaluate the damage of concrete, in which the damage parameter plays an important role. An experimentation method is designed in this paper, with which we can simulate the initial damage by mixing initiator into concrete. Using the elastic modulus of axial tension experimentation, the tension initial damage D0 and tension damage Peak value Df have been gained. The Size effect of concrete tension damage parameters is verified. The curve of damage-parameters and size is gained, the trend of the tension damage parameters is obtained.

Introduction

Concrete is one of the most important materials in contemporary civil engineering，which is widely used in civil engineering, hydraulic engineering and other fields[1]. Concrete is a multi-phase material, which consists of cement, aggregate and sand. There exists inevitably initial damage in concrete when the concrete structure is constructed, because of hydration heat, overflowing influence and so on. Additionally, the micro-cracks will happen on the interface of mortar and aggregate. Under the continuous external loading, these micro-cracks will extend and converge, and further become the macro-cracks. Meanwhile, new micro-cracks will be formed around these macro-cracks. Finally, the quality of concrete will be degraded severely[2]. It's well known that damage of concrete results in the degradation of the concrete property in concrete structure, which plays an important role in mechanics and actual engineering [3].

The carrying capacity decreases continuously as the material property deteriorates under the action of some external factors. Concrete is a damage field. It is necessary to consider the cumulative damage when we study on the reliability of structures. It is important to evaluate the damage parameters used in the actual structures because the damage parameters are essential in damage calculation. An experimentation method has been designed, which can simulate damage by mixed initiator into concrete. Using the elastic modulus of axial tension experimentation, the undamaged elastic modulus can be obtained. Then the initial damage D0 and damage Peak value Df of concrete in axial tension have been gained. It is unreasonable that the damage parameters of small concrete specimens are used for hydraulic structures and other mass concrete structures directly, for damage parameters have size effect. In this paper, concrete tension specimens in different sizes have been studied, the relation of tension damage parameters and size is gained, the trend of the tension damage parameters obtained. The size effect of concrete damage parameters is verified on the samples in different size. The damage parameters in any size of concrete structure can be determined through the size effect relation, which can be widely used in actual structures.

The principle of of analysis

According to Lemaitre Theory[4], the strain of damage material owing to the stress is equal to the strain of undamaged material owing to the effective stress. So we can use elastic modulus to express the damage parameter of concrete.

$$D = 1 - \tilde{E} / E \qquad (1)$$

Where E is the undamaged elastic modulus of concrete, $\tilde{E}$ is the elastic modulus of concrete.

We mixed air-entraining additive so as to form the different sizes of gaps in concrete. In this method, there exit many tiny air bubbles in concrete. These bubbles will reduce the effective area of concrete and result in damage. Through the tensile test of concrete with different quantity of air-entraining additive, we may fit the relation between the degree of damage and the quantity of air-entraining additive. Being based on this relation, we can calculate the elastic modulus of the concrete without air-entraining additive in theory, and further define this elastic modulus as undamaged initial elastic modulus E.

Test results and discussion

First the un-standard samples in size of 200*200*800 mm3 are made. The different elastic modulus of concrete with different quantity of air-entraining additive is shown in table 1

Table1 The modulus of concrete samples

NO	Quantity of additive (% of cement)	Elastic modulus(GPa)
1	0	30.38
2	0.1%	28.97
3	0.2%	27.36
4	0.3%	27.10

We can find that the elastic modulus of concrete without additive is larger than others. With the quantity of air-entraining additive X increasing, the elastic modulus E decreases gradually. The relation between E and X is confirmed by eq (2) and the curve is shown in Fig.1

$$E(x) = 9.94e^{-16.1x} + 26.61 \qquad (2)$$

In theory, E(0) is the elastic modulus of concrete without air-entraining additive, this elastic modulus is undamaged initial elastic modulus E, which is 36.55 GPa. So we can get the initial damage of concrete by eq(1) :

$$D_0 = 1 - \tilde{E}_0 / E = 1\text{-}33.01/36.55 = 0.097$$

The elastic modulus correspond to the Peak stress is 29.2 GPa, so we can get the Peak damage by eq(1):

$$D_f = 1\text{-}\frac{\tilde{E}_f}{E} = 1\text{-}29.2/36.55 = 0.201$$

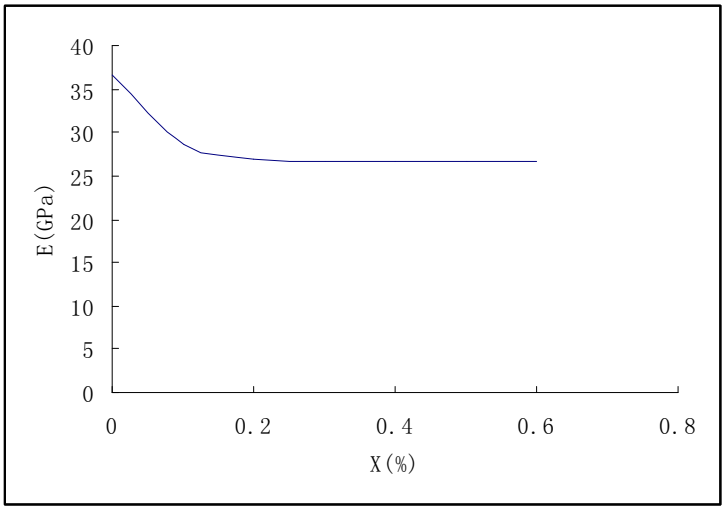


Fig1. Relation between elastic modulus and quantity of additive

In this tension test, there are concrete samples in three different sizes. The results are shown in table2.

Table2 Damage parameters of concrete samples with different sizes

Size/ mm^3	100*100*400	150*150*600	200*200*800
Initial damage D_0	0.054	0.079	0.097
Peak damage D_f	0.118	0.166	0.201

Size effect of initial damage and Peak damage

From literature [5] we know the formula about the size effect of initial damage

$$(1-D_{OL})/(1-D_{OS})=E_L/E_S \tag{3}$$

WhereD_{0L} is the initial damage of large concrete samples while D_{0S} is small. E_L is the initial elastic modulus of large concrete samples while E_S is small one.

With the data given by table 2, we can verify formula (3), and we can extrapolate initial damage of larger size concrete samples. Table 3 shows the results:

Table3 The initial damage of concrete samples

Size / mm^3	100*100*400	150*150*600	200*200*800	300*300*1200	450*450*1800
Initial damage D_0	0.054	0.079	0.097	0.122	0.146

Formula about size effect of damage threshold is given by literature [5]

$$(1-D_{fl})/(1-D_{fs})=(V_s/V_l)^{\frac{1}{\partial}} \tag{4}$$

Where D_{fl} is Peak damage of large concrete samples，D_{fs} is that of small one. V_S is volume of small concrete samples while V_L is that of large one. α is a statistical constant[6].

With the data given by table 2, we can verify formula (4), and we can extrapolate Peak damage of larger size concrete samples. Table 4 shows the results

Table4 The damage threshold value of concrete samples

Size / mm^3	100*100*400	150*150*600	200*200*800	300*300*1200	450*450*1800
Peak damageD_f	0.118	0.166	0.201	0.250	0.298

Conclusions

In this study, the tension experiment is done, which are not only the standard size samples but also un-standard size samples. The size effect of concrete tension damage parameters has been verified by comparing the results of concrete samples in different size. The damage parameters of samples in larger size are determined by the relation of tension damage parameters. The study results provide some reference for damage analysis of actual structure.

Acknowledgements

This work is supported by the National Nature Science Foundation of China (50878077)

This work is supported by the National Science and Technology Supporting Plan(2008BAB29B03)

References：

[1]Wang Xiandong: Study on initial damage of concrete, Key Engineering Materials, 2009, 418:633-636

[2]Wang Xiandong: Application of Concrete Damage Theory in the Simulation of Hydraulic Structure, Hohai University,2004,3

[3]Yu Tianqin, Qian Jicheng: Damage Theory and its Application (in Chinese), Press of National Defence and Industry 1993,50-100.

[4]Lemaitre J,Chabocha J L. a nonlinear model of creep fatigue damage cumulation and interaction.proe IUTAM,Symp of Mechauics of Viscoelastic Media and Bodies,Springs-Verlay,Gethenbure,1974.

[5]Wang Xiandong: Size effect of damage parameters of concrete structures. Journal of Hefei University of Technology,2005,28(3):308-310

[6]SL/T191—96，Design code for hydraulic concrete structures

© (2012) Trans Tech Publications, Switzerland
doi:10.4028/www.scientific.net/KEM.488-489.452

Elastic-viscoplastic Field At The Mixed-mode Crack-Tip Under Compression And Shear

Liang Wenyan[1, a], Wang Zhenqing[2,b] and Liu Fang[3,c]

[1]Smart Structures and Advanced Composites Laboratory, College of Aerospace and Civil Engineering, Harbin Engineering University, Harbin 150001, China

[a]liangwenyan@hrbeu.edu.cn, [b]wangzhenqing@hrbeu.edu.cn, [c]liufang@hrbeu.edu.cn

Keywords: mixed-load parameter; interface crack; viscosity; dynamic propagation;

Abstract. In the present paper, the mechanical model of dynamic propagation interface crack of the compression-shear mixed mode is proposed by using the elastic-viscoplastic constitutive model. Then the governing equations of propagation crack interface at crack tip are given. The numerical analysis is accomplished for the interface crack of compression-shear mixed mode by introducing a displacement potential function and some boundary conditions at interface crack tip. The distributed regularities of stress-strain fields of interface crack tip are discussed with several special parameters. The numerical results show that the viscosity effect is a main factor of interface propagating at crack-tip field, and the interface crack-tip is a viscoplastic field that is governed by viscosity coefficient, Mach number and singularity exponent.

Introduction

Williams[1] researched the isotropic bi-material interface crack problems with the asymptoticseries expansion method in 1959. Moreover, the oscillatory singularity ($r^{-1/2\pm i\delta}$) for stress field and singularity ($r^{1/2\pm i\delta}$) for displacement field were found near the crack tip. Viggo Tvergaard[2] analyzed the resistance curves for crack growth along an interface joining two elastic–plastic solids numerically, under conditions of small scale yielding. His work showed that for mode II crack plastic flow near the crack tip results in much larger resistance to crack growth. In consideration of the stress coupling, his analysis result had better accuracy. Then the fracture problems for non-uniform composite materials under the dynamic loads were solved. Chen and Lardner[3] used continuous distribution dislocations to simulate the cracks by applying the dislocation theory. They got the stress intensity factors near the interface by solving the singular integral equations. Shiyong Sun and Haoran Chen[4] studied sandwich beams with a viscoelastic interface crack under quasi-static and dynamic loading,. The numerical results show that the oscillating characteristic of dynamic J-integral is more evident with shorter loading rise time.The paper pointed out that the singularity index and the oscillation index were not only concerned with the material parameters, but also with the load frequencies. Ricci et al.[5] conducted an experimental study, in which the strain fields were used to investigate the behavior of subsonic crack propagation along the interface of anisotropic-orthotropic biomaterial system. The most research on the interface problems is concentrated in such areas as elastic, elastic-plastic and viscous, whereas the study of elastic-viscoplastic material is given less attention.

Formulation equations

The mechanical model of steady-state growing interface crack of the compression-shear mixed mode is shown in Fig.1. $X_\alpha(\alpha=1,2)$ denotes fixed plane coordinate system. Assume that a semi-infinite interface crack propagates along X_1 with constant velocity V between

elasto-viscoplastic material I which occupies zone I and rigid material II which occupies zone II. X_2 is vertical to the crack plane. For the steady-state growing crack, the material derivative of one physical quantity Ω in crack-tip field is

$$\dot{\Omega} = \frac{d\Omega}{dt} = -V\frac{\partial \Omega}{\partial x} = V\left(\frac{\sin\theta}{r}\frac{\partial}{\partial\theta} - \cos\theta\frac{\partial}{\partial r}\right)\Omega. \tag{1}$$

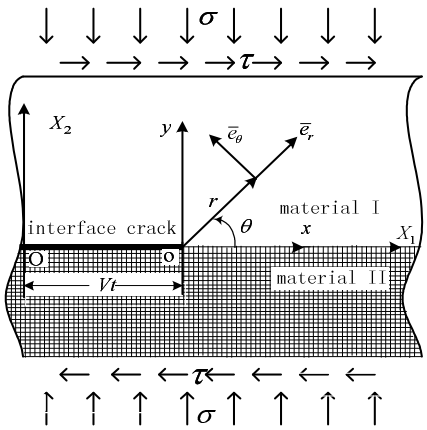


Fig.1 Mechanical model of Interface Mode I in Double Dissimilar Materials

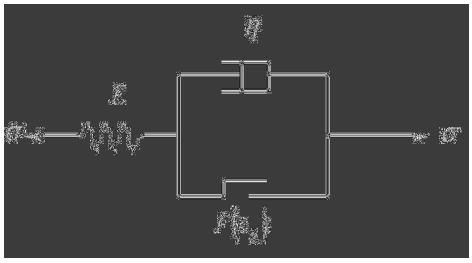


Fig.2 Elastic-viscoplastic constitutive model

Assume that the viscosity at crack-tip is related to the strain rate. Therefore, the viscosity coefficient η is as following

$$\eta = C\left(\dot{\bar{\varepsilon}}_p\right)^{-\beta} \quad (0<\beta<1). \tag{2}$$

Where C is a non-negative constant. The elastic-viscoplastic constitutive model is shown in Fig.2. After finishing operation, the three-dimensional elastic-viscoplastic constitutive equation of perfect plastic material is

$$\dot{\varepsilon}_{ij} = \frac{1+\nu}{E}\dot{\sigma}_{ij} - \frac{\nu}{E}\dot{\sigma}_{kk}\delta_{ij} + \frac{3S_{ij}}{2\bar{\sigma}}\left(\frac{2}{3C}\right)^{\frac{1}{1-\beta}} H\left[\bar{\sigma}-\sqrt{3}\xi\right]\left[\bar{\sigma}-\sqrt{3}\xi\right]^{\frac{1}{1-\beta}}. \tag{3}$$

Asymptotic equations of the mode I interface crack-tip field of Double Dissimilar Materials

Under incompressible situation, by introducing displacement potential function U, by magnitude matching, assume that the displacement potential function is

$$U = r^{2-\delta}\phi(\theta). \tag{4}$$

$r^{-\delta}$ singularity exists in σ_{ij}, the stress tensor in crack tip field. The stress tensor can be expressed as

$$\sigma_r = r^{-\delta}\left[F(\theta)+Z(\theta)\right], \sigma_\theta = r^{-\delta}\left[F(\theta)-Z(\theta)\right], \sigma_{r\theta} = r^{-\delta}L(\theta). \tag{5}$$

Where $F(\theta), Z(\theta)$ and $L(\theta)$ are the angular distribution functions

Introduce the following dimensionless quantities

$$\tilde{L} = \frac{L}{\mu}, \tilde{Z} = \frac{Z}{\mu}, \tilde{F} = \frac{F}{\mu}, \tilde{\Sigma} = \frac{\Sigma}{\mu}, f = \frac{\xi}{\mu} \tag{6}$$

Introducing the relevant quantities to equations of motion and constitutive equations, by dimensionless arrangement, we get the control equations of quasi-static extension crack-tip field in mode I Double Dissimilar material interface as following

$$\tilde{Z}' = \frac{2\delta\xi'}{\sin\theta} + 2\tilde{L} - \delta\tilde{Z}\frac{\cos\theta}{\sin\theta} - \frac{2D^*\tilde{Z}}{\tilde{\Sigma}\sin\theta}\left(\tilde{\Sigma} - \sqrt{3}f\right)^{\frac{1}{1-\beta}}. \tag{7}$$

$$\tilde{F}' = \frac{2\delta\xi'}{\sin\theta} - \delta\tilde{Z}\frac{\cos\theta}{\sin\theta} - \frac{2D^*\tilde{Z}}{\tilde{\Sigma}\sin\theta}\left(\tilde{\Sigma} - \sqrt{3}f\right)^{\frac{1}{1-\beta}} + \delta\tilde{L}. \tag{8}$$

$$\tilde{L}' = \delta\left(\tilde{F} + \tilde{Z}\right) - 2\tilde{Z}. \tag{9}$$

$$\xi'' = -\left(1-\delta^2\right)\xi - \delta\tilde{L}\cos\theta - \frac{2D^*\tilde{L}}{\tilde{\Sigma}}\left(\tilde{\Sigma} - \sqrt{3}f\right)^{\frac{1}{1-\beta}} - \delta\left(\tilde{F} + \tilde{Z}\right)\sin\theta. \tag{10}$$

Where: $\xi(\theta) = \sin\theta\phi'(\theta) - (2-\delta)\cos\theta\phi(\theta)$

Boundary conditions

Characterization parameters

The mixed-load parameter(M_P),supported first by Shih, is introduced for defining the stress state of crack tip

$$\begin{cases} M_P = \dfrac{2}{\pi} arctg\left(\lim\limits_{r\to 0} \left| \dfrac{\sigma_\theta(r,\theta=0)}{\sigma_{r\theta}(r,\theta=0)} \right| \right) \\ M_P = \dfrac{2}{\pi} arctg\left(\left| \dfrac{F(0)-Z(0)}{L(0)} \right| \right) \end{cases} \tag{11}$$

when $M_P = 1$, it denotes the mode I crack with the tension (compression) load; when $M_P = 0$, it denotes the mode II crack with the shear load; when $0 < M_P < 1$, it denotes the mixed mode crack with tension (compression) load and shear load at the same time. As an exceptional case, the closed crack surface would generate friction along the surface with the compression load.

The boundary conditions of compression-shear mixed mode interface crack include both contin uity conditions at the front of crack($\theta = 0$) and the friction conditions at crack surface($\theta = \pi$)

Continuity conditions in the front of crack($\theta = 0$)

$$g'(0) = 0, g(0) = 0, \tilde{F}(0) - \tilde{Z}(0) = 0, \tilde{L}(0) > 0 \tag{12}$$

Friction conditions at crack surface($\theta = \pi$)

The friction at crack surface is presumed to be compatible with Coulomb friction law. So the friction conditions are expressed as follows

$$\tilde{F}(\pi) - \tilde{Z}(\pi) \le 0, \tilde{L}(\pi) = -\mu[\tilde{F}(\pi) - \tilde{Z}(\pi)], g(\pi) = 0 \tag{13}$$

Numerical solution and analysis

In the process of solving equations of mixed mode interface growing crack tip field, there are five parameters needing to be selected. They are M (crack propagating velocity), D^* (denoted the material viscosity), β (index parameter), μ (friction coefficient) and M_P (mixed-load parameter). Because of the singularity of equations near crack tip, the numerical calculation of the start and end points are respectively $\theta = 10^{-4}$ and $\theta = \pi - 10^{-4}$. The solution of governing equation belongs to two-point boundary value problem. Owing to the absence of definite condition, $g''(0)$ and $F(0)$ are designated as adjustable parameter. By commissioning the two parameters, the boundary value problem can be change into initial value problem.

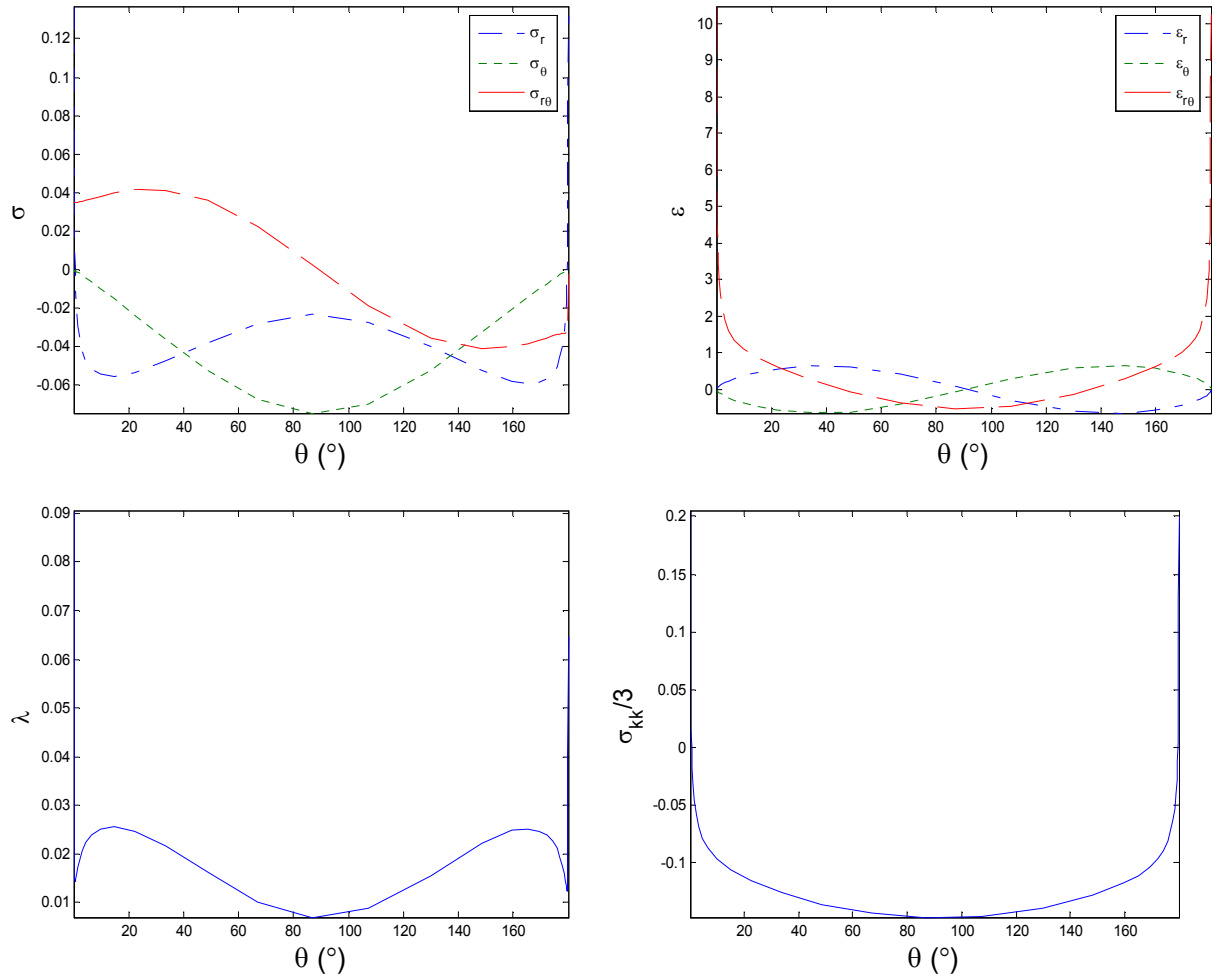


Fig.3 Angular variations of stress, stain, plastic flow factor and hydro-static stresses $\left(M=0.001, \beta=0.7, D^{*}=0.05, M_{P}=0.7, \mu=0.3\right)$

Summary

By the above analysis, we can see that

(1) The crack-tip singularity field of compression-shear mixed mode interface crack is controlled by the material viscosity coefficient, the Mach number (Ma), and the singularity exponent (β).

(2) The viscosity coefficient varies inversely with the power of the equivalent plastic strain rate. They are angular distribution functions and suited to the material nature with no loss of material uniformity.

Project supported by the the Fundamental Research Funds for the Central Universities （HEUCF20100201）

References

[1] Williams M L. Bulletin of the Seismoloical Society of America. Vol.49 (1959), p.199

[2] Viggo T. Journal of the Mechanics and Physics of Solids, Vol.49 (2001), p.2689

[3] B.Chen, T.J. Lardner: Int. J. Solids. Struct. Vol.30 (1993), p.1725

[4] Sun S Y, Chen HR. Composites Science and Technology. Vol.70 (2010), p.1011 (in chinese)

[5] V. Ricci, A. Shukla and V.B. Chalivendra: Theory. Appl. Frac. Mech, Vol.39 (2003), p.143

© (2012) Trans Tech Publications, Switzerland
doi:10.4028/www.scientific.net/KEM.488-489.456

Effect of rotational speed on thin-rim gear bending fatigue crack initiation life

Milan Opalić[1, a], Krešimir Vučković[1, b] and Dragan Žeželj[1, c]

[1]Faculty of Mechanical Engineering and Naval Architecture, University of Zagreb
Ivana Lučića 5, 10000 Zagreb, Croatia

[a]milan.opalic@fsb.hr, [b]kresimir.vuckovic@fsb.hr, [c]dragan.zezelj@fsb.hr

Keywords: thin-rim gear, rotational speed, bending fatigue, crack initiation, strain-life approach.

Abstract. Thin-rim gears are often used in aircraft applications in order to reduce weight. The objective of this study is to investigate the effect of rotational speed (centrifugal force) on bending fatigue crack initiation life of thin-rim gear manufactured from case carburized 14NiCrMo13-4 steel. Stresses in gear are determined from two-dimensional finite element model, assuming plane stress conditions. The fact that, in actual thin-rim gear operation, a significant reversed stress occurs at the root of the tooth adjacent to the loaded tooth is considered. Material is assumed to be homogenous, isotropic and linear elastic. Elastic strains are calculated from obtained stresses and corrected using Neuber's rule to account plasticity effects. The number of load cycles required to initiate bending fatigue crack is predicted using strain-life approach for variety of gear rotational speeds and rim thicknesses. Strain-controlled fatigue properties were approximated from material hardness, while the mean stress as well as residual stress effects are included through Morrow's mean stress correction. The proposed approach is validated by comparison with available experimental data from literature and used for parametric studies. Predicted numbers of load cycles required to initiate potential bending fatigue crack are presented for the variety of cases studied.

Introduction

A design goal for the gears in aircraft power transmissions is to transmit high loads at high speeds with both size and weight kept to a minimum. To achieve this goal, some gear designs incorporate thin rims. However, rims that are too thin may lead to additional bending fatigue problems at high speeds due to a centrifugal load that contributes to the applied loading of the gear.

A noteworthy amount of work has been done in the stress analysis of thin-rim gears [1, 2, 3]. Analytical and experimental study of actual thin-rim gear operation revealed that a significant amount of reversed stress occurs at the root of the tooth adjacent to the loaded tooth [3]. Bending fatigue tests showed that service life of thin-rim gears is reduced with decreased rim thickness [4].

The bending fatigue process can generally be divided into two main stages: crack initiation and crack propagation. Nevertheless, recent numerical investigations of thin-rim gear tooth root fatigue were mainly restricted to the crack propagation stage [5, 6], disregarding the fact that gears mainly operate in high-cycle fatigue, where the majority of the fatigue life is in the crack initiation stage [7]. The bending fatigue crack initiation life of thin-rim gears was investigated in analytical study [8]. However the effect of rotational speed on tooth root stresses is neglected in this study. Also the presence of reversed stress in tooth root fillet region is disregarded due to an assumption that loading cycle of thin-rim gear meshing is presumed as pulsating ($R = 0$).

The aim of this paper is to use advanced engineering tools for a numerical analyses in order to investigate the effect of rotational speed on bending fatigue crack initiation life of thin-rim gears manufactured from case carburized 14NiCrMo13-4 steel taking into account actual gear operation.

Fatigue crack initiation model

A proposed numerical model is based on the continuum mechanics approach and on the assumption that fatigue cracks are initiated on the surface of component. Bending fatigue crack initiation life is analyzed on a gear wheel with basic data adopted from [5] and shown in Table 1. The pinion is regarded as solid gear, having the same basic data as wheel.

Table 1 Basic data of studied thin-rim gears

Thin-rim gear					
Number of teeth	z	28	Root fillet radius of basic rack	ρ_{fP}	0
Module	m	3.175 [mm]	Addendum of basic rack	h_{aP}	$1.05 \cdot m$ [mm]
Profile shift coefficient	x	-0.05	Dedendum of basic rack	h_{fP}	$1.35 \cdot m$ [mm]
Face width	b'	6.35 [mm]	Tip diameter	d_a	95.25 [mm]
N. pressure angle of basic rack	α_{Pn}	20 [°]	Hub inner/outer diameter	-	29.72/50.8 [mm]

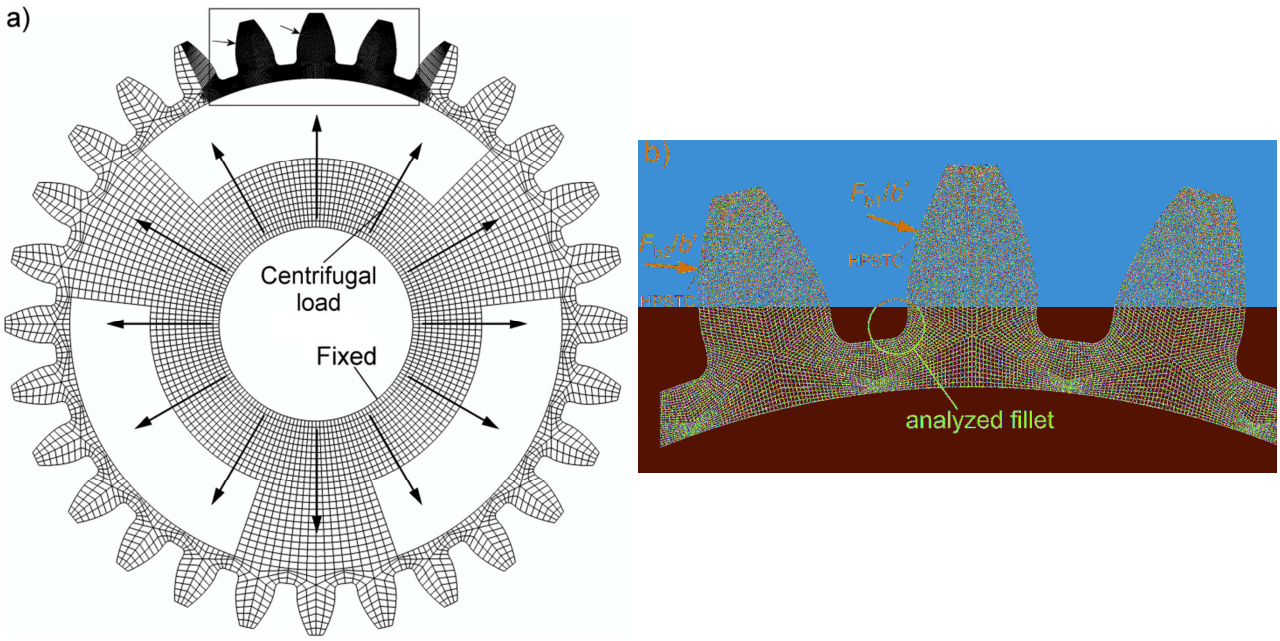


Figure 1 FE model of the whole gear: a) boundary and load conditions and b) detail view

Commercial finite element (FE) package ABAQUS/Standard is used to determine stresses in gear. Two-dimensional (2D) FE model of whole gear is created in order to avoid rim support issues, see Fig. 1. Plane stress conditions and uniformly distributed load on the tooth flank are assumed. An 8-node biquadratic plane stress quadrilateral elements (CPS8) are used for the mesh. The mesh is refined in the region of loaded tooth to improve accuracy. The material is assumed to be homogenous, isotropic and linear elastic. Values of the Young's modulus, E = 207 000 MPa, Poisson's ratio, ν = 0.3 and mass density, ρ = 7 700 kg/m^3 are adopted from [6]. In order to simulate actual gear operation the gear tooth engagement is broken down into two load steps which were then separately analyzed. In the first step analyzed tooth is loaded at the highest point of single tooth contact (HPSTC) with the normal load F_{b1}/b', where b' is the wheel tooth face width. In the second step load F_{b1}/b' is suppressed and tooth adjacent to the analyzed tooth is loaded at HPSTC with a new normal load $F_{b2}/b' = F_{b1}/b'$. This procedure is simplified version of the one proposed in [7]. In both steps, centrifugal load is applied through rotational body force option in FE software and the nodes of the inner hub diameter are fixed, see Fig. 1. Stress cycle is determined individually for each node in the region of analyzed tooth root fillet, assuming uniaxial stress. Elastic strains are calculated from obtained stresses and corrected using Neuber's rule to account plasticity effects. The number of load cycles required to initiate fatigue crack, N_i is calculated using strain-life approach trough Coffin-Manson relationship which is expanded to include the true mean stress, σ_m as well as the residual stress, σ_r effects through Morrow's mean stress correction method. The relationship is expressed through the following form

$$\frac{\Delta\varepsilon_1}{2} = \frac{\sigma'_f - \sigma_m - \sigma_r}{E}\left(2N_i\right)^b + \varepsilon'_f \cdot \left(2N_i\right)^c, \tag{1}$$

where $\Delta\varepsilon_1/2$ is the maximum principal strain amplitude, σ'_f the fatigue strength coefficient, b the fatigue strength exponent, ε'_f the fatigue ductility coefficient and c the fatigue ductility exponent. The residual stress value of -1 100 MPa at the tooth root fillet surface is adopted from [10]. Strain-controlled fatigue properties of the material are approximated from case hardness of 61 HRC [5] using Roessle-Fatemi method [9] and given in Table 2.

Table 2 Material parameters for crack initiation calculation

Case carburized 14NiCrMo13-4 steel					
Cyclic strength coefficient	K'	5146 [MPa]	Fatigue strength exponent	b	-0.09
Cyclic strength exponent	n'	0.161	Fatigue ductility coefficient	ε'_f	0.0404
Fatigue strength coefficient	σ'_f	3072.5 [MPa]	Fatigue ductility exponent	c	-0.56

Fatigue crack initiation model validation. Bending fatigue crack initiation life by means of gear running test and crack propagation gages was investigated in [5]. One solid and one thin-rim gear with the backup ratio (rim thickness divided by tooth height), $m_b = 0.3$ were investigated. Both were manufactured from the case carburized 14NiCrMo13-4 alloy steel. In the fillet region (loaded side) on one tooth of each of the test gears, notches were fabricated using electrodischarge machining (EDM) to promote crack initiation. Bending fatigue crack initiation time was determined as the time required to break the first strand of the gauge. The crack initiation was uniform throughout the tooth face width for solid gear; however this was not the case for the thin-rim gear where notable differences between front and rear flank crack initiation time occurred. Since, this study is based on 2D approach assuming uniform load and uniform crack initiation distribution over tooth face width, experimental results for the thin-rim gear are not considered as relevant.

In order to validate numerical model, by comparing it with the relevant experimental results, FE model of a solid gear with a notch in the fillet region is created. The notch width and length are 0.127 mm and it is located at a radius of 40.488 mm. Due to small difference at the notch tip and the fillet surface hardness [5], their strain-controlled fatigue properties are regarded the same. The residual stress value of -200 MPa for the notch tip is adopted from [10].

The numerically predicted bending fatigue crack initiation life for nominal gear torque, $T = 135.58$ Nm and gear nominal rotational speed of 10 000 rpm is $N_i = 48\ 845$. This value is notable lover than the experimental ones (100 300 on gear front and 78 300 on gear rear side [5]). This is primarily due to different initial crack lengths, a_i. In this study as well as in [7], the initial crack size a_i is estimated to be 0.01 mm, while the experimentally obtained ones were 0.229 mm on gear front and 0.178 mm on gear rear side. The number of cycles required to propagate crack from $a_i = 0.01$ to middle value of experimentally obtained initial crack lengths $a_i \approx 0.2$ mm is estimated to be 32 000, [7]. If this number of cycles is added to the numerically predicted number of cycles, $N_i = 48\ 845$ from this study, the obtained value of 80 845 cycles is in good agreement with the experimental results from [5].

Parametric studies

The effects of rotational speed and backup ratio on tooth root bending fatigue crack initiation are investigated. Five gears with the same basic tooth geometry and backup ratios, $m_b = 0.3$, 0.5, 1.0, 1.5 and 3.3 are studied. Gear rotational speeds 0, 5000, 10 000 and 15 000 rpm are used. All gears are with slots, except the one with $m_b = 3.3$ (solid gear). All of them are without notch. For all cases considered the applied tooth load corresponded to an applied torque, $T = 238.7$ Nm. The predicted numbers of load cycles, N_i required to initiate potential bending fatigue crack for various cases considered are given in Fig. 2. It can be observed that N_i is decreased as backup ratio, m_b is decreased and rotational speed increased. However, the change of N_i due to the effect of speed is significantly smaller compared to the effect of backup ratio. Regarding the effect of rotational

speed, the smallest increase by around 5 %, is obtained for $m_b = 3.3$, and the largest one by around 34 %, for $m_b = 0.5$. For all considered backup ratios rotational speeds lower than 5000 rpm have negligible effect on number of load cycles required to initiate bending fatigue crack.

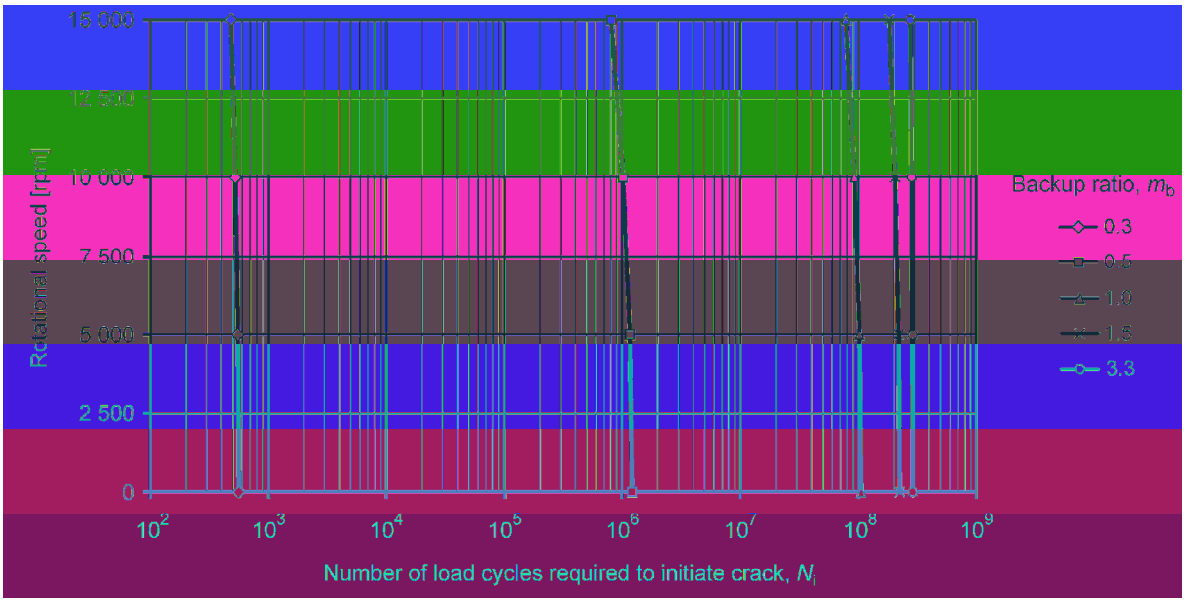


Figure 2 Predicted numbers of load cycles required to initiate potential bending fatigue crack for various gear backup ratios and rotational speeds

The crack initiation potential location is not changed with the varying rotational speed. However, we have found that its location does not coincide with location of maximum principal stress. It is shifted toward the tooth root. This finding will be thoroughly investigated in our future studies.

Conclusion

Compared to the effect of backup ratio, the rotational speed has little effect on the number of load cycles required to initiate bending fatigue crack in thin-rim gears. For speeds lower than 5 000 rpm this effect is negligible. However, for backup ratios lower than 1.0 and speed higher than 5 000 rpm it is advisable to considered it in order to obtain reliable results.

References

[1] R.J. Drago and R.V. Luthans: Journal of American Helicopter Society, Vol. 28 (1983), p. 19.

[2] M. Opalić and Z. Kolaček: Journal of Mechanical Engineering - DMMI '99 (1999), p. 173.

[3] N. Arai, S. Harada, N. Mori and M. Okamoto: Bull. JSME, Vol. 28, No. 236 (1985), p. 350.

[4] N. Arai, S. Harada and T. Aida: Bull. JSME, Vol. 24, No. 195 (1981) p. 1642.

[5] D.G. Lewicki and R. Ballarini: Int. J. Fatigue, Vol. 87, No. 1, (1997) p. 59.

[6] D.G. Lewicki: TM-2001-211117, ARL-TR-1314, NASA (2001)

[7] S. Podrug, D. Jelaska and S. Glodež: FFEMS, Vol. 31, No. 5 (2008), p. 327.

[8] J. Kramberger, M. Šraml, I. Potrč and J. Flašker: Eng. Fract. Mech., Vol. 71 (2004), p. 647.

[9] M.L. Roessle and A. Fatemi: Int. J. Fatigue, Vol. 22, No. 6, (2000) p. 495.

[10] D.P. Townsend: TP-2047, NASA (1982).

© (2012) Trans Tech Publications, Switzerland
doi:10.4028/www.scientific.net/KEM.488-489.460

Investigation on Damage Tolerance of Carbon/epoxy Laminate for Aircraft Structural Design

Hyunbum Park[1, a], Changduk Kong[1, b] and Kyungsun Lee[1, c]

[1]Department of Aerospace Engineering, Chosun University, Gwangju, Rep. of Korea

[a]swordship@daum.net, [b]cdgong@chosun.ac.kr, [c]kscraft@paran.com

Keywords: Composite structure, Low velocity Impact damage, Compressive strength

Abstract. In Korea, the KC-100, which is a small scale piston propeller general aviation aircraft, has been developed to establish a domestic certificate infrastructure and system through the BASA(Bilateral Aviation Safety Agreement) program by KAI(Korea Aerospace Industries, Ltd.). This aircraft adopted the whole composite structure concept for an environmental friendly aircraft through low fuel consumption due to structure weight reduction. However the carbon/epoxy composite structure, which is mainly used for this aircraft, is very weak against foreign object damage. Therefore the purpose of the damage tolerance design philosophy is to ensure that the aircraft can operate safely for a period of time with damage present within the airframe. This study is to investigate the residual compressive strength of the carbon/epoxy UD and fabric laminate due to impact damages. Through investigation on compressive strength, design allowable of carbon/epoxy laminate is determined by the experiment to address design criteria of the composite structure.

Introduction

Recently, as the utilization of small aircraft has been increasing, many countries have been developing various small aircraft. In Korea, the KC-100, which is a small scale piston propeller general aviation aircraft, has been developed to establish domestic certificate infrastructure and system through the BASA program by KAI and PMO (Project Managing Office). This KC-100 aircraft adopted the whole composite structure concept for environmental friendly through low fuel consumption due to structure weight reduction as well as for a competitive aircraft market. However the carbon/ epoxy composite structure, which is mainly used for this aircraft, is very weak against impact damage. Especially, the low velocity impact damage rather than the high velocity impact damage cannot be easily found to investigate the so called 'barely visible impact damage'. Thus the impact damage of the composite structure has become an important issue in composite structure design [1,2,3]. Therefore investigation on residual compressive strength after impact of composite structure due to low velocity impact is presented in this work.

Classification of Damage Criteria

According to a composite aircraft design handbook[4], the damage criteria are classified into five categories depending on the severity of damages for the damage tolerance design. The first category is the barely visible impact damage(BVID), and the second category is the visible impact damage(VID). Repair should be carried out from the second category. Thus the definition of the criteria for the VID category is important in structure design. In order to define the VID energy, this study produces impact damages with different impact energies in low velocity impact range, examines the visual finding possibility, and analyzes the decreasing tendency of compressive strength. Figure 1 presents schematic diagram showing design load levels versus categories of damage severity.

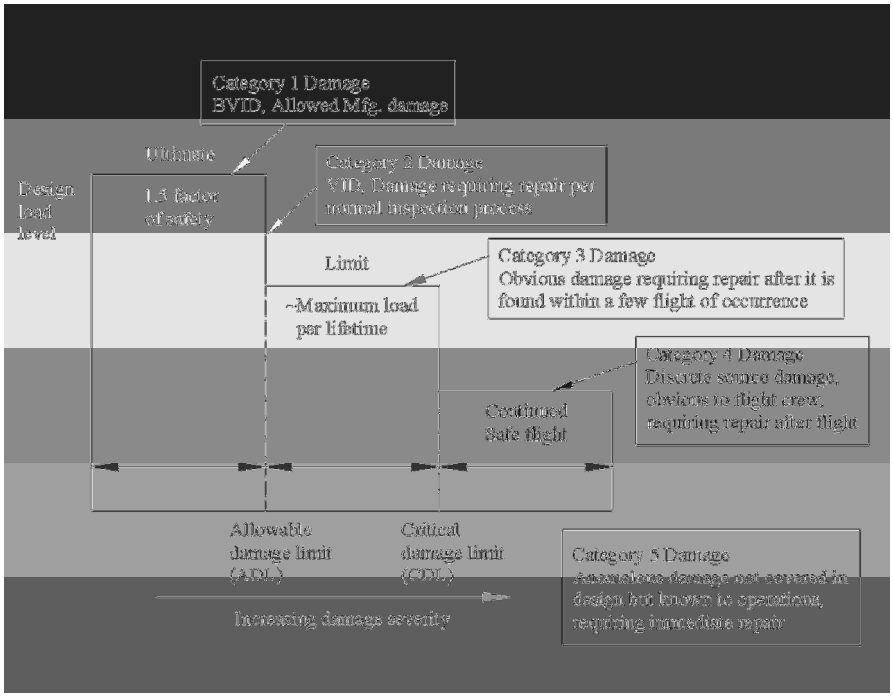


Fig. 1 Schematic diagram showing design load levels versus categories of damage severity

Manufacturing of Specimen

The candidate composite materials for the KC-100 aircraft are considered among some AGATE(Advance General Aviation Transport Experimental) materials which were proposed for increasing design reliability as well as promoting the small aircraft industry of the USA. According to this consideration, some composite materials, which are produced by Toray Industries Inc., are finally selected. Therefore, the main wing spar is designed with Carbon/Epoxy UD prepreg (P707AG-15), and the main wing rib is designed with Carbon/Epoxy fabric prepreg (F6273C-07M). In this study, specimens of spar and skin manufactured by autoclave molding and the impact damages on them are performed by drop-weight type impact test equipment. The lay-up sequence of the spar is 32 plies with $[45°/0°/-45°/90°]_{4s}$, and the lay-up sequence of the rib is $[(45°/-45°)/(0°/90°)]_{5s}$. Table 1 presents mechanical properties of UD and fabric prepreg.

Table 1 Mechanical properties of UD and Fabric prepreg

Mechanical properties of UD prepreg	
Longitudinal modulus[GPa]	124
Transverse modulus[GPa]	9
Shear modulus[GPa]	4
Longitudinal compressive strength[MPa]	1447
Transverse compressive strength[MPa]	198
Mechanical properties of Fabric prepreg	
Longitudinal modulus[GPa]	56
Transverse modulus[GPa]	54
Shear modulus[GPa]	4
Longitudinal compressive strength[MPa]	708
Transverse compressive strength[MPa]	702

Compressive Test after Impact Damage

Environmental conditions are firstly considered before producing impact damages simulated on the specimens. The room temperature dry condition and the elevated temperature wet condition should be taken into account because degradation of mechanical property of the composite material may take place frequently by environmental conditions. The specimens are immersed in a water tank with water temperature of 80℃ which is to simulate the elevated temperature wet condition[5]. When the specimens absorb moisture until saturation, their compressive strengths are measured at before and after impact damage. As the range of low velocity impact energy is less than 10J, the impact damages are gradually carried within 10J for the UD laminate specimens and the fabric laminate specimens according to ASTM D7136[6], and their compressive strengths are evaluated by ASTM D7137[7]. Finally, the damage criterion for repairable design is defined. Figure 2 is configuration of impact damaged specimen. Figure 3 is the fractured configuration of specimen after compressive test.

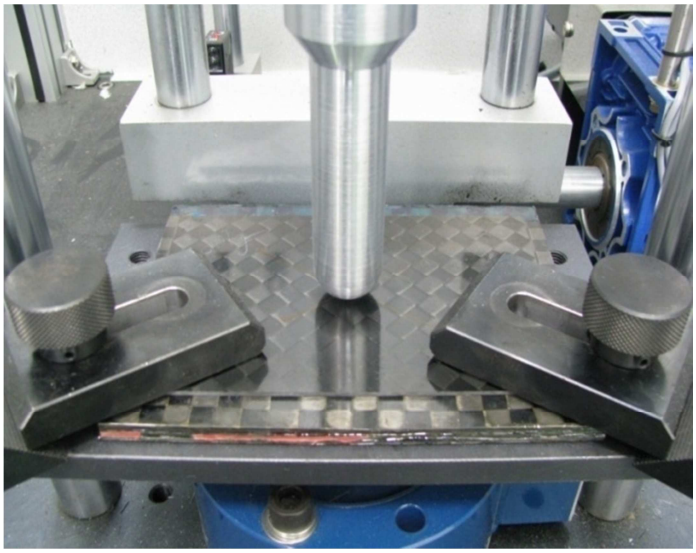


Fig. 2 Configuration of impact tested specimen

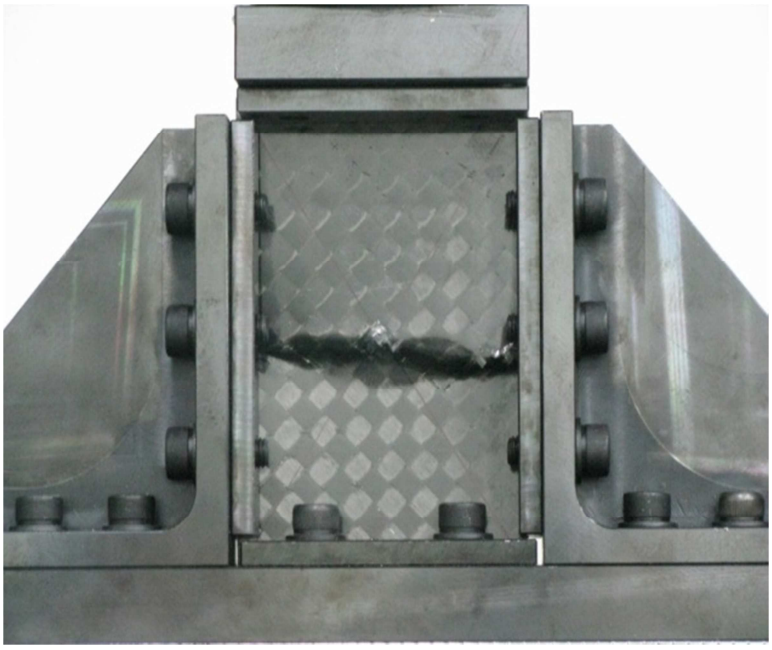


Fig. 3 Configuration of specimen after compressive test

In case of the UD laminate specimen, the compressive strength test results in the room temperature dry condition show that the compressive strength of the damaged specimen at impact energy of 5J is reduced to 4% than the compressive strength of the undamaged specimen. The damage at this impact is started to find visually. It is reduced to 19% at impact energy of 6J and to 32% at impact energy of 7J. However, the compressive strength test results of the UD specimen in the elevated temperature wet condition shows that the compressive strength of undamaged specimen is reduced to 5% than the strength of the undamaged specimen in the room temperature dry condition. Furthermore, the compressive strength is reduced to 11% at impact energy of 4J, 17% at impact energy of 5J, and 31% at impact energy 6J.
In case of the fabric laminate specimen, the impact damages are produced within impact energy of 10J at the same environmental conditions as the previous case. In the room temperature dry condition, its compressive strength is reduced to 3% at impact energy of 4J and 10% at impact energy of 5J which is possible to find visually the damage. It is reduced to 25% at impact energy of 6J and to 30% at impact energy of 7J. As the previous UD case, the strength test of the fabric laminate specimen also is carried out in the elevated temperature wet condition. The test results show that the compressive strength is reduced to 21% at impact energy of 4J and 25% at impact energy of 5J. It is reduced to 36% at impact energy of 6J.
Through the investigation above, the damage criteria for repairable design are suggested. Because the safety factor of 1.5 is used in most aircraft design, the repair of the damage tolerance structure can be performed at 33% reduction of its original strength. If this criterion is applied, the UD spar and fabric rib structure must be repaired if the structure has the impact damage equivalent to having impact energy of 6J in the elevated temperature wet condition.

Conclusions

This study carried out the low velocity impact damage evaluation of carbon/epoxy UD and fabric laminate adopted small aircraft composite structure. Through application of gradual impact energies and investigation of compressive strengths of the damaged specimens at different environmental conditions, the damage criteria for repairable design of both the impact damaged UD and fabric laminate structure are suggested.

References

[1] T. Anderson et al., “Experimental investigation of low-velocity impact characteristics of sandwich composites”, Composite Structures 50, 2000, 239-247

[2] C. T. Sun et al., “Quasi-static modeling of delamination crack propagation in laminates subjected to low velocity impact”, Composites Science and Technology 53, 1995, 111-118

[3] Chen, J. K., et al., “Impact response of buckled composite laminates”, Recent Adv. in Eng Mech. and their Impact on Civil Eng. Practice, Proc. 4th Eng. Mech. Div. Specialty Conf., Purdue University., West Lafayette. IN, May 23-25, 1983, 515-519

[4] AC20-107B, Composite Aircraft Structures, FAA

[5] ASTM D5229,"Standard Test method for Moisture Absorption Properties and Equilibrium Conditioning of Polymer Matrix Composite Materials", 2004.

[6] ASTM D7136,"Standard Test method for Measuring the Damage Resistance of A Fiber-Reinforced Polymer Matrix Composite to A Drop-Weight Impact Event", 2005.

[7] ASTM D7137, "Standard Test Method for Compressive Residual Strength Properties of Damaged Polymer Matrix Composite Plates", 2005.

© (2012) Trans Tech Publications, Switzerland
doi:10.4028/www.scientific.net/KEM.488-489.464

Damage Analysis of Concrete subjected to Freeze-thaw Cycles and Chloride Ion Erosion

Jize Mao[1,a], Zhiyuan Zhang[1,b], and Zongmin Liu[1,c],Chao Sun[1,d]

[1]College of Aerospace and Civil Engineering, Harbin Engineering University, Harbin 150001, China
[a]maojize@hrbeu.edu.cn, [b]edward_521@126.com,
[c]liuzongmin@hrbeu.edu.cn,[d]chaosun_825@126.com

Keywords: Concrete, Chloride ion, Freeze-thaw, Diffusion equation, Damage evolution

Abstract: With the development of damage mechanics, many researchers have used it to analyze the constitutive equation of concrete. Since the special environment in the cold marine regions, the offshore structures are common to subject to the comprehensive effects of freeze-thaw action and chloride erosion. This might cause concrete materials degradation and reduce the mechanical performance of concrete seriously. In this paper, based on the analysis and mechanical experiments of concrete materials under the comprehensive effects of freeze-thaw action and chloride ion erosion, the damage evolution equation of concrete elastic modulus along with the freeze-thaw cycles and chloride ion contents was established. The effects of chloride ion were investigated during the process of concrete degradation. According to the damage evolution equation, a new constitutive equation of concrete under freeze-thaw action and chloride erosion was established. And then, by means of the element simulation analysis of concrete beams when subjected to the comprehensive actions, the feasibility and applicability of the equation was examined and discussed. In this equation, both the freeze-thaw action and chloride ion erosion were considered together. It will be more suitable for analyzing the durability of concrete structures in the real cold marine regions. It will also provide some references for concrete constitutive theory.

Introduction

Freeze-thaw action and chloride ion erosion are the main durability problems for marine structures in the cold regions [1]. In order to enhance the durability of concrete materials in marine structures, many studies have been done recently [2-3]. However, most of them focus on the single action of either freeze-thaw action or chloride ion erosion. These methods could investigate the effects of single action on concrete materials, but could not exhibit the multi-factor actions on concrete in the real environment [4]. In this paper, based on gathering and analyzing the data of previous researches and experiments, the damage evolution equation of comprehensive effects of freeze-thaw action and chloride erosion on concrete was established. After that, the damage evolution was validated and the parameters were determined by the following tests. Finally, the feasibility of the damage evolution equation was discussed by simulation analysis of concrete beams.

The effects of freeze-thaw action on concrete materials

The effects of freeze-thaw action on concrete materials mainly respond on the change of pores. As the porosity increased and mechanical properties decreased, the concrete materials degrade when subject to freezing and thawing.

There are mainly two kinds of pores in concrete: gel pores (<10 nm), which are associated with the formation of hydration products, and capillary pores (10–10,000 nm). The capillary porosity is in dominant position in concrete [5].

During the freezing process, the volume of the pores contained freezing water and unfreezing cold water expanded. Along with the osmotic pressure increased from freezing of water in pores, the complicated tensile stress brought about in the concrete material. After some freezing and thawing circles, the porosity of concrete increased, as the capillary pores expanded and stretched and the new micro-crack formed in concrete, when the osmotic pressure was more than bearing capacity or the energy of water in the pores was not less than the energy needed by forming new micro-crack. With the increase of porosity, water absorption of concrete increased to generate more damage in concrete in the next freeze-thaw circle.

This process is the damage mechanism in concrete by freezing and thawing. Because the elastic modulus damage is based on the last cycle of freezing and thawing, we can assume that the increasing of elastic modulus damage in cement composite materials are in the proportion to the original elastic modulus with the increase of freezing and thawing cycles [6]. The relationship can be expressed as the following equation:

$$\frac{dE}{dN} = k' E . \tag{1}$$

Where, k' is a constant which can be determined by experiments.

The solution of this equation can be expressed as follow.

$$E_N = E_0 e^{k'N} . \tag{2}$$

Where, E_N is the elastic modulus of concrete after N cycles of freezing and thawing, E_0 is the original elastic modulus of concrete.

The effects of chloride ion erosion on freeze-thaw action

In order to investigate the effects of chloride ions on freeze-thaw action in concrete, freezing and thawing tests in water with 4 different contents of chloride ion were conducted. The concrete specimens went through 0, 22, 44, 66 freezing and thawing cycles respectively. The tests were operated according to Ordinary Concrete Long-term Performance and Durability Experiment Method Standard (GB/T 50082-2009). Table 1 shows the mixture proportion of the specimens.

Table 1 The mixture proportion of concrete specimens

Component	Cement	Water	Sand	Aggregate
Content（Kg/m^3）	458	165	707	1060

During the freezing and thawing test, it is clear to know that the damage of the specimens were aggravated along with the increasing of chloride ion content. Fig. 1 shows the scaling situation of specimens after 66 freeze-thaw cycles in water with 4 different chloride ion contents. From the left to the right, the concentrations of chloride in the specimens are 0%, 1.75%, 3.5% and 5.25% respectively. Similar to the surface, the damage in the internal materials is also a progressive increase along with the content of chloride ion.

After freezing and thawing tests, the mechanical tests were also carried out according to Ordinary Concrete Mechanics Performance Testing Method Standard (GB/T 50081-2002). In the tests, the strength and elastic modulus were mainly measured and the effects of chloride ion erosion on freeze-thaw action were investigated.

The damage evolution equation

The research shows that the chloride ion content in concrete can deeply affect the frost resistance of concrete. The effect can be converted to different freeze-thaw cycles according to different chloride ion content. This conversion also can be expressed by the following equation.

$$N' = (1 + \omega c)N . \tag{3}$$

Where, N' is converted freeze-thaw cycles according to chloride ion content; ω is the relative coefficient which can be decided by concrete component and can be obtained through experiments; c is the content of chloride ion in concrete; N is freeze-thaw cycles.



Fig. 1 The scaling situation of concrete specimens (Concentration of chloride from left to right: 0%, 1.75%, 3.5% and 5.25%)

Then combined with the equation (2), the elastic modulus of concrete along with freeze-thaw cycles according to chloride ion content could be expressed as the following equation.

$$E_{N'} = E_0 e^{k'(1+\omega c)N} . \tag{4}$$

Where, $E_{N'}$ is the elastic modulus of concrete when the content of chloride ion in concrete is c and the freeze-thaw cycles is N; E_0 is the elastic modulus of original concrete.

From the above analysis, a damage evolution equation of concrete under comprehensive effects of freeze-thaw action and chloride ion erosion can be obtained as follow [7].

$$D = 1 - e^{k'(1+\omega c)N} . \tag{5}$$

Where, D is the damage of concrete defined as elastic modulus.

However, the equation (5) is an ideal equation. As the chloride ion diffusion in concrete is long process and the distribution of chloride ion in concrete is inhomogeneous. Therefore, the damage of elastic modulus of concrete materials is also inhomogeneous. In this paper, in order to set up the relation between elastic modulus and comprehensive effects, the following rule should be conformed: the concrete is considered as semi-infinite homogeneous medium; chloride ion diffusion from one side; the inhomogeneous damage caused by chloride ion diffusion. Then the equation can express as follow.

$$dE_{N'}(x) = E_0 e^{k'(1+\omega c(x))N} dx . \tag{6}$$

Where, $E_{N'}(x)$ is the elastic modulus function along with the chloride ion diffusion direction; $c(x)$ is chloride ion diffusion function which can be determined by chloride ion diffusion equation.

So we can obtain the elastic constitutive equation of concrete after comprehensive effects as following equation.

$$d\sigma_{ij} = \frac{E_0 e^{k'(1+c\omega)N}}{1+\nu} d\varepsilon_{ij} + \frac{\nu E_0 e^{k'(1+c\omega)N}}{(1+\nu)(1-2\nu)} d\varepsilon_{kk}\delta_{ij} . \tag{7}$$

Where, $d\sigma_{ij}$ and $d\varepsilon_{ij}$ are stress and strain derivative along with the chloride ion diffusion direction.

Simulation Analysis

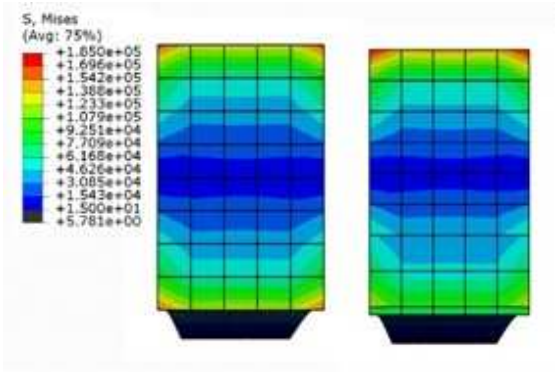


Fig. 2 Comparison with two cantilever beams under different stress states

In order to study the feasibility of the damage evolution equation, simulation of concrete beams was conducted. Combined with the previous experiments and analyses, the stress states of cantilever beams after comprehensive effects of freeze-thaw action and chloride ion diffusion were simulated. Fig.2 shows the simulated stress states of the root sections when the beams were under the same uniform load on the top. The two beams are all corroded by sea water from the bottom side. The beam in the left is analyzed by the elastic damage modulus, and the right one is simulated in the real conditions. Different colors express different stress states. During the simulation, the two beams have the same deformation but different stress states in the interior. The application of elastic damage modulus which has simplified calculation program can satisfy the project needs and doesn't need to consider the complicated chloride ion diffusion.

Conclusions

The research through experiments and analyses shows that the degradation speed of concrete under comprehensive effects was faster than that of concrete in single factor. Because of the inhomogeneous chloride ion distribution during its diffusion process, concrete showed properties of layered degradation when subjected to comprehensive effects. The damage evolution of elastic modulus can describe this change. The analysis indicates that the elastic modulus damage equation has its advantage on calculation programs and engineering applications.

Acknowledgments

The project was supported by National Natural Science Foundation of China (50908059), the Fundamental Research Funds for the Central Universities (HEUCFT1003), and Hei Long Jiang Postdoctoral Scientific Research Foundation.

References

[1] W. Yang and J. Qian: *Study on Test and Evaluation Methods of Frost-resistance and Chloride Ion Diffusion of Concrete in A Marine Environment*, Materials Review, 22(2008), p. 74-77
[2] J. Mao, H. Wang, Zh. Zhang and Z. Liu: *Finite Element Analysis for Concrete Damage under Freeze-thaw Action*, Key Engineering Materials, 417-418(2010), p. 133-136
[3] Ch. Zou, J. Zhao and F. Ling: Degradation of Mechanical Properties of Concrete Caused by Freeze-thaw Action, Journal of Building Structures, 29(2008), p. 117-123
[4] J. Hong, Ch. Liao and H. Wei: *Damage Caused by Freeze-thaw Cycles Influencing on Chloride Diffusion of Concrete*, Concrete, 1(2006), p. 36-38
[5] E.J. Garboczi and D.P. Bentz: *Computer simulation of The Diffusivity of Cement-based Materials*, Journal of Materials Science, 27(1992)
[6] M. Ru: *The Durability and Prediction of Concrete under Multi-factors of Freeze-thaw Action Cycles*, Southeast University, Doctoral Dissertation, (2000)
[7] K.E. Loland: *Continuum Damage Model for Load Response Estimation of Concrete*, Cement and Concrete Research, 10(1980), p.395-402

© (2012) Trans Tech Publications, Switzerland
doi:10.4028/www.scientific.net/KEM.488-489.468

Measurements of Mode I and Mode III Fracture toughness of Spring's Steel

Nenad Gubeljak[1, a], Vinko Močilnik[2,b] and Jožef Predan[1,c]

[1]University of Maribor, Faculty of Mechanical Engineering, Smetanova ulica 17, Maribor Slovenia

[2]Engineering Biro, Vinko Mocilnik s.p., Črneče 186, 2370 Dravograd, Slovenia

[a]nenad.gubeljak@uni-mb.si, [b]vinko.mocilnik@siol.net, [c]jozef.predan@uni-mb.si

Keywords: Bending, Torsion, Stress intensity factor, Mode 1, Mode 3, spring steel.

Abstract. The paper presents experimental measurements of fracture toughness for Mode I and Mode III loading of same spring's steel. The influence of notch effect on fracture toughness for Mode III has been discussed and confirmed by experiments. Circumferential notched spring bar with short fatigue pre-crack subjected to torsion shows significant plastic behavior in twist angle-torque plot. In contrast of circumferential pre-cracked spring (without notch) bar subjected to torsion, the fracture toughness in fully plain strain has been obtained. The K_{IIIC} value becomes more than two times lower than notched bar with short pre-crack K_{IIIQ}. Three point bending specimen with the crack shows fully plain strain condition for stress intensity factor K_{IC}. Different amount o plasticity corresponds to effect of notch root radius and notch angle on short fatigue pre-crack. The rough criteria for distinguishing short crack (affected by notch root radius) and long crack in the notches with 60° angle has been proposed.

Introduction

The experimentally obtained values of K_{Ic}, as fracture toughness parameter are possible to find in catalogue of different materials [1] or even at web side [2]. Generally there are three modes to describe different crack surface displacement [3].
However, if component is subjected to both Modes of loading I and II, it is necessary to determine K_{eq} value. The well known formula [4] for equivalent stress intensity factor is possible to use for two modes of loading:

$$K_{\text{eq}}^2 = K_I^2 + K_{II}^2 + (1+\upsilon)\cdot K_{III}^2 \qquad (1)$$

Where the K_{eq} is equivalent stress intensity factor (SIF), K_I is SIF for mode I, K_{II} is SIF for mode II, K_{III} is SIF for mode III, and ν is Poisson ratio. At present, Linear Elastic Fracture Mechanics allows us to study crack growth behavior and to perform structure integrity assessment, if SIF (K) solutions and material fracture toughness data are available. The aim of this paper is to compare fracture toughness of Mode III K_{IIIC} obtained by global approach (long crack and applied shear stress) and local approach (short crack and maximum shear stress in notch root).

Material and specimen preparation

The specimens were made from high-strength spring fine-grain steel, grade *VCN* [5, 6, 7, 8]. The chemical composition is listed in Tab. 1 as weight %. The used spring's material was rolled, forged, and soft annealed during the manufacturing process. The mechanical properties are listed in Tab. 2.

Table 1 Chemical composition of spring steel

Element	C	Si	Mn	Cr	Ni	Mo	V	Cu	P	S
% wieght	0.44	0.28	0.56	0.87	1.41	0.26	0.11	0.12	0.009	0.002

Table 2 Mechanical properties of spring steel

UTS R_m [*MPa*]	Yield strength $R_{p0,2}$ [*MPa*]	Torsion limit τ_e [*MPa*]	Shear modulus *G* [*GPa*]	Modulus *E* [*GPa*]	Hardness HRc
2010	1570	800	75	193	52 - 55

Material for specimens were prepared at the same technological procedure as regular spring production.

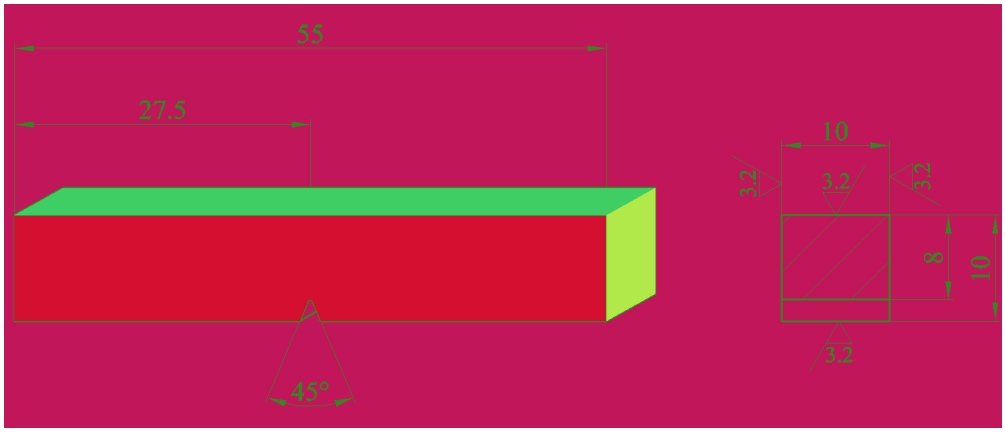


Fig. 1. Three point bend specimens (Chapry) with fatigue pre-crack for mode I

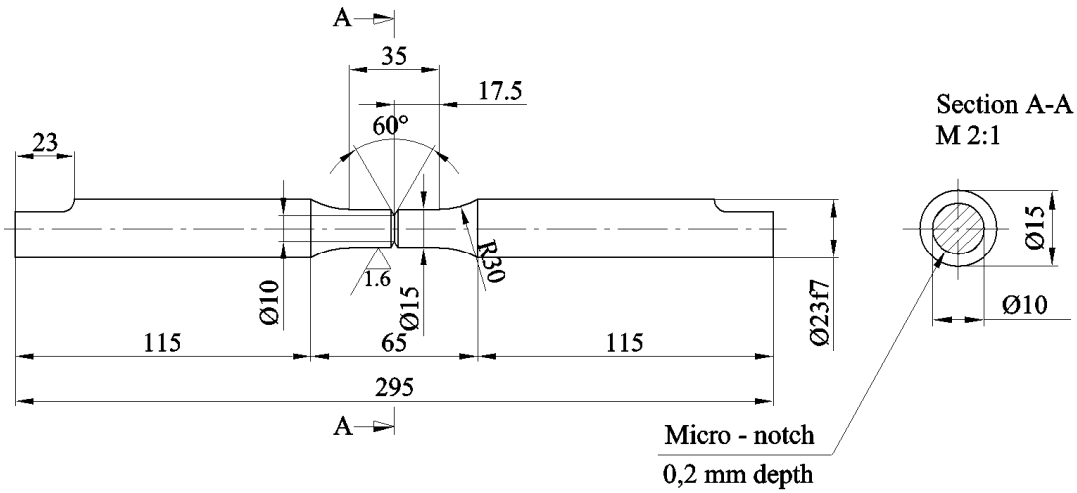


Fig. 2 Fully circumferential pre-cracked specimen for mode III

Fracture toughness testing

Mode I. Fracture toughness tests for mode I and mode III were performed on specimens, as is shown in Fig. 1 and Fig. 2, respectively. Fatigue pre-crack growth was carried out in both specimens. Three point specimens were subjected under load control under maximum fatigue load $F=7.79$ kN and R ratio $R=F_{min}/F_{max}=0.1$. After 3000 up to 4000 loading cycles N the fatigue crack a_f was between 0.2 up to 0.3 mm. Specimen failed when crack becomes longer. The three point bend specimens were subjected to steady bending as according to ASTM E-1820 standard [9] in order to determine fracture toughness K_{Ic}.

Table 3 Dimensions and calculated fracture toughness K_{IC}

Specimen	F_{max} [kN]	N [cycles]	B [mm]	W [mm]	Δa_f [mm]	a_0 [mm]	P_{max} [kN]	$CMOD$ [mm]	K_{IC} [MPa√m]
01	6.4	2717	10	10	1.99	2.351	11.86	0.095	111.03
02	7.79	3523	10	10	2.08	2.22	15.62	0.124	143.37
03	7.79	4039	10	10	2.04	2.226	14.62	0.097	134-37
average									**129.59**

Mode III The round bar specimen (Fig. 2) were subjected to rotate bending in order to create circumferential fatigue pre-crack in a bar. Short circumferential fatigue pre-crack was obtained with average depth a_f=0.215 mm. The specimen were subjected to Mode III loading. Experimentally obtained curve Torque-Twist angle shows that maximum torque is out of 5% offset line in compare with tests in Mode I. Therefore, in order to compare equivalent stress intensity factors by using Eq.(1) we used only torque M_5=238.67 Nm. Stress intensity factor K_{III} has been calculated by using general term for shear mode for cracked round bar [3]:

$$K_{\mathrm{III}} = \tau \cdot k \cdot \sqrt{\pi \cdot a} \tag{2}$$

where τ is applied shear stress, a is crack depth and shape function k=1.

However, in the case of notched round bar with short fatigue crack it is necessary to determine relevant shear stress t. find correct approach in order to determine relevant K_{III}. The applied shear stress τ_{appl} was calculated by using well known mechanics term

$$\tau_{appl} = \frac{16 \cdot M_5}{\pi \cdot D^3} \tag{3}$$

Where D=15 mm is round bar diameter and M_5 =238670 Nmm is torque. The maximum shear stress in notch is possible to calculate by using minimum diameter d=10 mm at middle section:

$$\tau_{\max} = \frac{16 \cdot M_5}{\pi \cdot d^3} \tag{4}$$

Table 4 Initial crack length, relevant shear stress, stress concetration factor and calculated fracture toughness K_{IIIC} and equivalent stress intensity factor:

Approach	a [mm]	τ^* [MPa]	k [-]	$k \cdot \tau$ [MPa]	K_{IIIQ} [MPa√m]	*Comments*
A	2.715	τ_{appl}=360	1	360	33.26	K_{IIIc}^*
B	2.715	τ_{appl}=360	$k_{\tau c}$=3.375	1215	112.26	K_{eq}=128.00
C	2.715	τ_{appl}=360	K_t=2.4	864	79.83	
D	0.215	τ_{max}=1215	1	1215	31.59	K_{IIIc}

The values of K_{IIIc} in A-global and D-local approach are practically the same (33.26 vs. 31.59 MPa√m):

$$\frac{1}{D^3}\sqrt{\pi\cdot(a_{notch}+a_f)} \approx \frac{1}{d^3}\sqrt{\pi\cdot a_f} \quad \rightarrow \quad \frac{1}{15^3}\sqrt{\pi\cdot 2.715} \approx \frac{1}{10^3}\sqrt{\pi\cdot 0.215} \tag{5.a, 5b}$$

Therefore, in case of Mode III loading it is possible applied local maximum shear stress, if fatigue pre-crack a_f is similar or greater than notch root radius ρ. It can be rough criteria for distinguishing short crack (affected by notch root radius) and long crack in the notches with 60° angle could be:

$$a_f \geq a_{notch}\frac{d^6}{D^6-d^6} \tag{6}$$

Conclusion

The influence of notch effect on fracture toughness for Mode III has been discussed and confirmed by experiments. The rough criteria for distinguishing short crack (affected by notch root radius) and long crack in the notches with 60° angle has been proposed. In contrast of circumferential pre-cracked spring (without notch) bar subjected to torsion, the fracture toughness in fully plain strain condition has been obtained. The K_{IIIC} value becomes more than two times lower than notched bar with short pre-crack K_{IIIQ}. However, fracture resistance of spring bar subjected by tension and torsion is possible to increase by machining notch root radius till depth of circumferential fatigue pre-crack. Different amount o plasticity corresponds to effect of notch root radius on short fatigue pre-crack.

References

[1] Rooke D.P., Cartwright D.J. Compendium of Stress Intensity Factor, Ministry of Defence, 1978, London

[2] SINTAP: British Energy Generation Ltd. *SI F and Limit Load Solution, 1998*.

[3] Hertzberg, Y. Mishing, in: *Diffusion Processes in Advanced Technological Materials*, edtied by D. Gupta Noyes Publications/William Andrew Publising, Norwich, NY (2004), in press.

[4] ABAQUS 6.10-3 solver).

[8] Močilnik V.: "*Vpliv prednapetja na dinamično nosilnost vzvojne vzmeti*", Ph. D. thesis, Oct. 2009, Faculty of Mechanical Engineering, University of Maribor,

[9] ASTM E-1820-05 Standard Test Method for Measurement of Fracture Toughness standard

[10] Noda N. A. and TAKASE Y., Stress concentration formulae useful for any shape of notch in a round test specimen under tension and under bending, Fatigue Fract Engng Mater Struct **22**, 1071–1082

© (2012) Trans Tech Publications, Switzerland
doi:10.4028/www.scientific.net/KEM.488-489.472

Numerical Implementation of Constitutive Material Law for Simulating the Kinkband Formation in Fiber Composites

Badrinath Veluri[a] and Henrik Myhre Jensen[b]

Department of Mechanical Engineering, Aarhus School of Engineering

Aarhus University

Dalgas Avenue 4, Aarhus C 8000 Denmark

[a]E-mail: vb@agse.dk ,[b]Email hmj@agse.dk , Web page: http://www.science.au.dk

Keywords: Kinkband, microbuckling, Strain localization, Finite Element Analysis, fiber composites, Constitutive model, Compressive strength.

Abstract. Finite element models with a constitutive material behavior that represents the non-linear response of fiber composites are used to simulate the compressive failure mechanism i.e. kinkband formation. A constitutive material law in framework of micromechanical modeling containing comprehensive constitutive equations for the constituent materials is adopted to model the non-linear behavior of the unidirectional layered materials. This material law is implemented as UMAT user subroutine in ABAQUS/Standard to study kinkband formation. The methodology provides a procedure to investigate the kinkband formation due to fiber misalignment for various complex structures having voids and material discontinuities that occur normally during the manufacture of these unidirectional fiber composites.

Introduction

Compressive strength is a limiting property of fiber composites made up of unidirectional laminae. Kinkband formation due to imperfections resulting from fiber misalignment interacting with matrix non-linearties is the dominating failure mode. The effect of fiber misalignment, matrix non-linearities and the bifurcation studies in fiber composites has been initiated by Rosen [1] and significant efforts have been extended by [2-5]. In 1990's an expanded activity on investigating the effects of fiber imperfections on the mechanical properties of the unidirectional fiber composites by [6-8]. In the case of rigid fibers was studied as a limiting case in [9], the axial shear deformation triggers matrix yielding leading to kinkband formation. In [10] the problem of predicting compressive strength of fiber reinforced materials is approached through an idealized composite model, with individual discretization of fiber and matrix material. In the present study, a two dimensional plane constitutive model is formulated within the framework of [9], and implemented as a user subroutine UMAT in the commercially available finite element program ABAQUS/Standard. The aim of this work is to provide a numerical approach to simulate the failure of fiber composites under compression.

The Constitutive Model

Following the frame work of [9] based on the following key assumptions:

1. *The fibers and the material lines which are parallel to each other are subjected to a common stretching/compression and rotation*
2. *Transmission of identical tractions in the planes parallel to the fibers*
3. *The constituents materials are elastic or elastic-plastic*

For the ease of decomposition of the constitutive equations the direction of fibers along the x_1 axis as shown in the Fig. (1) are predefined.

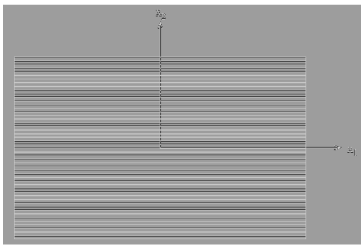


Fig. 1. Periodic fiber reinforced planar block of the composite material with alternate layup of matrix and fibers

A constitutive material behavior model which relates to various proven theories related to fiber reinforced structures has been developed. The first of these assumptions correspond to Voigt estimate for effective material properties where as the second corresponds to Reuss estimate. The third assumption is a standard specification of time independent materials. The general relation between the Cauchy stress and the strain rate is given by

$$\dot{\sigma}_{ij} = L_{ijkl}\varepsilon_{kl} \tag{1}$$

where L_{ijkl} are the plastic elastic-plastic tangent moduli. The strain rates are given by

$$\varepsilon_{ij} = \frac{1}{2}\left(v_{i,j} + v_{j,i}\right) \tag{2}$$

where $v_{i,j}$ is the velocity gradient of v_i.

The two dimensional constituent equations implemented in ABAQUS/Standard in the form of

$$\dot{s}_{ij} = C_{ijkl}v_{l,k} \tag{3}$$

where $\dot{s}_{ij}$ are the nominal stress rate components, C_{ijkl} nominal moduli tensor components which can be used to determine and is detailed in [9]

$$C_{ijkl} = L_{ijkl} - \frac{1}{2}\delta_{il}\sigma_{kj} - \frac{1}{2}\delta_{ik}\sigma_{lj} - \frac{1}{2}\sigma_{il}\delta_{kj} + \frac{1}{2}\sigma_{ik}\delta_{lj} \tag{4}$$

On describing the arbitrary time independent plasticity theory like J_2 flow theory for the constituents for modeling their behavior. The linear relation between Jaumann rates of Kirchoff stresses and strains is given by

$$\dot{L}_{ijkl} = G(\delta_{ik}\delta_{jl} + \delta_{il}\delta_{jk}) + (K - \frac{2}{3}G)\delta_{ij}\delta_{kl} - \frac{4}{3}(G - G_T)\mu_{ij}\mu_{kl} \tag{5}$$

where δ is korneker delta, G and K are the elastic shear modulus and bulk modulus and G_T is the shear tangent modulus given by

$$G = \frac{E}{2(1+v)},\ K = \frac{E}{3(1-2v)},\ \frac{1}{G_T} = \frac{3}{E_T} - \frac{1-2v}{E}, \mu_{ij} = \frac{1}{2\sigma_{eq}}(\sigma_{ij} - \frac{1}{3}\delta_{ij}\sigma_{kk}) \tag{6}$$

The von Mises' stress σ_{eq} is given by

$$\sigma_{eq} = \sqrt{\frac{3}{2}\sigma_{ij}\sigma_{ij} - \frac{1}{2}\sigma_{ii}\sigma_{jj}} \tag{7}$$

The nominal moduli tensor components are calculated by combined material properties of constituent's fiber and matrix in the composite structure. Ramberg-Osgood relation for the constituents as yielding condition that defines natural logarithmic strain considering the reference stress σ^y and hardening index n is given by

$$\varepsilon = \frac{\sigma}{E} + \frac{3\sigma^y}{7E}\left(\frac{\sigma}{\sigma^y}\right)^n \tag{8}$$

This constituent model has been implemented in ABAQUS/Standard as a user material UMAT to simulate the kinkband formation in the unidirectional fiber composites structures under compressive loading conditions.

Numerical Implementation

The current study is carried out with constant volume fraction remains constant throughout the deformation process with the properties of AS4 carbon fibers and PEEK (poly-ether-ether-ketone) thermoplastic matrix as stated in [10]. The domain was discretize with eight node bi-quadratic elements modeling the nonlinearity with the J_2 deformation theory of plasticity and Riks' method is used to trace the end shortening response during the kinkband formation in the unidirectional fiber composites under compressive loading. Fig. (2) demonstrates in detail the implementation and the functionality of the UMAT subroutine.

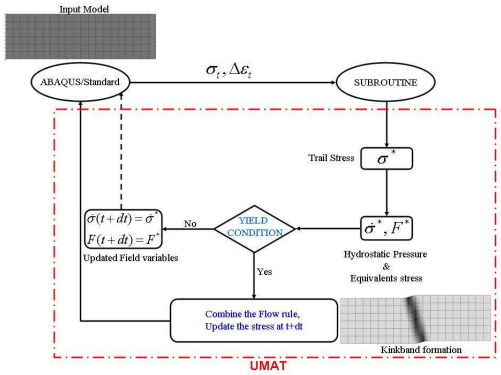


Fig. 2. Implementation of UMAT subroutine in ABAQUS/Standard UMAT

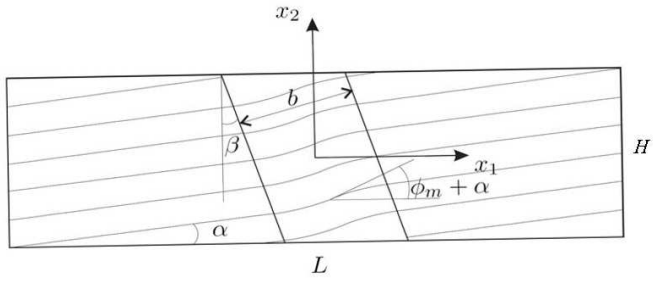


Fig. 3. Idealization of kinkband geometry

In the current investigation the volume fraction remains constant throughout the deformation process. The kinkband geometry is defined in Fig. (3) with the dimensions of height H, length L and band width of b and at inclination angle β with the direction of the fibers for a given initial imperfection ϕ_m. The direction of the fibers outside the band is given by the angle α and in the kinkband region the angle is considered as ϕ, which can be estimated using the geometrical parameters from the following

$$\phi(x_1, x_2) = \frac{1}{2}\phi_m \left[\cos\left(\frac{2\pi \cos\beta}{b}(x_1 + x_2 \tan\beta) \right) + 1 \right] + \alpha \tag{9}$$

To satisfy the following boundary conditions an initial imperfection value ϕ_m is added to fiber angle α

$$u_1 = 0 \text{ at } x_1 = -\frac{L}{2} \tag{10}$$

$$u_2 = 0 \text{ at } (x_1, x_2) = (-\frac{L}{2}, -\frac{H}{2}) \tag{11}$$

Results and discussion

The focus of this work was to implement the constitutive material law as UMAT in FEM code and to gain a better understanding of the influence of the micro-geometry (kindband width, inclination angle, initial misalignment) and macro-geometry (holes). Fig. (4) demonstrates the load-end shortening response with the various stages of kinkband formation for a moduli ratio of 35 fiber volume fraction of 0.6. Fig. (4) depicts the initial deformation is linear elastic and relatively stiff and becomes progressively nonlinear and reaches the peak load. This progressive reduction in the stiffness of the specimen is partly due to the geometric nonlinearity resulting from the imperfection combined with the nonlinearity of the matrix. Fig. (5) shows drop in the peak load due to the macro-geometrical imperfection like holes. Fig. (6) and Fig. (7) shows high sensitivity in the reduction og peak load response for different moduli ration and varying initial fiber misalignment.

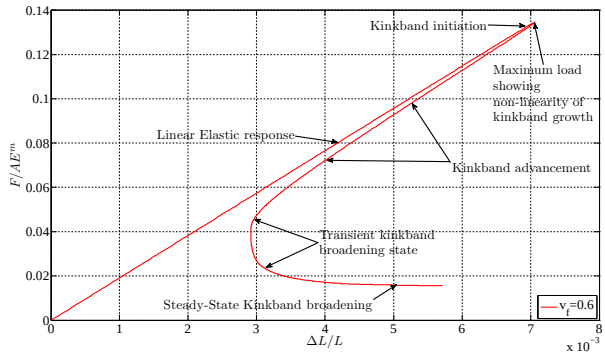


Fig. 4. Load-end shortening response for moduli ratio $E^f/E^m = 35$ and volume fraction $v_f = 0.6$

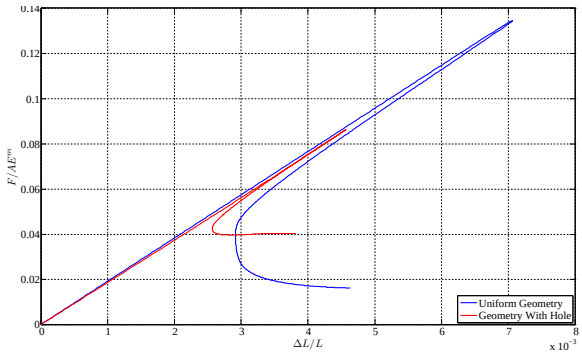


Fig. 5. Load-end shortening with macro geometric imperfection like hole for moduli ratio $E^f/E^m = 35$

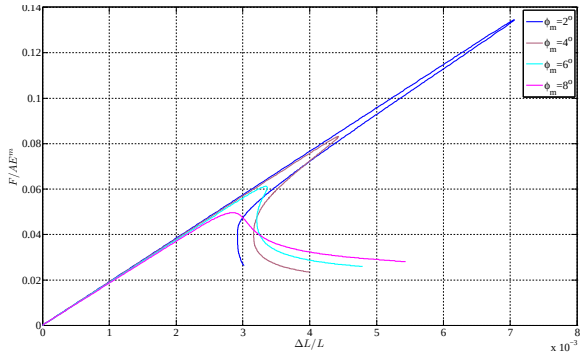


Fig. 6. Load-end shortening response for moduli ratio $E^f/E^m = 35$ varying initial fiber imperfection ϕ_m

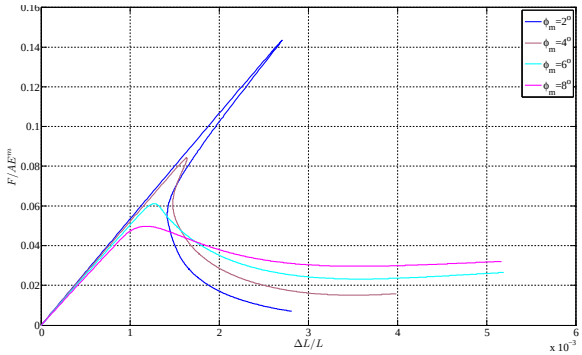


Fig. 7. Load-end shortening response for moduli ratio $E^f/E^m = 100$ varying initial fiber imperfection ϕ_m

Conclusions

The constitutive model was verified numerically for the consistency, convergence and stability in order to simulate the kinkband formation in the unidirectional fiber composites. The model shows a good consistency in simulating the kinkband formation and steady-state kinkband broadening numerically which demands the experimental validation.

References

[1] BW Rosen, Chapter 3: Mechanics of Composite Strengthening In: Fiber Composite Materials, ASM, Metals Park, OH, 1965.
[2] A Argon, Fracture of composites, in: Herman H (Ed.), Treatise on Materials Science and Technology, vol. 1 ed., Academic Press, New York, 1972, pp. 79-114.
[3] B Budiansky. Micromechanics, Computers & Structures. 16 (1983) 3-12.
[4] JG Davis, Compressive Strength of Fiber-reinforced Composite Materials, Composite Relaibility, ASTM STP 580 ed., ASTM International, West Conshohocken, PA, 1975, pp. 364-377.
[5] NA Fleck, Compressive Failure of Fiber Composites, in: John W. Hutchinson and Theodore Y. Wu (Ed.), Advances in Applied Mechanics, Elsevier, 1997, pp. 43-117.
[6] DC Lagoudas, AM Saleh. Compressive Failure due to Kinking of Fibrous Composites, Journal of Composite Materials. 27 (1993) 83-106.
[7] MR Piggott. The effect of fibre waviness on the mechanical properties of unidirectional fibre composites: A review, Composites Sci.Technol. 53 (1995) 201-205.
[8] MPF Sutcliffe, NA Fleck, Effect of geometry on compressive failure of notched composites, International Journal of Fracture. 59 (1993) 115-132.
[9] J Christoffersen, H Myhre Jensen. Kink band analysis accounting for the microstructure of fiber reinforced materials, Mech.Mater. 24 (1996) 305-315.
[10] S Kyriakides, R Arseculeratne, EJ Perry, KM Liechti. On the compressive failure of fiber reinforced composites, Int.J.Solids Struct. 32 (1995) 689-738.

© (2012) Trans Tech Publications, Switzerland
doi:10.4028/www.scientific.net/KEM.488-489.476

Fatigue Crack Propagation in New Generation Aluminium Alloys

Sébastien Richard [a], Christine Sarrazin-Baudoux [b] and Jean Petit [c]

Pprime Institute, ENSMA, Department of physics and mechanics of materials

Futuroscope site, Chasseneuil du Poitou, France.

[a] sebastien.richard@ensma.fr, [b] christine.baudoux@ensma.fr, [c] jean.petit@ensma.fr

Keywords: fatigue crack propagation, Al-Cu-Li and Al-Cu-Mg alloys, microstructure, atmosphere environment, crack closure, slip mechanisms, modelling.

Abstract. The fatigue crack propagation behaviour of a new third generation Al-Cu-Li alloy type 2050-T84 developed for aeronautical applications is studied in comparison to a new generation Al-Cu-Mg alloy type 2022-T851. The alloy resistance against crack growth is shown to depend on alloy composition, aging condition and atmosphere environment. The crack path and the growth rate at moderate ΔK and in the near-threshold domain are discussed in terms of the slip morphology with respect to the microstructure. The different crack propagation regimes, as identified by mean of micro-fractographic observations and EBSD analysis are discussed on the basis of a modelling framework elaborated for conventional metallic alloys.

Introduction

Weight saving is more than ever a strategic issue in aeronautics reinforced by the dramatic increase in fuel prices. Aluminum alloys, due to their good specific mechanical properties, are widely used and developed in aeronautical industry, to answer this issue. New generation aluminum alloys are developed to improve the properties through optimization of microstructures of conventional alloys as for 2022-T851 or through a reduction of the material density by mean of Lithium addition as for 2050-T84. Damage tolerance properties being of primary importance for aerospace structures, the aim of this paper is a study the fatigue crack propagation resistance of these new generation alloys. The objective of the present paper is to improve the understanding of the coupled influence of microstructure and of the atmosphere environment on the fatigue crack path and the fatigue crack growth rate in these new generations Al alloys in comparison to alloys of previous generations [1].

Experimentals

The alloys used in the present study were provided by Alcan in form of 40 mm thick plate of Al-Cu-Mg 2022 alloy in T851 temper, 15.5mm thick plate of 2050 alloy in the T84 temper. The microstructures of both Al-Cu-Mg alloys are very similar and consist of grains elongated in the rolling direction (670x200x80 μm3). The peak-aged heat treatment of the 2022 alloy is the standard temper designation T851 and consists of predominant incoherent θ' plates (Al_2Cu) of about 100 nm length, and a few S (Al_2CuMg) precipitates. The fibrous microstructure of the 2050T84 alloy (Figure 1) consists of partially re-crystallized grains strongly elongated in the rolling direction ($1000x100x30\mu m^3$), the hardening precipitation consisting mainly in incoherent T_1 plates (Al_2CuLi) of about 100 nm length. Chemical compositions of the alloys are given in Table 1, and the main mechanical properties are presented in Table 2.

Fatigue crack growth tests were performed on a servo hydraulic testing machine under load control. The loading signal was a sinusoidal waveform with a frequency of 35 Hz and a load ratio (R) of 0.1.

Table 1: Chemical composition (wt. %) of 2050-T84 and 2022-T851 alloys

	Cu	Li	Mg	Mn	Ag	Si	Fe	Zn	Zr	Cr	Ti
2050-T84	3.2- 3.9	0.7-1.3	0.2- 0.6	0.2- 0.5	0.2- 0.7	< 0.08	< 0.1	< 0.25	0.06- 0.14	-	-
2022-T851	4.5- 5.5	-	0.1- 0.45	0.15- 0.5	-	0.15	0.2	0.05- 0.3	-	0.05	0.15

Table 2 : Main properties of the studied alloys.

	Direction	E (GPa)	$R_{p0.2}$ (MPa)	R_m(MPa)	A (%)	K_{IC} (MPa.m$^{1/2}$)	d
2050-T84	T-L	77	500	530	11	37	2.70
2022-T851	L-T	72	380	440	14	41	2.80

The compact tension specimens were machined for a crack plane having orientation of table 2 with a width W of 50 mm and a thickness B of 10 mm. The crack length, a, was recorded with a traveling microscope. Threshold tests were performed using a load shedding procedure in accordance with the ASTM recommendation E 647. After the attainment of growth rates *da/dN* lower than 10^{-10} m/cycle, a constant load test was performed at R=0.1 up to the near-failure domain. Crack closure measurements were carried out using the compliance method, by means of a capacitive gauge mounted at the mouth of the notch of the specimens [2]. High vacuum tests were conducted inside the environmental chamber allowing a low pressure of $3x10^{-4}$ Pa.

Results and discussion

Figure 2 shows the experimental results of crack growth rate, *da/dN*, versus stress intensity factor range, *ΔK*, plotted in a log-log diagram.

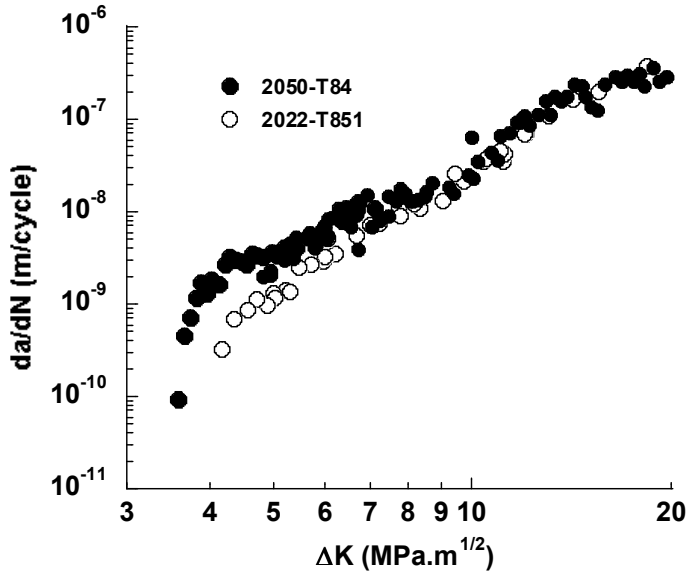
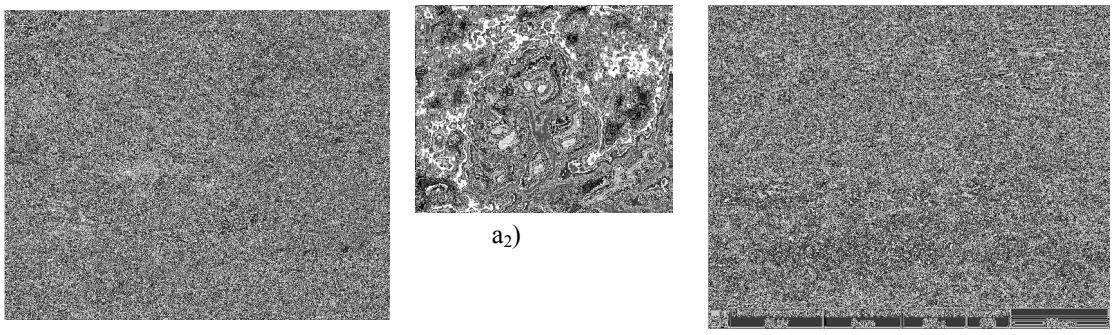


Figure 1: da/dN vs ΔK diagram in ambient air: room temperature, R=0.1 and 35 Hz.

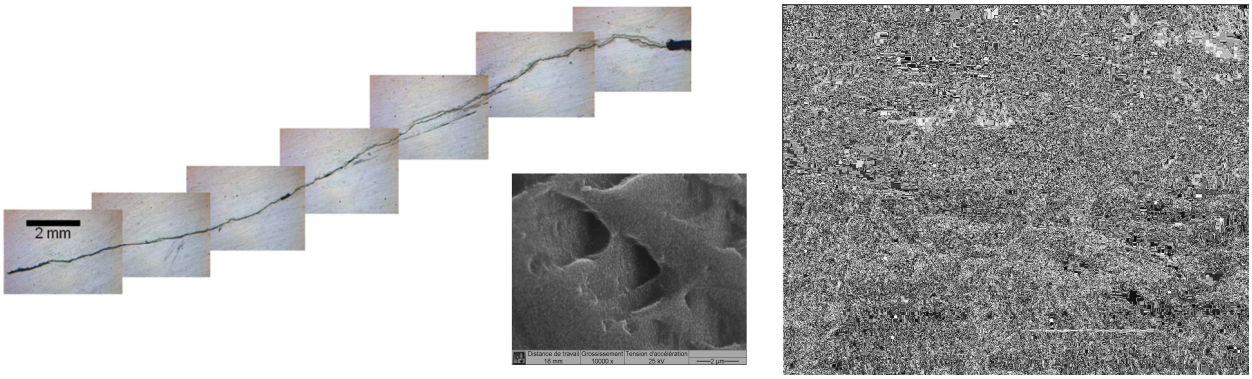
For *da/dN* higher than 10^{-8} m/cycle (or $\Delta K > 10$ MPam$^{1/2}$), the Li bearing alloy 2050-T84 and the Al-Cu-Mg alloy 2022-T851 present a very similar crack growth behavior. SEM observations of the crack surfaces are presented in figure 2.



a) a_2) b)

Figure 2: Fracture surface morphology at $\Delta K > 10MPam^{1/2}$: a) 2050-T84 and b) 2022-T851

On both alloys, typical stage II fracture surface morphology is observed at $\Delta K > 10MPam^{1/2}$. Etch pits obtained by the mean of a Keller chemical etching, are illustrated in the figure $2a_2$ for the 2022 alloy. Similar pits are obtained on both alloys in this rate range in ambient air. Such square shaped pits are consistent with (110) or (100) crack planes which had been analyzed as the result of alternative slip on two more or less symmetrical (111) planes. Such a mechanism associated to a mode I opening and a crack path normal to the load axis, is typical of a stage II crack generally poorly sensitive to the microstructure and to the ambient environment [3].At *da/dN* lower than 10^{-8} m/cycle, the 2050-T84 alloy shows progressively increased growth rates leading to a lower threshold range ΔK_{th} in comparison to the 2022 alloy. The crack path in the 2022 is comparable to the stage II regime observed at higher ΔK, but, for the 2050 alloy, a crack path deviated at an angle of about 26° is observed with a typical crystallographic regime with oriented facets corresponding to (111) planes as identified by mean of EBSD analysis, showing a [011] <211> brass texture, and triangular etch pits (figure 3).



a) b_2) b)

Figure 3: Crack path in 2050 T4: a) deviation for ΔK<10MPam1/2; b) crystallographic fracture surface with oriented facets; b_2) triangular etch pits on crystallographic facets.

The differences in the crack growth behaviour of the alloys can be related to different effects related to microstructure, to the atmosphere environment and to the contribution of crack closure. In figure 4 is presented the analysis of the fatigue crack propagation done on the basis of a frame work modelling previously proposed for conventional alloys. Four propagation regimes have been highlighted [4]:

1) Two intrinsic regimes operative in inert environment (high vacuum): i) intrinsic stage II (ΔK^4 dependence) which is favored by peakaged microstructures containing large and non-coherent precipitates as in the 2022 alloy; ii) intrinsic stage I-like propagation which is favored by microstructures containing fine shareable precipitates as the T_1 precipitation in the 2050-T84 alloy. The deformation is localized within each individual grain along the crack front giving retarded crystallographic crack propagation retardation due to the barrier effect of grain boundaries [5].

2) Two environmentally assisted regimes operative in air and in moist atmospheres: i) water vapor adsorption assisted stage II (ΔK^4 dependence) with reduced energy to create new fresh surfaces [6]; ii) hydrogen assisted stage II propagation [7] which is *CTOD* (crack tip opening displacement) controlled (ΔK^2 dependence).

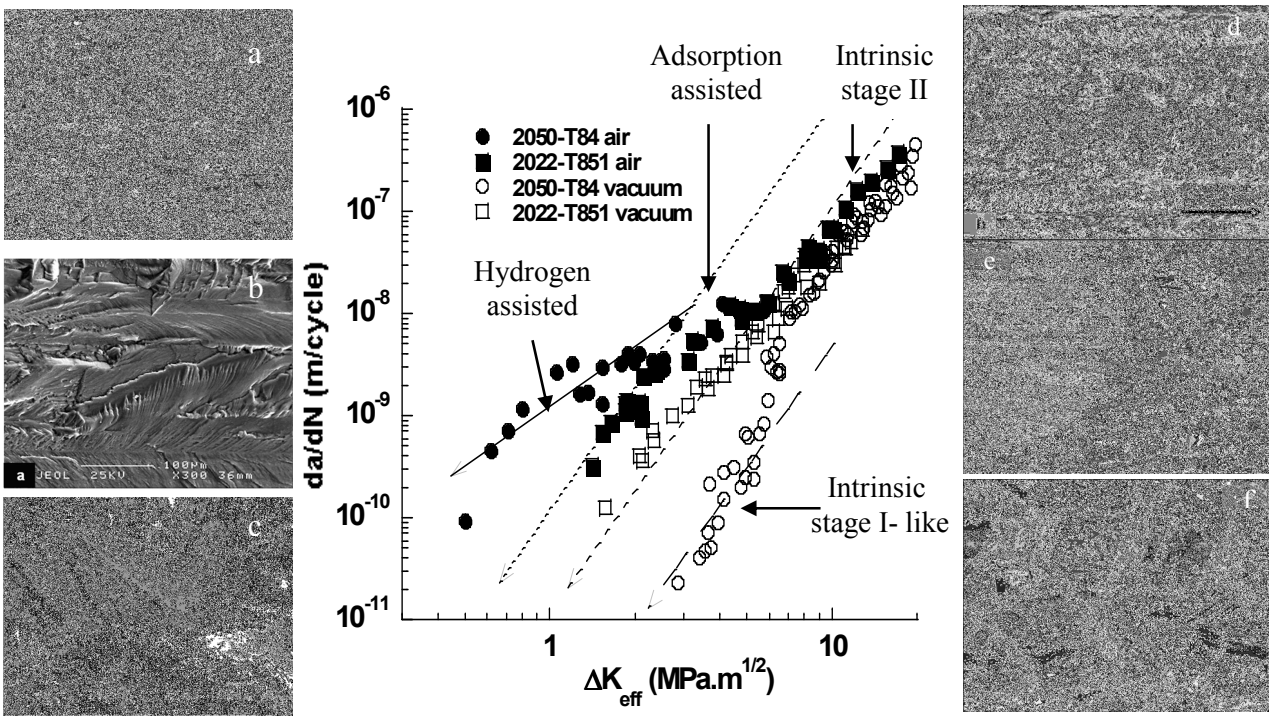


Figure 4: Propagation data compared to modeling frame work: a) adsorption assisted stage II in 2022 in air; b) oriented crystallographic propagation at low ΔK in 2050 in air; c) intrinsic near threshold stage II in vacuum in 2022; d) intrinsic stage II in vacuum at mid ΔK in 2050; e) transition in vacuum from intrinsic stage II to intrinsic stage I like in 2050; f) crystallographic intrinsic stage I like in vacuum near threshold in 2050.

Conclusions

From this comparative study, the following conclusions can be drawn:

i) a similar stage II crack propagation behavior for both alloys in the mid ΔK range with little influence of environment and microstructure;

ii) in the near threshold domain: - water vapor adsorption assisted stage II propagation for the 2022-T851 alloy in contrast to the intrinsic stage II in vacuum; - a high sensitivity to ambient air of the 2050-T84 alloy with enhanced *da/dN* and low threshold due to a *CTOD* controlled hydrogen assisted propagation in contrast to highly retarded crystallographic intrinsic stage I like in vacuum.

References.

[1] S. Richard, C. Gasquères, C. Sarrazin-Baudoux, and J. Petit Engng. Fract. Mech. (in press).
[2] J. Petit, G. Hénaff and C. Sarrazin-Baudoux, in: *ASTM STP 1372*, (2000), p. 3.
[3] C. Gasquères, C. Sarrazin-Baudoux, J. Petit and D. Dumont, Script. Mater. Vol. 53 (2005), p. 1333
[4] J. Petit, G. Hénaff and C. Sarrazin-Baudoux, in: *Comprehensive Structural Integrity: Environmentally-assisted Fracture*, J. Petit and P. Scott eds., Vol. 6 (2003), p. 211.
[5] K.J. Miller and E. R. De Los Rios: *The Behaviour of Short Fatigue Cracks,* (Mechanical Engineering Publications Limited, London 1986).
[6] S.P. Lynch*,* ASTM STP 675, (1978), p. 174.
[7] Y. Ro, S.R. Agnew, G.H. Bray and R.P. Gangloff, Mat. Sci. and Engng. A (2007), p. 88.

© (2012) Trans Tech Publications, Switzerland
doi:10.4028/www.scientific.net/KEM.488-489.480

An Effect of Shot Peening on Retardation and Growth of Short Fatigue Cracks in an Aircraft Al-alloy

Ivo Černý[1,a]

[1]SVÚM a.s., Podnikatelská 565, 19011 Praha 9, Czech Republic

[a]Ivo.Cerny@seznam.cz

Keywords: Shot peening; fatigue crack growth; fatigue life; aircraft Al-alloy

Abstract. The paper contains the main results of an investigation of an effect of shot peening on residual fatigue life of specimens made of an aircraft V-95 Al-alloy (equivalent to 7075 alloy) containing physically short fatigue cracks. In the first part, an adaptation and verification of direct current potential drop method for detection and measurement of short crack growth is described and discussed. The specific properties of the material and quite large dimensions of flat specimens with side necking with a low stress concentration factor had to be considered when the position of electrodes was specified. The specimen type and dimensions were proposed considering the investigation of shot peening effects. Physically short fatigue cracks of the length from 0.2 mm to more than 3 mm, most of them between 0.8 – 1.5 mm, were prepared under high cycle fatigue loading of the constant nominal stress amplitude ±160 MPa. Specimens with existing short fatigue cracks were shot peened using two different groups of parameters. Crack growth characteristics after shot peening were measured and compared with crack growth in specimens without shot peening. Retardation of crack growth was significant particularly for cracks shorter than 2 mm. Results are also discussed form the viewpoint of fracture mechanics approach. For the specific stress amplitude, evaluated results enable to estimate threshold length of defects, which after the application of shot peening will be reliably arrested.

Introduction

Present-day advanced design approaches in numerous fields of mechanical and transport engineering are connected with so called Damage Tolerance approach, which accepts presence of certain, well defined cracks or crack-like defects in structures provided that such defects are under control to exclude unexpected failure. The Damage Tolerance approach is being used not only in structures, where failure need not result in fatal consequences like e.g. ground transport vehicles, but also in aircraft industry. The main advantage of the Damage Tolerance philosophy namely is a considerable weight reduction, connected with a lower fuel consumption, higher payload, reduced environmental impact etc. On the other hand, a detailed knowledge about growth characteristics and mechanisms of such defects is a fundamental condition of safe and reliable operation of structures under the Damage Tolerance conditions.

There are other important factors affecting fatigue life of structures containing defects – possibilities to reduce their development. One of the methods is represented by shot peening, which is surface treatment applied to various metallic materials either separately or after previous surface treatments like plating, hard anodising etc., in order to locally improve the performance of mechanical components under fatigue loads [1,2]. This treatment creates compressive residual stresses and material local hardening that usually increases the operating life of the component.

The final effect of shot peening on fatigue resistance depends on numerous parameters and material which the technology is applied to. As an example, recent advanced shot peening methods are linked to development of nanostructures in the material surface [3]. In general, if the parameters of shot peening are not optimised for a specific material and for its basic structural and mechanical properties, shot peening may not be beneficial and fatigue resistance can even be deteriorated [4,5].

Recent advanced approaches are based on the hypothesis that compressive residual stresses are able to slow down or stop cracks propagation instead of preventing their formation, and therefore there are particularly suitable for applications under the Damage Tolerance conditions.

The evaluation of shot peening favourable effects is connected with high demands on sophisticated experimental methods, particularly preparation of physically short fatigue cracks in specimens of reasonable dimensions suitable for shot peening applications and exact measurement of actual crack length including not only surface path but also an estimation of crack profile inside the specimen. Length of short cracks is usually measured optically, which however does not enable to assess the subsurface length at all. Complex crack growth measurement including subsurface profile, which is an essential condition of application of fracture mechanics approaches, is not an easy task, particularly if specimens are of quite big dimensions.

In the first part of this paper, possibilities of measurement of short crack growth are analysed and discussed. The second part of the paper contains results of the experimental programme aimed at the evaluation of shot peening effects on retardation of short fatigue cracks applied to specimens of the Al-alloy containing short fatigue cracks preliminarily prepared by fatigue loading.

Method of Measurement and Evaluation of Short Crack Length

If homogenous direct current passes through a specimen with a constant rectangular cross section and the specimen of the width W contains an edge crack of the length a and potential is measured near the crack mouth at the distance y, then the crack length can be evaluated from the measured potential $V(a)$ using the well known Johnson´s formula [6]. A modification of the method for short specimens, where reference potential V_{ref} is measured in the area affected by the crack was described in [7,8].

There are two parameters affecting the measurement sensitivity, namely position of electrodes (distance y from the crack mouth) and specimen width W. To optimise these two parameters and explore possibilities and experimental limits, a kind of sensitivity analysis was carried out. Several situations were modeled and analytical calibration curves were calculated, namely:

– for the specimen of width W = 15.72 mm with three different mutual distances of potential electrodes near the crack mount – (i) y = 5 mm, (ii) y = 3 mm and (iii) y = 1 mm and
– for the same three values of distances y in case of specimen width W = 5 mm.

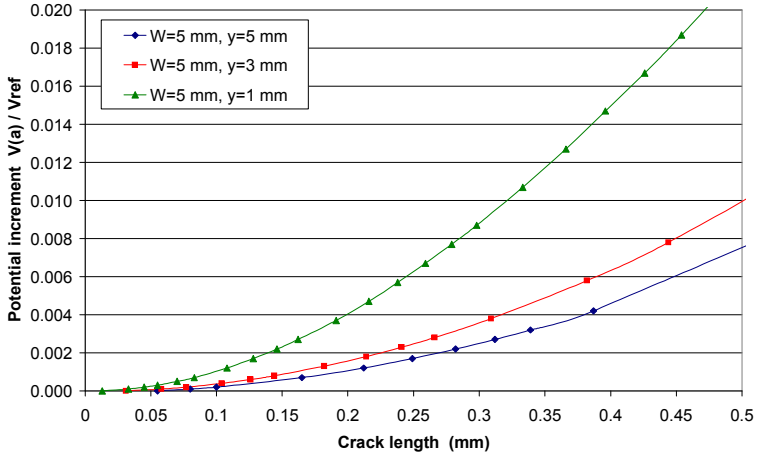


Fig. 1: Sensitivity of DCPD method as a dependence of distances of electrodes from crack mouth

Detail results of the sensitivity analysis were provided in [9]. The DCPD measurement was significantly more sensitive for the specimen of 5 mm width in comparison with the larger one. However, the sensitivity started to be higher for fairly long cracks with the length at least 30% of the total specimen width. The measurement sensitivity in the region of short cracks up to 1 mm was not unfortunately increased by the reduction of specimen width. Therefore, the model calibration curves were further calculated just for the specimen of 5 mm width – Fig. 1.

Considering the device resolution ≈ 0.001 of the potential ratio $V(a)/V_{ref}$ and the diagram in Fig. 1, it can be assessed that the minimum detectable crack length corresponds to approximately 0.10 mm, 0.16 mm and 0.19 mm for the electrode distances 1 mm, 3 mm and 5 mm, respectively. These results were quite encouraging. Unfortunately, a fairly large distance of electrodes had to be used due to fatigue cracking under the electrode instead of the free surface of the specimen edge [10].

Experimental Material and Procedure

The V-95 material is a Russian Al-alloy of Al-Zn-Mg type and is almost equivalent to a 7075 Al-alloy with just slightly lower content of Zn and Cu. Due to its high mechanical properties and fatigue resistance, it has been widely used for construction of aircraft structures, such as wings and fuselages, already for many years [11]. Typical values of basic mechanical properties of this material at heat-treated conditions are: strength up to 550 MPa and yield stress up to 480 MPa.

The V-95 alloy was available in the form of sheets of thickness 2.1 mm in Aeronautical Research and Test Institute in Prague, where specimens also were manufactured. The specimen were of quite big dimensions due to technological reasons of the shot peening application: total length 200 mm, width at gripping area 48 mm. To localize the area of crack initiation and to enable subsequent shot peening of specimen edges, shallow necking were made from both the specimen sides. The necking radius was 28 mm, the minimum width at the specimen centre was 24 mm.

Fatigue cracks of different length between 0.35 mm and 3.6 mm were prepared in 17 specimens, whereas the length of most of the cracks was between 0.87 mm and 1.49 mm (9 specimens). The nominal stress amplitude was constant, ±160 MPa, and common for all the specimens. After pre-cracking, the specimens were divided into two groups, each of them containing a similar spectrum of cracks lengths so that the groups could be compared to each other. Shot peening of two different parameters was applied at Technometra Radotín a.s. to the first and second group, respectively. Parameters of the shot peening were: Balottini sizes 0.43 – 0.7 mm and 0.21 – 0.32 mm for the first group and second group, respectively, Almen intensity A = 0.25 and A = 0.14 for the first and second group respectively. Shot peening angle was 60° and coverage 200% for both groups. Both edges in the central area of specimens were shot peened from both sides to the distance of 4 – 5 mm from the edge.

Experimental Results and Discussion

Residual fatigue life in terms of number of cycles to failure of specimens containing short cracks as a dependence on crack length and K-factor range are shown in Figs. 3 and 4, respectively.

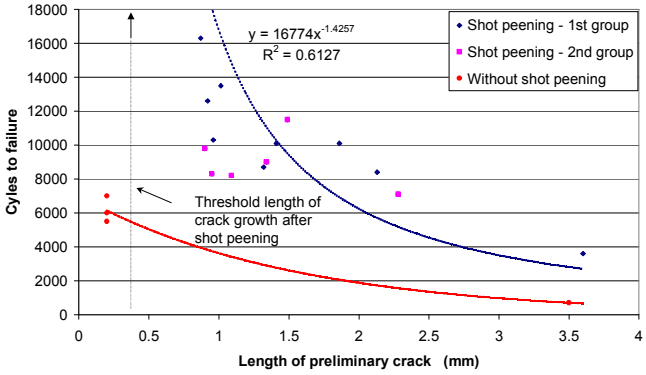


Fig.3: Residual fatigue life of specimens with short cracks after shot peening in comparison with untreated specimens

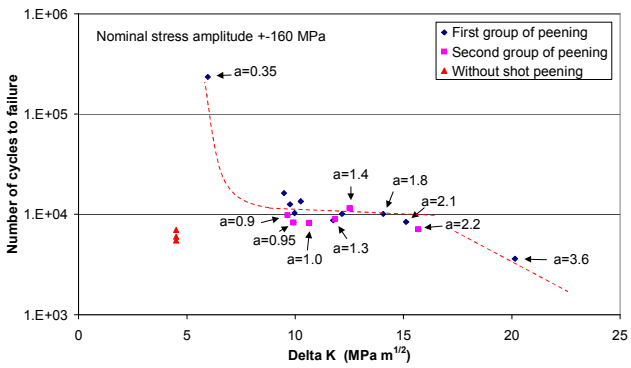


Fig.4: Residual fatigue life of specimens with short cracks as a dependence on stress intensity factor range

It follows from Figs. 3 and 4 that the retardation effect resulted from shot peening was significant. In the region of crack length around 1 mm, the estimated increase of fatigue life is at least between 2- and 3-times, the effect being stronger for the first group of shot peening parameters. However, even for cracks longer than 2 mm, some retardation effect is evident. Results in Fig. 3 enable to estimate the threshold length of the total crack arrest. The estimation was made on the basis of extrapolating the regression line for the shot peened specimen groups, the estimated value being approximately 0.35 mm. On the contrary, short crack growth in specimens without shot peening was much rapid, even bellow the threshold 0.35 mm: The residual life of not treated specimens with 0.2 mm long crack only was approximately 6000 cycles.

The plateau in Fig. 4 for ΔK between 8 and 16 MPa $m^{1/2}$ indicates a rather low sensitivity of residual life on K-factor in this interval, which may be connected with a characteristic behaviour of short fatigue cracks – with a local minimum of crack growth rates in the transient region between short and standard long fatigue cracks.

Conclusions

The main results of an investigation of shot peening with two groups of selected parameters on retardation of physically short fatigue cracks in a V-95 (7075) aircraft Al-alloy at repeated loading with stress amplitude ±160 MPa can be summarised as follows:

- Possibilities of the use of a modified direct current potential drop method for detection and measurement of short fatigue cracks of lengths starting from 0.2 mm were verified.
- Shot peening resulted in a considerable retardation of physically short fatigue cracks, the effect being most strong for crack lengths about 1 mm. Moreover, there was threshold crack length of approximately 0.35 mm, bellow which no further propagation occurred contrary to specimens without application of the shot peening technology with no such the threshold.

Acknowledgements

The work was carried out under the support of Ministry of Education, Youth and Sports of Czech Republic, grant MSM 2579700001.

References

[1] H.J.C. Voorwald, M.P. Silva, M.Y.P. Costa and M.O.H. Cioffi: Fatigue Fract. Eng. Mater. Struct. Vol. 32, No. 2 (2009), pp. 97-104.

[2] A. Camargo and H. Voorwald: Fatigue Fract. Eng. Mater. Struct. Vol. 30, No.11 (2007), p. 993.

[3] S. Bagherifard and M. Guagliano: submitted to Eng. Fract. Mech. (2011)

[4] F. Nový, M. Chalupová, M. Činčala and O. Bokůvka: Acta Mechanica Slovaca Vol. 11, No. 4 (2007), pp. 189-194.

[5] F. Nový, O. Bokůvka, M. Chalupová and V. Valovičová: Acta Mechanica Slovaca Vol. 12, No. 4-B (2008), pp. 209-214.

[6] H.H. Johnson: Mater. Res. Stand. Vol. 5, No. 9 (1965), pp. 442-445.

[7] I. Černý: Eng. Fract. Mech. Vol. 71, Nos. 4-6 (2004), pp. 837-848.

[8] I. Černý: Int. J. Press. Vessels Pip. Vol. 78, Nos. 11-12 (2001), pp. 893-902.

[9] I. Černý, in: *Proc. of the 1st Int. Conf. COMAT 2011*, edited by COMTES FHT a.s., Dobřany

[10] I. Černý: submitted to Procedia Engineering (2011).

[11] A.V. Karlashov, R.G. Gainutdinov and A.V. Golubnichii: Mater. Sci. Vol. 11 (1976), p.100.

© (2012) Trans Tech Publications, Switzerland
doi:10.4028/www.scientific.net/KEM.488-489.484

The Effect of Nonlinear Matrix on Crack Propagation in the Particulate Composite

Zdeněk Majer[1,a], Pavel Hutař[2,b]

[1]Faculty of Mechanical Engineering, Brno University of Technology, Technická 2896/2, 616 69 Brno, Czech Republic

[2]Institute of Physics of Materials, Academy of Sciences of the Czech Republic, Žižkova 22, 616 62 Brno, Czech Republic

[a]majer@fme.vutbr.cz, [b]hutar@ipm.cz

Keywords: particulate composites, FEM, interphase, fracture mechanics.

Abstract. In this paper polymer particulate composite was studied. The composite was modeled as a three-phase continuum – soft matrix, interphase and rigid particles. On the basis of fracture mechanics methodology the interaction of micro-crack propagation in the soft matrix filled by rigid particles (covered by the interphase) was analyzed. The properties of soft matrix (elasto-plastic material) were determined from the experiment and they were used for estimations of the crack behavior.

Introduction

The polymeric particulate composites, especially with the polypropylene matrix and mineral fillers (rigid particles), are of great practical importance due to the possibility both of modifying many different mechanical properties and reducing the price/volume ratio of resulting material [1,2]. Particulate composites are composed by the polypropylene matrix (PP) and rigid mineral fillers. The properties of the soft matrix, interphase and rigid particles (size, shape, material properties) can have a significant effect on the global behavior of the composite. The change of the general material properties of the particulate composites is the usual motivation for investigation particulate filled composites.

Generally, the addition of rigid particles to a polymer matrix will have an embrittling effect on the composite. The part matrix near the surface of the rigid fillers may have different properties, appear as a different thermodynamic phase, or even have a different chemical composition. To initiate the formation of the interphase, particles used as a filler are usually chemically treated. Moreover, the treatment of the particles contributes to their better dispersion in the polypropylene matrix. The presence of the interphase between particles and matrix can significantly change the final global mechanical properties of the composite.

In this contribution the composite composed of polypropylene matrix (PP) and rigid mineral fillers ($Mg(OH)_2$) was analyzed. The influence of the interphase on toughening mechanisms was discussed. The thickness of the interphases studied depends on the matrix and particle chemical composition only and is probably independent of the size of the particle [3]. As matter of fact, the thickness of the interphase was usually determined indirectly from a composite property, but results depend very much on the method of determination. The estimated interphase thickness of the composite, using various methods based on global material properties of this composite (modulus, yield stress, tensile strength), varies from 0.012 μm to 0.160 μm. In the paper [3] the interphase thickness for the studied composite (rigid particle - soft interphase) was estimated about 0.100 μm.

The polymer particulate composite with respect linear-elastic properties of soft matrix already was studied [4]. The FEM model was created with respect a few general terms [5]: (i) particles

should be of small size (less than 5 μm), (ii) aspect ratio must be close to unity to avoid high stress concentration, (iii) particles must debond prior to the yield strain of the matrix polymer in order to change the stress state of the matrix material and (iv) particles must be dispersed homogeneously in the matrix polymer.

Experiment

Used matrix was copolymer PP SHAC KMT 6100 (produce by Shell International Chemical Co. Ltd.). This material is using for injection of products (i. e. tools, cars components, equipment of household) [6].

As rigid fillers were used magnesium hydroxide in two commercial available versions, see Tab. 1; company named KISUMA 5AU and MAGNIFIN H 10. In addition MAGNIFIN H 10 by 2,5% stearic acid named ASTRA was modified [6].

Table 1 Different types of materials identification.

Material	S	F2	F4	F6	S2	S4	S6	N2	N4	N6
Filler	---	KISUMA 5AU company modified			MAGNIFIN H10 modified			MAGNIFIN H10 unmodified		
[%] VFF	0	20	40	60	20	40	60	20	40	60

The Young´s modulus of the particle was E = 72 GPa, and the value of Poisson´s ratio was ν = 0.29. The material properties characterizing the composite correspond to rigid particle ($Mg(OH)_2$) filled polypropylene obtained from experiment was used.

From experiment the ideal size of particles as rigid filler was determined too. Size dispersion is for both types of using filler similar and it can be said that assumption of particle size 1 μm is correct and valid [6].

Numerical model

For calculations of α was supposed that the particles are homogenously and regularly distributed in the matrix, the structure had to be strictly periodical and a unit cell with four particles should be regarded as representative for the composite structure, see Fig. 1.

Generally, a crack propagating in the matrix has a tendency to deflect to regions with stiffer materials (particles). If the particle is covered by a softer interphase, this effect is shielded and the trend of micro-crack propagation can be changed [7]. The composite was modelled as a three phase continuum and numerically simulated at a microscopic level by a unit cell scheme.

For determination of crack propagation direction the maximum tangential stress (MTS) criterion [8] has been used.

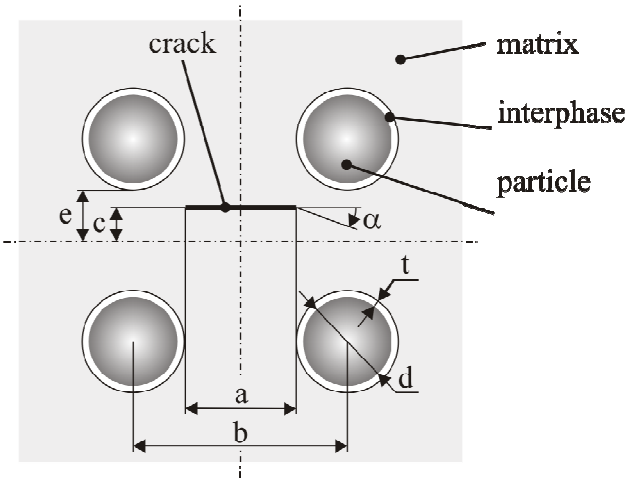


Figure 1 Geometry of the model.

The stress and strain distributions in the matrix have been determined for the following interphase properties: the value of Young's modulus of the interphase varies from maximum value for type of matrix (from experiment was determined different Young´s modulus for different temperature) to 0.1 GPa and it was assumed that Young's modulus of the interphase was constant through its thickness. A micro-crack of length corresponding approximately to the distance between the particles was modelled and the corresponding values of the stress intensity factors K_I and K_{II} and consequently the angle α were calculated.

Results of the numerical analysis

For all calculations the particles with interphase was considered. Generally, the presence of rigid particles in a polymer matrix leads to an embrittling effect on the composite. The existence of the interphase between matrix and particles can change significantly in many cases micro-crack behavior. Consequently, the global behavior of the polymer particulate composite is affected too. The fracture toughness of the polymer composite is influenced by several phenomena: (i) aggregation of the rigid particles, (ii) particles shape and size, (iii) distribution of the particles in the soft matrix (iv) and also material properties of the interphase (Young´s modulus). The present work is focused mainly on the effect of the interphase material properties. Assuming that particles were regularly distributed in the matrix, the behavior of the micro-crack (length of the crack *a* is comparable with distance between particles *b*) was studied for particle size 1μm with constant thickness of interphase 0.100 μm and temperature -50°C, see Fig. 2.

As a special case the configuration corresponding to perfect adhesion between particles and matrix (interphase Young modulus is equal to matrix E_i = 4.2 GPa) was considered as well. In this case the angle of deflection α is significantly positive all the time. That means the crack avoids regions with rigid particles and grows only in the pure matrix.

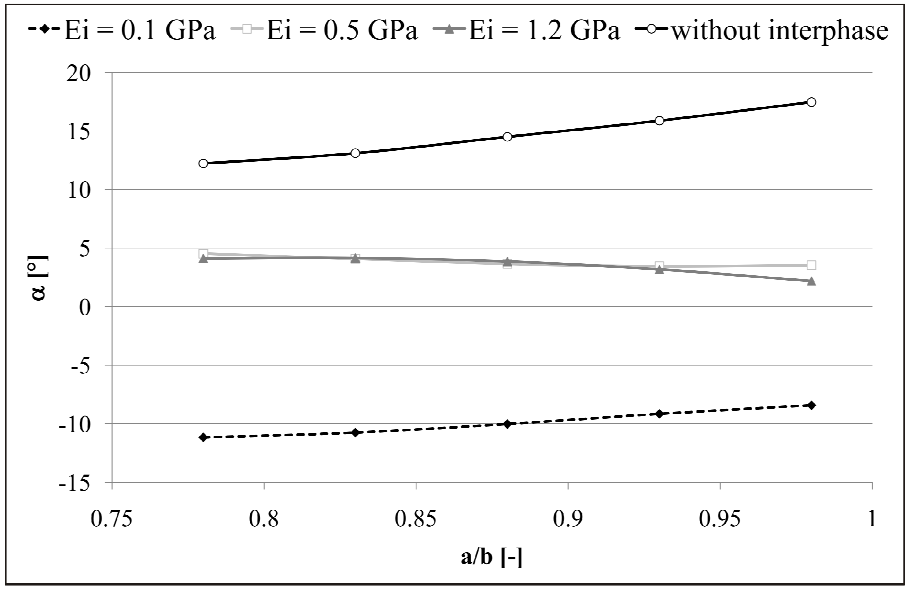


Figure 2 Dependence of crack propagation direction α on the ratio *a/b* for different values of the interphase Young´s modulus. Computations correspond to particle size 1μm, constant thickness of interphase 0.100 μm and temperature -50°C (temperature of experiment of matrix estimation).

If Young´s modulus of the interphase decreases and it is less than Young´s modulus of particles the effect of the rigid particles is partially attenuated by the softer interphase. The final effect on crack behavior is then indispensable (in this case interphase Young´s modulus is evaluated for approximately E_i = 0.5 GPa and E_i = 1.2 GPa, see Fig. 2). It is shown the micro-crack is not attracted or repelled. It means that the crack is growing independently of the presence rigid particles. In every way, this effect leads to contact of micro-crack and interphase.

For smaller values of the interphase Young´s modulus (E_i around 0.1 GPa) rigid particles are completely shielded by soft interface and the calculated angle of deflection α is always negative. It follows that the crack is attracted by the particles.

When the crack tip touches interphase, the interphase is damaged due to high stresses and the rigid particle becomes fully debonded. In context with this effect, the micro-crack is blunted. The stress singular field is changed and the micro-crack stays arrested near the particle. The blunting of the micro-cracks in connection with debonding can contribute to significant increase in fracture toughness of the composite [5], [9]. As a result, the micro-crack is blunted it needs some time (more energy) for re-initiation or better stays arrested on the particle.

Discussion and conclusions

The polymer particulate composite was studied. The composite was modelled as a three phase continuum (interphase, soft matrix and rigid particle) and numerically simulated at a microscopic level by a unit cell scheme using finite element model. The behaviour of the micro-crack was estimated for several interphase properties and material types of matrix.

It was determined that one of the basic mechanisms consists in the shielding of the rigid particles by a very soft interphase. This leads to the separation of interphase from the particle and to blunt of the micro-cracks. This effect is strongly material properties of matrix and interphase dependent.

In the case corresponding to matrix with Young´s modulus 4.2 GPa it is shown that the softest interphase properties leads to attraction of micro-crack by particles. For cases Young´s modulus of interphase 0.5 and 1.2 GPa it is shown that the micro-crack is not attracted or repelled. It means that the crack is growing independently of the presence rigid particles. In every way, this effect leads to contact of micro-crack and interphase.

Acknowledgment

This research was supported by grant P107/10/P503 of the Czech Science Foundation.

References

[1] B. Pukánszky: European Polymer Journal 41, 2005, pp. 645-662

[2] H.-G. Elias: *An Introduction to Plastics. 2ndEd.Weinheim*, Wiley-VCH GmbH&Co., Weinheim, 2003, ISBN 3-527-29602-6

[3] J. Moczó, E. Fekete, B. Pukánszky: The Journal of Adhesion 78, 2002, pp. 861-876

[4] P. Hutař, Z. Majer, L. Náhlík, L. Šestáková, Z. Knésl: Mechanics of Composite Materials 45, 2009, pp. 281-286

[5] W. C. J. Zuiderduin, C. Westzaan, J. Huétink, R., J. Gaymans: Polymer 44, 2003, pp. 261-275

[6] E. Molliková: Disertační práce, FSI VUT v Brně, 2003, pp. 103 (in czech)

[7] Z. Knésl, P. Hutař, L. Náhlík: Composites/nano-engineering ICCE 15, Haikou, China, 2007, CD

[8] F. Erdogan, G.C. Sih: Journal of Basic Engineering 85, 1963, pp. 519-527

[9] G. M. Kim, G. H. Michler: Polymer 39, 1998, pp.5689-5703

© (2012) Trans Tech Publications, Switzerland
doi:10.4028/www.scientific.net/KEM.488-489.490

On Effective Properties of Layers in Damaged Composite Laminates

Janis Varna

Lulea University of Technology, 97187 Lulea, Sweden

Janis.Varna@LTU.SE

Keywords: damaged laminate, laminate stiffness, intralaminar cracks, crack density, effective elastic constants.

Abstract. Methodology is suggested for calculation of effective elastic constants of layer containing intralaminar cracks. Trends are presented for layers with low and medium high crack densities, where the interaction between cracks can be neglected. The effective properties of the damaged layer are determined by back- calculation using previously developed GLOB-LOC model for thermo-mechanical properties of damaged laminate [1]. It is shown that the effective transverse modulus and shear modulus of a layer decrease linearly with increasing crack density, whereas longitudinal modulus and major Poisson's ratio do not change at all. Experimental data for multiple cracking are analyzed showing that linear approximation of crack density versus applied strain may have sufficient accuracy. These two linear trends are used to calculate the effective elastic properties of a layer as a function of strain.

Introduction

The most common approach of changing thermo-elastic properties of layers after introduction of damage is called "ply-discount model". In this paper we deal with intralaminar cracking which is caused by matrix failure and debonding and leaves fibers undamaged. Therefore the relevant modification of the ply discount model would be the one which leaves the longitudinal modulus and the major Poisson's ratio of the damaged layer unchanged but sets the transverse modulus and the in-plane shear modulus equal to zero.

In the presented paper this hypothesis is inspected by calculating stiffness of a laminate with fixed intralaminar crack state using GLOB-LOC model [1,2]. The laminate extensional stiffness matrix change with respect to the laminate theory values can be expressed in terms of changed stiffness matrix of the damaged layer. From there effective engineering constants of the damaged layer are calculated as functions of the damage state (intralaminar crack density).

The procedure is straight -forward and the back-calculation is unique if only one layer is damaged.

Methodology for effective properties determination

The analysis is valid for symmetric *N*- layer laminate. The *k*-th layer of the laminate is characterized by thickness t_k , fiber orientation angle with respect to the global x-axis θ_k and by stiffness in the local axes $[Q]$(defined by thermo-elastic constants $E_L, E_T, G_{LT}, \nu_{LT}$). The total thickness of the laminate, $h = \sum_{k=1}^{N} t_k$. The crack density in a layer is $\rho_k = 1/(2l_k \sin\theta_k)$ where average distance between cracks measured on the specimen edge is $2l_k$. Dimensionless crack density ρ_{kn} is introduced as $\rho_{kn} = t_k \rho_k$. The stiffness matrix of the damaged laminate is $[Q]^{LAM}$ and the stiffness of the undamaged laminate is $[Q]_0^{LAM}$. The extensional stiffness matrix of undamaged laminate is calculated as

$$[Q]_0^{LAM} = \sum_{k=1}^{N-1} [\overline{Q}]_k \frac{t_k}{h} + [\overline{Q}]_N \frac{t_N}{h} \quad . \qquad (1)$$

The stiffness matrix $[Q]_0^{LAM}$ is independent on the layer sequence in the laminate and therefore without loosing generality we can assume that the layer to be damaged (written separately in Eq. 1) has index N. When damage with given normalized crack density ρ_{Nn} is introduced in N-th layer, the stiffness matrix of the laminate $[Q]^{LAM}$ can be calculated using the GLOB-LOC model [1,2]. The result can be expressed also in terms of unknown effective stiffness of the damaged layer

$$[Q]^{LAM} = \sum_{k=1}^{N-1} [\overline{Q}]_k \frac{t_k}{h} + [\overline{Q}]_N^{eff} \frac{t_N}{h} . \tag{2}$$

In Eq.2 upper index "eff" stands for "effective". Subtracting Eq. 2 from Eq. 1 we obtain

$$[Q]_0^{LAM} - [Q]^{LAM} = \left\{ [\overline{Q}]_N - [\overline{Q}]_N^{eff} \right\} \frac{t_N}{h} . \tag{3}$$

From here the effective stiffness of the damaged N-th layer is

$$[\overline{Q}]_N^{eff} = [\overline{Q}]_N - \frac{h}{t_N} \left\{ [Q]_0^{LAM} - [Q]^{LAM} \right\} . \tag{4}$$

It can be transformed to local axes using expression

$$[Q]_N^{eff} = [T][\overline{Q}]_N^{eff} [T]^T \quad . \tag{5}$$

The effective compliance matrix of the damaged layer in local axes is calculated by inversion and effective engineering constants of the damaged layer (index N is omitted) follow from

$$E_L^{eff} = \frac{1}{S_{11}^{eff}}, \quad E_T^{eff} = \frac{1}{S_{22}^{eff}}, \quad -\nu_{LT}^{eff} = E_L^{eff} S_{12}^{eff}, \quad G_{LT}^{eff} = \frac{1}{S_{66}^{eff}} \quad . \tag{6}$$

If several layers are damaged instantaneously, the back-calculation using the described procedure is not unique and is not treated in this paper. If the interaction between damage in different layers can not be neglected, the most appropriate way of effective properties determination is iterative.

Results and analysis

In following examples cracks are in 90-layer only.

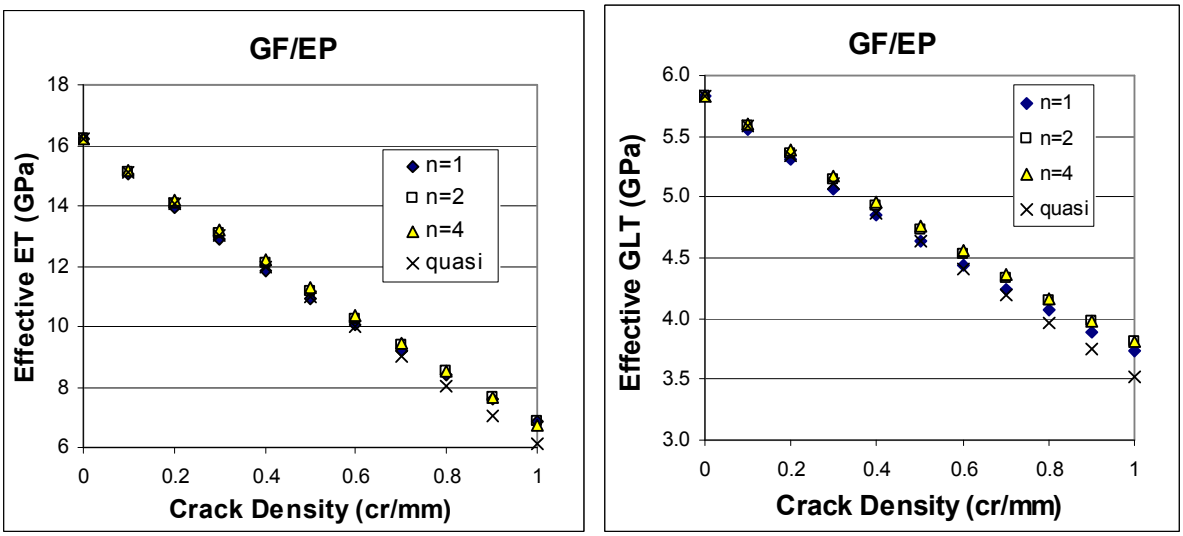
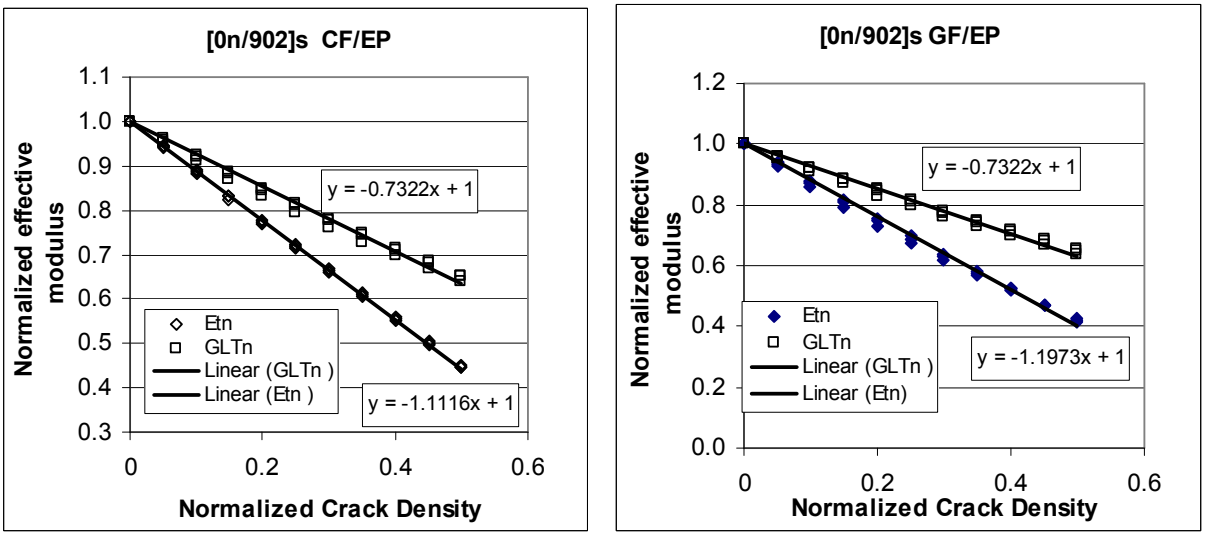


Figure 1 Reduction of 90-layer effective transverse modulus and shear modulus versus number of cracks in 90-layer of $(0n/90_2)s$ and $(-45_2/45_2/0_2/90_2)s$ laminates.

The back-calculation results in Fig. 1 show that the thickness ratio of plies in cross-ply laminate has negligible effect on effective transverse and shear modulus of the layer. The properties reduction with increasing crack density is linear. Calculations show that the effective longitudinal modulus and Poisson's ratio are exactly the same as in undamaged layer.



a) b)

Figure 2 Normalized effective elastic constants of damaged layer versus transverse crack density in this layer. Calculations and linear fit for $(0n/90_2)s$ cross-ply laminates with n= 1,2,4 : a) Glass fiber composite and b) carbon fiber composite.

According to Fig. 2 the shear modulus reduction slope is identical for CF/EP and GF/EP composites. The effective transverse modulus of GF/EP decreases slightly faster than that of CF/EP composite. Fig 3. presents experimental data on cracking in CF/EP cross ply laminates. The prepreg tape thickness was 0.3 mm leading to 90-layer thickness 0.3 mm and 1.8 mm for (0/90/0) and $(0/90_3)s$ respectively.

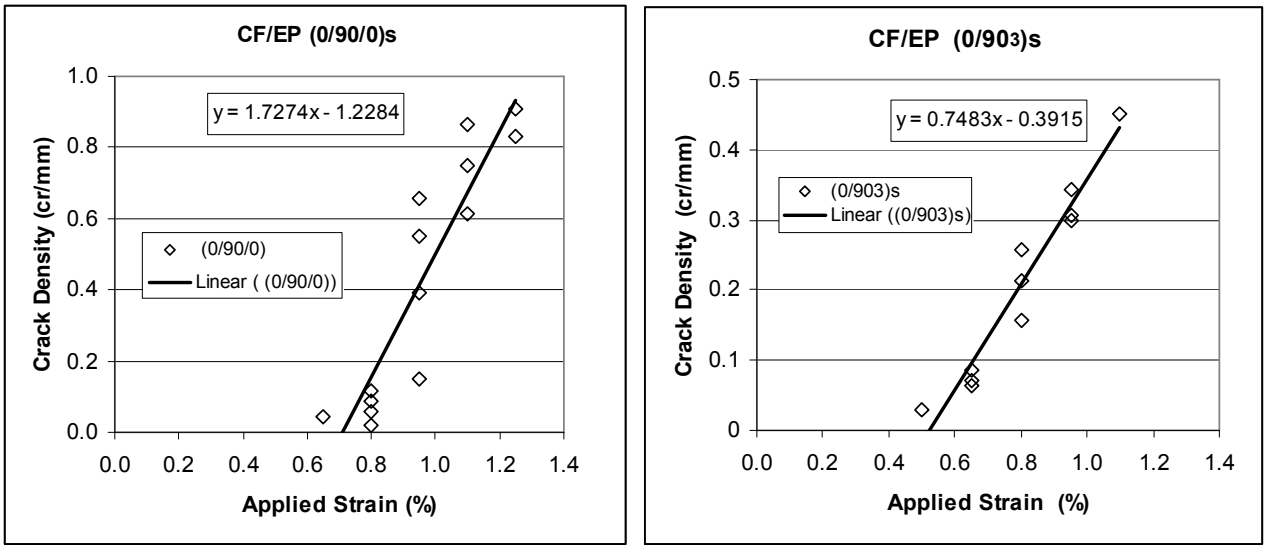
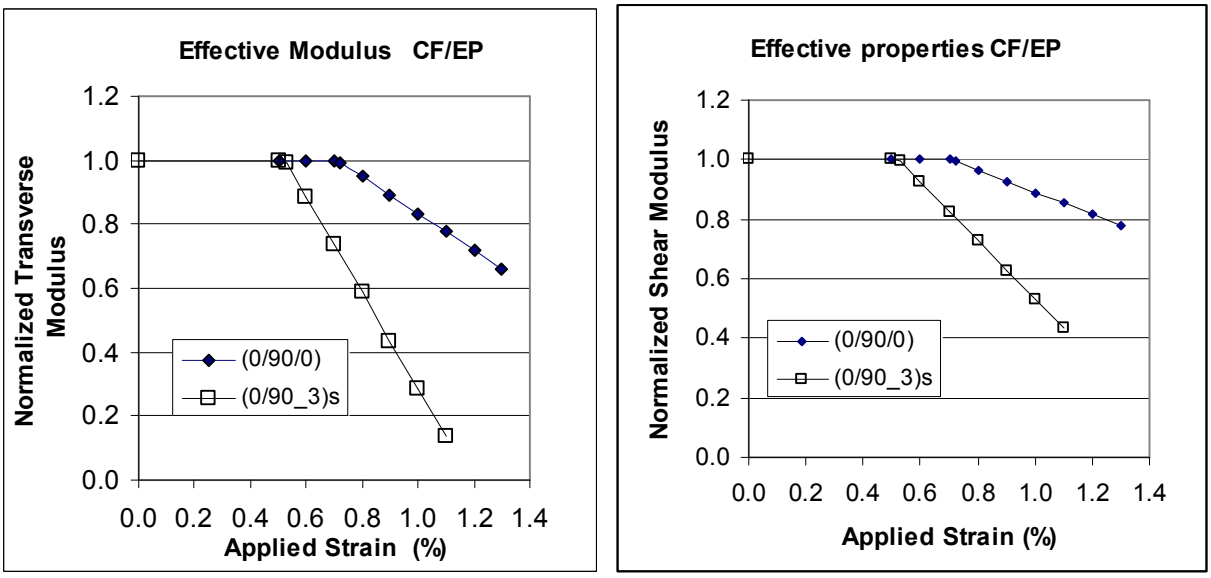


Figure 3 Crack density increase with applied strain in 90 layer of cross-ply laminates: a) CF/EP (0/90/0); b) $(0/90_3)s$

As expected cracking in the laminate with thinnest layer is delayed and is most probably controlled by crack propagation mechanisms described by fracture mechanics. In $(0/90_3)s$ the cracked layer is very thick and most probably strength based initiation controls the cracking process. Nevertheless, in both cases the crack density increase is rather linear in the considered region and linear trendline can be drawn as shown in Fig.3. It has to be noted that these specimens break as early as at 1.2 – 1.3 % strain and crack saturation was never observed.

The two obtained linear fitting lines: a) calculated normalized elastic constant dependence on crack density; b) experimental crack density dependence on strain can be used together to obtain the effective properties dependence on applied strain. The effective stiffness reduction in $(0/90_3)$s laminate, see Fig. 4, is much faster even if the crack density is lower. This is because cracks that cover the 90-layer thickness in this laminate are much larger and have more effect on laminate stiffness.



a) b)

Figure 4 Dependence of effective elastic constants on applied strain: a) axial modulus; b) shear modulus.

Summary

Using the GLOB-LOC model for damaged laminate stiffness matrix calculation and applying the described methodology for effective elastic properties back-calculation the following conclusions were obtained

a) intralaminar cracks do not affect the effective longitudinal modulus or Poisson's ratio of the damaged layer;
b) the effective elastic constants have linear dependence on crack density and the rate of reduction in normalized form depends very weakly on the used material and the layer thickness ratio;
c) the crack density increase with applied strain in damaged layer can be roughly considered as linear with slope which may depend on the damaged layer thickness;
d) the calculated linear dependence of effective properties on crack density and the experimental linear dependence of crack density on strain can be used to calculate the effective elastic constant dependence on strain.

References

[1] Lundmark P. and Varna J., Int. Journal of Damage Mechanics (2005); 14 (3); 235-261.
[2] Lundmark P. and J. Varna, Composites Science and Technology, 66, (2006), 1444-1454.

© (2012) Trans Tech Publications, Switzerland
doi:10.4028/www.scientific.net/KEM.488-489.494

Defect Size Measurement of Wall Thinned Pipe Using Shearography and Digital Image Correlation

Kyeongsuk Kim[1,a], Chansik Park[2,b], Dongpyo Hong[3,c], Manyong Choi[4,d], Hoseob Chang[5,e], and Hyunchul Jung[1,f]

[1]Dept of Mechanical Design Engineering, Chosun University, 375 Seoseok-Dong, Dong-Gu, Gwangju, 501-759, Korea

[2]Dept of Advanced Parts & Materials Engineering, Graduate School, Chosun University, 375 Seoseok-Dong, Dong-Gu, 5010-759, Korea

[3]Division of Precision Mechanical Eng., Chonbuk National University, 664-14 1Ga Duckjin-Dong, Duckjin-Gu, Jeonju, Jeonbuk, 561-756, Korea

[4]Korea Research Institute of Standards and Science (KRISS), Daejeon, 350-340, South Korea.

[5]Laser Center, Chosun University, 375 Seoseok-Dong, Dong-Gu, Gwangju, 501-759, Korea

[a]gsckim@chosun.ac.kr, [b]pcs9179@hanmail.net, [c]hongdp@jbnu.ac.kr, [d]mychoi@kriss.re.kr, [e]hschang@chosun.ac.kr, [f]yonggary@ieee.org

Keywords: Defect size, Wall thinning defect, Carbon steel pipe, Shearography, Digital Image Correlation, Displacement

Abstract. Defect size of wall thinned pipe is measured by using Speckle Shearing Interferometry (SSI) and Digital Image Correlation (DIC) techniques. A wall thinned defect of a carbon steel pipe was typically caused by flow accelerated corrosion (FAC). As wall thinned pipe can cause a huge accident at the nuclear power plant (NPP), a wall thinned defect should be detected for structure safety. SSI is one of the optical nondestructive techniques and can provide to inspect in real-time and to measure on the whole visible area at a time. DIC is a kind of the visual testing method. This method which uses a stereo vision system can measure the deformation or strain/stress of a structure in 3D. In this paper, ASTM A106 Gr.B carbon steel pipe is used as specimen. When the pressure load is provided by the pressure pump, the out-of-plane deformation along the longitudinal direction of a pipe can be detected quantitatively. Both results of SSI and DIC experiments are compared.

Introduction

The secondary loop system of the NPP consists of many pipelines. Many kinds of the defect (corrosion, the wall thinning defect, the leakage, etc.) have been occurred for these pipelines. Especially, the wall thinning defect is a typical type of the defect that is arisen for the carbon steel pipes. Most of wall thinning defects in the pipe are caused by flow accelerated corrosion (FAC) [1]. Because the wall thinning defect becomes a cause of the damage or the destruction of the pipeline, some techniques of the wall thinning defect measurement have been studied and developed.

Among many non-destructive methods, the optical methods are widely used for measuring the in-plane and out-of-plane displacements and the vibration of an object and detecting a defect on the internal and the outer surface of an object. The speckle shearing interferometry (SSI) [2] which is one of the optical methods is optimized to detect the defect and has some advantages. It is robust to the environmental disturbances and is very useful for the industrial fields because it has lower sensitivity than other optical methods. Recently, the digital image correlation (DIC) method using a stereo vision technique [3] has been developed for measuring the strain/stress distribution and the 3D shape of an object in the same time. This method uses a mapping technique that is a way to match up one specific point on the images acquired from 2 CCD cameras so that 3D deformation measurement of an object can be done.

In this paper, the wall thinned pipes were tested by the SSI and the DIC method and the results were compared each other.

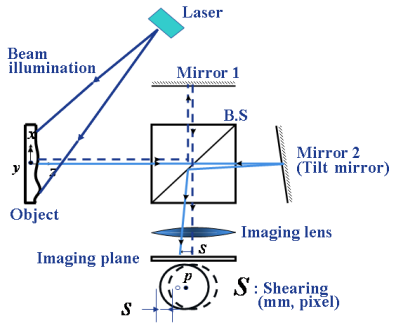


Fig. 1 Schematic of speckle shearing interferometry

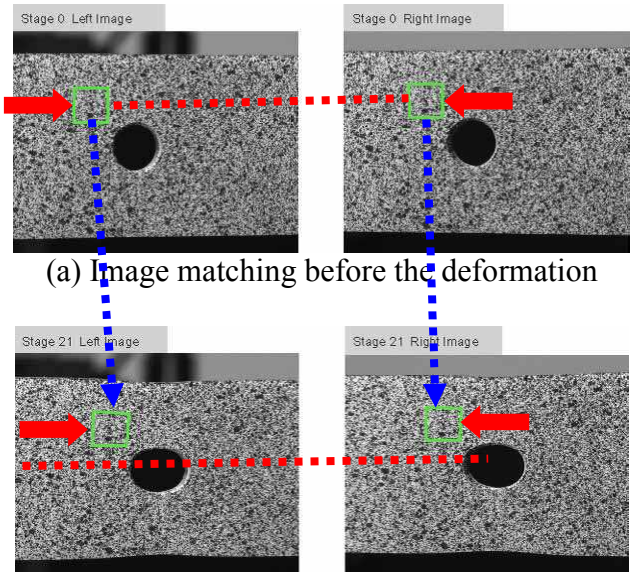
Displacement Measurement

Speckle Shearing Interferometry. When an object is illuminated by an expanded laser beam, a beam reflected on the object surface is divided into two laser beams by a beam splitter (B.S) as shown in Fig. 1. One beam is imaged to the CCD array after the reflection on the Mirror 1 while another beam is imaged to the CCD array after the reflection on the Mirror 2. If the Mirror 2 is tilted, then the wave-front reflected on the Mirror 2 is formed and it makes a sheared image to an image formed by the beam reflected on the Mirror 1. The interference fringe pattern resulted from two-beam interference presents the slope of the out-of-plane deformation of an object occurred after the deformation.

S expresses the shearing amount when the point P is moved to another point P'. The formation of the interference fringe can be controlled by the shearing amount and the shearing direction. When the incident direction of the laser beam illuminated to an object is the same as the vertical observation direction and Taylor series is used for calculating the deformation of x direction, the phase difference $\Delta\phi$ can be expressed as Eq. 1

$$\Delta\phi = \left(4\pi / \lambda\right)\left(\partial d / \partial x\right)\Delta x, \tag{1}$$

where, $\Delta\phi$ is the wavelength of the laser, $\left(\partial d / \partial x\right)$ is the deformation in x direction, and Δx is the shearing amount in x direction [4]. When $\Delta\phi$ can be quantitatively calculated by phase shifting method, the deformation of an object can be acquired in Eq. 1.



(a) Image matching before the deformation

(b) Image matching with point movement tracing after deformation

Fig. 2 Image matching process

Digital Image Correlation Method. In the DIC, two images are obtained by the stereo camera system. A unique point from each image can be selected and these points are tried to match. And after deformation of an image, these points are moved as much as an object is deformed. When the digital image processing technique is used, every moved point can be traced and the moved points on one image is mapped to the moved points on the other image. If the moved amount at each point can be calculated, then the displacement of an object by deformation is also calculated. Fig. 2 shows an example of the image matching process.

Experiment

Specimen. For predicting the length of the axial and radial direction of the wall thinning defect inside a pipe, an artificial defect was processed inner surface of a pipe specimen. The pipe specimens (SP-01 to SP-04) were made of ASTM A106 Gr.B material. The mechanical properties of A106 Gr.B are as shown in Table 1, and it is the seamless carbon steel pipe. The defect was prepared according to the minimum thickness of the defect. The maximum thickness of a pipe was 7.2 mm and the minimum thickness of each specimen is $\frac{7}{8}t$ (SP-01, 6.3 mm), $\frac{6}{8}t$ (SP-02, 5.4 mm), $\frac{4}{8}t$ (SP-03, 3.6 mm), and $\frac{2}{8}t$ (SP-04, 1.8 mm), respectively. The length of a defect (L/D_o) along the axial direction is 1.0 for all specimens.

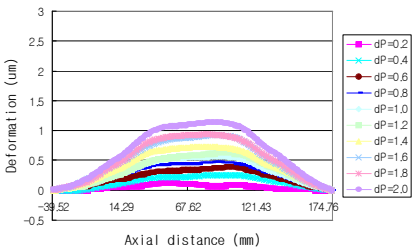
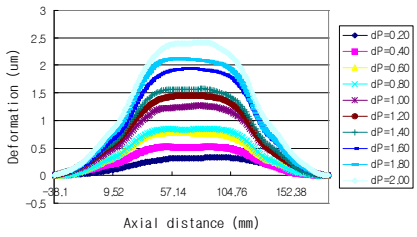
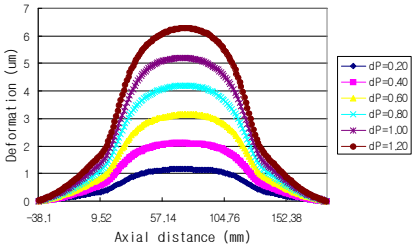
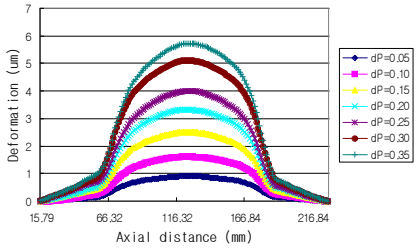
Table 1 Mechanical properties of A106 Gr.B

Yield strength [MPa]	Tensile strength [MPa]	Longitudinal elongation [%]
240	415	30

Experimental Apparatus. For Shearography experiment, Q-800HR (Dantec Dynamics Co.) was used. A diode laser (power: 50 mW, wavelength: 780 nm) is installed in the sensor head. For DIC experiment, ARAMIS (GOM Co.) was used. ARAMIS system is consisted of the sensor head with two CCD cameras, control unit, and control PC.

A manual loading type of hydraulic pressure pump was used to change the internal pressure. Each pressure difference step was 0.2 MPa for SP-01, SP-02, and SP-03 and 0.05 MPa for SP-04. It was because 0.2 MPa pressure difference generated too much deformation for SP-04 specimen.

Table 2 Deformation measurement result by Shearography (shear amount: 10 mm)

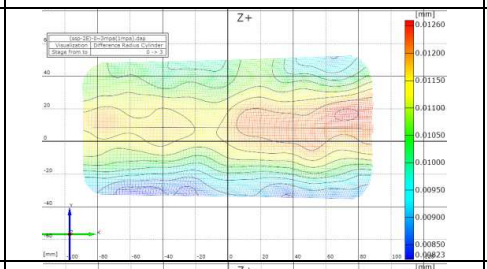
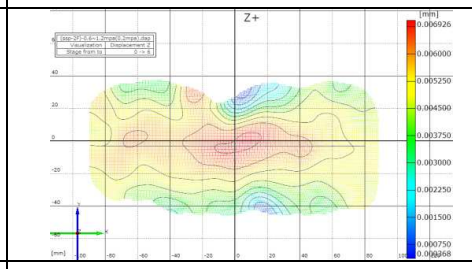
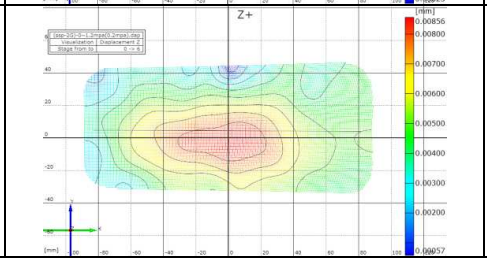
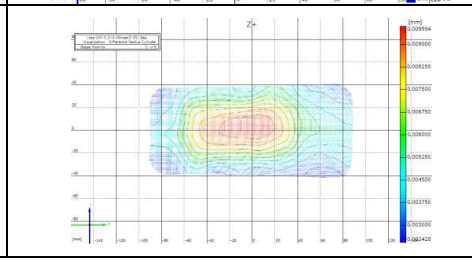
Specimen	Axial direction	Specimen	Radial direction
SP-01		SP-02	
SP-03		SP-04	

Results and Discussions

The deformation measurement results by Shearography are as shown in Table 2. In the case of SP-01, the defect length in the axial direction was measured from 0.4 MPa pressure difference. In the case of SP-02, SP-03, and SP-04, the defect length in the axial direction could be measured from 0.2 MPa pressure difference.

The deformation measurement results by DIC are as shown in Table 3. In the case of SP-01, the location of a defect was not measured though the pressure difference was 3 MPa. In the case of SP-02, the location of a defect was found roughly. For SP-03 and SP-04 specimen, the size of a defect as well as the location of a defect was found clearly.

Table 3 Defect deformation in the radial direction according to the minimum thickness of a defect by DIC

Specimen	Axial direction	Specimen	Radial direction
SP-01		SP-02	
SP-03		SP-04	

Conclusions

In this paper, Shearography and DIC experiments to measure the size of a wall thinning defect inside a pipe were compared. From the result, it was confirmed that both Shearography and DIC experiments are useful to detect a wall thinning defect, Shearography is optimized to detect the length of a wall thinning defect quantitatively, and DIC is suitable for finding the location and the size in both axial and radial directions of a wall thinning defect. Also, the minimum thickness what can be measured with Shearography should be greater than $\frac{6}{8}t$.

Acknowledgement

This research was supported by Basic Science Research Program through the National Research Foundation of Korea (NRF) funded by the Ministry of Education, Science and Technology (2010-0022523).

References

[1] J.W. Kim and C.Y. Park: Trans. of KSME (A) Vol. 29, No. 5 (2005), p. 734-742.

[2] K.S. Kang, K.S. Kim, H.C. Jung, and H.S. Jang: Key Engineering Materials Vol. 321(1) (2006), p. 112-115.

[3] M.A. Sutton, J.-J. Orteu, and H.W. Schreier: Image Correlation for Shape, Motion and Deformation Measurements (Springer, New York 2009).

© (2012) Trans Tech Publications, Switzerland
doi:10.4028/www.scientific.net/KEM.488-489.498

Fatigue focused optimization of treatment parameters – A case study about Deep Cryogenic Treatment –

Paolo Baldissera[1,a] and Cristiana Delprete[1,b]

[1]Politecnico di Torino, Corso Duca degli Abruzzi, 24 – 10129 Torino, Italy

[a]paolo.baldissera@polito.it,[b]cristiana.delprete@polito.it

Keywords: Optimization, DCT, fatigue, Genetic Algorithm, Neural Networks, Maximum Likelihood.

Abstract. The problem of treatment parameter optimization focused on the fatigue resistance is analysed through a case study about Deep Cryogenic Treatment (DCT) of AISI 302 steel. In particular, the possibility to integrate fatigue data fittings through the Maximum Likelihood Estimation (MLE) method in the optimization process is evaluated. Two levels of two parameters (soaking time and temperature) are considered and then expanded to three by proper scaling of their values in order to include the untreated case as a "zero" level. Fatigue focused optimization is then achieved by standard Response Surface Method (RSM) and by MLE with two models for comparison purposes.

Introduction

The application of thermal treatments and surface coatings often requires process parameter optimization in order to maximize the desired effect on a certain property. A wide range of consolidated methodologies [1-3] is available for single-value property optimization (i.e. hardness, elastic modulus, yield strength). However, when looking at the fatigue resistance, the optimization problem grows in complexity as the fatigue limit does not give an overall picture of the global behaviour and the number of cycles to failure is strongly influenced by other factors. In addition, fatigue data usually includes failures and run-outs, which must be accurately considered for proper statistical evaluation.

Parameter optimization is an important topic in almost all sciences and many suggestion and methodologies can be derived from disciplines far from the field of mechanical and materials engineering. However, the specific experimental conditions of each application introduce certain limitation and could lead to the exclusion of some approaches. Due to its expensive and time-consuming experimental requirements, the topic of material treatment for fatigue resistance introduces many of such limitations, often requiring a reduction of the parameter to be evaluated and/or the number of specimen to be tested. Such limitation affects the result accuracy and often leads to a partial understanding of the treatment under investigation. Evolutionary computational methods such as Genetic Algorithm [4] were successfully applied to fatigue problems [5, 6]. In particular, they are helpful when the model to be optimized is highly non-linear with the presence of singular points as traditional gradient methods could fall in local maxima or even being not able to startup.

The present paper is focused on the use of GA in conjunction with the Maximum Likelihood Estimation (MLE) method, which is a consolidated approach for the statistical representation of fatigue data by considering both failure and run-out specimens [7, 8]. The topic is presented through a case study about deep cryogenic treatment (DCT) of the solubilised AISI 302 austenitic stainless steel, whose experimental procedure and results were published elsewhere [9].

Materials and methods

Experimental data. The full factorial DOE fatigue data from a previous experimental work [13] were used as reference for the optimization purpose. One group of untreated specimens and four cryotreated groups with two levels of soaking-time (9 h and 24 h) and two levels of soaking-temperature (88 K and 143 K) were considered. All groups were tested with the stair-case method and nine additional failures were obtained at three levels of alternate stress.

Response surface method. The first approach to DCT parameter optimization was made through classic response surface methodology (RSM) [3]. Since the four available data groups with two levels of two parameters plus amplitude stress levels do not allow for a full quadratic model, the untreated group data were included with appropriate parameters [t = 0 h / T = 293 K]. Moreover, this condition was duplicated also as [t = 9 h / T = 293 K] and [t = 24 h / T = 293 K], under the likely assumption that the material is stable at room temperature and no variation of the fatigue behaviour would have noticed 9 or 24 h after the actual testing time without treatments.

Then, t and T levels were normalized as follow before to proceed with RSM:

$$\begin{cases} \tau = \dfrac{t}{24} \\ \theta = \dfrac{293 - T}{293 - 88} \end{cases} \quad \text{which gives:} \quad \begin{array}{llll} t\ [\text{h}] & 0 & 9 & 24 \\ \theta & 0 & 0.375 & 1 \\ \hline T\ [\text{K}] & 293 & 143 & 88 \\ \tau & 0 & 0.732 & 1 \end{array} \tag{1}$$

S-N curve fitting. The MLE method for data fitting were applied as suggested in [15] before to proceed with other optimization approaches. From the comparison of several models for the parameters of both log-normal and Weibull distributions, the maximum likelihood was obtained with Eq. (2).

$$\text{Log-normal distribution:} \begin{cases} \mu = \overline{\log N} = C_0 + C_1(\log(S - S_0) - \overline{\log S}) \\ \sigma = \exp(D_0 + D_1 \cdot S) \end{cases}, \tag{2}$$

where N is the number of cycles, S is the amplitude stress and σ is the standard deviation of $\log N$, while C_i and D_i are the parameters to be estimated through likelihood maximization and S_0 is the fatigue limit, which can be estimated or, as in this case, fixed to the value obtained from the stair-case. As first approximation, the MLE optimization was initially tested with the simplified model of Eq. (3)

$$\text{Log-normal distribution:} \begin{cases} \mu = \overline{\log N} = C_0 + C_1 \cdot S \\ \sigma = \exp(D_0) \end{cases}. \tag{3}$$

In order to optimize the DCT, its normalized parameters (θ and τ) were introduced into the C_i parameters of Eq. (2) and Eq. (3). The analysis was not extended to D_i parameters as no effects were noticed on data scatter, but nothing prevents an extension of the methodology in this direction.

Simplified model optimization. The model parameters of Eq. (3) were expressed as follow:

$$\begin{cases} C_0 = C_{0c} + C_{0\tau} \cdot \tau + C_{0\tau 2} \cdot \tau^2 + C_{0\theta} \cdot \theta + C_{0\theta 2} \cdot \theta^2 + C_{0\tau\theta} \cdot \tau \cdot \theta \\ C_1 = C_{1c} + C_{1\tau} \cdot \tau + C_{1\theta} \cdot \theta \end{cases}, \tag{4}$$

where C_{ix} represents the weighting factor for the DCT x parameter (θ or τ) on the ith parameter of the log-normal distribution model (linear, squared and interaction terms included). The DCT parameter influence on the fatigue life were considered up to the 2nd order only for the C_0 parameter as it was sufficient to obtain an acceptable result with a contained computational effort. Then, the likelihood maximization was applied to the model of Eq. (3) and Eq. (4) over the whole set of fatigue data (treated and untreated). With this model, the likelihood maximization was reached without difficulties through the Simplex method which is implemented into MATLAB®. By using the estimated weighting factors it was possible to calculate t and T values that maximize the fatigue life at given amplitude stress.

Extended model optimization. The above procedure was then applied to the model of Eq. (2). The non-linearity of the expression and the occurrence of singular points require a more powerful numerical approach as it could be difficult to find a proper starting point for the Simplex method. Good results were obtained through evolutionary computation with the Genetic Algorithm (GA), which has the advantage of exploring a wide space of solutions in order to avoid local minima and singularities.

In the GA approach the parameters to be estimated are handled as *genes* of a finite number of individuals forming a population of solutions. The population is evolved through generations in order to maximize the objective function. Since GA partially involves random selection processes, it rapidly gives a set of parameters resulting in finite likelihood value. Then, these *genes* are diffused to the rest of the population through evolution rules governing the process. In order refine the estimation, the GA output is then used as starting set of parameters for a further optimization through the Simplex method.

Results and discussion

In Figure 1 the fatigue life ratio of cryotreated over untreated material is plotted from the model obtained through RSM. This approach points out a gap between DCT effects at different amplitude stress: optimal DCT parameters change when passing from the near-limit fatigue to higher stress levels. However, the polynomial relation between N and S (at given θ and τ) is a very poor representation of fatigue data for S-N diagrams.

Figure 2 shows the S-N diagram obtained with the MLE linear model of Eq. (3) and Eq. (4). For this kind of procedure, the run-out data were reduced at 2E5 instead of 2E6 during the parameter estimation in order to achieve a more appropriate representation as the model is not able to describe the knee corresponding to the fatigue limit zone. Although very rough, the obtained model is able to catch the global effect of the DCT and could be used for a first attempt optimization. However, the linearization leads to large confidence intervals for the estimated parameters (about ±24%).

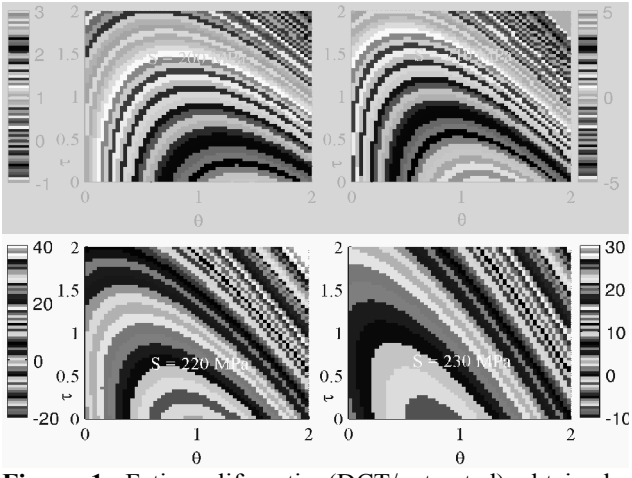


Figure 1: Fatigue life ratio (DCT/untreated) obtained with RSM at four stress amplitudes (different colormap scales).

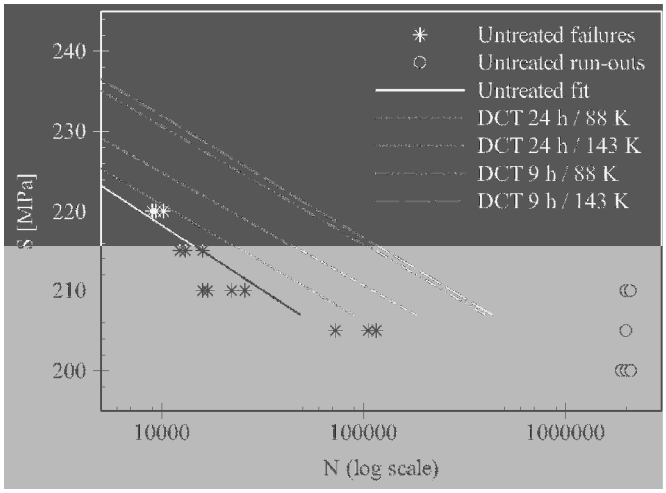


Figure 2: S-N diagram for the simplified linear model obtained through MLE methodology (50% survival).

Figures 4 and 5 report the *S-N* curves at 50% in reliability that were obtained through the logarithmic model with MLE and GA optimization. Data fitting is very accurate, resulting in narrow confidence intervals (about ±4%) for the estimated parameters. As with RSM, the optimal set of DCT parameters changes depending on the considered stress level, allowing to select the proper treatment for each working condition. In addition, while in this work the methodology was applied at 50% of survival probability, the estimation of σ given by MLE on Eq. 2 allows for parameter optimization at higher reliability levels and, if properly expanded, the model could also highlight the possible influence of the treatment on data scatter.

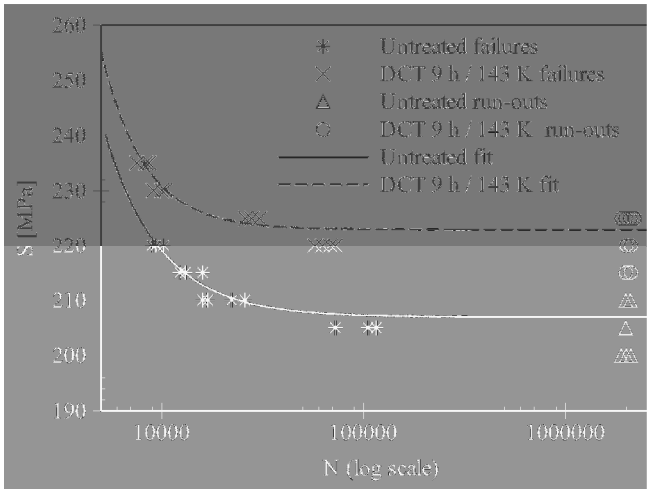


Figure 3: *S-N* fitting for two specimen groups with MLE and GA logarithmic model approach (50% survival).

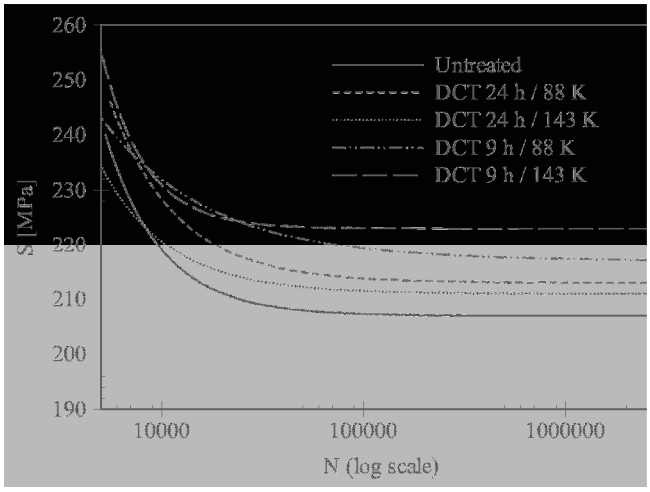


Figure 4: *S-N* diagram for all treatment groups with MLE and GA logarithmic model approach (50% survival).

Conclusion

In this work, three approaches to fatigue focused optimization of DCT parameters were analysed: RSM, MLE with a linear model and MLE with a logarithmic model optimized through GA. While all the methodologies allow for a good estimation of the optimal parameters, the latter has shown good potential for its accuracy and reliability in data fitting. In particular, this approach allows to optimize the treatment on the basis of a proper model for data representation by choosing the most appropriate distribution for fatigue data and its parameter expression. Moreover, potential treatment influence on data dispersion can be taken into account. At last, the fatigue focused optimization through MLE can return the proper set of treatment parameters for each working condition at any level of reliability.

References

[1] D.C. Montgomery, *Design and analysis of experiments* (Wiley, 2008).

[2] R.H. Myers and D.C. Montgomery, *Response surface methodology: process and product optimization using designed experiments* (Wiley, 2009).

[3] S.N. Sivanandam and S.N. Deepa, *Introduction to genetic algorithms* (Springer, 2007).

[4] V. V. Kurban, N.L. Yatsenko and V.I. Belyakova, Metallurgist, Vol. 51 (2007), p. 3.

[5] D.F. Cook, C.T. Ragsdale and R.L. Major, Eng. App. of Artif. Intell., Vol. 13 (2000), p. 391.

[6] J.C. Figueira Pujol and J.M. Andrade Pinto, Int. J. Fatigue, Vol. 33 (2011), p. 313.

[7] L. Jing and P. Jwo, Int. J. Fatigue, Vol. 19 (1997), Issue 5, p. 415.

[8] L. Goglio and M. Rossetto, Eng. Fract. Mech., Vol. 71 (2004), p. 725.

[9] P. Baldissera and C. Delprete, Mater. Des., Vol. 31 (2010), p. 4731.

© (2012) Trans Tech Publications, Switzerland
doi:10.4028/www.scientific.net/KEM.488-489.502

Fatigue Behaviour of Notched Ti-6Al-4V in Inert Environment

Sergio Baragetti[1,2,a], Stefano Cavalleri[1,b] and Federico Tordini[1,c]

[1]Department of Design and Technology, University of Bergamo, v.le Marconi 5, 24044, Dalmine, Italy

[2]GITT - Centre on Innovation Management and Technology Transfer, University of Bergamo, via Salvecchio 19, 24129, Bergamo, Italy

[a]sergio.baragetti@unibg.it, [b]stefano.cavalleri@unibg.it, [c]federico.tordini@unibg.it

Keywords: Titanium components, Fatigue, V-notch, Environmental effect, Step-loading technique.

Abstract. This work focuses on the fatigue behaviour of notched Ti-6Al-4V titanium alloy in inert environment. V-notched flat samples were cycled under axial fatigue (R = 0.1) under inert conditions by immersion in paraffin oil. A step-loading technique was used to determine the fatigue limit at the complete fracture for a constant fatigue life of 2×10^5 load cycles. The results were compared with previous data obtained with tests carried out in air and 3.5 wt.% NaCl solution. Fracture surfaces were examined under stereoscopic microscope.

Introduction

Ti-6Al-4V titanium alloy finds large application in the aerospace, automotive and naval industries because of the favourable ratio between strength and mass and the good corrosion resistance. The fatigue behaviour of smooth and notched Ti-6Al-4V samples in standard conditions has already been studied [1-5]. On the other hand, a better knowledge of the fatigue strength of Ti-6Al-4V in corrosive environments after foreign object damage (FOD) would be extremely important for aircraft or offshore applications to avoid unpredicted failures from environment-assisted fatigue or notch-induced fatigue crack growth [6-8]. In this respect, the fatigue behaviour of notched Ti-6Al-4V tested under inert conditions was compared with that observed with previous tests carried out in air and aggressive environment (recirculated 3.5 wt.% NaCl solution) [8]. V-notched flat samples were tested under axial fatigue (R = 0.1) by immersion in paraffin oil with an upper limit of 2×10^5 load cycles. The notches were formed in the middle of the gage length to obtain stress concentration factors ranging from 2.55 to 13.34. The inert conditions allowed highlighting the environmental effects of the other media. A step-loading method [4,5] was applied to draw data points on linear and Log-Log fatigue limit stress vs. K_t diagrams [9,10]. The features of some fracture surfaces were observed under stereoscopic microscope.

Material and methods

The chemical composition (average wt.%) of the Ti-6Al-4V hot rolled plate, which the fatigue samples were machined from, was: 5.97 Al, 4.07 V, 0.20 Fe, 0.1885 O, 0.003 C and Ti bal. Fig. 1 shows the dimensions of the samples tested with a detail of the notch geometry. The samples were formed with the notch axis parallel to the rolling direction of the Ti-6Al-4V plate, which was solution treated at 925°C (1 h) and vacuum annealed at 700°C (2 h) for stabilization before the machining operations (STOA treatment). The notches were machined by milling at very low speed to keep the residual stresses as low as possible. Notch root radii of 0.06, 0.26, 1.50 and 2.50 mm were then obtained by electrical discharge machining. These values are associated, respectively, with the following stress concentration factors calculated with FE models: 13.34, 6.63, 3.10 and 2.55. After the machining operations all the samples were stress relieved. The tensile properties along the transversal direction – i.e. that of load application – after the STOA treatment were determined using universal testing machine (INSTRON 1273).

Another universal testing machine (BRT T1000, Italy) was used to carry out axial fatigue tests (R = 0.1) at a frequency of 10 Hz under inert conditions (by immersion in still paraffin oil). The results were compared with previous experimental data obtained by testing samples having the same geometry in laboratory air or with the gage length immersed in recirculated 3.5% NaCl solution [8]. The maximum stress limit σ_{max_lim} (at 2×10^5 cycles) was calculated by implementing a step-loading procedure [4,5]. The alternating stress limit σ_{alt_lim}, which is half of the stress range associated with the fatigue limit, was then plotted vs. K_t. To apply the procedure, a stress level presumed to be lower than the fatigue limit according to previous results [11,12]

was initially assumed to run a first block of 2×10^5 load cycles. Once the sample had not failed during the first loading block, it was cycled again for 2×10^5 cycles at a stress level increased by a small percentage of 5%. By repeating the procedure the sample was eventually led to failure. The maximum stress limit at the complete fracture was interpolated between the maximum stress of the last and the last but one loading block, i.e. σ_{max_final} and σ_{max_prior} respectively, by solving to the following equation where N_{final} is the number of cycles to failure in the final loading block and the stresses are assumed as the nominal ones at the minimum sample cross section:

$$\sigma_{max_lim} = \sigma_{max_prior} + \frac{N_{final}}{2\times10^5}\left(\sigma_{max_final} - \sigma_{max_prior}\right)$$

Surface replicas were taken every 5,000-10,000 load cycles at the sample notch roots to detect the presence of propagating cracks as early as possible and to monitor their growth [8].

Coaxing takes place when a component cycled below the fatigue limit shows improved fatigue behaviour. This phenomenon might theoretically affect the reliability of the results, especially when several loading blocks are necessary before sample failure. Nevertheless, mainly ferrous materials are subjected to this phenomenon [10,13] and, furthermore, step-loading technique has already shown to be reliable for Ti-6Al-4V [4,5].

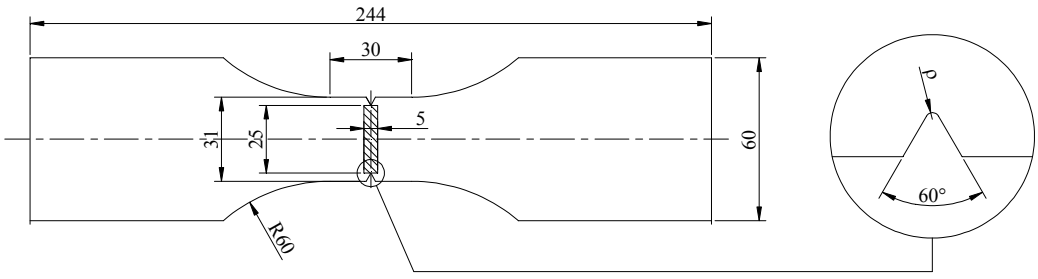


Figure 1 – Fatigue sample geometry (dimensions in mm) [8].

A selection of fracture surfaces was examined using stereoscopic microscope (Nikon SMZ800) to highlight some relevant features of the fatigue crack propagation process.

Results and discussion

Experimental tests. The tensile properties along the transversal direction of the STOA-treated Ti-6Al-4V plate were: tensile strength = 990 MPa, yield strength = 945 MPa and Young's modulus = 110,000 MPa. Fig. 2 shows the experimental results of the tests in inert environment and of the previous ones in air and NaCl solution in terms of σ_{alt_lim} vs. K_t linear and Log-Log diagrams at 2×10^5 load cycles. Similar values of fatigue limit stress were found at low and high K_t between the samples tested in air and paraffin oil. Both the samples tested in air and paraffin oil showed much better behaviour than the samples tested in NaCl solution with K_t lower than 6.63. By contrast, a remarkable fatigue strength fall was seen for the sample cycled in air at K_t = 6.63 – i.e. -19% and -28% with respect to the samples tested in NaCl solution and paraffin oil respectively –. It is worth underlining that at K_t = 6.63 the presence of the NaCl solution was not much detrimental to the fatigue resistance of Ti-6Al-4V in comparison with the tests in paraffin oil. The fatigue behaviour of the notched samples was improved more effectively under inert conditions at K_t = 6.63. Regardless of test environment, with increasing K_t the alternating stress limit tends asymptotically to approach a lower limit. Fig. 2 shows the fatigue limit stress vs. K_t plotted on a Log-Log diagram and a bilinear curve fitting all the data points. A threshold stress concentration factor could be seen between 6 and 7, after σ_{alt_lim} has rapidly decreased at low K_t. Beyond this threshold K_t the alternating stress limit could be assumed not to decrease significantly independently from the test environment. This is intended to be confirmed with further tests at higher K_t.

High crack growth rates were observed regardless of K_t and test environment. In all the tests the complete fracture occurred after a relatively low number of cycles after the propagating crack had been detected by replication [8].

It was believed that the good fatigue behaviour of the titanium samples tested under inert conditions could have been due to environment-assisted alteration of the slip band activity at the root of the V-notches which acted like pre-cracks [14].

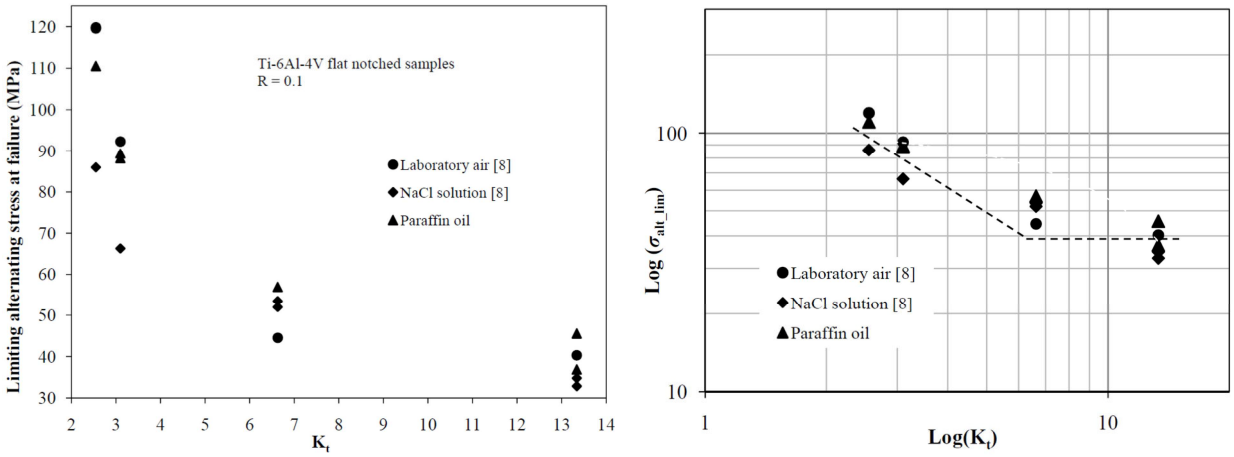
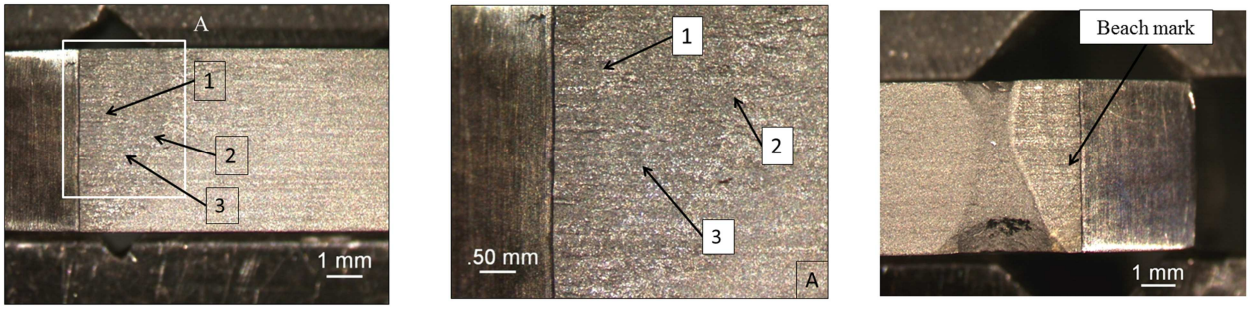


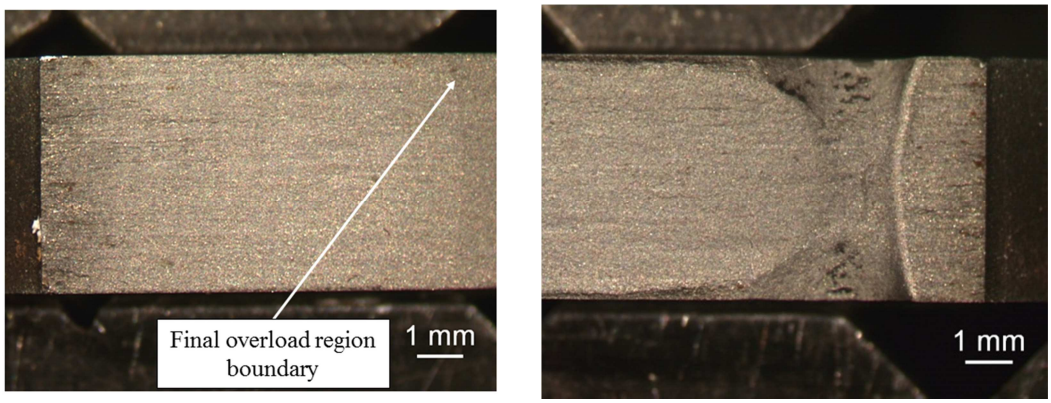
Figure 2 – Limiting alternating stress vs. K_t linear (on the left) and Log-Log (on the right) diagrams.

SEM observations. An overview of the main stable propagation region of the fracture surface of the sample with K_t = 13.34 cycled in paraffin oil is shown in Fig. 3(a). Fig. 3(b) shows a higher magnification of the stable propagation region behind the notch root. Some beach marks, which could be associated with the arrest and load increase operations between steps [8], are indicated in Figs. 3(a) and 3(b). Fatigue cracks propagated from both the notch roots, as the presence of a smaller crack propagation area behind the root of the notch on the right in Fig. 3(c) demonstrates. Beach marks emanating from this notch root as well as a region of large deformation associated with the final failure can be seen.



(a) (b) (c)

Figure 3 – Fracture surface of the sample with K_t = 13.34 cycled in paraffin oil: (a) overview of the main stable propagation area, (b) detail "A" of the same area and (c) overview of the final overload region where a secondary propagation area is visible.



(a) (b)

Figure 4 – Fracture surface of the sample with K_t = 6.63 cycled in air: overview of (a) the stable propagation region and of (b) the final overload area where a secondary stable propagation area is present.

Fig. 4 shows the fracture surface of the sample with $K_t = 6.63$ cycled in air. Fig. 4(a) shows an overview of the crack initiation and propagation area characterized by the higher crack growth rate. The boundary that separates the stable propagation region (on the left) from the final overload area is indicated. Crack initiation from both the notch roots occurred in this sample too. The appearance of the secondary stable propagation region (Fig. 4(b)) is similar to that of the sample shown in Fig. 3.

Summary

V-notched flat Ti-6Al-4V samples were tested under axial fatigue (R = 0.1) in inert environment (paraffin oil). The results were correlated with previous ones from tests in air and NaCl solution. Stress concentration factors of 2.55, 3.10, 6.63 and 13.34 were investigated. A step-loading method was applied to calculate the fatigue limit at 2×10^5 load cycles. Similar fatigue limit values were found at both low and high K_t between the samples tested in air and paraffin oil. A significant fatigue strength fall was seen for the sample with $K_t = 6.63$ cycled in air with respect to those tested in NaCl solution (-19%) and paraffin oil (-28%). Apparently, compared to the other environments the fatigue resistance of notched Ti-6Al-4V was improved more effectively under inert conditions at $K_t = 6.63$. By plotting the fatigue limit stress vs. K_t on a Log-Log diagram, a threshold K_t could be assumed between 6 and 7. Beyond this K_t the alternating stress limit was believed not to decrease significantly independently from the test environment. The overall good fatigue behaviour in inert environment could have been due to environment-assisted alteration of the slip band activity at the root of the V-notches which acted like pre-cracks.

Acknowledgements

The authors wish to thank prof. dr. A.K. Vasudevan of ONR (Office of Naval Research) – US Navy, for the discussion and his precious suggestions. The research was funded by ONR (Office of Naval Research) – US Navy (Contract Number: N00014-08-1-1197).

References

[1] D.B. Lanning, G.K. Haritos, T. Nicholas: Int. J. Fat., Vol. 21 (1999), p. S87.
[2] D.B. Lanning, G.K. Haritos, T. Nicholas, D.C. Maxwell: Fat. Fract. Eng. Mater. Struct. Vol. 24 (2001), p. 565.
[3] R.A. Naik, D.B. Lanning, T. Nicholas, A.R. Kallmeyer: Int. J. Fat., Vol. 27 (2005), p. 481.
[4] D.B. Lanning, T. Nicholas, A. Palazotto: Int. J. Fat., Vol. 27 (2005), p. 1623.
[5] D.B. Lanning, T. Nicholas, G.K. Haritos: Int. J. Fat., Vol. 27 (2005), p. 45.
[6] M.C. Kushan, S.F. Diltemiz, İ. Sackesen: Eng. Fail. Anal., Vol. 14 (2007), p. 1693.
[7] R. Boyer, G. Welsch, E.W. Collings: *Materials Properties Handbook: Titanium Alloys* (ASM International, US 1994).
[8] S. Baragetti, S. Cavalleri, F. Tordini: Proc. of the 11th Int. Conference on the Mechanical Behavior of Materials (2011).
[9] N.E. Frost, D.S. Dugdale: J. Mech. Phys. Solids, Vol. 5 (1957), p. 182.
[10] N.E. Frost, K.J. Marsh, L.P. Pook: *Metal Fatigue* (Clarendon Press, UK 1974).
[11] D.B. Lanning, T. Nicholas, A. Palazotto: Int. J. Fat., Vol. 25 (2003), p. 835.
[12] R.J. Morrissey, T. Nicholas: Int. J. Fat., Vol. 27 (2005), p. 1608.
[13] G.M. Sinclair: Proc. ASTM, Vol. 52 (1952), p. 743.
[14] Z.N. Ismarrubie, M. Sugano: Mater. Sci. Eng. A, Vol. 386 (2004), p. 222.

© (2012) Trans Tech Publications, Switzerland
doi:10.4028/www.scientific.net/KEM.488-489.507

A Comprehensive Study of the Performances of PVD WC/C-coated Racing Gears

Sergio Baragetti[1,2,a], Stefano Cavalleri[2,b] and Federico Tordini[1,c]

[1]Department of Design and Technology, University of Bergamo, v.le Marconi 5, 24044, Dalmine, Italy

[2]GITT - Centre on Innovation Management and Technology Transfer, University of Bergamo, via Salvecchio 19, 24129, Bergamo, Italy

[a]sergio.baragetti@unibg.it, [b]stefano.cavalleri@unibg.it, [c]federico.tordini@unibg.it

Keywords: Spur gears, PVD coatings, Fatigue, Rolling contact fatigue, Wear.

Abstract. In this work a preliminary data set including experimental results from fatigue tests on smooth and foreign object damaged (FOD) aluminium samples coated with WC/C deposited with PVD (physical vapour deposition) technique was considered before testing WC/C-coated spur gears for racing motorcycles under rolling contact fatigue (RCF). The fatigue behaviour of the samples was correlated with the results obtained with the RCF tests on the coated gears. A special device mounted on a universal testing machine was used to carry out the RCF tests.

Introduction

RCF is the most familiar source of failure for transmission gears. Tooth bending fatigue failure is less frequent, but it cannot be overlooked in the design process either. Case hardening or nitriding are typical surface treatments used to limit the progressive RCF damaging which develops from surface or subsurface crack initiation sites and causes pits or spalls to be formed on the tooth flanks. Physically vapour deposited coatings can improve the fatigue and RCF resistance of mechanical components made of both steel and light alloys [1-6]. This is associated with the presence of high residual compressive surface stresses produced by the deposition process. PVD-deposited WC/C is currently used for transmission gears because of its very low friction factor which can allow working even under poor lubrication. Nevertheless, the effects of this coating on the fatigue and RCF behaviour of the coated components have not been studied sufficiently yet. By contrast, the tribological and mechanical characterization of WC/C coatings have been studied quite thoroughly [7-9]. Based on previous authors' results [10,11], RCF tests on uncoated and WC/C-coated case hardened spur gears for racing motorcycles were carried out using a custom-made special device mounted on a universal testing machine [12]. The maximum service torque was applied under lubricated conditions for 100,000 load cycles. The contact surfaces and the profiles of the meshing teeth were carefully analysed after the tests to characterize the tooth damage. In fact, in order to verify the possibility to coat gears for advanced applications and/or under severe service loads, a thorough understanding of the performances of the thin film must be achieved, as both tooth bending fatigue and RCF failures can occur as well as wear phenomena. In this respect, the experimental results collected with rotating bending tests on smooth and foreign object damaged (FOD) 7075-T6 aluminium alloy samples coated with WC/C [13] were analysed in comparison with the results of the RCF tests on steel gears.

Materials and methods

The samples used for the fatigue tests were made of 7075-T6 aluminium alloy and the WC/C film was deposited at LAFER Spa (Piacenza, Italy) by magnetron sputtering (MS)-PVD at a nominal deposition temperature of 180°C. The main mechanical properties of the ceramic film were: thickness between 1 and 3 μm, Vickers hardness equal to 1600±100 HV0.025, friction factor of 0.15 and Young's modulus between 120 and 150 GPa [13].

The mechanical properties of both coated and uncoated samples were evaluated with standard tensile tests and gave a tensile and yield strength for the uncoated specimens equal to 656 and 585 MPa respectively, while values of 614 and 544 MPa were found for the WC/C coated ones. The Young's modulus was the same (75 GPa) for both treated and untreated material [13]. Hourglass shaped samples were machined from a bar 12 mm in diameter according to E 606 ASTM standard and five different series of fatigue samples were produced: smooth uncoated (S), smooth coated (SC), uncoated damaged by FOD (D), damaged and then coated (DC) and coated and then damaged (CD). A homemade testing device was used to carry out impact tests by means of a single shot towards the middle of the sample gage length perpendicularly to the longitudinal axis at a speed of 100 m/s; spherical hard steel balls with 2-mm diameter were used to produce FOD [13]. As regards the gears - constituting the sixth speed of a Ducati 1098R competition motorcycle - tested under RCF, the modulus was 2.5 mm and the tooth thickness was 13 mm [11]. The number of pinion teeth was 25 mm and the pitch diameter was 64.89 mm, whereas the same parameters for the driven gear were, respectively, 22 and 57.10 mm. The bulk material was UNI EN-16NiCr11 (AISI 3415) case-hardened steel alloy and the coating was the same 3 μm-thick WC/C ceramic film outlined previously. With the aim of accurately testing the gears by reproducing the rolling contact loading conditions on the tooth flank, testing equipment was expressly designed and assembled. The device was adaptable to a universal axial testing machine and it allowed one pair of meshing gears, respectively the pinion and the driven gear, to be subjected to the maximum service torque, i.e. 244 Nm. The gears were mounted on two shafts supported by suitable bearings and a leverage system enabled conversion of the axial load, provided by the testing machine actuator, into the desired loading torque on the pinion. The rotation of the driven shaft was constrained with a braking device designed to prevent transmission of parasite bending moments or axial forces. The torsional stiffness of the shafts enabled a relative rotation of the meshing gears which ensured that the whole contact arc was involved in the load transmission during the tests. A suitable video acquisition system and a torque load cell were arranged to control the initial position of the teeth and monitor the load transmitted.

The RCF tests on WC/C-coated high performance spur gears were carried out on a hydraulic axial testing machine (BRT T1000, Italy) with the RCF testing device outlined above, at a frequency of 1 Hz with a load ratio of 0.1. The lubricant used during the tests was F40 (SAE 15W-50, API SG) racing oil.

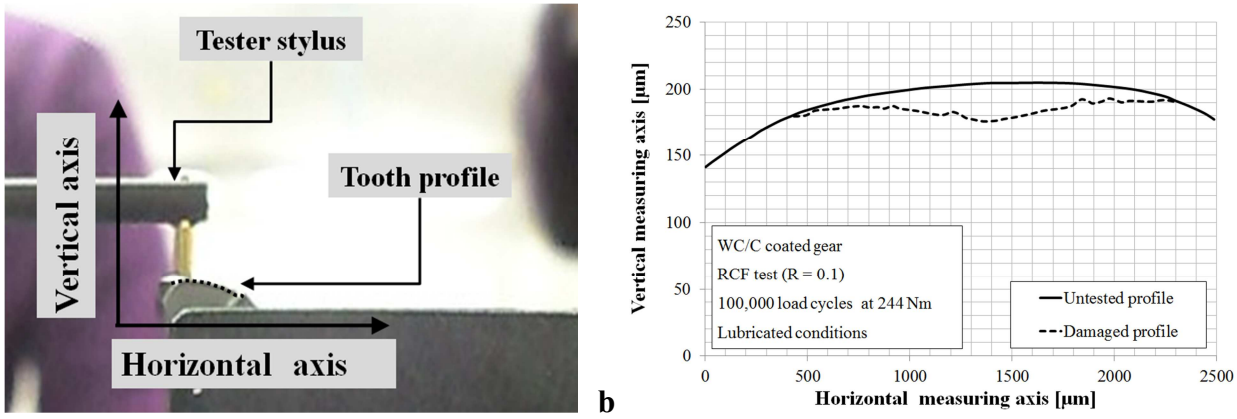


Figure 1. Example of tooth profile measurement with indication of the measuring axes of the roughness tester (a) and comparison between tested and untested tooth profiles in the middle of the tooth thickness for a WC/C-coated gear (b).

After each test the tooth flank was first investigated with an optical stereoscopic microscope (Leica MZ75) to qualitatively evaluate the appearance of the contact area and measure the damage extension in the thickness direction. A Form Talysurf 50 surface roughness tester was then used to capture the tooth profile in the middle of the tooth thickness. The measurement of the tested tooth profiles was processed with a two-dimensional CAD and compared with an untested one in order to determine the damaged cross section area and the maximum damage depth. The measuring axes of

the roughness tester are shown in Fig. 1: these axes define the measuring directions of the roughness tester stylus, which is electrically driven along the horizontal direction and is free to translate vertically to follow the tooth profile. According to the reference axes shown in Fig. 1(a), an example of comparison between tested and untested tooth profiles in the middle of the tooth thickness for a WC/C-coated driven gear is shown in Fig. 1(b).

Results and discussion

The results of the rotating bending tests are shown in the diagram of Fig. 2, where the fatigue limit is plotted vs. the number of cycles to failure for each series of samples. The WC/C coating was beneficial to the fatigue behaviour of both smooth and damaged samples, but it was rather detrimental for the fatigue resistance of the WC/C-coated samples damaged after deposition (CD series). The presence of the coating increased the fatigue resistance of about 8% and 11% with respect to the uncoated smooth and FOD samples respectively. FOD after deposition produced a mean decrease of about 8% in comparison with the uncoated damaged samples, as the presence of multiple cracks acting like severe micro-notches in the coating impact area was detrimental to the fatigue resistance [13].

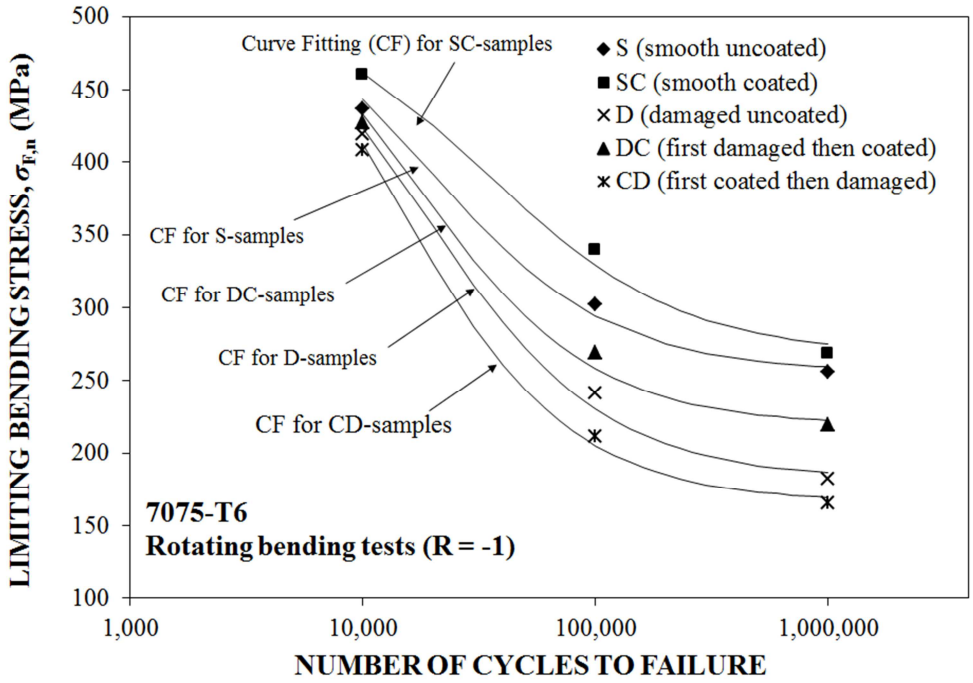


Figure 2. Limiting bending stress vs. number of cycles to failure diagram for the five series of samples tested in [13].

With regard to the RCF tests, the damaged cross section area and the maximum damage depth in the middle of the tooth thickness for a coated and an uncoated gear are listed in Table 1. Based on the fatigue results of the WC/C-coated samples subjected to FOD, the coating could have been detrimental to the RCF resistance of the gears. Nevertheless, the results of the tests in lubricated conditions pointed out that the WC/C coating was beneficial in reducing the surface damage due to RCF. Unlike the aluminium samples, in fact, the higher Young's modulus of the steel substrate was fundamental to properly support the ceramic coating and prevent its delamination or fracture. Furthermore, the absence of impacts between the meshing teeth during the torque transmission was believed to have limited the formation of micro-notches at the teeth surface. However, preliminary RCF tests carried out under dry conditions highlighted the fundamental effect of the lubricant in preventing the WC/C film from being damaged or delaminating from the base material [12]. The oil film, in fact, could reduce the contact pressures and the surface shear stresses due to the friction between the teeth flanks in relative sliding. Therefore, deposition of WC/C could be considered for high performance gears under lubricated conditions.

Table 1. Cross section area of removed material and maximum damage depth in the middle of the tooth thickness for a WC/C-coated and an uncoated gear tested for 100,000 load cycles.

	Uncoated gear	WC/C-coated gear
Damaged cross section area [μm^2]	1,352	319
Maximum damage depth [μm]	3.0	1.3

Summary

RCF tests on uncoated and WC/C-coated high performance steel spur gears were carried out. The results were compared with those obtained with previous rotating bending tests on uncoated and WC/C-coated 7075-T6 samples both in smooth and FOD conditions. The aluminium samples subjected to FOD after deposition showed a reduction in the fatigue limit that was probably due to the coating fractures produced by FOD acting like severe micro-notches. As far as the RCF tests on uncoated and WC/C-coated high performance spur gears are concerned, testing equipment was expressly designed to accurately reproduce the rolling contact conditions between the meshing gears. The measurements on the damaged teeth flanks pointed out a beneficial effect of the WC/C coating in preventing the RCF damage under lubricated conditions. In fact, unlike the aluminium samples, the higher Young's modulus of the steel substrate was fundamental to properly support the ceramic coating and prevent its fracture. The absence of impacts between the meshing teeth was believed to have also limited the formation of micro-notches at the teeth surface. Therefore, under lubricated conditions PVD WC/C coatings could be taken into account to improve the RCF behaviour of high performance transmission gears.

Acknowledgments

The Authors wish to thank DUCATI CORSE Srl for the drawings and the data on the spur gears.

References

[1] S. Stewart, R. Ahmed: Wear Vol. 235 (2002), p. 1132.
[2] *ASM Metals Handbook*, edited by ASM International, 10th ed., Materials Park, OH (1993).
[3] K.R. Kim, C.M. Suh, R.I. Murakami, C.W. Chung: Surf Coat Technol Vol. 171 (2003), p. 15.
[4] S. Baragetti, G.M. La Vecchia, A. Terranova: Int J Fat Vol. 27(10-12) (2005), p. 1541.
[5] S. Baragetti: Int J Fat Vol. 29 (2007), p. 1893.
[6] E.S. Puchi-Cabrera , M.H. Staia, J. Lesage, L. Gil, C. Villalobos-Gutiérrez, J. La Barbera-Sosa, E.A. Ochoa-Pérez, E. Le Bourhis: Int J Fat Vol. 30 (2008), p. 1220.
[7] P. Harlin, P. Carlsson, U. Bexell, M. Olsson: Surf Coat Technol Vol. 201 (2006), p. 4253.
[8] B. Navinšek, P. Panjan, M. Čekada, D.T. Quinto: Surf Coat Technol Vol. 154 (2002), p. 194.
[9] K. Persson, R. Gåhlin: Tribol Int Vol. 36 (2003), p. 851.
[10] S. Baragetti, A. Terranova, F. Tordini: Key Engineering Materials, Vols. 385-387 (2008), p. 57.
[11] S. Baragetti, S. Cavalleri, F. Tordini: Key Engineering Materials, Vols. 452-453 (2011), p. 589.
[12] S. Baragetti, S. Cavalleri, F. Tordini: Proceedings of the International Conference ICM11 (2011).
[13] S. Baragetti, R. Gerosa, B. Rivolta, G. Silva, F. Tordini: Proceedings of the International Conference ICM11 (2011).

© (2012) Trans Tech Publications, Switzerland
doi:10.4028/www.scientific.net/KEM.488-489.511

Effect of shot peening on the fatigue behavior of some sintered steels

S. Baragetti[1,a], R. Gerosa[2,b], G. Silva[2,c], B.Rivolta[2,d]
[1] Department of Design and Technology, University of Bergamo, v.le Marconi 5, 24044, Dalmine, Italy
[2] Dipartimento di Meccanica, Politecnico di Milano, Italy
[a]sergio.baragetti@unibg.it, [b]riccardo.gerosa@polimi.it, [c]giuseppe.silva@polimi.it, [d]barbara.rivolta@polimi.it

Keywords: sintered steels, shot peening, fatigue resistance.

Abstract
Shot peening is a mechanical treatment usually performed on metals for improving the mechanical properties of the surface layers. The application of such treatment to sintered steels causes a local surface densification and the birth of residual compression stresses. In this paper, the effect of different shot peening cycles, selected after a preliminary optimization, has been investigated focusing especially on the fatigue resistance measured by bending tests and on the surface residual stresses measured by XRD technique. Two high performances PM steels were considered: the former was sintered starting from a diffusion bonded powder, whereas the latter is based on a pre-alloyed powder. Two different nominal densities were considered, 6.9g/cm^3 and 7.1g/cm^3.

Introduction
The fatigue resistance of sintered components is considered a critical parameter, because the pores, especially the surface ones, can behave as local notches [1,2]. Fatigue life enhancements can be obtained by a shot peening treatment, able to increase the local density up to a fully dense material one [4,5]. In this experimental work two high performances PM steels have been investigated. Moreover two different nominal densities have been obtained: 6.9g/cm^3 and 7.1g/cm^3. Both the steels were studied by microscopic point of view characterizing both the pores area and roundness distribution and the microstructural constituents. The mechanical characterization of the as-sintered materials required micro and macro hardness tests, transversal rupture three point bending tests (ISO 3325), four point bending fatigue tests (R=0.1) and three point bending da/dN tests (R=0.1) (ISO 12108, ASTM E647), After a preliminary optimization, two shot peening cycles were selected and new samples were prepared and tested under four point bending fatigue loading. The quality of the shot peened surfaces were controlled by LOM and SEM observations, roughness measurements and micro-hardness tests. Finally, some measurements of the residual stresses induced by shot peening were carried out by XRD technique.

Materials and Methods
The investigated steels were obtained from high performances powders, whose chemical compositions are reported in Table 1.

Table 1 Different types of materials identification.

Steel	Ni [%]	Mo [%]	Cu [%]	Mn [%]	C_{tot} [%]
1	4.00*	1.41	2.00*	/	0.60
2	0.90	0.90	2.00*	0.20	0.60

*Diffusion bonded

Table 2: Materials codes and features.

Material Code	Steel	Density [g/cm^3]	Sintering temperature [°C]
1LL	1	6.9 (L)	1150 (L)
1HL	1	7.1 (H)	1150 (L)
2LL	2	6.9 (L)	1150 (L)
2HL	2	7.1 (H)	1150 (L)

The steels were sintered by STAME srl (Arosio (Co), Italy) at 1150°C, 25 minutes and fast cooled to room temperature. Finally a tempering was performed at 200°C, 1 hour. The whole heat treatment was performed under a protective N_2/H_2 (90/10) atmosphere. The materials were delivered as 65mm x 65mm x 10mm plates and their codes and features are summarized in Table 2. After a preliminary optimization, two shot peening cycles were selected and reported in Table 3.

Table 3: Selected shot peening cycles – shots are made of steel and their hardness is included between 60-62 HRC.

Shot peening cycle	Shot type	Coverage	Almen A [mm]
E	ASH 330 (0.8mm)	500%	0.5-0.6
G	ASH 330 (0.8mm) + ASH 70 (0.2mm)	100% + 500%	0.2-0.3 + 0.2-0.3

In Figure 1 the effect of shot peening is shown and in Table 4 the thicknesses of the shot peened layers and the dimensional variations are reported.

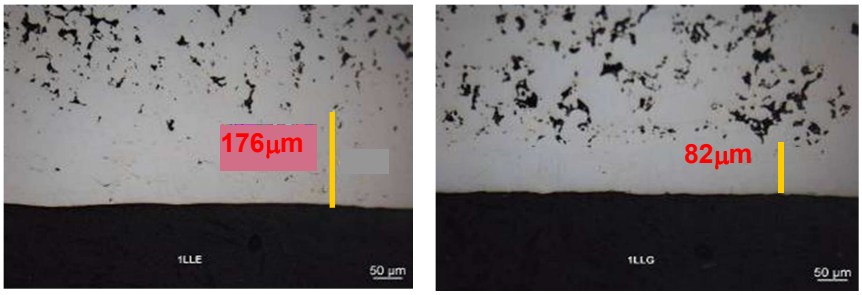


Figure 1: Densified layers for the selected shot peening cycles.

Table 4: Thicknesses and dimensional variations (Δh) of the shot peened layers.

Code	Densified layer [µm]	Δh [%]	Code	Densified layer [µm]	Δh [%]
1LL-E	188	-0.26	2LL-E	139	-0.19
1LL-G	82	-0.11	2LL-G	84	-0.12
1HL-E	184	-0.19	2HL-E	161	-0.17
1HL-G	91	-0.10	2HL-G	89	-0.09

Moreover, the shot peened surfaces were characterized by SEM observations (for detecting residual surface porosity, folds or cracks induced by the shot peening operation) and roughness measurements (R_a) using a Taylor-Hobson profilometer. All the roughnesses were small (about 3µm), even if E cycle generally resulted in higher values, probably due to its high impact energy.
Four point bending fatigue tests were performed on both the as-sintered and shot peened steels: samples 10mm x 10mm x 65mm were prepared and tested under a DMG ESH 2C 100 testing machine. The surfaces subjected to the tensile stress were respectively the sintered ones for the as-delivered samples and the densified ones for the shot peened samples. The lower supports distance was 40mm, whereas the upper knives distance was 20mm. In all the tests, the load ratio was kept constant and equal to 0.1. The fatigue limit was investigated at 10^5cycles by a staircase method (UNI 3964): for the as-sintered samples, this limit can be considered close to the infinite fatigue life because of the surface porosity that can be considered as existing defects [6]. The shot peened samples were tested at 10^5 cycles as comparison with the as-sintered materials.
Three point bending da/dN tests were finally performed on 10mm x 10mm x 65mm as sintered specimens. The notch length was equal to 1mm. The whole Paris curve was obtained for all the investigated materials by ΔK decreasing and ΔK increasing techniques.

Results

The pores features were studied and resulted in rather poor differences between the low and high density samples, even if the high density ones showed a slightly higher amount of pores with roundness close to 1 and smaller average area. A complete microstructural survey was performed in order to characterize the micro-constituents for both the materials.

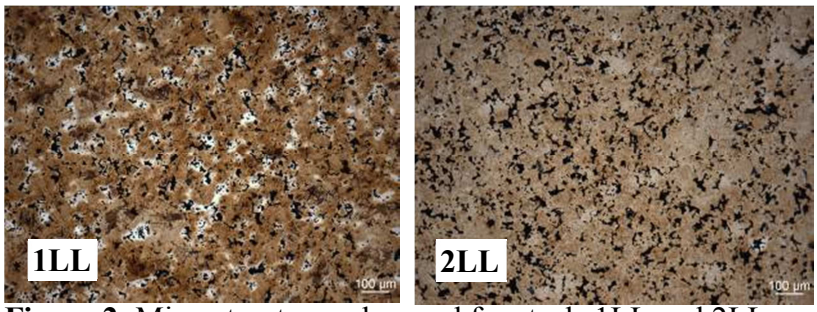


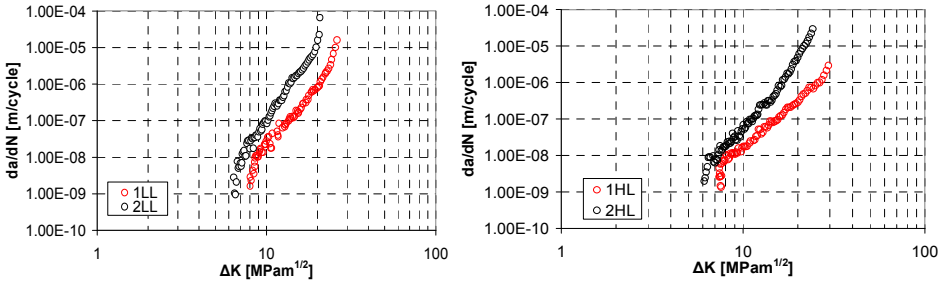
Figure 2: Microstructures observed for steels 1LL and 2LL.

In steel 1 the microstructure was prevalently martensite with retained austenite around the pores, whereas in steel 2 the microstructure was prevalently martensite. Macro-hardness tests (HV30) and transversal rupture tests were performed too. Generally, the hardness and the transversal rupture stresses of the high density samples were higher, even if a remarkable difference in the transversal rupture stresses was observed only for steel 2. Finally the fatigue limit (at 10^5 cycles) was determined by four point bending tests. In Table 5 a comparison between the materials is reported.

Table 5: Fatigue limits at 10^5 cycles for the as-sintered materials.

Material Code	Fatigue Limit [MPa]	Material Code	Fatigue Limit [MPa]
1LL	344±10	2LL	315±11
1HL	353±28	2HL	303±42

Fatigue crack propagation tests were performed on all the investigated materials. In Figures 3, a comparison between the Paris curves of steels 1 and 2 is reported.



Material Code	ΔK_{th} [MPa m$^{1/2}$]	*n* (Paris)
1LL	8.0	5.2
1HL	7.5	4.2
2LL	6.5	6.3
2HL	6.1	5.3

Figure 3: Comparison between steels 1 and 2 low and high density samples.

The shot peened samples, were first investigated with micro-hardness tests and compared with the micro-hardness profiles of the as-sintered materials. The results showed that the strain hardening induced by the shot peening was rather poor (probably due to the very hard martensitic microstructure of the as-sintered materials) even if in the residual austenite isles of steel 1, the micro-hardness strongly increased. Finally, some residual stresses measurements were carried out by XRD technique on the shot peened surfaces. The results are summarized in Table 6.

Table 6: Residual stresses measured on the shot peened surfaces.

Material Code	σ_{max} [MPa]	σ_{min} [MPa]	Material Code	σ_{max} [MPa]	σ_{min} [MPa]
1LL-E	-562	-583	2LL-E	-393	-439
1LL-G	-569	-673	2LL-G	-445	-508
1HL-E	-589	-682	2HL-E	-317	-358
1HL-G	-534	-586	2HL-G	-449	-515

Fatigue tests were carried out and the fatigue limit was determined at 10^5 cycles for comparison with the as sintered materials. In Table 7 the results are summarized.

Table 7: Fatigue limits for the as-sintered and shot peened materials.

Material Code	Fatigue Limit [MPa]	ΔL_f [%]	Material Code	Fatigue Limit [MPa]	ΔL_f [%]
1LL	344		1HL	353	
1LL-E	428	24.4	1HL-E	490	38.8
1LL-G	415	20.6	1HL-G	453	28.3
2LL	315		2HL	303	
2LL-E	378	20.0	2HL-E	453	49.5
2LL-G	390	23.8	2HL-G	440	45.2

Conclusions

The experimental results described in this work can be summarized as follows:

- from the microstructural point of view, the main difference between the investigated steels is the residual austenite around the pores of steel 1;
- the shot peening operation was effective in increasing the local density of the sintered materials. For the investigated steels, the strain hardening due to the shot peening was notably poor probably due to observed microstructures (prevalently martensitic with high hardness);
- by da/dN tests the ΔK thresholds and the Paris Law coefficients were determined. The comparison between the two steels led to some important considerations: steel 1 (low and high density) threshold values were higher than steel 2 ones, whereas the n exponents of the Paris law were lower. This results can be explained focusing on the observed microstructures: in steel 1, in fact, the presence of retained austenite, located around the pores, is able to retard both the nucleation and the propagation of fatigue cracks[1];
- the thresholds of the low density samples were very close to high density ones, whereas the n exponents of low density samples were higher. This can be explained considering that the threshold values are strongly dependent on the microstructure, while the crack propagation is influenced by the pores amount and morphology [3].
- the measured compressive residual stresses, resulted higher when the shot peenings were carried out on steel 1;
- from the fatigue resistance point of view, the as-sintered steel 1 resulted in higher limits (about 8% for low density materials and about 15% for high density ones). The shot peened samples resulted in higher fatigue performances, especially the high density materials.

Acknowledgements

Special thanks to MIC Italia (Piacenza (PC), Italy) for its cooperation in optimizing the shot peening cycles and for the preparation of the shot peened samples presented in this paper.

References

[1] German, R.M., Powder Metallurgy of Iron and Steel, Wiley Intersciences, New York, 1998.
[2] Danninger H., Weiss B., The influence of defects on high cycle fatigue of metallic materials, Journal of Materials Processing Technology, 143-144, 2003, 179-184
[3] R. Gerosa, B. Rivolta , A. Tavasci, G. Silva, A. Bergmark, Crack initiation and propagation in Chromium pre-alloyed PM-steel under cyclic loading, Engineering Fracture Mechanics 75 (2008), 750–759
[4] Sonsino C.M., Muller, F., Mueller M., Improvement of fatigue behaviour of sintered steels by surface rolling, International Journal of Fatigue, 1992, 3-13
[5] R. Bidulsky, M. Actis-Grande, M. Kabatova and J. Bidulska, Effect of Varying Carbon Content and Shot Peening upon Fatigue Performance of Prealloyed Sintered Steels, Journal of material science and technology, Vol.25, N°25, 2009
[6] N. Chawla, X. Deng, Microstructure and mechanical behavior of porous sintered steels, Materials Science and Engineering A 390 (2005) 98–112

© (2012) Trans Tech Publications, Switzerland
doi:10.4028/www.scientific.net/KEM.488-489.521

Effect of heat treatment on fracture during bending in AA6016 aluminium alloy sheets

Aleksandar Davidkov[1,a], Roumen Petrov[1,2,b], Peter De Smet[3,c] and Leo A.I. Kestens[1,d]

[1] Department of Material Science and Engineering, Gent University, Technologiepark 903, 9052 Gent, Belgium

[2] Department of Material Science and Engineering, Delft University of Technology, Mekelweg 2, 2628 Delft, The Netherlands

[3] Aleris Aluminum Duffel B.V.B.A., A. Stocletlaan 87, 2570 Duffel, Belgium

[a]Aleksandar.Davidkov@UGent.be, [b]Roumen.Petrov@UGent.be, [c]Peter.De.Smet@aleris.com, [d]Leo.Kestens@UGent.be

Keywords: High strength AA6016 aluminium alloy, bendability, quench rate, grain boundary ductile facture

Abstract. The bending properties of high strength precipitation-hardening AA6016-type Al alloy thin sheets in pre-aged T4P temper state were studied in this work. Microstructural features like grain boundary particles distribution and volume fraction of the matrix strengthening phases were considered as factors controlling the mechanical properties and the fracture of this grade. Remarkable decrease in ductility, accompanied by severe deterioration of bendability occurred when coarse precipitates were found into the grain boundaries. The in-situ fracture sequence investigations as well as the post-failure surfaces observations indicated that grain boundary ductile fracture mechanisms were involved in the propagation of the cracks during bending. Heat treatment simulations were carried out and the results showed that the precise control of the technological parameters during production of these sheets is the key factor responsible for obtaining an appropriate combination of strength and bendability. Only by providing both, homogeneous distribution of the matrix strengthening phases and a favourable grain boundary structure, the severe and often contradictory requirements for the functional properties of these alloys can be successfully satisfied.

Introduction

The bending of sheet materials is very often part of many forming processes. One of those is the sheet hemming, where severe bending to an angle of 180° over of a small radius is employed. The hemming is widely used in automotive, carpentry, frames, etc. industries, when it is necessary two or more sheets to be joined by plastic deformation of the edge of the outer one. In automotive industry, for example, door panels, engine- and trunk hoods, etc. are usually assembled by means of hemming joining operation. The hemming of high-strength aluminium alloy sheets is very often challenging and can act as a bottleneck in the industrial production process.

One distinctive feature of the bending process is the presence of geometrical constrains to the deformation. As a result, the strain is highly heterogeneously distributed in the through-thickness of the sheet and one-side surface localization phenomenon accompanies the severe elongation on the outer tensile surface of the formed bend. The geometrically related instabilities like diffuse- and localized necking/thinning typical for the tensile deformation are suppressed and do not appear. That is why the development of strain during bending is not limited and much larger strains to failure can be accomplished in bending than in most of the other sheet forming processes. Hence, the fracture during bending is mainly controlled by the ductility of the bent material itself [1,2].

In polycrystalline materials the development of local displacements along the grain boundaries happens in order to accommodate the plastic deformation in adjacent regions and to retain the grain-to-grain compatibility. Such displacements start developing at the earliest stages of bending and any

weakness of the grain boundary regions can have detrimental effect on the material ductility [3]. The fracture of the grain boundaries in precipitation hardening aluminium alloys could prevail over the other fracture mechanisms and can happen through: *(i)* micro-void growth at large grain boundary particles, *(ii)* strain localization in the soft and sometimes solute free grain boundaries precipitate free zones (PFZs) and *(iii)* matrix shear giving rise to inhomogeneous "planar" slip that apply large stresses to the grain boundaries at the end of the slip bands [4].

Dilatory quenching can reduce the fracture toughness of precipitation hardening aluminium alloys by provoking precipitation in the grain boundaries which reduces their cohesive strength [5]. The higher solute diffusivity in the grain boundary regions leads to higher precipitate rates compared to the interior of the grains. Coarse grain boundary particles can be formed there before the precipitation in the matrix starts. That is why the cooling rate during quenching is the most critical parameter determinative for obtaining satisfactory fracture properties of these alloys. This work studies the effect of the cooling rate during quenching on the bendability of 1 mm thick AA6016 aluminium alloy sheet used for automotive applications. The effect was estimated by carrying out interrupted laboratory hemming tests. The magnitude of grain boundary precipitation was estimated by qualitative observations of the formed microstructures.

Experimental

One millimetre thick cold rolled AA6016 high strength aluminium alloy sheet was used to simulate the heat treatment of this grade. Samples with a size of 100 × 150 mm were solutionized in a salt bath at temperature of 550°C for 70 seconds including 10 seconds heating time. Modified Jominy test [6] was used to simulate different cooling rates during the quenching of the sheet. The obtained cooling rates were ranging between about 6 and 150°C/s in the critical temperature interval between 400 and 280°C [7]. Two pre-aging steps were applied after the quench in order to stabilize the microstructures. Samples for scanning electron microscope observations, Vickers hardness measurements as well as for bending tests were prepared. The microstructure was observed in RD × TD plane after electropolishing the surface by means of 10% $HClO_4$ solution in methanol at 22°C and applied tension of 39 V for a time of 12 s. Environmental scanning electron microscope ESEM Phillips XL30 with LaB_6 filament employing acceleration voltages of 5 ÷ 25 kV and working distances of 10 ÷ 20 mm was used for the studies. Interrupted laboratory hemming tests were conducted as rectangular samples (10 × 20 mm) were bent over themselves around a bend line (BL) perpendicular to their rolling direction (RD). The applied bending was divided in three steps – bending to 90°, to 135° and to 180° with a final pressing. The assessment of the sample bendability was made by observing the micro- and macroscopic appearance (roughness, cracks) of the outer convex surfaces of the bent samples. The hardness of the samples was measured by applying a load of 0.3 kg and acting for 20 seconds in a Vickers hardness tester. According to the chemical composition shown in Table 1 the alloy is considered as excess Si alloy with a Mg/Si ratio of 0.67.

Table 1. Chemical composition, [wt. %]

Si	Mg	Fe	Cu	Mn	Al
0.90	0.60	0.10	0.17	0.15	rest

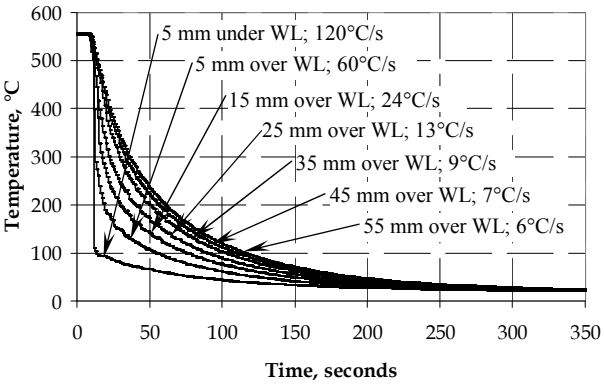


Figure 1. Variable cooling rates in the interval of 400 ÷ 290°C/s obtained by modified Jominy test; WL – water line

Results and discussion

It was already recognized [4,6,8] that in age-hardening Al alloys intergranular fracture can be easily triggered by precipitation of the strengthening alloying elements (Mg, Si, Cu) in the grain boundaries during quenching. To study this effect, variable cooling rates were simulated by a

modified Jominy test and correlated to the fracture behaviour of the material in bending through the amount of heterogeneously formed grain boundary particles. The typical set of thermocouple readings recorded during the quench test is presented in Figure 1.

The T4P hardness of the quenched samples was found to be independent on the cooling rate when varied between 6 and 150°C/s in the temperature interval of 400 ÷ 280°C. It was measured to be HV 74 ± 2.7% after one month of natural aging. The T6 hardness measured after artificial aging at 185°C for 20 min was HV 97 ± 2.2% which gives a hardening response of average 24%. The uniform hardness of all the samples as well as the good hardening response designates that there was no precipitation into the matrix during the quenching even at the slowest cooling rate of 6°C/s. This fact however was not true for the precipitation in the grain boundaries. The bendability of the quenched samples deteriorated with decreasing the cooling rate. Figure 2 presents the macro-images of the hemmed samples (BL ⊥ RD) together with the SEM-images of the microstructures obtained at some of the simulated cooling rates. The critical for the bendability rates were estimated to lie bellow 60°C/s. At this cooling rate the grain boundary precipitation is already present and small grain boundary particles (0.1 ÷ 1 μm) were formed along the grain boundaries. However, the macro-appearance of the bend was not affected and this sample showed good hemmability. At 24°C/s large amount of grain boundary particles are already present and visible in the surface of the sample as stringers aligned with the grain boundaries. This structure results in a considerable deterioration of the bendability. Further decrease in the cooling rate causes coarsening of the grain boundary particles (1 ÷ 5 μm) and increases the distance between them. The bendability of such a microstructure is severely deteriorated. Oppositely, the samples quenched at a cooling rate higher than 60°C/sec show no formation of grain boundary particles and, as expected, have good bendability.

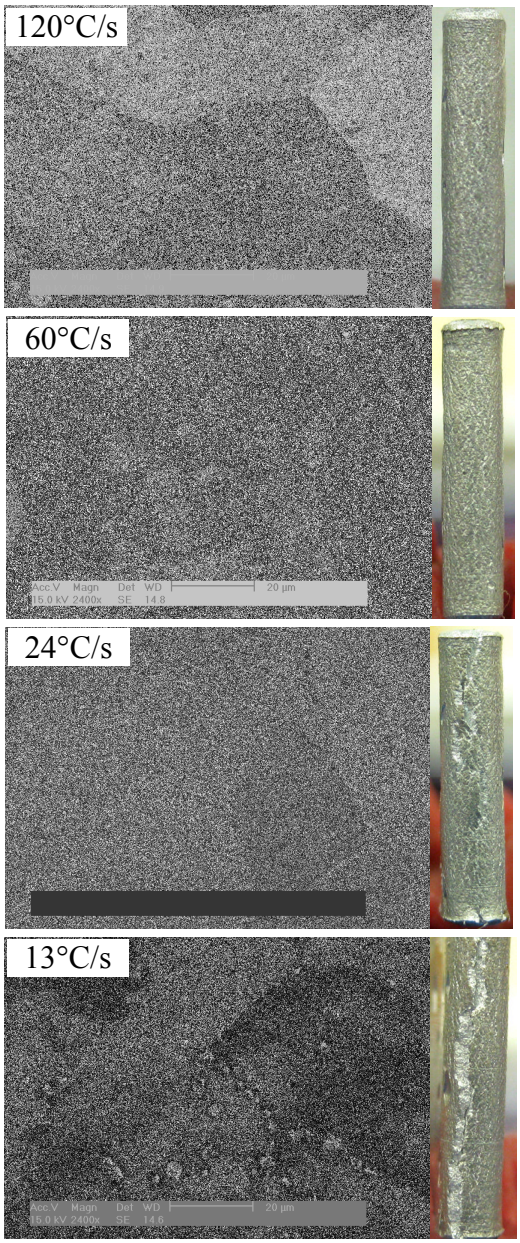


Figure 2. Microstructure and hemming ability of the samples

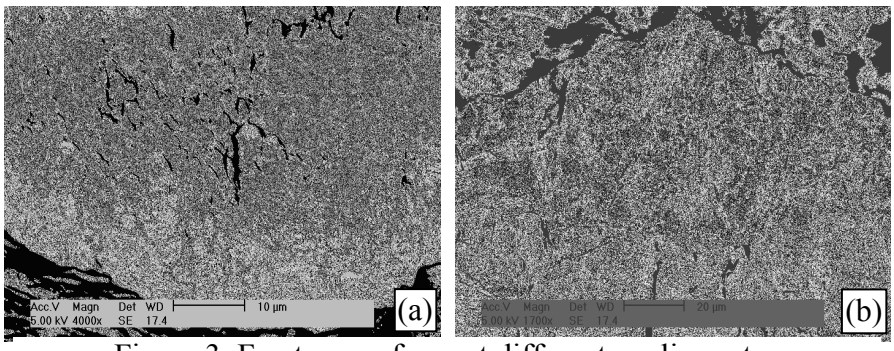


Figure 3. Fracture surfaces at different cooling rates
(a) 60°C/s, (b) 24°C/s

When observing the outer surface of the hem in the sample quenched at 60°C/s, significant number of deformation steps representing the high amount of strain accumulated in the interior of the grains was found. Shallow transgranular cracks were also discovered in some of the surface valleys. The images of the fractured surface show random micro-dimpling correlated to predominantly ductile type of crack growth – see Figure 3(a). The sample quenched at 24°C/s showed lower amount of accommodated strain and propagation of long intergranular primary crack. The fracture surface evidences separation of the grains caused by formation and growth of micro-voids at the grain boundary particles – see Figure 3(b). Sometimes deformation steps were also observed, which probably result from a planar slip inside the grains happening after a complete decohesion of the grains. Such decohesion can occur at the earliest stages of bending due to the presence of large amount of grain boundary particles.**Summary**

Different cooling rates during quenching of a high strength AA6016-type thin aluminium alloy sheets were simulated by performing a modified Jominy test. The recorded cooling rates varied between 6 and 120°C/s in the critical temperature interval between 400 and 280°C. The hardness of the samples in T4P temper state stayed always constant but the bendability deteriorated with decreasing cooling rates due to the precipitation of alloying atoms in the grain boundaries. It was found to happen much faster than in the interior of the grains, which allows the formation of coarse (1 ÷ 5 μm) grain boundary particles in a very short time before any significant precipitation in the bulk of the grains can occur. Cooling rates higher than 60°C/s were required for obtaining a satisfactory bendability in this alloy. The samples quenched at such conditions showed good bendability which was determined at micro-level from the intact grain boundary structure and the large amount of strain accommodated in the bulk of the grains. In samples, quenched at cooling rates lower than 60°C/s the amount of accommodated strain was limited by propagation of intercrystalline cracks growing by a mechanism including grain boundary decohesion and voids formation and growth at the grain boundary particles.

References

[1] A. Reyes, M. Eriksson, O.G. Lademo, O.S. Hopperstad, M. Langseth: Materials and Design Vol. 30 (2009), p. 596

[2] P.A. Friedman and S.G. Luckey: Practical Failure Analysis, Vol. 2, February (2002), p. 33

[3] D.J. Lloyd, D. Evans, C. Pelow, P. Nolan and M. Jain: Materials Science and Technology, Vol. 18 (2002), p. 621

[4] A.K. Vasudevan and R.D. Doherty: Acta metal. Vol. 35, No 6 (1987), p. 1193

[5] M. De Haas, J.Th.M. De Hosson: Journal of Materials Science 37 (2002), p. 5065

[6] D. Steele, D. Evans, P. Nolan, D.J. Lloyd: Materials Characterization, Vol. 58 (2007), p. 40

[7] C.R. Brooks, in Principles of Heat Treating of Nonferrous Alloys, edited by J.R. Davis, G.M. Davidson, S.R. Lampman, T.B. Zorc, J.L. Daquila, A.W. Ronke, K.L. Henniger and R.C. Uhl, volume 4 of ASM Handbook, Heat Treating, ASM Int., Materials Park, OH, USA (1991)

[8] D.J. Lloyd, D. Steele and J.H. Huang: Scripta Materialia Vol. 63 (2010), p. 426

© (2012) Trans Tech Publications, Switzerland
doi:10.4028/www.scientific.net/KEM.488-489.525

Fatigue growth models for multiple long cracks in plates under cyclic tension based on ΔK_I, ΔJ-integral and $\Delta CTOD$ parameter

Željko Božić[1, a], Siegfried Schmauder[2,b] and Marijo Mlikota[1,c]

[1,3]University of Zagreb, FMENA, I. Lucica 5, HR-10000 Zagreb

[2]Universität Stuttgart, IMWF, Pfaffenwaldring 32, D-70569 Stuttgart

[a]zeljko.bozic@fsb.hr, [b]siegfried.schmauder@imwf.uni-stuttgart.de,

[c]marijo.mlikota@fsb.hr mail

Keywords: fatigue crack growth, multiple cracks, stress intensity factor, J-integral, CTOD

Abstract. This paper presents the implementation of fatigue crack growth power law equations based on ΔK, ΔJ-integral and $\Delta CTOD$ fracture mechanics parameters determined in an FE analysis, to plates with multiple site damage (MSD). Results of fatigue tests with constant amplitude tensile loading carried out on mild steel plate specimens damaged with a single central crack and with three collinear cracks are presented. A relatively larger plastic zone occurred in the crack tip region at higher fatigue crack growth rate (FCGR), from 10^{-7} to 10^{-6} m/cycle. The crack growth models based on the elastic-plastic fracture mechanics (EPFM) parameters describe better fatigue crack growth in this range as compared to the liner elastic models.

Introduction

In thin-walled structures, fatigue cracks may initiate under a variety of loading and environmental conditions, at sites of stress concentration due to geometrical discontinuities. In ship deck structures very long cracks can occur due to the multisite damage (MSD), as the accident of Castor tanker showed [1]. The multisite damage can cause a disaster if allowed to progress [2]. From a damage tolerance design point of view, it is important to determine the fatigue crack growth in damaged structural parts.

A common approach to fatigue crack propagation analysis is to describe the crack growth rate by a differential equation, which is called a fatigue crack growth law or model. By integrating the differential equation one can obtain the crack length versus number of cycles, a-N curve, and predict the number of cycles required for the crack to grow from an initial to the final size. The well-known Paris law is based on the stress intensity factor (SIF) range, ΔK, which represents the difference of the maximum and minimum K value, $\Delta K = K_{max} - K_{min}$, associated with the maximum and minimum applied nominal stress in a loading cycle, σ_{min} and σ_{max}, respectively [3]. Excessive plasticity during fatigue violates linear elastic fracture mechanics (LEFM) assumptions and the SIF K no longer characterizes the crack tip conditions. In such cases the elastic plastic fracture mechanics (EPFM) parameters J-integral and $CTOD$ can be considered as a crack driving force. Dowling and Begley [4] used ΔJ-integral for fatigue crack growth modelling under large scale yielding conditions. Gasiak and Rozumek [5] presented a crack growth model based on ΔJ-integral and implemented it to various structural steel materials. Tanaka [6] demonstrated that $CTOD$ can be a suitable parameter for fatigue crack growth modelling under elastic-plastic conditions.

In this paper calculated fracture mechanics parameters K, J-integral and $CTOD$ are presented, by using linear elastic (LE) and elastic plastic (EP) FE analysis for plate specimens with a single crack and an array of collinear cracks. The experiments carried out on mild steel specimens showed higher crack growth rates and relatively larger plastic zones in the vicinity of a crack tip for longer cracks. The intention was to implement fatigue crack growth models based on EPFM parameters J-integral and $CTOD$ in modelling of higher crack growth rates observed in the experiment.

Fatigue Crack Growth Models

In a typical fatigue crack growth rate curve, da/dN versus stress intensity factor range, ΔK_I, one can distinguish three regions, commonly called region I, II and III. Region I is associated with an early fatigue crack development with FCGR typically of the order 10^{-9} *m*/cycle or smaller. Region II represents a stable growth zone for long cracks where the data follow a linear relationship between log d*a*/d*N* and log ΔK, and the FCGR is typically in the range from 10^{-9} up to 10^{-6} *m*/cycle. Region III represents a zone of very high FCGR, d*a*/d*N* > 10^{-6} *m*/cycle, associated with rapid and unstable crack growth.

Various fatigue crack growth prediction models have been developed to analyze propagation of long cracks. Paris used the ΔK parameter to explain FCGR behaviour based on the LEFM assumption. The Paris model does not take account of the SIF threshold, ΔK_{th}, a ΔK value below which crack growth practically does not occur. The ΔK_{th} can be taken into account considering the effective part of the SIF range ΔK_{eff}, as given by Eq. (1). This equation is also known as the Klesnil-Lukáš model [7]. In LEFM the parameters K and J-integral are correlated. Assuming the plane stress conditions, the following relation exists between the two parameters: $J=K^2/E$, where E is Young's modulus. The modified Dowling and Begley model which takes into account the J-integral threshold, ΔJ_{th}, is represented by Eq. (2), where $C_{\text{db eff}}$ and $m_{\text{db eff}}$ are the material constants and $\Delta J = J_{max} - J_{min}$, is the J-integral range. The crack growth model based on $\Delta CTOD$ parameter, which includes threshold $\Delta CTOD_{th}$ values, is represented by Eq. (3).

$$\frac{da}{dN} = C_{p_eff}(\Delta K^{m_{p_eff}} - \Delta K_{th}{}^{m_{p_eff}}) \tag{1}$$

$$\frac{da}{dN} = C_{db_eff}(\Delta J^{m_{db_eff}} - \Delta J_{th}{}^{m_{db_eff}}) \tag{2}$$

$$\frac{da}{dN} = C_{ctod_eff}(\Delta CTOD^{m_{ctod_eff}} - \Delta CTOD_{th}{}^{m_{ctod_eff}}) \tag{3}$$

The number of constant amplitude loading cycles due to which a crack grows from an initial crack length to a final crack length is determined by the integration of the Eq. (1-3).

Experimental and Numerical Simulation Results

A plate specimen with a single central crack P1 and a plate specimen with three collinear cracks P3 were exposed to cyclic tension using a hydraulic fatigue testing machine. The specimen geometry is shown in Fig. 1.

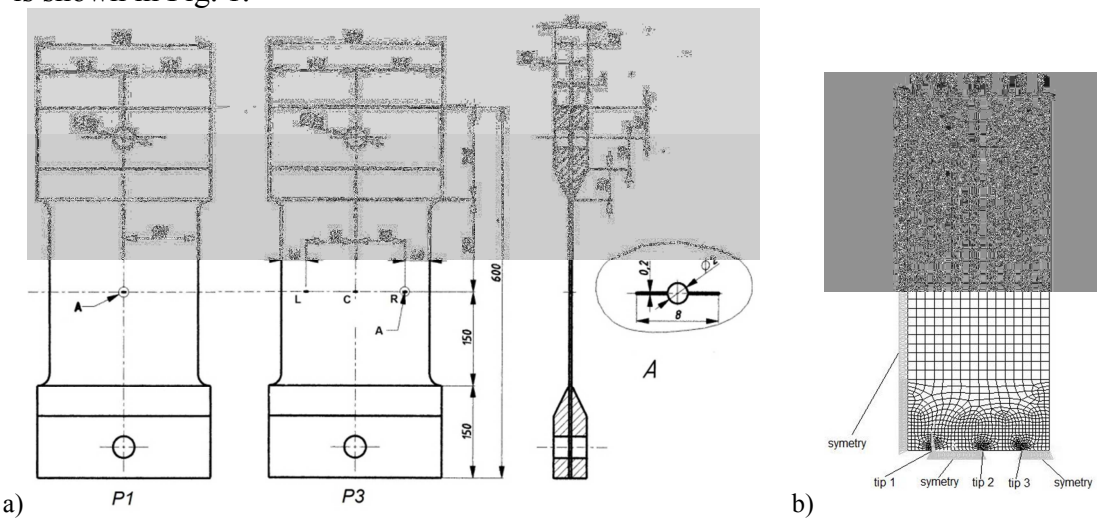


Figure 1 Fatigue test specimens P1 and P3: a) scantlings; b) FE mesh of P3 specimen.

The material used for the specimens is conventional mild steel for welded structures with the material properties specified as follows: ultimate strength is over 400MPa, yield strength is over 235MPa, Young's modulus is 206GPa, Poisson's ratio is 0.3, and the ΔK_{th}=6.8MPam$^{1/2}$. The applied average stress range related to a cross-section in the intact area was $\Delta\sigma_o$ = 80 MPa, with the loading frequency of 5 Hz, and the stress ratio, $R = K_{min}/K_{max} = 0.025$. The initial crack length was $2a$ = 8mm. Crack length data presented here were measured by using an optical microscope.

Fracture mechanics parameters: the Mode I SIF values, K_I, J-integral and *CTOD* were calculated by ANSYS [8] FEM software, where eight node quadratic isoparametric elements assuming plane stress conditions were used. Calculated ΔK_I values for P1 specimens and for the crack tip 1 of P3 are given in Fig. 2. ΔJ-integral calculated by linear elastic and elastic plastic FEA for P1 and for the crack tip 1 of P3 is given in Fig. 3. In Fig. 4 $\Delta CTOD$ values for P1 and P3 specimens are given as obtained from the EP FEA. In Fig. 5 plastic zone size values are compared which were determined analytically under LEFM assumptions and numerically in the EP FEA. Elastic-plastic FEA results for J-integral values agree well with the values obtained from LE FEA for lower FCGR. A larger plastic zone in the crack tip region is generated at higher FCGR. The material constants for the Eq. (1-3) were determined from the rate diagrams given in Figs. 6-9.

Based on the fracture mechanics parameters given in Figs. 2-4, and in Eqs. (1-3), fatigue crack growth life curves have been simulated, as given in Fig. 10. The models based on the EPFM parameters describe better fatigue crack growth at higher FCGR in comparison with the LEFM models, since they provide a steeper a-N curve, as observed in the experiment.

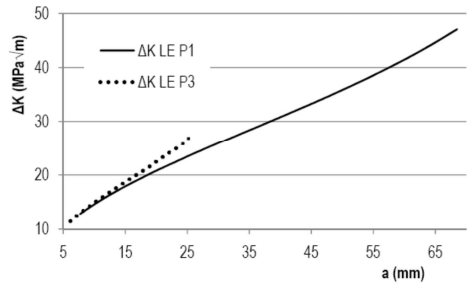


Figure 2 ΔK_I for P1 and the crack tip 1 of P3 specimen.

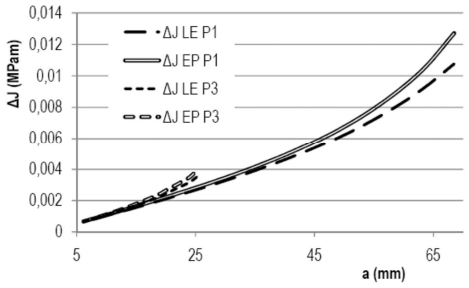


Figure 3 ΔJ for P1 and the crack tip 1 of P3 specimen.

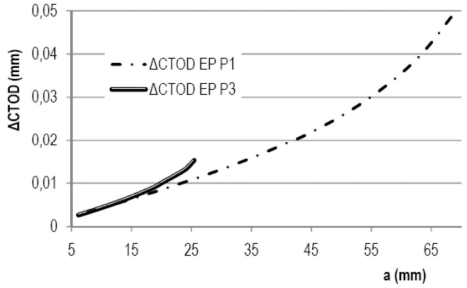


Figure 4 $\Delta CTOD$ for P1 and the crack tip 1 of P3.

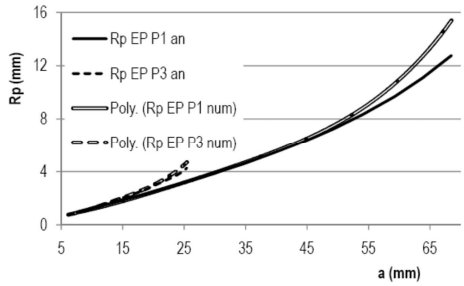


Figure 5 Plastic zone size *Rp*.

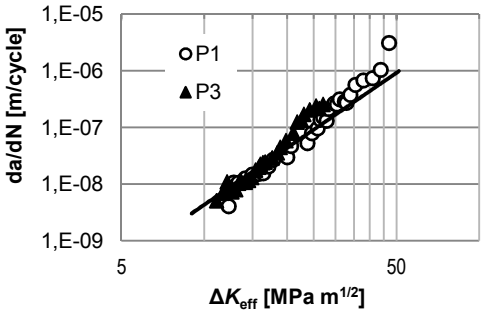


Figure 6 Rate diagram with respect to ΔK_{eff}.

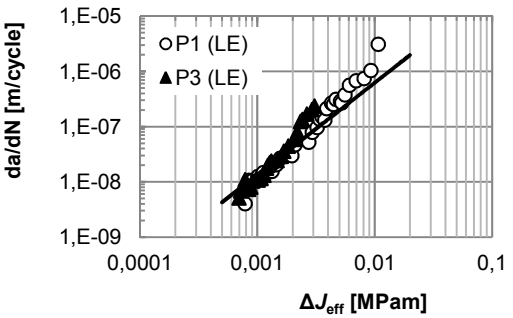


Figure 7 Rate diagram with respect to LE ΔJ_{eff}.

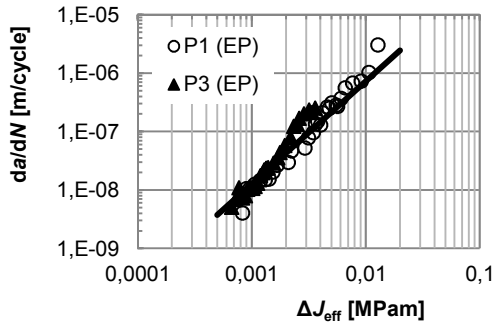


Figure 8 Rate diagram with respect to EP ΔJ_{eff}.

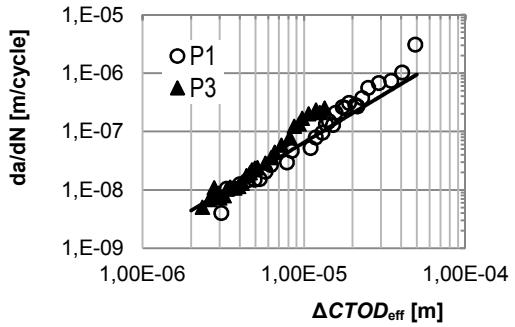


Figure 9 Rate diagram with respect to $\Delta CTOD_{\text{eff}}$.

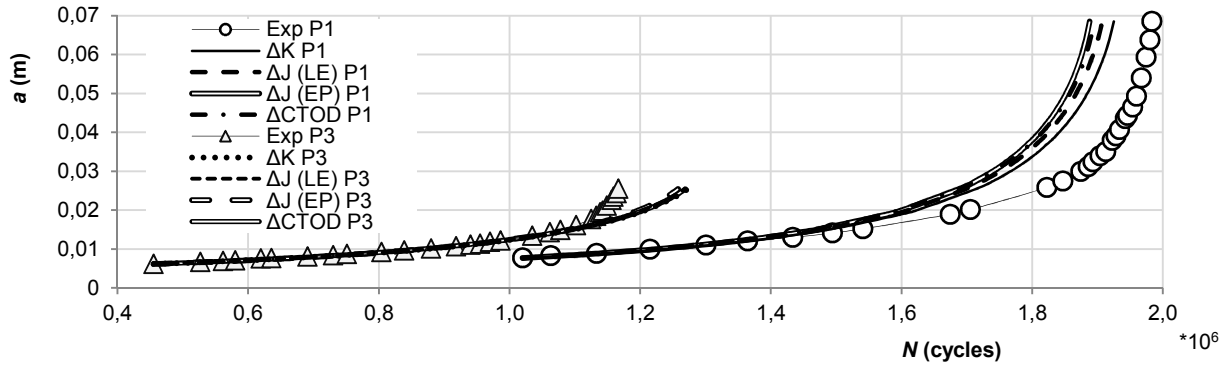


Figure 10 Fatigue life simulation results in comparison to experimental results for P1 and P3 specimens.

Conclusion

Experiments on mild steel plate specimens damaged with a single central crack and with three collinear cracks showed a high fatigue crack growth rate prior to unstable crack growth and final collapse. Elastic-plastic FEA results for *J*-integral were close with linear elastic analyses results at lower FCGR. A relatively larger plastic zone is generated in the crack tip region at higher FCGR, from 10^{-7} to 10^{-6} m/cycle. The models based on the EPFM parameters describe better fatigue crack growth in this range as compared to the LEFM models.

Acknowledgment

Financial support of the Deutsche Forschungsgemeinschaft (DFG-project SCHM 746/110-1) and of the Ministry of Science, Education and Sports of the Republic of Croatia (Project 120-0362321-2198) is gratefully acknowledged.

References

[1] R.J. Dexter, et al. International Journal of Fatigue, 25 (9-11) :1169-1174, 2003.

[2] Y. Sumi, et al. Journal of the Society of Naval Architects of Japan, 179 pp. 407-412, 1996.

[3] P. Paris and F.Erdogan: Journal of Basic Engineering 85 pp. 528–534, 1963.

[4] N.E. Dowling and J.A.Begley, ASTM STP 590, Philadelphia, PA, pp. 82-105, 1976.

[5] G. Gasiak and D. Rozumek, International Journal of Fatigue 26(2), pp. 135–140, 2004.

[6] K. Tanaka, ASTM STP 1020, Philadelphia, PA, pp. 82-105, 1989.

[7] Klesnil M., Lukáš P.: Fatigue of metallic materials. Materials Science Monographs, 7, 1980.

[8] Swanson Analysis System, Inc. ANSYS User's Manual Revision 11.0, 2009.

© (2012) Trans Tech Publications, Switzerland
doi:10.4028/www.scientific.net/KEM.488-489.529

Developed Random Tessellation for Modeling of Microstructure

Kh.Farhangdoost[1,a], S.Rahnama[1,b]

[1]Department of Mechanical Engineering, Ferdowsi University of Mashhad, Iran

[a]farhang@um.ac.ir

[b]sa_ra42@stu-mail.um.ac.ir

Keyword: random tessellation, microstructure, algorithm, grain, image processing

Abstract. The concept of random tessellation is extensively used in wide area of natural sciences, especially material sciences. In this paper a simple but complete explanation of the random tessellation and mathematical tools requirements is presented. Then introducing the algorithm and the program for display random tessellation diagram was written. This program, with high speed and simple algorithm for random tessellation has the ability to change the level of statistical parameters such as number, mean, variance of the area of the grain. The ability to model microstructures of metals and grains for mechanical application, such as estimation of mechanical properties and crack propagation model in microstructure scale is very important. Finally, the microstructure produced by this program show good fitness of random generation with real microstructure.

Introduction

Simulation of microstructure has a significant meaning because it can lead to predicting material behavior without executing complicated experiments. Furthermore, understanding the relationship between microstructure and material properties is very important [1]. For example, yield strength and electrical properties are clearly related to average grain size and grain size distribution (GSD) [2]. A microstructure is characterized by crystal structure, grains, orientation, and grain boundaries. Simulation of microstructures has been investigated by several researchers [3-7] for the purpose of assessing appropriate material properties. So far, several 2D microstructure simulation methods has been done for investigating mechanical characteristics of thin film such as Johnson-Mehl [6], Voronoi [2,3] and lattice model [5].

A division of the plane into polygons, or the space into polyhedral is called a tessellation. Each polygon is called a cell. In a random tessellation, the number of cells, the number of their segments and their shapes are all random. In material sciences, random tessellation is used to model the geometrical features of aggregates of grains in polycrystals, patterns of intergranular cracks and composites [6]. Fig. 1 shows a modeling of this type of crystals. One of the more applicable mathematical tools for constructing a random tessellation is Voronoi diagram [7]. This diagram consists of number of points in a plane and the borders between these points. These points are called sites. The bordering is such that the cells are sets of the nearest neighbor of its site. There are different mathematical algorithms to construct a Voronoi diagram. In this research we consider the most famous one, straight method, and develop it. In this paper, we state a very simple evidential explanation of Voronoi algorithm and we present the MATLAB program for constructing special Voronoi diagrams for a material science purpose and some required statistical inference for dealing with the problem of random tessellation.

This program, with high speed running and simple algorithm for random tessellation has the ability to change the level of statistical parameters such as number, mean, variance of the grains area. The ability to model microstructures of metals and grains for mechanical application, such as estimation of mechanical properties and crack propagation model in microstructure scale is very important. Finally, the microstructure produced by this program show good fitness of random generation with real microstructure by image processing.

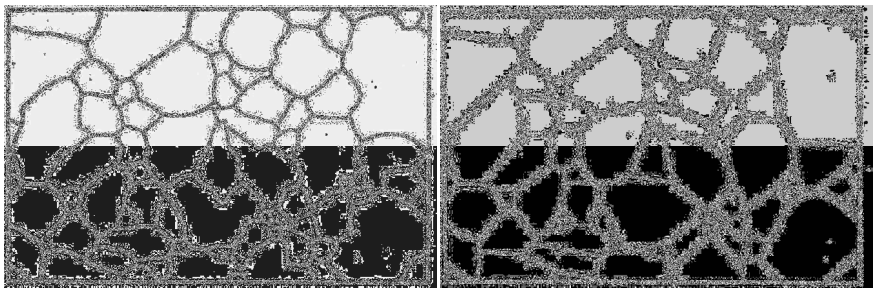


Fig. 1. Real crystal form and random tessellation with the similar topological form [7].

Theory of constructing the diagram

Different stochastic processes are used to define the random tessellation. Two more applicable processes which are used for constructing a random tessellation are the *Poisson point process* and the *Poisson line process*. The Poisson line process produces random lines in a plane by generating random angle of the line with the horizontal and random vertical distance of the line to the origin. These lines form boundaries of the cells of a random tessellation. The Poisson point process is more applicative and produces some random point on the 2D-plane. The coordinates of a point z is denoted by (z_x,z_y). Let S be the set of n random points in a plane, which are called sites. The distance between the points $z=(z_x,z_y)$ and $p=(p_x,p_y)$ is $d_p(z) = \sqrt{(p_x - z_x)^2 + (p_y - z_y)^2}$. The nearest distance of sites to a point z is $d(z) = min_{p\epsilon S} d_p(z)$. Using these notations, the Voronoi diagram on a set of sites $S = \{p_1, \dots, p_n\}$, V(S) is the set of all regions $\Omega_1,\dots, \Omega_n$ on the plane $\Omega \supset S$ such that $p_i \in \Omega_i$, $i = 1, \dots, n$ and $\Omega_i \cap \Omega_j = \emptyset$, for all $i \neq j, \bigcup_{i=1}^{n} \Omega_i = \Omega$ and for all $p_i \in S$ and $z \in \Omega_i$ we have $d_p(z) = d(z)$. A line with equal distance from two points, p and q is called bisector. The intersection of all bisectors of other sites is called the Voronoi region of that site.

To find the edges, we have to find bisectors of sites. The intersection of these bisectors gives us the edges. As it is shown in Fig. 2 further points from a point p produce bisectors which are ineffective for making its region's edges.

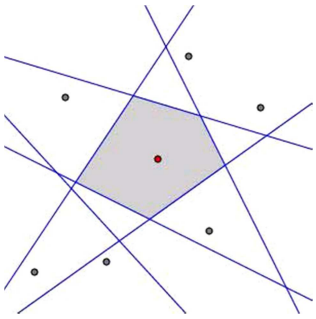


Fig. 2. Bisectors of a site with other sites

Computer programming

There are different mathematical algorithms, such as, straight method and Fortune's algorithm, to construct a Voronoi diagram. In this paper straight algorithm is applied to write a MATLAB program. This program constructs a Voronoi diagram on a limited square plane under a Poisson point process or other random process and patches it with two colors based on a special distribution with success probability parameter. These three parameters are initialized on the beginning of the program and can be updated by user. A sample output of this program is shown in Fig. 3. In this Fig. a Voronoi diagram is constructed on a limited square plane of width 5 under a Poisson point process with average intensity 50 and it patches with two colors based on a Bernoulli distribution with success probability parameter equal to 0.3.

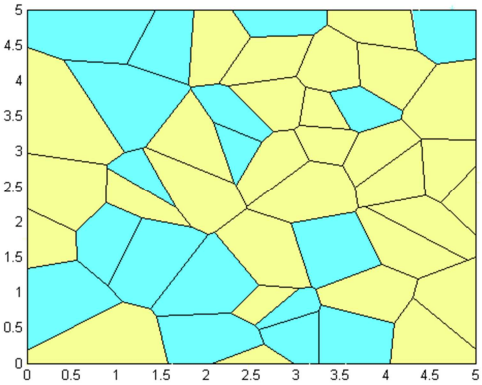
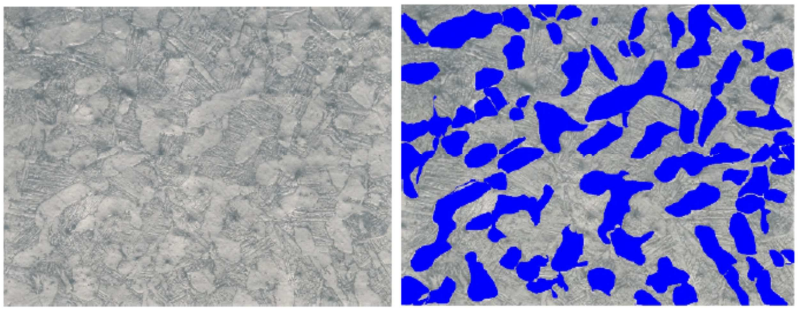


Fig. 3. Sample output of MATLAB program.

Validation

In this section, using real data obtained from image processing software, the program inputs obtained. After implementation of program, the results of the output image processing program are compared with actual results. First eighteen pictures of eighteen pieces of etched Ti-6Al-4V alloy which captured by optical microscope are entered to image processing software (CELEMEX), and processing is done. Fig. 4 shows a sample of the desired microstructure and its image has been processed. Number of alpha phase grain (brighter phase in actual picture) and beta phase grain (dark phase in the actual picture), the percentage of alpha phase and the distribution area of alpha phase are the image processing component outputs. Considering eighteen samples in a statistical distributions manner of the above parameters are obtained which forms inputs to the program.



(a) **(b)**

Fig. 4. (a) Actual microstructure picture. (b) Processed image of microstructure

In Fig. 4 total number of grain are 122 and area fraction of alpha phase is 0.4. In eighteen samples, number of grain has normal distribution with mean value of 98 and variance equal 2 and area fraction of alpha phase has normal distribution with mean value of 0.38 and variance equal 0.025. These parameters are inputs of MATLAB program. Fig. 5 shows the output of MATLAB program.

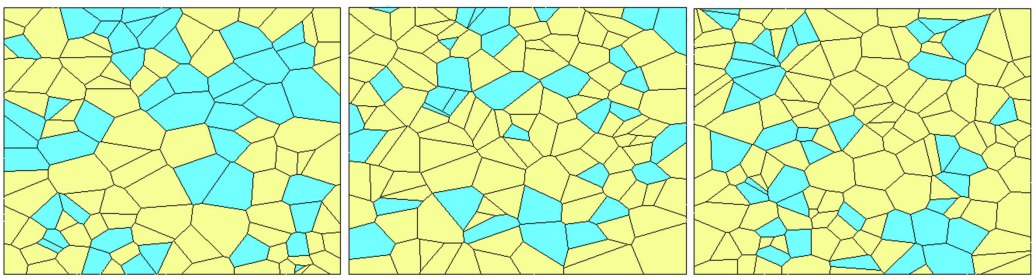


Fig. 5. Output of MATLAB program

After image processing on these outputs for eighteen runs of program, results show good fitness of random generation with real microstructure.

Conclusion

This investigation has capability to model two phase microstructure for the study of relation between microstructure and material properties in order to use for initiation and fatigue crack propagation in a random manner depend on generated microstructure. Some program efficiency have been mentioned as follow:

- Quick and simple for producing microstructure geometry
- Ability to define various statistical parameters and statistical distribution on the parameters influencing the microstructure geometry
- Ability to produce multiphase microstructure, as shown in Fig. 6.
- Ability to extract the coordinates of points for geometry used in other software such as FEM software

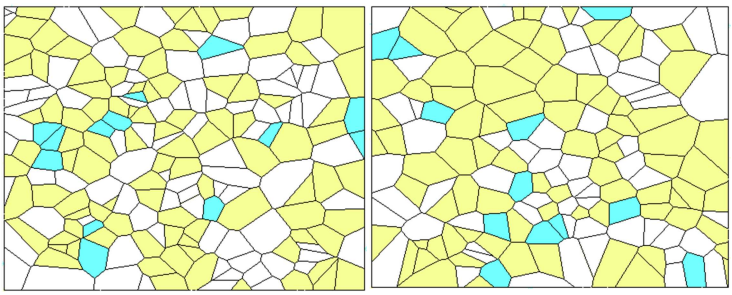


Fig. 6. Three phases microstructure

References

[1] Kh. Farhangdoost, S. Rahnama: *A Comparison of Macroscopic Fracture Surface and Crack Growth Rate of Ti-6Al-4V*, Advanced Materials Research Vols. 97-101 pp 687-690. (2010)

[2] W. Yu, C. D. Wright, S. P. Banks, and E. J. Palmiere: *Cellular automata method for simulating microstructure evolution*, Iee Proceedings-Science Measurement and Technology, vol. 150, pp. 211-213, (2003).

[3] G. Voronoi: *Nouvelles Applications des Parameters Continus a la Theorie des Formes,Quadratiques*, J.Reine Angew, Math, vol. 134, pp. 198-287, (1908).

[4] W. A. Johnson and R. F. Mehl: *Reaction Kinetics in Processes of Nucleation and Growth*, Trans. Am. Inst. Min. Metall., vol. 135, pp. 416-458, (1939).

[5] M. Castro, A. Sanchez, and F. Dominguez-Adame: *Lattice model for kinetics and grain-size distribution in crystallization*, Physical Review B, vol. 61, pp. 6579-6586, (2000).

[6] Mark de Berg, Marc van Kreveld, Mark Overmars, and Otfried Schwarzkopf, *Computational Geometry (2nd revised ed.)*, Springer-Verlag, ISBN 3-540-65620-0 Section 7.2: Computing the Voronoi Diagram: 151–160. (2000)

[7] Aurenhammer, F. Voronoi: *Diagrams-A Survey of a Fundamental Geometric Data Structure*, ACM Computing Surveys, vol. 23, no. 3, pages 345-405.

© (2012) Trans Tech Publications, Switzerland
doi:10.4028/www.scientific.net/KEM.488-489.533

Fracture Analysis of Cube- and Cylinder-shaped WST Specimens Made of Cementitious Composites with Various Characteristic Length

Ladislav Řoutil[1,a], Václav Veselý[1,b] and Stanislav Seitl[2,c]

[1]Institute of Structural Mechanics, Faculty of Civil Engineering, Brno University of Technology, Brno, Czech Republic

[2]Institute of Physics of Materials, Academy of Sciences of the Czech Republic, v. v. i., Brno, Czech Republic

[a]routil.l@fce.vutbr.cz, [b]vesely.v1@fce.vutbr.cz, [c]seitl@ipm.cz

Keywords: wedge-splitting test, cementitious composites, quasi-brittle fracture, brittleness, characteristic length, notch length.

Abstract. The paper is focused on finding reasonable proportions for both cube-shaped and cylinder-shaped silicate-based composite specimens subjected to wedge-splitting tests. The analysis is conducted using finite element method code with an implemented cohesive crack model. The aspect of the material's brittleness, related to the heterogeneity of the material and described by what is termed as the characteristic length of quasi-brittle material, is accented. The results yield some recommendations for the determination of parameters of nonlinear fracture models for cementitious composites by means of wedge splitting tests of laboratory specimens of the two standard shapes.

Introduction and motivation

Characterization of quasi-brittle cement-based building materials can be carried out using a set of fracture mechanical parameters which are obtained from fracture tests. These parameters, especially fracture energy, can then be employed for the definition of material models within an advanced numerical analysis of the quasi-brittle response based e.g. on cohesive crack models. In the previous analysis by the authors [1], [2], the optimal proportions of the cube-shaped specimen (particularly the minimal depth of the starting notch) necessary for the proper realization and evaluation of wedge splitting tests (WST [3], [4], Fig. 1a) performed on various cement-based composites were presented. This paper is focused on the numerical analyses of the failure mechanisms in core-drilled WST specimens conducted in order to tune the proportions (optimal/minimal starting notch depth) of a test specimen of a given shape (see Fig. 3a). The results of this analysis are utilizable within the preparation and conduction of real experiments. Note that a considerably large range of cement-based composites differing in their characteristic lengths is taken into account. The studied cylinder-shaped specimens/cores are important in the building industry – they can be taken from existing structures by drilling (convenient for the assessment of their residual life).

For the proper evaluation of the WST it is necessary that the failure should take place only in the specimen's ligament (Fig. 1b), although there are additional considerable stress concentrators –

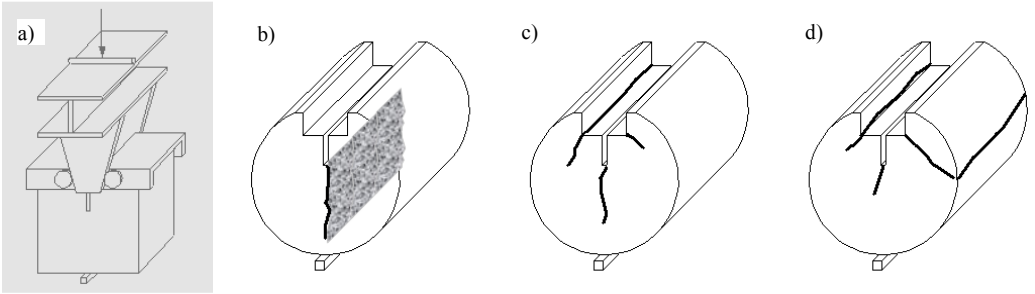


Fig. 1: WST configuration: a) test setup for the cube specimen; b) desirable and c), d) undesirable failures of the cylinder-shaped specimen, respectively

– the corners of the groove for the insertion of the steel loading platens – that can cause undesirable specimen failure (Fig. 1c, d). In the case of quasi-brittle materials, which are characterized by the formation of a fracture process zone (FPZ) around the stress concentrator before the crack starts to propagate, failure can take place at several points in the specimen simultaneously (Fig. 1c, d) unlike in (ideally) brittle materials. A major crack finally localizes, but undesirable damage may also occur elsewhere. The point of the primary crack localization may also depend on the material's brittleness.

Numerical Study

The study was conducted using a commercial finite element method code (ATENA, [5]) designed for the analysis of the failure of (reinforced) concrete structures. In this code, tensile failure is modelled according to nonlinear fracture theories for concrete, particularly the cohesive crack approach in its smeared version [6]. As was mentioned above, the primary goal of the study is to find the optimal specimen proportions for a successful wedge splitting test performance, which can be characterized as a test in which the only fracture process to develop is between the notch tip and the opposite specimen surface, and no other failure takes place in the specimen, e.g. cracking around the groove corners or crushing around the supports and steel platens. If the two above-described specimen geometries are considered, the objective of the study is simplified into one problem: that of finding the optimal starting notch length. This is investigated here for various types of cementitious composites which can significantly vary in their brittleness – in a wide range from a rather brittle hardened fine grained cement paste or geo-polymer up to a (somewhat quasi-ductile) coarse grained concrete or even fibre-reinforced concrete. Note that the measure of the mentioned (quasi-) brittleness vs. ductility is used here in relation to the considered specimens' sizes.

Material model. The tensile failure of the material model used for the virtually tested silicate-based composite is governed by the cohesive crack model with the following traction-separation law parameters: the tensile strength f_t, the shape of the softening function $\sigma(w)$ (σ is the cohesive stress, w is the crack opening), and the specific fracture energy G_f, specifying the area under the cohesive law function. A quantity referred to as the characteristic length is related to the cohesive law parameters f_t and G_f. This quantity is measured in meters and is defined (e.g. [7]) as $\ell_{ch} = EG_f/f_t^2$ (where E is the modulus of elasticity). The characteristic length can serve as a measure of the material's brittleness. It is also being given in context with the heterogeneity of the quasi-brittle material and has a certain correlation to the size of the FPZ.

The material model utilized for the study is referred to as 3D Non Linear Cementitious 2 in ATENA 2D software [5]. The basic set of parameters of this material model was generated by the program for a normal concrete of cubic strength f_{cu} = 75 MPa. This composite was marked as *C0*. Subsequently, other material parameter sets were prepared by modification of the G_f and f_t values, which shall correspond to cementitious composites with ℓ_{ch} equal to the chosen multiples (2, 4, 8, 16) or fractions (1/2, 1/4, ...,1/256) of the basic ${}^0\ell_{ch}$ for the *C0* concrete. They are referred to as *C2+*, …, *C16+* and *C2–*, …, *C256–*, respectively. The values of the parameters are presented in Tab. 1. A comparison of the corresponding shapes of the traction-separation laws (w is in logarithmic scale due to its range) is performed in Fig. 2.

Tab. 1: Cohesive law parameter values corresponding to material sets of different brittleness (with indications of their relation to the basic (*C0*) composite)

composite #	material parameters							note
	E	f_t		G_f		w_c	ℓ_{ch}	
	GPa	MPa		Jm^{-2}		mm	m	
C16+	41.9	2.13	${}^0f_t/\sqrt{4}$	426.8	$4\times{}^0G_f$	1.03E+00	3.93E+00	$16\times{}^0\ell_{ch}$
C4+	41.9	3.02	${}^0f_t/\sqrt{2}$	213.4	$2\times{}^0G_f$	3.63E-01	9.81E-01	$4\times{}^0\ell_{ch}$
C0	**41.9**	**4.27**	$\boldsymbol{{}^0f_t}$	**106.7**	$\boldsymbol{{}^0G_f}$	**1.29E-01**	**2.45E-01**	$\boldsymbol{{}^0\ell_{ch}}$
C4−	41.9	6.04	$(\sqrt{2})\times{}^0f_t$	53.4	${}^0G_f/2$	4.54E-02	6.13E-02	${}^0\ell_{ch}/4$
C16−	41.9	8.54	$(\sqrt{4})\times{}^0f_t$	26.7	${}^0G_f/4$	1.61E-02	1.53E-02	${}^0\ell_{ch}/16$
C64−	41.9	12.07	$(\sqrt{8})\times{}^0f_t$	13.3	${}^0G_f/8$	5.68E-03	3.83E-03	${}^0\ell_{ch}/64$
C256−	41.9	17.07	$(\sqrt{16})\times{}^0f_t$	6.7	${}^0G_f/16$	2.01E-03	9.58E-04	${}^0\ell_{ch}/256$

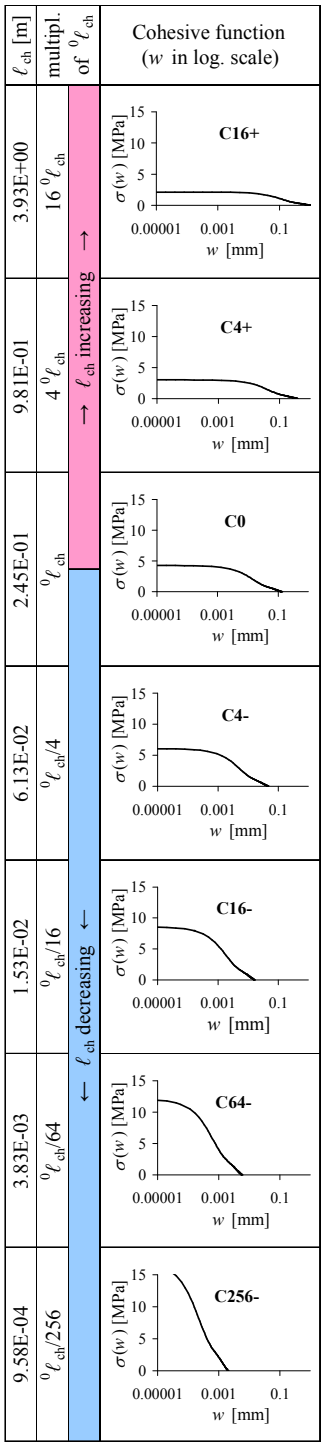


Fig. 2: Selected values of ℓ_{ch}, their relation to the basic ${}^0\ell_{ch}$ of *C0* concrete, and corresponding cohesive functions, i.e. the $\sigma(w)$ dependencies

Geometrical models. Specimens subjected to the WST have to be provided with a groove into which steel platens transferring the load from the testing machine to the specimen are inserted. The groove's dimensions for both cube- and cylinder-shaped specimens are considered the same in this study (Fig. 3a, compare to [2]). The cube-shaped specimen is prepared from a standard 100 mm edge length cube while the cylinder-shaped one is from a 150 mm diameter cylinder. The specimens' proportions are described in detail in [2] and Fig. 3a, respectively. Fig. 3b shows an FE model of the cylinder-shaped specimen including the loading platens, with an indication of boundary conditions.

The numerical study of the cube-shaped WST specimen presented in [1] is extended and supplemented by the analysis of the cylinder-shaped WST in this work. Similarly as in [1], the models were created in several variants. They differ in FE mesh density and in the properties of the interface of the loading steel platens with the cementitious composite specimen in the load application area (the groove). By alternation of the latter feature of the model a situation was simulated when failure propagates (symmetrically or asymmetrically) from the additional stress concentrator(s) introduced to the specimen, i.e. the groove corner(s). No-tension contact was considered as being either on both sides or on one side only. As an alternative, rigid contact between the platens and the specimen was modelled providing a situation when the failure may propagate only from the principal stress concentrator, the notch. This analysis, after its comparison to the preceding two analyses, can answer the question regarding the amount of energy being dissipated via failure around the groove corners [8].

Results, their subsequent analyses and discussion

Two types of outputs of the conducted nonlinear analyses (i.e. the load–displacement (*l–d*) diagrams and the crack patterns/crack width field, see e.g. [1], [8]) were further processed with a focus on the following aspects of the test performance.

Primary stress concentrator. The stress concentrator from which the final fracture started to propagate was investigated based on the crack patterns corresponding to the post-peak stages of the simulated fracture process (examples shown in Fig. 4). The observed trend resulting from simulations on the cylinder-shaped specimens can be seen in Fig. 3c. The curves plotted in the graph represent the considered values of the relative notch length nearest to the transition of the failure mode corresponding to the point of origin of the final failure at the notch tip or the groove corner, respectively, for both symmetrical and asymmetrical boundary conditions in the loading groove. The transitional relative crack length slightly decreases with increasing characteristic length.

Energy dissipated around secondary stress concentrators. The amount of energy dissipated outside of the final FPZ evolving from the notch tip to the opposite specimen's surface can be estimated by comparing the work of fracture values (the areas under the *l–d* curve) of the analysis variants enabling and disabling the failure in the groove corner(s). Research on this issue is currently in progress; however, from preliminary results it would seem that its value depends considerably on the material's brittleness and results in the need to increase the notch length (for example, in the case of the cube-shaped specimen it would be from 0.2 to 0.25 for the *C2+* material parameter set).

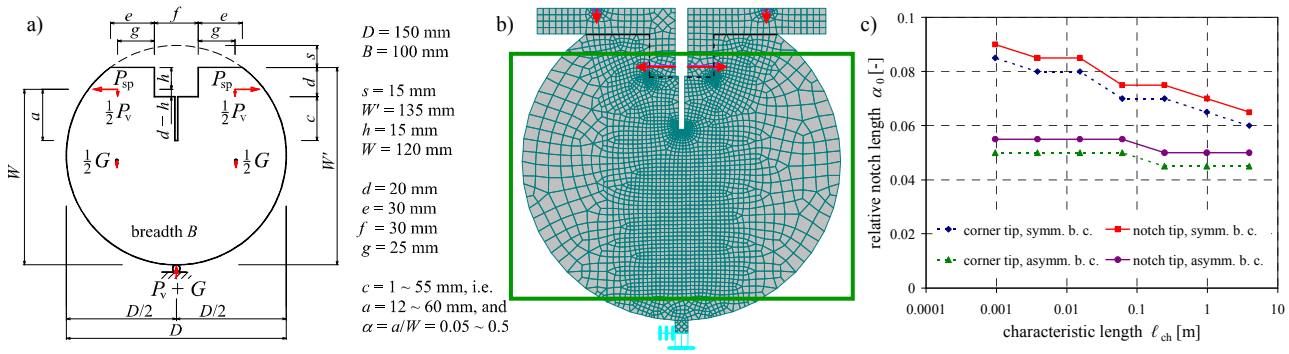


Fig. 3: a) Scheme of the cylinder-shaped WST specimen with an indication of the considered dimensions; b) the used FEM model of the WST; c) boundary between the onset of the final failure from the notch tip and the groove corner tip for both symmetrical and asymmetrical boundary conditions in the groove

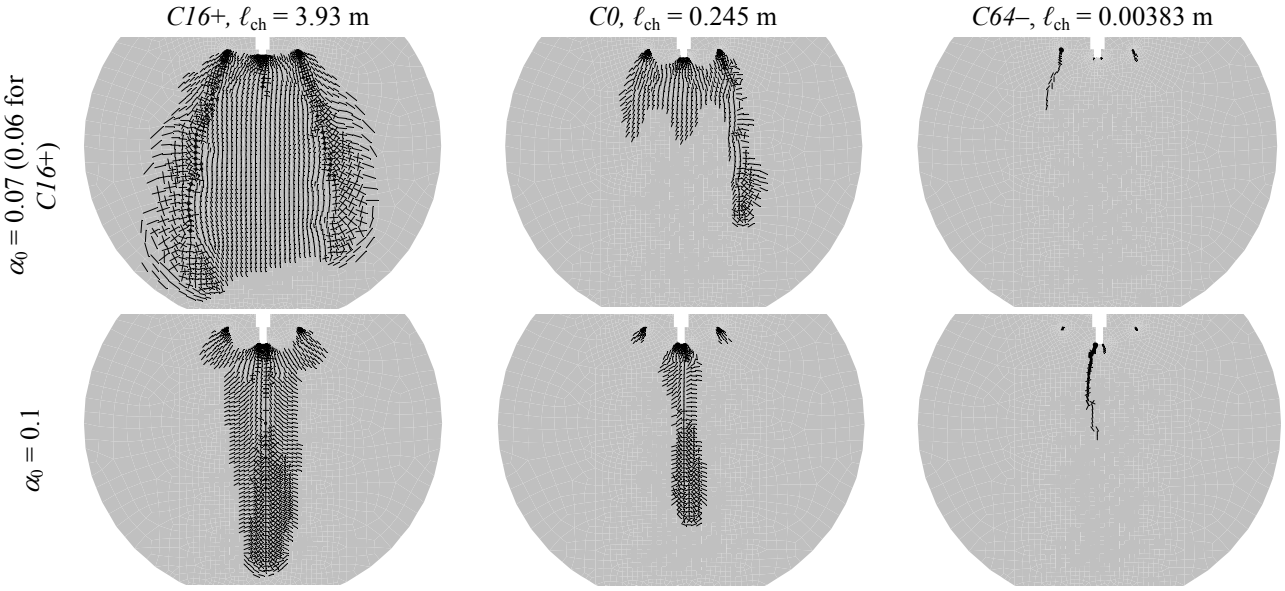


Fig. 4: Crack patterns representing the material failure extent for three selected material sets and two relative notch lengths α_0 (differing in the resulting failure mode) at the loading stage corresponding to 2/3 of the maximum load at the descending branch of the *l–d* curve (for the case when symmetrical boundary conditions exist in the loading groove)

Conclusions

The minimal starting notch length in a quasi-brittle cylinder-shaped specimen subjected to a wedge splitting test was numerically investigated in order to eliminate undesirable failure phenomena outside the specimen's ligament. It was found that there is a dependence between the minimal starting notch length and the brittleness of the composite (the larger the value of the characteristic length, the smaller the notch length), which has implications concerning experimental work.

Acknowledgement: Financial support from grants from the MSMF, project No. 1M0579 (CIDEAS), and the GA AV, project No. KJB200410901, of the Czech Republic is acknowledged.

References

[1] V. Veselý, L. Řoutil, S. Seitl: Key Engng. Mat., Vols. 452-453 (2011), p. 77.
[2] S. Seitl, J. Klusák, V. Veselý, L. Řoutil: Key Engng. Mat., Vols. 452-453 (2011), p. 81.
[3] H.N. Linsbauer, E.K. Tschegg: Zement und Beton 31 (1986), p. 38.
[4] E. Brühwiler, F.H. Wittmann: Engrg. Fract. Mech., 35 (1990), p. 117.
[5] V. Červenka et al.: *ATENA Program Documentation*, Cervenka Consulting, Prague (2005).
[6] Z.P. Bažant, B.H. Oh.: Mater. Struct., 16 (1983), p. 155.
[7] B.L. Karihaloo: *Fracture mechanics and structural concrete*, Longman, NY (1995).
[8] L. Řoutil, V. Veselý, S. Seitl, J. Klusák: Proc. of *IQCMEA-ICF*, Luxor, Egypt, 2011. In print.

© (2012) Trans Tech Publications, Switzerland
doi:10.4028/www.scientific.net/KEM.488-489.537

Finite Element Simulation on Failure Assessment of toughened epoxy adhesives

P. Akbarzadeh [a], Kh. Farhangdoost[b]

Department of Mechanical Engineering, Ferdowsi University of Mashhad, Iran

[a]po_akbarzadeh@yahoo.com, [b]farhang@um.ac.ir,

Keywords: adhesive joints, Finite-element, energy release rate, R-Curve

Abstract. The prediction of the strength of adhesively bonded joints has been investigated using a variety of failure criteria such as maximum stress or strain, and fracture mechanics approaches. Fracture mechanics approaches based on the critical strain energy release rate, for crack propagation are applicable to highly cross-linked structural adhesives and have the advantage of avoiding the explicit consideration of the bi-material singularities inherent in adhesive joints.
In the present work, the finite-element simulation of such adhesive joint has been performed and the R-curves of two different rubber-toughened epoxy adhesives were measured using double cantilever beam (DCB) specimens. The FE results are applied to be compared with the experimental results which were reported in the literature.

Introduction

The use of structural adhesives to bond composites and light weight alloys is now well established within the aerospace and automotive industries. The characterization of adhesive joints using a fracture mechanics approach is well established for mode I (the tensile opening mode) at slow rates in a British Standard [1] and an International Standard [2].

The prediction of the strength of adhesively bonded joints has been investigated using a variety of failure criteria such as maximum stress or strain, and fracture mechanics approaches. Fracture mechanics approaches based on the critical strain energy release rate, for crack propagation are applicable to highly cross-linked structural adhesives and have the advantage of avoiding the explicit consideration of the bi-material singularities inherent in adhesive joints.

Crack extension in rubber toughened adhesive joints begins with the cavitation of rubber particles followed by void growth and induced shear yielding of the matrix. These processes lead to the progressive development of a damage zone consisting of yielded material and distributed micro-cracks. As the load on the joint increases, the largest micro-cracks coalesce to form a macro-crack, which then grows as new micro-cracks and the damage zone advance into the adhesive layer. During these early stages of fracture, the damage zone continues to expand ahead of the growing macro-crack, leading to a progressive toughening of the joint as increasing amounts of strain energy are dissipated by the plastic deformation and micro-cracking. This process results in the fracture resistance curve (R-curve) of G_c versus the crack length. Eventually, the damage zone reaches a steady-state size and the G_c becomes constant, no longer increasing with macro-crack length. This steady-state value of G_c has been used to predict the ultimate strength of a wide range of adhesive joints [3].

In the present work, the finite-element simulation of such adhesive joint has been performed and the R-curves of two different rubber-toughened epoxy adhesives were measured using double cantilever beam (DCB) specimens. The FE results are applied to be compared with the experimental results which were reported in the paper by Ameli et al[4].

Finite element modeling

The DCB joint of Fig. 1 were modeled using finite elements (FE). Finite element analyses were performed to calculate steady-state energy release rate values, G_c.

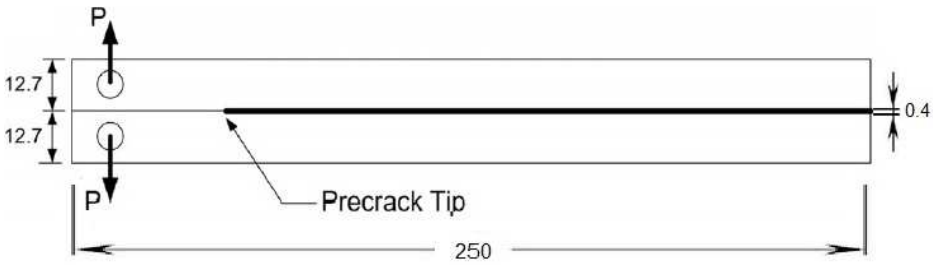


Fig. 1. Geometry of DCB (mode-I) specimen. All dimensions in mm.

The commercial code ABAQUS CAE (V 6.9) was used to create the finite element models. Taking advantage of symmetry it was sufficient to model one half of DCB specimen only as shown in Fig.2. The 24,000 element two-dimensional (2D) model used four-node bilinear plane strain quadrilateral element with reduced integration (CPE4R). The finite element mesh was refined within the region ahead of crack tip. Mesh sensitivity test was performed based on its influence on variation of stress strain distribution ahead of the crack front.

The analyses were performed for two different adhesives (Table 1) and the AA6061-T6 adherends were modeled as elastic. The load pin displacement at the onset of propagation of each crack length obtained from experimental test programme [4] were applied to the corresponding FE models.

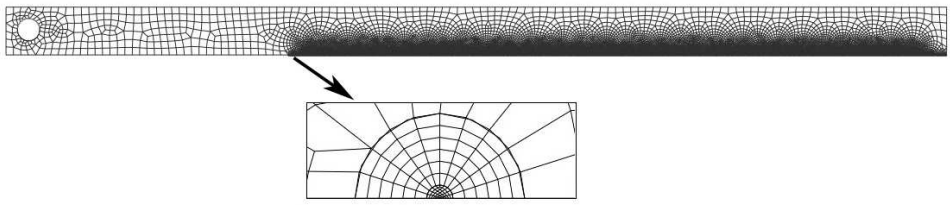


Fig. 2. Two-dimensional finite element model of a DCB specimen with a magnification of the adhesive elements in the crack tip region.

Table 1. Mechanical and physical properties of adhesives 1 and 2 [4]

Adhesive	Elastic modulus, E (MPa)	Poisson ratio, v	Tensile strength, σ_y (MPa)	Glass transition temperature, T_g (°C)	Cured density (g/cm^3)
Adhesive 1	1.96	0.45	44.8	125	1.50
Adhesive 2	1.73	0.39	N/A	122	1.14

The load versus load pin displacement curves for five different crack growth events obtained from FE analyses has been shown in Figure 3.

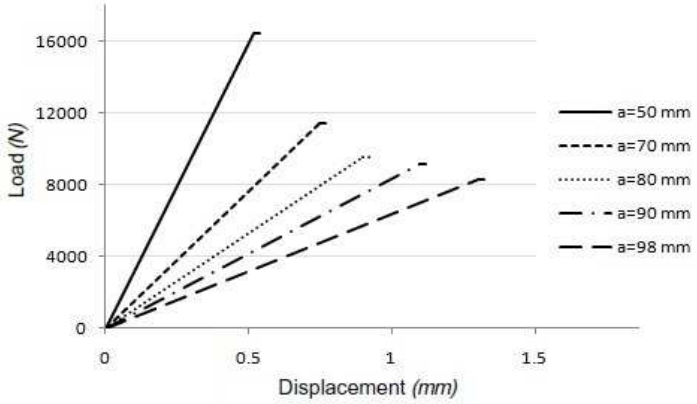


Fig. 3. Load vs. pin displacement up to adhesive crack extension with different initial crack lengths corresponding to the steady-state G_c.

The steady-state energy release rate values obtained from FE analyses and its comparison experimental results that reported by Ameli et al.[4] has been shown (Figs. 4 and 5).

Conclusion

The R-curves for two different toughened epoxy adhesive systems were measured using FE modeling. The data could be fit to a bilinear model representing the rising part and steady-state region of the R-curve. Figures 4 and 5 suggest that the results obtained from the FE analyses are in good agreement with the experiments. Therefore it can be concluded that the FE modeling could be applied to achieve reliable fracture prediction in adhesive joint structures and hence decrease the need for extensive fracture test experiments over a wide range of cases.

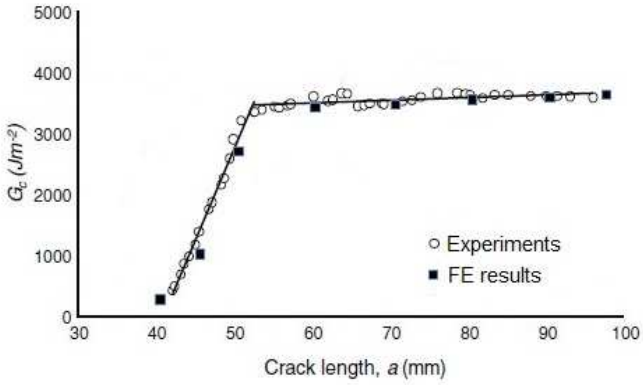


Fig. 4. Typical R-curve of adhesive systems 1.

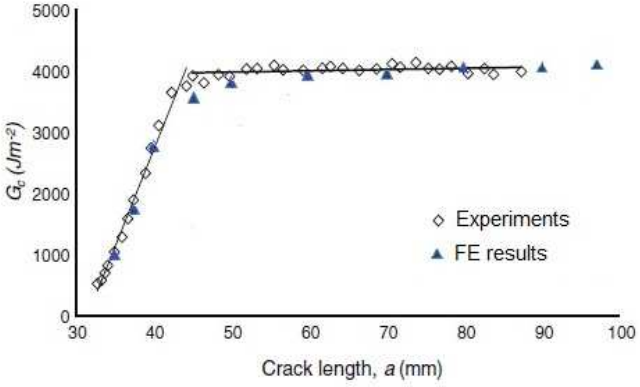


Fig. 5. Typical R-curve of adhesive systems 2.

References

[1] BSI. Determination of the mode I adhesive fracture energy, GIC, of structural adhesives using the double cantilever beam (DCB) and tapered double cantilever beam (TDCB) specimens; 2001 [BS 7991].

[2] ISO, Adhesives – determination of the mode I adhesive fracture energy GIC of structural adhesive joints using double cantilever beam and tapered double beam specimens. ISO; 2009 [25217].

[3] G.C. Jacob, J.F. Fellers, J.M. Starbuck, S. Simunovic. Crashworthiness of automotive composite material systems. J Appl Polymer Sci. 92(5) (2003) 3218–25.

[4] A. Ameli, M. Papini, J.A. Schroeder, J.K. Spelt. Fracture R-curve characterization of toughened epoxy adhesives. Engng Fract Mech. 77 (2010) 521–534

© (2012) Trans Tech Publications, Switzerland
doi:10.4028/www.scientific.net/KEM.488-489.541

Dynamic behavior of granular mixture solids

M. Buonsanti[1,a], G. Leonardi[2,b], F. Scopelliti[2,c] and F. Cirianni[2,d]

[1]MECMAT University of Reggio Calabria, Feo di Vito, 89100 Reggio Calabria, Italy

[2]DIMET University of Reggio Calabria, Feo di Vito, 89100 Reggio Calabria, Italy

[a]michele.buonsanti@unirc.it, [b]giovanni.leonardi@unirc.it, [c]francesco.scopelliti@unirc.it, [d]francis.cirianni@unirc.it

Keywords: Impact; FEM; Airport pavement; Aircraft landing, RVE analysis.

Abstract. In this paper a theoretical and numerical study of impulsive loads over a granular medium free surface has been developed. We will model a real case, as a high deformable solid impacting a less deformable surface, and consequently subject to micro and macro medium failure. Developing a macroscopic approach we resolve the macro-stress in the homogenized two-dimensional medium and subsequently apply a representative volume element (RVE) analysis modeling to the micro-scale. The problem is developed by energetic approach on an elasto-plastic element using an energy functional containing bulk and surface contributions. Finally, a numerical application is presented.

Introduction

The paper presents the application of a Finite Element Analysis for the study of the problem of the impact between a moving rubber wheel and a flexible infrastructure. Past flexible pavement models used multi-layer elastic analysis, which assume static loading, whereas in reality pavements are subject to loads both static and in motion [1]. Although involving a more complicated formulation than the multi-layer elastic theory, the application of FE techniques is generally thought to allow an accurate simulation of pavement problems [2]. More recently, the theory of visco-elasto-plasticity has been extensively used to analyses HMA materials [3]. The model encompasses the elastic, viscoelastic, plastic and visco-plastic components of asphalt concrete behavior.

The initially aim of this study is to assess the effects of a heavy impact caused by aircraft landing gear wheels on a flexible airport pavement. After this, we will to investigate at micro-scale the fracture or damage phenomenon which the solid is subject. We model a RVE considering the bond between two granular particles under sliding forces, formulating a variation approach. The energy functional is enriched by a further term that is comparable to a surface energy.

Finite Element Model

Flexible pavements can often be idealized as closed systems consisting of several layers; so it was decided to model the surface, base, sub-base and sub-grade material using three dimensional finite elements. The pavement structure and materials in the application is based on the structure as found for the runway of the Reggio Calabria airport. While an elastic constitutive model was assumed for the granular layers and the base course, a time hardening creep model was incorporated to simulate the viscoelastic behavior of the HMA surface layer [1]. The tire contact areas considered in the model were based on the Airbus 321 tire. The most common way of applying wheel loads in a finite element analysis is to apply pressure loads to a circular or rectangular equivalent contact area with uniform tire pressure [4]. To evaluate the pavement load in exceptional condition, the dynamic parameters of a “hard” landing, which cause the breaking of gear components, were considered [5]. The finite element model developed has the following dimensions: 10 m in x and y directions and 2.5 m in the z-direction (Fig. 1). The mesh presented has 126245 nodes and 29900 quadratic hexahedral elements of type C3D20R. The loads (vertical and horizontal) were uniformly applied to the element, which was created to be the same size as the wheel imprint of an A321.

Simulation

The results of the non-linear FE analysis are illustrated in the following figures. Fig. 1 *a)* shows the Mises stress distribution for the considered FE model at the landing aircraft impact instant.

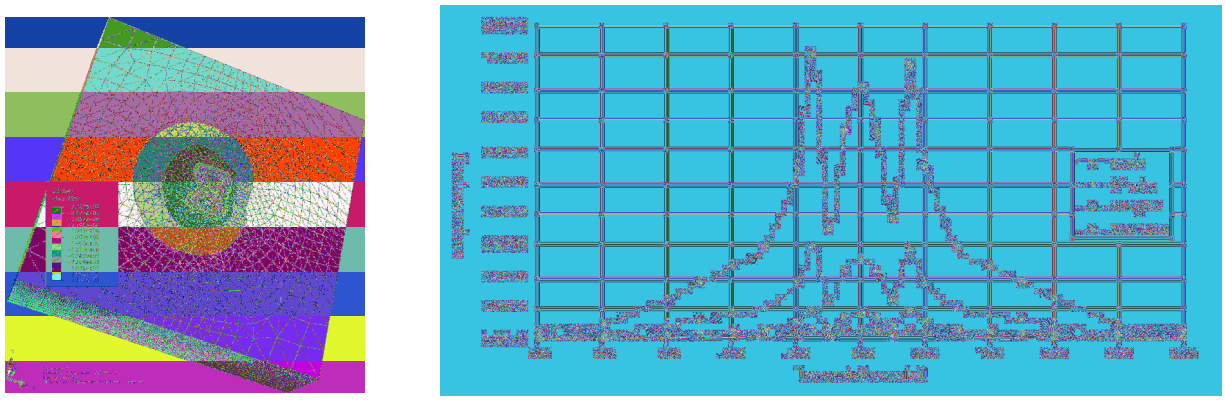


Fig. 1 *a)* Mises stress at the impact; *b)* Creep strain for 1, 10, 100 and 1000 loads repetitions.

In the graph of Fig. 1 *b)* the predicted transversal surface creep strain profiles are plotted along the transverse center line for 1, 10, 100 and 1000 wheels load repetitions.

Micromechanics analysis and conclusions

In this section our target will be to investigate the *RVE* (representative volume element) behavior when sliding forces are growing at macro-scale. We consider a *RVE* as formed by two granular particles (Fig. 2), where the first one lies fixed to the bottom and the second one free to move but constrained through adhesion bond joining either of the two particles.
The latter, made of the same material, are glued together by a viscoelastic thin sheet (i.e. asphalt). The fundamental theory governing the matter has been developed in literature as it regards three different behaviors, in the complexity of the phenomenon.

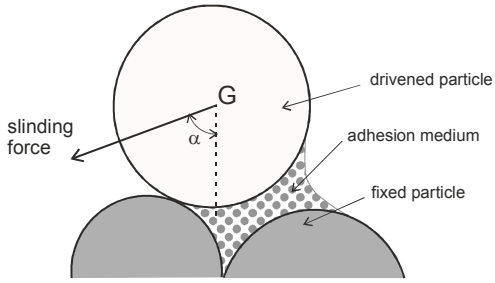


Fig. 2 *RVE* model

From the physical point of view the peeling is just an initial aspect, followed by sheet detachment and finally by bond breaking. In speaking terms, we have a contact dynamic problem with adhesion [6]. In the figure above an elementary volume is shown, and all the analytical considerations which follow from now were performed on it. Initially, we suppose a constant tension behavior on the adhesion sheet, normal to it plane. According to [7], we find the motion equation:

$$\rho u_{tt} - \sigma u_{xx} = 2f\,\delta(x) \tag{1}$$

where ρ is the medium density, $\delta(x)$ denotes the delta function and f the external force, while $u(x,t)$ is a small displacement. Extending in the thin sheet membrane we have likewise.

$$\rho u_{tt} - \sigma \nabla^2 u = f \tag{2}$$

clearly the Eq. 2 is defined over the domain sheet Ω where it's detached. At boundary ∂Ω of the detached part we have the condition $u = 0$. The boundary is, as yet unknown and to determine it there is a further condition called breaking conditions. Let us assume that the thin sheet membrane is linearly elastic with a stored energy as:

$$W = \tfrac{1}{2}\, C\, [\mathrm{I}^2 - (2+c)\, \mathrm{J}] \tag{3}$$

where C and c are constitutive constant, I and J, respectively, the first and the third invariant of the deformation gradient F. From now the analysis becomes deeper or even particularly specific. In the *RVE* model the small contact area among the two particles surfaces results very close to each other and consequently adhesion strength to be considered. If the contact stresses are large and growing the adhesion will be broken in the contact surface. So, in order to do this we should consider the transition from total adhesion to unilateral contact. Following [8] we have:

$$-f + C\, g(u)\beta^2 \geq 0 \tag{4}$$

where C is a constitutive parameter (in this case relative to the asphalt [8]), $\beta \in (0,1)$ the adhesion intensity and $g(u)$ a gap-function. In particular, focusing on the β parameter, by [9] we find:

$$\beta = -1/\eta(\omega - C g^2 \beta) \tag{5}$$

where η is the medium viscosity. From an energetic point of view the velocity field β should be take into account the eventual jump along the detachment line. Without loss of generality we consider the function β as a component in the surface energy part. Focusing our attention on the total energy functional we propose the form as sum of two contributions: the first one is the deformation energy and the second one is the surface energy.

$$W(u) = \int \tfrac{1}{2}\, c\, u'^2 + \beta(u) \tag{6}$$

Here u (x) represents the transverse displacement of the sheet and the admissible field $u(x)$ is assumed to satisfy the impenetrability constraint $u(x) \geq 0$. The potential of adhesive force is taken as well as Griffith criterion namely, zero values for $u = 0$ and equal to one for $u > 0$. Separation of elastic energy into bulk and surface (cohesive) parts is a classical assumption in phenomenological fracture mechanics. The first one is just a function of the strain while the second one is just a function of the components of relative displacement on the surface discontinuity [10].

The discontinuity mean fracture opening, for which the Eq. 6 is modified as follows:

$$W(u) = \tfrac{1}{2}\, c\, u^2 + \Sigma_i\, \beta[u(x_i)] \tag{7}$$

Performing an analysis as power develops the ε parameter to the altered energy $W(u + \varepsilon\eta)$, we find the two conditions:

$$\delta W(u, \eta) \geq 0; \qquad \delta^2 W(u, \eta) > 0 \tag{8}$$

If the deformation energy $w(u) = \tfrac{1}{2}\, c\, u^2$ has a convex graph, then the problem (Eq. 8) is fast to resolve, but this assumption not be able to confirm since non monotone stress-strain law are the material real response in finite elasticity.

We resolve the minimization of the non-convex functional using the gamma-convergence approach, since other direct methods fails. For this we refer to [11] putting the Eq. 7 in the Γ-convergence form, where *cw* is the sub-additive envelope convex.

$$W_\varepsilon(u) = (\varepsilon^{-1} w(u\varepsilon^{-1}) + \varepsilon|u|^2) \rightarrow W(u) = cw(|u|\, dx + \Sigma_{\beta(u)} |u^+ - u^-|) \quad (9)$$

After some calculation on the verified Γ*–limit* it is proven that:

$$W_\varepsilon(u) = (w(u) + |u|^2) \leq cw + \eta \quad (10)$$

Putting the set of the generic parameters *v*, *z*, and *t,* we have $u_\varepsilon(t)$ and the conditions over the functional (Eq. 9) become:

$$W_\varepsilon(u_\varepsilon) = (z/\varepsilon)\, \varepsilon\, w(v_T) + \varepsilon|\, v_T\,|^2 \leq (z/\varepsilon)\, \varepsilon(cw + \eta) \quad (11)$$

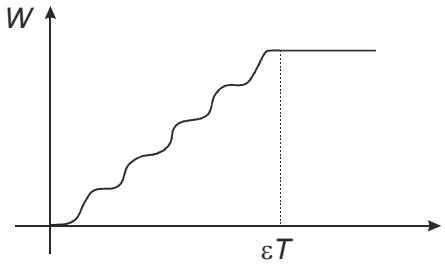


Fig. 3 Wiggles fracture energy

The shown graph in the Fig. 3 represents the gamma-convergence results over the fracture energy functional (Eq. 7). Here we find a graph as Griffith energy piecewise composition. The wiggles form represents continuous damage (i.e. Young's modulus reducing) until the total fracture. Any convex part, in Fig. 3, is joined to the other through a quasi-parallel piece of the horizontal axis and it will represent a fracture opening (or partial detachment) in the adhesive thin sheet joining the two granular particles.

References

[1] D. Johnson*, et al.*, "Three dimensional finite element analysis of flexible pavements to assess the effects of wander and wheel configuration," 2007.
[2] I. Al-Qadi*, et al.*, "In-Situ Validation of Mechanistic Pavement Finite Element Modeling," 2004.
[3] G. R. Chehab, *Characterization of asphalt concrete in tension using a viscoelastoplastic model*: North Carolina State University., 2002.
[4] Y. Huang, *Pavement analysis and design* vol. 367: Prentice Hall, 1993.
[5] AAIB, "AAIB Bulletin: 6/2009 EW/C2008/07/02," 2009.
[6] J. Moreau and P. Panagiotopoulos, *Nonsmooth mechanics and applications*, 1988.
[7] P. Villaggio, *Mathematical models for elastic structures*: Cambridge Univ Pr, 1997.
[8] J. M. Krishnan and K. Rajagopal, "On the mechanical behavior of asphalt," *Mechanics of materials,* vol. 37, pp. 1085-1100, 2005.
[9] P. Wriggers and G. Zavarise, "Computational contact mechanics."
[10] G. Del Piero and L. Truskinovsky, "Macro-and micro-cracking in one-dimensional elasticity," *International Journal of Solids and Structures,* vol. 38, pp. 1135-1148, 2001.
[11] A. Braides, "*Γ*-convergence for beginners, volume 22 of," *Oxford Lecture Series in Mathematics and its Applications*.

© (2012) Trans Tech Publications, Switzerland
doi:10.4028/www.scientific.net/KEM.488-489.545

Load Sequence Effect on Fatigue Damage

Y.G. Xu[1,a], L. Wang[2,b], Y. Chen[1,c], W. Tiu[1,d]

[1]School of Engineering and Technology, University of Hertfordshire, College Lane Campus, Hatfield, Hertfordshire, AL10 9AB, UK
[2]COMAC Building, No. 25 Zhangyang Road, Pudong New Area, Shanghai, China, 200120
[a]y.2.xu@herts.ac.uk, [b]kiddswang@hotmail.com, [c]y.k.chen@herts.ac.uk, [d]w.tiu@herts.ac.uk

Keywords: Fatigue Damage, Load Sequence Effect, Crack Closure, Spectrum Loading

Abstract. Reliable damage tolerant design of airframe structures relies on the accurate life prediction of fatigue cracks propagating from a detectable size to the critical size, which is challenging due to the complex load sequence effect under spectrum loading. This paper aims at gaining a further understanding of the complex influence of the loading history on fatigue damage through a detailed numerical simulation of the near-tip crack behaviour using the crack closure concept. The spectrum loading is broken down into a number of simple yet representative loading scenarios with overload/underload superimposed onto the baseline constant amplitude fatigue loading. Detailed finite element (FE) simulation of the plasticity-induced crack closure (PICC) has been carried out to catch the transient behaviour of PICC and link it to the fatigue damage. The load interaction effect has been analysed with the aim to identify the possible dominant loading cycle which could simplify the fatigue life prediction process in the industry. It is concluded that more reliable damage tolerant design can be achieved if the load sequence effect on fatigue damage can be taken into account more accurately for a structure under spectrum loadings.

Introduction

The current damage tolerance design philosophy in the aerospace industry was introduced in 1980s in response to the perceived limitations of the fail-safe and safe-life design approaches [1]. Under this philosophy an understanding of the fatigue crack growth behaviour is used to predict the crack growth life from an initial flaw size to a critical length in the structure, with an inspection program then being set up to ensure fatigue cracks are detected before the critical length is reached. A major challenge to the aerospace industry is the accurate prediction of the fatigue crack growth life of airframe structures under spectrum loading, where the load interactions due to the load sequence effect have to be fully understood and implemented [1,2,3].

The crack closure model is based on the finding of Elber [4] showing that crack surfaces may close under tensile loads. The premature contact of the crack surfaces during unloading reduces the crack growth driving force due to the load transfer in the wake of the crack tip. Various micro-structural and micro-mechanical factors will influence this premature contact of the crack surfaces, which explains the great capacity of the crack closure model in rationalizing various fatigue behavior [5,6,7,8,9]. Detailed near-tip crack opening profiles and stress distributed has been simulated by the authors [9] with a modified strip-yield model under both the constant amplitude and the single overload loading conditions. Strong correlations between the crack closure and the fatigue damage have been identified, which have been used in rationalizing important fatigue phenomena including the delayed fatigue crack growth retardation after the overload and the short crack growth behaviour, *etc*.

This paper aims at gaining a further understanding of the load sequence effects on fatigue crack growth using the crack closure concept. FE software ANSYS v10 is used to simulate the PICC under various loading conditions. Some basic issues related to the FE simulation of PICC were investigated first. Main efforts were focused on the simulation of the transient behavior of crack closure under various combinations of the overload/underload. The results were used to rationalize the load sequence effect on fatigue damage and crack growth under spectrum loading.

FE Simulation of PICC

Model Construction. Fig. 1 shows the schematic diagram of the centre-cracked tensile (*CCT)* panel used for the FE simulation of the PICC. The panel has a width (*W*) of 200*mm* and a length (*L*) of 400*mm* with the initial crack of a half-length a_0 = 5*mm*. Due to the symmetry, only a quarter of the panel is simulated. The material properties for the model represent typical high strength damage-tolerant aerospace aluminium alloys, e. g. AA2024-T351 and AA2124-T351, with Young's modulus E = 74 GPa, Poisson's ratio v = 0.33, yield stress σ_{ys} = 370 MPa, and the hardening modulus (bilinear model) H = 0.07E.

The mesh was generated with four node quadrilateral elements (Element 182). In maintaining the consistency and efficiency of the model, the transition region between the fine mesh near the crack tip and the coarse mesh further away from the crack tip was meshed by the same element but degraded to a triangular shape. The near-tip element size is 0.025*mm* to ensure enough number of elements in the plastic zone ahead of the crack tip. Cyclic stress is applied on the top edge of the model. Boundary conditions were applied to the left and bottom edges of the model to simulate the symmetry

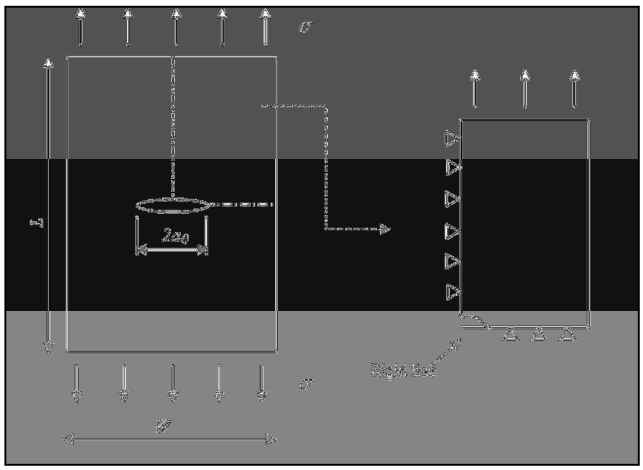


Fig. 1 Centre-cracked tensile panel.

conditions of the *CCT* panel. After some preliminary evaluation of various techniques to model the contact of the crack surfaces, the contact element method is used in the present investigation to simulate the closing process of the unloading phase and determine the corresponding closure stress level. Contact element (CONTA171) was attached to the crack surface and the corresponding target element (TARGE169) attached to a rigid line at the same place of the bottom line of the model to account for the symmetrical feature of the model and the prohibition of crack face interpenetration.

Basic Issues for PICC Simulation. To ensure the reliability of the FE simulation of PICC in this study, some preliminary investigation has been carried out to clarify the basic issues of mesh density, node release scheme, and the technique to define the crack closure level. The current study found that the variation of the forward plastic zone size quickly converged to a stable level when the near-tip element size is less than one-tenth of the forward plastic zone size, which is consistent to the general observation reported in the literature [10,11,12]. Four different node release schemes have been tested in the current study, namely node release at the minimum load every cycle, at the maximum load every cycle, at the minimum load every two cycles, and at the maximum load every two cycles. No significant difference in crack closure has been observed provided that the above mesh density criterion has been satisfied. It is however noticed that node release at the minimum load is computationally easier compared with the one with the node released at the maximum stress. This can be explained by the less amount of change in crack displacement when the node is released under the minimum load [11,13]. To maintain both the reliability and the efficiency of the FE simulation of PICC in this study, subsequent crack closure results were obtained with more than ten elements in the forward plastic zone and the crack was released every loading cycle at the minimum loading level.

The determination of a meaningful crack closure/opening level to define the effective crack propagation driving force remains a challenge to the fatigue research community [8,9,10,11,12,13]. Commonly used techniques for defining the crack closing/opening point include detailed monitoring of the crack surface displacement behind the crack, stress field variation at the crack tip, non-linearity of the specimen compliance curve, and the weight function method using the contact stress behind the crack tip at the minimum load. It is found in this study that, apart from the stress field method, all the other three techniques agree with each other quite well. The stress field method tends to predict a much high crack closure level and is considered questionable as indicated by other

researchers [11]. The difference among the displacement method, the compliance curve method, and the weight function method became negligible when a smaller load increment step (normally $\Delta\sigma<1\%\sigma_{max}$) was used in the simulation. The weight function method was chosen for the subsequent PICC simulation in this study due to its efficiency in the FE modelling as it only requires the contact stress on the crack surface at the minimum load without the need of monitoring the crack opening/closing processes under the cyclic loading.

Load Sequence Effect on PICC Variation and Fatigue Damage

Overload Effect. Fig. 2 shows the variations of the crack closure under two overloads of the same overload ratio of 100% (100%OL) applied onto a baseline constant amplitude loading of $R=0$ and $S_{max,BL}=100MPa$. The crack length increment (Δa) is normalized with the monotonic forward plastic zone size (r_f) at the maximum stress of the fatigue cycle. The second overloads were applied after the crack has propagated into the first overload plastic zone at a distance of $0.25(r_p)_{OL}$, $0.5(r_p)_{OL}$, $0.75(r_p)_{OL}$, $1.0(r_p)_{OL}$, and $3.0(r_p)_{OL}$, respectively. It is found that the first overload will interact with the second overload even if they are three times the overload plastic zone size apart. Enhanced crack closure has been observed for the second overload. Compared with the single overload case, the increase of the maximum crack closure level for the second overload ranges from 10% to 5% for the overload spacing changing from $0.25(r_p)_{OL}$ to $3.0(r_p)_{OL}$. It is also worth noting that the profile of the second post-overload crack closure variation was expanded with the increase of the spacing between the two overloads, indicating longer post-overload crack growth retardation due to the first overload. The sudden drop of the crack closure for the second overload is however nearly back to the level of the single overload scenario when the overload spacing is about $3.0(r_p)_{OL}$, indicating that the first overload has less effect on the initial acceleration of the crack growth than the retardation following the second overload.

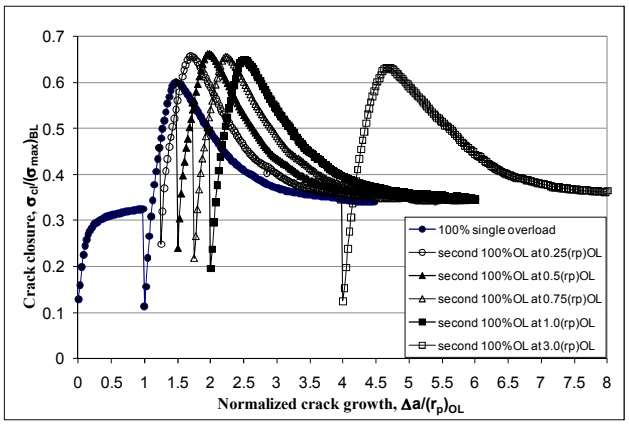


Fig. 2 Interactions of the two overloads.

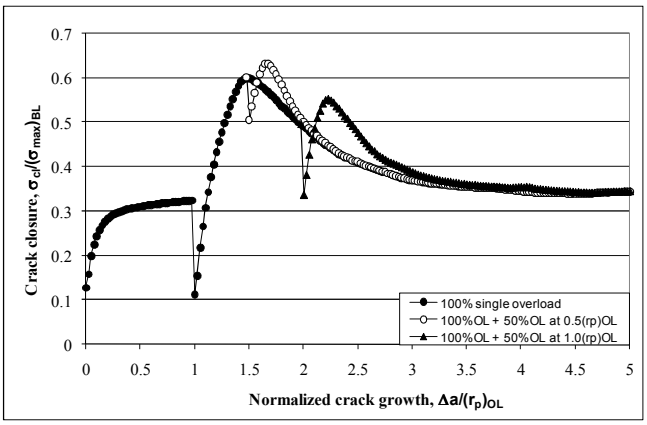


Fig. 3 Effect of the dominant overload.

Fig. 3 shows the effect of the dominating first overload (100%OL) on the variation of the crack closure of the second smaller overload (50%OL). In this study, the second overload of overload ratio of 50% was applied after the crack had propagated into the first overload plastic zone at a distance of $0.5(r_p)_{OL}$ and $1.0(r_p)_{OL}$, respectively. The overload plastic zone size $(r_p)_{OL}$ here is the one corresponding to the first overload. It is interesting to note that while the second overload introduced a brief decrease and then an enhanced PICC level, which is common to the single overload effect, the second overload did not increase the overload-affected distance of the dominating first overload. The PICC was back to the baseline PICC level after the crack growth of about $\sim 3.5(r_p)_{OL}$, which is different to the results in Fig. 2 where the second overload had the same magnitude of the first overload. Also worth noting is the fact that the maximum PICC level after the second overload (50%OL) can be higher or lower than the peak value due to the first overload alone, depending upon the position where the second overload was applied.

Underload Effect. Fig. 4 shows the effect of the underload on PICC variation with the 100% underload applied immediately before or after the 100% overload. It is found that the underload applied before the overload has no effect on the post-overload PICC variation, which is consistent to most of the literature results [2,3,4,5]. This statement remains valid for higher stress ratio baseline spectra as the simulation under R=0.3 supported the same claim. On the other hand, the underload applied immediately after the overload reduced the crack closure level significantly, which explains the accelerating effect of underload on crack growth if it is applied after the overload. An interesting point to note here is that the underload reduced the magnitude of the PICC level but did not shorten or prolong the overload-affected distance.

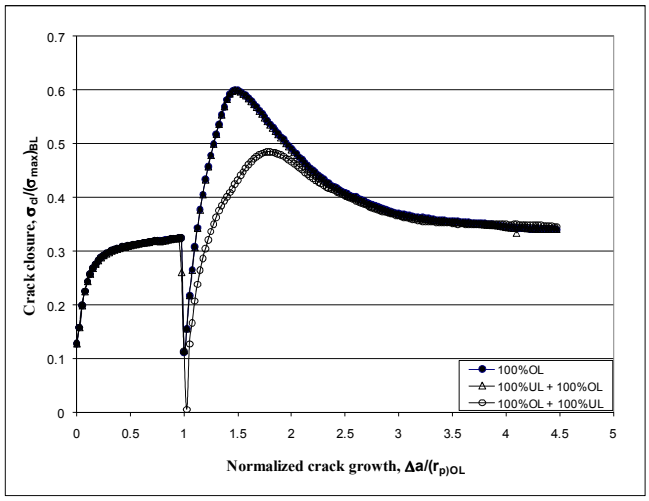


Fig. 4 Underload effect on PICC variation.

Summary

Basic issues related to the FE simulation of the PICC have been investigated to ensure the reliability of the simulation results. It is concluded that reliable crack closure level can be obtained with more than ten elements in the forward plastic zone and the node at the crack tip is released at the minimum load. The weight function method proves to be the reliable and efficient approach in the determination of crack closure.

The load sequence effect on the variation of crack closure and the corresponding fatigue damage has been investigated. The spectrum loading has been broken down into a number of combinations of overload(s)/underload(s) and has been simulated individually. Some interesting observations on double overload effect, the dominance of the overload, and underload effect on the variation of PICC have been made. These results should be implemented to improve the accuracy and efficiency of the life prediction for engineering purpose as the variation of the crack closure level is closely linked to the crack propagating driving force and the fatigue damage.

References

[1] T. Swift: Int. J. Fatigue Vol. 16 (1994), p.75-94.
[2] M. Skorupa: Fatigue Fract. Eng. Mater. Struct. Vol. 21 (1998), p. 987-1006.
[3] W. Cui: J. Mater. Sci. Technol. Vol. 7 (2002), p. 43-56.
[4] W. Elber: Engng. Fract. Mech. Vol. 2 (1970), p. 37-45.
[5] A. Ray, R. Patankar: Applied Mathematical Modelling Vol. 25 (2001), p. 979-94.
[6] J.C. Jr. Newman: Engng. Fract. Mech. Vol. 71 (2004), p. 2347-63.
[7] X. Huang, M. Torgeir: Int. J. Fatigue Vol. 29 (2007), p. 591-602.
[8] P.C. Paris, D. Lados, H. Tada: Engng. Fract. Mech. Vol. 75 (2008), p. 299-305.
[9] Lei Wang, Yongkang Chen, William Tiu, Yigeng Xu: Int. J. Modelling, Identification and Control Vol. 5 (2008), p. 77-91.
[10] K.D. Singh, K.H. Khor, I. Sinclair: Acta Materialia Vol. 56 (2008), p. 835-51.
[11] P.F.P. de Matos, D. Nowell: Engng. Fract. Mech. Vol. 74 (2007), p. 1579-601.
[12] K. Solanki, S.R. Daniewicz, J.C. Jr. Newman: Engng. Fract. Mech. Vol. 71 (2004), p. 149-71.
[13] H. Alizadeh, D.A. Hills, P.F.P. de Matos, D. Nowell, M.J. Pavier, R.J. Paynter, D.J. Smith, S. Simandjuntak: Int. J. Fatigue Vol. 29 (2007), p. 222-31.

© (2012) Trans Tech Publications, Switzerland
doi:10.4028/www.scientific.net/KEM.488-489.549

An Experimental and Numerical Investigation of the Mixed-Mode Fracture Toughness and Lap Shear Strength of Aerospace Grade Composite Joints

J. Mohan[1, a], A. Karač[1,b], N. Murphy[1,c] and A. Ivanković[1,d]

[1]School of Electrical, Electronic & Mechanical Engineering, University College Dublin, Belfield, Dublin 4, Ireland.

[a]joseph.mohan@ucd.ie, [b]aleksandar.karac@ucd.ie, [c]neal.murphy@ucd.ie, [d]alojz.ivankovic@ucd.ie

Keywords: Composite, adhesive joints, finite volume, fracture mechanics, DCB, lap-shear.

Abstract. In the present study, the mixed-mode fracture toughness of an adhesively bonded composite joint system was examined using a variety of linear elastic fracture mechanics (LEFM) based tests. These tests include the mode I double cantilever beam (DCB), mixed-mode asymmetrical DCB (ADCB) and mode II end load split (ELS) test. The joint system was also evaluated using the wide area lap shear (WALS) test that is often employed by the aerospace industry. While lap shear type tests are relatively simple to perform and post-process compared to their LEFM counterparts, the results can often be misleading and are greatly dependent on the overlap length, thickness of substrate and type of fillet. The experimental tests were also simulated using OpenFOAM, a finite volume based software package. Through this combined experimental-numerical approach, a greater understanding of the influence of the peel ply surface treatment and scrim cloth on the behaviour of the WALS test was achieved.

Introduction

The increasing use of composite materials in various industries, such as aerospace, automotive and renewable energy generation, has driven a need for a greater understanding of the fracture behaviour of bonded composite joints.

An important prerequisite for the adhesive bonding of composites is the existence of a uniform surface free from contaminants and mould release agents. While there are several ways in which this may be achieved, the use of peel plies has emerged as the preferred choice for many industries due to the repeatable nature of the resulting surface, particularly in the highly regulated aerospace industry. However, the use of peel plies can present some problems. It is possible that contamination from the peel ply can be transferred to the composite substrate and adversely affects the adhesive joint [1].

Composite joints are typically evaluated using lap shear type tests. While these tests are relatively simple to perform and post-process compared to their fracture mechanics based counterparts, the results can often be misleading and are greatly dependent on the overlap length, the thickness of the substrate and the type of fillet employed [2, 3].

The aim of this work is to show that composite joint systems can be modelled using material properties determined from fracture mechanics based tests. The fracture parameters will be used to develop numerical models of the fracture tests that accurately predict the wide-area lap-shear test.

Experimental

Materials & Manufacture of Bonded Specimens. A variety of aerospace grade materials were used in the present study. The substrates were manufactured from a carbon-fibre/epoxy prepreg manufactured by Hexcel. A Henkel wet peel ply was used to prepare the surface prior to bonding. A new generation two-part epoxy paste adhesive, manufactured by Henkel, was used to bond the substrates. The composite laminates were manufactured in-house at University College Dublin using a press-clave and vacuum bagging procedure as per the manufacturer's guidelines. Once cured, specimens were cut to a size of 25mm x 150mm using a diamond grinding disc. The peel ply

was removed just before application of the adhesive. Bondline thickness was controlled at 0.15mm using a nylon scrim cloth. The joints were cured in accordance with the manufacturer's guidelines in an air-circulated oven. A special curing jig was used to ensure alignment of the substrates.

Linear Elastic Fracture Mechanics (LEFM) Based Tests. Three LEFM based tests were conducted to determine the fracture toughness of the composite joints. The tests employed were a mode I double cantilever beam (DCB) test [4], a mixed mode I+II asymmetric double cantilever beam (ADCB) test [5] and a mode II end loaded split (ELS) test [6]. All tests were conducted at a constant crosshead displacement rate of 2 mm/min at room temperature on a screw-driven Hounsfield 50K tensile test machine. The propagation values for G_C were calculated using corrected beam theory (CBT).

Wide Area Lap-Shear (WALS) Tests. WALS tests were conducted in accordance with a Bombardier Aerospace (UK) test protocol. The bonded composite joints were notched using a diamond blade such that the overlap length was 12.5mm. The width of each specimen was 25mm. Tests were performed on an Instron servo-hydraulic tensile test machine. Hydraulic grips were used to minimise slippage. The samples were loaded at a rate of 0.1mm/min. The extension was recorded using a clip gauge with 50mm gauge length.

Numerical Method. A finite-volume based method was used for the numerical simulation of the experiments. A fully implicit time-differencing scheme is employed in the analysis, guaranteeing unconditional stability. The model was implemented in 'OpenFOAM' package, a C++ library for continuum mechanics [7]. Figure 1 shows a typical mesh used for simulation of mode I DCB tests and WALS tests. As can be seen, the tests were fully modelled, and proper material properties attributed to each specimen part. The aluminium loading block and composite substrate were modelled using a linear elastic material model with appropriate mechanical properties, whereas the adhesive was modelled using an elastic-plastic model with classical incremental J2 flow theory with von Mises plasticity. Plane strain conditions were assumed to dominate through specimen thickness, and hence 2D calculations were performed. Loading was applied to the loading boundary using a mixed boundary condition, to allow loading block rotation. Crack propagation was simulated using a Dugdale mixed-mode cohesive-zone model [8] applied to cell faces in the adhesive domain. Therefore, it was possible to simulate an arbitrary crack propagation path including a 'multi-cracking' process.



Figure 1. A typical mesh for DCB (left) and WALS (right) test simulations.

Results and Discussion

Fracture Tests: Experimental Results & Numerical Model. Figure 2 shows the failure envelope for the composite joint system under investigation. All joints resulted in interfacial failure. The total fracture toughness was essentially constant at approximately 200 J/m^2 until the condition of pure mode II loading was reached. At this point, the measured fracture toughness almost doubles to 400 J/m^2. However, the reason behind this increase was believed to be due to mechanical interlocking between the peel ply prepared surface and adhesive. From visual inspection of the fracture surface, segments of the wet peel ply resin were sheared off from the substrate. This damage was not seen to the same extent during mode I or mixed-mode loading.

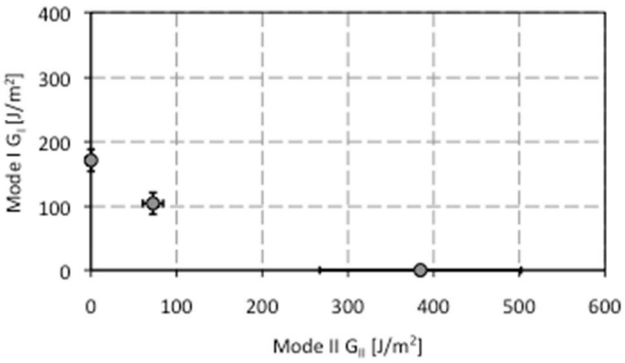


Figure 2: G_I/G_{II} failure envelope for composite joint system.

All DCB tests were simulated numerically using the procedure explained in the previous section. Cohesive-zone parameters were taken as follows: fracture energy G_{Ic} was set to the values obtained experimentally, ie. 200 J/m^2, while cohesive strength was equal to the tensile strength of the adhesive obtained from the standard tensile tests. Numerical simulations were then validated against experimental results comparing the load and crack length histories. In general, a good agreement between measured and predicted results was obtained. For example, Figure 3 (left) shows a comparison between the experimental and numerical load and crack length histories for a DCB test, where fracture toughness was set to 200 J/m^2, and cohesive strength of 30 MPa. At the time of writing, numerical models for ADCB and ELS geometries are being finalised.

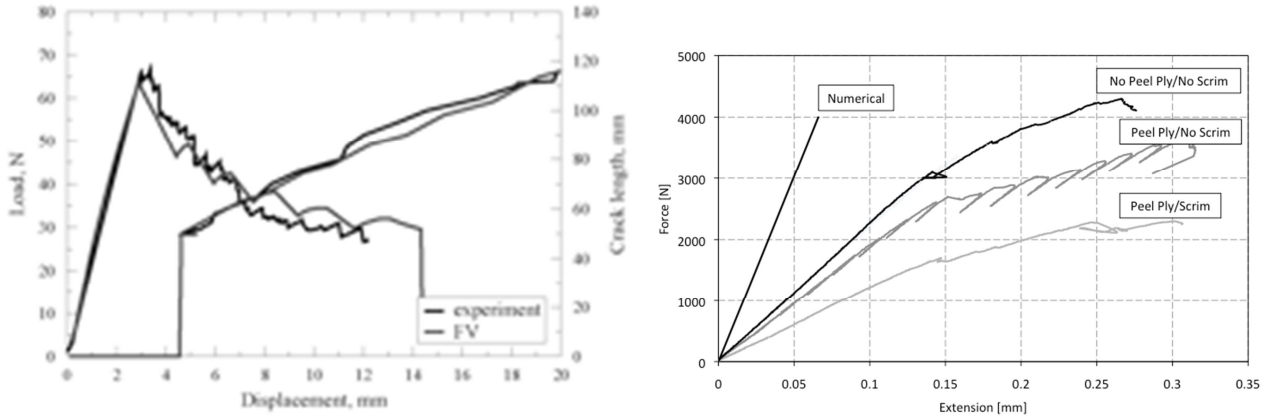


Figure 3: DCB experimental test and numerical load and crack length predictions (left). WALS experimental force-displacement curves for various combinations of peel ply and scrim cloth as well as numerical predictions (right).

WALS Tests: Experimental Results and Numerical Model: The numerical procedure used to simulate the classical DCB fracture tests was then applied to the WALS test configuration. It has to be noted that only part of the specimen between clip gauges was modelled. The reason for this was to circumvent any potential slippage in the grips that could not be controlled nor measured. Fracture

toughness was kept constant and equal to 200 J/m^2, while normal cohesive strength was set to 30 MPa. It can be seen from Figure 3 that the numerical prediction and initial experimental results (see force-displacement in Figure 3-right labelled 'Peel Ply/Scrim') were not in good agreement. This was investigated further by considering the effect of the peel ply surface treatment, which leaves behind a resin rich region on the surface of the substrate, and scrim cloth, which controls the bondline thickness, on the behaviour of the lap-shear specimens. WALS samples were manufactured using a peel ply but no scrim cloth and also without either peel ply or scrim cloth. Figure 3-right show that by removing these compliant materials, the compliance of the specimen was reduced and approaches the prediction of the numerical model. Current work is focused on further refinements to the numerical models and experimental tests in order achieve closer agreement.

Summary

While lap shear tests can provide a relatively quick and easy way to evaluate adhesive joints, the results can often be misleading. In the case of the present work, fracture mechanics based tests were carried out and numerically simulated in order to obtain parameters describing fracture process that can be used to accurately model the behaviour of lap shear joints. While accurate predictions of the WALS specimens were not achieved, the combined experimental-numerical approach provided valuable insight into the behaviour of lap-shear tests and highlighted the influence of the peel ply surface treatment and scrim cloth on the compliance of the joints. Further investigation is needed to refine these procedures that could conceivably be transferred to a structural component of any geometry used in the aerospace industry.

Acknowledgements

The authors would like to gratefully acknowledge the financial support of Enterprise Ireland. The materials supplied by Bombardier Aerospace (UK) and Henkel Loctite Ltd. are also gratefully acknowledged.

References

[1] Q. Benard, M. Fois and M. Grisel, *Composites: Part A*, 2005, 36, p. 1562-1568.

[2] Y. B. Park et al, *Composite Structures*, 2010, 92, p. 2173–2180.

[3] M.-G. Song et al, *Composite Structures*, 2010, 92, p. 2194–2202.

[4] B.R.K. Blackman and A.J. Kinloch, *In Fracture Mechanics Testing Methods for Polymers, Adhesives and Composites.* Elsevier Science, 2001.

[5] B.R.K. Blackman, A.J. Brunner, and P. Davies. *In Fracture Mechanics Testing Methods for Polymers, Adhesives and Composites,* 2001, p. 335-359. Elsevier Science, Amsterdam.

[6] B.R.K. Blackman, A.J. Kinloch, and M. Paraschi, *Engineering Fracture Mechanics*, 2005, 72, p. 877-897.

[7] OpenFOAM, www.wikki.co.uk, www.openfoam. co.uk, 2010.

[8] Camacho, G.T., Ortiz, M. *International Journal of solids and structures*, 1996, 33(20-22), p. 2899-2938.

© (2012) Trans Tech Publications, Switzerland
doi:10.4028/www.scientific.net/KEM.488-489.553

Numerical investigation into dynamic fracture of PCBN

D. Carolan[1,a], A. Ivankovic[1], N.Murphy[1]

[1]University College Dublin, Dublin, Ireland
[a] declan.carolan@ucd.ie

Keywords: PCBN, fracture, finite volume, high rate

Abstract. Polycrystalline Cubic Boron Nitride (PCBN) is a super-hard material, which is used in some of the most demanding material removal operations today. PCBN cutting tools are employed in turning of hardened steels as well as machining of other abrasive and aerospace grade alloys. In these applications the tools are subjected to high operating temperatures, abrasive and impact loading. Impact loading can lead to the sudden fracture and hence failure of the tool. Much of the recent developments in this industry have been focused on improving the fracture toughness of the PCBN compact. In this work a hypothesis based on induced thermal stresses at the crack tip has been put forward to explain the observed rate sensitivity of PCBN. The results show that the fracture toughness of PCBN is closely linked to the CBN grain size and that the rate sensitivity can be explained in part by induced thermal stresses at the crack tip at high rates of loading.

Introduction

The main application area for PCBN tooling is in the machining of hard steels (>45 HRC), aerospace alloys and both grey and hard cast irons [1]. PCBN is preferred over polycrystalline diamond (PCD) for the machining of ferrous materials as it is chemically stable in the presence of iron. PCBN, as used for cutting tools, is a sintered mass of CBN particles of the order of 1-10 microns with a variety of ceramic and metal phases. The advantage a polycrystalline material offers over a single crystal material is the greater toughness due to the random orientation of the crystalline cleavage planes in the sintered mass. However failure due to fracture and chipping is still a major problem in the industry today. In order to improve the fracture toughness of these materials it is firstly necessary to fully characterize the fracture properties and understand the fracture behaviour of the material under a wide range of operating conditions. In this work, the effects of loading rate and thermal shocking are considered.

In this study, a hypothesis to explain the observed rate sensitivity of the fracture toughness of PCBN has been put forward. Previous work by the current authors has shown that the measured fracture data for two grades of PCBN over a range of loading rates fit a well known thermal decohesion model [2, 3]. This work builds on that observation and focuses on thermally induced stresses at the crack tip at high rates of loading that could contribute to the failure of the observed decrease in fracture toughness.

Materials and Methods

A finite-volume method was used for the numerical simulation of the three-point bend experiment described in [4]. A fully implicit time-differencing scheme was employed in the analysis, guaranteeing unconditional stability. The models were implemented in *OpenFOAM*, a C++ library for solution of continuum mechanics problems [5]. Fig. 1 shows a typical mesh used for simulation of the three-point bend test. Due to the symmetry about the notch tip only one half of the specimen was modeled. Linear elastic material model was specified using mechanical properties measured in

[4]. Plane strain conditions were assumed to be dominant throughout the specimen thickness. Hence, only a 2-D analysis is performed. Loading was applied to the loading boundary using mixed boundary condition. The support was modeled as rigid using mixed boundary condition. Crack propagation was prescribed beforehand along a predefined cohesive patch using an appropriate cohesive zone model. The effect of both linear and Dugdale type cohesive zone modes was investigated.

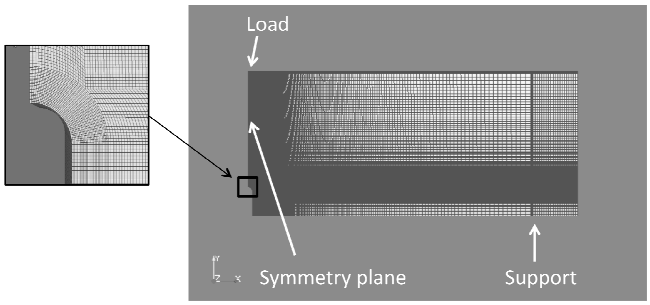
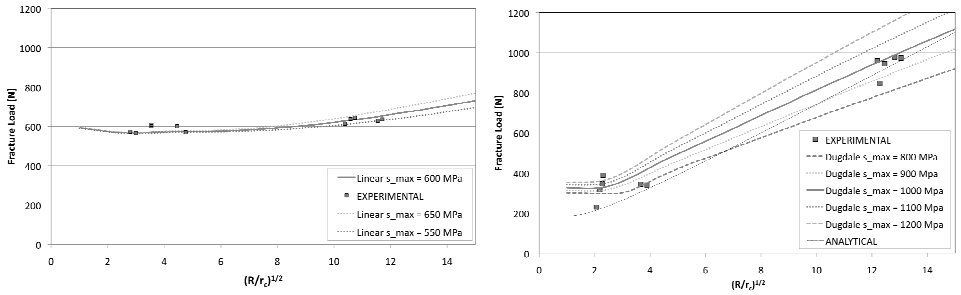


Fig. 1: Three point bend mesh employed in OpenFOAM

Results and Discussion

Fig. 2 presents the numerically predicted fracture load for the two grades of PCBN investigated in the current work at room temperature and quasi-static loading conditions versus normalised notch root radius. Normalised notch radius is simply the tip radius of the notched sample divided by the CBN grain size [6]. Both blunt and sharp-notched material was investigated. Table 1 lists the CZM parameters, which provide the best estimate of fracture load for the materials in question. The numerically predicted increase in fracture load with increase in notch root radius agrees well with an analytical model employed by the current authors to predict the fracture behaviour of PCBN [6].



(a) (b)

Fig. 2: CZM parameter fit for (a) large grained PCBN A and (b) small grained PCBN B

Table 1: CZM parameters used in the present study

	PCBN A	PCBN B
Model type	Linear	Dugdale/Linear
σ_{max} ***[MPa]***	600	1000
G_{Ic} ***[J/m²]***	70	11

It has been shown previously [2, 4] that the experimentally determined fracture loads of PCBN B does not change markedly at moderately high rates of loading whereas the fracture load decreases by approximately 40% for PCBN A at a loading rate of only 1 m/s. It is proposed that this can be explained by additional induced thermal stresses due to adiabatic conditions ahead of the crack tip due to the reduced timescale of loading, ~10-20 μs for loading rates of 1 m/s. In addition, the timescale for damage prior to crack initiation is also greatly reduced and is of the order of 1- 2 μs. Carslaw and Jaeger [3, 7] give a solution for predicting the maximum temperature rise at the crack tip. The maximum temperature predicted using the Carslaw and Jaeger infinite strip solution is less

than 2^o C, if one uses the bulk thermal properties of PCBN. Insertion of the binder thermal properties into the solution yields a maximum temperature rise of between 8^o and 10^o C. However, it should be pointed out that the thermal properties, particularly the thermal diffusivity, of the CBN grains and the surrounding binder are markedly different. Therefore it is reasonable to assume, that the temperature distribution in the system is more complicated and that large thermal gradients may be set up across the grain\binder interface, which may increase the level of thermal stresses.

To this end, a simple micromechanical model was employed in *OpenFOAM*. The model discretises the materials close to the notch into its constituent binder and CBN phases. The mesh, shown in Fig. 3 consists of an array of 10 by 5 CBN grains surrounded by the appropriate quantity of binder. To simulate thermal stresses due to cracking, the fracture energy is applied to the binder. The fracture energy is applied at a constant rate throughout the fracture process. The resultant temperature and hoop stress fields are shown in Fig. 4.

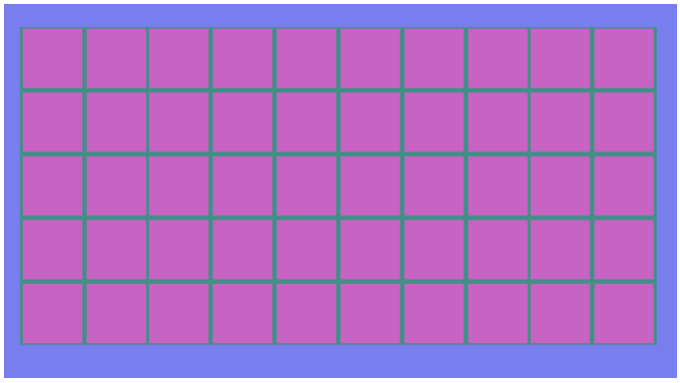


Fig. 3: Micromechanical model mesh with boundary conditions. Binder width artificially enhanced for clarity. The squares denote CBN grains while the black mesh represents the ceramic binder. The arrow indicates where the fracture energy is applied.

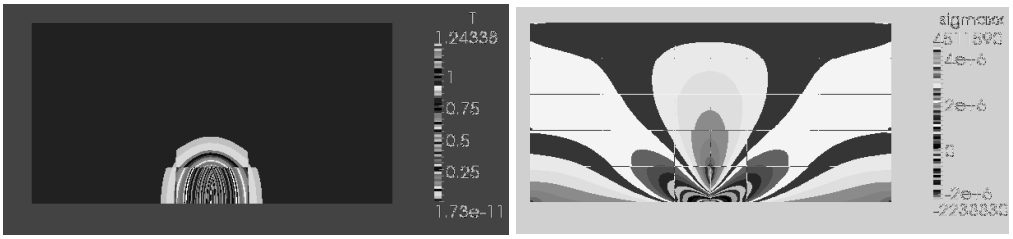


Fig. 4: Temperature and maximum hoop stress distribution in micromechanical model. Binder thickness is 1.25 microns in this case. G = 100 J/m^2 applied over 2 μs.

It can be seen that the difference in thermal properties is sufficient to induce a substantial thermal gradient across the closest binder CBN interface to where the fracture energy is applied. However for the test case shown, the maximum hoop stress was only 4.5 MPa. This is not sufficient to explain the experimentally observed drop in fracture toughness. Increasing the binder width has been observed to increase the peak temperature in the binder and hence the peak opening stresses.

Conclusions

Thermal stress assisted cracking has been qualitatively shown to be a plausible mechanism to explain the reduced fracture toughness at moderately high rates of loading of PCBN observed experimentally. The damage time prior to the failure is of key importance in determining the overall magnitude of the thermally induced stresses. It is also proposed that the binder thickness between the grains, modeled as uniform in this case could also play a role in influencing the final peak stress. Future work will concentrate on evaluating the effect of these parameters.

Acknowledgements

The authors gratefully acknowledge the support of *Enterprise Ireland, IRCSET* and *Element 6 Ltd., Shannon, Ireland.*

References

[1] Fleming, M.A., Bossom, P.K., 2000. PCBN – performance goals for the 21st century, Industrial Diamond Review.
[2] Carolan, D., Petrovic, M., Ivankovic, A., Murphy, N., 2011. Key Engineering Materials 452-453, 457-460.
[3] Carslaw, H.S., Jaeger, J.G., 1959. Conduction of heat in solids (2nd Ed.) London: Oxford University Press.
[4] Carolan, D., Ivankovic, A., Murphy, N., 2010. Key Engineering Materials 417, 669-672.
[5] OpenFOAM, www.wikki.co.uk, www.openfoam.co.uk, 2011.
[6] Carolan, D., Alveen, P., Ivankovic, A., Murpy, N., 2011 Engineering Fracture Mechanics, Submitted January 2011.
[7] Williams, J.G., Hodgkinson, J.M.m 1981. Crack-Blunting Mechanisms in Impact Tests on Polymers, Proceeding of the Royal Society (A), 375, 231-247.

© (2012) Trans Tech Publications, Switzerland
doi:10.4028/www.scientific.net/KEM.488-489.557

A methodological approach to the tolerance problems during the assembly process of deformable bodies

F. Caputo[1a], G. Lamanna[1b], F. M. Pannullo[1c], G. De Angelis[2d]

[1]Dept. of Aerospace and Mechanical Engineering, Second University of Naples, via Roma 29, Aversa (CE), Italy

[2]Fiat Group Automobiles S.p.A. via ex-aeroporto sn – 80038 Pomigliano d'Arco (NA), Italy

[a]francesco.caputo@unina2.it, [b]giuseppe.lamanna@unina2.it, [c]francesco.pannullo@gmail.com, [d]gustavo.deangelis@fiat.com

Keywords: assembly process, deformable bodies, tolerances analysis.

Abstract. The variations in shape compared to the initial project affect the performance and the appearance of any mechanical assembly. There are many commercial software that allow to conduct an analysis of tolerances but most of these are based on the assumption that the elements analyzed are rigid. This assumption is not found in many industrial processes. This is the typical case of the automotive industry, which widely uses assemblies of sheet metal elements, which are flexible. The major concern is how much variation (the output) of the assembly will be, as "staked-up" from possible sources of variation (the input). The sources of variation in the assembly process include parts variation, tooling variation, and their interactions. For clarity, only part variation is considered as the input in this paper. The present work aims to perform analyses of tolerances in presence of flexible elements; the analyses involve the finite element method.

Introduction

The variations in shape compared to the early design affect the performance and the appearance of any mechanical assembly. There are commercial software that allow to conduct an analysis of tolerances and many works in the scientific literature deal with this problem. Most of these, however, are based on the assumption that the analyzed elements are rigid. This assumption does not match with some industrial applications where machine parts undergo plastic deformation during the assembly process [1]. This is the typical case of the automotive industry, where the assembly of sheet metal elements, which are flexible, is widely diffused.

There are many deformable elements involved in an assembly process and as a consequence there are many causes of deformation during it; the strains coming from such deformation phenomena have to be added to those due to tolerance problems. The sequence and method of assembly heavily influence the final issue of a manufacturing process as theorized for the first time by Hu and Liu [2], which introduced the concept of mechanistic variation simulation. The present work aims to perform analyses of tolerances in presence of flexible elements. The analysesinvolve the finite element method.

A sheet metal assembly process consists of the following steps:

1. loading sheet metal parts to work-holding fixtures;
2. clamping parts to nominal position;
3. joining/welding the sheet metal parts;
4. releasing the clamp and/or fixtures.

Step 1: figure 1 [3] shows the part variation V when the parts are loaded onto the workholding fixture. For simplicity, only the variation of the part 1 at the tip of flange is show. If more than one sources of variation are considered, part variation will be expressed in a form of a vector $\{V\}$.

Step 2: clamps are applied to force the unwelded structures (parts) to their nominal positions. Finite element modeling can be used to calculate the forces applied by the clamp. Using an equation to represent this model, it can be written as:

$$\{F_u\} = [K_u]\{V_u\} \quad (1)$$

where $\{F_u\}$ is the force vector, $\{K_u\}$ is the stiffness matrix of the structures, computed by the numerical code, such as MSC/NASTRAN® [4], and $\{V_u\}$ is the random displacement (deviation) vector resulting from the variations at each node (grid). The components of the vector $\{F_u\}$ represent the forces provided by the clamps. Items with u represent quantities of unwelded structures.

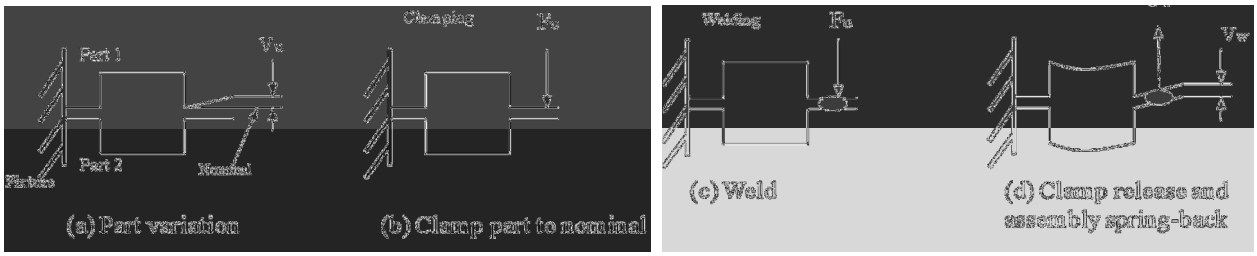


Fig. 1 – Sheet metal assembly process.

Step 3: the parts are joined by adding welds to form the assembly, thus the stiffness of the welded structure increases from $[K_u]$ to $[K_w]$. The welded stiffness matrix $[K_w]$ is also computed by the code. Item with subscript w represents quantities of the welded structures. The local deformation around the welded nugget caused by welding heat and pressure are ignored. A weld is considered as a binding agent to join the two points in space (in other words, a weld is indistinguishable from a rivet).

Step 4: the clamps are released from welded structures (assembly). The assembly will spring-back from its nominal position after the forces from the clamps are released. MSC/NASTRAN® can be used one more times to calculate the spring-back of the assembly:

$$[\mathrm{K_w}]\{\mathrm{U_w}\} = \{\mathrm{F_w}\} \quad \text{or} \quad \{\mathrm{U_w}\} = [\mathrm{K_w}]^{-1}\{\mathrm{F_w}\} \tag{2}$$

where $\{U\}$ is the spring-back of the welded structure at each node and $\{F_w\}$ is the force vector. This vector is identical to $\{F_u\}$ which has already been calculated in step 2.

$$\{\mathrm{F_u}\} = \{\mathrm{F_w}\} \tag{3}$$

The key to the Method of Influence Coefficients is to establish a linear relationship between the deviation $\{V_u\}$ and the spring-back deviation $\{U_w\}$. Substituting Eqs. (1) and (2) in Eq. (3), we have:

$$[\mathrm{K_w}]\{\mathrm{U_w}\} = [\mathrm{K_u}]\{\mathrm{V_u}\} \tag{4}$$

$$\{\mathrm{U_w}\} = [\mathrm{K_w}]^{-1}[\mathrm{K_u}]\{\mathrm{V_u}\} = [\mathrm{S_{w,u}}]\{\mathrm{V_u}\} \tag{5}$$

where $[S_{w,u}]$ is the sensitivity matrix [5]. Matrix $[S_{w,u}]$ represents how sensitive the assembly $\{U_w\}$ is to the part deviations $\{V_u\}$. For convenience, we drop the subscripts in Eq. (5):

$$\{\mathrm{U}\} = [\mathrm{S}]\{\mathrm{V}\}$$

The key to the method of influence coefficients is to establish a linear relationship between the deviation of the components$\{V\}$ and the spring-back deviation of the assembly $\{U\}$ [3].

Some application examples will be shown and results will be compared with those obtained by experimental data.

Problem definition

The validation work is applied on an automotive component that is shown in figure 2. The validation analysis consists in the experimental analysis of the processing products, the application of the method of influence coefficients and the comparison of experimental data with numeric ones.

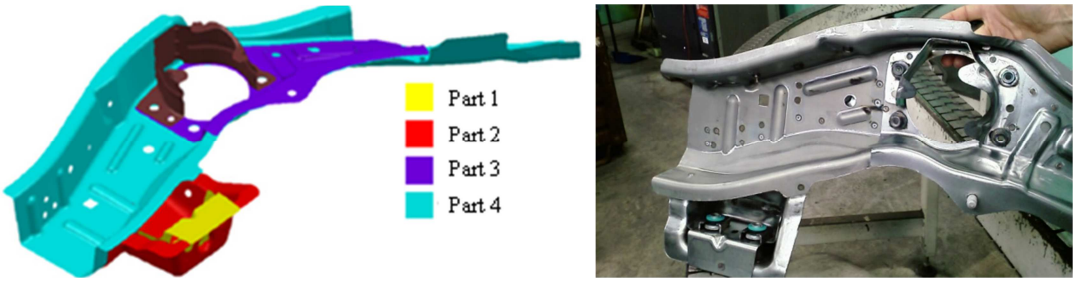


Fig. 2 – Automotive component analyzed.

The model we are going to study consists in two stages of assembly. We will study first the components of the first assembly station and then those of the second one, and will compare the distributions of variations of the control points with the experimental data. The work, therefore, begins with the collection of all necessary information, or inputs, which are used for analysis (CAD model). Then it will go on with the FE analysis and experimental measurements (input statistics) used for creating the model by the method of influence coefficients, analyze a significant number of possible configurations (solution) and summarize these results in the output statistics.

The thickness of each component is read and the material of which they are made is steel. The constraints are applied to the reset settings used for measuring experimental observations. They are applied across the whole surface to better simulate the real constraints. It has been considered, for simplicity, only the spotwelds as sources of variability. These points will be used for local adjustments of model mesh and for the definition of local reference systems. They will also be the points of the input variable in the model analysis by the method of influence coefficients. The process contemplates the mesh creation in order to start to prepare the model for analysis. Nodes are positioned at the points of welding and in the control ones in order to know the outcome of the analysis, the displacement, at that point. Local systems of reference are created, at each point of interest, in order to have the Z axis normal to the surface of storage node. Finally, the structure is constrained according to reset measure system. The analysis described above is performed for all components, individually and assembled. In the analysis of the components assembled, the individual components are joined by welds with c-weld elements. Once the model switches to writing the input file for analysis with MSC/NASTRAN®, the load cases are applied with the application of the unit force for each node of interest. The analysis results are then processed, stored and then imported into MatLab® [6] to create the analysis model.

Experimental measurements

Mean and variance of the distribution of variation sources are the inputs to be provided in MatLab®. These data refer to experimental testing. Since we assume that the variability is along the direction perpendicular to the surface, the experimental data must be found along this direction. The measurement process involves the monitoring of the pieces to be analyzed from the outset. In fact, the components analyzed are followed throughout the production process because you have to know the pieces, already been analyzed individually, which made the final assembly. In this case, there are two surveys to be conducted. The first measurement is after the pressing phase, and the second one is after the assembly stage. The measurements are performed for all points of interest and are analyzed by calculating the deviation from the nominal coordinates. From the series of surveys carried out we can calculate average values and standard deviation of the distributions of the single points analyzed.

The calculation model by the method of influence coefficients has been implemented in MatLab®. The creation process is performed by following five steps. The first step consists in importing the results of FE simulations. These results are then stored to be used to create the model. The second step involves the creation of the matrix of coefficients of influence. The matrices derived for individual components are then reversed. In the third step, the results of the experimental findings are used and then the generation of random numbers to simulate the variability is performed. The fourth step includes a series of simulations to generate a significant number of possible cases of settlement variability. The final step collects the numerical data generated and organizes them into histograms. which provide mean and standard deviation. The data of interest are those of the control points; these are compared with experimental measurements on the same control points.

The results are shown in the following charts (fig. 3). These distributions are obtained for all points of output in the second assembly station. The data are summarized in graphs reporting only mean and standard deviation. Graphs of mean and standard deviation by comparing the numerical results with experimental ones are reported.

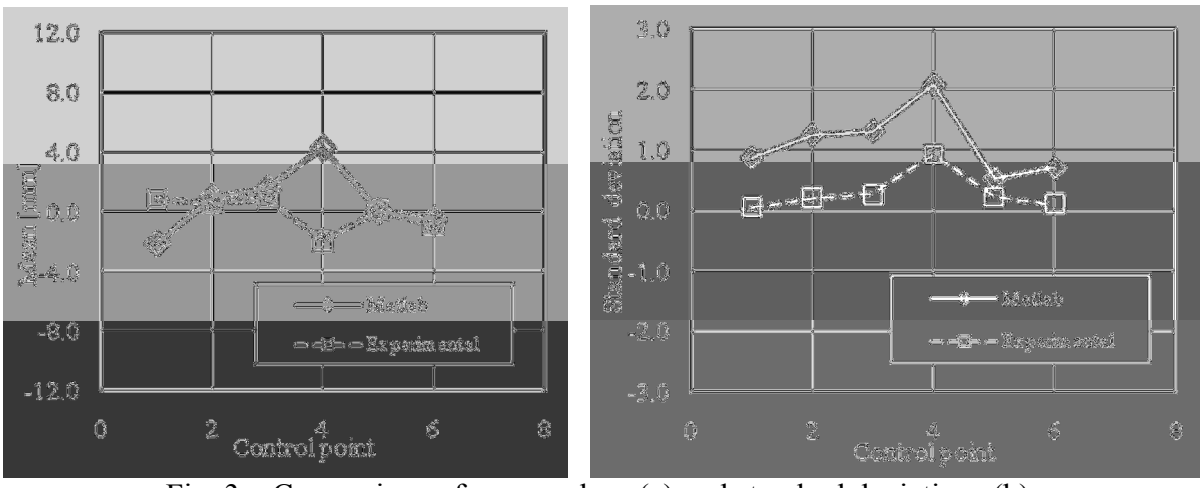


Fig. 3 – Comparison of mean values (a) and standard deviations (b).

The comparison shows an analogy between the trend of numerical and experimental data. Only a few control points are different because of the unreliability of their experimental measures. If we focus on the analysis of standard deviations it can be notice that from the numerical simulation results a higher variability; this determine a state of conservative analysis. The quality of a mechanical production process is generally defined as the fulfillment of standards for the product, and can be monitored through the tolerances assigned to the functional requirements of the finished product. The product is made by assembling together different parts, and each of them is subjected to their own tolerances, required for its implementation and monitoring. This gave rise to the need of rationalize the entire process that leads to the allocation, the implementation and the control of tolerances.

References

[1] Xie, K., Wells L., Camelio J. A. and Youn, B. D.: J Manuf Sci Eng Vol. 129 (2007), p. 934.

[2] S.C. Liu and S.J. Hu: Int J Mach Tool Manu Vol. 35 (1995), p. 1545.

[3] S.C. Liu and S.J. Hu: J Manuf Sci E-T Asme Vol. 119 (1997), p. 368.

[4] MSC/NASTRAN, User's Manual, The MacNeal-Schwendler Corporation.

[5] K.W. Chase and A. R. Parkinson: Res Eng Des Vol. 3 (1991), p. 23.

[6] MATLAB, User's Manual, Universityof Waterloo MathWorks.

© (2012) Trans Tech Publications, Switzerland
doi:10.4028/www.scientific.net/KEM.488-489.561

Energy absorption capabilities of a square tube system

F. Caputo[a], G. Lamanna[b], A. Soprano[c]

Dept. of Aerospace and Mechanical Engineering, Second University of Naples,
via Roma 29, Aversa (CE), Italy

[a]francesco.caputo@unina2.it, [b]giuseppe.lamanna@unina2.it, [c]alessandro.soprano@unina2.it

Keywords: crash box, aluminium foam, explicit FEM.

Abstract. In the present paper the authors refer about a series of experimental tests, where an aluminium alloy square tube, filled with an aluminium foam, was crushed by a longitudinal load at a speed of 10 m/s. The test apparatus consisted of a sled installed on a very stiff frame moving on appropriate guides, as the specimen was set on a home-made fixture. Two arrangements of square tubes were considered as specimens: a "standard" one and an "optimized" one. Both crushing behaviours and energy absorption capabilities were analyzed experimentally and numerically simulated by means of the explicit FE code LS-DYNA®; the complete numerical model consisted of the striker, the assemblage of square tubes and the base. A high-speed video recording system was used to capture the images from the physical test. The results from the numerical analyses were compared to those obtained from the experiments: those results showed that the force–deflection response had been overestimated by the numerical model. The authors attempted to justify this inconsistency by considering the influence of the strain rate parameters of the considered Cowper-Symonds analytical model on the results. It was shown that the "optimized" energy absorber exhibited a more desirable force–deflection response than the standard one due to some easy design changes, which involved the insertion of aluminium foam dampers.

Introduction

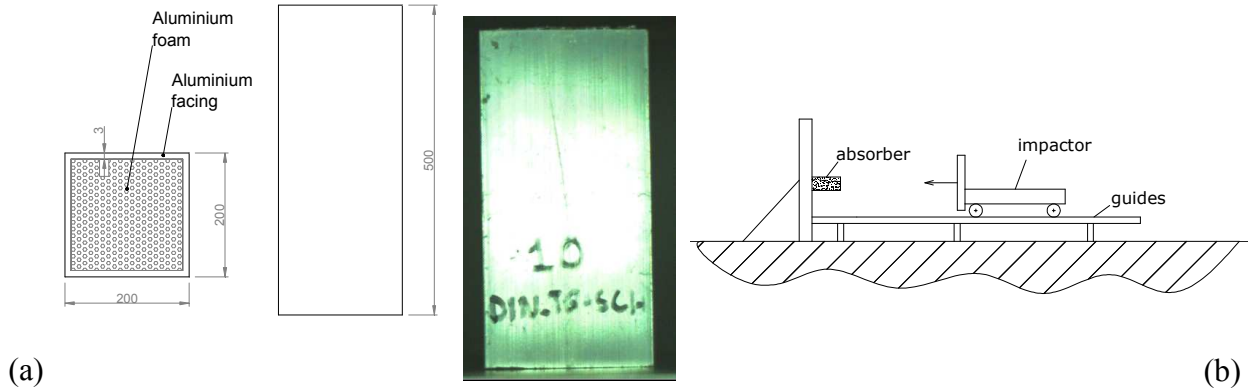
The present paper deals with the numerical simulation, by using the explicit finite element method, of the crash behaviour and energy absorption characteristics of thick-walled square tubular components made of an aluminium alloy (6000 series) filled with an aluminium foam, subjected to axial compressive load. The obtained numerical results have been compared with the experimental data from full-scale tests in terms of final deformation shape, energy absorption capability and load/deflection path. The energy absorption capability of an impact absorber element is largely affected by its structural design and material properties: prismatic structures, consisting of aluminium foam core inside an aluminium extruded tubular, are good candidates [1, 2]. They typically absorb energy by a localized crushing mechanism of the core and by bending and stretching of the walls [3]. Aluminium foams, with different mass percentage, are generally used for the core and aluminium alloys are used for the face plates.

In this work the tubular structure has been modelled by using finite element method and it has been analysed by using LS-Dyna® code; the aim is to identify a robust constitutive model [4] for the materials involved in the phenomenon and to define a more appropriate procedure for its correct setting through static, quasi-static and dynamic tests.

Test case description

The geometry and the materials of the absorber are shown in figure 1a, while the materials properties are those reported in Table I and figure 2. The tube material is an aluminium alloy of 6000 series, while the foam filler is an aluminium foam with specific mass percentage. The experimental test, performed at Polytechnic of Milan (Dept. of Aerospace Engineering), consisted in an axial compression of the structure at a speed of 10 m/s, by using the apparatus scheme showed in figure 1b. It consists of a flat rigid impactor installed on a sled with a total mass of 1300 kg; by means of a pneumatic system the selected speed (10.0 m/s) is imposed onto the sled. The very low

value of dynamic friction guarantees a small resistance to the sled. The absorber is installed perpendicular to the flat rigid barrier by fitting it on a convenient support. The latter is not to crash with the sled during the impact to leave the absorber free to express its great capacity to absorb energy. The tubular doesn't show any welded line because it has been manufactured by an extrusion process.



(a) (b)

Fig. 1 – Absorber (measures in mm) (a). Testing apparatus scheme (b).

Table 1 – Materials mechanical properties.

	Al 6000 series	Al-foam
Density [kg/m3]	2700	600
Elastic modulus [GPa]	66.6	7.2 (unloading)
Poisson ratio [-]	0.33	0.01
Yield stress [MPa]	251	3.15
Tangent modulus [MPa]	700	-

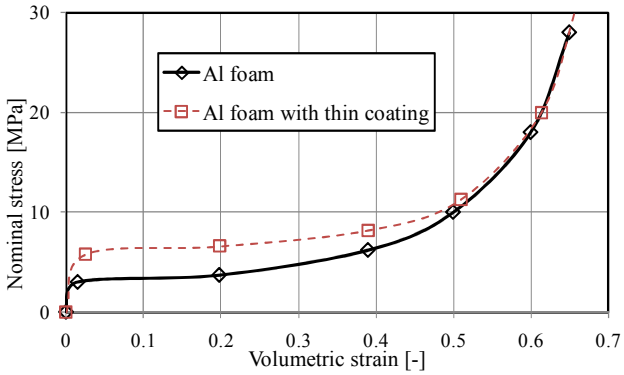


Fig. 2 – Uniaxial stress-strain curve.

Numerical models

In all the numerical models built in this work the absorber has been modelled with 176000 first order elements and 186000 nodes. The external walls have been modeled with 16000 shell elements and 16192 nodes, while the foam includes 160000 solid elements and 169781 nodes. Second order elements were been initially used, with to a number of nodes up to 717545. The preliminary results did not differ significantly from those obtained with first order elements, while the computation times had increased significantly. Therefore, the following numerical models have been built using only first order elements.

Many numerical models with different characterizations have been carried out in this study; for the characterization of the material of the external tube an elastic-plastic material model has been adopted, with an arbitrary stress vs. strain curve and an arbitrary strain rate dependency (model No. 24 of material library of LS-Dyna). For the characterization of the foam an elastic perfectly-plastic material has been chosen. This material type is dedicated to model crushable foam with optional damping; the unloading phase is elastic (model No. 63 of material library of LS-Dyna).

The four-noded shell elements formulation involves from one to five integration points located uniformly through the element thickness. The eight-noded solid element formulation involves just one integration point, in order to take advantages of substantial saving in computer time.

Different failure criteria have been adopted for the foam and for the wall material also based on the timestep calculation: erosion occurs when a certain minimum timestep is reached during numerical analysis [5]. Often, when the timestep decreases heavily during the simulation, the elements that govern this phenomenon are affected by large distortions and they lose their physical capacity to sustain the operative loading conditions. For the aluminium characterization an

enhanced material model combined with a specific failure criteria has been also adopted (model No. 123 of material library of LS-Dyna). Failure is based on effective plastic strain, plastic thinning, principal in-plain strain components; the tension cutoff in the foam material model represents another parameter to control the structure's integrity.

Up to four different contact types have been defined, two of these handling the interface between shell and solid elements. During the first phase a "tied contact" manages the interface between the foam and the walls; when the separation occurs, a surface to surface contact takes place. Another contact type manages the contact of the external walls with itself; this situation could occur in presence of large deformations that assume the characteristic wave shaped configuration (figure 3).

The tube has been considered to be fully clamped on one side, in particular the last two rows of nodes have been constrained in all their six degrees of freedom. The other side is completely free to move and it is crushed by a numerical rigid wall defined according to the experimental evidence. The rigid wall has a mass of 1300 kg and an initial velocity of 10.0 m/s; it has been positioned as near as possible to the impact side of the absorber in order to minimize the computational time which is necessary to move the rigid wall from its initial position to the crash front.

Results and discussion

Different types of numerical models have been worked out before reaching a good fitting between the numerical and experimental results. The starting model refers to a simple square-section tube filled with an aluminium foam where the interface between the two materials is regulated by a contact algorithm. The following numerical model includes also a system of bonding between the foam and the tube with a tensile strength of 4-5 MPa and a shear strength of 2.5-3 MPa (tied contact). The facing has been meshed not only with four-noded shell elements but also with eight-noded solid elements. The obtained results show an appreciable difference only in the case of the static analyses which have been performed preliminarily, therefore that modeling procedure hasn't been used for dynamic analyses.

The aluminium foam characterization represents another important aspect for the determination of the energy absorption capacity of the absorber. During the manufacturing process a thin coating surface was created around the foam. It changes the mechanical properties of the foam in particular it shifts to the top the characteristic stress-strain curve of such material (figure 2).

In this work the authors characterize this thin coating in two different ways: in the first one a further coating of shell elements has been modeled, in the second one a modified stress-strain curve has been adopted in order to take into account the effect of the coating surface on the standard foam's mechanical properties; both models have been opportunely calibrated by means of experimental testing.

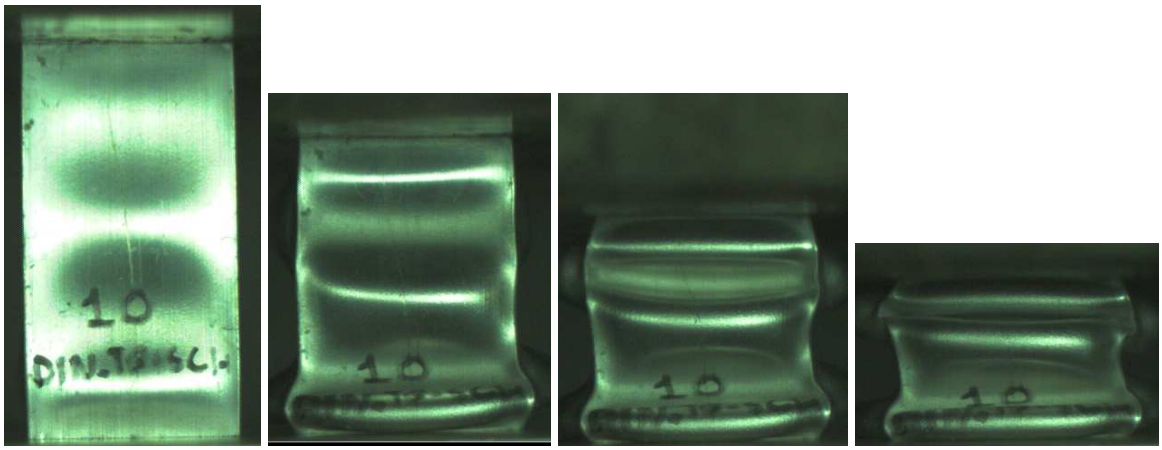


Fig. 3 – Deformation during the impact phenomenon.

Figure 4 shows that the force–deflection response has been overestimated by the numerical model (Tub_02i); this inconsistency is justified on the basis of the validity of strain rate parameters used in the Cowper–Symonds analytical relationship and of some of numerical characterizations

described above. The same figure and the table 2 show that the "optimized energy absorber" (Tub_14m) exhibited a more desirable force–deflection response than the standard one due to the design modifications.

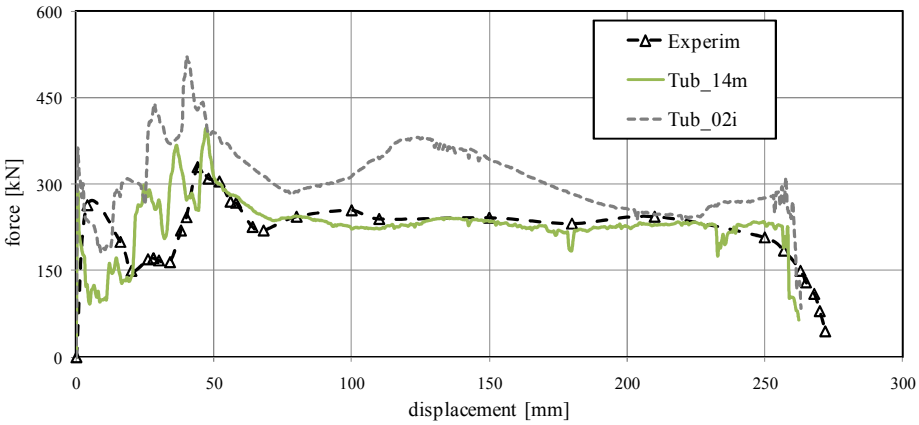


Fig. 4 – Reaction forces.

Table 2 – Main data of crash phenomenon.

	Experim.	Num Tub_02i	Δ%	Num Tub_14m	Δ%
Mean value [kN]	222.77	309.02	38.72%	229.98	3.24%
Max value [kN]	330.10	521.79	58.07%	355.68	7.75%
1st max v [kN]	263.98	359.13	36.04%	282.01	6.83%
Plateau v [kN]	237.86	300.14	26.19%	225.67	-5.12%
En absorbed [kJ]	57.92	77.25	33.38%	58.65	1.25%

Conclusion

Aluminium foams show their advantages primarily in combination with existing constructions. The combination of attributes like an high ratio between stiffness and weight and high energy absorption capability qualifies Al-foam for lightweight components with specific requirements. This work puts in evidence the problems related to the mechanical characterization of an aluminium impact absorber, it has been observed the influence of the different numerical solutions on the energy absorption capability.

The manufacturing process may affect the mechanical properties of aluminium foams with the same percentage of voids. In particular, the thin layer that surrounds the foam gives it higher rigidity. This study showed such differences by means of numerical and experimental tests identifying a robust constitutive model for the materials involved during the crash phenomenon and detecting an appropriate procedure for its correct setting.

References

[1] W. Johnson, S.R. Reid: Appl Mech Rev Vol. 31 (1978), p. 277 and Vol. 39 (1986), p. 315.

[2] F. Caputo, A. Soprano, G. Lamanna, G. Monacelli, V. Petrella: Trans Eng Sci Vol 1 (2005), p. 387.

[3] M. Seitzberger, F.G. Rammerstorfer, R. Gradinger, H.P. Degischer, M. Blaimschein and C. Walch: Int J Solids Struct Vol. 37 (2000), p. 4125.

[4] A.G. Hanssen, O.S. Hopperstad, M. Langseth, H. Ilstad: Int J Mech Sci Vol. 44 (2002), p. 359.

[5] F. Caputo, G. Lamanna, A. Soprano: Key Eng Mat Vol. 417 (2010), p. 685.

© (2012) Trans Tech Publications, Switzerland
doi:10.4028/www.scientific.net/KEM.488-489.565

Effects of Tolerances on the Structural Behavior of a Bolted Hybrid Joint

F. Caputo[a], G. Lamanna[b], A. Soprano[c]

Dept. of Aerospace and Mechanical Engineering, Second University of Naples, via Roma 29, Aversa (CE), Italy

[a]francesco.caputo@unina2.it, [b]giuseppe.lamanna@unina2.it, [c]alessandro.soprano@unina2.it

Keywords: Hybrid joint, CFRP, bolted joint, bolt-hole clearance.

Abstract. In this work, results from a study on bolted joints made of unidirectional, quasi isotropic Carbon Fiber Reinforced Polymer (CFRP) composites, subjected to tensile loads, are reported. CFRP composite materials are widely used in the mechanical industry, such as that of aerospace, where requirements of weight reduction and structural high performances are very compelling. Composite materials generally present a high resistance to fatigue and corrosion; however, the presence of joints produces the major problems and a poor design of joints leads to a drastic reduction of the reliability of structures made of these materials. A hybrid bolted joint involving a metal plate, made of aluminum alloy, and a CFRP composite plate has been considered; the plates are held together by a titanium bolt. Experimental results from literature are compared with those obtained through a numerical analysis developed with Abaqus code. Once the CFRP composite has been analyzed and the numerical model validated through numerical-experimental correlations, other possible configurations have been numerically analyzed in order to ensure the highest strength of the examined hybrid joint. Afterwards the effects of bolt-hole clearance on the stiffness and strength of the same joint have been investigated.

Introduction

Carbon fiber reinforced polymer (CFRP) composites are becoming widely used within the aerospace and automotive industries due to their very high specific strength and stiffness properties. These materials have a significant strength/weight ratio and find places into many technical applications. Generally, composite materials have a remarkable resistance to fatigue and corrosion, but the joint of such materials represents a critical point in the design process of the overall structure, as well as joint of metal components. There are different types of joints in the aerospace and automotive industry, among those bonding, riveting, brazing and bolting are widely diffused. The present work deals with bolted joints; in particular the connection of two components of different nature has been studied, the first is a CFRP composites material and the second is an aluminum alloy one; the two components are connected by a titanium bolt. A severe stress state characterizes the surrounding zone of bolted area and cracking phenomena can arise at the hole edge. However, this type of joint shows a remarkable reliability and can be applied with good results to several composites materials such as the mentioned CFRP or GFRE composites [1].

There are many studies, based on analytical and numerical methods, which try to predict and monitor the failure of a bolted joint [2] and the propagation path of damages around the bolted area. The development of a numerical simulation of a hybrid bolted joint includes the study of the non linear nature of such materials; in order to obtain a good correlation, the numerical results have been compared with the experimental ones in terms of strain values at different points of the jointed composite plates. Furthermore, the relative sliding between the two plates has been considered as described below.

Description of the numerical model

Carbon fiber reinforced polymer composites are quite susceptible to various typologies of damage. Common damage modes within CFRP composites include matrix cracking, delamination and fiber breakage [3]. For composite laminates, delamination is one of the major concerns since

this can significantly reduces the load carrying capacity of the laminate. Unlike metallic structures which are homogenous and have the ability to dissipate energy through yielding, composite structures are relatively brittle and exhibit weak interlaminar strength.

As a consequence, even low velocity impacts on CFRP composites can introduce significant delamination defects, which are not visible from the external surfaces of the component. The joints are another concern, since they can be cause of cracking. With reference to the bolted joints, one of the main causes of such cracking is the excessive closure force upon the bolts.

Two plates with different thickness and materials constitute the examined joint: the first plate is made of aluminum alloy (7000 class) while the second one is made of CFRP composite. Such plates measure 150 mm x 36 mm x 4/4.16 mm (metal/composite); both of them have a 6 mm diameter hole, located at 18 mm from the upper edge of the plate (see figure 1).

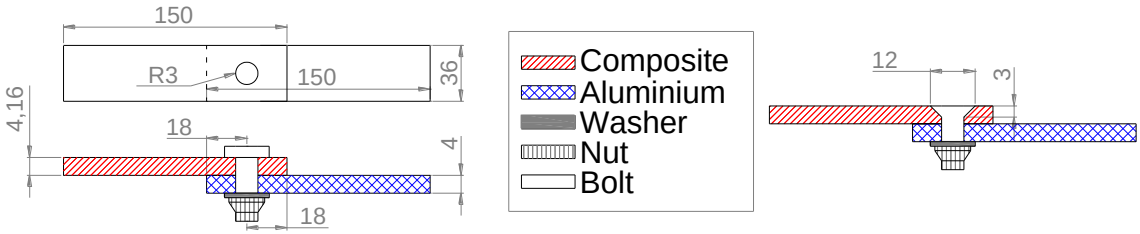


Fig. 1 – Specimens (measures in mm).

The titanium bolt is either countersunk or has a protruding head bolt (head diameter: 9.9 mm; head height: 3.5 mm). The clamping nut has a global height of 6.4 mm; it is partially conical and it pushes on a washer with an external diameter of 10.8 mm and a height of 2 mm. The washer lies between the metal sheet and the tapered nut (figure 1). The diameter of the bolt shank is 6 mm.

The CFRP composite is symmetric with respect to its mid-surface and contains equal numbers of ±45° plies; it has the following layup: [(±45,0,90)4]S32. The aluminium alloy of metal plate is the AA7475-T76 one, while the titanium alloy of bolt is the Ti6A114VSTA one; their mechanical properties are reported on Table 1.

Table 1 – Mechanical properties.

Ply	E_{11} [GPa]	E_{22} [GPa]	E_{33} [GPa]	E_{12} [GPa]	E_{13} [GPa]	E_{23} [GPa]	ν_{12}	ν_{13}	ν_{23}
properties	141	10	11	5.2	5.2	3.9	0.3	0.5	0.5

Aluminium	E [GPa]	ν	Titanium	E [GPa]	ν
AA7475-T76	69	0.28	Ti6A114VSTA	110	0.29

The matching between the hole and the bolt has been set up according to ISO f7/H10 regulation. The experimental test has been performed according the procedures described by Ireman [4].

A numerical model representative of a single lap joint was built. The whole model has about 40'500 elements and 48'000 nodes and has been entirely discretized with tridimensional elements, but for the interface elements between the contact surfaces, where C3D8 elements (Abaqus® element library) have been used.

The free end of the metal sheet has been fixed while a displacement has been imposed to the free end of the composite sheet in order to generate a traction load of 4 kN upon the specimen.

Modelling of interface elements on the contact surfaces by mean of “node to surface” algorithm (with “small sliding” option) has completed the numerical model: six different interfaces have been characterized in order to avoid undesired stress concentrations around the contact areas [5]. The friction coefficient is 0.15 at all contact surfaces. In consideration of the kind of adopted bolt, the tightening torque (T) of 1 Nm, applied to the bolt, changes into an axial load (L) of 2.63 kN with $A= T \cdot f(\mu, \alpha, \beta, P, dm)$, where μ = friction coefficient; α = helix slope; β = teeth angle; P = pitch; dm = notch diameter.

Results and discussion

Two different types of numerical results have been compared with experimental ones: the relative displacement between the two plates and the total strains at different locations of composite plate. In Figure 2 the locations where total strains of composite plate have been measured are showed.

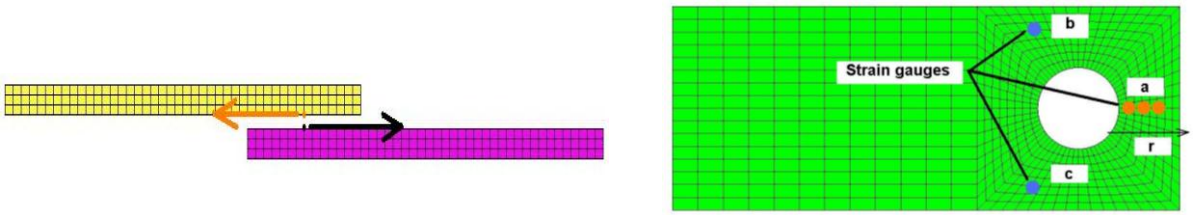


Fig. 2 – Relative displacement between two sheets and gauges positioning.

Figure 3a shows a good tuning between virtual and experimental relative displacements; the figure 3b and Table 2 confirm the final numerical-experimental correlation in terms of total strains. The obtained results demonstrate that the virtual model provides reliable results, in spite of the difficulties in characterizing the composite material and in calibrating the different contact parameters involved in the analysis.

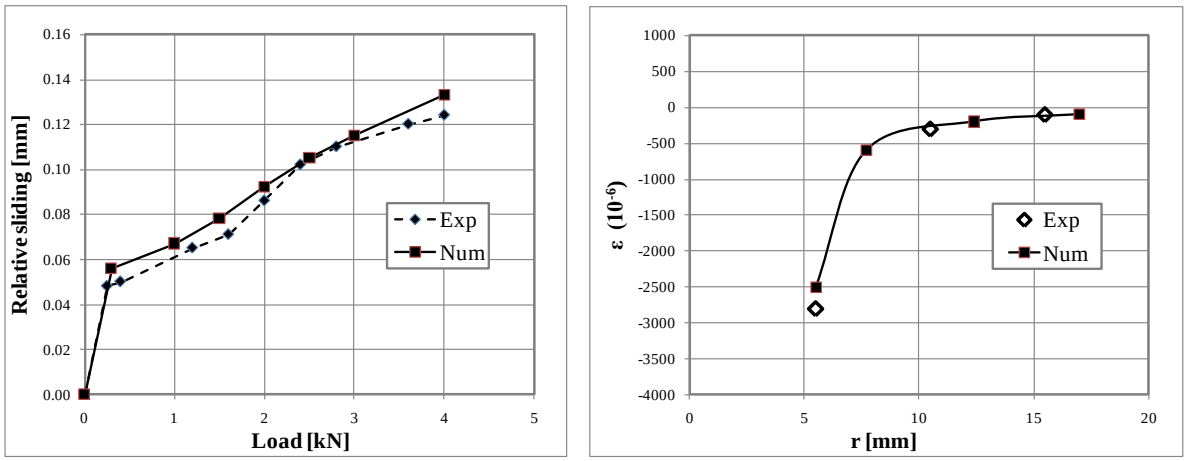


Fig. 3 – Relative displacement (a); strain at location “a”, load = 4 kN (b).

Table 2 – Strains at locations “b” and “c”, load = 4 kN

	Experimental	Numerical	Δ%
B location	1200	1230	+2.5%
C location	-500	-527	+5.2%

The validated model has been applied to the joint with countersunk bolt (figure 1b) and the effects of the bolt-hole clearance on the strength of the joint have been investigated. Comparing the stress of different configurations, the graphs illustrated in figure 4a indicates that the models with protruding head bolts are slightly stiffer than those with countersunk bolt (about 15%). This aspect comes from the regularity of bolt-hole contact in the countersunk bolt model.

The configuration studied was single-lap with single-bolt. Four different clearances have been considered, ranging from neat-fit to 180 μm. The models have been built in accordance to figure 1, with quasi-isotropic and zero-dominated lay-ups. Both protruding head and countersunk bolts have been used; a 4 kN total longitudinal traction load has been applied on the joint.

Within aerospace industry, 50-180 μm are typical clearance range, therefore this paper looks at clearances up to 3% of hole diameter, with a fixed 6 mm diameter bolt (Table 3).

Table 3 – Bolt-hole clearances.

d_{nom}	BOLT [μm] min - max	HOLE [μm] min - max	bolt-hole CLEARANCE [μm]
Protruding – 6 mm Countersunk – 6 mm	0 0	0 +60 0 +120 0 +180	0-180 (3% of 6mm diameter pin)

The results demonstrate that the single-lap joint modeled with protruding head bolt shows a certain dependency on clearance (figure 4b), with a drop of 14% at a clearance of 180 μm or 3% of hole diameter. Countersunk joints show no such dependency, as well as, strain values at 4 kN applied load value.

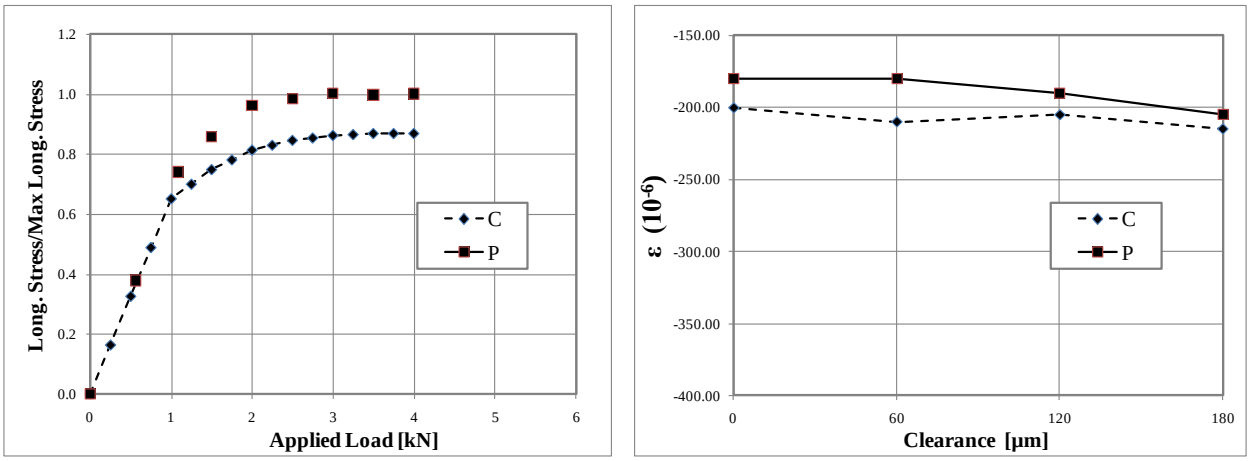


Fig. 4 – Relative stress for the different models (a). Strain at location "a" (x=12.4 mm, load = 4 kN) (b). P = protruding head bolt; C = countersunk head bolt.

Even though strains, as computed in this work, did not show much dependency on clearance for the two models, figure 4b shows a significant difference behaviour on clearance between the models with protruding and countersunk head bolt joint. It may be that, because of this increased loss of strength, the countersunk head bolt in the larger clearance joints loses its regularity of bolt-hole contact, resulting in larger strain in the larger clearance joints. This may not have any practical consequences for design of joints under in-service loads, but could be of interest in the design of joints to absorb energy (e.g. in crashworthy structures).

It has been found that three-dimensional finite element models of hybrid bolted joints, capable of being run in reasonable calculation time on a standard PC (ca 30 min. on intel 9400Q, ram 4GB), can produce results in close agreement with experimental ones. Three-dimensional effects such as secondary bending and through-thickness variations in stress and strain are well represented by such models. However, the process is far from routine and requires careful consideration of many issues.

References

[1] U.A. Khashaba, H.E.M. Sallam, A.E. Al-Shorbagy and M.A. Seif: Compos Struct Vol. 73 (2006), p. 310.

[2] P.P. Camanho and M. Lambert: Compos Sci Technol Vol. 66 (2006), p. 3004.

[3] J.H. Kweon, J.W. Jung, T.H. Kim, J.H. Choi, D.H. Kim: Compos Struct Vol. 75 (2006), p. 192.

[4] T. Ireman: Compos Struct Vol. 41 (1998), p. 195.

[5] T.J. Whitney, E.V. Iarve and R.A. Brockman: Int J Solid Struct Vol. 41 (2004), p. 1893.

© (2012) Trans Tech Publications, Switzerland
doi:10.4028/www.scientific.net/KEM.488-489.569

The Influence of Short Glass and Polypropylene Fibers on First Crack Formation and Toughness of Cement Based Composites after their Exposure to Fire Conditions

Z.G. Pandermarakis[1,a], A.B. Sotiropoulou[2,b] and N.D. Nikoloutsopoulos[3,c]

[1]Assistant Professor in Department of Civil and Structural Engineering Technology Teachers, School of Pedagogical and Technological Education, Athens-Greece

[2]Professor – Supervisor of Department of Civil and Structural Engineering Technology Teachers, School of Pedagogical and Technological Education, Athens-Greece

[3]Assistant Professor in Department of Civil and Structural Engineering Technology Teachers, School of Pedagogical and Technological Education, Athens-Greece,

[a]z.g.panderma@gmail.com, [b]a_b_sotiropoulou@yahoo.gr,

[c]nikolasnikoloutso@hotmail.com

Keywords: cement based composites, glass and polypropylene fibers, bending strength, first crack, complementary energy, structural integrity, fire exposure, high temperatures, time duration.

Abstract. The influence of glass and polypropylene short fiber addition on fracture response of cement based composites after their exposure to high temperatures up to 900^{o}C and for time intervals up to 2 hours was investigated during this study. These conditions simulate adequately closed those of a common real fire exposure. Measurements of their bending and compressive strength and also of ultrasonic wave propagation before and after their burning were carried out. Three distinct response zones are appeared that arise mainly by the incoming chemo-physical changes of constituents due to the attainment of remarked temperature levels. These changes involve the evaporation of physically bounded water in pores and paste in the region of 100^{o}C, the de-hydration of calcium hydroxide of cement paste in the region of 400^{o}C and the decomposition of calcium carbonate of limestone aggregates in the region of 900^{o}C. The fiber addition at common level volume percentage of about 0.3 %, improve only slightly their fracture features –as first crack formation, energy absorption, even their strength– up to 300 - 400^{o}C after of which this addition appears to have opposite effects. The essential changes seem to concern the improved cohesive features of cement based composites and the desired benefits arise mainly by ensuring better conditions for their durability and the restriction of their fragmentation and brittleness leading to a tougher future response.

Introduction

There are a lot of factors that can enter and alter the initial common mechanical response of typical cement based composites. Most of them are related to their manufacture process. The starting point of the cement based materials originates from hydration of the included active oxides. This procedure modifies radically the initial powdered – grained pozzolanic mixture that becomes gelly after the addition of adequate water amounts. The formed gel gradually will come to a more and more solid and stable expanded 3-dimensional network as the curing process through the above mention hydration proceeds. The resulting material will be appeared increasingly harder and tougher as the physico-chemical processes, especially of hydration, are evolved. The aqueous phases of mixture facilitate all processes and they give high rates of hydration, curing, hardening and so of the resulting strength. This more or less stable structure can easily be destabilised by chemical, thermal, mechanical and other physical and biological factors. Thus, the formed solid body that appears thermodynamically stability at ambient temperature, can easily be decomposed at a higher temperature to a system of other more stable to these conditions ingredients or/and initial

constituents [1]. As a physical consequence, the cohesiveness of a cement-based material is reduced and the appearing strengths became gradually minor in a reversed manner of the above mentioned [2].

In this study it is attempted to investigate if the observed, at high temperatures, chemical decomposition and subsequent degradation of the various chemical compounds in a mortar and also their physico-chemical and physico-mechanical bonds of the various phases and the incoming loss of their coherence may be restricted or even halted. In this way, the addition of uniformly distributed short fibres can improve mortars' achieved response, limiting their mechanical strength losses and also their durability [3]. Actually, the main role of the addition of fibres into a brittle body, which from its nature has the tendency to crack, is to restrict fragmentation, bridging the mouth of the appearing cracks (Fig.1).

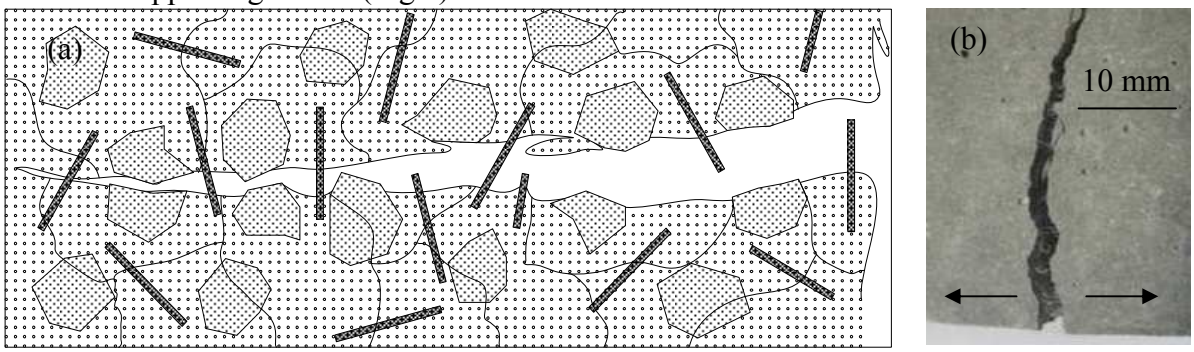


Fig.1a,b: The main role of fibres is to block crack development and help for the maintenance of body coherence that is deteriorated due to degradations, differentiated expansions and contractions and to the appearing cracking network (continuous lines in figure).

The conditions under which first crack is appeared and developed by the action of tensile stresses can give valuable information for the possibility to control it by adding fibres. As the temperature level and the duration of exposition are increased, the thermal decomposition and brittleness of mortar are facilitated and then the presence of fibres comes out the ultimate manner for their restriction [4].

The whole process of crack formation and fragmentation of a body requires energy consumption and the study of the fracture energy changes can be an additional magnitude for the estimation of the effectiveness of the various proposed methods for toughness improvements.

As the basic application of cement-based mortars is for repair, protection, layering and overlapping components of other building materials, in the case of an accidental fire, mortars are the first that come in direct contact with it, and then can be exposed to very high temperature levels of about 1000^{o}C or higher [5].

Experimental Procedure

The cement-based materials are consisted by sand and a bonding phase that comes by mixing cement and water. Here the proportion of sand with maximum grains of 4 mm to cement type I52.5 was established at 3/1 and the proportion of water to cement was fixed at 1/2. In this study the specimens were reinforced by 0.26 % PP and glass short fibres. Specimens were exposed to temperature levels from 100°C up to 900^{o}C and for time intervals from 10 up to 120min. They tested both by ultrasonic inspection and under bending and compression loadings in order to assess their remaining strength, flexibility, toughness and fracture response after their exposure to fire conditions. The prepared specimens had dimensions of 4cm x 4cm x 16cm and after their demoulding were immersed in tank water for 28 days at 20^{o}C.

Discussion of Results

In Fig. 2 bending stress-strain curves are given for various exposed temperature levels. It can be seen that as temperature is increased the mechanical response turns to lower strength and stiffness but in contrast to this, at the same time, the burned specimens appear higher ductility and toughness.

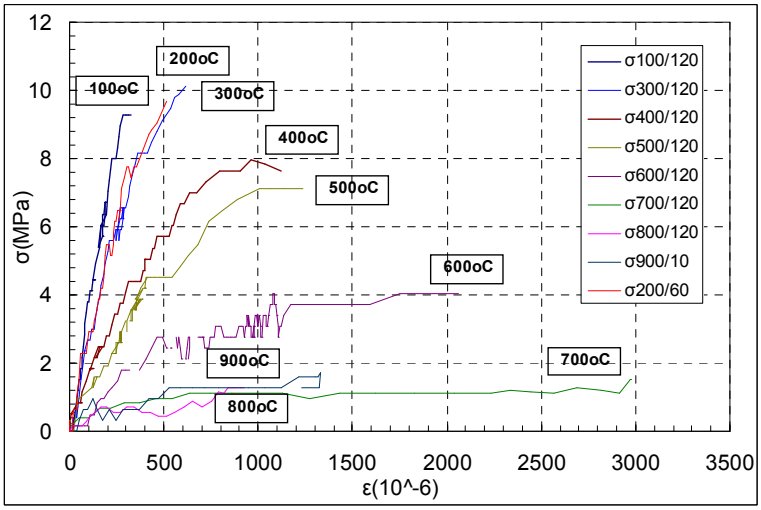


Fig. 2: Bending stress-strain curves of unreinforced specimens as comes by strain gauges for various exposure temperature levels. Similar curves came out also for reinforced specimens

A gradual degradation is appeared whereas at higher temperature levels the added fibres generally delay stiffness reduction (Fig. 2). Three distinct regions are appeared. The first is termed at 300°C, the second extends from 300°C up to 700°C, and the third above 700°C.

Several researchers have attempted to describe the demands of high performance cement-based composites, as V.C. Li and his collaborators [6] who focused on two basics magnitudes, that are closely connected with the first crack formation: the strength of first crack formation and the corresponding complementary energy (Fig. 3a,b). For a high performance material they must satisfy the following conditions:

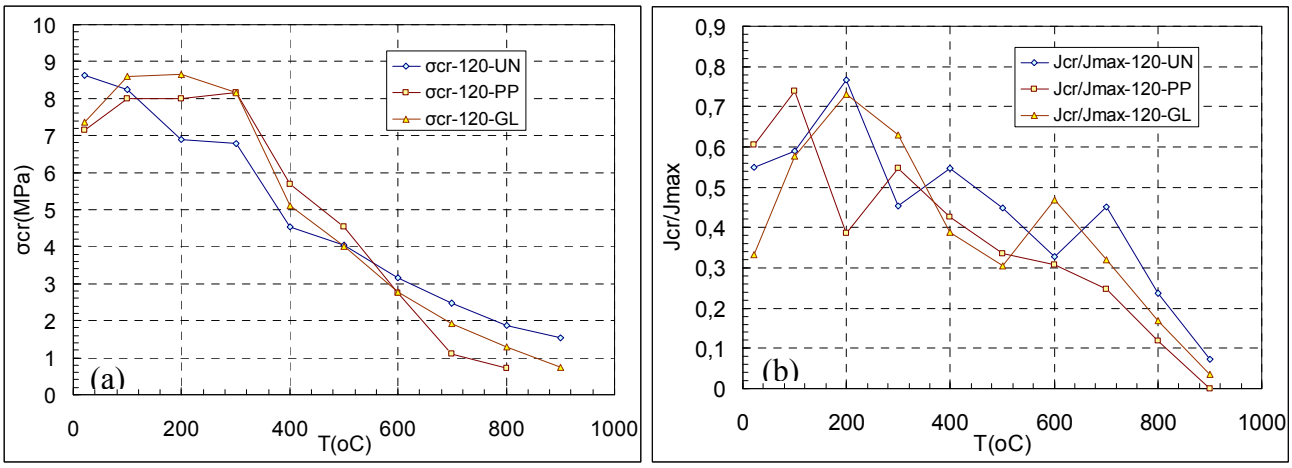


Fig. 3a, b: Variation of strength of first crack formation and of complementary energy ratio according to exposure temperature level for polypropylene and glass reinforced mortars and for unreinforced ones.

$$\sigma_{b,cr} / \sigma_{b,max} \leq 1 \quad \text{and} \quad J_{b,cr} / J_{b,max} \leq 1 \qquad (1a,b)$$

which easily comes that are true in our case due to fact they get valus in the rage of 0,6 to 0,8 for the stress ratio and in the range of 0.2 to 0.6 for the energy ratio.

Conclusions

By the above mention inspections and results, a series of valuable conclusions can picked up that gathered as follow:

Cement-based composites are essentially brittle bodies in common temperature conditions. When exposed to high temperatures as by an accidental fire, a more ductile response is appeared but is accompanied by a drop in their strength. Up to moderate temperatures i.e. 300^{o}C their strength can show a slight increase, remain the same or can even decrease due to the influence of many factors as an acceleration of curing, of water evaporation in cement matrix pores or by dehydration processes of cement paste and gel. In the region of 300^{o}C up to 700^{o}C a gradual degradation (which is accompanied by strength reduction up to 30% at 400^{o}C) appears as a result of decomposition of the hydrated oxides and especially those of calcium. Finally a total collapse of structural integrity is happened (up to 90% strength reduction) as the temperature of 900^{o}C is approached, due to the decarbonization of calcium aggregates. Ultrasonic inspection reveals a continuous degradation and loss of their structural integrity according to exposure temperature level, with the measured velocity in solid to change from 4500m/s for unaffected specimens to 1200m/s after heating at 900°C for two hours. As the temperature and the time duration increase the same happens to cracking grid on specimens, and also to the appearing mechanical, thermal and creep strains and to lateral and bending deflections. The addition of uniformly distributed short fibers, increases mortars ductility and thus their toughness as fibers act as cracking blockers. The fibers improve the mechanical response of cement-based composites mainly when they are exposed to high temperatures. The first crack strength $\sigma_{b,cr}$ and the corresponding complementary energy $J_{b,cr}$ are two magnitudes which can be used to assess the improvement of ductility and toughness and thus the higher performance of the investigated composites and at the same time to get a better insight of the predominant mechanisms for their response. The stress at the first crack during bending loadings $\sigma_{b,cr}$ is reduced up to 900^{o}C with a reduction up to 80% of the unaffected material. For short exposure times, the fiber reinforcement does not seem to give any significant improvement but for higher time intervals fiber cause higher strengths up to 500^{o}C. In the region of 300^{o}C the increase of toughness may reach this of 100% of unaffected material. However, at even higher temperatures, toughness is dramatically reduced, reaching at almost zero values. As with stress $\sigma_{b,cr}$, for the corresponding fracture energy $G_{b,cr}$ and complementary energy $J_{b,cr}$, the fibers improve fracture response reducing the available fracture potential as the temperature increases (Fig. 3b).

References

[1] J.P. Ingham, in: *11th Euroseminar on Microscopy Applied to Building Materials*, Porto Portugal (2007)

[2] C.V. Nielsen, in: *Featured at the XVII Symposium on Nordic Concrete Research*, Helsingor, June 2002

[3] D. Matesova, in: *Odborná konference doktorského studia,* Brno p. 23 (2003)

[4] K.K. Sideris, P. Manita, A. Papageorgiou and E. Chaniotakis, in: *14th National Concrete Conference*, p.194, Greece (2003)

[5] A.G. Gupta, in: *Fire in Buildings*, Chapter 25-SES02, Indian Instituted of Technology, Kharagpur (2006)

[6] T. Kanda and V.C. Li: J Adv. Conc. Techn. 4(1) p.59 (2006)

© (2012) Trans Tech Publications, Switzerland
doi:10.4028/www.scientific.net/KEM.488-489.573

Characterisation of the Fracture Energy and Toughening Mechanisms of a Nano-toughened Epoxy Adhesive

D. Mc Auliffe [a], A. Karač, N. Murphy and A. Ivanković

University College Dublin, Dublin, Ireland

[a]david.mcauliffe@ucd.ie

Keywords: Nano-particles, adhesive joints, toughening mechanisms

Abstract. In this study the adhesive joint fracture behaviour of a nano-toughened epoxy adhesive was investigated. Two experimental test methods were used; (i) the standard tapered double cantilever beam (TDCB) test to measure the mode I adhesive joint fracture energy, G_{IC}, as a function of bond gap thickness and (ii) a circumferentially deep notched tensile test to determine the cohesive strength of the adhesive for a range of constraint levels. It was found that the fracture energy of the adhesive followed the well-known bond gap thickness dependency [1]. SEM analysis of the TDCB fracture surfaces revealed significant plastic void growth. Finally, numerical modelling of the experimental tests suggested that most of the fracture energy was dissipated via highly localised plasticity in the fracture process zone ahead of the crack tip.

Introduction

Structural epoxy adhesives are commonly used to join materials placed in load bearing applications. Adhesive bonding has many advantages over conventional joining techniques such as the elimination of stress concentrations, improved rigidity and the possibility of joining dissimilar materials. These adhesives are typically based on a thermoset epoxy matrix. An epoxy matrix possesses a relatively high stiffness, but is prone to crack initiation and propagation. This limitation has been overcome by the addition of a dispersed second phase of particles, which can provide a significant increase in toughness [2]. The processes responsible for this increase in toughness are still not clear with different mechanisms reported depending on the type, size and concentration of particle added. The aim of this study is to determine the fracture toughening mechanisms that occur during mode I adhesive joint fracture of a core shell rubber (CSR) nano-toughened epoxy adhesive.

Experimental Materials and Procedure

Two experimental test methods were employed to examine the adhesive joint fracture behaviour of a nano-toughened epoxy adhesive. All tests were conducted at low-loading rates and ambient temperature.

Adhesive. The adhesive used in this study is an experimental grade, single part, nano-toughened epoxy adhesive produced by Henkel. It contains two grades of CSR nano-particles of diameters 50 nm and 200 nm, which occupy 16% and 22% of the adhesive volume respectively. A CSR particle consists of a rubber core surrounded by a thin layer of stiff material. All bulk and adhesive joint samples were cured at 180^0 C for 90 minutes. The basic mechanical properties of the adhesive and other substrates used are shown in table 1.

Table 1. Basic mechanical properties of materials used.

	E [GPa]	σ_{yield} [Mpa]	UTS [MPa]
Adhesive	1.76	31.4	45
Al 2014	72.4	425	475
mild steel	200	165	-

TDCB test. The standard Tapered Double Cantilever Beam (TDCB) test [3] was employed to measure the mode I fracture energy G_{IC}, (J/m^2) of the adhesive as a function of adhesive layer thickness. The test configuration, shown in Fig. 1 (a), consists of two contoured beams separated by an adhesive layer. The profile of the beam is such that the change in compliance with crack length, is linear, and is described by a geometry constant, m.

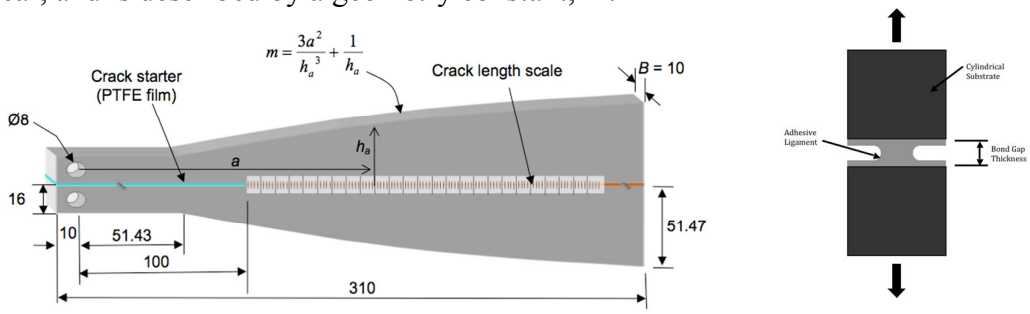


Fig 1. Schematic diagrams of (a) the TDCB geometry and (b) the CDNT geometry.

To prevent plastic deformation of the beams during testing, a high yield strength Aluminium alloy (Al 2014) was chosen as the substrate material. TDCB joints were produced with bond gap thicknesses ranging from 0.2mm to 2.5mm. A groove was machined along both sides of the adhesive layer for specimens with a bond gap thickness greater than 0.4 mm, this was to ensure pure mode I failure.

Testing was carried out with a standard tensile testing machine at a constant crosshead displacement rate of 0.5mm/min. During the test, the load, crosshead displacement and crack length, were recorded. From these measurements, GIC was calculated for each bond gap thickness, according to the corrected beam theory solution [3].

CDNT test. A new test method, the circumferentially deep notched tensile (CDNT) test has been developed to measure the cohesive strength of an adhesive in terms of constraint, the ratio of hydrostatic stress to equivalent von mises stress (σ_{Hyd}/σ_{eq}). This is especially useful to experimentally calibrate numerical cohesive zone models. The test involves bonding two cylindrical substrates at a given bond thickness. A notch is then machined circumferentially into the adhesive layer. Appropriate selection of the bond gap thickness, notch geometry, and substrate material produces the desired level of constraint across the remaining adhesive ligament. A typical specimen is shown schematically in Fig. 1 (b). Samples with bond gap thicknesses of 1.0mm and 1.6mm were manufactured with ligament to bulk area ratios of 25% and 50%, thus four specimen geometries each with a notch root radius of 0.3mm. The specimens were loaded in tension and the displacement and load were recorded.

Microscopy. During the fracture process, all the CSR particles debond from the epoxy matrix, followed by plastic growth of the resultant void. A microscopy study of the TDCB fracture surfaces was carried out to determine the dilatational void strain, ε_f, prior to fracture for each bond gap thickness. Fractured TDCB specimens were cut to provide sections containing the first 10mm of crack growth. These sections were then gold sputter coated and viewed under SEM. Images were taken along the centreline of the specimen in the direction of crack propagation¸ The radii of the voids remaining from debonding of the larger ~200nm particles were measured for each bond gap thickness. The average fracture strain, ε_f was then computed where $\varepsilon_f = u_r/r_{0,}$ and u_r is the radial displacement of the void and r_0 is the initial radius of the nano-particle, i.e. 100 nm in this case.

Experimental results

Steady state cohesive crack growth occurred for all TDCB tests. It was found that the G_{IC} steadily increased from 3400 J/m^2 at 0.2mm bond gap thickness up to 5600 J/m^2 at 1.6mm beyond which G_{IC} reduced slightly as shown in Fig 2. The CDNT tests resulted in cohesive failure across the adhesive ligament for all test geometries. It was found that all specimens failed at a ligament stress of 52Mpa ± 2%. From the microscopy study it was also found that the ε_f increased with fracture energy (Fig. 2).

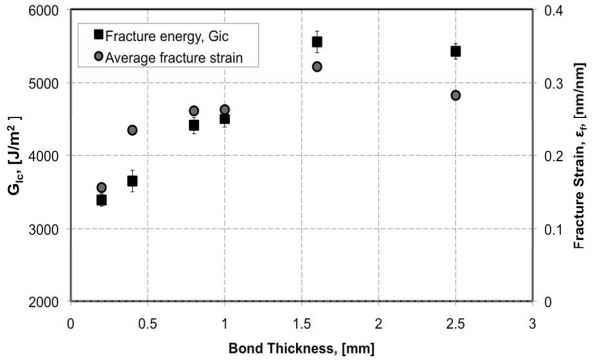


Fig 2. Typical SEM image of TDCB fracture surface, with two distinct void size distributions.

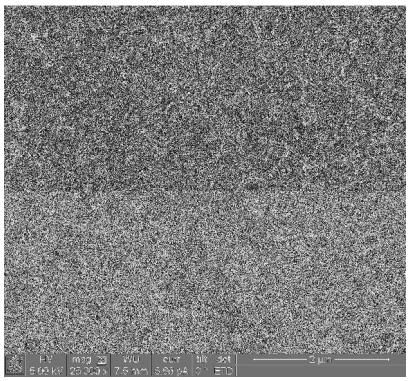


Fig 3. Typical SEM image of TDCB fracture surface, with two distinct void size distributions.

Numerical modelling

Numerical simulations of the CDNT and TDCB tests were performed with the OpenFOAM Finite Volume software package (version 1.4). A non-linear elastic plastic material model including conventional incremental J2 plasticity governed adhesive behaviour while all substrates were treated as being linear elastic. The fracture process was incorporated via a Dugdale cohesive zone model (CZM) specified by the cohesive strength, σ_{max} and the separation energy, $G_{0.}$ A cohesive strength of 52 MPa, based on the experimental CDNT tests, was selected for all simulations.

Analysis of the CDNT tests illustrated that the average level of constraint across the adhesive ligament prior to fracture was quite insensitive to the value of G_0 specified. Variations in G_0 only affected the extension to failure once the maximum stress was reached. A G_0 value of 2800 J/m^2 was used to obtain reasonable agreement with the experimental data (Fig. 4). The average constraint across the adhesive ligament prior to fracture was between 1.5 and 2.0 for the different test geometries. These values correspond to the range of constraints experienced during TDCB fracture.

Simulations of the TDCB tests were completed for bond thicknesses of 0.2, 0.4, 1.6 and 2.5 mm. To reproduce the experimental results it was necessary for G_0 to be between 90% and 95% of the experimentally measured fracture energy. The remaining fracture energy was dissipated through a small diffuse plastic zone ahead of the crack tip at the free surface of the adhesive layer.

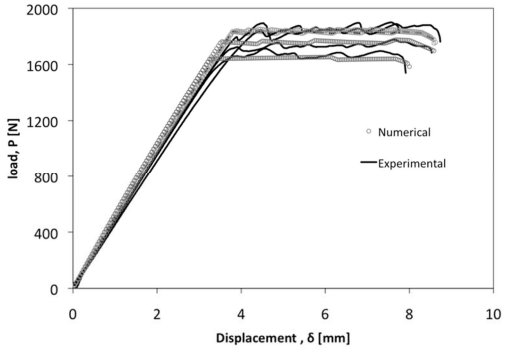


Fig 4. Comparison of experimental and numerical load displacement traces, for TDCB specimcens

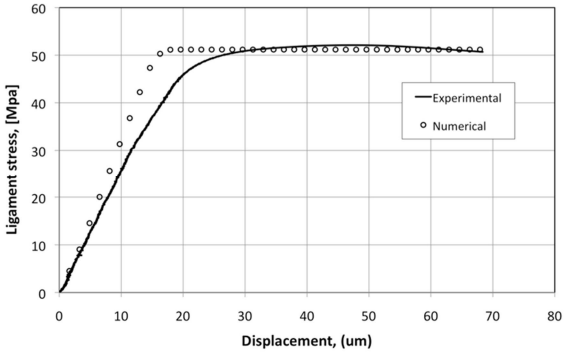


Fig 5. Typical CDNT load displacement trace and numerical simulation

Conclusions and Future Work

Two experimental test methods were used to examine the fracture behaviour of a nano-toughened structural epoxy adhesive. Under mode I testing the adhesive demonstrated the classical bond gap thickness dependency, whereby, the fracture energy increased steadily with bond gap thickness from 3400 J/m^2 to a maximum of 5600 J/m^2 after which the fracture energy reduced slightly. A CDNT test was developed to measure the cohesive strength of the adhesive for a range of constraint levels. It was found for the geometries tested, that the cohesive strength remained constant at 52 MPa. Also, the shape of the force displacement curves suggest that a constant stress damage model is a suitable representation of the traction separation law for this adhesive. A Dugdale cohesive zone model based on the experimental findings was implemented in numerical simulations to reproduce the experimental data. The cohesive strength was 52MPa for all simulations but the separation energy, G_0, was varied to reproduce the experimental tests. In the TDCB simulations the effects of the selected cohesive parameters became clear. The defined ratio of σ_{max} to yield strength of 1.65 prevented a significant diffuse plastic zone from developing before crack advance. Therefore, most of the fracture energy was dissipated in the cohesive zone. This suggests toughening is achieved via intense localised plasticity mechanisms in the fracture process zone ahead of the crack tip. Scanning electron microscopy of the TDCB fracture surfaces revealed that significant void growth occurred, up to 35% dilatational strain. Also, the extent of void growth prior to fracture increased with fracture energy. This indicates that the energy dissipated in the fracture process zone isn't constant but varies with fracture energy.

Further work is ongoing to characterise the fracture process zone, in particular to determine the depth and extent of void growth below the fracture surface. Also, the presence of shear bands will be investigated by use of polarised light microscopy. Bulk mechanical tests are being performed on the epoxy matrix alone to determine its deformation behaviour for a range of constraint levels. Furthermore, a partner research project is examining energy dissipation mechanisms by micro-mechanical modelling of the fracture process zone. This experimental and numerical description of the process zone should allow the energy dissipated in the FPZ and the associated mechanisms to be fully quantified.

Acknowledgements

The authors wish to acknowledge the support provided by the Irish Research Council for Science Engineering and Technology (IRCSET) and Henkel Ireland. The assistance provided by the surface engineering group in UCD is also greatly appreciated.

References

[1] Hunston, D. L., Kinloch, A. J. and Wang, S. S. (1989) 'Micromechanics of Fracture in Structural Adhesive Bonds', The Journal ofAdhesion, 28:2, 103 – 114

[2] Sultan, J. N., McGarry, F. (1973) 'Effect of rubber particle size on deformation mechanisms in glassy epoxy' , Polymer Engineering and Science, 13:1, 29-34

[3] British Standard Institution. BS 7991 Determination of the mode I adhesive fracture energy, G_{IC}, of structural adhesives using the double cantilever beam (DCB) and tapered double cantilever beam (TDCB) specimens, 2001.

© (2012) Trans Tech Publications, Switzerland
doi:10.4028/www.scientific.net/KEM.488-489.577

API J55 Steel Casing Pipe with an Initial Surface Crack under Internal Pressure - Determination of Fracture Parameters

M. Rakin[1,a], B. Medjo[1], M. Arsić[2], Ž. Šarkoćević[3], I. Ivanović[4] and A. Sedmak[5]

[1] Faculty of Technology and Metallurgy, University of Belgrade, Serbia

[2] Institute for Testing of Materials (IMS), Belgrade, Serbia

[3] High Technical School of Professional Studies, Zvečan, Serbia

[4] Innovation Center of Faculty of Mechanical Engineering, University of Belgrade, Serbia

[5] Faculty of Mechanical Engineering, University of Belgrade, Serbia

[a] marko@tmf.bg.ac.rs

Keywords: Casing pipe, Surface crack, Direct method for *J* integral evaluation, Finite element method, Pipe integrity

Abstract. Seam casing pipe used in an oil drilling rig, manufactured by high frequency (HF) contact welding of API J55 steel, is tested. The influence of an initial defect (machined surface crack) is analysed, by performing pressure test of a pipe segment closed at both ends. Besides the damages at the internal surface, casing pipes are exposed to damage at the external surface, which is why such configuration is analysed here. Measurement of strains and crack mouth opening displacement (CMOD) enabled the application of direct method for *J* integral evaluation. This procedure is based on the path independence of the *J* integral and can be applied both in laboratory conditions (on specimens) and on structures. However, it requires a demanding experimental - computational procedure, which is accomplished here using the developed routine. Additionally, the behaviour of the pipe under internal pressure, including fracture mechanics parameters determination, is modelled numerically (by finite element method) in software package Abaqus. The pressure is applied as distributed load acting on the inner surface of the three-dimensional model, and axial tension is applied at the end of the pipe to simulate the closed end. *J* integral values determined numerically and using direct method are used for estimation of the critical pressure corresponding to the crack growth initiation. Additionally, plastic limit load, i.e. pressure which causes yielding of the ligament, is determined. Based on the results, criteria for pipe integrity assessment are discussed.

Introduction

Insufficient crack initiation and propagation resistance is often one of the causes of pipeline failures in exploitation. Existing defects or defects initiated during operation can, under the working loads, develop to the level that poses a threat to the safe service. Determining the fracture behaviour and resistance is very important in structural integrity assessment of pipes, having in mind the requirements of structural safety and economical demands. Integrity assessment depends on an accurate estimate of the fracture mechanics parameters; for elastic-plastic material behaviour it is the *J* integral or crack tip opening displacement CTOD. These quantities enable a correlation between the level of damage (crack size) and operating conditions - fracture initiates when the applied crack driving force reaches the critical value.

Linear elastic stress intensity factors for circumferential and axial part-through surface cracked cylindrical geometries are considered in literature, e.g. [1,2]. Estimating non-linear fracture mechanics parameters, however, can still be problematic for part-through surface cracked pipes. Direct method is used here for experimental determining the applied crack driving force - *J* integral [3]. The result is compared with nonlinear finite element results, which enable assessment of the fracture mechanics parameters for various crack configurations, material properties and loading conditions.

Material properties

Chemical composition of API J55 steel, used for fabricating the examined pipe, is given in Table 1, while Table 2 contain its tensile properties.

Table 1. Chemical composition of API J55 steel, mass. % [4]

C	Si	Mn	P	S	Cr	Ni	Mo	V	Cu	Al
0.2924	0.233	0.963	0.013	0.0216	0.0995	0.0579	0.0123	0.003	0.131	0.025

Table 2. Tensile properties of API J55 steel [4]

$\sigma_{0.2}$ [MPa]	σ_m [MPa]	A [%]
380	562	33

Testing of the surface-cracked pipe

Experimental testing is conducted on pressurized vessel with a machined axial external surface crack in the base material. The vessel was made from a pipe segment with dished ends on both sides (wall thickness t = 6,98 mm), Fig. 1. The crack dimensions were: length $2c$ = 200 mm, depth a = 3,5 mm. Seam casing pipe, fabricated by HF welding, was in exploitation in an oil drilling rig and was withdrawn during a reparation procedure after about 70.000 hours (8 years); designed service life is up to 30 years. Strains were experimentally determined using the strain gauges (Figs. 2b and 2c), while crack mouth opening displacement (CMOD) was measured using COD gauges.

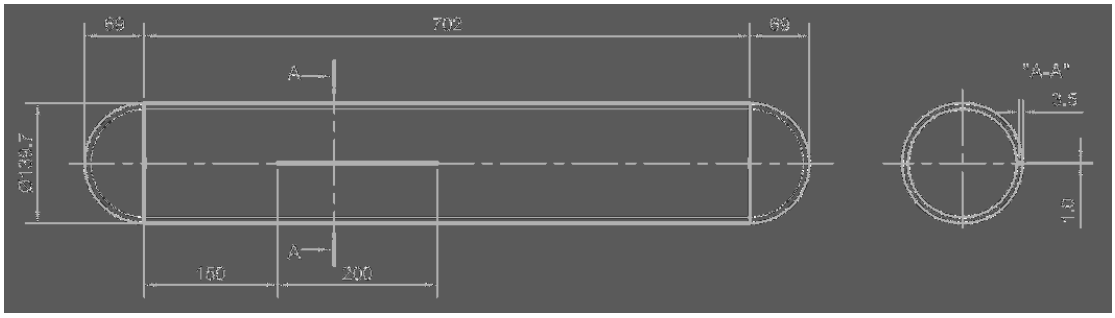


Fig. 1. Pipe dimensions

Direct method for J integral evaluation [3] is based on the path independence of J integral. This method is regarded as more universal in comparison with the standard ones, having in mind that the specimen shape and dimensions do not affect the results significantly. However, it is much more complicated and expensive, because it requires the use of the strain gauges at many locations. Basic principle is determining the J integral by calculating integrand expressions derived from the definition:

$$J = \int_{\Gamma} W dy - \vec{T}\left(\partial\vec{u}/\partial x\right) ds\,, \tag{1}$$

where x and y are Descartes coordinates originating from the crack tip. W is strain energy density, $\vec{T}$ is tensile stress at the integration contour Γ, $\vec{u}$ is displacement vector and ds is curvilinear element of Γ. Two integrands in Eq. (1) are calculated separately for contour segments OA, DO, BC, AB, and CD, Fig. 2a. Condition for application of this procedure on a pipe geometry is that the contour with a surface crack must have a shape that corresponds to the contour of a flat specimen ($t \ll R$). J integral values for contour segments (components: J_{OA}, J_{DO}, J_{BC}, J_{AB} and J_{CD}) are calculated using a C++ routine [5]; total value of the J integral is obtained by summation of these components, Fig. 2d.

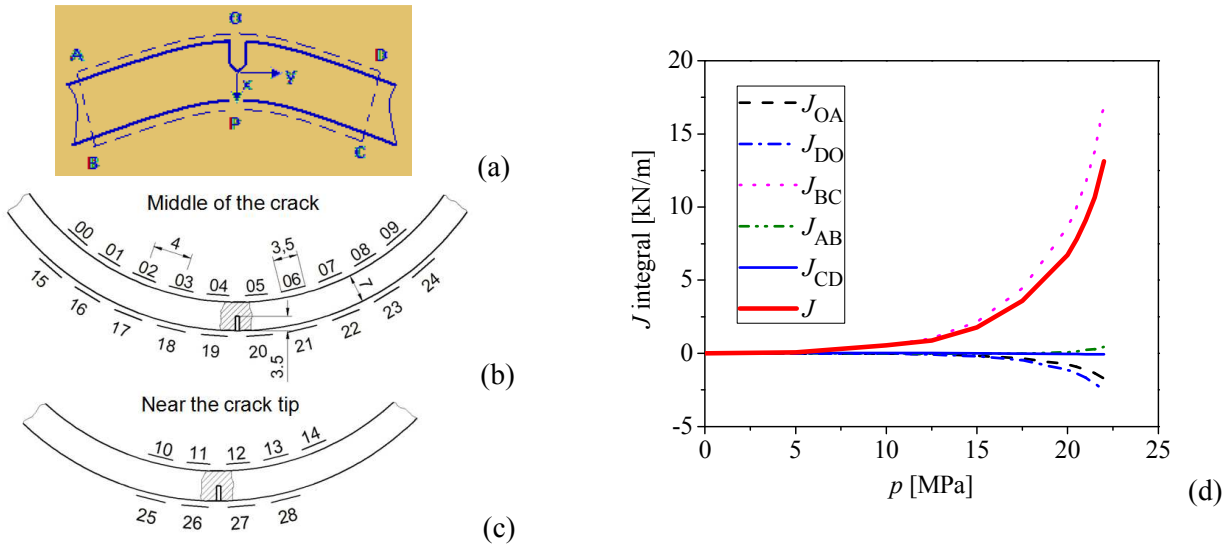


Fig. 2. Contour Γ in the cross section of the pipe (a), strain gauges locations – middle of the crack (b) and near the crack tip (c) and values of the J integral on the contour segments (d)

Numerical determination of fracture mechanics parameters

Numerical analysis of the pipe deformation due to the internal pressure is conducted using the finite element method (FEM), software package Abaqus. The mesh consists of 20-node reduced integration elements, Fig. 3a. Due to the symmetry, one quarter of the pipe is modelled. Loading is defined by prescribing the pressure at the inner side; to take into account the dished ends, axial loading is introduced at one end of the FE model. Crack geometry is approximated by the rectangular shape. The value of J integral is calculated using the domain integral (virtual crack extension) method. Fig. 3b shows the enlarged part of the mesh in the vicinity of the crack tip, with two out of four consecutively formed domains. For domains located further from the crack tip, the results converge and nearly coincide for domains 2-4; domain 4 is chosen as adequate.

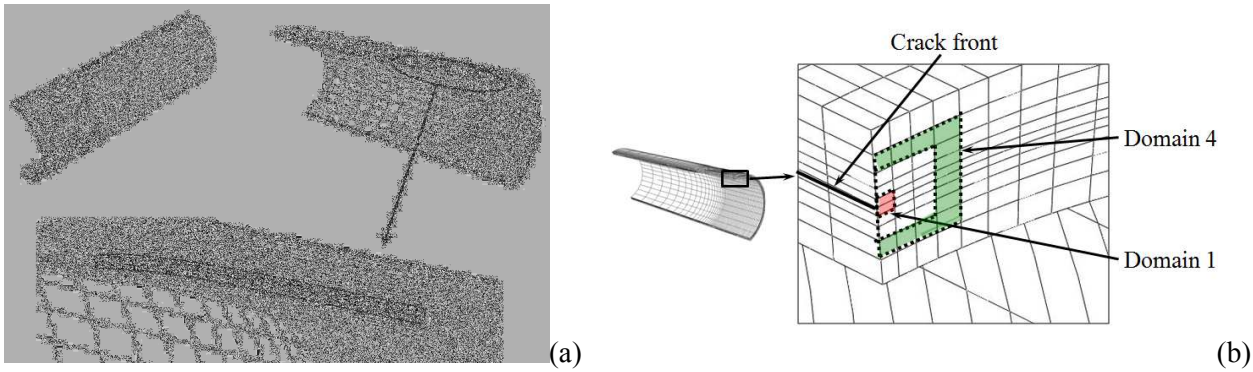


Fig. 3. FE mesh (a) and domains for J integral calculation (b)

Critical loading level

The values for CMOD (Fig. 4a) obtained numerically and experimentally exhibit very good agreement. J integral values obtained using domain integral method (domain 4, Fig. 3b) and experimentally by the direct method are given in Fig. 4b. Part of the experimental curve for pressure over 220 bar is obtained by extrapolation. Certain differences exist for the J integral, but they are getting lower with the increase of loading and are not significant for values approaching the critical value J_{Ic}. Based on the results shown in Fig. 4a and critical value of the J integral determined in [4] (J_{Ic} = 35.8 kN/m), it can be estimated that critical pressure is approx. 250 bar (corresponding to J_{Ic}), when reaching the critical value of fracture mechanics parameter is considered as a failure criterion.

Plastic limit load for the tested pipe is determined on the same FE model (Fig. 3a), by applying elastic - perfectly plastic material behaviour in FE analysis (to avoid problems associated with convergence, RIKS option was used). Pressure value 265 bar is obtained, i.e. the limit load is attained after the fracture mechanics parameter has reached its critical value, which should be taken into account for integrity assessment.

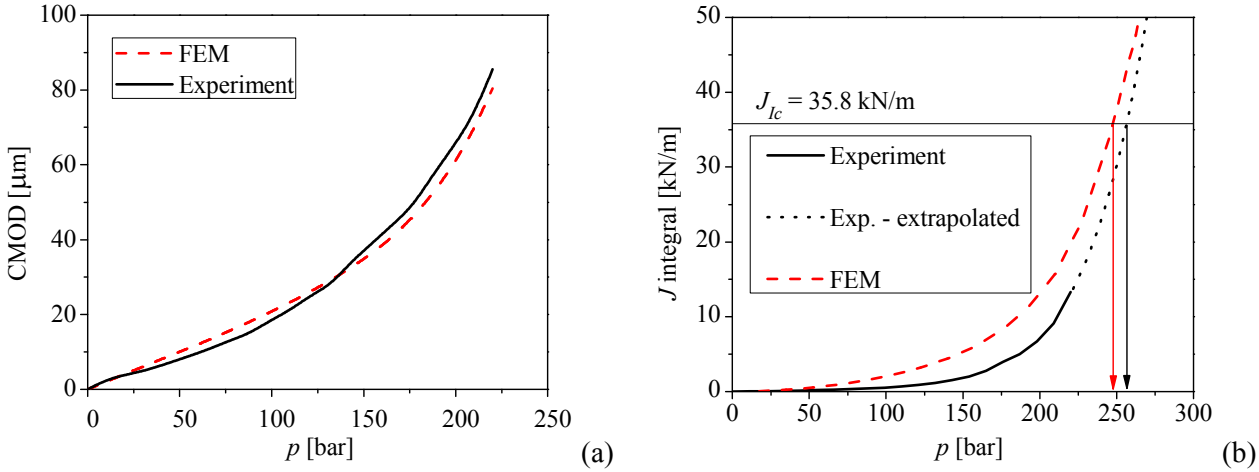


Fig. 4. Comparison of the results for CMOD (a) and *J* integral (b)

Conclusions

Surface-cracked casing pipe, fabricated by high frequency contact welding of API J55 steel, is tested. Experimental and numerical evaluation has shown that the behaviour of the pipe under the internal pressure is successfully predicted. The values of the *J* integral are experimentally determined by the direct method. Numerically determined values do not deviate significantly from the experimental ones, and similar solutions for critical pressure are obtained. Plastic limit load determined through FE analysis is somewhat larger in comparison with the critical pressure corresponding to the critical value of the *J* integral.

Acknowledgments

Authors acknowledge the support from the Serbian Ministry of Science under the projects TR 35002 and OI 174004.

References

[1] I.S. Raju, J.C. Newman: J. Press. Vess. Tech. Vol. 104 (1982), p. 293

[2] M. Bergman: Fat. Fract. Eng. Mat. Struct. Vol. 18 (1995), p. 1155

[3] D.T. Read, in: Fracture Mechanics: 14th Symposium - Vol. II, STP 791, ASTM (1983), p. 199

[4] Ž. Šarkoćević, M. Arsić, B. Medjo, D. Kozak, M. Rakin, Z. Burzić, A. Sedmak: Strojarstvo: J. Theory Appl. Mech. Eng. Vol. 51 (2009), p. 303

[5] I. Ivanović: Software for *J* integral calculation, Programming language C++, Belgrade (2009)

© (2012) Trans Tech Publications, Switzerland
doi:10.4028/www.scientific.net/KEM.488-489.581

Structural and Mechanical Properties of CN_x and CP_x Thin Solid Films

E. Broitman[1,a], A. Furlan[1,2,b], G.K. Geuorguiev[1,c], Zs. Czigány[3,d], H. Högberg[1,e], and L. Hultman[1,f]

[1]Thin Film Physics Division, IFM, Linköping University, SE-581 83 Linköping, Sweden
[2]Dept. of Materials Chemistry, Ångström Lab., Uppsala University, SE-751 21 Uppsala, Sweden
[3]Research Institute for Technical Physics and Materials Science, Budapest H-1525, Hungary

[a]esbro@ifm.liu.se, [b]andrej.furlan@mkem.uu.se, [c]gekos@ifm.liu.se, [d]czigany@mfa.kfki.hu, [e]hanho@ifm.liu.se, [f]larhu@ifm.liu.se

Keywords: carbon nitride, phosphorous-carbide, fullerene-like coatings, thin films, magnetron sputtering.

Abstract. The inherent resiliency, hardness and relatively low friction coefficient of the fullerene-like (FL) allotrope of carbon nitride (CN_x) thin solid films give them potential in numerous tribological applications. In this work, we study the substitution of N with P to grow FL-CP_x to achieve better cross- and inter-linking of the graphene planes, improving thus the material's mechanical and tribological properties. The CN_x and CP_x films have been synthesized by DC magnetron sputtering. HRTEM have shown the CP_x films exhibit a short range ordered structure with FL characteristics for substrate temperature of 300 ℃ and for a phosphorus content of 10-15 at.%. These films show better mechanical properties in terms of hardness and resiliency compared to those of the FL-CN_x films. The low water adsorption of the films is correlated to the theoretical prediction for low density of dangling bonds in both, CN_x and CP_x. First-principles calculations based on Density Functional Theory (DFT) were performed to provide additional insight on the structure and bonding in CN_x, CP_x, and a-C compounds.

Introduction

Amorphous carbon-based coatings have found many applications as protective coatings and solid lubricants. By tuning the C sp^3-to-sp^2 bonding ratio and by alloying the carbon with other elements, the properties of the coatings can be tailored. Recently, we have shown that it is possible to incorporate fullerene-like features to a solid matrix of C and N. The resulting so called fullerene-like (FL) compound consists of sp^2-coordinated graphitic basal planes that are buckled due to the presence of pentagons and cross-linked at sp^3-hybridized C sites, both of which are caused by structural incorporation of nitrogen. This fullerene-like carbon nitride (FL-CN_x), which possess a superior resiliency to mechanical deformation due to its unique superelasticity, show potential as protective top coat on computer hard disks and biocompatible coatings on orthopedic implants [1].

While the relatively weak adhesion of FL-CN_x films to ferrous substrates has been solved by the application intermediate layers of, e.g. CrN_x [1], we have proposed that the P substitution may improve their mechanical properties [2]. In this work we compare the structural and mechanical properties of CP_x and CN_x films deposited by DC magnetron sputtering. The film microstructure was characterized by high resolution transmission electron microscopy (TEM) and the mechanical characteristics were examined by nanoindentation testing. A quartz crystal microbalance (QCM) placed in a vacuum chamber was used to measure their water adsorption. To provide additional insight into the structural features of CP_x compounds, we performed first-principles calculations within the framework of Density Functional Theory (DFT).

Experimental Procedure and Modeling Details

CP_x and CN_x thin solid films has been deposited onto highly-doped Si(001) and NaCl(001) substrates by magnetron sputtering, as described previously [2]. For CP_x, we have used a compound target containing 12 at% of phosphorus prepared by statically pressing the mixture of graphite and red phosphorus. The high vacuum (HV) system applied for growth had a base pressure of

~5 ×10^{-7} Torr. The magnetron was operated in an Ar discharge with gas pressure (P_{Ar}) in the range of 3–9 mTorr. The substrate temperature (T_S) ranged between 150 °C and 600 °C and a bias voltage (U_b) between –20 V and –70 V was applied. The thickness of the as-deposited films was ~1.2 μm for the nanoindentation testing and ~ 50 nm for TEM characterization, with a deposition rate of ~0.4 Å/s.

The microstructure of the films deposited onto NaCl substrates was examined in a Technai G2 electron microscope (EM) for high resolution transmission electron microscopy (HRTEM) imaging and a Philips CM20 for selected area electron diffraction (SAED) pattern analysis, both operated at 200 kV.

The mechanical properties of the CP_x films were investigated by nano-indentation experiments using a 90° three-sided cube corner diamond tip in a Triboscope® (Hysitron Inc). Hardness and reduced modulus were calculated from the stiffness obtained by area function fitting to the unload part of the curve in the length 20% to 95% of penetration. Recovery was defined as $(h_{max} - h_r)/h_{max}$, where h_{max} is the maximum penetration depth and h_r is the residual depth of indent. Hardness was defined as $H = P_{max}/A$ where A is the area of contact at the peak load P_{max}. A was calculated from the area function obtained by indenting fused silica as reference material.

The water adsorption of the films was measured by a QCM placed inside a vacuum chamber operating in the range 10^{-8}–10^{3} Torr. The mass of water adsorbed on the surface of the quartz crystal was calculated using the Sauerbrey equation [3].

In what concerns the modeling, finite model systems simulating a-C, a-CP_x, as well as systems in which P is incorporated in strongly interlocked graphene sheets (to represent FL-CP_x) were considered. The study involved both geometry optimizations and cohesive energy (E_{coh}) calculations performed within the DFT framework in its Generalized Gradient Approximation (GGA). Differences in cohesive energies $|\Delta E_{coh}|$ for the possible structures were determined by an optimization strategy presented elsewhere [4], making use of the Gaussian 03 program.

Results and Discussion

Figure 1 displays a HRTEM image and the corresponding SAED pattern from a $CP_{0.1}$ film deposited at T_S = 300 °C, U_b = –25 V, and P_{Ar} = 3 mTorr. The film is essentially amorphous, but exhibits short-range ordering with fragments of curved graphene sheets. Although the presence of any larger packages of the FL structure similar to FL-CN_x cannot be ruled out from such HRTEM images due to the possible superposition of nanoscale features, it is not expected for CP_x since the calculations show a strong tendency for P-induced inter-linking of the graphene which breaks the continuity of the planes [2]. The SAED pattern shows that the $CP_{0.1}$ film has broad rings at ~1.6 Å, ~2.6 Å, and ~5.9 Å. These rings differ from those of other C allotropes, as well as from FL structures like FL-CN_x. This shows that incorporation of P in graphene has a unique influence on the film structure formation. In contrast, CP_x films deposited at T_s = 300 °C and working gas pressure of 6 mTorr and 9 mTorr show amorphous structure with close to graphitic short-range ordering. These samples exhibit SAED peaks at ~1.2 Å, ~2.15 Å, and ~4 Å. The first two peaks coincide with those also found in FL-CN_x [5], and some other amorphous C allotropes. The position of the third peak at ~4 Å, however, differs slightly from the ~3.5 Å peak typical for the FL structure known from FL-CN_x [5].

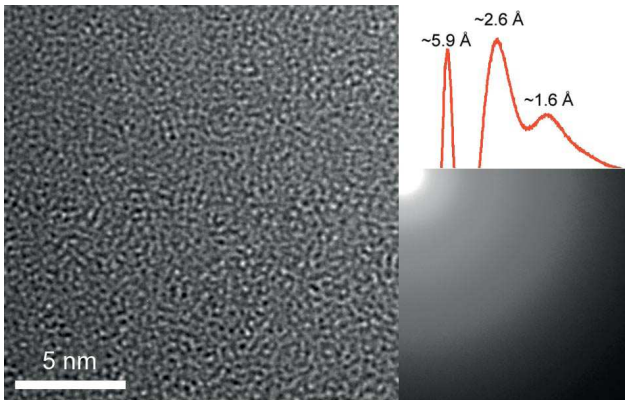


Figure 1: *HRTEM image and corresponding SAED pattern and its intensity distribution from a $CP_{0.1}$ thin film.*

Figure 2 shows nanoindentation load–unload curves for $CP_{0.1}$ films deposited at T_S = 300 °C and $CP_{0.025}$ films deposited at 600 °C. Both CP_x thin films are harder to indent than a characteristic FL-CN_x film. The $CP_{0.025}$ films had a hardness of 18.2 GPa at 2 mN indentation load. For comparison, the FL-$CN_{0.16}$ film has a hardness of 15.4 GPa for the same load. The work of plastic deformation, represented by the surface enclosed by load–unload curves, shows a more pronounced plastic deformation for $CP_{0.025}$ films compared to FL-$CN_{0.16}$. Specifically, the elastic recovery ratio of the $CP_{0.025}$ film is 0.63 compared to 0.74 for FL-$CN_{0.16}$. $CP_{0.1}$, on the other hand, displays a significantly reduced work of plastic deformation compared to $CP_{0.025}$, improved recovery to the value of 72%, and hardness of 24.4 GPa. Thus, the CP_x films exhibit a similar recovery to FL-CN_x, but are harder to indent. Mean surface roughness of the films, as determined by AFM, is ~0.5 nm for films deposited at T_S= 300 °C and ~0.9 nm for films deposited at T_S = 600 °C. Thus, the influence of the substrate roughness on the indentation results can be neglected for the used penetration depths.

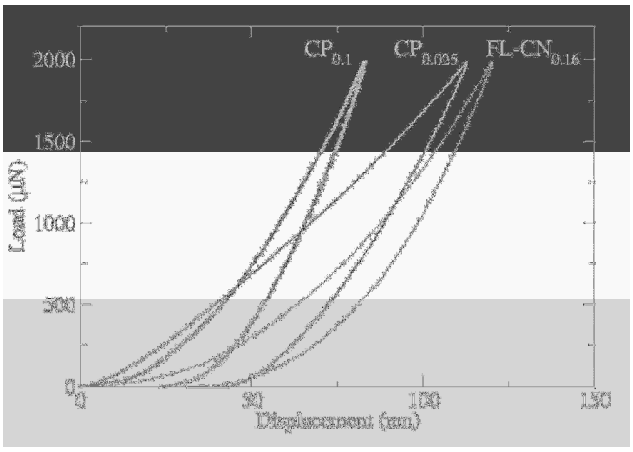


Figure 2: *Nanoindentation curves from CP_x thin fims deposited at 300 °C ($CP_{0.1}$) and 600 °C ($CP_{0.025}$). The FL-$CN_{0.16}$ film was deposited at 450 °C.*

Figure 3 shows the adsorption of water versus the water vapor pressure for films deposited under different conditions. All carbon-based films have a characteristic dependence of water coverage on the H_2O vapor pressure. There are, however, differences in the amounts of the adsorbed water:

i) Pure carbon films adsorb more water than phosphorous-carbide films;

ii) Fullerene films adsorb less water than amorphous films.

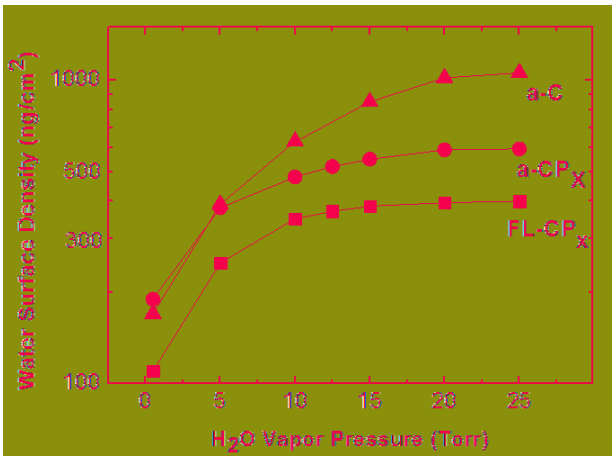


Figure 3: *The water surface density adsorbed on the surface of carbon overcoats at 50 °C versus water vapor pressure.*

It has been shown the surface roughness could play an important role on the water adsorption. However, surface roughness differences are small in our case, and only play a role in the adsorption of water at high levels of RH, where capillary condensation can occur in the valleys giving thicker water films [3,6].

The surface of the sputtered carbon-based films is heterogeneous and is composed of different hybridized carbon atoms (sp, sp^2, and sp^3) and dangling bonds. As soon as the surface is exposed to air, its dangling bonds react with oxygen and form oxygen containing polar groups such as C-O-C, C-OH, and C=O. Because of the hydrogen bonding tendency of water, the adsorption of water is sensitive to the polarity of the adsorbent surface and is enhanced by the presence of oxidized carbon. We should expect that, because of the fullerene structure, FL-CP_x films have the lowest number of dangling bonds and, in consequence, low water adsorption. Electron spin resonance measurements confirmed this assumption for carbon nitride coatings. In a previous work, we reported that FL-CNx shows the lower adsorption rate, and that a-C adsorbs more than 14 times the amount adsorbed by the fullerene coatings [6]. The differences in adsorption on our films must be understood in the context of their microstructural differences, as explained below by a theoretical model.

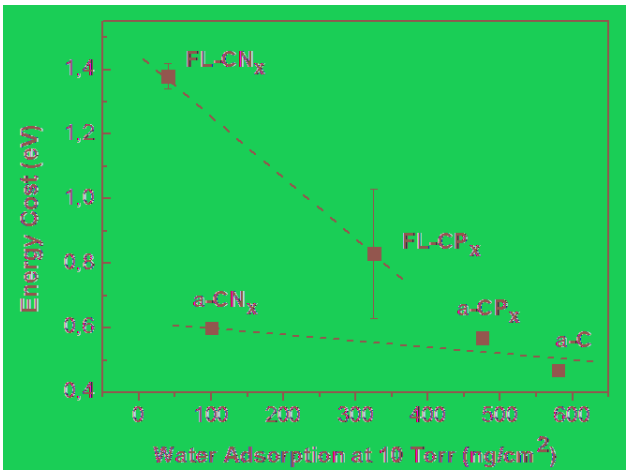


Figure 4: *Correlation of energy cost versus experimental water adsorption on amorphous and FL carbon-based compounds. Both dashed lines are only for guiding the eyes.*

Different model systems containing pentagons, tetragon defects, strongly interlocked graphene sheets and cage-like formations have been shown to correctly describe FL-CP_x [4]. Both a-CP_x and a-C were simulated by relaxing structurally disturbed model systems consisting on randomly intersected P-containing and pure grapheme sheets, respectively. Simulation results revealed that the energy cost for dangling bonds in different configurations is considerably higher in FL-CP_x than for amorphous films, being the lowest in pure a-C, which corroborates the experimental data that dangling bonds are less likely in FL-CP_x than in a-CP_x films. Figure 4 compares experimental values of water adsorption with the theoretically calculated values obtained for the energy cost of dangling bond formation. The error bars, displayed for FL compounds only, indicate the variation of the energy values due to the diversity of defects in these systems. The decrease of water adsorption on different FL and amorphous films correlates very well with the theoretically predicted reduction of dangling bonds on the film surfaces.

In conclusion, CP_x thin films deposited at 300 ^{0}C presents a unique microstructure with highly curved and interlinked FL features. In term of mechanical properties, $CP_{0.1}$ thin films are harder than FL-$CN_{0.16}$ counterparts, and can be considered as resilient with a hardness of 24 GPa and an elastic recovery of 72%. The $CP_{0.1}$ films present low water adsorption, which can be linked with a low amount of dangling bonds, as confirmed by our theoretical calculations.

Acknowledgements The authors acknowledge the support from the Swedish Foundation for Strategic Research (SSF) and the Swedish Research Council (VR).

References

[1] E. Broitman, J. Neidhardt, L. Hultman, in: *Tribology of Diamond -Like Carbon Films: Fundamentals and Applications*, edited by C. Donnet/A. Erdemir, Springer, N.Y., (2007), p. 620.

[2] A. Furlan, G.K. Gueorguiev, Zs. Czigány, H. Högberg, S. Braun, S. Stafström, and L. Hultman, Phys. Stat. Sol. (RRL) Vol. 2 (2008), p. 191.

[3] E. Broitman, A. Furlan, G.K. Gueorguiev, Zs. Czigány, A.M. Tarditi, A.J. Gellman, S. Stafström, and L. Hultman, Surface & Coatings Technology Vol. 204 (2009), p. 1035.

[4] G.K. Gueorguiev, E. Broitman, A. Furlan, S. Stafström and L. Hultman, Chemical Physics Letters, Vol. 482 (2009), p. 110.

[5] S.V. Hainsworth, T. Burlett, and T.F. Page, Thin Solid Films Vol. 236 (1993), p. 214.

[6] E. Broitman, G.K. Gueorguiev, A. Furlan, N.T. Son, A.J. Gellman, S. Stafström, L. Hultman, Thin Solid Films Vol. 517 (2008) p. 1106.

© (2012) Trans Tech Publications, Switzerland
doi:10.4028/www.scientific.net/KEM.488-489.585

SIMULATION OF RUBBER-COATED FABRIC MATERIAL DAMAGE

Agnieszka Derewońko[1,a], Pawel Baranowski[1,b] and Dariusz Rudnik[2,c]

[1] Department of Mechanics and Applied Computer Science, Military University of Technology
ul. Kaliskiego 2, 00-908 Warsaw, Poland

[2] Motor Transport Institute, 80 Jagiellońska Str., 03-301 Warsaw, Poland

[a] aderewonko@wat.edu.pl, [b] pbaranowski@wat.edu.pl, [c] dariusz.rudnik@its.waw.pl

Keywords: Finite Elements Analysis, experimental test, rubber-coated material

Abstract: The objective of this work is to describe part of the selecting process of a rubber-coated fabric material model. The material is used to construct an air cushion that is a carrying element of the cassette pontoon bridge unit. During operation the air cushion is permanently in contact with a metal component, fresh water and air. Therefore various interactions, such as a contact problem, flow of medium and thermodynamics can occur. The basic material model for numerical simulation was selected based on the uniaxial tensile test. The simple method was used to describe time-dependent material properties for numerical analysis, which allows computation to take a reasonable time. In order to assess the usefulness of the selected material model the impact puncture test was modelled with the same conditions and properties as in the laboratory testing machine called *Instron*. Moreover, an attempt of simulating the damage process is described. The energy absorbed by the material was registered during the laboratory test which was compared with the results of numerical analysis. An acceptable compatibility of the results is noticed.

Introduction

It can be said doubtlessly that constructed bridges have made people's life easier. One of the most interesting types of bridges is a pontoon bridge that floats on water with the support of various types of pontoons. In the paper a new construction of a such pontoon bridge is proposed [1]. The buoyancy and load capacity is assured by an air cushion filled with air. Rubber or plastic coated fabric is used to construct the air cushion due to its very high strength and elongation, gas-tightness, water resistance and lightweight. This material is very thick and flexible, and its structure usually consists of a layer of high tenacity woven fabric scrim, which is sandwiched (placed) between two coatings (Fig. 1a). During a common uniaxial tension test it was noticed that Poisson's ratio has a time-dependent characteristic for the analysed material (Fig. 1b).

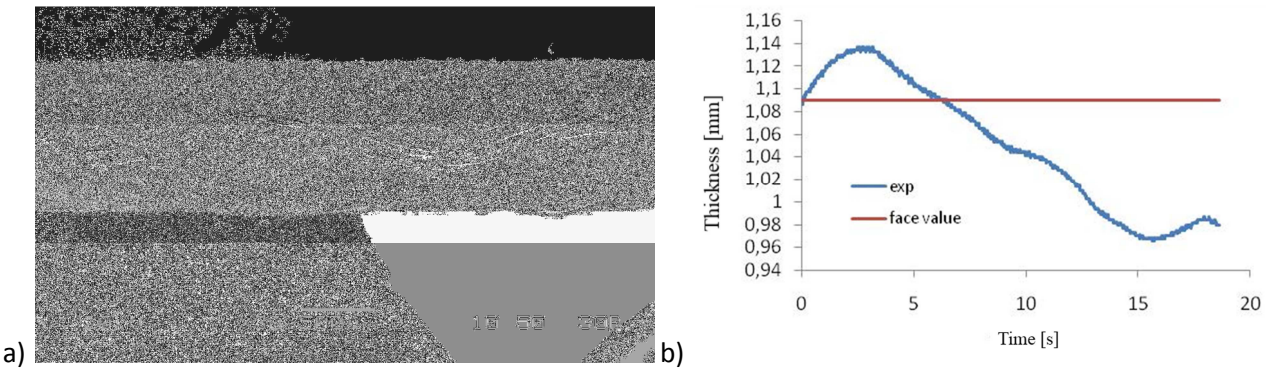


Fig. 1 a) Structure of plastic coated fabric, b) Poisson's ratio vs. time curves [1]

Numerical analysis of a new construction of the pontoon were performed with the use of the commercial engineering LS-Dyna code with an explicit time integration scheme. A fabric material model is strongly recommended for modelling the airbag in conjunction with membrane elements [2]. Although, orthotropic constants can be defined, it was necessary to describe

accurately time-dependent material behaviour. A simple method to determine parameters characterizing the material useful in a numerical simulation was proposed [3]. The results of the uniaxial tensile tests of samples cut in different directions are used. To validate this material model, a series of laboratory tests and numerical simulations were performed. The dynamic response of the material was investigated by simulating a puncture test. Displacements and energy absorbed by the material were compared with the results of an impact puncture test which was performed in Motor Transport Institute.

This paper presents one of the validation stages of a homogeneous material model useful to simulate the air cushion made of textile coated by rubber-like material filled with air.

Research object

Experimental test stand. The research object, which is presented in this paper is the materials testing machine called *Instron* with the gravity-operated column *Dynatup 9250V*. The described machine is equipped with the controlling and processing data system called *Impulse.* With the usage of the described test stand it was possible to perform impact resistance tests with parallel recording of such parameters as: impact velocity, energy variation, load characteristics or the deflection of a material sample. Impact strength tests were performed on the circular shaped samples. The samples were placed between two steel rings with a central hole. In order to perform a puncture test, a punch beater made of tool *NC3*steel with 48 *HRC* hardness was used. At its bottom, the cone was turned/shaped with the vertex angle of 30º. The gravity-operated punch with overall mass of 5,49 kg was dropped with the impact energy 25 J [4].

The magnitude displacement and force of material resistance were registered from the moment the beater touches the sample to perforate it (Fig. 2). Therefore, the absorbed energy is not the energy of the maximum resistance force of material. A value of the absorbed energy is less than the puncture energy, e.g. this is the work necessary to damage the sample.

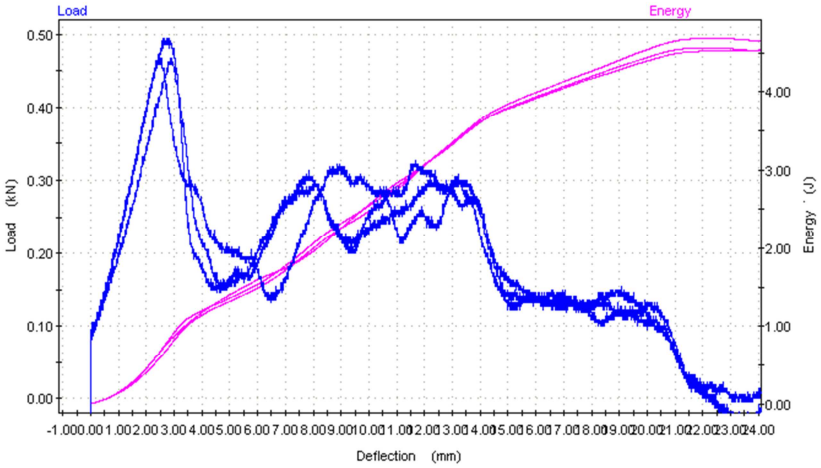
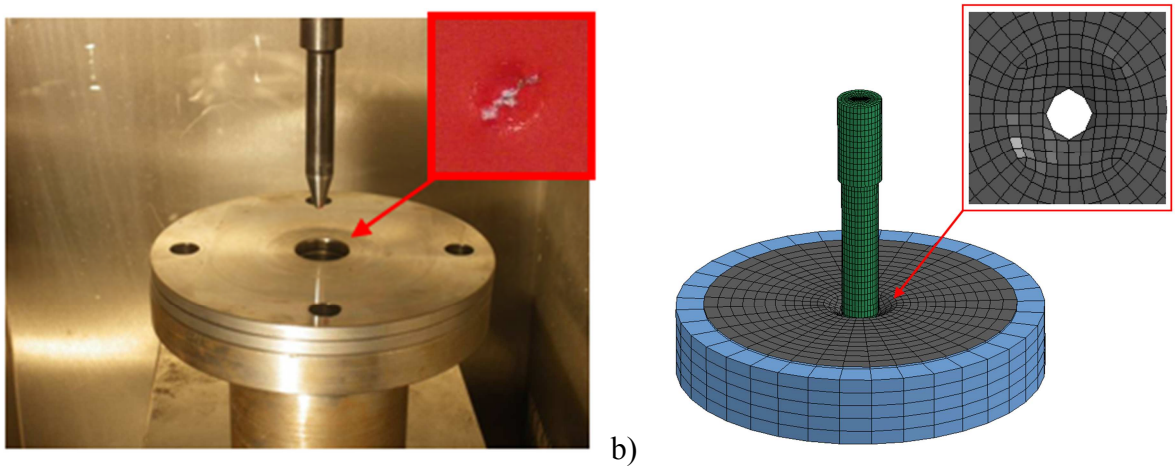


Fig. 2. Internal energy graph [—] and load force [—] vs. deflection during the puncture test of woven fabric H8545 [1]

Test stand numerical model. Based on the technical documentation of the presented test machine, a geometric model was carried out thanks to *CAD* software. Subsequently, the developed geometric model was discretized and next imported into *LS-Prepost* (*LS-Dyna*) program. Steel rings were replaced by one cylindrical body consisting of 2340 solid hexagonal elements. The punch beater was represented by rigid *HEX8* elements, whereas the circular sample consisted of 568 *Belytschko-Tsay* shell elements [2]. The test stand described above and its numerical model with the sample after tests (experimental and numerical) are presented in Fig. 3.



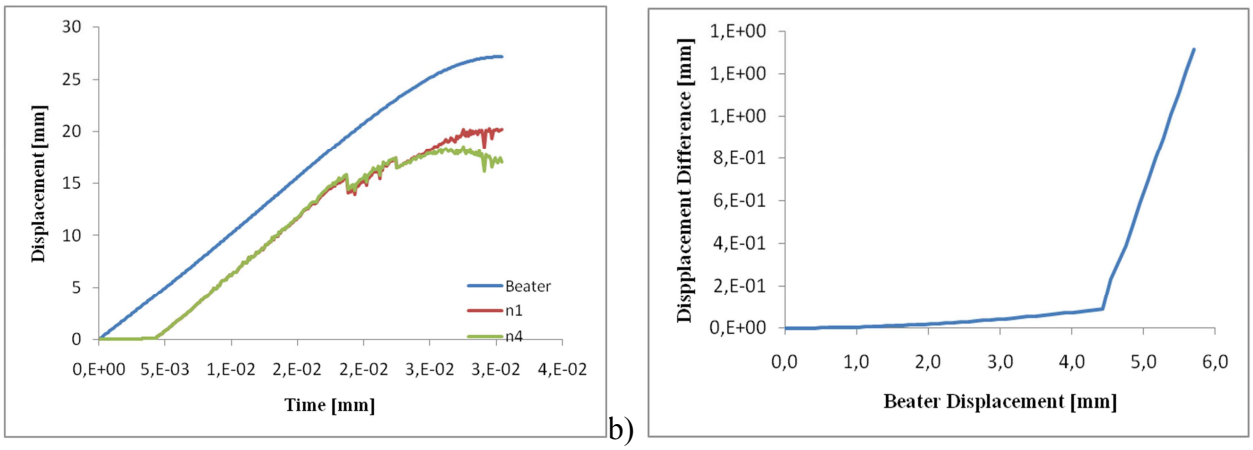
a) b)

Fig. 3 The test stand with the punch beater (a) and its numerical model (b)

Material properties (without the sample) and boundary conditions exactly corresponds to experimental tests. An interaction between the punch and the sample was simulated by the contact, while sample is permanently constrained to cylindrical ring tied contact. Contact algorithm is based on penalty function and penetration checking using a segment to segment approach. The authors decided to perform some modifications in the material fabric used as a sample material model in numerical computations. In order to implement the time-dependent material behaviour the stress versus strain along a longitudinal and transverse direction curve and shear stress versus shear strain plane characteristic were specially prepared based on the uniaxial tensile tests. It results in less time-consuming numerical computations. The fabric material model does not support any erosion or failure criteria. Since the location of the erosion failure is known (central area of the sample beneath the punch beater) the special feature is used to simulate sample failure. The coincident nodes in the middle of the sample are tied together and disconnected when the average volume weighted effective plastic strain in the adjacent element exceeds the specified value.

Effective plastic strain is calculated incrementally as a function of the plastic component of the rate of a deformation tensor. As the stress value increases, the recoverable strain, i.e. true stress/Young's modulus, increases as well. For plastic/polymer material elastic component of strain is large. Therefore, ultimate tensile strain of 0.00001 was used, which is the constraint critical value to disconnect any tied nodes once the element strain reaches this level.

Since tied nodes remain together, the difference in magnitude displacement of the coincident nodes is 0 and the damage does not occurred. Displacement of the end of the beater and two coincident nodes in respect to time is shown in Fig. 4a. The magnitude displacement difference of these two nodes versus beater displacement is presented in Fig. 4b.



a) b)

Fig. 4 Displacement of the end of beater and two coincident nodes in respect to time (a) and magnitude displacement differencen1-n4 nodes versus beater displacement (b)

The energy data, which are printed in the output files, are only useful to check on an analysis because internal energy includes elastic strain energy and work done in permanent deformation. Therefore, these values should not be compared with the results of the laboratory test. Absorbed energy of material W_{ae} is calculated as work done by resistance force f on displacement d according to formula (1) during contact of the beater and the sample right up to damage it.

$$W_{ae} = \sum \left(x^{t+1} - x^t\right)\left(f_x^{t+1} - f_x^t\right) + \left(y^{t+1} - y^t\right)\left(f_y^{t+1} - f_y^t\right) + \left(z^{t+1} - z^t\right)\left(f_{zx}^{t+1} - f_z^t\right) \tag{1}$$

Absorbed energy in respect to displacement of the beater is shown in Fig. 5.

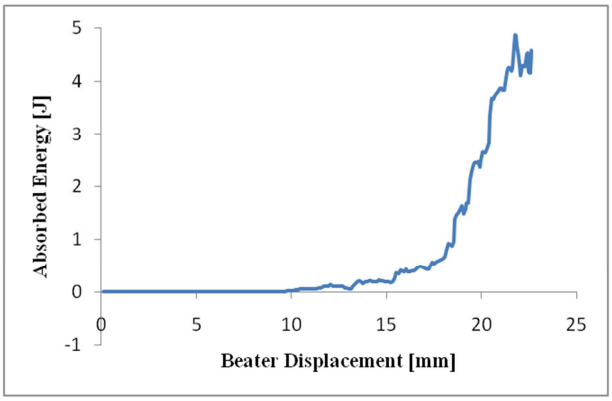


Fig. 5 Absorbed energy in respect to displacement of the beater

Conclusions

The paper presents the development process of materials testing machine *Instron* numerical model. A simple method to determine parameters characterizing the material useful in numerical simulation was also proposed. The material model, modified by authors, was implemented into the developed testing machine FE model. Moreover, in order to simulate material erosion, it was necessary to use a special method with failure criteria. The obtained results indicate that the proposed homogeneous material model i**n** conjunction with membrane elements can be applied for a dynamic analysis. Comparing the experimental testing results with the numerical ones an acceptable compatibility can be noticed, considering the fact of difficulty in modelling such structural complicated material as plastic rubber-coated fabric material.

Acknowledgements

The paper has been supported by a grant No. O R00 0079 09, financed in the years 2009-2011 by Ministry of Science and Higher Education, Poland.

References

[1] Patent EP10461514.1, *A sectional pontoon bridge* (2010).
[2].J.O. Hallquist in: *LS-Dyna. Theory manual*, California Livermore Software Technology Corporation (2006).
[3] Derewońko A., Kiczko A., Szurgott P. in : *Determination of a Rubber-Like Material Model as an Inverse Problem*, International Conference on Advances in Experimental Mechanics (ISEV), under review
[4] Z.L. Kowalewski, D. Rudnik and others in: *Opracowanie modułów i materiałów elastycznych o wysokiej wytrzymałości i odporności balistycznej w zastosowaniu na mosty przeprawowe,* Poland, Warsaw (2010).

© (2012) Trans Tech Publications, Switzerland
doi:10.4028/www.scientific.net/KEM.488-489.589

Elastic-plastic FEM modelling of the single overload effect on the fatigue crack front shape

Aleš Materna[1, a] and Vladislav Oliva[1, b]

[1] Czech Technical University in Prague, Faculty of Nuclear Sciences and Physical Engineering, Dept. of Materials, Trojanova 13, 120 00 Prague 2, Czech Republic

[a]ales.materna@fjfi.cvut.cz, [b]vladislav.oliva@fjfi.cvut.cz

Keywords: fatigue crack growth; FEM model; SWT parameter; low-cycle fatigue; node release schema; single overload.

Abstract. A 3D elastic-plastic FEM model for prediction of planar fatigue crack growth is presented. The model is based on the concept of local low-cycle fatigue of a small material volume in front of a high cycle crack. A local crack front advance is modelled by the successive release of finite element mesh nodes in the plane of propagation. The release of the nodes is controlled by the value of the Smith-Watson-Topper fatigue damage parameter in the surrounding elements. The effect of the single tensile overload on the fatigue crack growth and on the fatigue crack front shape is modelled.

Introduction

It is a well-known fact that a single overload cycle (OL) applied to a fatigue crack propagating under constant amplitude (CA) loading induces so-called delayed retardation [1]. Although there are a number of mechanisms which may account for this behaviour, e.g. a crack tip blunting and an additional strain hardening inside the plastic zone, the plasticity-induced crack closure appears to be the main cause. Concerning the stress state, the plastic zone size under plane stress is significantly larger than that under plane strain. Therefore, a crack closure is observed predominantly in the material surface layer. In addition, retardation after the overload is more intense at the material surface. In this contribution, a detailed theoretical study of this phenomenon in the case of a through-thickness planar crack is presented. A local crack growth rate after the OL is theoretically predicted from the cyclic elastic-plastic stresses and strains ahead of the crack front utilizing the Smith-Watson-Topper fatigue damage parameter. The crack front shape evolution after the OL is determined and compared with model shapes for crack propagating under CA loading.

Numerical model

Model basics and the governing equations. The model for prediction of the crack growth rate and crack front shape evolution is based on the cumulative low-cycle fatigue damage in front of the crack front. It was mainly inspired by the work [2], where the Smith-Watson-Topper (SWT, [3]) parameter

$$P_{\mathrm{SWT}} = \sigma_{\max} \frac{\Delta\varepsilon}{2} \tag{1}$$

was chosen for damage estimation. $\sigma_{\max}$ is the maximum stress and $\Delta\varepsilon/2$ is the strain amplitude. The SWT parameter can be related to the constant amplitude fatigue life N_{f} by the expression

$$P_{\mathrm{SWT}} = \frac{(\sigma'_{\mathrm{f}})^2}{E}(2N_{\mathrm{f}})^{2b} + \sigma'_{\mathrm{f}}\varepsilon'_{\mathrm{f}}(2N_{\mathrm{f}})^{b+c}, \tag{2}$$

where σ'_{f} is the fatigue strength coefficient, $\varepsilon'_{\mathrm{f}}$ is the fatigue ductility coefficient, b is the fatigue strength exponent, and c is the fatigue ductility exponent. The fatigue damage is calculated in material elements of a size typical for the given material. Damage fractions, calculated as reciprocal values of N_{f}, are summed up during the loading period using a linear cumulative hypothesis.

FEM implementation. The 3D finite element model of the growing fatigue crack was built in MSC.Marc. Fatigue damage evaluation, the change in boundary conditions and all other non-standard procedures were implemented using user subroutines [4].

FEM mesh and boundary conditions. Simulated central fatigue crack grows in a flat specimen with a thickness of 5 mm. The initial crack size is 12.5 mm. CA loading has a stress ratio $R = 0.1$, OL ratio is 1.5. With respect to the symmetry, only one eighth of the specimen is analyzed. The mesh is refined in the area of the supposed crack growth, where the dimensions of the elements in the planes parallel to the specimen surface are 40×40 μm. The dimension 40 μm was chosen as the optimum for the given material [5]. The element size in the direction of the specimen thickness increases gradually from 50 μm at the surface to 500 μm at the midsection (Fig. 1). It corresponds to higher expected stress and strain gradients in the subsurface layer.

The rigid contact surface in the plane of the propagation enables the proper simulation of the plasticity-induced crack closure.

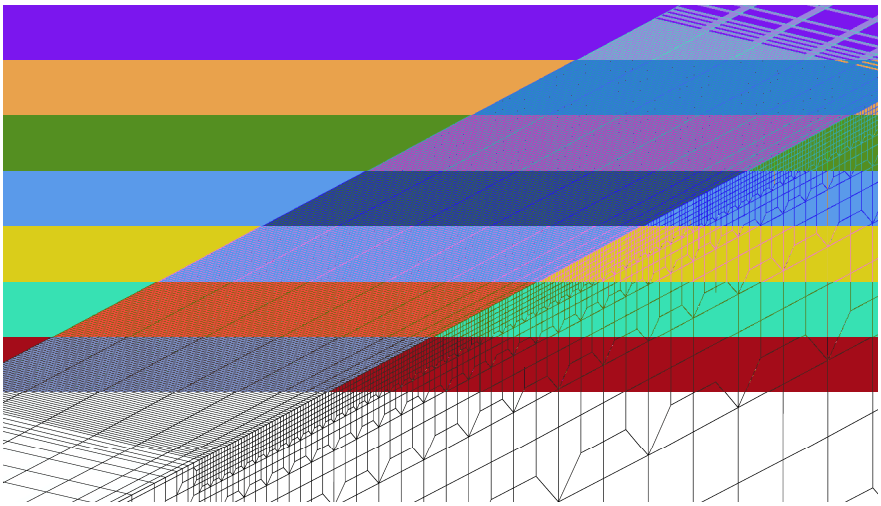


Fig. 1 – The finite element mesh in the region of the fatigue crack growth used for both analyses. Smaller elements are located near the crack plane and near the material surface.

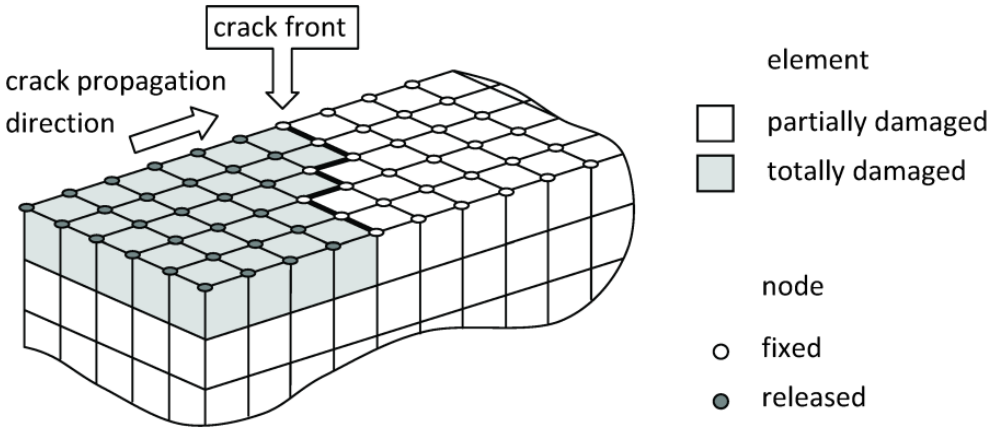


Fig. 2 – A finite element model of the planar crack propagation – the node release method in 3D.

Crack advance algorithm. After each loading cycle, the degree of the fatigue damage accumulated over each finite element ahead of the crack front was estimated with regard to eq. (2) as an average value over all the element integration points. The local crack front advance is realized by the release of the kinematic boundary condition in the node, for which all the surrounding elements had exhausted their fatigue lives (Fig. 2). The actual crack front position is determined as the boundary curve between the partially and fully damaged elements. The number of simulated loading cycles was reduced by the assumption that an increment of damage per one cycle would be constant for all subsequent cycles with a crack of an unchanged shape.

Material input data. All material data correspond to aluminium alloy 7010-T651 in the fibrous state and should reflect the change in mechanical properties and the rate of damage accumulation under the cyclic plastic deformation. Consequently, the input data were obtained from common low-cycle fatigue tests ($\sigma'_{\mathrm{f}} = 693.3\,\mathrm{MPa}$, $\varepsilon'_{\mathrm{f}} = 1.89$, $b = -0.061$, $c = -1.074$ [6]). The model $\sigma - \varepsilon_{\mathrm{p}}$ curve is the result of the tensile test performed after a previous intense cyclic loading with high plastic strain amplitude. The kinematic hardening rule is employed to simulate the observed Bauschinger effect.

Results and discussion. The comparison of results from both simulations, with and without OL, is carried out in Figs 3–5. The crack fronts are displayed every 1 000 cycles in Fig. 3. The local crack rates at the midsection of the specimen and at its surface are shown in Fig. 4 while Fig. 5 illustrates the difference in the crack length between the midsection and surface which is usually referred to as tunneling depth.

The initial model crack front is straight. At the beginning of the propagation, the crack growth rates in the middle are significantly higher than those at the surface (Fig. 4) – the crack front exhibits a gradual tunneling of its interior part (Fig. 5). After approximately 6000 simulated cycles, the 50% overload cycle is applied. After this a transient increase of the crack rate in the surface layer occurs which causes slight front straightening. This effect vanishes rapidly and is followed by a relatively long period of the crack growth retardation. The decrease in the crack rate is more intense and longer in the surface layer than in the midsection (Fig. 4), which corresponds to the increase of the tunneling depth (Fig. 5). 9000 cycles after the application of OL both the crack growth rates and the crack front shapes are comparable with the results of the simulation without OL. The length of the influenced region is 2 mm.

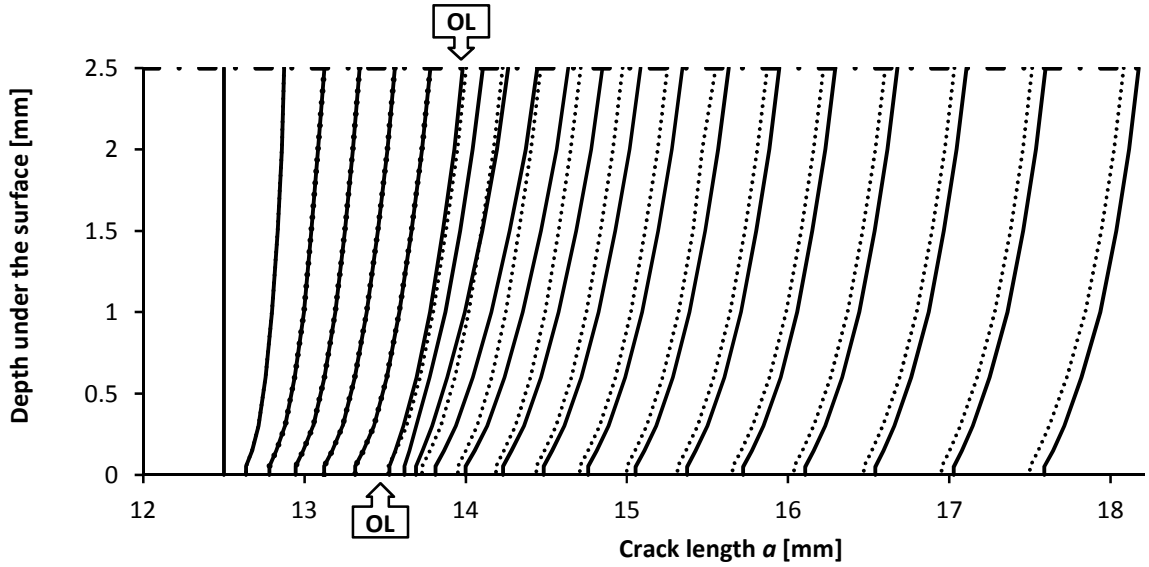


Fig. 3 – Simulated crack front shapes displayed every 1000 cycles. Full lines – loading with single overload cycle (OL), dotted lines – constant amplitude loading.

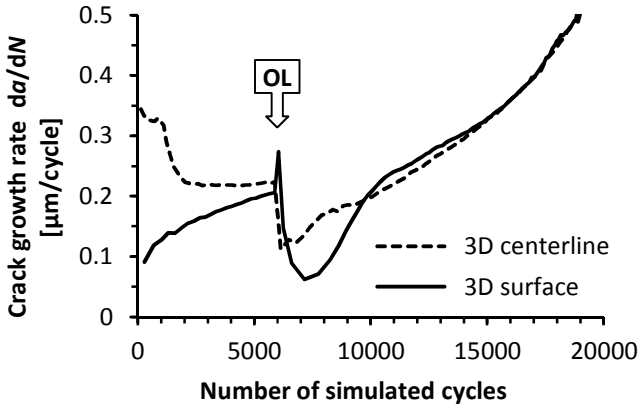


Fig. 4 – The effect of the overload cycle on the crack growth rate at the surface and in the midsection of the specimen

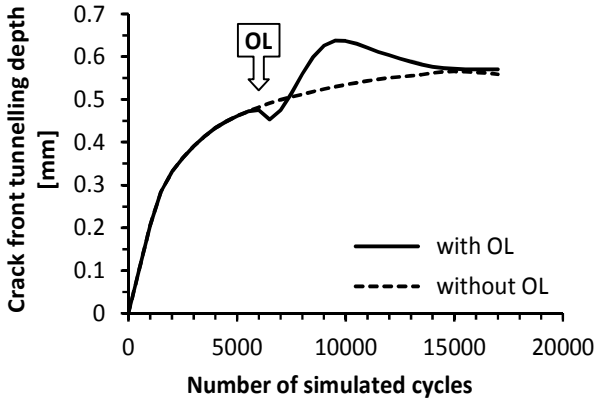


Fig. 5 – The effect of the overload cycle on the tunneling depth.

Summary

The simulation of the planar fatigue crack front shape evolution under constant amplitude loading with a single overload cycle was performed. The numerical model is based on a detailed FEM analysis of elastic-plastic stress and strain history ahead of the moving crack front along with the application of the Smith-Watson-Topper low-cycle fatigue damage parameter.

The three-dimensional nature of the model enables the study of miscellaneous phenomena such as the varying strain constraint and the crack closure along the crack front which leads to a varied local crack rate.

The comparison of the results of the two simulations, with and without the overload, leads to the following conclusions:

1. The retardation effect of the overload cycle is not uniform along the curved crack front.
2. The decrease of the crack rate is more significant at the material surface, where the plastic zone size is larger and the crack closure more intense, than in the midsection of the specimen.
3. The delay in retardation was primarily observed in the subsurface layer.

Acknowledgements

The authors would like to acknowledge funding from GA CR No. P108/10/2049.

References

[1] J. Schijve: *Fatigue of Structures and Materials* (Springer, 2009).

[2] A.H. Noroozi, G. Glinka and S. Lambert: Eng Fract Mech Vol. 75 (2008), p. 188-206.

[3] K.N. Smith, P. Watson and T.H. Topper: J Mater Vol. 5 (1970), p. 767–778.

[4] *Marc 2010 – Volume D: User Subroutines and Special Routines* (MSC.Software Corporation, 2010).

[5] A. Materna and V. Oliva, in: *Proceedings ECF17 – Multilevel Approach to Fracture of Materials, Components and Structures*, edited by J. Pokluda et al, VUTIUM Press, Brno (2008), p. 968–975.

[6] V. Oliva and I. Nedbal: *Properties of Al-Alloy 7010 (T7651–Fibrous Structure) – Low Cycle Behaviour*. [Technical Report V-KMAT-358/92], CTU-FNSPE, Praha (1992), 13 p.

© (2012) Trans Tech Publications, Switzerland
doi:10.4028/www.scientific.net/KEM.488-489.593

Energy Principle in Crack Propagation

SONG Haiyan[1, a], FAN Tao[1, b]

[1] College of Aerospace and Civil Engineering, Harbin Engineering University, Harbin 150001, China

[a] shyivg@yahoo.com.cn, [b] fantao19812005@ yahoo.com.cn

Keywords: energy release rate, crack propagation, energy functional, DCB speciment

Abstract. Fracture mechanics is an engineering discipline, which originated from Griffith energy-balance concept. The energy method is the most powerful analytical tool for fracture mechanics. Starting from energy principle in crack propagation, quasi-static governing equations and energy release rate of DCB specimen can be derived by energy principle in this paper. Finally, some correlative problems are discussed.

Introduction

Fracture mechanics is an engineering discipline. In its most basic form, it can be applied to relate the maximum permissible applied loads acting on a structural component to the size and location of a crack in the component. But it can also be used to predict the rate at which a crack can approach a critical size in fatigue or by enviromental influences, and can be used to determine the conditions in which a rapidly propagating crack can be arrested[1].

Based on the thermodynamic energy-balance concept, A.A. Griffith formulated a criterion for crack propagation of an ideally brittle material[2]. Irwin suggested that the Griffith theory for ideally brittle material could be modified and applied to both brittle material and metal that exhibit plastic deformation. When Griffith's concept was placed within a more general theoretical framework, Irwin's fracture mechanics theory had widely universality[3]. So the energy method is the most powerful analytical tool for fracture mechanics. The double cantilever beam (DCB) specimen was commonly used for the dynamic crack arrest experiment. Starting from energy principle in crack propagation, quasi-static governing equations and energy release rate of DCB specimen can be derived by energy principle in this paper. Finally, some correlative problems are discussed.

Energy release rate

Griffith A.A. approached the fracture of an ideally brittle material from a thermodynamic viewpoint[1]. It assumed that the work W done upon the body by the external forces was composed of strain energy U and surface energy S during an increment of crack propagation da, that is

$$dW = dU + dS \tag{1}$$

For a crack in a two-dimensional deformation field, it is convenient to define the energy as being per unit thickness of the body. If γ denotes the surface energy density per unit area, the two energy increments of fracture surfaces formed during crack propagation can be expressed as follow

$$dS = 2\gamma da \tag{2}$$

The energy release rate per unit thickness G was defined as follow[4]

$$G = -\frac{d(U-W)}{da} \tag{3}$$

where, $\frac{dW}{da}$ is the energy performed by the work of external forces per unit thickness during crack propagation, $\frac{dU}{da}$ is the increasing elastic energy caused by the work of external forces, $\frac{d(W-U)}{da}$ is the residual energy available for crack propagation. The physical meaning of Eq.(3) is that the work performed by external forces is equal to the increasing elastic energy and the energy available for crack propagation under constant load. According to strain energy theory of elasticity, Eq.(3) is rewritten as follow

$$G = -\frac{d\Pi}{da} \tag{4}$$

where, Π is the functional of potential energy, which consists of the functional obtained in fixed boundary and the functional obtained in variable boundary. The variational equation of energy functional Π is expressed as follow

$$\delta\Pi = -\iiint_V (\sigma_{ij,j} + \overline{F}_i)\delta u_i dV + \iint_{S_\sigma + S_c} (\sigma_{ij} n_j - \overline{T}_i)\delta u_i dS = 0 \tag{5}$$

where, σ_{ij} is stress, $\overline{F}_i$ is body forces, $\overline{T}_i$ is surface forces, u_i is displacement, S_σ is boundary of surface forces, S_c is boundary of crack surface.

Quasi-static governing equations and energy release rate of the DCB specimen

The model for dynamic crack propagation in the DCB specimen was presented in ref.[5]. It was commonly used for the dynamic crack arrest experiment. The DCB specimen and beam on an elastic foundation model is shown as Fig.1 (For the details, see ref.[1]).

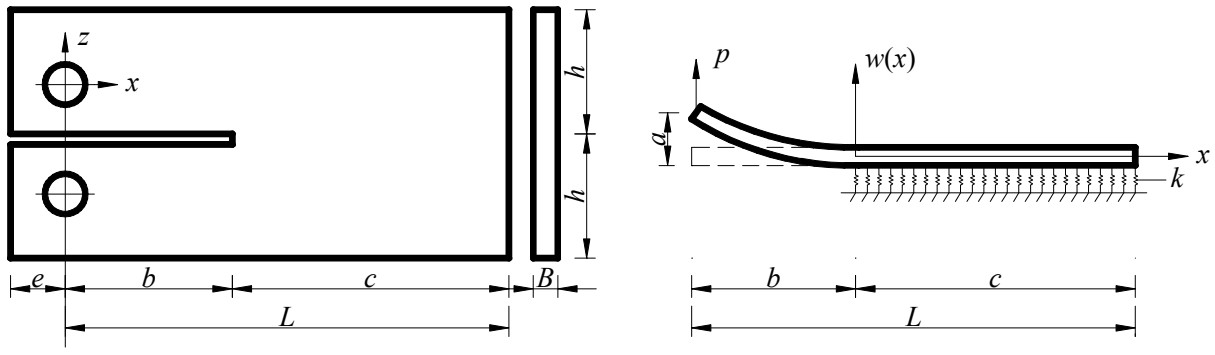


Fig.1 DCB specimen and beam on an elastic foundation model

Combined with assumed forms for the stress and displacement fields, governing equations of DCB specimen were obtained by Reissner's variational principle[6]. Although it is seldom made on a rigorous basis, the commonly used assumption that dynamic effects can be neglected in the arrest of rapid crack propagation in engineering structures is probably a reasonable one in most instances.

And quasi-static potential energy functional of DCB specimen Π per unit thickness can be expessed as follow

$$\Pi = \frac{1}{B}\int_{-e}^{L}[EI(\frac{\partial\varphi}{\partial x})^2 + \kappa\mu A(\frac{\partial w}{\partial x}-\varphi)^2 + (k_e w^2 + k_r\varphi^2)H(\theta_c-\theta)]dx \tag{6}$$

where, E is the elastic modulus, I is the centroidal moment of inertia, φ is the rotation of the centerline ($z=0$), κ is the shear deflection coefficient of beam, μ is the shear modulus, A is the area of cross-section, w is the vertical displacement of the centerline ($z=0$), k_e is the tension stiffness of the spring, k_r is the rotation stiffness of the spring, H is the Heaviside step function, θ is the parameter of crack propagation, θ_c is the critical value of θ.

Let variational functional $\delta\Pi = 0$, we have

$$\begin{aligned}\delta\Pi = \frac{2}{B}\int_{-e}^{L}[&EI\frac{\partial\varphi}{\partial x}\delta\frac{\partial\varphi}{\partial x} + \kappa\mu A(\frac{\partial w}{\partial x}-\varphi)\delta\frac{\partial w}{\partial x} - \kappa\mu A(\frac{\partial w}{\partial x}-\varphi)\delta\varphi + \\ &k_e wH(\theta_c-\theta)\delta w + k_r\varphi H(\theta_c-\theta)\delta\varphi + \frac{1}{2}(k_e w^2 + k_r\varphi^2)\delta H(\theta_c-\theta)]dx = 0\end{aligned} \tag{7}$$

Using Green theorem

$$\int_{-e}^{L} EI\frac{\partial\varphi}{\partial x}\delta\frac{\partial\varphi}{\partial x}dx = EI\frac{\partial\varphi}{\partial x}\delta\varphi\Big|_{x=-e}^{x=L} - \int_{-e}^{L} EI\frac{\partial^2\varphi}{\partial x^2}\delta\varphi dx \tag{8}$$

$$\int_{-e}^{L}\kappa\mu A(\frac{\partial w}{\partial x}-\varphi)\delta\frac{\partial w}{\partial x}dx = \kappa\mu A(\frac{\partial w}{\partial x}-\varphi)\delta w\Big|_{x=-e}^{x=L} - \int_{-e}^{L}\kappa\mu A(\frac{\partial^2 w}{\partial x^2}-\frac{\partial\varphi}{\partial x})\delta w dx \tag{9}$$

Substituting Eqs.(8) and (9) into Eq.(7), one can obtain

$$\begin{aligned}\delta\Pi = -\frac{2}{B}\int_{-e}^{L}\{&[EI\frac{\partial^2\varphi}{\partial x^2} + \kappa\mu A(\frac{\partial w}{\partial x}-\varphi) - k_r\varphi H(\theta_c-\theta)]\delta\varphi + \\ &[\kappa\mu A(\frac{\partial^2 w}{\partial x^2}-\frac{\partial\varphi}{\partial x}) - k_e wH(\theta_c-\theta)]\delta w\}dx + \\ &\frac{2}{B}EI\frac{\partial\varphi}{\partial x}\delta\varphi\Big|_{x=-e}^{x=L} + \frac{2}{B}\kappa\mu A(\frac{\partial w}{\partial x}-\varphi)\delta w\Big|_{x=-e}^{x=L} = 0\end{aligned} \tag{10}$$

The boundary conditions of DCB specimen are as follows

$$\varphi\big|_{x=-e} = \theta_c \ , \ \varphi\big|_{x=L} = 0 \tag{11}$$

$$w\big|_{x=-e} = a \ , \ w\big|_{x=L} = 0 \tag{12}$$

Considering Eqs.(11) and (12), Eq.(10) is rewritten as follow

$$\begin{aligned}\delta\Pi = -\frac{2}{B}\int_{-e}^{L}\{&[EI\frac{\partial^2\varphi}{\partial x^2} + \kappa\mu A(\frac{\partial w}{\partial x}-\varphi) - k_r\varphi H(\theta_c-\theta)]\delta\varphi + \\ &[\kappa\mu A(\frac{\partial^2 w}{\partial x^2}-\frac{\partial\varphi}{\partial x}) - k_e wH(\theta_c-\theta)]\delta w\}dx = 0\end{aligned} \tag{13}$$

Considering the arbitrary of $\delta\varphi$ and δw, the following equations can be derived from Eq.(13)

$$EI\frac{\partial^2\varphi}{\partial x^2}+\kappa\mu A(\frac{\partial w}{\partial x}-\varphi)-k_r\varphi H(\theta_c-\theta)=0 \quad (14)$$

$$\kappa\mu A(\frac{\partial^2 w}{\partial x^2}-\frac{\partial\varphi}{\partial x})-k_e wH(\theta_c-\theta)=0 \quad (15)$$

Eqs.(14) and (15) are quasi-static governing equations of DCB specimen. Under static loadin, it is always possible to obtain closed-form solutions to these equations. Substituting Eq.(6) into Eq.(4), the expression of energy release rate per unit thickness is rewritten as follow

$$G=\frac{1}{B}(k_e w^2+k_r\varphi^2)_{x=a} \quad (16)$$

The parameters k_e and k_r can be obtained from one-dimensional model, that are

$$k_e=\frac{2EB}{h} \quad (17)$$

$$k_r=\frac{\kappa\mu Bh}{2} \quad (18)$$

For the details, see ref.[7].

Summary

The energy method is the most powerful analytical tool for fracture mechanics. Starting from energy principle in crack propagation, quasi-static governing equations and energy release rate of DCB specimen can be derived by energy principle in this paper.

Acknowledgement

This research is supported by the Fundamental Research Funds for the Central Universities of China through Grant No.HEUCF100205.

References

[1] M.F. Kanninen, C.H. Popelar: *Advanced Fracture Mechanics* (Oxford University Press, New York 1985).

[2] A.A. Griffith: submitted to Philos. Trans. Roy. Soc., 1920, A221, pp.163-198.

[3] G.R. Irwin, in: *Handbuch der Physik*, edtied by S. Flgge, vol. 6, Springer-Verlag, Berlin, 1958, pp.551-590.

[4] M. Janssen, J. Zuidema and R.J.H. Wanhill: *Fracture Mechanics(2nd Edition)* (Spon Press, London and New York 2004).

[5] M.F. Kanninen, C. Popelar and P.C. Gehlen, in: *Fast Fracture and Crack Arrest*, edtied by G.T. Hahn, M.F. Kanninen, ASTM STP 627, Philadelphia, 1977, pp.19-38.

[6] S.J. Burns, C.L. Chow, in: *Fast Fracture and Crack Arrest*, edtied by G.T. Hahn, M.F. Kanninen, ASTM STP 627, Philadelphia, 1977, pp.228-240.

[7] M.F. Kanninen: submitted to J. Int. Fracture, 1974, 10, pp.415-430.

© (2012) Trans Tech Publications, Switzerland
doi:10.4028/www.scientific.net/KEM.488-489.597

Infrared Thermographic Analysis of Railway Brake Disc during Braking

Jeongguk Kim[a], Sung-Tae Kwon[b],
Sung-Cheol Yoon[c] and Byeong-Choon Goo[d]

Korea Railroad Research Institute, 360-1 Woulam Uiwang, South Korea 437-757

[a]jkim@krri.re.kr, [b]stkwon@krri.re.kr, [c]scyoon@krri.re.kr, [d]bcgoo@krri.re.kr

Keywords: Hot spots, Railway brake disc, Infrared thermography, Temperature evolution, Braking test

Abstract. The temperature monitoring on the surface of the railway brake disc was performed using high-speed infrared (IR) camera. The railway brake disc was developed for disc braking of maximum train speed of 180 km/h. The braking tests were conducted with a full scale dynamometer, and a high-speed infrared camera was employed to monitor temperature evolution on the brake disc during braking operation. The high-speed IR camera provides the measurement of temperature change during braking as well as the images of temperature contour on the brake disc surface. In general, the hot spot generation has been considered the main degradation mechanism in railway brake disc. In this investigation, damage evolution due to generation of hot spots on railway brake disc was investigated using the infrared thermography method.

Introduction

As the train speed increases, the brake system has been recognized as a critical and important part for the current railway applications [1-3]. Among the possible braking methods in railway brake applications, the mechanical braking is the typical braking type in railway industries. In consideration of mechanical braking, the hot spot generation has been considered as the main degradation mechanism in railway brake disc. Therefore, the understanding of hot spots, also called hot judder, which is undesirable low frequency vibrations developed by non-uniform contact area between brake pad and disc, is important for a better understanding of material design as well as enhancement of materials properties in railway brake disc [1-3]. Although there is an important aspect to understand hot spot phenomena in railway brake system, so far, not much attention has been given to the research of this field.

Also, infrared (IR) thermography is a powerful NDE technique for the characterization of thermal phenomenon in engineering components and/or systems including engineering materials [4-6]. The high-speed IR camera provides the measurement of temperature change during brake operation as well as the images of temperature contour on the brake disc surface.

In this investigation, damage evolution due to generation of hot spots on railway brake disc was investigated using the infrared thermography method. Moreover, based on obtained thermographic images of hot spots, the hot spots and thermal damage of railway brake disc during braking operation were qualitatively analyzed.

Brake Disc and Experimental Procedures

The Korean brake disc for passenger train, which is currently operating in the commercial line, was used for this investigation. The brake disc is composed of 12 holes with gray cast iron, and the disc has ventilation structure to emit the heat generated from the disc surface during brake operation.

An IR camera was used to monitor surface temperature change during braking operation. The high-speed capability of the IR camera guarantees high quality images as well as instant image capture during brake testing. Since the max speed of dynamometer was over 1,600 rpm, it was required to monitor the surface temperature analysis using high-speed infrared camera. In this investigation, the camera speed was 300 Hz with 300 thermographic image frames per second.

Braking tests were performed with brake disc and pads according to Korean railway standards (KRS) guideline with KRS BR 0007 (Non-Asbestos Disc Brake Pads). The braking force was 25 kN for both sides, and the initial braking speed (km/h) and sequences are as follows; 65, 35, 95, 150, 65, 125, 95, 95, 35, 125, 65, 65, 150, 95, 125, 125, 35, 35, 150, 65, 140, 180, 80, 100, 180, and 80 km/h. In order to prevent overheating of disc after braking, the next braking was proceeded when the temperature of brake disc reached under 60°C, which was measured by the thermocouples in brake disc. The thermocouples were embedded in the center of disc at 7 mm beneath the surface and 70 mm in depth. A total of 4 thermocouples were employed at the brake disc for this investigation. The braking tests were performed with the full scale dynamometer available at Korea Railroad Research Institute (KRRI).

Results and Discussion

Temperature Evolution of Disc and Pads During Braking. As described before, a total of 26 stops with different initial braking speed were performed, such as 35, 65, 80, 95, 100, 125, 140, 150, and 180 km/h. Among those temperature analyses results, in this paper, the cases of 65 km/h (relatively low speed) and 180 km/h (relatively high speed) were investigated.

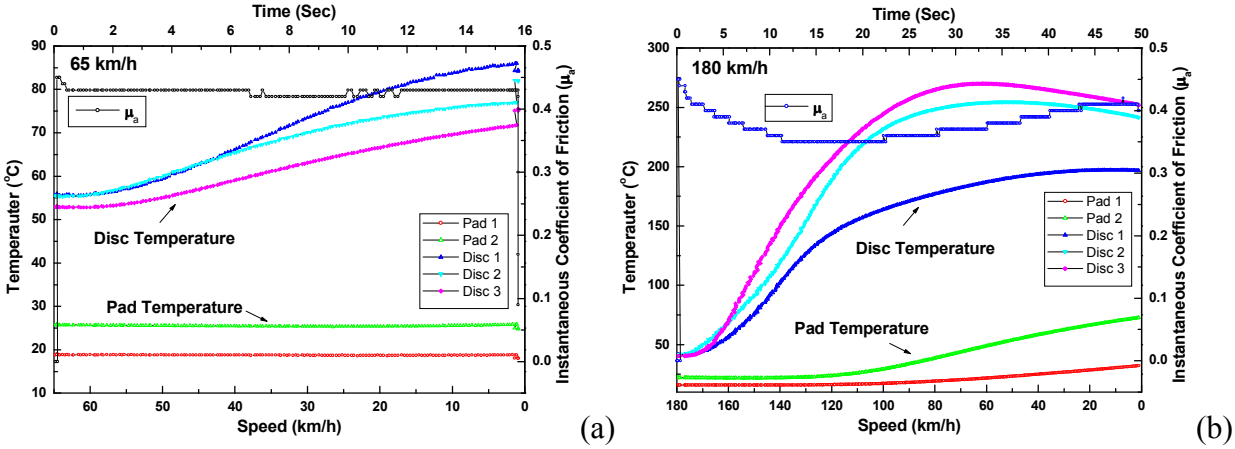


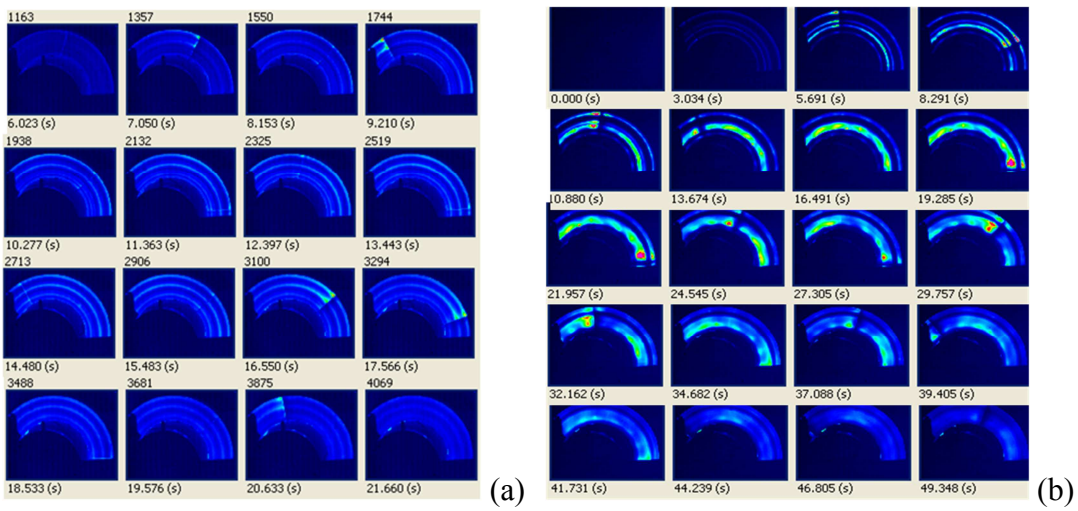
Fig. 1. Temperature evolution with instantaneous coefficient of friction during braking at the initial braking speeds of (a) 65 km/h and (b) 180 km/h. Note that the temperature measurements of disc and pad were conducted by thermocouples.

Figure 1 presents the temperature evolution results with instantaneous coefficient of friction during braking at the initial braking speeds of 65 and 180 km/h, respectively. Note that the temperature measurements of disc and pad were conducted by thermocouples. The temperature evolution during braking in both pads and discs showed gradual increases as the braking time increases. In terms of the instantaneous coefficient of friction, the initial value of instantaneous coefficient of friction was about 0.45 for the initial braking speeds of 65 and 180 km/h. However, as the braking time goes, the value of instantaneous coefficient of friction decreased for a while, then, the value of instantaneous coefficient of friction increased. The initial decreases in the instantaneous coefficient of friction could be due to increases in the temperature of brake disc or pads. Then, as the braking proceeded, the temperature of brake disc decreased after reaching the peak temperature as shown in Fig. 1. Those processes in temperature changes made the changes in the instantaneous coefficient of friction.

In Fig. 1(a), since the initial braking speed was relatively low with 65 km/h, not much changes in temperature of pads and the instantaneous coefficient of friction have been observed as compared with the case of 180 km/h. Especially, almost no changes in pad temperature have been observed during the braking, while the disc temperature increased gradually after the initial braking. The max disc temperature showed about 85°C at the time of complete stop.

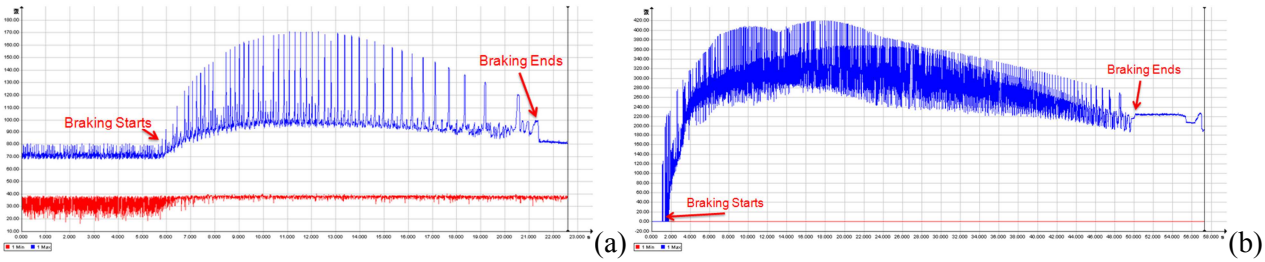
Unlike the temperature evolution pattern of the initial braking speed of 65 km/h, the temperature evolution pattern for 180 km/h exhibited somewhat different as shown in Fig. 1(b). Since the initial braking speed increased, much higher braking energy was required, and those differences made different temperature evolution patterns. For the case of 180 km/h, the disc temperature gradually increased, reached the highest temperature peak, and gradually decreased until final stop. Also, the temperatures of pads gradually increased until complete stop of brake disc as shown in Fig. 1(b).

Thermographic Analysis of Disc Surface Temperature During Braking. Figure 2 exhibits the thermographic evolution photos during braking tests at the initial braking speed of 65 km/h and 180 km/h, respectively. Also, the temperature profile during braking test for the initial braking speed of 65 km/h was shown in Fig. 3(a). The x-axis presents the time for braking, and the y-axis shows the temperature. The temperature profile in Fig. 3(a) was obtained based on the temperature analysis of the thermographic images in Fig. 2(a). In Fig. 3(a), the max temperature of disc surface at the beginning of braking showed about 80°C, and the disc surface temperature gradually increases as the braking continues. After reaching the max temperature of about 170°C, the gradual decreases in disc surface temperature have been observed. When the braking was completed, the surface temperature showed about 100°C. In order to correlate the temperature change with thermographic images, the thermographic images of brake disc were provided at the beginning stage, max temperature, and ending stage, respectively. Since the initial braking speed was relatively low value of 65 km/h, only the localized hot spot was observed at the max temperature in disc surface as shown in Fig. 2(a). The other stages of braking showed the thermal bands along the center line of the disc, which was expected in low braking speed, as shown in Fig. 2(a).



(a) (b)

Fig. 2. The thermographic evolution photos during braking tests at the initial braking speeds of (a) 65 km/h and (b) 180 km/h.



(a) (b)

Fig. 3. Temperature profiles during braking test for the initial braking speeds of (a) 65 km/h and (b) 180 km/h

Figure 2(b) presents the entire thermographic evolution photos during braking tests at the initial braking speed of 180 km/h. Unlike the braking pattern in relatively low braking speed shown in Figs. 2(a) and 3(a), Fig. 2(b) shows different braking pattern. In the light of thermographic images, at the relatively low speed of 65 km/h, the thermal band at the center line of the disc was observed. The

contour of thermal band was getting clear as the braking proceeded, and only localized hot spot could be observed. However, at the braking speed of 180 km/h, the thermographic pattern at the beginning stage of braking shows the formation of thermal bands with localized temperature evolution. The contour of thermal band was different from that of 65 km/h, and localized hot spots can be observed within thermal band as shown in Fig. 2(b). Especially, in Fig. 2(b), for the middle stage of braking, the growth of localized hot spots can be seen through the formation of the colony with small hot spots.

In terms of the temperature profile during braking, the temperature profile of 65 km/h showed the following steps; (1) initial temperature rising with slow slope, (2) reaching the max temperature (about 170°C), and (3) slow decreases in temperature until the stop (about 100°C) as shown in Fig. 3(a). The steps were well explained with the thermographic image results with the formation of thermal bands on disc surface without hot spots. However, the temperature profile of 180 km/h exhibits somewhat different aspects; (1) initial temperature rising with steep slope, (2) reaching the max temperature (about 420°C) with hump shape, and (3) gradual slow temperature decreases until the stop (about 230°C) as shown in Fig. 3(b). From the temperature analysis, the max temperature of hot spot in Fig. 2(b) was about 420°C.

From this investigation, the observation of surface temperature in brake disc during braking testing was introduced using the high-speed infrared camera. Based on these thermographic analysis results, the infrared thermography methods could be a powerful tool to monitor the temperature evolution during braking for different initial braking speeds.

Summary

The current research leads the following conclusions.
(1) Infrared thermography could be an effective way for the investigation of railway brake disc hot spot phenomena since the high-speed infrared camera could provide rapid and non-contact scanning of railway brake disc surfaces.
(2) The temperature evolution during brake operation in brake disc, which is currently employed for Korean railway operation, was introduced, and a high-speed infrared camera was used to measure the surface temperature of brake disc as well as for in-situ monitoring of temperature evolution.
(3) From the thermographic analysis results of disc surface temperature during braking, the temperature profile of the initial braking speed of 65 km/h showed the following steps; (1) initial temperature rising with slow slope, (2) reaching the max temperature (about 170°C), and (3) slow decreases in temperature until the stop (about 100°C). The steps were comparable with the thermographic image results with the formation of thermal bands on disc surface without hot spots. However, the temperature profile of 180 km/h exhibits somewhat different aspects; (1) initial temperature rising with steep slope, (2) reaching the max temperature (about 420°C) with hump shape, and (3) gradual slow temperature decreases until the stop (about 230°C)
(4) It was confirmed that the analyses of infrared thermographic images were necessary for the investigation of temperature evolution with thermal bands and hot spot phenomenon in railway brake disc.

References

[1] S. Panier, P. Dufrenoy, D. Weichert: Wear 256 (2004), p. 764.
[2] P. Dufrenoy: Proc. Instn Mech. Engrs Vol. 218 Part F: J. Rail and Rapid Transit, (2004), p. 17
[3] J. Kim, B.C. Goo, S.C. Yoon, and S.T. Kwon: Key Engineering Materials, Vols. 385-387 (2008), p. 669.
[4] J. Kim and P.K. Liaw: Journal of Engineering Materials and Technology, Vol. 127, (2005), p. 8.
[5] J. Kim, J.H. Lee, J.D. Chung, Y.U. Jeong: Key Engineering Materials, Vols. 297-300, (2005), p. 2533.
[6] J. Kim and P.K. Liaw: Materials Science and Engineering A, Vol. 409, (2005), p. 302.

© (2012) Trans Tech Publications, Switzerland
doi:10.4028/www.scientific.net/KEM.488-489.601

Structure Buckling Reliability Analysis for the Underwater Super-Speed Supercavitating Vehicle

Hai An [a], Weiguang An, Ling Zhou

College of Aerospace and Civil Engineering; Harbin Engineering University; Harbin 150001; Heilongjiang; China;

[a] anhai@hrbeu.edu.cn

Key words: structure buckling reliability analysis; semi-analytical FEM; critical buckling load coefficient; Limit Step Length Iteration Method; underwater super-speed supercavitating vehicle

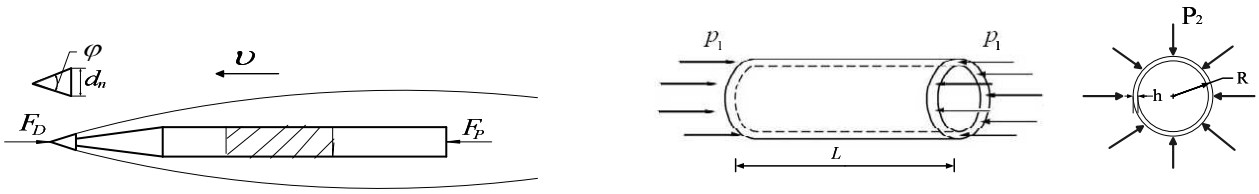
Abstract. An approach to the structure buckling reliability analysis for the underwater super-speed supercavitating vehicle is proposed in this paper. The circular ribbed part-cabin of the vehicle is simplified as the thin cylindrical shell with variable thickness. The critical buckling load coefficient of the thin cylindrical shell is solved by using semi-analytical FEM (finite element method). The structure buckling reliability index is obtained by SFEM (Stochastic Finite Element Method) combining Limit Step Length Iteration Method. A numerical example is given to analyze influences of the number of circular ribs, the coefficient of variation of elastic modulus and the coefficient of variation of the thickness of the thin shell on the structure buckling reliability index.

Introduction

Supercavitation is formed when the vehicle high-speed travels under water. In order to satisfy the demands for drag reduction and being encased by cavity, the supercavitating vehicle is designed to be slender body with high slenderness ratio. Because the super-speed supercavitating vehicle is acted on by the large longitudinal drag force of the cavitator of the front and the engine thrust of the trail, it is necessary to analyze structure buckling reliability for part-cabins of the vehicle. For this reason, this paper presents an approach to the structure buckling reliability analysis for the underwater super-speed supercavitating vehicle. The approach proposed in this paper give an applicable implication for the application of structure buckling reliability analysis for the underwater super-speed supercavitating vehicle.

The critical buckling load coefficient of the thin cylindrical shell

Force Analysis on the Thin Cylindrical Shell. The ventilated cavitation vehicle sails in a way as Fig.1(a). If not considering the trail to slide on the cavitation wall, the vehicle is acted on by the cavitator drag of the front, the engine thrust of the trail and the pressure in the cavitation. The sailing supercavitating vehicle is shown as Fig.1 (a). The dash area denotes the thin cylindrical shell part-cabin, d_n is the diameter of cavitator, φ is the angle of cone of cavitator, F_D is the drag of cavitator, F_P is the engine thrust. The geometric dimensioning and force model are shown as Fig.1 (b). R is the radius of the middle section, L is the length of the thin shell, is the thickness of the thin shell, P_1 is the axial stress, P_2 is the circular stress brought by the pressure in cavitation.



(a) (b)

Fig.1 The force model and geometric dimensioning of the thin cylindrical shell of supercavitating vehicle

The drag of cavitator F_D can be obtained as follows

$$F_D = \frac{1}{2}\rho_w \upsilon^2 A C_x(\alpha,0) = \frac{C_{x0}(1+\alpha)\rho_w \upsilon^2 \pi {d_n}^2}{8} \tag{1}$$

Where, ρ_w is the density of water, υ is the velocity of the vehicle, A is the cross-section area, α is the cavitation number, C_{x0} is the coefficient of drag of cavitator.

The axial stress P_1 is

$$p_1 = \frac{F_D}{2\pi Rh} = \frac{C_{x0}(1+\alpha)\rho_w \upsilon^2 \pi {d_n}^2}{16Rh} \tag{2}$$

The circular stress P_2 is

$$p_2 = \rho_w g H - \frac{1}{2}\rho_w \upsilon^2 \alpha \tag{3}$$

Then, the buckling stress $\boldsymbol{\sigma}$ of the thin cylindrical shell is

$$\boldsymbol{\sigma} = \begin{bmatrix}\sigma_x & \sigma_\theta & \tau_{x\theta}\end{bmatrix}^{\mathrm{T}} = \begin{bmatrix} p_1 & \dfrac{p_2 R}{h} & 0 \end{bmatrix}^{\mathrm{T}} \tag{4}$$

The buckling characteristics equation of the thin cylindrical shell

The cylinder coordinate system of the thin cylindrical shell is founded. The origin of coordinates is founded on the middle section of one side of cylindrical shell. Here x is the axial coordinate, r is the radial coordinate, θ is the angular coordinate. According to thin-shell theory, the strain of the thin cylindrical shell is $\boldsymbol{\varepsilon} = \begin{Bmatrix}\varepsilon_x & \varepsilon_\theta & \gamma_{x\theta}\end{Bmatrix}^{\mathrm{T}}$. According to the theory of large deflection, the strain can be expressed as follows

$$\boldsymbol{\varepsilon} = \boldsymbol{\varepsilon}^l + \boldsymbol{\varepsilon}^{nl} \tag{5}$$

Where, $\boldsymbol{\varepsilon}^l$, the vector of linear strain, and $\boldsymbol{\varepsilon}^{nl}$, the vector of non-linear strain, can be obtained through Yamaki geometric equation[1] and Hermite interpolation function.

The elastic and geometry stiffness matrixes of element of the *n*th harmonic wave can be obtained according to characteristics of orthogonality between linear/ non-linear strain energy equations and trigonometric function. The elastic stiffness matrix of element of the *n*th harmonic wave can be expressed as follows

$$\boldsymbol{k}_n^e = \pi \int_0^{L^e}\int_{-h/2}^{h/2} \boldsymbol{B}^{l\mathrm{T}}(n,r,x,\theta)\,\boldsymbol{D}\boldsymbol{B}^l(n,r,x,\theta) R\,dr\,dx\,d\theta. \tag{6}$$

Where, $\boldsymbol{B}^{l}(n,r,x,\theta)$ is the linear strain matrix, $\boldsymbol{D}$ is the elastic matrix.

The geometry stiffness matrixe of element of the *n*th harmonic wave can be expressed as follows

$$\boldsymbol{kg}_{n}^{e}=\pi\int_{0}^{L^{e}}\int_{-h/2}^{h/2}\boldsymbol{B}^{nl\mathrm{T}}(n,r,x,\theta)\hat{\boldsymbol{\sigma}}\boldsymbol{B}^{nl}(n,r,x,\theta)Rdrdxd\theta \tag{7}$$

Where, $\boldsymbol{B}^{nl}(n,r,x,\theta)$ is the non-linear strain matrix, $\hat{\boldsymbol{\sigma}}$ is the elastic matrix.

So, the buckling characteristics equation of the thin cylindrical shell can be obtained as follows

$$\left(\boldsymbol{K}_{n}+\lambda\boldsymbol{Kg}_{nref}\right)\Delta\boldsymbol{\delta}_{n}=0 \qquad n=1,2,\cdots \tag{8}$$

Where, $\boldsymbol{K}_{n}$ is the global elastic stiffness matrix, $\boldsymbol{Kg}_{nref}$ is the global geometry stiffness matrix acted on by loads.

The minimum eigen value λ_{cr} solved through Eqs.(8) is the critical buckling load coefficient. The eigen vector $\Delta\boldsymbol{\delta}_{n}$ corresponding to λ_{cr} is the failure wave shape. In this paper, semi-analytical FEM is employed to solve the critical buckling load coefficient λ_{cr}, because this method has higher accuracy and the fewer calculating degrees of freedom and work than traditional FEM.

Buckling reliability analysis for the thin cylindrical shell

The buckling safety margin equation of the thin cylindrical shell is founded according to the critical buckling load coefficient λ_{cr} as follows

$$M=g(\boldsymbol{X})=\lambda_{cr}-\lambda \quad . \tag{9}$$

Where, $\boldsymbol{X}=\left[X_{1},X_{2},\cdots X_{m}\right]^{\mathrm{T}}$ is the stochastic vector.

The reliability index of system is solved by using SFEM because of randomness of variables. The first partial derivative of the performance function is

$$\frac{\partial g}{\partial X_{i}}=\frac{\partial\lambda_{cr}}{\partial X_{i}}-\frac{\partial\lambda}{\partial X_{i}} \quad . \tag{10}$$

Where, the critical buckling load coefficient λ_{cr} is the implicit function of stochastic variables, the derivative to other variables is

$$\frac{\partial\lambda_{cr}}{\partial X_{i}}=\frac{-\Delta\boldsymbol{\delta}_{n}^{\mathrm{T}}\left(\dfrac{\partial\boldsymbol{K}_{n}}{\partial X_{i}}+\lambda_{cr}\dfrac{\partial\boldsymbol{Kg}_{nref}}{\partial X_{i}}\right)\Delta\boldsymbol{\delta}_{n}}{\Delta\boldsymbol{\delta}_{n}^{\mathrm{T}}\boldsymbol{Kg}_{nref}\Delta\boldsymbol{\delta}_{n}} \quad . \tag{11}$$

Because Eqs.(9) is the implicit limit function with higher non-linear degree, Limit Step Length Iteration Method [2] is adopted to solve Eqs.(10).

Numerical example

The circular ribbed part-cabin of the super-speed ventilated cavitation vehicle is shown in Fig.2. The circular ribbed spacing $L_{s}=0.6m$, the circular ribbed width $L_{w}=0.2m$.The sailing length $H=100m$, the sailing velocity $\upsilon=120m/s$, the water density $\rho_{w}=1025kg/m^{3}$, the saturated vapour pressure is 2350Pa, the angle of cone of cavitator $\varphi=180^{\circ}$, Poisson's ratio is 0.3. The other parameters are shown in Tab.1. Elastic modulus E, the mean value is 2.1×10^{11}Pa, the coefficient of variation is 0.06; the radius of the middle section R, the mean value is 266.5mm, the coefficient of variation is 0.003; the length L, the mean value is 4.0m, the coefficient of variation

is 0.005; the thickness h, the mean value is 4.0mm, the coefficient of variation is 0.08; the diameter of cavitator d_n, the mean value is 100mm, the coefficient of variation is 0.007; the ventilated cavitation number α, the mean value is 0.0788, the coefficient of variation is 0.09; the ribbed thickness h_f, the mean value is 5.5mm, the coefficient of variation is 0.05.

Adopting the buckling reliability analysis method above, the buckling reliability index of the thin cylindrical shell with six uniform spacing circular ribs can be solved to be $\beta = 3.07$, and the buckling reliability index with nine uniform spacing circular ribs is $\beta = 7.39$. Discuss the influence of changes of the coefficients of variation on the buckling reliability index, shown in Fig.3. Take the coefficient of variation of each variable in the numerical example as the standard V_0.

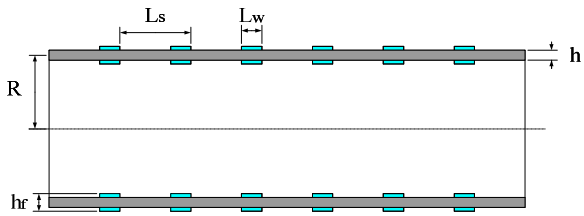


Fig.2. The circular ribbed thin cylindrical shell

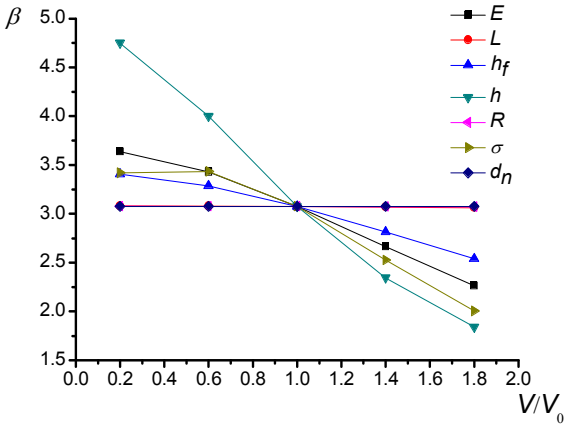


Fig.3. The variety of buckling reliability index with the change of coefficient of variation

It can be seen from Fig.3, the influences of the changes of coefficients of variation of the thickness h, elastic modulus E and the ribbed thickness h_f on the buckling reliability index are more obvious than other variables. The buckling reliability indexes fall sharply with the increases of their coefficients of variation.

Conclusions

This paper adopts SFEM to analyze the buckling reliability for the underwater super-speed supercavitating vehicle. According to the results of numerical example, the buckling reliability index can be improved by increasing the number of circular ribs, controlling material property and the coefficients of variation for geometrical dimension.

References

[1] Massimo Ruzzene: Dynamic Buckling of Periodically Stiffened Shells: Application to Supercavitating Vehicles. Int. J. Solids Struct., Vol.41(2004), P. 1039-1059

[2] Gong Jinxin: Reliability Methods for Engineering Structure, Dalian University of Technolgy Press, Dalian(2003), in press

© (2012) Trans Tech Publications, Switzerland
doi:10.4028/www.scientific.net/KEM.488-489.605

Finite Element Analysis of Secondary Cracks at a Crack Front under Pure Mode III Loading

M. Ressel[1, a], H. Theilig[2, b]

[1]Vattenfall Europe Generation AG, Production Hydro, Hohenwarte, Germany

[2]Department of Mechanical Engineering, University of Applied Sciences Zittau/Görlitz, Germany

[a]matthias.ressel@vattenfall.com, [b]h.theilig@hs-zigr.de

Keywords: crack growth, fracture criteria, mixed-mode loading, initial secondary cracks

Abstract. Several hypotheses and concepts exist for the prediction of crack deflection angles from the analysis of the undisturbed stress distribution at the crack front. In this paper, a finite element analysis of small penny shaped secondary cracks with deflection angles $\psi_0 = \pi/4$ at a pure mode III loaded crack front is presented. The results are compared with the solutions of the well-known 3D fracture criteria. The fracture mechanical analysis is performed by the highly effective MVCCI-method.

Introduction

The most important factor which determines the fracture surface morphology of a growing crack is the state of stress at the given crack front. It is well known that in cases with general 3D mixed mode loading crack growth occurs by initiating of a number of new secondary cracks in planes defined by the deflection angles φ_0 and ψ_0. This is consistent with the no-twist requirement of continuous crack growth in brittle solids [1]. Several hypotheses and concepts are given for the prediction of the crack deflection angles [2]. Especially for 3D cases, it is obvious that the basis of these concepts is only the known near-field solution for the undisturbed stress distribution at the crack front. Initial secondary cracks usually are not assumed in the models of these criteria. One reason for this is the diversity of the possible influences, especially the geometry, the number and the location of these propagating cracks at the primary crack front. In this paper, some first results of 3D-finite element analyses are presented for assumed secondary cracks at a crack front under pure mode III loading. Penny shaped secondary cracks are modeled that are expected to be found in this case [3]. As the primary crack problem, a central circular crack in a cylindrical bar under torsion has been chosen. This allows the analyzing of the interaction of the individual secondary cracks with each other without greater problems. The computational fracture analysis was performed by the effective modified virtual crack closure integral (MVCCI)-method [5,6].

3D-fracture criteria for pure out of plane shear

As the crack front cannot twist as a whole in the case of 3D-mixed mode loading, several new secondary cracks will be initiated at the given crack front. These cracks grow in planes, which are defined with the deflection angles φ_0 and ψ_0, Fig. 1. In the case of a pure Mode III loading these cracks are at an early stage obviously circular and grow in planes with $\varphi_0 = 0$ and $\psi_0 = \pi/4$. It can be seen in the experimental findings in Fig. 2 [3]. The well-known 3D fracture criteria give for $K_I = 0$ and $K_{II} = 0$ the predictions of the equivalent stress intensity factor and the deflection angles [2]:

$$K_v = K_{III},\ \varphi_0 = 0,\ \psi_0 = \pi/4. \tag{1}$$

For the initial secondary cracks it should be expected to have a pure Mode I load at least at $\gamma = 0$ with $K_I = K_V$ in the plans $\psi_0 = \pi/4$, Fig. 3.

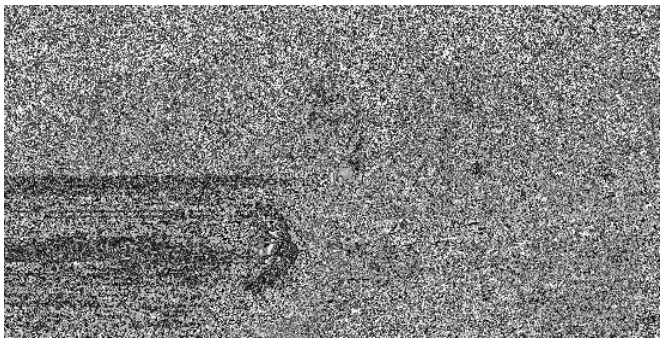


Figure 1: Experimental findings of secondary cracks under general mixed mode loading of the primary crack [4]

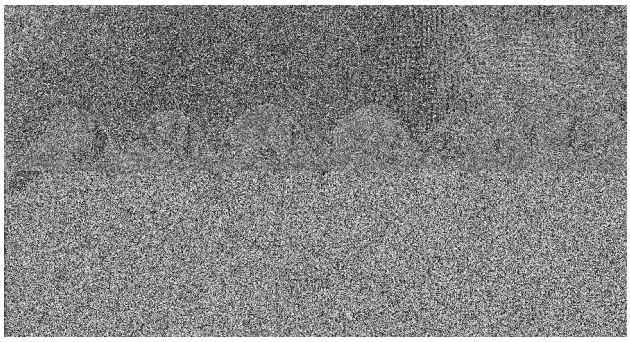


Figure 2: Experimental findings of secondary cracks under pure mode III loading of the primary crack (view perpendicular to the secondary cracks) [3]

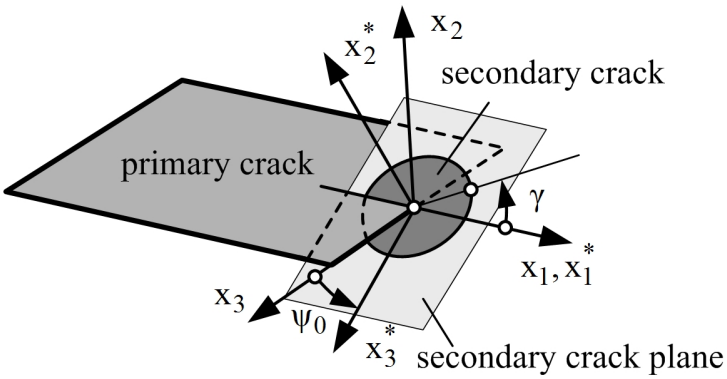


Figure 3: A circular initial secondary crack at a crack front under pure mode III loading.

Dimensions and loading of the model:
R = 10 mm
L = 40 mm,
a = 2 mm
M = 10^6 Nmm



Figure 4: Cylinder with central penny shaped crack under torsion

3D FE model

Pure mode III will be found at central penny shaped crack in cylindrical bar subjected with torsion at its ends, Fig. 4. In a first step, the numerical solutions for the stress intensity factors (SIFs) at the crack front are obtained from a FE-model by using MVCCI-methods for 3D problems [5,6]. The numerical results are compared with the well-known solution for a very long cylinder [7].

A half of the cylinder was modeled using the geometric symmetry of the crack problem and meshed with eight-node brick elements. Good results were found for a fine regular mesh along the crack front. Further, the numerical calculations have been shown, that for ratios L/R greater than four the change of accuracy was less than 2%. Therefore all numerical calculations has been carried out with L = 4R.

In a next step, cyclic boundary conditions were introduced. With this concept, it was possible to model a different number of secondary cracks along the crack front only by changing the angle of the sector, Fig. 5. Six and twelve cracks along the primary crack front are chosen. This means sectors with angles of $\pi/6$ and $\pi/3$. Especially consistent boundary conditions for cyclic symmetry and the use of the MVCCI-method had to be found for this approach.

For finally taking into account the secondary cracks along the primary crack front the adjacent volumes were regularly meshed now with 20-node brick elements, Fig. 6. This meshing strategy should be preferred for good results by the MVCCI-method. The remaining part of the model was meshed with tetrahedrons and pyramids are used at the boundaries of the regular meshed regions.

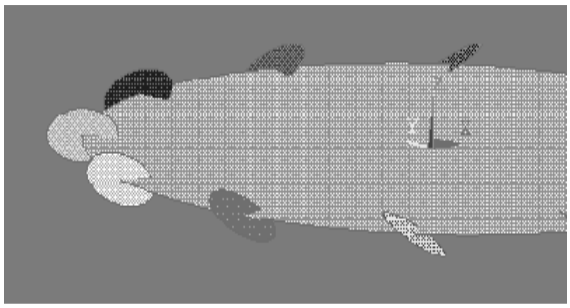


Figure 5: Initial secondary cracks at the penny shaped primary crack

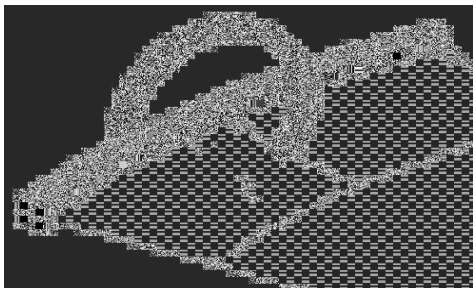


Figure 6: Regular brick meshing around the crack fronts for analysis with the MVCCI-method (faces of the secondary crack are not displayed)

Results and discussion

The results presented were found on a model with the geometrical parameters given in Fig. 4. With a loading of $M = 10^6$ Nmm the reference solution of [7] results in $K_{III} = 135.46$ N/mm$^{3/2}$. Therefore all numerical calculated SIFs are given normalized with this value as $f_i = K_i/135.46$ N/mm$^{3/2}$, i = I, II, III. The radius of the penny shaped secondary cracks was chosen as $a_{sec} = 0.2$ mm. The calculated SIFs along the primary crack front for twelve secondary cracks are given in Fig. 7.

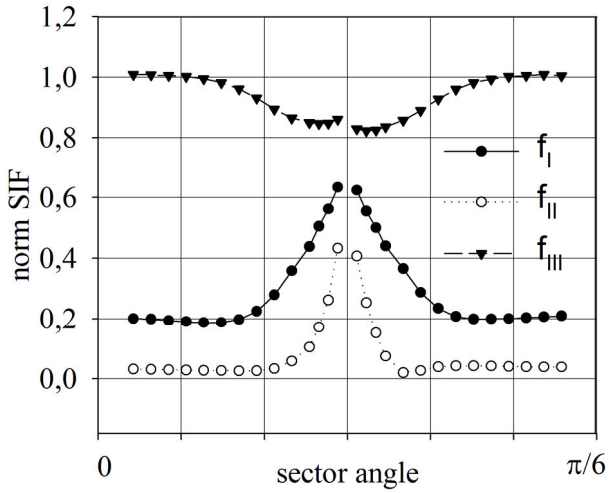


Figure 7: Normalized SIFs along a sector of the primary crack front with 12 secondary cracks

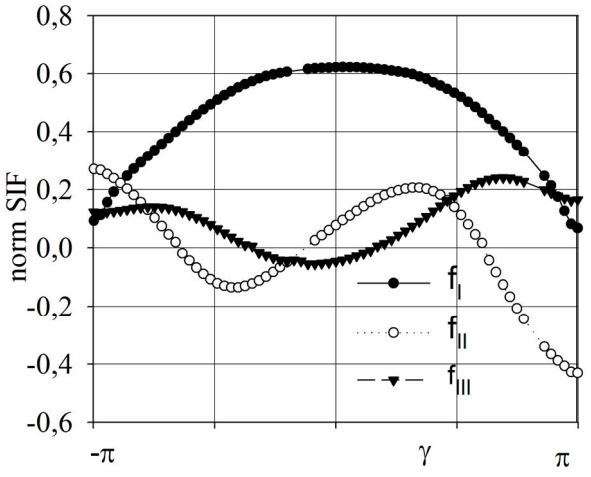


Figure 8: Normalized SIFs at the crack fronts of the 12 secondary cracks

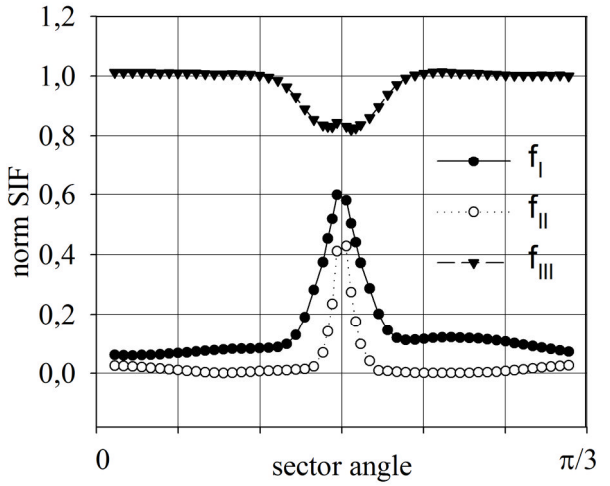


Figure 9: Normalized SIFs along a sector of the primary crack front with six secondary cracks

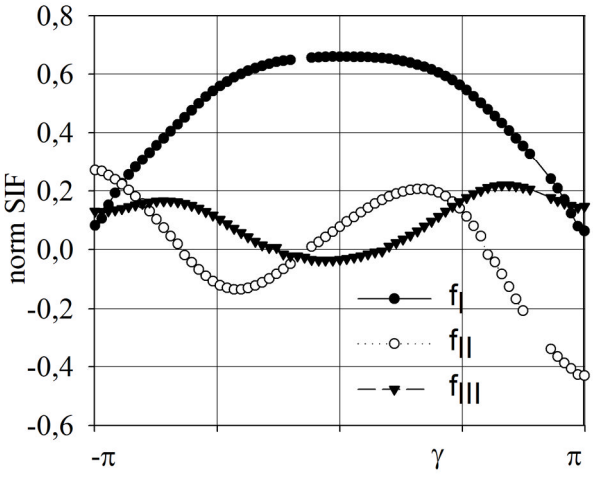


Figure 10: Normalized SIFs at the crack fronts of the six secondary cracks

As expected the secondary cracks release parts of the anti-plane shear load at the primary crack front. The value of K_{III} is still about 80%. Next to the secondary cracks, Mode I and II loads appear which leads to a spatial mixed mode situation. The assumed geometry of secondary cracks in the predicted plane $\psi_0 = 45°$ allows a crack opening at the primary crack which can be seen by the value of K_I along the primary crack front. The SIFs at the crack fronts of the secondary cracks (Fig. 8) show for $\gamma = 0$ an almost pure Mode I loading. Crack opening with Mode I loading at the primary crack leads to a Mode II and III loading situation at the secondary ones.

For a sector angle of $\pi/3$, which means six secondary cracks along the primary front the SIFs calculated for the secondary cracks, are almost the same, Fig. 10. A difference is noticeable at the primary crack front (Fig. 9) where now between the secondary cracks the load situation of the given undisturbed crack problem can be found.

Not surprising there is a Mode I loading at $\gamma = 0$. The value of K_I is less than expected after Eq. 1. A mixed Mode situation with Modes I, II and III appears at the crack fronts of the secondary cracks apart from $\gamma = 0$ and at the primary crack next to the secondary cracks. The ideal initial secondary cracks should have pure Mode I load by releasing the Mode III load at the primary one. Therefore penny shaped secondary cracks of finite size cannot be the result of fatigue crack growth at a purely Mode III loaded crack front. This can easily be seen from the resulting SIFs along the crack front of the secondary cracks. It can be concluded, that a crack formed by fatigue crack growth should not grow in the plane $\psi_0 = \pi/4$ apart from a small area next to $\gamma = 0$. Especially the intersections of the secondary cracks with the crack faces of the primary crack can be expected to be outside this plane.

The size of secondary cracks modeled was to be as small as possible with respect to the initial state. This was limited by the regularly meshed volume around the primary crack front. Therefore, the size of the secondary cracks can be a source of inaccuracy when comparing results with the prediction by 3D criteria. Nevertheless, it should be taken into account that a penny shaped crack of whatever small size would cause displacements in its surrounding as the ones found here. By scaling down the size of the secondary cracks the only thing that is changed is the ratio of the radiuses of the cracks a_{sec}/a. It seems therefore be more effective to search for a shape of the secondary cracks that would fulfill the Mode I condition in a better way.

Summary

On experiments small secondary cracks appeared if mode III loading was dominating. Expecting these secondary cracks to be penny shaped in the predicted plane leads to a spatial mixed mode situations along the primary and secondary crack fronts. In a next step the shape is to be varied in a way that gives almost pure mode I loading along the secondary crack fronts.

References

[1] Hull, D.: Int. J. Fract. 62 (2003), pp. 119 - 138.

[2] Richard, H. A, Buchholz, F.-G., Kullmer, G., Schöllmann, M.: Key Engineering Materials Vols. 251 - 252 (2003) pp. 251 - 260.

[3] Knaus, W.G.: Int. J. Fract. 6 (1970) pp. 183 - 187

[4] Buchholz, F.-G.: personal communication (2008)

[5] Buchholz, F.-G. in: Fracture mechanics, edited by A.V. Krishna Murthy, F.-G. Buchholz, Interline Publ., Bangalore (1994) pp. 7 - 12

[6] Shiwakumar, K.N., Tan, P.W., Newman, J.C. Jr.: Int. J. Fract. 36 (1988), R43- R50

[7] Benthem, J. P., Koiter, W. T.: in: G. C. Sih, Mechanics of fracture I, Noordhoff International Publishing Leyden (1973).

© (2012) Trans Tech Publications, Switzerland
doi:10.4028/www.scientific.net/KEM.488-489.609

On the evaluation of the R-curve including the self-weight contribution: mortar

N. Dourado[1, a] and S. Morel [2, b]

[1] *CITAB – Universidade de Trás-os-Montes e Alto Douro, Quinta de Prados 5000-911, Vila Real, Portugal*

[2] Université de Bordeaux I, UMR 5295 (CNRS), Institut de Mécanique et d'Ingénierie - Bordeaux (I2M), Dept. Génie Civil et Environnemental (GCE), Bordeaux, F-33000, France

[a] nunodou@gmail.com, [b] stephane.morel@u-bordeaux1.fr

Keywords: R-curve; Equivalent crack length; Fracture Process Zone; Cohesive zone model; Bilinear damage law; Self-weight.

Abstract. In fracture tests involving the Single-Edge-Notched beam loaded in Three or Four-Point-Bending as well as in other specimen shapes, the specimen weight contributes to the overall loading of the system. Unless special methods are put into practice, the contribution of the specimen weight is not compensated, leading to misevaluations of fracture parameters obtained in the experiments. In this work a method taking into account the exact contribution of the specimen self-weight is proposed to evaluate the Resistance-curve of mortar. Cohesive crack modeling accounting for the structure self-weight is used to generate the necessary load-displacement response to perform the validation of the proposed method.

Introduction

In notched structures, the fracture behavior of quasibrittle materials is characterized by the existence of a large Fracture Process Zone (FPZ) where various toughening mechanisms take place such as microcracking, crack branching or crack bridging [1]. Consequently, Linear Elastic Fracture Mechanics (LEFM) can not be applied, but rather Non-Linear Fracture Mechanics. An adaptation of LEFM (known as *eq*LEFM) provides a useful approximation of the quasibrittle failure, attributing the increase in the structure compliance, owing to the development of the FPZ, to the propagation of an effective crack, i.e., a sharp traction-free crack with a given length (called equivalent linear elastic crack length: a) which gives, according to LEFM, the same compliance as the one of the actual crack with its FPZ [2]. The main consequence of the development of a non-negligible FPZ is the so-called Resistance-curve (R-curve), which represents the evolution of the resistance to crack growth as a function of the equivalent linear elastic crack length $G_R(a)$.

In this work an Exact method is proposed to estimate the R-curve, within the framework of equivalent LEFM, taking into account the specimen self-weight. The method is numerically validated by means of the cohesive crack modeling (CCM) using a bilinear damage law, with a characteristic set of cohesive parameters characteristic of mortar. The FE analyses involve the simulation of the Single-Edge-Notched beam with different material densities.

R-curve evaluation: Exact method

The displacement of a point in the half-height mid-span (Figure 1) is given by the contribution of both the central load P and the linear distributed load q, corresponding to the beam weight,

$$\delta_P(a) = \delta_{PP}(a) + \delta_{Pq}(a) = \lambda_{PP}(a)\,P + \lambda_{Pq}(a)\,q \tag{1}$$

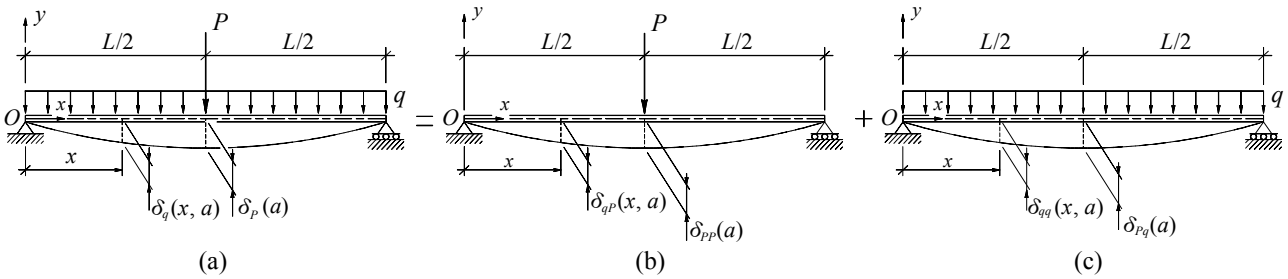


Fig. 1: SEN-TPB (a) showing the superposition of (b) central load P and (c) distributed load q.

(with λ_{PP} expressed in [m/N] and λ_{Pq} in [m^2/N], since P and q are stated in [N] and [N/m], respectively). It is possible to define the displacement field obtained along the specimen axis (middle-axis x in Figure 1), with respect to the abscissa x, and for a given crack length a, as follows,

$$\delta_q(x,a) = \delta_{qP}(x,a) + \delta_{qq}(x,a) = \lambda_{qP}(x,a)\,P + \lambda_{qq}(x,a)\,q \tag{2}$$

Let us consider the load-displacement response (P-δ_P) illustrated in Figure 2. In this figure the shift toward the right, noted as $\delta_{Pq}(a_0)$, corresponds to the initial displacement (measured in the axis of the applied load P) due to the specimen self-weight q, obtained for the initial crack length a_0, prior to the application of the external load P. As illustrated in Figure 2, the initial compliance $\lambda(a_0)$ may be defined from two points of the load-displacement curve [(δ_{P1}, P_1) and (δ_{P2}, P_2)] in the linear elastic domain, i.e., $\lambda(a_0) = \Delta\delta_P(a_0)/\Delta P$ (with $\Delta P = P_2 - P_1$). Thus, according to Eq. (1),

$$\begin{aligned}\Delta\delta_P(a_0) &= \delta_{PP2}(a_0) - \delta_{PP1}(a_0) \\ &= [\delta_{PP2}(a_0) + \delta_{Pq}(a_0)] - [\delta_{PP1}(a_0) + \delta_{Pq}(a_0)] \\ &= \lambda_{PP}(a_0)(P_2 - P_1)\end{aligned} \tag{3}$$

which yields,

$$\lambda(a_0) = \Delta\delta_P(a_0)/\Delta P = \lambda_{PP}(a_0) \tag{4}$$

Therefore, the initial compliance of the load-displacement curve (Figure 2) corresponds to the compliance related to the applied load P.

As shown in Figure 2, the equivalent crack length a corresponding to a given point M of the load-displacement response can be estimated from the slope $\gamma(a)$ of the straight line (OM), through

$$\gamma(a) = \delta_P(a)/P \tag{5}$$

According to Eq.(1), one can establish,

$$\gamma(a) = \frac{\lambda_{PP}(a)\,P + \lambda_{Pq}(a)\,q}{P} = \lambda_{PP}(a) + \lambda_{Pq}(a)\frac{q}{P} \tag{6}$$

Hence, knowing the applied load P associated to point M (Figure 2), as well as the distributed load q and the compliance functions: $\lambda_{PP}(a)$ and $\lambda_{Pq}(a)$, then it is possible to estimate the equivalent crack length a, which allows determining the value $\gamma(a)$. As a consequence, the equivalent crack length a can be assessed for all points of the P-δ_P curve.

Let us now consider any two consecutive points [$\delta_P(a_1)$, P_1] and [$\delta_P(a_2)$, P_2] of the load-displacement curve [with $\delta_P(a_2) > \delta_P(a_1)$]. As crack advances of an infinitesimal extension (i.e., $\delta a = a_2 - a_1$), the released elastic strain energy δE, can be expressed as

$$\delta E = \delta W - \delta U \tag{7}$$

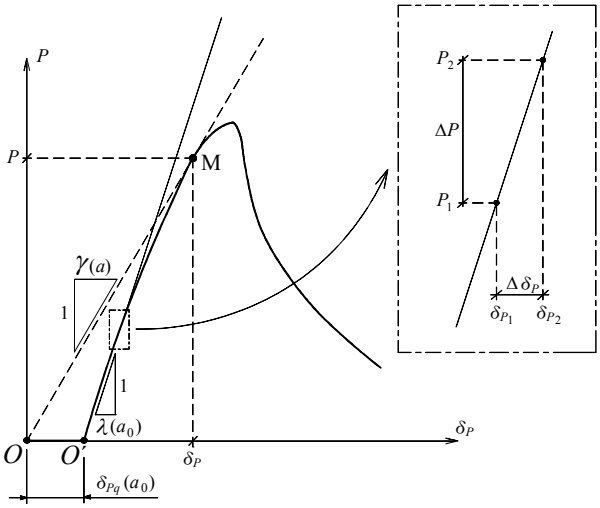


Fig. 2: Typical P-δ_P curve.

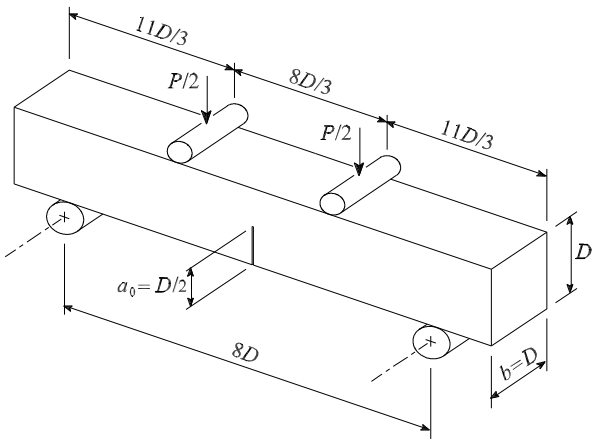


Fig. 3: Geometry of the SEN-FPB (D = 0.1 m).

with δW and δU denoting, respectively, the work of the external applied load P and the corresponding complementary energy. Then, taking into account the contribution of both the applied load P and the distributed load q, one can rewrite Eq.(7) as follows,

$$\delta E = \left(\delta W_P + \delta W_q\right) - \left(\delta U_P + \delta U_q\right) \tag{8}$$

The external work of the applied load P is computed through,

$$\delta W_P = W_{P2} - W_{P1} = \frac{P_1 + P_2}{2}\left[\delta_P(a_2) - \delta_P(a_1)\right] \tag{9}$$

while the external work due to the specimen self-weight q is given by,

$$\delta W_q = W_{q2} - W_{q1} = \int_0^L q\left[\delta_q(x, a_2) - \delta_q(x, a_1)\right] dx \tag{10}$$

In regards to the complementary energy due to the applied load P, one can establish,

$$\delta U_P = U_{P2} - U_{P1} = \frac{1}{2} P_2 \delta_P(a_2) - \frac{1}{2} P_1 \delta_P(a_1) \tag{11}$$

whereas the complementary energy due to the specimen self-weight q can be expressed by,

$$\delta U_q = U_{q2} - U_{q1} = \frac{1}{2}\int_0^L q\left[\delta_q(x, a_2) - \delta_q(x, a_1)\right] dx \tag{12}$$

Consequently, one can equate the released elastic strain energy δE, by substituting Eqs.(9-12) into Eq.(8). Thus, for a given elastic crack length a, the energy released during an infinitesimal crack extension δa, is obtained dividing both terms of the rewritten Eq.(8) by the infinitesimal crack surface (i.e., $b\delta a$), yielding,

$$G(a) = \frac{\delta E}{b\,\delta a} \tag{13}$$

Moreover, Eq.(13) being established for an infinitesimal crack extension (δa), allows estimating the resistance to crack growth $G_R(a)$, through $G_R(a) = G(a)$, whose plotting constitutes the R-curve.

Cohesive crack modeling (CCM): Numerical validation

In order to ensure a significant influence of the specimen self-weight mortar has been chosen as the target material, employing the Single-Edge-Notched beam loaded in Four-Point-Bending (SEN-FPB) as the loading system (Figure 3). In the numerical simulations the elastic properties of mortar were used (E = 18.3 MPa and ν = 0.2), considering the material density within the interval [1.7, 2.9]. Quasibrittle fracture behaviour was simulated through cohesive [3] crack model (bilinear

damage law [4]) using mortar characteristic cohesive parameters: $G_f = 0.022$N/mm and $f_t = 3.5$MPa [5], with the ratio of fracture energies [6] set to: $G_{f\mu}/G_f = 0.5$. As a consequence, the displacement associated to the specimen self-weight (i.e., $\delta_{Pq}(a_0)$) is attained (Figure 4) and no damage onset was observed in the crack ligament. Following this initial step, a displacement δ has then been imposed to the top rigid bodies (Figure 3) to complete the simulation of the experimental loading scenario.
Figure 5 shows the superposition of normalized R-curves obtained by means of the proposed Exact method, together with the corresponding cohesive zone extension l_{coh}, for the considered material densities. As a consequence, one observes that the Exact method permits to reveal with accuracy the character of the intrinsic material fracture property (i.e., toughness) independently of the material density. Indeed, since the CCM had been performed with a given (but characteristic) material property (i.e., $G_f = G_{Rc}$), the method is able to capture with accuracy the right (and unique) fracture energy [6]. This observation reveals the preciseness of the proposed method to evaluate the R-curve when the structure self-weight cannot be neglected.

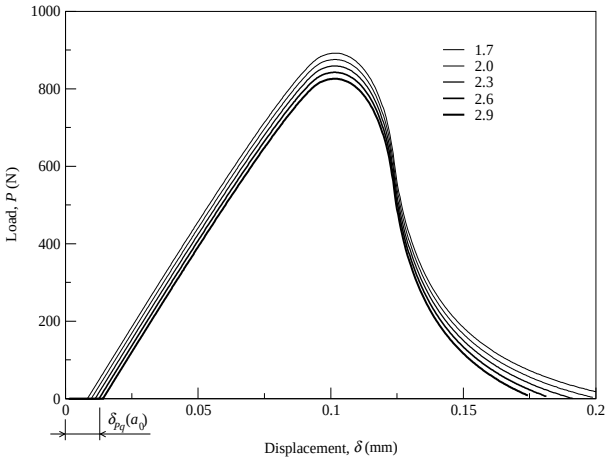


Fig. 4: Numerical P-δ curves (ABAQUS®).

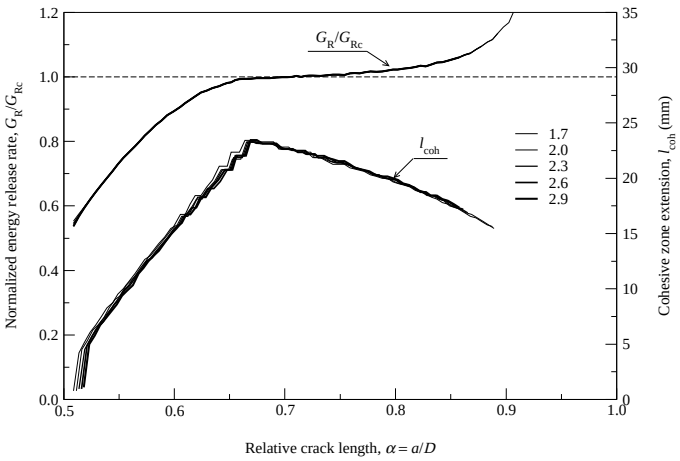


Fig. 5: R-curves.

Conclusions

An Exact method has been proposed to evaluate the Resistance-curve through the Single-Edge-Notched beam, accounting for the effect of the structure self-weight. As the load *vs* displacement curve is the result of the superposition of the external applied load plus the material self-weight, then the computation of compliance functions both in the applied loading axis and along the structure longitudinal axis is mandatory. Afterward, the obtained compliance functions have been used to assess the energy release rate associated to an infinitesimal crack extension, based on the work of the external applied load and the corresponding complementary energy. Finally, cohesive crack modelling accounting for the structure self-weight has been performed to prove that the method is able to evaluate the fracture toughness with accuracy.

References

[1] S. Morel: International Journal of Fracture Vol. 154 (2008), p. 15.
[2] Z.P. Bažant, M.T. Kazemi: Journal of American Ceramic Society Vol. 73 (1990), p. 1842.
[3] N. Dourado, M.F.S.F. de Moura, J. Morais: Int. J. Sol. Struct Vol. 48 (2011), p. 236.
[4] N. Dourado, S. Morel, M.F.S.F. de Moura, G. Valentin, J. Morais: Comp Part A Vol.39 (2008), p. 421.
[5] Z.P. Bažant, J. Planas: CRC Press LLC (1998), p. 168.
[6] S. Morel, C. Lespine, J.L. Coureau, J. Planas, N. Dourado: Int. J. Sol. Struct Vol.47(2010) p838.

© (2012) Trans Tech Publications, Switzerland
doi:10.4028/www.scientific.net/KEM.488-489.613

Influence of the secondary raw materials on the mechanical properties of multilayer films

R.Didžiokas [1, a], J.Janutėnienė [1,b], M.Gintalas [2,c], A.Tadzijevas [2,d]

[1]University of Klaipėda, Mechanical Engineering Department, Bijunu str.17, Klaipeda, LT- 91225, Lithuania

[2]University of Klaipeda, Materials and constructions Research Center, Bijunu str.17, Klaipeda, LT-91225, Lithuania

[a]rimantas.didziokas@ku.lt, [b]jolanta.januteniene@gmail.com, [c]marius_gintalas@yahoo.com,

[d]tadzijevas@gmail.com

Keywords: secondary raw material, recycling, mechanical properties, multilayer film, PET.

Abstract. Recycling and usage of secondary raw materials in production is one of the most topical issues. Usage of secondary raw materials is one of the most topical issues in both economic and ecological (environmental) sense. Such a layered film on the market has lower price because secondary raw material prices is significant lower compared with the original material, the PET granules.

Currently producing a layered film the middle layer composes up to 50 % of recycled material. In today's market in order to maintain a high level of competitiveness usage of 50 % of recycled materials is inadequate, therefore to use more recycled material amount and in such way to reduce product cost further researches are necessary.

1. Introduction

Usage of polyethylen teterephthalate (PET) in the packing area (water and soft drink bottles, food packaging) is very common due to physical and mechanical properties (lightness, impact resistance, gas impermeability). Growing consumption of this plastic causes the issues of recycling [1].

One of the areas of post-consumer PET (films, bottles) utilization is plastic films production with certain amount of post-consumer PET. It is found in literature cases of post- consumer PET application in composite materials for instance concrete production. Also influence of post consumer PET product to polymer matrix strength increasing is analyzed in scientific articles. In order to study the effects of the processes the polymer samples of virgin PET, post consumer PET which content varied by mass from 10-50% and their blends were prepared by different processing routes and tested in Rochester Institute of Technology.

A review of scientific works of PET waste recycling and application during last twenty years is presented in the paper [3]. In this work is assumed that recycled PET can be used in the blends with other polymers (polyethylene, polycarbonates, polyvinyl chloride, etc.)

Experimental investigation of five-layer food packaging films was studied in work [2]. Investigated films contained a middle buried layer of recycled low-density polyethylene (LDPE) comprising 25–50% by weight of the multilayer structure. During investigation it was determined that the post consumer LDPE scrap may be used in multilayer structures as a middle buried layer comprising up to 50% of the multilayer film without any significant adverse effect on the mechanical, thermal and permeation properties.

In terms of research practices each case of recycled materials usage due to different technological processes and the final product requires a detailed study definding the threshold quantities of post consumer materials and their influence on the newly formed material parameters [4].

This work presents the experimental research results of multilayer plastic films. Investigation's aim was to detect the influence of the post consumer PET (20-100 %.) quantity on films mechanical properties.

2. Experimental

2.1. Materials and methods

2.1.1. Materials

Film used in this study consists of three layers melted into one through the processes after extrusion. Films are made from A-PET and post consumer A-PET. Films used for experiments contains of two 10 % of cross-section external layers and 80 % of cross-section inner layer. External layer of films contains of 50 % post-consumer A-PET and 50 % virgin A-PET and 100 % virgin A-PET. The middle layer of films contains of 40 % to 100 % recycled A-PET and 0 % to 60 % virgin A-PET. All films used for tests are produced in extrusion line Lithuania, Klaipeda.
PET film samples of 33 different types have been selected for the experimental research. Film thickness ranged from 0.15 mm to 0.8 mm. Outer film layer thickness is 10 % and the inner film layer is 80 % of the cross-sectional area. Film layers are made of the materials shown in Table 1 in the respective amounts.

Table 1. Film layers materials

Amount of chopped film flakes in middle layer	Amount of chopped bottle flakes in middle layer	Amount of original material in inner layer	Amount of amorphous material in outer film layer	Amount of original material in outer film layer
0 – 50 %	0 – 50 %	0 – 80 %	0 – 40 %	60 – 100%

2.1.2. Test Specimens

According to the ASTM Standard 882-2:2004 following samples for experimental tests were made: 150mm length and 25mm wide specimens for determination of tensile strength, percent elongation at maximum force and at break; 300mm length and 25mm wide specimens for determination Young's modulus. Selected specimens length was 50mm greater then working part of the specimen. The samples were produced without narrowing of the work part. The samples were conditioned at 21°C and 45% relative humidity about 48 hours before tests.

2.1.3. Mechanical properties measurements

Tensile strength, percent elongation at maximum force and at break, Young's modulus where measured with an Zwick/Roell Testing Machine model ZC100 according to ASTM D 882-2 (ASTM, 2004) under the following conditions: crosshead speed was 12,5 mm/min and initial grip distance was 100 mm, for Young's modulus measurements were 300 mm x 25 mm, crosshead speed was 25 mm/min and initial grip distance was 250 mm. Tests were made at 21°C, 50 % relative humidity indoors. For each plastic sample five determinations were performed and results are reported as the mean of five determinations.

3. Results and discussion

3.1. Mechanical properties

After the tension tests, the tensile strength results are obtained. The results of tensile strength at break are given in Table 2.

Table 2. The experimental results of tensile test.

Amount of post consumer material, [%]	20	25	40	60	70	80	90	100
Tensile strength, [MPa]	63.47	63.60	66.10	56.59	55.48	58.14	57.98	55.40
Standard deviation, [MPa]	2.73	1.36	2.45	4.60	3.99	2.46	5.55	2.85
Coefficient of variation	4.30	2.14	3.76	8.13	7.19	4.22	9.57	5.15

Experimental studies showed that samples had a different failure mode: brittle fracture- Fig1 a., plastic fracture-Fig 1.b.

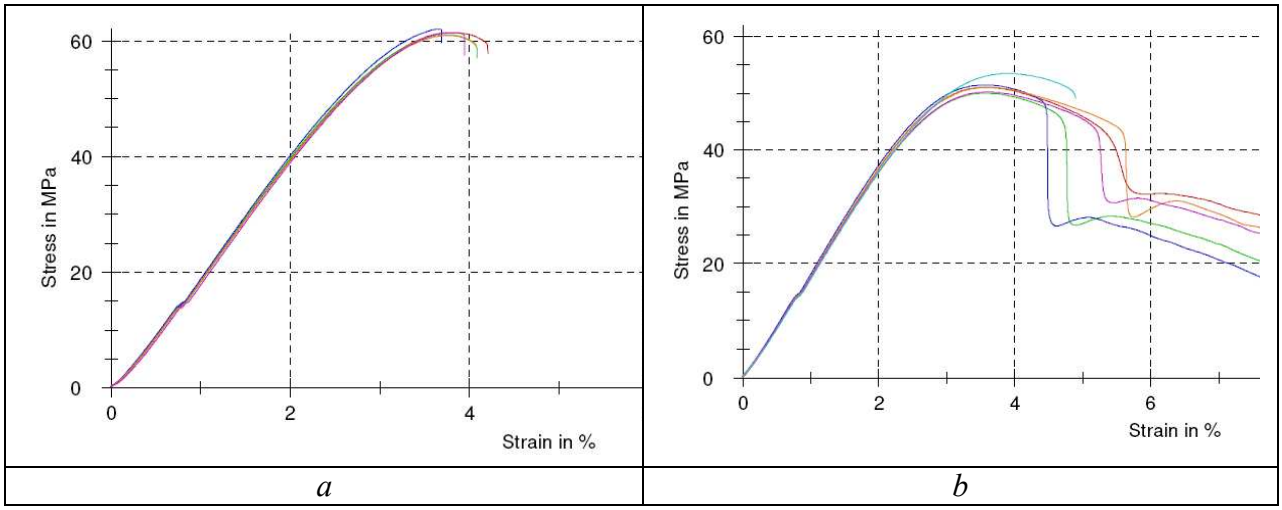


Fig.1 Stress-strain diagram: *a*-brittle fracture, *b*-plastic fracture

According to test results linear relationship between the amount of post consumer material and tensile stress was obtained (Fig. 2).

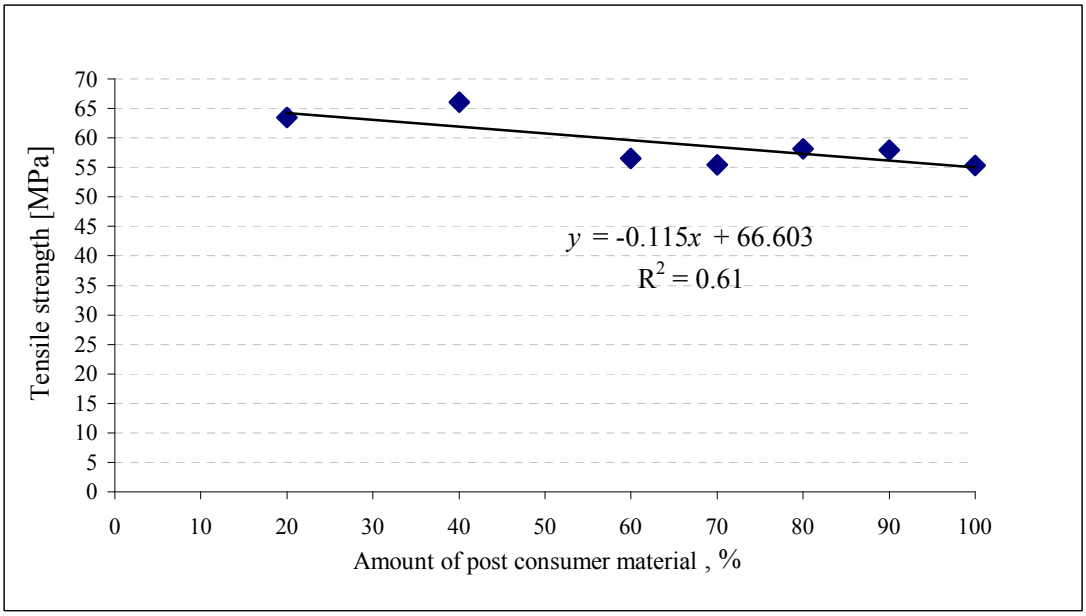


Fig.1 Relationship between the amount of post consumer material and tensile stress

Summary

1. Amount of post consumer material in the middle layer affects the strength toughness of multilayer plastic film. Increasing the post consumer material content from 20 up to 100 % tensile strength of film decreases about 12 -16 %.
2. From experimental results linear relationship between amount of post consumer PET and film's strength were evaluated: $y = -0.115x + 66{,}603$, where y- material's strength, x- amount of post consumer material in the middle layer of plastic film
3. Based on the experimental results of the study the maximum amount of secondary raw material providing the necessary film's mechanical characteristics can be determined.

References

[1] Firas Awaja, Dumitru Pavel. Recycling of PET: Review. European Polymer Journal: Vol. 41 (2005) p. 1453–1477.
Stavroula Chytiri, Antonios E. Goulas, Kyriakos A. Riganakos, Michael G. Kontominas. Thermal, mechanical and permeation properties of gamma-irradiated multilayer food packaging films containing a buried layer of recycled low-density polyethylene. Radiation Physics and Chemistry: Vol. 75 (2006) p. 416–423.

[2] Stavroula Chytiri, Antonios E. Goulas, Kyriakos A. Riganakos, Michael G. Kontominas. Thermal, mechanical and permeation properties of gamma-irradiated multilayer food packaging films containing a buried layer of recycled low-density polyethylene. Radiation Physics and Chemistry: Vol. 75 (2006) p. 416–423.

[3] V. Jankauskaitė, G. Macijauskas, R. Lygaitis. Polyethylene Terephthalate Waste Recycling and Application Possibilities: a Review. Materials science: Vol. 14 (2008) p. 119-127

[4] Alvin R. Caparanga, Blessie A. Basilia, Kevin B. Dagbay, Jonathan W.L. Salvacion. Factors affecting degradation of polyethylene terephthalate (PET) during pre-flotation conditioning. Waste Management : Vol. 29 (2009) p. 2425–2428

© (2012) Trans Tech Publications, Switzerland
doi:10.4028/www.scientific.net/KEM.488-489.617

Analysis of the Influence of Microstructure Heterogeneity and Mechanical Properties of Welded Joint Constituents on Fracture Toughness for Plane Strain, K_{Ic}

Ivica Čamagić[1, a], Nemanja Vasić[1, b], Zijah Burzić[2, c], Aleksandar Sedmak[3, d]

[1]Faculty of Technical Sciences, Kosovska Mitrovica, 7 Kneza Miloša Street, Serbia

[2]Military Institute of Techniques, Belgrade, 15 Katanićeva Street, Serbia

[3]Faculty of Mechanical Engineering, Belgrade, 16 Kraljice Marije Street, Serbia

[a]ivica.camagic@pr.ac.rs, [b]nemanja.vasic@pr.ac.rs, [c]zijah_burzic@rvkds.net, [d]asedmak@mas.bg.ac.rs

Keywords: welded joint, crack, notch, fracture toughness under plane strain

Abstract. The problem of fracture toughness, K_{Ic}, determination at a crack tip localized in a welded joint is placed in principle because fracture mechanics assumes homogenous material, not only around the crack tip but on a distance from it, in order to maintain valid theoretical assumptions and importance of the fracture toughness as the property measured by some of the fracture mechanics methods. Welded joint, as an integral part of a structure, represents inhomogeneity by microstructure and mechanical properties, often by geometrical form, and by the stress field as well, which are affected by various factors as well as residual stresses after welding [1]. However, these general difficulties did not disenable experimental determination of the fracture toughness under plane strain, K_{Ic}, in certain critical areas of a welded joint, or welded joint as a whole, but rather there are difficulties in interpreting the meaning of the measured values. Specimens for the fracture mechanics parameters determination are specimens with cracks, and cracks appears in welded joints as the most critical defects.

Introduction

Fracture mechanics opened new possibilities for safety insurance of welded structures by the analysis of brittle behavior of a body with a crack. According to the standard for determination of the fracture toughness under plane strain, K_{Ic}, ASTM E399 [2], development process of linear-elastic fracture mechanics is completed up to its application on real structures, made of high strength materials, when plane strain state is realized in presence of a crack. The validity condition for these testing is that plastic deformation seize only negligible small region around crack tip before crack propagation and fracture occurs. Since large area of plastic deformation develops around crack tip for majority of structural materials and welded joints, direct determination of K_{Ic} parameter is not possible, and its application is limited in real conditions.

The analysis of a material plastic behavior leaded to the definition of the two following parameters:

- crack tip opening displacement *CTOD*, δ, and
- contour *J* integral, independent on the integration path.

In the linear-elastic area these two parameters are directly connected with the K_{Ic} value and they represent critical values for which plane strain conditions are satisfied:

$$CTOD_c = \delta_{Ic} = \frac{\left(1-\nu^2\right)\cdot K_{Ic}^2}{E\cdot\lambda\cdot R_{p0,2}}, \tag{1}$$

$$J_{Ic} = \frac{\left(1-\nu^2\right)\cdot K_{Ic}^2}{E} = \lambda\cdot R_{p0,2}\cdot\delta_{Ic}, \tag{2}$$

where:

E - elastic modulus,

ν - Poisson's coefficient,

$R_{p0.2}$ - yield strength,

λ - factor of proportionality, $\lambda = 1 \div 2{,}6$.

Applicability of *CTOD* and *J* parameters is in possibility of their analysis after development of significant plastic deformations, as well as in suitability of their experimental determination, as legislated according to BS 5762 [3] for *CTOD* and according to ASTM E813 [4] and ASTM E1152 [5] for *J* integral.

Experimental Determination of the Fracture Toughness, K_{Ic}

Butt welded joint (2/3 X-weld) of Nionikral-70 low alloyed high strength steel was studied, in order to perceive more clearly the influence of microstructure heterogeneity and mechanical properties of welded joint on fracture toughness, K_{Ic}, under plane strain. Basic coated, low hydrogen electrode, Tenacito-75, in diameters of 3,25 mm and 4 mm were selected as additional material as defined in Acroni Jesenice catalogue, which was the material supplier. Testing of specimens taken from the welded plates was performed in order to determine the critical stress intensity factor, K_{Ic}. Specimens for three point bending (SEB), which geometry is defined according to ASTM E399 and shown in Fig. 1 [2, 6], were used for testing. Specimen for three point bending proved to be suitable for application, and it is widely used.

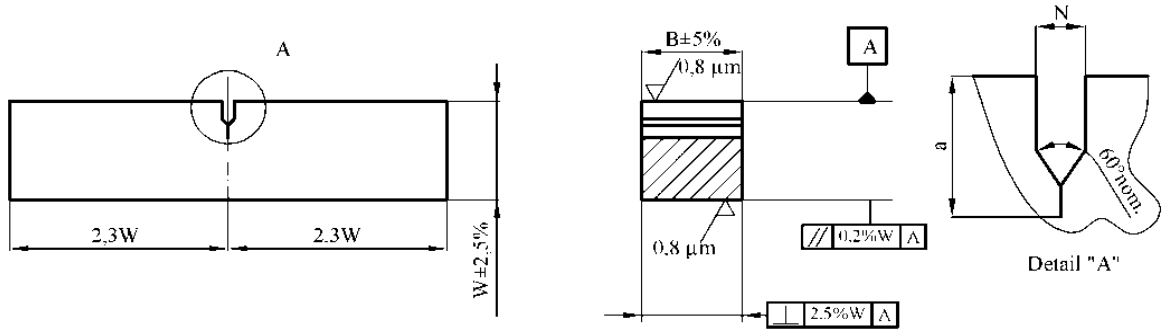


Figure 1. *Specimen for fracture mechanics testing*

The testing was performed at the room temperature, on the electro-mechanical testing machine Schenck Trebel RM 100. Crack tip opening was registered by the special extensometer Klip-Gage DD1, with measuring accuracy of ±0,001 mm.

Three groups of specimens were made, depending on the notch placement:

- I group - specimens with a notch in base metal (BM),
- II group - specimens with a notch in weld metal (WM),
- III group - specimens with a notch in heat affected zone (HAZ).

Fracture toughness, K_{Ic}, is determined based on the critical value of *J* integral, J_{Ic}, which is fracture toughness measure. Testing was performed according to the ASTM E813-89 [4]. Testing method of a single specimen consecutive partial unload was used for *J* integral determination. Points of the basic dependence curve are obtained by the pair of data: acting force, *F*, and crack tip opening, δ. Construction of the resistance curve, J-Δa, is requested by the procedure for the critical value determination of fracture toughness measure, J_{Ic}, in which the crack increment is determined by compliance alternation. F-δ and J-Δa diagrams for specimens with a notch in BM, WM and HAZ are shown in Fig. 2, 3 and 4 respectively. The influence of structure heterogeneity on the toughness properties of the welded joint components can be seen from the diagrams [7].

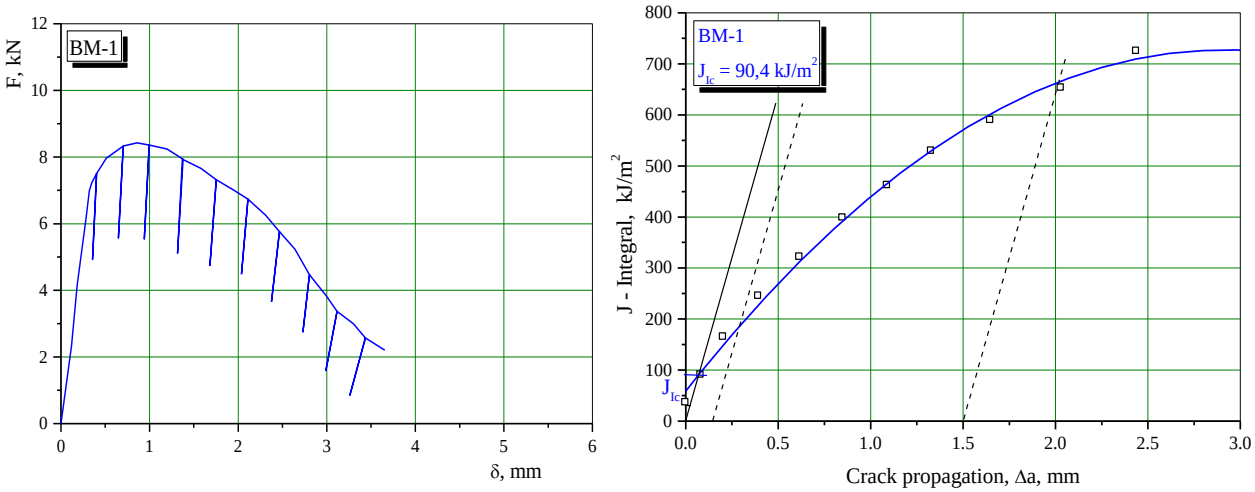


Figure 2. F-δ and J-Δa diagrams of the specimen with a notch in BM tested at the room temperature

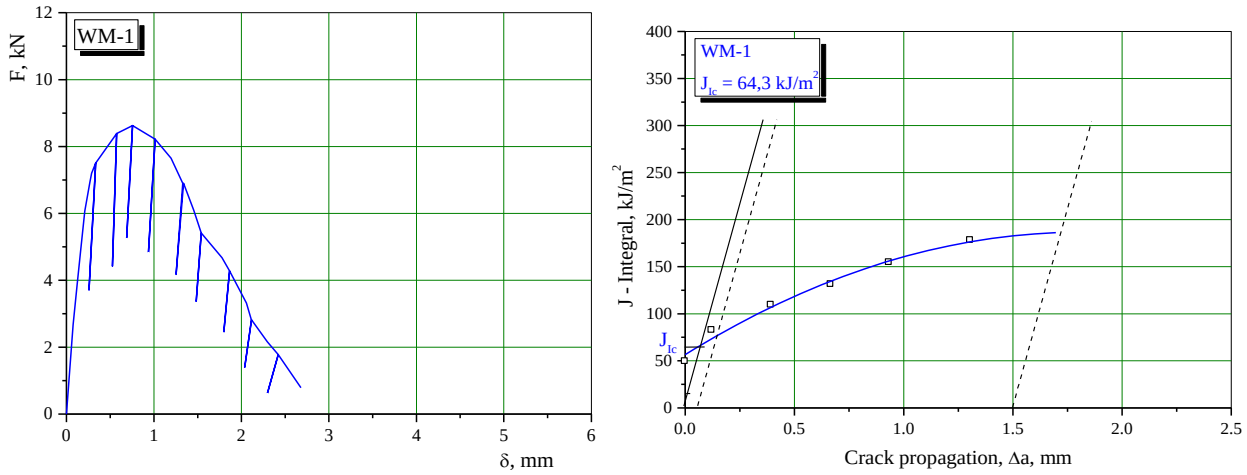


Figure 3. F-δ and J-Δa diagrams of the specimen with a notch in WM tested at the room temperature

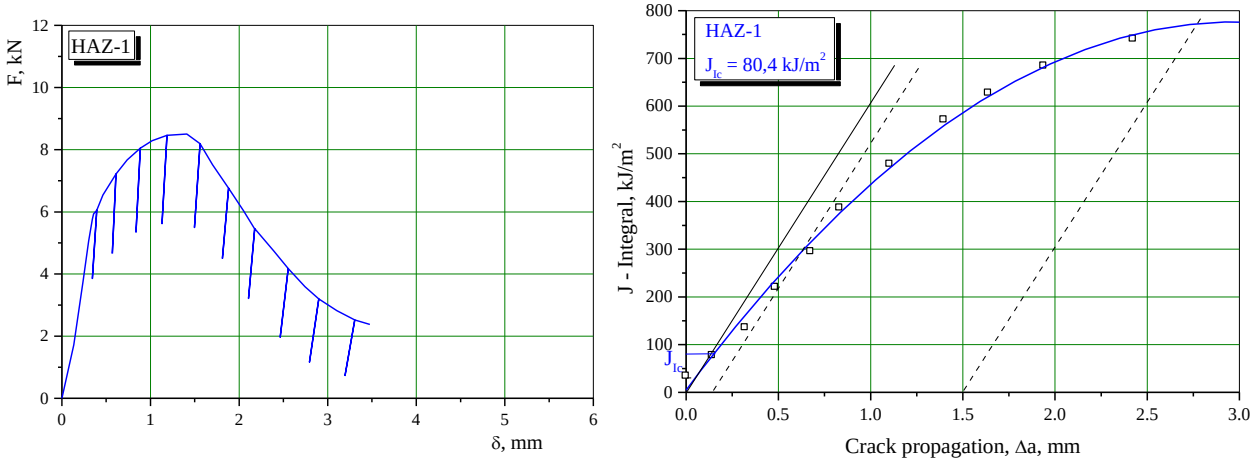


Figure 4. F-δ and J-Δa diagrams of the specimen with a notch in HAZ tested at the room temperature

Knowing the values of critical integral, J_{Ic}, value of the critical stress intensity factor or the fracture toughness under plane strain, K_{Ic}, can be calculated as:

$$K_{Ic} = \sqrt{\frac{J_{Ic} \cdot E}{1-\nu^2}}. \tag{3}$$

Calculated values of the fracture toughness under plane strain, K_{Ic}, are given in Table 1 [7].

Table 1. *Values of the fracture mechanics parameters*

Specimen mark	Critical J integral J_{Ic}, [kJ/m^2]	Critical stress intensity factor K_{Ic}, [MPa m$^{1/2}$]
BM-1	90,4	142,7
BM-2	94,3	145,8
WM-1	64,3	119,2
WM-2	61,5	116,6
HAZ-1	80,4	131,9
HAZ-2	74,9	127,3

Summary

Heterogeneity of welded joint mechanical properties, or its components, can be clearly seen from the obtained values of fracture toughness under plane strain, K_{Ic}, determined indirectly by the critical J_{Ic} integral. Specimens with a notch in BM had the highest measured value of K_{Ic}. Specimens with a notch in HAZ had slightly lower values of K_{Ic}, however in this particular case differences were relatively small and they were approximately 10-15 MPa m$^{1/2}$ in terms of minimal and maximal value [7]. These values do not have to have more significant influence on structures that are submitted to static load. However, if structural elements are submitted to constantly variable load, changes of K_{Ic} value are very significant, because critical crack length a_c directly depends on K_{Ic} value. Specimens with a notch in WM have the worst values of the critical stress intensity factor. Nature of the curves changes exclusively in dependence of a notch placement, or a crack penetration point. Almost identical dependence of individual curves nature in each group can be seen by analysis of obtained curves, taking into consideration that difference between specimens is only in the maximal force value, which is in direct dependence to the fatigue crack length [7].

References

[1] Z. Burzić, S. Sedmak and M. Manjgo: Eksperimentalno određivanje parametara mehanike loma zavarenih spojeva, Integritet i Vek Konstrukcija, No. 2, (2001), p. 97

[2] ASTM E399-89, Standard Test Method for Plane-Strain Fracture Toughness of Metallic Materials, Annual Book of ASTM Standards, Vol. 03.01. (1986), p. 522

[3] BS 5762-DD 19, Standard Test Method for Crack Opening Displacement, London (1976)

[4] ASTM E813-89, Standard Test Method for J_{Ic}, A Measure of Fracture Toughness, Annual Book of ASTM Standards, Vol. 03.01. (1993), p. 651

[5] ASTM E1152-91, Standard Test Method for Determining J-R Curve, Annual Book of ASTM Standards, Vol. 03.01. (1995), p. 724

[6] BS 7448-Part 1, Fracture Mechanics Toughness Tests-Method for Determination of K_{ic} Critical *CTOD* and Critical *J* Values of Metallic Materials, BSI (1991)

[7] I. Čamagić: Analiza napona i deformacija zavarenih spojeva niskolegiranih čelika povišene čvrstoće u prisustvu prslina, Master's thesis, Faculty of Technical Sciences, Kosovska Mitrovica (2009)

© (2012) Trans Tech Publications, Switzerland
doi:10.4028/www.scientific.net/KEM.488-489.621

R-curve and size effect in quasibrittle fracture: a rewriting of the Bazant's size effect law.

S. Morel[1, a] and N. Dourado[2,b]

[1] Université de Bordeaux , UMR 5295 (CNRS), Institut de Mécanique et d'Ingénierie - Bordeaux (I2M), Dept. Génie Civil et Environnemental (GCE), Bordeaux, F-33000, France

[2] *CITAB – Universidade de Trás-os-Montes e Alto Douro, Quinta de Prados 5000-911, Vila Real, Portugal*

[a]stephane.morel@u-bordeaux1.fr, [b]nunodou@gmail.com

Keywords: Quasibrittle failure; R-curve; Crack length at peak load; Size effect; Asymptotic behaviors; Cohesive zone model; Bilinear softening function.

Abstract. The recent rewriting of the Bazant's Size Effect Law which has suggested the existence of an additional asymptotic regime for intermediate structure sizes is compared to numerical simulations of fracture of geometrically similar notched structures of different sizes. The quasibrittle failure is simulated through Cohesive Zone Model (bilinear softening) using a constant set of cohesive parameters whatever the specimen size. The different asymptotic regimes expected for the size effect on the nominal strength are shown in fair agreement with the size effect observed on the results obtained from numerical simulations. The existence of the new asymptotic regime expected for intermediate structure sizes is, in particular, clearly revealed by this comparison.

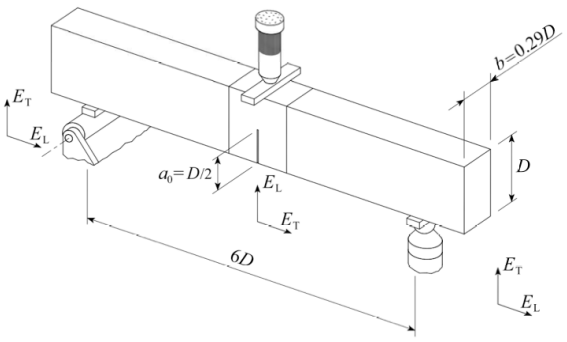
Introduction

The size effect phenomenon in solid mechanics concerns the effect of a structure size on its nominal strength σ_N. If one considers geometrically similar notched structures of different characteristic sizes D, the nominal strength σ_N of a structure of size D can be defined as:

$$\sigma_N(D) = c_N \frac{P_u}{bD} \quad , \tag{1}$$

where P_u is the maximum external load applied to the structure (commonly called the peak load), b is the thickness of the structure and c_N is a coefficient introduced for convenience. It is nowadays firmly established that the size effect of notched structures constituted by quasibrittle materials such as concrete, mortar, rocks or wood is an *energetic* size effect and not a *statistical* one in the sense of the Weibull's statistics [1]. The reference framework concerning the size effect phenomenon in quasibrittle fracture is due to Bazant [2-5] and is commonly called the Size Effect Law (SEL). In the last evolution of the SEL [4], Bazant has shown, from an energy-based asymptotic analysis founded on the assumption of a size-independent R-curve, that the size effect on nominal strength σ_N is expected to be transitional between two extreme asymptotic behaviors ('type 2' size effect [6]). In the case of small structure sizes (i.e., $D << D_0$), $\sigma_N \sim B f_t$ = const: no size effect is expected. For these small structure sizes, the FPZ is expected to occupy the whole volume of the structure, inducing no stress concentration and a failure with no crack propagation: this is the domain of strength theory. For large structure sizes (i.e., $D >> D_0$), $\sigma_N \sim D^{-1/2}$ which is the size effect expected from Linear Elastic Fracture Mechanics (LEFM). Indeed, in large structures, the FPZ is expected to lie within only an infinitesimal volume fraction of the structure and hence, the stress and displacement fields surrounding the FPZ are the asymptotic elastic fields expected from LEFM.

However, despite the success of Bazant's SEL, the crossover regime between both extreme asymptotic behaviors (estimated from the intermediate asymptotic theory) does not appear accurately defined. A precise description of the size effect for intermediate structure sizes is yet of great importance since this is usually the range of the experimental data.



Series	D (mm)
D_0	17.5
D_1	35
D_2	70
D_3	140
D_4	280
D_5	560
D_6	1120
D_7	2240
D_8	4480

Fig. 1: SENB wood specimen used for numerical simulations characterized by its characteristic dimension D (corresponding to the specimen height) submitted to three-point bending.

The lack of precision of the SEL in the range of intermediate structure sizes has been recently filled from the rewriting of the SEL using an analytical expression of the R-curve and an energy based asymptotic analysis [7]. This recent rewriting has suggested the existence of an additional asymptotic regime for intermediate structure sizes. The present study is devoted to the comparison between the predictions of the rewriting of the SEL and the size effect results obtained from numerical simulations of fracture of geometrically similar notched structures of different sizes using a cohesive zone model.

Numerical simulation of the fracture of geometrically similar notched specimens

The size effect on fracture properties of a quasibrittle material is studied from cohesive zone simulations performed on geometrically similar SENB wood specimens of different sizes submitted to three-point bending. All the specimen dimensions are proportional to the characteristic size noted as D which corresponds to the height of the beam as shown in Figure 1. Nine different specimen sizes were simulated corresponding to a ratio of 256 between the largest and the smallest specimen (i.e., 2.4 decades). The elastic properties of wood (Norway spruce, *Picea abies L.*), are E_L=9900 MPa, E_T=334 MPa, ν_{LT}=0.44 and G_{LT}=610 MPa where L and T correspond to the longitudinal and tangential wood directions, respectively (Fig.1). The simulations are performed under plane strain conditions and using cohesive zone model (CZM).

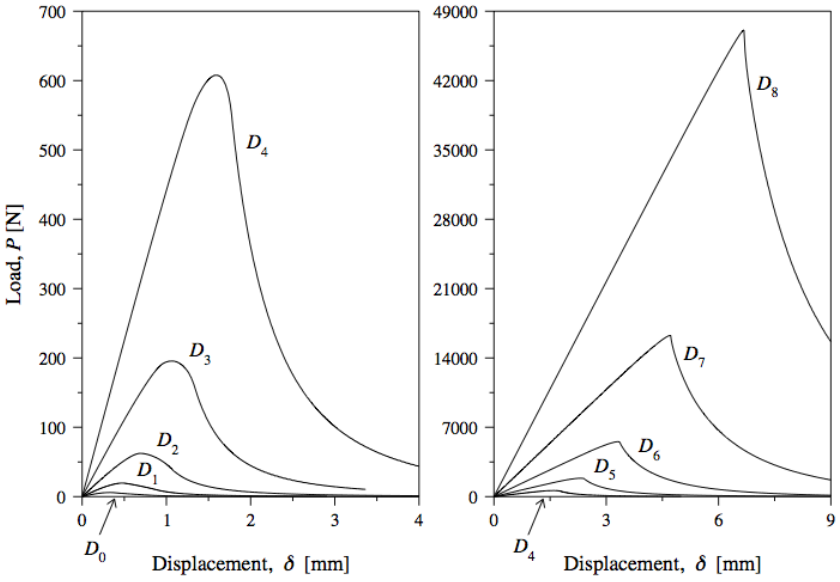


Fig. 2: Load-displacement curves obtained for all specimen sizes (D_0 to D_8). It can be observed that the peak load evolves from some Newtons for the smallest specimen (D_0) up to 48 kN for the biggest one (D_8). As intuitively expected, as the specimens increase in size, the macroscopic behavior revealed by the material proceeds from a ductile response toward a brittle one for higher sizes.

A bilinear softening diagram [8,9] is used with a constant set of cohesive zone parameters whatever the specimen size D. The cohesive fracture energy is G_f = 100 J/m^2, the tensile strength is f_t =1.75 MPa and the critical opening displacement corresponds to w_c=0.204 mm. Finally, the cohesive

interface is located in the plane of the initial notch and the length of each cohesive element has been fixed to 0.5 mm for all specimen sizes. The load-displacement curves obtained for each specimen dimension D are plotted in Figure 2.

Size effect : comparison between the analytical model's predictions and the numerical results.

The size effect observed from numerical simulations is analyzed within the framework of equivalent LEFM which is at the basis of the Bazant's SEL as well as of its recent rewriting. From the load-displacement curves plotted in Fig. 2, the corresponding R-curves are estimated within the framework of equivalent LEFM using the dimensionless energy release rate function $g(\alpha)$ characteristic of the structure geometry:

$$G_R(a) = G(a) = \frac{P^2}{E' b^2 D} g\left(\frac{a}{D}\right), \tag{2}$$

where P is the external load applied to the specimen, $\alpha = a/D$ corresponds the relative crack length (a being the eq. LEFM crack length) and E' is the effective modulus. With the exception of the smallest specimens (exhibiting a confinement of the FPZ), the R-curves are superimposed, leading to a single R-curve, i.e., an R-curve independent of the specimen size. As a consequence, as proposed in [7] , the R-curve can be fitted by a power law from which the resistance to crack growth G_R evolves as a function of the equivalent crack length increment $\Delta a = a - a_0$, as:

$$G_R(\Delta a) = \begin{cases} \phi \Delta a^{\beta} & si\ \Delta a < \Delta a_c \\ G_{Rc} & si\ \Delta a \geq \Delta a_c \end{cases}, \tag{3}$$

where the exponent β characterizes the curvature of the R-curve (and must lie between 0 and 1 in order to ensure convex R-curve), $\Delta a_c = a_c - a_0$ is the crack length increment for which the plateau value G_{Rc} of the resistance occurs and gives an estimate of the equivalent LEFM length of the FPZ commonly called *internal length*, and, $\phi = G_{Rc} / \Delta a_c^{\beta}$ is a prefactor (constant). The fit of the R-curves has led to the following parameters : G_{Rc} =100 J/m^2 which, as expected, corresponds to the value of the cohesive energy G_f [9], Δa_c = 21.0 mm and β =0.24. The assumption of a single R-curve being at the source of the recent rewriting of SEL (as well as of SEL itself) the size effect on the whole fracture properties at peak load (i.e., on the relative crack length, on the resistance to crack growth and on the nominal strength) can be predicted by the analytical model detailed in [7].

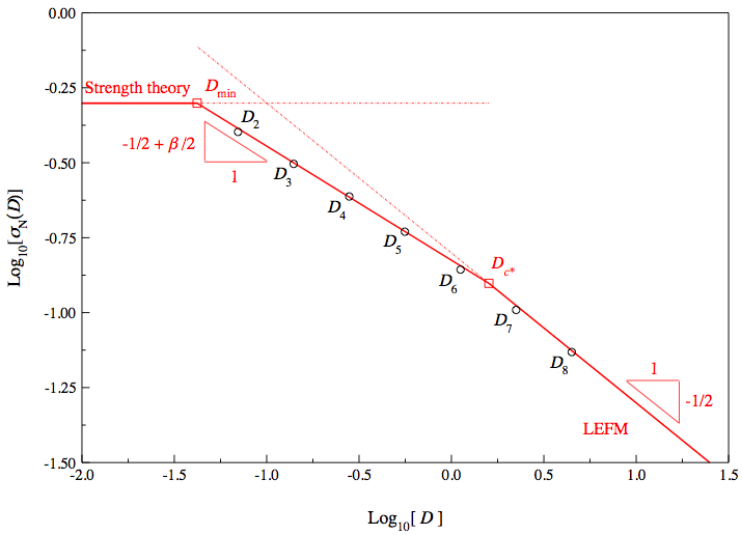


Fig. 3: Size effect on the nominal strength $\sigma_N(D)$ and expected asymptotic regimes according to Eq.(4). The existence of the new asymptotic regime expected for intermediate structure sizes, characterized by a slope of (-1/2+β/2) and extending over 1.58 decades, is clearly revealed by this comparison.

According to the rewriting [7] of the Bazant's SEL, the size effect on the nominal strength $\sigma_N(D)$ can be approximated through three asymptotic behaviors defined as:

$$\sigma_N(\alpha_u, D) = \begin{cases} \text{"strength criterion"} & \text{si } D < D_{\min} \\ D^{-1/2+\beta/2} & \text{si } D_{\min} < D < D_1 \\ D^{-1/2} & \text{si } D > D_1 \end{cases}, \quad (4)$$

where $D_{\min}$ and D_1 correspond to crossover sizes whose expressions are analytically defined in [7] and β is the exponent characterizing the curvature of the R-curve (3). Both extreme asymptotic regimes defined in Equation (4), i.e., the horizontal asymptote (strength theory) expected for structure sizes $D < D_{\min}$ and the LEFM asymptote expected for sizes $D > D_1$, are in agreement with the Bazant's SEL. The main difference lies at intermediate sizes for which an additional asymptotic regime occurs, characterized by a slope $(-1/2+\beta/2)$, instead of a simple crossover regime as expected from SEL. This new asymptotic regime expected at intermediate sizes can extend from 1 decade in the case of large β values up to more than 2 decades in the case of small β values (1.58 decades in the present case). The nominal strength $\sigma_N(D)$ obtained from the CZ simulations and the expected asymptotic regimes defined in Eq. (4) are plotted in Figure 3. In this Figure, one can see that the expected asymptotic regimes provide a very good description of the size effect on the nominal strength $\sigma_N(D)$ and especially that the existence of the new asymptotic regime expected for intermediate structure sizes is clearly revealed.

Conclusion

The recent rewriting of Bazant's Size Effect Law [7], based only on the R-curve (described by a simple power law) and of the dimensionless energy release rate function (easily estimated from a linear elastic FE analysis), provides an accurate description of the size effect on the nominal strength of structures through the estimate of different asymptotic behaviors. The main advantage of this rewriting compared to the original SEL lies in the fact that the size effect at intermediate structure sizes is accurately defined from a new asymptotic behavior (and not approximated as in SEL). Moreover, the new model is based on an analytical expression of the R-curve and hence, if the R-curve estimate is required, this one can be obtained from fracture experiments performed on a single structure size which limits the number of time consuming fracture tests.

References

[1] W. Weibull: Proc. Royal Swedish Inst. of Eng. Res. Vol. 153 (1939), p. 1.

[2] Z.P. Bazant: Journal of Engineering Mechanics Vol. 110 (1984), p. 518.

[3] Z.P. Bazant: Applied Mechanics Review Vol. 50 (1997), p. 593.

[4] Z.P. Bazant: International Journal of Fracture Vol. 83 (1997), p. 19.

[5] Z.P. Bazant: Z.P., 2000. International Journal of Solids and Structures Vol. 37 (2000), p. 69.

[6] Z.P. Bazant: Proceedings of the National Academic Sciences Vol. 14 (2004), p. 13400.

[7] S. Morel: International Journal of Fracture Vol. 154 (2008), p. 15.

[8] N. Dourado, S. Morel, M. de Moura, G. Valentin and J. Morais: Comp. Part A Vol. 39 (2008), p. 415.

[9] S. Morel, C. Lespine, J.-L. Coureau, J. Planas and N. Dourado: Int. J. Sol. Struct. Vol. 47 (2010), p. 837.

© (2012) Trans Tech Publications, Switzerland
doi:10.4028/www.scientific.net/KEM.488-489.626

Interaction of heat checks in aluminum pressure casting dies and their effect on fatigue life

P. Raninger[1,a], W. Ecker[1,b], T. Antretter[2,c], M. Leindl[2], R. Ebner[1]

[1]Materials Center Leoben Forschung GmbH, Roseggerstrasse 12, A-8700 Leoben;
[2]Montanuniversität Leoben, Institut für Mechanik, Franz-Josef-Strasse 18, A-8700 Leoben
[a]peter.raninger@mcl.at, [b]werner.ecker@mcl.at, [c]thomas.antretter@unileoben.ac.at

Keywords: Thermo-mechanical fatigue, crack shielding, pressure die casting, hot work tool steels, heat check networks, fatigue life

Abstract

Pressure casting dies are exposed to harsh service conditions consisting of cyclic thermal and mechanical loading and thus undergo thermo-mechanical fatigue. Due to cyclic plastic deformation of the material near the surface of the dies the loading conditions gradually change because of the formation of tensile residual stresses which add to the stress field from external loading. This change in the stress field influences the nucleation and the growth of cracks. Typically after a few thousand casting cycles a network of heat checks forms. In such a network crack shielding has a big influence on the evolution of the crack array. Firstly, it influences the propagation rates of the cracks and secondly it may change the propagation direction compared to the case where no neighbors are present. The crack growth rate and the length at which the cracks stop growing are also influenced by the thermo-physical and mechanical properties of the die material. It was found that the shielding effects of neighboring cracks are of equal importance. Crack deflection caused by the presence of neighboring cracks can lead to break-outs at the surface ensued by fast degradation eventually necessitating the replacement of the die. Consequently, the focus in this work is put on the investigation of the interaction of cracks in a network and their effect on the fatigue life. The problem is tackled by means of an automated strategy based on the finite element method.

1. Introduction

The elastic-viscoplastic material behavior of casting dies and the formation of heat check networks at the surface is described in [1] and [2]. The approach in [2] follows a method frequently applied for networks subjected to monotonic loads as described e.g. in [3] where cracks are evenly distributed and every second crack stops when a criterion is fulfilled. In [4] an approach for cyclic loading is discussed also considering the determination of an initial configuration. In this study an approach is presented where a unit cell of non-uniformly spaced cracks is allowed to grow freely including crack deflection and fatigue life calculation.

2. Characteristics of a typical crack array

Samples were taken from a pressure casting die provided by industry after 80000 load cycles. Fig. 1 shows a panorama view of a crack array in thickness direction at a typical position. The cracks in the plane are measured and the data obtained are summarized in Table 1 and depicted in Fig. 2. Cracks exceeding a final length of 100 μm are labeled separately.
In pressure casting dies first cracks usually appear after about 2000 casting cycles [5]. These cracks grow while other cracks may initiate in the areas between them. The probability of further crack initiation is dependent on the relaxation of stress and thus the length of the cracks in the vicinity of the possible initiation sites.

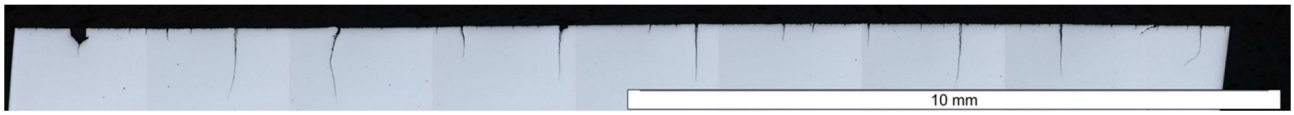


Fig. 1: Panorama view of a crack array at a characteristic position (50x)

The first cracks influence each other after penetrating a certain distance into the die but grow unhindered by the shorter cracks since those do not exist in the beginning. Assuming that the first cracks can be identified by a final length larger than 100 μm an average spacing of about 1000 μm can be measured. At a later stage new cracks initiate between the existing already comparatively long cracks. The younger cracks have little chance to grow since their corresponding driving forces, i.e. the stress intensity ranges may soon drop below ΔK_{th} under the shielding influence of the older ones. These so-called leading cracks propagate under arising and increasing mutual shielding effects. The influence of the long cracks on the short ones is significant but not the other way around, which is the reason why only cracks with a final length larger than 100 μm will be considered in the analysis.

Table 1: Data of a characteristic crack array. Cracks longer than 10 μm were measured and data of cracks longer than 100 μm extracted.

	Evaluated cracks	Average spacing/ [μm]	Maximum crack length/[μm]
	76	248	1217
>100μm	19	1012	1217

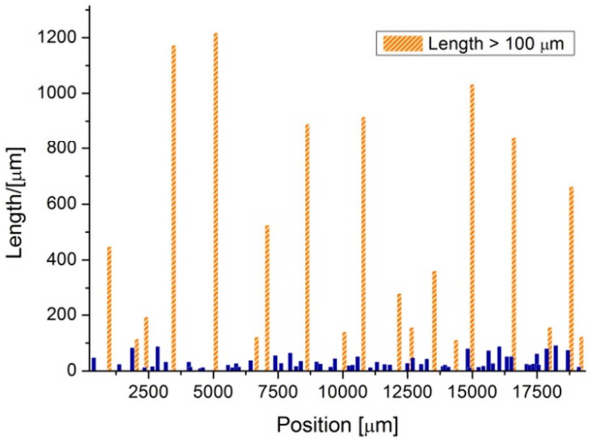


Fig. 2 (right): Evaluation of Fig. 1. Cracks exceeding 100 μm are indicated.

3. Modeling

The modeling of crack arrays due to thermal fatigue requires the implementation of various aspects concerning crack initiation and growth. In [4] Haddar et al. present a procedure to obtain an initial configuration based on grain sizes and Monte Carlo simulations. In this study which focuses on the crack array evolution rather than initiation the initial configuration is based on a metallographic section. Long crack behavior is assumed which can described with crack propagation curves. The cracks in the system undergo deflection due to the interaction with neighboring cracks and propagate according to Paris' equation.

3.1 FE-Modeling. An automated modeling path is implemented using the FE package Abaqus [6] which uses an initial configuration based on Fig. 2. The spacings are chosen to match the position of the cracks indicated and the initial lengths l_{0i} are set to 100 μm. The distributions of temperature and stabilized residual stresses after 100 casting cycles are computed separately and mapped onto the fatigue models (F-Models) which use elastic material behavior and periodic boundary conditions. In the F-Models the values for K_{max} occurring during spray cooling are computed. In auxiliary computations the load ratio (R) is determined for each crack which enters propagation criteria. The evolution of the array is investigated in a loop where a new F-Model is automatically generated for each propagation increment and cracks are propagated according to the criteria presented in the next section.

3.2 Crack propagation curves. Fig. 3 shows crack propagation curves measured at different load ratios (R) and thus show different crack closure behavior. The curve corresponding to R=0.7, where little closure effects are expected, is corrected according to Elber [7] in order to obtain an effective

curve. The parameters for the Paris' equation, which is used for the computation of propagation rates, are derived from it. The three remaining curves are evaluated as functions of K_{max} and shifted so that they coincide with the first curve (top left in Fig. 3). This way the ratios $\Delta K_{eff}/K_{max}$ are obtained for four load ratios including R=0.7 which can be computed directly. The corresponding data points are depicted in Fig 4. Since K_{max} and R are determined for each increment of crack growth ΔK_{eff} can be worked out and thus the propagation rate is found according to Paris equation.

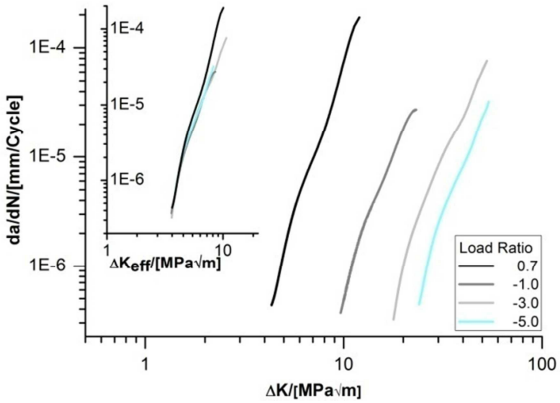


Fig. 3: Crack propagation curves for various load ratios. Top left: Curves shifted towards the effective curve which is the curve corresponding to R 0.7 corrected according to Elber.

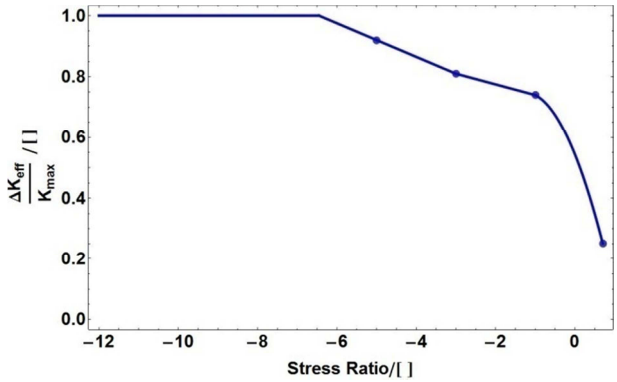


Fig. 4: $\Delta K_{eff}//K_{max}$ obtained by shift of propagation curves.

In each model the crack showing the maximum propagation rate $(da/dN)_{max}$, designated as p_{max}, is extended by an increment Δa_{max} which is kept constant at 100 µm. Δa_i of the other cracks are obtained by scaling Δa_{max} with p_i/p_{max}. If $\Delta K_{eff,i}$ drops below ΔK_{th} which is set to 3 MPa√m or Δa_i is smaller than $\Delta a_{max}/10$ the corresponding crack is no longer propagated in the model. The factor 10 results from meshing considerations.

3.3 Crack deflection. The propagation direction is computed according to the $K_{II}=0$ criterion described in [6]. In each model the angles of crack propagation are evaluated and used for the following increment. This way the changing shielding conditions are taken into account.

4. Results

Fig. 5 shows the final configuration of a crack array starting from an initial configuration consisting of the 19 cracks exceeding 100 µm in Fig. 2 with a uniform length of 100 µm. The analysis was continued until the number of load cycles exceeded 80000. The number of load cycles and the corresponding crack lengths of 5 predominant cracks are depicted in Fig. 7.

5. Discussion

It was assumed that the initial configuration of the first cracks in the system determine the final configuration of the array. The initiation scenario of those cracks, however, also decides which cracks prevail and which stop, thus making the system very sensitive. The first cracks at the die surface initiate within 2000 cycles. Still, the cracks will arrange dependent on the sequence of initiation which largely affects the propagation rates of the cracks in the system and can cause a buffering effect. In the actual case, cracks number 8 and 16 are predominant leading to very conservative results considering the penetration depth within the service life of the casting die which is about 80000 cycles. The maximum in the die is 1.2 mm compared to 3 mm in the simulation. Because the scenario of crack initiation is not known it is hard to reconstruct the evolution of a measured array in a die exactly. Furthermore, the simulation was started from 100 µm neglecting crack propagation up to this length. Due to the interplay of loading and crack length

stress intensities are very low in this regime leading to a significant contribution to fatigue life. Other artificial influences on the system are introduced by the stop criterion $\Delta a < \Delta a_{max}/10$ and the periodic boundary conditions causing crack 1 and 19 to be direct neighbors.

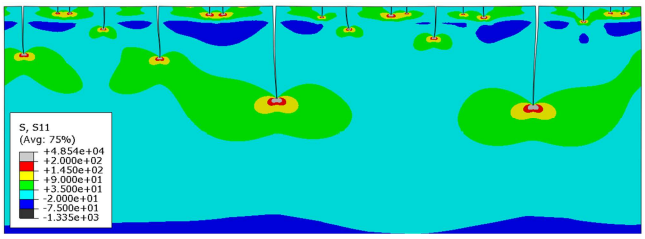


Fig. 5: Configuration after 85000 cycles

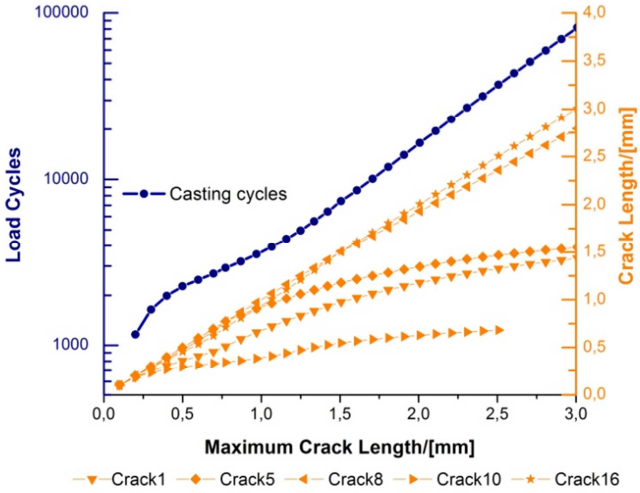


Fig. 6 (right): Number of casting cycles and penetration depth of 5 cracks over the maximum crack length in the system. E.g. if the leading crack penetrates 2 mm crack number 10 is about 0.6 mm long and the corresponding number of casting cycles is 17000

6. Conclusions

Crack array evolution is dominated by the cracks initiating first since they are not influenced by cracks initiated later and therefore grow fastest. The sequence of initiation of the first cracks and the growth in the short crack regime are also important, however. The model presented is capable of simulating the evolution of crack arrays in casting dies in an automated manner starting from arbitrary configurations. Furthermore, it provides data on R, ΔK_{eff} and load cycles for every crack in the model. A damage model combined with a finer resolution of the early stages of crack array evolution is a possible means to increase the precision of the modeling concept.

7. Acknowledgements

Financial support within the framework of the Austrian COMET Competence Center Program is gratefully acknowledged.

8. References

[1] W. Ecker, T. Antretter, and R. Ebner. Calibration and validation of an elasto-viscoplastic material model for a hot work tool steel used in pressure casting dies. *Key Engineering Materials*, 345-346 I:685–688, 2007.

[2] M. Leindl. *Untersuchung des Risswachstums in einem Druckgießwerkzeug mit Hilfe der Finite-Elemente-Methode*. PhD thesis, Montanuniversitaet Leoben, 2008.

[3] S. Nemat-Nasser. Stability of a system of interacting cracks. *International Journal of Engineering Science*, 16(4):277 – 285, 1978.

[4] N. Haddar and A. Fissolo. 2d simulation of the initiation and propagation of crack array under thermal fatigue. *Nuclear Engineering and Design*, 235(9):945–964, 2005.

[5] W. Ecker, M. Leindl, T. Antretter, R. Ebner, I. Siller, and S. Nissle. Effect of material properties on the thermo-mechanical loading and damage of pressure casting dies – a numerical study. In *Tool Steels – Deciding Factor in Worldwide Production. Proceedings of the 8th International Tooling Conference. Aachen*, pages 927–939, 2009.

[6] *Abaqus V6.10 Theory Manual*.

[7] W. Elber. The significance of fatigue crack closure. In *Damage tolerance in aircraft structures, ASTM STP 486*, pages 230–242, 1971.

© (2012) Trans Tech Publications, Switzerland
doi:10.4028/www.scientific.net/KEM.488-489.630

Dynamic *J*-integral evaluation of three-point-bend beams with various geometrical dimensions

Marius Gintalas[1,a], Antanas Ziliukas[2,b], Kaspars Kalnins[3,c]

[1]Research Center of Materials and Structures, Klaipeda University, Bijunu str. 17, Klaipeda, LT-91225, Lithuania

[2]Strength and Fracture Mechanics Center, Kaunas University of Technology, Kestucio str. 27, Kaunas, LT-44025, Lithuania

[3]Institute of Materials and Structures, Riga Technical University, Azenes iela 16/20-353, Riga, LV-1048, Latvia

[a]marius_gintalas@yahoo.com, [b]antanas.ziliukas@ktu.lt, [c]kaspars.kalnins@sigmanet.lv

Keywords: Dynamic fracture toughness, three-point-bend beam, ductile steel, single edge notch.

Abstract. *J*-Integral is the main effective and commonly used tool for cracked elastic-plastic material resistance assessment. Determination of fracture toughness under impact loading conditions is related with problems of crack length measurement. Nevertheless, current experimental techniques restrict the specimen's geometry taking into account span and height ratio, which is equal to four.

Evaluation of fracture toughness estimation method which requires only experimental load-line displacement curve of single specimen is research object of dynamic fracture mechanics.

This article proposes an approach of impact fracture toughness determination of elastic-plastic steel from single any size specimen test. Load-line displacement data obtained from three-point-bending tests of rectangular cross section specimens with V form single edge notch was used for *J*-integral calculation. Five series of specimens with different geometry were manufactured from ductile steel and tested.

Introduction

In most cases experimentally evaluating J integral it is separated into elastic J_{el} and plastic J_{pl} components. In this article method based on three components of energy amounts extracted from load – displacement curve (Fig. 2b) is presented for J_{tot} integral evaluation:

$$\mathrm{J_{tot}} = \mathrm{J_{el}} + \mathrm{J_m} + \mathrm{J_r} \tag{1}$$

Here a sum of $\mathrm{J_m}$ and $\mathrm{J_r}$ represents J_{pl} part. Calculation of these two components is based on Schindler's procedure.

1. J_{el} component

Elastic component of integral is calculated via stress intensity factor K. In international standards for fracture toughness testing there is limitations on specimen's geometry: specimen's span and height ratio α (Fig. 1) value must be equal to 4. Solution forms for ratio $\alpha = 8$ are found in the literature also. Formulas for stress intensity calculation are based on these ratio values. Expressions which can be used for stress intensity evaluation of any geometry of bend beam were proposed by Guinea et al [1]. Accuracy of these general expressions was studied by Karihaloo and Xiao for three point bend specimens with $\alpha = 6, 8$ and 12 [2]. Results confirmed that method suggested by Guinea at al could be used for determination of stress intensity factor of specimens with different α values.

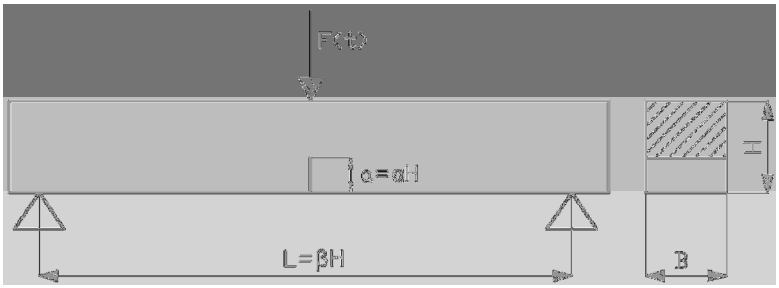


Fig. 1 Geometry of three points bend specimen

Elastic component of integral is calculated via stress intensity factor K_{Id}:

$$\mathrm{J_{el}} = \frac{\mathrm{K_{Id}^2}(1-\nu^2)}{\mathrm{E}} \tag{2}$$

Calculating dynamic stress intensity factor impact load F_{el} (Fig. 2a) up to the first drop point of load – displacement curve was applied:

$$K_{Id} = \frac{3F_{el}L\sqrt{\pi a}}{2BH^2} k_\beta(\alpha) \tag{3}$$

Geometry correction function valid for any size beam with rectangular cross section is:

$$k_\beta(\alpha) = \frac{\sqrt{\alpha}}{(1-\alpha)^{3/2}(1+2\alpha)} \left\{ p_\infty(\alpha) + \frac{4}{\beta}[p_4(\alpha) - p_\infty(\alpha)] \right\} \tag{4}$$

here $p_4(\alpha)$ and $p_\infty(\alpha)$ are functions when $\beta = 4$ and $\beta = \infty$:

$$p_\infty(\alpha) = 1.99 + 0.83\alpha - 0{,}31\alpha^2 + 0.14\alpha^3 \tag{5}$$

$$p_4(\alpha) = 1.99 - \alpha(1-\alpha)[2.15 - 3.93\alpha + 2.7\alpha^2] \tag{6}$$

2. Component $\mathrm{J_m}$ and $\mathrm{J_r}$

A single specimen technique based on a continuous force-displacement diagram has been developed by Schindler [3]. The input parameters are energy up to maximum load $\mathrm{U_m}$ and total fracture energy $\mathrm{U_t}$ amounts experimentally obtained from instrumented impact test.

$$\mathrm{J_m} = \left(\frac{2}{\mathrm{p}}\right)^{\mathrm{p}} \cdot \frac{\eta_{\mathrm{pl}}(\mathrm{a_0})}{\mathrm{B(H-a_0)^{1+p}}} \cdot \mathrm{U_t^p} \cdot \mathrm{U_m^{1-p}} (\Delta \mathrm{a})^{\mathrm{p}} \text{ when } \Delta \mathrm{a} \le \Delta \mathrm{a_m} \tag{7}$$

$$\mathrm{J_r} = \frac{2\eta(\mathrm{U_t - U_m})}{\mathrm{B(b_0 - \Delta a_m)^2}} \mathrm{s}[(\Delta \mathrm{a} - \Delta \mathrm{a_m}) - (\Delta \mathrm{a} - \Delta \mathrm{a_m})^2 / 2\mathrm{b_0}] \text{ when } \Delta \mathrm{a} \ge \Delta \mathrm{a_m} \tag{8}$$

$$\mathrm{p} = \frac{3}{4}\left(1 + \frac{\mathrm{U_m}}{\mathrm{U_t}}\right)^{-1} \tag{9}$$

$$\Delta a_m = \frac{U_m p b_0}{2U_t} \tag{10}$$

This method is based on the analysis of force-displacement test record it can be applied to any specimen geometry and loading rate.

3. Formula for η_{pl} determination

It is found in the literature that for η_{pl} determination usually are analyzed two cases. The first one is when specimen's geometry parameter $\alpha < 0.275$. This case represents shallow cracks. For deeply cracked beams $\alpha > 0.275$. Authors of paper [4] analyzed several formulas for η_{pl} calculation and evaluated formula which is valid for $\alpha > 0.05$. It means that this formula can be applied as well as for shallow and deep cracks and also for various rectangular cross sections sizes.

$$\eta_{pl} = 2.288(a/H)^5 - 16.754(a/H)^4 + 34.12(a/H)^3 - \\ -29.892(a/H)^2 + 12.065(a/H) + 0.139 \tag{11}$$

4. Crack length calculation

A measurement of crack size during impact is still relevant problem of dynamic fracture. Development of indirect crack length measurements methods remains relevant topic. Such method is proposed by author of paper [5]. Method requires only load and load line displacement values as input data for crack length calculation (Eq. 12). To verify the validity of formula under different loading rates authors have been performed three-point bend tests under static and dynamic loading with aluminum and high strength steel specimens. These two materials represented a brittle and ductile fracture behavior. Compliance of cracked beam is determined by equation:

$$BE\frac{u_P}{F} = \frac{1}{4}\left(\frac{L}{H}\right)^3\left[1 + \frac{12+11\nu}{5}\left(\frac{H}{L}\right)^2\right] + \left(\frac{L}{W}\right)^2 \cdot f(a/H) \tag{12}$$

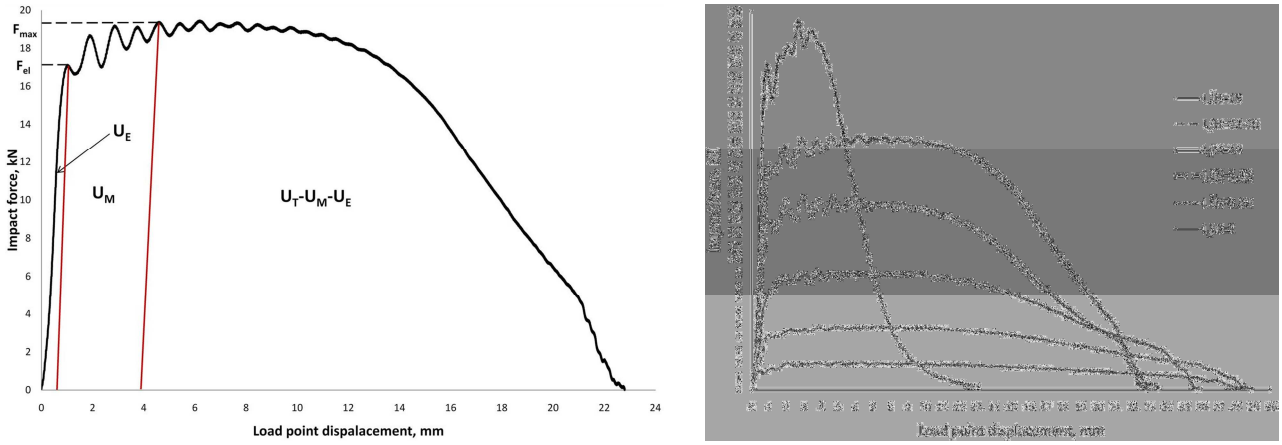
here E - Young modulus; F – load value mesured during experiment; u - load point displacement.

Bakker's function $f(a/H)$ is expressed by a fifth-order polynomial:

$$f\left(\frac{a}{H}\right) = \frac{(a/H)^2}{(1-a/H)^2} \cdot \left[8.9 - 33.717\left(\frac{a}{H}\right) + 79.616\left(\frac{a}{H}\right)^2 - 112.952\left(\frac{a}{H}\right)^3 \right. \\ \left. +84.815(a/H)^4 - 25.672(a/H)^5\right] \tag{13}$$

Eksperiment and results

Rectangular cross section specimens using three-point bending deformation scheme were tested under impact loading conditions (Fig. 1). Curves of impact force – load point displacement represent experimental results (Fig 2 b).



a b

Fig. 2 Experimental curves – a; energy separation approach – b

Five series of specimens with dimensions: L=90; B=10; a=2 mm (Fig. 2) and one series with - L=40; B=10; a=2 mm were manufactured. Each of five series had a different dimension H (5; 7; 9; 11; 13 mm). Specimens were cut from structural steel which chemical composition is listed in Table 1. As impact testing equipment drop weight tower INSTRON 9250HV was used. Initial impact velocity was 3.60 m/s.

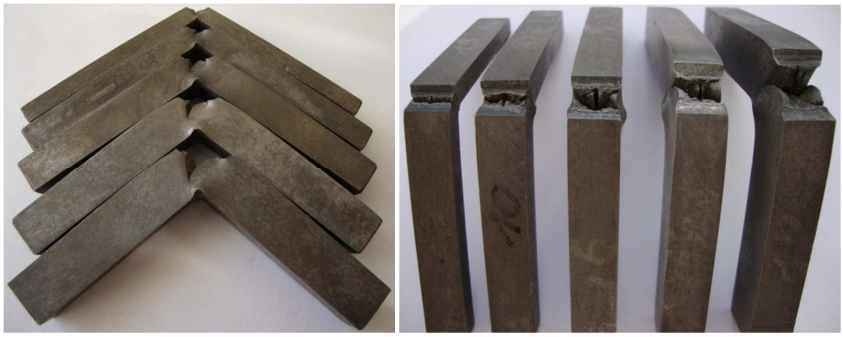


Fig. 3 Deformed specimens after test

Recorded experimental data was used for J integral determination (Table 2).

Table 1. Chemical composition of specimen's steel [%]

Fe	C	Si	Mn
98,4300	0,1400	0,3587	0,6986
P	S	Cr	Ni
<0,005	<0,005	0,0287	0,0391
Mo	Cu	Al	Ti
0,0352	0,0230	0,0940	<0,01
V	Co	Nb	W
<0,005	0,0201	0,0293	<0,05

Table 2. Calculated values of J integral [MJ/m^2]

Specimen's L/H	J_{el}	J_m	J_r	J_{tot}
18	0.579	0.417	2.190	3.187
12.86	0.295	0.542	2.762	3.599
10	0.159	0.609	2.980	3.749
8.18	0.130	0.726	2.906	3.762
6.92	0.079	0.717	3.103	3.900
4	1.409	0.762	2.028	2.931

Summary

Introduced method of J integral calculation and experimental results enable to compare fracture behavior of standard Charpy and non-standard (various dimensions) specimens.

References

[1] G. V. Guinea, J.Y. Pastor, J. Planas and M. Elices: Stress intensity factor, compliance and CMOD for a general three-point-bend beam. International Journal of Fracture: Vol. 83 (1998), p. 103-116.

[2] B. L. Karihaloo, Q. Z. Xiao: Higher terms of the crack tip asymptotic field for a notched three-point bend beam. International Journal of Fracture: Vol. 112 (2001), p. 111-128.

[3] H. J. Schindler and M. Veidt: Fracture toughness evaluation from instrumented sub- size charpy-type tests. Small Specimen Test Techniques, ASTM STP 1329 American Society for Testing and Materials (1997).

[4] P. R. Sreenivasen, and S. L. Mannan: Plastic η-factor for three-point bend specimen: Analysis of instrumented Charpy impact test results for AISI 308 weld and AISI 316 stainless steels. International Journal of Fracture: Vol. 101 (2000), p. 215-228.

[5] F. Jiang, A. Rohatgi, K. S. Vecchio, R. R. Adharapurapu: Crack length calculation for bend specimens under static and dynamic loading. Engineering Fracture Mechanics: Vol. 77 (2004) p. 1971-1985.

© (2012) Trans Tech Publications, Switzerland
doi:10.4028/www.scientific.net/KEM.488-489.634

Fracture Behavior of Directional TiAl Lamellar Structures

Ji Zhang

High Temperature Materials Division, China Iron and Steel Research Institute Group

No. 76 Xueyuan Nanlu, Beijing 100081, China

zhaji@public3.bta.net.cn

Keywords: TiAl alloy, Directional lamellar structures, Tensile test, Fracture behavior

Abstract: In order to assess the influences of macro- and microstructure as well as the cast flaw on the tensile properties, the fracture behavior of a number of ambient tensile TiAl specimens containing directional lamellar microstructure have been analyzed. It is found that all the fractures of tensile specimens are triggered by a critical Griffith crack. According to the desirable ambient tensile properties coincide with the initial cracking facets smaller than 600 μm, it is proposed that the detrimental effect of the random oriented lamellar colonies on the tensile properties can be eliminated through cast technology improvement.

Introduction

The long-range ordered crystal structure makes TiAl intermetallics possessing good strength and stiffness retentions at high temperatures. TiAl alloys are therefore considered as an attractive candidate material of turbine blades for its light-weight preponderance. The current roadblock includes intrinsically low room-temperature ductility，undesirable strength retention at high temperatures and not yet fulfilled cost control [1]. What the studies using polysynthetically twinned (PST) crystals have typically clarified the effect of lamellar orientation on the mechanical properties in TiAl alloys suggested that a good balance of strength and ductility can be obtained when the loading axis is parallel to the lamellar boundaries [2]. Accordingly, forming directional lamellar microstructures in the turbine blades is in principle a potent way to approach the designers' expectation, especially the increased endurance to the intermetallics' brittleness. Normally, seeding of the α phase in such casting operations is necessary since the lamellar structure of TiAl-base alloys consisting of γ-TiAl and α_2-Ti_3Al phases with the (111)γ // (0001)α_2 orientation relationship while the preferred growth direction of α dendrites is parallel to the [0001] direction [3]. It is therefore much cost-plus of course although it has shown a glimmer success in both lamellar orientation control and excellent mechanical properties [4]. On the other hand, simple casting operations that produce fully columnar macrostructures through α solidification should also result in the directional lamellar microstructure with the lamellar boundaries perpendicular to the growth direction, i.e., parallel to the blades' surfaces. It should also be beneficial to bear the service load in the turbine blades if the mechanical properties of TiAl alloys mainly depend on the lamellar orientation. The mechanical tests have proved that such oriented lamellar microstructures show excellent room temperature tensile properties, fracture resistance and also strength retention, creep rupture resistance and fatigue life at elevated temperatures [5]. It also brings out a potential way to approach the tradeoff between the mechanical behavior and cost. However, there are still many concerns about their reliability due to the existing macro-columnar boundaries and the final solidification area. Among those, the detrimental effect of columnar boundaries and cast flaws on the fracture behavior during ambient tensile tests is the major anxiety.

This study conducts a number of ambient tensile tests of the TiAl alloy containing directional lamellar microstructure with their boundaries being parallel to the loading direction. The influences of macro- and microstructure as well as the cast flaw on the tensile results deviation are thereafter assessed according to their effects on cracks initiation and propagation revealed through the fracture surface observations.

Experimental procedures

The cast Ti-47.5Al-2.5V-1.0Cr alloys was smelted in a vacuum cold crucible induction levitation-melting furnace and cast into an investment ceramic mould to produce $100\times80\times10$ mm^3 platy specimens. The hot isostatic pressing was carried out at 1240 – 1320°C in 120 – 150MPa Argon for 2.0 – 3.0 hours to remove the porosity in the cast specimens while remain the directional lamellar microstructure.

The metallographic specimens were mechanically polished, and those for microstructure observation were dip-etched by a hydro-solution containing 2%HF and 10%HNO_3 (by volume). The microstructure and porosity examinations were conducted under optical and scanning electronic microscopes. Tensile specimens were cut by spark erosion technique along the cast plates' longitudinal direction and then wheel ground to 25.0mm gauge length matching with 5.0mm diameter. The fracture surfaces were then examined by means of scanning electron microscopy.

Results and Discussion

Macro-observation showed that all the cast plates consisted of fully columnar macrostructure. As result, the γ-TiAl/α_2-Ti_3Al lamellae preferentially aligned vertical to the growing axis of the columnar crystals and therefore parallel to the surface of the cast plates as shown in Fig.1. The as cast specimens showed rather scattered tensile results with their strength ranging from 200 to 600 MPa and the ductility varying from 0.5% to 2.0%. This is coincident with the metallographic examination that the centre of the as-cast specimens contained gas and shrinkage pores as large as 300 μm. The HIPing at the temperatures above 1250°C was found effective to remove or shrink the pores to 20 μm or smaller. While, the specimens after the HIPing above 1280°C presented comparatively poor ductility around 1% and low strength about 470 MPa since they changed the morphology of the directional lamellar microstructure to a near fully lamellar microstructure. So, it is reasonable to figure out the cast directional lamellar microstructure ought to be hot-isostatically pressed at the temperatures between 1250°C and 1280°C as a normal procedure before tests and applications.

A large majority specimens experienced the appropriate HIPing showed excellent tensile results especially the plastic elongation ranging between 2 and 2.5% that is a very surpassing level in the so-far developed cast TiAl alloys [6]. But, there are still a few of specimens presenting the ambient tensile ductility lower than 1.0% unfortunately. The fracture surface observation is the intuitional means to reveal whether the ductility deviation was caused by columnar boundaries and cast flaws.

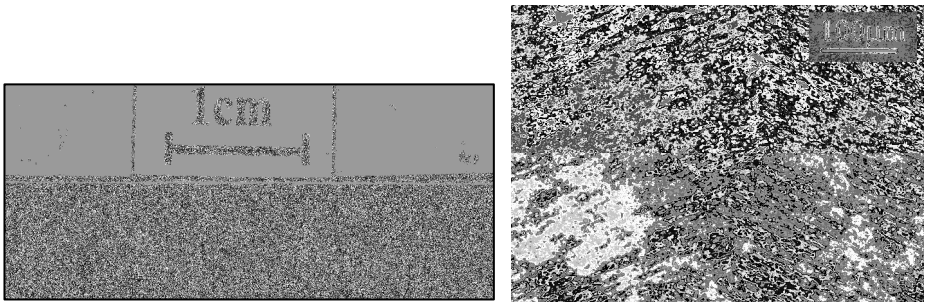


Fig.1 Optical macro- and microstructures of the cast TiAl plates

The macroscopic directional propagation of cracking shows that all the fractures of studied specimens are of a Griffths crack-triggering mode. The critical micro-cracks which trigger the final fracture locate at and extend from the outside surfaces of the round specimens (shown in Fig.2). Detailed observation found that the critical micro-cracks are composed of several coarse interlamellar microcracks characterized by smooth facet surfaces without obvious river pattern on them and the angles between the cleavage cracking planes of these sub-microcracks are very small (Fig.3).

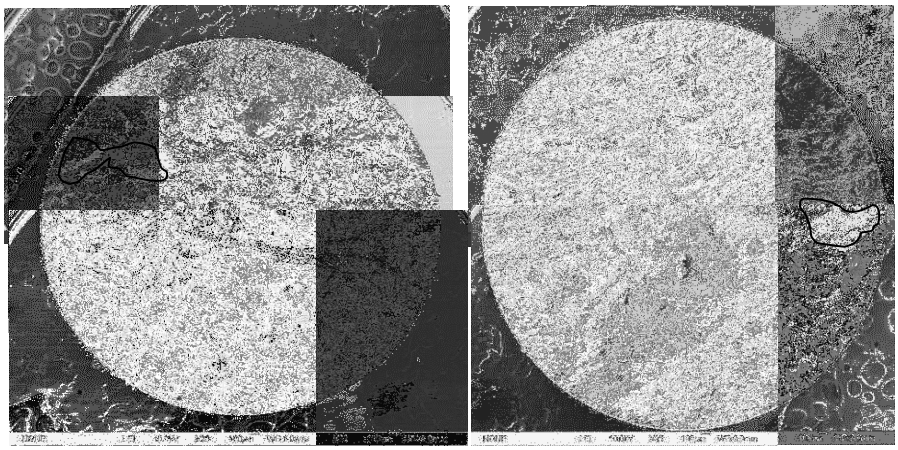


Fig.2 Typical macro-fracture surfaces of the tensile specimens of directional lamellar TiAl

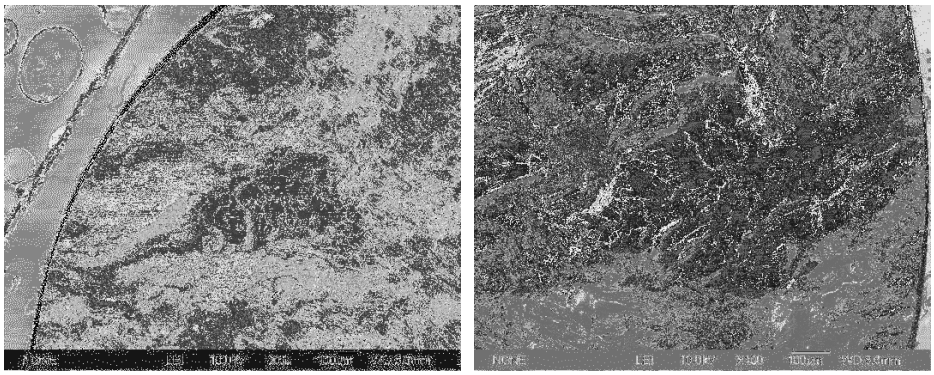


Fig.3 The critical interlamellar cracks that trigger the final fractures in Fig.2 respectively

According to the interlamellar strength being less than a third of the translamellar strength in TiAl lamellar structure [7], the size of the interlamellar crack should be the controlling factor for the failure of the studied TiAl tensile specimens. The statistic measurement of initial cracking facets suggests that the tilted lamellar colonies in the specimens with desirable ambient tensile properties are mostly smaller than 600μm.

The tilted lamellar colonies that are fragile in the tensile process are transformed from the equiaxed α grains that precipitate during final solidification due to not yet well optimized heat radiation condition. So, it is technologically possible to control the size of the random oriented lamellar colonies in order to have the area of interlamellar cracking surface being small enough to reach the critical value. The cast technology modification is on-going to produce more perfect directional lamellar microstructure.

Summary

All the fractures of tensile specimens taken longitudinally from the cast directional lamellar TiAl are triggered by a critical Griffith crack that is composed of several connected coarse interlamellar cracks. The desirable ambient tensile properties are coincident with the specimens with initial cracking facets smaller than 600μm when relating the test results to the area of critical integrated interlamellar crack. So that, the detrimental effect of the random oriented lamellar colonies on the tensile properties can be eliminated through cast technology improvement.

Acknowledgement

This study was financially supported by National Basic Research Program of China (973 Program contract number 2011CB605503) sponsored by the Ministry of Science and Technology of China. The authors wish to thank Ph.D student Sheng Li for carrying out the tensile tests and express gratitude to Dr. Rui Cao in Lanzhou University of Technology for her help with SEM work.

References

[1] R.E. Schafrik and S. Walston, in: Superalloys 2008, edtied by R.C. Reed, K.A. Green, P. Caron, T. P. Gabb, M.G. Famann, E.S. Huron and S.A. Woodard, TMS(2008), p. 3
[2] M. Yamaguchi, H. Inui and K. Ito: Acta mater. Vol48 (2000) , p.307
[3] D.R. Johnson, Y. Masuda, H. Inui and M. Yamaguchi: Acta Mater. Vol45 (1997) , p. 2523.
[4] M. Yamaguchi, D.R. Johnson, H.N. Lee and H. Inui: Intermetallics Vol8 (2000) p.511
[5] J.Zhang and Z.Y. Zheng: Materials China Vol9 (2010), P.9
[6] P. A. McQuay, in: Structural Intermetallics 2001, edtied by K.J. Hemker, D.M. Dimiduk, H. Clemens, R. Darolia, H. Inui, J.M. Larsen, V.K. Sikka, M. Thomas and J.D. Whittenberger, TMS (2001), p.3
[7] J.H. Chen, R. Cao, G.Z. Wang and J. Zhang: Metall. Mater. Trans.A Vol35A (2004), p.439

© (2012) Trans Tech Publications, Switzerland
doi:10.4028/www.scientific.net/KEM.488-489.638

Failure Mechanisms and Energy Absorption in Composite Elements under Axial Crush

A. F. Johnson and M. David

German Aerospace Center (DLR), Institute of Structures and Design,

Pfaffenwaldring 38-40, Stuttgart, Germany

alastair.johnson@dlr.de, matthew.david@dlr.de

Keywords: crashworthiness, energy absorption, crush test method, composites failure modes, finite element simulation

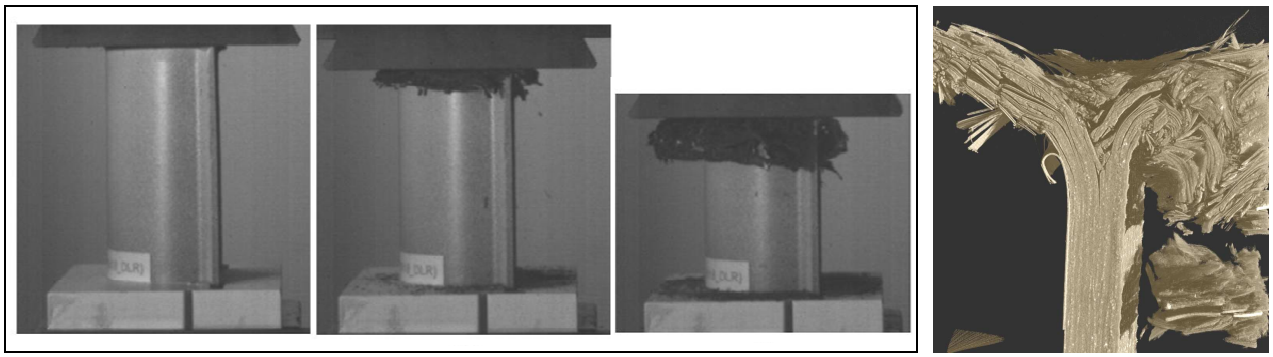
Abstract. Test methods are presented to determine failure modes and energy absorption properties of composite crash structural elements from quasi-static tests on chamfered carbon fabric/epoxy tube segment specimens under axial compression loads. High speed film and CT scans of failed specimens are used to identify trigger mechanisms, failure mode evolution at the crush front and failure processes during steady crushing. FE models of failure were developed which could be the basis for materials selection and design procedures for crashworthy composite structures. These are based on meso-scale composites ply damage models combined with cohesive interfaces to represent delamination failures, which damage and fail when the interface fracture energy is reached. The models are implemented in an explicit FE code and parameters for the ply damage and delamination models were obtained from related materials test programmes. The FE models were applied to simulate axial crushing in tube segments and C-channels, showing good predictions of measured peak forces at failure initiation, steady crush forces and total energy absorption.

Determination of composites crush failure and energy absorption properties

To measure and understand the energy absorption and failure mechanisms of composite structures requires the development of new test procedures and appropriate test specimens. Feraboli [1] reviews current test procedures and discusses the characteristics of flat plate and corrugated specimens for axial crush tests. The energy absorption (EA) properties to be measured are obtained from specimens which fail in a steady crush mode, requiring specially designed support fixtures or self-supporting specimens such as tubes and cylindrical profiles. DLR has developed chamfered tube segment specimens [2], which are easier to fabricate than tubes, are self-stabilising without lateral supports and give reproducible axial crush failures under both quasi-static and dynamic loading conditions. Quasi-static tests on the chamfered tube segment specimens are discussed here, and dynamic crush tests are described further in [2]. The test specimens consist of a half circle cylindrical segment with flanges at the longitudinal free edges to inhibit local buckling in axial compression. They were manufactured from Hexply M18-1/G939 carbon fabric/epoxy prepreg with eight fabric plies and a [0/90/0/90]s layup. Dimensions are length 75 mm, diameter 50 mm at flanges, nominal thickness 2.0 mm. The trigger mechanism was a 45º outside chamfer, which initiates a steady crush process at the chamfer tip. The base of the segment specimens is fixed in a support clamp to a lower steel platen mounted on the load cell of a quasi-static test machine. The chamfered edge is loaded in axial compression by a steel plate attached to the crosshead which loads the specimen at 1mm/s. Axial force-time and cross head displacement-time are measured in the test for typical crush distances of 50 mm.

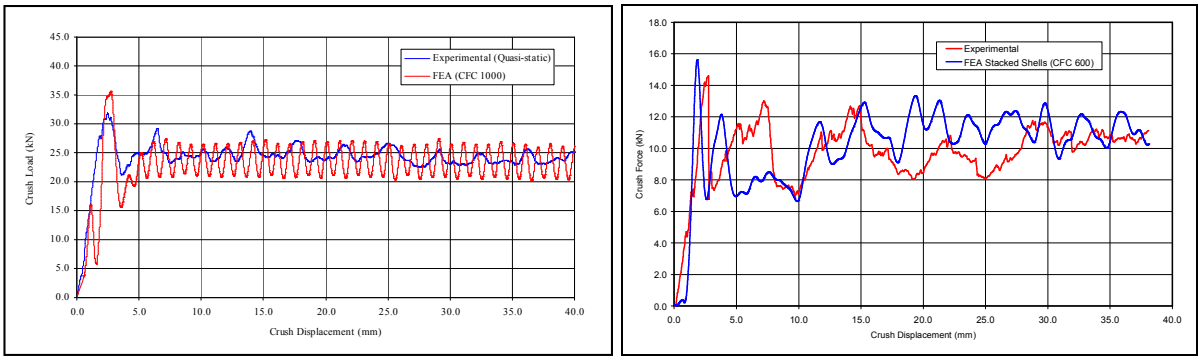
Fig. 1a shows images from the film of the crush test showing three phases, crushing down of trigger, splaying of the laminate into inner and outer laminae with a central delamination crack, followed by axial splitting of laminae bundles into petal-like fronds, as described in [3]. The steady state crush phase is composed of frond formation driven by the central delamination crack with a debris wedge as seen in Fig. 1b, which shows a computed tomography (CT) X-ray scan of the segment wall cross section at the crush front. The measured crush force - displacement curve of the segment specimen is plotted in Fig. 2a up to a displacement of 40 mm. The curve indicates a rapidly increasing load with peak at about 2 mm displacement which corresponds to loading the chamfer

trigger. This is followed by a sharp drop in load as the trigger fractures with load falling to a constant mean value in the steady state crushing phase. This steady crush is the basic mechanism used in the development of composites energy absorbing structures. Key parameters for design of such devices are the steady state crush force (SSCF), the energy absorbed (EA), defined as the area under the crush force-displacement curve, and Specific Energy Absorbed (SEA) the energy absorbed per unit mass of fractured material. In the test reported here SSCF = 24 kN, SAE = 87.1 kJ/kg, which are typical values for DLR segment tests with M18-1 carbon fabric prepreg materials, see data in the extended study of these specimens with different laminate lay-ups and manufacturing variants reported in Jackson et al [4].



a) Crush test sequence b) CT scan of crush front [3]

Fig. 1. Quasi-static crush test on carbon fabric/epoxy tube segment



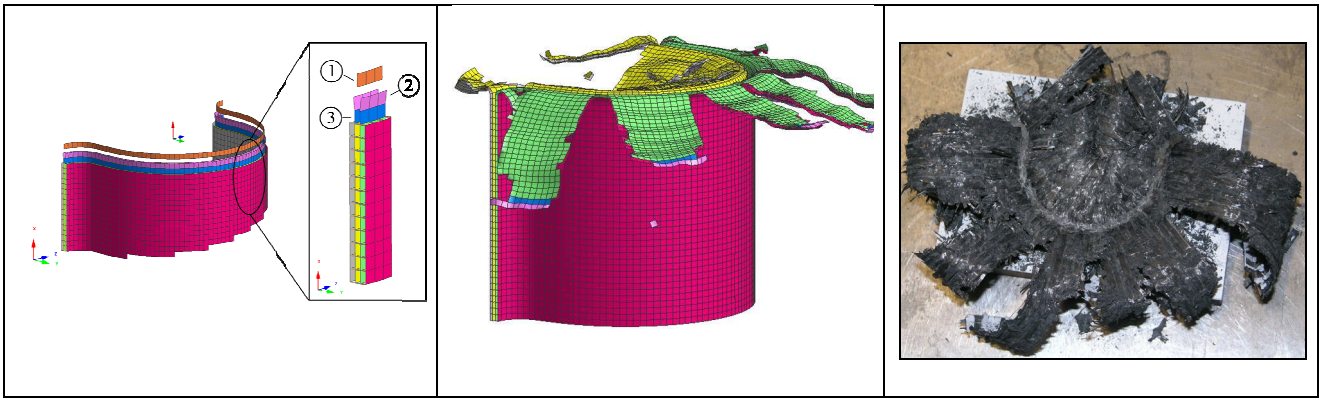
a) DLR half-tube segment b) C-channel section

Fig. 2 Crush force curves for composite sections: comparison of test data with FE simulation

FE simulation of composites crush elements

Modelling composites damage and failure. The segment crush tests provide data on crush failure mechanisms which may then be applied in design studies on crashworthy structures. Physical phenomena associated with impact damage and progressive collapse of composite structures are complex, and predictive models and simulation tools for design and analysis are urgently required to reduce the dependence on structural crash test programmes. A meso-scale composite model is used in which the composite laminate is modelled by layered shell elements. The shells are composed of composite plies assumed to be homogeneous orthotropic elastic or elastic-plastic damaging materials whose properties are degraded by micro-cracking prior to ultimate failure. The ply properties assigned were based on the Ladevèze [5] ply damage model for UD composites with shear plasticity, which was extended to fabric plies by Johnson et al [6]. Failure in the ply is controlled by fibre failure strains in tension or compression, or by reaching ply shear failure as determined by the shear damage energy at failure. The tests above on crush coupon specimens have shown the importance of interply delamination in controlling failure mode and energy absorption. The meso-scale FE models were extended in [6] to include stacked shell elements for the composite laminate connected through cohesive interfaces to model delaminations. This can be described as a 2.5D FE model, where the stacked shell technique allows a composite laminate to split into plies or

sublaminates when the cohesive interface fails and delamination occurs. The cohesive interface is controlled by an interface traction-displacement law such that interface contact is broken when the interface energy dissipated reaches the mixed mode delamination energy criteria. This contact interface is an efficient way of modelling delamination, with the advantage that the critical integration time step is relatively large since it depends on the area size of the shell elements not on the inter-ply thickness. The ply damage and failure models were implemented in the commercial explicit crash and impact code PAM-CRASH^{TM} in collaboration with the software company Engineering Systems International [7].



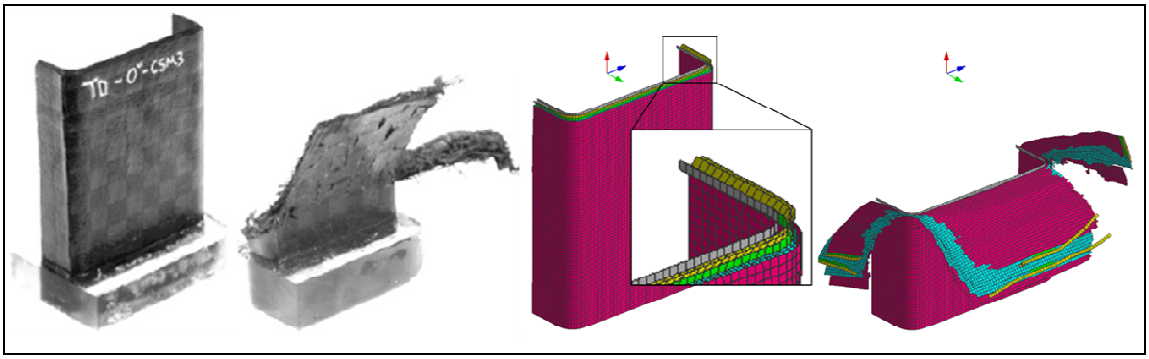
a) Chamfer trigger model b) Crush simulation c) Crush segment after test

Fig. 3. FE model of DLR carbon fabric/epoxy tube segment under axial crush

Simulation of segment crush behaviour. The numerical model selected for the segment test specimen consists of four stacked shells, as seen in Fig. 3a, b. Each shell in the stack is a 4-node layered composite shell which represents a ply or sublaminate ply group, with mesh size 1 mm. In the model here, each stacked shell represents two carbon fabric/epoxy plies. The ply properties assigned were based on the meso-scale fabric ply model discussed above. Material parameters were obtained from coupon tests previously conducted at DLR on the carbon fabric/epoxy material. The four stacked shells were connected using three cohesive interfaces whose failure behaviour was characterised by the delamination model. This requires interface fracture energy under mode I (G_{IC}) and mode II (G_{IIC}), which were determined from double cantilever beam (DCB) and end notched flexure (ENF) tests conducted at the DLR. Just as the chamfered edge is the key to initiate stable crushing in the segment specimen, the FE model requires a numerical trigger to produce a stable crush analysis as seen in Fig. 3a. This consists of a rigid element called a separation wedge which mimics the behaviour of the debris in the CT-scan image Fig. 1b. The elements representing the chamfer are then offset so that contact with the separation wedge initiates a central delamination crack in the stacked shells of the segment wall. The contact distance and friction coefficient between the segment shells and wedge are varied to control the delamination crack length, which in turn influences the degree of petalling in the fronds. Fig. 3b shows the segment simulation in the steady crush phase, which approximates quite well to the observed failure mode in the test segment shown in Fig. 3c. A critical test of the FE model is to compare computed crush load-displacement curves with test data as seen in Fig. 2a. These results are encouraging since the numerical simulations show an initial peak contact force, which after triggering drops to a steady crush force level close to that measured in the test, with similar good agreement in EA determined from the area under the force-displacement curves.

Simulation of C-channel crush behaviour. The modeling methods are now being applied to a range of composite structural elements being studied in the FAA CMH-17 Crashworthy WG, as described in some detail by Feraboli et al [8]. Fig. 4a shows one such element which is an open C-channel composed of eight plies of Toray T700/2510 carbon fabric/epoxy with a [0/90/0/90]s configuration and a nominal cured laminate thickness of 1.65mm. Channel dimensions are length 89 mm, width 63.5 mm and flange length 19 mm, with a 45° external chamfer at one end. Fig. 4a shows a C-channel test specimen before test and a failed specimen after a quasi-static axial

compression test, as performed in [8]. It is seen that the failure mode is no longer steady crushing as in the DLR segments, but the thin unsupported side walls bend outwards and cause a splaying failure mode with energy absorbed by tearing at the channel corners, which is unstable as indicated by the large oscillations in the measured load-deflection curve, Fig. 2b.



a) C-channel before and after crush test [8] b) Crush simulation with trigger and final failure

Fig. 4. FE model of carbon fabric/epoxy C-channel under axial crush

The FE model was again based on four stacked shells with three cohesive interfaces and mesh size 1 mm. Materials parameters were obtained from a standard ply dataset on the Toray T700/2510 material provided by CMH-17 to the WG, supplemented by DLR tests to characterise ply shear nonlinearity required in the ply damage model. To simulate the observed failure mode requires a numerical trigger to initiate shell bending rather than axial crushing. This consists of a bending wedge Fig. 4b at the inside of the central chamfer plies which causes transverse outward bending of the stacked shells. This in turn leads to axial tearing at the corner segments as the stacked shells impact the loading platen. The simulated failure mode in Fig. 4b shows outward bending of the three plate elements with fracture at the corners, corresponding to the failed test specimen. Fig. 2b compares measured and simulated axial crush forces for the C-channel, which are in good agreement on the main features. Because the tearing failure mechanism absorbs less energy than steady axial crush, it is seen that the steady crush load and hence EA is about half that measured in the half tube segments for specimens of similar size and mass.

Acknowledgements. The authors wish to thank R. Thomson and A. Jackson of CRC-ACS, Melbourne for manufacture of segment specimens and P. Feraboli, Chair of the CMH-17 Crashworthy WG, for test data on the C-channels.

References

[1] P. Feraboli, Development of a corrugated specimen for composite materials energy absorption, J. Comp. Mats. **42,** 229, 2008.

[2] M. David, Dynamic Crush Tests on Composite Segment Specimens, DLR Report IB 435-2009/**11**, 2009.

[3] A.F. Johnson, M. David, Failure Mechanisms in Energy-absorbing Composite Structures. Philosophical Magazine, **90** (31-32), 4245, Taylor & Francis, 2010.

[4] A. Jackson, S. Dutton, A.J. Gunnion and D. Kelly, Effect of manufacture and laminate design on energy absorption of open carbon fibre/epoxy sections, ICCM17, Edinburgh, UK, 2009.

[5] P. Ladeveze, , E. Le Dantec, Damage modelling of the elementary ply for laminated composites, Composites Science and Technology, **43**, 257, 1992.

[6] A.F. Johnson, A.K. Pickett, P. Rozycki, Computational methods for predicting impact damage in composite structures. Composites Science and Technology, **61**, 2183, 2001.

[7] PAM-CRASH™ FE Code, Engineering Systems International, F-94513 Rungis Cedex, France.

[8] P. Feraboli, B. Wade, F. Deleo, M. Rassaian, Crush energy absorption of composite channel section specimens. Composites Part A: Applied Science and Manufacturing, **40**/8, 1248, 2009.

© (2012) Trans Tech Publications, Switzerland
doi:10.4028/www.scientific.net/KEM.488-489.642

Experimental Fracture Behavior of Polypropylene Fiber Reinforced Concrete Specimens with Variable Width

Héctor Cifuentes[1, a], Fernando Medina[1,b]

[1]Grupo de Estructuras. Escuela Técnica Superior de Ingeniería. University of Seville. Spain

[a]bulte@us.es, [b]medinaencina@us.es

Keywords: Cross Section of Variable Width, Fiber Reinforced Concrete, Polypropylene Fibers.

Abstract. This paper presents a study of the influence of polypropylene fiber reinforcement of concrete on the fracture behavior and edge effect in elements of variable width. Experimental results of fracture behavior of specimens with different cross sections are available. It has obtained more ductile behavior for specimens with trapezoidal sections (with increasing width) and inverted T-sections. Therefore, we analyze the influence of the fibers addition on the fracture behavior of these sections. Sections with gradual variation of wide and sudden change of width were analyzed. Results allow us to quantify the increase of ductility and fracture performance improvements produced by polypropylene fiber addition to concrete in these sections.

Introduction

The cross section dimensions of the specimens used for the determination of the RILEM fracture energy [1] have a considerable influence on the obtained results [2, 3]. This influence is considered the size effect of concrete in the RILEM fracture energy of concrete [4].

Thus, many researchers have analyzed the dependence of the values of fracture energy with the size of the ligament area and the concept of edge effect in concrete structures was introduced [3-6].

On the other hand, the addition of polypropylene fibers to concrete increases the fracture properties of the material [7]. The favorable effect of fibers occurs mainly when the crack front approaches to the top free edge of the specimen (in rectangular sections). For this reason, a significant influence of the polypropylene fibers addition to concrete on edge effect is expected.

This paper presents an experimental analysis on the influence of the polypropylene fibers addition on the fracture behavior in variable width sections. The analyzed sections have been chosen appropriately, based on experimental results of fracture behavior. Two different types of cross sections with variable width are analyzed. The first type is a trapezoidal section with linear width variation in the ligament area. On the other hand, the second type is a T section with an abrupt change of width from flange to web. So, the edge effect will be revealed and analyzed.

Experimental Procedure

Specimens Geometry. Fig. 1 shows the geometric dimensions of the different cross sections of the specimens.

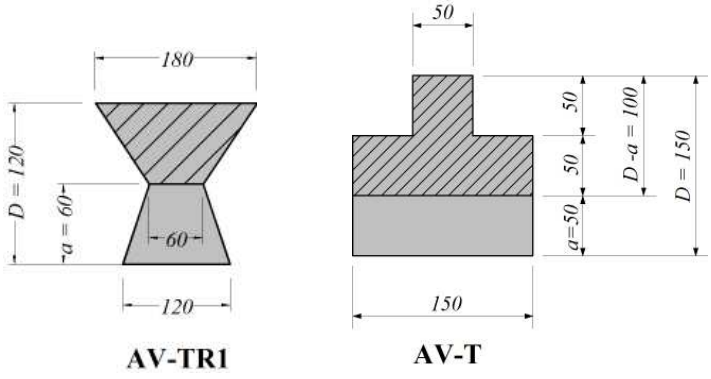


Fig. 1. Geometric shape of the different cross sections analyzed.

Where a is the initial notch depth. The length of all specimens is $L = 4.5D$ and the span between supports is $S = 4\ D$.

The AV-TR1 section is a trapezoidal section with linear width variation in the ligament area. So, the effect of a gradual variation of width is analyzed.

The AV-T section is a T section with an abrupt change of width from flange to web. So, the effect of a discrete variation of width is considered.

Materials. Two different types of concrete were manufactured. The only difference between them is the polypropylene fibers addition. The non-reinforced concrete (NRC) has been made with Portland cement type I/52.2 according to EN-197-1, siliceous aggregates of maximum size 6mm, adjusted according to the parable of Fuller, and mix proportions (AG / C / A) 4.6/1/0.5 with cement content of 400 kg/m^3. The fiber-reinforced concrete (FRC) has identical mix proportions than NRC concrete and the addition of polypropylene fibers (1200 g/m^3).

The properties of concrete were determined from standard specimens for normal strength concrete, i.e. 150 × 300mm cylinders (diameter × height), and the indirect tensile strength from split cylinder tests. The concrete modulus of rupture in bending was also determined from standard prismatic specimens, 150 × 150 × 600mm (thickness × depth × length). In Table 1 are shown the mechanical properties of the two types of concrete.

Table 1. Mechanical properties of concrete

Concrete	NRC	FRC
Compressive strength, f_c [MPa]	56.5 ±4%	57.8 ±2%
Split tensile strength, f_{cti} [MPa]	4.7 ±6%	4.9 ±9%
Modulus of rupture in bending, f_{ctf} [MPa]	6.5 ±1%	6.1 ±3%
Elastic modulus, E_c [GPa]	34.1 ±12%	34.3 ±15%

Polypropylene fibers are 24 mm in length, 33 μm in thickness and the ultimate tensile strength is 450 MPa.

Three-Point Bending Tests. In order to obtain the fracture energy G_f, by means of the work of fracture method [5], three-point bending tests were driven in a ±25 kN dynamic machine with a closed-loop servo control in vertical displacement at midpoint. The supports were antitorque, so parasite effects were no present. The CMOD displacement was measured with a clip gauge transducer and a LVDT displacement transducer was used to measure the vertical displacement at midpoint. So the load-CMOD and load-displacement curves for all specimens have been recorded. At least three specimens for each type of concrete were tested, according to RILEM procedure [1].

Fig. 2 shows a photograph of the three-point bending test for specimens with linear width variation of ligament area (left) and for specimens with abrupt change of width of ligament area (right).

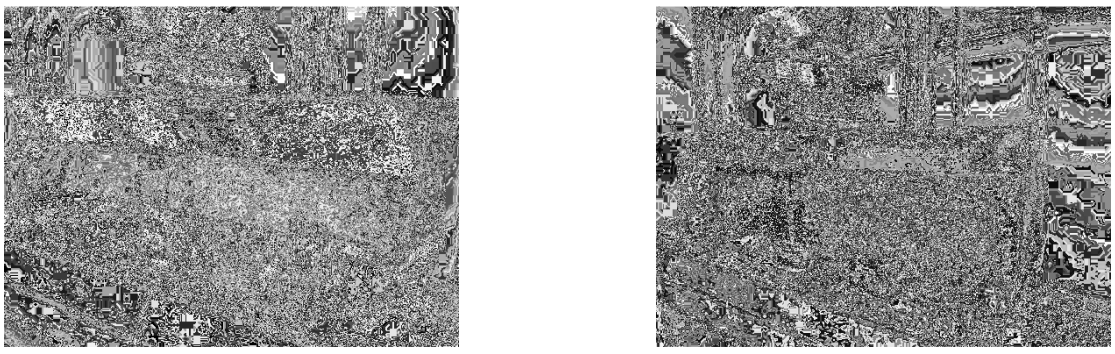


Fig. 2. Three-point bending test of AV-TR1 specimens (left) and AV-T specimens (right).

Results. Table 2 shows the results of RILEM fracture energy for each specimen and type of concrete analyzed. Moreover, with the material properties of concrete (Table 1) and the values of the fracture energy, the characteristic length ($l_{ch}= E_c G_f /f_{cti}^2$) of concrete was obtained for each specimen. As is shown, a shape dependence of fracture properties is obtained.

In order to analyze the ductility of the sections and taking into account that not all specimens have the same size, the inverse of the fragility number of Hillerborg (β_H) [8,9] have been obtained. This parameter is used for measuring the ductility of the cross section and is given by:

$$\frac{1}{\beta_H} = \frac{l_{ch}}{D} \tag{1}$$

Table 2. Fracture properties for different types of specimens and concrete

Specimen	G_f [N/m]	l_{ch} [mm]	$1/\beta_H$
AV-TR1-NRC	149.0 ±20%	218.5 ±20%	1.82
AV-T-NRC	169.6 ±6%	248.7 ±6%	1.66
AV-TR1-FRC	315.7 ±18%	451.2 ±16%	3.8
AV-TR1-FRC	429.2 ±21%	613.4 ±19%	4.1

As is observed from results in Table 2, there is a considerable increase of the RILEM fracture energy with the addition of polypropylene fibers to concrete. Comparing the results for AV-TR1-NRC and AV-T-NRC specimens with those corresponding to FRC concrete, is obtained that the RILEM fracture energy undergoes an increase of 112% for AV-TR1 specimens and 153% for AV-T specimens. The effect of polypropylene fibers addition to concrete is most remarkable in the case of the inverted T-sections analyzed (AV-T). In terms of ductility, AV-TR1 sections experience an increase of 109% and the corresponding increase for AV-T specimens is 147%. This increase in the values of the RILEM fracture energy and ductility of the material for each section considered is due to the bridging effect of the polypropylene fibers in the crack front (Fig. 3). As shown in results (Table 2) the bridging effect is most noticeable in the inverted T-sections (AV-T-FRC), where the fibers bridge the bottom flange of the section. Therefore, the addition of fibers interacts with the edge effect of the section more in the specimens with T cross section than in trapezoidal cross section specimens. This effect is also evident in the post-peak behavior of *P-CMOD* curves of the specimens tested. Fig. 4-left shows the *P-CMOD* curves for the specimens AV-TR1-NRC and AV-TR1-FRC. Similarly, in Fig. 4-right shows the curves of the samples AV-T-NRC and AV-T-FRC, which shows the addition of polypropylene fibers.



Fig. 3. Bridge effect of polypropylene fibers in the crack front.

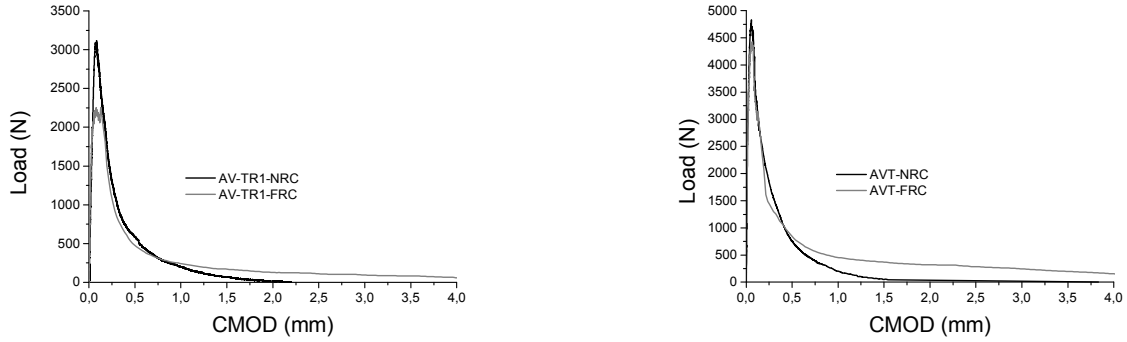


Fig. 4. *P-CMOD* curves for AV-TR1 specimens (left) and AV-T specimens (right) with NRC and FRC concrete.

Conclusions

From results, the following conclusions can be established:

The influence of polypropylene fiber addition to concrete is more remarkable in the inverted T section analyzed (AV-T).

The rise of fracture energy for the trapezoidal sections (AV-TR1) with the addition of polypropylene fibers is 112%. The increase of ductility in these sections was quantified by 109%.

Similarly, we have obtained a 153% increase in fracture energy for the case of the T-section specimens analyzed. The increase of ductility in this case is 147%.

Polypropylene fibers used as reinforcement in the specimens analyzed, presented a greater bridge effect in T-sections (AV-T) due to the bridging of the bottom flange of the section.

References

[1] RILEM TC-50 FMC: *Determination of the Fracture Energy of Mortar and Concrete by Means of Three-Point Bend Tests on Notched Beams*. Materials and Structures, Vol.18 (1995), pp.285-290.

[2] Z.P. Bazant and M.T. Kazemi: *Size dependence of concrete fracture energy determined by RILEM work-of-fracture method*. International Journal of Fracture, Vol. 51 (1995), pp. 121-138.

[3] X. Hu and F. Wittmann: *Size effect on toughness induced by crack close to free surface.* Engineering Fracture Mechanics, Vol. 65, pp. 209-221, 2000.

[4] X. Hu y K. Duan: *Size effect: Influence of proximity of fracture process zone to specimen boundary*. Engineering Fracture Mechanics, V. 74 (2007), pp. 1093-1100.

[5] H.M. Abdalla and B.L. Karihaloo: *Determination of size-independent specific fracture energy of concrete from three-point bend and wedge splitting tests.* Magazine of Concrete Research, V. 55 (2003), pp. 133-141.

[6] K. Duan, X. Hu and F. Wittmann: Thickness effect on fracture energy of cementitious materials. Cement and Concrete Research, V. 33 (2003), pp. 499-507.

[7] F. Medina, H. Cifuentes and M. Alcalde: *Efecto tamaño y ductilidad en hormigones de baja y alta resistencia reforzados con fibras de polipropileno.* Cemento – Hormigón, Nº. 930 (2009), pp. 32-42.

[8] G. Ruiz, M. Elices and J. Planas: *Experimental study of fracture of lightly reinforced concrete beams*, Materials and Structures, V. 31 (1998), pp. 683-691.

[9] Z.P. Bazant: Scaling of Structural Strength. (Elsevier, Great Britain, 2002).

© (2012) Trans Tech Publications, Switzerland
doi:10.4028/www.scientific.net/KEM.488-489.646

Influence of the wall thickness on the allowable and failure pressures of two- and tree-way globe valve bodies

M.Opalić[1,a], I.Galić[1,b] and K.Vučković[1,c]

[1]Faculty of Mechanical Engineering and Naval Architecture, University of Zagreb
Ivana Lučića 5, 10000 Zagreb, Croatia

[a]milan.opalic@fsb.hr, [b]ivica.galic@fsb.hr, [c]kresimir.vuckovic@fsb.hr

Keywords: Plastic collapse pressure, allowable pressure, failure pressure, two-way globe valve, tree-way globe valve.

Abstract. A globe valve is a linear motion valve used to shut off and regulate fluid flow in pipelines. Depending on the number of process connections, they are produced as two- or three-way valves. The main valve component carrying the internal pressure is the valve body. For safe exploitation, the valves are designed with the allowable internal pressure taken into consideration. The aim of this paper is to investigate the influence of the wall thickness on the allowable and failure pressures of two- and tree-way globe valve bodies, DN50 and DN100 respectively. Twice-elastic-slope (TES) and the tangent-intersection (TI) methods are used to obtain the plastic collapse pressures at the critical location which was determined (Fig. 1a and 1b) at the location where maximum equivalent plastic strain throughout the valve body thickness reaches the outer surface. Obtained values are used afterwards to calculate corresponding allowable pressures according to the limit design method, while the failure pressure at the same location was determined as the highest point from the load-maximal principal strain curve. Calculated allowable pressure values, for both valve bodies, are compared with the corresponding ones obtained using the EN standard.

Introduction

A globe valve is characterized by a baffle or partition separating the two halves of a body, with an interconnecting part at the centre which is opened and closed by a disc or plug mounted at the right angles to the body. For safe exploitation, the valves are designed with respect to the allowable internal pressure. In order to define the allowable load of the pressure vessel components according to the limit design method [1], it is necessary to determine the plastic collapse pressure due to the static load. Therefore, the plastic collapse pressure can be predicted by the limit load analysis of the finite element (FE), based on the large-scale strain theory, emphasizing the effect of strain hardening. Twice-elastic-slope (TES) and the tangent-intersection (TI) methods are used to determine the plastic collapse pressure. TES method [1] defines the collapse load as the load at the intersection of a line drawn from the origin of the load-strain curve, at twice the slope of the linear elastic part of the load-strain curve. In order to determine the collapse load by means of the TI method [2], it is necessary to draw the tangent line to the linear and nonlinear parts of the load-strain curve. The load in the tangent lines intersection defines the plastic collapse load.

The aim of this paper is to investigate the influence of the wall thickness on the allowable and failure pressures of two- and tree-way globe valve bodies, DN50 and DN100 respectively.

Finite Element Analyses

Tree-dimensional nonlinear FE analyses are performed using commercial FE software ABAQUS/Standard [3]. Because of the symmetrical geometry with respect to the vertical plane, only half of the body is modelled (Fig. 1). To simplify a numerical model and to reduce a number of finite elements, lateral flanges, due to their large stiffness, are not modeled [4, 5]. Since this is a case of a very complex geometry, a free-meshing algorithm is applied. For the model discretization, a modified quadratic tetrahedral element (C3D10M) is applied as adequate for both small and large deformations. Boundary conditions are defined by restraining displacements in all nodes in the

symmetry plane in the direction perpendicular to the plane. Internal pressure is applied to all internal surfaces of FE valve body model. Internal pressure affecting medial flanges is applied as the surface traction and assigned to the threaded holes in a direction normal to the flange surface. The real material hardening and geometrical nonlinearity are modeled. For this purpose, mechanical parameters of the cast steel GS-C25 are used, as described in [5]. Nonlinear material behavior is modelled using the incremental plasticity with the von Mises yield function, together with the associated flow rule and isotropic hardening.

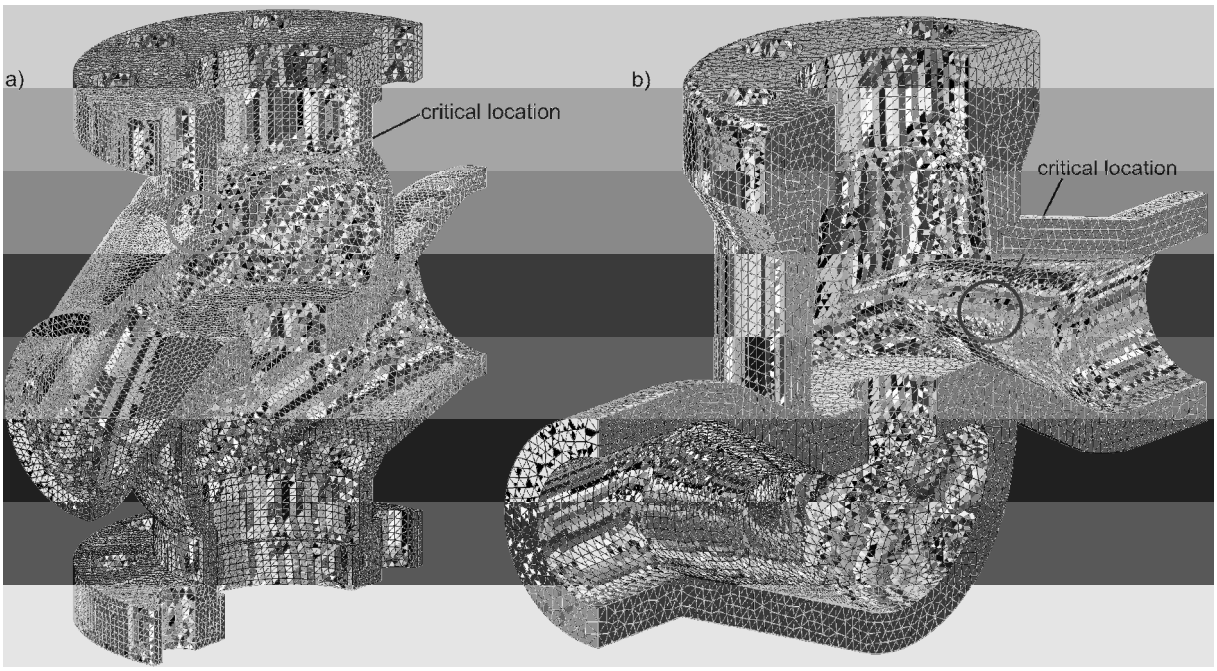


Fig. 1: Typical FE mesh with critical location: a) for DN100, b) for DN50

Comparison results from Finite Element method and EN12516-2

In Fig. 2a and 2b, FE results are given in pressures versus strain diagram at critical location for different wall thickness, where p_1 means plastic insatiability pressure. The zone with the maximum equivalent plastic strain throughout the valve body thickness, at the location where maximum equivalent plastic strain reaches the outer surface of the model is determined as the critical location.

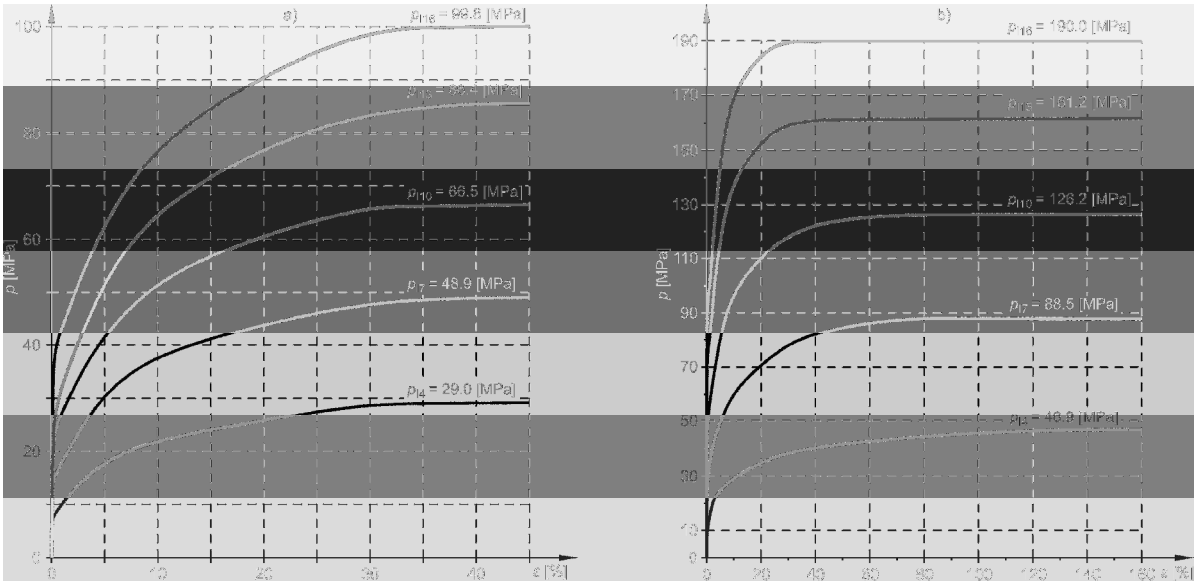


Fig. 2: Variation of pressure with maximal principal strain for: a) DN100 valve body and b) for DN50 valve body

From the pressure-strain curves shown in Fig. 2, the plastic instability pressure p_I is obtained as the highest point on the curve. In the FE analyses it is assumed that the material will fail in a ductile manner so that the plastic instability pressure p_I represents the failure pressure p_F that causes the plastic collapse of the body.

Based on the numerical results, plastic collapse pressure at critical location is determined. Collapse pressure–wall thickness diagrams at critical location are shown in Fig. 3 for DN100 and DN50 valve. It can be noticed in both cases that pressure collapse obtained by TES method is lower than the corresponding one obtained by TI method. For safety reasons, the allowable pressures are therefore calculated from pressure collapse values obtained by TES method.

For both analyzed valve bodies, the plastic collapse pressure is increased along with the thicker valve wall as anticipated. For the values obtained by TES method this change is almost linear, but this is not the case for the values obtained by the TI method. This nonlinearity can be explained by the fact that the TI method is sensitive to the selection of the point in which the tangent line is drawn to the nonlinear part of the curve.

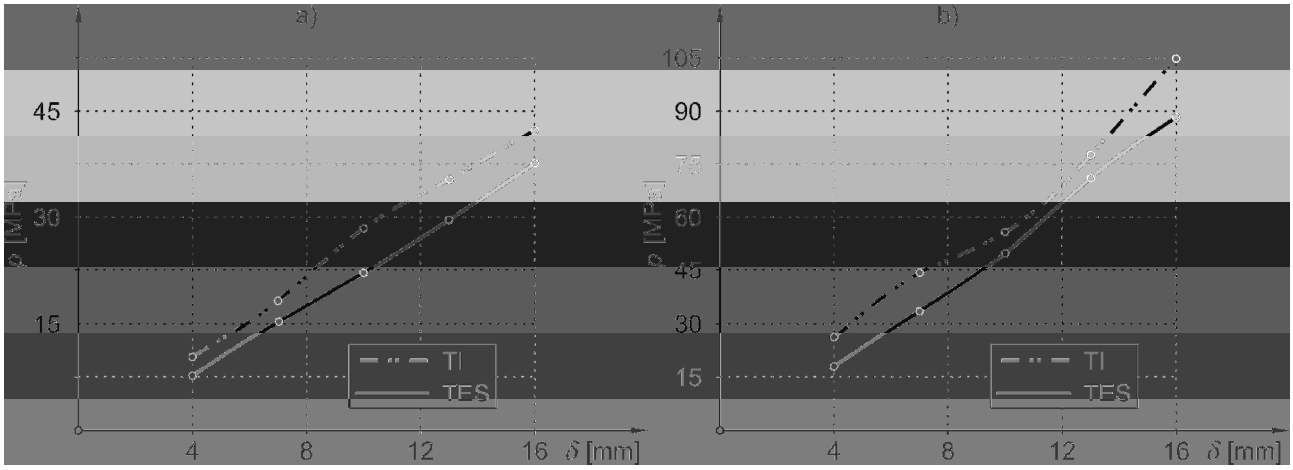


Fig. 3: Plastic collapse pressure variation with wall thickness for:
a) DN100 and b) DN50

In common engineering practice, the calculation of the valve body wall thickness is done in accordance with the EN 12516-2 standard [6]. The calculation has two steps: the calculation of the body main section wall thickness and calculation of wall thickness in the crotch area. Since the wall thickness in the crotch area cannot be calculated directly, the initial wall thickness in this area is assumed from the one calculated in the first step and then incrementally increased until the equilibrium of forces is reached. The investigated valve bodies DN50 and DN100 wall thickness calculations are, therefore, carried out only in the crotch area.

The maximum allowable pressures for the valve bodies are determined according to the expression

$$p \le \frac{f}{\left(\frac{A_p}{k_c \cdot A_f} + \frac{1}{2}\right)} \tag{1}$$

where $f = \sigma_y / 1{,}9$, $k_c = 1$ are used for a non-welded structure, σ_y - yield stress, A_p - pressurized valve body area, A_f - wall thickness area. Both areas, A_p and A_f, are determined graphically according to EN12516-2, and then inserted into expression (1).

In accordance with [1], the allowable pressure $p_{allowable}$ based on the limit design method is determined from the plastic collapse pressure p_c through the expression

$$p_{\text{allowable}} = \frac{2}{3} \cdot p_{\text{C}} \tag{2}$$

Table 1: Allowable pressure in [MPa]

Wall thickness		4	7	10	13	16
DN50	Left EN	26.44	30.93	35.25	39.69	43.98
	Right EN	7.91	14.29	22.27	30.04	37.47
	FEA	11.95	22.33	33.22	47.45	58.88
DN100	Left EN	25.39	25.27	25.76	28.22	30.79
	Right EN	4.18	9.24	13.40	18.84	23.99
	FEA	5.13	10.15	14.71	19,74	25.09

In the Table 1, comparison of the allowable pressure obtained by EN 12516-2 and FE are shown. Allowable pressure values for DN100 valve body obtained by FE analysis have good agreement with the corresponding ones calculated by the EN standard [6]. Unlike the allowable pressure values for the DN50 valve body calculated by the EN standard are highly conservative in comparison to corresponding ones obtained by FE analysis.

Conclusion

This paper is focused on two- and tree-way globe valve bodies, DN50 and DN100, with different wall thicknesses that are subjected to internal pressure. Three-dimensional nonlinear FE analyses are performed to obtain the plastic instability and collapse pressures. From the pressure - strain diagram that is obtained by the FE analysis, the failure pressure, i.e. the plastic instability pressure, is determined as the highest point on the curve. Based on the numerical results, the body plastic collapse pressures are determined.

As presented in this paper, the allowable pressure values are increased with increasing the wall thickness. This change is linear for both valve body types and for the values obtained by FE and by EN12516-2. In the case dealing with two-way globe valve body, DN50, it is shown that allowable pressure calculated by the application of the EN12516-2 standard is highly conservative compared with the one derived by the application of FE results. The wall thickness in the crotch area of the two-way globe valve body, according to the EN12516-2 standard, is calculated only in a symmetry plane. Although critical location obtained by the FEM is located in the crotch area, it is located away from the symmetry plane and thus away from both critical locations proposed by the EN12516-2 standard.

References

[1] ASME Boiler and pressure vessel code section III and VIII. New York: American Society for Mechanical Engineers, NY (1995)

[2] M. Save, in: *Pressure Vessel and Piping: Design and Analysis*, edited by G.J. Bohm, R.L. Cloud, 4th ASME, NY (1972), p. 382-416.

[3] D. Hibbitt, B. Karlsson and P. Sorensen, in: *ABAQUS/Standard. User's guide and theoretical manual*, Version 6.7, (2007)

[4] I. Galić, Z. Tonković and K. Vučković in: *Engineering Against Fracture*, edited by S.G. Pantelakis, C.A. Rodopoulos / Springer, Berlin, (2009), p. 487-497.

[5] I. Galić, Z. Tonković, K. Vučković, in: *Technical Gazette* / edited by P. Raos and M. Kljajin Slavonski Brod (2010), p. 67-74.

[6] EN 12516-2 (2004), Industrial valves - Shell design strength - Part 2: Calculation method for steel valve shells, Beuth Verlag GMBH, Berlin

© (2012) Trans Tech Publications, Switzerland
doi:10.4028/www.scientific.net/KEM.488-489.650

Analysis of shear strength of wood

Tihomir Štefić[1,a], Aleksandar Jurić[2,b] and Pavao Marović[3,c]

[1]J.J.Strossmayer University of Osijek, Faculty of Civil Engineering Osijek, Drinska 16a, HR-31000 Osijek, Croatia

[2]J.J.Strossmayer University of Osijek, Faculty of Civil Engineering Osijek, Drinska 16a, HR-31000 Osijek, Croatia

[3]University of Split, Faculty of Civil Engineering and Architecture, Matice hrvatske 15, HR-21000 Split, Croatia

[a]tstefic@gfos.hr, [b]ajuric@gfos.hr, [c]pavao.marovic@gradst.hr

Keywords: Shear strength, wood, fracture mode, FE analysis, shear test specimen.

Abstract. This paper presents the analysis of different types of shear strength of wood which can differ very much due to its structure and different orientations of applied load. These combinations of wood structure and load orientations lead to different modes of fracture. The main aim of the paper is to find a relation among all types of shear strength of the wood and to reduce the number of shear tests. Furthermore, different shear strengths will be analyzed both experimentally and numerically, i.e. experimentally by testing appropriate specimens and numerically with the help of the finite element structural analysis solver Robot AutoDesk. The testing specimens will be loaded parallel and perpendicular to the wood fibres and the radial and tangential planes will be analyzed. The paper will also investigate the relation to other strengths of wood (i.e. tensile strength parallel and perpendicular to the fibres) in order to simplify the testing procedure for shear strength determination.

I. Introduction

Wood as an anisotropic material is composed out of many small tubes (fibres) that correspond better to normal stresses in the longitudinal direction i.e. in the fibre direction, then to normal stresses perpendicular to the fibres and shear stresses in the longitudinal direction. Although it is often very difficult, it is recommended to avoid the mentioned unfavourable stresses in the process of design. Because of this weakness of the wood it is necessary to analyze all shear stresses and interaction of shear and normal stresses. In this paper an experimental analysis was performed on a short wooden specimens loaded with shear force, taking into account different combinations of fibre and load orientation. The results are presented with breaking forces and they are compared to the one obtained with the finite element structural analysis software by using linear numerical model. Critical shear stresses parallel and perpendicular to the fibres and to the radial plane are compared. For the design of shear stresses in timber elements, we use expressions from Eurocode EC5 [1] and literature [2, 3]:

$$\tau_{xz} = \frac{T_z S_y}{b I_y}; \quad \tau_{xy} = \frac{T_y S_z}{h I_z}. \tag{1}$$

$$\tau_{x,z} = \tau_{v,d} = 1{,}5\frac{V_d}{A} \leq f_{v,d}. \tag{2}$$

The mentioned expressions (1) and (2) were created for homogenous materials and their application is limited and questionable when applying to inhomogeneous and especially anisotropic material as wood. As all structures are in the state of different as well as combined normal and shear stresses, it is necessary to know characteristics of the material in all directions, so it would be possible to assure that stresses will not exceed the allowed values. In homogenous materials it is possible to check normal and shear stresses by using only one value, i.e. the yield strength for steel, which is not the case for wood. In order to check all possible states of normal and shear stresses when

designing timber elements, it is necessary to know several characteristics of the material. Unified experimental methods are very helpful when different characteristics of a material are needed. A mathematical connection that would give data for all material characteristic from a smaller number of experimental tests would also be appreciated. Considering all mentioned above this paper tries to make connections that would bound shear strengths of wood.

II. Analysis

In order to have a better insight into the critical shear stresses the analysis was conducted on short wooden specimens and all load cases were repeated four times. The experimental setup of one of the load cases and boundary conditions is shown in Figure 1, while the definition of axes considering longitudinal, tangential and radial direction of fibres is shown in Figure 2.

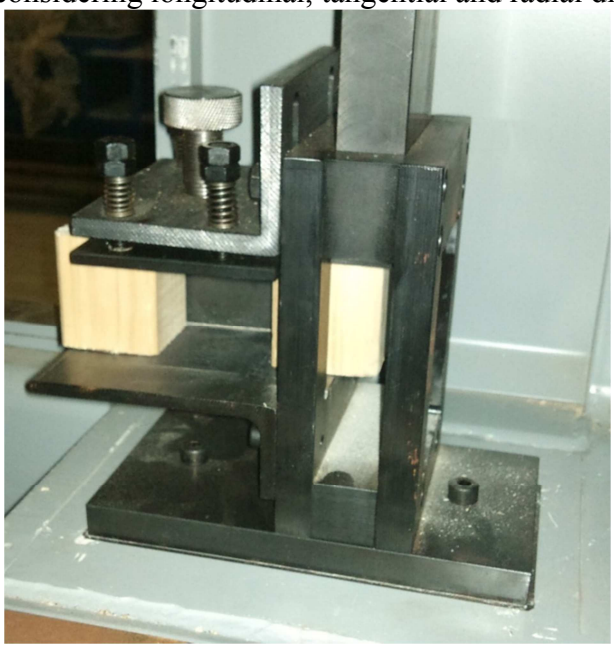


Figure 1. – Experimental setup

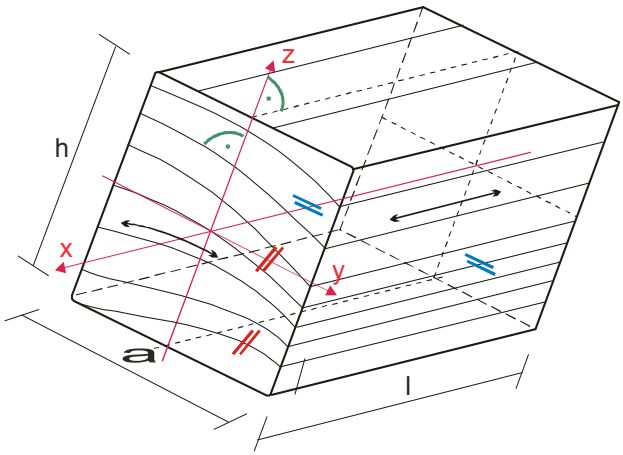
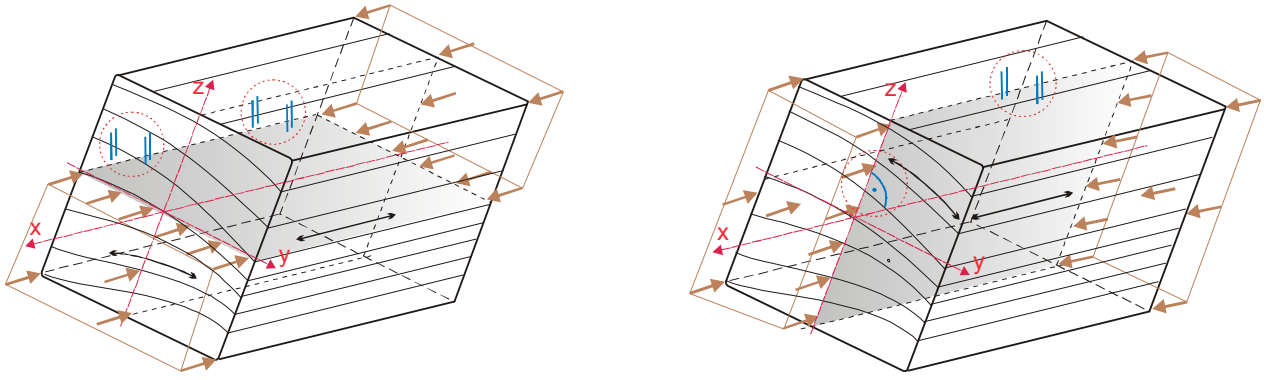


Figure 2. – Definition of axes

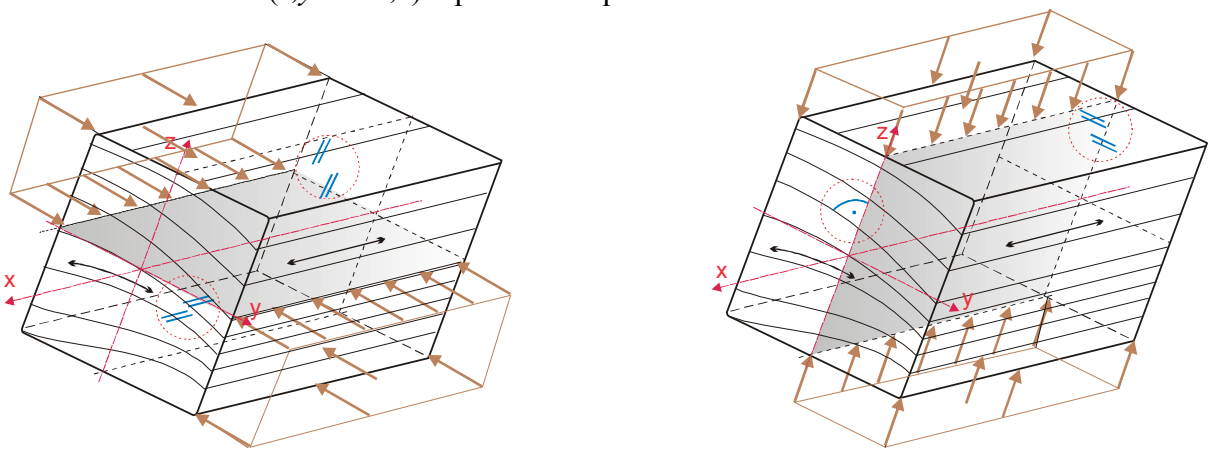
As presented in Figure 2, *x*-axis is the longitudinal axis of the element and is parallel to the fibres, *y*-axis is a tangent line on the radial distribution of fibres and is perpendicular to the fibres while *z*-axis is perpendicular to fibres and radial distribution of fibres. Figure 3 represents first two load cases, where the first capital letter (*X*) represents the load direction and the next two letters (*x,y* and *x,z*) represent the plane of shear stress.



a) $X - x,y$ b) $X - x,z$

Figure 3. – First load case

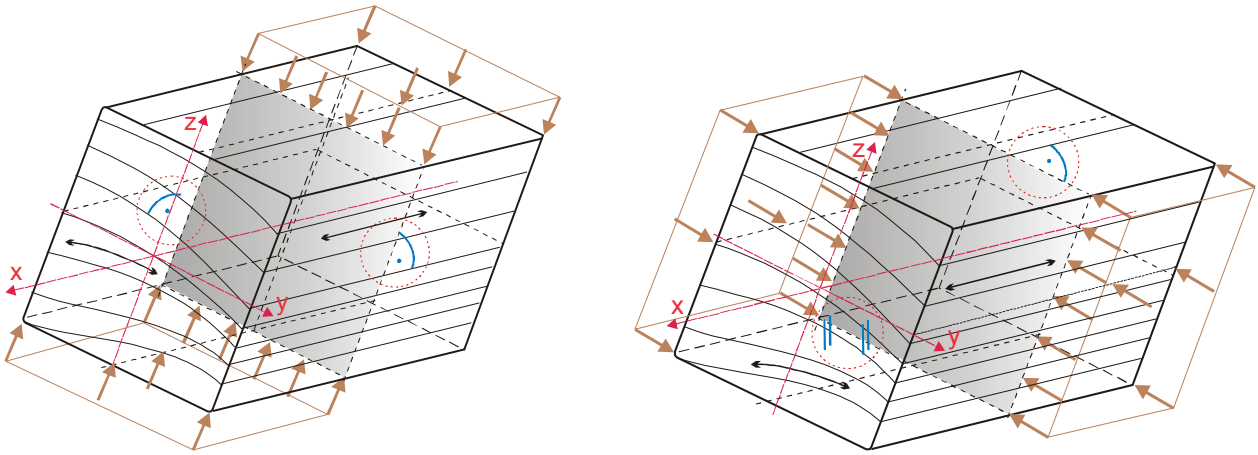
Figure 4 presents the second load case where the capital letters *Y* and *Z* represent the load direction and the next two letters (*x,y* and *x,z*) represent the plane of shear stress.



a) *Y* – *x,y* b) *Z* – *x,z*

Figure 4. – Second load case

The third load case is shown in Figure 5 where the capital letters *Z* and *Y* represent the load direction and the next two letters (*y,z*) represent the plane of shear stress.



a) *Z* – *y,z* b) *Y* – *y,z*

Figure 5. – Third load case

In order to have a complete insight of the stress distribution in the investigated specimens, a linear model was applied from Robot Autodesk software for structural analysis [4]. A characteristic distribution of normal stresses is shown in Figure 6 wherefrom the places of stress concentration can be seen indicating the most probable places of rupture. It can also be seen that the stresses, even when using relatively small specimens, are not evenly distributed, which can lead to the conclusion that the rupture does not happen only due to shear stresses.

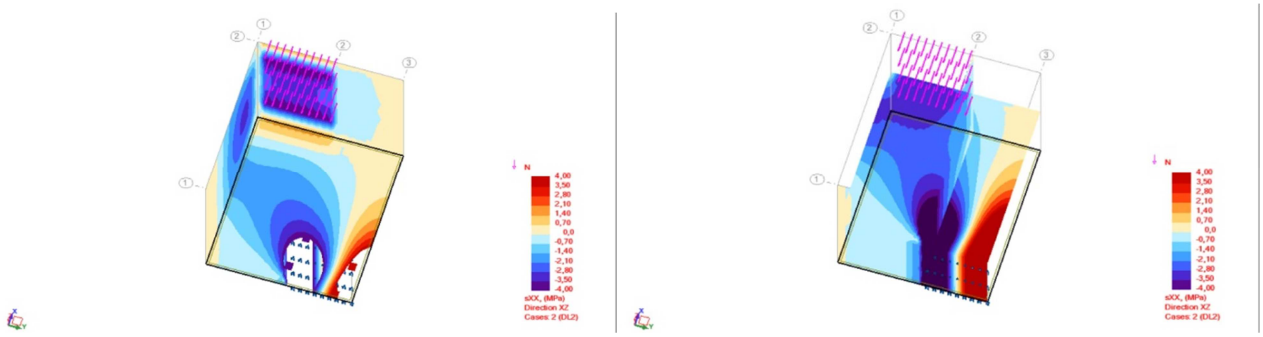


Figure 6. – Distribution of stress on the outer surface and in two sections of the specimen

The results of the experimental analysis according to the previously described load cases are shown in Table 1.

Table 1. – Experimental results

Load case	Sample	b	h/l	V	$f_{v,k}$ [N/mm^2]		Load case	Sample	b	h/l	V	$f_{v,k}$ [N/mm^2]		Load case	Sample	b	h/l	V	$f_{v,k}$ [N/mm^2]	
		[mm]	[mm]	[N]	V/A	mean			[mm]	[mm]	[N]	V/A	mean			[mm]	[mm]	[N]	V/A	mean
X - x,y	1	44	50	2067	0,940	**1,026**	*Y - x,y*	1	43	51	662	0,302	**0,324**	*Z - y,z*	1	43	42	1100	0,609	**0,618**
	2	43	52	2458	1,099			2	43	51	705	0,321			2	43	42	1020	0,565	
	3	43	52	2226	0,996			3	43	51	651	0,297			3	43	42	1221	0,676	
	4	43	51	2350	1,072			4	43	51	823	0,375			4	43	42	1120	0,620	
X - x,z	1	44	50	2629	1,195	**1,144**	*Z - x,z*	1	44	51	949	0,423	**0,367**	*Y - y,z*	1	43	42	1553	0,860	**0,872**
	2	44	49	2442	1,133			2	44	51	748	0,333			2	43	42	1440	0,797	
	3	44	51	2545	1,134			3	44	51	782	0,348			3	43	42	1582	0,876	
	4	44	50	2455	1,116			4	43	51	799	0,364			4	43	42	1724	0,955	

As shown in Table 1 the breaking force values for different load cases are similar but a notable difference exists in behaviour along radial and tangential plane. It is also visible that the peak value of nominal shear strength of wood of 1,7 N/mm^2 [2, 3] was not reached by any specimen.

Table 2. – Shear strength ratios

Load case	*X - x,y*						*X - x,y*	*Y - x,y*	*Z - y,z*
/	/						/	/	/
Load case	*X - x,y*	*X - x,z*	*Y - x,y*	*Z - x,z*	*Z - y,z*	*Y - y,z*	*X - x,z*	*Z - x,z*	*Y - y,z*
Ratio	1,000	1,115	0,316	0,358	0,602	0,849	0,897	0,882	0,708

In Table 2 the first load case shear strength (*X-x,y*) was adopted as the referent one. When analyzing the ratios we can see a variation of shear strengths from 31,6 to 111,5 % compared to the commonly used shear strength f_v. The difference of shear strengths between radial and tangential longitudinal plane orientations varies from 11,3 % to 11,8 % and 29,2 % for the cross-section plane.

III. Conclusion

The influence of anisotropy of wood to shear bearing capacity is shown through the experimental analysis of shear stresses caused by different shear forces. The calculated strength ratios emphasize the relevance of load direction and breaking plane orientation when calculating shear bearing capacity. As shear stresses can be caused by different internal forces (torsion, bending, etc.) it is difficult to estimate which one will exceed the shear strength. Comparison of shear strength and tensile strength parallel or perpendicular to the fibres without additional tests would not lead to an accurate conclusion, and is therefore excluded from this paper, but it should be the subject of future investigations of this problem.

References

[1] prEN 1995-1-1:2003 (E), Eurocode 5 – Design of timber structures – Part 1-1: General – Common rules and rules for buildings, 2003.

[2] Bjelanović, A., Rajčić, V., Wooden structures according to the Euronoms (Drvene konstrukcije prema europskim normama), Zagreb, Hrvatska sveučilišna naklada & Faculty of Civil Engineering of the University of Zagreb, 2005. (in Croatian)

[3] Šimić, V., Strength of materials 1 (Otpornost materijala 1), Zagreb, Školska knjiga, 1992. (in Croatian)

[4] Autodesk Robot Structural Analysis Professional 2010, Version 23.0.0.3128, Autodesk Inc., 2009.

© (2012) Trans Tech Publications, Switzerland
doi:10.4028/www.scientific.net/KEM.488-489.654

Application of two methods for notch fatigue life prediction

Radu Negru[1, a], Liviu Marsavina[1,b], Hannelore Filipescu[1,c], Cristiana Caplescu[1,d]

[1]"Politehnica" University of Timisoara, Victoriei Square, no.2, Timisoara, Romania

[a]radun@mec.upt.ro, [b]msvina@mec.upt.ro, [c]hannelore.filipescu@yahoo.com, [d]cristinacaplescu@yahoo.com

Keywords: notch fatigue, theory of critical distances (TCD), volumetric method.

Abstract. The aim of this paper is the application of two methods for notch fatigue life assessment, methods which are based on finite element analysis: the theory of critical distances and the volumetric method. Firstly, un-notched and notched specimens (for three different geometries) were tested in tension under constant-amplitude loading. The use of theory of critical distances (TCD) to predict the notch fatigue life involves the determination of the material characteristic length L based on experimental results obtained for the un-notched and one type of notched specimens. For the others notched geometries, based on linear-elastic finite element analysis, the fatigue strength is predicted using the TCD. In order to apply the volumetric method, elastic-plastic stress field around notches are considered and notch strength reduction factor are determined. Finally, the predictions of the two methods were compared with experimental fatigue data for notched specimens.

Introduction

A frequent cause of mechanical components failures is the fatigue damage that occur under cyclic stresses, usually from geometrical features which produce local stress concentration: notches, holes, shoulders, etc. Since these cannot be avoided in many structures, the prediction of the effect of notches or other stress concentration features on fatigue life is of great importance.

The fatigue behaviour depends not only on the local peak stress at the notch tip but also on other factors determined by stress distribution and notch geometry. For complex mechanical components, realistic information about the stress field can be generate trough finite element analysis, and thus the methods of fatigue estimation which use these results are of great applicability. In the last few years different methods for fatigue life prediction were proposed [1, 2]. Two of these methods, the TCD and the volumetric method, are applied in this paper to predict the fatigue life of notched specimens.

Experimental part

The tested material was aluminum alloy 2024-T3 with the following mechanical properties: Young's modulus $E = 70300\,[\mathrm{MPa}]$, Poisson's ratio $\nu = 0.33$, yield stress $\sigma_Y = 322.45\,[\mathrm{MPa}]$ and ultimate tensile strength $\sigma_{UTS} = 456\,[\mathrm{MPa}]$, obtained by static tensile tests.

The fatigue tests under tension loading were performed in the Strength of Materials Laboratory from "Politehnica" University of Timisoara, on a Walter+bai machine for static and dynamic tests of 100 [kN], under constant-amplitude loading, at a stress ratio $R = 0.5$ and with a loading frequency $f = 20\,[\mathrm{Hz}]$. There were tested un-notched and double edge notched specimens, for three different stress concentrators: double semicircular edge notch and rounded V-shaped notch, for an opening angle of 90° and two different notch tip radii, $\rho = 0.5\,[\mathrm{mm}]$ and respectively $\rho = 0.2\,[\mathrm{mm}]$. The geometrical configurations and the dimensions of the specimens in [mm] are presented in Fig.1.

The experimental results presented in Fig.2 are plotted on log-log coordinates, where σ_a is the amplitude stress in net section and N_f is the number of cycles to failure. For un-notched and rounded V-notch specimens, with tip radius $\rho = 0.2$, the S-N curves were modeled using Basquin's equation.

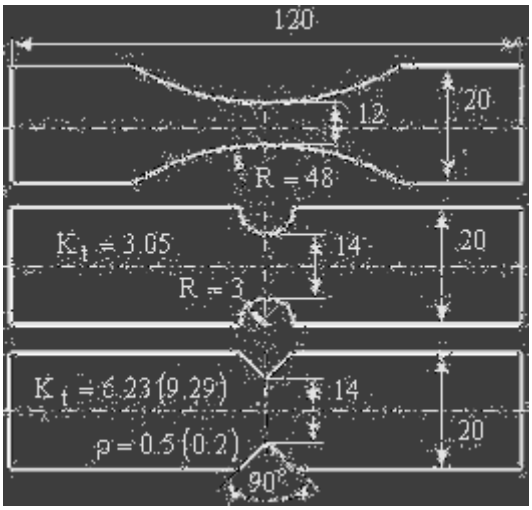


Fig.1 Geometry of specimens (K_t – elastic stress concentration factor)

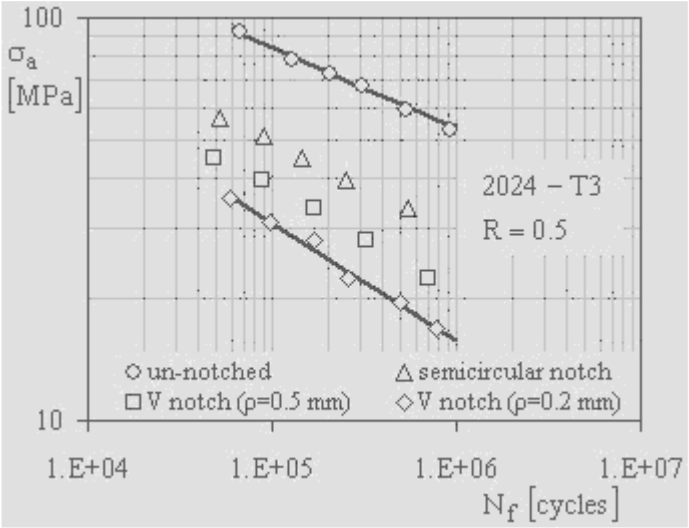


Fig.2 S-N curves for tested specimens

Because it is difficult to define an exact fatigue limit, the cyclic stress range $\Delta\sigma$ corresponding to 10^6 cycles was used in the present paper.

The Theory of Critical Distances

According to [3], the TCD represents a group of methods (the Point, Line, Area and Volume Method) which have a common approach – they use a characteristic material length parameter, the critical distance L, and a critical stress, in this case the fatigue limit of un-notched specimens $\Delta\sigma_0$. These two values depend on the stress ratio R and on the number of cycles to failure N_f. The Point Method (PM) could be expressed as follows [3]:

$$\Delta\sigma_{yy}\left(\theta = 0,\, r = L/2\right) = \Delta\sigma_0 \quad , \tag{2}$$

with the material characteristic length L defined as:

$$L = \frac{1}{\pi}\left(\frac{\Delta K_{th}}{\Delta\sigma_0}\right)^2 \quad , \tag{3}$$

where both $\Delta\sigma_0$ and ΔK_{th} have to be determined at the same stress ratio R. In other words, a notched component or specimen is in its fatigue limit condition when the range of the fatigue crack opening stress (or maximum principal stress) $\Delta\sigma_{yy}$ at a distance L/2 from the notch tip equals the un-notched fatigue limit $\Delta\sigma_0$.

In order to find the characteristic material length L, without the experimental determination of the threshold value of the stress intensity range ΔK_{th}, the alternative strategy presented in [4] was adopted. By using a finite element analysis, the linear-elastic stress field $\Delta\sigma_{yy}$ for the V-notched specimen, with notch tip radius $\rho = 0.2\,[\text{mm}]$, was plotted along the bisector, at an applied nominal stress in gross section equal to the notch fatigue limit $\Delta\sigma_{0n}$. As shown in Fig.3, the point at which

the straight horizontal line corresponding to un-notched fatigue limit $\Delta\sigma_0$ intersect the above stress-distance curve allows to determine the value of L/2, resulting the characteristic material length $L = 0.180\,[\text{mm}]$.

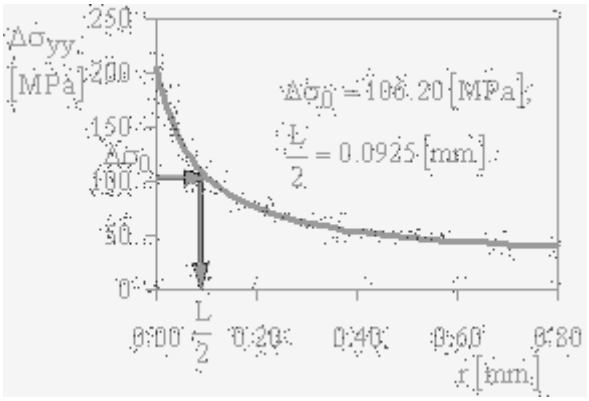


Fig.3 The PM to estimate the characteristic length L

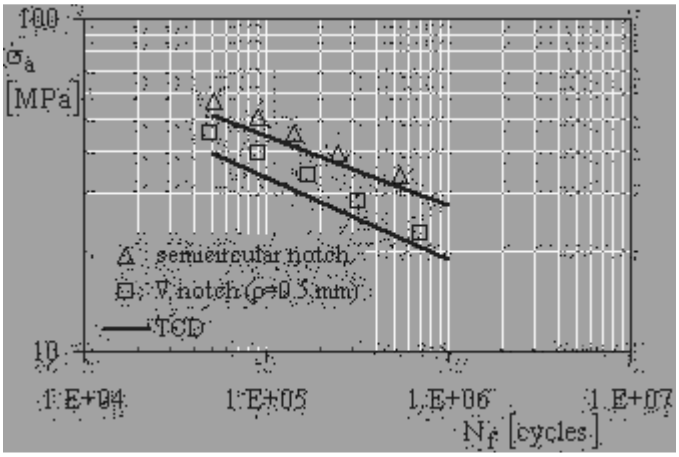


Fig.4 Notched specimen curves based on TCD and the experimental results

Finally, using the PM, the notch fatigue limits $\Delta\sigma_{0n}$ for the double semicircular edge notch and the rounded V-shaped notch ($\rho = 0.2$) specimens were estimated based on Eq. (2) and on a linear-elastic finite element analysis. Similarly, considering the number of cycles to failure $N_f = 500000\,[\text{cycles}]$, respectivelly at 70000 [cycles], the fatigue strength of notched specimens was also estimated. The obtained results presented in Fig.4 indicate that the TCD underestimates the fatigue strength of notched specimens with maximum 15%.

The Volumetric Method

The volumetric approach uses an elastic-plastic distribution and relative stress gradient χ to calculate the effective distance X_{eff}, the effective stress σ_{eff} and the notch strength reduction factor K_f:

$$K_f = \frac{1}{X_{eff}\,\sigma_n}\int_0^{X_{eff}} \sigma_{yy}(x)\times\varphi(x,\chi)\,dx \tag{4}$$

where $\sigma_{yy}(x)$ is the fatigue crack opening stress along notch tips, $\varphi(x,\chi)$ is the weight function and σ_n is net stress [5]. For better numerical results in volumetric method, the cyclic stress-strain cuve for this material was used in elastic-plastic finite element analysis [6]. To apply volumetric method calculation, the discrete stress results delivered by elastic-plastic finite element analysis were transformed in continuous and derivable functions through the polynomial curve fitting technique computed over a given number of elements near notch tips [7]. Adopting a 4 order polynomial function for $\sigma_{yy}(x)$, with a_i the polynomial coefficients:

$$\sigma_{yy}(x) = \sum_{i=0}^{n} a_i x^i\,, \quad n = 4\,, \tag{5}$$

the relative stress gradient is derived and the effective distance X_{eff}, which corresponds to minimum point of relative gradient, the effective stress σ_{eff} and the notch strength reduction factor K_f are determined with a Mathcad 14.0 routine, for an unit weight function $\varphi(x,\chi) = 1$.

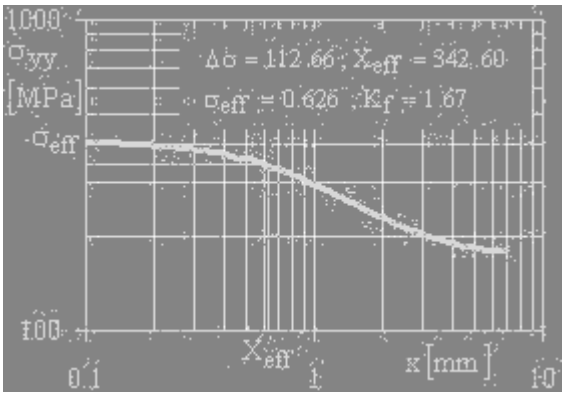


Fig.5 The elastic-plastic stress distribution for semicircular double edge notch

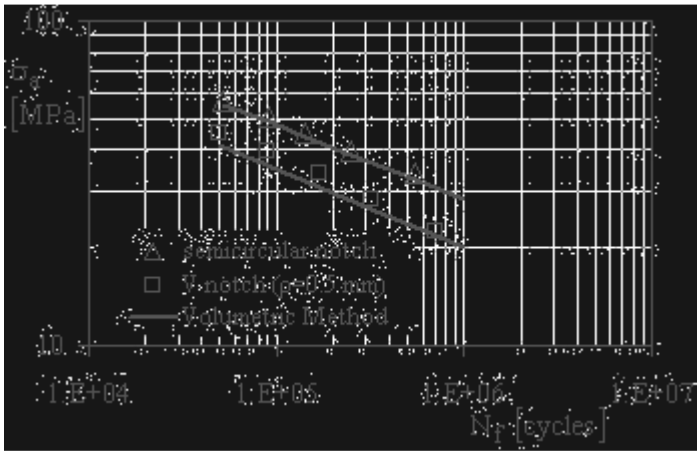


Fig.6 Notched specimen curves based on volumetric method and the experimental results

The obtained results presented in Fig.6 indicate that the estimations based on the volumetric method are in good agreement with the experimental results, with relative errors within ±10%. All the finite element analysis were performed using the commercial software package Cosmos/M 2.9.

Results and discussions

A comparative study of two recent methods, the TCD and the volumetric method, developed for the estimation of notch high-cycle fatigue behaviour was done in this paper. Using the stress field distribution generated by finite elements analysis the investigated methods predict reasonable accurate fatigue lifes. Moreover, these methods could be simply used for mechanical components in combination with linear-elastic or elastic-plastic finite element analysis.

Acknowledgments

This paper was supported by the project "Development and support for multidisciplinary postdoctoral programs in primordial technical areas of the national strategy for research – development – innovation" 4D-POSTDOC, contract nr. POSDRU/89/1.5/S/52603, project co-funded from the European Social Fund through the Sectorial Operational Program Human Resources 2007-2013.

References

[1] L. Susmel, D. Taylor: J. Strain Anal. Eng. 38 (2003), p.443.

[2] D. Bellet, D. Taylor, S. Marco, E. Mazzeo, J. Guillois, T. Pircher: Int. J. Fatigue 27 (2005), p. 207.

[3] D. Taylor: *The Theory of Critical Distances. A New Perspective in Fracture Mechanics* (Elsevier, UK 2007).

[4] L. Susmel, D. Taylor: Eng. Fract. Mech. 77 (2010), p.1492.

[5] H. Adib, G. Pluvinage: Int. J. Fatigue 25 (2003), p.67.

[6] J. Vázquez, C. Navarro, J. Domínquez: Fatigue Fract. Eng. M. 33 (2009), p.22.

[7] H. Adib-Ramezani, J. Jeong: Comp. Mater. Sci. 39 (2007), p.649-663.

© (2012) Trans Tech Publications, Switzerland
doi:10.4028/www.scientific.net/KEM.488-489.658

A Microstructural Sensitivity Study of 316H Austenitic Stainless Steel to Inter-granular Creep Fracture

B. Chen[1,a], P.E.J. Flewitt[2,3,b], D.J. Smith[1,c] and C.M. Younes[2,d]

[1]Department of Mechanical Engineering, University of Bristol, Bristol, BS8 1TR, UK

[2]Interface Analysis Centre, University of Bristol, 121 St Michael's Hill, Bristol, BS2 8BS, UK

[3]H.H. Wills Physics Laboratory, University of Bristol, Tyndall Avenue, Bristol, BS8 1TL, UK

[a]b.chen@bristol.ac.uk, [b]peter.flewitt@bristol.ac.uk, [c]david.smith@bristol.ac.uk and [d]c.m.younes@bristol.ac.uk

Keywords: Auger electron spectroscopy, Carbide precipitation, Segregation, Inter-granular fracture, Creep, Austenitic stainless steel

Abstract

A preliminary sensitivity examination of the ductility exhaustion based creep damage prediction model, currently used in the R5 high temperature assessment procedure, showed that material property inputs had significant effects on damage prediction. In the present work, the link between the microstructural factors and the susceptibility to inter-granular high temperature creep failure is considered. The latter was judged to be associated with the low creep ductility. Here, the longitudinal section of a creep specimen and the fracture surface were examined. Auger electron spectroscopy was used to investigate the grain boundary composition in this specimen, which failed after a creep test of 1038h at 550ºC under a triaxial stress state. The present results demonstrate that there is a possibility to correlate the susceptibility to high temperature inter-granular fracture from the low temperature fracture investigations. Finally, the susceptibility of the pre-treated 316H stainless steel to inter-granular high temperature failure and the contribution to the creep damage model are briefly discussed.

Introduction

Type 316H austenitic stainless steel welded components are widely used in the nuclear power generation industry for the purpose of high temperature operation [1]. Indeed inter-granular creep cracks have been observed in the heat affected zones (HAZs) of thick section weldments in high carbon austenitic stainless steel headers [2]. The R5 high temperature assessment procedure based on the ductility exhaustion concept was judged to provide a conservative prediction of this type of creep damage [2]. A preliminary sensitivity examination for the material parameters used in this empirical creep damage prediction model was undertaken systematically [2]. It showed that the prediction of crack initiation was strongly dependent on the material parameters selected, such as the uniaxial creep ductility. It is well established that inter-granular creep fracture, in general, promotes the low creep ductility to failure [2]. Therefore, it is necessary to evaluate the susceptibility to the inter-granular creep fracture so that the uniaxial creep ductility can be estimated.

In the present work, the susceptibility to the inter-granular fracture produced in a specimen after both high temperature creep failure at the notch and low temperature fracture of an unfailed notch are examined. The specimen was subjected to a prior solution heat treatment (ST) plus 12% compressive plastic straining (PS) at room temperature. A correlation was established between the concentrations of phosphorous and sulphur elements at grain boundaries and the presence of both creep and brittle fracture induced grain boundary facets. The contribution of these observations to creep damage model is briefly discussed.

Material and Creep Testing

Double notched bar creep specimen extracted from a Type 316H thick section austenitic stainless steel, was subjected to a solution heat treatment at a temperature of 1090ºC for 2.5h to remove previous thermo-mechanical history. Additional 12% plastic deformation in compression was applied to the notched bar specimen before fabrication of the creep specimen [2]. The dimensions of the specimen conform to the code of practice for conducting notched bar creep testing [3]. The creep testing was undertaken at 550ºC in air under a net stress of 320MPa using a constant load machine. The diameters of notched bar specimen at the notch throat plane, d_{no}, and the notch throat radius, r_{no}, were 3.99mm and 0.399mm respectively. The notch acuity of d_{no}/r_{no}=10 produced a von Mises equivalent stress of 195MPa and a maximum principal stress of 341MPa at the skeletal point of the specimen for an applied net stress of 320MPa [2]. The specimen failed at one notch throat after a 1038h. The accumulated creep strain at the unfailed notch throat was -0.0042, which was much lower than the value obtained from the same creep testing condition but using ex-service material [4]. The failure time for this ex-service material was 5718h under the same creep testing condition. The creep strain was measured using the shadowgraphic technique and was defined as the change in the diameter of the specimen at the notch throat [2]. Therefore, the creep lifetime and creep strain accumulation in the plastically strained specimen were much less than those for the ex-service condition. However, the latter was judged to be representative of the typical material behaviour of Type 316H stainless steel and the creep property data associated with it are currently used in the R5 high temperature assessment for predicting the creep damage accumulated in the HAZ [5].

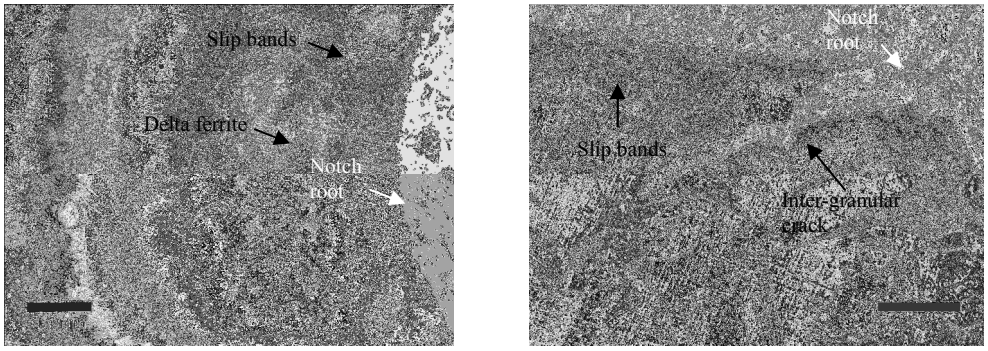
Auger electron spectroscopy (AES) studies were undertaken with a JEOL JAMP-30 instrument. The specimen examined was in the form of 1mm notched square bar, 12mm×2.2mm×2.2mm. Specimen was fractured in situ by impact loading within the AES instrument at a temperature of -140°C under a vacuum in the main analysis chamber of less than 6.6×10^{-8}Pa.

Results

Figs. 1(a) and (b) show the longitudinal sections of the unfailed and failed notches. Slip bands induced by the 12% plastic deformation at room temperature can be seen in both cases. The specimen in Fig. 1(a) was lightly etched with 5% oxalic acid to reveal the presence of any residual delta ferrite phase. A small percentage of this phase was often observed for thick section components, where the level of plastic deformation used to break down the heterogeneity in the ingot was limited [4]. A main inter-granular creep crack was observed in the longitudinal section of the failed notch, Fig. 1(b). The presence of the small intra-granular $M_{23}C_6$ precipitates at these slip bands and inter-granular $M_{23}C_6$ precipitates were confirmed [1]. The former accounted for the enhanced contrast of the slip bands.

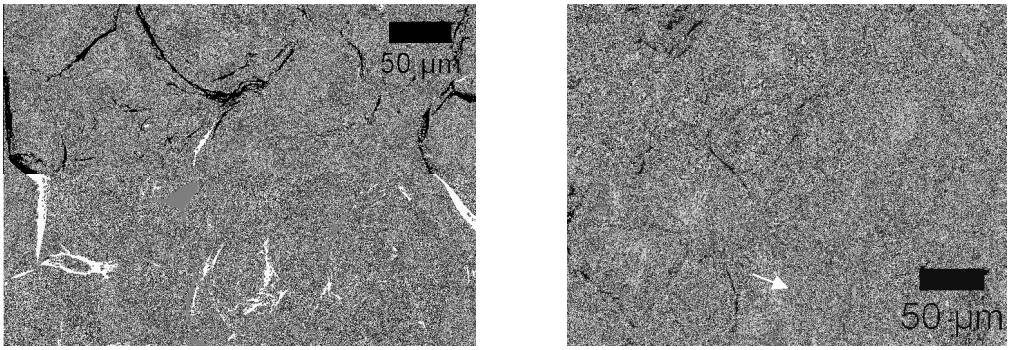
The creep failed notch of this specimen was examined using scanning electron microscopy (SEM) and the corresponding unfailed notch was fractured at a temperature of -196ºC to allow examination of the fracture mode. Figs. 2(a) and (b) show that the creep failure was inter-granular and the low temperature fracture surface also had an inter-granular path. In addition, the presences of creep cavities at some grain boundaries were observed in both high temperature and low temperature fracture surfaces. These were consistent with the introduction of a localised triaxial stress field at the sub-surface if the notch. From these observations it is possible to establish a correlation between the inter-granular brittle fracture after creep at high temperature and the inter-granular brittle fracture at low temperature. This confirmed the methodology of our previous study about the influence of thermo-mechanical history on grain boundary fracture [1]. Fig. 3(a) shows a typical creep cavitated grain boundary revealed by low temperature fracture. It should be mentioned that not all of the inter-granular fracture facets were decorated with the creep cavities. Fig. 3(b) shows a

typical spectrum of the grain boundary facets analysed with AES, where both phosphorous and sulphur peaks are observed. Table 1 shows individual grain boundary compositions. In total, eight measurements were carried out (illustrated by the letter A followed by a sequential number in the Table 1). This number was a compromise between good statistics and oxidation accumulation, as stated in elsewhere [1]. For the area A7, measurements were made before and after the Ar^+ etching the surface. The Ar^+ etching technique allowed identification of whether the measured elements were free segregated species. Thus, it can be concluded that most of the phosphorous, sulphur and antimony elements were free segregated species at grain boundaries. In addition, area A7 was measured at a heavily creep cavitated grain boundary and thereby accounted for the presence of antimony. This argument is consistent with previous findings that antimony segregates preferentially to the free surface of cavity [6].



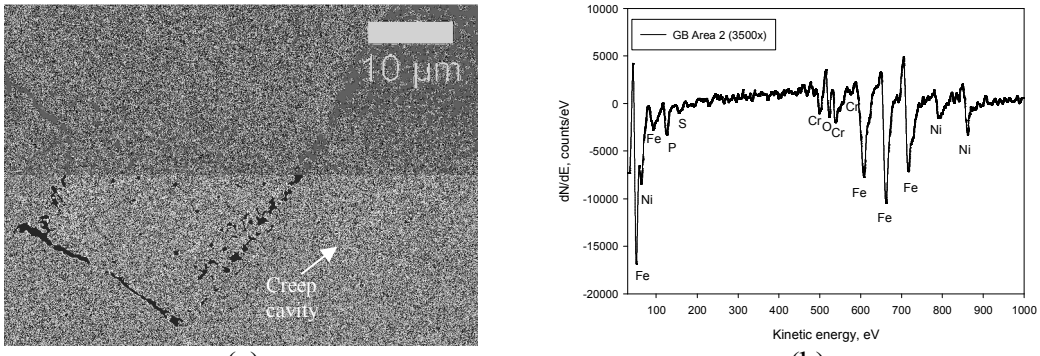
(a) (b)

Fig. 1: Optical micrographs of notched bar creep test specimen subject to a prior ST+PS pre-treatment: (a) unfailed notch showing the distribution of delta ferrite and presence of slip bands; (b) failed notch showing the presence of an inter-granular creep crack which grew into the specimen.



(a) (b)

Fig. 2: SEM photographs of fracture surfaces of (a) high temperature creep failed notch and (b) low temperature fractured notch, showing the presence of inter-granular facets.



(a) (b)

Fig. 3: SEM photograph of fractured surface by in situ AES impact loading fracture in (a) and the typical AES spectra obtained from the grain boundary in (b).

Table 1. Summary of individual grain boundary composition [wt%] in creep failed specimen.

Selected area	Fe	Ni	C	Cr	Mo	P	S	Sb	N
A1 (900x)	60.14	14.20	1.97	14.05	0.00	6.03	3.62	0.00	0.00
A2 (4300x)	48.16	14.90	0.00	16.10	13.58	4.16	3.11	0.00	0.00
A3 (3500x)	63.67	20.37	0.00	10.76	0.00	4.10	1.09	0.00	0.00
A4 (3500x)	67.70	16.32	1.00	9.25	3.05	2.68	0.00	0.00	0.00
A5 (3500x)	63.01	11.51	2.43	15.73	0.00	3.79	3.53	0.00	0.00
A6 (1800x)	66.22	10.61	3.78	13.47	0.00	2.93	2.99	0.00	0.00
A7 (before Ar^+) (19000x)	46.99	14.11	1.82	15.93	3.51	7.29	5.31	4.14	0.90
A7 (after Ar^+) (19000x)	71.67	12.55	2.28	8.51	4.09	0.90	0.00	0.00	0.00

Concluding Comments

It has been widely recognised that it is difficult to establish an absolute value of grain boundary energy but inter-granular fracture at a low temperature provides an indirect measure [1]. Impurity segregation of elements, such as phosphorous and sulphur, leads to a reduction in the cohesive energy of grain boundaries and thereby offer the potential to enhance the susceptibility to inter-granular fracture [7]. For the ST+PS pre-treated specimen, a large number of inter-granular facets were observed in the high temperature failed notch and low temperature fractured unfailed notch. The high susceptibility to creep inter-granular fracture was attributed to the presence of the phosphorous and sulphur elements at grain boundaries, and the presence of the creep cavities at some isolated grain boundaries. In addition, the tensile ledges induced by the 12% plastic deformation may facilitate the formation of creep cavities or wedge cracks in a micro-scale [4]. The high susceptibility to inter-granular fracture was consistent with the low value of creep ductility and short creep lifetime for this specimen. The creep damage prediction model currently used in the R5 high temperature assessment procedure does not consider the presence of low creep ductility, induced by the impurity segregation and cold work. The present work demonstrates that these two factors have a detrimental influence on creep ductility, although the quantitative assessment of these two factors was not established yet.

Acknowledgement

Bo Chen is grateful to the financial support from EDF/British Energy Ltd. and Great Western Research, UK.

Reference

[1] B. Chen, P.E.J. Flewitt, and D.J. Smith: Mater. Sci. Eng. A Vol. 527 (2010), p. 7387.
[2] B. Chen, D.J. Smith, P.E.J. Flewitt, and M.W. Spindler, *Effects of multiaxial stress state and microstructure on creep properties of austenitic stainless steel*, Int. Conf. on Eng. Struct. Integrity Assessment, Manchester, UK (2011).
[3] G.A. Webster, S.R. Holdsworth, M.S. Loveday, K. Nikbin, I.J. Perrin, and H. Purper: Fatigue Fract. Eng. Mater. Struct. Vol. 27 (2004), p. 319.
[4] B. Chen, *Effects of Thermo-Mechanical History on Creep Damage in 316H Austenitic Stainless Steel*, PhD thesis, University of Bristol (2011).
[5] British Energy Ltd., *R66, AGR materials data handbook*, Issue 5 (1999).
[6] C.L. White, J.H. Schneibel, and M.H. Yoo, *Report: sulfur and antimony segregation to creep cavity surfaces in Ni and an FCC Fe-Ni-Cr alloy*, Information Bridge: DOE Scientific and Technical Information.
[7] C.J. McMahon, and V. Vitek: Acta Mater. Vol. 27 (1979), p. 507.

© (2012) Trans Tech Publications, Switzerland
doi:10.4028/www.scientific.net/KEM.488-489.662

FEA of fretting fatigue: A comparison between ANSYS and ABAQUS

M. Abdel Wahab[a], R. Hojjati Talemi[b], P. De Baets[c]

Department of Mechanical Construction and Production, Faculty of Engineering and Architecture, Ghent University, Ghent, Belgium

[a]Magd.abdelwahab@ugent.be, [b]Reza.hojjatitalemi@ugent.be, [c]Patrick.DeBaets@UGent.be

Keywords: Finite Element Analysis; ANSYS; ABAQUS; Fretting Fatigue.

Abstract: Fretting fatigue occurs when two contact bodies undergo small oscillatory relative motion due to cyclic loading. It leads to fretting damage, which reduces the service life of the bodies in contact. This can be explained by the high stresses generated at the contact surface between the two bodies. Therefore, numerical analysis, such as Finite Element Analysis (FEA), would be useful to understand the fretting fatigue phenomenon and to investigate techniques to reduce its effect on fatigue lifetime of mechanical components. In this paper, FEA of fretting fatigue Aluminum specimen is carried out in order to study the stress distribution and crack initiation location. Two commercial FEA packages, namely ANSYS and ABAQUS are used to analyze the specimen. The stress distribution along the contact surface between the two bodies obtained using both codes is compared and analyzed.

Introduction

Fretting may take place between two contact surfaces, where sliding at micrometer level is present over a large number of cycles. This phenomenon could lead to fretting wear at the surfaces and fretting fatigue, which reduces the fatigue life of the components. The occurrence of fretting fatigue depends on the contact stresses between the two surfaces. These contact stresses, together with the micro-slip oscillatory motion, lead to crack nucleation and initiation. Once the crack is initiated, it will start to propagate under the fretting fatigue conditions. The conditions of fretting fatigue have been observed in many mechanical applications, e.g. bolded or riveted joints [1], shrink-fitted shafts [2] and blade dovetail of turbo machinery [3]. For more details on fretting fatigue, the reader may refer to the textbook 'Mechanics of Fretting Fatigue' by Hills and Novell [4]. Although fretting fatigue has been experimentally studied in the literature [5, 6], very few numerical models have been proposed [7]. This is because modeling of fretting requires the application of several theories including contact mechanics, stress analysis, damage mechanics and fracture mechanics. In this paper, we consider modeling fretting fatigue specimens using two commercial finite element packages, i.e. ANSYS and ABAQUS. First, the specimen's configuration, loading conditions and test set-up are presented. Then, the procedures of modeling the specimens using ANSYS and ABAQUS are described and followed by results and comparisons. Finally, conclusions are presented.

Experimental Set-up

The experimental set-up and the specimen's configuration are shown in Fig. 1. The specimen is made of Aluminum alloy 7075–T6, which has ultimate strength of 590 MPa and yield stress of σ_y 503 MPa. However, the two pads are made of stainless steel 410, which has ultimate strength of 700 MPa and yield stress of 420 MPa. A contact force F is applied to the specimen through the two bases of each pad. A cyclic axial stress σ is applied to the specimen, which varies from maximum to minimum as shown in Fig. 1. The cyclic elongation of the specimen at the contact surface gives rise to fretting fatigue.

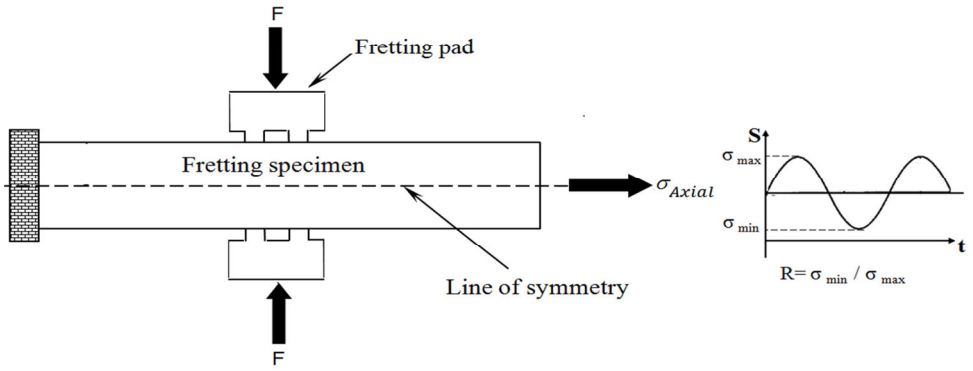


Figure 1: Fretting fatigue specimen

Finite Element Analysis

ANSYS. The ANSYS (version 12) model consists of four-noded plane stress elements (PLAN182) to model the specimen and the contact pad. Furthermore, contact elements CONTA172 and TARGE169 are used at interface between pad and specimen. The function of the contact elements is to allow load transfer between the contact pad and the specimen without penetration. The Augmented Lagrange method of friction is used with a coefficient of friction of 0.5. Due to symmetry, only one quarter of the specimen is modeled as shown in Fig. 2. Symmetric boundary conditions along the lines of symmetry are applied. The specimen is analyzed under the action of the load F and pressure σ_{axial}. The contact load, F is applied to establish contact between pad and specimen followed by either the maximum bulk stress, σ_{max}, or the minimum bulk stress, σ_{min}.

ABAQUS. In ABAQUS (version 6.10), the four-noded plane stress elements (CPS4R) are used to model both specimen and pad. The contact between pad and specimen is modeled using the master-slave interfacial algorithm, which makes use of Lagrange multiplier of friction. Similar to ANSYS, only one quarter of the specimen is modeled taking advantage of symmetry. The ABAQUS FE mesh is shown in Fig. 3. Loading conditions are also applied in three steps as explained above. A comparison of some modeling parameters used in ANSYS and ABAQUS are presented in Table 1.

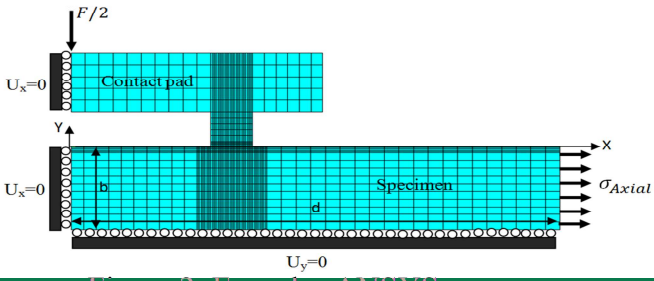


Figure 2: E mesh - ANSYS

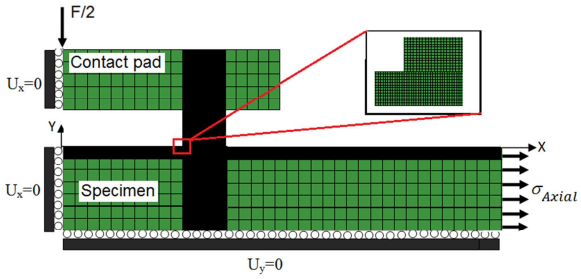


Figure 3: FE mesh - ABAQUS

Table 1: Comparison of modeling parameters

	Number of nodes	Number of elements	Number of DOF	CPU time (second)	Element size at contact (μm)
ANSYS	10 126	10 574	20 147	70.8	25×25
ABAQUS	14 264	14 025	28 434	16.8	25×25

It can be seen from Table 1 that although ABAQUS model has larger number of DOF than ANSYS model, its CPU time is much lower than ANSYS CPU time. It is clear that the solution solver of ABAQUS 6.10 is faster than that of the ANSYS 12.

Results and Comparisons

The contour plots of von-Misses stress obtained using ANSYS and ABAQUS are shown in Figs. 4 and 5, respectively. It can be seen from Figs. 6 and 7 that the stress distributions obtained using ANSYS and ABAQUS are very similar. However, the ANSYS maximum von-Misses stress is higher than the ABAQUS one. This may be due to the different contact algorithm using in each package. In commercial FE codes, there are in general four different contact algorithms, namely Pure penalty, Augmented Lagrange, Pure Lagrange multiplier and a mixed Lagrange-penalty (Lagrange multiplier on contact normal and penalty on frictional direction). In ABAQUS, Pure Lagrange (PL) contact algorithm was used. In such a method, Lagrange multipliers are used and contact forces are considered as separate DOF's. Therefore, contact stiffness does not need to be dealt with. In ANSYS, however, the PL algorithm did not shown convergence for this particular fretting fatigue specimen. Therefore, the Augmented Lagrange (AL) contact algorithm was used and convergence has been achieved. In this method, a penalty function together with Lagrange multipliers is used to solve the contact problem. The contact stiffness is automatically calculated once the penetration or sliding exceeds a certain limit. As the penetration should be minimized, high contact stiffness could be calculated resulting in higher contact stresses. Therefore, it is expected that ANSYS would produce higher stresses than ABAQUS. From FEA and analytical solution of a simple cylindrical pad contact carried out at our Department, it has been confirmed that the stresses produced using PL algorithm were closer to the analytical solution than those produced using AL algorithm.

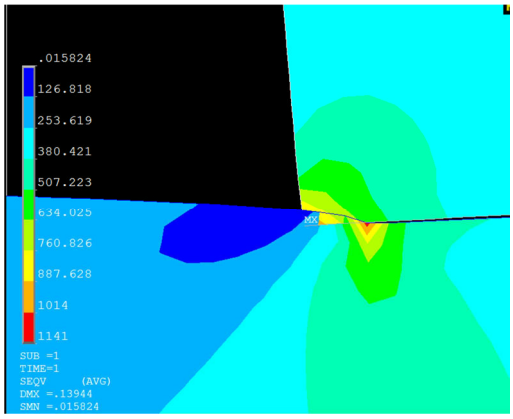


Figure 4: Von-Misses stress - ANSYS

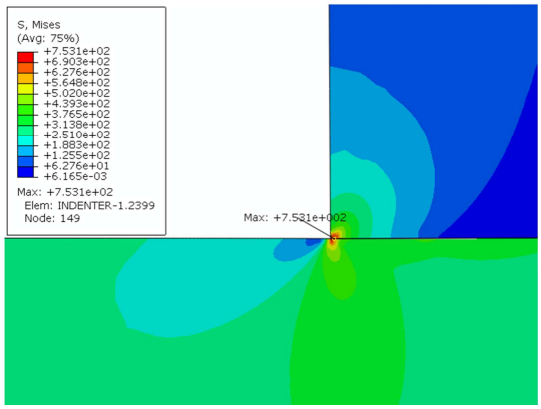


Figure 5: Von-Misses stress - ABAQUS

The tangential stress and shear stress distribution along the contact interface obtained using both softwares are compared in Figs. 6 and 7, respectively, and show good agreement between ANSYS and ABAQUS. As expected ANSYS gives higher maximum tangential stress than ABAQUS. According to Hills and Nowell [4], in fretting fatigue conditions crack will be initiated where the maximum tensile tangential stress takes place. Another crack initiation criterion for fretting fatigue is based on the fretting fatigue parameter F_1 [8], which is calculated as the product of the interfacial shear stress and the slip displacement. A further criterion F_2 takes into account the tensile stress parallel to the free surface, which is calculated as the product of F_1 and tangential stress. If any of these three mentioned criteria is used, both software's predict the same position of crack initiation.

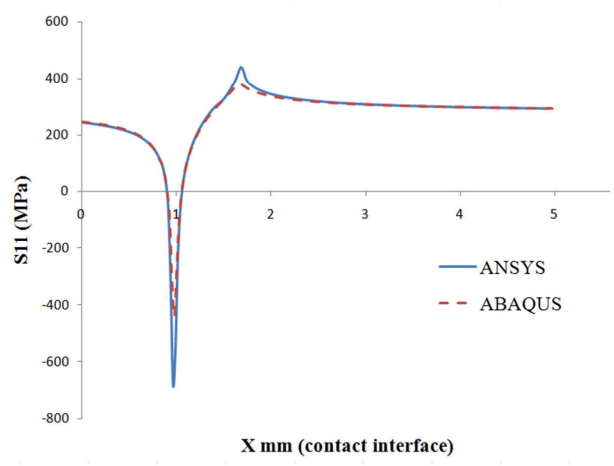


Figure 6: Tangential stress distribution

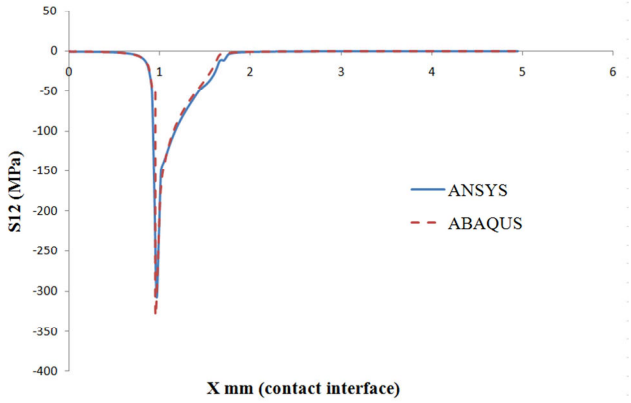


Figure 7: Shear stress distribution

Conclusions

In this paper, finite element analysis of fretting fatigue was carried out using two commercial FE packages, namely ANSYS and ABAQUS. The models consisted of quadratic elements to model fretting fatigue specimen and pads, and contact elements to model the interface. Contact loads on pads as well as fatigue loads on the specimen were applied and symmetric boundary conditions were considered. The results showed that both softwares produced similar stress distribution and predicted the same location of crack initiation based on the maximum tangential stress criterion. However, ANSYS predicted higher stresses than ABAQUS, which could affect the prediction of fatigue crack initiation lifetime. This has been attributed to the different contact algorithm using in each software. Comparing CPU times and FE models' size, it was concluded that the solution solver of ABAQUS 6.10 is faster than that of the ANSYS 12.

Acknowledgements

The authors wish to thank the Ghent University for the financial support received by the Special Funding of Ghent University (Bijzonder Onderzoeksfonds), in the framework of BOF project BOF 01N02410.

References

[1] A. Buch, Fatigue and fretting of pin-lug joints with and without interference fit, Wear (1977); 43:9.
[2] T. Hattori, S. Kawai, N. Okamoto and T. Sonobe, Torsional fatigue strength of a shrink-fitted shaft. Bull JSME (1981); 24(197):1893.
[3] R.L. Johnson and R.C. Bill, Fretting in aircraft turbine engines, NASA TM X-71606 (1974).
[4] D.A. Hills and D. Novell, Mechanics of Fretting Fatigue, Kluwer Academic, Publishers, Dordrecht (1994).
[5] T. Nicholas, A. Huston, R. John and S. Olson, A fracture mechanics methodology assessment for fretting fatigue, International Journal of Fatigue (2003); 25; 1069-1077.
[6] P. Golden and M. Shepard, Life prediction of fretting fatigue with advanced surface treatments, Materials Science and Engineering A (2007); 468-470; 15-22.
[7] H.A. Fadag, S. Mall and V.K. Jain, A finite element analysis of fretting fatigue crack growth behavior in Ti-6Al-4V, Engineering Fracture Mechanics (2008);75(6):1384-1399.
[8] C. Ruiz, P. Boddington and K. Chen, An investigation of fatigue and fretting in a dovetail joint, Experimental Mechanics (1984); 24(3), 208-217.

© (2012) Trans Tech Publications, Switzerland
doi:10.4028/www.scientific.net/KEM.488-489.666

Fatigue behavior in filled natural rubber: study of the mechanical damage dynamics

Luisa Munoz[1, a], Loïc Vanel[1, 2, b], Olivier Sanseau[1, c], Paul Sotta[1, d], Didier Long[1, e], Laurent Guy[3, f], and Ludovic Odoni[1, g]

[1] LPMA, UMR CNRS/Rhodia 5268, CRTL, Saint Fons, France
[2] LPMCN, Université de Lyon, Université Lyon 1 and CNRS, UMR 5586, France
[3] SILICA, Rhodia Operations, Collonges au Mont d'Or, France
[a]luisa-fernanda.munoz-meija-exterieur@eu.rhodia.com, [b]loic.vanel@univ-lyon1.fr, [c]olivier.sanseau@eu.rhodia.com, [d]paul.sotta-exterieur@eu.rhodia.com, [e]didier.long-exterieur@eu.rhodia.com, [f]laurent.guy@eu.rhodia.com, [g]ludovic.odoni@eu.rhodia.com.

Keywords: silica, natural rubber, pure shear geometry, fatigue, tear energy, crack velocity, sawtooth striations.

Introduction

Rupture dynamics in reinforced elastomers is a much more complex process than in pure elastomers due to the intrinsic heterogeneous mixture of a rubber matrix with filler particles at submicronic scale. In the case of natural rubber, an additional source of heterogeneity is the strain-crystallization effect. How rupture dynamics and crack path are affected by filler particles and strain-crystallization is still a matter of debate. Actually, understanding how rupture dynamics and crack path are correlated to each other is probably an important key in order to improve long time resistance of reinforced rubbers.

We present fatigue experiments performed on Silica-filled natural rubber and study the correlations between crack growth dynamics and fracture morphologies imprinted by an irregular crack path. Slow crack growth dynamics is obtained by cyclic fatigue. In order to control properly the crack growth dynamics, we use a pure shear test. The goal of this study is also to understand how rupture dynamics and morphologies depend on the control parameters of a fatigue experiment (frequency, stress or strain, strain rate, temperature). Here, we will focus our discussion on the crack velocity behavior and the appearance of sawtooth striations, showing that their formation follows a scenario that significantly differs from previous results reported in the literature [1,2].

Experimental protocol

The material considered is a natural rubber filled with 50 phr Silica particles. The material is molded into a pure shear test piece (Fig 1). An initial crack of length 30 mm is precut with a razor blade at one end of the sample. In mode I loading, fracture mechanics predicts that the elastic energy release rate is independent of the crack length at constant applied strain. In this case, crack growth is expected to occur at constant velocity.

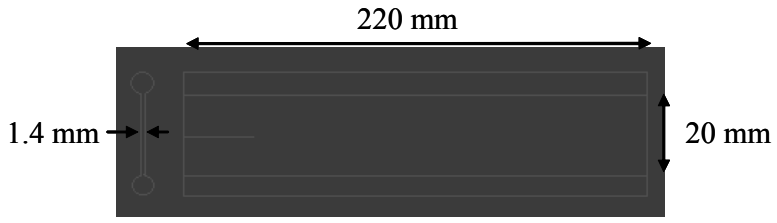


Figure 1: *Pure shear test geometry*

Uniaxial fatigue tests are performed using an Instron 8800 servohydraulic test machine. Fatigue cycles are applied using a trimodal control with the applied force returning to zero at the minimum position of the cycle and with a constant applied elastic displacement Δu_e. In that way, we take into account plastic creep elongation and avoid any compression of the sample. Also, it allows us to obtain a nearly constant elastic strain during the experiment.

Video tracking of the crack growth is done with an Imperx 4872x3248 pixels camera allowing a spatial resolution about 50 μm. Image acquisition is phase-locked to the fatigue cycles. Image analysis allows us to extract the crack tip position and measure the instantaneous crack velocity. In addition, SEM fractography measurements have been used to characterize *post-mortem* the crack path at spatial resolutions of 1 or 2 μm.

Results

Here, we present results that have been obtained during a fatigue test at room temperature with frequency 1Hz and maximum strain 90%. In Fig 2, we plot as a function of the crack velocity the elastic energy release rate G (tearing energy). In contrast with the expected behavior, there is a range of tearing energy where the crack velocity is not stationary but shows mainly two distinct velocity levels. This multistable behavior is reminiscent of the well-known intermittent crack growth behavior observed in a given range of mean velocity for different type of rubbers in trouser geometry [3] or for SBR in pure shear geometry [4]. When decreasing the maximum applied strain, we have observed that the multistable crack growth regime eventually disappears. On the other hand, we have found a very close relationship between crack velocity and rupture morphology.

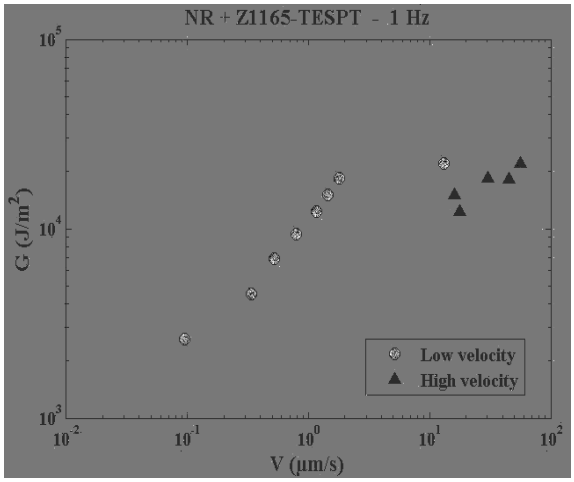


Figure 2: *Tearing energy as a function of the crack velocity. From a certain energy threshold, crack propagates at two main velocity levels (See Fig 3).*

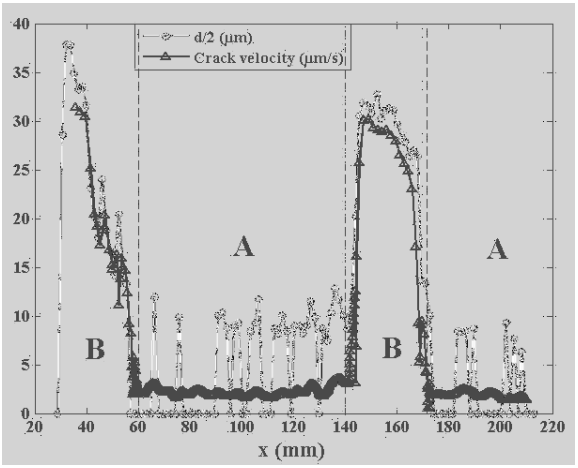


Figure 3: *Instantaneous crack velocity and half-width d/2 of the sawtooth striations.* **A** *and* **B** *refers to the morphologies shown in Figure 4. The excellent correlation between the two sets of data in* **B** *shows it takes two fatigue cycles to form a sawtooth striation.*

The corresponding morphologies of the fracture observed by SEM depend on the crack velocity and can be split into four types (Fig 4):

- At very low velocity, a rough disordered interface is observed (**A**),
- At high velocity are observed very regular and mainly straight sawtooth striations oriented perpendicularly to the crack propagation direction and extending across the whole sample thickness (**B**),
- Increasing the velocity starting from type **A** is observed a mixture of a rough disordered interface with small, slightly irregular, sawtooth striations (**A'**),
- Decreasing the velocity starting from type **B** are observed sawtooth striations that split into several zones across the sample thickness and are distributed in size, orientation and curviness (**B'**).

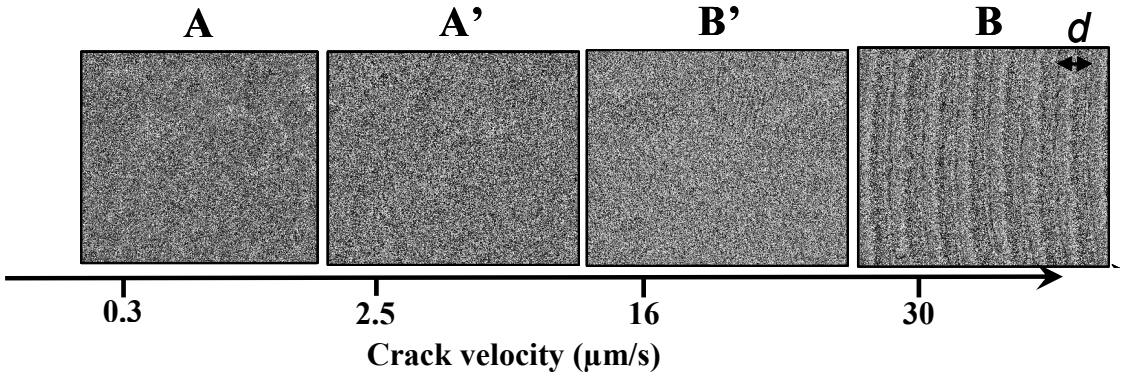


Figure 4: *Morphology (SEM) of rupture interface for increasing crack velocity.* **A***: Rough disordered surface.* **A'***: Mixture of sawtooth striations and rough disordered surfaces.* **B'***: Several zones with small sawtooth striations.* ***B****: Large sawtooth striations across the sample.*

From the SEM images, we can extract the striation width d (Fig 4) as a function of the crack tip x-position. In Fig 3, we plot the half striation width $d/2$. An excellent correlation is observed between the instantaneous crack velocity v and the striation half-width so that we can propose: $v\,T = d/2$, where T is the duration of one fatigue cycle (here T=1s). Note that the correlation is very good in the zones noted **B** of Fig 3 where morphologies **B** and **B'** are observed. In the zones noted **A** where morphologies **A** and **A'** are observed, a measurement of striation size is sometimes possible but does not correlate well with the macroscopic crack velocity. It is likely that the crack front velocity is not uniform and can locally be high enough to trigger striations without affecting much the overall crack velocity.

Summary

We have shown how fracture morphology and crack growth velocity are correlated during fatigue crack growth of filled natural rubber. In contrast with Bathias et al.[1] and Le Cam et al [2] claiming sawtooth striations occur in one fatigue cycle, we clearly show that it takes two cycles to form a striation. Our results suggest that striations result from the alternative selection of two symmetric inclined rupture planes.

We have also brought in light the existence of an energy threshold above which the crack velocity becomes unstable. For a given energy level, crack oscillates between two main velocities. More work is in progress to validate the generality of these observations, especially at higher frequencies and temperatures.

References

[1] C. Bathias, K. Le Gorju, C. Lu, L. Menabeuf, ASTM STP 1296, 505-513 (1997).

[2] J. Le Cam, and E. Toussaint, *Macromolecules* , **43**(10), 4708-4714 (2010)

[3] R. G. Stacer, and F. N. Kelley, *Rubber Chem. Tech.* **58**, 924-938 (1985).

[4] K. Tsunoda, J.J.C. Busfield, C.K.L. Davies, A.G. Thomas, *J. Mater. Sci.* **35**(20), 5187-5198 (2000).

© (2012) Trans Tech Publications, Switzerland
doi:10.4028/www.scientific.net/KEM.488-489.670

High Rate and High Temperature Fracture Behaviour of Polycrystalline Diamond

M. Petrovic[1, a], A. Ivankovic[1, b], N. Murphy[1, c]

[1]UCD School of Electrical, Electronic and Mechanical Engineering

University College Dublin, Dublin 4, Ireland

[a]marin.petrovic@ucd.ie, [b]alojz.ivankovic@ucd.ie, [c]neal.murphy@ucd.ie

Keywords: PCD, Fracture Toughness, Young's Modulus, Loading Rate, Temperature, Microstructure

Abstract. Polycrystalline diamond (PCD) materials have a variety of applications, mainly as cutting tools for machining non-ferrous metals and non-metallic materials. A significant application of PCD is in oil and gas industry for rock drilling operations. Other important areas, such as mining, have yet to reach their full potential. These cutters/tools are subjected to high operating temperatures, impact loads and abrasive wear during these operations, which may lead to their sudden failure. An advantage of these materials is that their structure and composition can be engineered to return properties required for specific applications and operations.

In this study, the mechanical and fracture properties of two grades of PCD have been determined at dynamic loading rates up to 5 m/s and elevated temperature up to 600°C in laboratory conditions using three point bending (TPB) and split-Hopkinson pressure bar apparatus (SHPB). The results show Young's modulus to be completely rate insensitive, while fracture toughness changes significantly. Two dominant regions can be observed on the rate scale: one predominated by the conductivity of the material and the other predominated by the rate of fracture where binder degrades locally at the crack tip. This behaviour was related to the material microstructure, where similarities and differences in the fracture of two different grades of PCD are shown examining polished fractured specimens using scanning electron microscopy, revealing mechanisms of fracture over the range of loading rates.

Introduction

Polycrystalline diamond is a sintered mass of randomly oriented, intergrown, diamond particles in the presence of cobalt as a catalyst, where the sintering process is achieved in high pressure and high temperature conditions. Premature failure of the cutting tool made of PCD, caused by tool fracture and chipping, is a frequent problem in the drilling industry. Considering the expenses of one day's drilling, changing the drill bit in the middle of the drilling process costs hundreds of thousands of euro. Therefore the most important demand on the cutting tool is to resist fracture. Having said that, the main aim for the manufacturers of the drilling bits is to understand the fracture process of these materials and try to improve their fracture properties. In this work, the effects of dynamic loading rates and high temperatures are considered.

Materials and Methods

In this study, high temperature testing chambers, a laboratory scale three point bend test rig and a split-Hopkinson pressure bar apparatus have been designed and used for testing the fracture and mechanical properties of two different grades of PCD: G6 grade constituted of 6μm average grain size and G30 grade constituted of 30μm average grain size. Standard fracture and material analysis were then carried out on each sample to determine its apparent fracture toughness K_{Ib} and Young's modulus E.

Young's modulus tests were performed on miniature size disk shaped PCD specimens of 9mm diameter and 3mm thickness at three different strain rates and at 300°C in air. Small, custom built, cylindrical heating unit was made of stainless steel and attached to the SHPB setup. Heating unit has a hole on top for easy inserting and removal of the test pieces. Two cartridge heaters with power rating of 200W each are connected in series and inserted into holes drilled and reamed on one side of the heating unit.

Normal procedure when testing the Young's modulus at SHPB is to use Kolsky analysis [1], where the reflected and transmitted strain signals are recorded by strain gauges placed onto the incident and transmitter bars, respectively. However, the problems encountered during testing necessitated modifications of conventional Kolsky analysis. The reason for this is the very high impedance of PCD material which effectively means that the reflected wave from the steel bar is very small and lost in the noise. This required instrumenting the specimen with a minute strain gauge and measuring the strain directly rather than the conventional method of integrating the reflected strain in the incident bar. Therefore, the strain was recorded by use of strain gauges connected to a Vishay 2310B Signal Conditioning Amplifier and the 100 MHz Handyscope HS3.

Elevated temperature tests with the SHPB method pose a problem if temperature gradients exist along the bar length because the propagation of elastic waves is affected through the effect of temperature on Young's modulus and wave velocity of the bar material. These gradients have two effects on the strain signal: a continuous change of amplitude and a continuous change of wave velocity. Correction factor is derived [2] and employed in the following form:

$$\frac{\varepsilon_0}{\varepsilon_T} = \left(1 + C_a\right)^{3/4}, \qquad \frac{t_T}{t_0} = \sqrt{\frac{E_0}{E_T}}\left(1 + C_a\right)^{3/4}, \qquad C_a = \frac{a_2}{a_1}\left(T - T_0\right), \tag{4.28}$$

where T_0 is ambient temperature,

T is temperature of the specimen,

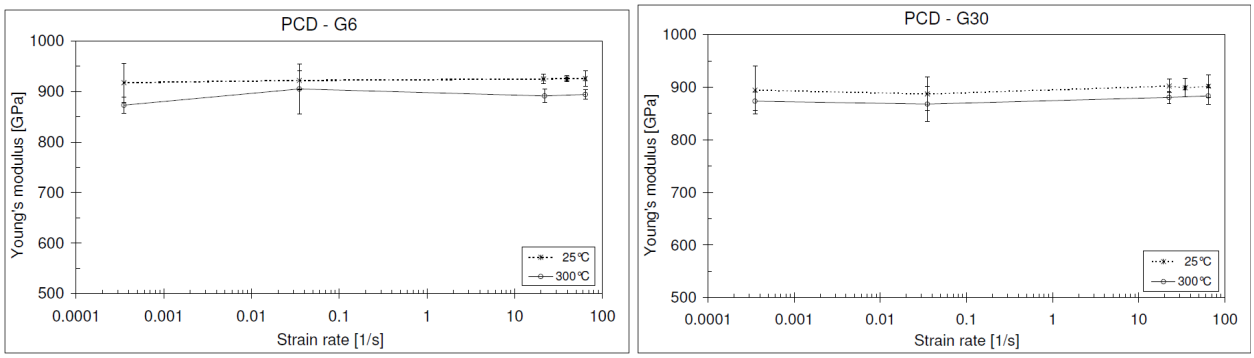
a_1, a_2 are constants that satisfy relation for linearly temperature dependent Young's modulus $E = a_1 + a_2\left(T - T_0\right)$.

Testing at temperatures above 300ºC is not feasible at present, due to absence of the appropriate miniature strain gauge pattern on the market.

Fracture toughness tests were performed in three-point bending on PCD Single Edge V-notched Bend (SEVNB) specimens with machined notch of 1.24 mm in depth and 150 μm notch root radius, using an instrumented Zwick-Roel drop-weight tower. The fracture toughness of PCD was evaluated at a temperature of 600°C and 3 different dynamic loading rates: 0.3 m/s, 1 m/s and 5 m/s. The load at initiation method was used in the analysis, as previously explained in [3,4], which is sufficiently accurate even for the dynamic tests as the specimens were instrumented with the minute strain gauges close to the crack tip from which the load was extracted. Strain gauges used were of Micro-Measurements type ZC-NC-G1262-120, which are free filament kanthal alloy gauges bonded by ceramic adhesive and with the measurement range of up to 1150°C.

Results

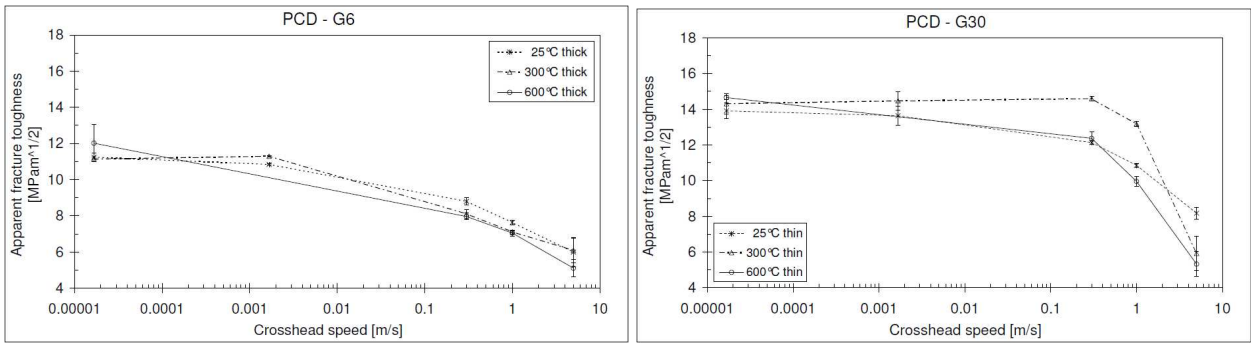
Dynamic Young's modulus results are presented in Figures 1a and 1b for G6 and G30 material, respectively, and compared with previously published quasistatic results [3]. At least three repeats at each combination of rate and temperature were conducted.



(a) *(b)*

Figure 1: Young's modulus of G6 (a) and G30 (b) as a function of strain rate and temperature

Apparent fracture toughness results determined in three-point bending are shown in Figures 2a and 2b for G6 and G30 material, respectively, and compared with previously published low temperature results [3].



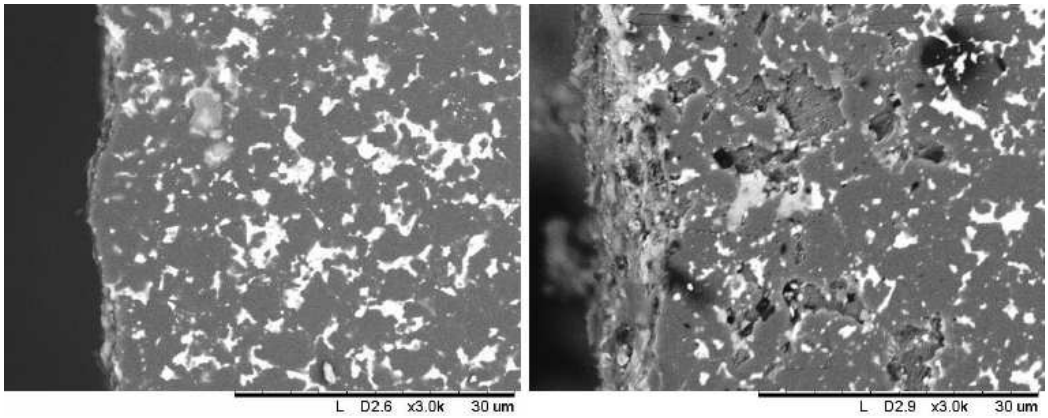
(a) *(b)*

Figure 2: Apparent fracture toughness of G6 (a) and G30 (b) as a function of crosshead speed and temperature

Thick and thin samples refer to two different production quality materials and can not be compared between themselves. However, relative change in fracture toughness can be compared as both grades have the same notch root radius.

Microscopy Analysis

In order to be able to get a better insight into the fracture process, eight G6 specimens and eight G30 specimens were sectioned and polished and these polished surfaces were examined by FEG-SEM. Using energy dispersive X-ray analysis (EDX), it was found that light greyish areas represent cobalt, while dark grey corresponds to diamond grains. Comparison between sectioned surfaces of one G6 specimen fractured at quasistatic rate and another fractured at dynamic rate is shown in Figure 3. Examined regions are very close to the initial crack tip, while the fracture surface is on the left on these images. It can be seen that the binder in regions close to the edge is considerably deteriorated during dynamic fracture which extends up to 30 μm off the fracture surface, as completely opposed to the fracture at quasistatic rate where the binder left undamaged.



(a) *(b)*

Figure 3: SEM images of the polished surface of G6 samples fractured at 1 mm/min (a) and 5 m/s (b)

Discussion and Conclusions

It has been shown that Young's modulus of both grades of PCD exhibits no rate sensitivity across five decades of the strain rate. Slight but consistent decrease of Young's modulus with increase of the temperature is also found at high strain rates. G30 grade appears to be still less susceptible to the temperature effects, due to higher average grain size and smaller cobalt content. When testing fracture toughness, two dominant regions can be observed on the rate scale: isothermal governed by the conductivity of the material and adiabatic governed by the rate of fracture where binder degrades locally at the crack tip. Isothermal region is longer for the coarser grain material due to higher conductivity. Apparent fracture toughness shows increasing behaviour with increase in the temperature at quasistatic rates, while this is reversed at dynamic rates. Microscopy analysis discloses the region of strong deterioration of cobalt at dynamic rates. It appears that binder gets damaged before the crack even reaches it by the temperature increase ahead of the crack tip. Considering huge difference between thermal expansion of diamond and cobalt, little change in temperature causes considerable change in expansions of these two materials, inducing shear locally in ligament of PCD binder between the grains. The stress intensity factor acting at the crack tip may be reduced due to these thermal stresses, thus causing microcracks and fracture to occur at lower load levels.

The undertaken study leads to improvement of understanding of PCD behaviour and thereafter allows recommendations to be made for the improved design of the material itself and of the corresponding manufacturing processes.

References:

[1] H. Kolsky. Stress waves in solids. Clarendon Press, Oxford, 1953

[2] U.S. Lindholm, L.M. Yeakley: Experimental Mechanics Vol. 8 (1968), p. 1-9

[3] M. Petrovic, D. Carolan, A. Ivankovic, N. Murphy: Key Engineering Materials Vol. 452 (2011), p. 153-156

[4] M. Petrovic, D. Carolan, V. Kanyanta, A. Ivankovic, Proceedings of the 6thICCSM (2009)

Acknowledgements: This work is funded by *Enterprise Ireland* and *Element 6 Ltd., Shannon, Ireland*

© (2012) Trans Tech Publications, Switzerland
doi:10.4028/www.scientific.net/KEM.488-489.674

Structural Analysis of Historic Masonry Arch Bridges: Case Study of Clemente Bridge on Savio River

Lucio Nobile[1, a], Veronica Bartolomeo[1,b] and Mario Bonagura[1,c]

[1] DICAM Department, University of Bologna, ITALY

[a]lucio.nobile@unibo.it, [b]veronica.bartolomeo@unibo.it, [c]mario.bonagura@unibo.it

Keywords: Masonry arch bridges, Structural Models, Discrete limit analysis, Collapse Mechanism

Abstract. The Clemente Bridge is a multi-span masonry arch bridge built during the 18th century on Savio River in Cesena. The aim of this paper is to assess its static capacity under live loads prescribed by Italian Standards in force. The analysis is performed employing RING 3.0, a computational tool based on Limit State Analysis. This method allows to individuate the minimum adequacy factor, that is the multiplier on vehicle loads required to cause collapse. In this way, a first assessment on the bridge safety can be obtained.

Introduction

Nowadays existing masonry arch bridges are very important to study because they represent a very significant part of National road and rail network, both in terms of numerical quantity and for the quality of their structural response and their environmental integration. In fact the masonry arch bridges continue to be used today without any evident change to their original shape, even if the majority of them was built between 17th and 19th century. This is possible thanks to the high self-weight together with masonry mechanical characteristics, that allow these bridges to have a relevant strength and stiffness regarding the loads which they are subjected. Maybe this is one of the most important aspects of the masonry arch bridges, that permits these ancient structures to keep in good health nowadays. However it can't be forgotten that weight, speed and traffic are increased during the last 100 years and these new elements will eventually lead to the deterioration of the bridge's fabric. This is the reason why is important check the existing bridges both through in-situ test and computational analysis. Structural assessment of this kind of structures is an important aspect for dealing with infrastructural systems efficiency, economy and with flexibility.

Computational tools for masonry arch bridges

In the last years, several strategies and computational tools have been developed to simulate the response of masonry arch bridges under the action of environmental or live loads actions. The major computational problem lays in the characterization of the behaviour of masonry, that isn't a homogenous material and as such it has to be modelled in the structural analysis. The most common idealizations of the material are elastic behaviour, plastic behaviour and non linear behaviour [1]. Among the principal computational strategies, the ones based on can be remembered: (i) Limit Analysis; (ii) Non Linear Incremental Techniques; (iii) Finite Element Method [2]. The first and the second ones usually concern bi-dimensional arches, while the third one refers to three dimensional model. Anyway, the Limit Analysis Method is just the most suitable to be applied to the arch masonry structures [3]. Heyman's statement for the masonry arch limit analysis provides that a structure is safe if a thrust line can be determined in equilibrium with the external loads, once satisfied specific hypothesis on the material [4]. So the arch shape, in relation to the applied loads, governs the stability. The use of aforementioned principle in combination with advanced numerical methods allows to develop powerful tools for the analysis of masonry arch bridges. Current tools based on the limit analysis theorem are: (i) ArchieM, that draws the trust-line for any given loading combination; (ii) Ring 3.0, that identify the limit state estimating the load factor that will lead to collapse. The last one will be adopted to analyze the case study presented in this paper.

The Case Study: Clemente Bridge on Savio River

The Clemente Bridge is a multi-span arch bridge on Savio River in Cesena, located about 90 km south-east of Bologna. The bridge, called also Old Bridge, was built between 1732 and 1772 under the Pope Clemente XII domain. Among the many designers that contributed to its realization, the famous Italian eighteenth century architects Ferdinando Fuga and Luigi Vanvitelli can be remembered [5].

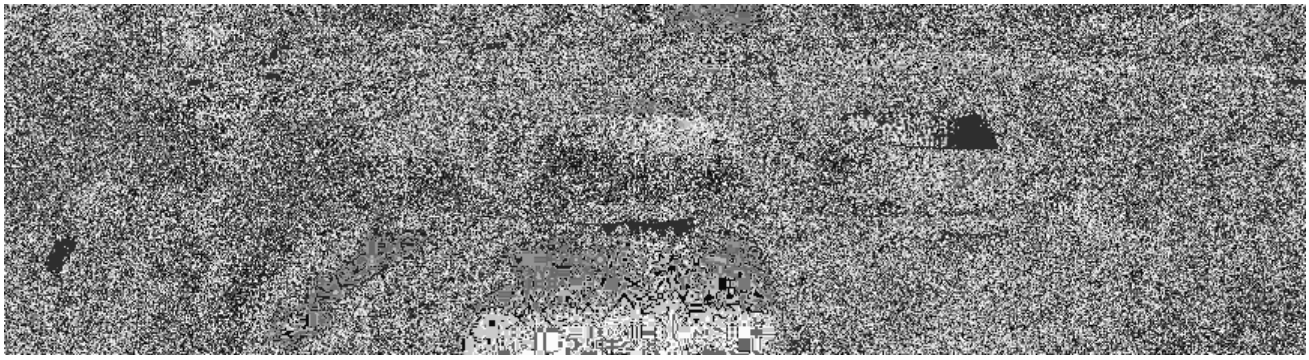


Fig. 1 Clemente Bridge aerial view

Clemente Bridge represents even now one of the most important accesses to the City, though in 1919 the Risorgimento Bridge was built down south and the Via Emilia was deviated. Before its construction, three bridges rose in the same place: the first in Roman Age, the second in masonry during Medieval Age, the third in wood during the Seventeenth Century. All these bridges were destroyed by Savio River in flood. This is the reason why Clemente Bridge has large piers, only three span and a relevant height on the water level. Over the years, the bridge withstood the river attacks and didn't suffered important damages until the Second World War, when the German troops in retreat mined the structure and blew the central arch. This one was rebuilt by Allies and by local administration between 1944 and 1945.

Clemente bridge is a road bridge and has a humpback pavement. The structure is symmetrical and was supported by three masonry arches that present a segmental shape, as illustrated in Figure 1. The arches are supported by massive piers, endowed with triangular cutwaters both at upstream and at downstream. The structure is composed by red bricks coming from a near furnace, while the cutwaters are reinforced on the edges with white limestone coming from Istria. The bridge reaches a total length of about 111 m and has an average width of 8.1 m, including the parapets. Its height is about 15 m in the maximum point. The most important geometric data regarding the three span, as the width or the rise, are provided in Table 1 and in Table 2.

Currently the bridge presents vertical cracks over the piers both on the south front and particularly on the north one. These cracks were present to a small extent on the parapets already in 1776, but in 1993 also the road surface next to the east pier presented an evident crack between the opposite platforms. Moreover the structure presents cracks on the walls of the lateral ramps and on the central arch between the old structure and the reconstructed one. Nowadays the bridge is considered a reduced loading bridge, because the heavy vehicles can not pass through it.

Table 1. Geometric Arch Data

	Span	Rise	Thickness
Span 1	22730 mm	7380 mm	1200 mm
Span 2	24900 mm	7900 mm	1200 mm
Span 3	22740 mm	7620 mm	1200 mm

Table 2. Geometric Pier Data

	Height	Thickness
Left Abutment	4185 mm	3180 mm
Pier 1	4250 mm	8490 mm
Pier 2	4150 mm	8520 mm
Right Abutment	4150 mm	3190 mm

Limit State Analysis of Clemente Bridge

As aforementioned, the structural analysis of the bridge is performed through RING 3.0, a computational modeling tool for masonry arch bridge. Built on Heyman theory, the software idealizes the bridge as an assemblage of rigid blocks and uses computational limit analysis methods to analyse the ultimate limit state, determining the amount of live load that can be applied before structural collapse. So the bridge is modelled as in-plane structure. The software introduce two important extensions to Heyman hypothesis: (i) it does not rule out the possibility that sliding fractures might occur; (ii) it allows to assume a finite crushing strength for masonry [6].

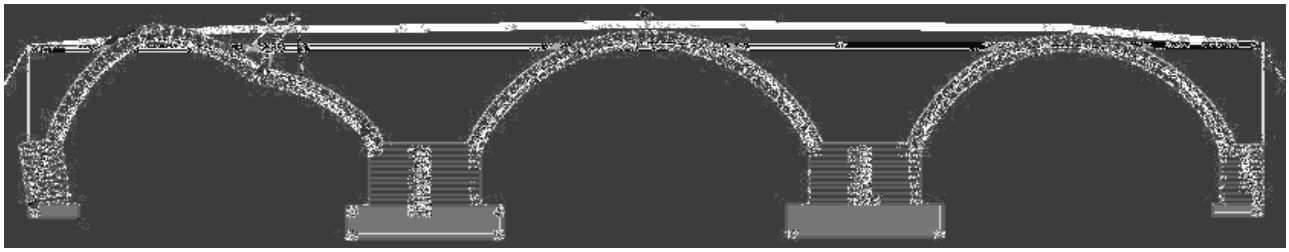


Fig. 2. North Front: Mode of response

The software RING 3.0 requires as input: (i) geometry; (ii) material properties; (iii) loading. The principal geometric data of the Clemente Bridge are provided in the previous paragraph and derived by a site survey. In order to save computational effort, in the software every arch ring is divided in 40 blocks and every pier in 20 blocks: this leads to a very small overestimate (up to 2 or 3 %) of the predicted carrying capacity of the real structure. Regarding the material properties and in absence of comprehensive in-situ test results, these are considered to assume typical values found in similar surveyed bridges. Finally concerning the loading, the Italian "Technical Standards for the Construction" of 2008 are considered [7]. These standards impose different load conditions according to the bridge category: Clemente Bridge belongs to the second category, because only reduced live loads can cross it. In this case, the Standards suppose to divide the bridge into two lanes, loading them with different point and distributed loads. Nevertheless, the Standards emphasize that the load disposition has to be chosen so to obtain the most unfavourable project conditions. Thus, refering to the Italian Standards but at the same time simulating a static test condition, the bridge is loaded symmetrically on the middle axle, overestimating the loads prescribed by the Standards. In this way, a combination of two types of loads is considered, ensuring higher safety standards: (i) double axle tandem point loads Q_{ik} of 440 kN, characterized by a loaded length of 400 mm and a width between the axles of 2000 mm; (ii) a distributed load q_{ik} of 7.20 kN/m^2 over all bridge length. To simulate the loading vehicle movement across the bridge and to identify the critical position, a series of load cases are taken into account. Firstly the whole bridge is divided into ten parts: eleven load combinations, as aforementioned, are considered. Once individuated the worst load position, the sequel step is to thicken the load cases around this zone to determine the exact condition that results in the lowest adequacy factor.

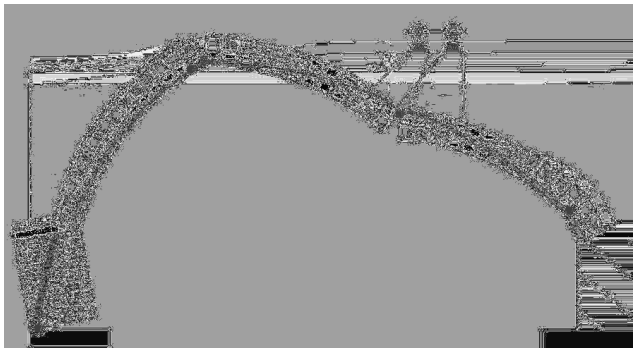


Fig 3. First Span: Failure mode and Bending moment

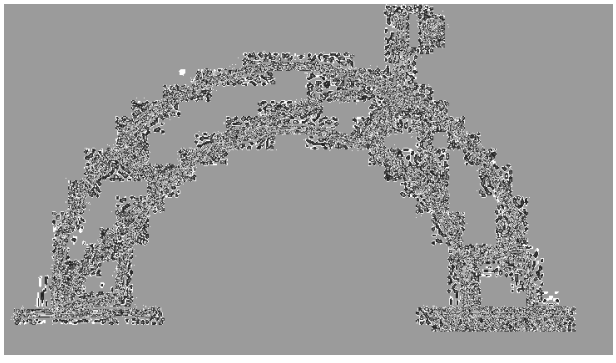


Fig. 4: J. Heyman: Point Load Case

Collapse mechanisms

In both cases the critical position is on the first span, with the double axle load spaced between 17,61 m and 19,21 m from the left springing. Obviously as the structure is symmetrical, there is a mirror-like collapse condition also on the third span. As illustrated in figure 2, at limit state the collapse is connected with the formation of a number of hinges enough to transform the stable arch in a unstable mechanism. In particular, on the first span the hinges open in alternating way in the intrados and in the extrados, following a pattern comparable to that described by Jacques Heyman for the point load case [4]. In figure 3 it can be observed also that the bending moment is equal to zero whenever the trust line pass the axle line, while it is maximum close to the hinges. In this case the *minimum adequacy factor* is equal to 3.98, so the bridge can be considered safe.

As there are no certainty on the constructive modes and the arch thickness is very high, the Authors have hypothesized also that every arch may be made also by two *debonded* rings, in the model separated by frictional contacts. In this last case, the value of the *minimum adequacy factor* decreases of almost 55% becoming 2,17: this factor highlights the loss of bearing capacity for the bridge. Also in this case the critical load position is on the first span, but obviously there are two trust line for every span and an higher number of hinges, as shown in Figure 5.

Conclusion

The results obtained employing Limit State RING 3.0 show a better behaviour for the bonded masonry arch bridge than the multi-ring *debonded* arch bridge. In fact the two solutions follow similar collapse mechanisms, but in the second case the *minimum adequacy factor* decreases evidently. Nevertheless in both constructive hypothesis, the bridge looks in fair conditions. In the future, the next analysis step will be to model also the actual crack distribution.

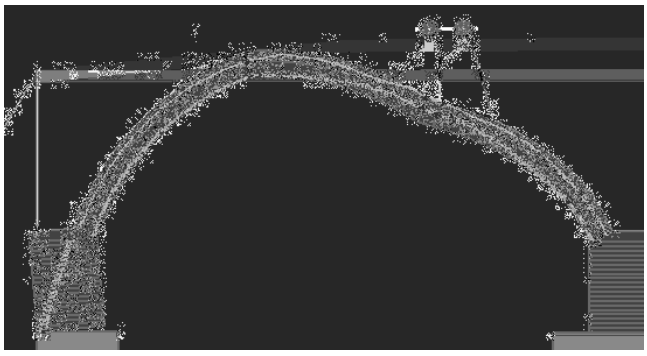


Fig 5. First multi-ring arch: Failure Mode

Acknowledgements

This research has been supported by University of Bologna, Italy. The authors gratefully acknowledge LimitState Ltd and Cantori Architectural Firm for supporting the present work.

References

[1] D. V. Oliveira, C. Lemos and P.B. Lourenço in: Proceedings of the Sixth International Conference on Arch Bridges, edited by B. Chen and J. Wei, Fuzhou, China (2010)

[2] P. Roca, M. Cervera, G. Gariup and L. Pelà: Archives of Computational Methods in Engineering, Vol. 17 (2010), pp. 299-325

[3] L. Nobile, V. Bartolomeo, M. Bonagura and C. Gentilini in: Proceedings of Twelfth International Congress on Mesomechanics, Taipei, Taiwan (2010)

[4] J. Heyman: *The stone skeleton* (Cambridge University press, Cambridge, 1995)

[5] S. D'altri Darderi: *Il ponte vecchio di Cesena* (Il Ponte Vecchio, Cesena, 1996)

[6] M. Gilbert in: Proceedings of Fifth International Conference on Arch Bridges '07, edited by P. B. Lourenco, D.V. Oliveira and A. Portela (Eds), Funchal, Madeira (2007)

[7] Technical Standards promulgated with Ministerial Decree of 14 January 2008

© (2012) Trans Tech Publications, Switzerland
doi:10.4028/www.scientific.net/KEM.488-489.678

Explosion and temperature resistance of underground structures by free hexagons

Petr P. Prochazka[1,a], Tat S. Lok[2,b]

[1]Association of Czech Civil Engineers, Prague 6, Komornická 15, Czech Republic

School of Civil and Environmental Engineering, NanyangTechnological University, Singapore

[a]petr.proch@gmail.com, [b]CTSLOK@ntu.edu.sg

Keywords: Extreme temperature, gas dynamics, plain concrete, fiber reinforced concrete, surface fissures, free hexagon method.

Abstract: It appears that sudden change of loading such as shock wave impinging on underground structures, which is mostly linked up with an extreme increase of temperature, causes immense disasters, which involve loss of human lives, heavy machine damage, long-lasting traffic troubles, decreasing of bearing capacity of the structural system, etc. A combination of shock wave due to both the elevated temperature accompanying explosion leads to cracking of the bearing system of underground openings, for example to cracking of concrete lining, i.e. to reduction of thickness of the bearing structures, etc. It has been previously proved that the free hexagon method serves for identifying the damage in the bearing system of underground structures very well. The dynamical influences have to be also emerged if extreme raise of temperature and explosion are involved in this problem; formulation is briefly mentioned and the results from numerical simulations are presented. It will be shown that the superheated vapor interacting with shock and temperature waves caused by the point charge inside of the underground open space may cause extensive occurrence of fissures on the surface exposed to the external loading envisaged.

Introduction

It is now commonly recognized that the actual behavior of concrete subjected to the high temperature and explosion effects is a result of many factors, including both environmental factors and constituent materials. Sudden change of temperature is accompanied by the volume amount of air and water in the voids within the trial material, see [1], for example. The superheated vapor causes spalling at the heated face of structure, [2]. On the other hand the combustion and gasdynamical waves coexist and interact with one another and solution of such a problem has to be obtained by numerical and computational means. The gasdynamical phenomena are, among others, described in [3], where application to shock wave impact on civil engineering structures is pointed out. It appears that free hexagon method is an appropriate numerical tool for the formulation and solution of problems of this kind, as were shown in [4] and [2]. Similarly to the problem studied in this paper a two-phase formulation is applied in both latter publications. Simplified three-phase medium is emerged in paper [5], for instance.

Under fire conditions, materials are subjected to transient processes and therefore there is a big need to quantify these properties being determined under transient conditions. Hereinafter the combustion (free hexagons) together with gasdynamics (discontinuous finite elements) is studied for underground concrete tunnel linings of a special shape (model structure), in order for free hexagons (perfectly describing possible damage of material) to apply to damage processes. Construction of theoretical models of solid materials that burn and release most of their energy in the gas-phase is carried out. A matter of validation of free hexagons is concerned for acquisition of a sufficiently accurate model of the complex processes that are involved in two-phase material, which consists of energetic solid part and the gases that, among others evolve from it.

The free hexagon method, which serves here as one of the numerical tools, starts with division of the domain (the material being confined within it) into non-overlapping hexagonal particles (elements). The particles create the solid phase while the influence of gas is concentrated in the surrounding of them. During the heating of a concrete face the tensile strength cannot be exceeded and if so, during the cooling process the tensile strength descends to zero and the admissible set of displacements turns to a cone.

Conservation equations for the gas

First the notation of the quantities under study is as follows: ρ is the density, $\boldsymbol{u} = \{u_1, u_2, u_3\}$ is the flow velocity vector, $E = e + \frac{1}{2} u_j u_j$ is the total energy density, e is the specific internal energy, which is a function of the pressure p and the specific volume $v = \frac{m}{\rho}$, m is the mass. Generally also the presence of sources of mass M, momentum F, and energy H can be taken into account. The complete set of basic conservation equations, which is linked up with gasdynamics, is found in [3]. Recall that they can be stored in the column vector notation as:

$$\frac{\mathrm{d}}{\mathrm{d}t}\int_{\Omega} \boldsymbol{U}\,\mathrm{d}\Omega + \int_{\Gamma} \boldsymbol{F}_j n_j\,\mathrm{d}\Gamma = \int_{\Omega} \boldsymbol{S}\,\mathrm{d}\Omega \tag{1}$$

where $$\boldsymbol{U} = \begin{pmatrix} \rho \\ \rho u_i \\ \rho E \end{pmatrix}, \quad \boldsymbol{F}_j = \begin{pmatrix} \rho u_j \\ \rho u_j u_i + p \\ \rho u_j (E + pv) \end{pmatrix}, \quad \boldsymbol{S} = \begin{pmatrix} M \\ F \\ H \end{pmatrix}. \tag{2}$$

The column vector $\boldsymbol{S}$ specifies the fact that point sources are in the field. Note that the effects of these quantities are of the principal importance in case the Sedov explosion is studied.

Suppose now that Ω is independent of time and is covered by a sum of $\Omega_g + \sum_{k=1}^{n} \Omega_k$, where volume Ω_g is occupied solely by gaseous material, and Ω_k with their boundaries Γ_k are n subdomains (particles) of the hexagonal shape. Since (1) is applied to the gaseous part only in the new set-up it is written as:

$$\begin{aligned} &\frac{\mathrm{d}}{\mathrm{d}t}\int_{\Omega_g} \boldsymbol{U}\,\mathrm{d}\Omega + \int_{\Gamma - \sum_k \Gamma_k} \boldsymbol{F}_j n_j\,\mathrm{d}\Gamma = \int_{\Omega_g} \boldsymbol{S}\,\mathrm{d}\Omega, \\ &\int_{\Omega_g} \frac{\mathrm{d}\boldsymbol{U}}{\mathrm{d}t}\,\mathrm{d}\Omega + \int_{\Gamma} \boldsymbol{F}_j n_j\,\mathrm{d}\Gamma - \sum_{k=1}^{n} \int_{\Gamma_k} (\boldsymbol{F}_j - \boldsymbol{U}u_j^k) n_j\,\mathrm{d}\Gamma = \int_{\Omega_g} \boldsymbol{S}\,\mathrm{d}\Omega \end{aligned} \tag{3}$$

where u_j^k is the velocity vector along the surface of the particle k and appears as a consequence of time-dependent volume Ω_k. The third term of the left hand side describes the mutual effect of gas and solid particle at the interfaces.

Two meshes are created, one for discontinuous finite elements, [3], and the other for free hexagons. The first mesh is depicted in Fig. 1 for the concrete example, which is to be presented here, and the second mesh is shown in Fig. 2. Obviously, both meshes are in compliance to compare the necessary quantities in representative element (RVE) its lay-out is seen in Fig. 3.

The RVE serves for pointing out of additional forces due to the exchanges in the gaseous phase and vice versa, for describing the effect of shape changes of the particles. The source $\boldsymbol{S}$ is active only outside of the solid phase, as the point of explosion or combustion ignition is considered inside

of the tunnel opening space, see Figs. 1, 2. Aside from the gas influence the particles are loaded by volume weight and the change of temperature. In the iterative process also dynamical forces are active, which are concentrated at the center in the particles, for simplicity. Note that the particles are assumed small enough, so that this simplification makes sense.

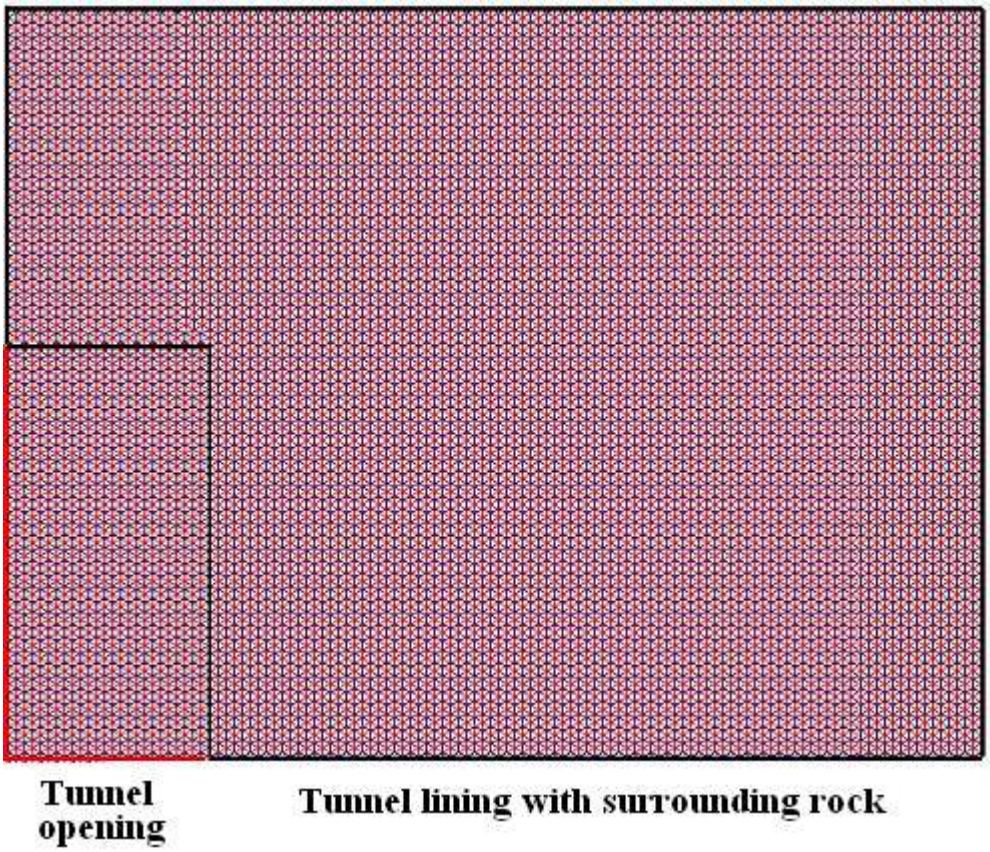


Fig. 1: Symmetric mesh for discontinuous finite elements

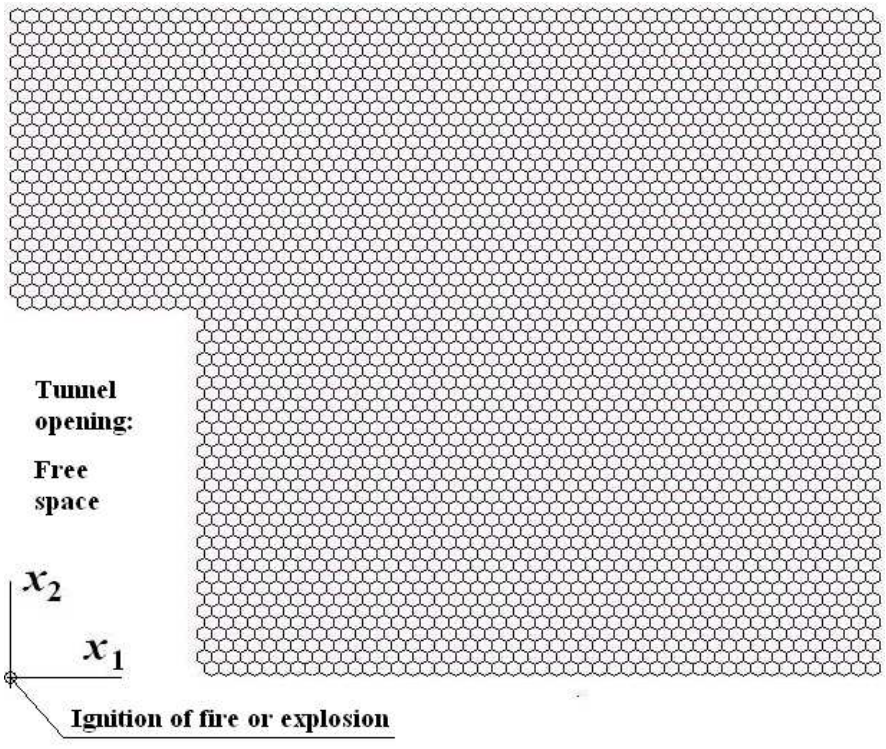


Fig. 2: Symmetric mesh for free hexagons

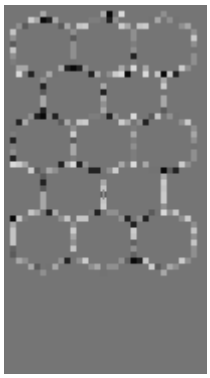


Fig. 3: Typical periodic RVE

Example and conclusions

Number of hexagons is 3064 and number of finite elements is 19320, which cover a cross-section of $30 \times 30\,\mathrm{m}^2$. Maximum applied temperature is 1200 ^{0}C, the ignition of which is located at the origin (Fig. 2), the igniter mass flux is 40 kg/(m^{3}s), which appears in H as a source term at $t = 0$, the molar gas constant R = 8.314472 J·K^{-1}·mol^{-1} . A simplification is made here that the material properties of the solid phase remain unchanged inside of the particles and are given in a standard way by modules taken for linear elasticity: $E = 208 \times 10^9$ N/m^2, volume weight is 2100 kg/m^3, ν = 0.29. Mirror symmetry is applied along x_2-axis, the other boundaries are defined by rollers. Movements of particles in cuts of the cross-section of the tunnel are depicted in Fig. 4 to Fig. 7 at different time instant. The fissures appear on the surface because of various interactions of vapor and gas states inside of the concrete and rock. The combination of free hexagons (admitting cracks in natural way as disturbed contacts) and finite elements solving one dimensional gasdynamics seems a promising tool for solving problems of this sort.

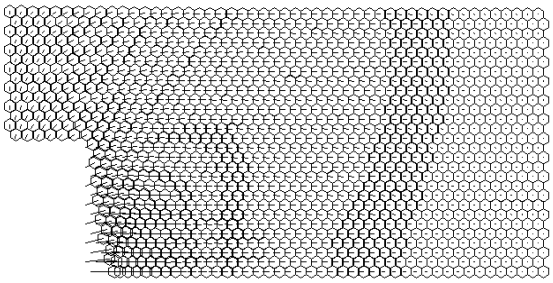


Fig 4: Movement at 0.01 sec

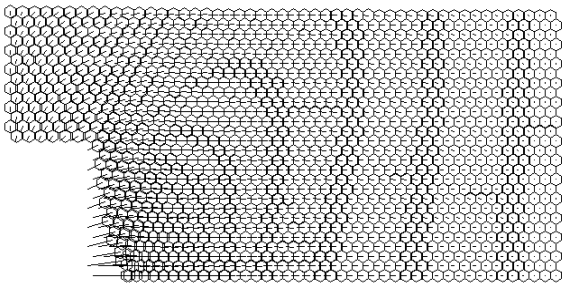


Fig. 5: Movement at 0.03 sec

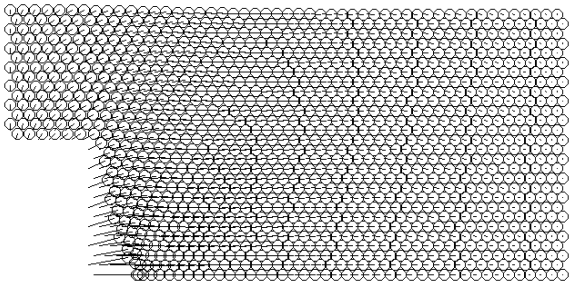


Fig. 6: Movements at 0.08 sec

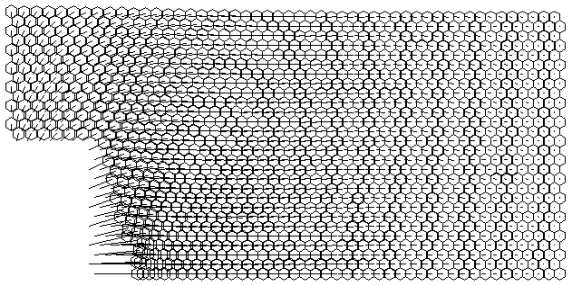


Fig. 7: Movements at 0.15 sec

Acknowledgment: This paper was financially supported by GAČR, project No. P104/10/1021. Financial support of Ministry of Education and Sport of the Czech Republic, project numbers MSM 6840770001 is also acknowledged.

References

[1] S. Peskova and P.P. Prochazka: CTU Reports 1, Vol. 12, (2008), pp. 150

[2] P.P. Prochazka, M.V. Valek, S. Peskova: Study on spalling of extremely heated FRC by free hexagons. Key Eng. Mater. 452-453: (2011), p. 693-696

[3] P. Prochazka, A. Kravtsov: Shock Waves as a Main Destructive Dynamical Loading of Structures. Czech Technical University in Prague (2010), pp. 132

[4] P.P. Prochazka: Application of discrete element methods to fracture mechanics of rock bursts. Engineering Fracture Mechanics 71 (2004) p. 601–618

[5] G.W. Ma, J.C. Li, J. Zhao: Three-phase medium model for filled rock joint and interaction with stress waves. Int. J. Numer. Anal. Meth. in Geomech. 35(1) (2011) p. 97-110

© (2012) Trans Tech Publications, Switzerland
doi:10.4028/www.scientific.net/KEM.488-489.682

Application of gradient based IR thermography to the GRP structures inspection

Lovre Krstulović-Opara[1,a], Endri Garafulić[2,b], Branko Klarin[1,c] and Željko Domazet[1,d]

[1]University of Split, Faculty of Electrical Engineering, Mechanical Engineering and Naval Architecture, R. Boskovica 32, 21000 Split, Croatia

[2]University of Split, Faculty of Science, Teslina 12, 21000 Split, Croatia

[a]Lovre.Krstulovic-Opara@fesb.hr, [b]endri.garafulic@pmfst.hr, [c]Branko.Klarin@fesb.hr, [d]Zeljko.Domazet@fesb.hr

Keywords: Infrared thermography, pulse heating, non destructive testing, thermal gradient

Abstract. The article presents application of non destructive testing method based on the pulse heating infrared thermography used to detect material anomalies for the case of glass reinforced polymer structures. The goal of presented research, based on the thermal gradient approach, is to establish the procedure capable of filtering out anomalies from other thermal influences caused by thermal reflections of surrounding objects, geometry influences and heat flows for observed object.

Introduction

The pulse (flash) heating infrared (IR) thermography is a non-destructive testing (NDT) method applicable to glass reinforced polymer (GRP) structures such as glider planes, sailing/power boats, wind turbine blades, aerospace components [1], etc. The method is based on a pulse source of heat, followed by the IR acquisition of structure cooling process. For the case of fast cooling materials such as metals (high heat conductivity), the heat pulse has to be applied in a relatively short time [2, 3, 4]. Fast cooling material requires cooled middle-wave IR cameras capable of acquisition at high frame rates. The heat source is a Xenon flash lamp capable of producing 6 kJ of energy in less than 20 ms, what makes special requests on needed equipment. For the case of slow cooling materials [1, 5, 6] such as GRP is (low heat conductivity), significantly cheaper equipment including heat source based on a Halogen lamp (e.g. 1 kW bulb on 1m distance and 2 min of heating) and long wave IR camera is enabling visualization of material anomalies such as fractures, delaminations, air pockets, as well as locating structural members and reinforcements. The presented research is conducted with 1 kW Halogen heat lamp and cooled middle-wave IR camera. Significant advantage of pulse heating thermography in comparison to the pure IR thermal acquisition is in shifting observed surface in higher temperature zones, away from radiating temperatures of surrounding objects. Thus, significant disturbances of surrounding object´s heat reflections, unavoidable for the case of on-field acquisitions, are avoided. The presented non-destructive method proved to be a reliable and robust approach to inspection of GRP structures. Nowadays in aircraft industry it is more and more common that in NDT of aircraft structures heat blankets are used to generate the transient propagating heat wave, making the similar effect as the halogen heat source described herein.

Pulse heating thermography

Heat flow introduced to the object of interest is causing different thermal responses depending on structure itself, thus enabling visualization of subsurface structural differences and material anomalies. For the case of common GRP structures (Fig. 1 to 3), structural reinforcements are clearly visible, what enables their detection and evaluation. Structural reinforcements for the case of the glider pane T-tail fin (Fig. 1), glider main spar (Fig. 2), or reinforcement of clamping region for the case of 600 W wind turbine blade (Fig. 3), are typical examples.

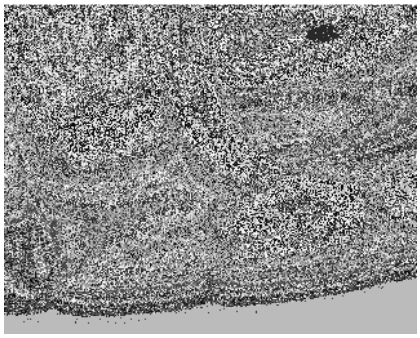


Fig.1 Reinforcements of T-tail fin

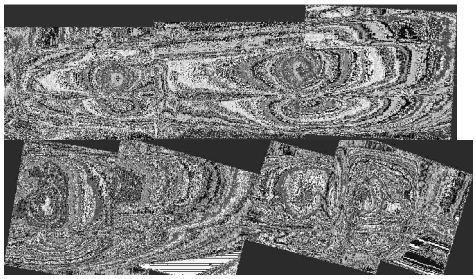


Fig. 2 Glider's main spar

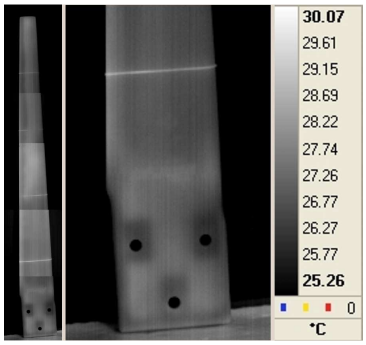


Fig. 3 Reinforcements of screw holes

Evaluation of the controlled impact damage of GRP plate is presented in reference [6], where impact is acquired by means of high frame rate thermography. In [6] the thermoelastic stress analysis is performed for case of uniaxial tension, while pulse heating thermography is used to locate the damaged zone. In [6] GRP roving is not covered with the gelcoat layer common for majority of GRP structures. In the case of fracture the gelcoat layer, as more brittle one, will show crack before the GRP, thus enabling the visual detection and evaluation of cracks (Fig. 4). For this case there is no significant advantage of using pulse heating IR approach. For cases of GRP structures without the gelcoat, e.g. free or pained surface, the pulse heating thermography is powerful method, as described in [6].

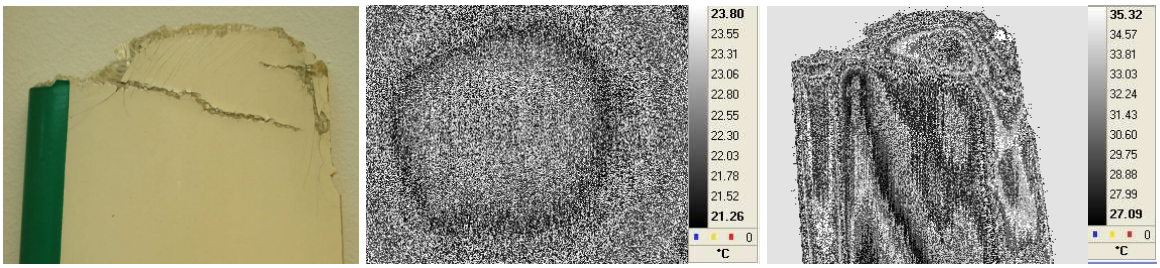


Fig. 4 Ruptured 900 W wind turbine blade: IR image before and after the pulse heating

Air bubbles in gelcoat, structural de-bonding of GRP layers and other anomalies of material can be detected by using the pulse heating thermography. In reality, observed objects are not flat and in laboratory environment, but curved and surrounded by objects radiating heat and causing thermal reflections that cannot be easily distinguished from material anomalies. When finding anomalies on a termogram several software tools such as various color palettes, image filters and isotherms can be used.

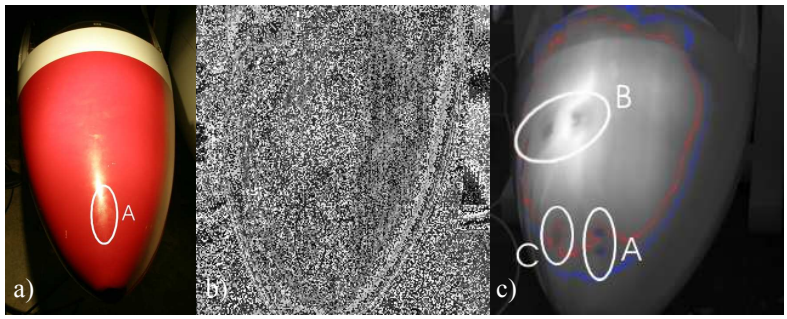


Fig. 5. Anomalies visible on glider's nose thermogram with and without pulse heating

A high pass filter generally increases the noise, making anomalies and sudden changes in temperature field appearing "sharper" (Fig. 10). Isotherms, the lines of same apparent temperature span, when reduced to small span size and slid over the temperature scale (level), are changing shape of their front line when passing over anomalies (Fig. 5c).

Gradient based approach to pulse heating thermography

Sliding isotherms is common procedure used in evaluation thermograms when detecting the heat concentration zones. A normal to front line of isotherm coincides with the temperature gradient, what inspired us to perform a themperature gradient function, grad (T), where T(x,y,t) is a temperature of each pixel forming the thermal image at observed (constant) time t, i.e.

$$\text{grad } T = (\partial T/\partial x, \partial T/\partial y). \quad (1)$$

Coordinates x, y are horizontal and vertical directions of a pixel position in the pixel map. Such an image processing enables flattening the differences in thermal signal with lower gradient and keeping visible zones with higher thermal gradient, i.e. enables visualizing the transition zones between anomalies and intact object.

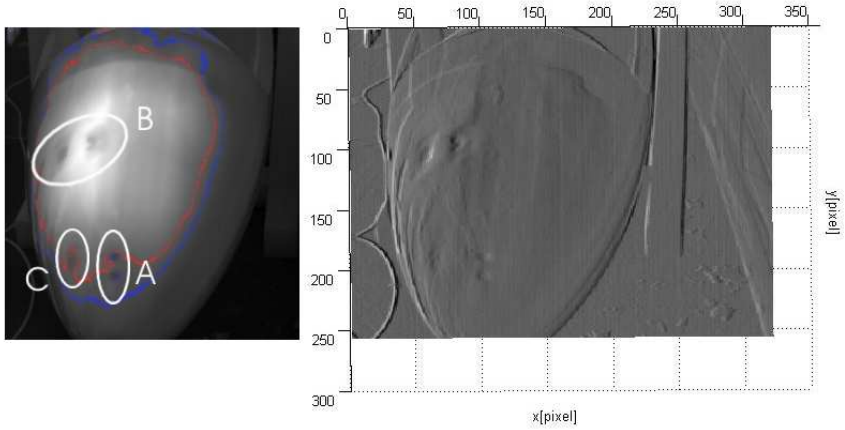


Fig. 6. A thermogram after the pulse heating and gradient of the same thermogram

Figures 7 to 11 summarize discussed approach. Anomalies of main spar junction, as a critical part of the glider plane, when observed in IR spectrum (Fig. 8) are not visible. IR image after the pulse heating (Fig. 9) shows structural reinforcements, trapped air pocket in GRP layers (zone D) and de-bonding of the GRP from the wooden main spar structure (zone E). High pass filtering (Fig. 10) enables clearer and sharper images.

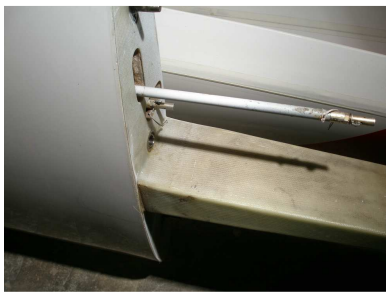


Fig. 7. Main spar junction

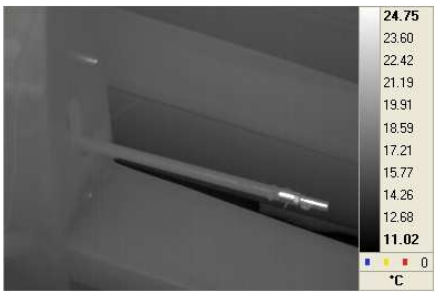


Fig. 8 Without the pulse heating

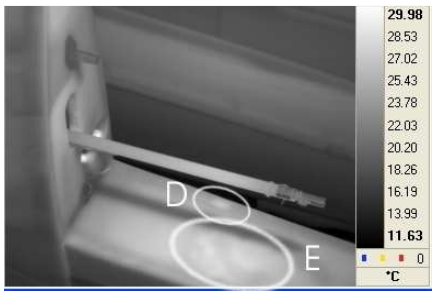


Fig. 9 After the pulse heating

Gradient based method (Fig. 11) applied on the pulse heating thermogram (Fig. 9), flattens the image and makes structural supports and anomalies visible and distinguishable.

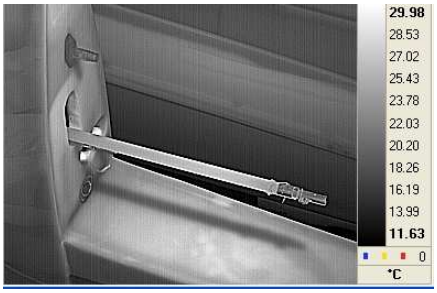


Fig. 10. High pass filtering of pulse heating image

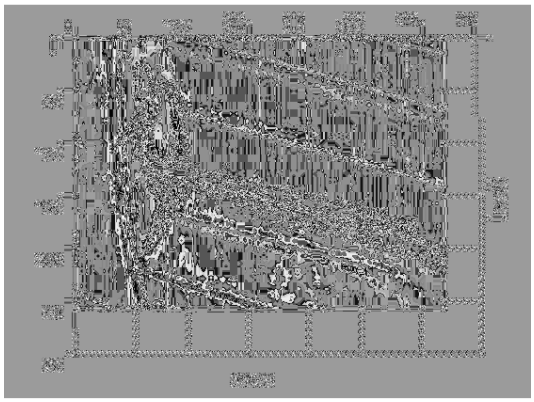


Fig. 11. Gradient of pulse heating image

Concluding remarks

Pulse heating thermography, as non-contact NDT method, has become standard procedure when evaluating the GRP structures. Detection of structural members and material anomalies, together with the elimination of surrounding objects reflections, are demonstrated in presented examples. The gradient based image processing approach enables differentiation of potential zones of material anomalies, what makes described method particularly applicable for on-field thermal acquisitions.

Acknowledgements: The financial support of the Ministry of Science, Education and Sports project "Fatigue strength of constructions and materials" is gratefully acknowledged.

References

[1] S. M. Shepard, Flash Thermography of Aerospace Composites, IV Conferencia Panamericana de END Buenos Aires, October 2007, 2007.

[2] V. Vavilov, E. Grinzato, P. G. Bison, S. Marinetti, M. J. Bales, Surface transient temperature inversion for hidden corrosion characterization: theory and applications, International Journal of Heat Mass Transfer 30 (1996) 355-371.

[3] X. Maladague, F. Galmiche, A. Ziadi, Advances in pulse phase thermography, Infrared Physics & Technology 43 (2002) 175-181.

[4] S. Marinetti, V. Vavilov, IR thermographic detection and characterization of hidden corrosion in metals: General Analysis, Corrosion Science 52 (2010) 865-872.

[5] S. Pickering, D. Almond, Matched excitation energy comparison of the pulse and lock-in thermography NDE techniques, NDT&E International, 41 (2008) 501-508.

[6] L. Krstulovic-Opara, B. Klarin, P. Neves, Z. Domazet, Thermoelastic Stress Analysis of impact damage of composite materials, Engineering Failure Analysis 18 (2011) 713–719.

© (2012) Trans Tech Publications, Switzerland
doi:10.4028/www.scientific.net/KEM.488-489.686

Tensile properties of random distribution short SMA fiber reinforced composites

Hongshuai Lei[a], Bo Zhou[b], Zhenqing Wang[c], Xiaoqiang Wang[d]

College of Aerospace and Civil Engineering, Harbin Engineering University, Harbin 150001, China

[a]lei123shuai@126.com, [b]zhoubo@hrbeu.edu.cn,

[c]wangzhenqiang@hrbeu.edu.cn, [d]wangxiaoqiang@hrbeu.edu.cn

Keywords: shape memory alloy; reinforced composites; short fiber; tensile mechanical properties; simulation

Abstract. Shape memory alloy (SMA) reinforced composites have been widely used in aerospace engineering fields. In this paper, four basic assumptions were presented to simply the research model based on the Eshelby's equivalent inclusion method and Mori-Tanaka scheme. Based on the three-phase equivalent system and two-step equivalent process, the effective elastic modulus and thermal expansion coefficient of unidirectional random distribution short SMA fiber reinforced composites were derived. The tensile mechanical properties of composites with fiber volume fraction (15%), size (L=3, D=1; L=5, D=1), and number (N= 30, 50), were simulated using software ANSYS12.0, and discussed the failure mode of the composites.

Introduction

Shape memory alloys (SMAs) have material properties which vary with applied stress, temperature, and load history. As such, they were uniquely suitable for using in composites. Many studies have shown that SMAs composites have significant potential applications in vibration and structural controls [1]. To design an intelligent composite or smart structure, particle and fiber of SMA was usually filled or embedded into other matrix materials, such as epoxy resin, metal matrix, ceramic matrix, and laminated particle-fiber-reinforced composite material. Therefore, it was valuable to investigate the mechanical behavior of SMAs composites.

Recently, many researchers have attempted to improve the properties of materials by embedding SMA in the form of tube, wires, long fiber, short fiber, particles and so on into either elastic-plastic matrix. Ni et al. (2007) [2] studied the mechanical behavior of SMA composite with short fiber and particle. Based on the Halpin-Tsai theory, a model for the laminated plates with SMA fillers was presented to predict the dynamic mechanical properties. In addition, some research has been done to understand and model the constitutive behavior of SMA composite. Cherkaoui et al. (2000) [3] regarded the composite as a two-phase system with ductile matrix and SMA second phase. Then, a macroscopic constitutive relation of the composite was established by using self-consistent approach where the micro-macro correlation was realized by volume averaging and by introducing the concept of stress and strain concentration tensors. Zhu et al. (2009)[4-5] developed an equivalent three-phase micromechanical model of composite with an elastic-plastic matrix and shape memory alloy reinforcement, based on Eshelby's equivalent inclusion method and Mori-Tanaka scheme.

On simulating the response of SMA composites, researchers have used a variety of methods including micromechanical methods and finite element analysis. These simulations are usually focused on the multilayered composite plates and beams. Few studies were focused on composites filled with SMA fibers and particles.

In the following sections of the paper, based on the three-phase equivalent system and two-step equivalent process, the effective elastic modulus and thermal expansion coefficient was derived. Then, the tensile properties of composite were simulated, with various fiber volume fraction, size, number and temperature. Finally, the failure mode of the composites was discussed.

The effective elastic modulus of composite

During the process of loading, stress will induce the phase transformation from austenite (a high symmetry parent phase) to martensite (a low symmetry product phase). The properties of SMA are various at different phase, therefore the SMA reinforced composite is considered as a three-phase equivalent system: matrix phase (defined as 0th phase), austenite phase (defined as 1st phase) and martensite phase (defined as 2nd phase). The volume fractions of austenite and martensite were denoted as c_1 and c_2 respectively, and the volume fraction of fiber was $c=c_1+c_2$. Then the volume fraction of matrix can be expressed as $c_0=1-c$.

Suppose a uniform strain boundary condition was applied to the composites in vertical direction, then the effective elastic modulus of composite can be expressed as follows:

$$\bar{E}_{ijmn} = E^0_{ijmn} + \sum_{r=1}^{R-1} c_r \left(E^r_{ijkl} - E^0_{ijkl} \right) B^r_{klmn} \tag{1}$$

where B^r_{klmn} and E^r_{ijkl} were the strain concentration factor and elastic modulus of the $r\,th$ phase material, respectively. R was the total number of the phase.

To solve the strain concentration factor, researchers have devoted a lot of energy and developed several effective methods. Based on Mori-Tanaka method, the strain concentration factor can be expressed as

$$B^r_{ijmn} = T^r_{ijkl} \left[c_0 I_{klmn} + \sum_{r=1}^{R-1} c_r T^r_{klmn} \right] \tag{2}$$

where I_{ijkl} was a fourth-order unit tensor, and

$$T^r_{klmn} = \left[I_{ijkl} + P^r_{ijkl} \left(E^r_{ijkl} - E^0_{ijkl} \right) \right]^{-1} \tag{3}$$

Substituting Eq. (2) and Eq. (3) into Eq. (1)

$$\bar{E}_{ijkl} = E^0_{ijkl} + \sum_{r=1}^{R-1} c_r \left[\left(E^r_{ijkl} - E^0_{ijkl} \right)^{-1} + c_0 P^r_{ijkl} \right]^{-1} \tag{4}$$

Considering the fibers had the same size and shape and was arranged in the same direction, R was set as 3. Thus, the above equation can be expanded as

$$\bar{E}_{ijkl} = E^0_{ijkl} + c_1 \left[\left(E^1_{ijkl} - E^0_{ijkl} \right)^{-1} + c_0 P^1_{ijkl} \right]^{-1} + c_2 \left[\left(E^2_{ijkl} - E^0_{ijkl} \right)^{-1} + c_0 P^2_{ijkl} \right]^{-1} \tag{5}$$

where P_{ijkl} was a fourth-order tensor and determined by the size of fiber.

The effective thermal expansion coefficient of composites

In order to estimate the effective thermal expansion coefficient of composites, a two-step equivalent process was introduced. The first step, the composites was regarded as a two-phase equivalent system consisting of fiber and matrix, and the thermal expansion coefficient of composite can express as

$$\bar{\alpha}_{ij} = \alpha_{ij}^{0} + \left(\bar{\alpha}_{ij}^{f} - \alpha_{ij}^{0}\right)\left(\bar{S}_{ijkl}^{f} - S_{ijkl}^{0}\right)^{-1}\left(\bar{S}_{ijkl} - S_{ijkl}^{0}\right) \tag{6}$$

where $\bar{\alpha}_{ij}^{f}$ and $\bar{S}_{ijkl}^{f}$ were effective thermal expansion coefficient and flexibility coefficient of fiber. The second step, fibers can be decomposed into austenite and martensite (generation phase). Thus,

$$\bar{\alpha}_{ij}^{f} = \alpha_{ij}^{1} + \left(\alpha_{ij}^{2} - \alpha_{ij}^{1}\right)\left(S_{ijkl}^{2} - S_{ijkl}^{1}\right)^{-1}\left(\bar{S}_{ijkl}^{f} - S_{ijkl}^{1}\right) \tag{7}$$

S_{ijkl}^{1} and S_{ijkl}^{2} were the flexibility coefficient of austenite and martensite respectively.

Substituting Eq. (7) into Eq. (6),

$$\bar{\alpha}_{ij} = \alpha_{ij}^{0} + \left(\alpha_{ij}^{1} - \alpha_{ij}^{0}\right)\left(\bar{S}_{ijkl}^{f} - S_{ijkl}^{0}\right)^{-1}\left(\bar{S}_{ijkl} - S_{ijkl}^{0}\right) + \left(\alpha_{ij}^{2} - \alpha_{ij}^{1}\right)\left(S_{ijkl}^{2} - S_{ijkl}^{1}\right)^{-1}\left(\bar{S}_{ijkl} - S_{ijkl}^{0}\right) \tag{8}$$

According to the literature [6],

$$\bar{S}_{ijkl}^{f} = S_{ijkl}^{1} + \xi\left(S_{ijkl}^{2} - S_{ijkl}^{1}\right)$$

here ξ was the martensite volume fraction of fiber ($\xi=c_2/(c_1+c_2)$).

In summary, Eq. (5) and Eq. (8) was obtained based on the three-phase equivalent system and two-step equivalent process. Therefore, comparing with other methods, they can predict the effective modulus of composite more precisely and comprehensively.

Numerical results and discussion

In order to evaluate the effect of short fibers on the elastic modulus and thermal expansion stress of composites, fiber volume fraction (15%), size (L=3, D=1; L=5,D=1), number (N= 30, 50) and temperature (343K) were simulated in present paper. Simulation was carried out on Ni-Ti (50%) fibers reinforced epoxy resin matrix under uniaxial tension. The length of matrix was 500mm, and the width was 200mm.

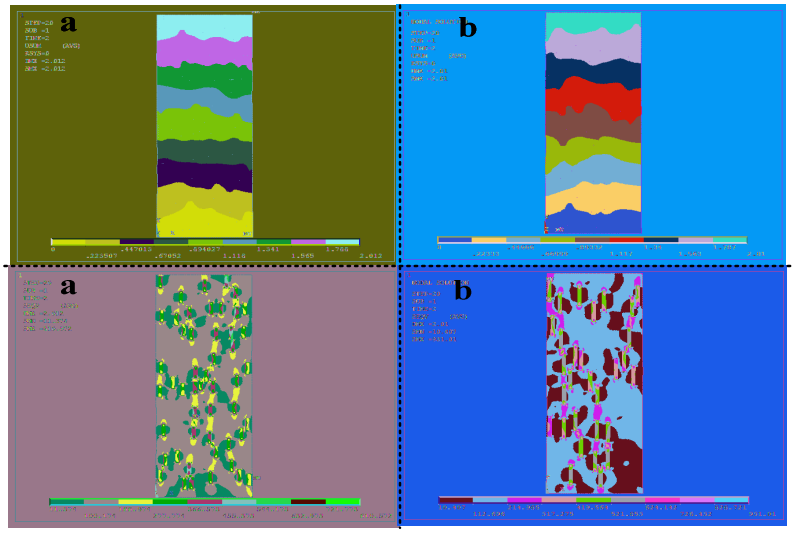


Fig.1 Contour plot of displacement and von Mises stresses in the composite at 343K: (a) L/D=3, c=15%; N=50 (b) L/D=5, c=15%; N=30

Fig.1 illustrates the influence of fiber length and number on the deformation and von Mises stress distribution of composites. It can be seen, at the same volume fraction, the deformation contour of short fiber composites is smoother than that of long fiber composites. Further, it could be obtained from the plots that most stress concentrations arise at the interfaces, especially in the areas where the fibers are close to each other. Due to the embedding of the fiber, the deformation of matrix was restricted. The stress distribution of composites was ununiform, and the average stress of long fiber is larger than that of short fiber. It indicates that the volume fraction of martensite and austenite was discrepant respectively in both cases.

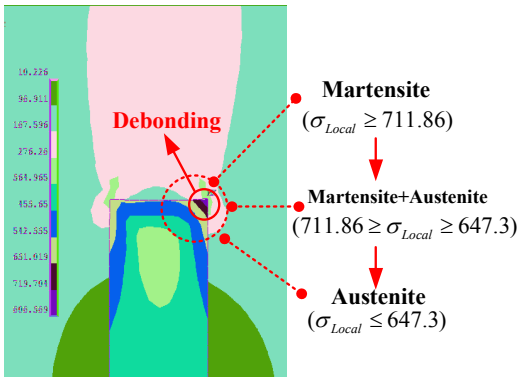


Fig.2 Contour plot of von Mises stresses in representative volume element (L/D=3, c=15%, T=343K).

The fibers are random distributed in the composites. Due to the different distribution of the fibers and the interaction between fibers, the overall stress of fiber was asymmetric. Fig.2 shows the contour plot of von Mises stresses in representative volume element (the maximum stress unit). The maximum stress occurs at the sharp point at both ends of fiber. σ_{Local} present the local stress of fiber. When $\sigma_{Local} \geqslant 711.86$MPa, the material was at the martensite phase; when $\sigma_{Local} \leqslant 647.3$MPa, the material was at the austenite phase, that's why we consider SMA reinforced composite as a three-phase equivalent system. With the increase of local stress, the interface between fiber and matrix will start debonding gradually, so the stress concentration point was considered as debonding start point. The failure mode was the interface debonding of SMA short fiber reinforced composites.

Conclusions

In this paper, tensile properties of unidirectional random distribution short SMA fiber reinforced composites were investigated through the theoretical analysis and numerical simulation respectively. At the same fiber volume fraction, the influence of fiber size on the effective modulus of composites cannot be ignored. Although the reinforcing effect of L/D=5 is more predominant than L/D=3, the deformation contour is not smooth and the material is more prone to debonding failure. During the process of loading, the Ni-Ti fibers will gradually phase transition; therefore it is reasonable to consider the composites as a three-phase equivalent system. Although the simulation model was too idealistic, it was still helpful for engineering application.

Acknowledgement

This work has been supported by the Fundamental Research Funds for the Central Universities (HEUCF20100201 and HEUCFZ1004), and the author wish to acknowledge Harbin Engineering University of China.

References

[1] J.S.Park, J.H Kim and S.H.Moon. Composite Structures 63 (2004) 179-188.
[2]Q.Q.Ni, R.X.Zhang, T.Natsuki and M.Iwamoto. Composite Structures 79 (2007) 90-96
[3]M.Cherkaoui, Q.P.Sun and G.Q.Song. International Journal of Solids and Structures 37 (2000) 1577-1594
[4] Y.P.Zhu, G.S.Dui. Journal of the Mechanical Behavior of Biomedical Material 2 (2009) 454-459
[5]Y.P.Zhu, G.S.Dui and D.Liu. Sci China Ser E-Tech Sci 52 (2009) 610-616
[6] L.C.Brinson and M.Panico. International Journal of Solids and Structures 46 (2009) 217-220

© (2012) Trans Tech Publications, Switzerland
doi:10.4028/www.scientific.net/KEM.488-489.690

Study on Static and Dynamic Mechanical Property of Sandwich plate with Aluminum Foam Core under Confining Pressure

Zou Guangping[1, a], Chang Zhongliang[1] and Wang Ruirui[1]

[1]College of Aerospace and Civil Engineering, Harbin Engineering University, Harbin 150001, China

[a]gpzou@hotmail.com

Keywords: Aluminum Foam; Sandwich plate; SHPB; Confining Pressure.

Abstract. In this paper, the sandwich structure which is consist by the aluminum foam core and CBF(continuous basalt fiber) composite plate is tested by the static and dynamic mechanical property under confining pressure, and the confining pressure experiment is done through add cylindrical tube to the sandwich structure circular specimens. The static mechanical property is tested by WDW3100 electronic universal testing machine, and its dynamic mechanical property is tested by the SHPB(Spilt Hopkinson Press Bar) device, Besides, the strain rate effect of this sandwich structure under confining pressure is tested too, From the experiment results we can see the static and dynamic mechanical properties of confining and no confining results is very different, and this study will provide references for further numerical simulation and damage studying of this kind of sandwich structure.

Introduction

Aluminum foam is a kind of novel light-weight functional material, it possesses large deformation and good energy absorption ability, so it is widely used in automobile, aviation, aerospace and other fields, especially in the buffer structure. As the anti-impacting and energy absorption material, the aluminum foam is always used for making the sandwich plate which the aluminum foam as the core material, and the plate is usually made by metal or composite material which can enhance stiffness of the sandwich structure. Now there are many researches about the static and dynamic mechanical property of this sandwich plate[1-2], but the research about its mechanical property under confining pressure is few[3], and this sandwich structure under confining pressure mechanical property should be considered when accurate calculate its impact resistance results. So in this paper, the static and dynamic mechanical properties of sandwich structure which consist by the aluminum foam core and CBF(continuous basalt fiber) composite plate under confining pressure is tested, and the confining pressure is done through add steel cylindrical tube to the sandwich structure circular specimens, the static mechanical property is tested by WDW3100 electronic universal testing machine, and its dynamic mechanical property is tested by SHPB, Besides, the confining pressure experiment results and the no confining pressure experiment results are detail compared.

Experiment Process

Specimen. The closed-cell aluminum foam average hole size is about 2.5mm, its density is 0.405g/cm^3, void fraction is 85%, and thickness is 10mm, the aluminum foam circle specimen as shown in Fig.1. The CBF plate thickness is 3mm, its density is 0.586g/cm^3. The sandwich plate is consist by the CBF plate and aluminum foam, and they were bonded by the epoxy resin adhesive, as shown in Fig.2, and the sandwich plate confining pressure is done through add steel cylindrical tube to the sandwich plate circular specimens, as shown in Fig.3. Because in the SHPB experiment the diameter of aluminum alloy bar is 37mm, so in the confining pressure experiment, all the sandwich plate specimens diameter are 37mm.

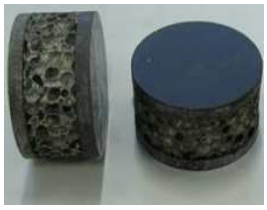
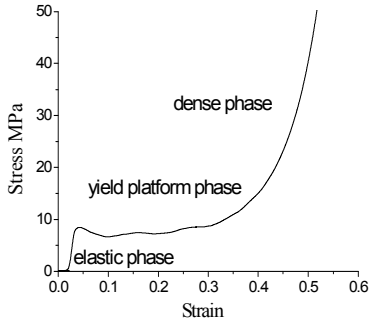




Fig.1 Aluminum foam Fig.2 Sandwich plate specimen Fig.3 Steel cylindrical tube and specimen

The Static Experiment Process. In the static mechanical property experiment, the WDW3100 electronic universal testing machine was used for testing the sandwich plate compression mechanical properties, including the confining and no-confining experiment, and the confining experiment also used the Fig.3 device. The compression data as shown in Fig.4 and Fig.5. From the two test results we can see the stress-strain curves are all have "three stage", elastic phase, yield platform phase and dense phase, while the yield stress of confining pressure is higher than the no confining result, and the strain and platform phase is less.



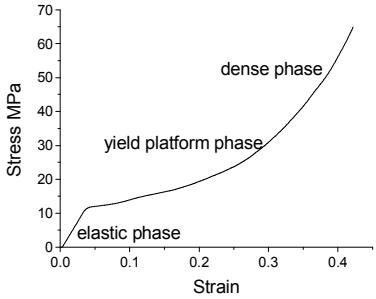


Fig.4. Static compression property of sandwich plate Fig.5 Static compression property of sandwich plate under confinging pressue

The Dynamic Experiment Process. The dynamic experiment was tested by the SHPB device, and the bar which SHPB experiment adopt is aluminum alloy bar, and its diameter is 37mm. In order to realize the dynamic sandwich plate confining pressure experiment, the sandwich plate specimen diameter is 37mm too, the facility of SHPB confining experiment as shown in Fig.6, and steel cylindrical tube was adopted to the sandwich plate circular specimens, and the tube diameter is 37mm too, as shown in Fig.7, and the steel tube on the SHPB facility as shown in Fig.8. Through one-dimensional elastic stress wave principle of SHPB, from Eq.1 we can get the stress, strain and strain rate of the sandwich plate specimen[4].

$$\sigma_s = \frac{AE}{A_s}\varepsilon_t, \quad \varepsilon_s = \frac{-2C_0}{l_s}\int_0^t \varepsilon_r dt \quad \dot{\varepsilon}_s = -\frac{2C_0}{l_s}\varepsilon_r \tag{1}$$

In the Eq.1, $\varepsilon_i, \varepsilon_r, \varepsilon_t$ respectively for the incident wave, reflect wave and transmit wave. C_0 is elastic wave velocity in the bars, l_s is the length of the specimen, E is the young's modulus of the bar, A is the section surface of the bar, A_s is the section surface area of the specimen.

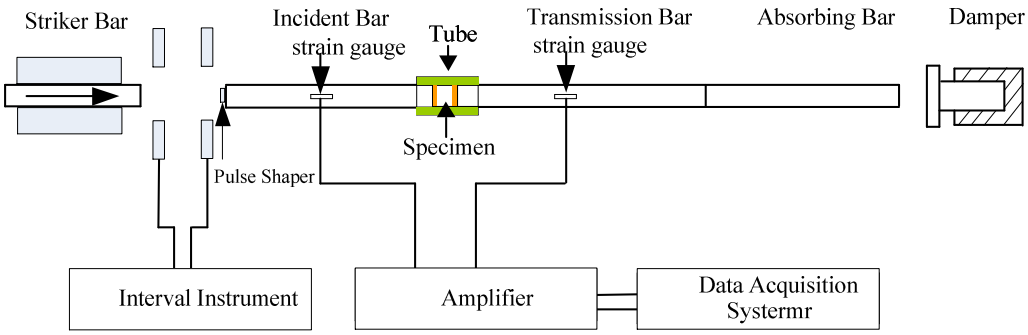


Fig.6 The experimental facility of SHPB



Fig. 7 SHPB specimen



Fig. 8 Steel tube used in SHPB

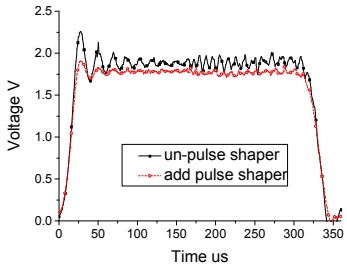


Fig.9 Incidence wave shaping

Because the aluminum foam of sandwich plate is relatively soft material, so the semiconductor strain gauge was pasted on the transmitted bar to measure the transmitted waveform. In the same time, the pulse shaper is used for shaping the incident wave, as shown in Fig.9. Through compare we can see that when use the pulse shaper, the incidence waveform became smooth, the high-frequency waves caused by the projectile impact were filtered. Also the incidence waveform amplitude of add pulse shaper just little lower than didn't add.

Experiment Results and Analysis

The sandwich plate core material-aluminum foam is rate-dependent material, so the SHPB was adopted to test the aluminum dynamic mechanical properties, the results as shown in Fig.10, Form the Fig.10 we can see that the materials deformation is basically same with static sandwich plate compression experiment and also has "three stage", and the dynamic yield stress is nearly two times higher than the static experiment, and strain rate phenomenon is very obvious.

Fig.11 is the sandwich plate dynamic mechanical properties under confining pressure. From the test results we can see the stress-strain curves have "three stage" too, elastic phase, yield platform phase and dense phase, the yield stress of strain-rate is $650s^{-1}$ is nearly two times higher than the strain rate is 0.033 s^{-1}, and near three times higher than the aluminum foam static yield stress. In the same time, the dynamic confining mechanical properties of sandwich plate is very different with the no confining dynamic mechanical properties of CBF-aluminum foam sandwich plate[5], as shown in Fig.12. Through compare with Fig.11, we can see under the confining pressure, the yield stress is higher, nearly two times than the no confining experiment, the dense phase is obvious, and the strain rate phenomenon is very obvious, while the yield platform is less.

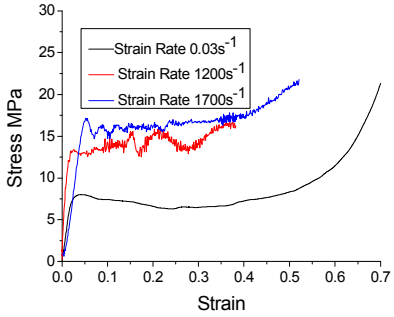


Fig.10 Dynamic mechanical properties of aluminum foam

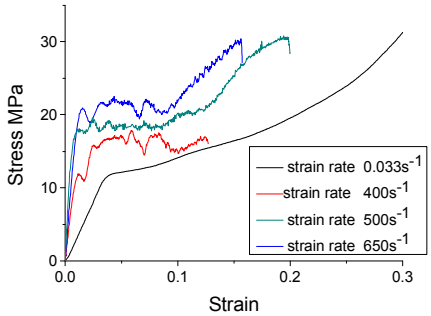


Fig.11 Dynamic mechanical properties of sandwich plate under confining pressure

Fig.13 is the typical experiment test curves (strain rate is $500s^{-1}$) of the dynamic confining pressure curve, from the reflect wave we can know the strain rate is nearly a constant value, and the incidence wave dispersion effect is very small, and the transmit wave of the semiconductor strain gauge tested is very good too. Fig.14 is the specimens after dynamic confining pressure, include the side view and front view, from the specimens we can see that the specimen thickness is similar, the aluminum foam become very dense and deformation is uniform, it didn't appear degumming phenomenon and crushing damage, so the mechanical properties of sandwich plate under confining pressure are very different with the no confining.

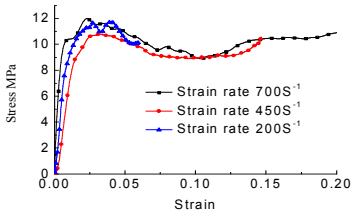


Fig.12 Dynamic mechanical properties of CBF-aluminum foam sandwich plate confining

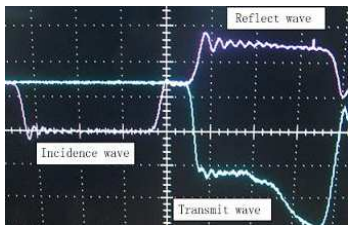


Fig.13 Experiment test curves



Fig.14 Specimens after SHPB pressure tested

Summary

In this paper, the dynamic mechanical properties of the sandwich plate under confining pressure was researched, and compared the results with the no-confining sandwich plate and aluminum foam dynamic mechanical test results. From the compare we can see the stress-strain curves are all have "three stage", under confining pressure, the yield stress is higher, nearly two times than the no confining experiment, its dense phase and the strain rate phenomenon is very obvious, its yield platform is less, and this means under the same strain, the sandwich plate under confining pressure possess obviously good energy absorption capability. From test results we can see the static and dynamic mechanical properties of under confining pressure is very different with the no confining, and also it need further study to research the failure mechanism of sandwich plate under confining pressure.

Acknowledgment

This work was supported by a grant from the Ph.D. Programs Foundation of Ministry of Education of China (No. 20092304110003).

References

[1] M.H.Zhang, H.S.Chen and H.Y.Zhao: Light Metals Vol.2(2008)p.55-58.

[2]H.S.Chen, H.Y.Zhao and M.H.Zhang: Journal of NingBo University (Natural Science & Engineering Edition) Vol. 20 (2007), p. 118-121.

[3] E.H.Wang: The Dynamic Mechanical Study of Aluminum Foam and Aluminum Foam Sandwich Beam .(University of Science and Technology PhD thesis.Hefei,2005)

[4] X. Q. Ma: *Impact Dynamics* (Beijing Institute of TechnologyPress, Beijing 1992).

[5] Z.L.Chang,G.P.Zou,W.L.Zhao,Y.Cao and R.R.Wang:Key Engineering Materials Vol. 452-453 (2011) , p.281-284

© (2012) Trans Tech Publications, Switzerland
doi:10.4028/www.scientific.net/KEM.488-489.694

Study on Quasi-static Growing Crack Field in Visco-Elastic Compressible Material

Yong Yang[1,a], Wu Guohui[1,b], Liqiang Tang[1,c]

[1]College of Aerospace and Civil Engineering, Harbin Engineering University, Harbin 150001, China

[a]yangharbin@163.com, [b]wuguohui@hrbeu.edu.cn, [c]tlq8854@126.com

Keywords: visco-elastic compressible material, crack tip, dynamic growing

Abstact. A mechanical model of the visco-elastic compressible material is established in order to investigate the viscous effect in quasi-static growing crack-tip field. The constitutive equations on the visco-elastic compressible material are deducted. Through asymptotic analysis, it is shown that in the stable creep growing stage, the elastic-deformation and the visco-deformation are equally dominant in the near-tip field, as $r^{-1/(n-1)}$. The asymptotic solutions of separative variable in the crack-tip field are aslo obtained. According to numerical calculation, the curves of stress, stain and displacement are given. The results indicate that the near-tip fields are mainly governed by the creep exponent n; the stress fields of mode I and mode II is slightly affected by the elastic compressible deformation; the strain and displacement fields of mode I are deeply affected by the elastic compressible deformation. However, the strain and displacement fields of mode II are less affected by the elastic compressible deformation. The asymptotic solutions of dynamic growing crack-tip field gained here can conveniently degenerate the incompressible case, when the Poisson ratio $\nu \to 0.5$, named as HR field. The conclusions can provide the references for further studying the dynamic growing crack-tip field in compressible material.

Introduction

Under high temperature, many metals show viscoelastic properties, which are closely related to environmental factors and strain rate. Engineering practice also shows that time-dependent deformation of materials have great effects on the structural strength, rigidity and life duration. So visco-elasticity has drawn much attention in the mechanical and engineering fields.

In 1968, Hutchinson[1], Rice and Rosengren[2] studied the asymptotic crack tip field for plane strain stationary crack independently. When elastic deformation is neglected, the so-called HRR field is obtained for power law hardening materials. Hui and Riedel[3] addressed the quasi-static mode III and mode I crack problem where elastic-power-creeping constitutive equations are introduced to model the rate-dependent materials. HR field was obtained, where stress and strain possess the same singularity, as $r^{-1/(n-1)}$, with n, the power law exponent. HR field is self-government which means that crack tip stress and strain fields are not dependent on the applied load, and no geometrical parameters related to the crack are included. Once the crack propagation velocity $\dot{a}$ is given, crack tip fields can be fully determined. Gao[4,5] gave a simplified elasto-visco-plastic model in which it was assumed that during the elastic deformation stage, viscous effects can be ignored. When plastic deformation occurs, viscous effects are taken into account. For mode I crack, solutions with logarithm singularity and power singularity were given separately. Tang[6] investigated the mode I crack tip field for incompressible elasto-viscous materials.

At present, more studies on the crack tip focus on the incompressible material. However, incompressibility is an ideal assumptation. In most cases, considering the material compressibility is more reasonable. Crack tip fields on mode I quasi-static growing crack in compressible visco-elastic material is given in present paper where the distribution law of the stress fields and the strain fields are discussed.

1. Basic Equations

Fig. 1 shows a mechanical model of a planar crack steadily propagating along the positive direction of X, in which the common origin is at the crack tip of planar crack , XOY is the fixed coordinate system, xoy is the moving coordinate system, and the moving rectangular and polar coordinate system denoted respectively by (x,y) and (r,θ). Supposing that the crack grows at the steady velocity V, the material derivative of any physical quantity $\boldsymbol{\Phi}$ in steady field can be expressed as

$$D = V\left[\frac{\sin\theta}{r}\frac{\partial}{\partial\theta} - \cos\theta\frac{\partial}{\partial r}\right]. \tag{1}$$

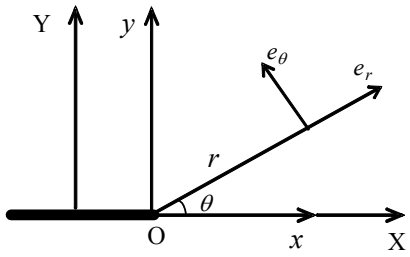


Fig.1 Coordinate with crack

The strain rate of the visco-elastic material is composed of elastic and viscous strain rate, named as

$$\dot{\varepsilon}_{ij} = \dot{\varepsilon}^e_{ij} + \dot{\varepsilon}^c_{ij}. \tag{2}$$

where, $\dot{\varepsilon}^e_{kk}$ and $\dot{\varepsilon}^c_{kk}$ is respectively expressed as elastic volume strain ratio and viscous volume strain ratio. The case where elastic deformation and viscous deformation are compressible is studied in this paper, as $\dot{\varepsilon}^e_{kk} \neq 0, \dot{\varepsilon}^c_{kk} \neq 0$. The constitutive equations are given by

$$\dot{\varepsilon}_{\alpha\beta} = \frac{1}{E}[(1+\nu)\dot{\sigma}_{\alpha\beta} - \nu\dot{\sigma}_{rr}\delta_{\alpha\beta}] + B(t)\sigma_e^{n-1}[(1+\nu)\sigma_{\alpha\beta} - \nu\sigma_{rr}\delta_{\alpha\beta}] \tag{3}$$

Where, the modulus of elasticity E, the exponent of creep strain n, the material parameters of power-law creep material B, and the equivalent stress is $\sigma_e^2 = \frac{2}{3}(\sigma_r - \sigma_\theta)^2 + \sigma_{r\theta}^2 + \frac{4+\nu}{6(1+\nu)}(\sigma_r + \sigma_\theta)^2$.

The case that the deformation is compressible is considered, so the Poisson's ratio $\nu < 0.5$. The equations of motion and geometry are

$$\nabla\cdot\boldsymbol{\sigma} + \mathbf{F} = \rho\,\ddot{\boldsymbol{u}},\ \ \boldsymbol{\varepsilon} = \frac{1}{2}\left(\boldsymbol{u}\nabla + \nabla\boldsymbol{u}\right),\ \ \nabla\times\dot{\boldsymbol{\varepsilon}}\times\nabla = 0. \tag{4}$$

2. Governing Equations

When $r \to 0$,supposed that the form of separate variable of potential function of displacement and separate variable of potential function of stress are

$$u_i = r^{s_1-1}u_i(\theta) \qquad (i = r,\theta), \tag{5}$$

$$\sigma_{\alpha\beta} = r^{s_2-2}\tilde{\sigma}_{\alpha\beta}(\theta) \qquad (\alpha,\beta = r,\theta). \tag{6}$$

In stable creep growing stage, elastic-deformation and visco-deformation are equally dominant in the near-tip field, as a result, the stress and the strain have the same singularity, as $s = s_1 = s_2 = (2n-3)/(n-1)$.

Introducing the relevant quantities to equations of motion and constitutive equations, by noticing that the derivation laws (1) of material derivative and by dimensionless arrangement, as:

$$
\begin{aligned}
&f'''(\theta)\sin\theta = f''(\theta)(s-2)\cos\theta - f'(\theta)(3s-2)\sin\theta + f(\theta)s(s-2)\cos\theta + (s-2)\widetilde{u}_r'(\theta)\sin\theta - (s-2)\widetilde{u}_\theta(\theta)\sin\theta \\
&\quad -(s-2)(s-1)\widetilde{u}_r(\theta)\cos\theta + \nu(s-2)(s-1)\left(f'(\theta)\sin\theta - sf(\theta)\cos\theta\right) - \widetilde{\sigma}_e^{n-1}\left[f''(\theta) + sf(\theta) - \nu(s-1)sf(\theta)\right] \\
&\widetilde{u}_\theta''(\theta)\sin\theta = (1-\nu^2)(s-2)(s-1)\left(f'(\theta)\sin\theta - sf(\theta)\cos\theta\right) - (s-2)(1-\nu)\widetilde{u}_\theta(\theta)\sin\theta + (s-2)\widetilde{u}_\theta'(\theta)\cos\theta \\
&\quad -\left[2+\nu(s-2)\right]\widetilde{u}_r'(\theta)\sin\theta + (s-2)\left[1+\nu(s-1)\right]\widetilde{u}_r(\theta)\cos\theta + \widetilde{\sigma}_e^{n-1}\left(1-\nu^2\right)(s-1)sf(\theta) \\
&\widetilde{u}_r''(\theta)\sin\theta = (s-2)\widetilde{u}_r'(\theta)\cos\theta + 2(1+\nu)\left[f''(\theta)(2-s)\sin\theta - (s-2)(1-s)f'(\theta)\cos\theta + s(2-s)\sin\theta f(\theta)\right] \\
&\quad -(s-2)\widetilde{u}_r(\theta)\sin\theta - (s-4)\widetilde{u}_\theta'(\theta)\sin\theta + (s-2)^2\widetilde{u}_\theta(\theta)\cos\theta + 2(1+\nu)\widetilde{\sigma}_e^{n-1}(1-s)f'(\theta)
\end{aligned}
\tag{7}
$$

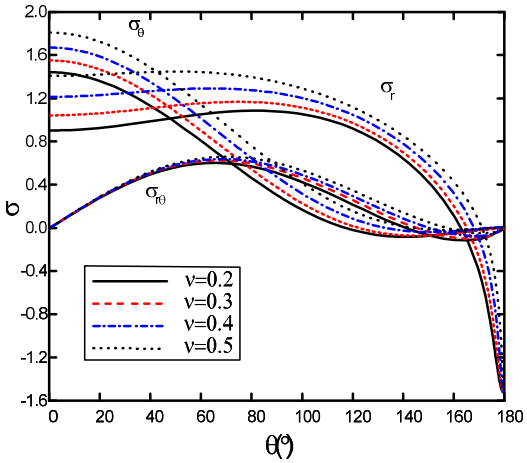


Fig.2 Curves of stresses of mode I with ν （$n=4$）

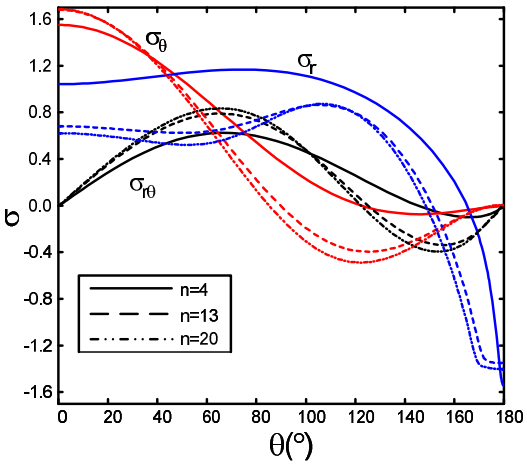


Fig.3 Curves of stresses of mode I with n （$\nu=0.3$）

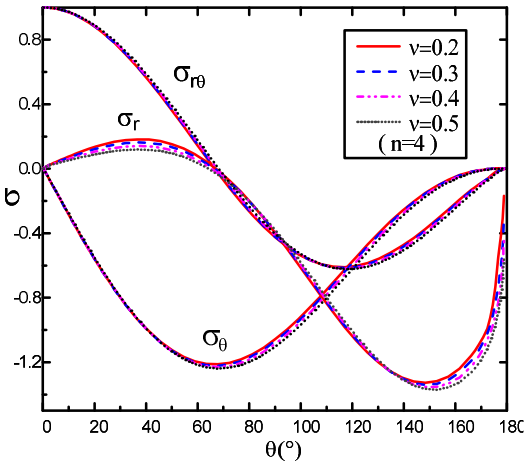


Fig.4 Curves of stresses of mode II with ν （$n=4$）

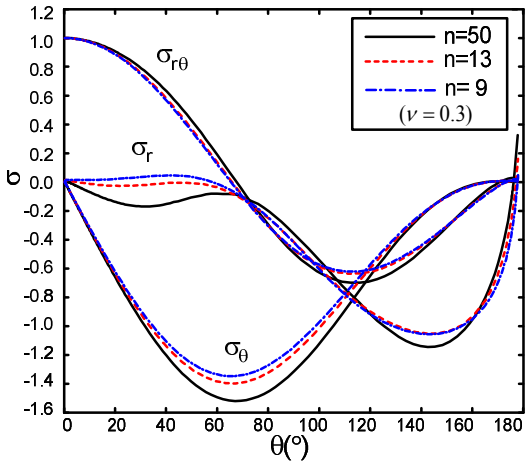


Fig.5 Curves of stresses of mode II with n （$\nu=0.3$）

3. Numerical calculation and Discussions

For mode I crack, the conditions to determine the solution are given as follows:

$$u_\theta|_{\theta=0}=0,\ \sigma_{r\theta}|_{\theta=0}=0,\ \sigma_\theta\big|_{\theta=\pi}=0,\ \sigma_{r\theta}\big|_{\theta=\pi}=0,\ u_r'(0)=u_\theta(0)=0,$$

$$u_\theta'(0)=[1+\nu(s-1)]u_r(0)+\frac{s}{s-2}(1-\nu^2)(s-1)[s-2-\sigma_e^{n-1}(0)]f(0)$$

$$u_r(0)=\frac{1}{(s-1)(s-2)}\{[\sigma_e^{n-1}(0)-s+2]f''(0)+s[1-\nu(s-1)](\sigma_e^{n-1}(0)-s+2)f(0)\} \tag{8}$$

For mode II crack, the conditions to determine the solution are given as follows:

$$\sigma_r\big|_{\theta=0}=0,\sigma_\theta\big|_{\theta=0}=0,\ \sigma_\theta\big|_{\theta=\pi}=0,\ \sigma_{r\theta}\big|_{\theta=\pi}=0,u_r(0)=0,\quad u_\theta'(0)=0,$$

$$u_r'(0)=2(1+\nu)(1-s)f'(0)+2(1+\nu)\frac{1-s}{s-2}f'(0)-(s-2)u_\theta(0) \tag{9}$$

4.Conclusions

(1) Crack tip fields on mode I and mode II quasi-static growing crack in visco-elastic material, where the elastic deformation is compressible and the viscous deformation is incompressible, are studied in this paper. By analysis, it shows that elastic deformation and viscous deformation are equally dominant in the near-tip, and the stresses, strains have the same singularity, namely, $(\boldsymbol{\sigma},\ \boldsymbol{\varepsilon})\propto r^{-1/(n-1)}$.

(2) Through Fig.2-5, the Poisson's ratio has more influence upon the stress fields. When the Poisson's ratio $\nu=0.5$, the March number $M=0$ the tip field tends towards HR field[6].

(3) The stress fields obviously change with the exponent of creep strain n, the stress components increase with the increasing creep exponent n. The trend of the stress fields in Fig.2-5 is consistent with Ref. [3].

Acknowledgments

The authors acknowledges the support by the fundamental research funds for the central universities (HEUCF100209).

References

[1] Hutchinson J.W.: Journal of Mechanics and Physics of Solids, Vol. 16(1968): p13.

[2] Rice J.R., Rosengren G.F.: Journal of Mechanics and Physics of Solids, Vol. 16(1968): p1.

[3] C.Y.Hui, H.Riedel. International Journal of Fracture, Vol.17(1981): p409.

[4] Gao Y.C.: Mechanics Research Communcations. Vol. 15, (1988):p307.

[5] Gao Y.C.: Theo. Appl. Frac. Mech., Vol. 14(1990): p233.

[6] Tang L. Q. and Can yanhong: Acta. Mater, Vol.37 (2005), p573 (in Chinese).

© (2012) Trans Tech Publications, Switzerland
doi:10.4028/www.scientific.net/KEM.488-489.698

Fatigue life prediction investigation on steel honeycomb sandwich beams at high-temperature

Jie Lu[1, a], Guang-ping Zou[b] , Yang Cao[c]

[1]Centre for Mechanics Testing, College of Aerospace and Civil Engineering, Harbin Engineering University, Harbin, 150001, P.R.China

[1,a]lujie@hrbeu.edu.cn, [b]gpzou@hotmail.com, [c]ycao1026@hotmail.com

Keywords: Honeycomb sandwich beams, flexural fatigue, high temperature, life prediction, stiffness degradation, displacement evolution

Abstract. The aim of this work is to investigate the fatigue behaviors of the steel honeycomb sandwich beams at 400°C through three point bending experiments. A stiffness reduction approach was adopted which was further based on the interpolation by the empirical functions of experimental results. For load control fatigue experiments, the evolution relations between number of cycles and displacement were obtained through real-time deformation monitoring of the specimens. A method based on exponential function fit was adopted in the further analysis, whose coefficients depended on the material properties, loading levels and high temperature conditions. This approach allowed us to predict the high temperature fatigue life of specimens while avoiding a large number of experiments. The results showed that experimental and prediction results were in a good agreement.

1. Introduction

Honeycomb structures have been received much attention in recent years because of their high strength/weight and stiffness/weight ratios, excellent heat resistance and favorable energy-absorbing capacity. They have been widely adopted in the aerospace, electronic and architectural industries. In the past, the strengths of honeycomb cells under static loading or impact loading conditions have been extensively studied, but the problem of the duration of the honeycomb cells and related sandwich panels under cyclic loading remains to be solved. The past studies investigating the fatigue behavior of the sandwich structures can be sorted based on the materials employed for the face sheets and the cores. Most sandwich specimens analyzed in the past fatigue studies were made of polymer foam cores with composite face sheets or with metal face sheets [1~4]. Relatively many efforts have been made on investigation of the fatigue strength of the sandwich structures with honeycomb cells. Demelio et al. [5] reported their experimental results for the fatigue behavior of the composite sandwich structures fastened with steel plates using blind fasteners. Belingardi et al. [6] investigated the four-point bending fatigue behavior of the undamaged and damaged sandwich beams with aluminum honeycomb cores and carbon-fiber composite face sheets. Jen et al. [7] presented a method of using local parameter to evaluate bending fatigue strength of aluminum honeycomb sandwich beams. Belouettar et al. [8] reported their experimental studies of static and fatigue behaviors of honeycomb sandwich composites, made of aramide fibers and aluminum cores through four-point bending tests. Sometimes honeycomb sandwich structures were served as vital parts at high temperature, thus an investigation on how temperature can affect damage and fatigue life is significant to be solved. Meanwhile studies of above mentioned literatures have seldom investigated. It is hence most important to have a comprehensive knowledge of the fatigue performance of sandwich structures at high temperature.

The aim of this work is to investigate the fatigue behaviors of steel honeycomb sandwich beams through three-point bending. For the need of some engineering requests, the fatigue behavior of specimens at 400°C is significantly studied. The prediction life model which can describe the flexural behavior of sandwich beams at high temperature is developed. The analytical results obtained from the developed model are compared with the results obtained from the fatigue experiments.

2. Method

2.1 Sandwich beam specimens

The mild-steel sheets Q235 were used as the honeycomb core and face sheets materials in the present study. The core structure was folded and brazed together with the upper and lower face layers forming a hexagonal cell structure. The length of side of core is 3mm. The schematic detailed description and geometrical dimensions of the honeycomb sandwich specimens are shown in Fig.1 and Table.1.

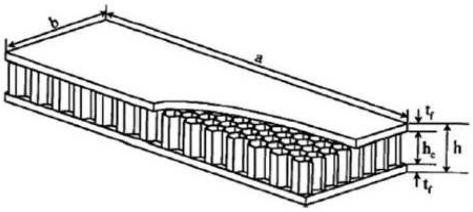


Fig.1 Schematic detailed description of the honeycomb sandwich structure

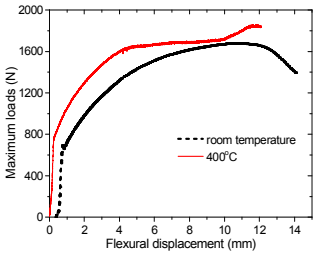


Fig.2 Comparison of the deflection according to the bending loads for room temperature and 400°C

Table.1 Specimen geometry dimensions

(mm)

a	b	h	h_c	t_f
100.00	14.50	9.72	8.12	0.80

2.2. Experimental method and results

Both static and fatigue tests were carried out through a three-point bending testing fixture device schematically shown in Fig.2. Such device, designed and built expressly for room or high temperature conditions, was connected to an electronic servo-hydraulic universal testing machine INSTRON 8801. The bending fixture material was refractory steel and the span was 80mm. Two kinds of tests, static and fatigue experiments were performed on undamaged specimens. Fig.2 shows the bending results at room temperature and 400°C.

2.3. Fatigue experiments

The objectives of the investigated tests were to obtain basic knowledge on the fatigue behaviors of steel honeycomb sandwich beams as the standard stress-life, SN diagrams. Tests were performed at 400oC under direct load control, while the load cycling amplitudes were chosen on the basis of the static test results. An INSTRON 8801 servo-hydraulic testing system with a special three-point bending jig and ceramic heat insulation box was employed to carry out these series of experiments. The experimental set-up is shown in Fig.3. The test load was sinusoidal with a frequency f=10 Hz. The loading ratio, defined as the minimum applied load to the maximum applied load in the fatigue cycle, was set at 0.2 for all fatigue tests and a constant amplitude loading. The maximum applied loads F_{max} in the fatigue tests were selected as 90%, 80%, 70%, 60% of the ultimate applied loads in the static bending tests. Three specimens were selected for different load levels. According to the stiffness degradation criterion [3] the fatigue life is defined as the number of cycles corresponding to a 30% decrease in tracing position of the specimen compared with the stable value. Also when the number of cycles arrives at 106, the test will be terminated. The S-N curve is shown in Fig.4. And for the tested load levels, the fatigue limit is nearly 450,000 at 400°C.



Fig.3 Three-points bending fatigue testing system

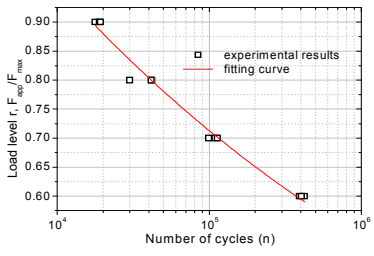


Fig.4 S-N curve of honeycomb sandwich beams at 400°C

3. Prediction model and discussion

3.1. Life prediction model

Although the failure mechanism is complex, it is significant to use a simple model to predict the fatigue life of honeycomb sandwich structures at high temperature. The residual stiffness is a parameter that can be monitored non-destructively, and therefore can be related to residual strength and fatigue life of the specimen [9]. A. El Mahi [3] used stiffness degradation method to develop the life and damage prediction models for sandwich composite materials. Our approach is basically inspired by the models used by the authors [3,9]. One of the important cases in our studies is that temperature condition must be considered in the prediction model. Fatigue tests were performed using load control. During the tests, increase in displacement according to the number of cycles was recorded.

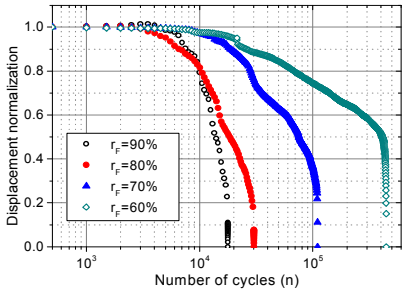


Fig.5 Displacement evolution versus cycles at different load levels

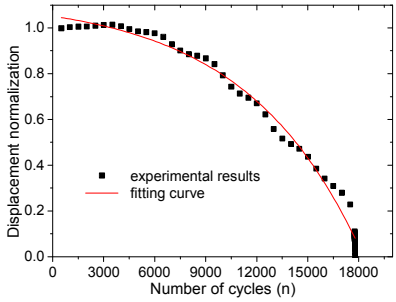


Fig.6 Relation curve between number of cycles and displacement normalization values

Fig.5 shows the relation between displacement normalization and number of cycles. d_{max} is denoted the mid-span maximum displacement, then the relation between the displacement evolution and the number of cycles can be denoted by an exponential function (as shown in Fig. 6) as:

$$\frac{d_{\max}}{d_{0\max}} = A + B\exp(Cn) \tag{1}$$

Parameter A depends on the initial conditions, temperature, load level and material properties. B is considered as a coupled parameter and denotes complex experimental conditions. C is connected with applied load level r and can be evaluated by a power function (as shown in Fig.7) as:

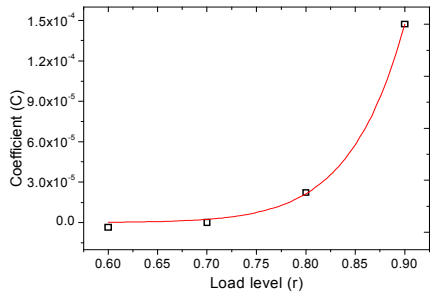


Fig.7 Curve between applied load level and coefficient C.

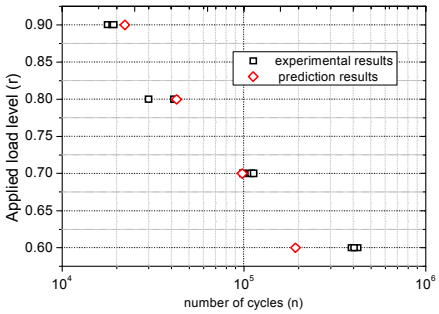


Fig.8 Compared results between experimental and predict model

$$C = ar^b \tag{2}$$

The other two parameters (A and B) can be similarly decided through the experimental results. Thus the prediction model can be derived from (1) and (2), namely:

$$N_{pre} = \frac{1}{ar^b}\ln\left(\frac{k-A}{B}\right) \tag{3}$$

where $k = \dfrac{d_{\max}}{d_{0\max}}$ (4)

3.2 Prediction results

Using the equation (3), the fatigue life of steel honeycomb sandwich beams can be predicted. The prediction results were compared with the experimental results in Fig.8. From compared results, for the high applied load levels, the prediction results are found in good agreement with experimental results. Due to relative short loading time and the low number of cycles, the influence of temperature is not dominant. While at low load levels, such as r=0.60, large deviation is appeared because the coupled mechanical and thermal experimental conditions are more complex. Thus, it is significant to consider the temperature influence on the long term flexural fatigue behaviors of honeycomb sandwich specimens.

4. Conclusion

The fatigue behaviors of steel honeycomb sandwich beams at 400^{o}C were investigated in this work. Life prediction model based on stiffness degradation were developed. The coefficients depended on the load level, temperature and material properties. The relation between the prediction life and load level was obtained. This approach enables the prediction of the fatigue life and reduces the number of experiments. A good agreement between the experimental and prediction results was found.

Acknowledgement

This work was financially supported by Research Fund for the Doctoral Program of Higher Education of China (Grant No. 20092304110003).

References

[1] Burman M, Zenkert D: Int. J. Fatigue. Vol. 19(1997), p.551-561.

[2] Burman M, Zenkert D: Int. J. Fatigue. Vol. 19(1997), p.563-578.

[3] El Mahi A, Khawar Farooq M, Sahraoui S, et al: Mater. Des. Vol. 25(2004), p.199-208.

[4] Kanny K, Mahfuz H: Compos. Struct. Vol. 67(2005), p.;403-410.

[5] Demelio G, Genovese K, Pappalettere C: Composites Part B: Eng. Vol. 32(2001), p. 299-308.

[6] Belingardi G, Martella P, Peroni L. Fatigue analysis of honeycomb-composite sandwich beams. Composites Part A: Appl Sci Manuf 2007;38(4):1183–91.

[8] S. Belouettar, A. Abbadi, Z. Azari, et al: Compos. Struct. Vol. 87(2009), p. 265-273.

[9] Clark SD, Shenoi RA, Allen HG: Compos. Sci. Tech. Vol. 59(1999), p. 471-486.

© (2012) Trans Tech Publications, Switzerland
doi:10.4028/www.scientific.net/KEM.488-489.702

Solving The Equivalent Function Of Failure Mode Based On Multiple Correlation

Chen Weidong[a] , LI Jiancao[b] ,Yu Yanchun[c]

College of Astronautics and Civil Engineering,

Harbin Engineering University, Harbin 150001, China

[a] chenweidong@hrbeu.edu.cn, [b] lijiancao@hrbeu.edu.cn, [c] yuyanchun@hrbeu.edu.cn

Keywords: failure mode; reliability; multiple correlation coefficient; equivalent plane method.

Abstract. To solve the problem of equivalent functions of failure mode and low computational efficiency, the coefficient expression of equivalent functions has been derived based on equivalent principle. The concept of multiple correlation was introduced to the reliability analysis of failure mode , the correlation problem between several components and a component has been explained rationally. The display recursive expression of equivalent functions involved two-dimensional integral computation has been given. The high calculation accuracy and efficiency of solving recursive equivalent functions has been indicated according to numerical results.

Introduction

In the reliability analysis of failure mode,the determination of function has been a difficult problem, and there is little research on it.

The coefficient expression of equivalent functions has been derived based on equivalent theory in this paper; the concept of multiple correlation was introduced to reliability analysis, the correlation problem between several components and a component in deducing process has been explained rationally. The explicit recursive expression involved two-dimensional integral computation has been given, the difficulties of solving equivalent functions and low computational efficiency have been solved.

1 Basic principles

1.1 principle of equivalence

Supposing the number of failure components is *m* in the failure mode, and the linear performance function of each component is as follows:

$$Z_i = \sum_{j=1}^{n} a_{ij} U_j + \beta_i \qquad (i = 1, 2, \cdots m) \tag{1}$$

Where, $U_1 \quad U_2 \quad \cdots \quad U_n$ are mutually independent standard normal random variables; $\boldsymbol{a}_i = (a_{i1} \quad a_{i2} \quad \cdots \quad a_{in})^T$ is a unit vector; β_i is reliability index corresponding to $Z_i \le 0$.

Because the relation between each component is in parallel, the failure probability of the failure mode is as follows:

$$P_f = \Phi_m \left(-\boldsymbol{\beta}; \boldsymbol{\rho}\right) = P(\bigcap_{i=1}^{m} \sum_{j=1}^{n} a_{ij} U_j + \beta_i < 0) \tag{2}$$

The generalized reliability index:

$$\beta_p = -\Phi^{-1} \left[\Phi_m \left(-\beta; \rho\right) \right] \tag{3}$$

Meanwhile, assuming the form of equivalent performance function as follows:

$$Z^e = \sum_{j=1}^{n} a_j^e U_j + \beta^e \tag{4}$$

Where, $\boldsymbol{a}_i^e = (a_{i1}^e \quad a_{i2}^e \quad \cdots \quad a_{in}^e)^T$ is a unit vector; β^e is reliability index corresponding.

Based on the principle of equivalence that were suggested by S. Gollwitzer and R. Rackwitz[1], and after normalizing there are[2]:

$$\beta^e = \beta_p \tag{5}$$

$$a_j^e = \frac{\partial \beta_p}{\partial U_j} \Bigg/ \sqrt{\sum_{k=1}^{m} \left(\frac{\partial \beta_p}{\partial U_k} \right)^2} \tag{6}$$

1.2 Multiple correlation coefficients

The degree of correlation between the a variable x_1 and a set of variables $x_2, \cdots, x_p$ can be described by correlation coefficient for linear combination of x_1 and $x_2, \cdots, x_p$, which called multiple correlation coefficient [3] $\rho_{1,2,\cdots p}$, then:

$$\rho_{1\bullet 2,\cdots p} = \max_{\boldsymbol{l} \neq 0} \rho\left(x_1, \boldsymbol{l}^T \boldsymbol{x}_2\right) = \left(\frac{\boldsymbol{\sigma}_{21}^T \boldsymbol{\Sigma}_{22}^{-1} \boldsymbol{\sigma}_{21}}{\sigma_{11}} \right)^{1/2} \tag{7}$$

As indicated in Eq. (1), variance of performance function is one, so its covariance matrix is:

$$\boldsymbol{z} = \begin{pmatrix} \boldsymbol{z}_{m-1} \\ \hline z_m \end{pmatrix}, \quad \boldsymbol{\Sigma} = \boldsymbol{\rho} = \left(\begin{array}{ccc:c} 1 & \rho_{12} & \cdots & \rho_{1m} \\ \rho_{21} & 1 & \cdots & \rho_{2m} \\ \vdots & \vdots & \ddots & \vdots \\ \hdashline \rho_{m1} & \rho_{m2} & \cdots & 1 \end{array} \right) = \begin{pmatrix} \boldsymbol{\rho}_{22} & \boldsymbol{\rho}_{12} \\ \boldsymbol{\rho}_{21}^T & 1 \end{pmatrix} \tag{8}$$

Therefore, the correlation coefficient is:

$$\rho_{1,2,\cdots m-1\bullet m} == \rho_{m\bullet 1,2,\cdots m-1} = \left(\boldsymbol{\rho}_{12}^T \boldsymbol{\rho}_{22}^{-1} \boldsymbol{\rho}_{12} \right)^{1/2} \tag{9}$$

2 Derivation for coefficient of the equivalent performance function

Then, the failure probability of failure mode is

$$P_f = P\left(\bigcap_{i=1}^{m} Z_i < 0 \right) = P\left(\bigcap_{i=1}^{m-1} Z_i < 0 \cap Z_m < 0 \right) = P\left(Z^{(m-1)} < 0 \cap Z_m < 0 \right) \tag{10}$$

the generalized reliability index is:

$$\beta_p = -\Phi^{-1}\left[P_f \right] = -\Phi^{-1}\left[P\left(Z^{(m-1)} < 0 \cap Z_m < 0 \right) \right] = -\Phi^{-1}\left[\Phi_2\left(\beta^{(m-1)}, \beta_m ; \rho \right) \right] \tag{11}$$

Where, $\Phi(\bullet)$ is the distribution function of standard normal variable.

The partial derivatives of the generalized reliability index to variables are:

$$\frac{\delta \beta_p}{\delta U_j} = \frac{1}{\varphi\left(\beta_p\right)} \left\{ \frac{\delta \Phi_2\left[\left(\beta^{(m-1)}, \beta_m ; \rho \right) \right]}{\delta \beta^{(m-1)}} \frac{\delta \beta^{(m-1)}}{\delta U_j} + \frac{\delta \Phi_2\left[\left(\beta^{(m-1)}, \beta_m ; \rho \right) \right]}{\delta \beta_m} \frac{\delta \beta_m}{\delta U_j} \right\} \tag{12}$$

There are:

$$\begin{aligned}\Phi_2\left[\left(\beta^{(m-1)},\beta_m;\rho\right)\right]&=\frac{1}{\sqrt{1-\rho^2}}\int_{-\infty}^{\beta_m}\int_{-\infty}^{\beta^{(m-1)}}\varphi\left(\frac{x_1-\rho x_2}{\sqrt{1-\rho^2}}\right)\varphi\left(x_2\right)dx_1dx_2\\&=\frac{1}{\sqrt{1-\rho^2}}\int_{-\infty}^{\beta^{(m-1)}}\int_{-\infty}^{\beta_m}\varphi\left(\frac{x_2-\rho x_1}{\sqrt{1-\rho^2}}\right)\varphi\left(x_1\right)dx_2dx_1\end{aligned}\tag{13}$$

Where, $\varphi(\bullet)$ is the probability density function of standard normal variable.

Therefore, there are:

$$\begin{cases}\dfrac{\delta\Phi_2\left[\left(\beta^{(m-1)},\beta_m;\rho\right)\right]}{\delta\beta^{(m-1)}}=\dfrac{1}{\sqrt{1-\rho^2}}\Phi\left(\dfrac{\beta_m-\rho\beta^{(m-1)}}{\sqrt{1-\rho^2}}\right)\varphi\left(\beta^{(m-1)}\right)\\\dfrac{\delta\Phi_2\left[\left(\beta^{(m-1)},\beta_m;\rho\right)\right]}{\delta\beta_m}=\dfrac{1}{\sqrt{1-\rho^2}}\Phi\left(\dfrac{\beta^{(m-1)}-\rho\beta_m}{\sqrt{1-\rho^2}}\right)\varphi\left(\beta_m\right)\end{cases}\tag{14}$$

From Eq.(10),ρ is the correlation between events $Z^{(m-1)}<0$ and events $Z_m<0$ in Eq.(14).ρ can be explained obviously by multiple correlation theory: $\rho=\rho_{1,2,\cdots m-1\bullet m}=\rho_{m\bullet 1,2,\cdots m-1}$;As found in Eq. (1) and Eq. (4)：$\dfrac{\delta\beta^{(m-1)}}{\delta U_j}=a_j^{m-1}$ ， $\dfrac{\delta\beta_m}{\delta U_j}=a_{mj}$ .Based on the above derivation, Eq.(6) can be wrote to:

$$a_j^m=\Phi\left(\frac{\beta_m-\rho_{m\bullet 1,2,\cdots m-1}\beta^{(m-1)}}{\sqrt{1-\rho^2_{m\bullet 1,2,\cdots m-1}}}\right)\varphi\left(\beta^{(m-1)}\right)a_j^{m-1}+\Phi\left(\frac{\beta^{(m-1)}-\rho_{m\bullet 1,2,\cdots m-1}\beta_m}{\sqrt{1-\rho^2_{m\bullet 1,2,\cdots m-1}}}\right)\varphi\left(\beta_m\right)a_{mj}\tag{15}$$

3 Numerical Example

Two methods were used to solve equivalent performance function:

1) Monte Carlo method and central difference method were used to calculate differential coefficients, and then the equivalent performance function was solved with normalization method[4];

2) The equivalent performance function was solved by the recursion formulas in this paper.

Example 1. the structure has ten basic random variables that obey standard normal distribution, and they are mutual independent. The performance functions of each failure component are:

$$g_i=0.707x_0+0.707x_i+0.5\qquad(i=1,2,\cdots,n)$$

The results of different number of failure component are shown in Table 1.

Example 2. There are four performance functions:

$$g_i(x)=2.5+0.25\cos(\pi i/5)-x_i-x_{i+1}$$

Where, $x_k(k=1,\cdots,5)$ are mutual independent standard normal random variables. The results of the equivalent performance function are shown in Table 2.

Example 3. the failure mode has four failure components, the performance functions of components are:

$$g_1(x)=-0.1431x_1-0.2817x_3-0.107x_4+0.9427x_6+0.5$$
$$g_2(x)=-0.1343x_1+0.9451x_2-0.266x_3-0.1343x_5+0.5$$
$$g_3(x)=0.9396x_1-0.1144x_2-0.3017x_3-0.1144x_4+0.5$$
$$g_4(x)=-0.107x_2-0.2817x_3+0.9427x_4-0.1431x_5+0.5$$

Where, $(x_1,x_2,\cdots,x_6)$ are mutual independent standard normal random variables. The results of the equivalent performance function of failure mode are shown in Table 2.

Table 1. Result of example 1

coefficients	N=4		N=6		N=8		N=10	
	Method 1	Method 2	Method 1	Method 2	Method 1	Method 2	Method 1	Method 2
a_0^e	0.894	0.894	0.926	0.926	0.943	0.943	0.953	0.953
a_1^e	0.221	0.210	0.149	0.142	0.118	0.106	0.090	0.085
a_2^e	0.220	0.218	0.159	0.157	0.119	0.106	0.095	0.085
a_3^e	0.221	0.226	0.150	0.159	0.111	0.119	0.091	0.095
a_4^e	0.232	0.237	0.161	0.160	0.124	0.120	0.093	0.096
a_5^e	0	0	0.153	0.161	0.123	0.121	0.096	0.096
a_6^e	0	0	0.154	0.163	0.119	0.122	0.096	0.097
a_7^e	0	0	0	0	0.113	0.123	0.091	0.098
a_8^e	0	0	0	0	0.116	0.125	0.099	0.099
a_9^e	0	0	0	0	0	0	0.103	0.100
a_{10}^e	0	0	0	0	0	0	0.099	0.102

Table 2. Result of example 2 and 3

Coefficients	example 2		example 2	
	Method 1	Method 2	Method 1	Method 2
a_1^e	-0.260	-0.257	0.433	0.422
a_2^e	-0.519	-0.513	0.331	0.341
a_3^e	-0.538	-0.545	-0.588	-0.584
a_4^e	-0.542	-0.551	0.420	0.418
a_5^e	-0.244	-0.253	-0.146	-0.139
a_6^e	—	—	0.400	0.410

4 Conclusions

The results of examples indicates that the result of the method in this paper are coincide with the results of numerical method, and the recursion formulas in this paper are credible for solving equivalent performance function. Meanwhile, the rationality and feasibility for reliability analysis with multiple correlations are proved from another perspective.

Because the recursive process only involves double integration, the method in this paper is more efficient for calculating the coefficients of equivalent performance functions, and it has obvious advantages for failure mode which includes many failure components especially. And the example 1 shows that the calculation accuracy is stable with the increase of the number of failure components, there is no degressive trend.

References

[1] M.Hohenbichl,R.Rackwitz.First-order concepts in system reliability: Struct Saf . vol .1(1983), p.177-188.

[2] Gong Jin-xin:*Computational methods for reliability of engineering structures*(Dalian University of Technology Press , Dalian2003)

[3] Zheng Cheng-de. *numerical calculation method* (Tsinghua university press ,Beijing 2010)

[4] Wang Xue-min. *Applied multivariate analysis* (Shanghai University Of finance & Economics Press, Shanghai 2009)

© (2012) Trans Tech Publications, Switzerland
doi:10.4028/www.scientific.net/KEM.488-489.706

Sensitivity Analysis for the Stiffened Plate Structure System with Crack Defects

Weiguang An[a], Hai An[b], Xianghua Song

College of Aerospace and Civil Engineering; Harbin Engineering University; Harbin 150001; Heilongjiang; China;

[a]anweiguang@hrbeu.edu.cn, [b]anhai@hrbeu.edu.cn

Key words: reliability analysis; crack defects; stiffened plate; reverse node forces ; sensitivity analysis

Abstract. The influence of crack defects on the ultimate strength of stiffened plate is analyzed, and reliability calculation and sensitivity analysis expressions of stiffened plate elements are given in this paper. An approach to sensitivity analysis for the global reliability index are proposed for the structure system which consists of stiffened plate elements with crack defects, providing the base for analyzing the contribution of design variables to the system reliability and seeking conveniently weak elements which reduce the reliability index of structure system. Finally, the validity of the approach is verified by taking a numerical example of a cabin section of the ship structure. The approach proposed in this paper provides an applicable reference for the safe design and maintenance of structure system.

Introduction

The problem of reliability evaluation for the structure with crack defects has been a hot topic all the time in engineering. It plays an important role to evaluate the reliability of the structure with defects in engineering, which will affect structure safety forecast, decision-making of maintenance and renewing. A new approach to reliability sensitivity analysis is proposed for the plate elements with crack defects and the system consisted of them in the paper.

Analysis for the Ultimate Strength of the Stiffened Plate Elements with Initial Crack Defects

The stiffened plate with initial crack defects is shown as Fig.1. The length and the width of plate are a and b respectively, the length of crack is c. The boundary condition of panel is simply-supported of four sides.

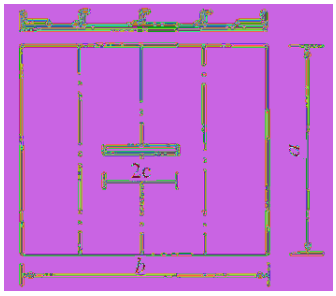


Fig.1. Stiffened plate

Considering cracks weakening to the section and assuming the stress to obey uniform distribution, the ultimate strength of stiffened plate [1] can be expressed as follow

$$\sigma_u = R_s \sigma_{u0} . \tag{1}$$

Where, σ_u and σ_{uo} denotes the ultimate strength of the plate with crack and without crack respectively. R_s, the discount factor of initial crack to the strength of stiffened plate, can be expressed as

$$R_s = \frac{\varphi_{ux} bt + \varphi'_{ux} nA_s}{bt + nA_s} . \tag{2}$$

Where, A_s denotes area of stiffened plate, n denotes numbers of stiffened panel, t denotes thickness of plate, φ_{ux} and φ'_{ux} are strength attenuation coefficients.

Sensitivity for the Reliability Index of Structure System

Sensitivity analysis of system reliability index to design variables. Structural reliability analysis is as follow. First, Branch-And-Bound Method[2] is adopted to searcher for significant failure modes, solving their correlation coefficient[3]. Then G delegable failure modes are given by using PNET method[3]. Moreover, structure failure probability can be obtained as follows

$$P_i = \Phi(-\beta_i) = 1 - \Phi(\beta_i) . \tag{3}$$

Where, P_i and β_i are the failure probability and reliability index of delegable failure modes, repectively.

Finally, reliability index of the system is

$$\Phi(-\beta_s) = 1 - \prod_{i=1}^{G} \Phi(\beta_i) . \tag{4}$$

Eqs.(4) is taken derivative to design variables X_q on its left side and right side simultaneity, we can obtain

$$\frac{\partial \beta_s}{\partial X_q} = \frac{\prod_{i=1}^{G} \Phi(\beta_i)}{\varphi(-\beta_s)} \sum_{k=1}^{G} \frac{\varphi(\beta_k)}{\Phi(\beta_k)} \frac{\partial \beta_k}{\partial X_q} . \tag{5}$$

So, sensitivity values of reliability index to design variables can be solved through Eqs.(4) and Eqs.(5). Hence, the influences of variables changing on the system reliability can be analyzed.

Sensitivity analysis for the safety margin of the stiffened plate with initial crack defects. The safety margin of the stiffened plate with initial crack defects can be expressed as follow

$$M = \sigma_{u0} R_s - \sigma . \tag{6}$$

Sensitivity of safety margin to design variables are, respectively

$$\frac{\partial M}{\partial \sigma_{u0}} = R_s, \quad \frac{\partial M}{\partial \sigma} = -1, \quad \frac{\partial M}{\partial (c/b)} = \sigma_{u0} \frac{\partial R_s}{\partial (c/b)}. \tag{7}$$

Where,

$$\frac{\partial R_s}{\partial (c/b)} = \frac{\partial \varphi_{ux}/\partial (c/b)\, bt + \partial \varphi'_{ux}/\partial (c/b)\, nA_s}{bt + nA_s}. \tag{8}$$

When σ is expressed through equivalent stress σ_{e0} at the centroid of the plate elements, it follows

$$\sigma = \sigma_{e0} = (\sigma_{x0}^2 + \sigma_{y0}^2 + 3\tau_{xy0}^2)^{\frac{1}{2}}. \tag{9}$$

Where, σ_{x0}, σ_{y0}, and τ_{xy0} denote stresses at the centroid of plate element.

The derivative of Eqs. (9) is taken with respect to design variable X_i as follows

$$\frac{\partial \sigma_{e0}}{\partial X_i} = \frac{1}{2\sigma_{e0}} \{2\sigma_{x0} - \sigma_{y0}, 2\sigma_{y0} - \sigma_{x0}, 6\tau_{xy0}\} \begin{Bmatrix} \frac{\partial \sigma_{x0}}{\partial X_i} \\ \frac{\partial \sigma_{y0}}{\partial X_i} \\ \frac{\partial \tau_{xy0}}{\partial X_i} \end{Bmatrix}. \tag{10}$$

Where, X_i denotes the plate thickness, the section area of beam element, loads and defects.

After solving the sensitivity of the safety margin to design variables, the sensitivity values of the reliability index of plate elements with crack defects or the system consisted of them to design variables can be solved from Eqs.(5). So, the influence of crack defects on the reliability index of plate elements or the system consisted of them can be analyzed.

Numerical Example

The wave load distribution chart of the cabin structure #165-#200 of the some type ship is shown in Fig.2. Sensitivity analysis of the global structural reliability index for elements with crack defects is carried out. Concrete messages of loads, the beam elements and the plate elements refer to literature [4].

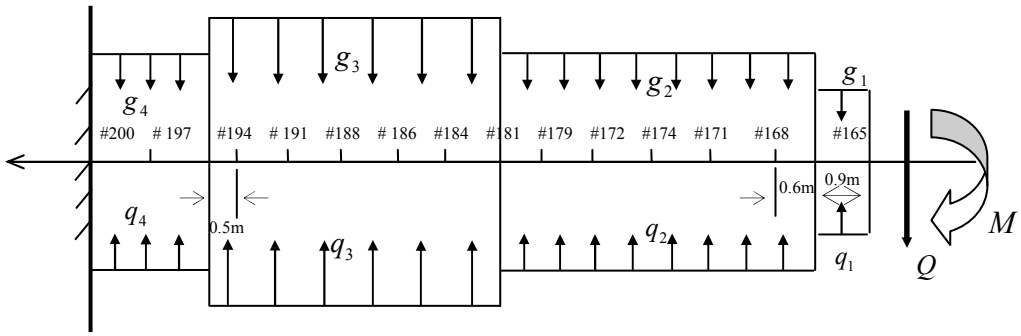


Fig.2. Distribution of loads of the cabin

It is assumed that cracks occur on plate element 74, $c/b = 0.45$. By computing, the reliability of the system $\beta_s = 3.56$, failure probability $P_{f_s} = 1.842\text{E-}4$. Sensitivity of reliability index to yield stress at the mean-value point, $\partial\beta_s/\partial\mu_{\sigma_s} = 1.041\text{E-}5$; Sensitivity of reliability index to cracks, $\partial\beta_s/\partial(c/b) = 3.45$; The sensitivity interval of the reliability index to the section area of the varying type of beam element at the mean-value point, $\partial\beta_s/\partial\mu_{A_i} = [\text{-}1.3\text{E+}02, 6.50\text{ E+}03]$, and the sensitivity interval of reliability index to varying thickness of plate element at the mean-value point, $\partial\beta_s/\partial\mu_{t_i} = [\text{-}1.60\text{E+}01, 6.4\text{ E+}02]$.

Conclusions

(1) Failure modes and the sensitivity expression of the system reliability index are given so that the contribution of varying variables to the system reliability index can be analyzed, providing the convenience for optimizing design variables and suitable design in practice.

(2) It is known from the results that the sensitivity of reliability index to cracks (3.45) is much bigger than the sensitivity of reliability index to yield stress (1.041E-5). Hence, it is not obvious for improving the reliability of system to only increase yield stress of material in the structure with crack defects.

In a word, the results of sensitivity analysis are significant for decision-making of maintenance and renewing under crack defects. So, Users can know the influence extent of varying variables on the system reliability after crack defects emerging. According to these results, we can make the global decision of maintenance and renewing with improving rationality and economy of decision.

References

[1] Hu Yong, Cui Wei-Cheng. Residual Ultimate Strength of Cracked Panels and Stiffened Panels under Combined Loading. Journal of Ship Mechanics (2003). 7(1), P. 63-78

[2] An Wei-guang, Cai Yin-lin, Chen Wei-dong: *Reliability analysis and optimum design forstochastic structure systems*. Harbin Engineering University Press, Harbin (2005), in press.

[3] An Weiguang: *Structural Reliability and Optimum Design Based on Reliability*. National Defence Industry Press, Beijin (1997), in press.

[4] An Wei-guang, Sun Ke-lin, Chen Wei-dong, Wang Bin-sheng, Cai Yin-lin. Optimum Design Based on Reliability in Stochastic Structure systems. Applied Mathematics and Mechanics (2005), 26(10), P. 1293-1302

© (2012) Trans Tech Publications, Switzerland
doi:10.4028/www.scientific.net/KEM.488-489.710

Failure conditions from push out tests of a steel-concrete joint: fracture mechanics approach

Jan Klusák[1,a], Stanislav Seitl[1,b], Wouter De Corte [2,3,c], Peter Helincks[2,3,d], Veerle Boel[2,3] and Geert De Schutter[3]

[1]Institute of Physics of Materials, Academy of Sciences of the Czech Republic, Žižkova 22, 616 62 Brno, Czech Republic

[2]Department of Construction, Faculty of Applied Engineering Sciences, University College Ghent, Schoonmeersstraat 52, 9000 Ghent, Belgium

[3]Department of Structural Engineering, Faculty of Engineering Sciences, Ghent University, Technologiepark-Zwijnaarde 904, 9000 Ghent, Belgium

[a]klusak@ipm.cz, [b]seitl@ipm.cz, [c]wouter.decorte@hogent.be, [d]peter.helincks@hogent.be

Keywords: Push out test, generalized linear elastic fracture mechanics, bi-material notch

Abstract. In order to evaluate the shear bond strength of a steel-concrete joint using an epoxy adhesive interlayer, push-out tests were carried out. The test samples consisted of two sandblasted steel plates and a self-compacting concrete sample, with the epoxy layer applied on the steel plates and gritted with granulates. During testing, an external force was applied to the concrete core and continuously recorded. To investigate the failure mechanism in detail, a fracture mechanics approach is required. In this paper theoretical-numerical assessment of the push-out test is performed. Regarding the finite element calculations, the locations suitable for failure initiation match bi-material (steel-concrete) notches. The most dangerous locations are evaluated from a generalized linear elastic fracture mechanics point of view. The critical load corresponding to the conditions of failure initiation is estimated and compared with the experimental results.

Introduction

Concrete and steel are two frequently used materials in the construction industry because of their specific characteristics regarding compressive and tensile strength. A good connection between both materials is essential to obtain a good structural performance of the composite structure. One of the techniques ensuring a connection between steel and concrete is the use of an epoxy adhesive. In this paper, the behaviour of a steel-concrete joint with a two-component epoxy adhesive is investigated from the fracture mechanics point of view and results are compared with experiments.

Fracture mechanics assessment

The push out test specimen is assessed from the generalized linear elastic fracture mechanics point of view [1, 2, 3]. Using analytical-numerical approaches, the test configuration is evaluated in order to estimate critical applied load corresponding to failure initiation in locations of stress concentration. The test specimen is considered as a perfectly bonded steel-concrete joint where the epoxy interlayer is neglected. The epoxy layer is considered only as a means ensuring bonding between steel and concrete. The most dangerous locations of the model exhibit singular stress concentrations. The *stress distribution* is found in the form of the sum of singular terms corresponding to two singularity exponents p_k, where k =1, 2. Then the singular stress components:

$$\sigma_{mij} = \sum_k \frac{H_k}{\sqrt{2\pi}} r^{-p_k} F_{ijkm} \tag{1}$$

where the subscripts i, j denote the polar coordinates r, θ (the origin of the polar coordinate system is in the notch tip) and the subscript m =1, 2 refers to material 1 or 2. H_k for the generalized stress intensity factors (GSIF) result from a numerical solution for given boundary conditions. F_{ijkm} are known functions of polar coordinates, geometry and materials of the notch [2, 3].

The stability criterion determines conditions of crack initiation from a bi-material notch and in this case is based on monitoring the tangential stress around the notch tip. The mean value of the $\sigma_{\theta\theta}$ component over a certain distance d

$$\overline{\sigma_{\theta\theta}}(\theta)=\frac{1}{d}\int_0^d \sigma_{\theta\theta}(r,\theta)\mathrm{d}r=\frac{H_1}{\sqrt{2\pi}}\frac{d^{-p_1}}{(1-p_1)}F_{\theta\theta 1m}+\frac{H_2}{\sqrt{2\pi}}\frac{d^{-p_2}}{(1-p_2)}F_{\theta\theta 2m} \tag{2}$$

is determined depending on the polar angle θ, and is considered as the controlling quantity. By analogy with cracks in the homogeneous case (MTS criterion, [4]) it is assumed that the crack at the bi-material notch tip is initiated in the direction θ_0 where $\overline{\sigma_{\theta\theta}}(\theta)$ has its maximum. Furthermore, it is assumed that the crack is initiated when $\overline{\sigma_{\theta\theta}}(\theta_0)$ reaches its critical value $\overline{\sigma_{\theta\theta\,C}}(\theta_0)$ that is ascertained for a crack in homogeneous media. The distance d has to be chosen with respect to the mechanism of a rupture, e.g. as a function of a crack increment length or as a size of material grain or it can be related to a fracture process zone (in the case of quasi brittle materials).

The *potential direction of crack initiation* is determined from the maximum of the mean value of tangential stress in both materials. The following relation fits for the direction of assumed crack initiation:

$$\frac{d^{-p_1}}{1-p_1}\frac{\partial F_{\theta\theta 1m}}{\partial\theta}+\frac{H_2}{H_1}\frac{d^{-p_2}}{1-p_2}\frac{\partial F_{\theta\theta 2m}}{\partial\theta}=0 \tag{3}$$

It is obvious that by inserting the ratio of the values $H_2/H_1 = \Gamma_{21}$ (obtained from the numerical solution) into the relation (3), we obtain a simple equation for the value of θ_0. The maximum of $\overline{\sigma_{\theta\theta}}$ can exist in both material 1 in the interval (0; ω_1) as well as in material 2 in (-ω_2; 0).

Critical loading. The value of the average stress $\overline{\sigma_{\theta\theta}}$ used for the stability assessment is calculated for the bi-material notch for the direction of θ_0 and it is compared with the critical stress $\overline{\sigma_{\theta\theta}}(\theta)_C$ corresponding to the crack subjected to the normal loading mode (the direction of assumed crack propagation $\theta_{0,\mathrm{crack}} = 0$). Then the critical mean tangential stress is:

$$\overline{\sigma_{\theta\theta\,C}}=\frac{2K_{IC}}{\sqrt{2\pi d}} \tag{4}$$

Comparing the relation (2) at the critical level (corresponding to the fracture toughness K_{IC}) and the relation (4) we obtain an expression for the critical value of the GSIF H_{1C}:

$$H_{1C}=\frac{2K_{IC}}{\frac{d^{\frac{1}{2}-p_1}}{1-p_1}F_{\theta\theta 1m}(\theta_{0,\mathrm{notch}})+\Gamma_{21}\frac{d^{\frac{1}{2}-p_2}}{1-p_2}F_{\theta\theta 2m}(\theta_{0,\mathrm{notch}})} \tag{5}$$

It is evident that the critical value H_{1C} depends on the fracture toughness for mode I (K_{IC}), which is a common material characteristic. Then the stability criterion can be suggested as (6), and for a better interpretation of results, the critical applied force can be determined as (7).

$$H_1(\sigma_{\mathrm{appl}})<H_{1C}(K_{IC}) \tag{6}$$

$$F_{\text{crit}} = F_{\text{appl}} \frac{H_{1C}}{H_1(F_{\text{appl}})} \tag{7}$$

The crack initiates in the tip of a bi-material notch if the value H_1 of GSIF exceeds its critical value H_{1C} and/or the applied loading force is over its critical value.

Numerical modelling of the push out test

The configuration and dimensions of the push out test are shown in fig. 1. In the finite element method (FEM) software ANSYS the model from fig. 2 was created. It represents a half of the specimen with symmetry conditions, and is rotated 90 degrees anticlockwise.

The most dangerous locations resulting from FEM analysis are assessed from the fracture mechanics point of view. According to the stress analysis, the point of the most probable crack initiation is assumed as shown in detail in fig. 2. Due to the material and geometrical discontinuity (the material interface, and the rectangular notch), there is a singular stress concentration in this corner. The stress distribution in the notch tip vicinity is shown in fig 3. There are the FEM distribution of tangential stress $\sigma_{\theta\theta}$ for polar coordinates with the origin in the notch tip and the dependence of the mean value $\overline{\sigma_{\theta\theta}}(\theta)$ on polar coordinate θ. The mean value of the tangential stress enters into the stability criteria and thus it is the leading quantity for the failure initiation. The white area in the fig. 3a) represents negative (pressure) tangential stress, which does not contribute to crack initiation.

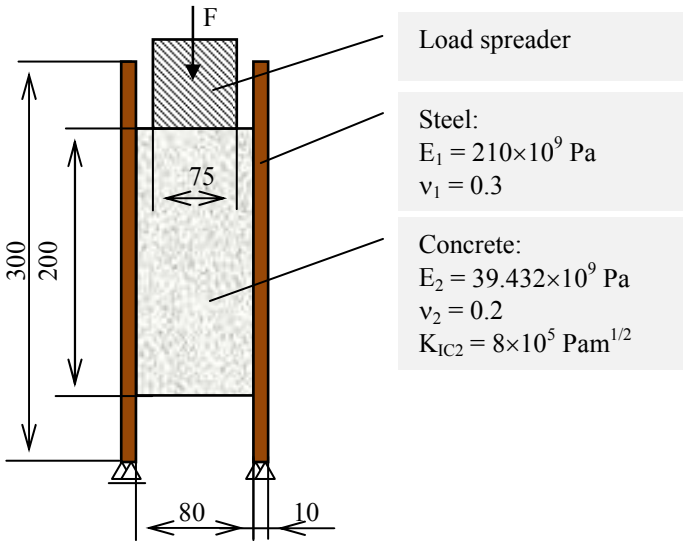


Fig. 1: The push out test configuration

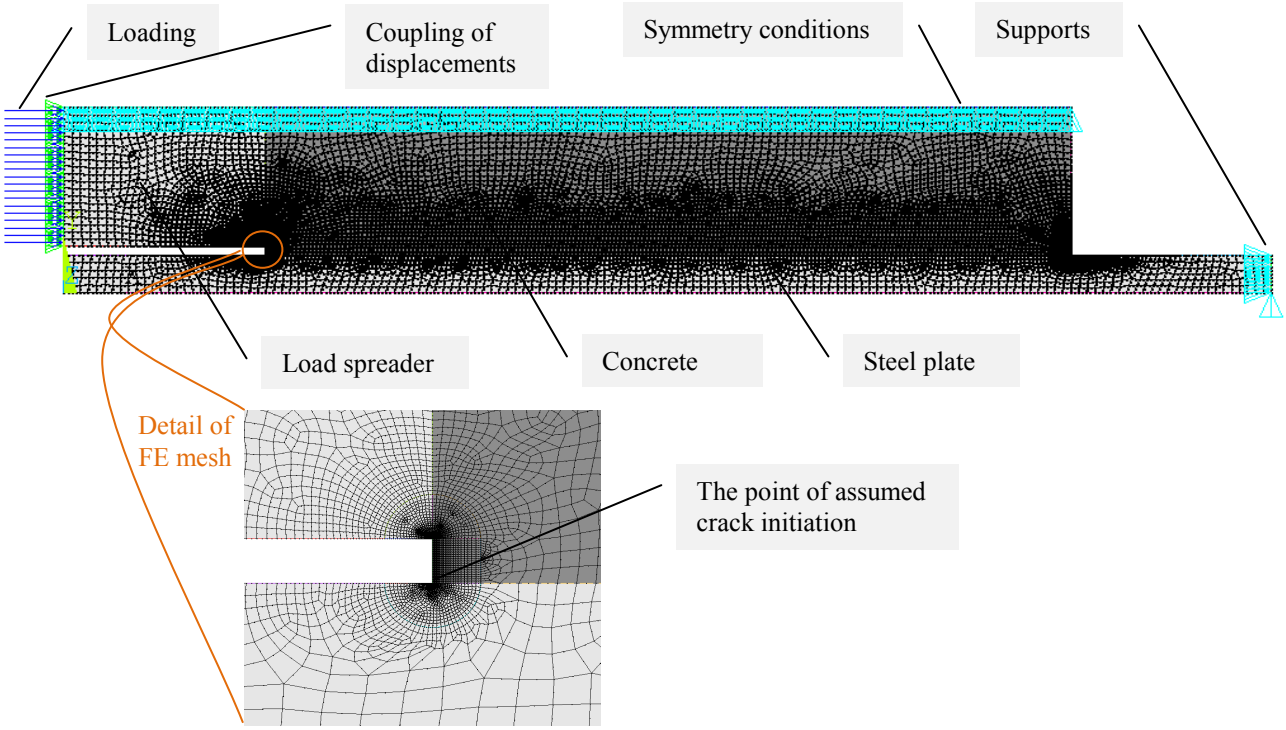


Fig. 2: The FEM model and a detail of the corner with the point of assumed crack initiation

Within the analytical-numerical assessment of crack initiation, the following inputs were used: steel: $E_1=210\times10^9$ Pa, $\nu_1=0.3$, concrete: $E_2=39.432\times10^9$ Pa, $\nu_2=0.2$, $K_{IC2}=0.8\times10^6$ Pam$^{1/2}$. The materials and geometry of the notch imply the stress singularity exponents $p_1=0.3124$, $p_2=0.0138$.

The results from the numerical solution are given in tab.1. Calculations are performed for the lengths $d=\{0.5;\ 1\}$ mm. According to the MTS criterion (3), the initiation angle θ_0 is oriented to steel (Fig. 3), but because the fracture toughness K_{IC} of steel is higher than K_{IC} of concrete, the crack initiation in the direction $\theta_0=0°$ (the crack parallel to the interface) into concrete is supposed. The ratio $\Gamma_{21}=H_2/H_1<<1$ means that the first singular term predominates and the use of the stability criterion based on K_{IC} is justified. The critical applied loading, under which a crack initiates, is estimated by means of (5) and (7). The values from the calculations (Tab.1) correspond well to the values gained form experimental observations, where for 4 specimens $F_{\max}\in\langle 262;\ 321\rangle$ kN.

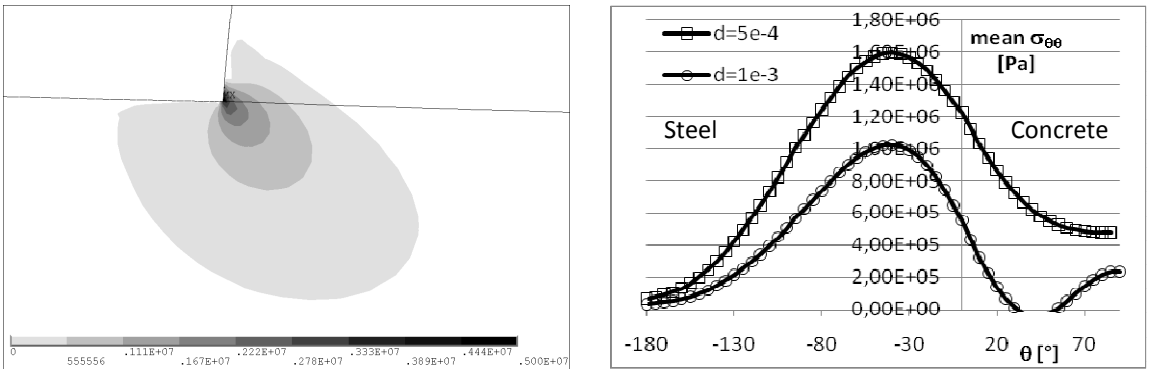


Fig.3: a) Tangential stress $\sigma_{\theta\theta}$ (origin of polar coordinates in the notch tip), b) mean value of $\sigma_{\theta\theta}$

Tab.1: Results of the calculations

d	[m]	0.0005	0.001
θ_0(steel)	[°]	-40.5	-41.5
θ_0(concrete)	[°]	0	0
Γ_{21}	[-]	-0.06804	-0.04361
H_1	[Pam^{p1}]	1.7940×10^5	1.4278×10^5
H_2	[Pam^{p2}]	-1.2206×10^4	-6.2270×10^3
H_{1C}	[Pam^{p1}]	3.8854×10^6	3.4342×10^6
F_{crit}	[kN]	308.62	342.74

Conclusions

The fracture mechanics procedure for the determination of conditions of crack initiation from a bi-material notch based on the mean value of the tangential stress has been presented. The procedure can estimate critical loading under which a failure of the push out specimen initiates.

Acknowledgements

The authors would like to thank the Czech Science Foundation (grants P108/10/2049 and P105/11/1551) and the Research Fund University College Ghent for financial support

References

[1] Williams M.L., Bull. Seismol. Soc. Amer., 49 (1959), 199-204

[2] Klusák J.; Knésl Z.: Determination of Crack Initiation Direction from a Bi-material Notch Based on the Strain Energy Density Concept, Comp. Mater. Sci., 2007, 39, 214-218.

[3] Klusák, J., Knésl, Z.: Reliability assessment of a bi-material notch: Strain energy density factor approach, Theor. Appl. Fract. Mech. (2010), doi:10.1016/j.tafmec.2010.03.001

[4] Erdogan, F., Sih, G.C.: On the crack extension in plates under plane loading and transverse shear. J. Basic Eng. 85 (1963), pp. 519–527.

© (2012) Trans Tech Publications, Switzerland
doi:10.4028/www.scientific.net/KEM.488-489.714

Failure conditions from push-out tests of a steel-concrete joint: experimental results

Peter Helincks[1,2,a], Wouter De Corte[1,2,b], Jan Klusák[3,c], Stanislav Seitl[3,d], Veerle Boel[1,2] and Geert De Schutter[2]

[1]Department of Construction, Faculty of Applied Engineering Sciences, University College Ghent, Schoonmeersstraat 52, 9000 Ghent, Belgium

[2]Department of Structural Engineering, Faculty of Engineering Sciences, Ghent University, Technologiepark-Zwijnaarde 904, 9000 Ghent, Belgium

[3]Institute of Physics of Materials, Academy of Sciences of the Czech Republic, Žižkova 22, 616 62 Brno, Czech Republic

[a]peter.helincks@hogent.be, [b]wouter.decorte@hogent.be, [c]klusak@ipm.cz, [d]seitl@ipm.cz

Keywords: steel-concrete joint, epoxy, push-out test, shear bond strength, stress distribution

Abstract. Steel-concrete joints can suffer from premature fail due to inadequate shear bond between the two surfaces. In this paper the shear bond strength between steel and self-compacting concrete (SCC) without mechanical shear connectors is evaluated through push-out tests. The test samples consist of two sandblasted steel plates (10 and 6 mm) and a concrete core, with connection between steel and concrete obtained by a 2-component epoxy resin, gritted with granulates. During the tests, the ultimate shear force is recorded as well as the slip between steel and concrete. All test members exhibited a concrete - adhesive failure, and indicate nominal shear bond stresses between 2.20 and 4.22 MPa. In addition, a substantial difference in measured shear bond stresses is found between the 6 and 10 mm steel plates, indicating unwanted secondary effects with the 6 mm plates. During testing, maximum slip values between 0.02 and 0.05 mm are recorded. In addition to the experimental tests, shear stress distribution in the epoxy – concrete interface is examined by finite element analysis (FEA). In this way, a non-uniform stress distribution between steel and concrete is found with the maximum shear value about 2.5 times higher than the nominal shear stress value. The FEA combined with the experimental results provide a reasonable understanding of the shear induced failure conditions at a steel-concrete joint, and create test data for a fracture mechanics approach.

Introduction

Concrete and steel are two frequently used materials in the construction industry because of their specific characteristics regarding compressive and tensile strength. Still, a good connection between both materials is essential to obtain a good structural performance of the composite structure. Mechanical shear connectors, welded on the steel surface, are often applied to ensure this connection (Fig. 1) [1]. However, the welding of these shear studs can degrade the performance of the steel (toughness, ductility, corrosion resistance), induce stress concentrations, and decrease the fatigue endurance of the structure [2].



Figure 1. Shear studs

Moreover, sometimes it is impossible to provide proper shear connectors in small composite elements. An epoxy adhesive can then be used to ensure the connection [3-4]. In this paper, the behaviour of a steel-concrete joint with a two-component epoxy adhesive is investigated. The maximum shear bond strength and according slip are examined by means of push-out tests. A uniform distributed shear stress is assumed to evaluate the results, but a theoretical finite element model (FEM) is also made to simulate the actual shear bond stress distribution in the contact surface between steel and concrete. As seen in an epoxy-based connection between FRP laminates and concrete, a non-uniform distribution is expected [5-6].

Experimental program

Materials. To cast the test members, a self-compacting concrete (SCC) mixture is made. The mixture has a W/C-ratio of 0.46 and contains sand 0/4 (853 kg/m³), river gravel 2/8 (263 kg/m³), rivel gravel 8/16 (434 kg/m³), limestone filler (240 kg/m³), CEM I 52.5 N (360 kg/m³), water (165 kg/m³), a polycarboxylic ether as superplasticizer (3.13 l/m³), and hooked-end steel fibres (55 kg/m³) with the following characteristics: length L_f = 30 mm, diameter D_f = 0.55 mm, and nominal tensile strength = 1100 N/mm². Sandblasted steel plates (S235, 6 or 10 mm thick) are used. They are cleaned with acetone before application of the adhesive layer to remove grease, oil, and dust, in order to achieve a better bonding performance. The adhesive applied in these experiments is a two-component epoxy, PC® 5800/BL, which has a good bonding at concrete, metal, carbon, etc.

Properties of concrete. Slump flow and V-funnel time define the fresh properties of the mixture. Hardened properties are determined at the age of 28 days on four 150 x 300 mm cylindrical specimens for each characteristic: compressive strength f_c (NBN EN 12390-3), split-tensile strength $f_{ct,sp}$ (NBN EN 12390-6), and static modulus of elasticity E_c (NBN B 15-203).

Table 1. Concrete properties

	SCC mixture
Slump flow [mm]	741 [55]
V-funnel [s]	10.5 [2.5]
f_c [N/mm²]	58.9 [3.5]
f_{ct} [N/mm²]	5.16 [1.00]
E_c [N/mm²]	39 213 [202]

Table 1 shows the mean mixture characteristics with the standard deviations between brackets. The tensile strength f_{ct} is calculated by $0.9 \cdot f_{ct,sp}$. [7].

Test members. The dimensions of the push-out specimens - which are based on these used in push-out tests executed by Aboobucker [4] - are shown in Fig. 2. The adhesive layer is applied on the steel surface with a toothed paddle (interval distance of 6 mm) and gritted with granulates (river gravel 2/4). According to the specifications, the cure time of the epoxy is 24h. After the curing of the adhesive layer, the SCC mixture is poured into the mould, between the prepared steel plates. The test members were demoulded after 24h, sealed and stored at 20 ± 2 °C until the age of testing.

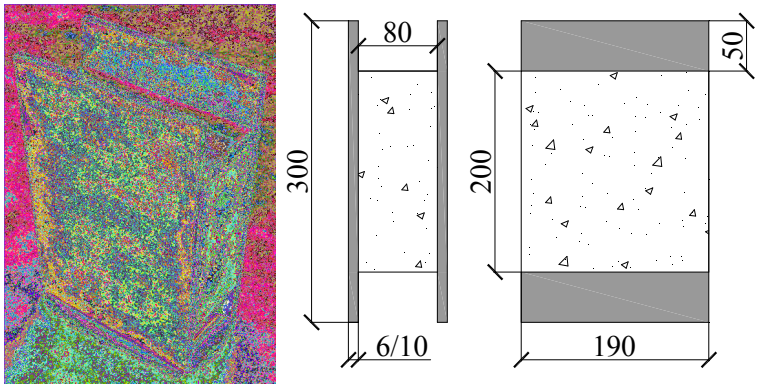


Figure 2. Dimensions of push-out test members [mm]

Test procedure. Test members were tested at the age of 28 days by means of push-out tests at a constant rate of 1 kN/s as shown in Fig. 3. Load spreaders with a width of 75 mm are used to spread the applied load over the concrete top surface. Two dial gauges are connected to the steel plates to measure the slip between concrete and steel. In order to exclude unevenness of the test specimen, one fixed and one roller support are used.

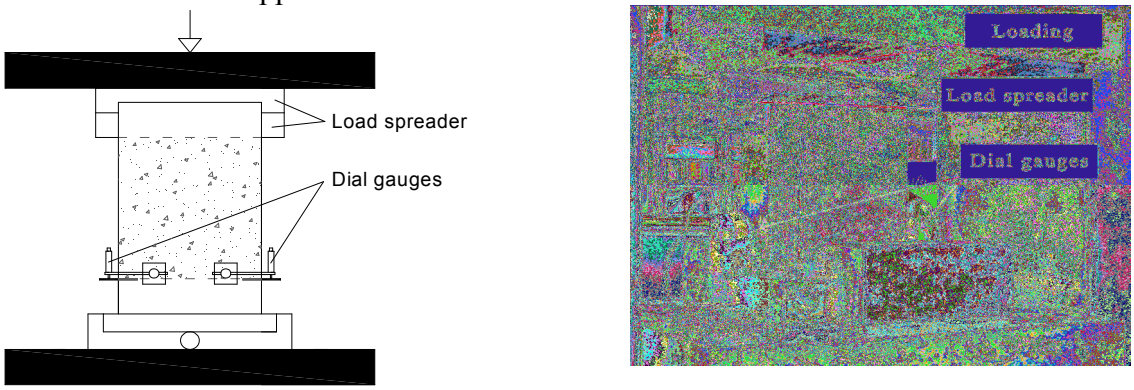


Figure 3. Test set-up push-out test

Experimental test results and discussion

Ultimate shear bond stress, slip, and failure mode. All test members exhibited a concrete - adhesive failure as seen in Fig. 4. In some cases, small cracks are visible in the concrete cores. To investigate this failure mechanism in detail, a fracture mechanics approach is recommended. The nominal shear bond stress τ_n [N/mm²] is calculated from the failure load F [N] by Eq. 1, where A [mm²] is the area of the contact surface between steel and concrete.

$$\tau_n = \frac{F}{A} = \frac{F}{2 \cdot 200\ \text{mm} \cdot 190\ \text{mm}} \quad (1)$$

Table 2 summarizes the failure load F, the nominal shear bond stress τ_n and the according maximum relative slip values s for all 8 test members (4 with 10 mm plates and 4 with 6 mm plates).

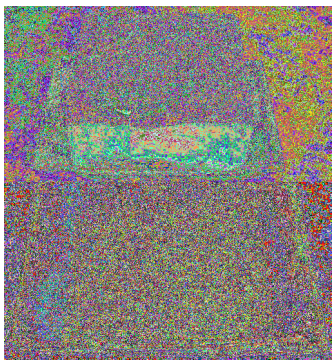


Figure 4. Concrete - adhesive failure

Table 2. Results push-out tests

Test member	Failure load F [kN]	Shear bond stress τ_n [N/mm²]	Maximum relative slip s [mm]
P10-1	320.97	4.22	0.04
P10-2	291.60	3.84	0.04
P10-3	261.51	3.44	0.02
P10-4	296.89	3.91	0.02
P6-1	167.29	2.20	0.02
P6-2	225.69	2.97	0.03
P6-3	193.09	2.54	0.04
P6-4	266.71	3.51	0.05

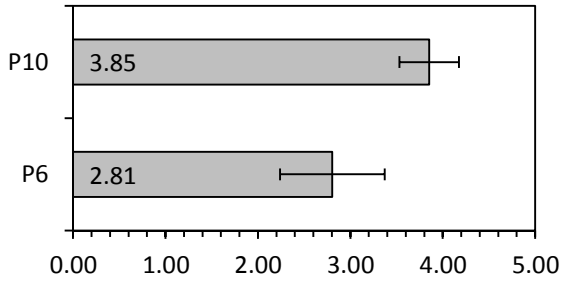


Figure 5. Mean nominal shear bond stress [N/mm²]

Test results point out bond stresses between 2.20 and 4.22 N/mm². The relative slip at failure is situated between 0.02 and 0.05 mm. The mean bond stresses and standard deviations are shown in Fig. 5. It can be observed that a substantial difference in shear bond stresses is found between the 10 and 6 mm steel plates. This can be explained by more explicit unwanted secondary effects that occur when loading the test specimens with 6 mm steel plates, as seen in the finite element analysis.

Finite element analysis

Modeling. A FEM was made with ABAQUS to compare the outcome of theoretical simulations with the experimental results. Steel plates were completely connected to the concrete core, so that no slip could occur. The parts of the assembly were meshed with 8-node linear bricks (C3D8R hex-elements) (Fig. 6). The mean experimental failure load was used in the FEA (292.77 and 213.20 kN for 10 and 6 mm steel plates, respectively).

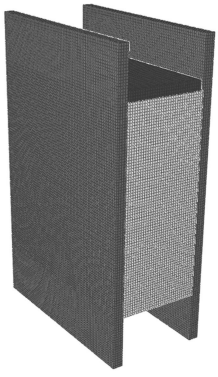


Figure 6. Meshed FEM

Comparison between test members. As the load increases, it is seen that the top and bottom of the steel plates move towards the inside of the test member, which indicates bending of the plates and, as a result, induces unwanted secondary forces.

It is observed that - under the same load conditions (213.20 kN) - the displacements are about 1.5 times higher when the test members with 6 mm plates is loaded. Therefore, higher secondary stresses occur and a premature failure is observed during the experimental tests.

Shear bond stress distribution. A non-uniform distribution of the shear bond stresses is found in the FEA's. The stress distribution is determined along two paths (in the middle and at the edge of the contact surface) and summarized in Fig. 7 for both test members. It is seen that in the middle of the bonding area, the bond stresses are lower than the nominal stresses. Near the top and the bottom, the stresses increase and even show some peak values.

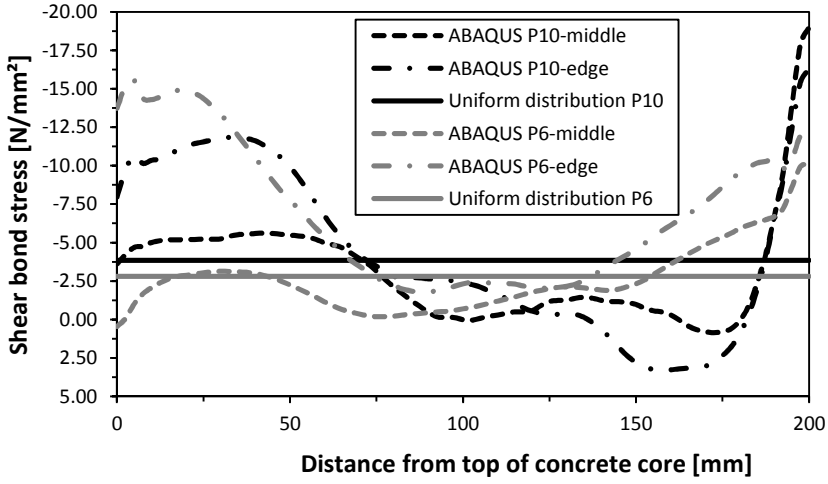


Figure 7. Shear bond stress distributions

Therefore, the effective maximum shear bond stress at failure is about 2.5 times higher than the nominal stress. This means that a good understanding of the stress distribution is necessary to determine the total direct shear bond strength that can be transferred between steel plates and concrete.

Conclusions

The aim of this research was to investigate the bond strength between steel and concrete using epoxy adhesive by means of push-out tests. For the 10 mm and 6 mm test members, a mean nominal shear bond stress of 3.85 N/mm² (stdev: 0.32) and 2.81 N/mm² (stdev: 0.56) is recorded. Lower bond stresses are found with the test members with 6 mm steel plates, due to bending of the steel plates and according secondary stresses. Also, a non-uniform stress distribution is found, with bond stresses about 2.5 times higher than the nominal stresses. Obviously, the scope of this study is too small to make a clearly defined conclusion of this subject. More research is needed, including a fracture mechanics approach.

Acknowledgements

The authors thankfully acknowledge the Research Fund University College Ghent and Czech Science Foundation (grants P108/10/2049 and P105/11/1551) for financial support and steel producer N.V. Bekaert S.A. for providing the steel fibres.

References

[1] Richard Liew J.Y., Sohel K.M.A. (2009), *Lightweight steel-concrete-steel sandwich system with J-hook connectors*, Engineering Structures 31, pp. 1166-1178

[2] Johnson R.P. (2000), *Resistance of stud shear connector to fatigue*, Journal of Constructional Steel Research 56, pp. 101-116

[3] Bouazaoui L., Perrenot G., Delmas Y., and Li A. (2007), *Experimental study of bonded steel concrete composite structures*, Journal of Constructional Steel Research 63, pp. 1268-1278

[4] Aboobucker M.A.M., Wang T.Y., and Richard Liew J.Y. (2009), *An experimental investigation on shear bond strength between steel and fresh cast concrete using epoxy*, The IES Journal Part A: Civil & Structural Engineering Vol. 2 (No. 2, May), pp. 107-115

[5] Guo Z.G., Cao S.Y., Sun W.M., and Lin X.Y. (2005), *Experimental study on bond stress-slip behaviour between FRP sheets and concrete*, Proceedings of the International Symposium on Bond Behaviour of FRP in Structures (BBFS 2005), pp. 77-84

[6] Sayed-Ahmed E.Y., Bakay R., and Shrive N.G. (2009), *Bond strength of FRP laminates to concrete: state-of-the-art review*, Electronic Journal of Structural Engineering 9, pp. 45-61

[7] European Committee for Standardization (2004), *Eurocode 2: Design of concrete structures - Part 1-1: General rules and rules for buildings*

© (2012) Trans Tech Publications, Switzerland
doi:10.4028/www.scientific.net/KEM.488-489.718

Numerical Stress Intensity Factors Determination for Fabrication Defects in Coronary Stents

Cristian-Sorin Nes[1,a], Angelica Enkelhardt[1,b], Nicolae Faur[1,c] and Adrian Birlan[1,d]

[1]"Politehnica" University of Timisoara, M. Viteazu nr.1, Timisoara, Romania

[a]cristianedonis@yahoo.com, [b]angelica_enkelhardt@yahoo.de, [c]ruaf2001@yahoo.com, [d]a_birlan@yahoo.com

Keywords: Stress Intensity Factor, coronary stent, ABAQUS, defect.

Abstract. *Objectives:* Numerical stress intensity factors (SIFs) computation for several fabrication defect geometries in coronary stents. XFEM crack initiation and propagation was also performed. *Methods:* The model represents a self-expandable coronary stent, made from a shape memory alloy (L-605). Several flaw shapes are considered. The analysis was performed using the ABAQUS code. The loads and boundary conditions simulate the interaction between the blood vessels and stents, immediately after the angioplasty was performed. The mesh contains 3d stress hexahedral elements. For global stress and strain distributions, the model of a complete stent was used. For crack propagation analysis and SIF determination, the model represented a single segment of the stent. The stress intensity factors were computed using the contour integral method. *Results and conclusions:* The stress and strain fields highlight the negative effects of crack initiation and propagation on the residual life of the stent. Furthermore, by compromising the structural integrity of the stent, large strains may occur, thus increasing the risk of restenosis and further stenosis-related complications. The stress intensity factors indicate the most dangerous locations for the flaws (cracks), as well as the most dangerous geometries.

Introduction

In recent years, stent grafts proved to be the optimal solution in treating arterial stenosis and arterial aneurysms. The relative simple procedure (angioplasty) has produced a large interest inside the medical community, due to the high success rate, short and complications-free convalescence period and reduced costs compared to classical invasive surgery. As well, the patient's lifestyle does not have to change drastically therefore the procedure meets general acceptance amongst the patients.

A vascular stent is a small metallic tube inserted in the artery in the narrowed zone; it behaves like an artificial support for the blood vessel. There are two major stent types: self-expandable stents, made of shape memory materials (stainless steel, nitinol, cobalt alloys) and balloon-expandable stents. The self-expandable stent can also contain the medication needed to prevent immune reactions that can jeopardize the patient's life.

The device failure issue has been previously analyzed by Beebe et al [1], Jacobs et al. [2], Chakfe et al. [3] and others. Finite element analysis regarding the stent-blood vessel interaction were also conducted by Lally et al. [4] Migliavacca et al. [5, 6] or Wu et al [7], but this paper focuses on SIF determination for different crack shapes, as a result of material defects. The numeric analysis was done using ABAQUS 6.9-3.

Model description

The stent model this paper analyses consists in 12 interconnected rings made of cobalt L-605 alloy wires (Fig.1.a). The tube is 22.4 millimeters long, has a diameter of 8.3 millimeters and is dedicated to stenosis-related applications.

Stress distribution. In order to identify the regions where failure is most likely to appear, a study of global stress distribution for the entire stent had to be performed. Considering that the blood vessel is covered with 56% stenosis, the exterior pressure on the wires was chosen p=2.5 MPa [4]. This rather elevated value of the exterior pressure, noticed numerically and experimentally confirmed in advanced stenosis imposes the usage of high-strength materials, with a minimum ultimate tensile stress (UTS) of 1000 MPa. The L-605 alloy has minimal UTS=1100 MPA, with the modulus of elasticity E=243000 MPa (www.euroflex-gmbh.de). The highest values for both the von Mises stress and the Maximum Principal Stress (MaxPS) were recorded at the tip of the wire winding (Fig.1.b).

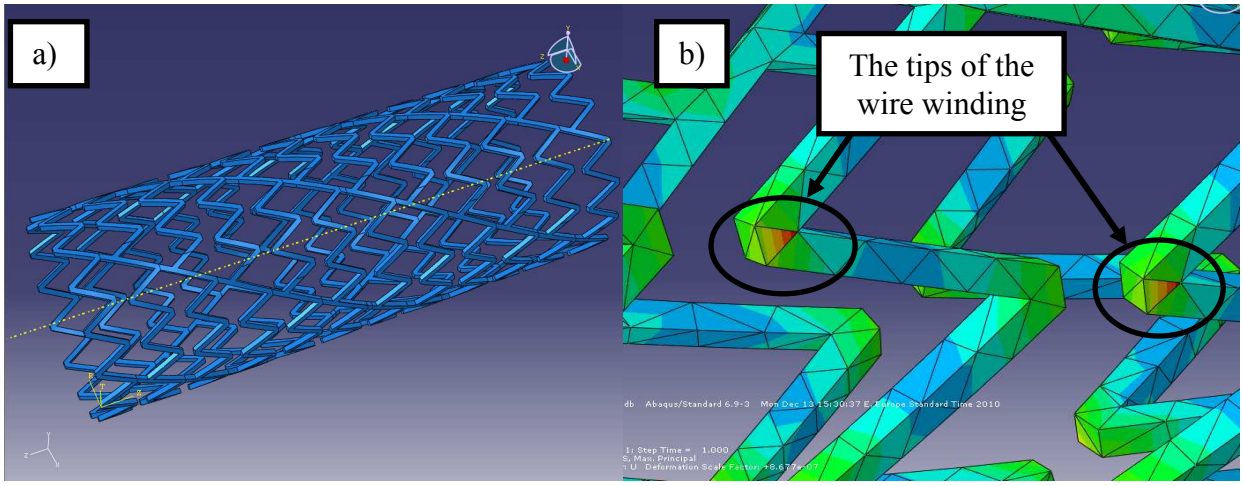


Fig.1. Self-expanding stent: a) the geometric model; b) the MaxPS at the tip of the wire winding

The fracture mechanics model. In order to perform fracture analysis, a single winding step has been extracted from the stent (Fig.2). The wire has a square, 0.2x0.2 mm section. Due to the reduced dimensions of the wire (0.2x0.2 mm) and sophisticated quality control procedures during fabrication, *any defect that may occur can be considered two-dimensional*, and can be modeled as a *plane crack*. Furthermore, this simplified model can be used to asses the stress intensity factors (SIFs) for eventual fatigue cracks.

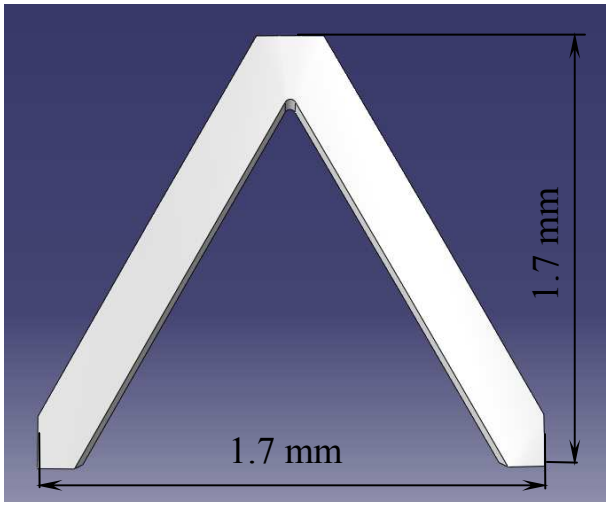


Fig.2. The fracture mechanics model

Crack propagation using XFEM. Using the XFEM module of the ABAQUS code, a virtual crack was propagated using the level set method (the PHILSM option was toggeled). The MaxPS damage model was implemented for this analysis. The mesh contained 1104 enriched hexahedral elements. The crack initiated in the fillet zone that connects the two elements (Fig. 3).

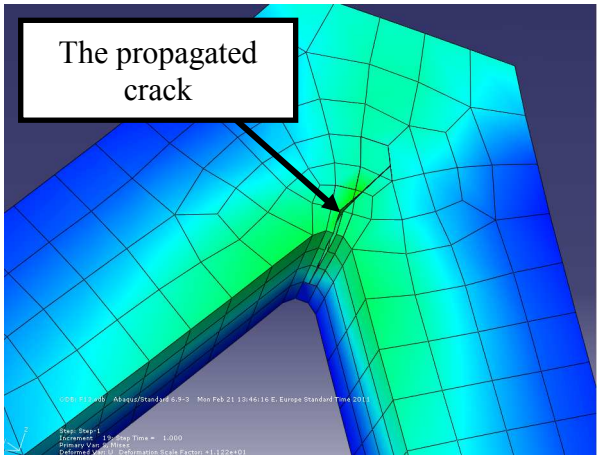


Fig. 3. The XFEM propagated crack

SIF determination for different crack geometries The presence of two-dimensional defects, modeled as plane cracks, can change significantly the stress distribution for a stent segment. The cracks have been modeled in all the zones of a single element. In order to provide means of comparison between different geometries, the crack were grouped in two categories: vertical cracks and horizontal cracks. The crack plane, crack front and growth direction are also highlighted in every picture.

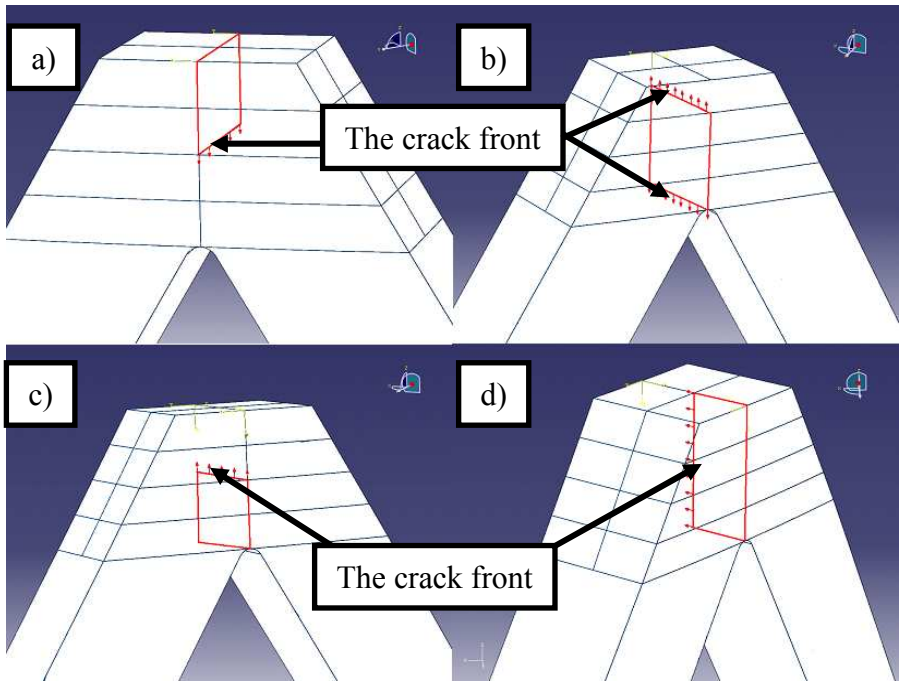


Fig. 4. The "vertical" cracks

Vertical cracks. These models simulate the presence of plane defects at the "tip" of the element. The crack plane contains the bisector of the angle described by the two segments. Four different geometries were chosen in this case (Fig. 4).

The SIFs were computed using the contour integral option of the ABAQUS CAE. For the configuration b), only the SIFs for the upper crack were considered (they had the biggest values). The maximal SIFs for each situation are plotted for comparison in Fig. 5.

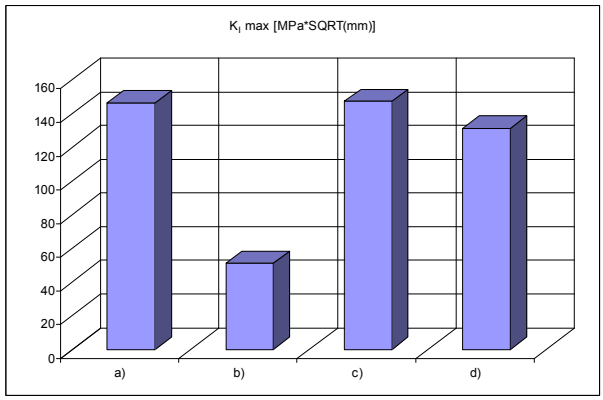


Fig. 5. Maximal K_I for "vertical" cracks

One can see that the geometries a), c) and d) produce similar behaviors, whilst the middle crack b) is four times less dangerous than the others.

Horizontal cracks. These models also simulate the presence of plane defects at the "tip" of the element. The crack plane is perpendicular to the bisector of the angle described by the two segments. In this case, three different geometries were chosen (Fig. 6). The maximal SIFs for each situation are plotted for comparison in Fig. 7.

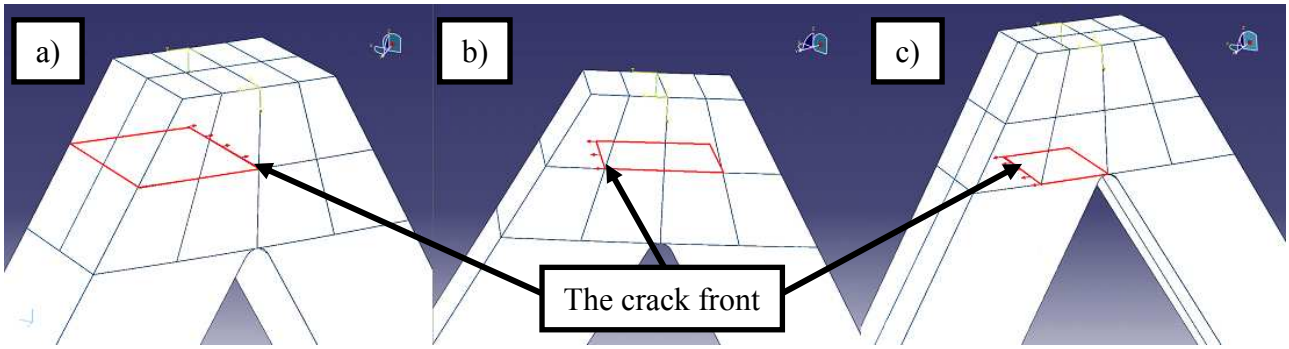


Fig. 6. The "horizontal" cracks

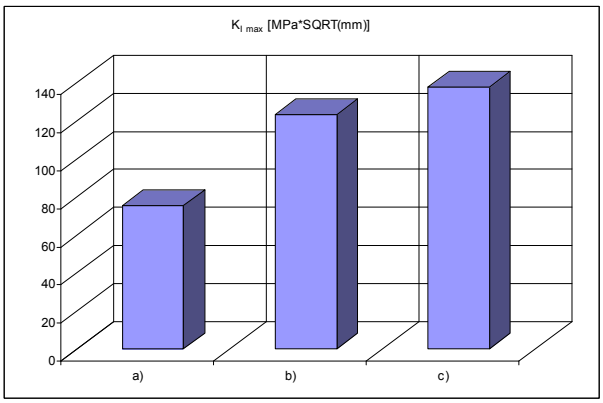


Fig. 7. Maximal K_I for "horizontal" cracks

One can see that all the situations provide relative high values for K_I, but they are still smaller than in the previous case. Nevertheless, the c) geometry generates a K_I of nearly $140\,MPa\sqrt{mm}$. For these configurations appear significant Mode II and Mode III stress intensity factors (K_{II} and K_{III}).

Conclusions

The computation of SIFs for different crack geometries that can be considered fabrication defects is a step forward in correct life time predictions for self-expandable stents. Considering the elastic behavior of the majority of the alloys used to manufacture coronary stents, these SIF determinations can be used for numerous similar stent geometries. As well, this paper shows that even if the loads are at the maximum, in biological terms, and the size of the defect is large (crack length/ wire width ratio of about 0.5), the SIFs remain in the tolerable zone even for a regular steel alloy. Future investigations should be directed towards establishing the fracture toughness (K_{cr}) for these special alloys. Mode II and Mode III fracture is virtually inexistent in the first case ("vertical cracks"), but it appears in the other case. Mode I fracture is the dominant component in all the situations.

Acknowledgment: This work was partially supported by the strategic grant POSDRU 6/1.5/S/13, (2008) of the Ministry of Labour, Family and Social Protection, Romania, co-financed by the European Social Fund - Investing in People.

References

[1] H.G. Beebe, J.L. Cronenwett, B.T. Katzen, D.C. Brewster, R.M. Green, *Results of an aortic endograft trial: impact of device failure beyond 12 months*, Journal of Vascular Surgery 33, 2001, S55–S63.

[2] T.S. Jacobs, J. Won, E.C. Gravereaux, P.L. Faries, N. Morrissey, V.J. Teodorescu, Hollier, L.H. Holl, M.L. Marin, *Mechanical failure of prosthetic human implants: a 10-year experience with aortic stent graft devices*, Journal of Vascular Surgery 37, 2003, pp.16–26.

[3] N. Chakfe, F. Dieval, G. Riepe, D. Mathieu, I. Zbali, F. Thaveau, C. Heintz, G. Kretz, B. Durand, *Influence of the textile structure on the degradation of explanted aortic endoprostheses*, European Journal of Vascular and Endovascular Surgery 27, 2004, pp.33–41.

[4] C. Lally, F. Dolan, P.J. Prendergast, *Cardiovascular stent design and vessel stresses: a finite element analysis*, Journal of Biomechanics 38, 2005, pp. 1574-1581.

[5] F. Migliavacca, L. Petrini, P. Massarotti, S. Schievano, F. Auricchio, G. Dubini, *Stainless and shape memory alloy coronary stents: a computational study on the interaction with the vascular wall*, Biomechan Model Mechanobiol 2, 2004, pp. 205–217.

[6] F. Migliavacca, L. Petrini, M. Colombo, F. Auricchio, R. Pietrabissa, *Mechanical behavior of coronary stents investigated through the finite element method*, J Biomech 35 , 2002, pp.803–811.

[7] W. Wu, W.-Q. Wang, D.-Z. Yang, M. Qi, *Stent expansion in curved vessel and their interactions: a finite element analysis*, Journal of Biomechanics 40, 2007, pp. 2580-2585.

© (2012) Trans Tech Publications, Switzerland
doi:10.4028/www.scientific.net/KEM.488-489.722

3-Dimensional Stress Intensity Factor Determination for a Notched Shaft under Mixed Mode Loading

Cristian-Sorin Nes[1, a], Nicolae Faur[1,b] and Liviu Marsavina[1,c]

[1]"Politehnica" University of Timisoara, M. Viteazu nr.1, Timisoara, Romania

[a]cristianedonis@yahoo.com, [b]ruaf2001@yahoo.com, [c]msvina@yahoo.com

Keywords: Stress Intensity Factor, mixed-mode, crack, ABAQUS, shaft, fillet.

Abstract. *Objectives:* Numerical determinations of Stress Intensity Factors (SIFs) for a shaft under mixed-mode load with a crack of different sizes in the connection zone between square and circular cross-sections. *Methods:* Linear-elastic Fracture Mechanics principles are used. The numerical analysis program used was ABAQUS CAE version 6.9-3. The shaft consists in a circular section and a square section, with a fillet connecting zone. Cracks of different lengths and different depths are modeled. The shaft is subjected to torsion and bending. The SIFs were determined using the contour integral method. *Results*: The stress distribution was determined and plotted, and the stress concentration effect of the notches was highlighted. Crack propagation was also performed, using the XFEM module of ABAQUS code. The computed SIFs were plotted along the crack front. *Conclusions:* Crack initiation and propagation matched the pattern obtained in experimental tests, thus validating the model. The results confirmed that the fillet zone between the two sections acts as a stress concentrator. The fillet radius determines the magnitude of stress concentration. Crack geometry has a significant influence on SIFs, as well as on the global stress distribution.

Introduction

In order to provide reliable life predictions for any mechanical structure under a certain array of loads, in the presence of cracks (caused by fatigue, material defects, technological defects, structure damages), the determination of the fracture parameters (Stress Intensity Factors - SIFs, Crack Tip Opening Displacement - CTOD, J-integral, Energy Release Rate - $\mathcal{G}$) is necessary. The existing literature provides analytical solutions for simple geometries, but for more complicated geometries or load cases, there are only two alternatives: numerical analysis and experimental testing. Experimental testing can be in most cases very expensive and may require a lot of time to be performed. Numerical analysis provides a cheap, fast and easy way to determine the fracture parameters for a given geometry and the performance level acquired by modern desktop computers allow fine meshing for accurate results.

This paper presents SIF determinations for a shaft with a circular section and a square section, subjected to torsion and bending. The two sections are connected by a fillet zone. Cracks of different sizes (different lengths and different depths) are then modeled, and the SIFs are computed using the contour integral method. The analysis was done using the ABAQUS code.

Model description

The loads, boundary conditions, materials and mesh. The shaft is subjected to a torsion moment and a bending moment. ABAQUS CAE does not allow defining moments on surfaces; instead these moments were created using distributed forces. The torsion moment is the result of the P_1 pressure, while P_2 generates the bending moment (Fig. 1):

P_1=213.33 N/mm^2 (M=60000 Nmm) (1),

P_2=10 N/mm^2 (F=500 N) (2).

The material properties used in these applications corresponds to JIS SS41 carbon steel, with the longitudinal modulus of elasticity E=210000 MPa, and Poisson's ratio ν=0.3.

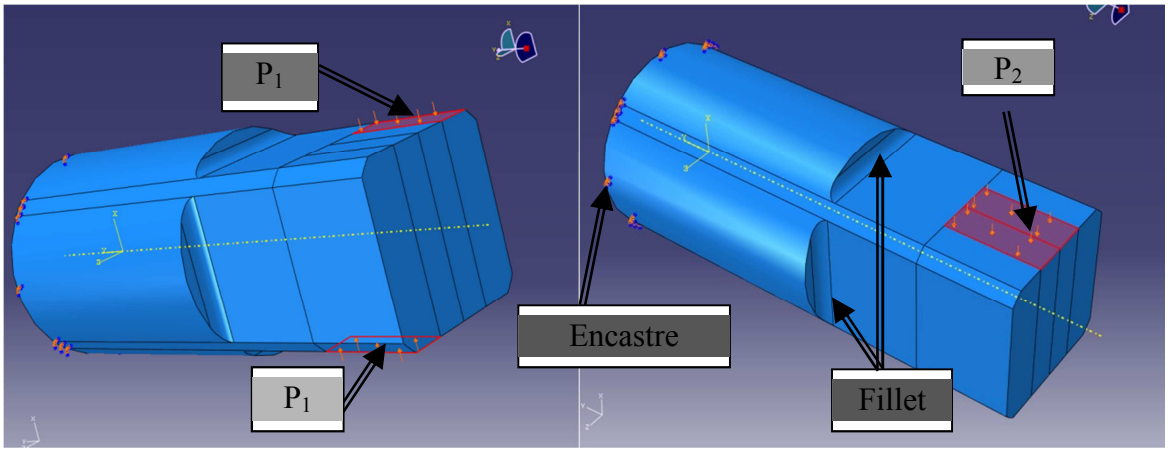


Fig. 1. The two distributed forces and the boundary conditions

The fillet radius between the square section and the circular section is 2 mm, the same value chosen for mass production.

In order to improve the accuracy by refining the mesh and also reduce the simulation time, only a portion of the shaft was considered. Each model consists of approximately 12500 hexahedral elements, obtained using the mesh sweep strategy (Fig. 2). Swept mesh is imposed in contour integral evaluations. Additional mesh refinement near the crack front was performed.

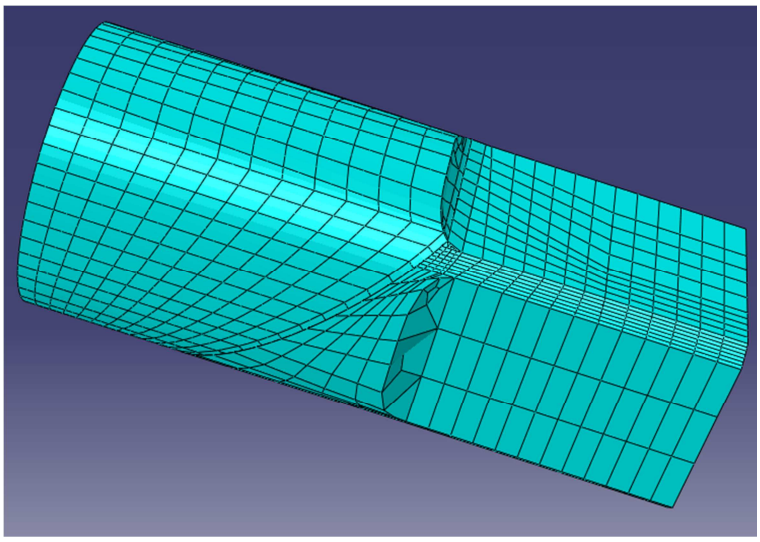


Fig. 2. The swept mesh

Model validation

Experimental studies conducted by Dumitru et al. [1] showed that the crack initiates near the fillet zone, and propagates by an average θ_{exp}=48.6° angle (Fig. 3.a). By using the XFEM module of the ABAQUS code, the initiation point and the propagation path of a virtual crack could be determined (Fig. 3.b); the propagation angle θ_{num}=49.22° confirmed the validity of the model. The XFEM model also determined the initiation point of the crack (the result matched the pattern obtained experimentally).

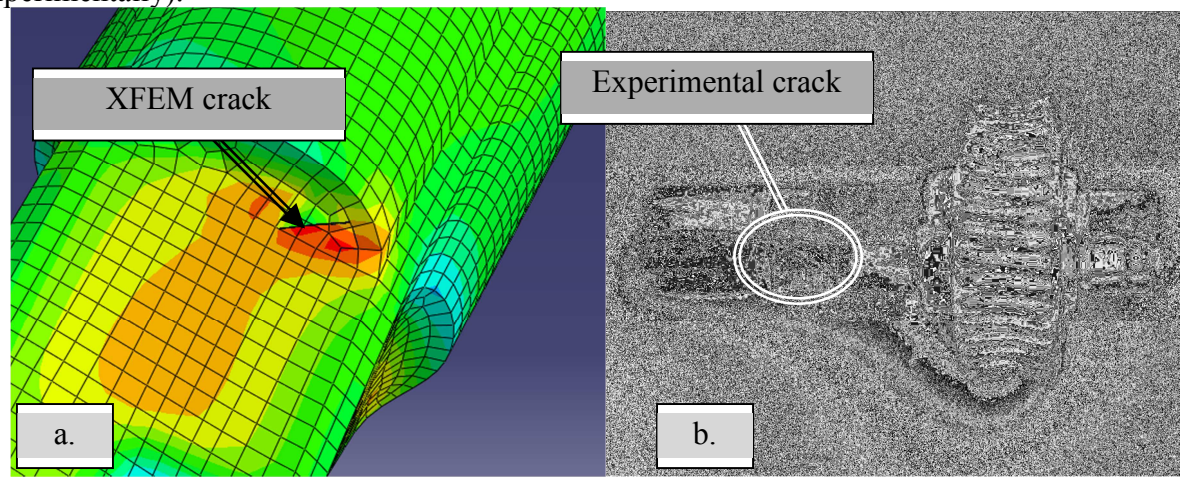


Fig. 3. The cracked shaft

SIF determination for various crack geometries

Fixed length, variable depth. A crack with a fixed length (11 mm), but with variable depth δ (0.4 mm, 0.7 mm, 1 mm, 1.3 mm and 1.5 mm) was modeled. One tip of the crack lied near the initiation point, while the other was placed according to the growth path determined experimentally. For each δ, the SIFs were determined using the contour integral crack definition of the ABAQUS CAE code. The SIFs (K_I, K_{II}, K_{III}) computed in the crack front nodes were plotted in Fig. 4. The first node is the nearest node to the initiation point.

Variable length cracks. Using the same model as in the previous case, this time the length of the crack was modified and the depth of the crack was chosen accordingly to the experimental results. Therefore, for each length, we had a different depth, in order to simulate the shape of a real crack. The crack length takes the following values: 4.5, 8 and 11 millimeters. These values have been chosen in order to cover an incipient phase, an intermediate phase and a phase close to the breaking point. The SIFs were determined using the same contour integral option.

The computed values for K_I, K_{II}, and K_{III} for variable length cracks are plotted in Fig. 5. The mesh parameters were kept unchanged for all the simulations.

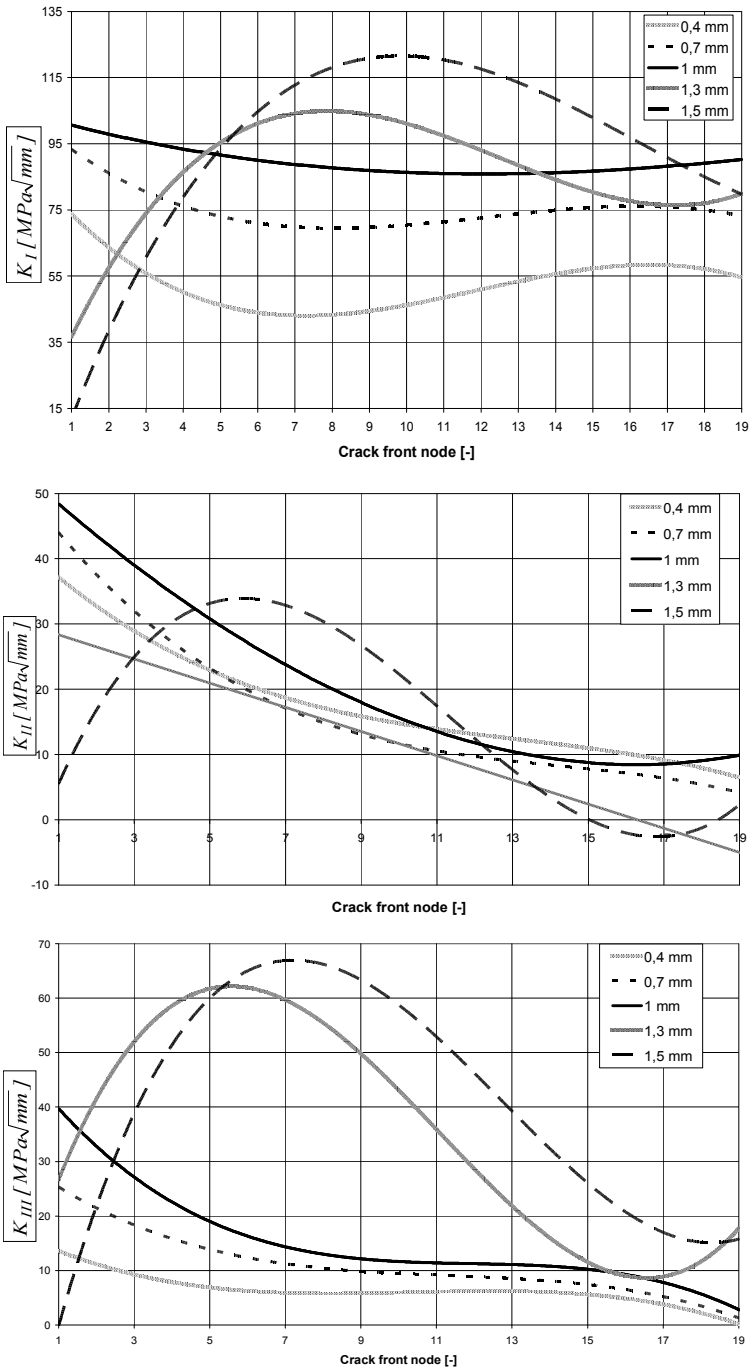


Fig. 4. The distribution of K_I, K_{II} and K_{III} along the crack front for different crack depths

Conclusions

The numerical analysis of the two-section shaft in mixed-mode loading confirmed the stress concentration effect of the fillet. Using enriched elements (XFEM), the initiation zone and the growth direction could be determined. The numerical results were confirmed by experimental testing. The SIF distribution along the crack front showed that the maximum values are reached near the tips; it also indicates the direction where the crack extends. Results have shown that the crack depth has a big influence on the SIFs: the values of K_I, K_{II} and K_{III} increase when δ increases. The margin effect tends to be more obvious for small δ. The results showed that Mode I fracture is predominant (K_I has superior values tu K_{II} and K_{III}). The numerical results helped improving the design of the real model by eliminating crack initiation throughout the component's life span.

Acknowledgment. This work was partially supported by the strategic grant POSDRU 6/1.5/S/13, (2008) of the Ministry of Labour, Family and Social Protection, Romania, co-financed by the European Social Fund - Investing in People.

References

[1] I. Dumitru, L. Marsavina, N. Faur: *Experimental study of torsional impact of shafts*, Journal of Sound and Vibration, Vol. 308, 2007.

[2] T.L. Anderson, *Fracture Mechanics*, CRC Press, ISBN: 0-8493-4260-0, USA, 1995.

[3] S. Mohammadi, *Extended Finite Element Method*, Blackwell Publishing Ltd, ISBN: 978-1-4051-7060-4, Singapore, 2008.

[4] ABAQUS 6.9-3 Documentation.

[5] Y. Murakami, *Stress Intensity Factors Handbook*, Pergamon Press, ISBN: 0-08-034809-2, Oxford, U.K., 1987.

[6] F.-P. Yang, Z.-B. Kuang, *Fatigue crack growth for a surface crack in a round bar under multi-axial loading condition*, Fatigue and Fracture of Engineering Materials and Structures, vol 28, 2005.

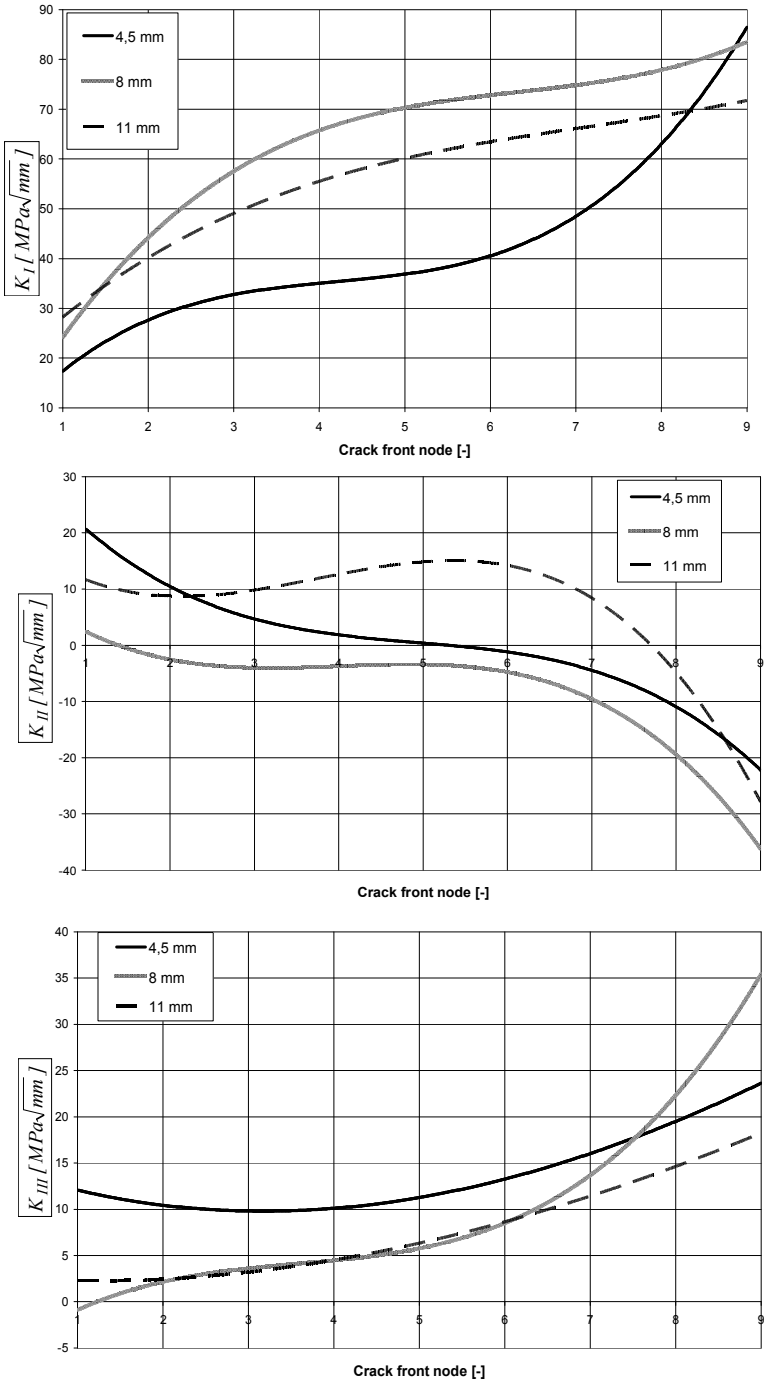


Fig. 5. The distribution of K_I, K_{II} and K_{III} along the crack front for different crack lengths

[7] R.S. Barsoum, *On the Use of Isoparametric Finite Elements in Linear Fracture Mechanics*, International Journal for Numerical Methods in Engineering, Vol. 10, No. 1, pp. 25–37, 1976.

[8] S.K. Chan, I.S. Tuba, W.K. Wilson, *On the Finite Element Method in Linear Fracture Mechanics*, Engineering Fracture Mechanics, Vol. 2, No. 1-A, pp. 1–17, 1970.

[9] R.D. Henshell and K.G. Shaw, *Crack Tip Finite Elements Are Unnecessary*, International Journal for Numerical Methods in Engineering, Vol. 9, pp. 495–507, 1975.

© (2012) Trans Tech Publications, Switzerland
doi:10.4028/www.scientific.net/KEM.488-489.727

Overview of the methods for service life prediction on gears

Boris Aberšek[1], Jože Flašker[2]

[1] University of Maribor, Faculty of Natural Science and Mathematics, Koroška 160, 2000 Maribor, Slovenia

[2] University of Maribor, Faculty of Mechanical Engineering, Smetanova 17, 2000 Maribor, Slovenia

boris.abersek@uni-mb.si, joze.flasker@uni-mb.si

Keywords: fracture mechanics, service life, mathematical models, experiment

Abstract For designing machines and devices the dimensioning with respect to service life is increasingly taken into account. This applies also for gearing which are still today one of very important components of almost all machines. The problem of determination of the service life of gearing is directly related to geometry of gears, multiaxial loadings, materials and appropriate models for prediction of the crack propagation. Obviously gears and gearing belong to the real complex structure, by correctly selected and carefully planned experiments we obtained results with which we can confirm and justified the mathematical model for calculating different parameters, i.e. service life.

In paper the past and the future of gears/gearings calculation will be point out, from deterministic calculations to mathematical modelling and from "classical" experimental techniques and procedure to more sophisticated one.

Introduction

All deterministic models according to different national standards are rough and give only approximate results since they do not take into account the actual conditions, so we developed the mathematical model for calculating different parameters connected with stress, strength and service life on gears.

For confirm mathematical model we developed different non-standard test pieces and on this pieces we used combination of mixed experimental methods. The aim of these combinations was to obtain as complete information about the individual influences as possible and to determine the interaction between magnitudes. In this way we confirmed the developed model as a whole and also determined some physical interpretations in models. With this we were able to ensure that the presented model is not purely a mathematical model.

Model for evaluation of service life

Model of crack initiation The linear elastic fracture mechanics is inapplicable for describing properties of very short cracks, since elastic stress cannot accurately describe high deformation fields near the tip of small defects in high-strength materials. Therefore, we used the theory of continuously distributed dislocation for analysis of crystallographic slip deformations before the tip of short fatigue crack in combination with crystal limits and on the basis of it we formed an appropriate model [1, 2]. The stress connected with dislocations can result in the slip of the inclusion or in generation of vacation. Dislocations can unite on any obstacle of the slip that causes their concentration in space. This results in nucleation of micro cracks and/or crack growth with uniting of remaining dislocations. The assumptions described above were used in our model for initiation and propagation of micro cracks.

For calculating the crack propagation in gears the most important parameters is gear stress concentration before crack or, more precisely, before crack increased for the size of the plastic zone. Thus the additional stress for this point $|\xi_o| \triangleright 1$ is:

$$\sigma(\xi_0) - T = A \int_{-1}^{1} \frac{f(\xi)}{\xi_0 - \xi} d\xi \qquad and\ |\xi_0| \triangleright 1 \tag{1}$$

and the number of dislocation in the plastic zone is obtained by integration of the distribution function between $\xi = 1$ and $\xi = d$. The tooth stress intensity factor Z which describes condition in the tooth root near the crack tip as a function of plastic displacement is the product of number of dislocation and of the Burger's vector. The result of this notation is:

$$Z = \frac{\boldsymbol{b}}{\pi^2 A} \frac{\left(1 - d^2\right)^{1/2}}{T} (T\, Y(a/S) \sqrt{\pi\, a})^2 = \frac{\boldsymbol{b}\left(1 - d^2\right)^{1/2} T\, Y^2(a/S)\, a}{\pi\, A} \tag{2}$$

By assuming that the crack growth rate is proportional to Z the present theory describes the model for calculation of service life. [1, 2].

Model of crack propagation Statistical analysis of experimental results shows that the material parameters in the equations of crack growth are random variables. As an example let as take the modified Paris - Erdogan equation in stochastically form:

$$\frac{da}{dt} = f(\Delta Z)\, A(t) = C\, f(\Delta Z)\, [\mu + Y(t)] \tag{3}$$

Where $\mu = E(A(t))$ and $A(t)$ is stochastic time process, and $Y(t)$ is random process with mean μ.

Experimental techniques

Traditional technigues

Since gears and gearings belong to the real complex structures by correctly selected and developed test pieces and carefully planned experiments we obtained results with which we confirmed and justified the use of the mathematical models [1, 3] for calculating the tooth stress intensity factor Z as well as the service life of gears.

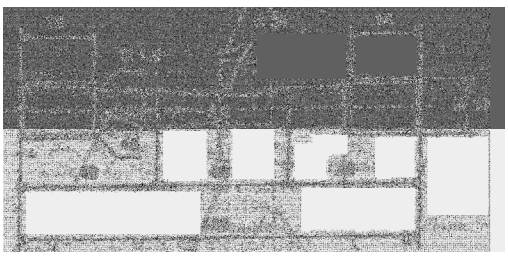


Figure 1: Standard (ASTM-E606) test piece

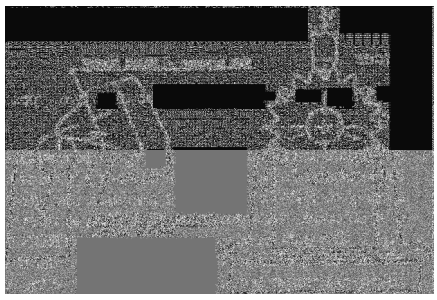


Figure 2: Gear test piece

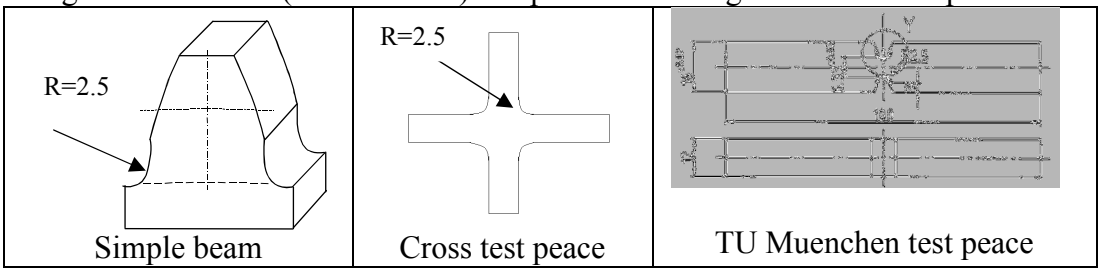


Figure 3: Non-standard gear test peace

Test pieces. We used in our laboratory two types of test pieces:

- Standard test piece for determination of fracture mechanics parameters of material AISI 4130 or 42CrMo4 according to DIN in the area of initiation and growth of short cracks according to ASTM-E606 as shown in Figure 1.
- Non-standard test pieces for determination of parameters of gears. These types of test pieces were gear test pieces developed during previous researches [1, 3]. The arrangement of the individual measuring instruments and test peace is shown in Figure 2. Different laboratories use different test peaces. Some of them are shown in Figure 3.

Measuring method used As we wanted to observe particularly initiation and propagation of short cracks and to determine the conditions occurring in this case [2] (stresses, strains, moment of beginning of fracture etc.), we used mixed experimental methods: photoelastic method, method of measuring of stress/strain by means of strain gauges, replica technique for determination of prevailing initials and measuring of microcracks by means of crack gauges. The a. m. methods were combined as follows:

- photoelastic examination with strain and crack gauges
- strain and crack gauges and
- gauges with replica method.

The aim of these combinations was to obtain as complete information about the individual influences as possible and to determine the interaction between these magnitudes.

Replicas on gears By the replica method we followed up the propagation of short fatigue cracks in the observed direction, i.e., along the tooth width. The test was performed so that the loadings, i.e., F_{max} = 50 kN, F_{min} = 5 kN and the ration $\Delta F = F_{min}/F_{max} = 0,1$ was checked. The test was performed at the frequency 50 Hz. Replicas were made in intervals $3x10^3$ during the first three measurements, then the step was increased to $6x10^3$ cycles. After $210x10^3$ the test was stopped and final impressions were made. All impressions were made in critical cross section at the point of maximum tensile stress. In the end we made ground section from the test piece on which we observed the process of occurrence of cracks and their size.

Measurements with crack gauges

For measuring the crack lengths greater than approximately 0,2 mm we used crack gauges made by Measurement Group Vishay Type TK-09-CPB02-005. The measuring gauges were glued to gear test pieces at approx. 0,11 - 0,2 mm from the edge as shown in Figure 2.

Measurements and fatigue

During the next step we started the fatigue test on the gear test piece at the room temperature and at 50 Hz frequency with the following loading: maximum force F_{max} = 50,1 - 50,2 kN, distance between supports L=294 mm and ratio $R = F_{max}/F_{min} = 0,1$. During fatigue we measured by means of strain gauges the change of strain as function of number of cycles in the area of micro cracks. The basic aim of the measurements was to obtain a correlation between the micro crack length and stresses and/or how to conclude from the stress what happen in the material, when the crack occurs.

Because of the possibility of examination and because of comparison of different methods the following measuring components were glued in addition to the photo elastic plastic sheet on the gear test piece front side:

- one strain gauge on the tooth flank in the critical cross section,
- another strain gauge on the rear side in the critical cross section.

Contemporary techniues

Vibro-acoustics We establish that the crack in the tooth root causes changes in tooth stiffness. The sound measuring was made on gear wheel with different cracks and without them. [5].

Stereo-photogrametry This method is suitable for accurate measuring of the position in space, three-dimensional displacement and with high number of points even measuring of object shape and deformation and is also very convenient for measuring cracks on the gear tooth's [4].

Conclusion

It can be seen above that for accurate calculations of service life of gearing the use of deterministic methods according to different standards is not sufficient. Therefore, for calculations we have developed the gear stress intensity factor *Z* that takes into account not only the stress of homogeneous material in critical cross section but also the stress concentration due to defects occurring there. On the basis of the factor *Z* we have developed the generalized model of growth of cracks by means of which it is possible to calculate accurately the actual service life. With our models we have reached the deviation of 5 - 12 % from experimental results, which is a very good accuracy in such calculations.

For confirm mathematical models we propose different experimental methods.

References

[1] B. Aberšek, and J. Flašker: *How gears break,* Wit Press, Southampton, Boston, (2004)

[2] B. Aberšek and J. Flašker: *Numerical methods for evaluation of service life of gear*, *Int. Journal for Num. Meth. in Eng.*, Vol. 38, 2531-2545, (1995).

[3] B. Aberšek, J. Flašker and S. Glodež *Review of mathematical and experimental models for determination of service life of gears*. *Eng. fract. mech.*. vol. 71, iss. 4/6, 439-453, (2004).

[4] B. Aberšek, N. Gubeljak, J. Predan and J. Flašker *Stereophotogrametric determination of crack initiation and propagation in tooth root. Key eng. mater.*, vols. 452-453, 761-764, (2010)

[5] A. Belšak, M. Ploj Virtič, B. Aberšek and J. Flašker *Vibration diagnostics of a gear unit. Key eng. mater.,* vol. 251-252, 457-462. (2003).

© (2012) Trans Tech Publications, Switzerland
doi:10.4028/www.scientific.net/KEM.488-489.731

Load-rate sensitivity in 1D non-linear viscoelastic model

Ivica Kožar[1, a], Joško Ožbolt[2,b] and Tatjana Pecak[1,c]

[1]Faculty of Civil Engineering University of Rijeka, Croatia

[2]Institut für Werkstoffe im Bauwesen Universität Stuttgart, Germany

[a]ivicak@gradri.hr, [b]ozbolt@iwb.uni-stuttgart.de, [c]tatjana.pecak@gradri.hr

Keywords: softening material, strain-rate, dynamic loading, bifurcation, localization, Kelvin material model.

Abstract. Load-rate sensitivity of material is important in impact and other dynamic loadings. It is assumed that the strain-rate sensitivity is not a material property but comes out naturally from dynamic equilibrium equations. Material is assumed non-linear, similar as used in the microplane model for quasi-brittle materials, and viscoelastic arranged into Kelvin scheme. The scheme is the simplest possible and consists of two Kelvin bars in series with an optional mass between them (Maxwell bars are considered in our previous paper). Loading is uniaxial tension with changing intensity in time, asymptotic or harmonic. The resulting differential equation (equations when a mass is present) is non-linear and stiff. Equations have been solved numerically using adaptive and Radau integration. For equal parameters nonsymmetrical (together with symmetrical) results could be obtained, meaning localization is possible without the localization initiator. System response is strongly influenced with the presence of a mass. Phase diagram show that some combination of parameters and loading demonstrate chaotic behavior.

Introduction

The paper is extension of our previous work [1] where a non-linear Maxwell bar model is described. It was concluded there that the model could exhibit localization without a localization initiator. Localization appeared only for sufficiently high loading rate. In contrast to this simple model, in [2] the influence of loading rate is shown on a rather complex model of a 3-D beam subject to impact load. However, the influence of some relevant parameters can be better studied on relative simple models.

Maxwell material model is traditionally connected with fluids but also some solids are described with it (e.g. glass) [3]. Traditional rheological description of solids includes Kelvin material model incorporated in some way. That is the reason for extension of the previous work hoping that similar results could be obtained with the Kelvin model. As before, the elastic component of the model is non-linear elastic, similar to the microplane material model for concrete, and the viscous component is linear. The model consists of two equal units connected in series with or without a mass in between. This is the simplest model of a bar under axial loading.

The loading is function of time and it is imposed through displacement control of the end of the bar (force control requires Neumann boundary conditions and displacement control requires simpler Dirichlet boundary conditions). Two types of loading have been used in the analysis: one starting from zero and asymptotically approaching the prescribed final value, and the other changing harmonically with the amplitude equal to the final value of the first type of loading.

Four cases have been analyzed: the bar without a mass and the bar with a mass, both under the asymptotic and under the harmonic loading. Different combinations of parameters demonstrate different possible responses of the model, some of them chaotic and some with attractors.

Non-linear Kelvin bar model described here is somewhat simpler (needs less differential equations) but equally interesting. Models that are more complicated are subject of further investigations.

Adopted material model

The model consists of two Kelvin units coupled in series (see Fig. 1). The elastic part is non-linear, similar to microplane model [4], and the viscous part is linear. The point where the two Kelvin bars connect may have a mass attached to it. The model has only one unknown displacement, since the end displacement ε_a is given (Maxwell model would have three unknowns).

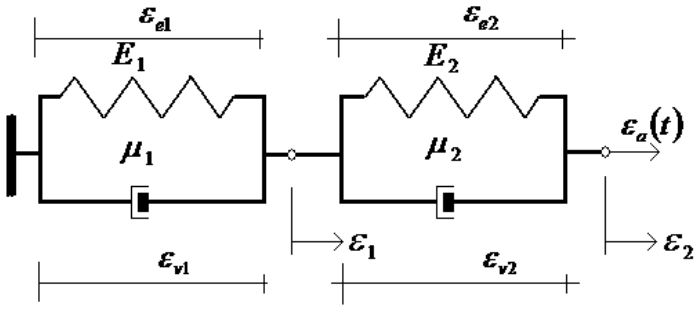


Figure 1. Kelvin model consisting of two non-linear bars.

Loading

Analysis has been performed with two types of loading: limited loading and harmonic loading. The first one represents sudden impact and the other one classical dynamic loading. Both loadings have first derivative. Here are shown results only for harmonic type of loading (see below).

Limited loading. Limited loading can be imposed using Heaviside function as in [5]. This type of description represents only the high-rate loading. In order to be able to vary the rate of the loading parametric representation has been introduced:

$$\varepsilon_a(t) = \varepsilon_0^2 \frac{ct^3}{1+ct^3\varepsilon_0} \qquad \text{with property} \qquad \lim_{t\to\infty} \varepsilon_a(t) = \varepsilon_0 . \tag{1}$$

where c is the rate varying parameter.

Harmonic loading. Harmonic loading has fixed amplitude ε_0 and adjustable period that is controlled with parameter p:

$$\varepsilon_a(t) = \frac{\varepsilon_0}{2}\left(\sin\left(\frac{2t-p}{2p}\right)+1\right). \tag{2}$$

Non-linear elastic viscous model without mass. Kinematic and equilibrium equations for the fodel shown in Fig. 1 are:

$$\varepsilon_{ei} = \varepsilon_{vi} = \varepsilon_i , \quad i=1,2 \quad \text{and} \quad \varepsilon_1 + \varepsilon_2 = \varepsilon_a , \tag{3}$$

$$\sigma_{ei} + \sigma_{vi} = \sigma_i , \quad i=1,2 \quad \text{and} \quad \sigma_1 = \sigma_2 , \tag{4}$$

$$\sigma_{ei}(\varepsilon_{ei}) = E_i w(\varepsilon_{ei}) \quad \text{and} \quad \sigma_{vi} = \mu_i \dot{\varepsilon}_{vi} , \quad i=1,2. \tag{5}$$

After appropriate substitutions the resulting differential equation reads:

$$\frac{d}{dt}\varepsilon_1(t) = \frac{1}{\mu_1+\mu_2}\left(E_2 w\big(\varepsilon_a(t)-\varepsilon_1(t)\big) - E_1 w\big(\varepsilon_1(t)\big) + \mu_2 \frac{d}{dt}\varepsilon_a(t)\right) \tag{6}$$

where $w(x)=x\ exp(-x/a)$ and $a=0.001$. This equation belongs to the class of 'stiff' differential equations and requires special integration techniques. Two methods are used for more confidence in results, adaptive and Radau integration. For completely symmetric parameters $E_1=E_2=1.00$, $\mu_1=\mu_2=0.05$ symmetric responses are obtained where $\varepsilon_1(t)=\varepsilon_2(t)$. For slightly different symmetric parameters $\mu_1=\mu_2=0.01$ we have managed to obtain asymmetric results as shown if Fig. 2.

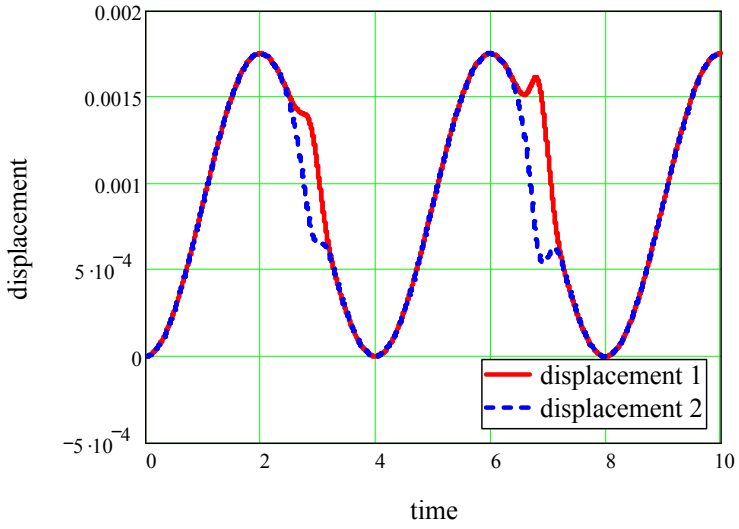


Figure 2. Displacements 1 (ε_1) and 2(ε_2) in time.

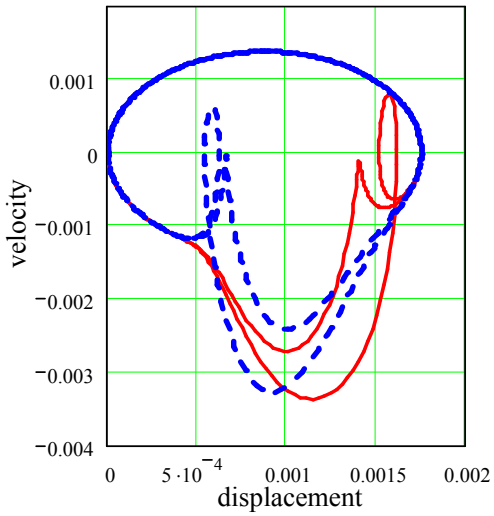


Figure 3. The phase diagram.

Figure 2. shows bifurcation in otherwise symmetrical results (symmetric solution still exists, only it is not the most probable one). Fig. 3. presents the phase diagram of Fig. 2. It is evident that the solution is dominantly periodic but with some non-periodicity within the periodic bounds. With proper parameters bifurcation can be almost anywhere and of almost any size. Results with similar characteristics are obtained with limit loading.

Non-linear elastic viscous model with mass. This model has an additional mass between the two Kelvin bars. The second part of Eq. 4 reads:

$$\sigma_1+\sigma_2+m_1\frac{d^2}{dt^2}\varepsilon_1=0\,. \tag{7}$$

With appropriate transformations we arrive to the system of two non-linear differential equations:

$$\frac{d}{dt}\varsigma_1(t)=\frac{1}{m_1}\left(E_2 w\left(\varepsilon_a(t)-\varepsilon_1(t)\right)-E_1 w\left(\varepsilon_1(t)\right)+\mu_2\frac{d}{dt}\varepsilon_a(t)-(\mu_1+\mu_2)\varsigma_1(t)\right), \tag{8}$$

$$\frac{d}{dt}\varepsilon_1(t)=\varsigma_1(t)\,, \tag{9}$$

with function w as before. Symmetric results could be obtained only for rather large viscosity ($\mu_1=\mu_2=0.5$). For completely symmetric parameters with smaller viscosity ($E_1=E_2=1.00$, $\mu_1=\mu_2=0.02$) solution with bifurcation (localization) may be detected as shown if Fig. 4.

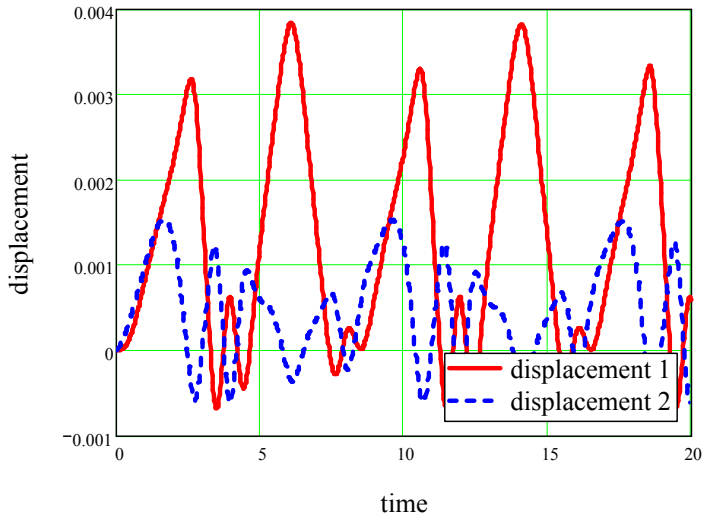


Figure 4. Displacements 1 (ε_1) and 2(ε_2) in time.

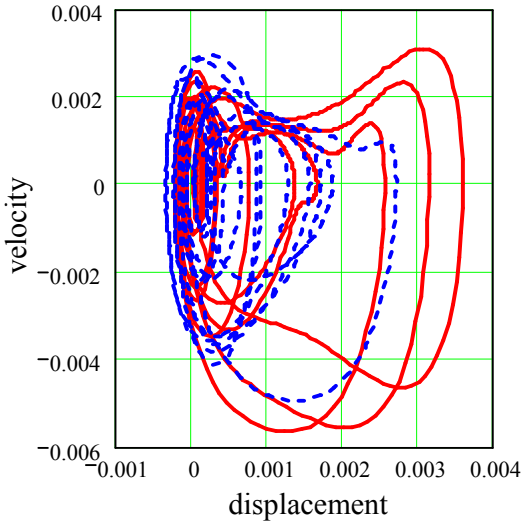


Figure 5. The phase diagram.

Fig. 5 demonstrates chaotic behavior of the system. Smaller mass tends towards periodic solution and larger mass tends towards chaos. Under the limit load, phase diagram shows two attractors in the place of chaos.

Summary

The simple two-part model from the paper shows expected sensitivity to the rate of loading as some quasi-brittle materials. There is no need for special material parameters, dynamic equations are sufficient to describe localization in the material.

References

[1] I. Kožar, J. Ožbolt: Computers and Concrete, Vol. 7 (2010), p. 317-329.

[2] V. Travaš, J. Ožbolt, I. Kožar: International Journal of Fracture, Vol. 160 (2009), p.31- 41.

[3] E.J. Barbero: *Finite Element Analysis of Composite Materials* (CRC Press, Taylor & Francis Group, 2008).

[4] J. Ožbolt, Y. Li, I. Kožar: International Journal of Solids and Structures, Vol. 38 (2001), p. 2683-2711.

[5] F.V. Souza, Y-R. Kim, G.A. Gazonas, D.H. Allen: Composites: Part B, Vol.40 (2009), p. 483 – 494.

© (2012) Trans Tech Publications, Switzerland
doi:10.4028/www.scientific.net/KEM.488-489.735

Effect of tensile dwell on low cycle fatigue of cast superalloy Inconel 792-5A at 800°C

Miroslav Šmíd[a], Karel Obrtlík[b], Martin Petrenec[c], Jaroslav Polák[d]

Institute of Physics of Materials, AS CR, Žižkova 22, Brno 616 62, Czech Republic

[a]smid@ipm.cz, [b]obrtlik@ipm.cz, [c]petrenec@ipm.cz, [d]polak@ipm.cz

Keywords: nickel base superalloys, elevated temperatures, low cycle fatigue, dwells.

Abstract. Effect of tensile dwell on low cycle fatigue of cast Inconel 792-5A is studied in symmetrical strain cycling at 800°C. Cyclic hardening/softening curves, cyclic stress-strain curves (CSSC) and fatigue life curves were obtained in continuous cycling and in cycling with tensile dwells. Dwells have slight effect on hardening/softening curves at high strain amplitudes. CSSC in cycling with dwells is shifted to lower stress amplitudes. No significant effect of dwells on Basquin curves is observed. Density of slip markings in continuous cycling is significantly higher in comparison with cycling with dwells. Samples cycled with dwells are typical of high density of secondary cracks, although sporadic slip markings were also found.

Introduction

Inconel 792-5A (IN 792-5A) is cast polycrystalline nickel-based superalloy with wide applications in aerospace and power generation industry. Especially turbine blades, components with requirement of high reliability, are subjected to complex stress conditions. Straining of these components is a result of temperature gradients during start-up and shut-downs, vibrations caused by service, and centrifugal forces. Low cycle fatigue with introduction of dwells, is a reasonable way how to simulate fatigue-creep interaction in service [1].

Goswami [2,3] summarized the effect of dwells on low cycle fatigue behavior of numerous materials including superalloys. It was found that the fatigue behavior of superalloys depends on the type of dwells. Some materials are sensitive to tensile and/or compression dwells. In some cases dwells have insignificant or even beneficial influence on fatigue life. Sporadic experimental data on the fatigue behavior of IN 792-5A can be found in continuous cycling [4-6] while the effect of dwells wasn't studied so far. The aim of this paper is to investigate influence of tensile dwells on the fatigue life, stress-strain behaviour and cyclic strain localization under symmetrical total strain cycling at 800°C.

Experimental

Cast polycrystalline superalloy IN 792-5A was provided by PBS Velká Bíteš as conventionally cast rods. Chemical composition is 12.28 Cr, 8.87 Co, 3.98 Ti, 3.36 Al, 4.12 Ta, 4.1 W, 1.81 Mo, 0.1 Nb, 0.16 Fe, 0.031 Zr, 0.078 C, 0.015 B, the rest is Ni (all in wt. %). Structure consists of coarse dendritic grains with carbides at grain bondaries and shrinkinge pores up to 0.5 mm in diameter - see [7,8] for comparison. The linear intercept method revealed average grain size 3 mm. Characteristic microstructure of the superalloy comprises γ matrix strenghtened by γ′ precipitates, which have bimodal shape. They are distributed in the form of spherical particles of average diameter 0.190 μm and near cuboidal particles with edge length of 0.630 μm. The low cycle fatigue test with tensile dwells were conducted on button-end specimens with gauge length 15 mm and diameter 6 mm. Fatigue tests were performed in a computer controlled electro-hydraulic MTS testing system at total strain rate of 2.10^{-3} s^{-1} with fully reversed total strain cycle (R_ε= - 1). The

strain was measured and controlled with a sensitive extensometer with a 12 mm base. The hysteresis loops for selected numbers of cycles were recorded. Subsequently plastic strain amplitude and stress amplitude were evaluated. Heating was provided by a three-zone resistance furnace controlled by thermoregulators. Specimen temperature was monitored by three thermocouples.

Selected specimens were mechanically and electrolytically polished before straining to obtain sufficiently smooth surface for subsequent observation, which was performed by scanning electron microscope TESCAN Lyra 3XMU with FEG source.

Results and Discussion

Figure 1a shows the stress amplitude as a function of cycles from continuous cycling held at different total strain amplitudes. IN 792-5A exhibits stable cyclic behavior, which is in agreement with previous works on the material at this temperature [5,8]. The final stage of the fatigue life with distinct cyclic softening is caused by the magistral fatigue crack propagation. Cyclic stress response is significantly influenced by large scatter of elastic moduli of individual specimens originating from coarse macrostructure. Namely, the gauge length can consist of several grains only. The fatigue test with the highest stress amplitude shows initial cyclic fatigue hardening with subsequent short saturation and mild cyclic softening. Stable stress response is observed for medium and low amplitudes. Hardening/softening curves of tests with tensile dwells are shown in Figure 1b. Stable cyclic behavior was found in the low amplitude domain. Initial cyclic softening, followed by saturation is typical for high and medium amplitudes.

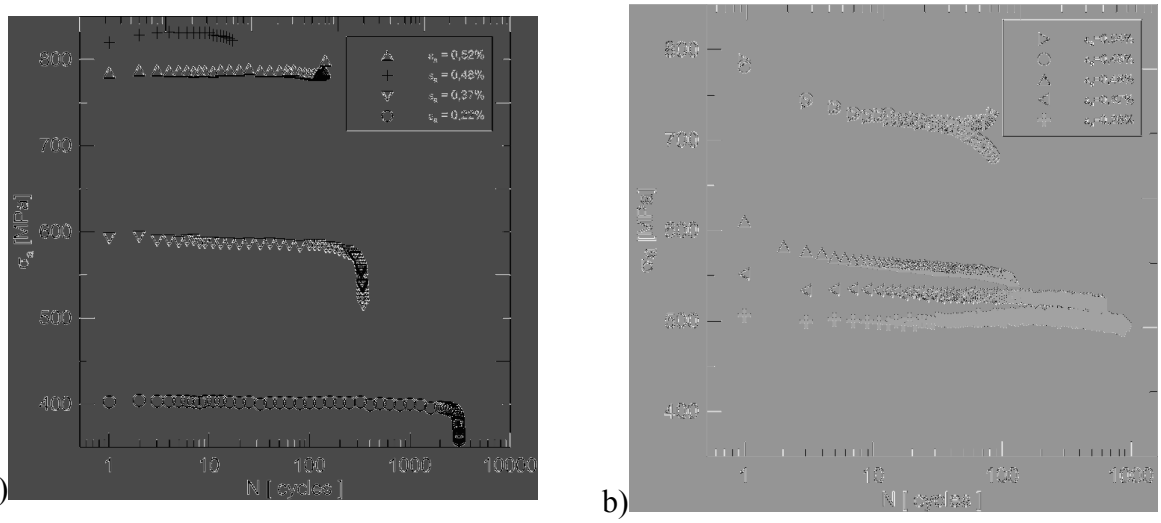


Fig. 1 Cyclic hardening/softening curves for a) continuous cycling and b) cycling with 10 min dwells.

Cyclic stress-strain curves (CSSCs) are presented in Fig. 2 as the stress amplitude σ_a versus the plastic strain amplitude ε_{ap} at half life for both types of experiments. Experimental data were fitted by the power law

$$\log \sigma_a = \log K' + n' \log \varepsilon_{ap} \qquad (1)$$

Material parameters of equation (1), fatigue hardening coefficient K' and fatigue hardening exponent n', were evaluated by regression analysis and their values are presented in Table 1. The effect of dwells is clearly visible in Fig. 2. The CSSC for continuous cycling is shifted to higher stress amplitudes in comparison with that obtained in cycling with dwells. The hardening/softening behavior of IN 792-5A in continuous cycling differs from that in cycling with dwells – see Fig. 1. The cyclic softening found in fatigue tests with dwells can contribute to the CSSC shift in Fig. 2.

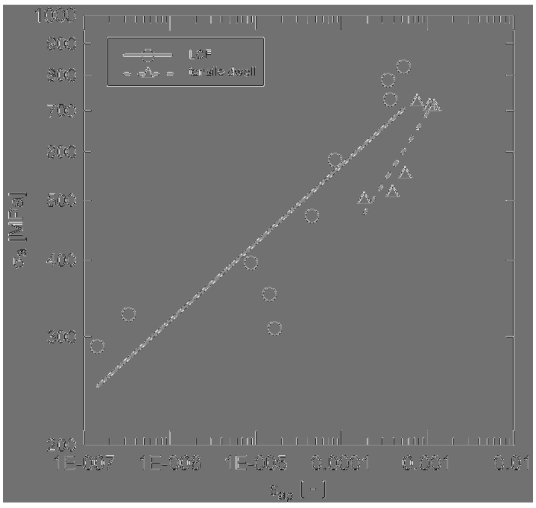


Fig. 2 Cyclic stress strain curves.

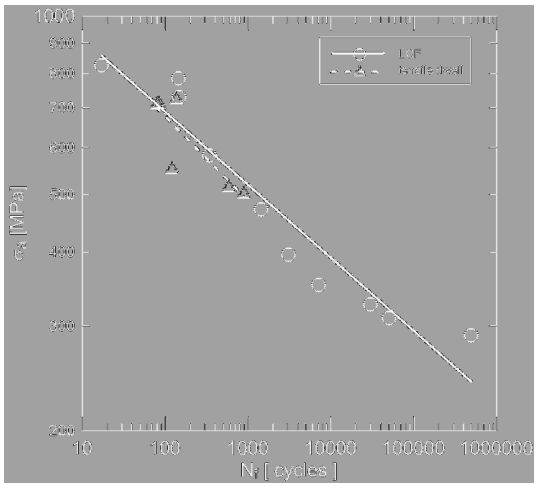


Fig. 3 Basquin curves.

Fatigue life curves in the representation of stress amplitude σ_a at half life vs the number of cycles to fracture N_f are shown in Fig. 3. Experimental data were fitted with the Basquin law:

$$\sigma_f = \sigma'_f \left(2N_f\right)^b \tag{2}$$

Fatigue strength coefficient σ'_f and fatigue strength exponent b were evaluated by regression analysis and their values are presented in Tab. 1. It can be seen from Fig. 3 that both Basquin curves are identical within the scatter of experimental data. Thus, Basquin curves are not sensitive to tensile dwells in IN 792-5A.

Tab. 1. Values of paramaters of CSSC and Basquin curves of IN 792-5A.

	K' [MPa]	n' [-]	σ'_f[MPa]	b [-]
LCF	1829	0.126	1216	-0.123
Dwell	3239	0.222	1303	-0.142

Surface relief of selected specimens was studied in SEM after cyclic loading. Specimens cycled at high total strain amplitudes were preferentially chosen. Figure 4 shows surface relief of a specimen strained in continuous cycling. Well developed persistent slip markings (PSMs), resulting from cyclic plastic strain localization, are apparent in majority of grains in the gauge length. One slip system along planes of the type {111} is activated in numerous grains and several suitably oriented grains to the stress axis show multiple slip. The length of well developed PSMs was hundreds of micrometers going over whole grains. Secondary fatigue cracks along grain boundaries are documented. Surface relief of a specimen after cyclic loading with tensile dwells is shown in Figure 6. It is clearly obvious that cyclic strain localization is not so well developed as in the case of continuous cycling. Just several PSMs occurred in few grains. On other hand the density of fatigue cracks along grain boundaries was significantly higher in cycling with dwells. The cracks are predominantly oriented nearly perpendicular to the stress axis. It can be suggested that introduction of dwells changes the fatigue damage mechanisms. Namely, the role of PSMs as fatigue crack initiation sites is less important and grain boundary crack nucleation is the dominant damage mechanism. Similar findings have been published recently [9,10]

Conclusions

The results of low cycle fatigue tests with continuous cycling and with tensile dwells on cast polycrystalline Inconel 792-5A at temperature 800 °C can be summarized as follows:

(i) Stable cyclic stress response in continuous cycling tests changes into moderate cyclic softening with introduction of dwells.

(ii) Fatigue life curves of IN 792-5A in the Basquin representation law are not dwell sensitive.

(iii) Introduction of tensile dwells results in distinct changes in surface relief topography. Formation of persistent slip marking is reduced and the grain boundary crack initiation becomes more frequent.

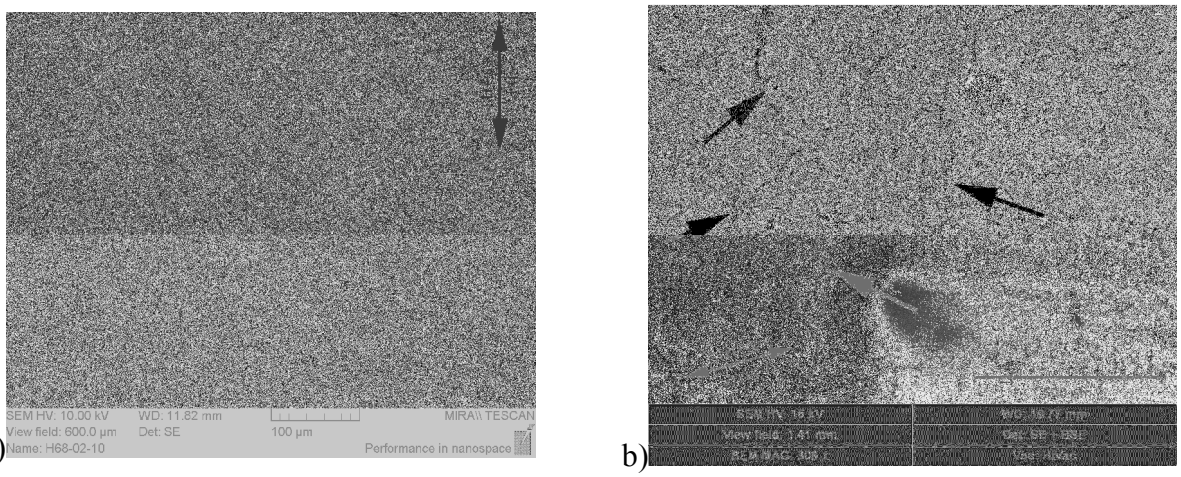


Fig 4 SEM micrographs of surface reliefs of a) continuous cycling (ε_a = 0,51%) and b) cycling with dwells (ε_a = 0,49%). Arrows show cracks along grain boundaries.

Acknowledgement: This research was financially supported by the grants Nos. P2004/11/1453 and P107/11/2065 of the Grant Agency of the Czech Republic.

References

[1] P. Rodriguez, K. Bhanu Sankara Rao: *Progr. Mater. Sci.*, Vol. 37, (1993), p. 403-480.

[2] T.Goswami: *Int. J. Fatigue*, Vol. 21, (1999), p. 55-76.

[3] T. Goswami, H. Hänninen: *Materials and design*, Vol. 22, (2001), p. 199-215.

[4] K. Obrtlík, M. Petrenec, J. Man et al.: *J. Mat. Sci*., Vol. 44, (2009), p. 3305-3314.

[5] T. Beck, G. Pitz, K.-H. Lang et al.: *Mater. Sci. Eng. A*, Vol. 234-236, (1997), p. 719-722.

[6] P. Shahinian, K. Sadananda: *Mater. Sci. Eng. A*, Vol. 108, (1989), p. 131-140.

[7] M. Petrenec, K. Obrtlík, J. Polák: *Key Eng. Mater.*, Vol. 348-349, (2007), p. 101-104.

[8] M. Petrenec, K. Obrtlík, J. Polák, J. Man: *Key Eng. Mater.*, Vol. 345-346, (2007), p. 383-386.

[9] K. Obrtlík, J. Man, M. Petrenec et al., in: *Proceedings on 12th International Conference on Fracture*, NRCan – CANMET, 2009.

[10] D.W. Kim, J.H. Chang, W.S. Ryu: *International Journal of Pressure Vessels and Piping*, Vol. 85, (2008), p. 378-384.

© (2012) Trans Tech Publications, Switzerland
doi:10.4028/www.scientific.net/KEM.488-489.739

Assessment of Existing Concrete Buildings

L. Nobile[1, a], M. Bonagura[1,b] and V. Bartolomeo[1,c]

[1]DICAM Department, University of Bologna, Italy

[a]lucio.nobile@unibo.it, [b]mario.bonagura@unibo.it, [c]veronica.bartolomeo@unibo.it

Keywords: Concrete strength, non-destructive tests (NDT), ultrasonic pulse velocity (UPV), rebound index (RI), SonReb combined methods.

Abstract. Assessment of concrete strength in existing structures is a very fundamental task today, because the mechanical characteristics are strictly connected to seismic protection and performance estimation of the material. To this aim, several compression tests has been carried out on drilled core samples in conjunction with different NDT methods. The activity presented in the paper is still under development and is intended as a reference in the choice of the methods and correlations for structural survey of existing buildings.

Introduction

The evaluation of structural performance of existing concrete buildings, built according to standards and materials quite different to those available today, requires procedures and methods able to cover lack of data about mechanical material properties and reinforcement detailing. This issue is more relevant when seismic zones are concerned and structural strengthening needs to prevent failures due to earthquakes. Recent seismic codes give relevance to procedure and methods to establish the performance levels of existing structures. To this end detailed inspections and test on materials are required. It is recognised that different levels of knowledge (KL) can be reached depending on available technical design reports, structural drawings and material acceptance data: KL1 Limited Knowledge, KL2 Normal knowledge, KL3 Full Knowledge. As a consequence tests on drilled cores are required; on the other end, it is stated that non-destructive testing (NDT) cannot be used as the only mean to get structural information, but can be used in conjunction with destructive testing (DT) by a representative correlation between DT and NDT.

The aim of this study is to verify the accuracy of some formulas of correlation available in literature between measured parameters, i.e. rebound index, ultrasonic pulse velocity and strength (SonReb Method). To this end a relevant number of DT tests and NDT tests has been performed on many school buildings located in Cesena (Italy). The above relationships have been assessed on site correlating ND test results to strength of core drilled in adjacent locations.

On site concrete strength

The experimental campaign for the assessment of onsite concrete strength has been carried out in the framework of research grant in partnership with the City of Cesena (Italy). For each points of investigation, three concrete core samples were taken to be tested (specifications to use core testing are given in several standards, e.g. ASTM C/42-1988, ACI 228-1988 and in Italy UNI EN 12504-2002). Afterwards all the samples were tested in compression. Even if core testing represent the most reliable method to evaluate the concrete strength, it has to be noted that the values obtained on laboratory are slightly different from the actual onsite. For this reason the core samples strength f_{core} are converted in the corresponding onsite compression strength f_c through the well known relationship:

$$f_c = \frac{2{,}5}{\left(1{,}5 + \frac{h}{d}\right)} \cdot f_{core} \tag{1}$$

Where h represents the height and d the diameter of the core cylinder samples tested in laboratory.

Non Destructive Methods (NDT) for assessment of concrete strength

1. Rebound Hammer

Rebound hammer is a method developed in 1948 by the Swiss engineer Ernst Schmidt for testing concrete based upon the rebound principle. This NDT method is described in ASTM C805, BS 1881:2002, DIN 1048 and UNI EN 12504: 2001. The results of the rebound hammer test is the Rebound Index (RI), an adimensional parameter employed to measure the surface hardness that can be connected to the compression strength of concrete. This test is very fast and simply to perform but presents too much drawbacks linked to geometrical characteristics and phoenomena of deterioration of the material. For this reason, two calibration curves are taken into account: one given directly by the instrumentation producer and the other one taken from literature [1], that is:

$$R_c = 0{,}0034 \cdot (RI)^{2{,}5245} \quad \text{[MPa]} \quad [1] \tag{2}$$

2. Ultrasonic Pulse Velocity (UPV)

The Ultrasonic pulse velocity (UPV) method is a stress elastic wave propagation method that involves measuring the travel time (and as a result the *virtual velocity V*), over a known path length, of a pulse of ultrasonic waves. This NDT method is able to provide quantitative and qualitative information and is described in ASTM C597, BS 1881-203:1986, DIN/ISO 8047: 1983 and UNI EN 12504-4:2004. It is well known that also the UPV method can be influenced by different variables (i.e. path length, age of the concrete, different mixture proportion, moisture content of the concrete etc..). Therefore between the numerous correlations proposed to limit the uncertainty of this method, two of the most reliable formula [2,3] are taken into account, that are:

$$R_c = (-307 + 0{,}157 \cdot V) / 10 \quad \text{[MPa]} \quad \text{(Giannini [2])} \tag{3}$$

$$R_c = 1{,}88 \cdot 10^{-21} \cdot (V)^{6{,}184} \quad \text{[MPa]} \quad \text{(Hisham-Qasrawi [3])} \tag{4}$$

3. SonReb Combined method

The poor reliability of rebound hammer and ultrasonic pulse velocity due to different aspects could be partially contrasted by using both methods together. One of the most employed NDT combined methods in practice is the SonReb method, described in RILEM 7 NDT and 43 CND. This technique achieves an improvement of the accuracy by the use of various *correction factors* taking into account the influence of different concrete mixture proportion. Several correlation equations have been developed and presented by numerous authors. In this paper some of the most reliable and employed formulations available in literature are considered [4,5,6,7]:

$$R_c = 7{,}695 \cdot 10^{-11} \cdot (RI)^{1{,}4} \cdot (V)^{2{,}6} \quad \text{[MPa]} \quad \text{(Giacchetti-Lacquaniti [4])} \tag{5}$$

$$R_c = 1{,}2 \cdot 10^{-9} \cdot (RI)^{1{,}058} \cdot (V)^{2{,}446} \quad \text{[MPa]} \quad \text{(Di Leo-Pascale [5])} \tag{6}$$

$$R_c = 0{,}0286 \cdot (RI)^{1{,}246} \cdot (V)^{1{,}85} \quad \text{[MPa]} \quad \text{(Gasparirik [6])} \tag{7}$$

$$R_c = 0{,}9 \cdot (RI) + 0{,}022 \cdot (V) - 94 \quad \text{[MPa]} \quad \text{(Tanigawa-Baba-Mori [7])} \tag{8}$$

The main distinction between this formulations lies especially in the different relevance given to the correction factors and the two parameters determined onsite: the rebound index (*RI*) and the virtual ultrasonic pulse velocity (*V*). For this reason it seems to be interesting to take into account also the results obtained by combining two or more expressions (Technical Standards of Toscana Region).

Table 1. Summary of collected data and correlations for onsite concrete strength.

Onsite strength [MPa]	Rebound Hammer [MPa]		UPV [MPa]		Sonreb combined method [MPa]			
f_c	$R_{c\ (IR)}$	Eq. 2	Eq. 3	Eq. 4	Eq. 5	Eq. 6	Eq. 7	Eq. 8
18,34	34,00	24,62	13,73	4,17	11,12	14,92	17,26	1,01
19,60	39,50	29,00	15,30	5,17	13,34	17,40	19,96	5,41
19,81	32,00	21,69	20,87	10,48	15,28	20,38	21,37	9,42
22,41	42,00	30,83	18,60	7,93	16,51	21,14	23,38	10,88
26,83	35,00	25,29	24,25	15,51	19,66	25,42	25,97	16,15
30,71	44,00	34,18	23,78	14,71	22,67	28,19	29,60	19,64
31,29	38,00	28,18	24,09	15,24	20,68	26,37	27,20	17,33
59,33	56,50	47,80	33,59	40,96	42,01	48,65	47,46	38,69

Comparisons

An experimental testing program (see Tab.1) is carried out to evaluate the reliability of three of the most used NDT methods for evaluation of onsite concrete compressive strength: rebound hammer tests, ultrasonic pulse velocity (UPV) and Sonreb combined methods. A poor correlation between rebound hammer test and concrete strength was evidenced for all the results. Fig.1a shows for the two correlation curves a similar progress even if they provide values that on average overestimate the actual strength. Better results can be found employing the ultrasonic pulse velocity methods (UPV) and in particular with the Eq. 3. In fact for strengths minor than 27 MPa, the curve stay very close to the idealized one (Fig.1b).

With regards to the SonReb combined method all the expressions taken into account have shown a progress similar to the concrete strength curve (Fig.3). Excluding the Eq. 8 that presents values too much far from the actual onsite, the other three expressions are very close to the referenced f_c curve. In particular for the Eq. 6 and Eq. 7 it can be observed that the mean percentage deviation is significant lower than the other one (Fig.2a), i.e. respectively 10,7% and 7,48% while for Eq. 5 is 29,56%. This value strongly decreases if the range of data considered is included between 20MPa and 32MPa. Finally if we consider as SonReb curve the mean values of the first three formulations (as Technical Standards of Toscana Region suggests to take into account), it can be seen that each data lay close to the f_c curve.

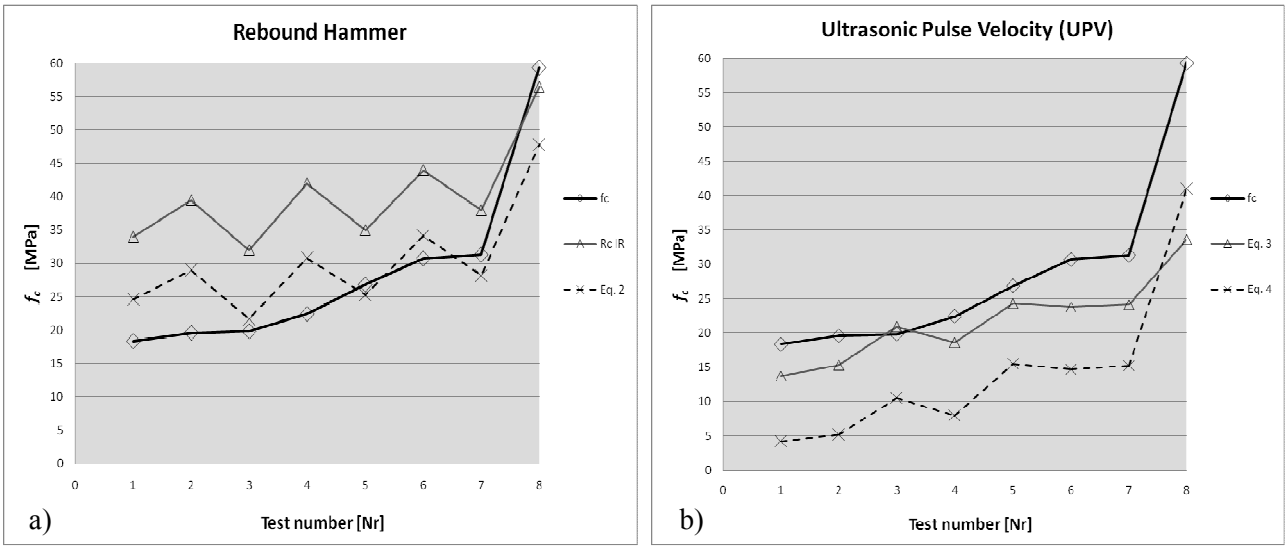


Fig.1. Diagrams 'f_c – *Test number'* experimentally obtained for Rebound Hammer (a) and UPV (b).

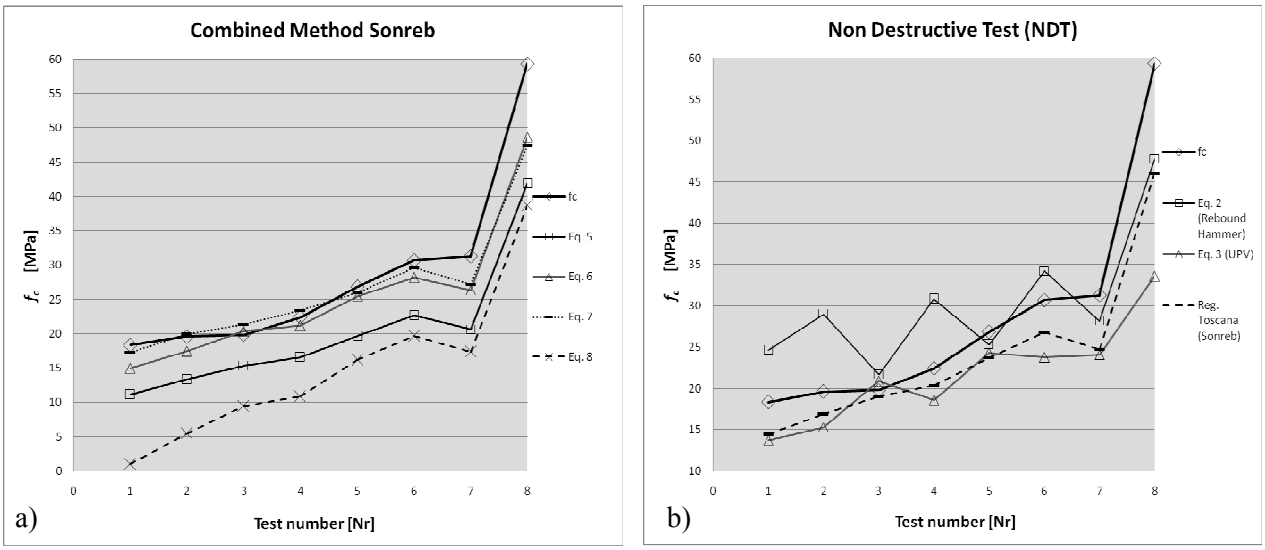


Fig.2. Diagrams 'f_c – *Test number*' experimentally obtained for Sonreb method (a) and a comparison of the most reliable formula for every NDT methods (b).

Conclusion

The results of this in-place NDT testing program have shown an unreliable behaviour for the rebound hammer test and ultrasonic pulse velocity method for the assessment of the mechanical characteristics of existing concrete. The reliability of this two techniques increases if they can be used in a combined method, i.e. SonReb (Fig.2b). In particular, combining different correlation formulas (Fig.3) there aren't any overestimation, and this behaviour can ensure higher safety standards.

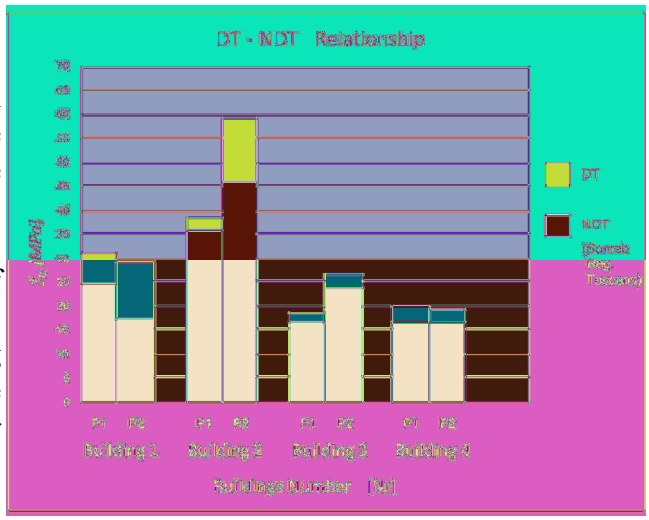


Fig.3. Diagram 'f_c – *Buildings number*' experimentally obtained that highlight the reliability of SonReb method.

Acknowledgments

This research has been supported by University of Bologna, Italy.
The authors gratefully acknowledge the City of Cesena for supporting the present work.

References

[1] G. Menditto, S. Menditto: *Indagini semidistruttive e non distruttive nell'ingegneria civile: disciplina tecnica, applicative e normative*, Pitagora Editrice, Bologna, Italy (2008).

[2] R. Giannini et al. in: *10° Congresso Nazionale AIPnD*, Ravenna, Italy (2003).

[3] Y.H. Qasrawi in: *Cement and Concrete Research*, Vol. 30, pp. 739-746 (2000).

[4] R. Giacchetti, L. Lacquaniti in: *Nota tecnica 04* (1980).

[5] A. Di Leo, G. Pascale in: *Convegno Sistema e Qualità e Prove non Distruttive per l'Affidabilità e la Sicurezza delle Strutture Civili*, Bologna, Italy (1994).

[6] J. Gasparirik in: *Quaderno didattico*, edited by AIPnD, Brescia, Italy (1992).

[7] Y. Tanigawa, K. Baba, H. Mori in: *ACI SP 82*, Vol. 1, pp. 57-65 (1984).

© (2012) Trans Tech Publications, Switzerland
doi:10.4028/www.scientific.net/KEM.488-489.743

Residual Fracture Toughness of Concrete Subject to Elevated Temperatures

YU Jiangtao[1,a], YU Kequan[1,b], LU Zhoudao[1,c]

[1]Research Institute of Engineering and Disaster Reduction, Tongji University, Shanghai, China
[a]yujiangtao@tongji.edu.cn, [b]zjzjykq@163.com, [c]luzhoudao@163.com

Keywords: fracture toughness, post-fire, elevated temperature, wedge splitting

Abstract. This paper presents an experimental investigation on the variation of residual fracture toughness of concrete after being exposed to elevated temperatures. A total of 60 specimens, with a uniform size of 200x200x230mm and precast notches of 80mm in height, were heated to constant temperatures of 65℃, 120℃, 200℃, 300℃, 350℃, 400℃, 450℃, 500℃ and 600℃ respectively. After cooling, standard wedge splitting tests, according to the corresponding Chinese Specification, were employed. The results indicate that the elevated temperature has significant influence on the residual fracture toughness of concrete. The magnitude of fracture toughness decreases drastically with increasing temperature. Additionally the relationship between residual fracture toughness and weight loss of specimens with respect to temperatures is also investigated.

Introduction

As to the reinforced concrete structures frequently subjected to elevated temperature environments, for example, cooling towers in the power plants or prestressed concrete pressure vessels in nuclear industry, the information about the mechanical properties such as value of strength, stiffness, toughness or brittleness is inevitably required for design. Concrete structures exposed to fire will suffer damage to some extent. Establishing the relationship between residual mechanical properties and temperatures will be helpful for civil engineers to identify the level of damage. Most studies concentrated on the reduced strength or modulus of concrete subjected to elevated temperatures. So far, limited test focused on the fracture behavior parameters (fracture energy and fracture toughness), which are very useful for the post-fire safety assessment, structural analysis and numerical simulation.

Based on the three-point bending and eccentric compression tests on both dry and saturated concrete specimens heated up to 200℃, Bazant and Prat[1] found that the fracture energy monotonously decreased with increasing temperature and that saturated specimens yielded much smaller fracture energy. Baker [2], B.zhang [3] and Nielsen [4] conducted the three-point bending tests on the notched preheated beams, and found that the fracture energy bore an increase-decrease tendency with increasing temperature. B.zhang and N.Bicanic [5] investigated the effects of heating temperatures up to 450℃ and testing conditions (hot and cold) on the fracture energy of high-performance concrete, and found that the fracture energy generally sustained a decrease-increase tendency with the heating temperature for hot concrete but a hold-increase-decease tendency for the cold concrete.

G.Prokopski [6] and Hisham Abdel-Fattah [7] investigated the fracture toughness at high temperature and after cooling respectively by conducting the three-point bending tests on the concrete beams. Both experiments demonstrated the fracture toughness was greatly influenced by temperatures and decreased steadily.

This research investigated the residual fracture toughness K_{IC} of concrete and its relationship with temperatures T_m by conducting the wedge splitting test. The ultimate weight losses w of specimens at specified temperatures were recorded. Thus the relationship between K_{IC} and T_m could be established.

1. Experimental details

Overall 50 concrete specimens with the same dimensions 230×200×200mm were prepared in the test. All the specimens had a precast notch of 80mm height and 3mm thickness by placing a piece of steel plate into the molds prior to casting. After 60 days of curing, compressive test at ambient temperature gave the cube compressive strength of 35.5Mpa, elastic modulus of 32800Mpa.

Nine heating temperatures were adopted (T_m =65℃, 120℃, 200℃, 300℃, 350℃, 400℃, 450℃, 500℃, 600℃). 20℃ is taken as the ambient temperature. Since it was recognized that the fracture behavior measurements were generally associated with significant scatter, 5 repetitions were performed for each heating case to reduce discrepancy. In the subsequent text, each test datum is the average value from five specimens.

Electric furnace was employed to heat the specimens. Thermocouples embedded in specimens helped to control temperatures. After cooling for 7 days, a closed-loop servo controlled hydraulic jack with the maximum capacity of 1000kN was employed to conduct the wedge splitting test at a fixed rate of 0.4mm/min. Two Clip-on Extensometers were suited respectively at the mouth and the tip of crack respectively to measure the crack mouth opening displacement (CMOD) and crack tip opening displacement (CTOD).The test picture is shown in Fig. 1.



Fig. 1 Test set-up

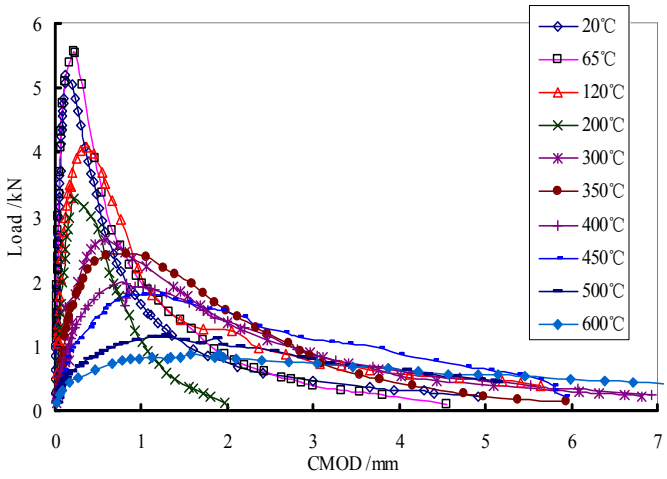


Fig. 2 Load vs. CMOD curves for different heating temperatures

2. Experimental results

2.1 Test phenomena

In the cases of loading test on specimens exposed to relatively lower temperature (20℃~200℃), the splitting load generally reached its peak with no visible crack observed. Once the first crack initiated, the value of load dropped dramatically. Cracks propagated vertically and rapidly to the bottom of prism. Coarse aggregates and mortar paste were seen, after test, split on the fracture surfaces. As to the specimens exposed to higher temperatures, it was obvious that more than one cracks branching from the tip of notch and competing to form the final fracture. The fracture surfaces tended to be more tortuous and much less cracks across the grains were observed. It can be attributed to degradation of cohesion between the coarse aggregates and mortar paste.

2.2 Load vs. CMOD curves and the ultimate weight loss for different heating temperatures

Fig 2 shows that the ultimate load P_u did not change largely up to 200 ℃ and then continuously decreased with T_m. P_u slightly increased by 7% from 20℃ to 105℃, and then monotonously declined to 600℃with a final drop of 80%. Meanwhile the critical CMOD corresponding to P_u increased by 13 times with T_m from 20℃ to 600℃.

Fig 3 shows the ultimate weight loss corresponding to T_m. In general, w increased with three typical stages. Firstly, w increased rapidly with T_m until 200℃, which could be regarded as a predominantly physical process associated with the evaporation of capillary water in concrete. When T_m was increasing to 450℃, w kept increasing at a lower rate and the further weight loss was mainly caused by the evaporation of gel water. The smaller evaporation rate was attributed to the difficulty for gel water to escape from gel pores. This stage could be described as a physical-chemical process. In the third stage, *weigh loss* was mainly due to the dehydration and decomposition of hardened cement paste and aggregates, representing a chemical process.

2.3 The residual fracture toughness

The residual fracture toughness K_{IC} is calculated based on the following equation [8]:

$$K_{IC} = \frac{F_{HMAX} \times 10^{-3}}{th^{1/2}} f(\alpha) \quad . \tag{1}$$

where F_{HMAX} is the maximum horizontal load, h is the specimen depth, t is the specimen thickness. f(a) is the function of deformability of wedge splitting specimens, determined according to literature [8]. The temperature effect on the residual fracture toughness which sustained a hold-increase-decrease tendency was illustrated in Fig. 4 and the relationship between K_{IC} and T_m are derived as follows:

$$K_{IC}=0.0054T_m+0.6271 \qquad R^2=0.9444 \qquad 200℃\leq T_m\leq 500℃ \tag{2}$$

$$K_{IC}=-0.129T_m+9.6799 \qquad R^2=1.0000 \qquad 500℃\leq T_m\leq 600℃ \tag{3}$$

Toughness commonly characterizes the capacity of material to resist deformation and fracture. Fig.4 indicates the values of residual fracture toughness basically keep constant before 200℃, which means the removal of capillary water due to heating do not cause evident structural changes. From 200℃ to 500℃, K_{IC} increases significantly due to the escape of gel water. However when the dehydration and decomposition of mortar paste occurring, the huge thermal damage causes the capacity of fracture resistance decline and so with the fracture toughness.

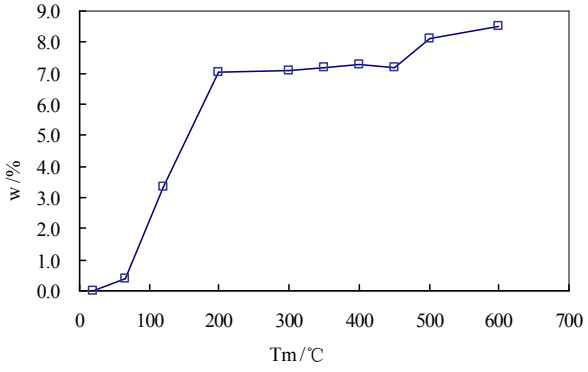


Fig. 3 Weight loss for different heating temperatures

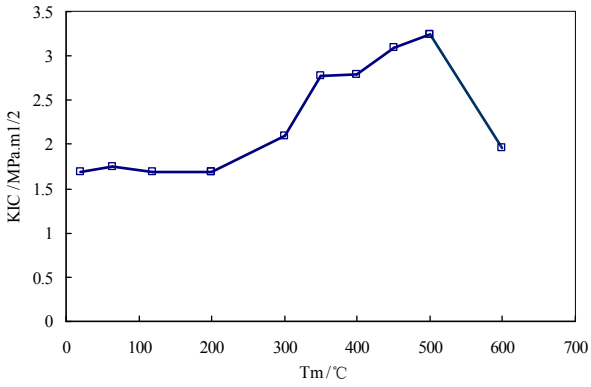


Fig. 4 Residual fracture toughness

3. Conclusions

The effects of heating temperatures on the residual fracture properties of concrete have been investigated by conducting wedge splitting test on the preheated standard specimens. The following conclusion could be drawn:

1. The weight loss, as a continuous non-reversible process, steadily increased with heating temperature T_m.

2. Elevated temperatures have significant effects on the fracture performance of concrete. The increasing temperature results in monotonously decrease in the peak load and increase in the critical CMOD of splitting test.

3. Before 200℃, temperature seems to have limited influence on the fracture toughness. Afterwards, with the increase of temperature from 200℃ to 500℃, the brittleness of concrete reduced significantly. However when the temperature is above 500℃, the residual fracture toughness decreased. It is generally sustained a hold-increase-decease tendency with heating temperature T_m. The relationship between the K_{IC} and T_m is established. According to the proposed equation, K_{IC} can be easily obtained corresponding to T_m.

References

[1] Bazant Z.P. and Prat P.C: Effect of temperatures and humidity on the fracture energy of concrete. ACI Materials Journals, 1988, 85, No.4, p. 262.

[2] Baker G: The effect of exposure to elevated temperatures on the fracture energy of plain concrete. RILEM Materials and Structures, 1996, 29, No.190, p.383.

[3] Zhang B., Bicanic N., Pearce C.J. and Balabanic G.: Residual fracture properties of normal and high-strength concrete subject to elevated temperatures. Magazine of Concrete Research, 2000, 52, No.2, p.123.

[4] Nielsen C.V. and Bicanic N.: Residual fracture energy of high-performance and normal concrete subject to high temperatures.RILEM Materials and Structures, 2003, 36, No.262, p.515.

[5] B. Zhang and N. Bicanic:Fracture energy of high-performance concrete at high temperatures up to 450℃: the effects of heating temperatures and testing conditions (hot and cold). Magazine of Concrete Research, 2006, 58, No.5, p.277.

[6] G.Prokopski:Fracture toughness of concretes at high temperature. Journal of Materials Science, 1995, 30, p.1609.

[7] Hisham Abdel-Fattah, and Sameer A.Hamoush.: Variation of the fracture toughness of concrete with temperature.1997, Vol 11,No.2, p. 105.

[8] Shi Lang Xu and Hans W.Reinhardt.: Determination of double-K criterion for crack propagation in quasi-brittle fracture, Part III: Compact tension specimens and wedge splitting specimens. International Journal of Fracture, 1999, Vol 98, p.179.

© (2012) Trans Tech Publications, Switzerland
doi:10.4028/www.scientific.net/KEM.488-489.747

Taking full advantage of nominal stresses to design notched components against variable amplitude multiaxial fatigue

Luca Susmel[1,a], David Taylor[2,b]

[1]Department of Civil and Structural Engineering, University of Sheffield, Mappin Street, Sheffield, S1 3JD, UK

[2] Department of Mechanical Engineering, Trinity College, Dublin 2, Ireland

[a]l.susmel@sheffield.ac.uk, [b]dtaylor@tcd.ie

Keywords: Critical plane approach, notch, variable amplitude loading, multiaxial fatigue.

Abstract. The present paper is concerned with the use of the Modified Wöhler Curve Method (MWCM), applied in terms of nominal stresses, to estimate lifetime of notched components subjected to variable amplitude multiaxial fatigue loading. The MWCM is applied by defining the critical plane through that direction experiencing the maximum variance of the resolved shear stress: since the shear stress resolved along the above direction is a monodimensional quantity, fatigue cycles are directly counted by the classical Rain-Flow method. The performed validation exercise, based on an extensive experimental investigation, seems to strongly support the idea that the MWCM applied along with the classical nominal stress based approach is capable of accurately estimating fatigue damage also in notched components subjected to variable amplitude multiaxial load histories.

Introduction

Since the pioneering work done both by Neuber [1] and Peterson [2], the classical approach based on the correction of the plain fatigue curves through appropriate fatigue strength reduction factors, K_f, has been widely used by structural engineering to perform the fatigue assessment of notched components subjected to either pure axial, pure bending, or pure torsional loading.

Even if, in such circumstances, the above design methodology has proven to allow components to be designed by always reaching an adequate level of safety, examination of the state of the art shows that the scientific community has not agreed yet a universally accepted strategy suitable for using the nominal stress based approach to estimate fatigue damage in notched components subjected to variable amplitude multiaxial fatigue loading. Accordingly, the present paper summarises an attempt of formalising a novel design methodology, based on the MWCM, capable of efficiently addressing, in situations of interest, such an intractable problem.

Our fatigue design methodology

Consider a notched component subjected to a complex system of time-variable forces resulting in a multiaxial stress state at the critical section (Fig. 1a). According to the classical approach due to Neuber [1] and Peterson [2], the above stress state has to be determined in terms of nominal quantities calculated with respect to the reference section (Fig. 1a). After defining the necessary nominal stresses, the orientation of the critical plane at point O can directly be determined by locating that plane containing the direction experiencing the maximum variance of the resolved shear stress (direction MV in Figure 1b) [3]. The shear stress amplitude relative to the critical plane, $\bar{\tau}_a$, can then be calculated from the variance of stress signal $\tau_{MV}(t)$, i.e. [4]:

$$\mathrm{Var}\left[\tau_{MV}(t)\right]=\frac{1}{T}\int_0^T\left[\tau_{MV}(t)-\bar{\tau}_m\right]^2\cdot dt \Rightarrow \bar{\tau}_a=\sqrt{2\cdot \mathrm{Var}\left[\tau_{MV}(t)\right]}, \quad (1)$$

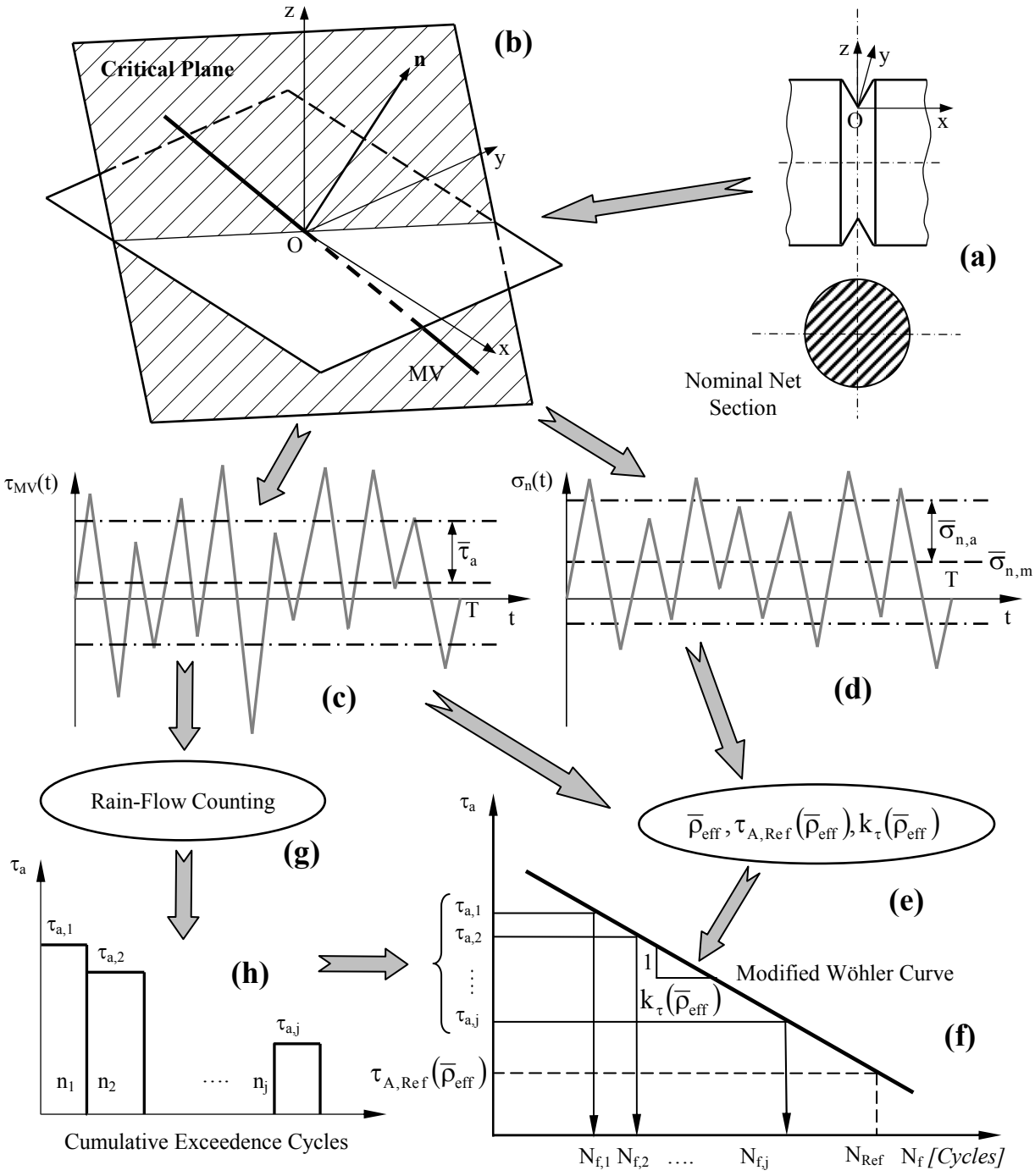


Figure 1: In-field use of the proposed method.

where $\tau_{MV}(t)$ is the shear stress resolved along direction MV (Fig. 1b), whereas T is the time interval over which the assessed load history is defined (Fig. 1c). In a similar way, the mean value, $\overline{\sigma}_{n,m}$, and the amplitude, $\overline{\sigma}_{n,a}$, of the stress, $\sigma_n(t)$, normal to the critical plane take on the following values [4] (Fig. 1d):

$$\overline{\sigma}_{n,m} = \frac{1}{T}\int_0^T \sigma_n(t)\cdot dt\,;\ \overline{\sigma}_{n,a} = \sqrt{2\cdot \mathrm{Var}\left[\sigma_n(t)\right]} \Leftrightarrow \mathrm{Var}\left[\sigma_n(t)\right] = \frac{1}{T}\int_0^T \left[\sigma_n(t) - \overline{\sigma}_{n,m}\right]^2 \cdot dt\,. \tag{2}$$

Subsequently, the degree of multiaxiality and non-proportionality of the assessed load history has to be evaluated as follows [4]:

$$\overline{\rho}_{\text{eff}} = \frac{m \cdot \overline{\sigma}_{n,m} + \overline{\sigma}_{n,a}}{\overline{\tau}_a}, \tag{3}$$

where mean stress sensitivity index m is a material constant measuring the sensitivity of the investigated material to the presence of superimposed static stresses [5, 6]. As soon as ratio $\overline{\rho}_{\text{eff}}$ is known (Fig. 1e), the position of the corresponding modified Wöhler curve can be estimated according to the following linear relationships [5] (Fig. 1f):

$$k_\tau(\overline{\rho}_{\text{eff}}) = (k_n - k_{0n}) \cdot \overline{\rho}_{\text{eff}} + k_{0n} \tag{4}$$

$$\tau_{A,Ref}(\overline{\rho}_{\text{eff}}) = \left(\frac{\sigma_{An}}{2} - \tau_{An} \right) \cdot \overline{\rho}_{\text{eff}} + \tau_{An} \,. \tag{5}$$

In the above identities, k_n and σ_{An} are, respectively, the slope and the nominal stress amplitude extrapolated at N_A cycles to failure characterising the fully-reversed uniaxial fatigue curve, whereas k_{0n} and τ_{An} are instead the corresponding quantities associated with the fully-reversed torsional fatigue curve, nominal stresses σ_{An} and τ_{An} being referred to the reference section.

By taking full advantage of the classical Rain-Flow method, the resolved shear stress cycles can now be counted (Figs 1c and 1g) to build the corresponding load spectrum (Fig. 1h). Finally, the calculated load spectrum has to be used to estimate the damage content associated with any counted shear stress level (Figs. 1h and 1f), the estimated number of cycles to failure being equal to:

$$D = \sum_{i=1}^{j} \frac{n_i}{N_{f,i}} \Rightarrow N_{f,e} = \frac{D_{cr}}{D} \sum_{i=1}^{j} n_i \,. \tag{6}$$

To conclude, it is worth observing that according to the classical rule due to Palmgren and Miner, the critical value of the damage sum, D_{cr}, can directly be taken equal to unity.

Validation by experimental data

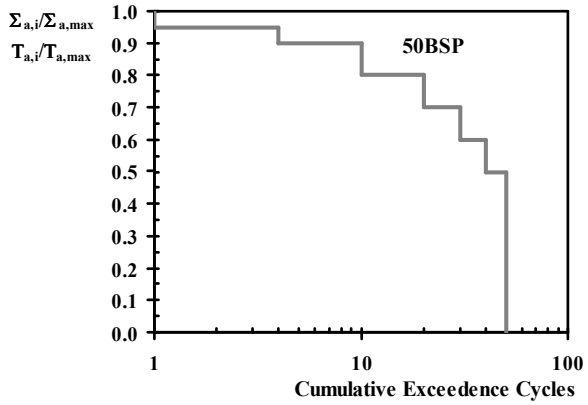


Figure 2: Investigated load spectrum.

In order to check the accuracy of the design methodology summarised in the previous section, an extensive investigation was carried out by testing V-notched cylindrical samples having gross diameter equal to 12mm and made of carbon steel C40 (σ_{UTS}=852 MPa, σ_Y=672 MPa). The following three geometrical configurations were investigated: (i) sharply V-notched samples having net diameter, d_n, equal to 9.15 mm, root radius, r_n, to 0.225 mm, notch opening angle, α, to 35°, resulting in a net stress concentration factor of 4.42 under axial loading, K_t, and of 2.38 under torsion, K_{tt}; (ii) intermediate V-notched specimens having d_n=9.00mm, r_n=1.2mm, α=90° (K_t=2.19, K_{tt}=1.42); (iii) bluntly U-notched cylindrical bars having d_n=9.00mm and r_n=3.0mm (K_t=1.62, K_{tt}=1.21). The above notched samples were tested under the load spectrum shown in Figure 2, where $\Sigma_{a,i}$ and $T_{a,i}$ are the amplitudes of the axial and torsional nominal stresses at the i-th stress level, respectively, $\Sigma_{a,max}$ and $T_{a,max}$ being the maximum values of the amplitudes in the spectrum itself. The results summarised in Figure 3 were generated under combined tension and torsion by exploring the following variable amplitude loading paths: in-phase (IPh) and 90° out-of-phase (OoPh) situations at a ratio, F, between the axial and torsional frequency equal to 0.5, 1 and 2, with zero (ZMS) and non-zero mean stress (N-ZMS). In particular, nominal mean values Σ_m and T_m for the axial and torsional channel, respectively, were set as follows: $\Sigma_m=0.2\Sigma_{a,max}$ and $T_m=0.2T_{a,max}$.

The fully-reversed axial and torsional fatigue curves, expressed in terms of nominal quantities, were directly derived from the corresponding un-notched one, generated under fully-reversed loading, by taking fully advantage of Peterson's relationships, i.e. [2, 7]:

$$K_f = 1 + \frac{K_t - 1}{1 + \frac{0.0254}{r_n}\left(\frac{2079}{\sigma_{UTS}}\right)^{1.8}}\ ;\ K_{ft} = 1 + \frac{K_{tt} - 1}{1 + \frac{0.01524}{r_n}\left(\frac{2079}{\sigma_{UTS}}\right)^{1.8}}\ . \tag{7}$$

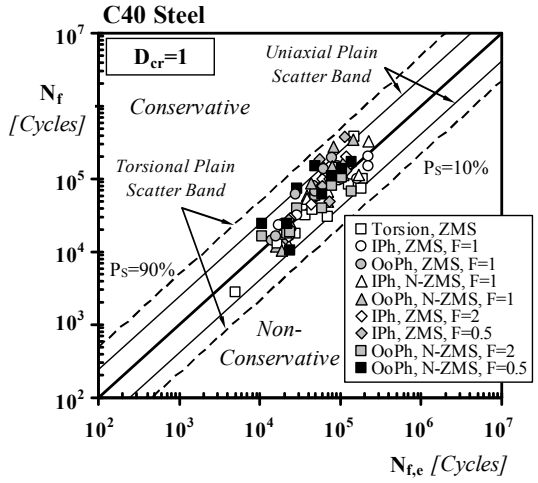


Figure 3: MWCM's accuracy.

The fully-reversed plain uniaxial fatigue curve had negative inverse slope equal to 9.4 and reference stress amplitude at 10^6 cycles to failures equal to 292.8MPa. The fully-reversed plain torsional fatigue curve was instead characterised by a slope of 12.8 and a reference shear stress amplitude at 10^6 cycles to failures of 231.7MPa. Finally, a mean stress sensitivity index, m, of 0.19 was directly determined from the plain uniaxial fatigue curve generated under zero-tension. The experimental, N_f, vs. estimated, $N_{f,e}$, lifetime diagram reported in Figure 3 makes it evident that the proposed methodology proved to be capable of estimates falling within the widest scatter band between the two associated with the plain fatigue curves used to calibrate, through Eqs. (7), the method itself, the target error bands being delimited by the two straight lines calculated for a probability of survival, P_S, equal to 10% and 90%, respectively.

To conclude, it is worth observing that such a high level of accuracy was obtained independently from tested geometrical feature as well as from investigated variable amplitude loading path.

Conclusions

1) The MWCM applied in terms of nominal quantities is seen to be successful in estimating fatigue lifetime of notched components subjected to variable amplitude multiaxial fatigue loading;

2) More works needs to be done to reformulate such a variable amplitude design methodology to make it suitable for being applied in terms of local quantities.

References

[1] H. Neuber: *Theory of notch stresses: principles for exact calculation of strength with reference to structural form and material* (II Edition, Springer Verlag, Berlin, Germany 1958).

[2] R.E. Peterson, in: *Metal Fatigue*, edited by G. Sines and J. L. Waisman, McGraw Hill, New York, p. 293.

[3] L. Susmel: Int. J. Fatigue 32 (2010), p. 1875.

[4] L. Susmel, R. Tovo: *Estimating Fatigue Damage under Variable Amplitude Multiaxial Fatigue Loading*. Fatigue Fract. Engng. Mater. Struct., in press, 2011.

[5] L. Susmel: *Multiaxial Notch Fatigue* (Woodhead, UK, 2009).

[6] L. Susmel, D. Taylor: Fatigue Fract. Engng. Mater. Struct. 31 12 (2008), p. 1047.

[7] Y.-L. Lee, J. Pan, R. B. Hathaway, M. E. Barkey: *Fatigue Testing and Analysis* (Elsevier Butterworth–Heinemann, USA 2005).

© (2012) Trans Tech Publications, Switzerland
doi:10.4028/www.scientific.net/KEM.488-489.751

Semi-permeable cracks in magnetoelectroelastic solids under impact loading

M. Wünsche[1], A. Sáez[2], Ch. Zhang[1] and F. García-Sánchez[3]

[1] Faculty of Science and Technology, University of Siegen, Paul-Bonatz-Str. 9-11, D-57068 Siegen, Germany, e-mail: wuensche@bauwesen.uni-siegen.de, c.zhang@uni-siegen.de

[2] Departamento de Mecánica de Medios Continuos, Teoría de Estructuras e I. del Terreno, Universidad de Sevilla, Camino de los Descubrimientos s/n, 41092 Sevilla, Spain, e-mail: andres@us.es

[3] Departamento de Ingeniería Civil, de Materiales y Fabricación, E.T.S. de Ingenieros Industriales, Universidad de Málaga, 29013 Málaga, Spain, e-mail: fgsanchez@uma.es

Keywords: magnetoelectroelastic materials, semi-permeable electrical and magnetical crack-face condition, impact loading, dynamic intensity factors, Galerkin BEM

Abstract. In this paper, transient dynamic crack analysis in two-dimensional, linear magnetoelectroelastic solids by considering different electrical and magnetical crack-face boundary conditions is presented. For this purpose, a time-domain boundary element method (TDBEM) using dynamic fundamental solutions is developed. The spatial discretization of the boundary integral equations is performed by a Galerkin-method while a collocation method is implemented for the temporal discretization of the arising convolution integrals. An explicit time-stepping scheme is applied to compute the discrete boundary data and the generalized crack-opening-displacements. Iterative algorithms are implemented to deal with the non-linear electrical and magnetical semi-permeable crack-face boundary conditions.

Introduction

Magnetoelectroelastic composites are widely used for broadband sensing, actuating devices and many other smart structures which are required in advanced engineering sciences [1]. The transient dynamic crack analysis in linear magnetoelectroelastic solids has important applications in fracture and damage mechanics and the corresponding results have a direct relevance to the design and optimization of composite materials. Since analytical solutions are limited to very simple crack configurations, numerical solution algorithms have to be used in general cases. The boundary element method is very attractive and efficient for solving dynamic crack problems in linear magnetoelectroelastic solids. An important role in the crack analysis of magnetoelectroelastic solids plays the definition of the electrical and the magnetical crack-face boundary conditions [2].

Problem statement

Let us consider a homogeneous and linear magnetoelectroelastic cracked solid. In the absence of body forces the cracked solid satisfies the equations of motion

$$\sigma_{iJ,i}(\mathbf{x},t) = \rho\delta^{*}_{JK}\ddot{u}_{K}(\mathbf{x},t), \quad \delta^{*}_{JK} = \begin{cases} \delta_{JK}, J,K = 1,2 \\ 0, \text{otherwise} \end{cases} \tag{1}$$

and the constitutive equations

$$\sigma_{iJ}(\mathbf{x},t) = C_{iJKl}u_{K,l}(\mathbf{x},t), \tag{2}$$

where ρ, u_I and σ_{iJ} are the mass density, the generalized displacements and the generalized stresses

$$u_I = \begin{cases} u_i, I = 1,2 \quad \text{(mechanical displacements)} \\ \varphi, I = 4 \quad \text{(electrical potential)} \\ \phi, I = 5 \quad \text{(magnetical potentials)} \end{cases}, \quad \sigma_{iJ} = \begin{cases} \sigma_{iJ}, J = 1,2 \quad \text{(mechanical stresses)} \\ D_i, J = 4 \quad \text{(electrical displacements)} \\ B_i, J = 5 \quad \text{(magnetical inductions)} \end{cases} \tag{3}$$

and C_{iJKl} is the generalized elasticity matrix as given in [1]. Further the initial conditions

$$u_i(\mathbf{x},t) = \dot{u}_i(\mathbf{x},t) = 0 \ \text{ for } \ t \le 0, \tag{4}$$

the boundary conditions

$$t_I(\mathbf{x},t) = \bar{t}_I(\mathbf{x},t), \ \mathbf{x} \in \Gamma_t, \tag{5}$$

$$u_I(\mathbf{x},t) = \bar{u}_I(\mathbf{x},t), \ \mathbf{x} \in \Gamma_u, \tag{6}$$

and the electrical and magnetical semi-permeable crack-face boundary conditions

$$D_i(\mathbf{x} \in \Gamma_{c^+},t) = D_i(\mathbf{x} \in \Gamma_{c^-},t) = -\kappa_c^e \frac{\varphi(\mathbf{x} \in \Gamma_{c^+},t) - \varphi(\mathbf{x} \in \Gamma_{c^-},t)}{u_i(\mathbf{x} \in \Gamma_{c^+},t) - u_i(\mathbf{x} \in \Gamma_{c^-},t)}, \tag{7}$$

$$B_i(\mathbf{x} \in \Gamma_{c^+},t) = B_i(\mathbf{x} \in \Gamma_{c^-},t) = -\kappa_c^m \frac{\phi(\mathbf{x} \in \Gamma_{c^+},t) - \phi(\mathbf{x} \in \Gamma_{c^-},t)}{u_i(\mathbf{x} \in \Gamma_{c^+},t) - u_i(\mathbf{x} \in \Gamma_{c^-},t)} \tag{8}$$

are satisfied [2]. Here, t_I denote the generalized traction components, Γ_t is the boundary where the tractions t_I are prescribed, Γ_u is the boundary where the displacements u_I are given, Γ_c^+ and Γ_c^- are the upper and the lower crack-faces and $\kappa_c^e = \kappa_r^e \cdot 8.85 \cdot 10^{-3}$C/(GVm) and $\kappa_c^m = \kappa_r^m \cdot 1.26$H/Mm are the electrical permittivity and the magnetical permeability, with κ_r^e and κ_r^m being the relative permittivity and permeability of the medium inside the crack. Lowercase subscripts take the values 1, 2 (elastic) and uppercase subscripts take the values 1, 2 (elastic), 4 (electric), 5 (magnetic).

Time-domain BIEs

The Galerkin time-domain BIEs for a cracked solid are defined by

$$\begin{aligned} \int_{\Gamma_b} \psi(\mathbf{x}) u_j(\mathbf{x},t) d\Gamma_x = & \int_{\Gamma_b} \psi(\mathbf{x}) \int_{\Gamma_b} \left[u_{ij}^G(\mathbf{x},\mathbf{y},t) * t_i(\mathbf{y},t) - t_{ij}^G(\mathbf{x},\mathbf{y},t) * u_i(\mathbf{y},t) \right] d\Gamma_y d\Gamma_x \\ & + \int_{\Gamma_b} \psi(\mathbf{x}) \int_{\Gamma_{c^+}} t_{ij}^G(\mathbf{x},\mathbf{y},t) * \Delta u_i(\mathbf{y},t) \, d\Gamma_y d\Gamma_x, \end{aligned} \tag{9}$$

$$\begin{aligned} \int_{\Gamma_{c^+}} \psi(\mathbf{x}) t_j(\mathbf{x},t) d\Gamma_x = & \int_{\Gamma_{c^+}} \psi(\mathbf{x}) \int_{\Gamma_b} \left[v_{ij}^G(\mathbf{x},\mathbf{y},t) * t_i(\mathbf{y},t) - w_{ij}^G(\mathbf{x},\mathbf{y},t) * u_i(\mathbf{y},t) \right] d\Gamma_y d\Gamma_x \\ & + \int_{\Gamma_{c^+}} \psi(\mathbf{x}) \int_{\Gamma_{c^+}} w_{ij}^G(\mathbf{x},\mathbf{y},t) * \Delta u_i(\mathbf{y},t) \, d\Gamma_y d\Gamma_x. \end{aligned} \tag{10}$$

In Eq. (9) and (10), an asterisk denotes the Riemann convolution, u_{ij}^G are the displacement fundamental solutions, t_{ij}^G, v_{ij}^G are the traction fundamental solutions and w_{ij}^G are the higher-order traction fundamental solutions, Δu_i are the generalized crack-opening-displacements (COD) and $\Gamma_b = \Gamma_u + \Gamma_t$. The dynamic fundamental solutions for homogenous and linear magnetoelectroelastic solids, expressed in the 2D case by line-integrals over the unit circle, are implemented.

To solve the BIEs (9) and (11) numerically, a spatial Galerkin-method with linear elements is implemented while a collocation method is applied for the temporal discretization using linear shape-functions [3]. Special crack-tip elements are implemented for a direct calculation of the dynamic intensity factors (IFs) from the computed CODs. Iterative algorithms are developed to solve the electrical and magnetical semi-permeable crack-face conditions (7) and (8).

Numerical Results

Let us consider a crack of length 2a in a infinite magnetoelectroelastic solid under impact tensile loading $\sigma(t)=\sigma_0 H(t)$ as shown in Fig. 1. $BaTiO_3$-$CoFe_2O_4$ composite is investigated [1]. The crack is discretized by 20 elements and a normalized time-step $c_L\Delta t/a=0.05$ is used. The numerical results are presented in Fig. 2 for different electrical permittivities κ_c^e and magnetical permeabilities κ_c^m.

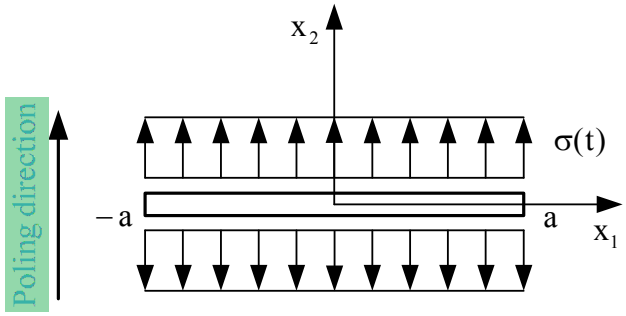
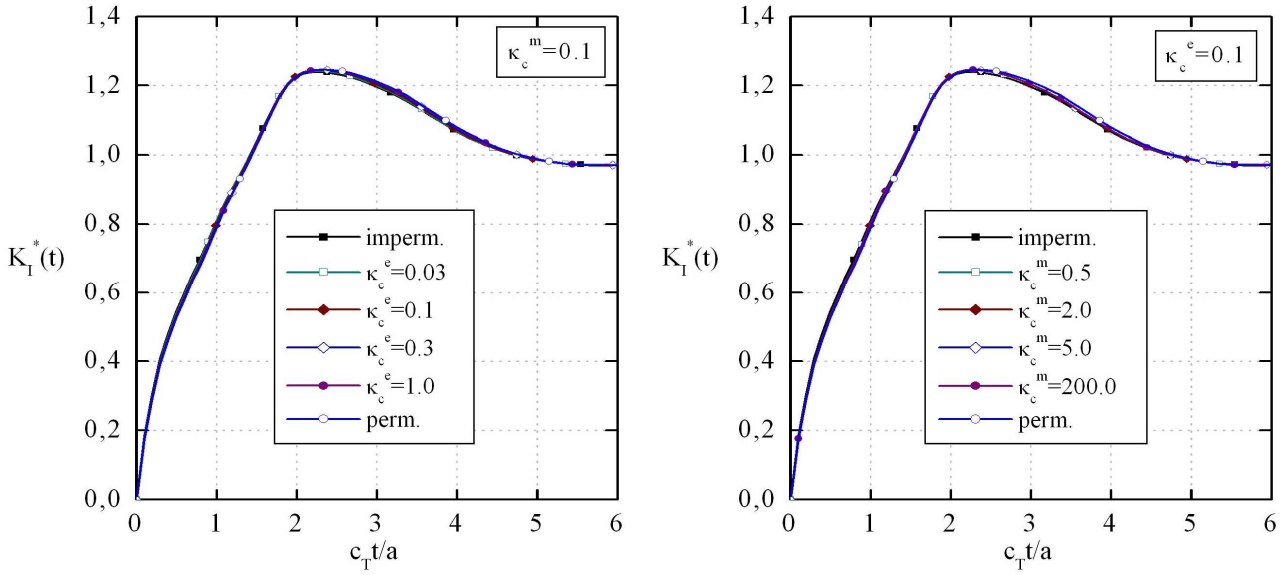


Fig. 1: A crack in a infinite magnetoelectroelastic solid under tensile loading

The normalized dynamic mode-I IFs are very similar without a significant difference for all investigated κ_c^e and κ_c^m values. The mode-II dynamic IF vanishes, since no shear stress components are induced in the case of the investigated loading. In contrast, the electrical permittivity and the magnetical permeability have a significant influence on the normalized dynamic mode-IV and the mode-V IFs. As well expected, the results of the semi-permeable cracks are between the bounds given by the impermeable and permeable results.



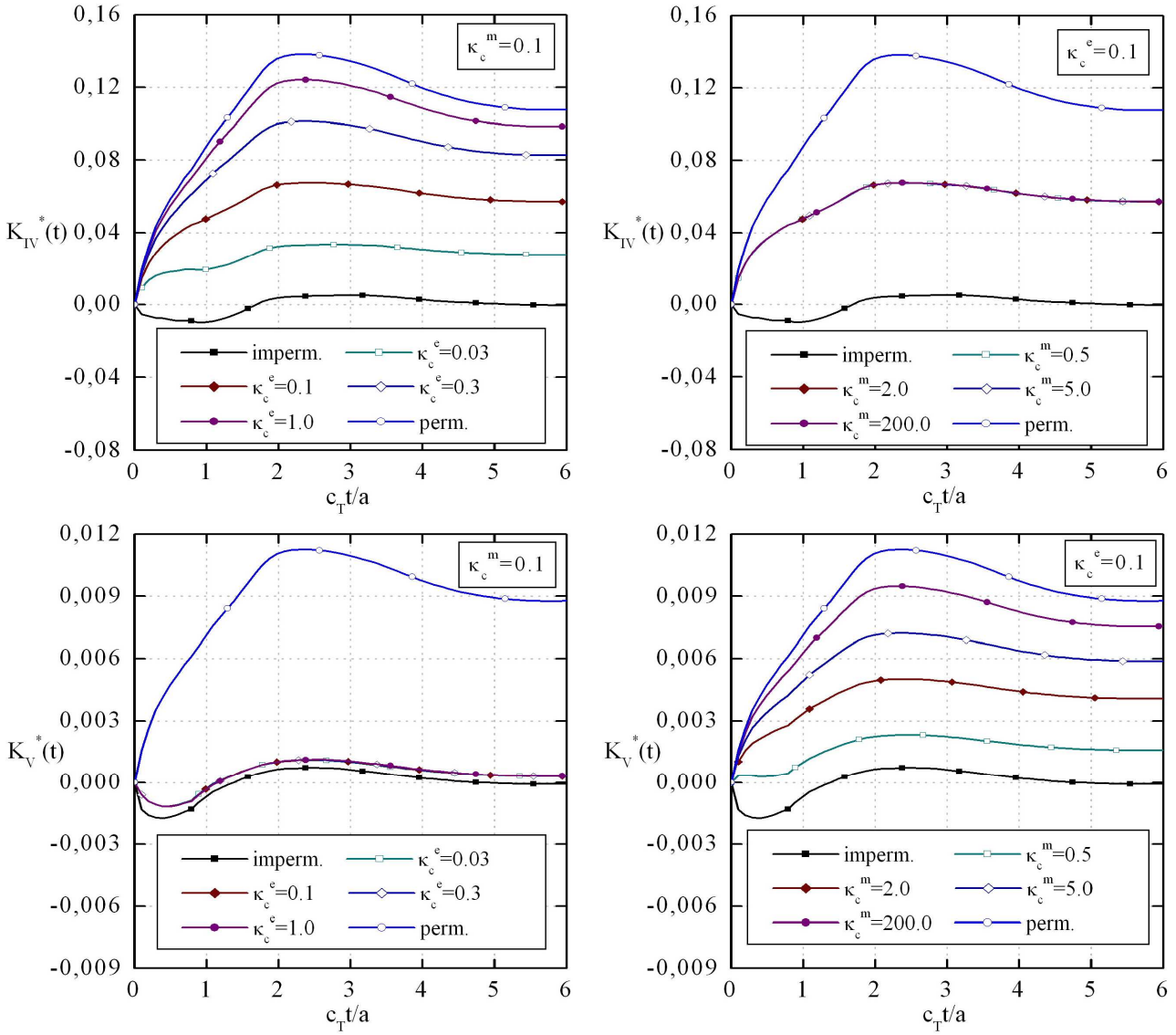


Fig. 2: Normalized dynamic IFs for different electrical and magnetical crack-face conditions

Summary

In this paper an improved 2D transient dynamic crack analysis in linear magnetoelectroelastic solids is presented. A time-domain BEM is developed for this purpose. The spatial discretization is performed by a Galerkin-method while a collocation method is adopted for the temporal discretization. To solve the non-linear electrical and magnetical semi-permeable crack-face conditions, an efficient iterative algorithm is implemented. Numerical examples demonstrate the suitability and the efficiency of the present time-domain BEM for transient dynamic crack analysis.

References

[1] Nan C.W., Magnetoelectric effect in composite of piezoelectric and piezomagnetic phases, Phys. Rev. B 50, 6082-6088, (1994).

[2] Wang B.L. and Mai Y.W., Applicability of the crack-face electromagnetic boundary conditions for fracture of magnetoelectroelastic materials, Int. J. Solids Struct. 44, 387-398 (2007).

[3] Wünsche M., Sáez A., García-Sánchez F., Zhang Ch., A 2D time-domain collocation-Galerkin BEM for dynamic crack analysis in piezoelectric solids, Eng. Anal. Boun. Elem. 34 377-387 (2010).

© (2012) Trans Tech Publications, Switzerland
doi:10.4028/www.scientific.net/KEM.488-489.755

A THREE DIMENSIONAL GRAPHICAL AID FOR FATIGUE DATA ANALYSIS

[a]Atzori B, [b]Meneghetti G, [c]Ricotta M

University of Padova, Department of Mechanical Engineering, via Venezia 1, 35131 Padova - Italy

[a]bruno.atzori@unipd.it, [b]giovanni.meneghetti@unipd.it, [c]mauro.ricotta@unipd.it

Keywords: compatibility conditions, cyclic stress-strain curve, fatigue data analysis, strain-life curve, stress-life curve, stress-strain curve

Abstract. The fatigue behaviour of materials is usually synthesised in terms of stress-life (S-N) curve or in terms of strain-life (ε-N) curve, the latter being described by the so-called Manson-Coffin equation. It is known that the assumption of equality of the plastic and elastic components between the Manson-Coffin and the stabilised stress-strain curves leads to the so-called compatibility conditions which connect the equations theoretically. The material constants of the Manson-Coffin and of the stabilised stress-strain curve are commonly determined by best fitting separately the experimental data obtained from strain-controlled fatigue tests. As a consequence the compatibility conditions may not be fulfilled. In this paper a method for fatigue data analysis that ensures the compatibility conditions is proposed and validated against experimental data.

Introduction.

The fatigue behaviour of materials is usually experimentally investigated by carrying out stress or strain controlled fatigue tests and the fatigue data are then synthesised in terms of stress-life (S-N) or strain life (ε-N) curves, respectively. The stress-life law is described in terms of reversals to failure in the following form:

$$\sigma_a^k \cdot 2N_f = \sigma_A^k \cdot 2N_A \tag{1}$$

where σ_a is the applied stress amplitude, k the inverse slope of fatigue curve, $2N_f$ the number of reversals to failure, σ_A the fatigue strength evaluated at N_A number of cycles to failure (e.g. 2 million cycles). The unknown parameters of Eq.1 (k, σ_A) are evaluated by fitting the experimental fatigue data.

The relation between the total strain amplitude ε_a and the fatigue life ($2N_f$) is expressed by Manson-Coffin equation, in which ε_a is divided in its elastic ($\varepsilon_{a,el}$) and plastic ($\varepsilon_{a.pl}$) components:

$$\varepsilon_a = \varepsilon_{a,el} + \varepsilon_{a,pl} = \frac{\sigma_f'}{E}(2N_f)^b + \varepsilon_f'(2N_f)^c \tag{2}$$

where σ_f' is the fatigue strength coefficient, E the material modulus of elasticity, b the fatigue strength exponent, ε_f' the fatigue ductility coefficient and c the fatigue ductility exponent. Besides the modulus of elasticity E, Eq. 2 contains four material parameters σ_f', b, ε_f' and c.

The unknown parameters of Eq. 1 and Eq. 2 can be calculated following ASTM E739-10 Standard [1] that presents a statistical analysis of fatigue data, in which the selected and controlled variable (namely, stress or strain) is considered as independent variable and the number of cycles to failure as dependent variable. Different procedures for statistical analysis of strain-life data can be found as an example in [2,3].

The stabilised stress-strain relationship due to cycling loadings is usually described by following equation, where the first term represents the elastic component, while the second is the plastic component:

$$\varepsilon = \varepsilon_{el} + \varepsilon_{pl} = \frac{\sigma}{E} + \left(\frac{\sigma}{K'}\right)^{\frac{1}{n'}} \tag{3}$$

K′ and n′ are the hardening coefficients relevant to the stabilised cyclic curve. The material parameters K′ and n′ are usually evaluated by fitting the experimental data obtained from strain controlled, constant amplitude fatigue tests.

Since Eq. 2 and Eq. 3 have similar structures, under the hypothesis that material parameters do not depend on the number of cycles (after material stabilisation), by comparing the elastic and plastic components the so-called compatibility equations can be obtained [4]:

$$n' = b/c\,; \qquad K' = \sigma_f' \Big/ \left(\varepsilon_f'\right)^{b/c} \tag{4}$$

Eq. 4 establishes a bridge between parameters of Eq. 3 and of Eq. 2.

The common methods for determining material constants do not ensure compatibility so that Eq. 4 is satisfied only approximately. In fact the material constants are usually determined separately, i.e. the set of data is treated as experimental results independent of each other.

This possible inconsistency can be overcome following the recent procedure proposed in [5], where the Authors suggest to fit the experimental data in a three-dimensional strain-stress-life space and then to calculate the material parameters directly from the projections of a straight line on suitable planes.

In this paper, following the idea of representing the data in a strain-stress-life space, a novel procedure is proposed for fatigue data analysis that starts from the stress-life and the strain-life curves and ensures the compatibility conditions. Finally some experimental fatigue data are re-analysed and the results are compared with those obtained according to [5] and to the conventional procedures [1].

The proposed methodology and experimental validation.

The proposed methodology for fatigue data analysis is developed under the hypothesis that the parameters of stress-life curve as well as the plastic strain life curve have already been determined according to the procedure proposed in [1], that in this paper will be referred as “conventional procedure”.

Let us define:

$$x = \log\left(\varepsilon_{a,pl}\right),\ y = \log\left(\sigma_a\right),\ z = \log\left(2N_f\right) \tag{5}$$

so that Eq. 1 and the plastic component in Eq. 2 can be linearised. A straight line in a three-dimensional space can be defined as intersection of two planes (see Fig. 1):

$$\begin{cases} ky + z - \left(k \log \sigma_A + \log\left(2N_A\right)\right) = 0 \\ x - cz - \log\left(\varepsilon_f'\right) = 0 \end{cases} \tag{6}$$

where the first equation represents a plane parallel to x-axis (S-N plane) and the second a plane parallel to the y-axis (plastic plane).

By projecting Eq. 6 to y-x plane, the plastic component of Eq. 3 is defined, by ensuring compatibility conditions. Then the hardening parameters can be evaluated from Eq. 7 :

$$n' = -(c \cdot k)^{-1}\,; \qquad K' = \sigma_A \left(2N_A\right)^{\frac{1}{k}} \cdot \left(\varepsilon_f'\right)^{\frac{1}{c \cdot k}} \tag{7}$$

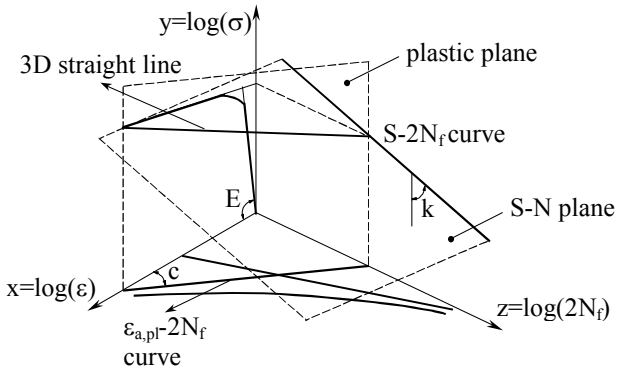


Fig.1 Schematic view of proposed methodology

From the elastic component of Eq. 2, the stress amplitude can be written as $\sigma_a = \sigma_f^{'} \cdot (2N_f)^b$, that is a different form of Eq. 1. Therefore the following conditions must be ensured:

$$b = -1/k\,; \qquad \sigma_f^{'} = \sigma_A \cdot (2N_A)^{1/k} \tag{8}$$

Then, after fitting the elastic component of strain controlled fatigue data, the dynamic elastic modulus E can be derived. Finally, by substituting Eq. 8 into Eq. 7, the compatibility conditions (Eq. 4) are obtained.

Constant amplitude, strain-controlled fatigue tests were carried out on alloyed ductile iron provided by Anselmi SpA foundry. The experimental tests were conduced on the specimens' geometry reported in Fig. 2 by using a MTS Minibionix test machine equipped with a 15 kN load cell and a MTS extensometer having gauge length of 25 mm. A sinusoidal wave form characterised by a nominal strain ratio R_ε (defined as the ratio between the minimum and the maximum strain) equal to –1 was imposed. Test frequencies between 0.1 and 5 Hz were adopted.

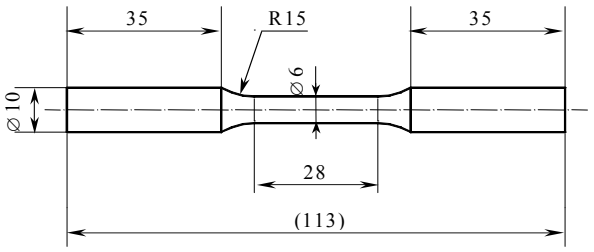
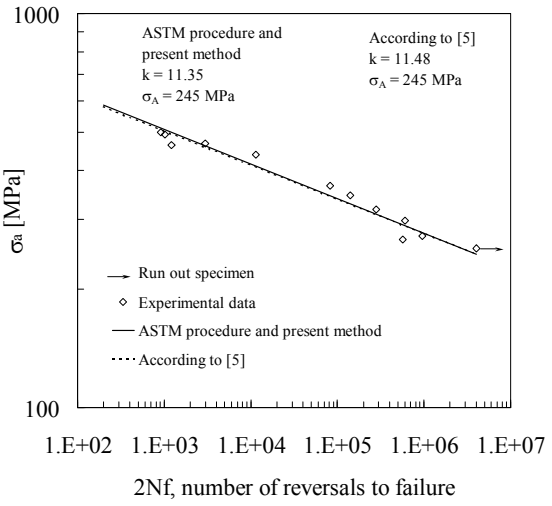


Fig. 2: Specimen's geometry adopted in the fatigue tests for the alloyed ductile iron



(b)

Fig. 3: S-N curves obtained following different procedures

The S-N curve was determined by considering the stabilised stress amplitude vs $2N_f$ experimental data. The S-N curve evaluated according to [1] is shown in Fig. 3 and compared with that calculated following [5]. For the set of experimental data analysed in the present work, both procedures give very similar results.

The parameters of plastic component of Eq. 2 were calculated by considering the experimental data having the plastic component greater than a limit value ε_0 [2,5]. On the basis of the accuracy of adopted experimental equipment, the limit value was set equal to 0.004%. The plastic component of the strain amplitude was evaluated considering the width of the recorded stable hysteresis loops. The Manson-Coffin curves obtained following Refs [1,5] and the present procedure are shown in Fig. 4-a, where E_s represents the elastic modulus measured by means of previous static tests. Finally, the cyclic curves were calculated and the results are compared in Fig. 4-b, where the thin line represents the cyclic curve evaluated by fitting the relevant experimental data separately

according to a least square "classical method". In this case compatibility conditions are satisfied only approximately, but nevertheless both the Manson-Coffin curve and the stabilised curve are close to those calculated according to [5] and the present method. It is the author's opinion that higher discrepancies between compatible and non-compatible procedures may arise when analysing different sets of experimental data.

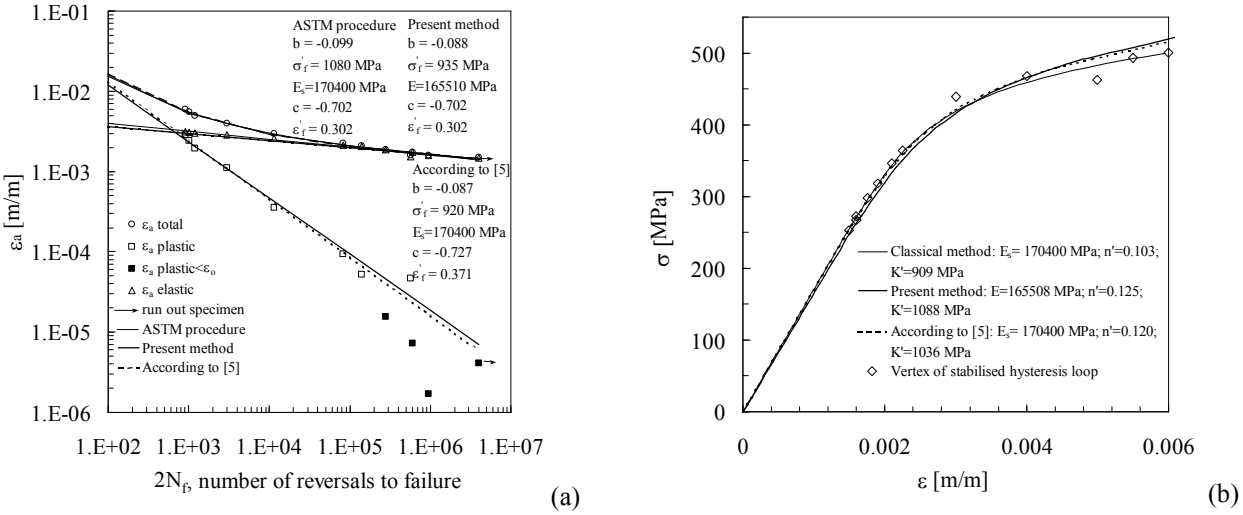


Fig. 4. a) Manson-Coffin curves and b) cyclic curves for the analysed alloyed ductile iron obtained by using different procedures

Conclusions

In this paper a novel methodology for fatigue data analysis is presented. In the proposed method a straight line, defined in a 3D strain-stress-life space (ε-σ-N), is calculated starting from the knowledge of the stress-life and of the plastic strain-life curves, evaluated according to the in force Standards by means of a simple 2D statistical analysis. As final result, by projecting the 3D-line on the stress-strain plane, the stabilised cyclic curve is obtained and its parameters ensure the compatibility conditions.

Acknowledgments

We would like to acknowledge Anselmi Spa for supplying material and specimens adopted in the present research.

References

[1] ASTM E739 – 10: Standard practice for Statistical Analysis of Linear or Linearized Stress-Life (S-N) and Strain-Life (ε-N) fatigue data.

[2] C.R. Williams, Y.-L. Lee, J.T. Rilly: Int J Fatigue 25 (2003) p. 427-436.

[3] E. Castello, A. Canteli, H. Pinto, M. López-Aenlle: Mater Lett 62 (2008) p. 3639-3642.

[4] E. Dowling in: *Mechanical Behavior of Materials*, Pearson Prentice Hall (2007).

[5] A. Niesłony, C. Dsoki, H. Kaufmann, P. Krug: Int J Fatigue 30 (2008) p. 1967-1977.

© (2012) Trans Tech Publications, Switzerland
doi:10.4028/www.scientific.net/KEM.488-489.759

Meshfree Continuum Damage Mechanics Modelling for 3D Orthogonal Woven Composites

L.Y. Li[1,a], M.H. Aliabadi[2,b] P H Wen[3]

[1, 2] Department of Aeronautics, Imperial College, London, UK, SW7 2BY

[3] School of Engineering and Materials, Queen Mary University of London E1 4NS

[a] l.li08@imperial.ac.uk, [b] m.h.aliabadi@imperial.ac.uk

Keywords: Meshfree, Radial basis, Moving kriging, Galerkin, Continuum damage, 3D orthogonal woven composites, Weibull

Abstract. A Meshfree approach for continuum damage modeling of 3D orthogonal woven composites is presented. Two different shape function constructions, Radial basis (RB) function and Moving kriging (MK) interpolation, are utilized corresponding with Galerkin method in the Meshfree approach. The failure of two different unit cell models, straight-edge and smooth fabric unit cell model respectively, is compared.

Introduction

Damages in many fibrous composite materials play an important role with non-ductile matrices. There are many attempts to address the issue of damage growth in laminated fibre-reinforced plastic composites using the continuum damage mechanics (CDM). The Weibull [1] distribution function is selected to describe the failure of bundle of fibers with initial defects both for normal stress and shear stress conditions. Wen and Aliabadi [2,7] applied Weibull function to CDM of plain woven composites and showed a good agreement between analytical and Meshfree results.

In terms of more complicated woven composites, like 3D orthogonal woven composites, Meshfree method shows significant advantages comparing with finite element method, as it does not require mesh generation. During the last decades, Meshfree method was developed with a rapid speed, from Element free Galerkin (EFG) [3], that uses Moving least square (MLS) approximation as the shape function construction, to more recent approaches using RB functions. Wen and Aliabadi [2, 4] applied RB function on various problems including micro-mechanics modeling and CDM modeling of plain woven composites. It was shown that the meshfree approach is efficient and accurate when comparing with the finite element method. A new formulation of EFG through the MK interpolation is proposed by Lei Gu [5] recently in order to eliminate the shortcoming that EFG shape function does not satisfy the Kronecker delta property.

In this paper, RB functions and MK interpolation are both applied in the meshfree approach for CDM modeling of 3D orthogonal woven composites by using straight-edge unit cell model and smooth fabric one. The results are compared with each other.

Shape Function Constructions

Consider a problem domain Ω which is represented by a set of nodes in the domain Ω and on the boundary Γ, as shown in Fig. 1. Let u($\mathbf{A}$) be the function of the field variable defined in the domain Ω. The approximation of function u at point $\mathbf{A}(x_A, y_A, z_A)$ can be defined by

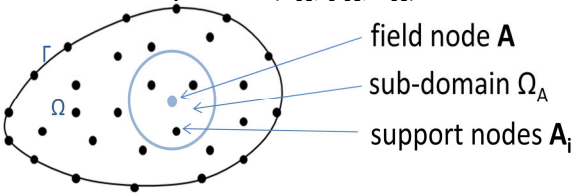


Fig. 1 *Sketch of domains and boundaries of 2D cases for Meshfree Method*

$$\mathrm{u}(\mathbf{A}) = \boldsymbol{\Phi}(\mathbf{A}, \mathbf{A}_\mathrm{i})\mathbf{u} = \sum_{\mathrm{i}=1}^{\mathrm{n}} \phi_\mathrm{i}(\mathbf{A})\mathrm{u}_\mathrm{i} \tag{1}$$

where $\boldsymbol{\Phi}(\mathbf{A}, \mathbf{A}_\mathrm{i})$ is the matrix of shape functions and $\mathbf{u}$ is the matrix of displacements of the support nodes $\mathbf{A}_\mathrm{i}$. n is the number of nodes in the sub-domain Ω_A.

By using RB functions interpolation [4], the shape function $\boldsymbol{\Phi}(\mathbf{A}, \mathbf{A}_\mathrm{i})$ in Eq. 1 has the form of

$$\boldsymbol{\Phi}(\mathbf{A}, \mathbf{A}_\mathrm{i}) = \mathbf{R}^\mathrm{T}(\mathbf{A}, \mathbf{A}_\mathrm{i})\mathbf{R}_0{}^{-1} \tag{3}$$

By using MK interpolation [5], the shape function $\boldsymbol{\Phi}(\mathbf{A}, \mathbf{A}_\mathrm{i})$ in Eq. 1 can be defined by

$$\boldsymbol{\Phi}(\mathbf{A}, \mathbf{A}_\mathrm{i}) = \mathbf{p}^\mathrm{T}(\mathbf{A})\mathbf{M} + \mathbf{e}^\mathrm{T}(\mathbf{A})\mathbf{N} \tag{4}$$

Weibull CDM model

In the commonly used train equivalence approach, a material containing damage can be represented as an equivalent undamaged material subject to the same strain. Therefore, the effective stress-strain relationship is obtained by $\{\sigma\} = [C(\omega)]\{\varepsilon\}$, here $[C(\omega)]$ is the damaged or effective stiffness tensor and the function of the damage factor ω.

The Weibull [1] distribution function of the defects in the fibres is selected and the damage factors ω_i are evaluated by

$$\omega_i = 1 - \exp\left[-\frac{1}{m_i e}\left(\frac{|\varepsilon_i|}{\varepsilon_i^0} \right)^{m_i} \right] \qquad i = 1,2,3 \tag{5}$$

By implementing the damage factor related stress-strain relationship into Galerkin method, the global discrete system equation in matrix form becomes

$$[\mathbf{K}]_{3n\times 3n}\,\hat{\mathbf{u}}_{3n} = \mathbf{f}_{3n} \tag{6}$$

where $\mathbf{f}_{3n}$ is nodal force vector in matrix form and

$$[\mathbf{K}(\omega)] = \int_\Omega \mathbf{B}^\mathrm{T}[\mathrm{C}(\omega)]\mathbf{B}d\Omega \tag{7}$$

Note that for woven fabric composites, the constitutive matrix $[\mathrm{C}(\omega)]$ also depends on the location of each integral point and represents the directions of the fibres in different yarns.

Unit Cell Models

3D orthogonal woven composites, as shown in Fig. 2a, is one of the most common choices for finite element analysis because of its relatively simple weave pattern comparing with other 3D woven composites.

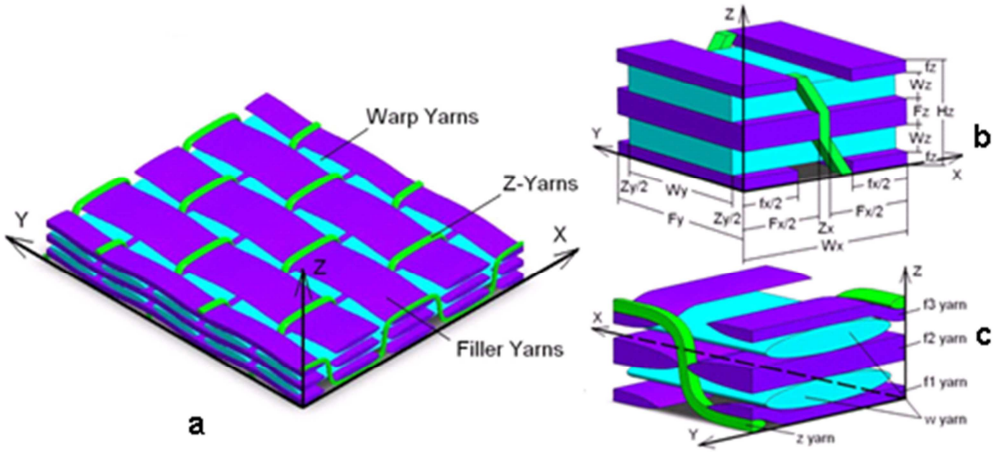


Fig. 2 a *Representative model of 3D orthogonal woven fabric*
b *Straight-edge* c *Smooth fabric Unit cell model of 93oz fabric composites*

In the approach proposed by A. E. Bogdanovich [6], a straight-edge unit cell model as shown in Fig. 2b is generated according to direct measurements of the produced fabric and composites. In this paper, a more realistic representation of the 3D orthogonal woven fabric model is formulated and implemented into meshfree method. For comparison, Fig. 2c shows a representative smooth fabric model using the same basic dimensions with the straight-edge unit cell model.
The determined characteristics of this geometric model are listed in Table 1.

Table 1 The determined characteristics of the geometric model [mm]

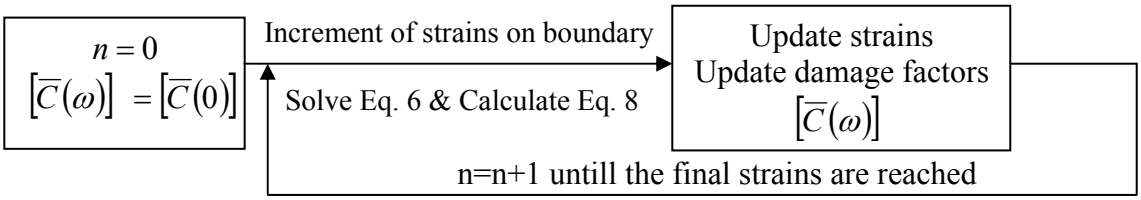
fx	fz	Fx	Fy	Fz	Wx	Wy	Wz	Zx	Zy	Zz	Hz
3.082	0.292	4.326	5.08	0.614	4.618	4.171	0.637	0.292	0.909	0.292	2.472

Results and Discussion

Increment of strain technique is applied to evaluate the constitutive matrix in this paper. The average stress can be determined by an integral

$$\overline{\sigma_x} = \frac{\int \sigma_x dV}{V} \tag{8}$$

Suppose the final strains are given, the algorithmic details at a time station $t_n = t_{n-1} + \Delta t$ can be determined as follows:



Note that the calculations in the blocks above need to be done for each integral point.

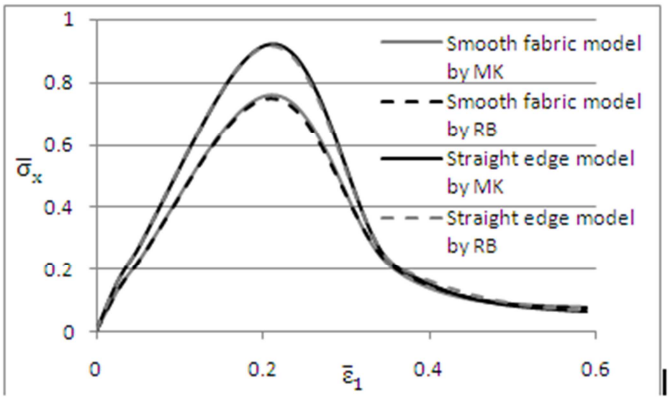


Fig. 3 *Variations of unit cell stress $\bar{\sigma}_x$ with unit cell strain $\bar{\varepsilon}_1$ by using different Meshfree methods*

The results of average stress $\bar{\sigma}_x$ of two different unit cell models by using two different Meshfree shape functions are compared in Fig. 3. Obviously, satisfied agreements are achieved between two different Meshfree shape function constructions, RB function and MK interpolation, for both unit cell models. The maximum value of average stress for smooth fabric unit cell model is about 18% lower than that for straight-edge unit cell model by using both Meshfree shape functions. The failure unit cell strain is approximately 0.21 for both straight-edge model and smooth fabric one.

Summary

Two Meshfree shape functions, RB function and MK interpolation, dealing with the CDM micromechanical models of 3D orthogonal woven fabric composites are presented in this paper. The unit cell model of this type of woven composites is improved to be smoother and more realistic. The Weibull distribution function is used to describe the damage factors in matrix and yarn in RVC. Incremental technique of applied strain is utilized to deal with highly non-linear problems. It is shown that the CDM modeling for complex structured 3D woven composites becomes simple with the utilization of Meshfree method.

References

[1] W. Weibull: A statical theory of the strength of materials, IVA Proceedings Nr. 151, Stockholm, 1939

[2] P. H. Wen and M. H. Aliabadi: Continuum damage mechanics modeling for woven fabric composites (to be published)

[3] T. Belytschko, Y. Y. Lu, and L. Gu: Element-Free Galerkin Methods, *Int. J. Numer. Meth. Engineering*, 37, 229-256, 1994

[4] P. H. Wen and M. H. Aliabadi: Mesh-free micromechanical model for woven fabric composite elastic moduli, *Journal of Multiscale Modelling,* 1, No. 2, 303-319, 2009

[5] Lei Gu: Moving kriging interpolation and element-free Galerkin method, *Int. J. Numer. Meth. Engng,* 56, 1-11, 2003

[6] A. E. Bogdanovich: Multi-scale modelling, stress and failure analyses of 3-D woven composites, *J Mater Sci*, 41, 6547-6590, 2006

[7] P.H.Wen and M H Aliabadi Elastic Moduli of Woven Fabric Composite by Meshless Local Petrov-Galerkin (MLPG) Method, Computer modeling in Engineering and Sciences, Vol 61, P. 133-154, 2010.

© (2012) Trans Tech Publications, Switzerland
doi:10.4028/www.scientific.net/KEM.488-489.763

A Novel Methodology for Fatigue Delamination Growth Analysis of Composites

O. Bacarreza[1, a], M. H. Aliabadi[2, b]

[1]Imperial Consultants, 58 Prince's Gate, SW7 2PG, London, UK

[2]Department of Aeronautics, Imperial College London, SW7 2AZ, London, UK

[a]o.bacarreza-nogales@imperial.ac.uk, [b]m.h.aliabadi@imperial.ac.uk

Keywords: Fatigue, Delamination, Composites, VCCT, XFEM.

Abstract. A novel methodology for analysis of fatigue delamination growth, capable of dealing with complex delamination shapes and mixed-modes in a computationally efficient way, is proposed. It combines the VCCT to find the energy release rates and the XFEM to update the geometry during the progressive failure, thus making it very robust and computationally efficient. The methodology is demonstrated at coupon level.

Introduction

Composite materials are increasingly being used as structural materials in several engineering components. Fatigue is one of the most common causes of failure in aerospace structures [1-2]. It is the product of cyclic loading on a structural component. The fatigue process involves several damage mechanisms depending on the geometry, boundary conditions, stacking sequence, etc. Fatigue damage can occur in the bulk material, i.e. intralaminar damage, or in the boundary between the different layers in the composite layup, i.e. interlaminar damage or delamination.

The behaviour of composite materials is more complicated than the one of homogenous and isotropic materials. In fibre reinforced composites, a damage process zone develops at the crack tip, where the material around is highly heterogeneous and anisotropic. The gradual progressive damage leads to continuous stress redistributions and reduction of stress concentrations. Thus, delamination under fatigue involves the same micro mechanics and processes that occur under static loading: there is an initiation or onset process followed by a propagation or crack growth.

An efficient way to deal with fatigue delamination growth is by means of Linear Elastic Fracture Mechanics (LFEM). The Virtual Crack Closure Technique (VCCT) [3] criterion is a method based on LEFM, therefore, is appropriate for problems in which brittle crack propagation occurs along predefined surfaces as it is the case for fatigue delamination. The VCCT technique is based on Irwin's assumption that when a crack extends by a small amount, the energy released in the process is equal to the work required to close the crack to its original length. Based on this assumption, the components of the energy release rate are computed from the nodal forces and nodal relative displacements.

Although valuable information about delamination can be obtained using the VCCT, its use in the simulation of delamination growth may require complex moving mesh techniques to advance the crack front when the local energy release rates reach a critical value, it is also possible to use other techniques to avoid the complex remeshing during delamination as it is the case of the extended finite element method (XFEM) [4-5].

Proposed Methodology

The crack growth rate is defined as the crack extension per number of cycles and the energy release rate is referred to as the rate of strain energy flux flowing toward a crack tip as the crack tip extends. This relation between the fatigue crack growth rate and the variation of the energy release rate is commonly represented in a log-log diagram. The curve is divided into 3 regions according to the

curve shape. In Region I there is a threshold value G_{th}, below which cracks do not propagate or the additional crack growth is negligible. Region II defines a stable crack growth zone showing a linear behaviour in the log-log scale. Finally in Region III the curve raises to an asymptote corresponding to the critical fracture toughness value G_c where static fracture is achieved.

Paris law [6] is widely used and accepted for modelling fatigue damage propagation despite the fact that it describes only the linear portion of the curve (Region II):

$$\frac{da}{dN} = C\Delta G^m \quad . \tag{1}$$

In Eq.(1) parameters C and m depend on the mode-ratio and they must be determined experimentally; ΔG depends on the loading conditions and geometry.

The integration of Paris law, Eq.(1), can be evaluated once the difference in energy release rates ΔG and the delamination growth Δa for each increment are known. The result of the numerical integration is the increment of the number of cycles ΔN_i necessary to extend the crack area between the previous step, (*i -1)*, and the current step, (*i)*:

$$\Delta N_i = \frac{\Delta a_i}{C\Delta G_i^m} \tag{2}$$

and the total number of cycles at the n^{th} increment is evaluated as:

$$N_n = \sum_{i=1}^{n} \Delta N_i \tag{3}$$

The difference in energy release rates ΔG and the delamination growth Δa can be calculated as follows: The material toughness is artificially reduced to a fraction of the real one, so that delamination growth will occur at low load levels, as the ones expected during cyclic load. The model with an initial delamination is subjected to static monotonically increasing load, making the initial delamination grow, and since XFEM is being used, there is no need to remesh the model to obtain the updated geometry at a given load level. The delamination shape at this given load level is therefore known and consequently the energy release rates can be calculated using the VCCT.

Fatigue Delamination Growth in a Laminate Coupon

A composite laminate $[\pm 45, 0, 90]_s$ with an initial circular delamination between the 5th and the 6th layers was loaded cyclically with amplitude between maximum stress σ_{max} = 0MPa and minimum stress σ_{min} = -150MPa on the upper surface. The lower surface was fixed, and the side surfaces where allowed to slide in the direction parallel to the load only. The width of the panel is W = 120mm and the length L = 230mm. The initial delamination is situated at the centre of the panel, and it has a radius r = 32mm. The Paris law parameters were assumed to be: C = 0.05 and m = 1.15.

Figure 1 shows the delamination shape at a given number of cycles after postprocessing the results obtained from the static analysis. The numbers of cycles shown below each frame were calculated using the proposed methodology. It can be seen that the shape of the delamination areas can be complex even for a simple geometry, boundary conditions and load.

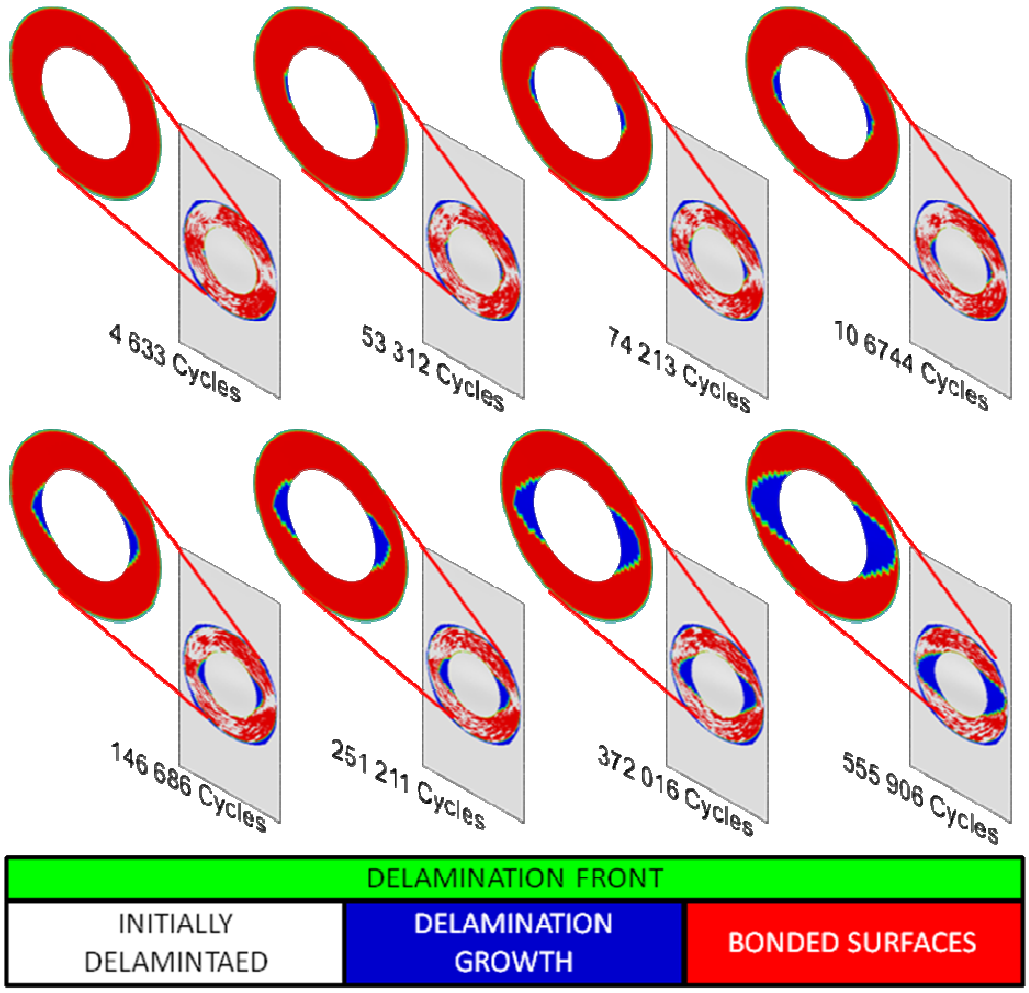


Figure 1. Fatigue Delamination Growth at coupon level

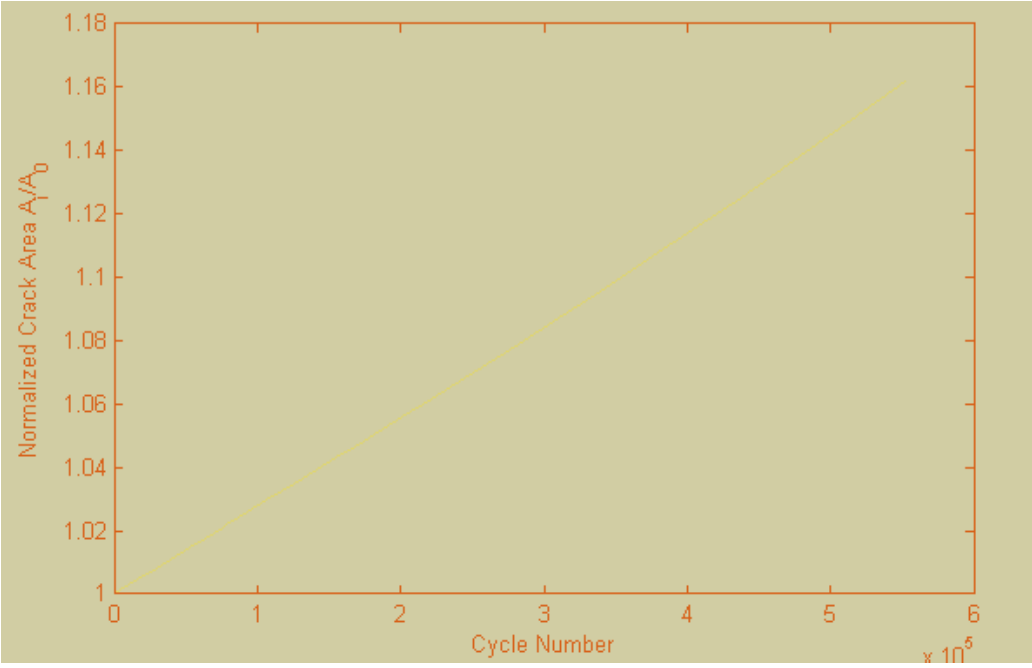


Figure 2. Normalized crack area versus cycle number

Figure 2 shows the growth of the delaminated area with respect to the cycle number. It should be noted that the crack area was normalized with respect to the originally delaminated area. For this given geometry, boundary conditions and material parameters, a fairly linear growth of the delaminated area occurs with the increasing number of cycles.

Conclusions

A Fatigue Delamination Growth Methodology was developed, capable of dealing with complex geometries and complex mixed-mode fatigue delamination growth in a very robust and computationally efficient manner combining the Virtual Crack Closure Technique to find the energy release rates and the eXtended Finite Element Method to find the new geometry for different load levels. The process of finding the necessary number of cycles for a given delamination shape is straight forward by means of integrating Paris law.

References

[1] M H Aliabadi Nonlinear Fracture and Damage Mechanics, WIT Press, Southampton, 2001
[2] M. Guagliano and M H Aliabadi *Fracture and Damage of Composites*, WIT Press, Southampton, 2006
[3] R. Krueger, "Virtual crack closure technique: History, approach, and applications," *Applied Mechanics Reviews,* vol. 57, p. 109, 2004.
[4] J. M. Melenk and I. Babuska, "The partition of unity finite element method: basic theory and applications," *Computer methods in applied mechanics and engineering,* vol. 139, pp. 289-314, 1996.
[5] T. Belytschko and T. Blacky, "Elastic Crack Growth in Finite Elements with Minimal Remeshing," 1998.
[6] P. Paris*, et al.*, "A rational theory of fatigue," *The Trend in Engineering,* vol. 13, pp. 9–14, 1961.

© (2012) Trans Tech Publications, Switzerland
doi:10.4028/www.scientific.net/KEM.488-489.767

Impact Detection using Artificial Neural Networks

M. Ghajari[1,a], Z. Sharif Khodaei[1,b] and M. H. Aliabadi[1,c]

[1]Department of Aeronautics, Imperial College London, South Kensington Campus,

Roderic Hill Building, Exhibition Road, SW7 2AZ, London, UK.

[a]m.ghajari@imperial.ac.uk, [b]z.sharif-khodaei@imperial.ac.uk, [c]m.h.aliabadi@imperial.ac.uk

Keywords: impact, structural health monitoring, finite element method, artificial neural network

Abstract. In this work, a number of impacts on a composite stiffened panel fitted with piezoceramic sensors were simulated with the finite element (FE) method. During impacts, the contact force history and strains at the sensors were recorded. These data were used to train, validate and test two artificial neural networks (ANN) for the prediction of the impact position and the peak of the impact force. The performance of the network for location detection has been promising but the other network should be further improved to provide acceptable predictions about the peak force.

Introduction

One of the major concerns about the increased usage of composite materials in modern aircraft structures is their susceptibility to impact damage. Two typical impacts that may occur during life of an aircraft are runway debris impact and tool drop. The types of damage that could result from such impacts include fibre fracture, matrix cracking, fibre/matrix debonding and delamination in laminar structures. After sustaining an impact, a composite panel may return to its original shape, owing to its brittle nature, without any visible sign of damage while it has suffered massive internal damage. Hence, determining the impact location and force helps assess the health of the structure, especially for barely visible impact damage (BVID).

There are two types of structural health monitoring systems; the active sensing system, which has been addressed in many studies such as [1-4] and the passive sensing system. The latter, which is the main concern of the current study, refers to determining the impact force and location from the response of the structure recorded by sensors attached to its surface. Worden and Staszewski [5] used artificial neural networks to quantify the impact force applied on a stiffened panel and detect its location. For the training, 80 impacts were carried out but the level of the force was kept below 0.1 N. Their approach was successful in finding the impact location, but it failed to detect the magnitude of the impact force. They commented [6] that the low level of the impact force was probably the reason for not being able to build a predictive ANN. To determine the location of the impact on a composite plate, Haywood et al. [6] established an ANN. Several features of the signal, its spectrum and envelope were employed to train the network. Eventually, it was found when the time of the beginning of each signal envelope and the maximum of each envelope were used as features the network could predict the impact location with highest precision. In a recent work [8], several forces were applied to an FE model of a composite stiffened panel, composed of 2710 shell elements, and the strain was recorded at the sensor locations. These data were used to train a linear finite difference model, which is called an auto-regressive with exogenous input (ARX). No information was provided in this study as to whether the force history has been obtained from experiments or some arbitrary data has been used.

This brief review shows that the training data for an impact force detection model is usually obtained from simple FE models or experiments. However, performing a number of experiments on relatively large stiffened panels used in aircrafts, to generate enough training data, is a time

consuming and expensive task. This is the reason that for most of models based on experimental training data very simple panels are analysed to show the capabilities of the proposed method. Consequently, there remains a crucial need for implementing these methods to rather complex stiffened panels.

The increasing capabilities of the FE method have enabled simulating the impact of an object onto complex composite structures. In the current work, the impact of rigid objects onto an aircraft stiffened panel is simulated by using the ABAQUS FE software [9]. The analysis outputs, including the impact force and strains measured at sensors placed over the panel, are used to train ANNs in order to predict the impact position and its force magnitude.

Impact simulation

An aircraft stiffened panel (Fig. 1, a) was employed in this study. It is composed of a skin, five stringers and four frames made of unidirectional and woven carbon/epoxy laminates. Since the impact force was not too high to cause considerable damage in the skin or debonding at the skin/stringer interface, elastic properties were defined for the materials and the stringers were rigidly tied to the skin. The panel was meshed with four node reduced integration shell elements and laminas were defined with through-thickness integration points. The PZT sensors were modelled with an integration point added to the elements located inside the areas occupied by the sensors. The panel was fitted with a dense distribution of sensors, which would be used for sensor placement optimisation in future studies. For this study, the focus was on the 1/6 of the panel distinguished in Fig. 1 (a) with dashed lines; the impacts occurred inside this area. The in-plane strains recorded by the 18 highlighted sensors were used, after feature extraction, to form the input vector of two ANNs explained later. It should be noted that there is a linear relationship between the voltage change at two faces of a PZT sensor and the sum of the in-plane strain components measured at the sensor/plate interface at the centre of the sensor [10]. Since the sensor is relatively small, it can be assumed that the variation of the strain components over the sensor area is negligible and calculate the average strain of the elements within the sensor area.

Intermediate mass and small mass impacts were simulated, representing debris collisions. The impactor was modelled as a discrete rigid sphere. For the intermediate mass impact, the impactor's radius was 12.7 mm, its mass was 0.3 kg and the impact velocity was 6 m/s, colliding the panel from outside. The impact location varied in a grid with 50 mm spacing. For the small mass impact, a radius of 6.35 mm, mass of 0.01 kg and velocity of 10 m/s was defined for the sphere and the impact location grid was shifted by 25 mm in both directions. In total, 200 impacts were simulated. The contact at the impactor/skin interface was modelled with the softened penalty algorithm; the pressure-overclosure data were produced by employing the Hertz relation [11].

Artificial neural networks

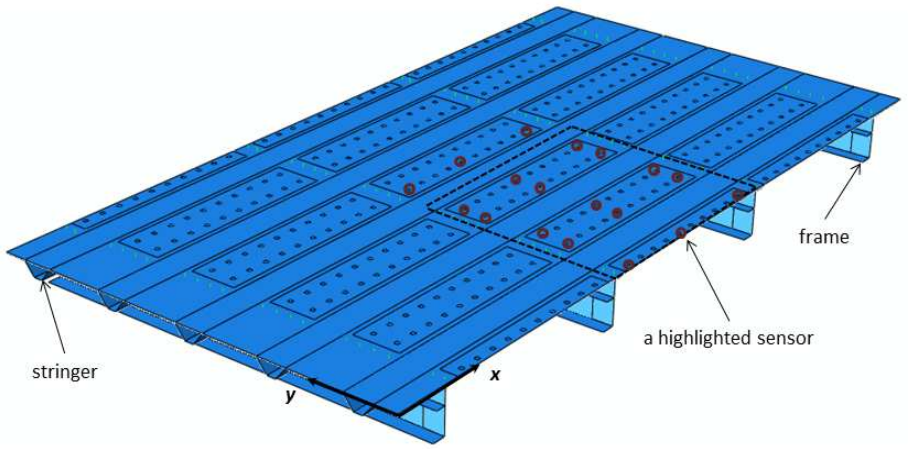
In order to predict the impact position and the force amplitude, two separate neural networks were built and trained using the ANN toolbox of MATLAB [12]. Both networks were feedforward with a backpropagation training algorithm. After trying available activation functions, it was found that the log-sigmoid function provides better results. The networks were trained with a 60% of the impact data generated with the SMART FE model; they were randomly selected. The remaining of the data was randomly divided into a validation set and a testing set. Since the outcome of training is very much dependent on the initial values given to the weights, which are selected randomly, networks were trained for 100 times to find the one with the best performance.

Results and discussion

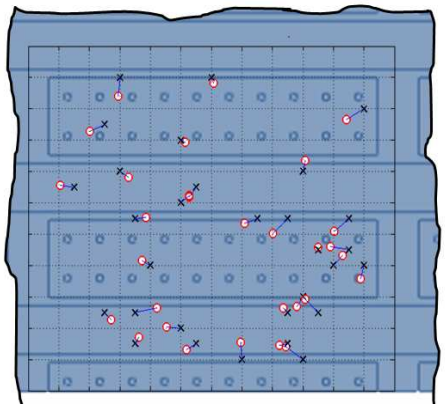
ANN for detection of the impact position. For this network, the arrival time of the strain waves at the sensors composed the input vector. This time was measured with respect to the shortest arrival time. The outputs were x and y coordinates of the impact location. After trying several structures for

the network, it was concluded that using one hidden layer with 20 neurons, yielding a 18:20:2 structure (depicted in Fig. 2, a), provides accurate results for the impact location and its training process is relatively fast.

For the network with the best performance among the 100 trained networks, the root mean square (RMS) errors for the x and y coordinates were ±8.1 mm and ±7.5 mm respectively; the errors were calculated using the testing set. The actual and predicted impact positions are shown in Fig. 1 (b). In terms of the length and width of the impact area, the percentage errors were equal to 3%, which indicates that the network could accurately detect the impact location. The performance of this network is superior to the one established by Stazewski et al. [6] ; although their ANN had a quit complex structure (34:30:20:10:2), the percentage errors for the x and y coordinates were 9.4% and 26.7%. This poor performance may be ascertained to the features extracted from sensor signals. Haywood et al. [7] obtained better results for impact position with a 24:20:2 structure: 8.6% error in x direction and 9.9% error in y direction. Nonetheless, its performance is still inferior to the ANN established in the current study.



(a)

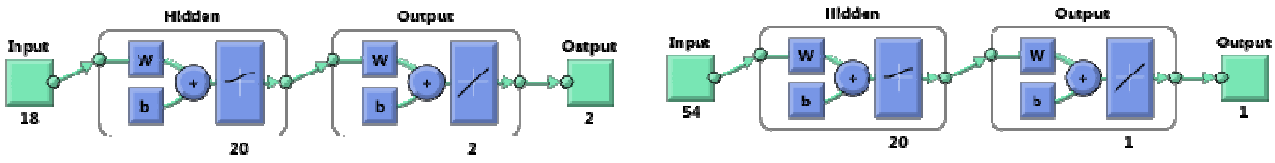


(b)

Fig. 1 (a) The stiffened panel fitted with a number of sensors (the focus was on the area distinguished with the dashed lines and the 18 highlighted sensors), (b) Actual (×) and predicted (○) impact positions for the testing data set; the grid distance is 50 mm.

ANN for detection of the impact force magnitude. The features used for this network and its structure were selected through trial and error. The structure was 54:20:1 (depicted in Fig. 2, b), which is relatively simple and its training is fast. The signal features were maxima of the approximation and detail coefficients of the first level Wavelet decomposition of the signal and the peak of the signal. The RMS error was ±243 N, which was obtained from presenting the testing set to the network that had the best performance. Compared to the mean of the force magnitudes, the percentage error was 26%, which is remarkably high. Nonetheless, the performance of the network is better than the relatively complex network (34:20:10:1) established in [6]. For the current study,

data from impacts of only two combinations of the impactor's mass and velocity were used to train the network. Probably using data from more combinations would improve the performance of the network.



(a) (b)

Fig. 2 Structure of the ANNs established for (a) impact position and (b) magnitude of the impact force; **w**: weights vector, **b**: bias vector (the images are produced by the MATLAB's ANN toolbox).

Conclusions

Small and intermediate mass impacts onto a composite stiffened panel fitted with PZT sensors have been simulated using the FE method. The results have been used to train, validate and test two separate artificial neural networks established for detection of the impact position and the impact force magnitude. The former ANN detects the impact position with a high degree of accuracy but the latter one still should be improved by using more impact data for the training. The advantage of the established ANNs is their simple structure, which reduces the training time and therefore makes them suitable for the sensor placement optimisation problem.

References

[1] S. Khodaei and M. H. Aliabadi, "Damage Identification Using Lamb Waves," *Key Engineering Materials,* vol. 452, pp. 29-32.

[2] Z. Su and L. Ye, *Identification of Damage Using Lamb Waves: From Fundamentals to Applications*: Springer Verlag, 2009.

[3] I. Benedetti, M H Aliabadi, A Milazzo "A Fast BEM for analysis of damaged structures with bonded piezoelectric sensors," Computer Methods in Applied Mechanics and Engineering Vol 199, p. 490-501, 2010.

[4] S. S. Kessler, S. M. Spearing, and C. Soutis, "Damage detection in composite materials using Lamb wave methods," *Smart Materials and Structures,* vol. 11, p. 269, 2002.

[5] K. Worden and W. J. Staszewski, "Impact location and quantification on a composite panel using neural networks and a genetic algorithm," *Strain,* vol. 36, pp. 61-68, 2000.

[6] W. J. Staszewski, K. Worden, R. Wardle, and G. R. Tomlinson, "Fail-safe sensor distributions for impact detection in composite materials," *Smart Mater and Struc,* vol. 9, p. 298, 2000.

[7] J. Haywood, P. T. Coverley, W. J. Staszewski, and K. Worden, "An automatic impact monitor for a composite panel employing smart sensor technology," *Smart Materials and Structures,* vol. 14, p. 265, 2005.

[8] J. F. C. Markmiller and F. K. Chang, "Sensor Network Optimization for a Passive Sensing Impact Detection Technique," *Structural Health Monitoring,* vol. 9, p. 25, 2010.

[9] ABAQUS, "Abaqus Analysis User's Manual," Simulia, 2010.

[10] C. Yang, L. Ye, Z. Su, and M. Bannister, "Some aspects of numerical simulation for Lamb wave propagation in composite laminates," *Composite Structures,* vol. 75, pp. 267-275, 2006.

[11] M. O. Pierson and R. Vaziri, "Analytical solution for low-velocity impact response of composite plates," *AIAA journal,* vol. 34, pp. 1633-1640, 1996.

[12] MATLAB: The Mathworks Inc., 2011.

© (2012) Trans Tech Publications, Switzerland
doi:10.4028/www.scientific.net/KEM.488-489.771

Failure Analysis of Bolted Composite Joint Based on Extended Finite Element

Zhenqing Wang [a], Song Zhou [b], Jiansheng Zhou [c], Xiaodi Wu [d]

College of Aerospace and Civil Engineering, Harbin Engineering University, Harbin 150001, China
[a]wangzhenqiang@hrbeu.edu.cn, [b]dagaier@163.com,
[c]zhoujiansheng@hrbeu.edu.cn, [d]wuxiaodi528@163.com

Keywords: composite; joint; Extended Finite Element Method (XFEM); geometrical parameters; failure

Abstract. In this paper, the influence of geometrical parameters on failure load of bolted single-lap composite joint was investigated. The composite laminate was manufactured from HTA/6376, a high-strength carbon fiber–epoxy material currently used in primary structures in the European aircraft industry. Two geometrical parameters which were plate width-to-hole diameter ratio (W/D), and the edge-to-hole diameter ratio (E/D) were analyzed. To avoid modeling each ply of the laminates discretely, the laminates were modeled using equivalent linear elastic properties. the failure analysis was modeled by Extend Finite Element Method (XFEM) in ABAQUS. Maximum principal stress criterion (Maxps) was used to determine the failure load.

Introduction

Composites are widely used in different branches of engineering and structural systems like those in aerospace and automobile industries, power plants, etc. Since the ratio of strength to weight and stiffness of such materials in many cases is higher than other conventional engineering materials, applications of composites have been widely expanded, the composite joints have become a very important aspect because the structural properties of the composite structure are determined by its joints, not by its basic structure [1].

Joint design in the composite structures is a very important consideration because improper design may lead to overweight of defective structures. The joining of composites has traditionally been achieved by mechanical fastening or adhesive bonding. Adhesive boding dose not require the holes, but adhesive bonding joints are sensitive to the environmental condition [2-3].

Traditionally the finite element method is chosen of the calculation of the failure load of joint, but when the crack appear in the material, the crack tips need to be re-meshed, which will increase the computation cost and maybe result in the calculation result not converge. In 1999 Belytschko [4] presented the extended finite element method (XFEM), the partition of unity (PUM) and level set method (LSM) are the basic idea and the mathematical foundation of XFEM. Some recent improvements in the method can be found in Stazi et al [5] where the method was extended to higher order elements. Sukumar et al [6], Moes et al [7] and Gravouil et al [8] extended the method to three dimensional problems by using LSM to track the evolution of the crack. An extensive survey can be found in Karihalooo and Xiao [9].

In this paper we used XFEM in ABAQUS to predict the failure of bolted single-lap composite joint with different geometrical parameters. Two geometrical parameters shown in Fig. 1 which were plate width-to-hole diameter ratio (W/D) and the edge-to-hole diameter ratio (E/D) were analysed. The geometric parameters and the finite model are shown in Fig.1

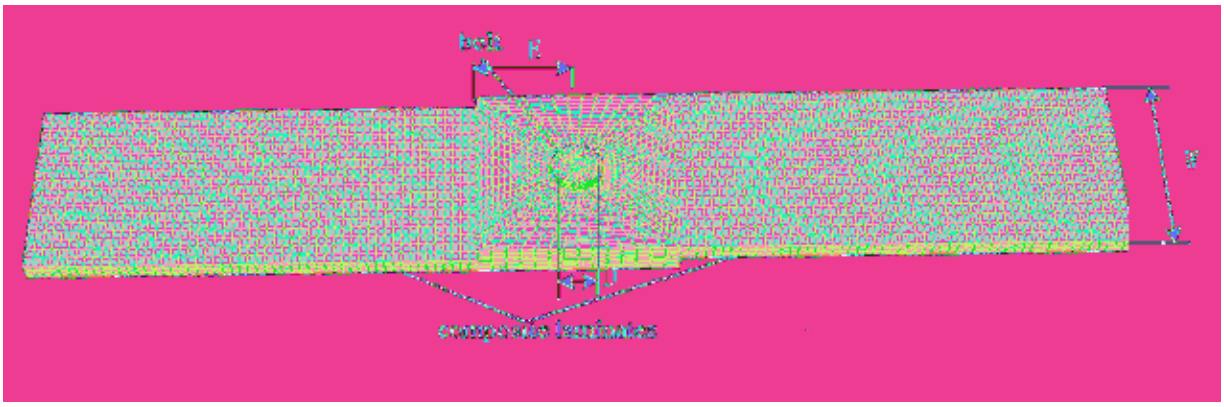


Fig.1 The geometric parameter schematic diagram of composite laminate

The Extended Finite Element Mehtod

For the purpose of fracture analysis, the enrichment functions typically consist of the near-tip asymptotic functions that capture the singularity around the crack tip and a discontinuous function that represents the jump in displacement across the crack surfaces. The approximation for a displacement vector function u with the partition of unity enrichment is

$$u(x)=\sum_I N_I(x)\left[u_I+\underbrace{H(x)a_I}_{I\in K_\Gamma}+\underbrace{\sum_{\alpha=1}^{4}\varphi_\alpha(x)b_I^\alpha}_{I\in K_\Lambda}\right] \tag{1}$$

where $N_I(x)$ are the usual nodal shape functions; the first term on the right-hand side of the above equation, u_I is the usual nodal displacement vector associated with the continuous part of the finite element solution; the second term is the product of the nodal enriched degree of freedom vector, a_I and the associated discontinuous jump function $H(x)$ across the crack surfaces; and the third term is the product of the nodal enriched degree of freedom vector, b_I^α and the associated elastic asymptotic crack-tip functions $\varphi_\alpha(x)$. The first term on the right-hand side is applicable to all the nodes in the model; the second term is valid for nodes whose shape function support is cut by the crack interior, K_Γ are the nodes which crack interior passes through; and the third term is used only for nodes whose shape function support is cut by the crack tip, K_Λ are the nodes which crack tip passes through. As shown in Fig.2 K_Γ and K_Λ enrichment nodes are represented by square and circle respectively.

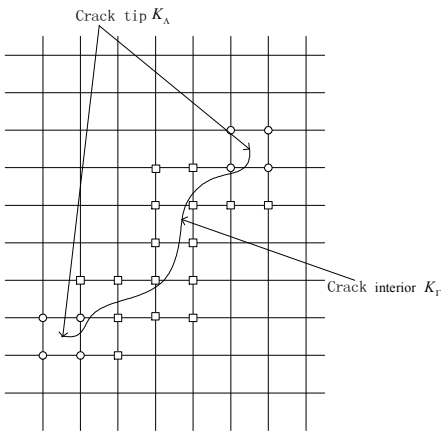


Fig.2 Crack tip and crack interior enrichment nodes

As shown in Fig. 2, the asymptotic crack tip functions $\varphi_\alpha(x)$ was given by

$$\left\{\varphi_\alpha(\mathrm{r},\theta)\right\}_{\alpha=1}^{4}=\left\{\sqrt{r}\sin\left(\frac{\theta}{2}\right),\sqrt{r}\cos\left(\frac{\theta}{2}\right),\sqrt{r}\sin\left(\frac{\theta}{2}\right)\sin(\theta),\sqrt{r}\cos\left(\frac{\theta}{2}\right)\sin(\theta)\right\} \tag{2}$$

where (r,θ) is a polar coordinate system with its origin at the crack tip, and $\theta=0$ is tangent to the crack at the tip. This function spans the asymptotic crack-tip function of elasto-statics, and $\sqrt{r}\sin\left(\frac{\theta}{2}\right)$ takes into account the discontinuity across the crack face.

Numerical results and discussion

Finite element model for bolted single-lap composite joint consisted of two laminates and bolt. The laminates the laminates are manufactured from HTA/6376, a high-strength carbon fiber-epoxy material currently used in primary structures in European aircraft industry. The unidirectional stiffness properties are shown in Table 1 with a stacking sequence of $\left[45^\circ/0^\circ/-45^\circ/90^\circ\right]_{5s}$, and the equivalent material engineering constants of laminate are shown in Table 2. The titanium bolt was modeled with isotropic material properties, with material constant $E_b=110GPa, \upsilon_b=0.29$.

Table 1 Unidirectional stiffness properties for HTA/6376

E_{11} $[GPa]$	E_{22} $[GPa]$	E_{33} $[GPa]$	G_{12} $[GPa]$	G_{13} $[GPa]$	G_{23} $[GPa]$	υ_{12}	υ_{13}	υ_{23}
140	10	10	5.2	5.2	3.9	0.3	0.3	0.5

Table 2 Equivalent homogeneous material properties used for laminates

E_{xx} $[GPa]$	E_{yy} $[GPa]$	E_{zz} $[GPa]$	G_{xy} $[GPa]$	G_{xz} $[GPa]$	G_{yz} $[GPa]$	υ_{xy}	υ_{xz}	υ_{yz}
54.25	54.25	12.59	20.72	4.55	4.55	0.309	0.332	0.332

Since the joint had different geometrical parameters, we select E/D=3, W/D=4, 5, 6 as the example to explain the finite element model in ABAQUS. The simulation results are shown in Fig.3. The geometric parameters are shown in Table 3.

Table 3 Geometric parameters of composite laminate

W[mm]	E[mm]	D[mm]	W/D	E/D
24	24	8	2	3
32	24	8	3	3
48	24	8	4	3

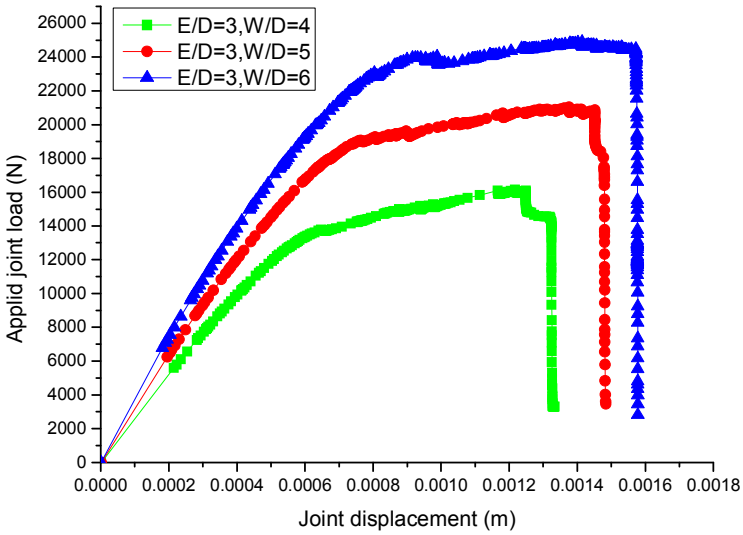


Fig.3 Displacement-load curve, E/D=3, W/D=4, 5, 6.

Conclusions

In this paper, failure load of single-lap bolted composite joint was predicted by Extended Finite Element Method, the influence of geometric parameters on failure of joint was investigated. As shown in Fig.3 the failure load rises with the increase of W/D. So we can know that when E/D was selected, W/D can obviously improve the load bearing capacity of composite joint, and this conclusion can be adopted for the design of bolted composite.

Acknowledgement

This work has been supported by the Fundamental Research Funds for the Central Universities (HEUCF20100201 and HEUCFZ1004), and the author wish to acknowledge Harbin Engineering University of China.

References

[1]Choi, JH, and Chun. J. Compus. Mater. 37(2003) 2163-2177.
[2]Mallick PK: Marcel Dekker Inc. (1988), p, 418.
[3]Choc JH, Lee DG. J Adhes. 55 (1996) 245-60.
[4] Belytschko T. and Black T: International journal of Fracture Mechianics, 45, 601-620
[5] Stazi FL., Budyn E., Chessa J. and Belytschko T. Computational Mechanics. 31 (2000) 131-150
[6]Sukumar N., Moes N., Moran B. and Belytschko T. International Journal for Numerical Methods in Engineering. 48 (2000) 1549-1570
[7]Moes N., Gravouil A. and Belytschko T. International Journal for Numerical Methods in Engineering. 53 (2002) 2549-2568.
[8]Gravouil A., Moes N., and Belytschko T. International Journal for Numerical Methods in Engineering. 53 (2002) 2569-2586.
[9]Karihaloo B.L. and Xiao Q.Z. Computers & Structures. 81 (2003) 119-129.

© (2012) Trans Tech Publications, Switzerland
doi:10.4028/www.scientific.net/KEM.488-489.775

Influence of drawing straining path on hydrogen damage of prestressing steel wires

Jesús Toribio[1,a], Miguel Lorenzo[2,b] and Diego Vergara[1,c]

[1]Department of Materials Engineering, University of Salamanca,

E.P.S., Campus Viriato, Avda. Requejo 33, 49022 Zamora (Spain)

[2]Department of Mechanical Engineering, University of Salamanca,

E.T.S.I.I., Avda. Fernando Ballesteros, 2, 37700 Béjar (Spain)

[a]toribio@usal.es, [b]mlorenzo@usal.es, [c]dvergara@usal.es

Keywords: hydrogen embrittlement, residual stress and strain states, wire drawing, straining path.

Abstract. Residual stress and strain states, produced during cold drawing, play a key role in hydrogen embrittlement (HE) of prestressing steel wires, because of hydrogen accumulation in certain places of the material is affected by stress and strains fields. Taking into account that the *drawing straining path* directly affects *both* residual stress and plastic strain distribution, the aim of the present paper is to clarify the influence of drawing straining path in the residual state and, consequently, its influence on the HE process of prestressing steel wires.

Introduction

Hydrogen embrittlement (HE) of prestressing steel wires is an important technological problem for the assessment of damage tolerance and structural integrity of civil engineering structures surrounded by harsh environments [1,2]. To evaluate HE phenomenon, the knowledge of the residual stresses and plastic strains distributions in wires generated after cold drawing is a key issue to obtain a successful prediction of prestressing wire lives. These stress and strain states are not negligible [3] and, so, the relevant role of *plastic strain* in HE of prestressing steel was revealed in a previous paper [4] and, thus, the necessity of considering such a variable in hydrogen diffusion analyses was established to avoid a dramatic underestimation of the hydrogen content given by the stress-only assisted diffusion approach in which the strain field is *not* taken into account.

In this sense, the *drawing straining path* directly affects *both* residual stress and plastic strain distribution and, consequently, the mechanical behaviour of cold drawn wires subjected to cathodic conditions where HE takes place. A previous paper [5] analyzed the influence of different drawing straining paths on HE of cold drawn wires, but only one step of the manufacture chain was considered. Taking this into account, the present paper goes further analyzing the influence on HE of *both* residual stress and plastic strain distribution induced by two *whole* real cold drawing chains (following two different drawing straining paths) of two commercial (*real*) prestressing steel wires. Obtained results prove the relevance of considering the *straining path*, and consequently its associated residual stress and plastic strain states, in the design of cold drawing process to achieve a better wire performance against hydrogen damage and, therefore, avoid the catastrophic failure of the structure surrounded by a corrosive environment.

Numerical modelling

Two different *real* (*industrial*) drawing processes whose main difference is the *reduction of cross-sectional area* at the first drawing stage are considered in the present paper. Both processes use a hot rolled bar of the same dimensions at the beginning of the process (diameter d = 12 mm) and at the end the dimensions of the commercial wire are equal as well (diameter d = 7 mm). In spite of this similitude, there are two important differences: the number of stages or steps in which the process is divided and the reduction of the cross-sectional area applied at the first stage of drawing, i.e., *the*

straining path undergone by both prestressing steel wires is obviously different. The main difference between both straining paths is the diameter reduction achieved at the first drawing step (cf. Table 1, where ε^{p}_{cum} represents the cumulative plastic strain, $\varepsilon^{p}_{cum} = 2\ln(d_0 / d_i)$, d_0 being the diameter of hot rolled bar and i the number of drawing stage). The two commercial prestressing wires analyzed are eutectoid steels with a similar chemical composition: Steel A (0.800% C, 0.690% Mn, 0.265% Cr, 0.230% Si, 0.060% V, 0.012% P, 0.009% S, 0.004% Al) and steel B (0.789% C, 0.698% Mn, 0.271% Cr, 0.226% Si, 0.078 % V, 0.011% P, 0.005% S, 0.003% Al).

Table 1. Wire diameter and plastic strains achieved during the two drawing processes.

	Stage	**0**	**1**	**2**	**3**	**4**	**5**	**6**	**7**
A	***d* (mm)**	12.00	10.80	9.81	8.94	8.22	7.56	7.00	--
	ε^{p}_{cum}	0.00	0.21	0.40	0.59	0.76	0.92	1.08	--
B	***d* (mm)**	12.00	11.23	10.45	9.68	9.02	8.54	8.18	7.00
	ε^{p}_{cum}	0.00	0.13	0.28	0.43	0.57	0.68	0.77	1.08

Fig. 1 plots the evolution of mechanical parameters of both drawing processes (σ_Y, yield stress; σ_R, ultimate tensile strength or UTS). It can be observed that while UTS follows a common trend for both drawing processes, the yield stress σ_Y changes significantly at the first and the last drawing stages, reaching at last drawing stage (commercial prestressing steel wires) an *identical* value in the two cases. Then, according to Fig. 1, the straining path affects the mechanical properties and, presumably, the corresponding residual stress state, that influences the mechanical behavior of the steel wires under HE environmental conditions [4,5].

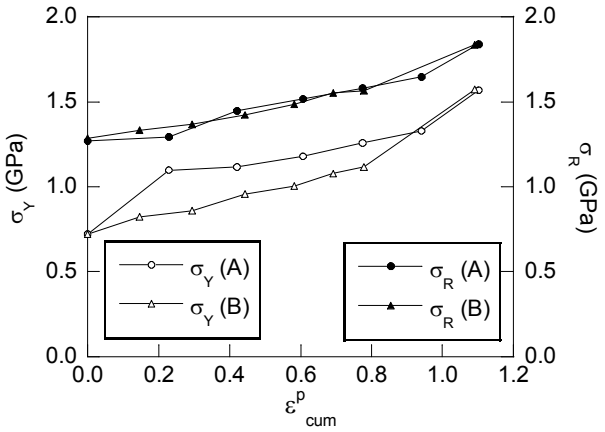


Fig. 1. Evolution of mechanical parameters during different straining paths of two industrial cold-drawing processes.

Cold drawing consists of the pass of the steel wire through a hard die [4,5]. In this work, both real (commercial) cold drawing processes in several passes or stages (A and B) were modelled by finite element method (FEM), their constitutive model being an elastoplastic solid with von Mises yield surface, associated flow rule and isotropic strain-hardening following the experimental stress-strain curve of respective hot rolled bars (not cold drawn at all). The die was modelled with an inlet angle of 7º, and the material of the die (tungsten carbide) was considered to be rigid due to its very high Young modulus in relation to that of the wire. Friction between the wire and the die was not considered in the numerical modelling. Initial dimensions of the both wires (A and B) were d_0 = 12 mm (initial diameter) and L_0 = 60 mm (initial length). In the case of the commercial cold-drawn pearlitic wires used in this analysis, the progressive (or repetitive) cold drawing processes are divided into six passes for steel A and into seven passes for steel B, so as to produce a commercial prestressing wire from a hot rolled bar (Table 1). The axisymmetric formulation is suitable for simulations. Corresponding

finite element model was created to model the drawing process in cylindrical coordinates [cf. 5]. Elastoplastic large deformation – large strain calculations were performed using a general-purpose finite element code with updated lagrangian formulation.

Residual stress and strain generated by cold drawing

Results of numerical simulations were focused on the mechanical variables that rule hydrogen diffusion process inside a metal according to the model fully described in [6] where hydrogen flux (***J***) (eq. 1) is considered to be dependent on the stress and strain states in terms of the hydrostatic stress (σ) and the hydrogen solubility ($K_{S\varepsilon}$) which is directly dependent of equivalent plastic strain (ε_P)

$$\boldsymbol{J} = -D(\varepsilon_P)\left\{\nabla C - C\left[\Omega\nabla\sigma + \frac{\nabla K_{S\varepsilon}(\varepsilon_P)}{K_{S\varepsilon}(\varepsilon_P)}\right]\right\} \tag{1}$$

where Ω is a constant dependent of partial volume of hydrogen (V_H) and temperature (T), D is the hydrogen diffusion coefficient and C is the hydrogen concentration.

The amount of hydrogen at wire surface Γ, $C_{eq}(\Gamma)$, can be obtained from the following equation

$$C_{eq}(\Gamma) = (1 + 4\varepsilon_P(\Gamma))\exp(\Omega\sigma(\Gamma)) \tag{2}$$

Fig. 2a and Fig. 2b show respectively the equivalent plastic strain (ε_P) and the hydrostatic stress (σ) distribution throughout the radial coordinate (r) for the two cold drawing processes.

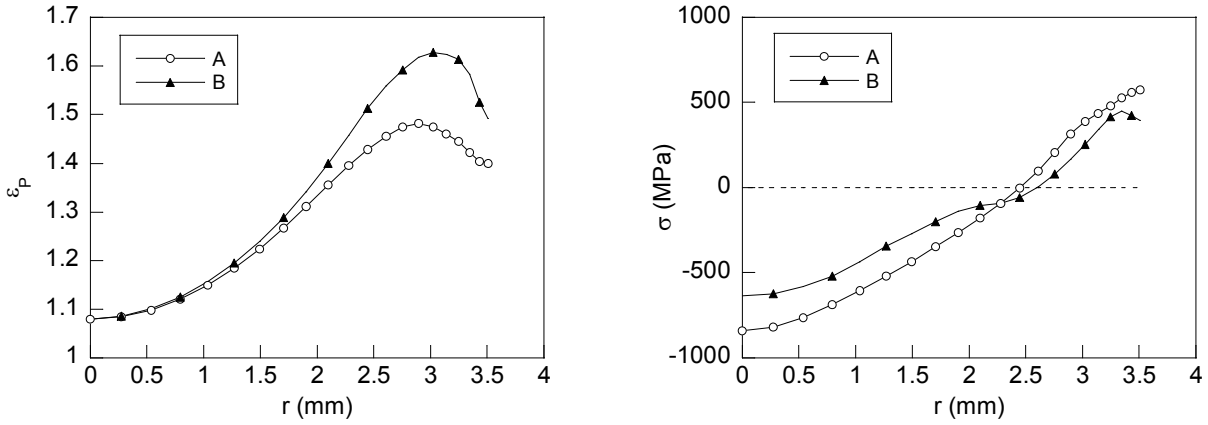


Fig. 2. Residual states distribution throughout the wire radius of the two cold drawing processes: (a) equivalent plastic strain; (b) hydrostatic stress.

Straining path does not modify the shape of plastic strain distributions (ε_P). In both analyzed processes the profile is similar: increasing from wire surface until a maximum value (placed close to surface) is reached and then decreasing with depth towards wire center. However, sensible differences are obtained after each one of the process analyzed over the outer half radius (1.75 mm < r < 3.5 mm) while over the inner half radius (0 mm < r < 1.75 mm) the differences decrease progressively with depth becoming negligible at wire center (r = 0). So, inner points of the wire are not affected by the differences in drawing straining path (as could be expected due to the fact that the local effect of diameter reduction on the wire vanishes with depth) and, consequently, the plastic strain obtained at deeper points is equal to the one given by the cumulative plastic strain, i.e., considering an uniform plastic strain distribution.

The hydrostatic stress distributions (σ) generated after drawing exhibit in both processes tensile stress at surface and compression at inner points. However, the values and shape are different in the two processes analyzed. Wire drawing A generates a profile with a uniformly decreasing tend with depth while wire drawing B generates a profile which decreases with depth as well, but with a *plateau* in the middle of wire radius. In addition, an important change for HE analysis is obtained in wire obtained after drawing B: the maximum value is placed not at wire surface, as in wire drawn B, but slightly moved to inner points. This displacement supposes the existence of a positive *gradient of hydrostatic stresses* and, therefore, according to eq. 1, hydrogen flux would be increased.

HE susceptibility can be *qualitatively* estimated from obtained residual stress and plastic strains distributions in the following way. Two competing effects can be considered. Firstly, the gradient of plastic strain is two times higher in wire drawn B than in wire drawn A. In addition, the gradient of hydrostatic stress in wire drawn B is positive, i.e., enhancing hydrogen entry, while in wire A is negative and, therefore, the effect on hydrogen diffusion is the opposite, i.e., difficult hydrogen entry and diffusion. Secondly, the hydrogen amount at surface, given by eq. 2, is higher in wire A due to the higher value of hydrostatic stress σ at surface (cf. Fig. 2b) in spite of a lower value of equivalent plastic strains ε_P at surface (cf. Fig. 2a). So, from the later, it can be considered that in wire A surface there is more hydrogen available for entering into the material but the driving forces (gradient of hydrostatic stresses and gradient of equivalent plastic strains) are lower than in wire drawn B where a faster hydrogen accumulation and, therefore, damaging action could be expected.

Conclusions

The straining path applied during wire drawing significantly affects the residual stress and plastic strains generated after the conforming process. Depending on the sequence of wire diameter reduction applied during the process, different residual stress and strain states are obtained in the wire after straining. This way, wire drawn A (heavy first reduction stage) generates a smoother plastic strain profile than the one in wire drawn B (heavy last reduction step). Hydrostatic distributions generated in wire drawn B exhibit a positive gradient enhancing hydrogen entry while in wire drawn A the gradient is negative, thereby delaying hydrogen entry. These changes affect the hydrogen diffusion process and, therefore, the hydrogen susceptibility of such wires depending of two competing effects: the *amount of hydrogen at surface* (higher in wire drawn A due to the higher value of hydrostatic stresses at surface) and the higher *gradient of the driving force for hydrogen diffusion* (higher in wire drawn B for both gradients, hydrostatic stress and equivalent plastic strain), the latter effect producing heavier hydrogen damage in wire B.

Acknowledgements

This work was financially supported by the following Spanish Institutions: MCYT (Grant MAT2002-01831), MEC (Grant BIA2005-08965), MCINN (Grant BIA2008-06810) and JCYL (Grants SA067A05, SA111A07 and SA039A08).

References

[1] L. Vehovar, V. Kuhar and A. Vehovar: Eng. Fail. Anal. Vol. 5 (1998), p. 21

[2] M. Perrin, L. Gaillet, C. Tessier and H. Idrissi: Corros. Sci. Vol. 52 (2010), p. 1915

[3] M. Lorenzo, D. Vergara, V. Kharin and J. Toribio: Anal. Mec. Fract. Vol. 1 (2007), p. 123

[4] J. Toribio, V. Kharin, D. Vergara, J. Blanco and J. Ballesteros: Corros. Sci. Vol. 49 (2007), p. 3557

[5] J. Toribio, M. Lorenzo, D. Vergara and V. Kharin: Corros. (*In press*).

[6] J. Toribio, V. Kharin, D. Vergara and M. Lorenzo: Adv. Mat. Res. Vol. 138 (2010), p. 117

© (2012) Trans Tech Publications, Switzerland
doi:10.4028/www.scientific.net/KEM.488-489.779

Structural Integrity of CO2 Transport Pipelines – A Review

Amir Chahardehi[1,a]

[1]School of Engineering, Whittle Building, Cranfield University, Beds, MK43 0AL, UK.

[a]a.chahardehi@cranfield.ac.uk

Keywords: CO2 Transport Pipelines, Structural Integrity, Stress Intensity Factor, Toughness, Ductile Failure, Brittle Failure, Crack Propagation.

Abstract. A recent trend in the development of CO2 pipelines is the shift from the predominance of transport of CO2 for enhanced oil recovery (EOR) to the transportation of CO2 as part of the carbon capture and storage (CSS) process for global warming mitigation. Among the processes of capture, transport, and storage, less attention has been paid to transport as it is assumed to be for granted, existing technology. This paper presents a focused analysis of the problem of structural integrity of CO2 pipelines through reviewing the state-of-the-art literature and practice, and highlights the need for a unified code of practice for the modelling of integrity and, due to the potentially hazardous nature of CO2, safety, in these pipelines.

Introduction

The need to control and reduce the emission of CO2 into the atmosphere has been the driving force behind the development of CCS technologies. Initiatives such as the EU Emissions Trading Scheme, usually requiring companies to limit or reduce greenhouse gas emissions, mean there will be a serious economic driver for power generation companied to consider CCS technology. Moreover, for the CCS process to be cost-effective and safe all three areas of capture, transport and storage should be developed and possibly standardised. However, as the Congressional Research Service Report on CO2 pipelines indicates the general focus of CCS and related legislation is on the capture and storage of CO2 and not its transportation. As the report suggests, "this reflects the perception that transporting CO2 via pipelines does not present a significant barrier to implementing large-scale CCS." [1]. It is evident that pipelines will be the primary mode of transport of CO2 in the context of CO2 [2, 3]. Compared with hydrocarbon transport pipelines, there is very little experience in the design and maintenance of CO2 pipelines. Also, since some or most of the storage locations are offshore, the requirements for pipelines in the offshore environment need to be considered. Design and construction of new dedicated pipelines for CO2 transport, or, in some cases, the conversion of existing infrastructure, both require a thorough understanding of the safety issues associated with the transport of CO2.

Safety Considerations – Leakage Scenario and Crack Propagation

Makino et al. highlight the existing issues with the prediction of crack propagation in ultra-high-pressure natural gas pipelines [4]. In the words of Hood [5], "a high pressure pipeline is a unique type of structure that may offer uninterrupted fracture paths.". Whereas the catastrophic failure mode in pressurised pipelines is clearly demonstrated in burst tests as being ductile [5-7], crack initiation at low temperatures is more likely to be due to the metal lacking sufficient toughness, i.e. brittle failure mode [8]. In many cases the failure is a mixture of brittle and ductile fracture [9]. Cravero et al. recommend a constraint-modified failure assessment diagram which takes into account both ductile and cleavage (brittle) mode failures [10].

Safety analysis of the pipeline should include the important 'what-if' scenario, where a defect is assumed to be created in the pipeline. As stated by Burdekin [11], "...without defects, the problems of fracture in service would hardly arise". The existence of a defect in the pipeline would lead to rapid escape of fluid CO2 from the hole. Mahgerefteh et al. have proposed an outflow model which predicts the decompression behaviour of the CO2 flow through the pipe defect [12]. Starting from liquid or supercritical phases, the saturation pressure – at which liquid and gas phases are in equilibrium – is determined by the initial pressure of the fluid in the pipe; the higher the initial pressure the higher the saturation pressure. For a pure component, the temperature is a function of pressure and therefore the temperature of the escaping gases is wholly dependent on the depressurisation trajectory. Eldevik et al. [13] argue that, as a result of pipeline failure, rapid depressurisation may cause the CO2 to cool to the triple point and the low temperatures could cause associated operational and structural problems. A detailed discussion on the decompression behaviour of CO2 from a pipeline defect can be found in [12]. In a review article, Eldevik emphasises that the likelihood of solid CO2 deposition on the pipe as a result of decompression may bring the local temperature as low as - 78˚C [14]. This can have a severe impact on the pipeline material's toughness or resistance to fracture.

Model Development – Component Testing vs. Specimen Testing

Typical pipeline steels, i.e. X65, X70, X80 and the 'next generation' X100, used by TransCanada [15], show a ductile-to-brittle transition at low temperatures. Knowledge of the exact behaviour of the material is key in the development of a structural integrity model for the pipeline. As part of the development of the model, a database containing toughness characteristics of the material as a function of temperature should be compiled.

Current test standards relevant to the evaluation of pipeline toughness include testing methods such as the Drop Weight Tear Test (DWTT) [16-18] and Notched Bar Impact Test [19]. Some authors have recommended the use of pre-cracked test specimens in the impact test and report a closer correlation with the plane-strain fracture toughness (KIC) [20]. However, there is a considerable amount of uncertainty as to the correlations between the actual fracture toughness value pertinent in the design and analysis of CO2 pipelines and the results from the Charpy impact test or DWTT [21]. This is also true for the problem of analysis of crack arrest behaviour [22]. The conclusion of the Health and Safety Executive report on the subject is that whereas individual correlations have been introduced and summarised, "no single correlation describes completely the KIC temperature transition although some attempt to do so." [21]. The Det Norske Veritas Recommended Practice [2] rather vaguely suggests that the pipeline should be designed such that any rupture is arrested within a small number of pipe joints. Notwithstanding the fact that the predictive requirements of any structural integrity model demand accurate knowledge of material characteristics at different temperatures, a more rigorous standard practice should be devised for CO2 pipelines considering their growing importance and the potential hazards of pipeline failure and CO2 leakage. There are currently a relatively large number of test programmes dedicated to developing systematic understanding of the structural integrity issues and requirements of these pipelines. A rigorous, robust structural integrity model for CO2 pipelines can only be obtained after material characteristics tests, such as DWTT, Charpy and fundamental fracture mechanics tests involving the direct determination of KIC or CTOD, are used in conjunction with component testing, full-scale or otherwise. Large-scale component testing gives invaluable information about the transferability of the results obtained from specimen tests to the real world. Depending on the type of steel used in the pipeline, for low strength steels there could be a difference between the resistance to initiation and propagation while for ultra high strength steels there is little difference between the two [11]. A critical part of the structural integrity model should deal with the arrest and initiation stress intensity factors; Gray et al. have conducted tests on mild steels and demonstrated that the two values are identical in sub zero temperatures [23]. This being dependent on the type of steel, fundamental tests should include crack initiation and measurements of the onset of unstable crack growth as well as

crack arrest in regions of temperature gradient, where the crack in the pipeline is likely to grow from a region of low temperature in the vicinity of the defect to a region where the temperature is effectively in equilibrium with the environment. The low toughness value of the metal in the neighbourhood of the defect would mean that crack initiation is likely even though the normal 'working temperature' toughness of the metal is sufficient to ensure lack of crack growth [14, 23]. Robertson devised a test to characterise this temperature gradient effect on the propagation of cleavage fracture in steels [24]. This type of test, modified to account for the requirements of CO2 pipelines in terms of steel type, thickness and geometry constraint, can be used as a tool in the generation of the material property database. The resulting model should include the effect of local cooling and the consequences on stress (local thermal stress) and toughness (reduced toughness due to temperature drop) and at the same time, incorporate residual stresses e.g. at weldments, allow for anisotropy in pipeline materials [25] and also use beneficial residual stresses advantageously through the application of weight functions [26] in order to construct a robust, predictive structural integrity model for CO2 pipelines.

Conclusions

A review of the structural integrity issues concerning the CO2 transport pipelines has been presented. The scope of the relevant aspects of pipeline integrity and the ambiguity of existing standards call for a comprehensive and dedicated research into the modelling of the structural integrity of these pipelines. Furthermore, the expansion of the CO2 pipelines and the risks associated with the CO2 would mean that a standard code of practice needs to be clearly defined for this class of pipelines. The fundamental fracture mechanics based model is at the core of this standard but pertinent matters ranging from the choice of suitable material through to the establishment of the inspection regime, based on the integrity model are also key elements of this practice.

References

[1] P.W. Parfomak, P. Folger, *Carbon Dioxide (CO2) Pipelines for Carbon Sequestration*, Emerging Policy Issues, Congressional Research Service Report for Congress, 19 April 2007, Order Code RL33971.
[2] Det Norske Veritas, *Recommended Practice DNV-RP-J202, Design and Operation of CO2 Pipelines*, April 2010.
[3] S. Holloway, *Carbon dioxide capture and geological storage*, Philos Transact Royal Soc A Math Phys Eng Sci, 2007, 365:1095–1107.
[4] H. Makino, T. Kubo, T. Shiwaku, et al., *Prediction for Crack Propagation and Arrest of Shear Fracture in Ultra-high Pressure Natural Gas Pipelines*, ISIJ Int, 2001; 41(4):381–388.
[5] J.E. Hood, *Fracture of Steel Pipelines*, Int J Pressure Vessels Piping, 1974; 2:165-178.
[6] W.A Maxey, *Factors Affecting Ductile Fracture in Offshore Gas Pipelines*, Proceedings of the Offshore Technology Conference, OTC4241, 14th Annual OTC, May 1982, Houston, USA.
[7] G.D. Fearnehough, G.M. Lees, J.M. Lowes, R.T. Weitner, *The Role of Stable Ductile Crack Growth in the Failure of Structures*, Practical Application of Mechanics to Pressure Vessel Technology, Institution of Mechanical Engineers, 1970.
[8] F.M. Burdekin, J.F. Knott, J.D.G. Sumpter, A.H. Sherry, *TAGSI views on aspects of crack arrest philosophies for pressure vessels with thicknesses up to 100mm*, Int J Pressure Vessels Piping, 1999; 76:879–883.
[9] G.D. Fearnehough, *Fracture Propagation Control in Gas Pipelines: A Survey of Relevant Studies*, Int J Pressure Vessel Piping, 1974; 2:257-282.
[10] S. Cravero, C. Ruggieri, *Structural integrity of axially cracked pipeline using conventional and constrain-modified failure assessment diagrams*, Int J Pressure Vessels Piping, 2006; 83:607–617.
[11] F.M. Burdkin, The *Practical Application of Fracture Tests to Prevent Service Failures*, Welding Research Supplement, March 1968, pp. 129-139.

[12] H. Mahgerefteh, O. Atti, *Modeling Low-Temperature-Induced Failure of Pressurized Pipelines*, AIChE J, 2006; 52(3):1248– 1256.
[13] F. Eldevik F, B. Graver, L.E. Torbergsen, O.T. Saugerud, *Development of a Guideline for Safe, Reliable and Cost Effective Transmission of CO2 in Pipelines*, Energy Procedia, 2009; 1:1579–1585.
[14] F. Eldevik, *Safe Pipeline Transmission of CO2*, Pipeline Gas J, 2008; 235(11):76–77.
[15] Information on http://www.transcanada.com/customerexpress/update/march_2004/article_4.html
[16] *Recommended Practice for Conducting Drop-Weight Tear Test on Line Pipe*, API RP 5L3, American Petroleum Institute Standard.
[17] *Metallic materials – Drop weight tear test*, BS EN 10274:1999, British Standard.
[18] *Standard Test Method for Drop-Weight Tear Test of Ferritic Steels*, ASTM E436-91, ASTM International Standard.
[19] *Standard Test Methods for Notched Bar Impact Testing of Metallic Materials*, ASTM E23-07a, ASTM International Standard.
[20] J.C. Radon, C.E. Turner, *Fracture Toughness Measurement by Instrumented Impact Test*, Eng Fract Mech, 1969; 1:411–428.
[21] *Critical Examination of Correlations between Fracture Toughness and Charpy Impact Energy*, Offshore Technology Report – OTO 96 710, Health and Safety Executive.
[22**]** C.S. Weisner, *Predicting Structural Crack Arrest Behaviour using Small-scale Material Characterisation Test*, Int J Pressure Vessels Piping, 1996; 69:185-196.
[23] I. Gray, A.H. Priest, *The Arrest of Propagating Cracks*, Practical Applications of Fracture Mechanics to Pressure Vessel Technology, Institution of Mechanical Engineers, 1971.
[24] T.S. Robertson, *Propagation of Brittle Fracture in Steel*, J Iron Steel Inst, 1953; 175:361–374.
[25] J.B. Ju, J.S. Lee, J.I. Jang, *Fracture toughness anisotropy in a API steel line-pipe*, Mater Lett, 2007; 61:5178–5180.
[26] A. Chahardehi, F.P. Brennan, A. Steuwer, *The Effect of Residual Stresses Arising from Laser Shock Peening on Fatigue Crack Growth*, Eng Fract Mech, 2010;77(11):2033–2039.

© (2012) Trans Tech Publications, Switzerland
doi:10.4028/www.scientific.net/KEM.488-489.783

Damage mechanics in G/E tubes under tension-torsion cyclic loading

Carraro P.A, Quaresimin M.

Department of Management and Engineering - University of Padova, Stradella S. Nicola 3, I-36100 Vicenza, Italy

carraro@gest.unipd.it, marino.quaresimin@unipd.it

Keywords: multiaxial fatigue, composite materials, damage, crack propagation

Abstract. In this work, multiaxial fatigue tests results on $[0_F/90_{U,3}/0_F]$ glass/epoxy tubes are discussed. Specimens are subjected to combined tension-torsion loadings, resulting in the stress components σ_2 and τ_{12} in the 90° layers of the tubes. The effect of shear stress on damage mechanics has been investigated and a strong influence on both damage onset and propagation has been observed. SEM investigation of fracture surfaces shows the dependence of damage modes, at the microscopic scale, on the multiaxiality condition. Comparison with previous results on tubes with different lay-ups ($[90_4]$, $[0_F/90_{U,3}]$) shows the strong influence of the constraining 0° fabric layers on the damage onset and propagation.

Introduction

Few criteria for multiaxial fatigue behavior of composite materials can be found in the literature. Some of them have been analyzed and compared to experimental data [1], obtaining not always satisfactory results. Most of the criteria in the literature are empirical and they do not take into account the actual damage modes, which are strongly dependent on the multiaxiality condition. In order to define a reliable prediction model it is important to understand and describe quantitatively the damage mechanisms and their nucleation and propagation till the final failure. The aim of this work is to investigate the damage mechanisms of glass/epoxy composite tubes subjected to a cyclic loading condition resulting in a non fiber-dominated behavior. In a previous paper [2] fatigue tests on glass/epoxy tubes subjected to combined tension-torsion, with two different lay-ups, $[90_4]$ (UD) and $[0_F/90_{U,3}]$ (FU) were presented. In the present work, tubes with lay-up $[0_F/90_{U,3}/0_F]$ (FUF) are tested under different values of the biaxiality ratio $\lambda_{12} = \tau_{12}/\sigma_2$ in the 90° plies, in order to analyze its influence on the damage onset and propagation in these layers.

Materials and experimental results

Tubular specimens are used for fatigue testing. Tubes are produced by mandrel wrapping and cured in autoclave (6 bars, 140°C, 1 hour). The internal and external diameters are 19 and 22 mm and the total and calibrated lengths are 150 and 70 mm respectively. The following materials are used:
- UE 400 REM by SEAL, G/E UD tape, thickness = 0.38mm, for the inner 90° plies;
- EE106-ET443 by SEAL, G/E fabric, thickness = 0.13mm, for the internal and external plies.

An axial-torsional MTS 809 testing system is used for fatigue testing (load-controlled cycles, load ratio R = 0, frequency 10 Hz). Damage onset and evolution are monitored during the tests by an infrared camera FLIR SC7600 MW and by eye observations. When an UD lamina is subjected to a cyclic loading condition leading to a non-fiber-dominated response, it fails suddenly and without a progressive damage evolution. Conversely, if the same lamina is constrained between other layers with higher strength (i.e. 0° layers), it undergoes multiple cracking and stable crack propagation. This allows us to analyze with more accuracy the damage modes and their dependence on the biaxiality ratio in the specimens of the FUF and FU type, with respect to the UD ones. Another advantage of the FUF tubes is that the damage nucleation in the 90° layers is insensitive to the surface finishing and surface defects, as instead may happen instead for FU specimens. In Fig.1 the S-N data for the nucleation of the first visible crack are plotted and compared to the curves for the UD tubes [2], which correspond in this case to the final failure. For both types of specimens, a

detrimental effect of the increasing shear component can be clearly observed. It is important to notice that the curves for the UD tubes slightly underestimate the fatigue resistance of the 90° layers in the FUF specimens in terms of first crack nucleation. This is due to the constraining effect of the stiffer fabric layers (increasing the in-situ strength of the 90° plies) and the entity of this effect depends on both the number of 90° plies and the stiffness of the constraining fabric layers [3].

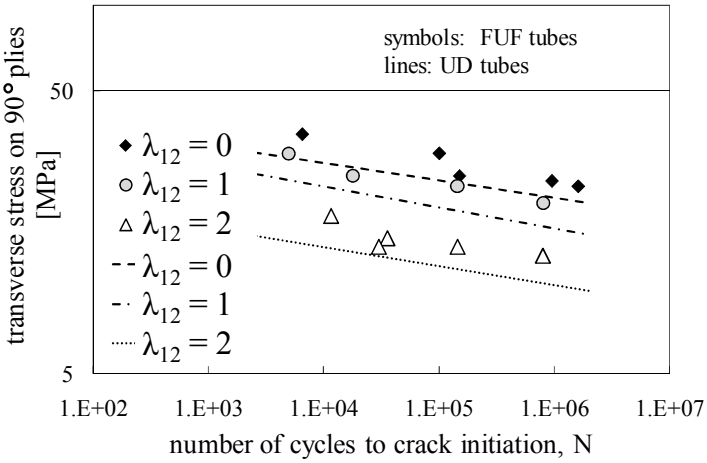


Fig.1 Comparison between crack nucleation data for FUF tubes and crack nucleation/final failure curves for UD samples

With the aim of understanding the influence of the shear stress on damage evolution, crack propagation analyses are made on FUF tubes keeping a maximum cyclic transverse stress of 30 MPa and varying the biaxiality ratio (and thus the applied shear stress) from 0 to 1,5. The average Crack Growth Rate (CGR) is calculated as the average slope of the propagation curves for the various λ_{12}. In Fig. 2 the angle of propagation, calculated as $(2\alpha - 2\alpha_i)$, where $2\alpha_i$ is the initial crack angle at the moment of its identification, is plotted against the number of cycles of propagation. The slope of the curves, i.e. the CGR, increases with increasing the shear stress contribution. Qualitatively similar propagation curves have been reported in [2], where the FU specimens were subjected to a maximum cyclic transverse stress of 23.7 MPa, with λ_{12} varying from 0 to 2. The average CGRs for FU tubes are higher than in the present case, though they are subjected to a lower stress state. This is explained if the results are analyzed in terms of Strain Energy Release Rate, as shown later on. Tensile loading is associated to a mode I propagation, while torsion loading to a mode II crack growth.

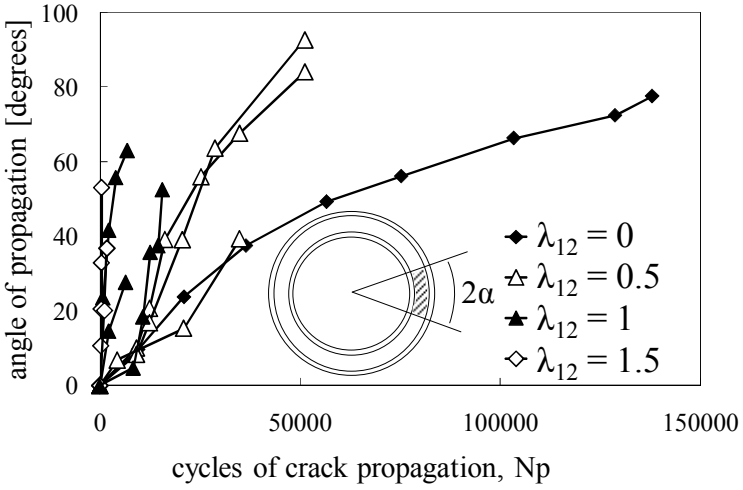


Fig.2 Crack propagation curves (maximum cyclic transverse stress = 30 MPa)

The mode I and II components of G are calculated via FE analyses of a cracked tube subjected to pure tension and torsion loadings. Only one half of the tube is modelled with different crack angles (Fig. 3), and the compliance method is used for SERR calculation, with equations (1a and b):

$$G_I = \frac{F^2}{2}\frac{dC_I}{dA}, \qquad G_{II} = \frac{T^2}{2}\frac{dC_{II}}{dA} \tag{1a and b}$$

where A is the cracked area.

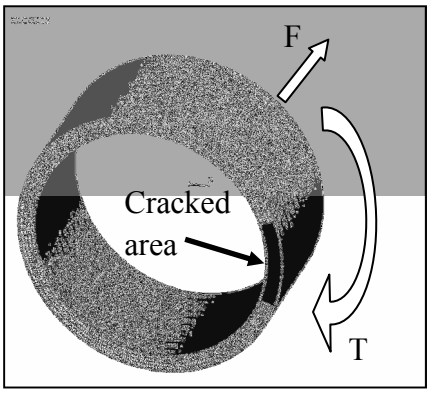


Fig. 3 FE model of a cracked tube

Axial and tangential constrains are applied on the non-cracked portion of the front surface of Fig.3. Tension and torsion loading conditions are simulated by applying a uniform axial displacement on the back surface and a uniform tangential displacement on the external circumference of the back surface respectively. When a cracked ply is constrained between other layers, in a flat coupon under mode I, the SERR value reaches a plateau after a crack length about twice the layer thickness [4]. According to Eq. (1a and b), this means that the compliance's derivative with respect to the crack area becomes pretty constant. A similar trend is found even in the tubes investigated here, as shown in Fig. 4 a) and b).

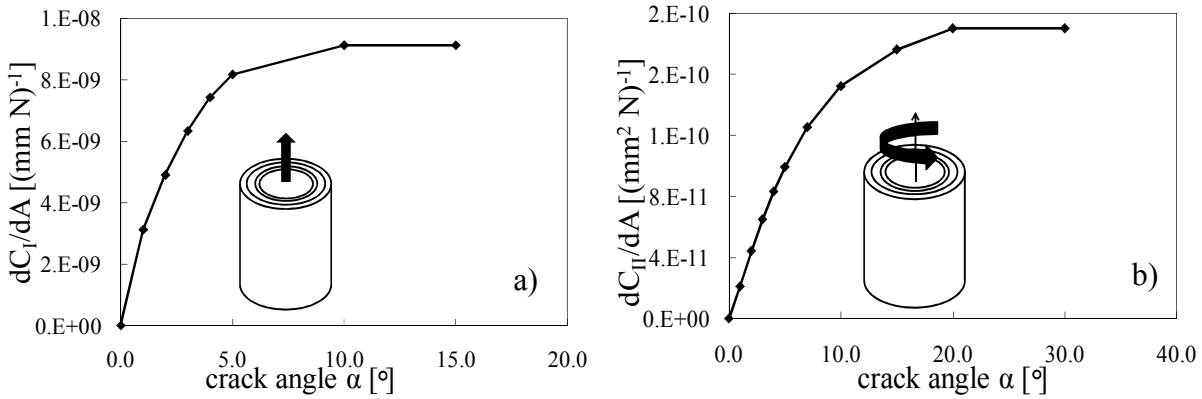


Fig. 4 Compliance derivative with respect to the crack area for a) mode I and b) mode II loadings

Since crack propagation occurs mainly in the plateau region, a single value of G_I and G_{II} has to be associated to each of the propagation curves in Fig. 2, both for FU and FUF tubes. By keeping G_I constant and increasing the Mode Mixity, the average CGR increases, in a similar way for the two kinds of samples (Fig.5). FU tubes are subjected to a higher SERR even though the stress level is lower, and this is due to reduced constraining effect of the single internal fabric layer with respect to the case of FUF tubes where the 90° plies are constrained from both the internal and external fabric layers.

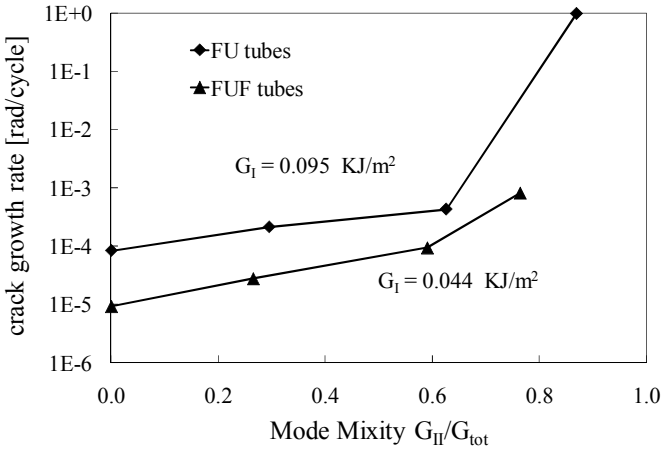


Fig. 5 Average CGR vs mode mixity for a fixed G_I, for FU and FUF samples

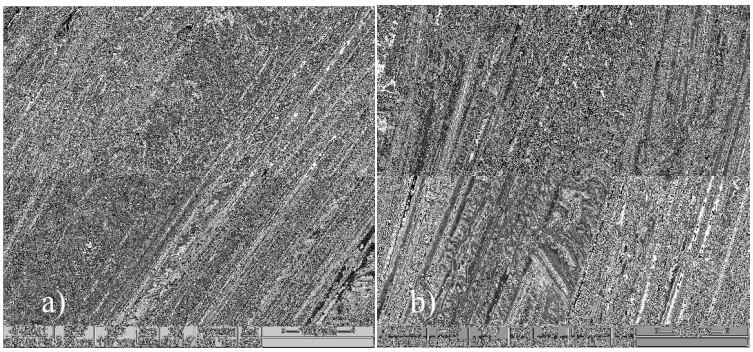


Fig.6 Fracture surfaces for a) $\lambda_{12} = 0$ and b) $\lambda_{12} = 2$

Fracture surfaces analysis

SEM analysis indicates that for low values of λ_{12} (0 and 0.5) the fracture surfaces are rather smooth, while for higher λ_{12} values (1 and 2) shear cusps are widely present, which are typical for shear failure. All the samples show some clean fiber surfaces, suggesting that fiber-matrix debonding may play a role in the fracture process, however not being necessarily the leading damage mode.

Conclusions

The behavior of G/E tubes under tension/torsion loading has been investigated and the main conclusions are as follows:

- A strong detrimental effect of the shear stress is found for damage onset and evolution;
- Crack nucleation resistance for FUF tubes is slightly higher than that for UD ones, this is attributed to the constraining effect of the internal and external fabric layers.
- Average CGR increases with increasing shear stress contribution for FU and FUF samples;
- The external fabric layer on FUF specimens plays an important role in decreasing the SERR and therefore the CGR;
- Fracture surfaces and damage modes are seen to be strongly dependent on the biaxiality ratio.

References

[1] Quaresimin M., Susmel L., Talreja R., International Journal of Fatigue, 32, 2-16, 2010.
[2] Quaresimin M., Talreja R, Proceeeding of ECCM14, 7-10 June 2010, Budapest, Hungary.
[3] Wang J., Karihaloo B. L., Composite Structures, 47, 635-641, 1999.
[4] Ho S., Suo Z., Journal of applied mechanics, 60, 890-894, 1993.

© (2012) Trans Tech Publications, Switzerland
doi:10.4028/www.scientific.net/KEM.488-489.787

Acoustic damage analysis of a gear system

Ales Belsak[1, a], Jure Prezelj[2, b]

[1]University of Maribor, Faculty of Mechanical Engineering,
Smetanova 17, 2000 Maribor, Slovenia

[2]University of Ljubljana, Faculty of Mechanical Engineering,
Askerceva 6, 1000 Ljubljana, Slovenia

[a] ales.belsak@uni-mb.si, [b] jurij.prezelj@fs.uni-lj.si

Keywords: Gear, Failure, Acoustic Emission, Acoustic Image.

Abstract. In diagnostics, noise can be a very reliable way of defining the condition of mechanical systems. There are different methods to visualise the noise source. Primarily, they deal with a specific noise source in a specific acoustic environment. This paper presents a visualization method of complex noise sources, using an acoustic camera. This method makes it possible to visualise all types of different complex noise sources; a special acoustic algorithm is applied for this purpose. Also, it is possible to observe various transient acoustical phenomena.

Introduction

The purpose of maintenance is to maintain the characteristics of a technical system at the most favourable or still acceptable level. First it is required to collect precise data, which must be then appropriately analysed, compared and processed to effectively determine the condition of a technical system.

Gear units are most frequent machine parts or couplings; they are of different types and sizes and consist of a housing, toothed wheels, bearings. The major causes for durable damages in gear units are as follows: geometrical deviations or unbalanced component parts, material fatigue [1], which results from the engagement of a gear pair, or damages of roller bearings.

The condition of mechanical systems is often determined, using vibrations and noise measuring methods. When data is acquired, this data is analysed, using different tools [2], which make it possible to define the features denoting the presence of damages and faults.

Identification of noise sources and analysis of signals

Visualization method of all types of different complex noise sources, with an acoustic camera, is based on a new algorithm of digital signal processing.

The method based on an acoustic camera is very different from the acoustic ray reconstruction method [3,4]. Signals are obtained with microphones, placed on the ring or the cross of an acoustic camera. The signals are then processed in a rather complex way, using the acoustic camera algorithm, which corrects the delay of individual signals (i.e. the length of the path of the sound waving from the elementary source to an individual microphone on the camera) in relation to time. This delay is appropriately corrected in time domain, whereas this is carried out on the basis of phases in frequency domain when using the sound ray reconstruction method [5,6].

Sound waves travel from the elementary acoustic source to an individual microphone; microphones are fixed on the ring of an acoustic camera (Fig. 1). The lengths of the paths r_i, along which sound waves travel, differ. Due to different path lengths of sound waves $|r_i|$, signal delays Δ_i of the same sound wave, created at the elementary sound source $V(x_j)$, vary.

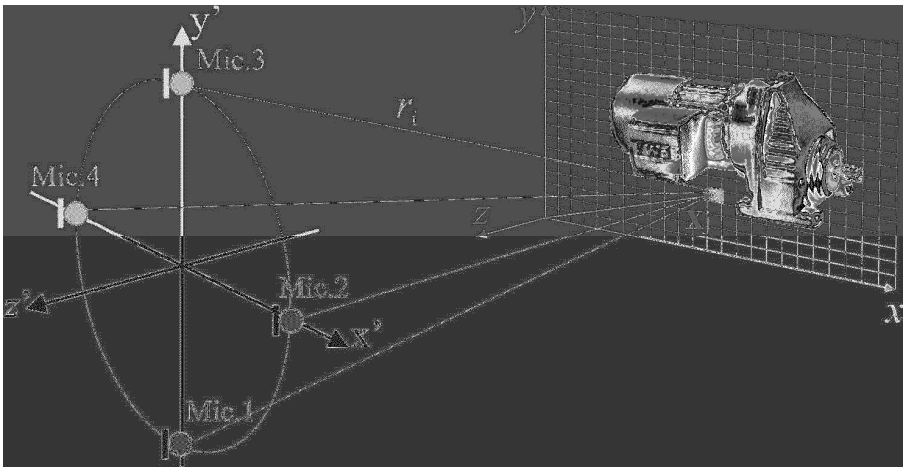


Fig. 1: Path length of an elementary source to individual microphones, which are fixed on an acoustic camera

The method using the acoustic camera is the only method of acoustic sources visualization that functions exclusively in time domain. It is not necessary to use the Fourier transform to calculate the acoustic image. Consequently, the limitations relating to the use of the Fourier transform do not apply when using an acoustic camera. Frequency analysis is a part of the user system; the algorithm, however, calculates the acoustic image first and the Fourier transform only after that.

The measurement is based on the use of an acoustic camera (GFaI with dRec48C192) and 32 phase coordinated microphones, placed on a ring in reference to the work in a free acoustic field. Prepolarised condensation microphones with linear frequency of 23 kHz (–3 dB) are used. Their response is gradually reduced from 6 dB per decade to 40 kHz. In order to obtain an adequate image resolution, high frequency area microphones must be used. Higher sampling frequencies or better phase coordination of microphones are necessary to get higher resolution. The highest sampling frequency is 196 kHz per channel and an analogue-digital converter resolution is 21 bit. Digitalised signals are temporarily stored in this converter during the measuring process. The data is transferred to a PC first, afterwards it is possible to calculate the sound source acoustic image.

The rotating movement of a gear unit, which enables the transmission of rotating movement, is most frequently periodical. The presence of local and time changes in vibration signals denotes faults and damages, which represent a disturbing quantity or impulse. Thus, time-frequency changes can be expected, which indicate faults or damages.

Certain frequency components fairly often appear in signals only from time to time. Time-frequency analysis makes it is possible to find out how frequency components of non-stationary signals change with time and to identify their intensity levels.

Practical tests

A single stage gear unit SEW-EURODRIVE RX47 DR63S4 (electromotor with power 120W) with a helical gear unit with straight teeth integrated into it was used. As the distance between the teeth of the smaller gear unit was very small, it would have presented a great difficulty to produce a fatigue crack in a tooth root by means of a machine for dynamic tests. Consequently, a notch in the tooth root was made with wire erosion. Two pairs of spur gear-units, integrated in a single stage gear-unit, were used for noise measurements. One of them had a notch and the other one was without it (faultless). The operating conditions were such as are usually associated with this type of a gear unit. A ground gear pair with a notch was a standard gear pair with teeth quality 6; it is presented in Fig. 2. The notch with the length of 0.85 mm was located in the tooth root of a pinion. The pinion had 14 teeth, whereas the gear unit had 79.

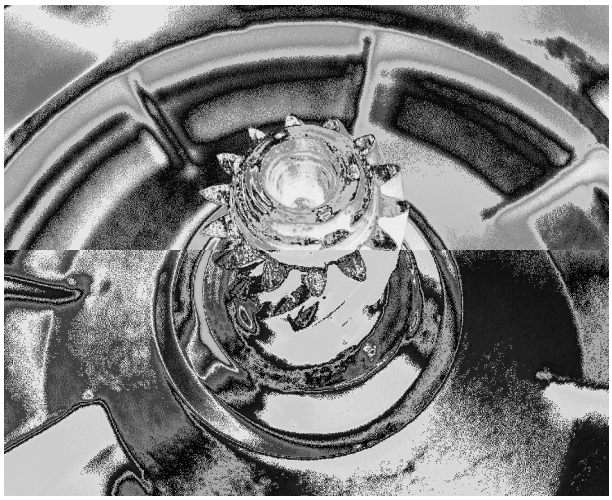


Fig. 2: Pinion with a notch in the tooth root

A comparison between the measured signal of a faultless gear unit and the signal of a faulty gear unit was performed. The presence of a notch in the tooth root was identified, using short time frequency transform. The signal was, on an average, composed of 192000 measuring points and the length of the signal of measured values was 3 s. The rotational frequency was 38 Hz during measurement.

Fig. 3 shows the acoustic image and the spectrogram. No pulsation of harmonics can be observed, with the exception of typical frequencies, determined on the basis of typical frequencies components. Monitoring appropriate frequency components with pulsating frequency, which is typical for meshing frequency (530 Hz) and for high harmonics, is very interesting. Pulsation is expressed only in case of a notch. Fig. 4 presents this phenomenon. Pulsation reflects a single engagement of a gear pair with a notch.

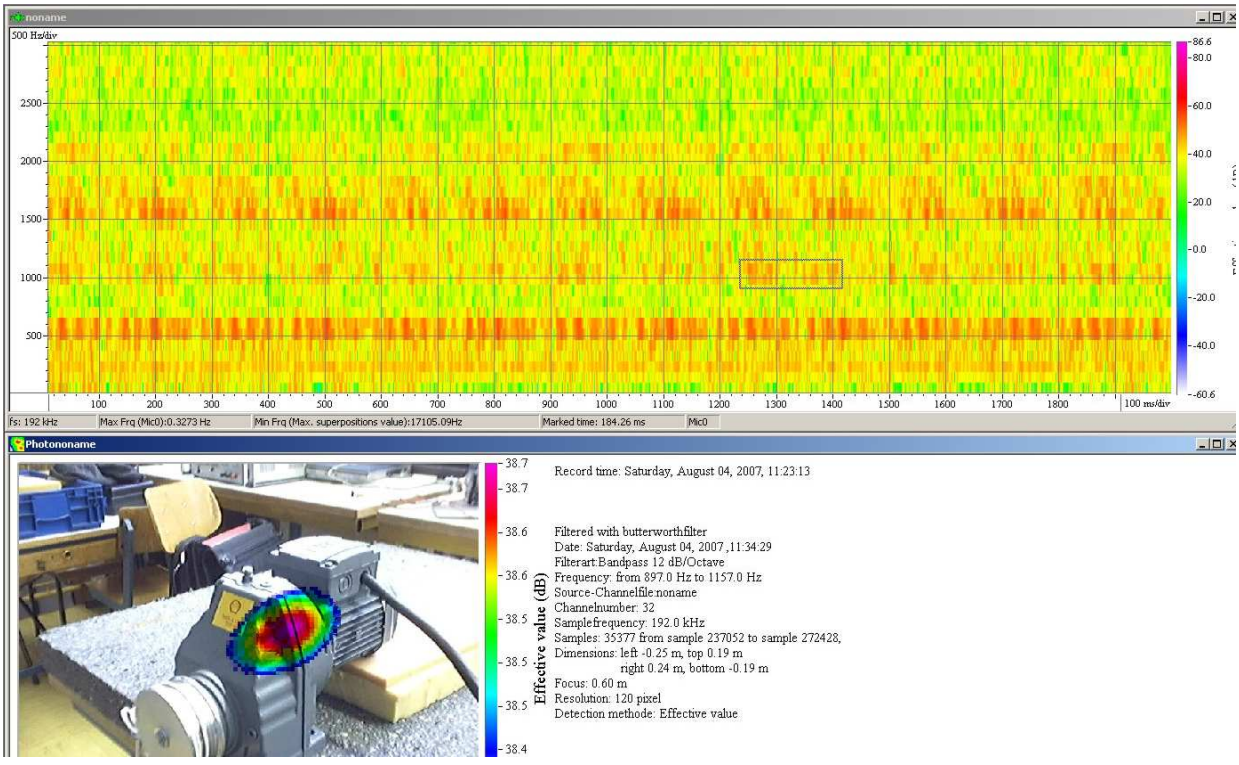


Fig. 3: Spectrogram with acoustic image of faultless gear

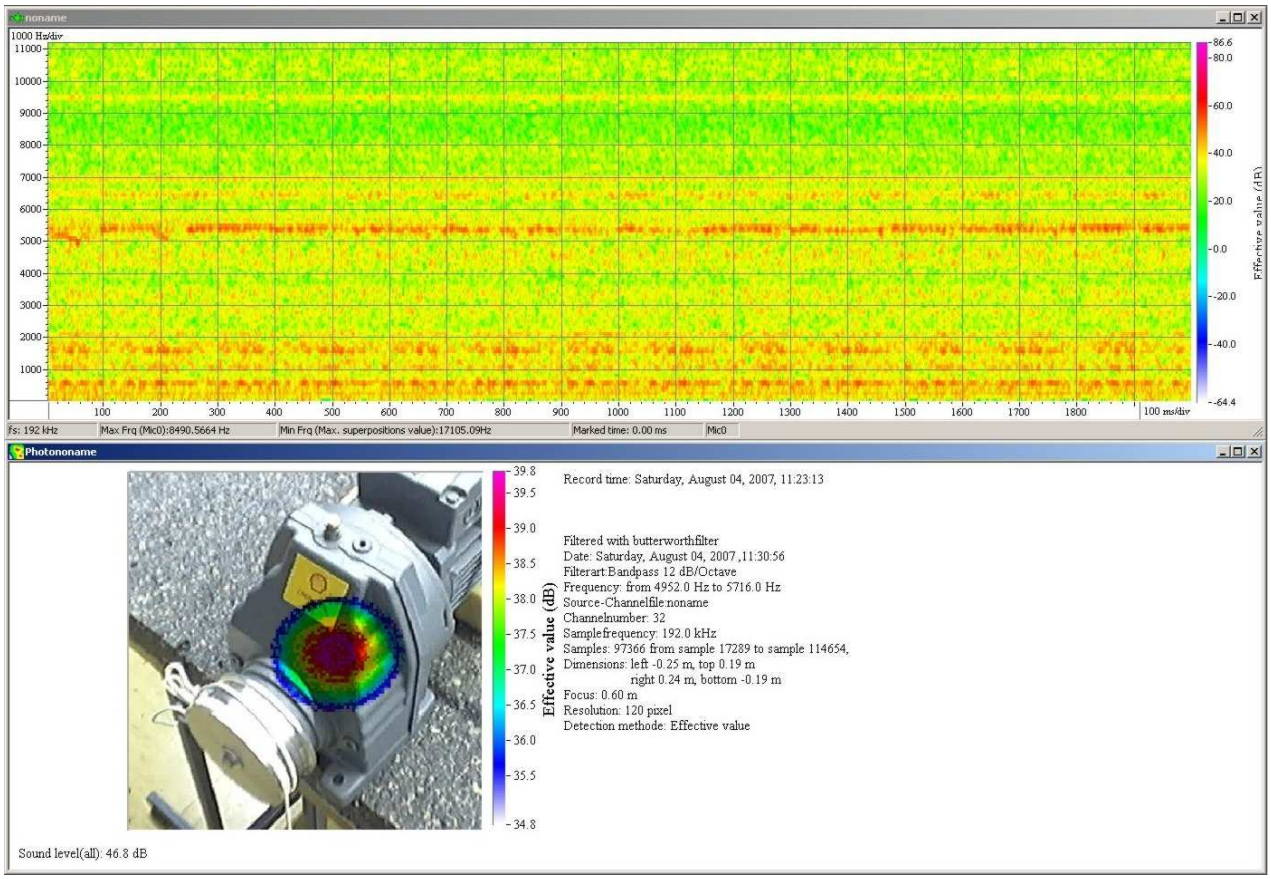


Fig. 4: Spectrogram with acoustic image of a gear unit with a notch in the tooth root

CONCLUSION

Faults can be identified by noise analysis. Presented methods increase safety of operation and reliability of monitoring operational capabilities. The method with an acoustic camera enables better resolution in time and place of the acoustic sources visualisation than any other acoustic system. For the method with an acoustic camera, a specific algorithm functioning in time domain and on specifically located microphones is used. The reliability of monitoring the life cycle of a gear unit is improved by means of appropriate spectrogram samples and a clear presentation of the pulsation of individual frequency components. Early detection of faults and damages increases the control of the reliability of operation. With more reliable methods for faults detection, the remaining life cycle of a gear unit can be predicted in a more reliable way.

REFERENCES

[1] A. Mertins, Signal Analysis, John Wiley & Sons Inc., New York, 1999.

[2] P. Fladrin, Time-Frequency/Time-Scale Analysis, Academic Press, 1999

[3] J. Christensen and J. Hald, Beamforming, B&K technical reviev 1, 2004

[4] J. Hald, Combined NAH and Beamforming Using the Same Array, B&K technical rev. 1, 2005

[5] G. Heinz, Locating Noise Sources, A Comparison Between Different Noise Localization Techniques, GFaI Report 001-06-21, 2004

[6] J. Prezelj, M. Cudina, Dipole in orthogonal direction as a secondary source for active noise control in ducts. *Acta acustica united with acustica*, , vol. 93/1, pp. 63-72, 2007

© (2012) Trans Tech Publications, Switzerland
doi:10.4028/www.scientific.net/KEM.488-489.791

Meshless Local Integral Equation Method with Analytical Formulation and its Application to Computational Fracture Mechanics

P.H. Wen[1,a] and M.H. Aliabadi[2,b]

[1] School of Engineering and Material Sciences, Queen Mary, University of London, UK

[2]Department of Aeronautics, Imperial College, London, UK

[a]p.h.wen@qmul.ac.uk, [b]m.h.aliabadi@imperial.ac.uk

Keywords: Meshless local integral equation method, radial basis function, crack opening displacement.

Abstract. In this paper, the exact forms of integrals in the meshless local boundary integral equation method are presented and applications were demonstrated for fracture mechanics. A weak form for a set of governing equations with a unit test function or polynomial test functions is transformed into local integral equations. Each node has its own support domain and is surrounded by a local integral domain with different shapes of boundaries. The meshless approximation based on the Radial Basis Function (RBF) is employed for the implementation of displacements. For cracked plate, opening displacement on the crack surface can be obtained with satisfactory accuracy without special treatment for stresses singularities at crack tip.

Introduction

In recent years, several effective advanced computational methods for solving fracture mechanics problems have been developed [1-4]. The application of mesh free method to linear elastostatic fracture mechanics, i.e. evaluation of stress intensity factors and analysis of crack growth, were demonstrated in [3]. Wen et al [4] developed a mesh free Galerkin method using enriched radial basis functions. In this paper, the analytical formulations for the meshless local boundary integral method are presented and applied to fracture problems without domain or boundary integrals. With the use of radial basis functions, the analytical solutions for all domain integrals in the weak form of are derived. The weak formulation for the governing equations with a unit test function or any polynomial test functions are obtained exactly for the local domain integrals. As the closed form of the local boundary integrals are obtained, the computational time are reduced significantly.

Local integral equation method

Consider a linear elastic body in three dimensional domain Ω with boundary $\partial\Omega$. The equations of equilibrium can be written as

$$\sigma_{ij,j} + f_i = 0 \tag{1}$$

where σ_{ij} are stresses and f_i is the body force ($i = 1, 2$ for 2D and $i = 1, 2, 3$ for 3D). The boundary conditions are given as

$$u_i = \bar{u}_i \quad \text{on} \quad \Gamma_u \quad \text{and} \quad t_i = \sigma_{ij} n_j = \bar{t}_i \quad \text{on} \quad \Gamma_t \tag{2}$$

in which $\bar{u}_i$ and $\bar{t}_i$ are the prescribed displacements and tractions respectively on the displacement boundary Γ_D and on the traction boundary Γ_T, and n_i is the unit normal outward to the boundary Γ. In the local boundary integral equation approach, the weak form of differential equation over a local integral domain Ω_s can be written as

$$\int_{\Omega_s} (\sigma_{ij,j} + f_i) u_i^* d\Omega = 0 \tag{3}$$

where u_i^* is a test function. By use of divergence theorem, Eq.(3) can be rewritten in a symmetric weak form as

$$\int_{\partial\Omega_s} \sigma_{ij} n_j u_i^* d\Gamma - \int_{\Omega_s} (\sigma_{ij} u_{i,j}^* - f_i u_i^*) d\Omega = 0 \tag{4}$$

If there is an intersection between the local boundary and the global boundary, a local symmetric weak form in linear elasticity may be written as

$$\int_{\Omega_s} \sigma_{ij} u_{i,j}^* d\Omega - \int_{L_s} t_i u_i^* d\Gamma - \int_{\Gamma_D} t_i u_i^* d\Gamma = \int_{\Gamma_T} \bar{t}_i u_i^* d\Gamma + \int_{\Omega_s} f_i u_i^* d\Omega \tag{5}$$

in which, $\partial\Omega_s = \Gamma_s \cup L_s$, Γ_s is a part of the local boundary located on the global boundary and L_s is the other part of the local boundary inside the local integral domain Ω_s; Γ_D is the intersection between the local boundary $\partial\Omega_s$ and the global displacement boundary; Γ_T is a part of the traction boundary as shown in Figure 1.

The local weak forms in Eq.(4) and Eq.(5) are a starting point to derive local boundary integral equations if appropriate test functions are selected. A step functions can be used as the test functions u_i^* in each integral domain

$$u_i^*(\mathbf{x}) = \begin{cases} \varphi_i(\mathbf{x}) & \text{at } \mathbf{x} \in (\Omega_s \cup \partial\Omega_s) \\ 0 & \text{at } \mathbf{x} \notin \Omega_s \end{cases}. \tag{6}$$

where $\varphi_i(\mathbf{x})$ is arbitrary function. For $\varphi_i(\mathbf{x}) = 1$ and zero body force $f_i = 0$, the local weak forms Eq.(4) and Eq.(5) are transformed into simple local boundary integral equations (equilibrium of local integral domain) as

$$\int_{\partial\Omega_s} t_i d\Gamma = 0 \tag{7}$$

Analytical formulation of weak forms of governing equation

Consider a local domain $\partial\Omega_s$ shown in Figure 1, which is the neighbourhood of a point $\mathbf{x}$ $(=\{x_1, x_2\})$ and is considered as the domain of definition of the RBF approximation for the trail function at $\mathbf{x}$ and also called as support domain to an arbitrary point $\mathbf{x}$. Generally the support domain is chosen as a circle centred at $\mathbf{x}$. To interpolate the distribution of function u in the local domain $\partial\Omega_s$ over a number of randomly distributed nodes $\boldsymbol{\xi}$ $[=\{\boldsymbol{\xi}_1, \boldsymbol{\xi}_2, ..., \boldsymbol{\xi}_K\}$, $\boldsymbol{\xi}_k = (\xi_{k1}, \xi_{k2})$, $k = 1,2,...,K\ ]$, the approximation of function u at the point $\mathbf{x}$ can be expressed by

$$u_i(\mathbf{x}) = \sum_{k=1}^{K} R_k(\mathbf{x}, \boldsymbol{\xi}) a_k + \sum_{t=1}^{T} P_t(\mathbf{x}) b_t = \mathbf{R}(\mathbf{x})\mathbf{a} + \mathbf{P}(\mathbf{x})\mathbf{b} \tag{8}$$

$$\mathbf{b} = \boldsymbol{\beta}\mathbf{u}, \quad \mathbf{a} = \boldsymbol{\alpha}\mathbf{u}$$

$$\boldsymbol{\beta} = \left(\mathbf{P}_0^T \mathbf{R}_0^{-1} \mathbf{P}_0\right)^{-1} \mathbf{P}_0^T \mathbf{R}_0^{-1}, \quad \boldsymbol{\alpha} = \mathbf{R}_0^{-1}\left[\mathbf{I} - \mathbf{P}_0\left(\mathbf{P}_0^T \mathbf{R}_0^{-1} \mathbf{P}_0\right)^{-1} \mathbf{P}_0^T \mathbf{R}_0^{-1}\right] \tag{9}$$

where $\mathbf{I}$ denotes the diagonal unit matrix. Substituting the coefficients $\mathbf{a}$ and $\mathbf{b}$ from Eq.(18) into Eq.(12), we can obtain the approximation of the field function in terms of the nodal values

$$u(\mathbf{x}) = \boldsymbol{\Phi}(\mathbf{x})\mathbf{u}, \quad \boldsymbol{\Phi}(\mathbf{x}) = \mathbf{R}(\mathbf{x})\boldsymbol{\alpha} + \mathbf{P}(\mathbf{x})\boldsymbol{\beta}. \tag{10}$$

in which $\boldsymbol{\Phi}(\mathbf{x})$ is defined as shape function, matrix $\mathbf{R}(\mathbf{x})$ and $\mathbf{P}(\mathbf{x})$ are scale $(1 \times K)$ and (1×6) matrix respectively. It is worth noting that the shape function depends uniquely on the distribution of scattered nodes within the support domain and it has the Kronecker Delta property.

Firstly, consider a unit test function, i.e. $\varphi_i(\mathbf{x}) = 1$ and the local domain is enclosed by several straight lines as shown in Figure 2, therefore, the local boundary integral equation becomes

$$\sum_{k=1}^{K}\sum_{l=1}^{L}\left[\sum_{i=1}^{K}\left(\frac{E}{1-\nu^2}F_{1il}n_1^l+\mu F_{2il}n_2^l\right)\alpha_{ik}+\sum_{t=1}^{T}\left(\frac{E}{1-\nu^2}G_{1tl}n_1^l+\mu G_{2tl}n_2^l\right)\beta_{tk}\right]u_1^{(k)}+$$
$$\sum_{k=1}^{K}\sum_{l=1}^{L}\left[\sum_{i=1}^{K}\left(\frac{E\nu}{1-\nu^2}F_{2il}n_1^l+\mu F_{1il}n_2^l\right)\alpha_{ik}+\sum_{t=1}^{T}\left(\frac{E\nu}{1-\nu^2}G_{2tl}n_1^l+\mu G_{1tl}n_2^l\right)\beta_{tk}\right]u_2^{(k)}=0 \quad (11a)$$

$$\sum_{k=1}^{K}\sum_{l=1}^{L}\left[\sum_{i=1}^{K}\left(\frac{E\nu}{1-\nu^2}F_{1il}n_2^l+\mu F_{2il}n_1^l\right)\alpha_{ik}+\sum_{t=1}^{T}\left(\frac{E\nu}{1-\nu^2}G_{1tl}n_2^l+\mu G_{2tl}n_1^l\right)\beta_{tk}\right]u_1^{(k)}+$$
$$\sum_{k=1}^{K}\sum_{l=1}^{L}\left[\sum_{i=1}^{K}\left(\frac{E}{1-\nu^2}F_{2il}n_2^l+\mu F_{1il}n_1^l\right)\alpha_{ik}+\sum_{t=1}^{T}\left(\frac{E}{1-\nu^2}G_{2tl}n_2^l+\mu G_{1tl}n_1^l\right)\beta_{tk}\right]u_2^{(k)}=0 \quad (11b)$$

for $\mathbf{x}_k, k=1,2,...M_\Omega$, where E is Young's modulus, ν is Possion ratio and $\mu=E/2(1+\nu)$ the shear modulus and the integral functions

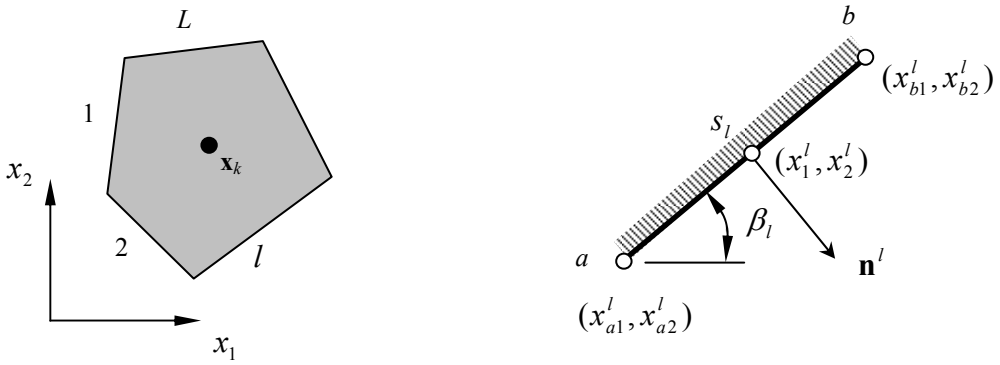


Figure 2. Local integral domain with straight boundary lines.

$$F_{jil}=\int_0^{s_l}\frac{\partial R_i}{\partial x_j}ds,\quad G_{j1tl}=\int_0^{s_l}\frac{\partial P_t}{\partial x_j}ds \quad (12)$$

Consider $n_1^l=\sin\beta_l, n_2^l=-\cos\beta_l$, we have solutions in closed form

$$F_{1il}=(r_2-r_1)\cos\beta_l-[(x_{a1}^l-\xi_{i1})\sin\beta_l-(x_{a2}^l-\xi_{i2})\cos\beta_l]\sin\beta_l\ln(d_1/d_2)$$
$$F_{2il}=(r_2-r_1)\sin\beta_l-[(x_{a2}^l-\xi_{i2})\cos\beta_l-(x_{a1}^l-\xi_{i1})\sin\beta_l]\cos\beta_l\ln(d_1/d_2)$$
$$r_1=\sqrt{c^2+(x_{a1}^l-\xi_{i1})^2+(x_{a2}^l-\xi_{i2})^2}$$
$$r_2=\sqrt{c^2+(x_{b2}^l-\xi_{i1})^2+(x_{b2}^l-\xi_{i2})^2} \quad (13)$$
$$d_1=(x_{a1}^l-\xi_{i1})\cos\beta_l+(x_{a2}^l-\xi_{i2})\sin\beta_l+r_1$$
$$d_2=(x_{b1}^l-\xi_{i1})\cos\beta_l+(x_{b2}^l-\xi_{i2})\sin\beta_l+r_2$$

Next considering a linear test function $\varphi_i(\mathbf{x})=x_i$ with a rectangular local integral domain, the weak forms of the governing equations can be derived as following

$$\sum_{k=1}^{K}\left[\sum_{i=1}^{K}\left(\frac{E}{1-\nu^2}H_{il}^{111}+\mu H_{il}^{221}\right)\alpha_{ik}+\sum_{t=1}^{T}\left(\frac{E}{1-\nu^2}I_{tl}^{111}+\mu I_{tl}^{221}\right)\beta_{tk}\right]u_1^{(k)}+$$
$$\sum_{k=1}^{K}\left[\sum_{i=1}^{K}\left(\frac{E\nu}{1-\nu^2}+\mu\right)H_{il}^{121}\alpha_{ik}+\sum_{t=1}^{T}\left(\frac{E\nu}{1-\nu^2}+\mu\right)I_{tl}^{121}\beta_{tk}\right]u_2^{(k)}=0 \quad (14a)$$

$$\sum_{k=1}^{K}\left[\sum_{i=1}^{K}\left(\frac{E\nu}{1-\nu^2}+\mu\right)H_{il}^{122}\alpha_{ik}+\sum_{t=1}^{T}\left(\frac{E\nu}{1-\nu^2}+\mu\right)I_{tl}^{122}\beta_{tk}\right]u_1^{(k)}+$$
$$\sum_{k=1}^{K}\left[\sum_{i=1}^{K}\left(\frac{E}{1-\nu^2}H_{il}^{222}+\mu H_{il}^{112}\right)\alpha_{ik}+\sum_{t=1}^{T}\left(\frac{E}{1-\nu^2}I_{tl}^{222}+\mu I_{tl}^{112}\right)\beta_{tk}\right]u_2^{(k)}=0 \quad (14b)$$

for $\mathbf{x}_k, k=1,2,...M_\Omega$, where the integral functions

$$H_{il}^{pqr} = \int_{x_{a1}x_{a2}}^{x_{b1}x_{b2}} \frac{\partial^2 R_i}{\partial x_p \partial x_q} x_r dx_1 dx_2 , I_{tl}^{pqr} = \int_{x_{a1}x_{a2}}^{x_{b1}x_{b2}} \frac{\partial^2 P_t}{\partial x_p \partial x_q} x_r dx_1 dx_2 \tag{15}$$

It is not difficult to obtain all integrals in the closed form by Wen and Aliabdi [5]

A part from the collocation points in the domain, we need to consider the traction/displacement boundary conditions for the nodes collocated on the boundary. For the nodes on the traction boundary, Eq.(7) should be introduced

$$\int_{\Gamma-\Gamma_T} t_i d\Gamma = -\int_{\Gamma_T} \bar{t}_i d\Gamma \quad \text{for } \mathbf{x}_k \;\; k = 1,2,...,M_T \tag{16}$$

For the displacement boundary nodes, we can introduce the displacement equation directly, i.e. $u_i(\boldsymbol{\xi}_k) = \bar{u}_i, k = 1,2,...M_D$. Therefore, there are total $2\times(M_\Omega + M_T + M_D)$ linear algebraic equations which are used to determine the same number unknowns of displacements either in the domain or on the traction boundary.

Example

A square plate of width 2*a*, containing a central crack of length $2c$ ($c = a/2$) subjected to a uniform tension σ_0 on the top and bottom is analysed. Regular mesh with 1681(41×41) nodes is used in the domain and on the boundary. Due to the symmetry, we only need to consider a quarter of the plate, as shown in Figure 10. The opening normalised displacement u_2 (x_1) is plotted in Figure 11 for comparison. In this example, the results of meshless method proposed in this paper, finite element method and boundary element method are presented. Dual boundary element method (see Wen, Aliabadi and Young [5]) is considered as a highly accurate method for crack problems, since the singularity of stresses around the crack tips is avoided successfully during numerical process. For DBEM, 4×16 quadratic elements on the boundaries and 32 discontinuous quadratic elements on the crack surfaces are used. Opening displacement on the crack surface can be used to evaluate the stress intensity factors directly.

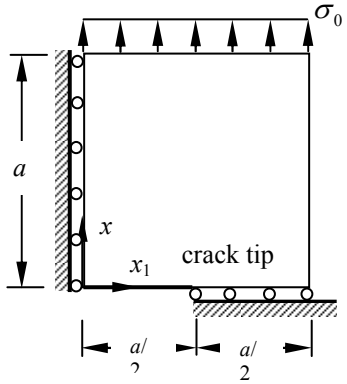


Figure 1. Square plate with a central crack under tension load σ_0.

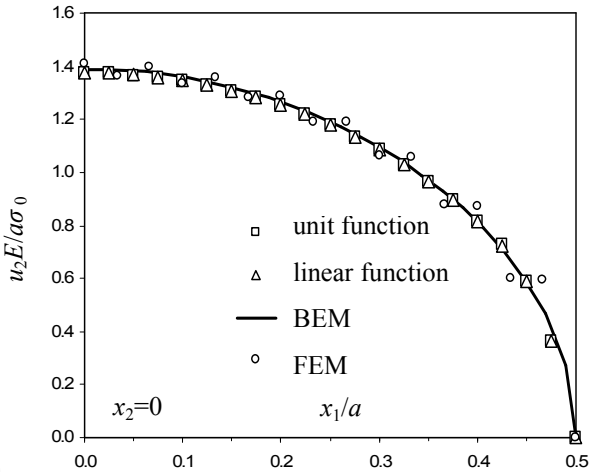


Figure 2. Normalized opening displacement on the crack surface.

References

[1] Portela,A, Aliabadi,MH, Rooke,DP The Dual Boundary Element Method – Effective Implementation for Crack Problems, Int. J Numerical Methods in Engineering, Vol 33, p. 1269-1287 1992

[2] Portela,A, Aliabadi,MH, Rooke DP Dual Boundary Element Analysis of Cracked Plates – Singularity Subtraction Technique, Int. J. Fracture, Vol 55, p.17-28, 1992.

[3] Wen,P.H. and Aliabadi,M.H. A Varitional Approach for Evalaution of Stress Intensity Factors using the Element Free Galerkin Method, Int. J. Solids and Structures, Vol. 48, P. 1171-1179, 2011.

[4] Wen, P.H. and Aliabadi, M.H., Meshless method with enriched radial basis functions for fracture mechanics, Structural Durability & Health Monitoring, 3(2), 107-119, 2007.

[5] Wen, P.H. Aliabadi, M. H. and Young A., Stiffened cracked plates analysis by dual boundary element method, Int. J. Fracture, 106, 245-258, 2000.

© (2012) Trans Tech Publications, Switzerland
doi:10.4028/www.scientific.net/KEM.488-489.795

Experimental study to verify the fatigue limit found by thermal analysis of specimen surface in mono axial traction test

Giacomo Risitano[1, a], Carmelo Clienti[2,b]
[1]Faculty of Applied Science and Technology, Guglielmo Marconi University, Rome, Italy
[2]Department of Industrial Engineering, University of Catania, Catania, Italy
[a]g.risitano@unimarconi.it, [b]cclienti@diim.unict.it

Keywords: fatigue, mono axial traction test, infrared thermography, mechanical characterization.

Abstract. Following the first experimental results concerning the possibility to estimate the fatigue limit by semi-static tensile traction test, the authors are continuing the experimental thermo-analysis of the curve zone between the origin and the yield stress; that is rich of indication about the fatigue failure process. The tests carried out on the AISI 304 steel by thermal analysis, confirmed the good approximation between the values of the fatigue limit estimated by fatigue test and by the quasi-static test. The results shoed the importance of the thermo-analysis of the part of the stress-strain curve (distant from the yield point) where only in macroscopic terms the behavior is perfectly elastic.

Introduction

In previous work, the authors, proposed a methodology to find the fatigue limit of the materials by means of a thermo-analysis of the specimen surface during a classic mono-axial traction test. Following the results, the aim of this work is the use of the procedure for a different material (in terms of released heat under stress) and, in the same time, the use a more complete approach to verify the validity of the method.

The calorimetric effect associated to elastic deformation and plastic deformation is observed by different researchers. The thermoelastic effect was studied by Lord Kelvin [1] and the termoplastic effect was analyzed by Taylor and Quinney [2]. With the possibility to read the surface temperature of specimen during tests by infrared image processing, many authors worked to use the thermoplastic effect to define mechanical characteristics of materials. In 2000, Chrysochoos and Louche [3] analyzed the surface temperature by infrared camera during static traction test of a flat and thin parallelepiped sample. They using infrared image processing, based on Fourier's techniques, observed a sudden dissipative effect due to the propagation of the Luders band during local plastic deformation. In 2009 Plekhov and Naimark [4] with use of high sensitivity infrared camera demonstrated that in static traction test the plastic strain localization are accompanied by emergence of heat waves and their propagation over the specimen surface. In all literature examined never it was been linked the heat released to the dynamic failure of the specimen. Risitano et Al. [5] noted that the slope changing in the temperature vs strain curve was linked with the first plastic local deformation (local necking). Knowing that fatigue failure happens for a load able to induce in the specimen (or mechanical component) local plasticization, they defined as the fatigue limit, the stress corresponding to the slope's change of the temperature curve in a static traction mono-axial test and proposed to find the fatigue limit by a simple classic test accompanied to the analysis surface temperature or analysis of the released heat. In [6] it is indicated how it could be possible to evaluate the limit stress of the thermo-elastic phase of deformation by thermo-analysing the surface of the specimen during a static traction test. Adding the temperature curve measured on a small area of the surface (the hottest) to the classic stress-strain curve, it is possible to evaluate a limit temperature T_0 coincident with the beginning of the non linear trend of the curve. The corresponding stress value is coincident with the fatigue limit of the analyzed component.

In this work, the authors are continuing the experimental thermo-analysis of the curve zone between the origin and the yield stress during tensile traction test that is rich of indication about the fatigue failure process. Using AISI 304 steel specimens, they compared the fatigue limit found by the thermoanalysis of the static stress-strain curve wiht that found by thermo-analysis of the specimen surface during fatigue test. Table 1 summarizes the all test programmed.

Table 1: Summary of all tests.

Specimen	Static Test	Broken in Static Test	Speed Crossbar in Static Test [mm/min]	Fatigue Test	Broken in Fatigue Test	Max Cycles Number in Fatigue Test
Mean value for 3 specimens in the static characterization phase	yes	yes	1,421	no	no	-
Mean value for 3 specimens in the fatigue characterization phase	no	no	-	yes	yes	4,76E+05

Testing procedure

As reported in [5, 6, 7], to estimate the fatigue limit for R=-1, it is sufficient to perform a classic static test and recorder the temperature surface during the static test by means of a adequate remote system. The subsequent image processing permits one to define the end of the thermo elastic behavior and permits to estimate the T_0 temperature as the beginning of the local micro-plasticization and consequently the zone where the plasticization appears for the first time. The increase in temperature depends:

1. on the material characteristics and ambient conditions (for steel at an ambient temperature of 23°C there is an increase of approximately 0,1 °C, for each 100 N/mm^2 of stress);
2. on the sensibility of the thermal sensors;
3. on the image analysis quality;
4. on the signals synchronization of the three parameters:
    a. load;
    b. elongation;
    c. surface temperature.

As a general indication, we can say that during the first phase (perfectly elastic) for which at any point of the surface is $\Delta T = -K_m T \sigma_m$, the temperature variations are proportional to the thermo-elastic coefficient K_m (approximately $3{,}3 \times 10^{-12}$ [Pa^{-1}] for steel and 10×10^{-12} [Pa^{-1}] for aluminum alloy) and to the point value of the stress. The temperature variations are more evident near the high stress concentration point.

The authors applied this procedure and they found the value of σ_0 and compared the values to those determinate by Risitano's methods [8] for R=-1. The method was applied to steel AISI 304 (Allegheny Ludlum Stainless Steel Chromium-Nickel Type 304, 10% Cold Rolled - UNS S30400) specimen with a rectangular section (12x5 mm) and length of 90 mm. The testing machine was an Instron model 8501 100 kN Servo Hydraulic Machine and the thermographic scanner was Flir System model SC-3000. The image processing was also performed by Flir system. The frequency of image acquisition was 1 Hz. The minimum measurable value of temperature was 0.02°C. The emissivity coefficient was 0,9.

Analysis of results

With the first tests, the material was characterized. Therefore 3 specimens, for the static and thermo-static characterization, were used and other 3 for the thermo-fatigue characterization. The figure 1, for the sake of brevity, reports only one of the classic traction load-displacement curve of the three specimens tested. The other two had a very similar trend. In the diagram of figure 1, the temperature of the hottest surface point recorded during the test, is reported. The temperature curve has an evident inflection point for 7 kN (corresponding stress of 117 MPa). For what has been said above, this value can be considered an estimated value of the fatigue limit of the material. The percentage errors of the measured values of the Yield Stress (525 MPa) and Ultimate Stress (692 MPa) compared to those in the literature (Literature Yield Stress 517 MPa and Literature Ultimate Stress 676 MPa) are very small (1,5% and 2,3%).

Other 3 specimens were subjected only to the fatigue test until they were completely broken (in table 1 the average number cycles at failure is reported); the specimens were loaded with a load ratio R=-1. To determine the fatigue limit, we used the method Risitano [8] and for each step of load, the stabilization temperature has been measured. Figure 2-a, shows the temperature variation as average value of the temperature acquired for the three specimens tested. For each load step, the difference between the average value and the others was not more than 1,2%. According to the Risitano method, the mean values of the stabilization temperature were reported as a function of the square of the load (stress) and the intersection of the trend line with the x-axis is the value of fatigue limit (figure 2-b). The mean fatigue limit σ_0, for the 3 specimen, is 102 MPa. Finally, the Wohler diagram using the data of figure 2-a and according to the previous mentioned method, was created (figure 3-c). In this way we have characterized the material in static and fatigue terms. As it is possible to note, the difference between the found values of the fatigue limit (117 MPa and 102 MPa) is very low.

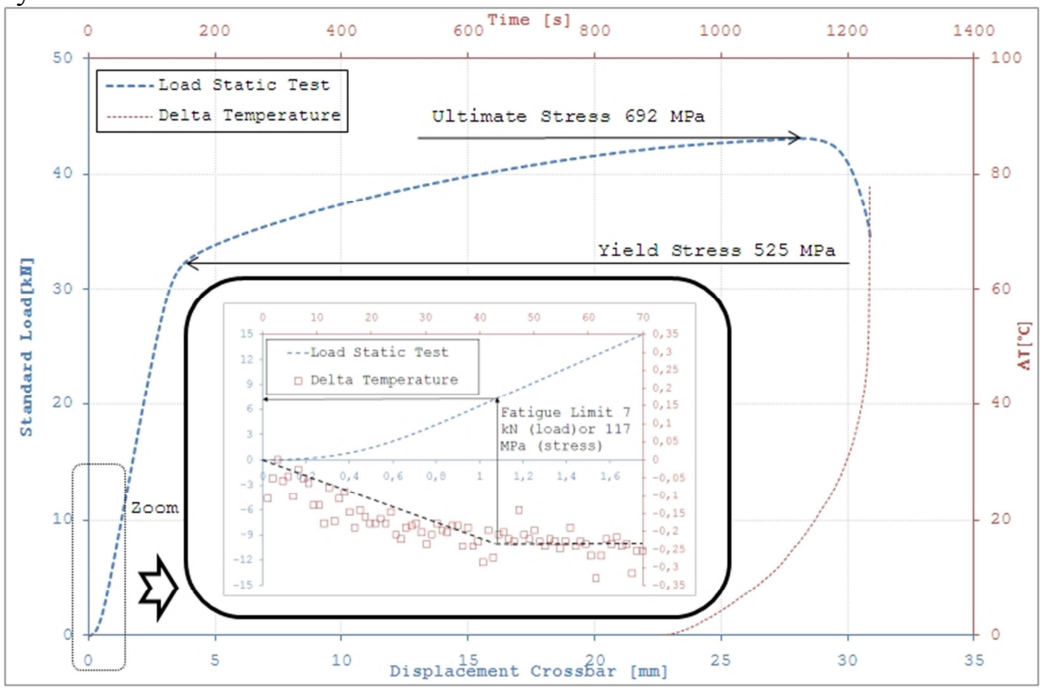


Fig. 1: Monoaxial Tensile Static Test. Standard load vs displacement of crossbar (blue line) and ΔT vs time (red line).

Conclusion

The Authors, in recent works, proposed a method to estimate the fatigue limit of a material by thermographic analysis of a simple traction static tests [5, 6, 7]. In this work, they have carried out tests to verify the methodology with a steel characterized by different released heat under stress, compared those used in other applications. The tests conducted were of two different types. Using 6 specimens, 3 were performed as static tests and 3 as fatigue tests. The material has been used for the specimens was AISI 304. The method that the authors are carrying out is completely different from the others proposed by other authors that use cyclic loading to find the fatigue limit of the material. In different way of other researchers, the authors are analysing the part of the classic stress strain curve between the end of the completely elastic phase and the beginning of the macroscopic plastic phase, near the yield stress. The dispersion of the data found, confirmed by the literature shows that the difference between the fatigue limit obtained by static monoaxial tensile test and the fatigue limit determined by thermal fatigue tests (Risitano method) is in the order of 13%. In this application the reading of the fatigue limit is clear and is a good approximation with that found by the traditional method and by the Risitano method.

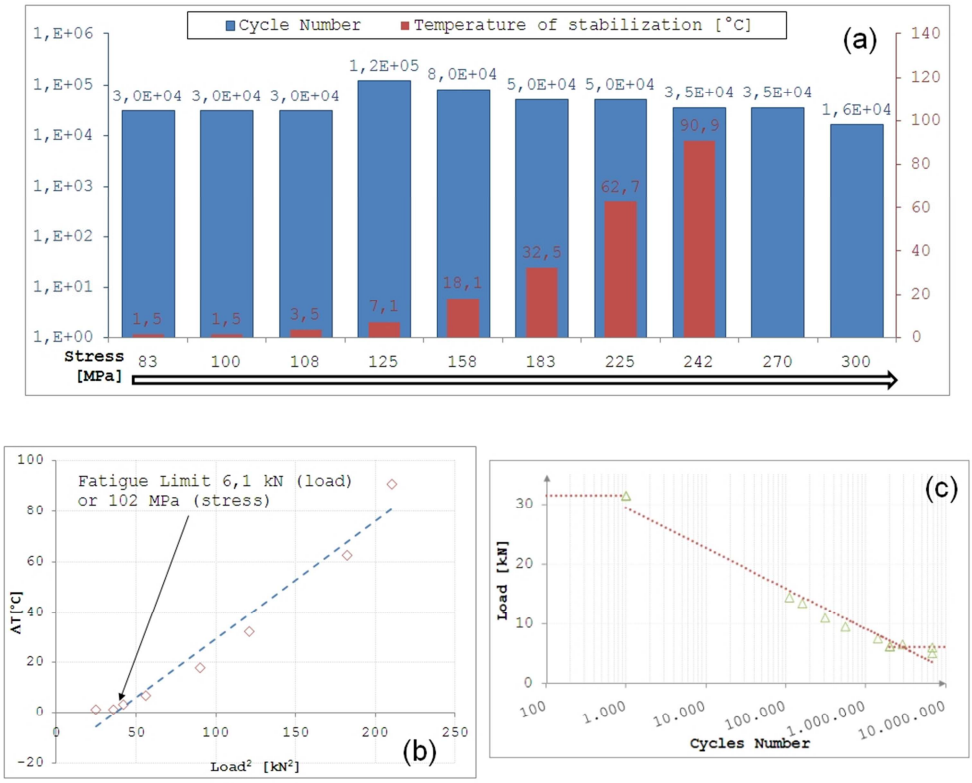


Fig. 2: (a) Mean values of acquired cycle number and temperature stabilization; (b) Determination of fatigue limit; (c) Wohler Diagram.

References

[1] Lord Kelvin, in: *On the thermo-elastic and thermo-magnetic properties of matter*, Roy. Soc. Edimb.20 (1853), 161.

[2] G.I. Taylor, and H. Quinney, in: *The latent Energy remaining in a metal after a cold working*, Proceedings of the Royal Society, London (1934).

[3] A. Chrysochoos, and H. Louche, in: *An infrared image processing to analyse the calorific effects accompanying strain localisation*, International Journal of Engineering Science 38 (2000), pp. 1759-1788.

[4] O.A. Plekhov, and O B. Naimark, in: *Theoretical and experimental study of Energy dissipation in the course of strain localization*, Journal of applied mechanics and technical physics, vol. 50 No. 1, (2009), pp. 127-136.

[5] A. Risitano, and G. Risitano, in: *L'importanza del "parametro energetico" temperatura per la caratterizzazione dinamica dei materiali*; IGF "Frattura ed Integrità Strutturale", 9, (2009), pp. 123-124.

[6] A. Risitano, C. Clienti, and G. Risitano, in: *Determination of fatigue limit by mono-axial tensile specimens using thermal analysis*, Key Engineering Materials Vol. 452-453 (2011).

[7] D. Corallo, G. Risitano, A. Sirugo, in: *Analisi numerico-sperimentale dei processi dissipativi su materiali duttili*, Congresso Nazionale AIAS XXXIX, Maratea, 7-10 settembre 2010.

[8] G. La Rosa, A. Risitano, in: *Thermographic methodology for rapid determination of the fatigue limit of materials and mechanical components*, Int. J. Fatigue 22, (2000), pp. 65–73.

© (2012) Trans Tech Publications, Switzerland
doi:10.4028/www.scientific.net/KEM.488-489.799

Measurement of Deformation on Welding Specimen Using ESPI

Kyeongsuk Kim[1,a], Dongsoo Kim[2,b], Kyungsu Kim[2,c], Changdoo Kee[3,d], Jinweon Kim[4,e] and Mangyun Na[4,f]

[1]Dept. of Mechanical Design Eng., Chosun Univ., 375 Seosuk dong, Dong-Gu, Gwangju, Korea

[2]Dept. of Advanced parts and Materials Eng., Graduate School, Chosun Univ., 375 Seoseok Dong, Dong-Gu, Gwangju, Korea

[3]School of Mechanical Systems Engineering, Yongbong-dong 300, Buk-gu, Gwangju, Korea

[4]Department of Nuclear Engineering, Chosun Uni- versity, 375, Seoseok-dong, Dong-gu, Kwangju

[a]gsckim@chosun.ac.kr, [b]victoryehdtn@naver.com, [c]kyungsukorea@naver.com, [d]cdkee@chonnam.ac.kr, [e]jwkim@chosun.ac.kr, [f]magyna@mail.chosun.ac.kr

Keywords:, Welding, ESPI, Interferometry, Residual stress, Measurement

Abstract. The residual stress was measured through the proposed method with ESPI measurement system. The proposed measurement method as a basic study combined with theory and experiments applied for residual stresses prediction and developments of safety estimation technique.

Introduction

Generally welding is a technique that joins two kinds of metal materials by heating. It has been recognized important technique that becomes an indispensable presence for joining of iron and nonferrous metals due to development of various welding methods with modern industry development. Adhesion Strength of welding joint is higher than the strength of rivet joint that is used in conventional structure joint. Also, a structure using welding joint could be made earlier than a structure using rivet joint.

Welding plays a pivotal role in various industry fields such as shipbuilding, nuclear power plant, airplane, automobile and architecture industry because welding has many strong points like water tightness and air tightness. However, welding structures can be able to destroy unexpectedly due to the fact that quality of the material, residual stress, deformation, welding defects have an aptitude to happen easily in welding structures because welding is a kind of joint method by increasing heat. Especially, a main reason for leading to defects or destruction of structure can be residual stress.

In this study, therefore, the method for measuring residual stresses using ESPI technique that is one of the laser applied measurement technique excellent in the view of field application was proposed.

In-plane ESPI.

Two object beam speckle patterns can be combined coherently to make a new speckle pattern. The optical setup sensitive to measure in-plane displacement for ESPI is shown in *Fig. 1*. This arrangement was described first by Leendertz (1970). In this case, the object surface is supposed to lie in the x - y plane. The surface is illuminated by two beams of coherent light propagating parallel to the x - y plane and incident at equal angles θ on either side of the surface normal. The two beams generate their own speckle patterns, and the scattered light is imaged on to a image plane. There is no separate reference beam falling on the image plane. Serving as references to each other, the pair of independent speckle patterns combines coherently to produce the resulting speckle pattern. The motion of an elementary part of the surface in the z-direction induces, as a consequence of the equal angle θ, an equal amount of phase change in the two speckle patterns. The cancellation of these terms in the calculation of the relative phase change renders the method insensitive to the movement.

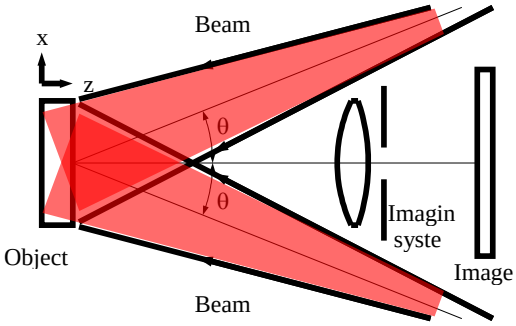


Fig. 1 Schematic optical setup sensitive to measure in-plane displacement.

Experiment setup and Result

Fig. 2 and Table 1 shows the shape and the dimension of a welding specimen. SM490 steel were tested. This time, the welding method executed CO_2 welding method. And the welding executed in the both sides of the specimen.

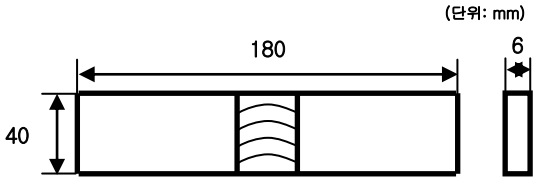


Fig. 2 Shape and size of specimen

Table 1 Mechanical properties of base metal of specimen

Type	Elasticity(GPa)	Yield Strength(MPa)	Tensile Strength (MPa)	Elongation of Length direction(%)
SM490	**204**	**345**	**513**	**29.6**

For this study, measurement system of ESPI is shown in *Fig. 3*. And load was increased by step of 2 KN from base state with 5KN. The variation distribution which occurs in the base metal department of the specimen and the welding region used ESPI and measured. For the observation which the specimen welding department, CCD camera image measure the maximum size.

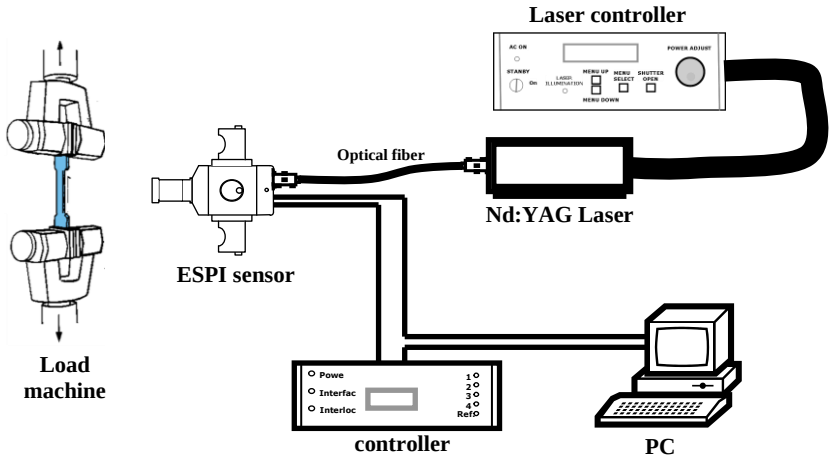
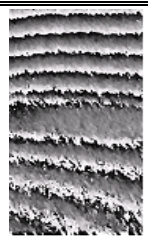
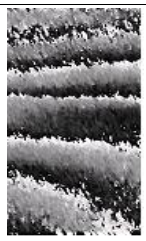


Fig. 3 Experimental setup

Table 2 is phase map which measured of load. And this phase map is tensile/compression phase map according to load condition. Also, Table 2 show that interference stripes of phase map increasing, according to the load which was given in the specimen. And deformation is increased.

Fig. 4 shows analysis result(Case; 5KN) of phase map of measured image. And we get the color image, profile(y-direction), 3D-plot.

Table 4-1 ESPI phase-map of CO2 butt welded (both sides) specimen

	5kN	7kN	9kN	11kN
Tensile				
compression				

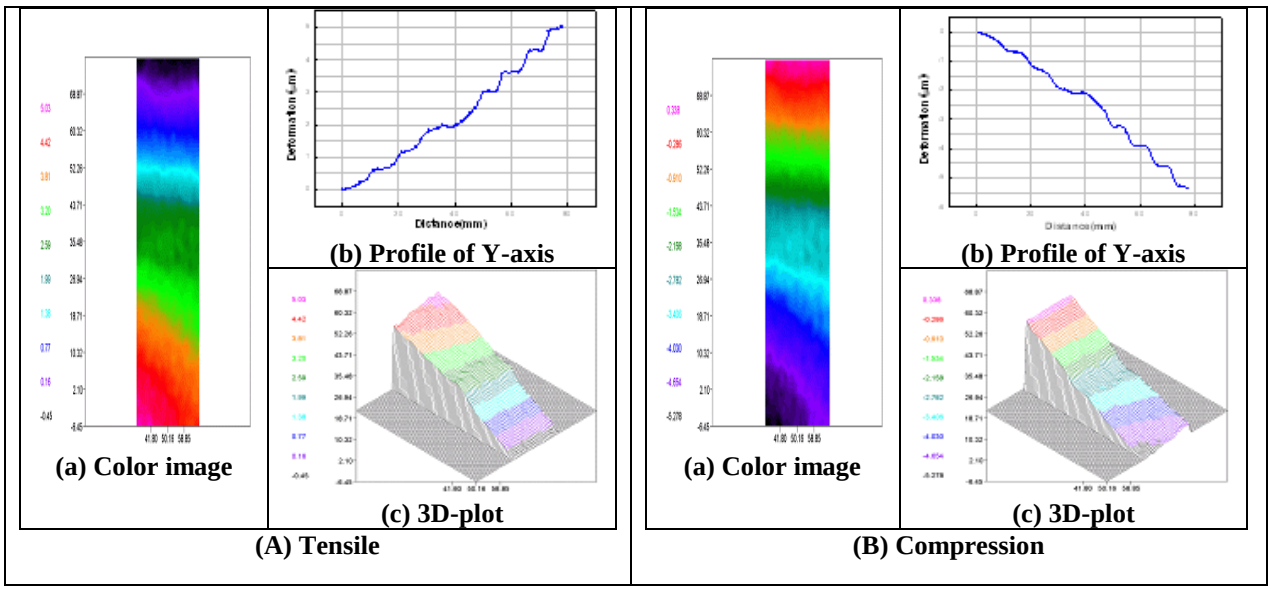
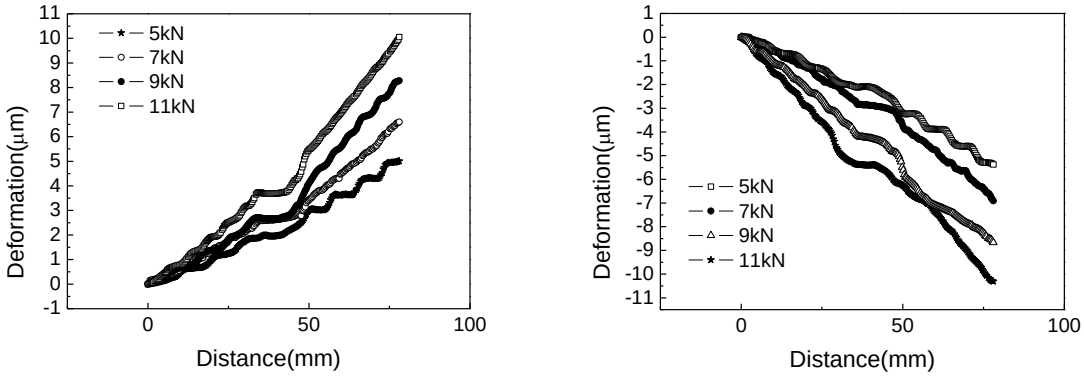


Fig. 4 Analysis results of phasemap of CO2-both sides butt welded specimen(F=5kN)

Drew the profile on the center of the specimen and measured followed tried the variation of the base metal department and the welding department. The result confirmed that deformation of the base metal department is bigger deformation of the welding department. The variation suddenly rise or the tendency which falls appeared from the specimen all welding department in compliance with the case CO_2 welding method of the welding specimen. This case, the welding at the time of being twisted, and becomes feed with the fact that follows in welding bead form. Fig. 5 shown profile data graph according to each load condition.



(a) Tensile (b) Compression

Fig. 5 Deformation comparison of CO2-both sides butt welded specimen by forces

Summary

In this paper, we measure the deformation distribution of welding specimen by using ESPI system. And this paper proposes residual stress measurement method on the welding department. In the test, test results shows the change of stress distribution resulted from the load change measured. Experiment result of the base metal department and the welding department was able to discover a difference.

We measured stress deformation distribution of the base metal department and the welding department by each load condition(Case; tensile, compression). Also, specimen by welding method (CO2 welding method) appears different. Namely, the two-sided welding the variation to be smaller compared in the base metal department.

The welding department residual stress method of measurement which proposes from the study which sees is the fundamental study where the residual stress prediction and case sincere evaluation engineering development etc. theory and experiment are combined. Also, safety and case malleability of the welding infrastructure, with the fact that will contribute in the base establishment will be able to increase conservativeness.

Acknowledgement

This work was supported by the Nuclear Research and Development of the Korea Institute of Energy Technology Evaluation and Planning (KETEP) grant funded by the Korea Government Ministry of Knowledge and Economy.

References

[1] W. H. Kearns: Welding handbook. American. Welding Society 7th edition Vol. 5 (1984), p. 276 - 311

[2] P. Michaleris and A. DeBiccari: Prediction of welding distortion. Welding Journal Vol. 76 No. 4(1997), p. 172 – 179

[3] F. A. Kandil, J. D. Lord, A. T. Fry, P. V. Grant: review of residual stress measurement methods. National Physical Laboratory Report MATC(A)(2004)

[4] Ulf Schnars: *Digital holography*, Springer, p. 18-20 (2003)

[5] J. C. Dainty: *Laser speckle and related phenomena 2nd edition*, New York, Springer-Verlag,(1984)

3D Crack Analysis 363
3D FEM 85
3D Orthogonal Woven Composites 759
7050 Aluminium Alloy 61
θ-Method 363
Ψ-Integral 416

A

AA6060 Alloy 343
AA7178 T6 105
ABAQUS 662, 718, 722
Acoustic Birefringence 315
Acoustic Emission (AE) 146, 787
Acoustic Emission Test 432
Acoustic Image 787
Actuator 282
ADAPCRACK3D 109
Adhesion 117
Adhesive Joint 537, 549, 573
Advanced Gurson Model 77
AE Technique 436
Aircraft Al-Alloy 480
Aircraft Landing 541
Airport Pavement 541
Al 6061-T6 89
Al-Cu-Li and Al-Cu-Mg Alloys 476
Algorithm 529
Alkali-Activated 198
Alkali-Activator 411
All Fracture Modes (AFM) Specimen 258, 266
Allowable Pressure 646
Alloy Steel 53
Aluminium Foam 561, 690
Aluminum Alloy 33
Anisotropic Damage 49
Annular Notched Shaft 174
ANSYS 270, 662
Armor 25
Artificial Neural Network (ANN) 767
Artificial Pre-Crack 319
Asperity 101
Assembly Process 557
ASTM A470 61
Asymptotic Behavior 621
Atmosphere Environment 476
Atmospheric Exposure Test 57
Auger Electron Spectroscopy (AES) 658
Austenitic Stainless Steel 97, 234, 658

B

Bamboo 214
Bao-Wierzbicki Method 89
Bendability 521
Bending 468
Bending Fatigue 456
Bending Strength 569
Bending Test 105
Bending-Torsional Loading 166
Betti's Reciprocity Theorem 416
Bi-Material Notch 710
Bi-Modal Tram 81
Bifurcation 731
Big Circular Arc Postulation Method 226
Bilinear Damage Law 609
Bilinear Softening Function 621
Bolt-Hole Clearance 565
Bolted Joint 565
Bone-Cement Interface 391
Bone Characterization 371
Bottom Ash 198, 278, 411
Boundary Condition 399
Boundary Element Method 363
Braking Test 597
Brittle Element 29
Brittle Failure 779
Brittleness 533
Buckling 222

C

$Ca(OH)_2$+NaCl 1
Carbide Precipitation 658
Carbon Nitride 581
Carbon Steel Pipe 494
Carbon/Carbon Composites 295
Casing Pipe 577
CBF Composite Plate 436
Cellular Automata (CA) 339

Cellular Solid 286
Cement-Based Composite 569
Cementitious Composite 533
Ceramic 303
CFRP 565
Characteristic Length 533
Chloride Ion 464
Circular Lining Structure 440
Circular Section Beam 379
CO_2 Emission 278
CO_2 Transport Pipelines 779
Coating 331
Cohesive Zone Model (CZM) 609, 621
Cohesive Zone Modeling 117
Collaborative Research Centre Transregio 30 109
Collapse Flow 69
Collapse Mechanism 674
Compatibility Condition 755
Complementary Energy 569
Composite 41, 355, 549, 763, 771
Composite Flywheel 134
Composite Material 783
Composite Material Body 81
Composite Structure 25, 460
Composites Failure Modes 638
Compression Strength 214
Compressive Strength 198, 274, 278, 460, 472
Compressive Stress 130
Computational Analysis 258
Concrete 29, 448, 464
Concrete Fracture 270
Concrete Strength 739
Confining Pressure 690
Constitutive Model 472
Contact Fatigue 113
Contact Load Distribution 113
Container Vessel 218
Continuum Damage 759
Coronary Stent 718
Corrosion 57
Corrosion-Fatigue 1, 97
Corrosion Inhibition 61
Cortical Bone 186
Crack 202, 383, 617, 722
Crack Bifurcation 130
Crack Closure 476, 545
Crack Crowth 428
Crack Defect 706
Crack Density 490
Crack Front Curvature 178
Crack Growth 13, 109, 182, 605
Crack Growth Rate 343
Crack Initiation 456
Crack Initiation Predictions 266
Crack Length at Peak Load 621
Crack Opening Displacement 791
Crack Path Simulation 444
Crack Propagation 97, 158, 323, 593, 779, 783
Crack Shielding 626
Crack Tip 694
Crack-Tip Field 399
Crack Tip Opening Displacement (CTOD) 525
Crack Velocity 666
Crackable Steel 21
Crash Box 561
Crashworthiness 638
Creep 186, 303, 315, 658
Creep Damage 339
Critical Buckling Load Coefficient 601
Critical Plane Approach 747
Cross Die Drawing 49
Cross Section of Variable Width 642
Crush Test Method 638
Crystallography 395
Curing Temperature 198
Cycle Extraction 93
Cyclic Crack Propagation 93
Cyclic Hardening/Softening Curve 307
Cyclic Stress-Strain Curve 307, 755

D

Damage 41, 202, 246, 315, 371, 375, 448, 783
Damage Evolution 464
Damage Identification 5
Damage Mechanism 351
Damage Parameters 448
Damage Progression 230
Damage Tolerance 407
Damaged Laminate 490
Damaged Structure 347
DCB 549

DCB Speciment 593
DCT 498
Defect 194, 718
Defect Size 494
Deflection Coefficient 282
Deformable Body 557
Delamination 117, 763
Diffusion Coating 307
Diffusion Equation 464
Digital Image Correlation (DIC) 494
Dimensionless Stress Intensity Factor 174
Direct Method for J Integral Evaluation 577
Directional Lamellar Structures 634
Discrete Limit Analysis 674
Displacement 494
Displacement Evolution 698
DP Steel 49
Dual-Phase Steel 77
Ductile Damage 33
Ductile Failure 779
Ductile Fracture 77
Ductile Frame 359
Ductile Steel 630
Duration Time 569
Dwell 735
Dynamic Antiplane Behavior 206
Dynamic Characteristics 81
Dynamic Fracture Toughness 630
Dynamic Growing 694
Dynamic Intensity Factor 751
Dynamic Loading 731
Dynamic Propagation 452
Dynamic Stress Concentration 226
Dynamic Stress Concentration Factor (DSCF) 37, 206

E

Earthquake 142, 351
EBSD Analysis 89
Edge Strength 331
Effective Elastic Constants 490
Effective Property 327
Eigen-Equation 170
Eigen-Value 170
Elastic Large Strain Constitutive Model 424
Elastic Modulus 286
Electric Field Intensity Concentration Factor 206
Elevated Temperature 735, 743
Elliptic Hole 37
Energetic Network 351
Energy Absorption 638
Energy Functional 593
Energy Release Rate 537, 593
Environmental Effect 502
Epoxy 714
Equivalent Crack Length 609
Equivalent Load 218
Equivalent Plane Method 702
ESPI 799
ESSPI 436
Expansive Admixture 242
Experiment 182, 202, 270, 727
Experimental Study 347, 351
Experimental Test 585
Explicit FEM 561
Extended Finite Element Method (XFEM) 763, 771
Extreme Temperature 678
Extruded 7075-T6 45

F

Failure 89, 355, 771, 787
Failure Assessment Diagram 444
Failure Mode 702
Failure Pressure 646
Fatigue 17, 45, 182, 230, 238, 290, 311, 323, 343, 420, 498, 502, 507, 666, 763, 795
Fatigue Crack 65
Fatigue Crack Growth 480, 525, 589
Fatigue Crack Path 101
Fatigue Crack Propagation 1, 476
Fatigue Damage 391, 545
Fatigue Data Analysis 755
Fatigue Failure 190
Fatigue Life 21, 307, 480, 626
Fatigue Limit 210, 319
Fatigue Resistance 511
FCC Crystals 387
FE Analysis 650
Feature Extraction 432

FEM Model 589
FGM 222
Fiber Composites 472
Fiber Distribution 295
Fiber Reinforced Composite 150
Fiber Reinforced Concrete 642, 678
Fiber Reinforcement 214
Fillet 722
Finishing 290
Finite Element (FE) 150, 371, 383, 537
Finite Element (FE) Simulation 638
Finite Element Analysis (FEA) 33, 41, 190, 335, 472, 585, 662
Finite Element Model (FEM) 134, 367, 375, 407, 484, 541, 577, 767
Finite Element Modeling 182, 186
Finite Fracture Mechanics 130
Finite Volume 549, 553
Fire Exposure 569
First Crack 569
Flaky-Zn-Epoxy Coating 262
Flexural Fatigue 698
Flexural Strength 214
Flexural Wave Scattering 37
Flowability 274
Focused Ion Beam 319
Forged Steel 21
Fractography 323
Fracture 17, 150, 154, 303, 553
Fracture Behavior 214, 634
Fracture Criteria 605
Fracture Design 170
Fracture Mechanic 343, 379
Fracture Mechanics 117, 158, 162, 407, 484, 549, 727
Fracture Mode 238, 650
Fracture Origin 238
Fracture Process Zone FPZ 609
Fracture Resistance 367
Fracture Toughness 53, 670, 743
Fracture Toughness under Plane Strain 617
Free Hexagon Method 678
Free Surface Effect 178
Freeze-Thaw 246, 464
Fretting Fatigue 662
Friction Stir Channelling 105
Friction Stir Welding (FSW) 311, 343
Full Factorial Design 138
Fullerene-Like Coatings 581

G

Galerkin 759
Galerkin BEM 751
Gas Dynamics 678
Gas Turbine Blade 17
Gaussian Heat Source 218
Gear 787
Generalized Linear Elastic Fracture Mechanics 710
Genetic Algorithm (GA) 138, 498
Genetic Minimization Algorithm 69
Geometrical Parameters 771
Geopolymer Mortar 411
Geopolymers 198
Girth Weld 126
Glass 331
Glass and Polypropylene Fibers 569
Glass Fiber 150
Glass Transition Temperature 286
Goodman Diagram 210
Graded Structure 158
Gradient-Dependent 246
Grain 29, 529
Grain Boundary Dissolution 428
Grain Boundary Ductile Facture 521
Granular-Zn-Epoxy Coating 262
Green Concrete 278
Green's Function 440
Growth Mechanism 45
Guided Wave 371, 375

H

Health Monitoring 371, 375
Heat Check Networks 626
Hertzian Approach 395
Heterogeneous Welded Joint 367
High Chromium Steel 299
High Rate 553
High Strength AA6016 Aluminium Alloy 521
High Strength Steel Pipe 126
High Temperature 307, 569, 698
Higher Order Terms 399
Hot Spot 597
Hot Strip Mill 299

Hot Work Tool Steel 626
Humidity 45
Hybrid Joint 565
Hydrogen Embrittlement 234, 323, 775
Hydroxyapatite (HA) 428
Hyper-Elastic Property 190
Hypervelocity Impact 122, 202

I

Image Processing 529
Impact 541, 767
Impact Absorption 25
Impact Damage (ID) 5
Impact Load 751
Impact Testing 420
Impact Toughness 53
Inconel 738LC 307
Inelastic Dynamic Step by Step Analysis 359
Infrared Thermography 597, 682, 795
Inherent Strain 218
Initial Secondary Cracks 605
Inter-Granular Fracture 658
Interaction 65
Interaction Effect 383
Interface Crack 452
Interferometry 799
Internal Pressure Test 105
Interphase 484
Intralaminar Cracks 490
ISO Standard 85

J

J-Integral 525
Joint 771

K

Kelvin Material Model 731
Kinkband 472

L

$LaCl_3$-Zn Epoxy Coating 254
Lamb Waves 5, 65
Laminar Ceramics 130
Laminate Stiffness 490
Lap-Shear 549
Large Simple Shear Deformation 424
Large Three-Row Roller Slewing Bearing 113
Lattice 29
Level Set 69
Life Prediction 698
Lifetime Calculations 403
Limit Analysis 69
Limit Step Length Iteration Method 601
Load Sequence Effect 545
Loading Rate 670
Localization 731
Localized Déformation 69
Logarithmic Strain 424
Low Alloy Steel 250
Low-Constraint Toughness 126
Low Cycle Fatigue 166, 307, 589, 735
Low-Velocity Impact Damage 460

M

Magnetoacoustic Emission 315
Magnetoelectroelastic Material 751
Magnetron Sputtering 581
Marine Environment 250, 254
Martensite 234
Masonry Arch Bridge 674
Matched Asymptotic Expansion 416
Material Constant 190
Material Gradation 109
Material Mismatch 367
Mathematical Model 727
Matrix Crack 170
Maximum Likelihood 498
Maximum Principal Stress σ1'-Criterion 266
Measurement 799
Mechanical Characterization 795
Mechanical Property 331, 613
Medium Carbon Steel 166
Mesh Bumper 202
Mesh Density Dependency 29
Mesh Free Method 69
Meshfree 759
Meshless Local Integral Equation Method 791
Mesostructure 29
Metal Fatigue Fracture 432
Metal Foam 122
Microbiological Influenced Corrosion (MIC) 250, 254, 262

Microbuckling 472
Micromechanics 327, 391
Microplane Model 150
Microstructure 476, 529, 670
Mission Analysis 93
Mixed-Load Parameter 452
Mixed-Mode 93, 109, 722
Mixed-Mode I+II+III Fracture 258
Mixed-Mode Loading 605
Mode I 101, 468
Mode III 468
Modeling 25, 476
Modified Virtual Crack Closure Integral Method 266
Molecular Dynamics (MD) 154
Mono Axial Traction Test 795
Mooney-Rivlin 190
Moving Kriging 759
Multi Local Complex Coordinate 37
Multiaxial Fatigue 747, 783
Multilayer Film 613
Multilayer Polymer Pipe 162
Multiple Correlation Coefficient 702
Multiple Crack Systems 444
Multiple Cracks 440, 525
Multiscale Modelling 339, 387

N

Nanoindentation 395
Nanoparticle 573
Nanovoids 387
Natural Frequency 138
Natural Rubber (NR) 666
Neural Network (NN) 138, 498
Neutron Diffraction 335
Nickel Alloy 403
Nickel Base Superalloy 735
Nitriding 238
Node Release Schema 589
Nodular Cast Iron 182
Non-Combustible Mg Alloy 311
Non Conservative Forces 383
Non-Destructive Testing (NDT) 436, 682, 739
Non Invasive Technique 375
Non-Linear Behavior 347
Non-Linear Static Analysis 359
Nonlinear 270
Nonlinear Analysis 142
Nonlocal 246, 355
Notch 617, 747
Notch Fatigue 654
Notch Length 533
Notched Parameter 166
Notched Specimen 77
Nuclear Glass 154
Numeric Simulation 109
Numerical Model 113
Numerical Modeling 1, 150
Numerical Simulation 270
Numerical Solution 395
Nylon 286

O

Off-Axis 41
Ogden Model 190
Optimal Elastic Design 295
Optimization 295, 498
Orthotropic Bi-Material Notch 416
Over-Deterministic Method 399

P

Particulate Composite 484
PCBN 553
PCD 670
Peridynamic Theory 355
PET 613
Phosphorous-Carbide 581
Piezoelectric Material 363
Piezoelectric Sensor/Actuator 5
Pipe Integrity 577
Plain Concrete 678
Plane Mixed-Mode 101
Plastic Collapse Pressures 646
Plastic Limit Load 444
Polyamide Foam 286
Polymer 150
Polymer Mass 347
Polymer Matrix Composite (PMC) 230
Polymer Weld 158
Polypropylene Fiber 642
Pop-In Effect 395
Pores of Irregular Shapes 327
Porosity 295
Post-Fire 743
Pre-Stressed Rotor 134
Pressure Die Casting 626
Prestressing Steel Bars 1
Probabilistic Fracture 53

Probability-Based Imaging 5
Progressive 355
Pseudoelasticity 146
Pulse Heating 682
Pure Shear Geometry 666
Push-Out Test 710, 714
PVD Coating 507

Q

Quality Control 53
Quarter Infinite Piezoelectric Medium 206
Quasi-Brittle Fracture 533
Quasibrittle Failure 621
Quasicontinuum Method 387
Quench Rate 521

R

R-Curve 537, 609, 621
Radial Basis 759
Radial Basis Function (RBF) 791
Radiation Effect 154
Rail Defect 13
Railway Brake Disc 597
Railway Components 407
Railway Safety 13
Railway Wheel 194
Random Tessellation 529
Rebound Index (RI) 739
Recovery 186
Recycling 613
Reinforced Composite 686
Reliability 702
Reliability Analysis 706
Repair of Damage 347
Replication Test 194
Residual Deformation 218
Residual Strain and Stress 335
Residual Stress 194
Residual Stress and Strain States 775
Restrained Shrinkage 242
Reverse Node Forces 706
Rolling Contact Fatigue 101, 299, 507
Rotating Bending 45
Rotational Speed 456
Roughness 117
Rubber-Coated Material 585
Rubber Component 190
RVE Analysis 541

S

Sandwich Plate 690
Sawtooth Striations 666
Scattering of SH-Wave 226, 440
Secondary Raw Material 613
Segregation 658
Seismic Isolation 142
Self-Weight 609
Semi-Analytical FEM 601
Semi-Permeable Electrical and Magnetical Crack-Face Condition 751
Sensitivity Analysis 706
Service Life 727
Shaft 722
Shakedown 146
Shape Memory Alloy Actuator 146, 282, 686
Shape Recovery 282
Shear Bond Strength 714
Shear Mode Crack 45
Shear Strength 650
Shear Test Specimen 650
Shearography 494
Ship Plate Steel 254
Short Fiber 686
Shot-Peening 21, 290, 480, 511
SHPB 690
Shrinkage Reducing Agent 242
Silica 666
Silica Fume 274
Simulation 686
Single Edge Notch 630
Single Overload 589
Sintered Steel 511
Size Effect 448, 621
Slant Crack 138
Slip Mechanisms 476
Slow Crack Growth 162, 303
Slurry Coating 420
Small Fatigue Crack Growth Analysis 319
SMC 282
Smith-Watson-Topper (SWT) Parameter 444, 589
SMP 282
Softening Materials 731
Soil-Structure Interaction (SSI) 142
SonReb Combined Methods 739
Space Debris 122

Spalling 101
Spatial Statistical Analysis 57
Spectrum Loading 545
Spheroidal Graphite Cast Iron 238
Splitting Tensile Strength 214
Spring Steel 468
Spur Gear 507
SSRT 234
Stability 383
Steam Turbine 61
Steel-Concrete Joint 714
Steel Honeycomb Sandwich Beams 698
Step-Loading Technique 502
Stiffened Plate 706
Stiffness Degradation 698
Strain Energy Release Rates (SERRs) 258
Strain-Life Approach 456
Strain-Life Curve 755
Strain Localization 472
Strain Path 775
Strain-Rate 731
Strain Rate Dependency 49
Stress Concentration 327
Stress Concentration Factor (SCF) 174
Stress Corrosion 61
Stress Distribution 134, 714
Stress Field 170, 174
Stress Intensity Factor (SIF) 17, 379, 468, 525, 718, 722, 779
Stress-Life Curve 755
Stress Method 299
Stress Singularity Exponent 178
Stress-Strain Curve 755
Structural Damage 142
Structural Health Monitoring (SHM) 5, 767
Structural Integrity 569, 779
Structural Model 674
Structure Buckling Reliability Analysis 601
Stuffed Whipple Shield 122
Substrate Curvature 9
Subsurface Circular Cavity 226
Subsurface Circular Inclusion 206
Sulfate-Reducing Bacteria (SRB) Solution 262
Superalloy CMSX4 9
Surface Crack 577
Surface Displacement 440
Surface Elastic Layer 226
Surface Fissures 678
Surface Roughness (SR) 290

T

Tear Energy 666
Temperature 670
Temperature Change 222
Temperature Evolution 597
Tensile Mechanical Properties 686
Tensile Mode Crack 45
Tensile Test 634
Tension 448
Tension Test 126
Texture 45, 89
Theory of Critical Distance (TCD) 654
Thermal Barrier Coating (TBC) 9
Thermal Damage 194
Thermal Gradient 682
Thermally Grown Oxide 9
Thermo-Mechanical Fatigue (TMF) 403, 626
Thermography 146
Thin Film 581
Thin Plate 37
Thin-Rim Gear 456
Thin-Rimmed Gear 85
Three-Point-Bend Beam 630
Threshold Stress Intensity Factor Range 311
TiAl Alloy 634
Tip Rubbing 17
Titanium Components 502
Tolerance Analysis 557
Tooth Root Stress 85
Torsion 468
Toughening Mechanism 573
Toughness 779
Tree-Way Globe Valve 646
Truck 210
Turbo-Expander 61
Two-State Integral 416
Two-Way Globe Valve 646

U

U-Notch 174
UHPC 274
Ultimate Tensile Stress (UTS) 315

Ultra High Performance Concrete 242
Ultrasonic Pulse Velocity (UPV) 739
Underwater Super-Speed Supercavitating Vehicle 601
Uniaxial Cycling 21

V

V-Notch 174, 502
Vapor Phase Inhibitors 61
Variable Amplitude Loading 747
Variational Principle 222
VCCT 763
Vertex Singularity 178
Virtual Testing 33
Visco-Elastic Compressible Material 694
Viscoelasticity 186, 391
Viscoplastcity 186
Viscosity 274, 452
Volumetric Method 654

W

Wall Thinning Defect 494
Wavelet Packet (WP) 432
Wear 507
Weathering Steel 57
Wedge Splitting 743
Wedge Splitting Test 399, 533
Weibull 759
Weld Joint 617
Weld Width 367
Welded Joint 335
Welding 799
Wheel Tread 194
Wire Drawing 775
Wood 650

Y

$YbCl_3$-Zn-Epoxy Coating 250
Yield Load 367
Yield Point 315
Yield Stress 210
Young's Modulus 315, 670

A

Abdel Wahab, M. 662
Aberšek, B. 727
Acevedo, C. 335
Akbarzadeh, P. 537
Al-Qureshi, H.A. 25
Alfredsson, B. 101
Aliabadi, M.H. 5, 759, 763, 767, 791
An, H. 601, 706
An, W.G. 601, 706
Anthymidis, K.G. 420
Antretter, T. 626
Aoki, T. 282
Ariza, M.P. 387, 391
Arsić, M. 577
Asadikouhanjani, S. 17
Atzori, B. 755
Augustyniak, B. 315
Austrell, P.E. 142
Avila, J.A. 359

B

Bacarreza, O. 763
Bagherifard, S. 290
Baik, K.S. 210
Bakić, A. 182
Balan, T. 77
Baldissera, P. 498
Baldizzone, C. 89
Bandini, M. 290
Bang, B.J. 202
Baragetti, S. 502, 507, 511
Baranowski, P. 585
Bartolomeo, V. 674, 739
Baumann, S. 303
Bavarian, B. 61
Behdinan, K. 230
Belsak, A. 787
Ben Bettaieb, M. 77
Birlan, A. 718
Boel, V. 710, 714
Bonagura, M. 674, 739
Bouquet, J.B. 117
Božić, Ž. 525
Bradsell, C.H. 286
Broitman, E. 581
Buonsanti, M. 541
Burzić, Z. 617

C

Čamagić, I. 617
Čanžar, P. 182
Cao, Y. 698
Caplescu, C. 654
Caputo, F. 557, 561, 565
Carolan, D. 553
Carraro, P.A. 783
Cavalleri, S. 502, 507
Černý, I. 480
Chahardehi, A. 779
Chang, H.S. 494
Chang, S.K. 81
Chang, Z.L. 436, 690
Chen, B. 174, 658
Chen, D.N. 226
Chen, L. 436
Chen, Q. 45
Chen, S. 436
Chen, W.D. 702
Chen, X.D. 246
Chen, Y. 545
Chen, Y.S. 432
Choe, K.Y. 210
Choi, M.Y. 494
Cifuentes, H. 642
Cirianni, F. 541
Clienti, C. 795
Czigány, Z. 581

D

D'Alvise, L. 335
David, C. 420
David, M. 638
Davidkov, A. 521
De Angelis, G. 557
De Baets, P. 662
De Corte, W. 710, 714
De Iorio, A. 13, 407
De Schutter, G. 710, 714

De Smet, P. 521
Delaye, J.M. 154
Delprete, C. 498
Dembowski, P. 351
Deng, A.M. 270
Derewonko, A. 585
Dhondt, G. 93
Dias, A. 25
Didžiokas, R. 613
Domazet, Ž. 682
Dourado, N. 609, 621
Drach, B. 327
Drezet, J. 335
Drobne, M. 299
Dunand-Châtellet, C. 146
D'Urso, G. 343

E

Ebner, R. 626
Ecker, W. 626
Eichlseder, W. 403
Eliáš, J. 29
Enkelhardt, A. 718
Escuadra, J. 1
Esteban, H. 391

F

Falborski, T. 347
Fan, T. 222, 593
Fansi, J. 77
Fantuzzi, N. 379, 383
Farhangdoost, K. 529, 537
Faur, N. 718, 722
Fawaz, Z. 230
Filipescu, H. 654
Flašker, J. 727
Flewitt, P.E.J. 9, 658
Fluch, R. 97
Foot, P.J.S. 286
Fu, Y.D. 250, 254, 262
Fukunaga, K. 282
Fulland, M. 109
Furlan, A. 581

G

Galić, I. 646
Garafulić, E. 682
García-Sánchez, F. 751
Gerosa, R. 511
Ghafari-Namini, N. 41
Ghajari, M. 767
Ghasemnejad, H. 41
Ghelichi, R. 290
Ghorbani, R. 17
Gianetto, J.A. 126
Giardini, C. 343
Giglio, M. 33, 89
Gilioli, A. 33
Gintalas, M. 613, 630
Glažar, V. 85
Glodež, S. 113, 299
Göncz, P. 113, 299
Gong, H.P. 122
González, B. 1
Goo, B.C. 210, 597
Goto, M. 45
Grasso, M. 13, 407
Gregov, G. 85
Grellman, W. 158
Gruttadauria, A. 89
Guagliano, M. 290
Guan, G.S. 202
Gubeljak, N. 367, 468
Gueorguiev, G.K. 581
Guo, J. 37
Guy, L. 666

H

Habraken, A.M. 77
Hadavinia, H. 286
Hajhosseini, M. 138
Hallam, K.R. 9
Hamada, S. 311
Hannes, D. 101
Hayashi, K. 311
He, Y.Z. 424
Helincks, P. 710, 714
Henkel, S. 444
Hewson, K. 286
Högberg, H. 581
Hojjati Talemi, R. 662
Holländer, D. 444
Hong, D.P. 494
Horníková, J. 395
Hotza, D. 25
Hua, X. 448
Hultman, L. 581

Hutař, P. 158, 162, 178, 484
Hutařová, S. 307
Hwang, K.H. 278, 428

I

Infante, V. 105
Ionescu, I.R. 69
Ivanković, A. 549, 553, 573, 670
Ivanović, I. 577
Izzard, V.G. 286

J

Jankowski, R. 142, 347, 351
Janßen, R. 25
Janutėnienė, J. 613
Jensen, H.M. 472
Jeong, Y.S. 57
Jha, R.N. 53
Jia, B. 122
Johnson, A.F. 638
Juliš, M. 307
Jung, H.C. 494
Jurić, A. 650

K

Kaidu, Y. 234
Kainuma, S. 57
Kalnins, K. 630
Kang, S.T. 198, 274, 411
Karač, A. 549, 573
Kariya, K. 45
Kawagoishi, N. 45, 238
Kee, C.D. 799
Kestens, L.A.I. 521
Kieu, L.H. 154
Kim, D.S. 799
Kim, J.G. 210, 597
Kim, J.W. 799
Kim, K.S. 494, 799, 799
Kim, M.C. 278
Kim, S.H. 198, 411
Kim, S.W. 242
Kim, Y.S. 81
Klarin, B. 682
Kloster, V. 109
Klusák, J. 416, 710, 714
Knésl, Z. 158, 162, 178
Köberl, H. 403
Kodvanj, J. 182
Koh, K.T. 198, 274, 411
Kong, C.D. 460
Konjatić, P. 367
Kotoul, M. 130, 416
Kotsikos, G. 13
Kowalewski, Z.L. 315
Kozak, D. 367
Kožar, I. 731
Krolo, J. 150
Krstulović-Opara, L. 682
Kuna, M. 363
Kwiecień, A. 347
Kwon, S.J. 194
Kwon, S.T. 194, 597

L

Lach, R. 158
Lacković, V. 150
Lamanna, G. 557, 561, 565
Lebet, J.P. 331
Lee, D.H. 194
Lee, J.H. 198, 411
Lee, J.K. 278, 428
Lee, K.S. 460
Lefebvre, J.P. 335
Lei, H.S. 686
Leindl, M. 626
Lemoine, X. 77
Leonardi, G. 541
Lezana, A.G.R. 25
Li, C.H. 250, 254, 262
Li, D. 206
Li, F. 122
Li, G.L. 218
Li, H. 218
Li, H.L. 37
Li, J.C. 702
Li, K.F. 134
Li, L.Y. 759
Li, Q.F. 134, 250, 254, 258, 262, 266
Li, Y. 379
Li, Y.T. 166, 170, 174
Liang, W.Y. 452
Limbachiya, M. 41
Lindqvist, M. 331
Liu, D. 9

Liu, F. 452
Liu, J.N. 134
Liu, Z.M. 246, 464
Lok, T.S. 678
Long, D. 666
Longo, M. 343
Lorenzo, M. 775
Louter, C. 331
Lovrenić-Jugović, M. 186
Lu, J. 698
Lu, Z.D. 743

M

Ma, P. 166
Madenci, E. 355
Maeda, H. 45
Mahmoud, S. 142
Majer, Z. 484
Makowska, K. 315
Malzbender, J. 303
Manes, A. 33, 89
Manzano, J.C. 359
Mao, J.Z. 246, 464
Mapelli, C. 89
Marcassoli, P. 343
Marović, P. 650
Marsavina, L. 654, 722
Marunić, G. 85
Marzani, A. 371, 375, 383
Materna, A. 589
Matos, J.C. 1
Mc Auliffe, D. 573
Medina, F. 642
Medjo, B. 577
Meinders, T. 49
Meneghetti, G. 755
Merhej, T. 206
Minami, K. 214
Miniaci, M. 371, 375
Mirzazadeh, M.M. 21
Mlikota, M. 525
Močilnik, V. 468
Mohan, J. 549
Mok, J.K. 81
Mombelli, D. 89
Montesano, J. 230
Moon, K.H. 81
Morel, S. 609, 621
Mori, G. 97
Morino, K. 238
Morris, V.J. 286
Moumni, Z. 146
Munoz, L. 666
Murphy, N. 549, 553, 573, 670

N

Na, M.Y. 799
Náhlík, L. 158, 162, 178
Nahvi, H. 138
Neckel, L. 25
Negru, R. 654
Nes, C.S. 718, 722
Niazi, M.S. 49
Nikoloutsopoulos, N.D. 569
Nishimoto, A. 323
Nishimura, F. 238
Niu, R.T. 202
Nobile, L. 674, 739
Noguchi, H. 311, 319, 323
Noijen, S.P.M. 117
Nowak, K. 339
Nu, Y. 45
Nussbaumer, A. 335

O

Obrtlík, K. 307, 735
Oda, Y. 323
Odoni, L. 666
Oliva, V. 589
Opalić, M. 456, 646
Ortiz, M. 387
Oterkus, E. 355
Oudet, E. 69
Ožbolt, J. 150, 731
Ozolinsh, E. 65

P

Pandermarakis, Z.G. 569
Pang, B.J. 122
Pannullo, F.M. 557
Panzenböck, M. 97
Park, C.S. 494
Park, D.Y. 126
Park, H.B. 460
Park, H.S. 190
Park, J.J. 242, 274

Pastore, T. 343
Pavelko, I. 65
Pavelko, V. 65
Pecak, T. 731
Pećanac, G. 303
Penta, F. 13, 407
Petit, J. 476
Petrenec, M. 735
Petrov, R.H. 521
Petrović, M. 670
Piat, R. 295
Pippan, R. 97
Plumtree, A. 21
Podrábský, T. 307
Pokluda, J. 395
Polák, J. 307, 735
Ponga, M. 387
Poon, C. 230
Potočnik, R. 113
Predan, J. 468
Prezelj, J. 787
Prochazka, P.P. 678
Profant, T. 130, 416
Pucillo, G.P. 13, 407

Q

Qi, H. 226
Qiu, D.L. 218
Qu, J. 424
Quaresimin, M. 783

R

Rahnama, S. 529
Rakin, M. 577
Raninger, P. 626
Ray, K.K. 53
Reiner, L. 61
Ren, H.L. 218
Ren, Z.Y. 134
Ressel, M. 605
Richard, H.A. 109
Richard, S. 476
Ricotta, M. 755
Risitano, G. 795
Rivolta, B. 511
Rojas-Diaz, R. 5
Romero, I. 387
Řoutil, L. 533
Rudnik, D. 585
Ryu, G.S. 198, 274, 411

S

Sáez, A. 751
Sakamoto, J. 319
Sakamoto, M. 311
Šandera, P. 395
Sanseau, O. 666
Sanz-Herrera, J.A. 391
Šarkoćević, Ž. 577
Sarrazin-Baudoux, C. 476
Schmauder, S. 525
Schramm, B. 109
Scoppelliti, F. 541
Sedmak, A. 577, 617
Seitl, S. 399, 533, 710, 714
Seo, D.S. 428
Seo, G.D. 278
Seo, J.W. 194
Šestáková, L. 399
Ševčík, M. 158, 178
Ševeček, O. 130, 416
Shao, X.H. 37
Sharif Khodaei, Z. 5, 767
Shen, G. 126
Shi, Y. 226
Shigematsu, I. 311
Shimamoto, A. 282
Shin, W.G. 190
Silva, G. 511
Sinchuk, Y. 295
Skozrit, I. 186
Šmíd, M. 735
Smith, D.J. 658
Song, H.Y. 246, 593
Song, K. 432
Song, T.S. 206
Song, X.H. 706
Soprano, A. 561, 565
Sotiropoulou, A.B. 569
Sotta, P. 666
Stainer, D. 25
Stasiuk, G. 295
Štefić, T. 650
Stolz, C. 154
Sun, B.T. 440
Sun, C. 464
Susmel, L. 747

Szymczak, T. 315

T

Tadzijevas, A. 613
Takahashi, Y. 319
Takano, N. 234
Tang, L.Q. 694
Taylor, D. 747
Terai, M. 214
Theilig, H. 444, 605
Timmermans, P.H.M. 117
Tiu, W. 545
Tonković, Z. 182, 186
Tordini, F. 502, 507
Toribio, J. 1, 775
Trakali, A. 420
Tsipas, D.N. 420
Tsukrov, I. 327
Tyson, W.R. 126

V

van der Sluis, O. 117
Vanel, L. 666
Varna, J. 490
Vasić, N. 617
Veluri, B. 472
Vergara, D. 775
Veselý, V. 399, 533
Vichytil, C. 97
Vidal, C. 105
Vilaça, P. 105
Viola, E. 371, 375, 379, 383
Vořechovský, M. 29
Vučković, K. 456, 646

W

Wang, J. 250, 254, 262
Wang, L. 545
Wang, Q. 432
Wang, R.F. 170
Wang, R.R. 690
Wang, X.D. 270, 448
Wang, X.Q. 686
Wang, Y. 448
Wang, Y.F. 448
Wang, Z.Q. 452, 686, 771
Wen, P.H. 759, 791
Wilson, L.M. 286
Winter, G. 403
Wippler, K. 363
Wisselink, H.H. 49
Woo, C.S. 190
Wu, G.H. 694
Wu, X.D. 771
Wu, Y.J. 448
Wünsche, M. 444, 751

X

Xu, D.Y. 270
Xu, H.N. 440
Xu, M.J. 440
Xu, Y.G. 545

Y

Yan, S.Y. 258
Yang, L.H. 424
Yang, Y. 694
Yang, Z.L. 440
Yang, Z.X. 278
Yoo, D.Y. 242
Yoon, S.C. 210, 597
Yoon, Y.S. 242
Younes, C.M. 658
Yu, J.T. 743
Yu, K.Q. 743
Yu, Y.C. 702

Z

Žeželj, D. 456
Zhang, C.Z. 751
Zhang, J. 61, 634
Zhang, X.N. 258
Zhang, Z.Y. 464
Zhao, J.M. 278
Zhou, B. 686
Zhou, J.S. 771
Zhou, L. 601
Zhou, S. 771
Zhu, L. 258, 266
Zhu, S.F. 266
Ziliukas, A. 630
Zou, G.P. 436, 690, 698
Zouhar, M. 162